

MICROBEAM ANALYSIS

1988

Dale E. Newbury, *Editor*

Proceedings of the 23rd Annual Conference
of the
Microbeam Analysis Society
Milwaukee, Wisconsin, 8 - 12 August 1988



San Francisco Press, Inc.

Box 6800, San Francisco, CA 94101-6800

PUBLISHER'S NOTICE

The Microbeam Analysis Society (MAS) and San Francisco Press, Inc., are not responsible for the information and views presented in this volume by the several contributors.

Permission to reprint portions of this volume in professional journals published by scientific or technical societies (with suitable acknowledgment) will be given free of charge on application to the publisher; a nominal fee may be charged for reprint rights given to book publishers, commercial journals, company publications, and other media.

Copies of this volume are available to members of the Microbeam Analysis Society (MAS) and of the Electron Microscopy Society of America (EMSA) *who send prepayment by personal check* at a 20% discount from the list price. (Californians add tax.) The same discount is available to members of both societies for the MAS triennial *Analytical Electron Microscopy*, and for the *Proceedings* of the annual EMSA meeting. The following books are available (some back issues at reduced prices):

Proceedings EMSA

1983, 1984, 1985, 1986, \$45 each

1987, 1988, \$65 each

Microbeam Analysis

1975, 1977 (8th ICXOM), 1979, 1980, 1981, \$25 each

1982, 1984, \$30 each

1986, 1987, \$50 each

1988, \$60

Analytical Electron Microscopy

1981, \$25

1984, \$40

1987,* \$50

Early History of the Electron Microscope (L. Marton), \$5

Electron Microscopy Safety Handbook, \$15

*AEM-1987 also contains the MAS-1987 papers on surface analysis.

TABLE OF CONTENTS*

1. TUTORIALS (R. B. Marinenko)

Echlin, P., Ambient-temperature chemical specimen preparation for biological microanalysis	1
--	---

2A. PRESIDENTIAL SESSION: COMPUTER-AIDED IMAGING I (W. F. Chambers, D. S. Bright)

Jeulin, D., Sequential random functions for image modeling and simulation	9
Russ, J. C., Computers in stereology and image analysis	14
Bright, D. S., Newbury, D. E., and Marinenko, R. B., Concentration-concentration histograms: A new analysis technique applied to quantitative compositional maps	18
Bright, D. S., Usefulness of various computer algorithms for locating spots and arrays in electron diffraction patterns	25
Fritz, G. S., and Schamber, F. H., The integration of x-ray analysis and digital imaging into an SEM	33

2B. COMPUTER-AIDED IMAGING II (W. F. Chambers)

Marinenko, R. B., Newbury, D. E., Myklebust, R. L., and Blendell, J. E., Application of wavelength-dispersive digital compositional mapping to high-temperature superconductors	37
Friel, J. J., Juzwak, T. J., and Johnson, P. F., Quantitative EDS mapping of a ceramic superconductor	41
Buskes, H. A., and Baughman, G. D., Quantitative large-area x-ray mapping with an SEM: A study of low-level elemental segregation in continuous-cast steels	44

3. ANALYTICAL ELECTRON MICROSCOPY (R. D. Leapman, J. R. Michael, M. J. Kaufman, D. B. Williams)

Disko, M. M., Ahn, C. C., Meitzner, G., and Krivanek, O. L., Temperature dependence of aluminum EXELFS	47
Statham, P. J., Impact of low noise design on x-ray microanalytical performance	50
Liu, D.-R., Plasmon energy measurement in the electron energy loss spectrum of the $\text{YBa}_2\text{Cu}_3\text{O}_{7-x}$ superconducting ceramics	55
Gauvin, R., L'Esperance, G., and Kennedy, G., On the computation of k_{AB} factors for $K\alpha$ lines	57
Michael, J. R., Probe size measurement in a field-emission STEM	60
Titchmarsh, J. M., Materials analysis by STEM-EDX at high spatial resolution	65
Butler, J. H., and Treacy, M. M. J., High-spatial-resolution microanalysis in the petrochemical industry	69
Eades, J. A., Glide planes and screw axes in convergent-beam diffraction: The standard procedure	75
Sarikaya, M., Local structure variations in $\text{YBa}_2\text{Cu}_3\text{O}_{7-x}$ by electron microdiffraction	81
Liu, D.-R., Application of decomposition table in the analysis of the Gjønnes-Moodie lines in convergent-beam electron diffraction	84
Liu, D.-R., and Williams, D. B., Possible ambiguity in the structural analysis of TiBe_2 by convergent-beam electron diffraction	87
Liu, D.-R., and Williams, D. B., EELS microanalysis of Be-Ti alloys with calibrated partial cross sections	91

4. SECONDARY ION MASS SPECTROMETRY (H. Storms)

Levi-Setti, R., Chabala, J. M., and Hallégot, P., High-resolution ion probe imaging and analysis	93
Odum, R. W., SIMS molecular ion imaging of simple neuro-compounds	102
Newbury, D. E., and Bright, D. S., Compositional mapping with a TV camera-based imaging system on an ion microscope	105
Slodzian, G., Effects of aberrations upon the collection efficiency of sputtered ions	109
Corcoran, S. F., Woodward, W. S., Linton, R. W., and Griffis, D. P., A PC based bus interface for the Cameca IMS-3f	111
Williams, D., Recent developments in quantitative analysis with the use of sputtering techniques	114
Simons, D. S., and Chi, P., Ion implantation artifacts detected by SIMS	117
Inoue, K., and Isogai, A., Characterization of silicon-oxide films by a new SIMS technique	120
Chi, P., Simons, D. S., and Roitman, P., Artifacts observed in oxygen profiles of SIMOX samples by SIMS	121
Gay, A. J., Henderson, D. K., van Duin, P. J., and Humphrey, P., The use of SIMS in the study of toxic trace elements on FBC fly ash particles	123
Satoh, H., Owari, M., and Nihei, Y., Quantitative analysis of small particles by submicron SIMS	126

5. ELECTRON-BEAM DAMAGE (P. J. Lea, R. F. Egerton)

Blake, D. F., Allard, L. F., Echer, C. J., and Freund, F., Characterization of electron-beam induced damage structures in natural fluorite, CaF_2 , by AEM	129
--	-----

6. MONTE CARLO METHODS IN MICROSCOPY AND ANALYSIS (D. E. Newbury)

Murata, K., Extending Monte Carlo techniques to low primary-beam energies	133
Newbury, D. E., and Myklebust, R. L., Performance of a "conventional" Monte Carlo program at low beam energy	139
Joy, D. C., Simulation of high-resolution SEM images	143
Rothwell, T. E., and Russell, P. E., Secondary electron yield measurements in the SEM	149

7. OPTICAL MICROPROBE ANALYSIS (E. S. Etz, B. Wopenka)

Delhaye, M., Dhamelincourt, P., and Barbillat, J., The evolution and perspective of Raman microanalysis	153
Ikeda, T., Yumoto, M., and Okahana, H., Accurate (5.1×10^7 dyne/cm ²) stress evaluation of silicon by micro-Raman mapping system	159
Exarhos, G. A., and Hess, M. J., High-pressure Raman microprobe studies of phosphazene trimers	161
Lewis, A., Lieberman, K., Habib, V., Isaacson, M., Harootunian, A., and Betzig, E., Near-field optics: Applications of microbeams of light with wavelength-independent resolution beyond the diffraction limit	164
Butler, I. S., Gilson, D. F. R., Paroli, R. M., Kawai, N. T., and Lord, G., Application of high-pressure micro-Raman spectroscopy in the detection of phase transitions in orientationally disordered solids ..	165
Huong, P. V., Boutinaud, P., Kazaoui, S., and Leycuras, A., Chemical bonds at the interface of GaAs/Si studied by micro-Raman spectroscopy	167
Ishitani, A., Katagiri, G., Ishida, H., and Masaki, T., Raman microprobe study on fracture behavior of yttrium oxide containing tetragonal zirconia polycrystals (Y-TZP)	169
Sharma, S. K., Pandya, N., and Muenow, D. W., Calibration of a multichannel micro-Raman spectrograph with plasma lines of argon and krypton ion lasers	171
Purcell, F. J., and Heinz, R. E., The practical advantages of FT-Raman spectroscopy for macro- and micro-sampling	175
Veirs, D. K., Rosenblatt, G. M., Dauskardt, R. H., and Ritchie, R. O., Two-dimensional spatially resolved Raman spectroscopy of solid materials	179
Huong, P. V., Grenier, J. C., and Bezdzicka, P., Polarized Raman spectra of single crystals of YBa ₂ Cu ₃ O ₇ , EuBa ₂ Cu ₃ O ₇ , and YBa ₂ Cu ₃ (O/F) ₇	182
Etz, E. S., Wong-Ng, W., and Blendell, J. E., Micro-Raman spectroscopy of high T _c superconductors in the Y-Ba-Cu-O system	187
Hegemann, B. E., Jahanmir, S., and Hsu, S. M., Microspectroscopy applications in tribology	193
Wopenka, B., and Pasteris, J. D., "Graphites" in geological samples: Raman spectroscopic misfits?	196
Vry, J. K., Brown, P. E., and Beauchaine, J., Analysis of individual fluid inclusions by micro-FTIR spectroscopy	201
Hartcock, M. A., Atkin, S. E., and Davis, B. L., Infrared microspectroscopy functional group imaging as a probe into the compositional heterogeneity of polymer blends	203
Sommer, A. J., and Katon, J. E., Infrared and Raman microspectroscopy: Critical factors in sample purity, preparation, and size	207
Messerschmidt, R. G., and Reffner, J. A., FT-IR microscopy of biological samples: A new technique for probing cells	215
Baker, M. T., and Von Endt, D. W., Nondestructive analysis of art and archeological objects by infrared microspectroscopy	218
Ishatani, A., Kamoto, R., and Ishida, H., Recent applications of Fourier transform infrared microscopy	221
Carl, R. T., Analysis of fiber optics by infrared microspectroscopy	223
Reffner, J. A., Mineral analysis by FT-IR microscopy	227
Burgi, D. S., and Dovichi, N. J., The comparison of two optical designs for the crossed-beam thermal lens scanning laser microscope	230
Mirabella, F. M., Jr., and Shankernarayanan, M. J., Characterization of polymer blends by simultaneous Fourier transform infrared microspectroscopy and differential scanning calorimetry	233
DeBlase, F. J., and Harrick, M. J., Micro/nano-sampling internal reflection FT-IR spectroscopy	236

8. QUANTITATIVE ELECTRON PROBE ANALYSIS (K. F. J. Heinrich, J. Henoc)

Armstrong, J. R., Quantitative analysis of silicate and oxide materials: Comparison of Monte Carlo, ZAF, and $\phi(\rho z)$ procedures	239
Love, G., and Scott, V. D., Curve fitting for EPMA correction procedures: An assessment	247
Henoc, J. R., Modern computer procedures for electron probe analysis	251
Lábár, J. L., Effect of Coster-Kronig transitions on x-ray microanalysis	253
Packwood, R., Parker, C., and Moore, V., $\phi(\rho z)$ for tilted specimens in the electron probe and SEM	258
Myklebust, R. L., and Newbury, D. E., A redetermination of x-ray loss due to electron backscatter by Monte Carlo simulation	261
Small, J. A., Newbury, D. E., Myklebust, R. L., Fiori, C. E., Bell, A. A., and Heinrich, K. F. J., An electron/x-ray optical bench for the measurement of fundamental parameters for electron probe microanalysis	263
Harrowfield, I. R., and MacRae, C. M., The collection of continuum spectra by energy-dispersive spectrometry for the derivation of modeling expressions	267
Brown, J. D., Analysis of thin films by electron probe microanalysis	271
Heinrich, K. F. J., Newbury, D. E., and Myklebust, R. L., Calculation of depth distributions of x-ray generation by the Monte Carlo technique	273
Karduck, P., and Rehbach, W., Progress in the measurement and calculation of the depth distribution of low-energy x-ray generation	277
Rehbach, W., and Karduck, P., Verification of the Gaussian $\phi(\rho z)$ approach and determination of the limits of validity by tracer experiments and Monte Carlo calculations	285
Bastin, G. F., Heijligers, H. J. M., and Pinxter, J. F. M., Quantitative EPMA of nitrogen in Ti-N compounds ..	290
Xu, L., Jin, G.-X., Wu, Z.-Q., and Lee, R. J., A directly calculated quadrilateral model for $\phi(\rho z)$	295
Okumura, T., Quantitative analysis of Ti-N films on stainless-steel substrate with EPMA	297
Xu, L., Jin, G.-X., Wu, Z.-Q., and Lee, R. J., Standardless EDS analysis based on a calculated quadrilateral model	300

Armstrong, J. T., Accurate quantitative analysis of oxygen and nitrogen in minerals with a W/Si multilayer crystal	301
Cheng, W., and Lee, R. J., Step shape $\phi(\rho z)$ model and nonstandard ultra-light element analysis program	305
Willich, P., Obertop, D., and Krumme, J. P., Quantitative electron-probe microanalysis of oxygen in Y-Ba-Cu-O superconducting materials	307
Waldo, R. A., An iteration procedure to calculate film compositions and thicknesses in electron probe microanalysis	310
Pouchou, J. L., and Pichoir, F. M. A., A simplified version of the "PAP" model for matrix corrections in EPMA	315
Pouchou, J. L., Determination of mass absorption coefficients for soft x rays by use of the electron microprobe	319
9. QUANTITATIVE ANALYSIS: INSTRUMENTATION (J. A. Small)	
Gastin, G. F., and Heijligers, H. J. M., Contamination phenomena in the electron probe microanalyzer	325
Matsuya, M., Fukuda, H., Kawabe, K., Sekiguchi, H., Inagawa, H., and Saito, N., Electron probe microanalyzer for ultra-large specimens up to 12 in. square	329
Glover, E. D., Stability of an SEMQ microprobe	333
Konopka, J. F., Micro Consultant: A FORTH-based expert system for quantitative microanalysis	338
Kawabe, K., Takagi, S., Saito, M., and Tagata, S., Layered synthetic microstructure dispersion elements for electron probe microanalysis of carbon, boron, and beryllium	341
Nagatsuka, Y., Otsuki, M., Saito, M., and Tagata, S., Improved analytical capability of a new WDS/EDS combined EPMA system	345
Mershon, W. J., Powers, W. H., Jr., Lentz, H. P., and Baughman, G. D., Application of micro-imaging to computer-controlled SEM	349
10. LASER MICROPROBE MASS SPECTROMETRY (R. A. Fletcher)	
Van Vaeck, L., Bennett, J., Lauwers, W., Vertes, A., and Gijbels, R., Laser microprobe mass spectrometry: Possibilities and limitations	351
Seydel, V., Haas, M., and Lindner, B., In vitro drug effects monitored by single bacterial cell mass analysis with LAMMA	353
Musselman, I. H., Simons, D. S., and Linton, R. W., Effects of sample geometry on interelement quantitation in LAMMS	356
Daniel, W. M., Delorenzo, D. J., and Wilson, H. R., LAMMS analysis of Schottky barrier diode leakage	365
Fletcher, R. A., and Currie, L. A., Pattern differences in laser microprobe mass spectra of negative ion carbon clusters	367
Housden, J., Hutt, K. W., Leake, J. A., and Wallach, E. R., The question of ion yield in LAMMS	371
Hutt, K. W., and Wallach, E. R., Initial results of a current-probe investigation of laser microprobe (LAMMS) plasma conditions	374
Brenna, J. T., and Creasy, W. R., Laser microprobe Fourier transform ion cyclotron resonance mass spectrometry	377
Kelland, D., and Wallach, E. R., Quantification of a pesticide by LAMMA	379
Schmidt, P. F., Quantitation of LAMMA result on the distribution of elements and chemical compounds in biological and medical specimens	383
Odom, R. W., and Niemeyer, I. C., Laser microprobe analysis of zirconium compounds: Survey mass spectra and relative ion yields	387
11. UNIQUE APPROACHES TO MICROANALYSIS (D. B. Wittry)	
Nichols, M. C., and Boehme, D. R., X-ray microfluorescence: A new elemental imaging tool that complements the SEM	389
Carpenter, D. A., Lawson, R. L., Taylor, M. A., Poirier, D. E., Morgan, K. Z., and Haney, G. W., A scanning x-ray microprobe with glass capillary collimation	391
Wittry, D. B., and Golijanin, D. M., Detection limits in microprobe x-ray fluorescence analysis	394
Golijanin, D. M., and Wittry, D. B., Microprobe x-ray fluorescence: New developments in an old technique	397
Leyde, D. E., Leland, D. J., Bilbrey, D. B., Wobrauschek, P., and Aiginger, H., Total-reflection x-ray fluorescence: Principles and applications	403
Kinney, H. H., Johnson, Q. C., Nichols, M. C., Bonse, U., Saroyan, R. A., Nusshardt, R., and Pahl, R., Three-dimensional x-ray microtomography: Principles and applications	405
Lindstrom, R. M., Fleming, R. F., and Rook, H. L., Neutron microprobe: Prospects and potential applications	407
12. SURFACES AND SMALL PARTICLES (J. A. Venables, S. Iijima, M. M. J. Treacy, S. Kim)	
Sakai, Y., Kitamura, S., and Ichinokawa, T., Observation of Si crystal surface by scanning RHEED microscopy	409
Gavrilovic, J., Surface analysis of small particles	412
13. LIGHT AND ACOUSTIC MICROSCOPY (C. L. Reider, W. C. McCrone)	
Isaacson, M., Betzig, E., Barshatzky, H., Lin, K., and Lewis, A., Near-field optical imaging	417
Kessler, L. W., Acoustic microscopy	419
Dodd, J. G., and DeNoyer, L. K., Super-resolution in light microscopy	421

14. BIOLOGICAL MICROANALYSIS (A. J. Sauberman)

Cantino, M. E., and Johnson, D. E., Elemental imaging techniques in studies of striated muscle	427
Statham, P. J., Progress and application of quantitative elemental mapping	429
Ingram, P., LeFurgey, A., Davilla, S. D., Sommer, J. R., Mandel, L. J., Lieberman, N., and Herlong, J. R., Quantitative elemental x-ray imaging of biological cryosections	433
Colonna, K. N., and Oliphant, G., Capacitation and decapacitation: Ionically distinct physiological states of the mammalian sperm	440
Marshall, A. T., and Conron, R. J., Quantitative comparison of low-temperature preparation methods for the x-ray microanalysis of biological bulk samples	443
Burns, M. S., Chabala, J., Hallégot, P., and Levi-Setti, R., Effects of tissue preparation on distribution of CN ⁻ and O ⁻ in scanning ion microprobe analysis	445
Herlong, J. R., LeFurgey, A., Ingram, P., Shelburne, J. D., Mandel, L. J., and Hawkey, L. A., Quantitative x-ray imaging of human cystic fibrosis nasal epithelium	447
Echlin, P., Biological electron-probe x-ray microanalysis: An unfulfilled promise? ..	451

15. SCANNING ELECTRON MICROSCOPY (J. Pawley, M. T. Postek, P. E. Russell)

Roitman, P., and Davis, G. E., Selected-area channeling pattern and defect etch study of silicon implanted with oxygen	456
Apkarian, R. P., and Joy, D. C., Analysis of metal films suitable for high-resolution SE-I microscopy	459
Russell, P. E., Low-voltage SEM for metrology and inspection	463
Steel, E. B., SEM imaging and analysis of submicrometer particles in air and water samples	466

16. APPLICATIONS IN GEOLOGY (P. H. Hlava, G. Jarosevich)

Armstrong, J. T., Bence-Albee after 20 years: A review of the accuracy of a -factor correction procedures for oxides and silicate minerals	469
Yang, S. V., and McKay, G. A., Evaluation of standards and creation of artificial standard records through ZAF-backward calculations in quantitative electron microprobe analysis	477
Shoemaker, G. L., Stephens, J. D., and Teller, R. G., Microdiffraction and microanalysis of iron-titanium mineral samples with a VG STEM	480
Harrowfield, I. R., MacRae, C. M., and Simmonds, P. F., The automated SEM as a tool for gold microprospecting	481
Knowles, K. R., and Kiilsgaard, T. H., Rare earth minerals in black sands of the Big Meadow Placer deposit, Idaho	483
Solberg, T. N., Electron microprobe trace element analysis	485
Kracher, A., Benjamin, T. M., Duffy, C. J., and Rogers, P. S. Z., Analysis of meteoritic minerals by proton microprobe (PIXE)	491
Jercinovich, M. J., and Keil, K., Electron microprobe analysis of basaltic glasses and associated alteration products	495

17. APPLICATIONS IN MATERIALS SCIENCE (A. D. Romig Jr.)

Metin, E., Romig, A. D., Jr., Inal, O. T., and Semarge, R. E., Nitride layer growth in iron and titanium alloys: Studies by EPMA	498
Carr, M. J., and Graham, R. A., Microscopy and microanalysis of shock-processed materials	503
Heikinheimo, E., Kivilahti, J., and Pajunun, M., The formation of titanium silicides in diffusion couples	509
Hepburn, J. S., Stenger, H. E., and Lyman, C. E., Rh and Pt distributions in Rh/Al ₂ O ₃ and Pt/Al ₂ O ₃ catalysts	511
Ayer, R., Mueller, R. R., Leta, D. P., and Sisak, W. J., Phase transformation at steel/IN625 clad interfaces	514
Klein, C. F., and Ayer, R., Stability of second-phase dispersoids in austenitic stainless steels	517
Lifshin, E., Peluso, L. A., and Arendt, R. H., Electron microprobe analysis of YBa ₂ Cu ₃ O _{6+x} high-temperature superconductors	519
Fitch, L. D., and Votava, W. E., Identification of particulate defects in cast products by ASEM	523

Author index	527
--------------------	-----

Officers of the Microbeam Analysis Society

MAS Executive Council

President: W. F. Chambers, Sandia National Laboratories, Albuquerque, N.M.

President Elect: D. B. Wittry, University of Southern California, Los Angeles

Past President: C. E. Fiori, National Institutes of Health, Bethesda, Md.

Treasurer: A. D. Romig Jr., Sandia National Laboratories, Albuquerque, N.M.

Secretary: J. T. Armstrong, California Institute of Technology, Pasadena, CA 91125
(818) 356-6253

Directors

Gary Aden, Kevex Corp., Foster City, Calif.

Tom Huber, JEOL (USA) Inc., Peabody, Mass.

Peter Ingram, Research Triangle Institute, N.C.

Rich Lee, ETC, Monroeville, Pa.

Rich Linton, University of North Carolina, Chapel Hill, N.C.

John Small, National Bureau of Standards, Gaithersburg, Md.

Honorary Members

L. S. Birks, Naval Research Laboratory, USA

Raymond Castaign, University of Paris (Orsay), France

V. E. Cosslett, University of Cambridge, Great Britain

Peter Duncumb, Tube Investment Research Laboratories, Great Britain

T. A. Hall, University of Cambridge, Great Britain

K. F. J. Heinrich, National Bureau of Standards, USA

R. E. Ogilvie, Massachusetts Institute of Technology, USA

Gunji Shinoda, Osaka University, Japan

D. B. Wittry, University of Southern California, USA

1988 MAS Paper Awards

Birks Award: D. M. Golijanin and D. B. Wittry, "Alignment and characterization of doubly curved x-ray diffractors"

Macres Award: M. A. Harthcock and S. C. Atkin, "Compositional mapping with the use of functional group images obtained by infrared microprobe spectroscopy"

Castaign Award: M. Lakshminarasimha and P. F. Johnson, "Computer-generated three-dimensional microstructures"

Procter & Gamble Award: R. Levi-Setti, J. M. Chabala, Y. L. Wang, and P. Halégot, "High-resolution ion probe imaging and analysis"

1988 MAS Presidential Awards

Significant technical achievement: James D. Brown

Service to the Society: C. Gordon Cleaver

K. F. J. Heinrich Award for outstanding young MAS scientist: David B. Williams

Sustaining Members' Information

AMRAY, INC.

160 Middlesex Turnpike
Bedford, MA 10730

Product Contacts:

Technical Data:	Dr. Sheldon Moll	(617) 275-1400
Delivery & Prices:	Gerald Cameron, Jr.	(617) 275-1400

Product Line: Manufacturer of Scanning Electron Microscopes

Regional Sales Offices:

George Bruno	New England	(617) 275-8310
Ed Griffith	Mid-Atlantic North	(609) 662-3922
Tom Richards	Mid-Atlantic South	(609) 662-3922
Ken Lindberg	Southeast	(305) 767-4220
Rich Lantz	Southwest	(214) 247-3542
Gerry O'Loughlin	Northern California	(408) 748-1300
Don Brayton	Southern California	(408) 748-1300
Fred Feuerstein	Mid-West	(312) 695-6117
Matt Gohlke	Mid-East	(216) 579-0035

BIO-RAD, MICROSCIENCE DIVISION

19 Blackstone Street
Cambridge, MA 02139

Product Contact: Robert Schoonhoven (617) 864-5809

Product Line: Laser Confocal Fluorescent Imaging Systems, Vacuum Evaporators, SEM/TEM Consumables, SEM/TEM Processing Equipment.

Regional Sales Offices:

James Steele, 780 Montequa Expressway, San Jose, CA 95131 (408) 435-5530

CAMBRIDGE INSTRUMENTS, INC.

P.O. Box 123
Buffalo, NY 14240

Product Contact: Peter W. Boutell (716) 891-3009

Product Line: Scanning Electron Microscopes - EDX and WDX x-ray systems.

Regional Sales Offices:

W. Wuestenhoefer, 2840 San Tomas Expsrwy., Suite 16,
Santa Clara, CA 95051
M. Cohen, 40 Robert Pitt Drive, Monsey, NY 10952
R. Kanishak, 9360 Chartwell Drive, Dallas, TX 75243

CAMECA INSTRUMENTS, INC.

2001 West Main Street
Stamford, CT 06902

Product Contact: Thomas C. Fisher (203) 348-5252

Product Line: Scanning Electron Microprobes and Secondary Ion Mass Spectrometers.

DAPPLE SYSTEMS

355 West Olive, Suite 100
Sunnyvale, CA 94086

Product Contact: Bill Stewart (408) 733-3283

Product Line: Microcomputer-based analytical instrumentation including image analysis and energy-dispersive x-ray analysis.

DENTON VACUUM, INC.
2 Pinoak Ave.
Cherry Hill, NJ 08003

Product Contacts: Robert Specht, Chris O'Connor, (609) 424-1012

Product Line: Gold sputter coaters for SEM; High-vacuum carbon coaters for TEM, Laboratory research vacuum evaporators.

EDAX INTERNATIONAL, INC.
P.O. Box 135
Prairie View, IL 60069

Product Contacts:
Technical Data: Ken Mason (312) 634-0600
Delivery and Prices: Marilyn Tillman (312) 634-0600

Product Line: Energy-dispersive x-ray analysis systems for x-ray microanalysis and image collection, display, and processing in SEMs, TEMs, and electron microprobes.

Regional Sales Offices:
Richard Feller, Bannockburn, IL (312) 634-0600
Frank Gibson, Spring, TX (713) 350-8654
Brad Lawrence, San Jose, CA (408) 729-6442
Eugene Martin, Silver Spring, MD (301) 598-8881
Larry Williams, Snellville GA (404) 979-5441

ELECTROSCAN CORPORATION
100 Rosewood Drive
Danvers, MA 01923

Product Contacts:
Technical Data: Dick Harniman (617) 777-9280
Delivery and Prices: Barry A. Weavers (617) 777-9280

Product Line: Multi-environmental Electron Microscopes - operating up to 20 torr specimen chamber pressure. Secondary and backscattered high-resolution imaging is available throughout this pressure range (from 10 to minus 5 torr to 20 torr). Dynamic imaging provided by variable specimen chamber control and real-time (TV) imaging of any experiment irrespective of specimen's physical state.

Regional Sales Offices:
San Francisco: Rick Kanishak (415) 831-9986
North East: early 1988
Middle Atlantic: early 1988
Southern California: early 1988

EMTEK (Electron Microprobe Technologies Corp.)
24932 Avenue Kearny, Suite 1
Valencia, CA 91355

Product Contacts: D.J. Bleu, President
Technical Data: Bob Matchett (805) 257-1215
Delivery & Prices: Ed North (805) 257-1215

Product Line: Service and provision of parts and upgrades for SEMQ scanning electron microprobes.

Regional Sales Offices:
Donald P. Leshner Warren, Ohio (216) 856-4830
Roland T. Henry Morton, Pennsylvania (215) 544-0924
Gernot Winkler Langen, West Germany 49-6103-24064

CHARLES EVANS AND ASSOCIATES

301 Chesapeake Drive
Redwood City, CA 94063

Product Contact: Shaun Wilson (415) 369-4567

Product Line: Charles Evans and Associates is an independent service analysis and materials research laboratory specializing in state-of-the-art lateral and in-depth microanalysis. Commercial services are available on a day-to-day or contract basis, and have been provided to numerous government, industry, and university laboratories.

GATAN, INC.

6678 Owens Drive
Pleasanton, CA 94566

Product Contact: Kevin Scudder (412) 776-5260

Product Line: Specimen preparation equipment for material science, specialized TEM specimen holders, parallel-detection electron energy loss spectrometers.

Regional Sales Office:

Kevin Scudder, 780 Commonwealth Dr., Warrendale, PA 15086 (412) 776-5260

GW ELECTRONICS, INC.

6981 Peachtree Industrial Boulevard
Norcross, GA 30092

Product Contact: Bob Lewis (404) 449-0707

Product Line: Electronic accessories for SEMs and microprobes.

INSTRUMENTS SA, INC.

6 Olsen Ave.
Edison, NJ 08820

Product Contact: Bruce D. Perrulli

Product Line: MOLE - Raman Molecular Microprobes, U 1000 and S 3000

INTERNATIONAL SCIENTIFIC INSTRUMENTS, INC.

1457 McCarthy Blvd.
Milpitas, CA 95035

Product Contact: Dr. Robert Buchanan (408) 945-2233

Product Line: Full range of Scanning Electron Microscopes, Cassette to Cassette Critical Dimension Line Width Measurement Systems, and E-Beam Probers.

Regional Sales Office:

ISI, Avon Park South, Bldg. 2, 20 Tower Lane, Avon, CT 06001
William Maguire (203) 677-0016

JEOL USA, INC.

11 Dearborn Road
Peabody, MA 01960

Product Contacts: Charles Nielsen, Steve Hamilton (617) 535-5900

Product Line: Electron Microscopes (TEM, SEM, TEMSCAN), Microprobes (Auger, electron, x-ray), linewidth measurement systems, electron beam lithography systems.

Regional Sales Offices:

Thayer Brickman, Jack Francis, JEOL USA, Inc., 3500 Bayshore Road,
Palo Alto, CA 94303 (415) 493-2600

KEVEX CORPORATION

1101 Chess Drive

Foster City, CA 94404

Telex: 760-7256 KEVEX UC Fax: 415-573-1539

Product Contact: Andrew Isaacs (415) 573-5866

Product Line: Complete product line of materials analysis systems for qualitative and quantitative x-ray and digital image analysis. Product line includes instrumentation for energy-dispersive and wavelength-dispersive x-ray analysis, Auger and electron energy loss spectrometry, and digital image acquisition and feature analysis. Also featured are systems for automated chemical and digital image analysis. Analyzers may be multitasked for simultaneous use by several operators and interfaced with VAX and other computers. X-ray detectors for all elements heavier than Be and digital beam control systems are available for all models of electron microprobes, SEMs, TEMs, and STEMs.

Regional Sales Offices:

9989 Windsor Way, San Ramon, CA 94583	(415) 828-2188
71 Rising Trail Drive, Middleton, CT 06457	(717) 639-2330
16 Barberry Hill Road, Gainesville, GA 30506	(404) 889-1363
2617 N. Central Park, Chicago, IL 60647	(312) 384-1260
109-F Corporate Blvd., S. Plainfield, NJ 07080	(201) 754-2277
19635 Cottonwood Trail, Strongsville, OH 44136	(216) 238-8666
107 Danbury Drive, Oak Ridge, TN 75043	(201) 754-2277
6417 Glenmoor Avenue, Garland, TX 75043	(214) 699-1944
PO Box 200, Mercer Island, WA 98040	(206) 232-3444
PO Box 505, Thornhill, Ontario L3T 4A2 Canada	(416) 731-2161

KRISEL CONTROL, INC.

16 Farsta Court

Rockville, MD 20850

Product Contact: Christos Hadidiacos (301) 762-1790

Product Line: Automation equipment for electron microprobe/microscope, featuring on-line data acquisition and reduction with Alpha and ZAF correction schemes. Single-crystal automation system for on-line data collection, centering, calculation of orientation matrix, and refinement of cell parameters for an x-ray diffractometer.

LINK ANALYTICAL

240D Twin Dolphin Drive

Redwood City, CA 94065

Product Contact: Frank Brown, Dave Edwards (415) 595-5465

Product Line: Energy-dispersive x-ray microanalysis and x-ray fluorescence systems.

LOGETRONICS, INC.

7001 Loisdale Road

Springfield, VA 22150

Product Contact: Lynell D. Cameron (703) 971-1400, Telex 89-455

Product Line: Manufacturer of photographic enlargers and reducers which are used to produce enhanced prints from electron microscope films or similar imagery such as industrial x-ray films.

WALTER C. McCRONE ASSOCIATES, INC.

850 Pasquinelli Drive

Westmont, IL 60559

Product Contact: John Gavrilovic (312) 887-7100

Product Line: Analytical and consulting services - ultramicroanalysis, small-particle analysis, light microscopy, analytical electron

microscopy, electron microprobe analysis, secondary ion mass spectrometry, micro x-ray diffraction, organic microanalysis for small particle and sub-nanogram samples. Failure analysis on solid state devices, bond failures, corrosion problems, thin-film analysis. Microscopy supplies and accessories, microscope sales (Olympus microscope dealer) light microscopy supplies. Asbestos consulting and testing, analysis of suspect materials for asbestos by light microscopy and/or electron microscopy, building surveys, air sampling, monitoring during abatement projects.

Regional Sales Offices:

Ian M. Stewart/Bonnie L. Betty, McCrone Associates and Components,
2508 S. Michigan Ave., Chicago, IL 60616 (312) 842-7100
Richard L. Hatfield, McCrone Environmental Services, 5500 Oakbrook
Parkway, Suite 200, Norcross GA 30090 (404) 449-8474 or 8461

MICRON, INC.

3815 Lancaster Pike
Wilmington, DE 19805

Product Contact: James F. Ficca, Jr. (302) 998-1184

Product Line: analytical services including SEM, EPA, TEM, XRF, XRD, OES, DSC, FTIR, ESCA.

MICROSPEC CORPORATION

45950 Hotchkiss Street
Fremont, CA 94539

Product Contact: H.S. Culver (415) 656-8820

Product Line: WDX-3PC Wavelength-dispersive x-ray spectrometer for use on SEMs; WDX-2A Wavelength-dispersive x-ray spectrometer for use on SEMs.

NISSEI SANGYO AMERICA, LTD.

HITACHI SCIENTIFIC INSTRUMENT DIVISION
460 Middlefield Road
Mountain View, CA 94043

Product Contact: Hideo Naito (415) 961-0461

Product Line: Scanning electron microscopes, transmission electron microscopes.

Regional Sales Offices:

Nissei Sangyo America, Ltd., 2096 Gaither Rd., Rockville, MD 20850
Nissei Sangyo America, Ltd., 1701 Golf Rd., Suite 401, Rolling Meadows,
IL 60008
Nissei Sangyo America, Ltd., 89 Galaxy Blvd., Suite 14, Rexdale, Ontario
M9W 6A4, Canada

OVONIC SYNTHETIC MATERIALS, INC.

1788 Northwood
Troy, MI 48084

Product Contact: Steven A. Flessa (313) 362-1290

Product Line: The OVONIX line of multilayer x-ray monochromators are replacing natural crystals and Langmuir-Blodgett pseudocrystals for light-element analysis in WD/XRF and EPMA spectrometers. Increased peak intensities and suppression of higher orders improves analysis of Al-B in XRF and of Na-Be in EPMA.

OXFORD INSTRUMENTS NORTH AMERICA, INC.

3A Alfred Circle
Bedford, MA 01730

Product Contact: Glenn Kinnear (617) 275-4350

Product Line: Accessories for SEM and TEM, including the following:
Liquid nitrogen and liquid helium cold stages, cryo-preparation systems,
heating stage, tensile stage, automatic and cathodo-luminescence systems.

PERKIN-ELMER
PHYSICAL ELECTRONICS DIVISION
6509 Flying Cloud Drive
Eden Prairie, MN 55344

Product Contact: Marlin A. Braun (612) 828-6318

Product Line: Full line of analytical instruments for surface and thin-film analysis, including scanning Auger microprobes, Auger, ESCA, and SIMS, and components including LEED and ion guns, for research and production applications. Contract services for all of these techniques.

Regional Sales Offices:

Guy R. Messenger, 7310 Ritchie Hwy., Suite 520, Glen Burnie, MD 21061
(301) 761-3053

Edward T. Grabey, 5 Progress St., Edison, NJ 08820 (201) 561-6730

Tom J. Swanson, 564 Forbes Ave., Suite 1312, Pittsburgh, PA 15129
(412) 261-6760

Christopher J. Macey, 2 Taunton St., Plainville, MA 02762 (617) 695-7181

John J. Kadlec, 1011 S. Sherman St., Richardson, TX 75081 (214) 669-4419

Jude H. Koenig, Meredith J. Bigley, 151 Bernal Rd., Suite 5, San Jose CA
95119 (408) 629-4343

Elm W. Sturkol, 325 Canyon Center, 1881 Ninth St., Boulder, CO 80302
(303) 449-4573

Dave Harris, Bill Stickle, 1161-C San Antonio Rd., Mountain View, CA
94043 (415) 967-2600

Europe: Bahnhofstrasse 30, D-8011 Vaterstetten, West Germany
Tel. 011-49-8106-3810

Hong Kong: 303 Fourseas Bldg., 208-212 Nathan Rd., Tsimshatsui, Kowloon,
Hong Kong Tel. 3-7210788, TLX 37753 HKPHIHX, Dr. John P. Chan

Japan: ULVAC PHI, Inc., 2500 Hagisono, Chigasaki-shi, Kanagawa-ken,
Japan Tel. 0467-85-6522, TLX 3862157

India: Blue Star, Ltd., Sahas, 414/2 Vir Savarkar Marg., Probhadev 1,
Bombay 400 025, India

PHILLIPS ELECTRONIC INSTRUMENTS, INC.
85 McKee Drive
Mahwah NJ 07430

Product Contact: John S. Fahy (201) 529-3800

Product Line: Transmission analytical electron microscopes, scanning
electron microscopes, and accessories for electron microscopes.

Regional Sales Offices:

A. Hugo, 55 Virginia Ave., West Nyack, NY 10994

D. Ahr, 6231 Executive Blvd., Rockville, MD 20852

H. Ittner, 155 N.E. 100th St., Suite 403, Seattle, WA 98125

T. Bates, 7094 Peachtree Industrial Blvd., Suite 220, Norcross, GA 30071

B. Smick, Suite D45, 2525 East Oakton, Arlington Heights, IL 60005

Ms. Jo Long, 7302 Harwin Dr., Suite 106, Houston TX 77036

S. Spiers, 3000 Scott Blvd., Suite 113, Santa Clara, CA 95050

POLAROID CORPORATION
575 Technology Square
Cambridge, MA 02139

Product Contact: Elinor Solit (617) 577-4337

Product Line: Cameras, films, and associated equipment.

Regional Sales Offices:

Call 1-800-225-1618 for local dealers, contacts, and information.

PRINCETON GAMMA-TECH
1200 State Rd.
Princeton, NJ 08540

Product Contacts:

Technical Data: Doug Skinner (609) 924-7310
Delivery and Prices: Mark Smith (609) 924-7310

Product Line: Princeton Gamma-Tech's product line consists of the PGT System 4+ microanalysis system with complete EDS x-ray analysis capabilities for SEM, TEM, and STEM. Also highlighted in our product line is PGT Imagecraft, digital image processing, enhancement, and quantitative image analysis for light microscopy as well as electron microscopy.

SPECTRA-TECH, INC.
652 Glenbrook Road
Stamford, CT 06906

Product Contacts:

Technical Data: Joan M. Kwiatkoski (203) 357-7055
Delivery & Prices: Sally Mobilio (203) 357-7055

Product Line: Full line of "Leading Edge" IR/FTIR sampling accessories, the CIRCLE - liquid sampling accessory, the COLLECTOR - diffuse reflectance accessory, and the SPECTRA-BENCH microsampling accessory. FTIR microscopes: the IR-PLAN - Visible/Infrared microscope for high-performance FTIR microspectrometry and the SPECTRA-SCOPE in-compartment infrared microscope accessory.

Regional Sales Offices:

Spectra-Tech Europe, Ltd., Genesis Center, Science Park South, Birchwood, Warrenton, WA3 7BH England, Tel. National Padgate (0925) 810 418, International +4492 581 0418
Sanyo Shuppan Boeki Co., Inc., PO Box 5037, Tokyo International, 100-31 Japan Tel. (02) 699-3761

SPI SUPPLIES
DIVISION OF STRUCTURE PROBE, INC.
535 East Gay Street
P.O. Box 656
West Chester PA 19381-0656

Product Contact: Charles A. Garber, Ph.D. (215) 436-5400

Product Line: SPI Supplies: Small instruments and consumables for electron microprobe and electron microscope laboratories including sputter coaters, table-top vacuum evaporators, and microprobe standards. Structure Probe: Independent laboratory providing SEM/EDS, TEM, probe, Auger, XPS, XRD, and other services for industry and government. Member of American Council of Independent Laboratories; accredited by American Association for Laboratory Accreditation.

Laboratories:

230 Forresta St., Metuchen, NJ 08840 (201) 549-9350
63 Unquowa Rd., Fairfield, CT 06430 (203) 254-0000
1015 Merrick Rd., Copiague, L.I., NY (516) 789-0100

Regional Sales Offices:

SPI Supplies/Canada, PO Box 187, Station "T", Toronto, Ontario, Canada M6B 4A1 (416) 787-9193

C.M. TAYLOR CORPORATION
289 Leota Avenue
Sunnyvale, CA 94086

Product Contact: Dr. Charles M. Taylor (408) 245-4229

Product Line: Standards for microbeam analysis by SEM, microprobe, and ion probe using energy-dispersive, wavelength-dispersive, and mass spectrometers. Standards available exceed 175 different metals, alloys, glasses, and compounds or minerals. Bence-Albee standards are available. Manufacture many types of sample holders, polishing jigs, and other equipment for sample preparation. Also offer electron microprobe analytical services using a MAC-5 instrument, with FRAME B or Bence-Albee correction procedures.

M.E. TAYLOR ENGINEERING, INC.
21604 Gentry Lane
Brookeville MD 20833

Product Contact: M.E. (Gene) Taylor

Product Line: Scintillators, SEM supplies, secondary and backscatter electron detectors, vacuum foreline traps, specimen stubs, filaments and related items. Precision machine work and scientific glass blowing. Repair most EDS detectors.

Regional Sales Office:
Dave Ballard, 15817 Crabbs Branch Way, Rockville, MD 20855 (301) 330-0077

TRACOR NORTHERN, INC.
2551 W. Beltline Hwy.
Middleton, WI 53562

Product Contacts:
Technical Data: Jerry Shattuck (608) 831-6511
Delivery & Prices: John Santroch (608) 813-6511

Product Line: Scanning electron microscopes, energy-dispersive x-ray microanalysis systems, image analysis systems for microscopy, confocal light microscopes.

Regional Sales Offices:
TN-East: Don Dunkin, 4001 G, Greentree Executive Campus,
Marton, NJ 08053 (609) 596-6335
TN-South: Tom Levesque, 4270 Kellway Circle, Dallas, TX (214) 380-1942
TN-Midwest: Dennis Masaki, 6313 Odana Rd., Suite 2N, Madison, WI 53719
(608) 274-1666
TN-West: Mike Ivey, 70 Whitney Place, Fremont, CA 93539 (415) 656-9898

VG INSTRUMENTS, INC.
32 Commerce Center
Cherry Hill Drive
Danvers, MA 01923

Product Contact: Dr. Michael Wells (617) 777-8034

Product Line: UHV analytical instrumentation; those pertinent to MAS include High-Resolution Auger, UHV dedicated STEM, imaging SIMS.

Regional Sales Offices:
Ellen Flentye, 7910 Ivanhoe Ave., La Jolla, CA 92037
Howard Danaceau, 966 Hungerford Dr., Rockville, MD 20850
Randy Aramburn, 1128 Sunset Dr., Roanoke TX 76262

CARL ZEISS, INC.
One Zeiss Drive
Thornwood, NY 10594

Product Contacts: William I. Miller, III (914) 747-1800

Product Line: EM/CEM 902 Electron Spectroscopic Microscope, EM 10 Transmission Electron Microscope, DSM/CSM Digital Scanning Electron Microscope.

Regional Sales Offices:

Dietrich Voss, PO Box 2025, Willis, TX 77378 (409) 856-7678

Frank Coccia, 183 Lake Shore Dr., Pasadena, MD 21122 (301) 437-7382

Virginia Hanchett, 14870 Marie Court, San Martin, CA (408) 779-0100

AMBIENT-TEMPERATURE CHEMICAL SPECIMEN PREPARATION FOR BIOLOGICAL X-RAY MICROANALYSIS

Patrick Echlin

Any preparative technique for x-ray microanalysis must result in reasonably recognizable structural detail while preserving in situ the elemental constituents to be analyzed. In practice, the adequate preparation of biological tissues so that they should retain elemental integrity, withstand electron irradiation, and provide sufficient image detail for ultrastructural studies is doubtless the greatest weakness of the whole analytical procedure. In many respects the principles of specimen preparation resemble those used in electron microscopy generally, but with the added caveat that the preservation should not be solely at the expense of the soluble cell constituents, which are the principal components most usually analyzed. Many approaches have been adopted to achieve optimum specimen preparation and it is generally agreed that as far as the chemical methods of preparation are concerned, every tissue and each element requires its own method, not the application of a general or universal technique to all biological samples.

This is not the case with low-temperature techniques, where there is now sufficient evidence to suggest that the generalist approach of rapid, nonequilibrium cooling followed by appropriate sample manipulation of frozen hydrated samples is the only reliable method for the study of diffusible elements. The low-temperature techniques will not be discussed here; they are the subject of another tutorial at this meeting¹ and additional information may be found in the book by Newbury et al.² and the chapters by Zierold and Steinbrecht³ and Marshall.⁴

The discussion that follows is not intended to provide innumerable recipes for chemical techniques that could be applied to specific biological systems, but rather to consider the principles underlying the methodology and thus allow experimenters to devise their own methods for the particular samples in question. The subject is not new; an attempt will be made to give details of some of the more recent advances, but reference should be also made to the recent reviews by Chandler,⁵ Harvey,⁶ and Morgan.⁷

Nature and Extent of the Problems of Sample Preparation

X-ray microanalysis of samples may be defined as the detection and measurement of small amounts of elements with high spatial resolution in a biological matrix of low mass

density. The analytical method does not distinguish among elements in a dissolved, ionized, or crystalline form, or whether they are part of a molecule or even a macromolecule. Under ideal conditions, it is possible to measure elemental amounts as small as 10^{-18} g in concentrations down to 1 mmol kg and at a spatial resolution of 10 nm.⁸

The ideal specimen for x-ray microanalysis would be a thin smooth section of a stable low-atomic-number material with good thermal and electrical properties containing discrete inclusions of high local elemental concentration. A thin 200nm aluminum foil containing gold inclusions would be the nearest one could hope to approach such a specimen. Unfortunately, biological samples are far removed from this ideal. Biological samples are three dimensional, unstable, wet insulators composed primarily of organic molecules and macromolecules bathed in low concentrations of ions and electrolytes. The bonding of the elemental components ranges from the strong covalent bonds found in sulfur-containing proteins to the weak ionic interactions associated with sodium and potassium ions in the cytosol.

A characteristic feature of living material is that it moves. At the cellular level this movement ranges from cytoplasmic streaming to the movement of ions, molecules, and macromolecules relative to each other in the cell. These latter movements are usually very fast. The average diffusion rate of water and electrolytes at 293 K is about 10 μ m in 5×10^{-7} s and the time for translational diffusion and reorientation of a water molecule is a mere 10^{-12} s. Biological material is constantly changing as patterns of metabolism form, destroy, rebuild the functional architecture of the cell. This very instability militates against any precise x-ray microanalysis being carried out on living material unless ways may be found instantaneously to arrest cell activity and hold it in this state until the investigations are complete. If these were not problems enough, the environment in which the x-ray microanalysis has to be performed is totally alien to the life processes we wish to analyze. A typical cell can synthesize many hundreds of compounds by precisely regulated processes, can replicate itself, and is capable of genetic evolution and modification of these processes. If one wanted a quick way of destroying this uniquely delicate and balanced mechanism, there is probably no better tool than a flux of fast electrons that can boil away water many times the weight of the sample in a second. Even in the most consummately prepared samples, the problems of radiation damage during examination and analysis remain.

The author is at the Department of Botany, University of Cambridge, Cambridge, England CB2 3EA.

If we are to carry out microanalysis on biological material, we must accept a compromise between the properties of the sample and the conditions under which the analysis must be performed. Because unalterable restraints are imposed on the conditions under which the analysis is carried out, we have to seek ways of modifying the sample. Most preparative procedures that have been devised are based on the methods used in scanning and transmission microscopy that rely on preserving structural macromolecules, usually at the expense of the smaller molecules we would like to retain for x-ray microanalysis. All the procedures that have been devised for conventional histological analysis of cells and tissues result in a gross loss and/or redistribution of elements. The loss is not uniform for various elements in the same tissues, nor for the same element in various tissues. Although there are severe restraints to the use of the so-called "wet chemical" techniques for preparing biological samples, some useful information has been obtained by careful and considered application of these methods. We shall first discuss the types of analytical investigations and applications to biological systems, since that will give us a measure of the restraints of which we must be aware during sample preparation. We shall then consider the types of samples to be examined before discussing the general strategy and specific tactics for optimal specimen preparation by ambient-temperature chemical methods.

The Biological Applications of X-ray Microanalysis

It is useful to consider briefly the main types of investigations undertaken by x-ray microanalysis, for they provide some measure of the care that must be taken with the sample preparation. Although these investigations are categorized below, the categories frequently overlap.

1. Localization at the cell and tissue level of ions of known physiological function.
2. The distribution of elements in relation to a particular structural feature of the cell.
3. The study of systems that have been naturally or deliberately perturbed, e.g., by drugs, disease, histochemical stains, or precipitating agents.
4. Localization of regions of metabolic activity.
5. Microchemical analysis of very small volumes of expressed or extracted biological fluids.

In all five categories, the element(s) to be analyzed can exist in several forms: as amorphous or crystalline deposits, strongly or weakly bound to molecules or macromolecules or as the unbound ion or soluble element freely diffusible in the cell and tissue fluids. Each situation demands a different approach to sample preparation.

Types of Biological X-ray Investigations

The investigations may be carried out at two levels of sophistication. The most usual goal of qualitative analysis is to find out either whether an element is present or absent in a sample, or whether one part of a sample has more of a given element than another part. Small losses of an element from the sample during preparation will probably not have a serious effect on the result; if adequate care is taken during sample preparation, valid biological information may be obtained. In quantitative analysis one attempts to measure as accurately as possible how much of a given element is present in a given volume of tissue. In this situation the preparative techniques are far more exacting because one is trying to measure elemental concentrations as they exist naturally in the cells or tissues.

Types of Biological Specimens Studied by X-ray Microanalysis

The different types of specimen show varying degrees of x-ray spatial resolution depending on the volume of the sample contributing to the analysis. This volume is a function of the beam diameter, depth of electron penetration, and electron and x-ray scattering within the specimen.

Bulk Sample. These are defined as specimens that are too thick to allow transmission of electrons or photons and for which the morphological information can be obtained only with a reflected signal. The major limitation of the use of bulk samples is the poor x-ray spatial resolution, which is of the order of 3-5 μm . Hard tissue such as bones, shells, wood, and fossils may be fractured and such specimens are useful for qualitative analysis, but their irregular surfaces makes accurate quantitative analysis very difficult. This problem may be partly overcome by polishing of the surface but pure abrasive must be used to avoid contamination. The fracture faces of soft material may be analyzed, but only after the tissue has gone through fixation, dehydration, and hardening, all of which involve chemical intervention.

Isolated Cells and Organelles. Although these types of specimen are usually only a few micrometers thick, they are usually treated as bulk samples. The elemental content of individual rat blood platelets and their dense granules have been determined by x-ray microanalysis and the use of a direct quantification method with microdroplets as standards.⁹ Magnesium, calcium, and phosphorus concentrations were measured in whole air-dried platelets and there was a close correlation between the magnesium and phosphorus concentration in the dense granules.

Inorganic Particles and Fibers. It is sometimes necessary to carry out analysis on particulate matter which has either been eluted from tissues with physiological saline, or individually isolated from the tissue matrix by micromanipulation. Dry particles may be analyzed in situ on a filter as long as they are

sufficiently well dispersed and not embedded in the filter pad. Alternatively, the particles may be embedded in resin which is either fractured and polished, or cut into sections. Particles may also be resuspended in a non-aqueous solvent and spread as a thin layer on a suitable substrate. Particles are frequently found within a matrix of organic material, which may be removed either by washing in sodium hypochlorite solution, boiling in potassium hydroxide, or cold-plasma ashing. The last method is to be preferred as it does retain the inorganic particles at some semblance of their natural location in the tissues.

Liquid Samples. A number of applications in biological x-ray microanalysis center on the study of physiological fluids from renal, reproductive, and excretory systems that may be derived from single cells or from spaces surrounded by a few cells. The electron microprobe can be used for the analysis of microvolumes (10^{-10} l) of fluid that can be extracted from cells and tissues by ultrafine pipettes.¹⁰ The method permits the measurement of minimal detectable limits as low as 0.05 mmol l⁻¹ and is the only technique of detecting several elements in very small fluid volumes. Most of the analysis has been carried out on droplets mounted on a solid substrate such as beryllium or carbon, with wavelength-dispersive spectrometers (WDS) rather than energy-dispersive spectrometers (EDS) because of the low peak-to-background ratios. It is also possible to analyze microdroplets on thin film supports by both EDS and WDS.¹¹ Sprayed droplets of solubilized biological tissue samples deposited on thin films may also be analyzed by EDS.¹² The microdroplet technique has been extended by being combined with specific microprecipitation techniques to analyze quantitatively organic materials such as urea.¹³

Thick Sections. Thick (0.2-2 μ m) sections are a useful sample compromise, because reasonably good morphological information can be obtained by scanning transmission images and the specimens are sufficiently thick to contain enough material for good x-ray spatial resolution. As most tissues are very soft, they first must be stabilized and strengthened before any sections can be cut, all of which can cause serious losses of soluble materials from the sample.

Thin Sections. Thin (less than 200nm) sections show the greatest amount of morphological detail and potentially the highest x-ray spatial resolution. However, their thinness may reduce the amount of material to be analyzed to very low levels. If one is restricted to using ambient temperature techniques, thin sections may only be prepared following extensive chemical intervention and one must be prepared for all the losses that will ensue. Thick and thin sections are the most useful type of specimen for biological microanalysis and many of the more successful preparative methods are centered on this type of sample.

The General Strategy of Sample Preparation

Before attempting sample preparation, one must appreciate a number of parameters that affect the preparation, examination, and analysis of biological material by electron beam instruments. The experimenter is advised to make a list of these general physical properties, together with any other parameters peculiar to the sample being analyzed, as they will help in the design of the experimental protocol. It is important to have information about the following matters.

1. The type of analytical equipment available and an appreciation of its attributes and limitations.
2. The imaging facilities available for viewing the sample.
3. Knowledge of the structure of the tissue being studied.
4. Information on the elements to be analyzed and where they are likely to be found in the tissue.
5. The probable chemical associations and binding states of the elements being analyzed (e.g., covalently bound to proteins, soluble in the extracellular spaces, or weakly bound to structural features of the cytomatrix).
6. Some measure of the osmotic properties and normal hydration state of the cells and tissues.
7. A clear understanding of the structural and analytical spatial resolution required by the experiment.
8. The degree of analytical sophistication, i.e., qualitative or quantitative analysis.
9. An appreciation of why the analysis is being performed, what it is expected to show, and whether x-ray microanalysis is the best technique for the given problem.

For example, quite a different approach to specimen preparation is indicated for, say, the qualitative analysis of a heavy metal covalently bound in a liver biopsy sample by means of a scanning electron microscope fitted with a simple EDS system and operating in the reflective mode, and the quantitative analysis of sodium and potassium in a thin section of plant root by means of a computerized electron probe microanalyzer fitted with a comprehensive WED system and operating in the transmission mode.

Criteria for Satisfactory Sample Preparation

Having designed a preparative protocol on the basis of the constraints and attributes of the total experimental system, one should have some guidelines to judge whether the procedures that have been adopted are satisfactory. It is not sufficient to end up with a sample whose image appears satisfactory as measured by the unfortunate set of criteria we have adopted to judge the quality of electron micrographs. Some criteria are listed below that may help the experimenter to evaluate the quality of sample preparation, primarily from the analytical point of view.

1. The normal structural relationships of the sample should be adequately preserved. It is difficult to set limits for the preservation of ultrastructure, but a good guideline would be to aim for structural spatial resolution one order of magnitude better than the hoped-for x-ray spatial resolution.

2. The gross amount of material lost from (or gained by) the specimen during the course of sample preparation. In most chemical preservation methods, such losses can easily amount to 70-90% of the electrolyte concentration. These gains and losses can be measured easily by atomic absorption spectroscopy of one half of an identical sample before and after preparation. Although this procedure measures only the total changes in the sample, it is an important initial indication of the effectiveness of the experimental protocol. Gains in the total elemental concentration of the sample are largely a matter of common sense. One would not, for example, use phosphate-buffered saline as a fixative vehicle for a sample that is to be analyzed for sodium and phosphorus.

3. The general location from which material has been lost (or gained) on the sample should be known. Elements in biological specimens are usually partitioned into different compartments, each of varying composition. Within any one compartment, elements are in different binding states, and a preparative procedure may selectively affect the concentration of a particular element.

4. The amount of elemental distribution and translocation within the sample should be known. Although a particular preparative procedure may not change the gross concentration of an element in a sample, it may well cause considerable redistribution. It is very difficult to assess this phenomenon properly; the only guideline is to be suspicious of abnormally high or low concentrations of elements, such as unusual crystallites or voids in regions of the sample where, on the basis of normal cell physiology, such concentrations would not be expected. Distinct chemical boundaries and gradients of electrolyte concentration would indicate that elemental redistribution had not occurred. If different preparative techniques give varying distribution patterns, elements may have been moved from their natural location in the cell.

5. The chemicals used to prepare the sample should not mask the elements being analyzed. A simple but complete list of the elements used during sample preparation and the elements being analyzed in the sample, together with their characteristic x-ray lines, should obviate this problem. This list should also include the chemical identity of support grids, conductive films, stains, and the background radiation from the microanalyzer. For example, the copper La line can virtually mask the sodium Ka line from a sample being analyzed in an EDS system.

6. The actual process of analysis may remove material from even the most carefully prepared sample. Analysis of biological

tissue is limited by the transformation of elemental composition under the electron beam. The general mass loss of organic components and the loss of specific inorganic elements depend on the molecular structure of the sample, the conditions of analysis, the temperature, and the chemical identity of the element. Sodium, potassium, chloride, and sulfur are at particular risk, as are bulk samples and thick sections. Frozen dried samples are at greater risk than resin-embedded samples and mass losses are higher at ambient temperatures and high beam currents.

In many instances it may not be necessary to go through an elaborate pretesting of the preparative procedures, as parallel physiological and biochemical studies show whether the preparative procedures are causing problems. However, it is most important to have a measure of the gross changes in the sample, which can be measured easily by independent chemical means. The changes and redistribution of elements within the sample are much more difficult to measure as there are few other reliable analytical procedures that can verify the accuracy of microanalysis at the cellular level. It is important to avoid the uncomfortable position of having to rely on the electron microprobe to assess the accuracy of x-ray microanalysis.

Preparative Procedures Before Fixation

In general, there should be a minimum delay in obtaining the piece of tissue or cells from the experimental organism. Enough is known about the structural changes associated with anoxia, stress, and post mortem changes to suggest that local elemental concentrations will be similarly affected. Care must be taken to remove any contaminating body fluids such as blood, mucus, and extracellular fluids that may infiltrate the sample and give spurious x-ray signals. Speed and cleanliness are of paramount importance in this first step.

Preparative Procedures During Chemical Fixation

It is probably impossible to find a chemical fixative that does not cause some degree of loss, redistribution, or masking of the elements one hopes to analyze. Small-molecular-weight organic fixatives such as glutaraldehyde penetrate biological material at an average rate of $1-2 \mu\text{m s}^{-1}$, and it takes at least half a minute before transcytoplasmic movements are arrested in a cell placed in a chemical fixative.¹⁴ The average diffusion rate of electrolytes is about $10 \mu\text{m in } 10^{-7} \text{ s}^{-1}$ and it is for this reason that cryofixation at rates of $5 \times 10^{-4} \text{ s}^{-1}$ within the first $10 \mu\text{m}$ of a sample are mandatory for any investigations involving the x-ray microanalysis of electrolytes. Chemical fixation is too slow and too disruptive. Very few systematic studies have been undertaken to examine the effects of chemical fixation on the elemental concentrations in tissues. Work on animal tissue^{4,15,16} and plant tissue¹⁷ indicate

varying losses from samples during chemical fixation.

The best one can hope for is to minimize these losses. Some of the newer organic fixatives¹⁸ may prove useful in this respect. For example, the diimidoesters are a class of bi-functional reagents which cross link proteins by reacting with their α and ϵ amino groups. They carry an amido group (NH_2^+) adjacent to each functional group and as a result leave the charge distribution of the protein unaltered. These and related compounds are beginning to be used in microscopy and there is hope that they may help diminish the loss of soluble components from biological tissues during fixation. The loss of soluble elements is exacerbated by treatment with heavy-metal fixatives containing osmium and manganese, which have the added disadvantage of masking a number of the elements commonly found in biological material. If it is quite clear that some sort of tissue stabilization is necessary, and if chemical fixatives have to be used, the fixation time should be as brief as possible and the fixative should be used in the vapor rather than the liquid phase. If liquid fixation is unavoidable, the chemicals should be used with organic buffers (such as bicarbonate or piperazine-N-N'-bis-2-ethanol sulfonic acid) that avoid the problem of adding unwanted elements to the sample. (Cacodylate buffer, for example, contains arsenic.) The pH of the fixative and buffer should be adjusted so that it does not cause changes in elemental solubility.

Preparative Procedures for Histochemical Elemental Localization

Light and electron microscopists are able to localize areas of physiological and/or metabolic activity by the use of highly specific dyes and histochemical agents. The same idea can in principle be applied to x-ray microanalysis. A detailed review of the techniques used in x-ray analytical cytochemistry are provided by Sumner,¹⁹ Bowen and Ryder,²⁰ and Van Steveninck and Van Steveninck.²¹ The techniques have been applied in a variety of cytochemical fields, including immunocytochemistry, autoradiography, identification of reaction products, analysis of reaction mechanisms, simultaneous identification of more than one reaction product, and ultrastructural cytochemistry. The preparative procedures are in many ways no different from those used in conventional light-microscopical histochemistry. The now-familiar caveats of sample preparation must be applied and the substance of interest must not be lost from the tissue, or blocked or inactivated by the preparative procedures. The cytochemical reaction is most usually carried out before or during the initial fixation.

The technique seems to be most useful in the identification of unknown reaction products and in investigations of reaction mechanisms, where its ability to identify colorless reaction products and the facility of quantitation are particularly valuable. X-ray

microanalysis is also useful for comparing the distribution of the products of more than one cytochemical reaction. The spatial resolution generally achieved is not much greater than can be achieved by light microscopy. A typical procedure would be to modify the standard Gomori technique for acid phosphatases so that the end product is a deposit of lead phosphate or cobalt sulfide rather than a colored reaction product. The end product need not necessarily be a heavy metal as long as it is sufficiently distinct from the bulk of the sample matrix. For example, the Alcian Blue stain for mucin contains copper, sulfur, and chlorine, all of which may be detected by x-ray microanalysis.

Preparative Procedures of Elemental Localization by Precipitation

Several workers have attempted to precipitate diffusible elements in situ before chemical fixation takes place and thus reduce the leaching influences of aqueous preparative media while still retaining the structural integrity of the specimen. The technique is based on the reaction of an ion with a compound (usually a heavy metal) that can be detected either by virtue of its increased electron scattering or x-ray emission. Alternatively, if the ion itself is a heavy element, organic reagents may be used as the precipitating agents. The same principle can be applied to the intracellular localization of certain enzymes whose reaction products are inorganic ions.

The type of reactions used include chloride precipitation by silver formate or acetate; calcium precipitation with oxalate salts; sodium, potassium, magnesium, and calcium precipitation with pyroantimonate; and potassium precipitation with sodium cobaltinitrite or sodium tetraphenyl boron. The precipitating agent is usually included in the initial fixative and in some of the subsequent aqueous processing fluids. Although the precipitation methods have been widely used, they are an unsatisfactory alternative for diffusible electrolytes, which are best prepared by low temperature methods. Many of the precipitating reactions are nonspecific and ineffective,⁵ and take a long time to diffuse to the site of the reaction. Losses can still occur after precipitation, for example during dehydration and embedding, and formation of the reaction product usually results in endogenous translocation of the element from outlying regions to a focal precipitating site. The pyroantimonate reaction is notoriously nonspecific (it precipitates a wide range of monovalent and divalent cations), and even when the elements have been characterized by x-ray microanalysis, interpretation is difficult and quantitation virtually impossible. If precipitation methods are to be used, the specificity of the reaction must be adequately tested. A review of the pyroantimonate method²² provides criteria that may be usefully applied when this method is used with cations.

Preparative Procedures for Sample Dehydration

There is no doubt that chemical dehydration contributes to the further loss of diffusible substances from cells and tissues. Although no critical comparative studies have been made on elemental losses, there appears to be little difference in the effect of ethanol, methanol, or acetone. Plant material dehydrated in 1-2 dimethoxypropane showed considerably improved ion retention (Na^+ , K^+ , and Cl^-) compared with dehydration in acetone. One may circumvent the classical "wet chemical" dehydration procedures either by freeze drying (the best option) or by employing inert dehydration procedures,²³ water soluble resins, or the glutaraldehyde-urea method.²⁴ An alternative procedure²⁵ involves infiltrating fixed specimens with increasing concentrations of polyvinyl alcohol, up to 20%. Water is then removed by dialysis and the resultant hard gel may be sectioned. Unfortunately, none of these procedures significantly reduces the loss of diffusible substances. Simple air drying of whole cells in fluid suspension (e.g., blood and semen) and cells containing dense cytoplasmic inclusions such as mineral deposits avoids the use of both chemical fixatives and dehydration fluids. Provided some measure of sample distortion may be tolerated, and the experimentally significant regions of the sample can be recognized, air drying is a useful alternative procedure. Critical point drying may have a severe effect on elements normally considered to be firmly bound to the cytoplasmic matrix, as fluids in a supercritical state have an enhanced ability to dissolve substances.

Preparative Procedures for Sample Embedding

Most fixed and dehydrated biological material needs infiltrating with either paraffin wax or epoxy or acrylate resin, which is then solidified and hardened to enable sections to be cut for examination and analysis. The wax or resin, which essentially replaces the water that has been removed during dehydration, effectively dilutes the cellular constituents by increasing the specimen mass. The embedding step may be omitted only if very thin specimens or fine suspensions are to be examined or if the sample is to be treated as a bulk sample.

Resins can extract and redistribute elements as well as organic molecules, although this process is strongly influenced by the embedding medium and temperature. Thus, more than 99% of the protein and 88% of the lipid were retained in bacterial cells that had been dehydrated in either ethanol or acetone and embedded in methacrylate at 223K.²⁶ The embedding media can also contribute elements to the materials being analyzed. Some of the epoxy resins contain small amounts of sulfur, and resins based on epichlorhydrin contain small amounts of chlorine. Even the low (0.73%) levels of chlorine in Spurr's low-viscosity resin are too high when critical studies for chloride are being carried out. If trace ele-

ment analysis is to be performed on resin-embedded material, it is advisable either to carry out an elemental analysis on the polymerized resin or to carry out x-ray microanalysis on sections of the polymerized resin that do not contain the specimen. Methacrylate resins usually contain fewer contaminants than the epoxy resins, although they shrink during polymerization and are unstable in the electron beam.

Some recent studies^{27,28} have shown that the low-temperature resins Lowicryl, which are based on water-soluble acrylates, may have a useful application as embedding media for analytical studies. Unlike the conventional resins, which are polymerized at high temperatures, Lowicryl infiltration and polymerization is carried out at 223K with UV irradiation. This feature, together with the fact that there is no water production during polymerization of methacrylates, would enhance elemental immobilization and insure minimal losses during tissue preparation for x-ray microanalysis. Morphological preservation is adequate and allows the major compartments of cells to be recognized. In a comparative study on muscle tetany,²⁸ the characteristic increased levels of Na^+ and Cl^- and decreased levels of K^+ were observed in Lowicryl-embedded material, although the Na^+ levels were significantly lower in freeze-dried and Araldite-embedded samples. X-ray microanalysis of the resin in the immediate vicinity of the sample failed to show any redistribution of ions into the embedding medium from the sample.

Preparative Procedures During Sectioning and Fracturing

It may be difficult to see how sectioning and fracturing could affect the analytical results, but several possible effects should be considered. Knife edges do not stay sharp indefinitely and they are progressively worn away by interaction with the specimen. Glass knives contain boron, sodium, potassium, and silicon, and traces of these elements could contaminate the sections or fracture faces. Diamond knives are pure carbon and would be unlikely to contaminate the specimen. Steel and tungsten carbide knives are used to cut thick sections and may also be a source of contamination. It is important to clean thoroughly metal knives with acetone, followed by methanol, after they have been sharpened to remove any traces of the honing compound. New razor blades should always be cleaned before use.

During sectioning, the trough liquid should be kept clean and it should be remembered that diffusible elements can leach out of resin-embedded sections. Material embedded in the water-soluble resins, including Lowicryl, are best sectioned with a dry knife. If resin sections need flattening, it is better to avoid using chloroform vapors, which can be readily absorbed by resin sections and result in high levels of chlorine contamination. If samples are to be fractured rather than sectioned to reveal the internal regions, one should insure that the fracture surface is free of any

fragment by blowing clean air across the surface.

Preparative Procedures for Specimen Staining

All the cautionary remarks related to the use of fixatives apply equally to staining. If anything, the problem is more acute, for the chemicals used to increase the contrast of biological material are invariably derivatives of heavy metals. In view of the danger of further extraction of soluble materials and the certainty of introducing heavy elements whose x-ray peaks will mask or interfere with the elements of interest, it is probably best to avoid staining entirely. If the contrast of the sample is unacceptably low, then some compromise may have to be made, or the specimen examined by alternative techniques with an enhanced contrast mechanism such as the dark-field STEM mode. With experience, a lot of detail can be seen in unstained biological material; analytical accuracy is the prime objective of the exercise and structural acuity should take second place.

Preparative Procedures for Sample Coating

It is usual to coat specimens with a thin conductive layer prior to examination to minimize undue heating and prevent local charge build-up. However, provided the specimen is in good contact with the specimen support, the coating procedures can usually be omitted for thin sections that are to be analyzed by EDS systems. The higher specimen currents and longer counting times normally associated with WDS systems may require samples to be coated. Thick sections usually need coating and bulk specimens must be coated to prevent unwanted charging and spurious x-ray signals. The coating layer should neither mask the elements being analyzed nor give rise to spectral overlaps that might be difficult to deconvolute. In addition, the thin coating layer should be sufficiently thick to provide a good thermal and electrical pathway, but not so thick as to attenuate the incoming primary electron beam or absorb the emitted x-ray photons.

For obvious reasons, the noble metals and their alloys should not be used for coating biological samples prior to x-ray microanalysis. Beryllium, carbon, aluminum, and chromium are the four elements of choice. The high thermal radiation flux from carbon evaporation can easily damage delicate specimens; the procedure of flash evaporation of carbon fibers²⁹ overcomes many of these problems. The extreme toxicity of beryllium has led most workers to avoid using this metal, although methods have been devised for using this material safely.³⁰ Aluminum may be used, but it will interfere with some of the lighter elements (Na, Mg, Si, P). Chromium is relatively easy to use and has no toxic effects. Although the characteristic K and L lines of chromium are sufficiently far away from most of the light elements of common interest not to cause any interference, the background associated with the chromium peaks may contrib-

ute to the background of the light elements being analyzed. It is necessary to strip the chromium spectrum from the spectrum of the biological material in order to obtain quantitative data. These procedures, and the merits and disadvantages of the various coating materials are discussed in a recent paper by Echlin and Taylor.³¹

Preparative Procedures for Specimen Supports

Ideally, the specimen support should be a good conductor and made of a material that either makes no contribution to the x-ray signal from the sample, or generates a recognizable and measurable signal that may be removed during spectral processing. For bulk specimens, microdroplets, or thick sections to be examined by secondary electrons, it is usual to place the specimens on highly polished ultrahigh-purity carbon, beryllium, or aluminum disks. If appropriate, single crystals of silicon doped with boron are also useful. All these materials are reasonably good conductors and make only a small contribution to the x-ray background. Samples to be examined by transmitted-light optics should be placed on quartz or clear plastic slides, which should be thinly (~5-7 nm) coated with aluminum to provide a conductive layer. Glass or mica should not be used as supports because they contain a number of light elements.

Thick and thin sections are usually supported on standard TEM grids, which are readily available in a variety of mesh sizes and shapes and elemental constitution. The grids may be used naked or coated with a thin plastic and/or carbon layer. There is a tendency to use grids made of low-atomic-number elements such as beryllium, aluminum, or pyrolyzed graphite. Other materials may be used, provided their contribution to the total x-ray spectrum may be eliminated or avoided, or is of no consequence. Aluminized or carbon-coated nylon films also make good supports for sections. Woven nylon grids should be avoided. Bulk samples should be fixed to the specimen support with a high-purity colloidal graphite paint, and all samples should be stored in a clean, dry, dust-free container if they are not to be immediately examined and analyzed.

The Application of Ambient-temperature Preparative Procedures

The chemical methods of sample preparation are not now generally used where the analysis of diffusible ions is the prime objective, because so many compromises have to be made to the sample that the experimental results will probably have little validity. Diffusible elements may be confidently preserved in situ by low-temperature preparation methods that entirely avoid chemical intervention. However, it is more difficult to use low-temperature methods properly and it may require specialist equipment. A reasonably satisfactory halfway stage is to embed unfixed,

freeze-dried samples in resin and use the resulting thin sections for x-ray microanalysis. The elemental losses appear diminished.

It is impossible to set down guidelines for preparing all the other types of biological specimens that are likely to be studied by x-ray microanalysis. Each sample will require its own recipe and the properties and exigencies of the sample must be thoroughly researched before any chemical intervention place.

References

1. A. LeFurgey, "Cryotechniques for the application of x-ray microanalysis to biological systems," *Proc. 46th Ann. Meet. EMSA*, 1988, xiii.
2. D. E. Newbury, D. C. Joy, P. Echlin, C. E. Fiori, and J. I. Goldstein, *Advanced Scanning Electron Microscopy and X-ray Microanalysis*, New York: Plenum, 1986.
3. K. Zierold and R. A. Steinbrecht, "Cryofixation of diffusible elements in cells and tissue for electron probe microanalysis," in R. A. Steinbrecht and K. Zierold, *Cryotechniques in Biological Electron Microscopy*, Berlin: Springer, 1987.
4. A. T. Marshall, "Scanning electron microscopy and x-ray microanalysis of frozen hydrated bulk samples, in Ref. 3.
5. J. A. Chandler, "X-ray microanalysis of biological tissues: An examination of comparative specimens preparation methods using prostate tissue as a model," *SEM/1985 II*, 731.
6. D. M. R. Harvey, "Applications of x-ray microanalysis in botanical research," *SEM/1986 III*, 953.
7. A. J. Morgan, "X-ray microanalysis in electron microscopy for biologists," *Royal Microscopical Society Microscopy Handbook 05*, Oxford University Press, 1985.
8. T. A. Hall, "Capabilities and limitations of probe methods for the microanalysis of chemical elements in biology: A brief survey," *Ultramicroscopy* 24: 181, 1988.
9. A. Boeckstein et al., "Elemental analysis of individual rat blood platelets by electron probe x-ray microanalysis using a direct quantification method," *Histochemistry* 82: 257, 1985.
10. N. Roinel and C. L. de Rouffignac, "X-ray analysis of biological fluids: Contribution of microdroplet technique to biology," *SEM/1982 III*, 1155.
11. C. A. G. van Eekelen et al., "X-ray microanalysis of picolitre microdroplets: Improvements to the method for quantitative x-ray microanalysis of samples of biological fluids," *Micron* 11: 137, 1980.
12. A. J. Morgan, "The electron microprobe analysis of sprayed microdroplets of solubilized biological tissues: A useful preliminary to localization studies," *SEM/1983 II*, 861.
13. R. Beeukes, "Techniques for the quantitative organic analysis in microdroplets," *SEM/1979 II*, 767.
14. B. Ph. M. Mersey and M. E. McCulley, "Monitoring of the course of fixation of plant cells," *J. Microscopy* 114: 49, 1978.
15. R. Yaron et al., "Calcium in myonuclei: Electron microprobe x-ray analysis," *Experientia* 31: 154, 1975.
16. K. A. Holbrook et al., "A comparison of the effects of sample preparation on the x-ray microanalysis and ultrastructure of thin sectioned specimens of skin," *SEM/1979 I*: 265.
17. J. Coetzee and C. F. van den Merve, "Penetration rate of glutaraldehyde in various buffers into plant tissue and gelatin gels," *J. Microscopy* 137: 129, 1985.
18. G. R. Bullock, "The current status of fixation for electron microscopy," *J. Microscopy* 133: 1, 1984.
19. A. T. Sumner, "X-ray microanalytical cytochemistry," *SEM/1984 II*, 905.
20. I. D. Bowen and T. A. Ryder, "The application of x-ray microanalysis to cytochemistry," in D. A. Erasmus, Ed., *Electron Microprobe Microanalysis in Biology*, London: Chapman and Hall, 1979.
21. R. F. M. Van Steveninck and M. E. Van Steveninck, "Ion localization," in J. L. Hall, Ed., *Electron Microscopy and Cytochemistry of Plant Cells*, Amsterdam: Elsevier North Holland, 1978.
22. J. A. V. Simpson, H. L. Bank, and S. S. Spicer, "X-ray microanalysis of pyroantimonate precipitable cations," *SEM/1979 II*, 779.
23. D. C. Pease, "Glycol-methacrylate copolymerization with glutaraldehyde and urea as an embedment retaining lipids," *J. Ultrastructure Res.* 45: 124, 1973.
24. D. C. Pease and R. G. Peterson, "Polymerizable glutaraldehyde-urea mixtures as polar, water containing embedding media," *J. Ultrastructure Res.* 41: 133, 1972.
25. S. Munoz-Guerra and J. A. Subirana, "Glutaraldehyde cross linked polyvinyl alcohol as a water soluble embedding media for electron microscopy," *Proc. 7th Europ. Congr. EM Leiden*, 2: 724, 1980.
26. C. Weibull and A. Christiansson, "Extraction of proteins and membrane lipids during low temperature embedding of biological material for electron microscopy," *J. Microscopy* 142: 79, 1986.
27. R. Wroblewski et al., "Freeze drying and related preparation techniques for biological microprobe analysis," *SEM/1985 I*, 447.
28. J. Wroblewski and R. Wroblewski, "Why low temperature embedding for x-ray microanalysis investigations? A comparison of recently used preparation methods," *J. Microscopy* 142: 351, 1986.
29. K-R. Peters, "Precise and reproducible deposition of thin and ultrathin carbon films by flash evaporation of carbon yarn in high vacuum," *J. Microscopy* 133: 17, 1984.
30. A. T. Marshall and D. Carde, "Beryllium coating for biological x-ray microanalysis," *J. Microscopy* 134: 113, 1984.
31. P. Echlin and S. E. Taylor, "The preparation and x-ray microanalysis of bulk frozen hydrated vacuolate plant tissue," *J. Microscopy* 141: 329, 1986.

Presidential Session: Computer-aided Imaging I

SEQUENTIAL RANDOM FUNCTIONS FOR IMAGE MODELING AND SIMULATION

Dominique Jeulin

Sequences of images occur in various fields of image analysis. In microstructures it may concern the genesis of a material, or perhaps a crystallization process, as for the microprobe maps of Fig. 1. Other sequences appear in images where individual features located in the foreground partially mask features in the background, such as in perspective views, or in SEM micrographs (Fig. 2). In that case the microscopist would appreciate finding estimators of the size distribution of particles from the SEM micrographs. A solution to this problem is given in the frame of the Digital Dead Leaves model introduced in this paper.

Random Function (R.F.) Modeling: The Mathematical Morphology Approach

The Mathematical Morphology¹⁻³ gives a set theory methodology to get a quantitative description of disordered textures, or to build models or random structures. Within this approach and the Random Sets theory of G. Matheron,^{1,2} a Random Function R.F., with support in Euclidean space R^n , is studied as a random closed set R.A.C.S. by means of its subgraph^{3,4} $X = SG(Z) = \{x, z; Z(x) \leq z\}$. We use:

$$Q(B, x, z) = P[B, x, z \subset X^c] = F_{X+B}(z, x) \\ = P[Z + \check{B}(x) \leq z] \quad (1)$$

$$P(B, x, z) = 1 - P[Z - \check{B}(x) < z] \quad (2)$$

where B is a compact set in R^{n+1} and $Z + \check{B}$ (or $Z - \check{B}$) is the result of the *dilation* (or *erosion*) of $Z(x)$ by B .³ When B is a subset of R^n (a flat structuring element), we have

$$Z + \check{B}(x) = V[Z(y); y \in Bx] \quad (3)$$

$$Z - \check{B}(x) = \Lambda[Z(y); y \in Bx] \quad (4)$$

where V and Λ stand for supremum and infimum. When B is made up of a finite set of points, we can deduce from Eqs. (3) and (4) the well-known *spatial law*⁴ (or n -points probability function)

$$F_n(x_1, \dots, x_n; z_1, \dots, z_n) \\ = P[Z(x_1) < z_1, \dots, Z(x_n) < z_n] \quad (5)$$

$$T_n(x_1, \dots, x_n; z_1, \dots, z_n) \\ = P[Z(x_1) \geq z_1, \dots, Z(x_n) \geq z_n] \quad (6)$$

Particular cases of Eqs. (5) or (6) are the

The author is with the Centre de Géostatistique, Ecole des Mines de Paris, F-77305 Fontainebleau, France.

univariate and bivariate distribution functions, from which it is easy to deduce the *covariance* of the random function.

For spatially homogeneous structures, we use stationary and ergodic models of R.F., where the laws of Eqs. (1) and (2) do not depend on the location of x . For a given model, the laws of Eqs. (1), (2), (5), and (6) are calculated from the genetic assumptions as a function of parameters. On a studied microstructure, the laws may be estimated from area or volume fraction measurements after erosions or dilations obtained by image analysis. Thus, it is possible to provide estimates of the parameters of the model and to test the validity of assumptions. This approach is illustrated in what follows.

The Digital Dead Leaves (D.D.L.) Model

This section is a brief introduction to the D.D.L. model and to its properties. For a detailed study of bivariate distributions, second-order statistics, and estimation of the parameters, and for more general sequential R.F. models, see Refs. 5-7.

Construction of the D.D.L. Model and Basic Properties. We consider a family of *primary* R.F. $Z_t'(x)$ with a compact support $X_0'(t)$, which are meant to simulate the intact dendrites in Fig. 1 or the particles in Fig. 2. Between times t and $t + dt$, independent realizations of Z_t' are implanted at random sites x_k in R^n , according to an infinitesimal Poisson point process with intensity $\theta(t)dt$. During a finite time interval $[0, t]$ there are in point x in R^n changes of observed values $Z_t'(x - x_k)$ when a primary function covers x . We use two different rules of construction of the D.D.L. R.F., from these observed values:

(1) we assign to x the last observed value

($\neq 0$)

(2) we assign to x the first observed value

($\neq 0$)

Other rules of combination can be used:⁵⁻⁷ the sum of observed values, or the supremum or infimum value; the last give the Boolean R.F.^{3,4,11} derived from G. Matheron's Boolean models of R.A.C.S.^{1,2}

Rules (1) and (2) are digital versions of the construction of the dead leaves tessellation⁸ or the color of dead leaves:^{9,10} imagine dead leaves with a texture (gray-level variations) falling from trees, seen from above (1) or from below (2). The color dead leaves model is a particular case of the D.D.L. where $Z_t'(x)$ are cylinders with random heights Z .

A comparison of the results of the two modes of construction and of the Boolean R.F.

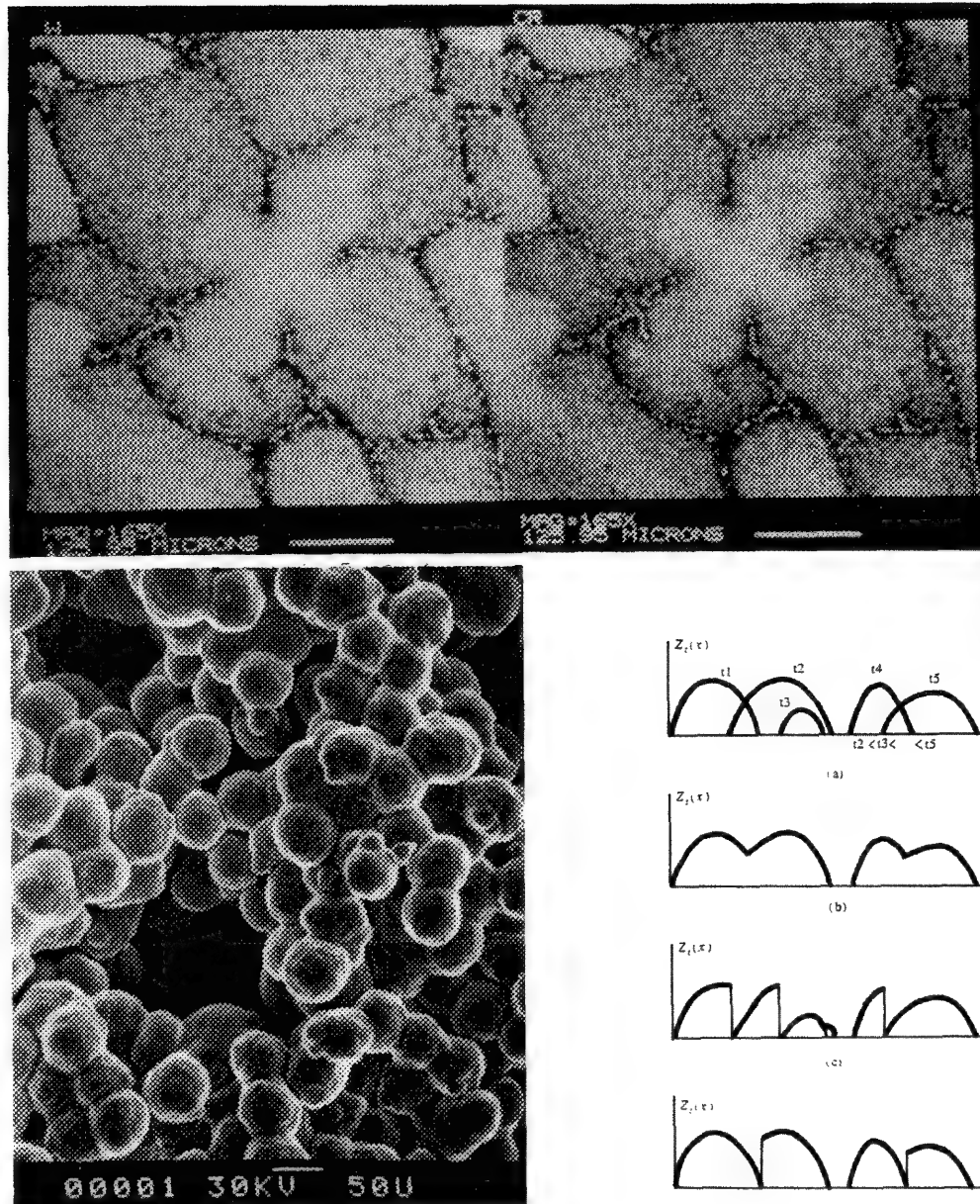


FIG. 1.--Microprobe digital maps of tungsten (left) and chromium (right) inside dendrites of superalloy. (Micrographs by V. Parienti, Centre P. M. Fourt, Paris School of Mines.)

FIG. 2.--SEM micrographs showing powder deposit obtained by electrophoresis. (D. Fayeulle, Centre P. M. Fourt, Paris School of Mines.)

FIG. 3.--Comparison between Boolean F.F. (b) and D.D.L. R.F. (1) in (c) and (2) in (d), obtained from same sequence of primary functions (a).

is provided from the same sequences on a profile in Fig. 3. It is interesting to note some properties of the trajectories of $Z_t(x)$: the D.D.L. trajectories are *stochastic processes with Markovian jumps*; "vertical" sections of the D.D.L. (i.e., profiles) generate R.F. of the same type, with a support embedded into a lower-dimension space. The property is interesting for the solution of stereological problems, such as inferring the properties of the R.F. from information obtained on their profiles; any anamorphosis (e.g., a gray-scale enhancement) of the R.F. is obtained from the same transformation on the primary R.F. $Z_t'(x)$. (This property can be used to gener-

ate families of R.F., or to model data obtained after an anamorphosis transformation.)

The support $X_0(t) = \bigcup [X_0'(u); u \leq t]$ is a Boolean R.A.C.S.^{1,2} with primary grains $X_0'(t)$. For this model, the moment $Q(B)$ is given by

$$Q(B, t) = \exp\left\{-\int_0^t \theta(u) \bar{\mu}_n [X_0'(u) + \tilde{B}] du\right\} \quad (7)$$

Probabilistic Properties of the D.D.L. Model. The Markovian character of the trajectories results in Chapman-Kolmogorov types of equations that yield the main probabilistic properties of the model. Here we only give some examples for definition (1).

The univariate distribution function is given by

$$T(z, t) = 1 - F(z, t) = p_0(t) \int_0^t \frac{\theta(u) K(0, z, u)}{p_0(u)} du$$

$$= p_0(t) \int_0^t \frac{\mu(0, u)}{p_0(u)} [1 - G(z, u)] du \quad (8)$$

where $p_0(t) = \exp[-\int_0^t \theta(u) K(0, u) du]$ and $K(0, u)$ is the Lebesgue measure (area in R^2) of $X_0'(u)$. The moments $M_n(t)$ are derived from Eq. (8) and from the moments of Z_t' [with $\mu(0, u) = \theta(u) K(0, u)$]:

$$M_n(t) = E[Z^n(t)] = p_0(t) \int_0^t \frac{\mu(0, u)}{p_0(u)} M_n'(u) du \quad (9)$$

The moment $P(B, z, t)$, obtained by erosion of $Z_t(x)$, is given by

$$P(B, z, t) = \int_0^t \theta(u) \mu_n[X'(t) - \check{B}]z \frac{Q(B, t)}{Q(B, u)} du \quad (10)$$

where $Q(B, t)$ is given by Eq. (7), with $B_0 = B \cap \Pi_0$ (Π_0 is the horizontal hyperplane $z = 0$).

Equation (10) is valid if the primary function is such that, with B connected,

$$\mu_{n-1}[X_z'(t) \cap X_0'(t)] = 0 \quad \forall z$$

and

$$\Lambda[Z_t'(x); x \in B] = m$$

This relation gives the statistical changes of the R.F. $Z_t(x)$ after erosions by B (change of support implying the operator Λ as seen in the case of a flat structuring element in Eq. (4). Erosions by segment are detailed elsewhere.^{5,7}

The probability density function (p.d.f.) $h(z, t)$ of the height of apparent summits of the D.D.L. is deduced from the corresponding p.d.f. $h'(z, t)$ of the R.F. $Z_t'(x)$, when $Z_t'(x)$ possesses a single summit:

$$h(z, t) = \int_0^t \theta(u) h'(z, u) \frac{p_0(t)}{p_0(u)} du \frac{1}{N(S, t)} \quad (11)$$

where $N(S, t) = \int_0^t \theta(u) \exp[-\int_0^u \mu(0, v)] dv$ is the total number of apparent summits at time t per unit volume in R^n .

The Homogeneous Digital Dead Leaves (D.D.L.) Model

An important particular case of D.D.L. model is obtained when θ and $Z_t'(x)$ do not depend on time. In each point x of R^n the trajectory is a time-homogeneous Markov stochastic process and leads to simple results. Moreover, the two definitions (1) and (2) are equivalent (up to a reversion of time t).

The support $X_0(t)$ of $Z_t(x)$ is a Boolean R.A.C.S., with intensity t and primary grain X_0' :

$$p_0(t) = \exp[-\theta t K(0)] = \exp[-t \mu(0)] \quad (12)$$

$$Q(B, t) = \exp[-\theta t \mu_n(X_0' + \check{B})] \quad (13)$$

From Eq. (8) we get the univariate distribution and the moment $M_n(t)$

$$1 - F(z, t) = [1 - G(z)] \{1 - \exp[-t \mu(0)]\} = T'(z) [1 - p_0(t)] \quad (14)$$

$$M_n(t) = E[Z^n(t)] = M_n' [1 - p_0(t)] \quad (15)$$

When $t \rightarrow \infty$, $T'(z) \rightarrow T'(z)$; the distribution of $Z_\infty(x)$ is the distribution of $Z'(x)$ but that is not the case for the bivariate distribution.^{5,7}

The moment $P(B, z, t)$, with the conditions prevailing for the validity of Eq. (10), is given by

$$P(B, z, t) = \frac{\bar{\mu}_n(X' - \check{B})z}{\mu_n(X_0' + \check{B}_0)} [1 - Q(B, t)] \quad (16)$$

$$P(B, z) = \frac{\bar{\mu}_n(X' - \check{B})z}{\mu_n(X_0' + \check{B}_0)} \quad (17)$$

for $t \rightarrow \infty$.

The number of apparent summits at time t is obtained from

$$N(S, t) = \int_0^t \theta(u) \frac{p_0(t)}{p_0(u)} du = \frac{1 - p_0(t)}{K(0)}$$

The p.d.f. of apparent summits $h(z, t)$ is given by

$$h(z, t) = \frac{1}{N(S, t)} \int_0^t \theta h'(z) \frac{p_0(t)}{p_0(u)} du = h'(z) \quad (18)$$

that is, the p.d.f. of the summit of Z' . When $t \rightarrow \infty$, $N(S, \infty) = 1/K(0)$.

The Intact Primary Functions in the Homogeneous D.D.L. Model

In this section, we assume that we can locate the intact primary function $Z_t'(x)$ (which remained completely uncovered by further implantation of functions after their own arrival). That can be the result of an image segmentation procedure that we shall not discuss here. The population of intact $Z_t'(x)$ is biased with respect to the initial population, as largest supports $X_0'(t)$ tend to mask lower-size supports.

The correction of this bias is of primary importance for two reasons: for estimates of the parameters of the model from available data (see below), and, more practically, for estimates of a size distribution of particles from micrographs such as those in Fig. 2.

To simplify, we give here the correction of the bias in the homogeneous model; the general case is given in Refs. 5 and 7. We assume that $Z'(x)$ depends on a finite number of parameters, with multivariate p.d.f. ϕ_X' ; for instance, when X' is deduced from X_0' by a random change of scale λ , we have $\phi_X' = \phi(\lambda)$. We look for the relationship between the ϕ_X' and the observed $\phi_{X_i}'(t)$ on the population of intact X' at time t .

The average number of intact primary grains at t is given by

$$N_i(t) = E y' \frac{1 - Q(Y_0', t)}{\bar{\mu}_n(X_0' + Y_0')} \quad (19)$$

The p.d.f. of intact primary functions at t is

$$\phi_{Y_i}'(t) = \frac{\phi_{Y'}[1 - Q(Y_0', t)]}{\bar{\mu}_n(X_0' + Y_0')} \frac{1}{N_i(t)} \quad (20)$$

When $t \rightarrow \infty$

$$\phi_{Y_i}' = \frac{\phi_{Y'}}{\bar{\mu}_n(X_0' + Y_0')} \frac{1}{N_i} \quad (21)$$

That is, the bias of the initial p.d.f. ϕ_Y is given by

$$\frac{1}{N_i \bar{\mu}_n(X_0 + Y_0)}$$

Further results for $t \rightarrow \infty$ are obtained when the support X' is almost surely convex (with Minkowski's functionals^{2,3} W_k): from Eq. (21) we get

$$N_i \left(\sum_{k=0}^n C_n^k \bar{W}_{k,c} \bar{W}_{n-k} \right) = 1 \quad (22)$$

$$N_i \left(\sum_{k=0}^n C_n^k \bar{W}_{n-k} \overline{W_{k,i} W_{k,i}'} \right) = 1 \quad k' = 0, 1, \dots, n$$

The system of (22) gives an estimate of the \bar{W}_k (valid for X_0') from the $\bar{W}_{k,i}, \bar{W}_{k,i}'$ and \bar{W}_k' measured on intact primary functions; in the case of functions with support in R^2 , such as images, we have $W_0 = A(X_0')$ (area) $2W_1 = L(X')$ (perimeter) and $2W_2 = 2\pi$. Then from Eq. (21) and the observed ϕ_{Y_i}' , the underlying histogram ϕ_Y is estimated. This is a satisfactory answer to the size-distribution estimation of convex particles from SEM micrographs of a packing.

Estimation of the Parameters of the D.D.L. Model and Tests

We give a short summary of the situations where estimators of the parameters and tests of the D.D.L. model can be proposed.⁵⁻⁷

The parameters of the model are the intensity $\theta(t)$ (i.e., a function) and the properties of $Z_t'(x)$.

For the general nonhomogeneous model, realizations of $Z_t(x)$ at different times are required. By derivation in t , we can get separate estimates of properties of $X_0'(t)$ and of $Z_t'(x)$, after extraction of the intact primary functions.

For the homogeneous model, the estimate is feasible from a realization at any time t . For t infinite, the intensity θ disappears from the results: it is no longer a parameter of the model. In other situations, parameters can be estimated from a single realization, like a semihomogeneous model, where the intensity is constant, and the primary functions are transformed by an affinity [with ratio $\alpha(t)$] from an initial population $Z'(x)$; that may occur in SEM, where objects in the background may, on average, appear darker than in the foreground.

Tests of the model can be proposed when the support $X_0'(t)$ is a convex R.A.C.S. They are derived from classical tests of the Boolean R.A.C.S. model. Additional tests can be performed by comparisons of predicted properties (deduced from the model and its parameters) with measured properties.

Conclusions

The D.D.L. model presented in this paper illustrates the mathematical morphology approach for modeling images. It provides descriptions of physical situations, like microstructures or SEM micrographs, and allows calculation of the main statistical properties that can be measured on samples, in order to estimate the model parameters. Within the model, a correction of bias in the estimation of size distributions is proposed. Last, simulations of the D.D.L. model can be provided with very low computational effort by use of an image analyzer, as it only involves writing procedures in image memories.

References

1. G. Matheron, *Éléments pour une théorie des milieux poreux*, Paris: Masson et Cie, 1965.
2. G. Matheron, *Random Sets and Integral Geometry*, New York: Wiley, 1975.
3. J. Serra, *Image Analysis and Mathematical Morphology*, London: Academic Press, 1982, chap. 12.
4. D. Jeulin and P. Jeulin, "Synthesis of rough surfaces by random morphological models," *Stereol. Jugosl.* 3(Suppl. 1), 239.
5. D. Jeulin, "Modèles de fonctions aléatoires séquentielles," Internal Report N-1/88/CG, Paris School of Mines, 1988.
6. D. Jeulin, "Sequential random functions models," Proc. 3rd Intern. Geost. Congress, Avignon, Sept. 1988 (in preparation).
7. D. Jeulin, "Morphological modeling of images by sequential random functions," *Signal Processing* (submitted).
8. G. Matheron, *Schéma Booleen séquentiel de partitions aléatoires*, Internal Report N-83, Paris School of Mines, 1968.

9. D. Jeulin, *Morphologie mathématique et propriétés physiques des agglomérés du minerai de fer et du coke métallique*, Doctorate Thesis, Paris School of Mines, 1979, chap. 5.

10. D. Jeulin, "Multicomponent random models for the description of complex microstructures," *Mikroskopie* 37S: 130, 1980.

11. J. Serra, "Boolean random functions," in *Image Analysis and Mathematical Morphology*, vol. 2, London: Academic Press, 1988, chap. 15.

COMPUTERS IN STEREOLOGY AND IMAGE ANALYSIS

John C. Russ

Stereology is a coined word introduced about three decades ago to cover a growing collection of methods that describe three-dimensional structures and relationships between objects based on measurements obtained from conventional two-dimensional images. These techniques have been primarily applied to microscope images (light, electron, etc.) of organic and inorganic materials, such as the grain structure of metals, description of pores in ceramics roughness of worn surfaces, structure of agglomerated soot particles, alignment of fibers in muscles, orientation of root hairs on plants, determination of surface/volume relationships in the lung, and arrangement of organelles within a cell. Of course, the principles are general and can be applied at larger scales, such as studies of irregularity in the spatial distribution of particular types of stars, mapping of terrain or vegetation from satellite photos, or determining spatial relationships between mineral deposits from geological maps. Besides application to research, they are also used in industrial quality control applications for such diverse purposes as controlling the absorbance of diaper materials, the porosity and texture of bread, and grading the size of rice grains.

It is the goal of stereology to provide quantitative measures for structurally based parameters. The algorithms are based on geometric probability and make heavy use of mathematics, yet their routine applications is often extremely simple, requiring only a counting operation by the user. Few stereological parameters have meaning for a single isolated object or feature. Rather, they are properly applied to assemblages or populations of features, or to complete three-dimensional structures, to provide statistically correct, unbiased measures that can be used for comparison or description of the population or structure as a whole. There are two somewhat different approaches to obtaining the desired parameters. One deals only with global parameters, the most fundamental of which is the volume fraction of a "phase." (The word is used in a more general sense than its normal materials meaning to refer to any identifiable structure or type of feature.) Global parameters do not treat the details of how the phase is organized within its matrix. However, they provide an extremely efficient description of the volume density of the phase, its bounding surfaces and their curvature, mean spacings between phase regions, and so on. These values

can be obtained with minimal effort by counting the occurrences of points, intersections and so forth in random section images through the structure. They are most often performed by humans directly, and their interpretation is generally well understood.

When it is desired to measure directly individual objects or features in one or more images to characterize a population, it is necessary to distinguish between two different types of images, because each obscures some of the desired information and requires different interpretation of the measured data. A "section" image represents a cut (usually planar) through a structure, on which are visible the intersections of the surface with the features of interest. A typical metallurgical specimen is an example of this situation, as is a TEM image if the specimen thickness is small compared to the size of objects. These intersections do not in general show the full extent of the objects. Conversely, a "projection" image shows entire objects by their shadows or upper surfaces. Transmission light or electron microscope images of small objects, or an SEM image of particles on a substrate, fit into this category. The maximum extent of objects (at least in one direction) is shown, but surface indentations and other shape irregularities may be hidden.

In each case, it is necessary to utilize an appropriate set of models to derive expected values for the three-dimensional objects present from the measurements of the features seen in the image. Many such models have been derived for both general and specific situations. The basic types of measurements can be grouped into four classes.

1. *Measures of Size.* This includes such directly accessible values as the area of a feature in the image, its perimeter, length (longest chord), breadth (shortest caliper dimension), and perhaps the convex area and perimeter defined by a "taut string" around the feature. From these primary values, derived or secondary parameters can be calculated. Some apply to two-dimensional images, such as the width (for instance, the thickness of the lines used to form the letter "S" as opposed to the breadth of the letter itself), and others describe the three-dimensional object which the feature is assumed to represent. Examples include the volume and surface area of the object.

2. *Measures of Position.* This includes the location of each feature, for instance as given by the coordinates of its centroid or the corners of a bounding rectangle, and

The author is at the Department of Materials Science and Technology, North Carolina State University, Raleigh, NC 27695.

generally the orientation (usually the angle of the longest chord, or the axis of minimum moment). From these parameters, it is possible to derive information about the mean distance between objects, the mean distance from an object to its nearest neighbor, etc. It is also possible to search for patterns in object position (such as clustering) or gradients in object position or orientation, especially as correlated with measures of size or other parameters.

3. *Measures of Shape*. This is one of the most powerful categories of data, yet also one of the least familiar to humans who simply lack the ready vocabulary to describe shapes (although we routinely use shape information for object recognition). At one extreme, there is a collection of a dozen or so dimensionless shape parameters such as *formfactor* ($4\pi \text{ Area} / \text{Perimeter}^2$) or *convexity* (the ratio of taut string perimeter to perimeter) that are widely used and often allow feature classification but do not seem to describe a really fundamental property of the features. At the other extreme, Fourier shape coefficients obtained by unrolling the feature perimeter and expressing it as a series expansion of harmonics allow similar objects to be classified and compared, but are hard to relate to what humans see in the image. A third, more recent development is the use of fractal dimensions to describe quantitatively the irregularity of boundaries and the roughness of surfaces. Determining the full topological parameters of three-dimensional objects requires more than a single two-dimensional image.

4. *Measures of Density or Color*. This is perhaps the least used of the types of measurement parameters, because the process of obtaining images often does not preserve a quantitative relationship between object properties and the brightness or color of the feature in the image. Density measurements of stained structures in the transmission light or electron microscope can be quantified by suitable calibration methods. Color imaging in the light microscope can provide enhanced ability to discriminate features, but few systems are equipped at this time to use the information. In electron microscopy, any multisignal imaging system (for instance various use of energy x rays, back-scattered electrons, etc.) can be considered roughly analogous to color imaging in this context.

When information is required on a population of objects, it is usually impractical to obtain it by manual image measurement. Instead, automatic image analysis computers are employed to measure hundreds or thousands of features in dozens of images, to build up a database suitable for statistical interpretation. Machine methods are generally more consistent than human measurements, and also faster, but lack the ability to make the subtle discrimination required in some instances to distinguish the features to be measured. Algorithms that mimic some of the human vision operations

are applied to image processing in these cases, or in the extreme case humans are required interactively to select the features, trace their boundaries, and so forth.

Computer image measurement involves a series of steps, starting with the digitization and storage of the image. This often employs video technology; a standard camera connected to the microscope, a VCR as an intermediate storage device, or a slow-scan signal that may have somewhat different raster size. The number of stored picture points ("pixels") varies from about 256 to 1024 across the width of the image, and the number of discrete brightness values at each point is usually digitized to one part in 256. (By comparison, the human eye can generally distinguish about 20-30 gray levels in a typical photograph, but the lateral resolution is far higher—as much as a thousand points per inch.)

To assist in selecting the features in the image to be measured, it is sometimes helpful to apply image processing methods. These include smoothing to reduce noise, subtracting or ratioing successive images to look only at changes that have occurred between two views of the same field, and a variety of edge-enhancing operations designed to assist in distinguishing objects from their surroundings and from each other. There is a rich literature in the image-processing field, much of which received its initial impetus from space probe and satellite imagery, and has also been abetted by research into the physiology of human vision.

Discrimination of features in images is usually accomplished by selection of a range of brightness values (either in the original or in a processed image) that correspond to the features of interest, to produce a "binary" image in which the original gray-scale or color values are reduced to black and white, or figure and ground. These binary images may also require morphological processing before measurement, for instance to smooth outlines, separate touching objects, or join broken ones. Reduction of features to their skeletons may more directly characterize their shape than the original, for example. Another class of operations applies Boolean logic to combine several binary representations, perhaps showing different objects in the same field. These can be used, for instance, to select for measurement only features that meet several criteria or objects of one type that lie within another, or even to measure the extent to which one type of object lies adjacent to another.

The measurement of the size, shape, location, and brightness parameters for each feature present produces a lot of data. Although these data occupy much less storage space than the original image, they still do not usually provide a direct answer to the real purpose behind the image analysis effort. This question is not always well understood at the start of the work. It may be as general

as "what is the difference between these two materials?" or as specific as "are any cancerous cells present?" The tools to answer these questions are statistical and usually interactive. They involve plotting values for several measured variables against one another to look for correlations, and the ability to examine distribution plots for the measured variables and/or the derived parameters obtained from them using stereological relationships. Distribution plots come in many forms, including cumulative, logarithmic, and probability axes, and two or more dimensions. They are rich in stereological information.

Comparisons require careful use of the proper statistical tools. Chi-squared tests of distributions, t-tests and r-tests of correlation, and both parametric (e.g., Anova) and nonparametric (e.g., Wilcoxon) comparisons between populations are important, but often misapplied or misinterpreted. It is also usually necessary to work with quite large data files. If the features of interest represent only a few percent of the total objects present, and statistically precise results are desired, it may be necessary to measure a total of tens of thousands of objects. Since individual images may contain tens or hundreds of objects, it is easy to see that many such images must be obtained (by proper random sampling) and the data acquired.

The descriptions so far have dealt primarily with single, two-dimensional images. In some cases, multiple images allow an even more direct study of three-dimensional structure with fewer assumptions and models. A particularly simple and powerful method called the "disector" allows the determination of the number of features per unit volume of the sample by counting the number of features that appear in one image but not in another produced by cutting or polishing a small distance deeper into the matrix. Otherwise, determining this apparently simple value from a single plane section image requires making some limiting assumptions about the shape of the objects. The extension of this method to a complete set of "serial sections" allows reconstruction of a three-dimensional structure in its entirety, so that topological information can be determined. Sometimes these images are obtained by physical sectioning (e.g., microtoming), and sometimes by in-situ methods (e.g., by ion sputtering with intermittent imaging, or sequential polishing of the sample). In some cases, the images can be obtained nondestructively by optical focusing at various depths below the surface. This applies to light microscope images of optically transparent specimens, as well as to the newer confocal scanning light microscope and the scanning acoustic microscope.

Stereoscopy is a set of measurement techniques that allow the three-dimensional arrangement of objects, or the relief and topography of a surface, to be determined from two images taken of the same field but with different viewing angles. Parallax of objects in the two images allows computation of their

distances. When more than two views are available tomographic reconstruction of internal structure can also be performed. Originally applied to x-ray images in medical diagnosis, these methods have now been extended to microscopic dimensions, and to the use of electrons and other radiation. (It has even been used to map the earth's core by use of seismic waves.) Tomographic image reconstruction has been used to view internal structure, but only limited use of measurements has been attempted thus far.

Many examples of representative applications can be shown. The following list of references is intended as a basic library for would-be researchers in the field. It is not comprehensive or exhaustive, but includes books that will at least introduce most of the concepts discussed, and give references to much of the periodic literature. Publication of articles on current theory and applications can often be found in the *Journal of Microscopy* (Royal Microscopical Society), in *Acta Stereologica* (International Society for Stereology), and in the forthcoming *Journal of Computer-Assisted Microscopy* (Plenum Press). The author has also published a number of relevant articles in earlier annual issues of *Microbeam Analysis*.

- D. H. Ballard and C. M. Brown (1982). *Computer Vision*, Prentice Hall, Englewood Cliffs, N.J.
- P. R. Bevington (1969), *Data Reduction and Error Analysis for the Physical Sciences*, McGraw-Hill, New York.
- K. R. Castleman (1979), *Digital Image Processing*, Prentice Hall, Englewood Cliffs, N.J.
- M. Coster and J.-L. Chermant (1985), *Précis d'analyse d'images*, Editions du Centre National de la Recherche Scientifique, Paris.
- R. T. DeHoff and F. N. Rhines (1968), *Quantitative Microscopy*, McGraw-Hill, New York.
- G. T. Herman (1980), *Image Reconstruction from Projections: The Fundamentals of Computerized Tomography*, Academic Press, New York.
- S. Inoue (1986), *Video Microscopy*, Plenum Press, New York.
- M. G. Kendall and P. A. Moran (1963), *Geometrical Probability*, No. 10 in Griffith's Statistical Monographs, Charles Griffith, London.
- B. B. Mandelbrot (1982), *The Fractal Geometry of Nature*, W. H. Freeman, San Francisco
- D. Marr (1982), *Vision*, W. H. Freeman, San Francisco.
- G. Matheron (1975), *Random Sets and Integral Geometry*, Wiley, New York.
- R. Nevatia (1982), *Machine Perception*, Prentice Hall, Englewood Cliffs, N.J.
- W. K. Pratt (1978), *Digital Image Processing*, Wiley, New York.
- F. N. Rhines and R. T. DeHoff (1986), *Microstructology: Behavior and Microstructure of Materials*, Dr. Riederer-Verlag, Stuttgart.

- A. Rosenfeld and A. C. Kak (1982), *Digital Picture Processing*, Academic Press, London.
- J. C. Russ (1986), *Practical Stereology*, Plenum Press, New York.
- J. Serra (1982), *Image Analysis and Mathematical Morphology*, Academic Press, London.
- E. E. Underwood (1970), *Quantitative Stereology*, Addison-Wesley, Reading, Mass.
- E. R. Weibel (1979), *Stereological Methods* vols. I & II, Academic Press, London.

CONCENTRATION-CONCENTRATION HISTOGRAMS: SCATTER DIAGRAMS APPLIED TO QUANTITATIVE COMPOSITIONAL MAPS

D. S. Bright, D. E. Newbury, and R. B. Marinenko

Compositional mapping with the electron microprobe requires standardization of, and instrumental and matrix corrections to, the raw x-ray data in order to achieve a quantitative elemental analysis at each pixel location in a map.¹⁻³ The resulting arrays of compositional values are then displayed on a cathode-ray tube³ as images with selected gray or color scales to encode the range of compositional values. Often it is of interest to establish the spatial correlation of two or more constituents. Such correlations can be conveniently presented in visual form by the use of the well-known technique of primary color overlay, in which two or three "single band" (or single constituent) images are overlaid with the red, green, and blue guns of a color CRT. By the laws of color addition, the appearance of secondary colors in the image field reveals regions of overlap of any two constituents. This powerful and widely used technique suffers from the deficiency that it is difficult to visualize the compositional ranges of the single-band images in a meaningful way in the final color composite image.

As an alternative, the composition-composition histogram (CCH) provides a numerical view of the relationships of the constituents^{4,5} and promises to be useful for diagnosing experimental problems and evaluating data.

Method

Concentration-Concentration Histogram (CCH). Histograms of images are often obtained by scaling the images to cover a concentration range of 0-255, and then accumulating the intensities of each pixel in a one-dimensional array of 256 bins in the usual manner. The concentration-concentration histogram (CCH) is a two-dimensional analog, a type of scatter diagram.^{4,5} Each pixel in one image, $A(x,y)$, representing element A at coordinates (x,y) , is associated with the corresponding pixel in the other image $B(x,y)$. The concentrations represented at this location are accumulated in a 256×256 pixel array CCH, where the abscissa of the CCH corresponds to the concentration of A and the ordinate to the concentration of B by the following procedure:

For every location (x,y) , increment the CCH as follows:

$i = A(x,y)$ = concentration of element A for current pixel in map A

$j = B(x,y)$ = concentration of element B for current pixel in map B

$CCH(i,j) = CCH(i,j) + 1$

The accumulated number in each pixel in the CCH can be displayed with selected gray or color scales to represent the CCH as an image. Such a visual display of the CCH allows the analyst to recognize quickly and quantitatively the compositional value pairs that occur commonly in the original single-band images.

As an example, Figs. 1 and 2 are respectively Cu and Ti maps of an aligned eutectic alloy, and Fig. 3 shows the CCH of this pair of images. The CCH often shows intense spots where most of the pixel pairs tend to clump, as shown in Fig. 3, along with some points or bins of very low intensity representing only one or two pixel pairs for the original quantitative maps. The points outside of the clumps do not fall randomly but in a strip between the clumps.

We have found the scattered low-intensity points to be as important as the clumps. To visualize these low intensity points as well as the high intensity clumps, the accumulated number in each pixel in the CCH can be displayed by means of a scale that presents the wide dynamic range of the data to an observer (Fig. 4). A "thermal color scale" is especially effective for this application.

Locating Features in the Original Images. A powerful aspect of the CCH is the trace-back capability to highlight selected compositional features in the original images according to features recognized in the CCH. Once a feature of interest in the CCH has been identified, the procedure is reversed to identify the specific pixel locations in the original compositional maps that correspond to selected concentration-concentration conditions. Examples are shown (a) Figs. 5 and 6, where the lower right or high-Cu low-Ti clump correspond to the Cu-rich phase (labeled "c"); (b) Figs. 7 and 8, where the upper left clump corresponds to the Ti-rich phase (labeled "t"); and (c) Figs. 9 and 10, where the strip between the clumps corresponds to the boundary region between the two phases.

Selecting Areas in the CCH. The algorithms here were implemented with an image-processing system⁶ written in both the LISP and FORTRAN programming languages. To simplify programming, we choose rectangles to outline or make up the areas of interest. The left and right sides of each rectangle define a concentration range for element A. We then use this concen-

The authors are at the Center for Analytical Chemistry, National Bureau of Standards, Gaithersburg, MD 20899.

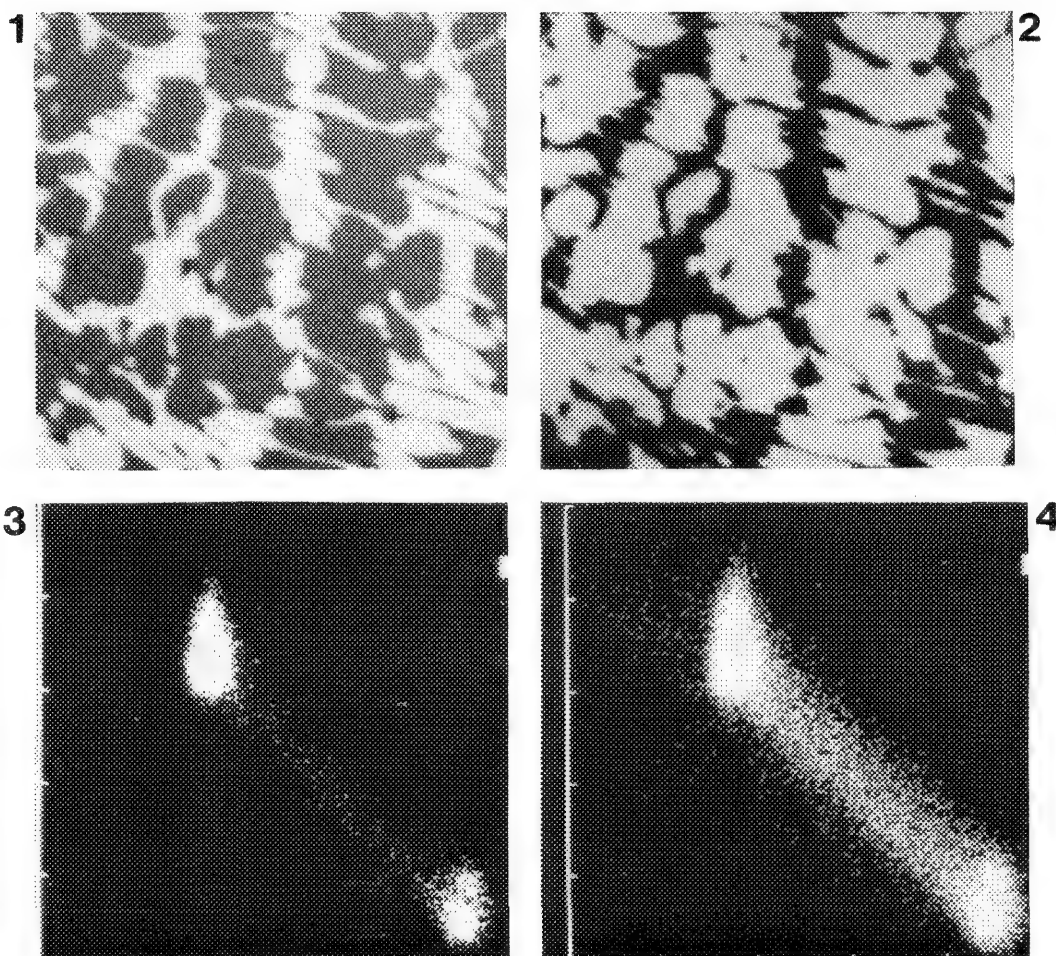


FIG. 1.--Cu x-ray map for Cu-Ti alloy.

FIG. 2.--Ti x-ray map for Cu-Ti alloy.

FIG. 3.--CCH for corresponding concentration maps of binary alloy of Cu and Ti. Abscissa, Cu concentration, range 20-56%; ordinate, Ti concentration, range 43-73%. Intensity proportional to number of pixels of original maps with appropriate Cu and Ti concentration values. Most pixels fall into two large clumps on CCH.

FIG. 4.--Same CCH as Fig. 3, but with low intensities enhanced to visualize pixels or points representing only one or two pixel pairs. Most of these points fill in strip between the two intense clumps.

tration range to select (with intensity thresholds) the pixels in map A by making a mask marking all the pixels of map A that fall within this range. The same can be done with the top and bottom of the rectangle for map B. The two masks can be combined with a logical AND operation to show areas of the sample that satisfy the concentration conditions both for map A and map B, and that therefore represent all the points on the inside of the rectangle in the CCH. If necessary one can use more than one rectangle by simply accumulating the appropriate locations for all the rectangles in the CCH into a final mask that can overlay the original map or maps.

Applications

The CCH for a homogeneous silver-gold alloy is shown in Fig. 11. Because the Ag and Au are uniform, the map pixels should accumulate into one bin (pixel) in the CCH. Instead, the

effect of counting statistics has resulted in a rounded clump of points, where the absence of slant shows that the variation in the Ag concentration is not correlated with the variations in the Au concentration.

The CCH of an inhomogeneous Fe-Cr-Ni steel alloy (Fig. 12) has a different appearance. There is still a central clump (Fig. 13) representing the major continuous phase that is high in Ni (Fig. 14; see Ni map in Fig. 12b). A broad tail streaking to the left toward lower Ni concentrations and slightly up toward higher Cr concentrations (Fig. 15) represents the thin dendritic phase (Fig. 16, see Cr map in Fig. 12c). A very sparse section (Fig. 17) just above the main clump represents pixels anomalously in high Cr (Fig. 18), corresponding to the upper left corner of the Cr map (Fig. 12c), which may represent slight errors in the quantitation of the map, or an anomalous area of the sample.

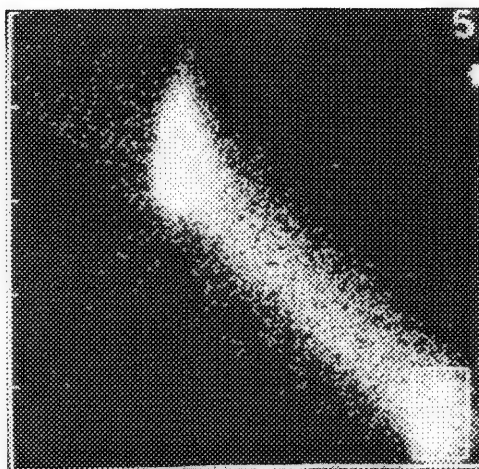


FIG. 5.--Same CCH as Fig. 3, but with bottom right clump outlined.

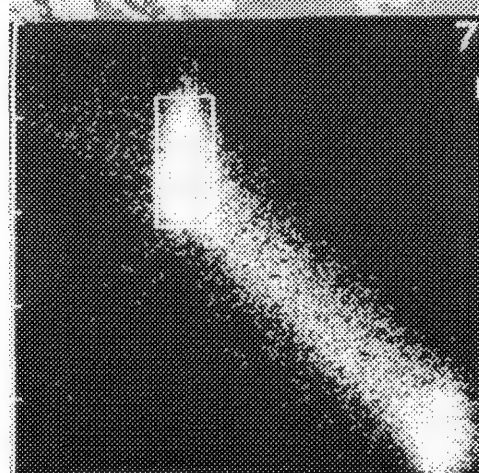
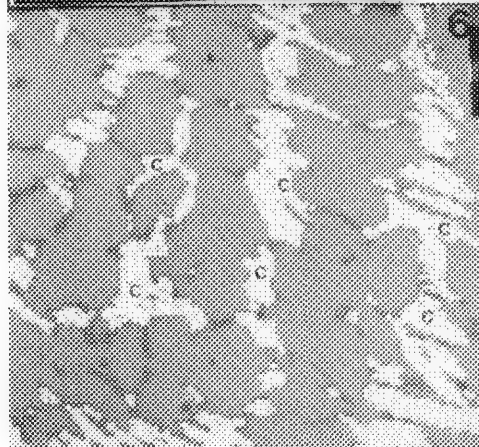
FIG. 6.--X-ray maps in Figs. 1 and 2 overlapped, with pixels 'c' rendered white that correspond to clump outlined in Fig. 5. Note correspondence of these 'c' pixels with Cu-rich pixels in Fig. 1.

FIG. 7.--Same CCH as Fig. 3, but with top left clump outlined.

FIG. 8.--X-ray maps in Figs. 1 and 2 overlapped, with pixels 't' rendered light gray that correspond to clump outlined in Fig. 7. Note correspondence of these 't' pixels with Ti-rich pixels in Fig. 2.

FIG. 9.--Same CCH as Fig. 3, but with strip between clumps outlined.

FIG. 10.--X-ray maps in Figs. 1 and 2 overlapped, with white pixels (on Cu-Ti boundary) corresponding to strip outlined in Fig. 9.



Figures 19 through 26 are CCHs and corresponding maps for the lamellae of an Al-Cu alloy. The maps have roughly equal areas of the Al-rich phase and the Cu-rich phase, so the CCH has two major clumps at the corresponding concentration combinations as expected. The clump representing the Cu-rich phase is outlined in Fig. 19 and the corresponding lamellae centers are outlined in Fig. 20. What is less expected is that the pixels on the boundaries do not accumulate in the CCH as a single band or area between the two major clumps but rather as two bands looping around a sparsely populated area. Figures 21 and 22, and Figs 23 and 24, show that the bands correspond to edge pixels with the Cu-rich phase (lighter phase) on the right or left side, respectively. This correspondence can be explained by the position of the spectrometer measuring the Al x-ray intensity, which is above and to the left of the maps in the figures. In order to reach the detector, the Al x rays from positions along the left side of the aluminum lamellae and below the sample surface must pass through a wedge of a Cu-rich lamella and are attenuated by it. The analogous x rays from the right edge of the Al lamellae pass through only Al-rich material and thus suffer less attenuation.

Figure 25 selects the region between the strips and major clumps, where there is still a noticeable number of pixels that cannot be attributed to noise. Figure 26 shows the x-ray map pixels that correspond to these points and that cluster on discontinuities of the lamellae--where the lamellar boundaries are not vertical. (Extraction of defect lines shown by similar discontinuities in lamellae have been selected automatically from images with a complex algorithm involving mathematical morphological operations.^{7,8}) This finding might be explained again by the position of the Al detector. Pixels on these boundaries represent x rays whose paths are not entirely in either the Cu-rich or Al-rich phases, but are in a combination of both phases. A pixel represents a finite sample area. For a horizontal boundary, a fraction of the x rays would be at-

tenuated along a path in Cu-rich material, and some would not; the pixel value represents the average between the two. Other less common cases, also shown in Fig. 26, are due to lamellar boundaries that slant so that the path of the x rays penetrates varying proportions of the Cu-rich phase.

Conclusions

The CCH promises to be a useful diagnostic tool for detecting inhomogeneities in materials, spotting errors in quantitative corrections of x-ray maps, and evaluating sampling and measurement statistics. The CCH also promises to be useful for selecting phases or features of interest for further analysis. Examples include measuring volume fractions or other properties of sample phases and measuring the degree of diffusion across grain boundaries.

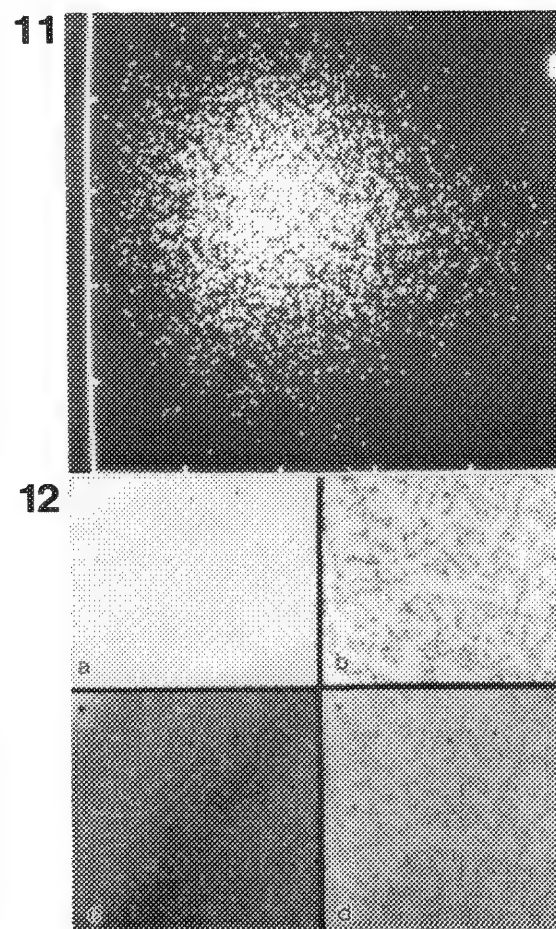
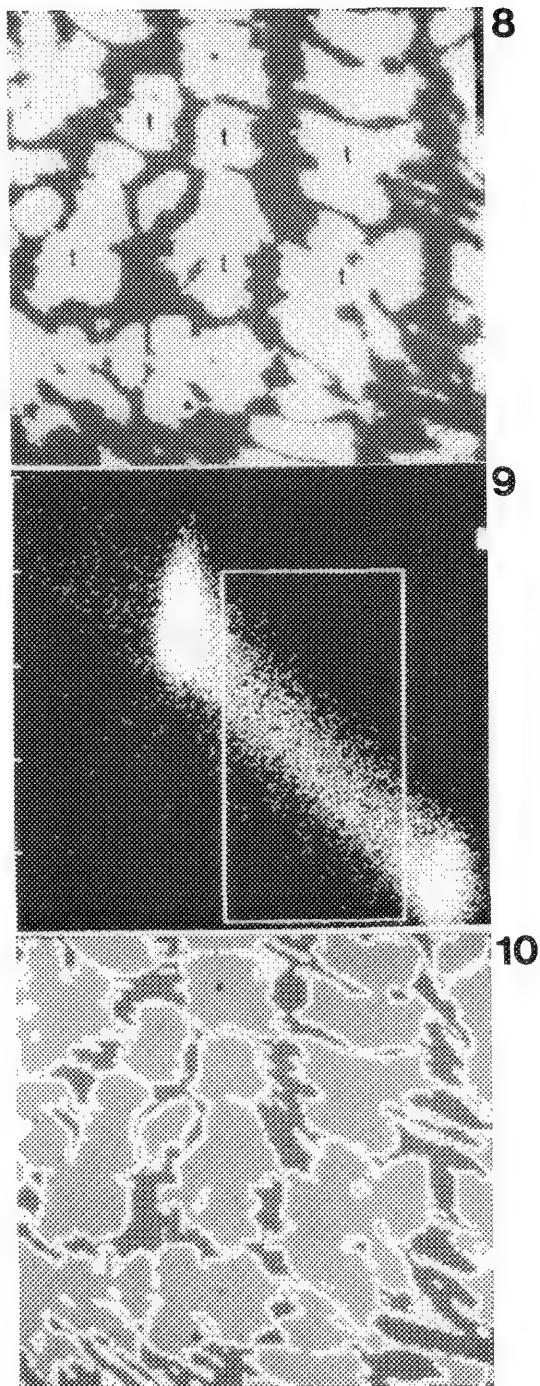


FIG. 11.--CCH for homogeneous Ag 20%-Au 80% alloy. Abscissa, Ag concentration, range 19-23%; ordinate, Au concentration, range 71-90%. Scatter in points due to counting statistics.
 FIG. 12.--(a) Fe map, (b) Ni map, (c) Cr map, (d) color composite (printed in black and white) of steel alloy. (Ni and Cr maps are discussed in text.)

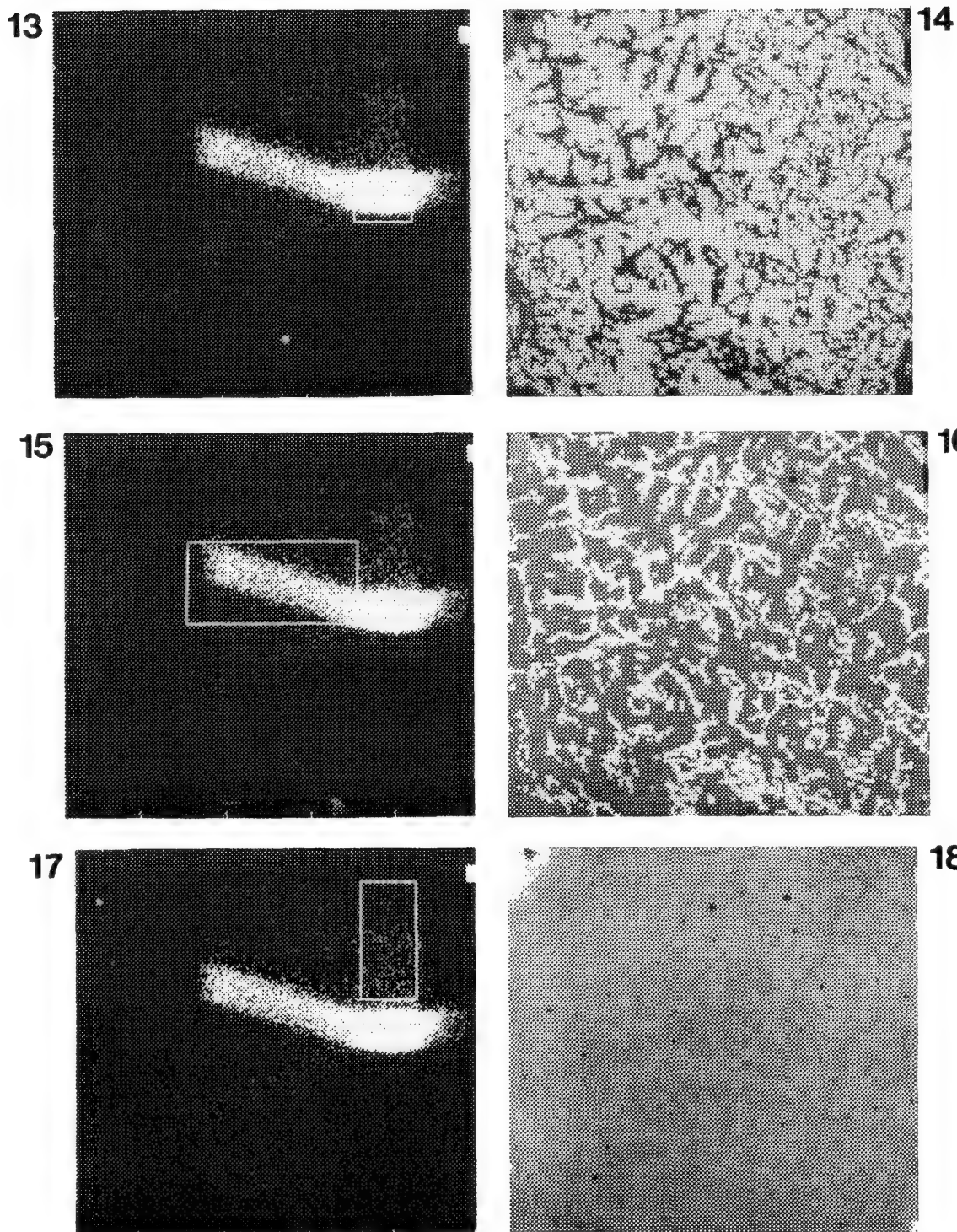


FIG. 13.--CCH for Ni (abscissa, 0-10%) and Cr (ordinate, 0-50%) phases of alloy in Fig. 12. Rectangle outlines major clump.

FIG. 14.--Light-gray pixels of map selected by rectangle in Fig. 13, corresponding to major phase of alloy.

FIG. 15.--Same CCH as Fig. 13 but with rectangle outlining the broad tail to left of major clump.

FIG. 16.--White pixels selected by rectangle in Fig. 15, corresponding to dendritic phase of alloy.

FIG. 17.--Same CCH as 15, but with sparse area above main clump outlined by rectangle.

FIG. 18.--White pixels on Cr map selected by rectangle in Fig. 17. This isolated area of image is anomalously high in Cr, as seen in Fig. 12c.

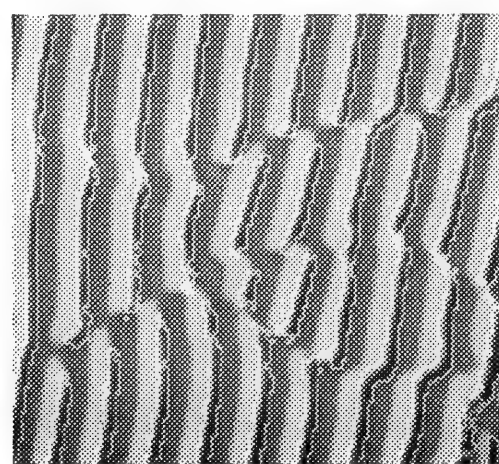
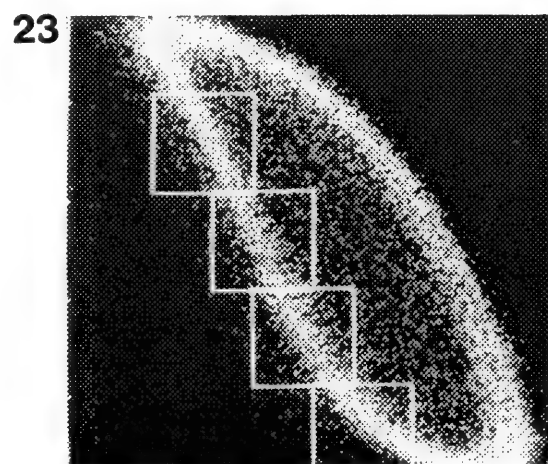
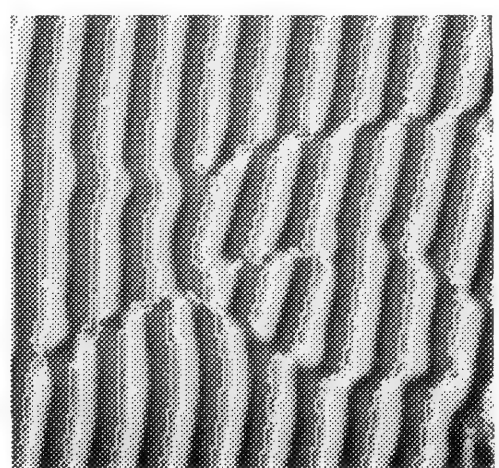
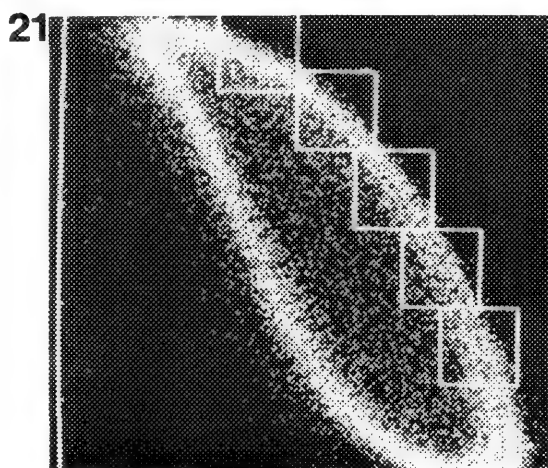
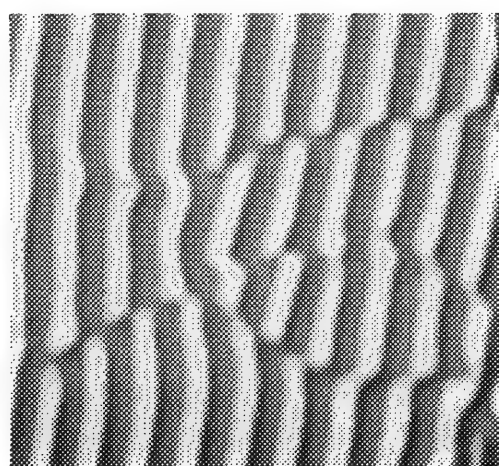
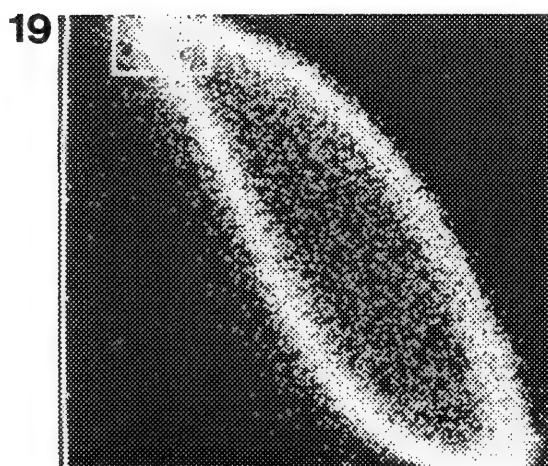
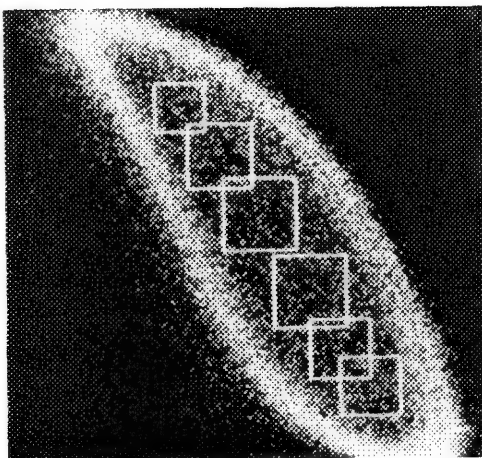


FIG. 19.--CCH of Cu-Al alloy. Abscissa: Al concentration, 52-89%. Ordinate: Cu concentration, 7-51%. Rectangle outlines major clump representing Cu-rich phase.
 FIG. 20.--Black-and-white copy of color composite of x-ray maps for Al-rich lamellae (dark gray) and Cu-rich lamellae (light gray). Regions outlined selected by rectangle in Fig. 19.
 FIG. 21.--Same CCH as Fig. 19, but with rectangles to outline top strip between major clumps. This strip represents pixels with intermediate concentrations, therefore on phase boundaries, and apparently rich in Cu or poor in Al.
 FIG. 22.--Areas outline in white correspond to top strip of Fig. 21. Pixels are on boundaries with Al on left and Cu on right. Al x rays have been attenuated by Cu lamellae.
 FIG. 23.--Analogous CCH to Fig. 21, but with other strip outlined with rectangles.
 FIG. 24.--Analogous to Fig. 22, but this time boundaries with phases on opposite side outlined in white.

25



26

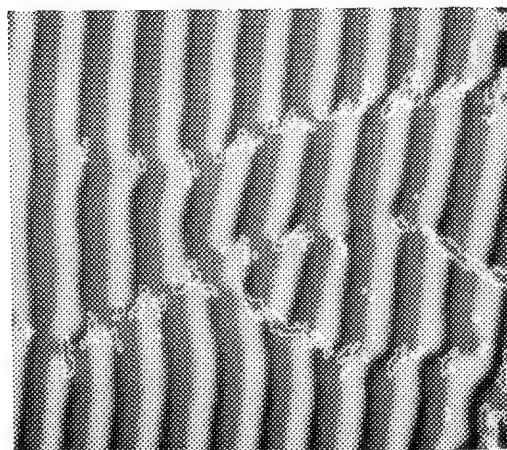


FIG. 25.--Same CCH as Fig. 19, but with rectangles outlining sparse area surrounded by strips and major clumps.

FIG. 26.--Pixels outlined in white correspond to selected points in Fig. 25 that cluster at discontinuities in lamellae.

References

1. R. B. Marinenko et al., "Wavelength-dispersive techniques for compositional mapping in electron-probe microanalysis," *Microbeam Analysis--1985*, 159-162.
2. R. L. Myklebust, D. E. Newbury, R. B. Marinenko, and D. B. Bright, "Defocus modeling for compositional mapping with wavelength-dispersive x-ray spectrometry," *Microbeam Analysis--1986*, 495-497.
3. R. B. Marinenko, R. L. Myklebust, D. B. Bright, and D. E. Newbury, "Digital x-ray compositional mapping with 'standard map' corrections for wavelength dispersive spectrometer defocusing," *J. Microscopy* 145: 207-223, 1987.
4. M. Prutton et al., "Quantitative imaging in the scanning Auger microscope," *Analytical Electron Microscopy--1987*, 304-310.
5. R. Browning, "Materials analysis by scanning Auger microscopy: Why the information crunch is needed," *Analytical Electron Microscopy--1987*, 311-316.
6. D.S. Bright, "A LISP-based image analysis system with applications to microscopy," *J. Microscopy* 148: 51-87, 1987.
7. Jean Serra, *Image Analysis and Mathematical Morphology*, New York: Academic Press, 1982, 410-412.
8. Jean Serra, "Introduction to mathematical morphology," *Computer Vision, Graphics and Image Processing* 35: 283-305, 1986.

USEFULNESS OF VARIOUS COMPUTER ALGORITHMS FOR LOCATING SPOTS AND ARRAYS IN ELECTRON DIFFRACTION PATTERNS

D. S. Bright

Electron diffraction patterns of small polycrystalline particles are routinely obtained by use of the transmission electron microscope in the selected-area diffraction mode. In some cases, several particles contribute to the diffraction image and yield several superimposed diffraction patterns. Automated analysis of these patterns is difficult because of the overlapping diffraction images with complex combinations of rings and spots. The search for regular arrays of spots in the electron diffraction patterns is an image analysis problem with some typical stages: (1) acquire, process, and store the image; (2) segment the image into spots; (3) measure the spot locations; (4) enhance the patterns, or (5) measure line spacings, or (6) find arrays and measure basis vectors. Computer algorithms and methods are recommended for each stage.

Algorithms

1. *Image Acquisition.* The images to be discussed were acquired from photographic negatives with a spot scanner or with a TV camera and light table. To reduce camera and digitization noise, the TV digital images were sums of $256 \times 512 \times 512$ pixel images. The summed pixels, 16 bits each, were truncated to 8 bits. The resulting $512 \times 512 \times 8$ -bit images had sufficient dynamic range to represent the original films.

2. *Isolation of Diffraction Spots.* First the images must be segmented into the diffraction spots and background (everything else). For algorithms in this paper, the objects are assumed to be brighter than the background. The images were not enhanced, but negative images (bright background, dark spots) were inverted to make the diffraction spots bright against a dark background.

The diffraction spots were isolated or enhanced by various means, depending on the nature of the image.

A. *Constant threshold.* The background in some images is constant enough to allow segmentation of the spots from the image simply by choice of a threshold above which any pixel is considered as part of a spot rather than as part of the background. A single threshold was not satisfactory for any of the images used in this paper.

B. *Top-hat filter.* Simply setting a constant threshold is often not sufficient to iso-

late the spots, because any one threshold is appropriate for only a small area of the image. If the spots are all roughly of the same size, or the smallest spot-to-spot separation is greater than the largest spot radius, the spots can be isolated by means of a two-dimensional top-hat filter.¹ (A single application of the top-hat filter is used in an application covered later, Fig. 5b).

C. *Two top-hat filters.* Figure 1a shows a diffraction pattern with two distinct sizes of spots. One threshold setting or one top-hat filter operation is not sufficient to resolve all the spots. Since the top-hat filter is size specific, two applications can be used to separate out the large (Fig. 1b) and small (Fig. 1c) spots. However, the blob-splitting algorithm (E. below), which gives all of the spots as a list (Fig. 1d shows locations), is easier to use because this algorithm does not require "tuning" for size but isolates all the spots at one time. Spots can be selected later on the basis of brightness or size or both.

D. *Gradient.* The gradient (Fig. 2) of a diffraction image (Fig. 1a) highlights the spots by showing the edges, but it is difficult to extract the spot positions from a gradient image. The spots are shown only as outlines, and even though the threshold was carefully selected, the outlines are noisy and sometimes are not continuous. Performances of the gradient (Fig. 3) is worse for an image such as Fig. 5a. Many spots are highlighted, but the gradient image is cluttered with background noise and with the outline of the beam stop (compare with top-hat filter, Fig. 5b).

E. *Blob-splitting algorithm.* The blob-splitting algorithm² has worked for most patterns tried to date. It is especially useful where the background varies widely, the spots do not fall in a few size groups, or the spots have no sharp edges (e.g., Figs. 1c and 4). The algorithm defines objects as brighter areas within a local darker background, and with no internal areas that could themselves be objects.

3. *Localization of Spot Centers.* Once the pixels belonging to spots have been assigned, the coordinates of each spot center are calculated as the intensity weighted averages of the coordinates of the pixels assigned to that spot. For this calculation to be carried out, the spots must be given unique labels, or they must be known to lie within a rectangle with no other spot. The labels are given with our image-processing system by a blob function³ that assigns a common label to pixels that are adjacent to each other; i.e., that are part of

The author is at the Center for Analytical Chemistry, National Bureau of Standards, Gaithersburg, MD 20899.

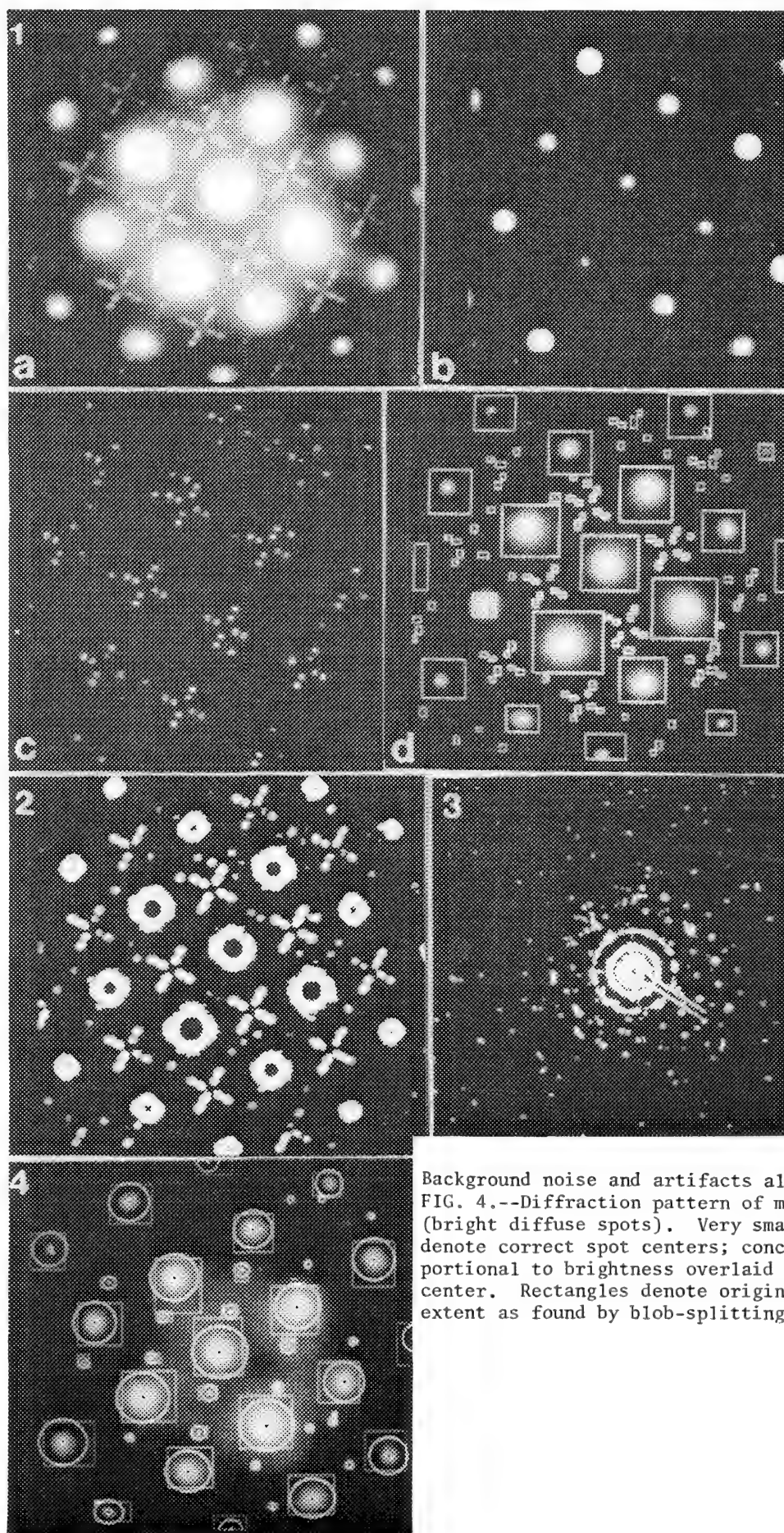


FIG. 1.--Diffraction pattern of metallurgical sample with superlattice reflections; (b) top-hat filtered pattern in (a) with parameters chosen to select large spots; (c) same as Fig. (b) but for small spots; (d) both sizes of spots are found by blob-splitting algorithm, which does not need spot sizes as input. FIG. 2.--Gradient of diffraction pattern in Fig. 1a, thresholded at optimal setting to highlight spots. FIG. 3.--Gradient of diffraction pattern in Fig. 5a, thresholded to highlight most spots.

Background noise and artifacts also highlighted. FIG. 4.--Diffraction pattern of metallurgical sample (bright diffuse spots). Very small black or white dots denote correct spot centers; concentric circle radius proportional to brightness overlaid to help visualize spot center. Rectangles denote original (off-center) spot extent as found by blob-splitting algorithm.

TABLE 1.--Part of list of spots for Fig. 9, for use by basis vector algorithm. Not all decimal places are necessarily significant.

```

...
((TYPE SPOT) (TOL 0) (XY (343.0 197.99)) (INTENS 90) (AREA 75))
((TYPE SPOT) (TOL 0) (XY (276.85 197.3899)) (INTENS 143) (AREA 176))
((TYPE SPOT) (TOL 0) (XY (310.0 249.3999)) (INTENS 149) (AREA 388))
((TYPE SPOT) (TOL 0) (XY (343.0799 249.8999)) (INTENS 160) (AREA 473))
((TYPE SPOT) (TOL 0) (XY (366.35 302.6799)) (INTENS 142) (AREA 606))
((TYPE SPOT) (TOL 0) (XY (342.8099 301.8099)) (INTENS 72) (AREA 55))
...

```

a continuous blob (spot) of pixels.

The center locations measured as averages over the entire spot can be displaced because large "skirt" areas around the spot centers may be included as part of the spots. For example, the asymmetrical nature of the spot skirts (not shown but outlined by rectangles in Fig. 4) throws the spot positions off center. Use of only the brightest 10% of the pixels of a spot determines the correct spot location (small dots in center of spots, Fig. 4), since this approach avoids the asymmetric skirts but still averages a number of pixel locations for more precision: the coordinates are determined to a fraction of a pixel (e.g., Table 1).

4. *Enhancement of Regular Arrays by Convolution.* Convolving the image of the spots with itself forms a two-dimensional Patterson function which is a map of inter-atomic vectors.⁴ The convolution of an image⁵ with a kernel of the size of the image itself is computationally intensive. Convolving with a kernel about the size of a single spot can highlight spots in a narrow size range, but other features in the image are highlighted as well.¹ Use of a kernel between these two size extremes shows promise. Figure 5b shows the spot locations from the top-hat-filtered diffraction pattern of Fig. 5a as a 256 × 256 image of bright spots. Figure 5c, the convolution kernel, is a 64 × 64 pixel region from the upper right quadrant of Fig. 5b. The result of the convolution of Fig. 5b by Fig. 5c is shown in Fig. 5d, where the intensity scale is adjusted to show only the brightest points--the points that show the regular hexagonal pattern in the array. There are still extraneous points; the extraction of the hexagonal pattern is not clean. The basis vector method explained below^{6,7} leaves no extraneous points.

5. *Measure Line Spacings.* The Hough transformers^{8,9} can be used to select lines or a colinear series of spots. A dot in the Hough transform corresponds to a line in the original image. The x coordinate of the dot gives the orientation of the line; the y coordinate, the distance of the line from a point of reference.

The first example is a diffraction pattern, which is best described not in terms of basis vectors and a simple array of spots but as lines, is shown in Fig. 6a, where the diffraction spots fall in lines or streaks. If the spot positions (Fig. 6c) are represented as disks (Fig. 7a), then the Hough transform of the disk pattern can be thresholded (Fig. 7b) to select the vertical row of points in Hough

space where each point corresponds to one of the slanted rows of spots in the original diffraction pattern (Fig. 6a) and the vertical spacing of the Hough spots correspond to the line spacings in the diffraction pattern. The idea and mathematics are similar to the technique of measuring line spacings in transition electron micrographs of replicas of optical diffraction gratings.¹⁰

A second example concerns the small spots in Fig. 1a or c. The larger spots (Fig. 1b) form an array that can be found by the algorithm explained below; the smaller spots do not, but they do lie on regularly spaced lines. The Hough transform of Fig. 1c is shown in Fig. 8. The major spacing (between rows of small spots in the diffraction pattern, Fig. 1a) can be discerned in Fig. 8 as the vertical spacing between the brightest spots.

6. *Find Arrays and Measure Basis Vectors.* Sometimes the sizes of spots can be used to associate them with one array or another as in Fig. 9a. In this pattern, the brighter spots are part of the coarser array but there is an exception; spot D is small and dim, yet part of the coarser array. A more robust method, the basis vector algorithm, does not rely on spot brightness classifications to distinguish between the two arrays in this figure. This algorithm avoids pitfalls resulting from use of only the characteristics of individual spots, by use of the spatial relationships between the spots. It completes the analysis steps presented here by extracting the basis vectors that denote the arrays of spots. Examples for which this method works are the patterns in Figs. 4, 5a, 9, and 10.

With this method it helps to replace the image representation of the data as a large array of pixels by a list of the spot centers and intensities. We retain the images for diagnostic display and illustration only. Table 1 shows part of the list of spots for the diffraction pattern in Fig. 9a.

In Table 1, "xy" denotes the spot center, "intens" the intensity (full range of 0 to 255 units) above the immediate surrounding area, and "area" the number of pixels in the spot (currently not being used by the algorithm). "Type" and "tol" are used internally by the algorithm,⁷ but are not discussed here.

The algorithm searches the list of spots from the entire diffraction pattern for regular arrays of spots that can be described in terms of a pair of basis vectors, and a list of the

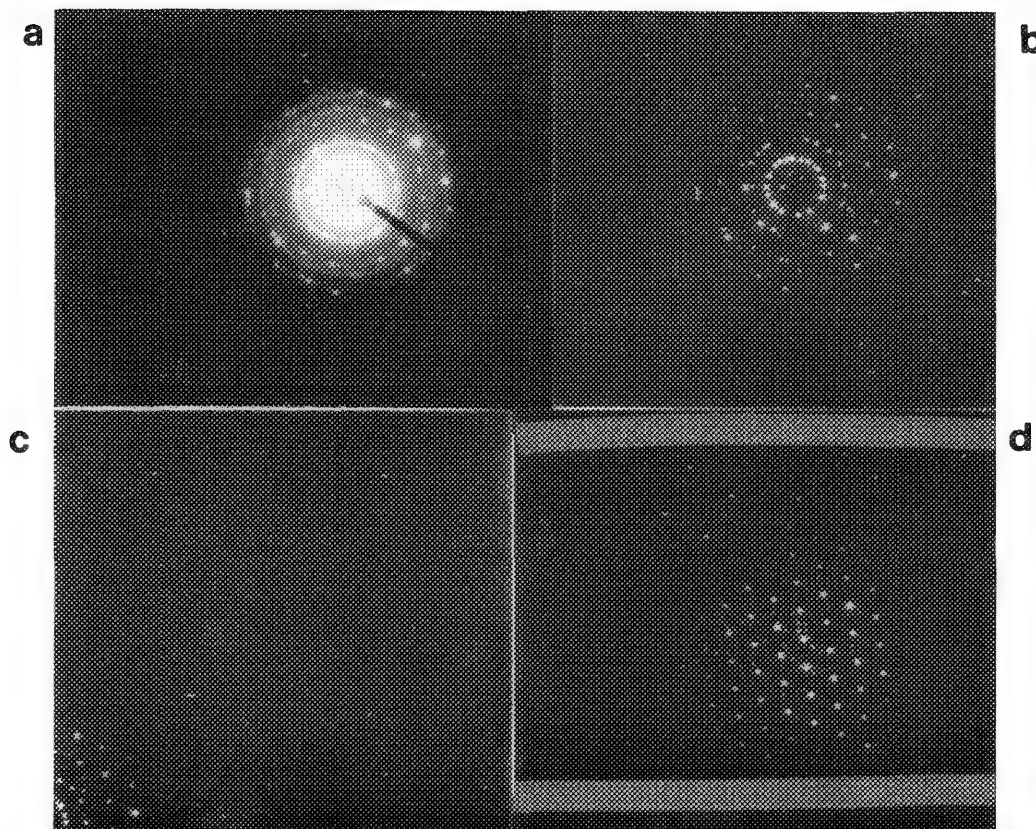


FIG. 5.--(a) Diffraction pattern with large diffuse background, but where spots are approximately of same size and smaller than smallest spot-spot separation; (b) top-hat filter applied to Fig. 5a, with filtered result shown as 256×256 rather than a 512×512 pixel image; (c) selected portion of Fig. 5b, 64×64 pixels; (d) convolution of Fig. 5b by Fig. 5c with contrast adjusted to show only brightest points, with regularities in Fig. 5b enhanced.

associated spots. The details of the basis vector algorithm are in Bright and Steel.^{6,7}

The algorithm is given a minimum amount of information on the nature of the image: the patterns to be found can be described by two basis vectors, there are at least half a dozen spots per pattern, and the spots to check first are the bright ones near the center of the image. The search is controlled by only three parameters that limit the range of search; here are the values for searching Fig. 9a:

```
((*V_TOL_FACTOR* 0.1) (*MAX_BV_LENGTH* 200)
(*MIN_BV_LENGTH* 10))
```

The first is an estimate of the image distortion or error in spot locations. The next two are the minimum and maximum lengths that a basis vector may have. Searches on simple spot patterns do not require the last two parameters, but those on complex patterns do. If reasonable bounds to these parameters are not given, for example, closely spaced spots due to crystal twinning can give erroneously short trial basis vectors, very long search times, and nonsensical results.

In order to determine the basis vectors for each array of spots, the steps of the basis

vector algorithm are: (A) Search for a starting spot from which two trial basis vectors can be found; (B) search over the entire diffraction pattern for other spots in the array that can be reached by the trial basis vectors and collect the spots; (C) give final values for the basis vectors as averages of the spot-to-spot displacements for adjacent spots over the entire array; and (D) repeat steps A-C until all spots have been tried.

A. To start the search for an array of spots, a bright spot near the center of the pattern is chosen as a likely candidate for being part of a regular array. If a few spots nearby are found that are regularly spaced with the first spot, trial basis vectors are determined (Fig. 10a) and from them, a search pattern is constructed (upper left, Fig. 10b). If no trial basis vectors can be found, other starting spots are tried, in turn. One carries out the search here by scanning a list of spots, calculating distances and directions, and comparing them with other distances and directions. One does not search by determining a distance and direction from one spot, and then looking at pixels in the original image near this location to try and determine whether a spot exists there.

B. Once the search pattern is found, one collects spots in the array by starting at

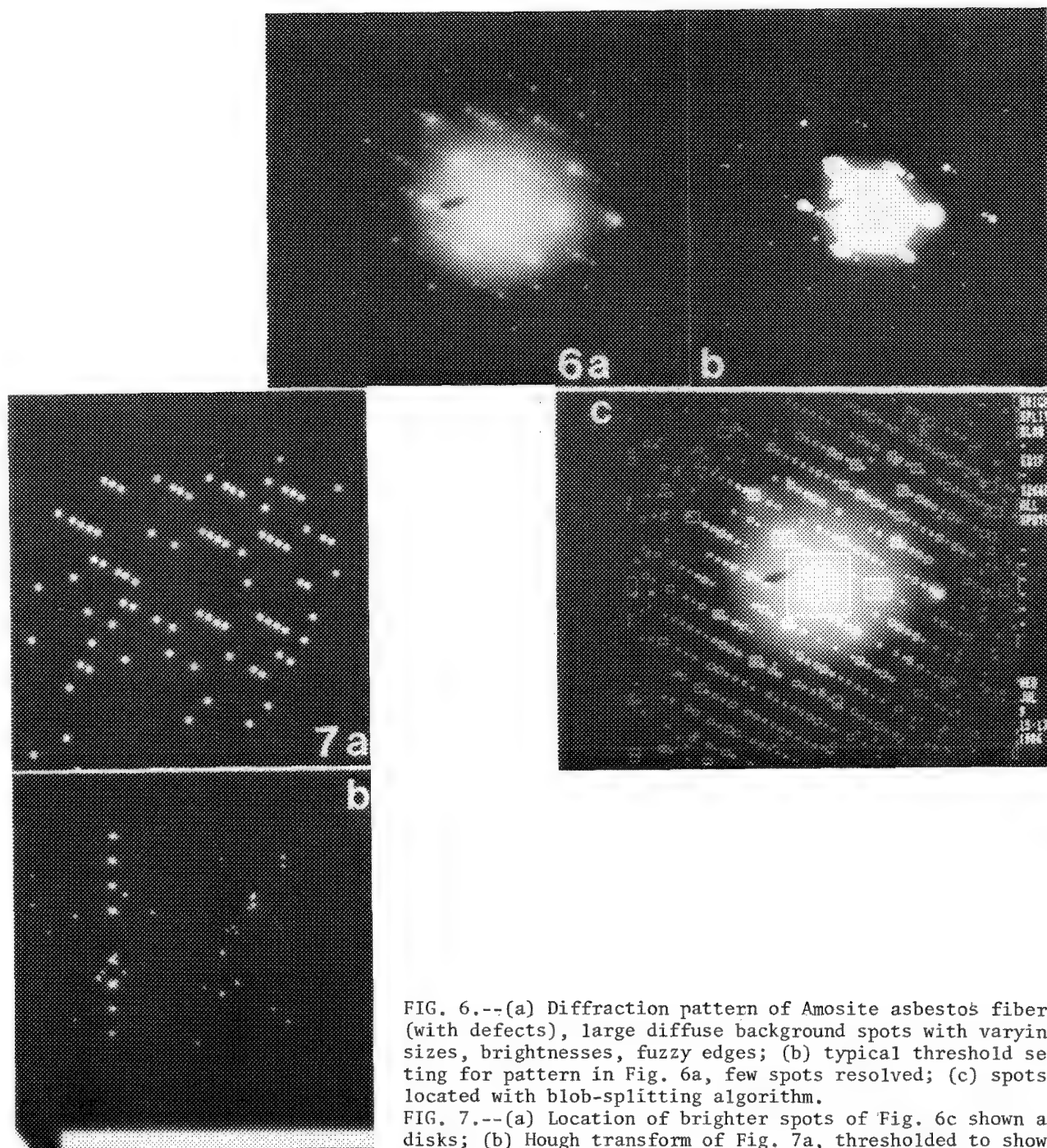


FIG. 6.--(a) Diffraction pattern of Amosite asbestos fiber (with defects), large diffuse background spots with varying sizes, brightnesses, fuzzy edges; (b) typical threshold setting for pattern in Fig. 6a, few spots resolved; (c) spots located with blob-splitting algorithm.

FIG. 7.--(a) Location of brighter spots of Fig. 6c shown as disks; (b) Hough transform of Fig. 7a, thresholded to show only brightest spots, which correspond to lines of spots in Fig. 6a.

the initial spot (that resulted in the trial basis vectors and search pattern) and looking in all the appropriate directions for the presence of another spot. If such a spot is found, the same search pattern is again applied to this spot, and so on, until the list of spots is exhausted. Figures 10b-d illustrate this collection procedure.

C. After the spots in the regular array have been collected, a more accurate determination of the basis vectors is made by averaging all of the instances of these vectors that occur between the spots in the array (Fig. 11).

D. If all of the spots in the original image have not been accounted for as being a rejected starting spot, or as part of an array already collected, the list is searched again with a new starting spot for an occurrence of another array of spots. Figure 9b shows instances where two overlapping arrays of spots were found. Note that the algorithm was given no other information than the three parameters mentioned above. Since choice of these parameters is not critical and can be approximated by prior knowledge of experimental conditions, this algorithm is suitable for automating

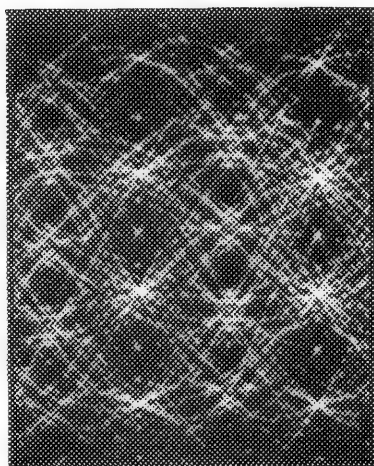
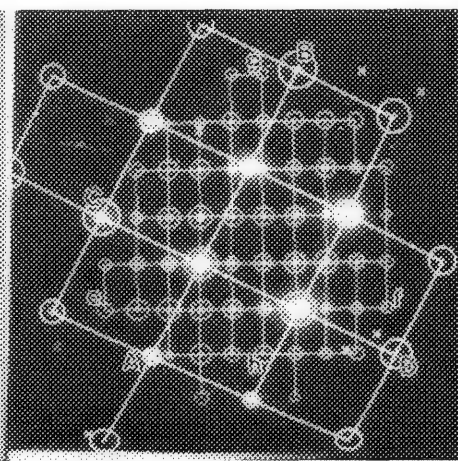
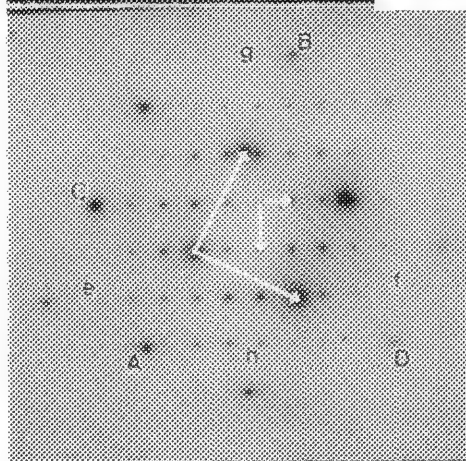


FIG. 8.--Hough transform of Fig. 1c (actually transform of image with all spots of Figs. 1c and 1b represented as small disks).
FIG. 9.--Diffraction pattern of pyroxene mineral sample (thin section), spots and basis vectors marked (see Table 3); (b) lines and circles depicting arrays of Fig. 9a (diffraction pattern inverted in background, see Table 3), spots marked.

8

9a

b



initial stages of the analysis of diffraction patterns^{11,12} that are normally done by hand.

The basis vector algorithm starts with lists of spots and finishes with the spots grouped into arrays and the associated basis vectors, and a list of rejected spots. Table 2 shows part of the result used to generate Fig. 9b. This result is in LISP⁵ association-list form, where the items are grouped together by name. The main list, "av bvp," is a pair of averaged basis vectors and associated information. The items in the list include the averaged basis vectors as coordinate pairs and the statistics associated with each, the original trial basis vectors used to find the spots, and finally a list of the spots in the array. One diffraction pattern may result in two or more such lists, one for each array. The above list was from the coarse array of spots shown in Fig. 9a (long arrows). The labels are for comparison with measurements taken by hand (Table 3). The hand measurements were made by moving a cursor on the digitized image to the visual spot centers. The spots used are labeled with letters in Fig. 9a and b. The directed line segments A-B and C-D (Fig. 9b) were divided by three, for example, to get visual estimates of the coarse basis vectors. The results in Table 3 are in pixel units, where the image is 512 pixels on an edge.

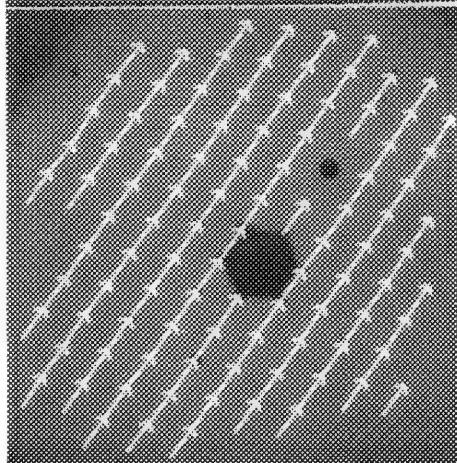
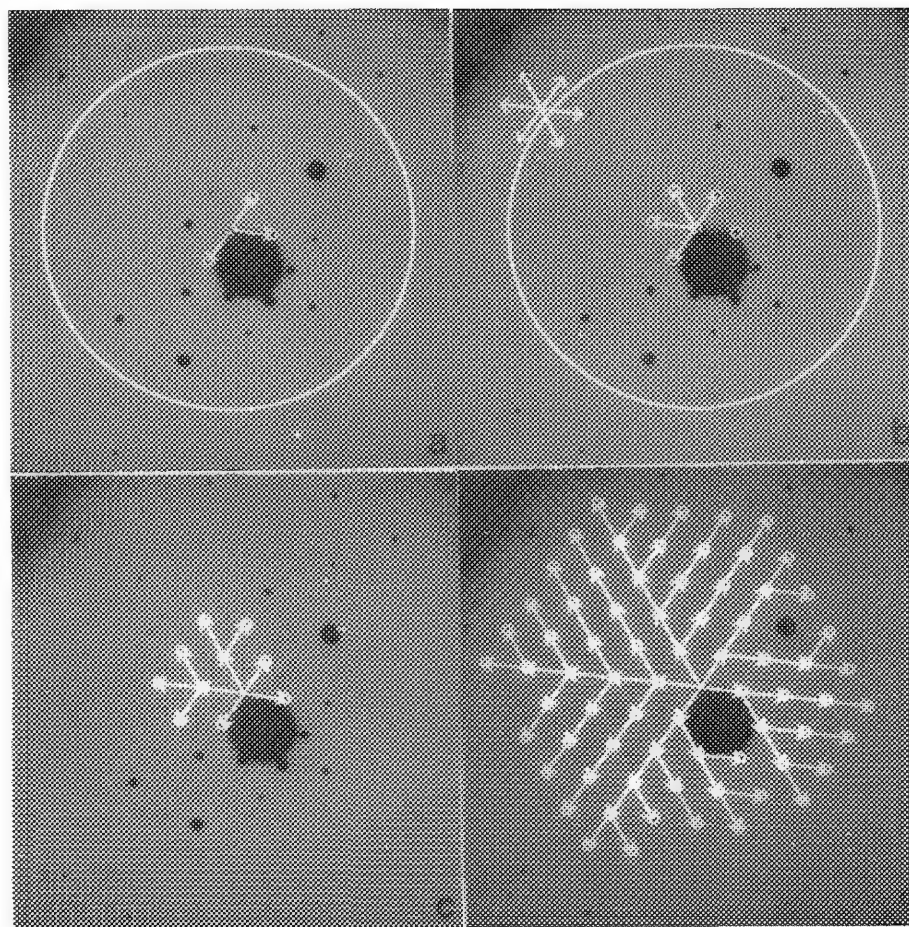
The more familiar hand measurements correspond well with the results of the basis vector algorithm. The algorithm results should be more accurate because the precision of the spot centers is greater (averaged over many pixel locations rather than just a cursor position which must be at a particular pixel), and more vectors (in the sense of Fig. 11) are averaged together.

Conclusion

Image analysis algorithms have been presented to search for arrays of spots in electron diffraction patterns. Image processing algorithms that work at the pixel-by-pixel level representation of the image are used for the earlier stages of the problem; algorithms based on more abstract information are used for the final stages.

References

1. D. S. Bright and E. B. Steel, "Two dimensional top hat filter for extracting spots and spheres from images," *J. Microscopy* 146: 191-200, 1987.
2. D. S. Bright, "An object finder based on multiple thresholds, connectivity and internal structure," *Microbeam Analysis--1987*, 290-292.
3. D. S. Bright, "A LISP-based image



11

FIG. 10.--(a) Trial basis vectors for hexagonal diffraction pattern (background image) of Zambian Crocidolite asbestos; (b) search pattern (upper left) from trial basis vectors in Fig. 10a, and beginning of search tree (center) for spot array; (c) subsequent stage for search tree shown in Fig. 10b; (d) advanced stages of search tree of previous two figures, with lighter arrows showing steps analogous to Fig. 10c, for all peripheral spots (bright arrows and circles).

FIG. 11.--All instances of one basis vector, all averaged (length and direction) for final value.

analysis system with applications to microscopy," *J. Microscopy* 148(Pt. 1): 51-87, 1987.

4. G. Y. Fan and J. M. Cowley, "Auto-correlation analysis of high-resolution micrographs of near-amorphous thin films," *Proc. 43rd Ann. Meet. EMSA*, 1985, 60-61.

5. R. C. Gonzalez and P. Wintz, *Digital Image Processing*, 2nd ed., Reading, Mass.: Addison-Wesley, 1987, 187.

6. D. S. Bright and E. B. Steel, "Automated method for analyzing images containing electron diffraction spots," *Microbeam Analysis--1985*, 163-165.

7. D. S. Bright and E. B. Steel, "Automated analysis of regular spot patterns in electron diffraction images," *J. Microscopy* (in press).

8. C. R. Dyer, "Gauge inspection using Hough transforms," *IEEE Trans. PAMI*-5: 621-623, 1983.

9. R. O. Duda and P. E. Hart, "Use of the Hough transformation to detect lines in curves in pictures," *Comm. Assoc. Comp. Mach.* 15: 11-15, 1972.

10. D. S. Bright and E. B. Steel, "STEM calibration by analysis of Hough transformed

TABLE 2.--Part of description of one array in Fig. 9b, as given by basis vector algorithm. Not all decimal places are necessarily significant.

```
((AV BVP
  ((TYPE VECTOR) (XY (104.6307 -51.2053)) (TOL 11.64885)
  (X STATS
    (MEAN 104.6307) (COUNT 13) (STD_DEV 1.3451) (MEDIAN 104.9001)
    (MAX 106.19) (MIN 100.6799)))
  (Y STATS
    (MEAN -51.2053) (COUNT 13) (STD_DEV 0.778955) (MEDIAN -51.5301)
    (MAX -49.6898) (MIN -52.21)))
  ((TYPE VECTOR) (XY (51.08232 105.7215)) (TOL 11 74156)
  (X STATS
    (MEAN 51.08232) (COUNT 13) (STD_DEV 1.450989) (MEDIAN 51.4001)
    (MAX 53.02011) (MIN 47.32999)))
  (Y STATS
    (MEAN 105.7215) (COUNT 13) (STD_DEV 0.688155) (MEDIAN 105.8498)
    (MAX 106.63) (MIN 103.9299))))
(BVP
  ((TYPE VECTOR) (XY (105.0101 -51.66)) (TOL 11.70293))
  ((TYPE VECTOR) (XY (49.60989 106.0899)) (TOL 11.71163)))
(SPOTS
  ((TYPE SPOT) (TOL 0) (XY (368.4299 38.59999)) (INTENS 32) (AREA 610))
  ((TYPE SPOT) (TOL 0) (XY (419.5198 144.6199)) (INTENS 81) (AREA 904))
  ((TYPE SPOT) (TOL 0) (XY (3.99 350.07)) (INTENS 36) (AREA 935))
  ((TYPE SPOT) (TOL 0) (XY (105.8798 36.88999)) (INTENS 32) (AREA 703))
  ...
```

TABLE 3.--Basis vectors for Fig. 9: lengths in pixels \pm sample standard deviation; ** lengths in pixels of lines A-B, C-D, e-f, and g-h (Fig. 9b) divided by 3, 3, 10, and 6, respectively.

Coarse Array - 18 spots			
	Computer Algorithm * 13 vectors averaged	Hand Measurement **	
x1	51.1 \pm 1.5	51.7	A-B
y1	105.7 \pm 0.7	106.3	A-B
x2	104.6 \pm 1.3	105.3	C-D
y2	-51.2 \pm 0.8	-51.3	C-D
Fine Array - 55 spots			
	Computer Algorithm * 44 vectors averaged	Hand Measurement **	
x1	33.4 \pm 0.8	33.4	e-f
y1	0.4 \pm 0.2	0.4	e-f
x2	0.4 \pm 0.8	0.3	g-h
y2	-51.7 \pm 0.3	-51.6	g-h

images of optical grating replicas," *Microbeam Analysis--1985*, 155-158.

11. M. J. Carr, "A technique for computer-assisted acquisition and analysis of electron diffraction patterns," *Analytical Electron Microscopy--1981*.

12. M. Tokiwai et al., "Automatic computer analysis of electron diffraction patterns," *JEOL News* 21E(2): 2-6, 1983.

THE INTEGRATION OF X-RAY ANALYSIS AND DIGITAL IMAGE PROCESSING INTO A SCANNING ELECTRON MICROSCOPE

G. S. Fritz and F. H. Schamber

During the past 15 years, there has been a concerted effort to automate various functions of the scanning electron microscope (SEM) and its sister instrument the electron microscope. In the early years, this effort was primarily confined to x-ray microanalysis and included the mechanical automation of the stage, wavelength spectrometers, and beam current monitoring.^{1,2} As the years progressed, the level of automation expanded to meet the needs of developing applications and has come to include such functions as image acquisition and analysis.³⁻⁶ All these applications were usually addressed with "add-ons" to existing SEMs. More recent additions to the conventional SEM have commonly become more sophisticated than the microscopes themselves and have included the latest computer and digital electronics in their designs. The "add-on" philosophy has been pushed to the limit as the applications for these hybrid systems have become more demanding. In fact, in many of these systems, normal SEM functions and hardware are duplicated, for example in the inclusion of scan generators into many of the microanalysis systems. In other instances, many of the advanced microscopes containing microprocessors for control do not allow functions of the microscope to be accessed efficiently or accessed at all from computers controlling an application that involves multiple technologies. The next step in the evolution of the electron microscope is thus to combine these technologies into one instrument. Advantages in user friendliness and ease of operation by unification of these subsystems to include the use of one console and keyboard. However, to realize the full potential of such an integrated system requires a re-evaluation of the traditional SEM architecture.

System Design and Description

In designing an integrated system, many aspects of both hardware and software must be evaluated in light of the ultimate needs of the analyst. The system to be described has essentially been designed as an analytical work station which combines all the technologies previously located in various instruments into a single package.

In developing an integrated system, one must take a close look at the design of the chamber and associated detectors. Since this microscope has been designed as an analytical work station, getting microanalysis data along with

image data is of prime concern. In this instrument, the energy-dispersive x-ray spectrometer (EDS) detector and optional wavelength spectrometers (WDS) have been designed to have a high take-off angle (40°) and a short working distance (24 mm). The EDS detector has also been designed to share a common port with the secondary electron detector, so that both look at the sample in a colinear geometry. When the bias voltage of the secondary electron detector is turned off, this configuration may be used as a "gun sight" to image the exact same features that the EDS detector is "seeing," which allows the correlation of x-ray data and image data on samples with rough surfaces.

In the basic electronic and software configuration (Fig. 1), all of the several subsystems are controlled by one central processor, in this case a Motorola 68020. These subsystems (which have their own microprocessors) in turn take care of the lower-level hardware functions such as controlling motor movements or vacuum logic. All the hardware in the system has been designed to be accessible and monitored via software in the central processor. This type of software control at a central location realizes many advantages when one is creating an integrated system. These advantages can be best highlighted as we examine the several subsystems of the instrument.

One of the main features of the instrument is a six-axis computer eucentric stage. The motors for this stage are incorporated within the vacuum system, which reduces mechanical complexity, increases speed and precision of motion, and eliminates vacuum feedthroughs. By coordinating the control of the axes via microprocessors, one can achieve complex orientations while retaining a feature within a field of view. Since the host computer has complete access to the stage, the system can automatically change the focus of the objective lens to keep features in focus when the sample height is changed as the z axis of the stage is moved.

Another feature of the microscope is an automated anode that allows the spacing between the Wehnelt electrode and the anode to be optimized for whatever accelerating voltage is selected. As a result, the microscope is able to perform optimally over the complete accelerating voltage range when the voltage is selected from an automated sequence.

The system is equipped with an automated aperture, which adds another option that can be controlled by the central computer. As a result, application software can select different apertures for different portions of

The authors are with Tracor Electron Beam Instruments, 2305 Parview Road, Middleton, WI 53562-2697.

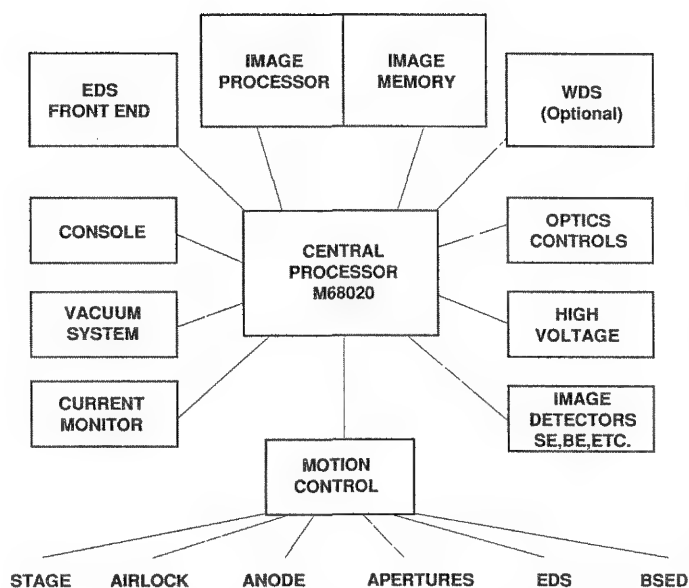


FIG. 1.--Basic architecture of an integrated electron microscope.

automated analyses. For example, one aperture could be used to obtain the desired image information and another used to obtain x-ray information. Having an automated aperture also allows the computer to assist in the alignment of the apertures.

At the basic heart of the instrument is the integrated digital image processor. Since the image processor is not an "add-on," many advantages are realized. A very fundamental advantage is the total elimination of "scan flicker" at moderate and slow scan rates, since the viewed image is displayed from the computer's memory and refreshed at 60 times a second. The same advantage allows the microscope to be used in normal lighting and thus removes a serious environmental restriction on SEM usage.

The image processor also provides frame-by-frame averaging (Kalman and exponential), by which the entire image is formed during the first frame and merely improved in signal-to-noise ratio as additional frames are averaged. This type of frame averaging results in less charging and specimen damage for beam-sensitive samples, since the beam does not dwell at any one point of the specimen for any length of time. Frame averaging also averages out certain transient image artifacts, which show up on some samples at conventional slow-raster rates (e.g., when insulating materials or uncoated specimens are imaged). As a result of the integrated design, the same averaging can be made to start and stop automatically when any instrument parameter such as focus, magnification, or stage position is altered by the user. This feature results in the image quality automatically improving when all adjustments by the user or automated functions have been completed.

Once an image has been acquired by the system, a number of new capabilities are achieved with the integrated image processor. Images

can be enhanced digitally and/or features analyzed for size, shape, brightness levels, etc. Images, along with all the conditions under which they were collected (beam current, accelerating voltage, stage positions, etc.) can be stored to disk for retrieval at a later time. Since images may be stored to disk, the operator is freed up from photographing every shot that might be of interest to the recipient of the data. Selected images may then be photographed at a later time with a digital color camera integrated into the system.

X-ray microanalysis systems have become very common accessories on SEMs. To obtain acceptable analytical results in traditional instruments, the analyst must tell the EDS system the current microscope operating parameters. With the architecture used in this system, all the operating parameters are automatically recorded with each x-ray spectrum, including beam current, stage and beam position, accelerating voltage, and take-off angle. The take-off angle can be automatically calculated for the user since the system knows the position of the EDS detector, the working distance, and the bank and tilt of the stage. The beam current is obtained with a fast-acting Faraday-cup device designed into the system, which monitors the beam current in conjunction with a computer-controlled current monitor.

Included in the system is a motorized device for inserting and retracting an annular solid-state backscatter electron (BSE) detector. The BSE detector may be retracted automatically to protect it when not in use and provide more freedom of movement for the sample. Furthermore, the insertion and retraction process are coupled with both the stage and the EDS detector controllers in such a manner that the stage and EDS detectors are moved out of the way automatically and then returned to their original positions, if possible, after the BSE detector has finished moving.

As a result of the integration of all aspects of the instrument under a single main processor, the instrument is capable of "beam on demand." This feature automatically unblanks the beam when any type of acquisition is to be performed, including an image of x-ray data. Once the data collection has been completed the beam is automatically blanked from the specimen. This approach protects sensitive samples from beam damage and contamination. The integration also allows the user to simply point at a feature in a stored image and have an entire x-ray analysis performed at that point.

The real power of a system integrated under the control of one processor is realized when applications are addressed. One such application is the automatic analysis of particulates or complex features. In this application, the system is capable of moving the stage from one field to the next, focusing the image, adjusting the contrast and brightness, locating and

sizing features, and performing chemical analyses on the features all automatically. The system can also monitor and adjust the beam current to keep image quality the same during the entire analysis.

By having one computer control the entire system, the user can also write program sequences or schedules to perform a variety of operations over and over. These schedules can even be learned by performing the sequence once manually, which allows even the novice operator to program the instrument. All aspects of the instrument may be controlled, including functions such as setting the voltage, autofocusing, auto contrast and brightness, stage and beam motions, aperture selection, and image or x-ray acquisitions. Other functions considered to be analysis routines may also be executed from a schedule including image enhancement, image analysis, and x-ray analysis. Storage of all data to disk is also possible from a schedule.

Summary

A computer-based system has been described which merges an electron microscope, x-ray analyzer, and image processor into a single instrument. All the hardware of this system has been designed to be accessible to the software of the central processor. Because it has a software environment, the instrument can continue to evolve and be refined to meet the expanding needs of developing applications.

References

1. W. F. Chambers, *SANDIA-TASK '78: An Electron Microprobe Automation Program*, SAND78, 1149, 1978.
2. W. F. Chambers and J. H. Doyle, "A user-oriented software system for electron microprobes," *Microbeam Analysis--1979*, 279-280.
3. J. J. McCarthy, G. S. Fritz, and R. J. Lee, "Acquisition, storage, and display of video and x-ray images," *Microbeam Analysis--1981*, 30-34.
4. R. J. Lee, J. S. Walker, and J. M. McCarthy, "Microimaging: A link between microscope, image analysis, and image processing," *Microbeam Analysis--1985*, 153-154.
5. G. S. Fritz, J. J. McCarthy, and R. J. Lee, "Interactive software for automated particulate analysis," *Microbeam Analysis--1981*, 57-60.
6. G. S. Fritz and A. T. Laudate, "Automated measurements of integrated circuit linewidths," *Microbeam Analysis--1983*, 1-4.

APPLICATION OF WAVELENGTH-DISPERSIVE DIGITAL COMPOSITIONAL
MAPPING TO HIGH-TEMPERATURE SUPERCONDUCTORS

R. B. Marinenko, D. E. Newbury, D. S. Bright, R. L. Myklebust, and J. E. Blendell

The new high- T_c superconductors are advanced ceramic materials prepared from oxide powders which are pressed and sintered. Their physical properties depend on the microstructure, which in turn depends strongly on the processing sequence used in their production. We have used wavelength-dispersive (WDS) x-ray compositional mapping to study the microstructure of the $\text{Ba}_2\text{YCu}_3\text{O}_{6+x}$ ceramics being produced at the National Bureau of Standards so as to understand better the processing procedures and the resulting physical properties.

Experimental

The Cameca electron microprobe used in this work is equipped with three spectrometers, a standard Tracor Northern TN-2000 analyzer, and a TN-1310 automation system.* The instrument automation includes a PDP-11/34 computer, which is configured with 48K words of memory, including memory management.

The WDS digital x-ray maps were obtained with the Tracor Northern XIP program and the accompanying Tracor Northern WDS module, which were modified in our laboratory to take counts directly from the WDS scalers at each pixel in the map.¹ Maps from the three spectrometers can be acquired simultaneously and are then transferred from disk to a Digital Equipment Corp. VAX 11/780 computer, where the data are separated into individual maps for each spectrometer, and each pixel (after background and dead-time corrections are made) is quantitated with the NBS matrix correction procedure FRAME.² The maps are displayed on an IP 8400 DeAnza Image Analysis System.

The maps described here were prepared from the Ba $L\alpha$ line on the PET crystal of the inclined spectrometer, the Cu $K\alpha$ line on the LiF crystal, and the Y $L\alpha$ line on the TAP crystal

of the vertical spectrometers. All maps were 128×128 pixels and the excitation potential was 20 kV. Constant current was maintained with the beam-current regulator. The quantitative program uses a background correction based on the average atomic number of the pixel being quantitated.³ The defocus modeling procedure was used for maps below $2000\times$ magnification; at magnifications above $2000\times$, data from point-beam analyses of the standards were used to correct the entire map, since no obvious defocus correction was needed. For the quantitative calculations, pure element standards were used for copper and yttrium, and a glass standard, K-309, containing more than 13 wt% barium (plus the elements silicon, aluminum, calcium, iron, and oxygen) was used as the barium standard. The weight percent of oxygen was calculated on the assumption that it was stoichiometrically related to the other elements. Ba and Cu were assigned valences of +2, and Y a valence of +3. These were valid assumptions for the calculation of oxygen, because for most pixels the total composition from the three analyzed elements plus oxygen was close to 100% with deviations generally not more than $\pm 2-3\%$. Maps of the oxygen concentration distribution calculated in this way were useful in identifying the compositions of the phases. A direct concentration determination of oxygen would be preferred since a variation in the Cu valence is known to exist but can be done with EPMA only if absorption corrections are improved.

The bulk specimens were prepared from a mixture of powders of BaCO_3 , Y_2O_3 , and CuO , which was pressed into large pellets and reacted at 900 C for 24 h. These pellets were ground, re-pressed, and heated at 900 C again for at least 24 h. Then these samples were milled in acetone, dried in air, pressed into disks again, and sintered under a variety of conditions. The thin films were formed by simultaneously RF sputtering of the three oxides onto a substrate, followed by annealing at temperatures below 950 C.

Results

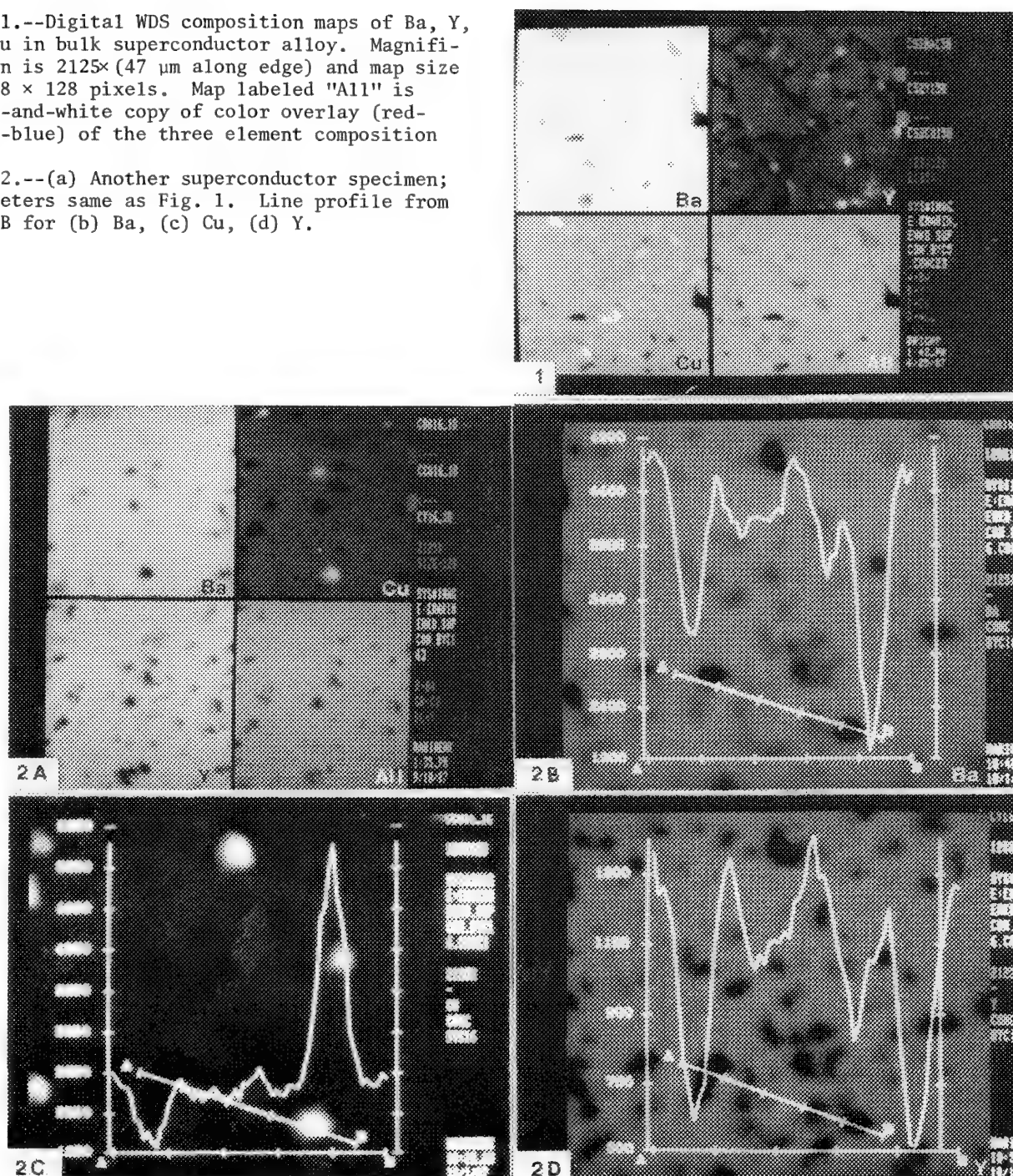
Quantitative maps of one of the first superconductor specimens we studied are in Fig. 1. These maps were taken at a magnification of $2125\times$, which corresponds to $47 \mu\text{m}$ along an edge. The yttrium map in this case was acquired from the $L\alpha$ line on the PET crystal instead of the TAP crystal, which was used in all subsequent maps. The individual element maps in Fig. 1 are displayed with a gray-level scale, with the absence of an element shown in black and the maximum abundance of that

R. B. Marinenko, D. E. Newbury, D. S. Bright, and R. L. Myklebust are at the Center for Analytical Chemistry, and J. E. Blendell is at the Institute for Materials Science and Engineering, National Bureau of Standards, Gaithersburg, MD 20899. They thank L. Stearns for her work on the preparation of the sinter-forged specimen and K. Kreider for providing the thin-film specimen.

*Certain commercial equipment, instruments, or materials are identified in this paper to specify adequately the experimental procedure. Such identification does not imply recommendation or endorsement by the National Bureau of Standards, nor does it imply that the materials or equipment identified are necessarily the best available for the purpose.

FIG. 1.--Digital WDS composition maps of Ba, Y, and Cu in bulk superconductor alloy. Magnification is 2125 \times (47 μ m along edge) and map size is 128 \times 128 pixels. Map labeled "All" is black-and-white copy of color overlay (red-green-blue) of the three element composition maps.

FIG. 2.--(a) Another superconductor specimen; parameters same as Fig. 1. Line profile from A to B for (b) Ba, (c) Cu, (d) Y.

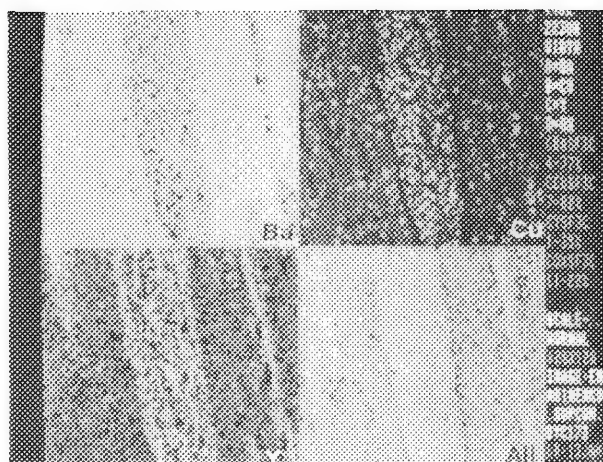


element, white. The map to the lower right (labeled "All") is a black-and-white copy of a color overlay map in which each is displayed as one of the three primary colors--red, green, or blue. Distinct phases can be identified in the original color composite map, and to some extent these phases can be seen in the black-and-white copy here; but one should not use gray-level relationships to interpret this map quantitatively.

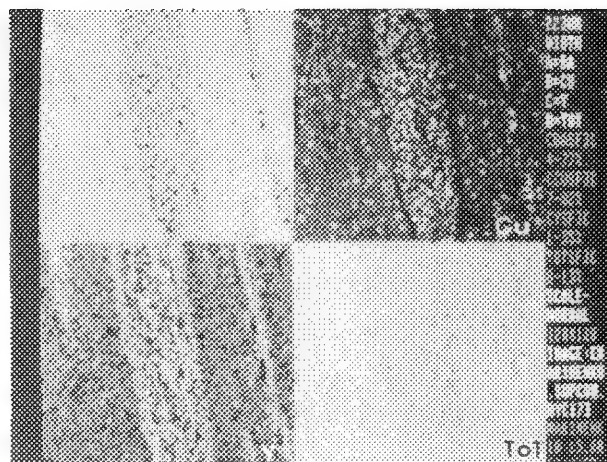
This superconductor specimen is obviously not homogeneous, and many voids, of pores, are present. The pores can be identified by the presence of corresponding black areas in all

four images. Pores in bulk specimens such as this one are an asset in the production of the superconducting phase as they allow more oxygen into the specimen during sintering. Excess oxygen is needed in the formation of this superconducting phase.

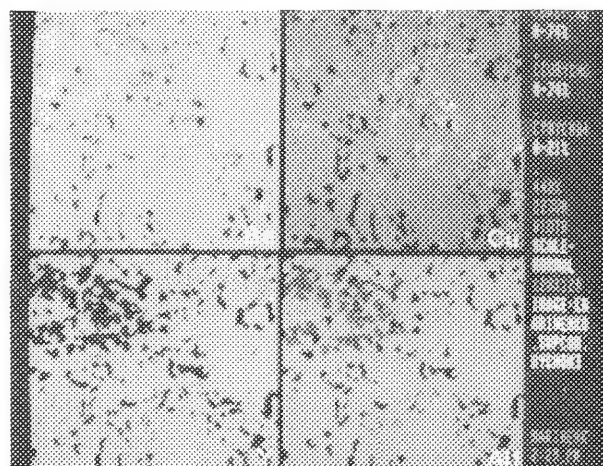
The presence of other phases cannot be attributed to unreacted material because the grain sizes of these other phases are 5 times larger than those in the starting powder. Their presence is attributed to some unexpected melting, during sintering, which results in segregation.⁴ These segregated phases have been identified from the phase diagram.⁵ One



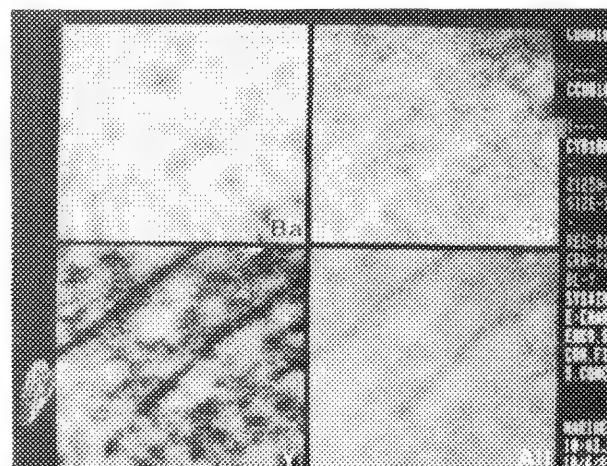
3A



3B



4



5

FIG. 3.--(a) Sinter-forged superconductor specimen. Magnification is 448 \times (223 μ m along edge); map size is 128 \times 128 pixels. Map labeled "All" is a red-green-blue overlay of the three maps. (b) Same as (a) but lower right map is total map obtained compositions of barium, copper, yttrium, and oxygen (calculated from stoichiometry) are added at each pixel.

FIG. 4.--Another superconductor specimen; parameters same as Fig. 3(a).

FIG. 5.--A 1 μ m thin-film specimen; parameters same as in Fig. 1.

might be a combination of CuO and BaCuO₂; another, called the "green" phase, is BaY₂CuO₅. Details of the identification of these phases can be found in Ref. 4.

In Fig. 2 are the element maps for another superconductor specimen, also taken at 2125 magnification. Figures 2b-d are line profiles of each of the element maps from point A to point B. Such profiles can be made between any two pixels on these concentration maps. They are very useful for the identification of phases, since the weight percent concentration can be read off the left vertical axis (100 wt% is equal to 10 000 units on the y-axis).

In an effort to increase critical current density of the Ba₂YCu₃O_{6+x} superconductor, sinter-forging was used to achieve texturing in the final product. The result was an alignment of elongated grains (Fig. 3). These maps were taken at a 448 \times magnification, which corresponds to 223 μ m on an edge. This specimen has some porosity and a multitude of small inclusions. The yttrium-rich BaY₂CuO₅ and some of the copper-rich (partly CuO) inclusions are

located in the dark "bands" that run perpendicular to the stress axis and parallel to the elongation direction. Most of the barium-rich inclusions (BaCuO₂) are in the lighter (superconductor) matrix region. Two or three other phases have been identified in this specimen.

In Fig. 4 are the maps of a recent specimen which was expected to be more homogeneous than the previous samples. Compositional mapping at 448 \times magnification has shown that this specimen too is composed of several phases and voids.

The specimens above were in bulk form. Another preparation technique being tried is RF sputtering of thin films. Maps of a film that is about 1 μ m thick are seen in Fig. 5. The magnification is 2125 \times , which corresponds to 47 μ m on an edge. Homogeneity again has not been achieved; several phases are still present but the voids are absent and are more consistently distributed than in the previously described bulk specimens.

Conclusion

EPMA compositional mapping is obviously an invaluable technique for understanding the microstructure of materials. As applied to superconductors, it is helping the materials scientist define the phases that are present and their orientation, which in turn aids in the understanding of the observed physical properties such as conductivity and magnetic susceptibility.

References

1. R. B. Marinenko et al., "Digital x-ray compositional mapping with 'standard mapping' corrections for wavelength dispersive spectrometer defocusing," *J. Microsc.* 145: 207, 1987.
2. H. Yakowitz, R. L. Myklebust, and K. F. J. Heinrich, *FRAME: An on-line Correction Procedure for Quantitative Electron Probe Microanalysis*, National Bureau of Standards Technical Note 796, 1973.
3. R. L. Myklebust et al., "Background correction in electron microprobe compositional mapping with wavelength-dispersive x-ray spectrometry," *Microbeam Analysis--1987*, 25.
4. J. E. Blendell et al., "Processing-property relations for $\text{Ba}_2\text{YCu}_3\text{O}_{7-x}$ high T_c superconductors," *Adv. Ceram. Matls.* 2: 512, 1987.
5. R. S. Roth et al., "Phase equilibria and crystal chemistry in the system Ba-Y-Cu-O," *ibid.* (in press).

QUANTITATIVE EDS MAPPING OF A CERAMIC SUPERCONDUCTOR

J. J. Friel, T. J. Juzwak, and P. F. Johnson

Quantitative x-ray microanalysis is an established technique, and the logical extension to quantitative compositional mapping has been discussed by a number of authors over the last few years.¹⁻⁴ Digital x-ray imaging systems have made quantification possible, because the computer stores the number of x-ray counts at each pixel. The magnitude of these numbers, and thus the precision of the analysis, is limited by the time the beam dwells on each pixel. Accordingly, high-quality x-ray maps cannot be obtained in minutes, and overnight runs are often required for maps of trace elements. Inasmuch as precision is limited by counting statistics, and the goal of quantitative mapping is to determine the spatial distribution of elements, ultimate accuracy in each pixel is not crucial.

A rapid method of quantifying digital x-ray maps consists of establishing a calibration curve that relates x-ray counts to composition in the same way it was done in the early days of electron probe microanalysis.⁵ Once a curve is established that encompasses the range of composition to be measured, the background-subtracted, live-time-corrected counts in each pixel can be converted directly to weight percent. The many phases in the BaO-Y₂O₃-CuO system are a class of materials for which this technique is particularly well suited. The system contains several stoichiometric phases that make fine standards, but it also contains the superconducting YBa₂Cu₃O_{7-x} phase with variable stoichiometry and properties that depend on the oxygen concentration.

Operating Considerations

Most authors who discuss quantitative mapping use wavelength-dispersive spectrometers, which have the advantage of higher count rates than one generally obtains with EDS; therefore, higher precision is possible in the same amount of time. WDS also has the advantage of a greater P/B, which makes it the method of choice for trace element analysis. EDS, on the other hand, is capable of analyzing all elements of interest simultaneously and under the same geometric conditions. EDS also avoids the spectrometer defocusing problem that plagues WDS when the beam rather than the stage is moved. Moreover, digital EDS systems typically have image processing and image analysis capabilities so that it is easy to make comparisons

among images. Consequently, EDS is the method of choice for routine quantitative compositional mapping, particularly at low magnification or when precise stage control is not available.

If the mapping resolution (i.e., the number of pixels) can be varied, it should be chosen such that each pixel corresponds approximately to the x-ray range. For example, in ceramic superconductors at 10 kV, the x-ray range is about 0.6 μm . At 750 \times magnification, an imaging resolution of 256 \times 256 beam steps results in about 0.5 $\mu\text{m}/\text{pixel}$, calculated as follows: $R = L/nM$, where R = the pixel resolution, n = the number of pixels in one direction (i.e., 256), L = length of the line digitized on the CRT, and M = magnification, all in the same units of length. Use of fewer pixels would result in undersampling, but it would also decrease the time required to collect the map. Use of more pixels would be a waste of counting time that could be more profitably added to dwell time at each pixel.

Method

Samples of Ba-Y-Cu-oxide materials were prepared by various methods, including (1) solid-state synthesis, (2) nitrate precipitation, (3) sol-gel processing, and (4) partial melting followed by crystallization. The details of the synthesis procedures, property measurements, and microstructural description have been reported previously.⁶ Secondary and backscattered electron images were obtained with an ISI SS40 SEM, and x-ray maps of Ba, Y, Cu, and O were collected with a PGT microanalysis system with windowless detector. The SEM was operated at 10 kV and 5 nA, and the La lines were used to analyze all elements except oxygen, for which the K α line was used. The x-ray maps were corrected for background by subtracting the map of an adjacent element not present in the sample.

The BaO-Y₂O₃-CuO system is well suited to quantification by the method of calibration curves, because most bulk compositions in the system consist of multiple phases, and many of them are stoichiometric. Consequently, they may be used as standards to analyze the entire microstructure and in particular the composition of the 123 superconducting phase, which is not stoichiometric. For example, Y₂BaCuO₅ known as the "green phase" or the "211" phase is stoichiometric and ubiquitous. Y₂O₃, CuO, and various oxides containing only two of the three cations are also commonly present. A curve can thus be established that relates x-ray intensity to concentration for each element. Figure 1 shows examples of such curves for Y La and O K α x rays. The gray scale on

J. J. Friel and T. J. Juzwak are with Princeton Gamma-tech, 1200 State Road, Princeton, NJ 08540; P. F. Johnson is with the New York State College of Ceramics at Alfred University, Alfred, NY 14802.

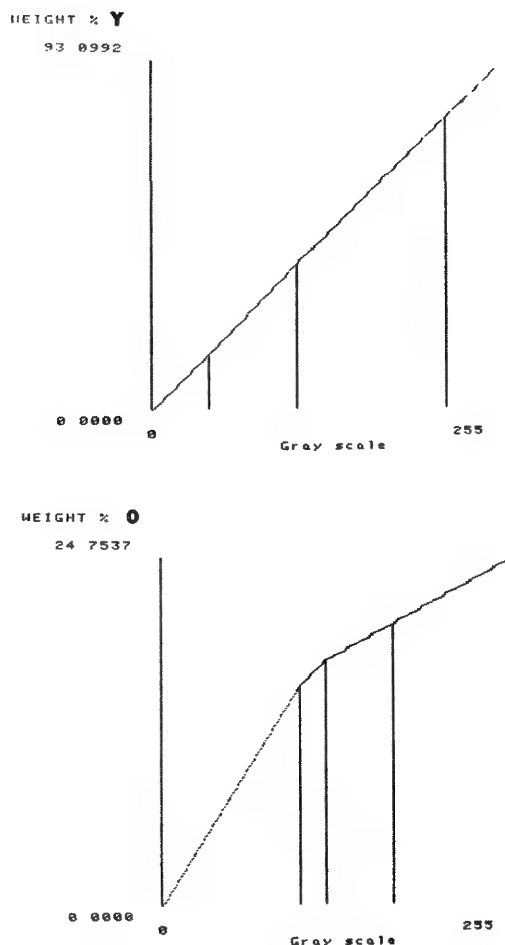


FIG. 1.--Calibration curves of image gray scale to (a) yttrium concentration and (b) oxygen concentration. Image gray scale for each element is derived directly from x-ray counts for that element.

the x axis corresponds directly to the number of x-ray counts stored on disk. If internal standards were not so conveniently available, several standards would have to be collected for each element, although these standards could be used repeatedly as long as the analytical conditions did not change.

In this study, digital x-ray maps were collected with a windowless detector for maximum sensitivity. The x-ray counts were digitized at either 256×200 pixels for 0.2 s/pixel to achieve maximum spatial resolution or at 128×100 pixels for 1 s/pixel to achieve better counting statistics. Under the latter conditions, on average, 1000 counts were collected in the oxygen peak at each pixel, corresponding to an analytical sensitivity of about 1.2% absolute or about 7% relative.⁷ To do better by WDS would require very high beam current. In all cases the actual x-ray counts were stored on disk; consequently, there was no loss of precision because of scaling. In addition to the precision defined by counting statistics, any inaccuracy associated with the background subtraction or the calibration curve must also

be considered. Of course, pixel in a quantitative map will never have the precision of point analysis because of the limited dwell time, but it is often an ideal starting point for image analysis. Furthermore, when all the pixels corresponding to a particular phase were considered together, more than 10^7 counts were present for each element.

Results

Maps were obtained for samples prepared by the various ceramic synthesis methods, and the major phases were clearly distinguishable in x-ray contrast. However, unlike for analog maps, it was easy to identify minor phases on the basis of their composition. The most interesting results, though, came from the oxygen maps. Figure 2 shows quantitative maps of Ba, Y, Cu, and O at a resolution of 256×200 pixels. This sample had about 35 vol% of the 123 superconducting phase and about 50% of the 211 phase, and the remainder consisted mostly of binary oxides and ternary phases such as BaCuO_2 that could be easily identified on the basis of elemental concentration. Area fractions were readily measured by image analysis.

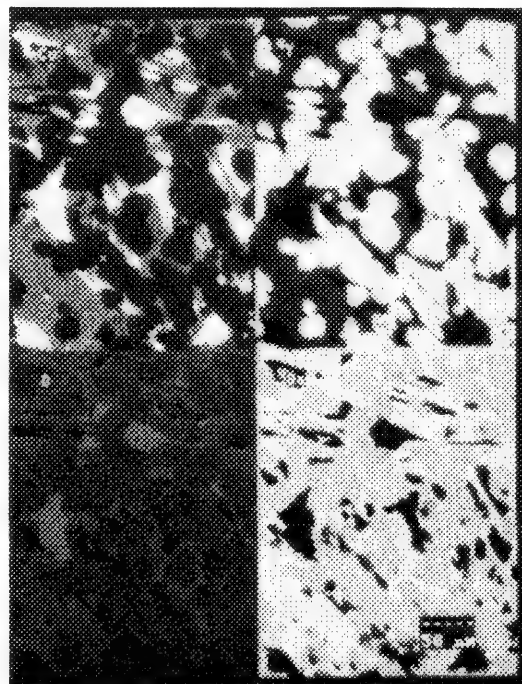


FIG. 2.--Quantitative compositional maps of Ba, Y, Cu, and O in ceramic superconductor after aging 9 months.

Originally, it was impossible to distinguish the 123 from the 211 phase in backscattered electrons, because they differed by only 0.06 average atomic number. However, as the sample aged, contrast began to appear. This contrast turned out to be the result of oxidation or hydration of the 123 phase that was originally defect in oxygen. The maps shown in Fig. 2 were

TABLE 1.--Oxygen concentrations in $\text{YBa}_2\text{Cu}_3\text{O}_{7-x}$.

Oxygen conc.	solid state synthesis			liquid phase synthesis	
	original	4 mo aging	9 mo aging	original	2 mo aging
wt%			vol%		vol%
13			3		0
14			3		0
15			7		0
16			7		1
17			14		1
18			43		36
19			19		59
20			4		3
21			0		0
Average oxygen conc. (wt%)	15.5	17.4	17.2	15.9	18.6

collected about 9 months after the sample was prepared, and the oxygen content in the 123 phase averaged 17 wt% compared with 15.5 wt% originally. Maps collected 4 months after synthesis also revealed 17 wt% oxygen. Because gray levels in a quantitative map are equivalent to weight percent, it is possible to determine the distribution of composition by measuring the area fraction of each gray level. Table 1 shows the variation in oxygen concentration after aging. One sample was prepared by solid state sintering and another by partial melting and crystallization of a bulk composition identical to that of the 123 phase. The original distribution of oxygen is not available because these samples were not mapped for oxygen when they were first prepared, although numerous spot microanalyses were obtained. It is evident that the superconducting phase oxidizes within several months of preparation, and synthesis at a temperature high enough to produce liquid produces a more oxidized compound but with a narrower distribution of oxygen concentration than does solid-state synthesis.

A change of 1.0 wt% oxygen corresponds to a change of about 0.5 atom of oxygen in the formula $\text{YBa}_2\text{Cu}_3\text{O}_{7-x}$. In each pixel this is about the limit of precision; however, the average composition calculated from all the pixels is limited only by the factors that affect accuracy. When x changes by 0.5, the average atomic number changes by 0.6. Hence, if a sample is oxidized by 2 wt%, the structure can change from defect to excess oxygen, and atomic number contrast between the 123 and the 211 phases becomes clearly visible.

Conclusions

The method of calibration curves provides reasonably accurate quantitative compositional maps providing suitable standards are available. It is particularly powerful when combined with image analysis, which can be performed either before or after quantification. The phases in the Ba-Y-Cu-oxide system can be

easily distinguished on the basis of composition, and the effect of oxidation of $\text{YBa}_2\text{Cu}_3\text{O}_{7-x}$ on BSE contrast can be quantified.

References

1. D. E. Newbury, "Applications of compositional mapping in materials science," *Microbeam Analysis--1987*, 33.
2. R. L. Myklebust, D. E. Newbury, R. B. Marinenko, and D. S. Bright, "Background correction in electron microprobe compositional mapping with wavelength-dispersive spectrometry," *Microbeam Analysis--1987*, 25.
3. R. L. Myklebust, R. B. Marinenko, D. E. Newbury, and D. S. Bright, "Quantitative calculations for compositional mapping techniques in electron probe microanalysis," *Microbeam Analysis--1985*, 101.
4. C. E. Fiori, "Quantitative compositional mapping of biological cryosections," *Microbeam Analysis--1984*, 183.
5. J. I. Goldstein, H. Yakowitz, D. E. Newbury, E. Lifshin, J. W. Colby, and J. B. Coleman, *Practical Scanning Electron Microscopy*, New York: Plenum, 1975, 424.
6. E. C. Behrman et al., "Synthesis, characterization, and fabrication of high temperature superconducting oxides," *Advanced Ceramic Materials* 2: 539, 1987.
7. J. I. Goldstein, D. E. Newbury, P. Echlin, D. C. Joy, C. Fiori, and E. Lifshin, *Scanning Electron Microscopy and X-ray Microanalysis*, New York: Plenum, 1981, 434.

QUANTITATIVE LARGE-AREA X-RAY MAPPING WITH AN ANALYTICAL SCANNING ELECTRON MICROSCOPE: A STUDY OF LOW-LEVEL ELEMENTAL SEGREGATION IN CONTINUOUS CAST STEELS

H. A. Buskes and G. D. Baughman

Large area x-ray mapping has become an important analytical tool for the study of the segregation of low-level elements in continuously cast steels.^{1,2} A general x-ray mapping utility, developed for electron-optical equipment with computer-controlled specimen stage and wavelength dispersive spectrometer (WDS) movement, provides the means by which the appropriate elemental data may be collected. The technique, using stage movement, allows specific elemental x-ray intensity profiles to be mapped over large sample areas with spatial resolutions commensurate with electron-probe microanalysis. Data acquisition, synchronized to noninterrupt-driven stage movement, allows fast x-ray map generation at up to 1024 × 1024 pixel resolution for sample areas from less than 0.5 mm² to over 50 mm². Elemental concentration maps which are derived from the direct x-ray counts by the use of specific image processing techniques provide an important database for mathematical models, thus aiding in the understanding of the mechanisms that lead to segregation. We shall illustrate with examples of quantitative elemental maps and qualify some of the techniques used.

Principles and Instrumentation

High-speed data acquisition by uninterrupted stage movement and low concentrations for elements of interest in steels dictate the use of wavelength-dispersive (WD) spectrometers for x-ray counting. Some important considerations in large-area x-ray mapping are the aspects of sample "flatness" over the analytical area, counting statistics, beam stability, and data processing with a view to quantification.

Our system for assessing low-level element segregation in steels is based on a JEOL JXA-840 scanning electron microscope fitted with three WD spectrometers. Computer control of the X and Y stage axes and data acquisition/processing is provided by Tracor Northern's TN-5500/TN-5600 system and modified versions of the Large Area Mapping (LAMAP) and Image Processing Programs (IPP).

Measurement Techniques

Data acquisition times can be minimized by counting while traversing the sample in both the forward and reverse directions (bidirectional scan mode) with the beam defocused to the "effective" analytical spot size. Direct

mapping in bidirectional mode introduces a relative phase shift, or "pixel offset," the magnitude of which is determined by a test scan across a phase boundary. Synchronization is then achieved with the appropriate delay for the start of the counting sequence. (Other methods proved ineffective at high stage speeds.)

Spectrometer defocusing and the inherent complexity required to correct for this effect may be avoided by producing "flat" samples. Where this approach is not practical, a focus correction may be applied that approximates the specimen surface with a hyperbolic paraboloid.³ Let (X_i, Y_i, Z_i) represent the coordinates of the *i*th corner of a square which defines the analytical area of interest. The Z coordinate at any point within this area may be computed by:

$$Z = Z_1 + (Z_2 - Z_1) \frac{X - X_1}{X_2 - X_1} + (Z_4 - Z_1) \frac{Y - Y_1}{Y_4 - Y_1} \\ + (Z_1 - Z_2 + Z_3 - Z_4) \frac{X - X_1}{X_2 - X_1} \frac{Y - Y_1}{Y_4 - Y_1}$$

The effective dwell time per pixel is a function of the dimensions of the analytical area of interest, the collected image resolution, and the scan speed. The effective dwell together with the counting statistics (which in turn are a function of beam current, spectrometer efficiency, and the concentrations of the elements being measured) define the statistical accuracy of relative variations in element concentrations. Our mapping of the elements phosphorus, carbon, and manganese (typical levels of 0.02%, 0.04%, and 1.6%, respectively) has allowed respective variations of 100%, 40%, and 10% to be measured with a high degree of accuracy for effective dwell times of 30 ms at 3 μA of beam current.

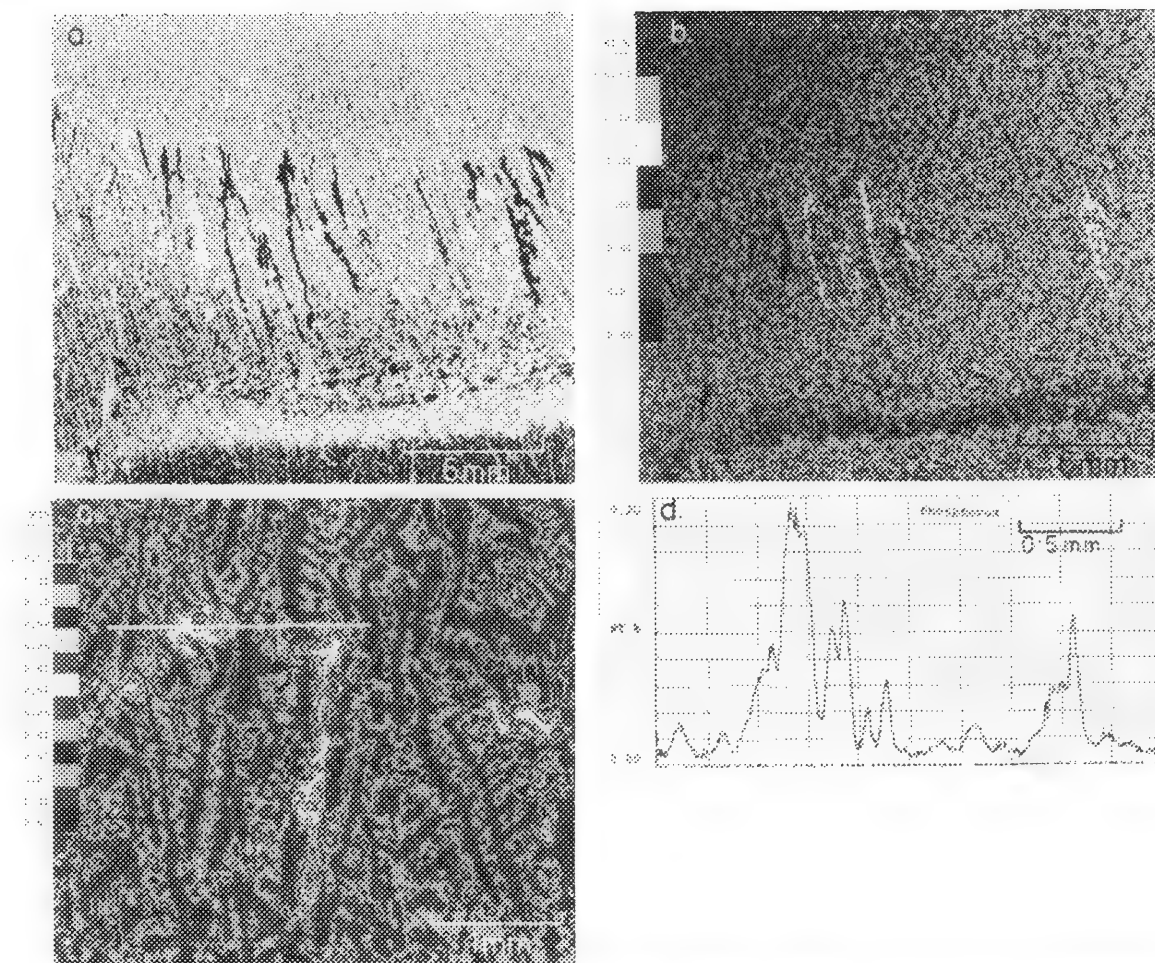
Beam-current stability is critical for Large Area Mapping, where for 512 × 512 pixel maps typical acquisition times are on the order of 3 h. Feedback circuitry is the obvious solution but, as with our instrument where design prevents its use, an alternative of regular beam current measurement with appropriate scaling of the data has been very successful.

Processing Techniques

Maps are stored as single-byte arrays, so that the range available for counts is 0 to 255. True x-ray counts outside this range would need to be clipped or scaled down. Scaling down causes rounding errors, which could be severe for the important low-level counts in an environment where high counts are also measured.

H. A. Buskes is with the BHP-Melbourne Research Laboratory, Victoria, Australia; G. D. Baughman is with Tracor Northern Inc., Middleton, WI 53562-2697.

1



2

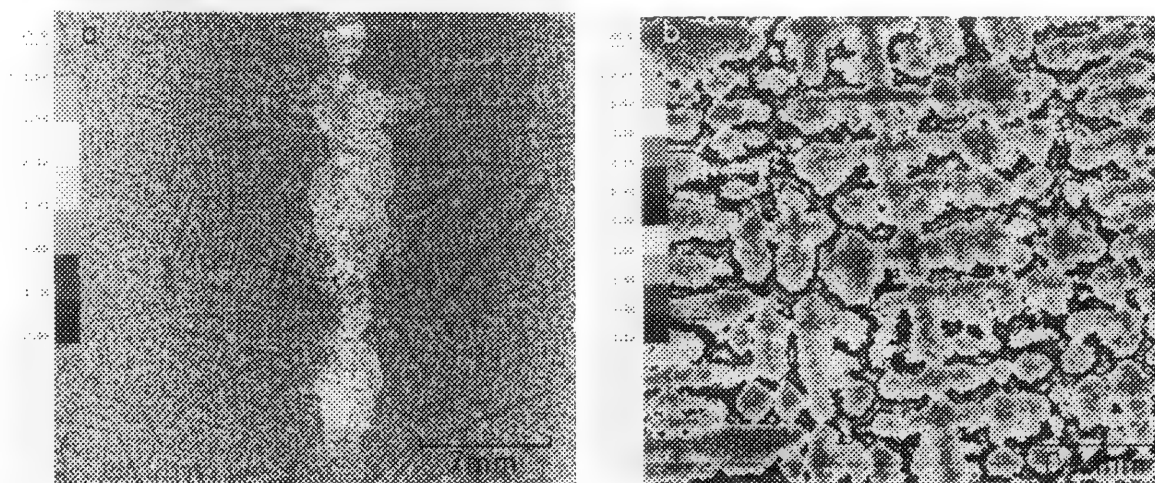


FIG. 1.--Continuous cast steel exhibiting back-filled cracks showing (a) and (b) an optical micrograph for a 20 × 30 mm etched sample with a corresponding phosphorus concentration map, respectively; (c) a phosphorus map over a 5 × 5 mm area; (d) a 2.5 mm phosphorus linescan corresponding to the trace on (c).

FIG. 2.--Manganese concentration maps for a continuous cast steel highlighting (a) center-band segregation in a 35 × 35 mm sample; (b) the dendritic structure over a 2 × 2 mm area.

In our measurements the necessary scaling factors are predetermined to allow the count range of interest to be suitably represented at the expense of clipping the high counts.

Map data may be quantified according to the following equation: $Cu/Cs = (Iu/Is)(Mu/Ms)$

where Cu, Iu, Mu and Cs, Is, Ms represent the concentrations, background-corrected x-ray intensities, and matrix correction factors for the element of interest in an unknown and a standard, respectively. Low-level elements in steel present a simple task for quantification

since it may be assumed that the background is, apart from statistical fluctuations, effectively constant for each element and, provided a standard of similar composition is available, matrix correction is unnecessary. That means that the above equation reduces to $Cu/Cs = Iu/Is$ where background measurements are made via averaging test scans and the mean counts for maps from a standard specimen represent some base level concentration.

Results

Some examples of large area x-ray concentration maps produced for continuous case steels are presented in Figs. 1 and 2. In all cases the maps were required over 512×512 analytical points for an effective x-ray counting time of 30 ms per point with a 15kV, 3 μ A electron beam. The linescan in Fig. 1d represents a two-pass, 512 point trace for a 0.5s dwell per point with a 15kV, 1 μ A beam. The use of image-smoothing filters has been adopted for some maps to reduce resolution in order to emphasize gross features. In the original maps, x-ray counts representing specific concentration ranges are color-coded. Experience has shown that the choice of ranges of specific color tones is important: although color set may adequately define intensity variations, the structural information in the map may actually be "washed out."

Conclusion

Large area x-ray mapping has proven itself as an invaluable tool for the study of continuous elemental distributions, as opposed to discrete phases, and specifically for segregation in continuous cast steels. The success of this technique with equipment in the current context shows that its practical use is not restricted to the complex and expensive analyzers dedicated to this technique.

Future work will entail more extensive image processing/analysis of segregation maps to define some parameters which uniquely characterize the segregation.

References

1. I. Taguchi, H. Hamada, and S. Tani, *Nippon Steel Technical Report*, No. 26, 1985, 59.
2. I. Taguchi, H. Hamada, and M. Kama, *JEOL News* 20E(No.3): 3, 1982.
3. M. Mayr and J. Angeli, *X-ray Spectrometry* 14: 89, 1985.

3 Analytic Electron Microscopy

TEMPERATURE DEPENDENCE OF ALUMINUM EXELFS

M. M. Disko, C. C. Ahn, G. Meitzner, and O. L. Krivanek

The temperature variation of the extended electron energy loss fine structure (EXELFS) amplitude can be analyzed in order to obtain a localized measurement of the Debye temperature (θ_D). This procedure has been used in extended x-ray absorption fine structure (EXAFS) studies with great success for monatomic FCC metals such as Cu and Pt.¹⁻³ We have performed such a study on a thin aluminum foil using a prototype of the Gatan 666 parallel detection EELS system.⁴ EXELFS analyses of the first nearest neighbor oscillations in the temperature range 86 K to 236 K demonstrate the capability to determine θ_D localized within a sample volume of approximately $0.01 \mu\text{m}^3$. Thus it is possible to relate inhomogeneities in θ_D to corresponding variations in fundamental properties such as elastic constants and heat capacity.⁵

Experimental

The present experiment would not have been practical with a serial acquisition system. Parallel detection made it possible to obtain excellent counting statistics within the first 900 eV of the aluminum K edge onset in acquisition times of 100 s. Measurements were made with a Philips EM430 TEM operated at 300 kV, probe size ~ 500 nm, and a beam current of ~ 5 nA. The spectrometer was operated in the diffraction coupling mode (image on viewing screen). Hence the region from which inelastic scattering was collected is limited by the spectrometer entrance aperture, which gave an effective diameter of 250 nm. The energy resolution at the aluminum K edge was ~ 3 eV, which is adequate for EXELFS analysis. A liquid-nitrogen stage equipped with a heating element was used to control the temperature. Three Al K edges were acquired at each of the following temperatures: 86, 117, 148, 176, 206, and 236 K. One of the set of edges for 86 K is shown in Fig. 1 after removal of the background extrapolated from the pre-edge region.

The sample volume that was analyzed showed a total inelastic mean free path fraction t/λ_T of 0.6 for the collection semiangle of ~ 100 mrad, 300 kV accelerating voltage, and energy losses up to 150 eV.⁶ Multiple inelastic scat-

tering is not expected to be significant. An approximation of λ_T can be obtained from values given by Egerton and Cheng for 100 kV incident electrons (85 nm), by scaling to allow for 300 kV electrons, to obtain $\lambda_T \sim 180$ nm.^{7,8} A value of t/λ_T of 0.6 thus corresponds to an approximate thickness of 110 nm. Several nanometers of amorphous Al_2O_3 scale cover each surface of the foil and contribute a significant signal to the transmission EXELFS.

Results

The nearest-neighbor EXELFS oscillations can be described by the single scattering formula for neighbors at R_1 ,^{1,2,9}

$$\begin{aligned} \chi_1(k) &= A_1(k) (N_1/R_1^2) \exp(-2k^2\sigma_1^2) \sin[2kR_1 + \phi_1(k)] \\ &\quad (1) \end{aligned}$$

where $A_1(k)$ is the electron backscattering amplitude function characteristic of aluminum, N_1 is the number of atoms in the first coordination shell, σ_1^2 is the mean square relative displacement (MSRD) at a given temperature, and $\phi_1(k)$ is the phase shift. The MSRD for any particular shell is the average relative displacement between the excited atom and the coordination shell.^{1,11} One can readily compute $\Delta\sigma_1^2$ (the change in σ_1^2 between two temperatures) from a given pair of $\chi_1(k)$ functions. The log of the ratio of $\chi(k)$ functions is plotted vs k^2 , and then the slope of the resultant line gives $\Delta\sigma_1^2$. But the determination of σ_1^2 requires that the amplitude function $A_1(k)$ is known accurately. The procedure in the determination of θ_D involves the use of the data from one temperature as a reference point. Data from other temperatures are then used to obtain experimental $\Delta\sigma_1^2$ values. Finally, the experimental values are compared with differences between theoretical MSRD values.

In order to obtain the $\chi_1(k)$ functions, the initial step involves the isolation of the EXELFS oscillations and mapping from energy loss to momentum k . The threshold ($k = 0$) position was assigned to the maximum in the first derivative at the absorption edges. A cubic spline polynomial with five knots evenly spaced between 1565 and 2264 eV was fit to the high-energy side of the absorption edge and subtracted to isolate the EXELFS oscillations. The EXELFS oscillations were normalized to the edge height calculated from the difference between a linear fit to the pre-edge region and the fit to the post-edge region. Plots of $k\chi(k)$ versus k for $T = 86$ K and 236 K show that the overall amplitude of the oscillations does decrease with increasing temperature

M. M. Disko and G. Meitzner are at Exxon Research and Engineering Company, Route 22 East, Annandale, NJ 08801; C. C. Ahn is at the California Institute of Technology, Keck Laboratory of Engineering Materials, Pasadena, CA 91125; and O. L. Krivanek is at Gatan, Inc., 6678 Owens Drive, Pleasanton, CA 94566. The aid of Carl Klein in the preparation of the aluminum foils, and of Arizona State University for use of the Philips EM430, is acknowledged.

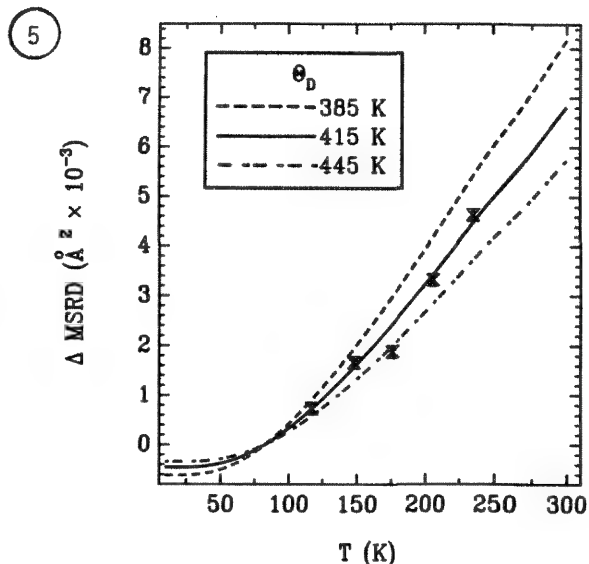
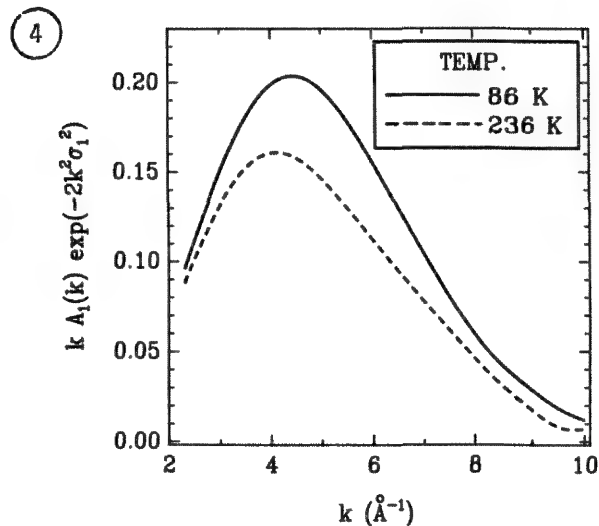
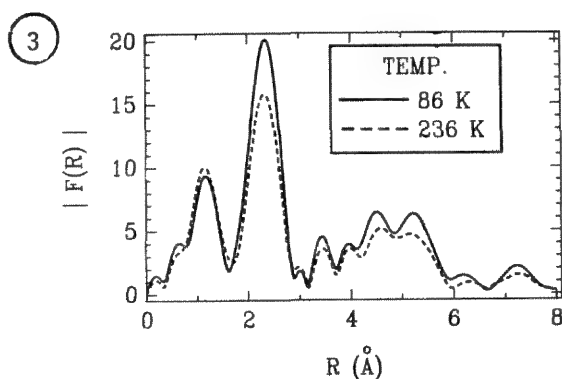
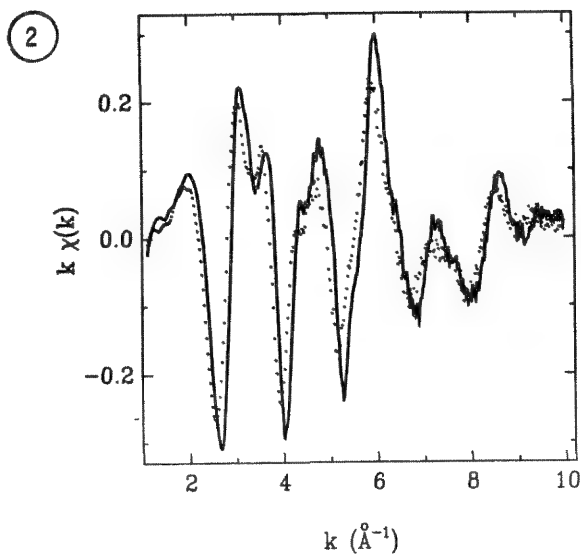
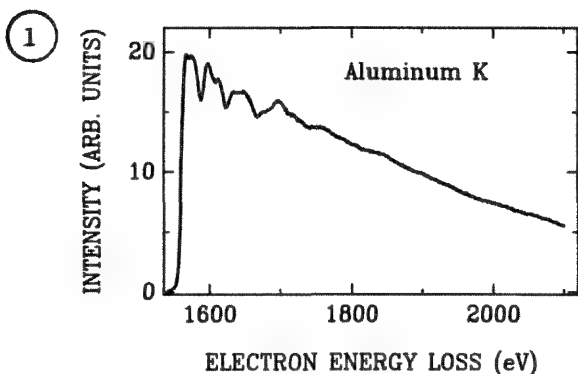


FIG. 1.--Aluminum K edge obtained at 86 K.

FIG. 2.-- $k\chi(k)$ for 86 K (solid) and 236 K (dots).

FIG. 3.--Magnitude of Fourier transform of $k\chi(k)$ EXELFS for 86 and 236 K aluminum K edge oscillations.

FIG. 4.--Nearest-neighbor peak amplitude functions obtained from back-transforms of 86 and 236 K structure functions in Fig. 3.

FIG. 5.--Experimental $\Delta\sigma_1^2$ (symbols), and theoretical ΔMSRD for θ_D values of 385, 415, and 445 K.

(Fig. 2). A first power in k weighting was applied to $\chi(k)$ in order to amplify the high- k part of the spectrum.

Fourier transforms (radial structure functions) of $k\chi(k)$ from samples at 86 and 236 K were calculated with data between $k = 2.36 \text{ \AA}^{-1}$ and 10.05 \AA^{-1} (Fig. 3). The first peak in Fig. 4, corresponding to $R = 2.3 \text{ \AA}$, shows that the amplitude is due mainly to the first nearest neighbors. The actual distance is 2.871 \AA , but no phase correction has been applied. A peak that is probably due to the presence of surface oxide occurs near 1.2 \AA . This oxide peak is clearly separated from the metal-metal bond length contribution.

First nearest neighbor oscillations $k\chi_1(k)$ were isolated with a 1.57 \AA to 3.06 \AA back-transform window on radial structure functions in Fig. 3. Figure 4 demonstrates the temperature dependence of the amplitude of the EXELFS oscillations $kA_1(k) \exp(-2k^2\sigma_1^2)$ between 86 and 236 K. The lowest temperature data were used as a reference function in order to fit the higher temperature data while holding the bond length and number of atoms constant. The fitting technique and details of the analysis are described in a separate report.¹⁰ Experimental values for $\Delta\sigma_1^2$ are plotted as symbols in Fig. 5.

A fit of experimental $\Delta\sigma_1^2$ values with theoretical MSR values relative to the lowest temperature data was performed in order to estimate the Debye temperature. The temperature dependence of the nearest neighbor MSR based on the correlated Debye model of the density of states, $(\sigma_1^2)_D$, is given by^{9,11}

$$(\sigma_1^2)_D = 2[\text{MSD} - \text{DCF}] \quad (2)$$

where the mean squared displacement (MSD) and displacement correlation function (DCF) can be calculated in terms of the atomic mass, temperature, Debye temperature, and bond length.⁹⁻¹¹ Equation (2) shows correctly that the MSR is twice the difference between the MSD and DCF, which differs by a factor of 2 from Eq. (19) in the paper by Beni and Platzman.

An estimate of θ_D was made by computing the total squared deviations between experimental and theoretical Δ MSR values for a range of θ_D . A single minimum in the resulting parabolic error function was found at $\theta_D = 415 \text{ K}$. This value might be compared with literature values of θ_D for bulk Al, for example 428 K ⁵ and 396 K .¹² Figure 5 shows theoretical Δ MSR curves for three values of θ_D along with the experimental $\Delta\sigma_1^2$ values obtained with the lowest temperature data as a reference. Calculated Δ MSR curves for θ_D values of 385 and 445 K show poor agreement with experiment.

Conclusions

The use of a parallel detection data acquisition system for the acquisition of transmission EXELFS data makes quantitative studies localized within extremely small sample volumes possible. Spectra thus obtained provide

signal qualities which, in the soft x-ray regime, are comparable to those found in EXAFS experiments conducted with synchrotron radiation.¹³ Excellent agreement was obtained between the transmission EXELFS determined Debye temperature and values given in the literature. This finding suggests that the temperature measurements were not significantly affected by the high flux of the incident electron beam. Future applications of this work include the correlation of $\Delta\sigma_1^2$ values with dislocation and defect densities at interfaces or within minority phases.

References

1. E. A. Stern, D. E. Sayers, and F. W. Lytle, "Extended x-ray absorption fine structure technique: III. Determination of physical parameters," *Phys. Rev. B* 11: 4836-4845, 1975.
2. D. G. Stearns and M. B. Stearns, "Microscopic methods in metals," in U. Gonser, Ed., *Topics in Current Physics* 40, Berlin: Springer-Verlag, 1986, chap. 6.
3. E. Sevillano, H. Meuth, and J. J. Rehr, "Extended x-ray absorption fine structure Debye-Waller factors: I. Monatomic crystals," *Phys. Rev. B* 20: 4908, 1979.
4. O. L. Krivanek, C. C. Ahn, and R. B. Keeney, "Parallel detection electron spectrometer using quadrupole lens," *Ultramicroscopy* 22: 103-115, 1987.
5. C. Kittel, *Introduction to Solid State Physics*, New York: Wiley, 5th ed., 1976, chap. 5.
6. R. D. Leapman, C. E. Fiori, and C. R. Swyt, "Mass thickness determination by electron energy loss for quantitative x-ray microanalysis in biology," *J. Microscopy* 133: 239-253, 1984.
7. R. F. Egerton, *Electron Energy Loss Spectroscopy in the Electron Microscope*, New York: Plenum, 1986, 180.
8. R. F. Egerton and S. C. Cheng, "Thickness measurement by EELS," *Proc. 43rd EMSA Meeting*, 1985, 398-399.
9. D. R. Sandstrom, E. C. Marques, V. A. Biebesheimer, F. W. Lytle, and R. B. Gregor, "Thermal disorder in Pt and Ir metal: Comparison of model and experimental extended x-ray-absorption fine structure," *Phys. Rev. B* 32: 3541-3548, 1985.
10. M. M. Disko, G. Meitzner, C. C. Ahn, and O. L. Krivanek, "Temperature dependent transmission EXELFS of aluminum," *Appl. Phys. Lett.* (submitted).
11. G. Beni and P. M. Platzman, "Temperature and polarization dependence of extended x-ray absorption fine-structure spectra," *Phys. Rev. B* 14: 1514-1517, 1976.
12. P. P. Debye, "On the theory of specific heats," *Ann. Phys.* 39: 789-839, 1912.
13. E. A. Stern, "Comparison between electrons and x-rays for structure determination," *Optik* 61: 45-51, 1982.

THE IMPACT OF LOW-NOISE DESIGN ON X-RAY MICROANALYTICAL PERFORMANCE

P. J. Statham and T. Nashashibi

The traditional method of assessing energy-dispersive spectrometer (EDS) performance is by the full width at half maximum (fwhm) of the Mn K α peak. Whereas there have been only slight improvements in this parameter over the last ten years, there have been dramatic changes in electronic noise performance as a result of a more thorough understanding of noise sources at the detector head. Recently, a radical change in FET structure has enabled a noise fwhm of 40 eV to be achieved and further improvements are likely once the full potential of the novel head design has been exploited. This paper attempts to demonstrate the impact these noise improvements have for the microscopist in terms of practical microanalytical performance.

Low-noise Design for Solid-state Detectors

The resolution fwhm of a spectral peak can be calculated from

$$\text{fwhm}^2 = \text{fwhm}_0^2 + 21.4FE \quad (1)$$

where fwhm_0 is the fwhm resolution in eV of the electronic noise contribution, E is the x-ray energy in eV of the photons responsible for the peak, and F is the "Fano factor" of the detector. For a Fano factor of 0.11, the minimum possible resolution for Mn K α x rays (5.9 keV) is thus 118 eV. Conventional electronic feedback methods produce too much noise to exploit this potential; it was the use of opto-electronic charge restoration^{1,2} that revolutionized the design of head amplifiers for x-ray spectrometry. Alternative techniques are reviewed elsewhere;³ the most successful commercial implementation is "drain feedback," but "pulsed optical restoration" (POR) has now been almost universally adopted by manufacturers of EDS systems and a noise contribution of 92 eV, equivalent to a resolution of 150 eV at Mn K α , is representative of average performance to date.

Though POR was responsible for a large reduction in electronic noise, the use of "time-variant" pulse processing produced a further major improvement.⁴ Although this claim was a subject of controversy for several years, it was eventually confirmed and explained by the observation that there was a major noise component due to dielectric or "1/f" noise, which had previously been omitted from noise calculations.⁵ During the development of a new FET, a detailed study of noise sources led to

the use of an extra electrode which improved noise performance by obscuring the contribution due to defect centers in the FET channel. In conjunction with time-variant pulse processing, this "tetrode" device enabled a noise fwhm of around 60 eV to be achieved.⁶

In order to minimize spectral broadening and distortion due to the aftereffects of POR, a dead time is always imposed at the end of each restore; the duration necessary depends on the detector and FET design but can be in excess of 1 ms. In TEM and STEM applications, although the photon rate may be low, the energy \times rate product can often demand a high rate of charge neutralization. In this case, the total dead time due to charge restoration can be a major fraction of the acquisition time. The tetrode FET design was stimulated by the problem of analyzing radioactive specimens where the aftereffects of POR were originally severe enough to obscure all spectral detail. With the improved device, restore times could be as low as 20 μ s and energy deposition rates in excess of 1 MeV/ μ s could be accommodated. There seemed to be little opportunity for further improvement without a radical change in electronic design at the detector head, but just this opportunity has arisen recently with the invention of a new device designed specifically for EDS.

Pentafet

The pentafet⁷ is a novel 5-terminal integrated solid-state device incorporating a low-noise junction FET (JFET) and a fast, nonoptical charge restore facility. Charge restoration is achieved by injecting a pulse of minority carriers into the channel of the FET: the gate leakage current therefore increases by many orders of magnitude and neutralizes the charge accumulated on the feedback capacitor. This process is much faster than the widely used optical method and can operate in only 1 μ s. In doing so, the operating conditions of the FET are not disturbed and the gate leakage current reverts to its low value a fraction of a microsecond after the restore pulse.

Since the FET package no longer has to be light tight, the need to use lossy dielectrics (which add to the noise of the detector system) is avoided. Furthermore, the JFET is specially designed to give a low equivalent noise voltage and an input capacitance which is ideally matched to the total capacitance of the detector. With this device, a noise resolution of 40 eV has recently been achieved on a 10mm² Si(Li) detector.

Implications for Microanalysis

Detection of Low-energy Peaks. The effec-

The authors are with Link Analytical Ltd., Halifax Road, High Wycombe, Bucks, England HP12 3SE, and are indebted to M. Jones for considerable technical assistance in the experimental work for this paper.

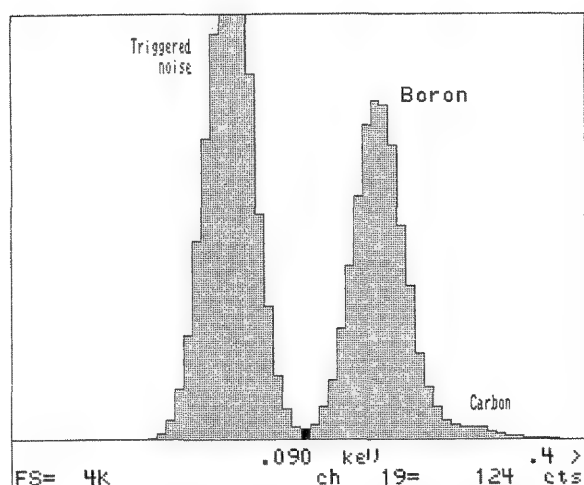


FIG. 1.--Spectrum of boron metal obtained at 10 kV in SEM showing P/V of 30 for a noise fwhm of 52 eV.

tive signal from a low-energy photon can easily be masked by electronic noise; in the recorded spectrum this means that the low-energy peak will be overlapped by a "noise" peak which is due to measurements triggered by noise excursions rather than genuine signal pulses. Sensitivity to such radiation ultimately relies on effective separation of these two peaks and the ratio of peak height to that of the valley on the low energy side, P/V, can be used as a convenient quality factor to assess performance.⁸ P/V values of 2.1 for Be and 20 for B have been reported.⁸ Figure 1 shows an example of a boron peak with P/V = 30 for a noise fwhm of 52 eV. The noise distribution is clearly displayed and the boron peak is clean and symmetrical so that the true valley height can be measured; if the processing electronics are incorrectly set or are defective, the tail of the noise distribution may be obscured, which can lead to a false estimate of sensitivity.⁹ Any reduction in electronic noise will clearly have a major impact on detection limits for peaks with energies below 200 eV.

Detection Limits. The relationship between spectrometer resolution and detection limit is often a subject of confusion and argument, possibly because no single equation can cover every possible situation. Most basic treatments apply to a single peak on a uniform background where it can be shown¹⁰ that, with optimal processing, the detection limit is proportional to fwhm^{0.5}. From this standpoint, even a 20% reduction in fwhm would only produce about 10% improvement in detection limit, so that it would seem that there is little to be gained from such modest improvements in resolution.

The perspective is quite different when there is more than one peak in the spectrum, in which case the resolution influences the width of regions that are "peak free" and suitable for background fitting and corrections for peak overlap may also be necessary. With the wide variety of techniques currently used to process spectral data, it is impossible to generalize any quantitative advantage of resolution improvement, but a simple example will serve to illustrate the potential gain.

If we consider the overlap of a single peak into a window integral region with width set to match the fwhm of a peak (Fig. 2), the fraction of counts that fall in this window is given by

$$\int_a^b 0.4 \exp(-0.5 x^2) dx \quad (2)$$

where $a = (2.355 s/w) - 1.18$ and $b = (2.355 s/w) + 1.18$ (Fig. 2). If the resolution is improved, the overlap fraction drops for two reasons: the interfering peak becomes more compact and the integration window is narrower (since it is set to fwhm). Table 1 provides an example to show that an improvement of 20% in fwhm can reduce the interference of a nearby peak by large factors in situations that could occur in practice. For a large nearby peak

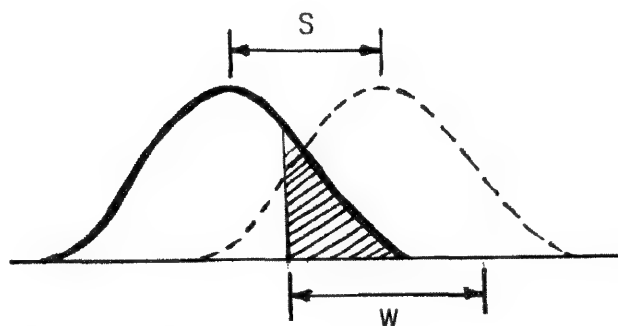


FIG. 2.--Shaded area indicates overlap of (solid) peak into window integration region w for (dashed) peak. Width w is set to fwhm and s is separation of x-ray lines.

TABLE 1.--Overlap as a fraction of peak area for a peak separation s of 100 eV computed from Eq. (2).

Fwhm	80eV	100eV	125eV
overlap	0.039	0.119	0.239

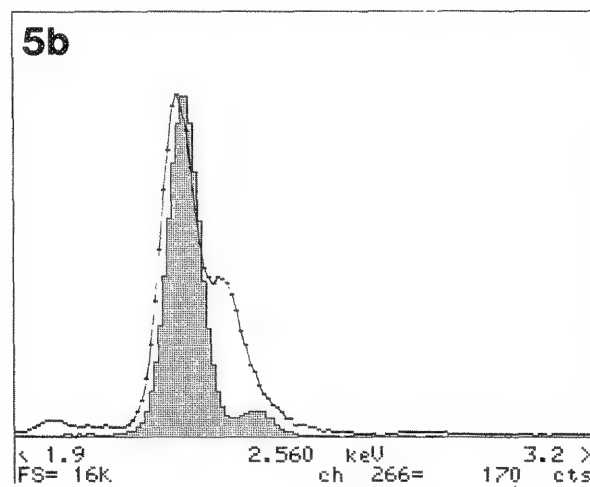
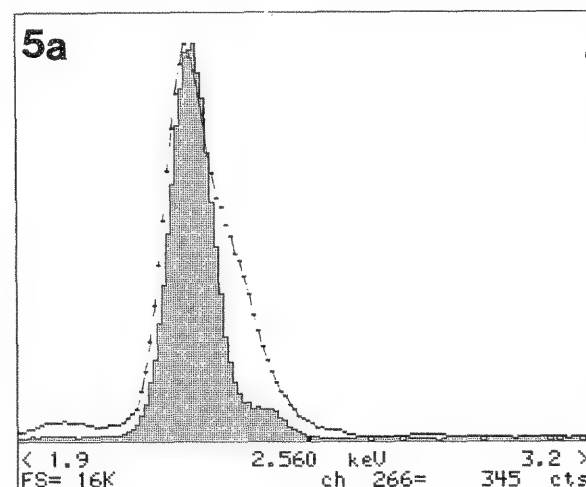
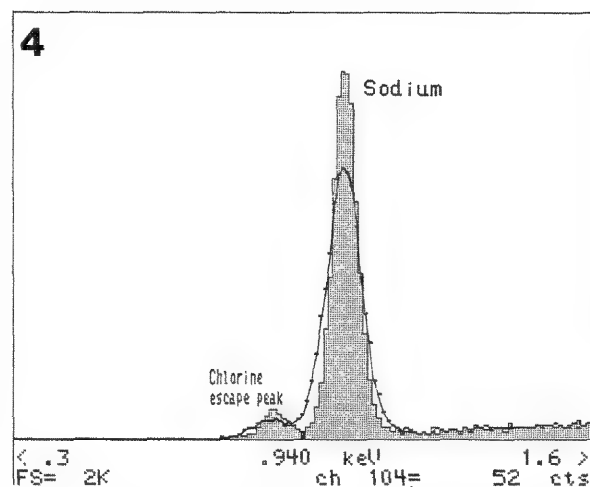
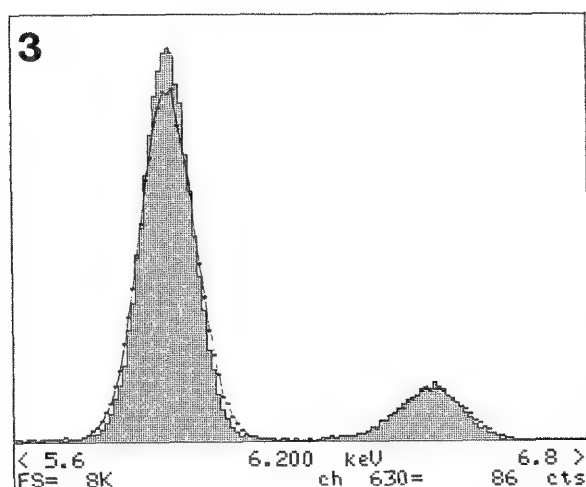


FIG. 3.--Mn K peaks at various noise fwhm. (Bars = 40 eV noise, dots = 80 eV noise.)

FIG. 4.--Na K peaks at various noise fwhm. (Bars = 40 eV noise, dots = 80 eV noise.) Sample was NaCl and small peak to left is escape peak corresponding to Cl K parent.

FIG. 5.--Peak profiles at (a) 80, (b) 40 eV noise fwhm. (Bars = S K, dots = Mo L.)

from another element or electronic noise perhaps) overlap could exceed the contribution from bremsstrahlung background and thus represent the dominant effect on statistical precision. In this case, Table 1 shows one situation where a 20% improvement in resolution, in reducing overlap by a factor of 3, could almost halve the detection limit. Obviously, this analysis is no proof that performance will always depend so critically on resolution, and it is important to assess each application in detail, but we see here at least one reasonable demonstration where a 20% improvement could be as valuable as having up to 3 times as many counts in the spectrum!

Figure 3 compares the resolution achieved at Mn K α with 40 eV of electronic noise with that for 80 eV of noise. Although the above discussion extols the advantages of even a modest reduction in fwhm, benefits are greater at low energies where, as Eq. (1) shows, the noise contribution dominates; with 40 eV of noise, Na K α peak in Fig. 4 is only 64 eV fwhm as opposed to 94 eV fwhm for 80 eV of noise, and the improvements in peak-to-background ratio and thus detection limits are more apparent.

Spectroscopy. The detailed structure of an x-ray spectrum has always been masked by the poor resolution of EDS and consequently it has been appropriate to refer to x-ray "peaks" rather than "lines" when discussing EDS data. As the noise performance improves, structure begins to appear in profiles that have been hitherto regarded as a single peak. Figure 5 shows that with only 40 eV of noise, the S K α line and Mo L α lines are apparent but they are not resolved in a system with 80 eV of noise, even though this would previously have been regarded as one of "premium resolution!"

High Count Rate. If the sample can resist strong excitation, the only limit to the data accumulation rate is the time taken to process and measure each photon. The noise contribution to the final spectrum will be greater if this processing time is reduced, so poorer resolution is the price to be paid for high data-rate capability. If the intrinsic noise component is sufficiently low, even at short processing times the resolution can be acceptable. Figure 6 shows an orthoclase spectrum showing satisfactory resolution of Al and Si

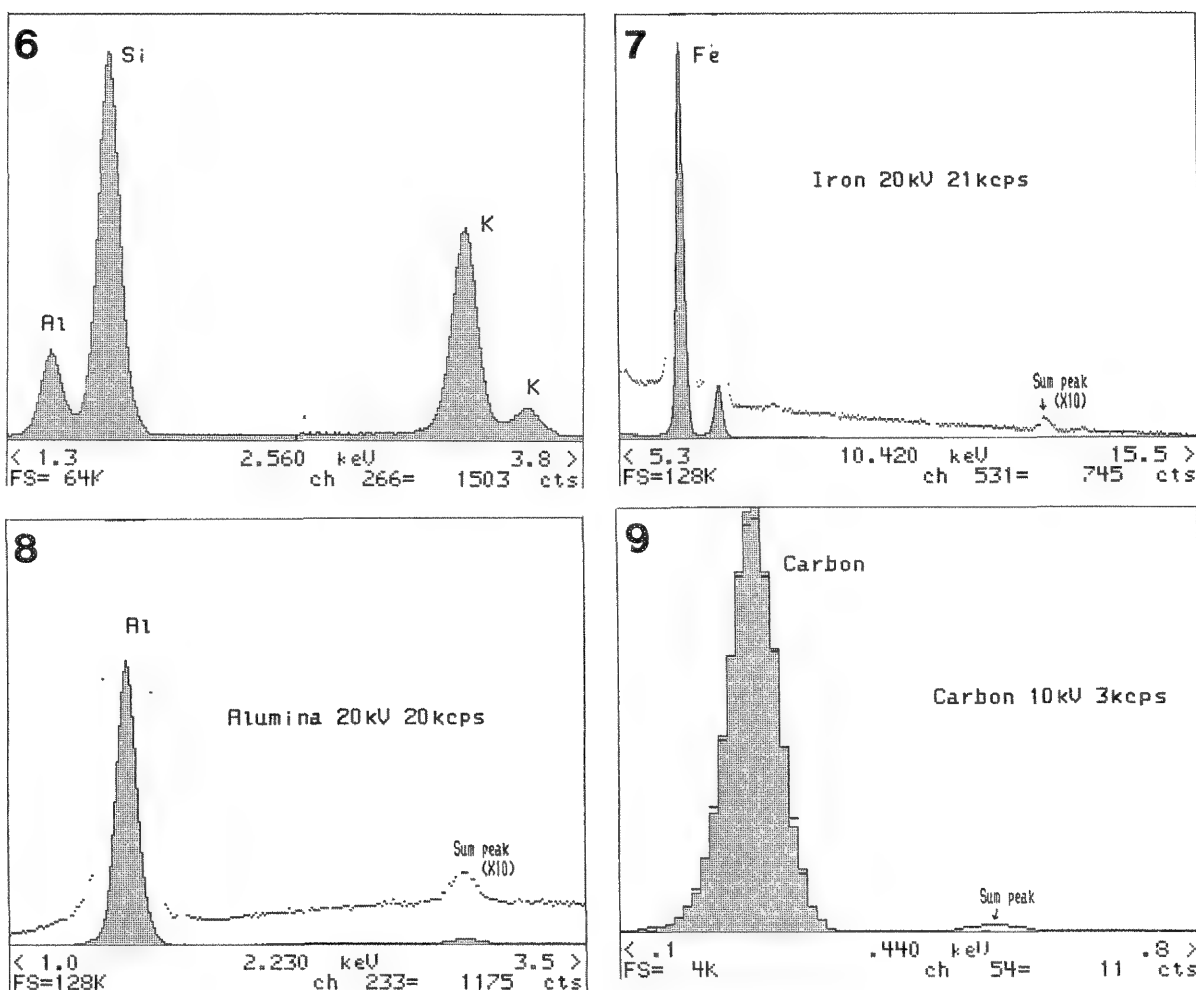


FIG. 6.--Spectrum of orthoclase at high input rate. Noise fwhm = 80 eV for pulse time-to-peak of 10 μ s.

FIG. 7.--Spectrum obtained on Fe specimen in 100 live seconds. Sum peak = 2500 cts, Fe K α = 1 033 000 cts, i.e., t_r = 0.97 μ s.

FIG. 8.--Spectrum obtained on alumina specimen in 100 live seconds. Sum peak = 9700 cts, Al K α = 1 001 000 cts, i.e., t_r = 0.97 μ s.

FIG. 9.--Spectra obtained from carbon specimen. (Bars = 3 kcps, dots = 400 cps input rate.) For 3kcps data, sum peak area = 4000 cts, C K α = 231 000 cts, livetime = 200 s, so t_r = 15 μ s.

peaks and a clearly resolved K K β peak; in this case, the pulse peaking time was only 10 μ s (total processing time of 28 μ s per photon), yet the noise fwhm was 80 eV, a value more often associated with processing times of 80 μ s or greater even on a good system.

Pile-up and Sum Peaks. The problems of peak shift and broadening at high photon rates have been largely eliminated through the use of special time-variant pulse-processing techniques.⁴ However, pile-up still represents a fundamental problem which is inextricably linked with noise performance. If a photon arrives while a pulse measurement is in progress, the result will be greater than expected and a count will appear in the spectrum at too high an energy. The "pile-up inspection" channel is designed to detect and eliminate such events from the spectrum but it can only do so if it can discriminate between a genuine pulse and a random noise excursion. If the inspector is effective, two genuine spectral peaks will give rise to a

third "sum peak" whose area is proportional to the resolving time for the corresponding pulses;¹¹ if not, a plateau or pile-up continuum will appear that extends up to the sum peak energy. Whereas computer correction for a well-defined sum peak is feasible, correction for pile-up continuum is extremely costly and impractical.¹¹

Of greater concern for microanalysis is loss of counts from a peak, through pile-up, to higher energy channels,¹¹ which causes k-factors to vary with count rate, a defect that will be most noticeable on thin-windowed and windowless detector systems because of the difficulty of detecting pile-up involving very low energy events. Therefore it is important to quantify the ability of a system to sense pile-up. In the simplest case where a peak with area A_E counts is accumulated in T livetime-corrected seconds, the area of the sum peak at twice the energy is given by

$$A_{2E} = A_E^2 t_r / T \quad (3)$$

where t_r is the pulse pair resolving time for two pulses of energy E .¹¹ If time constants are reduced, noise in the inspection channel will eventually swamp pulses of energy E and a pile-up continuum will appear instead of a clean sum peak; in this case, counts in the pile-up continuum should be added to A_{2E} in order to get an estimate of t_r suitable for estimating losses from a peak.¹¹

We have tested a new pulse processor (Link Analytical 2040) which includes three inspection channels with pulse peaking times of 0.1 μ s, 1 μ s, and 10 μ s. Figure 7 shows that the fastest channel can resolve two Fe K α pulses within 0.23 μ s according to Eq. 3. The intermediate speed channel provides protection well below 1 keV and Fig. 8 demonstrates an effective pulse pair resolution time of 0.97 μ s for 1.5 keV Al K α pulses; note in particular the absence of any pile-up continuum between the Al K and sum peaks. The slowest channel is required to cover the very low energy region and the spectrum from carbon in Figure 9 suggests a resolving time of 15 μ s for 282 eV pulses; Even at 3kcps, there is no pronounced pile-up continuum, and at 400 cps, the C + C sum peak is less than 0.3% of the C peak in area. The low noise performance of the pentafet enhances pile-up rejection capability by extending the effective range of each channel to lower energies.

Since elements such as Fe, Co, and Ni have low-energy L lines, pile-up will present a limitation to high rate work, even with a three-channel inspector, if this radiation is allowed to enter the detector. In this respect, the presence of an absorbing Be window is an asset rather than a disadvantage; if there is neither an absorbing window nor an inspection channel effective at very low energies, spectra will exhibit plateaus of various heights extending for several hundred eV above every major peak. Since each plateau contains counts which should have appeared in the peak, this feature will influence calculation of k-ratios, as explained above.

Future Developments

Most of the results for this paper were obtained on a prototype detector; until we have several production systems to test we shall not know whether the 40eV result is the best, average, or worst example of performance to be expected. In the absence of further supportive experimental data we can only speculate that:

1. In TEM and STEM applications the energy \times rate product and thus restore rate is high, so we would expect there to be a substantial reduction in deadtime through use of the fast restore time of the pentafet.
2. With the freedom to choose alternative dielectric materials and to modify the head design with no worry of light leakage, noise resolutions below 40 eV would seem attainable.
3. If a satisfactory head design can be achieved for a germanium detector, then results obtained to date¹² suggest that a resolution at Mn K α of less than 110 eV should be achievable.

References

1. K. Kandiah, *Proc. Conf. on Radiation Measurements in Nuclear Power*, London: Inst. of Physics and Physical Society, 1966, 420.
2. F. S. Goulding, J. T. Walton, and D. F. Malone, *Nucl. Instr. and Meth.* 71: 273, 1969.
3. P. J. Statham, *Proc. Workshop on Energy-dispersive X-ray Spectrometry*, NBS Special Publication 604, 1979 (issued 1981), 141.
4. K. Kandiah, A. J. Smith, and G. White, *IEEE Trans. NS-22*: 2058, 1975.
5. J. Llacer and D. F. Meier, *Nucl. Instr. and Meth.* 142: 597, 1977.
6. K. Kandiah and G. White, *IEEE Trans. NS-28*: 613-620, 1981.
7. T. Nashashibi and G. White, Link Analytical Ltd., private communication.
8. P. J. Statham, *Microbeam Analysis--1986*, 281.
9. P. J. Statham, *J. Microsc.* 130: 165-176, 1983.
10. P. J. Statham, *Microbeam Analysis--1982*, 1.
11. P. J. Statham, *X-ray Spectrom.* 6: 94, 1977.
12. C. E. Cox, B. G. Lowe, and R. A. Sareen, *Proc. 1987 Nuclear Science Symposium, IEEE Trans. Nucl. Sci.* (in preparation).

PLASMON ENERGY MEASUREMENT IN THE ELECTRON ENERGY LOSS SPECTRUM OF THE $\text{YBa}_2\text{Cu}_3\text{O}_{7-x}$ SUPERCONDUCTING CERAMICS

Dang-Rong Liu

An electron energy loss spectrum (EELS) collected in the low-loss region (from 0 to ~100 eV) can reveal the electronic structure, including the plasmon energy, of the sample examined in a transmission electron microscope (TEM).¹ For normal materials, this plasmon energy is no more significant than other valence-band features of the spectrum. When this technique is applied to the new superconducting materials, however, the plasmon energy can provide quantitative information on many important parameters of superconductivity. The present work is to demonstrate this potentiality.

Experimental

The $\text{YBa}_2\text{Cu}_3\text{O}_{7-x}$ specimen was prepared in the usual way.² A piece of sample was crushed into fine powder, which was then picked up onto a TEM grid covered with a holey carbon film. The specimen was examined in a Philips EM400T analytical microscope equipped with a Gatan 607 spectrometer. Spectra were collected in the diffraction mode, with the transmitted beam being displaced ~1 mrad relative to the 2mm spectrometer entrance aperture, in order to suppress the surface loss component of a spectrum.³ A select area diffraction aperture was used to select a region of 0.5-1.0 μm in size from which a spectrum was to be collected.

Results

A typical spectrum is shown in Fig. 1. The first prominent feature in the spectrum is at 4.8 eV, which must be the plasmon energy.¹ Other features can be attributed to various valence energy levels of the electronic structure of the specimen, which will not be further discussed in this paper. The importance of the plasmon energy is that the carrier density n can be related to the plasmon energy ω_p as follows:⁴

$$\omega_p = \sqrt{4\pi n e^2 / m} \quad (1)$$

where e is the electron charge and m the electron rest mass. The hole-like carrier⁵ density in the present case is then calculated to be $n = 2.1 \times 10^{22} \text{ cm}^{-3}$. In fact, the above expression is based on the free-electron gas model. The value so obtained can be compared

The author is with the Department of Materials Science and Engineering, Whitaker Laboratory #5, Lehigh University, Bethlehem, PA 18015. He thanks Drs. D. B. Williams, D. M. Smyth, and W. B. Fowler for useful discussions. This work is supported by the National Science Foundation under contract NSF-DMR-8400427.

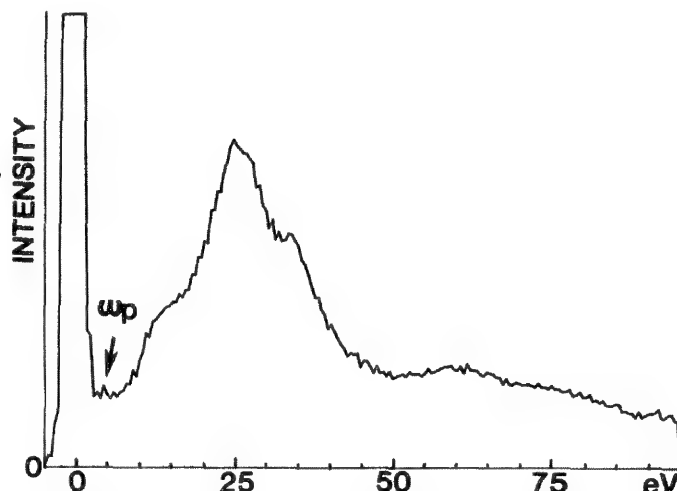


Fig. 1.--Typical EEL spectrum collected from $\text{YBa}_2\text{Cu}_3\text{O}_{7-x}$ sample.

with the results $n \approx (0.3 - 1.0) \times 10^{22} \text{ cm}^{-3}$ from the other methods.^{6,7} This result clearly demonstrates the compatibility of the value of the carrier density deduced from the plasmon by the EELS approach. We can go further to deduce other superconductivity parameters. For example, the magnetic-field penetration depth λ_0 can also be computed from ω_p by the following expression:⁴

$$\lambda_0 = c / \omega_p \quad (4)$$

where c is the speed of light. In the present situation, the value of λ_0 can be computed as 248 nm. This is the penetration depth at the absolute zero temperature. At the finite temperature T , the following expression is used:

$$\lambda = \lambda_0 / \sqrt{1 - (T/T_C)^4} \quad (3)$$

For $T_C = 95 \text{ K}$ and $T = 4 \text{ K}$, λ is practically the same as λ_0 and quite close to the value $\lambda = 200\text{--}250 \text{ nm}$ obtained by other methods.^{6,8} The lower critical magnetic field H_{C1} can then be computed from the equation:⁹

$$H_{C1} = \phi_0 / \pi \lambda^2 \quad (4)$$

where ϕ_0 is the fluxoid quantum and is equal to $2.07 \times 10^{-7} \text{ Gs cm}^2$. The lower critical field is then 110 Gs, which compares favorably with $H_{C1} = 100 - 150 \text{ Gs}$ measured by independent methods.¹⁰

Conclusions

We have demonstrated for the first time that the plasmon energy acquired by using the EELS in a transmission electron microscope can yield a lot of information pertinent to the electric properties of a superconducting material. With the plasmon energy value from the EELS experiment, the values of many electric/magnetic properties thus deduced compare quite favorably with those obtained with other independent approaches. Yet it is relatively easy to obtain in a microscope and can be complementary to the information from the imaging, diffraction, and other microanalytical techniques.

References

1. H. Raether, *Excitation of Plasmons and Interband Transitions by Electrons*, Berlin: Springer-Verlag, 1980.
2. C. M. Sung, P. Peng, A. Gorton, Y. T. chou, H. Jain, D. M. Smyth, and M. P. Harmer, "Microstructure, crystal symmetry and possible new compounds in the system $Y_1Ba_2Cu_3O_{9-x}$," *Adv. Ceramic Mat.* 2: 668, 1987.
3. D. R. Liu, "An experimental method of separation of the volume and surface loss components in an electron energy loss spectrum," *Phil. Mag.* B57: 619, 1988.
4. J. M. Ziman, *Principles of the Theory of Solids*, Cambridge, England: University Press, 1972.
5. J. T. Chen, C. J. McEwan, L. E. Wenger, and E. M. Logothetis, "Determination of charge carriers in superconducting La-Ba-Cu-O by thermoelectric measurements," *Phys. Rev.* B35: 7124, 1987.
6. G. Aeppli, R. J. Cava, E. J. Ansaldo, J. H. Brewer, S. R. Kreitzman, G. M. Luke, D. R. Noakes, and R. F. Kiefl, "Magnetic penetration depth and flux-pinning effects in high-Tc superconductor $La_{1.85}Sr_{0.15}CuO_4$," *Phys. Rev.* B35: 7129, 1987.
7. D. R. Harshman, G. Aeppli, E. J. Ansaldo, B. Batlogg, J. H. Brewer, J. F. Carolan, R. J. Cava, and M. Celio, "Temperature dependence of the magnetic penetration depth in high-Tc superconductor $Ba_2YCu_3O_{9-\delta}$," *Phys. Rev.* B36: 2386, 1987.
8. W. J. Kossler, J. R. Kempton, X. H. Xu, H. E. Schone, Y. J. Uemura, A. R. Moodenbaugh, and M. Suenaga, "Magnetic field penetration depth of $La_{1.85}Sr_{0.15}CuO_4$ measured by muon spin relaxation," *Phys. Rev.* B35: 7133, 1987.
9. C. Kittel, *Introduction to Solid State Physics*, 5th ed., New York: Wiley, 1976.
10. H. Maletta, A. P. Malozemoff, D. C. Cronmeyer, C. C. Tsuei, R. L. Greene, J. G. Bednorz, and K. A. Muller, "Diamagnetic shielding and Meissner effect in the high Tc superconductor $Sr_{0.2}La_{1.8}CuO_4$," *Solid State Comm.* 62: 323, 1987.

ON THE COMPUTATION OF K_{AB} FACTORS FOR $K\alpha$ LINES

Raynald Gauvin, Gilles L'Espérance, and Gregory Kennedy

There are several reasons that theoretical K_{AB} factors calculated from first principles are generally less accurate than experimental K_{AB} factors obtained with standards of known composition. One reason is that computation of accurate theoretical K_{AB} factors requires a good parametrization of ionization cross sections Q . Inspection of the Bethe formula for Q shows that if the b_k parameter is not a function of atomic number, only the C_k parameter is needed to compute K_{AB} . In this paper, the C_k parameter is computed by a method¹ that uses ratios of experimental K_{AB} factors obtained at various accelerating voltages.

Theoretical

The absolute x-ray net intensity I_A for an element A in a thin foil free of absorption and fluorescence is given by

$$I_A = i(\Omega/4\pi)(Q\omega\alpha\epsilon/A) \rho N_0 t C_A \quad (1)$$

where i is the total electron dose, $(\Omega/4\pi)$ is the fractional solid angle, Q is the ionization cross section, ω is the fluorescence yield, α is the relative transition probability $(K\alpha/K\alpha + K\beta)$, ϵ is the Si(Li) detector efficiency, A is the atomic weight, ρ is the sample density, N_0 is Avogadro's number, t is the distance traveled by the electrons in the specimen, and C_A is the weight fraction of element A.

In practice, a frequently used quantification procedure is that due to Cliff and Lorimer,² in which the net intensities I_A and I_B are related to the concentrations C_A and C_B of two elements A and B by the following equation:

$$\frac{C_A}{C_B} = K_{AB} \frac{I_A}{I_B} \quad (2)$$

The constant of proportionality K_{AB} can either be determined experimentally from a sample of known composition and sufficiently thin to neglect absorption and fluorescence within the sample; or calculated from

The authors are at Ecole Polytechnique de Montréal, C.P. 6079, Succ. A, Montréal, Canada H3C 3A7. R. Gauvin and G. L'Espérance are with the Center for Characterization and Microscopy of Materials, Département de Génie Metallurgique; G. Kennedy is in the Département de Génie Energétique. This work was supported by grants from the Natural Sciences and Engineering Research Council of Canada and from l'Association des Diplômés de Polytechnique (R. Gauvin).

$$K_{AB} = \frac{(Q\omega\alpha/A)_{B\epsilon_B}}{(Q\omega\alpha/A)_{A\epsilon_A}} \quad (3)$$

obtained by substitution of Eq. (1) into Eq. (2).

Experimental K_{AB} factors are generally more accurate than computed K_{AB} factors because of uncertainties in ϵ and in Q .³ The ionization cross section is given by³

$$Q_{n\ell} = \frac{6.5 \times 10^{-20} Z_{n\ell} b_{n\ell} \ln(C_{n\ell} U)}{E_{n\ell}^2 U} (\text{cm}^2) \quad (4)$$

where $Z_{n\ell}$ is the number of electrons in the shell, $E_{n\ell}$ is the binding energy for that shell (keV), $U = E_0/E_{n\ell}$, E_0 is the energy of incident electron (keV), and $B_{n\ell}$ and $C_{n\ell}$ are constants for the $n\ell$ shell.

In the 100-400kV range, relativistic effects are present for incident electrons and an expression to correct the incident energy has been proposed³ to compute Q from Eq. (4). Another expression to compute Q , which includes a relativistic correction, can also be used.⁴ These relativistic corrections change the absolute values of Q but do not change the ratio of Q_A/Q_B needed to compute a K_{AB} factor (Fig. 1). Equations (4) and (3) can thus be used to calculate a K_{AB} factor and no correction for relativistic effects need be carried out.

The value of $C_{n\ell}$ in Eq. (4) can be obtained from¹

$$C_{n\ell} = \exp \left[\left(\frac{\psi^2}{4} - \frac{R_{AB}^{E_1-E_2} \alpha - \beta}{R_{AB}^{E_1-E_2} - 1} \right)^{\frac{1}{2}} - \frac{\psi}{2} \right] \quad (5)$$

where

$$\psi = \ln(U_B^{E_1} U_A^{E_2}) = \ln(U_B^{E_2} U_A^{E_1}) \quad (6)$$

$$\alpha = (\ln U_B^{E_1})(\ln U_A^{E_2}) \quad (7)$$

$$\beta = (\ln U_B^{E_2})(\ln U_A^{E_1}) \quad (8)$$

$$R_{AB}^{E_1-E_2} = \frac{K_{AB}^{E_2}}{K_{AB}^{E_1}} = \frac{Q_B^{E_2} Q_A^{E_1}}{Q_B^{E_1} Q_A^{E_2}} \quad (9)$$

where $K_{AB}^{E_1}$ and $K_{AB}^{E_2}$ are obtained at two different accelerating voltages E_1 and E_2 . Taking the ratio $R_{AB}^{E_1-E_2}$ means that ϵ , α , ω , and A at the numerator and denominator will cancel and so remove the uncertainties associated

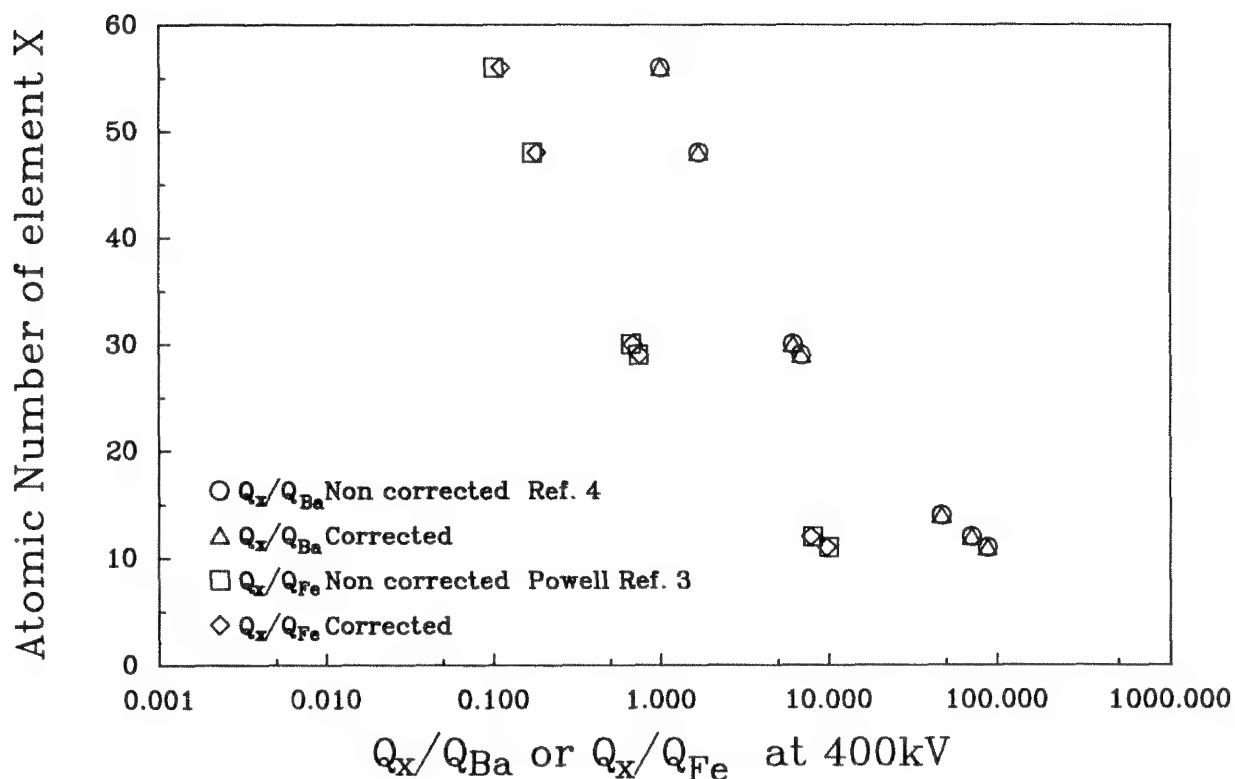


FIG. 1.--Ratios of ionization cross sections with and without relativistic correction. In Ref. 3, incident energy is corrected in Eq. (4). In Ref. 4, experimental cross sections from 80 to 200 kV were obtained. The authors then obtained b_k and C_k using Eq. (4) without relativistic correction and also using expression that includes relativistic correction. Relativistic correction does not change ratio of cross sections needed to compute K_{AB} factor.

with these values, particularly that with ϵ . This equation is valid when K_{AB} is obtained with the same type of lines (K, L, M) for both elements A and B.

Experimental

K_{AB} factors were obtained at 120 kV in a JEOL 100-CX coupled with a Tracor Si(Li) EDS x-ray detector. K_{Ni-Fe} and K_{Cr-Fe} were obtained with a 16Cr-24Fe-60Ni alloy, K_{Nb-Fe} was calculated from K_{Fe-Ni} and K_{Nb-Ni} obtained with a 10Nb-90Ni alloy, and K_{Zn-Fe} with a synthetic powder of FeS-ZnS. The alloys were tested for homogeneity by electron microprobe and the powder by x-ray diffraction. The alloys were jet electropolished to produce thin foils and the powder was crushed in methanol and deposited on a copper grid covered with a carbon film. Thirty spectra were recorded for each K_{AB} factor; K_{Fe-Ni} was corrected for fluorescence as in Ref. 3. The thickness was determined by the spot contamination method.

Results

Table 1 shows the value of the C_k parameter computed from Eqs. (5) to (9) and the values of K_{Cd-S} , K_{Ba-S} , and K_{Zn-S} for K α lines obtained at 100 and 200 kV by Schreiber and Wims.⁵ An average value of 0.74 is obtained which is between the C_k value obtained by Paterson et al.⁴ and Powell.⁶ We did not use, from the values

of Schreiber and Wims,⁴ K_{Cu-S} because of some Cu probably arising from the microscope column, K_{Na-Cl} because of the evaporation of Na, and K_{Mg-Si} because of the small variation of this K_{AB} factor with voltage.

The other constant needed to compute Q from Eq. (4) is the b_k parameter. However, as shown by many workers,^{4,6-8} the value of b_k is not a function of atomic number. This constant therefore cancels in Eq. (4), so that only the value of C_k is needed to compute K_{AB} factors from that expression. Table 2 shows K_{X-Fe} factors computed by use of $C_k = 0.74$ and with the cross-section parametrization of Powell;⁸ ω , α , and ϵ were taken from Ref. 3. Also shown are our experimental K_{X-Fe} factors and those obtained by Wood et al.³ Since the detector efficiency ϵ is microscope dependent for elements lighter than Cr and heavier than Nb, only K_{X-Fe} factors for which ϵ is likely to be close to 1 are shown.

Clearly, the agreement between experimental and our computed K_{AB} factors is good, which shows the potential of taking the ratios of K_{AB} factors obtained at various accelerating voltages to compute the C_k parameter of Eq. (4). Also, with two K_{AB} factors obtained at two different accelerating voltages, it is possible to compute a K_{AB} factor at any other accelerating voltage from Eq. (9) without the knowledge of detector efficiency.

TABLE 1.-- C_k calculated from (5) to (9) using experimental K_{AB} factors obtained by Schreiber and Wims⁵ at 100 and 200 kV.

K AB	100-200 R AB	C k
Zn-S	0.91	0.83
Cd-S	0.67	0.62
Ba-S	0.61	0.76
		AVERAGE 0.74

TABLE 2.--Experimental and computed K_{x-Fe} factors at 120 kV.

K x-Fe	COMPUTED		EXPERIMENTAL	
	This work	Powell ⁸	This work	Wood ³
Cr	0.86	0.917	0.94	0.90
Mn	0.92	0.97	----	1.04
Co	1.01	1.074	----	0.98
Ni	1.04	1.096	1.14	1.07
Cu	1.16	1.227	----	1.17
Zn	1.23	1.305	1.26	1.19
Nb	3.30	3.50	3.53	2.14

Conclusions

A method to compute K_{AB} factors for K_{α} lines on the knowledge of the C_k parameter of the Bethe formula for the ionization cross section has been presented. The agreement between K_{AB} factors computed with this method and our experimental K_{AB} factors and some from the literature is very good. A useful feature of the method in the context of intermediate voltage analytical electron microscopy is that it allows one to calculate a K_{AB} factor for any accelerating voltage from two K_{AB} factors obtained at different voltages without the need to know the detector efficiency (Eq. 9).

References

1. R. Gauvin and G. L'Espérance, "The determination of C_{nl} parameter in the Bethe formula for the ionization cross-section by the use of Cliff-Lorimer K_{AB} factors obtained at different accelerating voltages in a TEM," *J. Microsc.* (submitted).
2. G. Cliff and G. W. Lorimer, *J. Microsc.* 103: 203-207, 1975.
3. J. E. Wood, D. B. Williams, and J. I.

Goldstein, *J. Microsc.* 133(pt. 3): 255-274, 1984.

4. J. H. Paterson, W. A. P. Nicholson, J. N. Chapman, and R. H. Geiss, *Analytical Electron Microscopy--1987*, 96-98.
5. T. P. Schreiber and A. M. Wims, *Ultra-microscopy*, 6: 323-334, 1981.
6. N. F. Mott and H. S. W. Massey, *The Theory of Atomic Collisions*, 2nd ed., London: Oxford University Press, 1949.
7. M. Green and V. E. Cosslett, *Proc. Phys. Soc.* 78: 1206-1214, 1961.
8. C. J. Powell, *Rev. Mod. Phys.* A48: 33-47, 1976.

PROBE SIZE MEASUREMENT IN A FIELD-EMISSION STEM

J. R. Michael

An accurate knowledge of the electron probe size and the current distribution in the probe is required for effective utilization and interpretation of the results of high spatial resolution microanalysis obtained from a modern analytical electron microscope (AEM). It is the purpose of this paper to describe a technique for probe size determination in an AEM equipped with a cold field-emission gun, and to compare the measured probe sizes with those calculated from geometrical electron optics considerations.

The most popular method for measuring probe size on scanning electron beam instruments involves scanning the probe across a suitably sharp knife-edge and monitoring, with a suitable detector, the intensity change that occurs.¹⁻⁵ This technique yields an integrated intensity profile and, as will be shown later, does not directly give the full width at half maximum (FWHM) of the electron distribution in the probe. In some transmission electron microscope/scanning transmission electron microscope (TEM/STEM) instruments, it is possible to image the electron probe on the TEM screen and measure the probe size directly.⁶⁻⁸ This direct method is probably the best way to determine the probe sizes generated by thermionic sources in TEM/STEM instruments. In order to measure the very small probe diameters generated by a cold field-emission gun (FEG), in a dedicated scanning instrument, direct imaging of the probe is not possible and a knife-edge technique must be used.

Many definitions of probe size have been used. The current distribution in the electron probe is usually assumed to be Gaussian, although recent experimental studies have shown that to be the case only when the electron probe is properly limited by the second condenser aperture.^{7,8} It is important to specify the fraction of the total probe current that is included in a specified probe diameter. Instrument manufacturers usually report probe diameters containing 50% of the total current (the FWHM). Other equally valid definitions could be the diameter that contains 40% of the current which represents a single standard-deviation (σ) diameter; or 90% of the current, which is the full width at tenth maximum (FWTM). For a Gaussian distribution, the FWHM is 2.35 times larger than the standard deviation and the FWTM is 1.8 times larger than the FWHM. Since the standard deviations, FWHM, and FWTM are all consistently related for a Gaussian distribution, any one of them can be used as a definition of a probe

size provided the diameter used is specified. For microanalytical use, the FWTM definition is particularly useful in that the commonly used equations to calculate the broadening of the electron probe as it traverses a thin sample describe a diameter which contains 90% of the incident electrons. The FWTM definition of the probe size has been proposed previously.⁹

Experimental

A Vacuum Generators HB-501 dedicated STEM was used in this study. The microscope is equipped with a cold field-emission source (<310> tungsten), operated at 100 kV. The illumination system consists of a gun lens, two condenser lenses, and a high-excitation objective lens with a spherical aberration coefficient C_s : 3.2 mm.¹⁰ The illumination system also utilizes a virtual objective aperture (VOA), which is similar to a C2 aperture in a TEM/STEM, and also reduces spurious x rays to an extremely low level. The VOA is in a plane that is approximately optically conjugate to the objective aperture of the STEM and is physically placed after the gun lens and before the condenser lenses.¹¹ This configuration has the disadvantage that the VOA is very close to the electron source, which causes the alignment of the aperture to be extremely critical. The advantage of this configuration is that probe current is essentially independent of the C1 and C2 settings. Thus, convergence angles (and hence probe sizes) may be selected without changes in the probe current at the specimen. If the objective aperture is used, the convergence angle is fixed by the aperture size and is independent of C1 settings.

Since it is not possible to image the electron probe directly in a dedicated STEM, a variation of the knife-edge technique was used. Small MgO smoke particles were generated by burning Mg ribbon, and collected on flamed 400 mesh Cu grids. The grid was immediately placed into the microscope and heated to $\sim 90^\circ\text{C}$ for 5 min in a vacuum of 1×10^{-8} torr. The specimen was then transferred into the microscope vacuum of 1×10^{-9} torr. Cube-shaped MgO crystals (~ 10 -50 nm in size) were oriented so that the electron beam was parallel to one of the crystal faces. No visible contamination of the specimen was observed. The beam was scanned across the crystal and the annular dark field (ADF) signal was recorded at $5 \times 10^6\times$. The focus of the objective lens was adjusted (underfocused) to yield the most abrupt change in intensity on the ADF signal as the probe was scanned across the edge of the crystal. The probe size was then determined from the line profiles as is described later. The beam currents measured at the specimen were ~ 4 nA for

The author is at the Homer Research Laboratories, Bethlehem Steel Corp., Bethlehem, PA 18016.

the $\sim 100\mu\text{m}$ VOA, ~ 1 nA for the $50\mu\text{m}$ VOA, and ~ 0.3 nA for the $25\mu\text{m}$ VOA. Probe convergence angles were measured by recording stationary diffraction patterns from pure Ni.¹²

Results and Discussion

The final probe size may be calculated by assuming that it is determined by an initial Gaussian diameter d_g and the diameter of the disks of minimum confusion due to spherical aberration d_s , and diffraction from the probe forming aperture d_d .^{3,12,13} The final probe size may then be estimated by adding the three contributions to the probe size in quadrature.^{3,12-17} Thus, the total probe size d_t is given by

$$d_t = (d_g^2 + d_s^2 + d_d^2)^{1/2} \quad (1)$$

which gives a first-order estimate of probe size, although it is clear that d_s and d_d are not invariably Gaussian. The initial Gaussian diameter is given by:

$$d_g = \frac{2}{\pi} \frac{I_p}{\beta} \alpha^{-1/2} \quad (2)$$

where α is the convergence semi-angle, I_p is the probe current, and β is the brightness of the source. The brightness for an FEC operated at 100 kV was assumed to be $\sim 1 \times 10^5$ A/cm²/sterad.¹⁰ The diameter of the disk of minimum confusion caused by spherical aberration is given by

$$d_s = 0.5 C_s \alpha^3 \quad (3)$$

where C_s is the spherical aberration coefficient for the objective lens. A diameter that represents the FWHM of the intensity distribution would replace the 0.5 coefficient by 0.3.^{3,14} However, the diameter of the spherical aberration disk in the Gaussian image plane (which would normally represent a focused image) would replace the coefficient 0.5 by 2.0. Depending on the size of the aperture used, the intensity distribution may or may not be Gaussian. The diffraction-limited diameter is given by

$$d_d = 1.22 \lambda / \alpha \quad (4)$$

where λ is the electron wavelength and 1.22 gives the diameter of the first minimum in the interference function, which is a diameter that contains 85% of the incident intensity. This distribution is not Gaussian. Probe diameters calculated in this manner have been used to estimate the FWHM of the electron distribution.¹² Two of the components of the probe size may not be Gaussian, so that this calculation actually represents some unknown fraction of the total probe intensity. Since the FWHM of the probe intensity is normally quoted in the literature, this study compares the experimentally measured FWHM with the results of the above calculations.

The FWHM of the electron probe may be determined by measuring the horizontal distance between the 12% and 88% points on the integrated intensity profile (not as commonly used, the distance between the 25% and 75% points). As the probe is scanned across the edge of the MgO crystal, the intensity of the probe is not integrated radially, but from one side of the two-dimensional Gaussian to the other. This integration has been described previously.¹⁸ Figure 1 is a schematic of the integrated intensity profile that results when a Gaussian distribution is scanned over an edge. The distances that represent the various fractions of the distribution are also indicated. As can be seen, the FWHM is the distance between the 12% and 88% points on the integrated intensity scan. In order to determine the FWTM of the distribution, the distance between the 2% and 98% points must be measured. If a Gaussian distribution is assumed, the FWTM may be determined by measuring the FWHM and multiplying it by 1.8.

Figure 2a is an ADF integrated intensity profile one obtains by scanning the probe across the edge of a MgO cube using a $100\mu\text{m}$ VOA and a first condenser setting of 17. Figure 2b is similar to Fig. 2a, except that a $50\mu\text{m}$ VOA aperture was used. It is apparent that the smaller VOA results in a smaller probe size due to the smaller convergence angle. Figure 2c is an ADF intensity profile for the $25\mu\text{m}$ VOA. If Gaussian intensity distributions are assumed, the FWTM probe sizes are 7.4 nm for the $100\mu\text{m}$ VOA, 1.8 nm for the $50\mu\text{m}$ VOA, and 3.5 nm for the $25\mu\text{m}$ VOA.

Figure 3 shows the calculated and experimentally measured probe sizes for the 50, 100, and $25\mu\text{m}$ VOA. The agreement between the calculated and experimental values for the $50\mu\text{m}$ aperture shown in Fig. 3a is good. The optimum combination of a $50\mu\text{m}$ VOA and a C1 setting of 17 results in a convergence angle of 6.75 mrad and a probe size of 1.0 nm with ~ 1 nA of current. Figure 3b shows the data for the $100\mu\text{m}$ VOA. Due to spherical aberration, the minimum probe size is increased to over 2.0 nm and the measured values are not in good agreement with the calculated values, probably as a result of the intensity distribution within the probes not being Gaussian. Figure 3c shows the data for the $25\mu\text{m}$ VOA, which allows small convergence angles to be obtained. As the convergence angle is reduced from 6.1 mrad to 1.5 mrad, the probe size increases. The increase in the probe size with decreasing convergence angle may be the result of the probe being diffraction limited by the VOA and may cause the intensity distribution within the probe to deviate substantially from Gaussian, which results in the measured and calculated probe sizes differing. The optimum aperture size needed to limit a given probe properly can be calculated and is given by⁷

$$d_t = 1.1 C_s \alpha^3 \quad (5)$$

If a 1.0nm FWHM probe is desired, the opti-

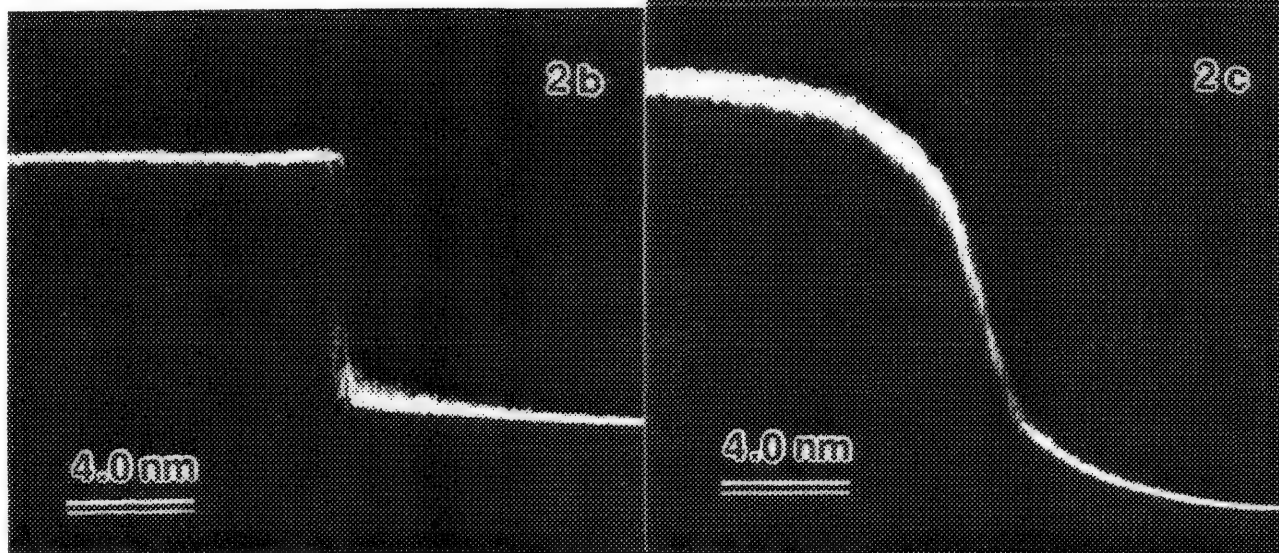
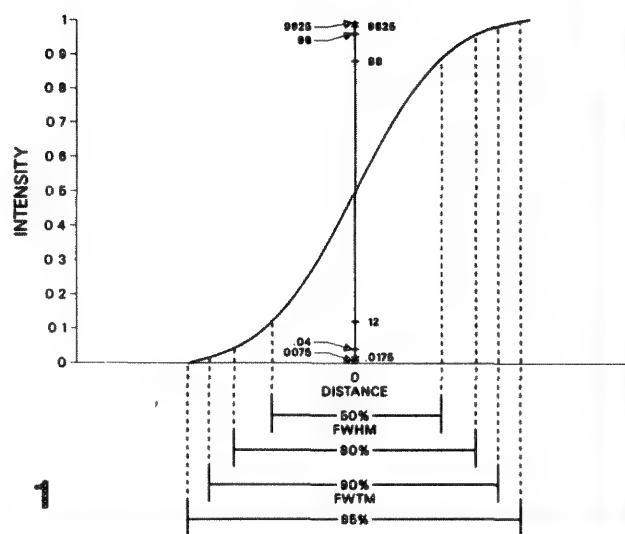


FIG. 1.--Schematic integrated intensity profile obtained by scanning Gaussian probe across knife-edge, along with distances that represent various probe size definitions.

FIG. 2.--Annular dark-field integrated intensity profile obtained by scanning electron probe across edge of MgO crystal. (a) 100 μ m VOA, C1 = 17; (b) 50 μ m VOA, C1 = 17; (c) 25 μ m VOA, C1 = 17.

mm aperture would be $\sim 60 \mu\text{m}$, which is close to the 50 μm VOA used in this study; thus, the 1.0nm FWHM probe generated in this study may be considered to be Gaussian. Probes generated with larger apertures may be spherically aberrated.

Figure 4 is a log-log plot of the measured probe sizes (FWHM) from all the three VOAs vs the convergence angle. It is apparent that the probe size decreases with decreasing convergence angle until a minimum is reached, at about 6-7 mrad. As the convergence angle is reduced further, the probe size begins to increase as a result of the probes being diffraction limited by the 25 μm VOA.

The probe sizes (FWHM) for the 50 and 100 μm VOAs may be described by

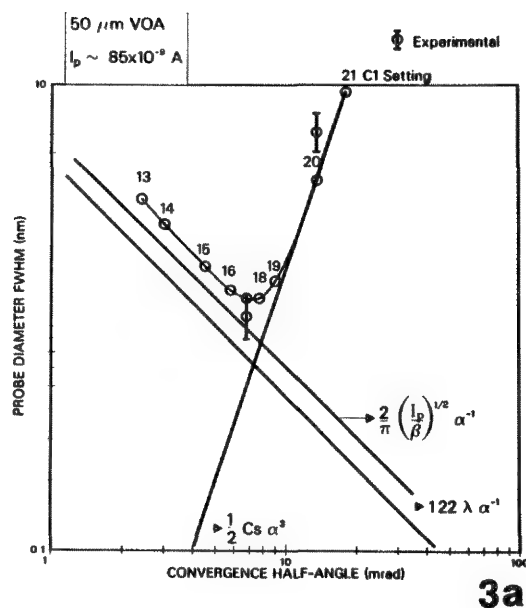
$$d_{\text{FWHM}} = 1.22C_s \alpha^3 \quad (6)$$

which is very similar to Eq. (3) except that the coefficient is different. A previous study found that the probe size as measured by scanning the probe across the edge of a thin gold film, and monitoring the x-ray count rate could be described by the same equation except that the coefficient was 1.56.¹² These coefficients lie between those for the spherical aberration disk in the Gaussian image plane ($2.0C_s \alpha^3$) and the size of the disk of minimum confusion ($0.5C_s \alpha^3$).

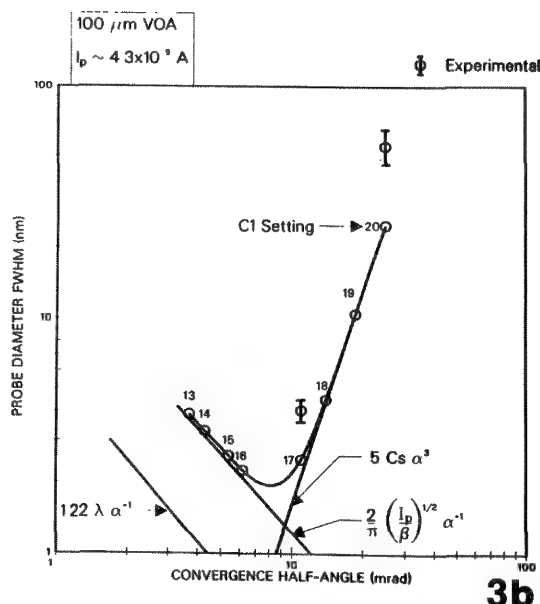
The data for the 25 μm VOA as shown in Fig. 6 may be described by

$$d_{\text{FWHM}} = 0.60\lambda/\alpha^{1.3} \quad (7)$$

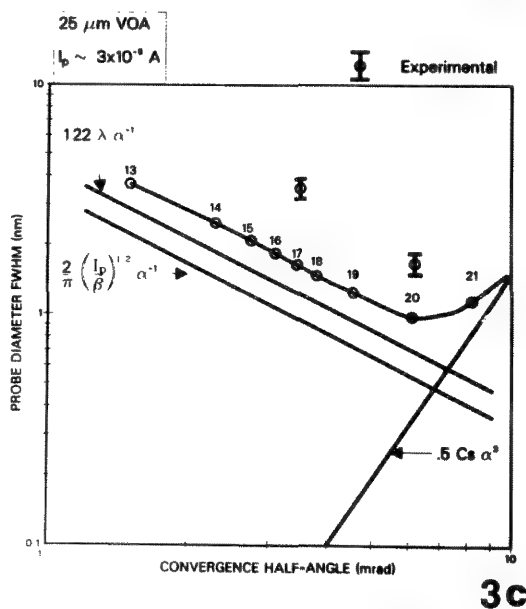
This equation is similar to Eq. (4). More experimental data are needed to draw any conclusions from these data, although the line



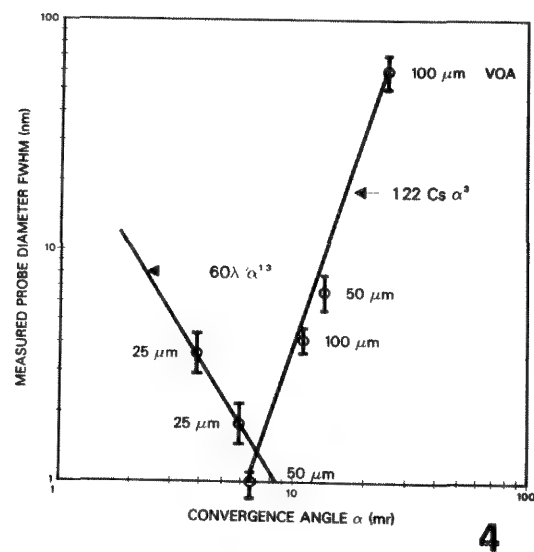
3a



3b



3c



4

FIG. 3.--Calculated probe sizes (FWHM) vs convergence angle α over range of C1 settings for (a) 50 μ m VOA, (b) 100 μ m VOA, and (c) 25 μ m VOA. Also shown are two experimentally determined probe sizes at C1 = 17 and C1 = 20.

FIG. 4.--Log-log plot of measured probe size (FWHM) vs convergence angle for 100, 50, and 25 μ m VOA.

through the data points has a slope close to the theoretical value when plotted on a log-log scale.

The knowledge of the probe sizes and beam currents generated in an AEM allow the operator to make intelligent choices of operating conditions for a particular experiment. If microanalysis were being performed on a specimen that did not require the highest resolution, the 100 μ m VOA and a C1 setting of 17 would generate a probe \sim 2-3 nm (FWHM) in size with \sim 4nA of current. This probe would provide the required resolution and the high probe current would provide high x-ray count rates for microanalysis. If higher resolution is required, the 50 μ m VOA could be used with

a C1 setting of 17 to provide a probe 1.0 nm FWHM in size which contains 1 nA. For microanalysis, there is no advantage to using the 25 μ m VOA since the probe sizes are slightly larger and the probe currents much lower than those generated with the 50 μ m VOA. The small convergence angles produced by the 25 μ m VOA may be useful in electron diffraction work.

Conclusions

1. It is possible to measure small probe sizes using MgO crystals as knife-edges, provided the instrument is capable of high magnification in a scanning mode, and the vacuum system is clean to avoid contamination.

2. The minimum FWHM probe size in the FEG-equipped AEM used in this study was 1.0 ± 0.2 nm with 1 nA of current, and was obtained with a beam convergence of 6.75 mrad.

3. Convergence angles of ~ 7 mrad or more result in probes limited by spherical aberration; convergence angles of 5 mrad or less result in probes limited by diffraction effects.

4. Probe sizes quoted in the literature should specify either the FWHM or FWTM probe size and what size probe limiting aperture was used.

References

1. D. C. Joy, *SEM/1974*, 327.
2. W. H. Vaughan, *SEM/1976*, 746.
3. T. Hanai and M. Hibino, *J. Electron Microsc.* 33: 116, 1984.
4. E. Oho et al., *J. Electron Microsc. Tech.* 2: 463, 1985.
5. E. Oho et al., *J. Electron Microsc. Tech.* 3: 159, 1986.
6. J. Bentley, *Proc. 38th Ann. Meet. EMSA*, 1980, 72.
7. G. Cliff and P. B. Kenway, *Microbeam Analysis--1982*, 107.
8. C. F. Klein et al., in *Intermediate Voltage Microscopy and Its Application to Material Science*, Mahway, N.J.: Electron Optics Publishing Group, 1987.
9. J. R. Michael and D. B. Williams, *J. of Microsc.* 147: 289, 1987.
10. C. Colliex, *Ultramicroscopy* 18: 131, 1985.
11. I. R. M. Wardell, *Ultramicroscopy* 7: 39, 1981.
12. L. E. Thomas, *Ultramicroscopy* 9: 311, 1982.
13. E. Zeitler, in *Proceedings of a Specialist Workshop in Analytical Electron Microscopy*, Cornell University, 1987, 1.
14. O. C. Wells, *Scanning Electron Microscopy*, New York: McGraw-Hill, 1974, 69.
15. L. Reimer, in *Quantitative Electron Microscopy*, Scottish Universities Summer School of Physics, Glasgow, Scotland, 1984, 217.
16. J. A. Venables and G. Cox, *Ultramicroscopy* 21: 33, 1987.
17. C. Colliex and C. Mory, in Ref. 15, p. 149.

MATERIALS ANALYSIS BY STEM-EDX AT HIGH SPATIAL RESOLUTION

J. M. Titchmarsh

Surface analysis methods such as Auger spectroscopy (AES) have been traditionally used to measure the chemical composition at grain boundaries in polycrystalline alloy systems. A prerequisite is the ability to reveal boundaries by fracture. Even when that is possible, the presence of fine-scale precipitation on the boundaries might not be noticed, which might cause errors in data interpretation. Energy-dispersive x-ray analysis (EDX) in the scanning transmission electron microscope (STEM) offers an alternative technique for measuring interface composition. Examples are described of the use of STEM-EDX to reveal the presence of equilibrium and nonequilibrium segregation in alloys. Quantitative analysis is aided by comparison of experimental data and calculated composition profiles. A method of analysis of equilibrium segregation is suggested that requires less stringent control of experimental variables.

Spatial Resolution

The relationships among the experimental parameters of importance to high spatial resolution EDX and electron energy loss spectroscopy (EELS) have been described previously.^{1,2} There is an increasing number of reports showing high-spatial-resolution profiles in a range of materials (e.g., Refs. 1-10, and others). Obviously, the best resolution obtainable is determined by the probe current distribution, which is a complex function of probe convergence angle and defocus,¹¹ with an additional broadening (usually negligible in EDX) due to localization.¹² High-angle elastic scattering of the electron probe ("beam broadening") causes spurious x-ray fluorescence in EDX in regions laterally distant from the beam impact point.¹³ Although this effect can cause extended tails on otherwise narrow profiles, which increase with foil thickness t , experimental evidence and calculation suggest that the most important consequence of beam broadening is a reduction in the measured concentrations of small homogeneities; the full-width half-maximum (FWHM) values of profiles do not change rapidly with thickness.^{3,5} Moreover, the use of a field-emission gun (FEG) provides sufficient current in a 2nm-diameter probe to allow detected count rates of several hundred x rays per second in a foil thickness t of only a few tens of nanometers,

The author is at MPMD, Harwell Laboratory, Didcot, Oxon, England OX11 0RA. This work was undertaken as part of the UKAEA Underlying Research Programme. The support of I. A. Vatter, A. W. James, and Dr. M. Wall is gratefully acknowledged.

so that the need to use thick foils is reduced.

Equilibrium segregation at grain boundaries can be sometimes detected with a heated W filament electron source.^{14,15} These workers have also derived quantitative values for segregation. However, detection limits and accuracy of measurement are improved by the use of a FEG STEM.^{1,16}

Experimental and Theoretical Procedures

The experimental data were measured with the following equipment: a VG Microscopes HB501 FEG STEM, a VG ELS501 EELS spectrometer, a Link Analytical windowless EDX detector, and a Link Analytical AN10/85 computer. Foils were prepared by electropolishing and by ion milling. Resolution test specimens were made by collection of MgO smoke particles on holey carbon films. The procedures for collecting EDX composition profiles have been described previously.⁵

Foil thicknesses were calculated from measurements of t/λ by EELS, where λ , the total mean free path for inelastic scattering, was estimated from a parametric equation.¹⁷ Probe sizes were measured from the annular dark-field (ADF) signal line scans across accurately oriented edges of MgO cubes. Similar measurements have been reported by experimenters using the EELS signal.¹⁸

Concentration profiles were calculated by use of a Monte Carlo program to determine the likely effect of beam broadening, with a choice of various specimen geometries, including a film of segregation.¹⁸ It is similar to other programs in using a screened Rutherford scattering potential,^{14,19} but can also use a Doyle-Turner potential for greater accuracy with very fine probes.

Results

The probe size dependence on condenser lens excitations is shown in Fig. 1. Probe diameter ϕ_{80} is defined as the distance over which the ADF signal changes from 10% to 90% as the probe is scanned across the MgO cube face. Three curves are shown, each for a different combination of the gun lens excitation and virtual objective aperture (VOA), which must be used during x-ray acquisition to define the probe convergence, instead of the objective aperture. The probe current is constant along each curve, and Fig. 1 is used to choose the excitations to give the smallest probe diameter. In practice, the lowest curve (A) usually has too little current for x-ray analysis of thin ($t < 50$ nm) foils in the typical analysis times (< 200 s), and curves (B) and (C) represent the limits of the range of condi-

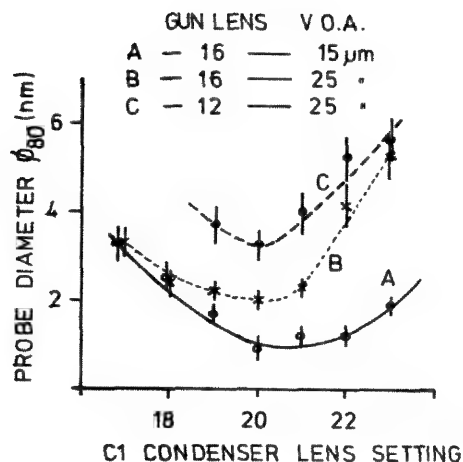


FIG. 1.--Variation in measured electron probe size as function of condenser lens excitation; different combination of gun lens excitation and VOA size was used for each curve.

tions used for analysis. These curves would all have the same minimum value (at different condenser excitations) if the source size in the object plane of the objective lens was vanishingly small, which is clearly not the case.

The demonstration of a finite source size by the results in Fig. 1 is important because it suggests that oscillations in the probe current distribution, which are predicted for a point source and which change rapidly with focus,¹¹ will not be present in our probe. To support this result, Fig. 2 has been computed to show how the fluctuations predicted for a point source at one specific optical configuration are almost eliminated when convoluted with a 1nm-diameter spread function with a "top-hat" profile. The resulting curve (C) becomes roughly Gaussian in shape.

An example of grain boundary segregation in an Al-Cu-Zn alloy is shown in Fig. 3. The profiles of Zn, Cu, and Mg have similar widths and are roughly symmetrical. These results are consistent with equilibrium segregation, because the profiles show no significant broadening compared with the probe diameter ϕ_{80} of ~ 2.5 nm. If the segregated elements are confined to one or two atom planes adjacent to the boundary, then the measured profile is simply a convolution of the probe with an approximate δ -function.^{1,5} There was sufficient Zn at this boundary in the specimen to enable an elemental map to be acquired, of 128×128 pixels, in ~ 30 min. Figure 4a shows the boundary as a rippled line because of drift induced by thermal changes as the air-conditioning unit switched on and off. A straight boundary was recorded when this anomaly was eliminated, and some variation of Zn along this section of boundary is suggested by the contrast changes in the image.

The quantification of data in the form of symmetric profiles to derive an equivalent atomic layer value has been reported previously.⁵ When the foil is very thin and "beam-

broadening" is ignored, the profile shape and height provide enough information. Beam broadening in thicker foils changes the profile height and shape, and scaling of the experimental profiles against Monte Carlo computations is then made to derive the level of segregation.

Computations are shown in Fig. 5 for the case of a 25% atomic layer of P segregation in an Fe foil. In Fig. 5a the profiles are shown as a function of electron probe diameter; in Fig. 5b the effect of inclining the boundary plane up to 5° from the ideal orientation is shown. When the areas under these curves are measured with a digitizer, it is found that they are equal, within experimental error. This is also true for changes in t up to 100 nm, for a fixed probe size and orientation.²⁰ These observations suggest that one can measure the level of segregation by integrating the area in a profile and then scaling to a single value, computed for a known amount of segregation. A precise knowledge of t , ϕ , and boundary inclination is not necessary. This method may become inaccurate as t increases above 100 nm (for a steel foil), because the total electron trajectory length has a greater dependence than unity on t . More detailed comparisons of experimental and theoretical profiles will then be necessary.³ However, we have found that we rarely measure profiles from foils where $t > 100$ nm because x-ray counting rates then can become too large.

Analysis of the profiles in Fig. 3 yields equivalent fractional monolayer coverages of 0.39 ± 0.04 , 0.15 ± 0.02 , and 0.08 ± 0.02 , respectively, for Cu, Zn, and Mg. The detection limits for Zn and Cu in Al are approximately 1% of a monolayer. For the case of P in a ferritic steel the detection limit is estimated to be $\sim 5\%$.⁵

Nonequilibrium segregation causes a gradual variation in the chemical concentration in the vicinity of sinks such as a precipitate or a grain boundary. Austenitic stainless steels can become susceptible to corrosion by nonequilibrium segregation of Cr and precipitation of Cr-rich particles during thermal aging. Recently we have examined steels sensitized by irradiation with neutrons at low temperatures ($< 450^\circ\text{C}$), and revealed very narrow profiles that clearly showed nonequilibrium character.²¹ An example is shown in Fig. 6. The high spatial resolution of the profiles enabled a successful comparison to be made with profiles calculated from diffusion models, for a range of temperatures. In a second study the transition from equilibrium to nonequilibrium segregation of Cr and Mo in type 316 stainless steels has been studied as a function of aging.²² Again, it is possible to determine the likely effect of beam broadening on measured profiles by the use of Monte Carlo computations.⁵ Not unexpectedly, it is found that the major effect is to change drastically the minimum measured value as t and ϕ increase. The FWHM of the profiles is fairly insensitive to such changes. Because the true concentration gradient may be large over a few planes of atoms adjacent to a boundary, the use of

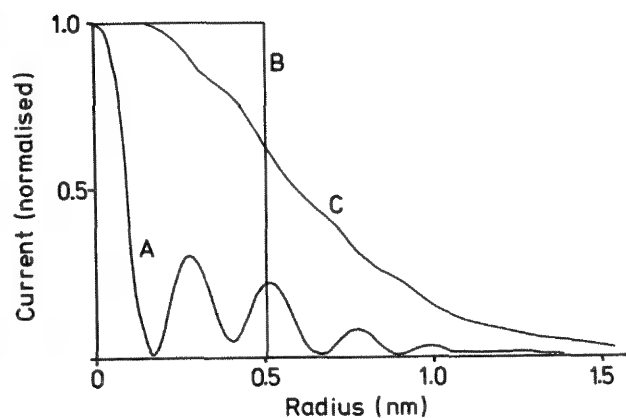


FIG. 2.--Theoretical radial current distributions: A, point source, 100 kV electron beam, objective lens defocus = 210 nm, convergence angle = 11.9 mrad, spherical aberration coefficient = 3 mm; B, "top-hat" distribution; C, convolution of A and B.

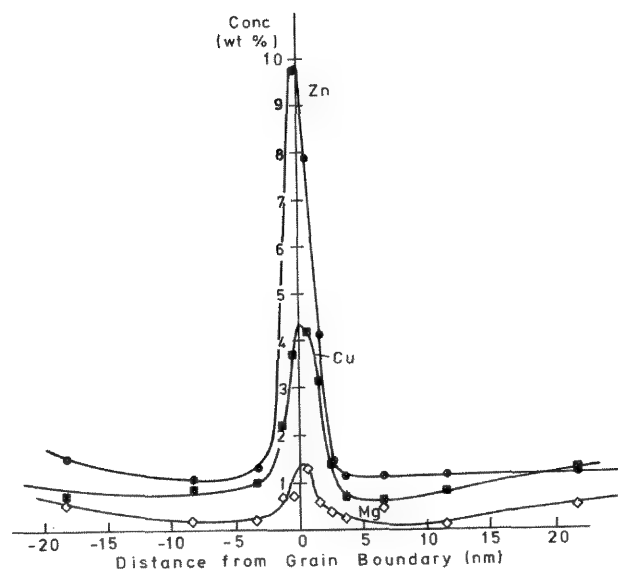


FIG. 3.--Profiles of chemical composition for Zn, Cu, and Mg at grain boundary in aluminum alloy.

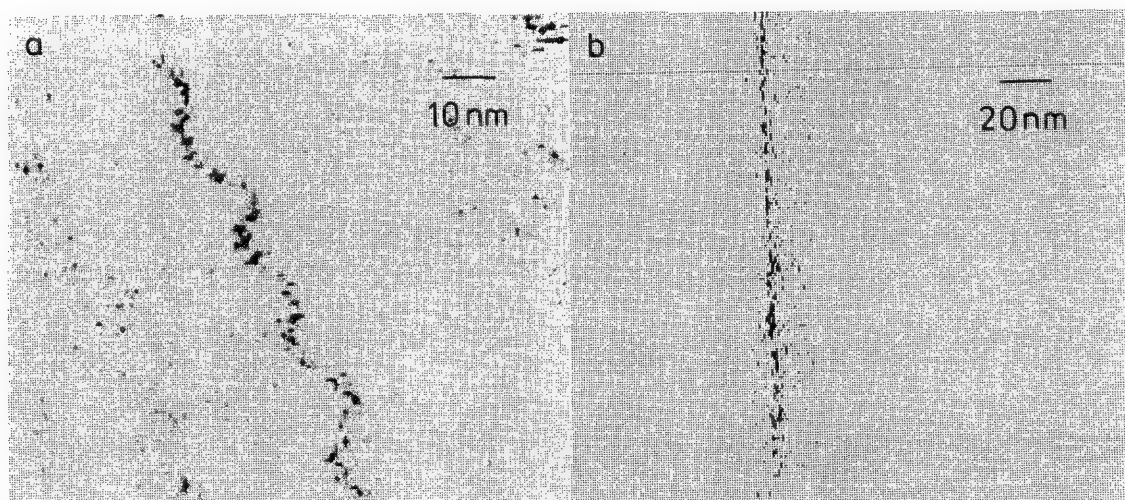


FIG. 4.--X-ray elemental maps (Zn-K α) showing ~ 0.4 monolayers of Zn segregated to grain boundary.

the finest probe in the thinnest foil is still unlikely to reveal an accurate measurement of boundary concentration.

Conclusions

STEM-EDX analysis is an alternative method to surface analysis for the study of equilibrium segregation. Quantitative measurements of segregation levels can be made by integration of the area of the segregation profile and scaling to a value calculated for a known segregation level. Sensitivity limits can be as small as 1% of a monolayer, depending on the alloy system, and elemental mapping of segregated species is feasible. The measurement of nonequilibrium profiles is limited by the finite probe diameter and concentration gradient.

References

1. A. J. Garratt-Reed, *SEM/1985 I*, 21.
2. C. Colliex, *Ultramicroscopy* 18: 131, 1985.
3. E. L. Hall, D. Imeson, and J. B. Vander Sande, *Phil. Mag.* A43: 1569, 1981.
4. C. R. M. Grosvenor, P. E. Batson, D. A. Smith, and C. Wong, *Phil. Mag.* A50: 409, 1984.
5. J. M. Titchmarsh, *Proc. 11th ICOM*, London, Ontario, 1986, 337.
6. M. Scheinfein, A. Muray, and M. Isaacson, *Ultramicroscopy* 16: 233, 1985.
7. P. Sainfort and P. Guyot, *Phil. Mag.* A50: 575, 1985.
8. E. A. Kenik, *Scripta Met.* 21: 811, 1987.
9. M. M. Disko and H. Shuman, *Ultramicroscopy*, 20: 43, 1986.
10. J. F. Bullock, J. M. Titchmarsh, and C. J. Humphreys, *Semicond. Sci. Technol.* 1: 343, 1986.

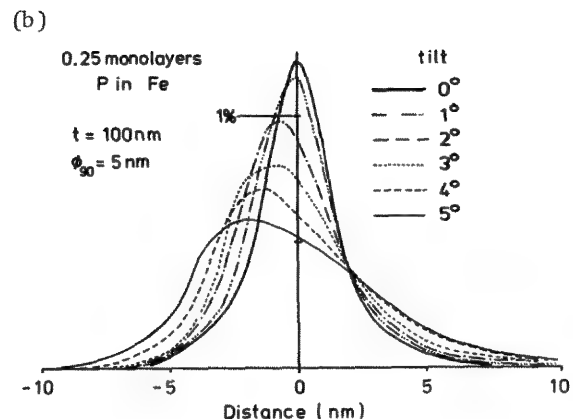
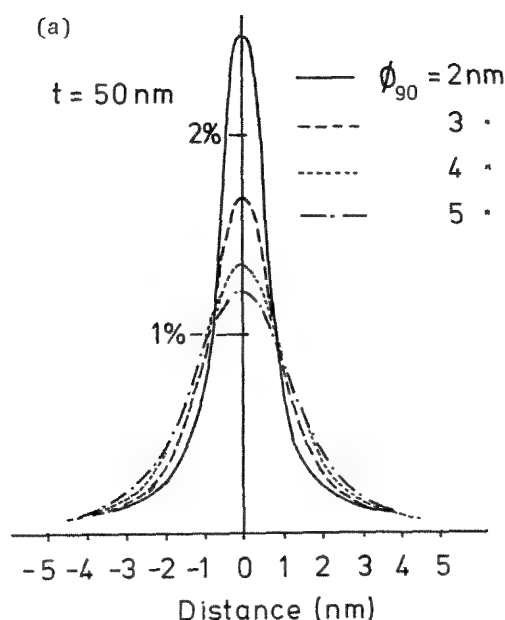


FIG. 5.--Theoretical profiles of chemical composition for 0.25 monolayers of P in Fe foil; (a) beam parallel to boundary plane, probe size varying, $t = 50$ nm; (b) probe size constant, varying angle of beam to boundary plane, $t = 100$ nm. Ordinate shows ratio of electron trajectory lengths in P to Fe, which is proportional to x-ray signal.

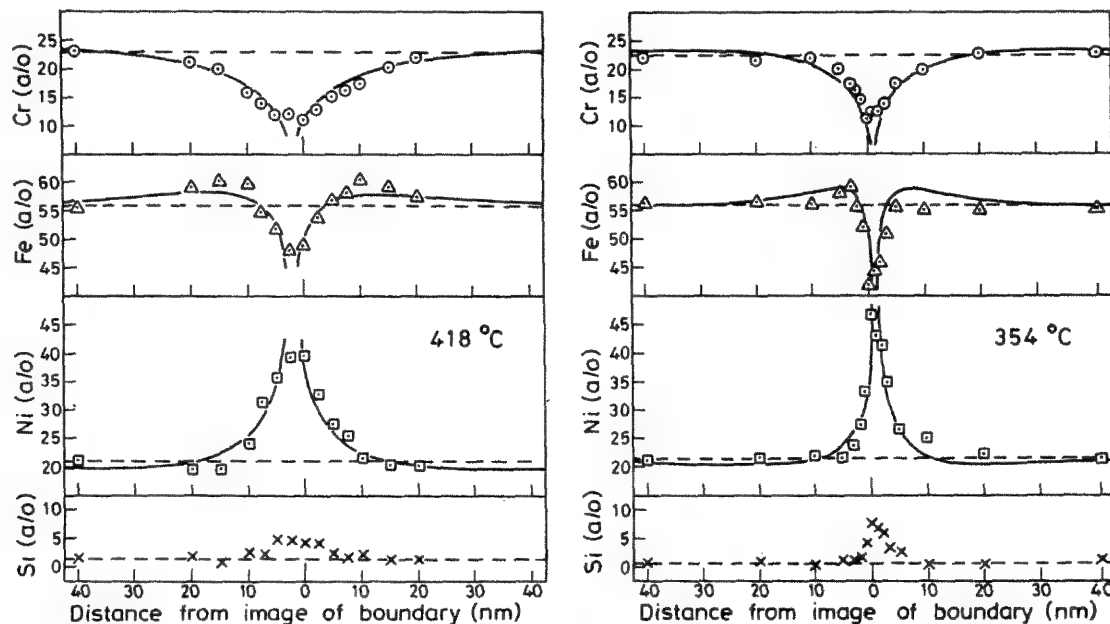


FIG. 6.--Profiles of chemical composition for Fe, Ni, Cr, and Si at grain boundary in irradiated stainless steel. Concentrations in atomic % (a/o). For irradiation at 418 C diffusion is faster and profiles are wider than for 354 C.

11. C. Colliex and C. Mory, in J. N. Chapman and A. J. Craven, Eds., *Proc. Scottish Universities Summer School in Physics*, 1984, 25.
12. A. Howie, *J. Microscopy* 11: 117, 1979.
13. J. I. Goldstein, J. L. Costley, C. W. Lorimer, and S. J. B. Reed, *SEM/1977 I*, 315.
14. J. R. Michael, G. Cliff, and D. B. Williams, *SEM/1984 IV*, 1697.
15. P. Doig and P. E. J. Flewitt, *J. Microscopy* 112: 257, 1978.
16. J. M. Titchmarsh, R. T. Kerr, and E. D. Boyes, *Analytical Electron Microscopy--1984*, 64.
17. T. A. Malis, S. C. Cheng, and R. F.

Egerton, *J. Electron Microscopy Techniques* (in preparation).

18. S. D. Berger, D. Imeson, and R. H. Milne, *Ultramicroscopy* 21: 293, 1987.

19. D. E. Newbury and R. L. Myklebust, *Analytical Electron Microscopy--1981*, 21.

20. I. A. Vatter and J. M. Titchmarsh, unpublished results.

21. D. I. R. Norris, C. Baker, and J. M. Titchmarsh, in *Materials for Nuclear Reactor Core Applications*, London: BNES, 1987, 277.

22. A. W. James and C. M. Shepherd, Harwell Report AERE-R12766.

HIGH-SPATIAL-RESOLUTION MICROANALYSIS IN THE PETROCHEMICAL INDUSTRY

J. H. Butler and M. M. J. Treacy

Catalysts used for the production of chemical commodities from petroleum feedstocks invariably contain active sites that are located on particles of unique, and usually complex, chemical structure. The directness of electron microscope methods can be important in establishing the nature of these materials;¹ however, the submicron (and even subnanometer) particle dimensions are frequently smaller than the probe diameter that can be formed with a conventional electron source. Because a very fine probe is required to address individual particles, elemental distribution analyses of these materials can only be conveniently performed on a microscope with a field-emission electron source. Ultrahigh-vacuum field-emission instruments with controlled atmosphere sample loading capabilities can further facilitate the examination of highly air-sensitive catalysts (which rapidly deteriorate under vacuum conditions found in most conventional microscopes) as well as subject the sample to simulated chemical reaction environments. This paper presents examples of EDS, EELS, and high-angle-detector (HAD) studies used to determine the spatial distribution of elements in olefin polymerization, petroleum cracking, and cyclic reforming catalysts.

Polyolefin Catalysts

Polyolefin (i.e., polyethylene, polypropylene, etc.) catalyst technology is based on a complex formulation of Ti supported on Mg halides, an organometallic component, and a Lewis base (which serves as an electron donor).² A variety of these "Ziegler-Natta" type catalysts are available depending on whether they are to be used in liquid slurry, gas phase, liquid bulk, or a combination of these production processes. The synthesis of these materials often results in a "cocktail" of chemical species distributed among a range of submicron morphologies. High-resolution analytical microscopy can be used to determine the relative abundance and types of these species, as well as the structure of particular species that

contain the catalytically active sites. Particle morphology plays a key structure/property role on two microlevels: characterization of the atomic structure is essential to the complete understanding of the polymerization process and bulk structure information is important for learning how the particles fragment during polymerization (which determines reactor operability and resin marketability).

A typical focus for this sort of investigation is the commercial polypropylene catalyst, ball-milled $\text{MgCl}_2/\text{TiCl}_4$ /ethylbenzoate. Figure 1a is a low magnification (25 000 \times) image which reveals the existence of no fewer than four distinct morphologies in this catalyst: (1) small (100–500Å) spheres, (2) stringy agglomerates of tiny (~ 400 Å) crystallites, (3) larger (several μm), flat platelets, and (4) another structure, which appears to be a platelet-like particle with about a 1000Å thick coating. EDS was performed with the incident probe position at the coincidental locations as labeled in Fig. 1a and shown in Figs. 1b–f.

Spectrum 1b is a bulk analysis made while scanning the probe over the entire field of view. As expected, Mg, Ti and Cl are the dominant elements. However traces of K and Ca are also in evidence. This bulk spectrum also provides an estimate of the Cu and Fe background (from the Cu grid and the pole pieces) which is evident in all subsequent spectra.

Spectrum 1c is from small (~ 300 Å) particle #1. It shows a complete absence of Mg and a great deal of Ti over Cl. These spherical particles could be oxidized TiCl_3 , TiCl_4 or a $\text{TiCl}_4 \cdot \text{EB}$ complex. Spectrum 1d is from one of the larger ($\sim 2 \mu\text{m}$) thin, platelets; evidence of a $\text{MgCl}_2/\text{TiCl}_4$ complex is present. Spectrum 1e is from the shell-like region #4 in Fig. 1a. Here we see a comparatively large Ti/Cl ratio. Spectrum 3f is from the coated particle (bulk region #5); we observe a sharp decrease in Ti and qualitatively conclude that these particles are some sort of Mg/Ti/Cl complex with a Ti-rich "skin." Spectra from the "stringy" agglomerate labeled #2 in Fig. 1a suggest that this structure could be unsupported (no MgCl_2), polycrystalline TiCl_3 .

A second polyolefin catalyst material is neat, polycrystalline, Shatterboxed (intensively ground) TiCl_3 , a precursor of many Ziegler-Natta type systems, and the first compound used to polymerize isotactic polypropylene. Although high resolution TEM can contribute much to the knowledge of this material's structure,³ it is only through combined, complementary, chemical analyses (such as electron spin resonance, magnetic susceptibility, and x-ray line broadening), as well as

J. H. Butler is at the Exxon Chemical Company, Baytown Polymers Center, Box 5200, Baytown, TX 77522; M. M. J. Treacy is at the Exxon Research and Engineering Company, Corporate Research Science Laboratories, Clinton Township, Route 22 East, Annandale, NJ 08801. They are honored to acknowledge the aid of their Exxon colleagues for their many contributions throughout various phases of this work: Dr. P. Brant, G. M. Brown, Dr. T. J. Burkhart, Dr. M. M. Disko, Dr. J. L. Kao, S. B. Rice, and Dr. T. H. Vanderspurt.

careful examination of the corresponding polymer products, that the complete picture of the active site arrangement within the Shatter-boxed particles begins to emerge.

TiCl₃ has a layer lattice structure (similar to MoS₂) comprised of two HCP Cl layers sandwiched about a (non-HCP) layer of Ti; these "sandwiches" are then stacked in such a manner as to give rise to a number of polytypes (with their associated Greek prefixes). Fig. 2a shows a model of α -TiCl₃; from the top view (of a single layer) it is apparent that each Ti atom is coordinated to six Cl atoms. Ti atoms at the edge planes of the tiny α -TiCl₃ crystallites do not have their full complement of six nearest-neighbor Cl atoms; these uncoordinated Ti atoms serve as the active sites for polymerization. Figure 2b ($\times 2.5M$) shows a high resolution STEM image of a small α -TiCl₃ crystallite. Assignment of dimensions for such crystallites is difficult because it is not clear where one fragment begins and another ends; there is bending at the indicated places while there appears to be some continuity of layers across the bend planes (white lines).

In order to gain insight with regard to the local electronic configuration in the vicinity of the (active site) edge planes, high resolution EELS with a narrow STEM probe sighted directly along the edge planes was performed after the method of Disko et al.⁴ Our intention was to be able to identify variations from the bulk Ti edge fine structure which might initially be correlated with possible Ti edge atom coordination and, ultimately (after some EXELFS analysis), with catalytic performance.

The results of this endeavor can be summarized with regard to Fig. 2c, a typical spectrum from a very thin crystallite edge. The Cl-K edge at 200 eV and Ti-L_{2,3} edge at 456 eV are dominant in spectra from all thin regions of the sample. However, when spectra are collected from the very edges of crystallites, the superposition of the O-K edge on the Ti fine structure of 532 eV gives rise to the type of spectrum shown here. This spectrum is nearly identical to that referenced for TiO₂,⁵ and serves to emphasize the practical difficulties involved in the analyses of such highly reactive specimens.

Even though care was taken to insure that this sample was synthesized, mounted and inserted into the microscope under controlled atmosphere conditions, it is evident that after only a few days in $\sim 5 \times 10^{-9}$ T vacuum, enough residual oxygen found its way onto the TiCl₃ edge planes to reduce the uncoordinated Ti atoms and render Ti energy loss fine structure examinations meaningless. Since the catalyst is made in the plant under less stringent conditions than those used for this study; the tendency to place importance on these results is strong: surely the plant-synthesized catalyst has at least as much reduced oxygen on the edges of its crystallites and therefore the results obtained here should be applicable to the real catalyst. But, as previously mentioned, an organometallic co-catalyst (such as

Al(Me)₃) must also be present in order for polymerization to proceed. In the reactor model, the co-catalyst is hypothesized to be a chemical scavenger, constantly cleaning oxygen off the TiCl₃ edge planes. Thus it is apparent that, for this particular system at least, the acquisition of meaningful micro-analytical data about the active sites of real catalysts is not straightforward, and probably not even possible without a reaction cell microscope stage. For analytical microscopy of catalysts, the challenge of the future is to enable the observation of chemical reactions.

Cracking and Reforming Catalysts

Conversion of the light naphtha component of crude oil into higher value products is a chief petrochemical interest. Usually this means taking short chain carbon molecules (with their complete complement of isomers) and converting them to cyclized or aromatic compounds. Historically this has been accomplished by any number of noble metals supported on γ -alumina. Thus the size and dispersion of the noble metal particles on the support are the key parameters of analytical interest.

Although not a true spectroscopic technique, the high angle detector method of dark-field STEM imaging must in some measure be regarded as a microanalytical method since the contrast observed in HAD images is sensitive to the atomic number, Z .⁶ This can be especially true when digital image acquisition and processing capabilities are available; then the image signal corresponding to the (comparatively) light support material can be scaled and subtracted from the composite signal to produce a final image of just the high Z component.⁷ This is demonstrated in Fig. 3 for the case of 2% by weight Pt-Ir on γ -Al₂O₃ by using concentric HADs and subtracting the weighted signal from the inner annulus from that of the outer, which is comparatively more sensitive to high Z elements. In this case the contribution to the image background from the (nonuniform thickness) alumina support has been removed from the final image.

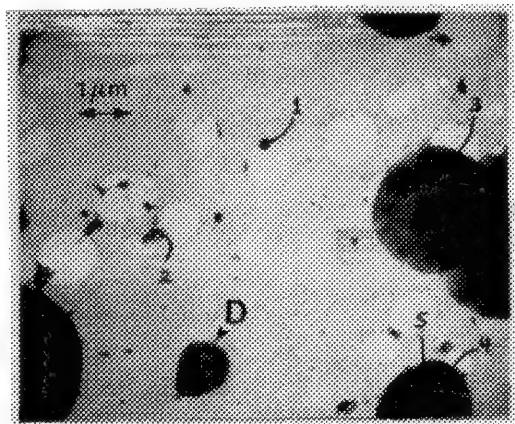
Many current petroleum and petrochemical processes are based on a rapidly developing zeolite technology. The micropores within the aluminosilicate framework of a zeolitic structure promote selected catalytic conversion reactions because of their ability to act as molecular "sieves"; among other steric functions, they prevent undesirable hydrocarbon reactants from accessing the minute noble metal particles buried inside the zeolite channels. Thus the potential for converting feedstock streams into higher quality raw materials (which contain larger amounts of cyclic, aromatic and olefinic hydrocarbons and less of the principle by-product, methane) exists both directly in the initial cracking process as well as in a number of postcracking operations.

The catalytic activity and selectivity of zeolitic materials are sensitive to subtle

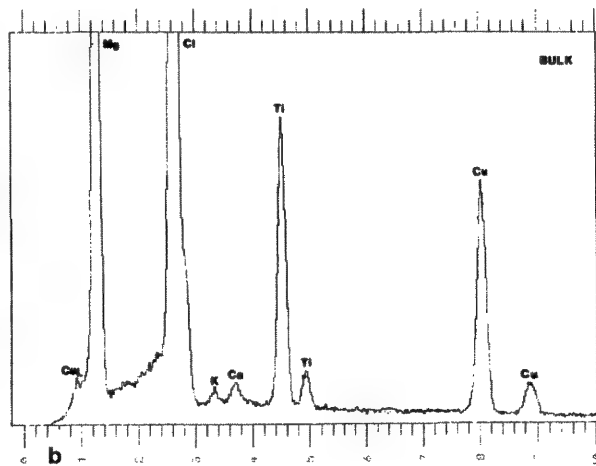
changes in channel topology and morphology. An important aspect of zeolite synthesis is to try to tailor a zeolite system which is optimized for a specific chemical reaction or process. To this end, substitutional cations are often incorporated into the framework of (well-established) zeolite structures during syntheses in order to induce slight changes in channel dimensions. Since the primary crystallite particles are nominally of submicron dimensions, high resolution analytical electron microscopy is required in order to produce elemental dis-

tribution maps of the cation concentrations across an individual crystallite.⁸ However, one must exercise caution in such EDS studies of zeolites; due to the uneven beam damage rate across zeolite crystallites, cation concentrations measured via EDS are systematically low because of cation migration away from the probe.⁹

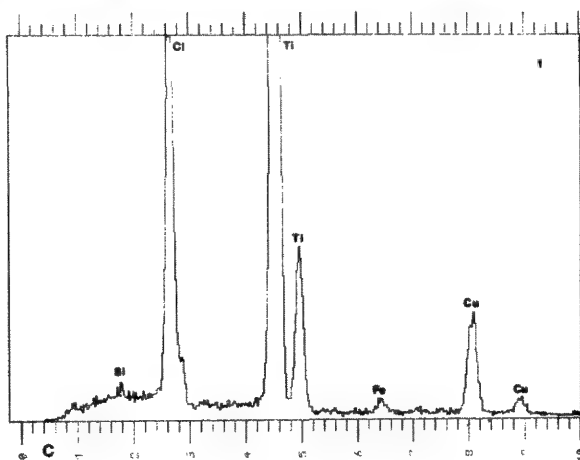
However, the issue of noble metal impregnation within zeolitic channels can be addressed with the use of HAD DF imaging. HAD techniques are based on the collection of elastically



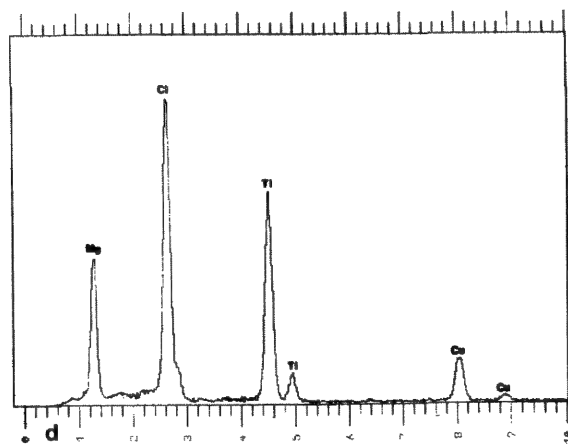
a



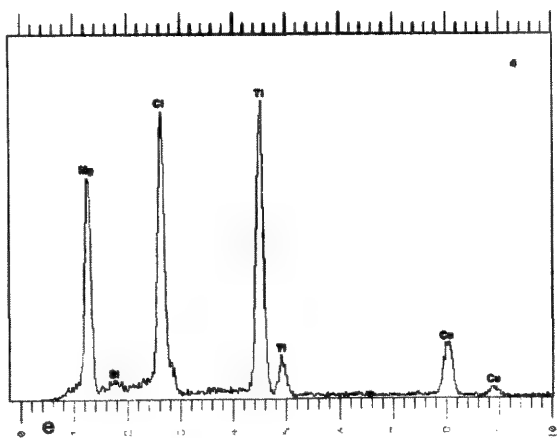
b



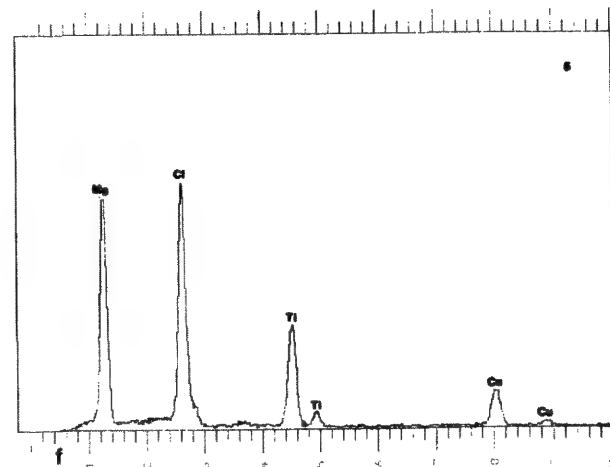
c



d



e



f

FIG. 1.--STEM low magnification image of ball milled $\text{MgCl}_2/\text{TiCl}_4$ /ethyl benzoate and EDS spectra from indicated points.

scattered "Rutherford" electrons. Because Rutherford scattering cross sections are highly localized near the atomic cores, HAD methods can provide much higher resolution than most amplitude contrast mechanisms. Figure 4 shows high resolution STEM BF and HAD DF images of Pt loaded zeolite L. Although most of the Pt particles can be identified in the BF image, many particles in the thicker zeolite regions are obscured. The HAD image shows all of the Pt particles, independent of zeolite substrate thickness variations. Particles as small as 7 Å (arrows) can be seen; particles in this size range are not detected in BF images.¹⁰

Conclusions

Ultrahigh vacuum, field-emission gun analytical electron microscopes are invaluable tools for high spatial resolution microanalysis of petrochemical catalysts. The correct choice and application of any specific method is strongly influenced by the behavior of the sam-

ple within the microscope environment. High resolution AEM will be invaluable in directing the synthesis of newer generation petrochemical catalyst materials.

References

1. J. V. Sanders, *J. Elec. Microsc. Tech.* 3: 67, 1986.
2. A. W. Langer, *Ann New York Acad. Sci.* 295: 110, 1977.
3. R. T. Murray, R. Pearce, and D. Platt, *J. Polym. Sci: Polym. Lett. Ed.* 16: 303, 1978.
4. M. M. Disko, M. M. J. Treacy, S. B. Rice, R. R. Chianelli, J. A. Gland, T. R. Halbert, and A. F. Ruppert, *Ultramicroscopy* 23: 313, 1987.
5. C. C. Ahn and O. L. Krivanek, *EELS Atlas*, HREM Facility, Center for Solid State Science, Arizona State University, Tempe, Ariz., 1983.
6. M. M. J. Treacy in T. E. Whyte, R. A. Dalla Betta, E. G. Derouane, and R. T. K. Baker, Eds., *Catalytic Materials: Relationship between Structure and Activity*, ACS Symposium Series No. 248, 1984, 367.
7. J. H. Butler, *Proc. 39th Ann. Meet. EMSA*, 1981, 137.
8. C. E. Lyman, "Symposium on the new surface science in catalysis," *Ann. Meet. ACS*, Philadelphia, 1984, 840.
9. M. M. J. Treacy and J. M. Newsam, *Ultramicroscopy* 23: 411, 1987.
10. I. Y. Chan, R. Csencsits, M. A. O'Keefe, and R. Gronsky. *J. Catal.* 103: 466, 1987.

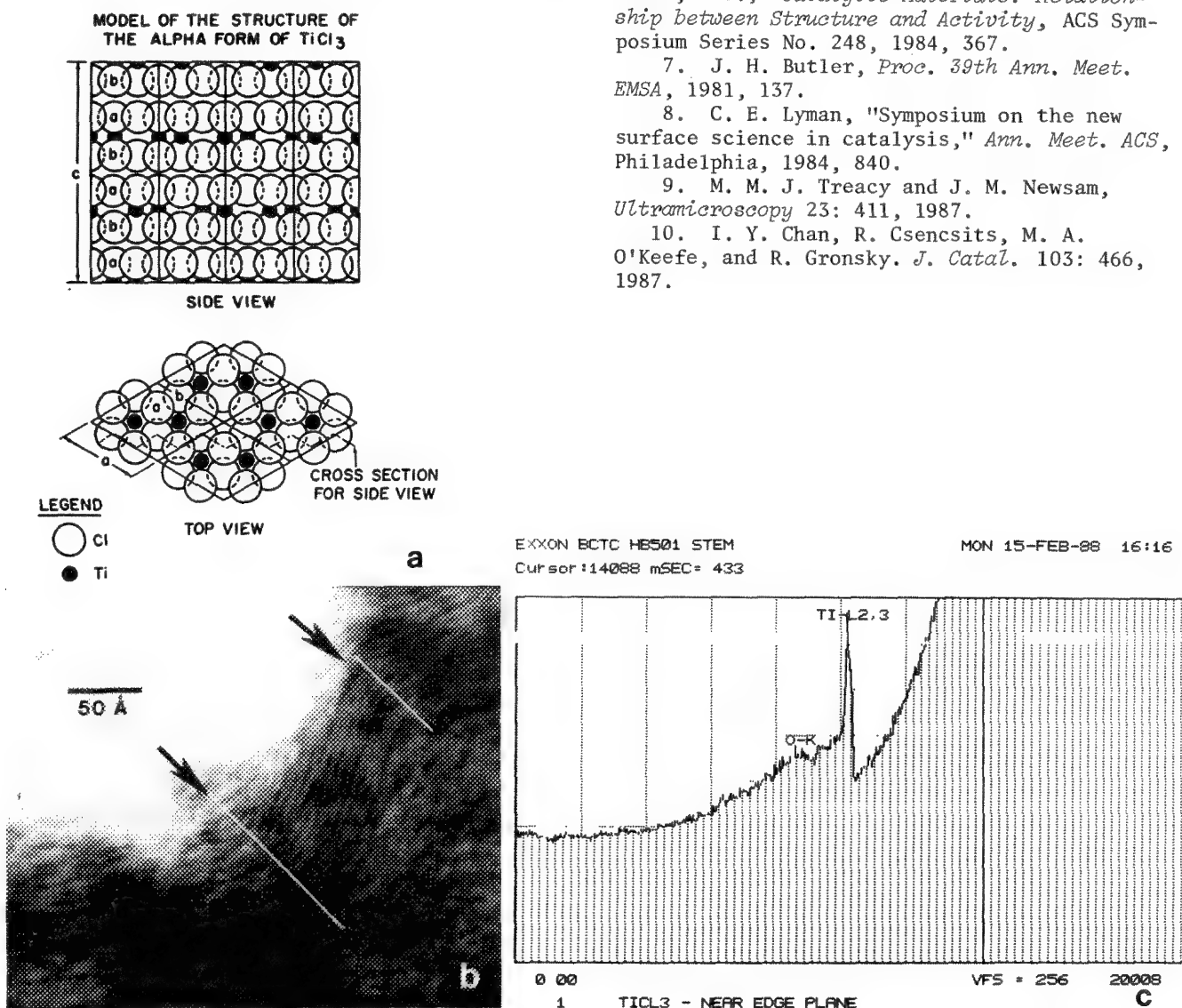


FIG. 2.--Shatterboxed α - TiCl_3 : (a) Model structure, (b) high resolution BF STEM image, (c) Ti EELS spectrum from crystallite edge plane.

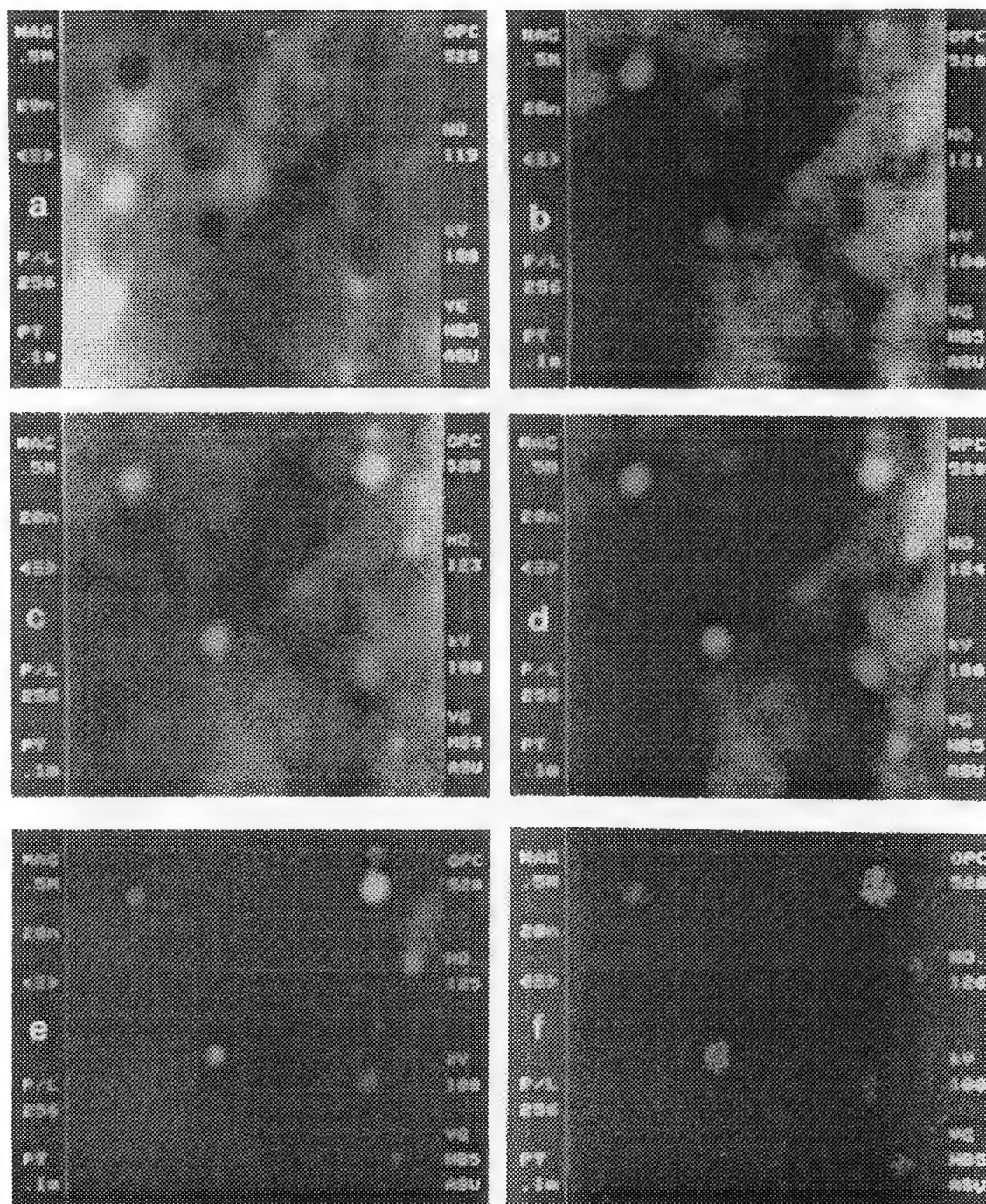


FIG. 3.--Pt/Ir supported on γ -Al₂O₃ with image processing: (a) Amplitude bright field: BF, (b) high angle dark field: HAD, (c) very high angle dark field: VHAD, (d) VHAD-BF, (e) VHAD-HAD, (f) VHAD-HAD, with processing.

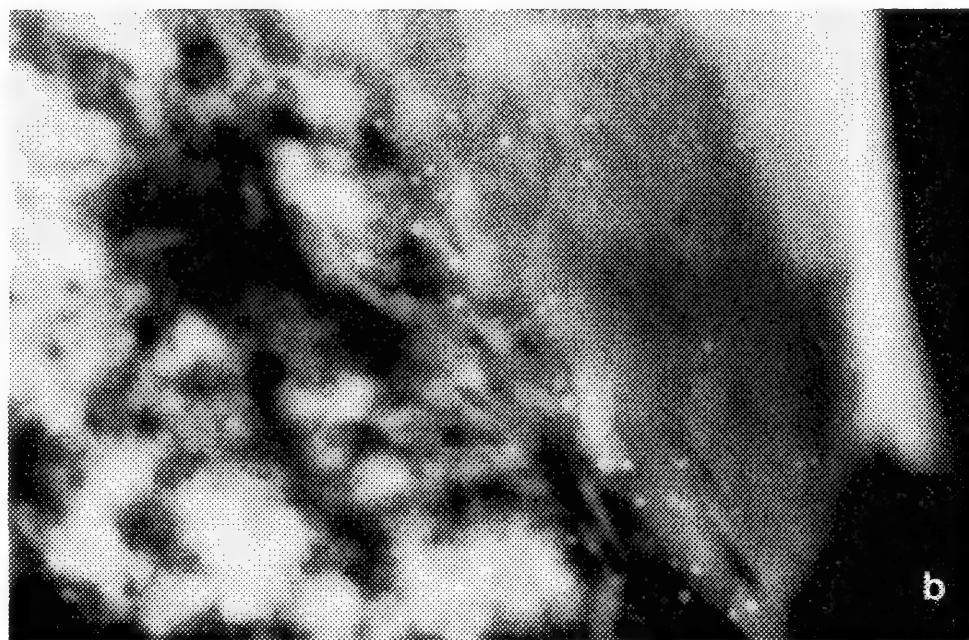
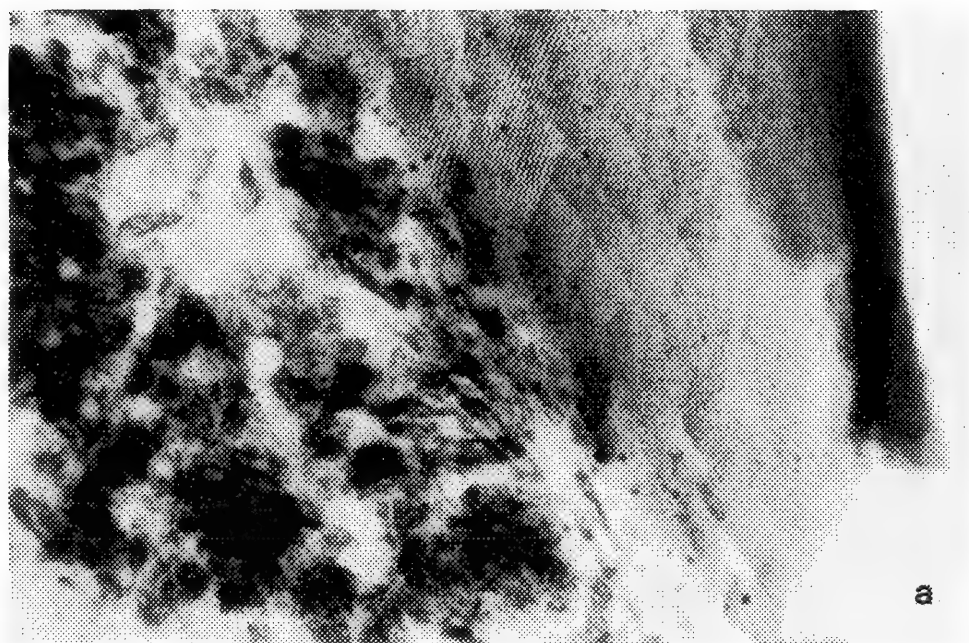


FIG. 4.--STEM of small ($< 15\text{\AA}$) Pt clusters within zeolite L channels: (a) BF image, (b) HAD DF image of same areas as (a). Note enhanced visibility of Pt particles.

GLIDE PLANES AND SCREW AXES IN CONVERGENT-BEAM DIFFRACTION: THE STANDARD PROCEDURE

J. A. Eades

The electron-diffraction determination of crystal symmetry proceeds in two stages. First, the symmetry of convergent-beam patterns is used to find the crystal point group.¹⁻³ Next, the presence of screw axes and glide planes is determined in order to complete the identification of the space group. Screw axes and glide planes in the crystal structure produce clearly identifiable features in convergent-beam diffraction patterns and these features are used to deduce the presence of the symmetry elements. The features in question are zeroes in the diffracted intensity. They are known variously as black crosses, dark bars, Gjønnes and Moodie lines, GM lines, or dynamical extinctions.⁴ This paper does not discuss the theoretical explanation and understanding of these features; it is limited to a discussion of their use in symmetry determination.

Forbidden Reflections

Dynamical extinctions occur only in reflections that are kinematically forbidden as a result of the presence in the crystal structure of two-fold screw axes (2₁) and/or glide planes. Such reflections may be excited by double diffraction. It may be useful to point out that seven of the fourteen Bravais lattices are centered—the conventional unit cell contains more than one lattice point. The centering gives rise to forbidden reflections of a different kind, that cannot be excited by double diffraction (e.g., 100 for fcc) and hence are not relevant to this discussion.

A 2₁ screw axis (along 010, say) gives rise to a single row (parallel to the screw axis) of reflections in which every second reflection (± 010 , ± 030 , ± 050 , etc.) is "forbidden"; that is, these reflections have structure factor zero.

Similarly, a glide plane gives rise to a single plane (parallel to the glide plane) of reflections in which every second row is "forbidden." The forbidden rows lie perpendicular to the glide direction, so that, for example, if the glide lies on an 010 plane and the glide direction is c, then the forbidden reflections are $\pm h01$, $\pm h03$, $\pm h05$, etc., whereas if the glide were diagonal the forbidden rows would be the reflections with $(h + 1)$ odd. (It might appear that diamond glides behave differently; the rule for extinction is, say,

$h + k \neq 4n$. However, the space groups with diamond glides are all face centered or body centered and, when the reflections forbidden due to centering are taken into account, it is still true that the glide makes alternate rows of reflections in one plane kinematically forbidden.

When considering the above, remember that only screws and glides alone give forbidden reflections: if a screw axis (2₁) is parallel to a two-fold axis (2), no forbidden reflections result; and if a glide plane (a,b,c,n,d) is parallel to a mirror (m), there are no forbidden reflections.

In electron diffraction, the intensity of these "forbidden" reflections is often as great as for reflections that are not forbidden, as a result of multiple diffraction.

Dynamical Extinctions

It has been shown that the intensity of diffraction into these kinematically forbidden reflections must be zero at certain well-defined orientations.⁴ Gjønnes and Moodie gave rules for these zeroes of intensity and subsequent tabulations^{2,5-7} have made clear how these rules can be applied to the determination of space groups.

Convergent-beam patterns display the variation of diffracted intensity as a function of the angle between the incident beam and the crystal structure. The zeros of intensity due to screws and glides occur at particular orientations of the incident beam. Therefore these features appear particularly clearly in convergent-beam patterns as dark lines or points.

There are two relevant lines (Fig. 1): a line at the Bragg angle for that reflection (B) and a radial line perpendicular to it (A).

Dynamical extinctions can conveniently be divided into three classes:

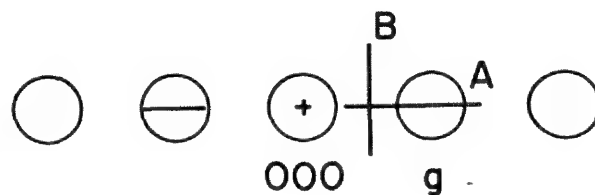


FIG. 1. Dynamical extinctions occur along two lines: radial line A and line at Bragg position B. Line B (shown here for reflection *g*) does not lie inside disk of on-axis convergent-beam pattern.

The author is at the Center for Microanalysis of Materials, Materials Research Laboratory, University of Illinois, Urbana, IL 61801. The work was supported by DOE contract DE-AC02-76ER01198.

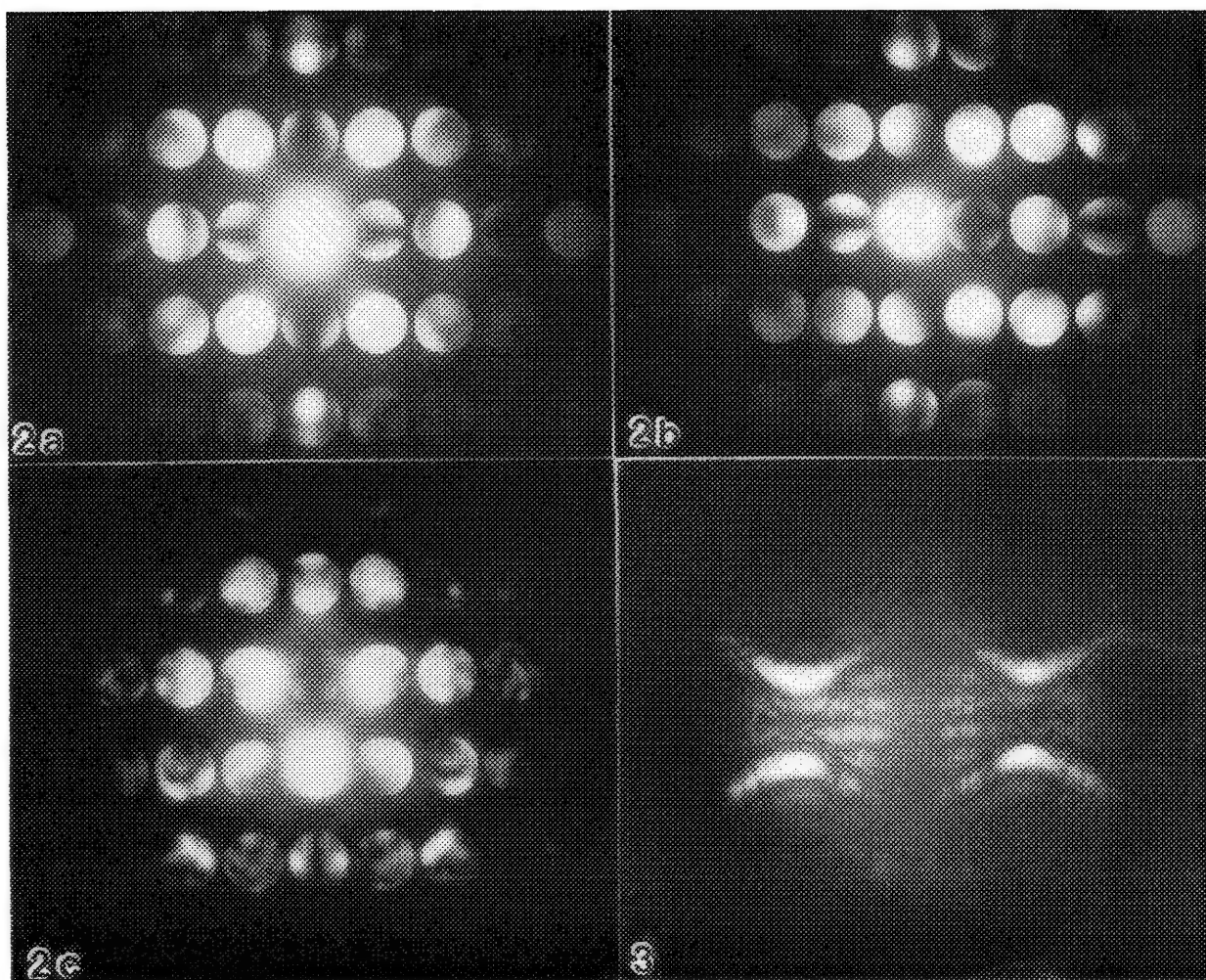


FIG. 2.--Dynamical extinctions in FeS_2 (cubic: space group 205, $\text{Pa}\bar{3}$) at the $[110]$ zone axis, 120 kV. (Courtesy K. C. Hsieh.). (a) On-axis pattern showing radial dark bars (along A) in alternate reflections along both 00ℓ (ℓ odd) and $h\bar{h}0$ (h odd). (b) Tilted to bring 001 to the Bragg angle so that the black cross (dark bars along both A and B) is visible. Dark bars remain in alternate reflections along the row. (c) Tilted to bring 110 to the Bragg angle--black cross visible. This is also from a thicker area, showing that dynamical extinctions persist.

FIG. 3.--Dark-field Tanaka pattern from Ni_3Mo at $[120]$ zone axis. In this case there is some intensity from HOLZ lines along one arm of the black cross (the horizontal arm as printed). This is a class Ib extinction.

I. those in zero-layer reflections when there are zero-layer double diffraction routes.

II. those in zero-layer reflections when there are no zero-layer double diffraction routes and all intensity comes from diffraction involving HOLZ (higher-order Laue zone) reflections.

III. those in reflections in higher-order Laue zones.

The most obvious and most useful are those of class I. These are the normal 'dark bars' or 'black crosses' that are familiar in convergent-beam patterns (Figs. 2 through 5). In principle, there are three distinct situations in class I.

Ia. There is a zero of intensity along both A and B, which can occur when both a screw axis and a glide plane are present in the orienta-

tion given for Ic and Ib, respectively. (Tanaka's symbol: $\begin{smallmatrix} A_2B_2 \\ A_3B_3 \end{smallmatrix}$.)

Ib. There is a zero of intensity along A. Along B there is no intensity diffracted by zero-layer interactions but there may be intensity resulting from double diffraction via HOLZ reflections. This result can arise when there is a glide plane parallel to the zone axis. The reflections with extinctions will be along a line parallel to the glide plane. The glide *direction* does not affect the result. (Tanaka: $\begin{smallmatrix} A_2B_2 \\ A_3 \end{smallmatrix}$.)

Ic. There is a zero of intensity along B. Along A the intensity from zero-layer interactions is zero but there may be intensity from interactions with HOLZ reflections. This result can occur when there is a screw axis

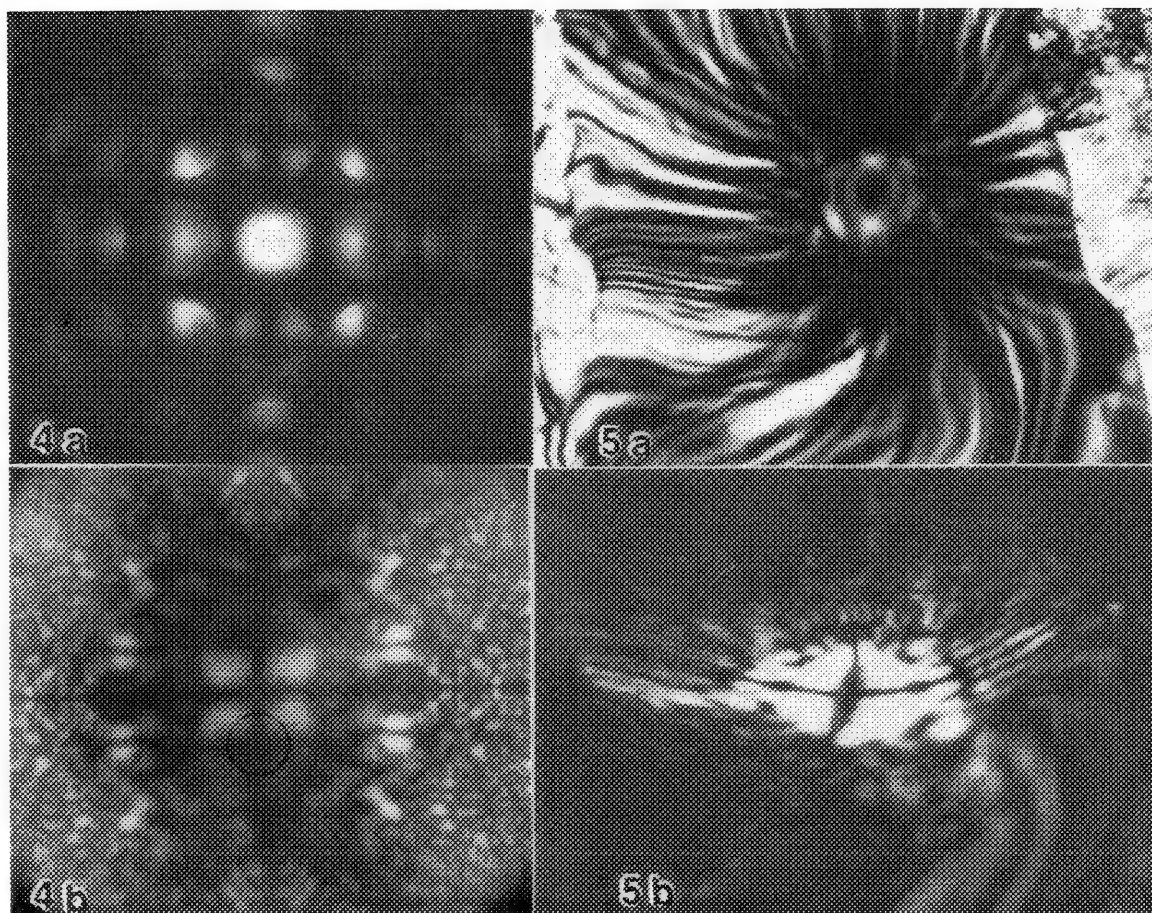


FIG. 4.--Dynamical extinctions in Ni_3Mo (orthorhombic: space group 59, Pmmn) at the $[100]$ zone axis, 120 kV. (a) Normal on-axis convergent-beam pattern. The dark features perpendicular to the radial line are not dynamical extinctions (they are not at the Bragg angle); they are there by coincidence. (b) Tanaka pattern in the 010 reflection showing that the radial line is a dynamical extinction. Both arms of the black cross are now visible. Distortion (the horizontal line is not straight due to buckling of the specimen) does not prevent recognition of the zero of intensity. The circle marks the position of the corresponding disk in 3a.

FIG. 5.--(a) Bright-field bend contour pattern from CaTa_2O_6 . (b) Dark-field bend-contour pattern from CaTa_2O_6 . Even the severe distortion of this bend-contour pattern permits the identification of the black cross. It is also possible to see how the intensity drops off away from the zone axis as double diffraction routes are weakened.

perpendicular to the zone axis. The reflections with extinctions lie along a line parallel to the screw axis. (Tanaka: A_2B_2 .)

In practice the zero-layer interactions are so much stronger than those via HOLZ reflections that Ia, b, and c are usually indistinguishable (except in high-index zone axes, where HOLZ effects are relatively stronger; see Fig. 3): all three cases look like case Ia. However, it is possible to decide whether the extinctions are due to a screw, a glide, or both from a knowledge of the diffraction group for the zone axis (Table 1 and Ref. 6).

Class II dynamical extinctions are unlikely to be seen unless they are specifically sought because the intensities are so weak. They can

occur only when there is a glide plane perpendicular to the zone axis, so that half the reflections are "missing" in the zero layer. (This condition is easy to spot: the density of reflections in the HOLZ is twice that in the zero layer.) In this case there are no zero-layer double diffraction routes to the forbidden reflections, but there are double diffraction routes via HOLZ reflections; so the reflections are not truly missing but they will be so weak that they will tend to appear so. Again there are three types.

IIa. A radial zero of intensity (along A) resulting from a glide plane parallel to the zone axis.⁸ (Tanaka: A_3 .)

IIb. A line of zero intensity along B, resulting from a screw axis perpendicular to

the zone axis. (Tanaka: B_3 .)

IIc. A point of zero intensity at the intersection of A and B, given by the glide plane perpendicular to the zone axis. The presence of this glide is already deduced from the "missing" reflections. Therefore, although it has been observed (by Tanaka's group)⁹ it is not useful in space group determination and Tanaka does not give it a symbol nor include it in his tabulation.

In general, class II dynamical extinctions will not be very useful in determining space groups since (unless I have made a mistake) there are no cases when the inability to observe them makes a difference to the possibility of distinguishing between space groups. However, they may be useful in particular situations if they appear (or not, as the case may be) at zone axes that are accessible when other zone axes with class I extinctions (or not) cannot be reached.

The third class of dynamical extinctions, those that occur in HOLZ reflections, can arise from glide planes parallel to the zone axis. (That is, the same conditions as Ia, Ib, or IIa.) They appear as radial lines of extinctions (i.e., along A). They will normally be useful when there are no zero-layer reflections that show the extinctions. This situation can arise as follows. Consider a c-glide plane on (010) viewed down $[201]$. Then the zero-layer reflections along a line parallel to the glide plane are ± 102 , ± 204 , etc., none of which is kinematically forbidden, since the forbiddens for the c-glide have l odd. Therefore no extinction is visible in the zero layer. However, it is possible that in the HOLZ ring there is a reflection like 6, 0, 11, which would have a radial line of extinction through it. On the other hand, if the sample were tilted from $[201]$ to $[101]$, then the reflections along the glide would be ± 101 , ± 202 , etc., and there would be a line of dynamical extinctions in the zero layer that would be much more obvious.

A tabulation of the occurrence of dynamical extinctions in HOLZ reflections will be published shortly (Tanaka, private communication).

Experimental Details

One question that arises in the use of dynamical extinctions is how to distinguish a dark bar in a convergent-beam disk that arises from dynamical extinction from one that arises as a part of the normal pattern in the disk (i.e., a coincidence). There are three indications that permit the distinction. Dynamical extinctions occur not just in single reflections but in every alternate reflection along a row (Fig. 2). (This may not apply to one in a HOLZ reflection.) They occur at all thicknesses and all voltages. If there is some doubt as to the origin of the dark bar in a convergent-beam disk, try moving to an area of different thickness and/or changing the voltage of the microscope. Also check that every alternate reflection has the feature (Fig. 2). In addition,

it may be valuable to use, say, the Tanaka method to observe this pattern over a wider angular range when the extinction becomes even more dramatic (Figs. 4 and 5).

In an on-axis pattern, none of the zero-layer disks includes the Bragg orientation for that reflection (assuming no overlap of disks). Therefore of the two dark bars in the black cross, only the radial dark bar (along A) is visible in on-axis patterns (Figs. 1 and 2). As indicated above, normal (class I) extinctions all look the same, so that no loss of information results.

In the determination of point groups there can be concern over the correct assignment of symmetry as a result of strain in the crystal (in a normal convergent-beam pattern) or from thickness variation and buckling (in a Tanaka pattern). However there seems to be no such problem in the use of dynamical extinctions. The zeros of intensity may bend and twist in, say, a distorted Tanaka pattern, but remain recognizable for what they are (Figs. 4 and 5).

Using Black Crosses to Determine Space Groups

Assume that the point group of the crystal is known from a symmetry analysis of convergent-beam patterns and the centering is known, e.g., from short camera length patterns.^{8,10} Then the first step toward determining the space group is to obtain convergent-beam patterns from as many zone axes as possible and examine them for the presence of dynamical extinctions (of class I, initially).

From Table 1, it is then possible to determine the presence of glide planes and screw axes, and their orientations (i.e., they can be indexed). It should also be possible to deduce that, at other orientations, the corresponding symmetry elements are 2-fold axes and mirrors (rather than screws and glides). Depending on how many zone axis patterns could be obtained, the experimental part of the determination may be complete or not. In either case the next step will be to see whether sufficient information is available to complete the determination, either from Tanaka's tables^{5,7} or from the International Tables for X-ray Crystallography¹¹ (the diagrammatic representation of the symmetry elements in each space group is most valuable for grasping what is going on), or better still, from both.

Because of the improved layout, the tables in the book by Tanaka and Terauchi⁷ are easier to use than those in the original paper.⁵ There is also a small unexplained change of notation. Some of the indices have subscripts, e.g., for space group 9 -- h_0l_0 . The subscript 0 means "odd" and indicates the line of reflections with extinctions. The subscript e means "even" and reflects the fact that for this centered cell odd values cannot occur (and has nothing directly to do with the extinctions).

Remember that that 2₁ screw axis is contained in 4₁, 4₃, 6₁, 6₃, and 6₅ screw axes (but not 4₂, 3₁, 3₂, 6₂, or 6₄) and the

TABLE 1.--Origin of dynamical extinctions in zero-layer reflections. (The table permits the proper interpretation of zero-layer black crosses when the diffraction group is known.)

Single row of zero-layer black crosses	Perpendicular rows of zero-layer black crosses	Deduction	Tanaka Symbol
mR 2mRmR	2mRmR 4mRmR	Screw axes parallel to each row of black crosses	A ₂ B ₂ B ₃
m 2m	2mm 4mm	Glide planes parallel to the zone axis and each row of black crosses	A ₂ B ₂ A ₃
2RmmR	4RmmR	Glide, if parallel to whole pattern mirror <u>or</u> Screw, if perpendicular to whole pattern mirror	A ₂ B ₂ A ₃ <u>or</u> A ₂ B ₂ B ₃
	2RmmR	Glide parallel <u>and</u> Screw perpendicular to whole pattern mirror	A ₂ B ₂ A ₃ <u>and</u> A ₂ B ₂ B ₃
m1R 2mm1R	2mm1R 4mm1R	Glide plane <u>and</u> Screw axis parallel to each line of black crosses: see note	A ₂ B ₂ A ₃ B ₃

Note: This is the case for double diffraction routes in the zero layer. If the black cross is produced by double diffraction via HOLZ reflections there are space groups for which the black cross can be produced by a glide or a screw alone.

extinctions that arise from a screw axis could be associated with one of these alternatives rather than just a 2₁.

If the information available is not enough to complete the determination, examination of the tables should make clear what further experiments are needed.

This procedure provides as complete a determination of the space group as is possible from dynamical extinctions and will uniquely identify 181 of the 230 space groups (Table 2). A further 27 space groups can be uniquely identified if "forbidden" reflections can be identified even though they do not contain black crosses (for example, because the screw that gives rise to the forbidden reflections is one that does not contain a two-fold screw). Such forbidden reflections might be identified from their tendency to disappear in very thin samples or from the way they are localized in wide angle patterns (Tanaka patterns). In a dark-field

Tanaka pattern a normal reflection shows intensity along a continuous line about the Bragg angle, whereas a forbidden reflection shows intensity that comes and goes as double diffraction routes become available.

Of the remainder, 18 space groups correspond to 9 enantiomorphic pairs (i.e., space groups that are identical except for a reversal of handedness); they can be distinguished by methods that involve detailed calculation--and hence a knowledge of the crystal structure including the positions of the atoms in the unit cell.¹²⁻¹⁴ The final 4 space groups are two pairs (I222 and I2₁2₁2₁; I23 and I2₁3) in which the same symmetry elements occur in each member of the pair, but they are distributed differently in space. There is therefore no way, based on symmetry, to distinguish them.

Conclusions

This paper attempts to provide a tutorial

introduction to the use of dynamical extinctions for the determination of crystal space groups. It may be read with another tutorial paper, on point group determination, given at another 1988 meeting.¹⁵

References

1. B. F. Buxton, J. A. Eades, J. W. Steeds, and G. M. Rackham, "The symmetry of electron diffraction zone axis patterns," *Phil. Trans.* 281: 171-194, 1976.
2. J. W. Steeds and R. Vincent, "Use of high-symmetry zone axes in electron diffraction in determining crystal point and space groups," *J. Appl. Cryst.* 16: 317-324, 1983.
3. M. Tanaka, R. Saito, and H. Sekii, "Point-group determination by convergent-beam electron diffraction," *Acta Cryst.* A39: 357-368, 1983.
4. J. Gjønnes and A. F. Moodie, "Extinction conditions in the dynamic theory of electron diffraction," *Acta Cryst.* 19: 65-67, 1965.
5. M. Tanaka, H. Sekii, and T. Nagasawa, "Space-group determination by dynamic extinction in convergent-beam electron diffraction," *Acta Cryst.* A39: 825-837, 1983.
6. J. A. Eades, M. D. Shannon, and B. F. Buxton, "Crystal symmetry from electron diffraction," *SEM/1983 III*, 1051-1060.
7. M. Tanaka and M. Terauchi, *Convergent-Beam Electron Diffraction*, Tokyo: JEOL, 1985, 192 pp.
8. J. W. Steeds and N. S. Evans, "Practical examples of point and space group determination in convergent beam diffraction," *Proc. 37th Ann. Meet. EMSA*, 1980, 188-191.
9. M. Tanaka, M. Terauchi, and H. Sekii, "Observation of dynamic extinction due to a glide plane perpendicular to an incident beam by convergent-beam electron diffraction," *Ultramicroscopy* 21: 245-250, 1987.
10. M. Raghavan, J. Y. Koo, and R. Petrovic-Luton, "Some applications of convergent beam electron diffraction in metallurgical research," *J. Metals* 35(No. 6): 44-50, 1983. Reproduced (with better figures) in *Norelco Reporter* 31(No. 1EM): 32-38, 1984.
11. *International Tables for Crystallography* (Vol. A: Space group symmetry) (International Union of Crystallography, Reidel, Holland, 1983); or *International Tables for X-ray Crystallography* (Vol. I: Symmetry groups) (International Union of Crystallography, Kynoch Press, Birmingham, 1969).
12. M. Tanaka, M. Takayoshi, M. Ishida, and Y. Endoh, "Crystal chirality and helicity of the helical spin density wave in MnSi: I. Convergent-beam electron diffraction," *J. Phys. Soc. Japan* 54: 2970-2974, 1985.
13. P. Goodman and T. W. Secomb, "Identification of enantiomorphously related space groups by electron diffraction," *Acta Cryst.* A33: 126-133, 1977.
14. P. Goodman and A. W. S. Johnson, "Identification of enantiomorphically related space groups by electron diffraction: A second method," *Acta Cryst.* A33: 997-1001, 1977.

15. J. A. Eades, "Symmetry determination by convergent-beam diffraction," *Proc. 9th European Cong. Electron Microscopy*, York, 1988.

TABLE 2.--Space groups that cannot be distinguished from analysis of dynamical extinctions. (Space groups that are underlined can be distinguished by means of forbidden reflections that do not have dynamical extinctions.)

23	24		I222	I212121	
<u>75</u>	<u>77</u>		P4	P4 ₂	
76	78		P4 ₁	P4 ₃	
<u>79</u>	<u>80</u>		I4	I4 ₁	
<u>83</u>	<u>84</u>		P4/m	P4 ₂ /m	
<u>85</u>	<u>86</u>		P4/n	P4 ₂ /n	
<u>89</u>	<u>93</u>		P422	P4 ₂ 22	
<u>90</u>	<u>94</u>		P4212	P4 ₂ 212	
<u>97</u>	<u>98</u>		I422	I4 ₁ 22	
<u>143</u>	144	145	P3	P3 ₁	P3 ₂
<u>149</u>	151	153	P312	P3 ₁ 12	P3 ₂ 12
<u>150</u>	152	154	P321	P3 ₁ 21	P3 ₂ 21
<u>168</u>	171	172	P6	P6 ₂	P6 ₄
169	170	<u>173</u>	P6 ₁	P6 ₅	P6 ₃
<u>177</u>	180	181	P622	P6 ₂ 22	P6 ₄ 22
178	179	<u>182</u>	P6 ₁ 22	P6 ₅ 22	P6 ₃ 22
197	199		I23	I213	
<u>207</u>	<u>208</u>		P432	P4 ₂ 32	
<u>209</u>	<u>210</u>		F432	F4 ₁ 32	
<u>211</u>	<u>214</u>		I432	I4 ₁ 32	
212	213		P4 ₃ 32	P4 ₁ 32	

LOCAL STRUCTURAL VARIATIONS IN $\text{YBa}_2\text{Cu}_3\text{O}_{7-x}$ BY ELECTRON MICRODIFFRACTION

Mehmet Sarikaya

There is a growing interest in the effect of substructural features on the phase transformation characteristic, stability, and superconducting properties of $\text{YBa}_2\text{Cu}_3\text{O}_{7-x}$ which shows zero resistance at about 90 K.^{1,2} Both in single crystal and polycrystal forms, twinning takes place where the twin boundary is $\{110\}$ parallel to $[001]$ orthorhombic direction.³⁻⁵ Other planar defects such as stacking faults,⁶ ninety-degree twins,⁷ and nonstoichiometric oxygen domains³ have also been observed but their real nature has so far not been determined.

The $\{110\}$ twins form as a necessity to accommodate the transformation strains that develop as a result of the lattice parameter differences in the tetragonal and orthorhombic forms of $\text{YBa}_2\text{Cu}_3\text{O}_{7-x}$ phase.^{4,5} It is known from the bulk measurements that due to oxygen ordering along $[010]$ directions of the orthorhombic phase, b slightly expands and a contracts.⁸ The largest difference between the bulk b and a corresponds to $\Delta a/a = 1.8\%$ and to T_c of 90 K. The study presented in this paper describes the measurements of $\Delta a/a$ by microdiffraction in the TEM and relates the local variations in $\Delta a/a$ to oxygen ordering in the matrix. It further discusses the consequences of these structural variations in terms of anomalies observed⁹ in superconducting properties of these materials.

Experimental Procedures

Polycrystalline superconducting samples were prepared by a dry-powder processing technique in which Y_2O_3 , BaO , and CuO were mixed in stoichiometric amounts to result in a 1:2:3 composition. After drying, the samples were heated (5 C/min) to 950 C, held there 1 h, and cooled (1 C/min) to room temperature. Samples exhibited T_c at 90 K with a transition width of about 2 K. The TEM samples were prepared by ion-beam (Ar) milling by use of liquid nitrogen holder to reduce damage to the structure. TEM studies were conducted with a Philips EM430T at 300 kV. The liquid nitrogen holder was used (with the measured sample temperature of 110 K) to eliminate the radiation damage. It has been found that low-temperature ion milling and TEM observation are essential to eliminate the beam damage in these materials.

The magnitudes of reciprocal lattice vectors a^* and b^* and the amount of splitting were mea-

The author is at the Department of Materials Science and Engineering, and the Advanced Materials Technology Program, Washington Technology Center, University of Washington, Seattle, WA 98195. This work is supported jointly by AFOSR and DARPA under Grant AFOSR-87-0114.

sured directly on the microdiffraction patterns by a toolmaker's microscope with an accuracy of 2.5 μm . A microdensitometer with a variable slit size was used to increase the resolution of the measurements, to distinguish the shape of the diffraction spots, and to delineate the existence of extra spots.

Results and Discussion

The structures of the tetragonal and orthorhombic $\text{YBa}_2\text{Cu}_3\text{O}_{7-x}$ phase have been determined by neutron diffraction, which gives space groups of $4/mmm$ and $Pmmm$, respectively.⁸ Although the orthorhombicity of the structure can readily be distinguished by the symmetry features developed within convergent beam patterns, slight changes in lattice parameter cannot be measured because of lack of necessary diffraction lines within the disks due to local changes in thickness, strain, and orientation. The convergent beam electron diffraction pattern given in Fig. 1 (taken from region P in Fig. 3) reveals a 2mm diffraction group in the $[001]$ projection of the orthorhombic phase. For better sampling of the structure, microdiffraction is used, and all the variations in Δa are measured in $[001]$ projection.

During a martensitic transformation, the amount of transformation strains dictates the degree of deformation in the product phase.¹⁰ For example, if the transformation strains are accommodated by the formation of twins, as in high-carbon steels, then the twin spacing in the final phase is determined by the amount of strain (that is, by the amount of carbon) in the matrix. Analogously, higher strain (i.e., higher $\Delta a = b - a$) means narrower twin spacing in the orthorhombic $\text{YBa}_2\text{Cu}_3\text{O}_{7-x}$ on the basis of the analysis given below. In addition, bulk Δa is related to the oxygen content,^{1,2} and hence varying values of twin spacing observed in the orthorhombic $\text{YBa}_2\text{Cu}_3\text{O}_{7-x}$ may be due to varying oxygen concentration, or ordering, across a single grain.¹¹

The twin spacings can be determined from the energy¹¹ and the geometrical considerations.⁵ In the former case, the minimization of total energy due to twins results in twin spacing λ , given by $\lambda = \sqrt{2}E_T/\Omega(\Delta a/a)^{-1}$, where E_T is the twin boundary energy and Ω is the shear modulus. Hence λ is inversely proportional to $(\Delta a/a)$.¹¹ The geometrical considerations require a basic distance $d = ab/\sqrt{2}\Delta a$ for the twin spacing for the formation of strain-free matrix containing twins.⁵ Here $\lambda = nd$, where n is an integer.

In order to check the inverse relationship between the twin spacing λ and $(\Delta a/a)$, micro-

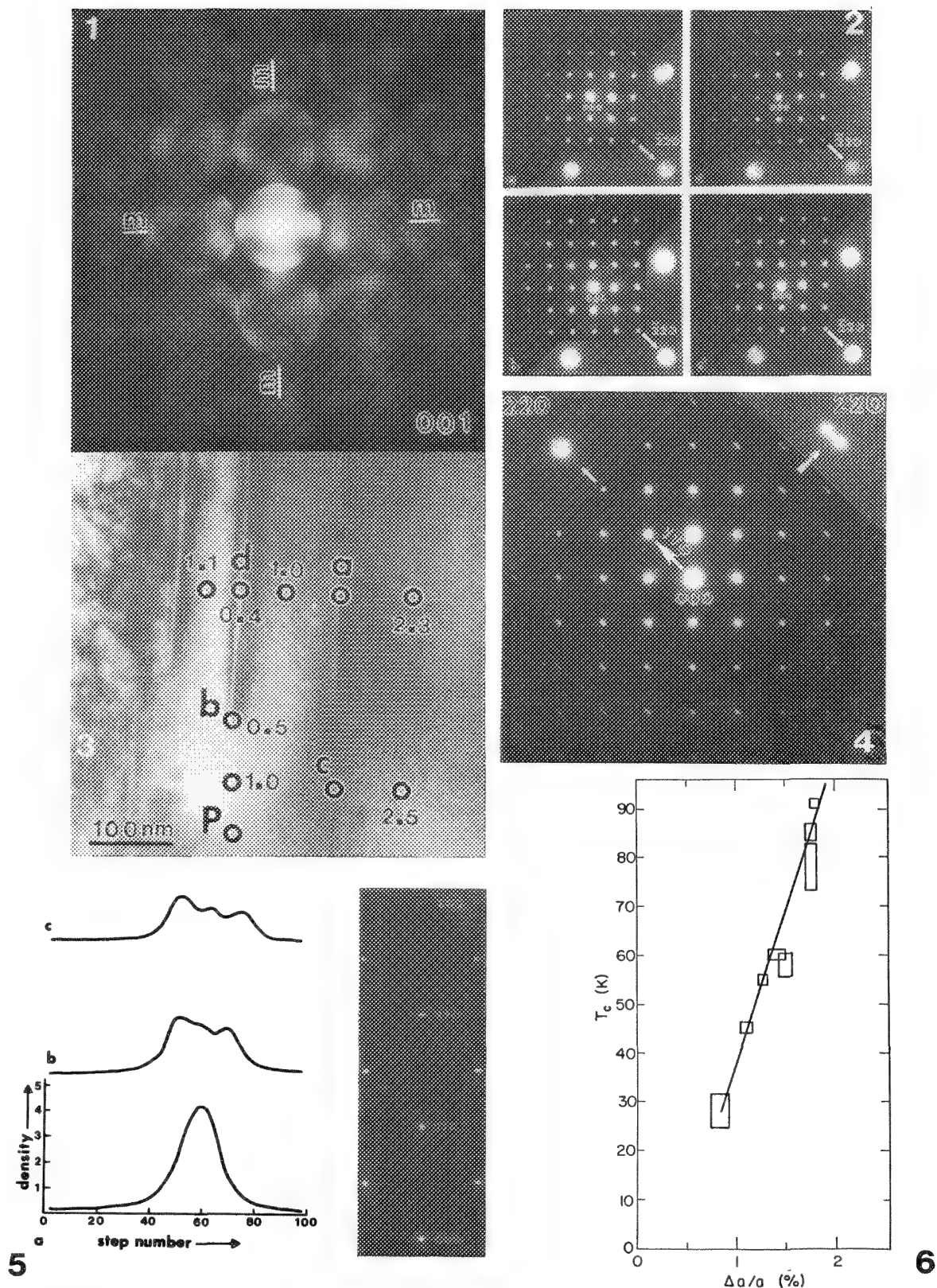


FIG. 1.--CBED pattern (taken from region P in Fig. 3) along $[001]$ reveals 2mm projection diffraction symmetry (recorded at 200 kV; probe diameter 10 nm; convergence angle 3 mrad).

FIG. 2.--Microdiffraction patterns recorded from region indicated in Fig. 3.

FIG. 3.--BF image with indicated values of $\Delta a/a$ percentages. Dots correspond to positions of microdiffraction patterns.

FIG. 4.--SAD pattern revealing spot splitting along $[110]$.

FIG. 5.--Microdensitometer traces in (a), (b), and (c) correspond to the first-, second-, and third-order reflections shown in enlarged portion (d) of SAD pattern from region shown in Fig. 3.

FIG. 6.--Plot of T_c vs bulk $\Delta a/a$ percentage.

diffraction experiments were performed with a 10nm probe. A set of microdiffraction patterns is shown in Fig. 2, corresponding to the region in Fig. 3. The numbers in Fig. 3 are $\Delta a/a$ percentages. In this and other regions, not only was no relation found between $\Delta a/a$ and λ , but also local values of $\Delta a/a$ varied from 0.0 to 4.0, which differs greatly from the macroscopic values quoted in the literature.^{1,2}

For a better sampling of the foil, selected area diffraction can be used. Figure 4 shows such a pattern from a different part of the sample. As noted, spot splitting occurs with ($\bar{1}10$) type of spots for a twin plane on (110). The angle of splitting is given by $\delta \approx (\Delta a/a)$.

For two extreme values of a and b , two discrete spots should appear. Diffraction information was taken by use of an SAD aperture centered at the tip of the twin, shown in Fig. 3 covering several twins. The portion of the SAD pattern along $[\bar{1}10]$ is shown in Fig. 5 with the corresponding microdensitometer traces along the $[110]$. It is clear from the higher order reflections that more than two peaks appear, confirming the microdiffraction results given in Fig. 3. High-resolution x-ray diffraction data obtained by use of single crystals exhibit multiple peaks corresponding to large variation in Δa and are in agreement with the above results.⁷

Measurements made on twin spacing also indicate a large deviation from the integer multiple of the basic distance d , implying there is a variation in b and a locally, resulting in various values of d , and hence λ .⁵ The cause of variation in measured values of $\Delta a/a$ has not been determined in our measurements but may be related to samples being in metastable states. Coexistence of orthorhombic and tetragonal phases at low temperatures had already been predicted by theoretical phase diagram calculations.^{12,13}

A plot of the literature data^{1,2} for bulk $\Delta a/a$ vs T_c yields a straight-line relationship (Fig. 6).¹¹ The bulk value of $\Delta a/a = 1.8$ corresponds to $T_c = 90$ K. From this plot the maximum value of $\Delta a/a$ (i.e., 4.0, measured by microdiffraction) corresponds to $T_c \approx 220$ K. Since the samples are at a metastable equilibrium, proper annealing should produce higher T_c samples. In fact, low-temperature annealing, which has already been noted in the literature,¹⁴ gives a T_c of ≈ 155 K in $\text{YBa}_2\text{Cu}_3\text{O}_{7-x}$.

Since $\Delta a/a$, and hence oxygen ordering, varies locally, on cooling different portions of the sample with weak links should be superconducting at different temperatures. The bulk values of 1.8% corresponding to $T_c = 90$ K may be associated with the condition where weak links are connected. The change in $\Delta a/a$, and the corresponding T_c , may explain the origin of superconducting glassy state in high T_c oxides and may be the cause for large variations in anomalous magnetic properties.

Conclusions

Microdiffraction experiments performed on

the orthorhombic phase of $\text{YBa}_2\text{Cu}_3\text{O}_{7-x}$ at 110 K show local variations of $\Delta a/a$ over distances of several hundred nanometers. The value of $\Delta a/a$ is the percentage difference between the b and a dimensions of the orthorhombic structure. The values of $\Delta a/a$ vary from 0.0 to 4.0 in regions defined by the electron probe size within the same grain. Here, the former $\Delta a/a$ value indicates tetragonality and the latter high orthorhombicity, and they both differ from the bulk value of 1.8. These variations are related to changes in oxygen ordering or strain present in the matrix and are attributed to the samples being in a metastable state, consistent with the phase diagram predictions in the literature. These results also indicate that the samples are in a superconducting glassy state. A linear relationship exists between the macroscopic $\Delta a/a$ and T_c , the critical superconducting temperature, which for $\Delta a/a = 4.0\%$ implies a T_c of about 220 K.

References

1. J. M. Tarascon et al., in V. Kresin and S. Wolf, Eds., *Workshop on Novel Mechanisms of Superconductivity*, Berkeley, New York: Pergamon, 1987, 705.
2. R. J. Cava et al., *Phys. Rev. Lett.* 58: 1676, 1987.
3. M. Hervieu et al., *Phys. Rev.* B36: 211, 3920, 1987; *Europhys. Lett.* 4: 205, 1987.
4. G. Van Tendeloo et al., *Solid St. Comm.* 63: 603, 1987.
5. M. Sarikaya et al., *Physica C*152: 161; see also M. Sarikaya et al., *Proc. 46th Ann. Meet. EMSA*, 1988.
6. H. W. Zandbergen et al., in *High Temperature Superconductors*, Proc. MRS Fall Meeting, 1988, 553.
7. H. You et al., *Phys. Rev. B* (in press).
8. I. K. Schuller et al., *Solid State Commun.* 63: 385, 1987.
9. G. Deutscher and K. A. Müller, *Phys. Rev. Lett.* 59: 1945, 1987.
10. Z. Nishiyama, *Martensitic Transformations*, New York: Academic Press, 1978, 162.
11. M. Sarikaya and E. A. Stern, *Phys. Rev. B* 37(16), June 1988.
12. A. G. Khachaturyan et al., *Phys. Rev. Lett.* B (in press).
13. L. T. Wille et al., *Phys. Rev. B* (in press).
14. R. N. Bargawa et al., *Phys. Rev. Lett.* 59: 1468, 1987.

APPLICATION OF DECOMPOSITION TABLE IN THE ANALYSIS OF THE GJØNNES-MOODIE LINES IN CONVERGENT-BEAM ELECTRON DIFFRACTION

Dan-Rong Liu

Convergent-beam electron diffraction (CBED) in a transmission electron microscope is now widely used for determination of the space group of a specimen. Compared with the use of x-ray diffraction for the same purpose, CBED offers more information on space groups and yet is much simpler to use. However, the basic physical principle behind the two techniques is the same, in that the presence of some microscopical symmetry elements can be deduced from the observation of kinematically forbidden reflections in a diffraction pattern. In the case of CBED, the dark lines/bands appear in kinematically forbidden reflections in the pattern of the material in question. This fact was first pointed out by Gjønnes and Moodie¹ and therefore the lines are commonly called G-M lines. Their argument is based on the general "physical optics" theory developed by Cowley and Moodie.² The basic idea is to use the concept of pairing the appropriate product terms in the expansion expression of the final scattering wave function of a particular dynamic reflection, according to the symmetry related by the glide plane or screw axis, so that the intensities represented by the two paired terms cancel one another at the center of that reflection disk. However, the presence of such a cancellation is judged in fact according to certain intuitive arguments. This approach can be valid for cases of simple space groups, but it could become inappropriate for some complicated space groups. Therefore, in the present paper, a rigorous analytical approach is developed to solve this problem. The major point is to devise a decomposition table with which any dynamic scattering event can be decomposed into a series of kinematic reflections that can be rigorously analyzed based on the well-established knowledge of x-ray crystallography.

Decomposition of a Multiscattering Process

Any dynamic scattering reflection of h can be expressed by the sum of the product terms:²

$$F(\underline{h}_1)F(\underline{h}_2) \dots F(\underline{h}_n) Z(\zeta_1, \zeta_2 \dots \zeta_{n-1}) \quad (1)$$

where $F(\underline{h}_i)$ is the structure factor of the kinematic reflection \underline{h}_i and ζ_r is the excitation error of the reflections $\sum_{j=1}^r \underline{h}_j$ and $\underline{h} = \sum_{j=1}^n \underline{h}_j$.

The author is with the Department of Materials Science and Engineering, Lehigh University, Bethlehem, PA 18015. Useful discussions with Dr. D. B. Williams are acknowledged. This work is supported by the National Science Foundation under contract NSF-DMR-8400427.

These product terms can be paired so that it is possible for every two paired terms to have the same magnitude but opposite sign when a dynamic extinction is present in that reflection h .¹ When this principle is applied to the simple planar group pg , the following conditions should be utilized:

$$F(h, k) = F(\bar{h}, k) \quad \text{for } k = 2n,$$

$$F(h, k) = -F(\bar{h}, k) \quad \text{for } k = 2n+1 \quad (2)$$

For such a simple case, the intuitive pairing of dynamic scattering events is adequate for the determination of the possible presence of the G-M lines. However, for situations where high-order Laue zones (HOLZ) are involved, that might not be the case, as will be clear later. Therefore, an analytical scheme is developed within which each dynamic scattering event is decomposed into individual kinematic scattering steps that occur in sequence. Every kinematic scattering step is then rigorously analyzed with the knowledge of x-ray crystallography. Let us now to apply this principle to the case of the planar group pg explored in the paper.¹

The pairing of dynamic scattering events to the third order is drawn in Fig. 1. The three events AB-BC-CD, AG-GH-HD, and AE-EF-FD can be decomposed into single kinematic scattering events as shown in Table 1. The indices are tabulated according to $\underline{h} = \underline{h}_1 + \underline{h}_2 + \underline{h}_3$, where \underline{h}_1 , \underline{h}_2 , and \underline{h}_3 are the decomposed kinematic reflections, as shown in the first column of the table. With regard to the assignment of the concrete indices to each individual reflection, this kinematic scattering step should be referenced to the origin (0,0) of the diffraction pattern in order to be comparable with the knowledge from x-ray crystallography. Although the scattering step BC, for example, is produced in the route from the reflection spot (1,0) to the spot (1,2), it really is in essence a kinematic scattering event from (0,0) to (0,2), and, in this sense only must this elemental event BC satisfy the rules for kinematic scattering reflections, well established in x-ray crystallography.³ Similarly, the indices (\underline{h}_i, k_i) of all other elemental scattering steps are established, as shown by the second and third columns in the table. When all the dynamic scattering events have been broken into kinematic steps, the rules for the individual kinematic reflections as expressed by Eq. (2) can be applied to determine the signs of these reflections, i.e., the structure factors $F(\underline{h}_i)$. For the purpose of comparison, we can define

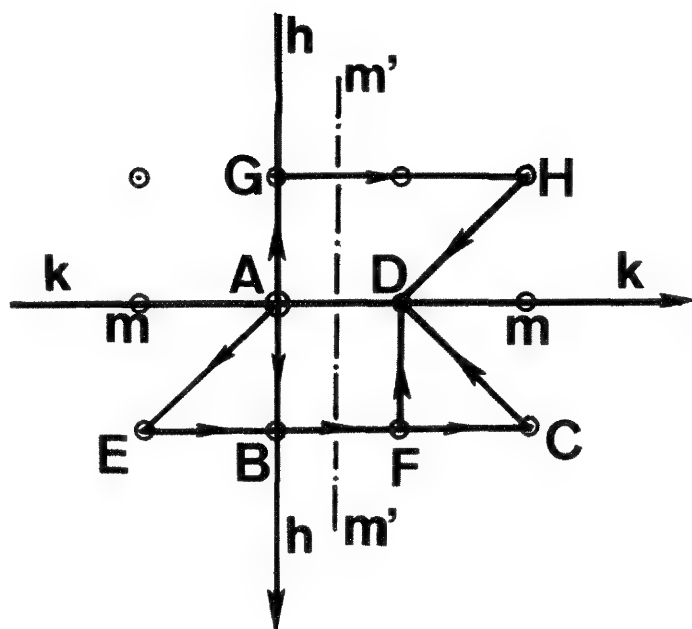


FIG. 1.--Multiscattering diagram for the third-order processes: mm and $m'm'$ are symmetric planes due to the presence of a vertical glide plane or a screw axis along kk .

all structure factors in the route $AB-BC-CD$ as positive. That will then enable us to determine the signs of the individual factors as shown in the fourth column of the table. Then the sign of each product term of the form of Eq. (1) is easily determined. The cancellation of the pair $F(AB)F(BC)F(CD)$ and $F(AE)F(EF)F(FD)$ is obvious if the appropriate excitation errors for each route are also maintained.

Application to Three-dimensional Cases

The decomposition procedure clearly demonstrates the formation of possible G-M lines in the planar group pg . However, its usefulness lies in the capability of rigorous analyses for possible formation of G-M lines due to HOLZ reflections, especially for the cases where complicated interactions among the glide planes and/or screw axes are present and manifested by the characteristics of the index sum $h + k + l$. To illustrate this complexity, let us assume in Fig. 1 that the three reflection disks C , H , and E are located at the first order Laue Zone (FOLZ) ring, and the others all on the zero-order Laue zone (ZOLZ) plane, the same as in the above case. The indices of the three corner disks are then $C(1, m, 1)$, $H(-1, m, 1)$ and $E[1, -(m-1), 1]$, respectively, where m can be a positive, odd or even integer. A similar decomposition table can be produced for this case (Table 2). The cancellation of the dynamic scattering pairs of $AB-BC-CD$ and $AG-GH-HD$, as well as $AB-BC-CD$ and $AE-EF-FD$, is possible only when the condition set by Eq. (2) is strictly obeyed in the presence of HOLZ reflections. In the present case, the sign of the structure factors $F(h, k)$ with respect to

$F(\bar{h}, k)$ in the two corresponding pairs should depend only on whether k is odd or even, as in the values shown in the column 3, not on the characteristics of the indices sum of $h + k + 1$. For some space groups involving interactions between glide planes and/or screw axes, their structure factors could be different according to whether, for example, the indices sum $h + k + 1$ is $4n$, $4n + 1$, $4n + 2$, or $4n + 3$. There are about 20 space groups in this category.³ If it happens that one needs to investigate a space group of this type, the elemental reflection CD in the route $AB-BC-CD$ and the elemental reflection HD in the $AG-GH-HD$, for example, may have different indices sum as $-1-m$ and $1-m$, respectively, though these two events seem to have exactly the same scattering geometry and are symmetric about the line kk as seen in Fig. 1.

For a concrete example, we may assume $m = 19$ (an odd number) and $m = 20$ (an even number) and compute the type of indices sums as shown by columns 6-9. One can see immediately that any pair of the apparently equivalent structure factors, either in the pair of $AB-BC-CD$ and $AG-GH-HD$, or in the pair of $AB-BC-CD$ and $AE-EF-FD$, might be in fact different. Checking through the structure factor tables in the *International Tables for X-ray Crystallography*,³ we find that for the space group $Fd\bar{3}m$, for example, depending upon whether the indices sum is the type $4n$, $4n + 1$, $4n + 2$, or $4n + 3$, the elemental structure factors are different. Further, a complete decomposition procedure is carried out for a practical G-M line analysis of CBED patterns from materials with the space group $Fd\bar{3}m$.⁴ All these analyses reveal that the intuitive pairing method for the G-M line determination might not be applicable for some complicated space group as characterized by their indices sum $h + k + l$. For these space groups the signs and the amplitudes of the two corresponding structure factors in the identified dynamic pair might appear to be equivalent but in fact different, so that a cancellation of the pair is impossible.

Conclusions

The commonly used approach in the G-M line analysis of the space group determination is examined. A decomposition table is devised so as to make use of the well-established knowledge of x-ray crystallography for the space group determination in CBED. It is concluded that the intuitive pairing method for the G-M line analysis might not be applicable for some space groups where there are complicated interactions between the glide planes or/and screw axes as manifested by the sum of the indices $h + k + l$. The decomposition table method, on the other hand, is based on rigorous analysis of the elemental kinematic reflections and should be applicable to all space group analyses.

TABLE 1.--Decomposition of multiscattering processes of Fig. 1. The relation $h_1 + h_2 + h_3 = h$ is used in tabulation. The sign \pm at the lowest right corner is for the product F_i s.

(a) Route AB-BC-CD

		h	k	Sign of F_i
h_1	AB	1	0	+
h_2	BC	0	2	+
h_3	CD	-1	-1	+
h	AD	0	1	+

(b) Route AG-GH-HD

		h	k	Sign of F_i
h_1	AG	-1	0	+
h_2	GH	0	2	+
h_3	HD	1	-1	-
h	AD	0	1	-

(c) Route AE-EF-FD

		h	k	Sign of F_i
h_1	AE	1	-1	-
h_2	EF	0	2	+
h_3	AD	-1	0	+
h	AD	0	1	-

TABLE 2.--Decomposition of multiscattering process of Fig. 1 but with FOLZ reflections involved. The relation $h_1 + h_2 + h_3 = h$ is used for tabulation. The numbers under the columns with $m=19$ and 20 are for $h+k+1$.

(a) Route AB-BC-CD

		h	k	1	$h+k+1$	$m=19$	type	$m=20$	type
h_1	AB	1	0	0	1	1	$4n+1$	1	$4n+1$
h_2	BC	0	m	1	$1+m$	20	$4n$	21	$4n+1$
h_3	CD	-1	$-(m-1)$	-1	$-1-m$	-20	$4n$	-21	$4n+3$
h	AD	0	1	0					

(b) Route for AG-GH-HD

		h	k	1	$h+k+1$	$m=19$	type	$m=20$	type
h_1	AG	-1	0	0	-1	-1	$4n+3$	-1	$4n+3$
h_2	GH	0	m	1	$1+m$	20	$4n$	21	$4n+1$
h_3	HD	1	$-(m-1)$	-1	$1-m$	-18	$4n+2$	-19	$4n+1$
h	AD	0	1	0					

(c) Route for AE-EF-FD

		h	k	1	$h+k+1$	$m=19$	type	$m=20$	type
h_1	AE	1	$-(m-1)$	1	$3-m$	-16	$4n$	-17	$4n+3$
h_2	EF	0	m	-1	$-1+m$	18	$4n+2$	19	$4n+3$
h_3	FD	-1	0	0	-1	1	$4n+3$	-1	$4n+3$
h	AD	0	1	0					

References

1. J. Gjønnes and A. F. Moodie, "Extinction conditions in the dynamic theory of electron diffraction," *Acta Cryst.* 19: 65, 1965.
2. J. M. Cowley and A. F. Moodie, "The scattering of electrons by atoms and crystals: I. A new theoretical approach," *Acta Cryst.* 10: 609, 1957.
3. N. F. M. Henry and K. Lonsdale, Eds., *International Tables for X-ray Crystallography*, Birmingham, Eng.: Kynoch Press, 1952, vol. 1.
4. D. R. Liu, "Observation of dynamic extinction from high-order laue zones by convergent beam electron diffraction," *Ultramicroscopy* 23: 35, 1988.

POSSIBLE AMBIGUITY IN THE STRUCTURAL ANALYSIS OF TiBe_2 BY CONVERGENT-BEAM ELECTRON DIFFRACTION

Dang-Rong Liu, M. Wall, and D. B. Williams

The space group of TiBe_2 has been determined by the x-ray powder diffraction method as $\text{Fd}\bar{3}\text{m}$.^{1,2} However, the powder method essentially provides one-dimensional information out of a three-dimensional structure, so that a more satisfactory approach to the determination of its structure seems warranted. This need can be illustrated by the controversy over the structure of the MgAl_2O_4 spinel, which has a structure similar to TiBe_2 . Though the space group of the MgAl_2O_4 spinel was determined by the powder method as $\text{Fd}\bar{3}\text{m}$ in 1915, some researchers have suggested its structure might be the lower symmetry space group, $\text{F}\bar{4}3\text{m}$, by showing the presence of the weak $\{200\}$ reflection spots in the $\langle 100 \rangle$ zone axis selected area diffraction (SAD) patterns.^{3,4} In general, convergent-beam electron diffraction (CBED) can provide three-dimensional symmetry information. However, even with CBED, ambiguity still exists for the space group determination of the MgAl_2O_4 spinel.⁵

Experimental

The metallic TiBe_2 samples were made by the usual procedure: disk punching, grinding, and electrolytical polishing. The diffraction work was carried out in a Philips EM400T transmission electron microscope with the specimen being cooled by liquid nitrogen. Unless stated otherwise, all CBED patterns were taken at 120 kV.

Results

A series of zone axis patterns (ZAPs) are shown in Fig. 1, which were subsequently identified as $\langle 111 \rangle$ ZAPs, consistent with other results presented later. Both the bright-field (BF) symmetry and the whole-pattern (WP) symmetry can be determined as 3m .⁶ The dark-field (DF) symmetry can be identified as m_2 from the HOLZ lines in the DF disks. The $\pm\text{G}$ dark-field pattern ($\pm\text{DF}$) symmetry can be seen to be 2Rm .⁷ Then the corresponding diffraction group could be uniquely determined as 6rmmr . This leaves the choice of the point group to be either $\text{m}\bar{3}\text{m}$ or $\bar{3}\text{m}$. To distinguish further between the two possible point groups,

D.-R. Liu and D. B. Williams are with the Department of Materials Science and Engineering, Lehigh University, Bethlehem, PA 18015; M. Wall is in the Chemistry and Materials Science Department, Lawrence Livermore National Laboratory, Livermore, CA 94550. They thank Dr. L. E. Tanner of Lawrence Livermore National Laboratory for his interest and encouragement. This work was supported by the National Science Foundation under contract NSF-DMR-8400427. The work at Livermore was supported by Department of Energy contract W-7405-ENG-48.

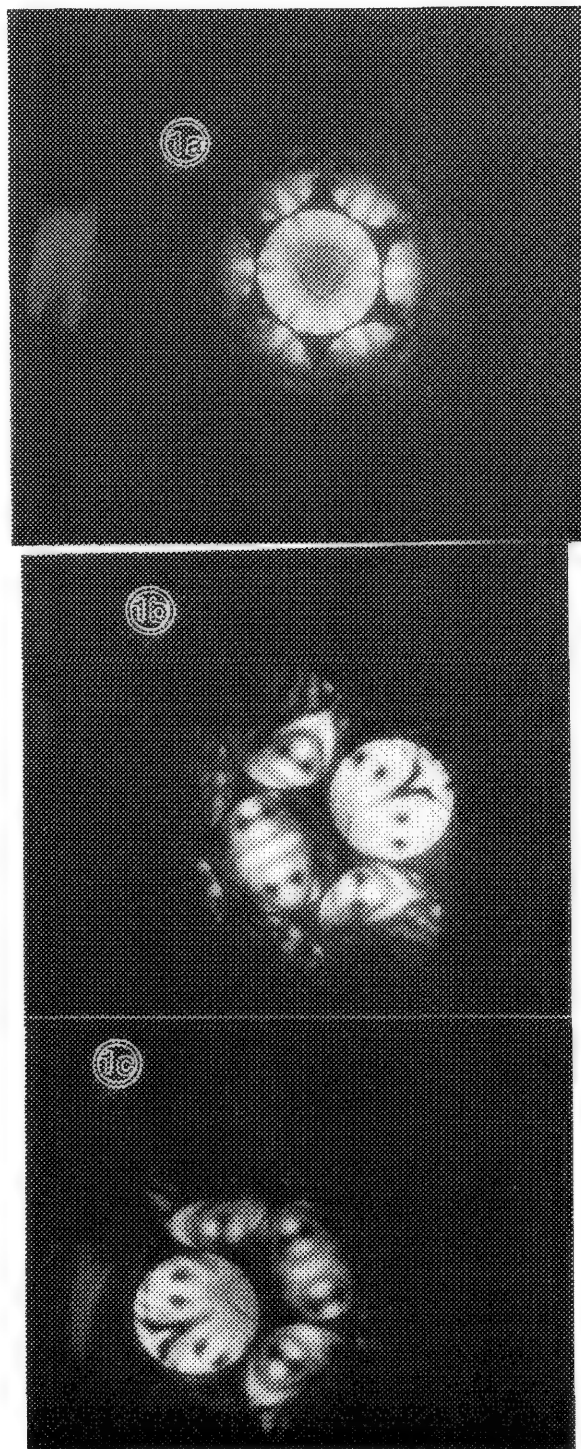


FIG. 1.-- $\langle 111 \rangle$ zone axis of TiBe_2 : (a) in exact zone axis, (b) the 220 reflection in Bragg condition, (c) $\bar{2}20$ reflection in Bragg condition.

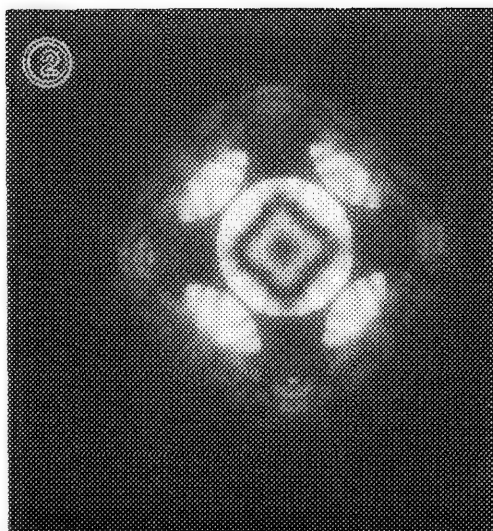


FIG. 2.--<100> zone axis patterns of TiBe₂.

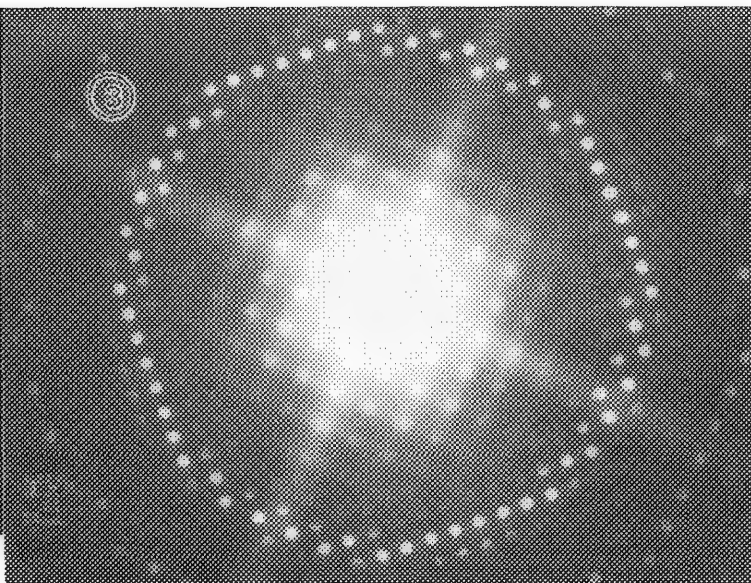


FIG. 3.--<001> zone axis pattern of TiBe₂.

the <100> zone axis pattern was taken (Fig. 2). The BF symmetry and the WP symmetry are 4mm. This information alone leads to two possible diffraction groups: 4mm and 4mm1q. However, none of them could result from the point group $\bar{3}m$. Therefore, the point group is determined as $m\bar{3}m$. Next we will determine the Bravais lattice of the sample. For the diamond structure, the measurement should be performed in the <100> orientation, because only along this zone axis can the {200} spots in the ZOLZ plane be truly forbidden. Their absence then enables one to distinguish unambiguously the diamond-type structure from others. The <100> CBED pattern of the TiBe₂ shows that it is indeed the diamond structure (Fig. 3).⁸ Two more <100> zone axis patterns are shown in Fig. 4, taken at 118 and 116 kV. Black lines of diffraction intensity deficiency are present in all {200} disks and must result from the presence of some microscopical symmetry elements in the space group of TiBe₂.⁹ Based on all this evidence, we can immediately deduce the possible space groups Fd $\bar{3}m$.

Discussion

We have followed the standard procedure to determine the structure of TiBe₂ and clearly demonstrated that it should be Fd $\bar{3}m$. It is apparent that no ambiguity exists in the information gained from the diffraction patterns in the <100> orientation. It was found that when the specimen was thin, the diffraction pattern had no {200} diffraction spots unless it was tilted slightly (Fig. 5a). However, when the area examined became thicker, the {200} spots clearly appeared (Fig. 5b). Therefore, as in the controversy over the space group of MgAl₂O₄, the intensity within the {200}-type spots could result either from HOLZ reflections or from the nonzero structure factor at {200}

reciprocal lattice points. For MgAl₂O₄, this structure effect arises due to a possible small displacement of the Al³⁺ cation in the <111> direction from the center of the octahedral interstice.^{10,11} It has already been proposed that the space group of MgAl₂O₄ be Fd $\bar{3}m$ (to a first-order approximation), even if its true space group is F $\bar{4}3m$. A similar question could be raised whether the space group of TiBe₂ could also be F $\bar{4}3m$ though it might be approximated to Fd $\bar{3}m$.¹² We have therefore investigated two possible approaches to distinguish the two space groups.

a. The first approach is whether, in general, we can reliably distinguish between $m\bar{3}m$ and $\bar{4}3m$ using the CBED patterns shown in Fig. 1. We are effectively asked to distinguish between the diffraction groups 6 $\bar{2}mm$ and $\bar{3}m$. According to the tables, this distinction is possible if we look into the difference in the DF symmetry and \pm DF symmetry of these two point groups.^{6,7} However, no such symmetry difference has been observed in practice in many published CBED works on crystals of Si, Ge, and diamond having Fd $\bar{3}m$ and crystals of GaAs family having F $\bar{4}3m$.^{6,13} In fact, all <111> CBED patterns of the latter family show the same symmetry as the former. For the <110> zone axis patterns of the GaAs class, the situation seems clear. The CBED patterns of GaAs have shown its \pm DF symmetry lower than that of Ge.^{6,13} The reasons can be analyzed as follows. In the GaAs unit cell there is a polarization in the <111> direction, which is about 4% in terms of the atomic potential difference. Therefore, the net effect of asymmetry caused by the <111> polarization is too small to be observed. But the beam would fully sample the polarization along the <110> direction, because the polarization projection is the largest in the (110) projection plane.

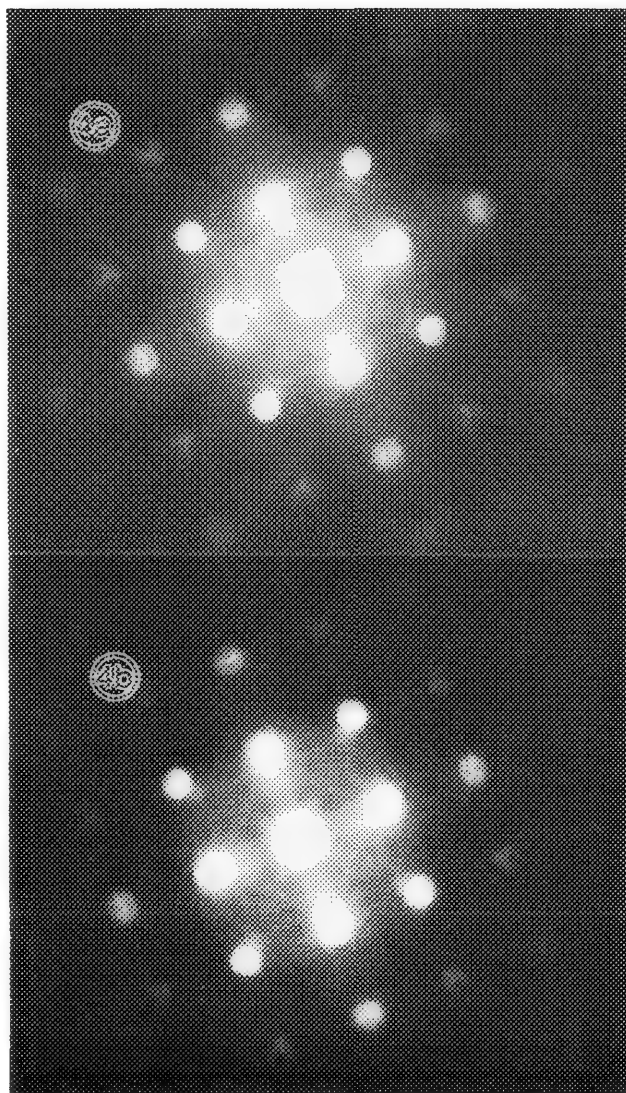


FIG. 4.--Two $\langle 001 \rangle$ zone axis patterns taken at (a) 118 kV and (b) 116 kV.

Further inspection of the $\langle 110 \rangle$ CBED patterns of GaAs shows that the polarity is manifested as some small local intensity difference between two patterns of $\bar{4}3m$ and $m3m$.^{6 13} In the case of $MgAl_2O_4$, the polarity in the $\langle 111 \rangle$ directions, if it exists, may be estimated to be 0.4% from the amount of the Al^{+3} cation displacement,^{10,11} about 10 times smaller than that of GaAs. Therefore, the expected intensity difference would probably be much less, and it may not be sufficient to resolve the long-standing controversy even in the $\langle 110 \rangle$ orientation. The same problem would exist for $TiBe_2$, if it also had a small noncentrosymmetry.

b. The second method is developed out of comparison of our Fig. 4 with the CBED pattern of GaAs given as Fig. 11 in reference 6. Here we focus our attention upon the fine HOLZ lines along the $[100]$ and $[010]$ directions in the $\{200\}$ disks. In the case of $TiBe_2$, the sym-

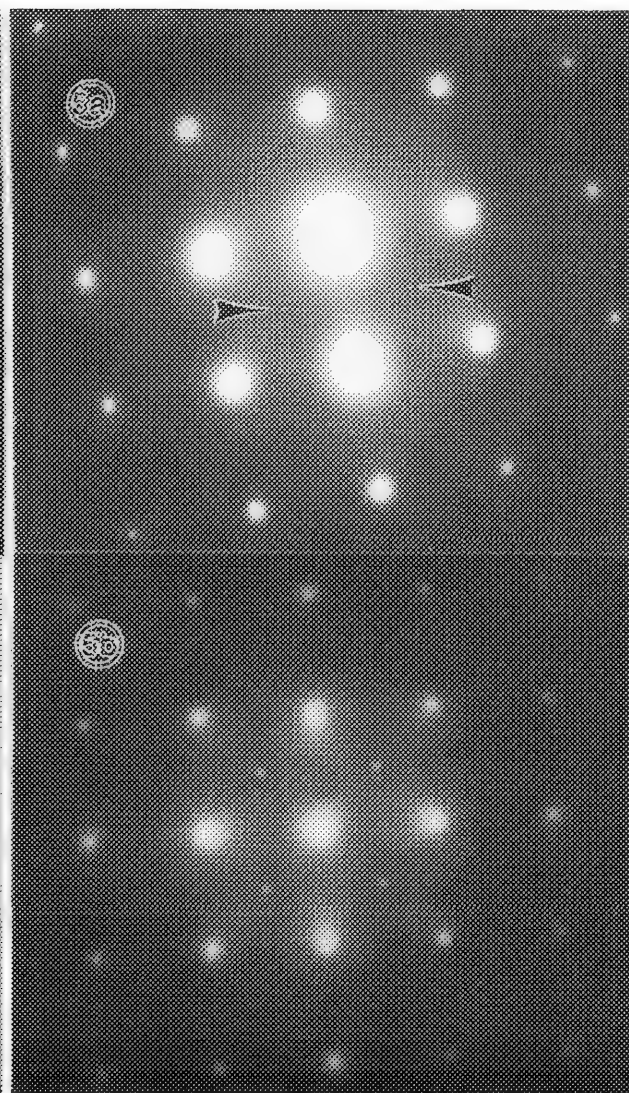


FIG. 5.-- $\langle 100 \rangle$ selected area diffraction patterns of $TiBe_2$ taken at (a) thin region, (b) thick region.

metrical black central lines are clear evidence for the presence of a glide plane/screw axis. However, for $F\bar{4}3m$, there should not be such symmetrical black central lines in the $\{200\}$ disks, as is shown in the $\langle 100 \rangle$ ZAP of GaAs.⁶ Therefore, $TiBe_2$ must have the $m3m$ point group, given the two possible choices of $m3m$ and $\bar{4}3m$. This approach essentially makes use of the HOLZ line pattern and therefore possesses a great sensitivity, probably better than 0.02-0.05%, in detecting a small noncentrosymmetry.

Conclusions

We have followed the standard procedure to establish the point group and space group of $TiBe_2$ to be $m3m$ and $Fd3m$. However, when we considered a slight hypothetical possibility that $TiBe_2$ may be in the space group $F\bar{4}3m$, rather than $Fd3m$, it was found that the standard procedure might not be sufficient to dis-

tinguish them. We have therefore proposed to use the CBED features of microscopical symmetry elements possessed by the space group $Fd\bar{3}m$, but not by the space group $F\bar{4}3m$, to distinguish between the point groups $m\bar{3}m$ and $\bar{4}3m$. This method should be highly sensitive to detect any possible degeneration of the space group $Fd\bar{3}m$ to the space group $F\bar{4}3m$. Any possibility that $TiBe_2$ possesses $F\bar{4}3m$ is ruled out.

References

1. Powder Diffraction files, JCPDS file 12-587, Swarthmore, Pa., International Center for Diffraction Data, 1982.
2. A. L. Giorgi, B. T. Matthias, G. R. Stewart, F. Acker, and J. L. Smith, "Itinerant ferromagnetism in the C-15 Laves phase $-TiBe_{2-x}Cu_x$," *Solid State Commun.* 32: 455, 1979.
3. L. Hwang, A. H. Heuer, and T. E. Mitchell, "On the space group of $MgAl_2O_4$," *Phil. Mag.* 28: 241, 1973.
4. R. H. Mishra and G. Thomas, "Structural phase transition in the spinel $MgAl_2O_4$," *Acta Crystallogr.* A33: 678, 1977.
5. B. C. De Cooman and B. C. Carter, "On the point group of stoichiometric spinel $MgO \cdot Al_2O_3$," *Phil. Mag.* A51: 175, 1985.
6. B. F. Buxton, J. A. Eades, J. W. Steeds, and G. W. Rackham, "The symmetry of electron diffraction zone axis pattern," *Phil. Trans. Roy. Soc.* A281: 171, 1976.
7. M. Tanaka, H. Sekii, and T. Nagasawa, "Point group determination by convergent beam electron diffraction," *Acta Crystallogr.* A39: 825, 1983.
8. J. W. Steeds, "Convergent beam electron diffraction," in J. I. Hren, J. I. Goldstein, and D. C. Joy, Eds., *Introduction to Analytical Electron Microscopy*, New York: Plenum, 1979, 410.
9. J. Gjønnes and A. F. Moodie, "Extinction conditions in the dynamic theory of electron diffraction," *Acta Cryst.* 19: 65, 1965.
10. A. H. Heuer and T. E. Mitchell, "Further discussion on the space group of spinel," *J. Phys.* C8: L541, 1975.
11. N. W. Grimes, P. Thompson, and H. F. Kay, "New symmetry and structure for spinel," *Proc. Roy. Soc. Lond.* A386: 333, 1983.
12. A. M. Burns, *Space Group for Solid State Scientists*, New York: Academic Press, 1978, 163.
13. M. Tanaka and M. Terauchi, *Convergent Beam Electron Diffraction*, Tokyo: JEOL Ltd., 1985.

EELS MICROANALYSIS OF Be-Ti ALLOYS WITH CALIBRATED PARTIAL CROSS SECTIONS

Dang-Rong Liu, M. Wall, and D. B. Williams

The compositional analysis of Be-Ti alloys on a submicron level is best performed by electron energy loss spectroscopy (EELS). The quantification procedure for EELS has been well established.¹ An important parameter in obtaining good quantitative results is the ratio of the partial inelastic-scattering cross sections of the elements of interest. The conventional way to obtain this ratio is to employ the SIGMAK2/SIGMAL2 programs to compute the relevant cross section values.¹ However, the accuracy of the value computed, in general, is limited to $\sim \pm 20\%$. If the error propagation law is strictly followed, the atomic ratio of two elements would have an error figure of $\sim \pm 40\%$ resulting from cross-section errors alone. We have attempted to improve this accuracy by using a specimen of known composition as a standard in the quantification of the Li content of Al-Li alloys.² The same approach is used here for quantification of the Be content of Be-Ti alloys.

Experimental

Two groups (A and B) of Be-Ti specimens, suitable for use in a transmission electron microscope, were prepared from cast samples by the usual procedure: disk punching, grinding, and electrolytic polishing. The samples were nominally stoichiometric; group A had the approximate formula TiBe_2 and group B was $\text{TiBe}_{1.2}$. A Philips 120 kV EM400T analytical microscope, equipped with a GATAN spectrometer and a serial recording system was used for the EEL spectrum collection. The collection semi-angle used was 2.9 mrd. All spectra were collected under identical electron optical conditions: in the TEM mode with a defocused illumination.²

Results

The two groups of specimens were both single phase, as confirmed by the dark-field images. Six EEL spectra were collected from each group of specimens. Typical spectra from each of the two groups of specimens are shown in Fig. 1. It is easy to see qualitatively that group B sam-

ples (Fig. 1b) contain much more Be than group A (Fig. 1a). The full quantification procedure was carried out on spectra collected from the two groups of specimens. The ratio equation used for quantification is¹

$$N_1/N_2 = [\sigma_2(\beta, \Delta)/\sigma_1(\beta, \Delta)] [I_1(\beta, \Delta)/I_2(\beta, \Delta)]$$

where the N_1/N_2 is the atomic ratio of Be to Ti and I_1/I_2 is the intensity ratio of the Be K edge and Ti L_{23} edge signals obtained with a collection semi-angle β and a signal integration window Δ . The term σ_1/σ_2 is the corresponding cross-section ratio. The thickness t of sample regions was usually 0.6-0.7 λ , as conveniently determined by the ratio of the intensities of the first plasmon peak, to the zero-loss peak. For these preliminary results, no deconvolution was performed to remove the plural scatterings. The background extrapolation was based on a direct least-squares fit with weighting of the channels toward the onset of the edge.³ The integration window was 60 eV for both edges. With a student distribution analysis and assuming a 95% confidence, the intensity ratio of Be/Ti in the spectra from group A samples is 10.2 with a relative error $\pm 6.6\%$. For reasons discussed below, it was reasonable to assume that the composition of the group A specimens was indeed TiBe_2 . Therefore the ratio of Be to Ti in group A samples could be used to calibrate the partial cross-section ratio $\sigma(\text{Be})/\sigma(\text{Ti})$. The composition of the group B specimens was then determined to be $\text{TiBe}_{7.5 \pm 0.7}$, with a relative error of $\pm 9.3\%$.

Discussion

This result was surprising in that it was far from being the formula composition $\text{TiBe}_{1.2}$ previously assigned to the group B specimens. We have carefully investigated the structure of the group A specimens using convergent-beam electron diffraction, and unambiguously determined its space group to be $\text{Fd}\bar{3}m$, which corresponds to the type 1 Laves phase.⁴ Therefore, the formula must be TiBe_2 . We checked whether any significant errors could have been introduced into the EELS quantification. The reason to collect spectra from relatively thick regions was to have these spectra as representative of bulk specimens as possible. It is known that a finite thickness might introduce a certain amount error to the quantification results in a few examples.¹ However, in the case of the Be-Ti alloys, spectra collected from regions thicker or thinner than 0.6-0.7 t/λ showed nearly the same results. (One of the spectra was collected from a region of $t = 1.2\lambda$.) The difference between the computed results from spectra collected from

D.-R. Liu and D. B. Williams are with the Department of Materials Science and Engineering, Lehigh University, Bethlehem, PA 18015; M. Wall is in the Chemistry and Materials Science Department, Lawrence Livermore National Laboratory, Livermore, CA 94550. They thank Dr. L. E. Tanner of Lawrence Livermore National Laboratory for his interest and encouragement. This work was supported by the National Science Foundation under contract NSF-DMR-8400427. The work at Livermore was supported by Department of Energy contract W-7405-ENG-48.

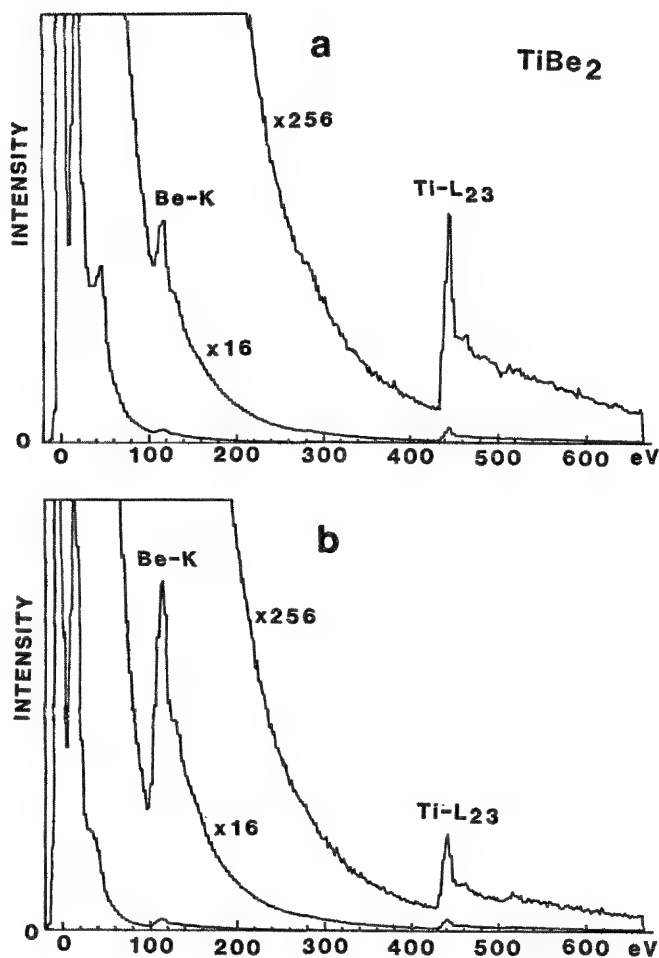


FIG. 1.--EEL spectra of (a) TiBe_2 and (b) the group B specimens.

various areas did not show a definite correlation with their difference in thickness. Furthermore, deconvolution might not always improve the results. More important, since the thickness of the regions selected for spectrum collection in the two groups of specimens was about the same, the degree of influence of the plural scatterings should be the same for the two groups of spectra. By use of one group of spectra from specimens of known composition for calibration of the partial cross sections in the quantification of the other group, the influence of plural scattering in the latter group could be reasonably ignored, without a deconvolution step. It is then clear that no other significant error has been introduced in the quantification of the group B spectra. Assuming the group A specimens are of stoichiometric composition TiBe_2 , the group B specimens are clearly not TiBe_{12} . It is possible from the phase diagram that they could be the intermetallic compound $\text{Ti}_2\text{Be}_{17}$,⁵ but the actual composition of the group B specimens used in this work is $\sim\text{Ti}_2\text{Be}_{14.9\pm 1.4}$.

Conclusion

An accurate partial cross section ratio for Be/Ti was obtained with the use of spectra

from specimens of known composition. We were then able to identify positively the composition of another group of specimens as $\text{Ti}_2\text{Be}_{14.9\pm 1.4}$, closer to the compound $\text{Ti}_2\text{Be}_{17}$ than TiBe_{12} , as originally thought.

References

1. R. F. Egerton, *Electron Energy Loss Spectroscopy in the Electron Microscope*, New York: Plenum, 1986.
2. D. R. Liu and D. B. Williams, "Progress toward precise composition determination of Al-Li alloys by electron energy loss spectroscopy," *Microbeam Analysis--1986*, 425.
3. D. R. Liu and D. B. Williams, "A new background extrapolation procedure for quantification in EELS," *Proc. 45th Ann. Mtg. EMSA*, 1987, 118.
4. D. R. Liu and D. B. Williams, "Possible ambiguity in the structural analysis of TiBe_2 by convergent beam electron diffraction," *Microbeam Analysis--1988*, this volume.
5. J. L. Murray, "The Be-Ti (beryllium-titanium) system," *Bull. Alloy Phase Diagrams* (in press).

Secondary Ion Mass Spectrometry

HIGH-RESOLUTION ION PROBE IMAGING AND ANALYSIS

R. Levi-Setti, J. M. Chabala, Y. L. Wang, and P. Hallégot

Two distinct methods can be used to obtain mass-resolved images by secondary ion mass spectrometry (SIMS): direct imaging ion microscopy, and scanning ion probe microanalysis. The direct imaging method, pioneered by Castaing and Slodzian in 1960,¹ has developed into a mature and widespread technique. Recently, scanning ion microanalysis has emerged as a procedure with many attractive features, including unsurpassed lateral resolution, low specimen damage, and parallel mass detection. At the 1985 MAS conference, we presented early results obtained with the University of Chicago-Hughes Research Laboratories scanning ion microprobe (UC-HRL SIM).² Through a gradual process of instrumental modification, the analytical capabilities of this instrument have been improved considerably since that time. In addition, the experience we have gained in our attempts to optimize the information that can be obtained from high-resolution mass-resolved images has taught us much about the potential and limitations of the scanning ion microprobe technique.³⁻⁴ We discuss these issues in the context of examples from a selection of interdisciplinary fields.

The Scanning Ion Microprobe

Conceptually, the UC-HRL scanning ion microprobe consists of two decoupled systems operating in tandem (Fig. 1): the primary and secondary ion optical columns.⁵ In the primary ion optical column, a strong electric field (~ 1 V/Å) extracts, by a field evaporation process, heavy ions (usually Ga⁺) from a liquid metal ion source. The primary ions emerging from this high-brightness source ($\sim 10^6$ A cm⁻² sr⁻¹) are drawn through a beam-defining aperture that serves to collimate the ions and, consequently,

to reduce spherical and chromatic optical aberrations. The ion current extracted from the source is in the microampere range; only a small fraction, in the picoampere range, passes through this aperture to bombard the sample. The ion beam is focused by two electrostatic lenses, accelerated to 20-60 keV energy, and scanned by two sets of octupole deflectors. Two channel electron multiplier detectors positioned above the target provide secondary electron or non-mass-resolved secondary ion signals; these signals yield topographic information. The entire length of the primary optical column is only 25 cm.

The full-width-half-maximum Gaussian diameter of the resultant probe depends on the diameter of the beam-defining aperture and can be made, theoretically, smaller than the dimensions of the ion emitting region (possibly less than 10 nm). Unfortunately, probes of this diminished size would be of curiosity value only: they would not induce the emission of enough secondary ions for relevant analysis with current technology.⁴ Furthermore, the lateral dimensions of the primary-ion-induced collisional cascade are typically in the 5-20 nm range,⁶ negating any resolution advantage gained by use of ultranarrow probes. In practice, 20 nm (~ 1.6 pA for the UC-HRL SIM) beams are sufficient for specialized applications involving the analysis of high-ion yield or segregated materials.⁷ Routine microanalysis is possible with 35-70 nm diameter probes (10-40 pA). The evaluation of image spatial resolution must include, as its most important factor, consideration of secondary ion yield statistics.^{4,8} As a result, because of differing elemental emission characteristics, image resolution is sample-dependent in the low-counting-statistics regime (<1 count per probe setting).

The operation of the secondary ion optical system is not affected by any adjustments, such as probe focusing, made on the primary ion column. Ion-induced secondary ions emerging from the sample are accelerated by a small (~ 100 V) potential. These ions traverse a compact, 8 mm-diameter cylindrical sector energy analyzer positioned 1 mm above the target. The sample voltage can be varied to explore various regions of secondary ion energy spectra. A series of electrostatic transport elements shape the beam for optimal insertion into an RF quadrupole mass spectrometer. Finally, the mass-filtered ions are detected by a channel electron multiplier operated in pulse mode. The resulting digital signal (one detected ion, one pulse) is subsequently routed to photo-display oscilloscopes and to arrays of digital image memory in a KONTRON

The authors are at the Enrico Fermi Institute and Department of Physics, The University of Chicago, Chicago, IL 60637. This material is based on work supported by the National Science Foundation under grants DMR-8612254 and BBS-8610518. Additional support was obtained from the Allied Signal Engineered Materials Research Center. We thank our collaborator, Dr. E. Olsen of Field Museum of Natural History, Chicago, for providing the Chainpur meteorite sample. The Al alloy and tooth examples were obtained as part of a collaboration with Dr. A. Lodding of Chalmers University of Technology and Dr. J. Norén of the Dental School, both of Gothenburg, Sweden. We are indebted to these colleagues for making these materials available for use in this forum. Finally, we thank Dr. D. Kern of the IBM Thomas J. Watson Research Center for providing the test circuit.

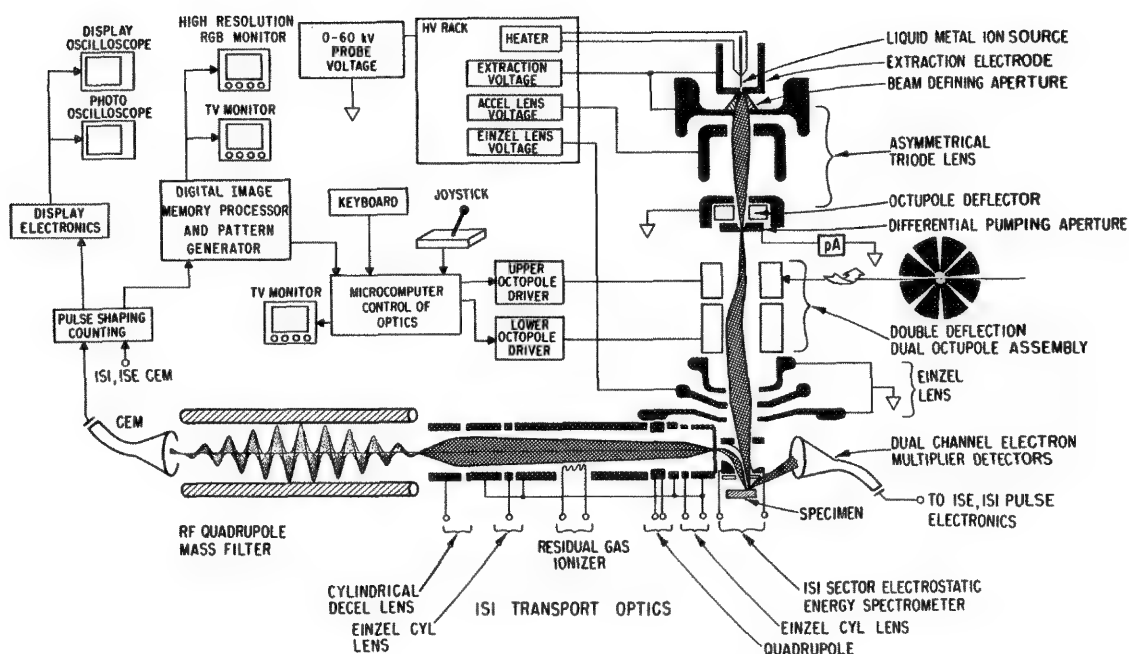


FIG. 1.--Schematics of current implementation of UC-HRL scanning ion microprobe at University of Chicago.¹⁶ Adapted from reference 5.

image processing system (IPS). Positive or negative secondary ions can be analyzed by reversal of the polarity of the optical elements in the secondary ion handling system. Residual currents, such as secondary electrons originating from electrodes in the primary optical column, are small ($\sim 10^{-15}$ A) and therefore do not interfere with SIMS analysis. Parallel mass detection systems have been implemented on several microprobe instruments.^{9,10}

Microprobe Control and Data Acquisition

The operations of the primary and secondary ion optical systems are unified by a computer-controlled electronics network. The primary ion probe can be maneuvered in either a raster or a vector-scan mode. For raster scanning, custom hardware generates a square digital X-Y sweep similar to that customarily used in scanning electron microscopes; the speed (500ns to 16ms dwell time per probe setting) and dimensions (16×16 to 1024×1024) of this sweep are widely adjustable. A microcomputer controls other scan parameters, including scan rotation, astigmatism correction and magnification.

For quantitative analysis, secondary ion mass spectrometry images, once stored in digital memory, are evaluated by the KONTRON IPS utilizing a pipelined image array processor. Current hardware allows the storage of fourteen $512 \times 512 \times 8$ images in RAM. Operations performed within computer memory typically include the construction of intensity plots along any operator-defined curve (line scans), and the computation of intensity histograms for selected image areas. Image features can also be selected by a variety of densitometric criteria; for example, submicrometers-scale areas corresponding to a segregated phase can be

isolated from a bulk matrix according to area, intensity, or shape and relevant properties evaluated. If more information (e.g., mass spectra) is desired from any arbitrary subarea of the original field of view, the processor can steer the probe to perform a vector scan exclusively of such subareas. In this manner, quantitative analyses can be obtained from submicrometer domains (microSIMS). This procedure, equivalent to a gated scan, is also useful for minimizing certain resputtering artifacts.^{3,11} The vector-scan capabilities of this system also facilitate the machining of microphysics devices.

Many additional image processing operations are occasionally performed, including fast Fourier transform filtering (to eliminate periodic image artifacts) and the registration with color coding of correlated images for superposition. These functions do not improve the image resolution.

Applications

As demonstrations of the versatility and power of a high lateral resolution scanning ion probe, we present examples from ongoing research on a number of disparate subjects. These projects involve studies of silicate minerals in meteorites, of sintered ceramics, of aluminum alloys, of microcircuits on silicon substrates, and of mineralized biological tissue.

Stone Meteorite. The scanning ion microprobe is well suited for the analysis of the silicate minerals and other inclusions found in stone meteorites (chondrites). The extraordinary diversity in elemental composition and size of the microstructures found in these bodies, generally highly insulating, provides tests of both analytical sensitivity and

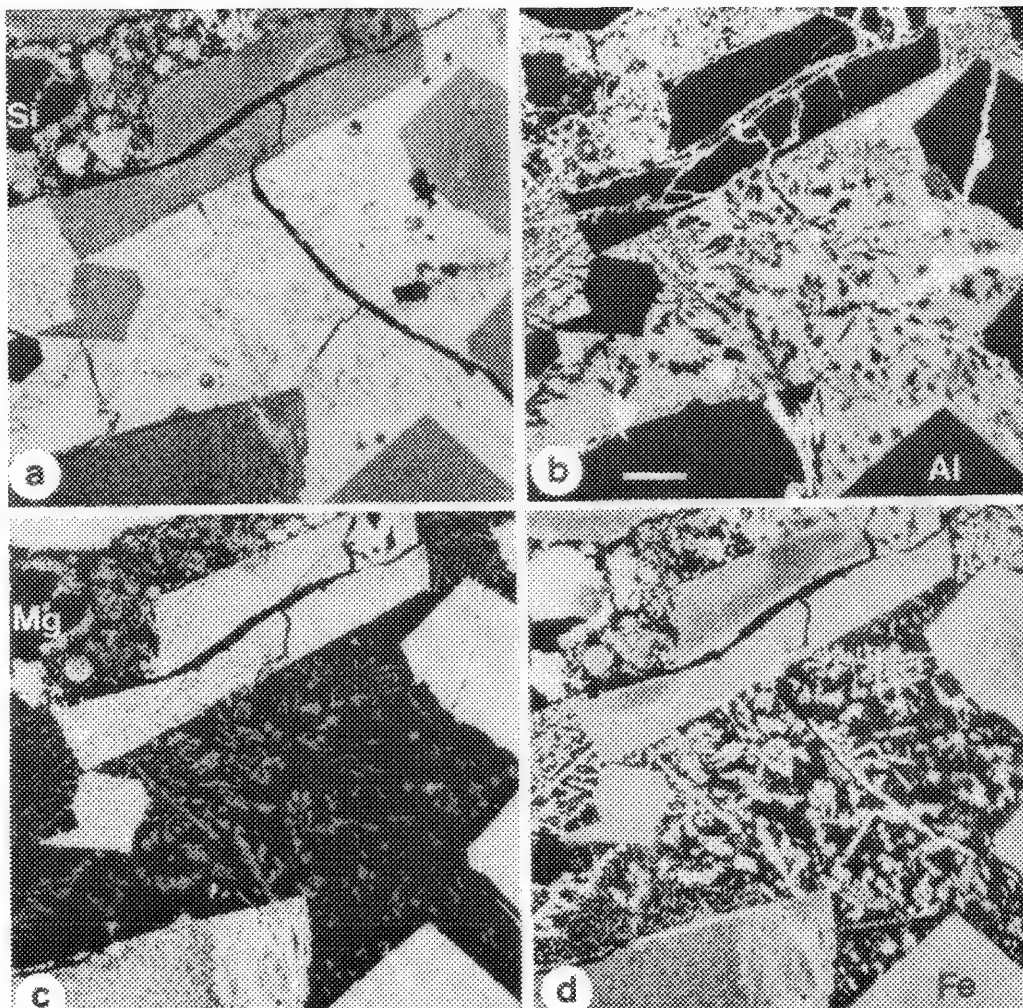


FIG. 2.—SIMS elemental distribution images of interior of Chainpur meteorite chondrule. 20 pA, 40 keV Ga^+ probe. Scale bar, 20 μm . (a) $^{28}\text{Si}^+$; 8.3×10^6 counts accumulated in 524 s. (b) $^{27}\text{Al}^+$; 14×10^6 counts, 157 s. (c) $^{24}\text{Mg}^+$; 12×10^6 counts 524 s. (d) $^{56}\text{Fe}^+$; 7.5×10^6 counts, 524 s.

spatial resolution. Most important, the study of chondrites with a novel instrument promises to unravel several still controversial aspects related to their origin and formation.

Chondrites typically consist of aggregates of spherical or ovoid bodies called chondrules, which in turn are primarily composed of crystalline silicates such as olivine $[(\text{Mg},\text{Fe})_2\text{SiO}_4]$ and pyroxene $[(\text{Mg},\text{Fe})\text{SiO}_3]$ cemented by a glassy matrix rich in Si, Al, Na, and K. There is evidence that chondrules underwent a melting and quenching cycle before their final aggregation into meteorite-size objects. The mechanism of this thermal process is not well understood.¹²

We are examining chondrules and their rims in a primitive stone meteorite called Chainpur (LL-3 chondrite).¹³ The sample analyzed here is a doubly polished thin section about 30 μm thick, affixed with epoxy to a 25mm-diameter glass disk. The entire assembly was coated with a $\sim 30\text{nm}$ layer of gold to inhibit charging artifacts.

Figure 2 shows elemental images (maps), $160 \times 160 \mu\text{m}^2$ in size, of the interior of a porphyritic chondrule. These wide-field survey

images convey information about the principal structural features of the sample. The central bright areas in the $^{28}\text{Si}^+$ and $^{27}\text{Al}^+$ maps (Figs. 2a and b) are representative of the glassy component of the chondrule interior. The complementary bright areas in the $^{24}\text{Mg}^+$ and $^{56}\text{Fe}^+$ maps (Figs. 2c and d) indicate the presence of large olivine crystals. Within the glass phase, fine-grained, dendritic olivine precipitates suggest a rapid quench from a melt.

Mass spectra of positive and negative secondary ions were obtained from the area imaged in Fig. 2. These spectra, presented in Fig. 3, reveal an extraordinarily complex composition. Correlative maps have been obtained for most prominent element peaks in these spectra. Of particular interest, relevant to the history of the chondrules prior to their aggregation into the meteorite body, would be the imaging of C_2 and CN distributions. Indeed, images of quality comparable to those shown in Fig. 2 have been obtained for these components. However, we believe these latter results are unreliable because the plastics used for section preparation may have infiltrated the porosities and fissures of the sample. This issue

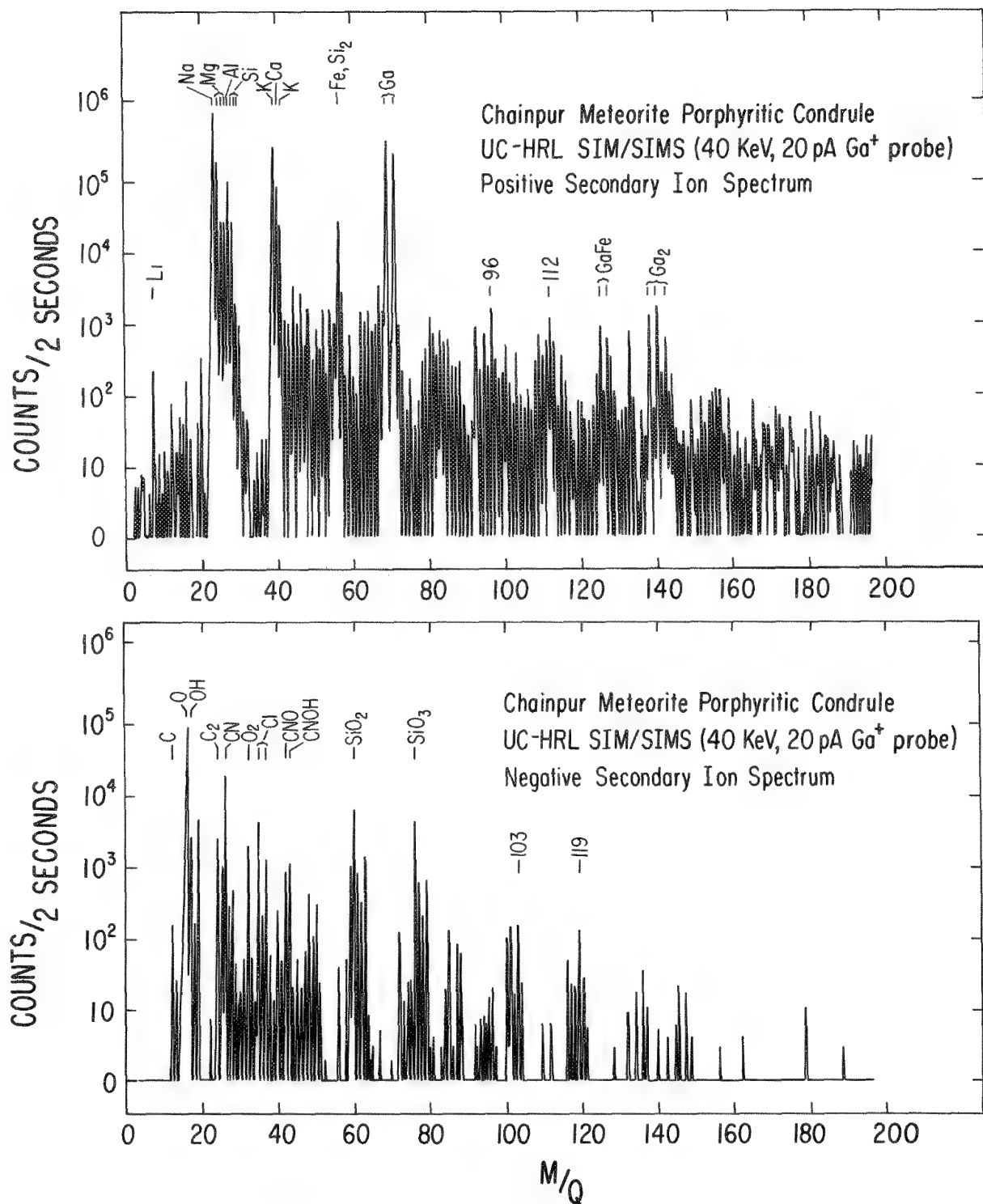


FIG. 3.--Positive and negative secondary ion mass spectra of area imaged in Fig. 2., interior of Chainpur meteorite chondrule.

will be resolved following the analysis of contamination-free samples.

From a technical standpoint, we note that the elemental counting rates obtained at present with the UC-HRL SIM are greater by more than a factor of ten than those reported previously from the analysis of a similar sample.¹⁴ This improvement is the result of a careful redesign of the secondary ion collection, transport, and detection systems.

Sintered Silicon Nitride Ceramic. Sintered silicon nitride (Si₃N₄) is an advanced ceramic often used for high-temperature applications. Used as sintering agents, yttrium oxide (Y₂O₃), magnesium oxide (MgO), and others, present in 1-10wt% concentrations, react with the silicon nitride phases and allow sintering to occur at temperatures between 1600 and 1900 C in a nitrogen overpressure environment. The mechan-

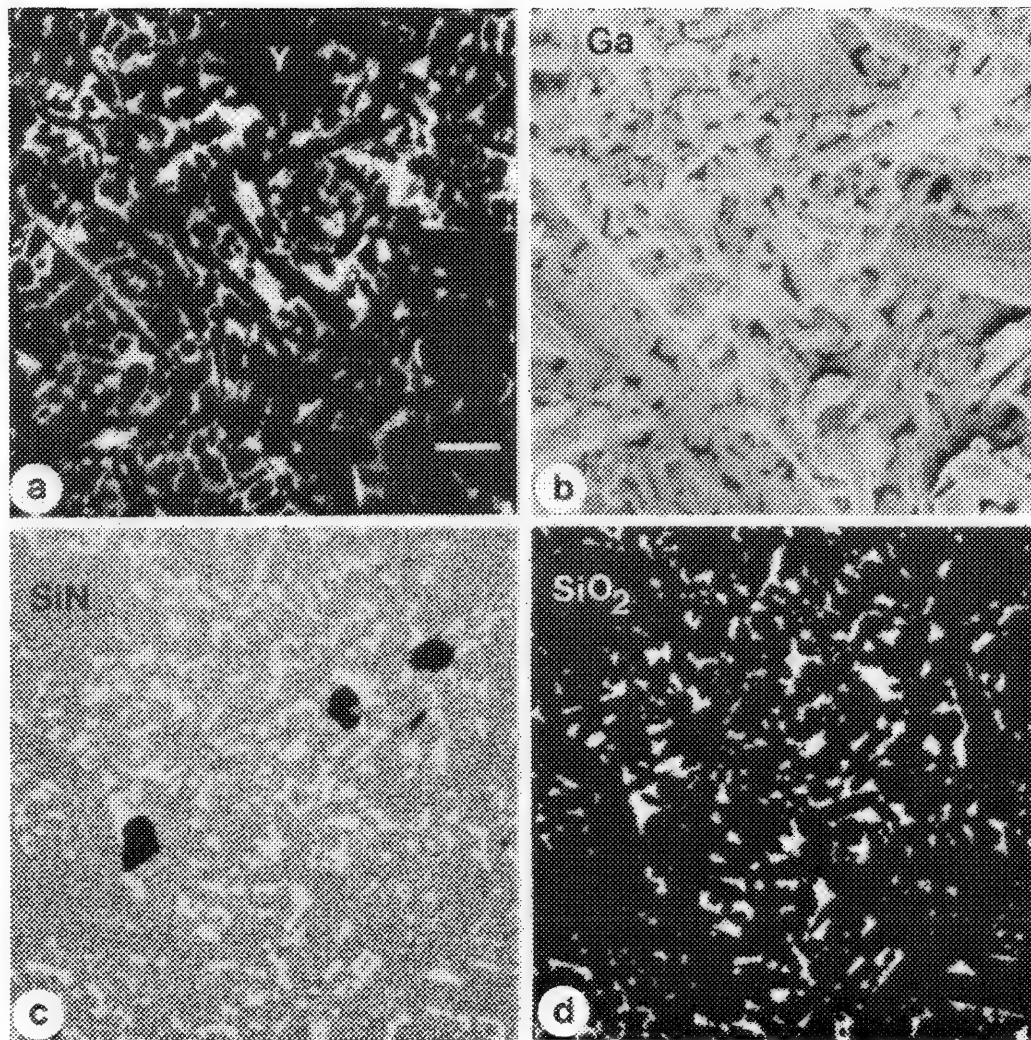


FIG. 4.--SIMS images of yttria-sintered (8 wt% Y_2O_3) silicon nitride (Si_3N_4) ceramic. Images (a) and (b) from fractured surface; (c) and (d) from polished surface. 50 pA, 40 keV Ga^+ probe. Scale bar, 2 μm . (a) $^{89}\text{Y}^+$; 1.9×10^6 counts accumulated in 524 s. (b) Resputtered $^{69}\text{Ga}^+$; 10×10^6 counts, 524 s. (c) $^{42}\text{SiN}^-$, 2.6×10^6 counts, 524 s. Black areas due to contamination inclusions. (d) $^{60}\text{SiO}_2^-$, 1.9×10^5 counts, 524 s. Image resembles Y^+ distribution for same area.

ical properties of these ceramics are ultimately determined by the properties of resulting secondary phases which form along grain boundaries. When Y_2O_3 is used as a sintering additive for Si_3N_4 , an interboundary YSiO_2N phase develops that can oxidize to $\text{Y}_2\text{Si}_2\text{O}_7$. We summarize here the results of a study¹⁵ of a silicon nitride system produced by a reaction bonding process. Compacted silicon powder was nitrated at high temperature; final sintering occurred at 8 wt% Y_2O_3 .

Numerous charged molecular fragments are copiously emitted under probe bombardment from both the Si_3N_4 matrix and the interboundary phase. The analysis and two-dimensional display of these signals provides information about the volume, distribution, and content of both components.

Fractured and polished surfaces of this ceramic were examined; representative maps are shown in Fig. 4. Figure 4a shows the yttrium distribution within a $16 \times 16 \mu\text{m}^2$ area of a

fractured surface. Because the fracture occurs preferentially along grain boundaries, the secondary phase may partially blanket the exposed Si_3N_4 crystals. Consequently, this image may not provide a faithful representation of the size of the intergranular pockets. Peculiar to the use of a gallium probe, the differential resputtering of Ga atoms implanted during previous microprobe scans yields structure and density information about the sample. This process is demonstrated by the $^{69}\text{Ga}^+$ map in Fig. 4b, which corresponds to the area imaged in Fig. 4a. The crystalline structure of the matrix is clearly outlined in this map: the interboundary phase is less emissive than the matrix. Roughly, the yttrium and gallium distributions are complementary to each other.

A better description of the interboundary pocket profile is provided by the $^{42}\text{SiN}^-$ and $^{60}\text{SiO}_2^-$ distribution obtained from a polished section of this ceramic, shown in Figs. 4c and

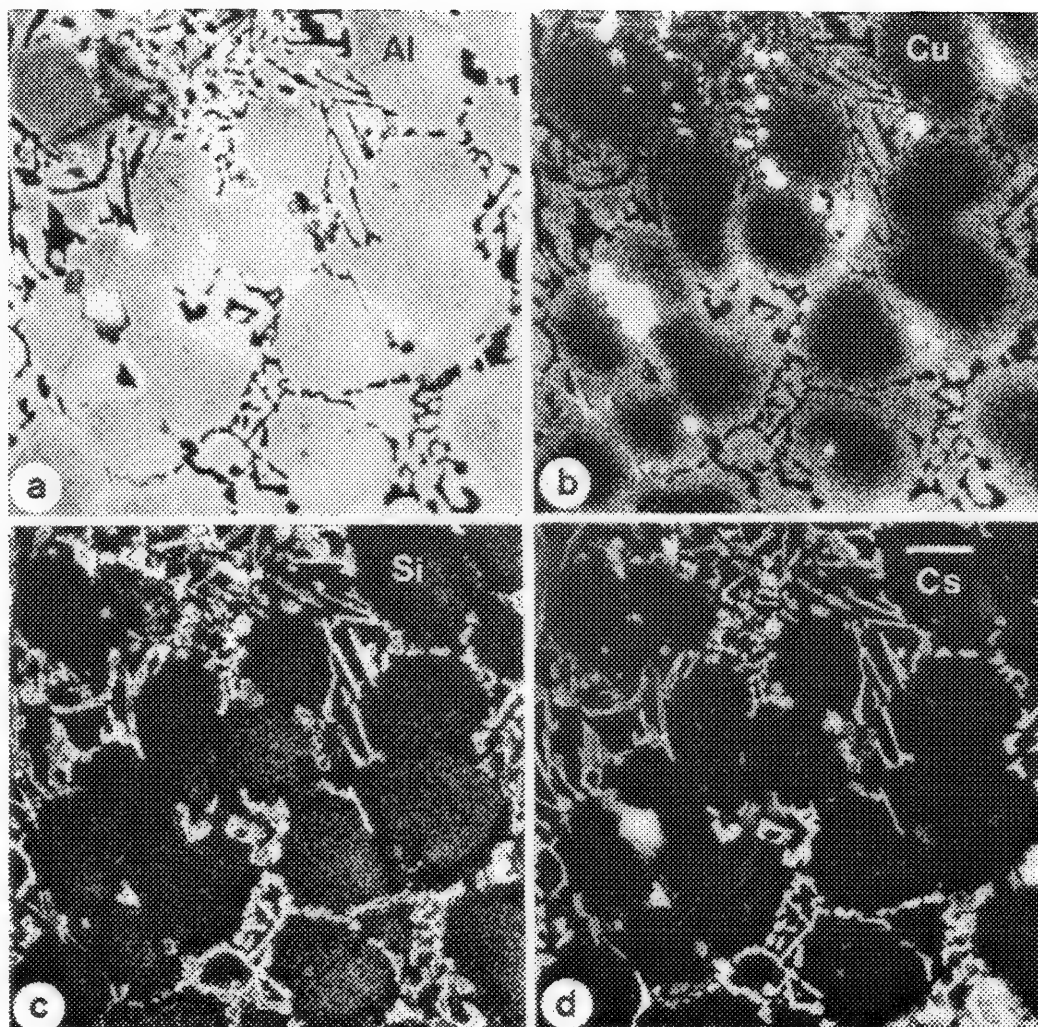


FIG. 5.--Correlative SIMS maps of Al-based alloy. 10 pA, 40 keV Ga⁺ probe. Scale bar, 10 μ m. (a) ²⁷Al⁺; 4.6×10^7 counts accumulated in 128 s. (b) ⁶³Cu⁺; 1.3×10^6 counts, 524 s. (c) ²⁸Si⁺; 1.0×10^6 counts, 524 s. (d) ¹³³Cs⁺; 3.2×10^6 counts, 524 s.

4d. Quantitative study of these and of other maps (O,Si) leads to an unambiguous characterization of this engineered material. A thin coating of gold, plus the metallic gallium primary ion implant, are sufficient to allow repeated high-magnification scans of one area without charging artifacts.

Aluminum-based Alloy. SIMS imaging microanalysis of alloys can provide detailed characterization of primary, eutectic, intermetallic, and solid solution phases. We are engaged in a long-range study of binary and multicomponent aluminum-based alloys. As a glimpse of the complex multidimensional information that can be extracted from a nominal Al-Si-Cu-Mg casting alloy, we present in Fig. distribution maps for ²⁷Al⁺, ⁶³Cu⁺, ²⁸Si⁺, and ¹³³Cs⁺ (additional maps for ²⁴Mg⁺, ³⁹K⁺, ¹⁶O⁻, ¹⁹F⁻, ²⁴C²⁻, and ²⁶CN⁻ are not shown). Figure 5a shows the typical Al primary (α) dendrite structure with interdendritic precipitates. These precipitates consist of several intermetallic and eutectic phases. The ⁶³Cu⁺ map (Fig. 5b) shows moderately large copper- (and aluminum-) rich

crystallites, presumably intermetallic CuAl₂. The Cu also exists in solid solution within the Al phase, visible as a diffuse gradient that increases in concentration toward the interdendritic boundaries. The interdendritic Al-Si eutectic is clearly marked by a web of silicon-rich precipitates (Fig. 5c). Like Cu, Si exists in solid solution within the Al dendrites. However, the Si concentration is depleted in the vicinity of the interdendritic region in a manner that is complementary to the Cu distribution pattern. Intense ¹³³Cs⁺ emission is observed (Fig. 5d) in coexistence with the Si precipitates and the intermetallic CuAl₂. The presence of cesium in this alloy is puzzling; it may have been used as a modifier. Indeed, abundant emission of K, a common Al-Si alloy modifier, is observed to mimic the Cs concentrations. We have also detected an intense ¹⁹F⁻ signal directly associated with the Al distribution. This pairing suggests that fluorine is a residue of the alkali-AlF₆ used in the electrolytic extraction of aluminum; the potassium and cesium could also have originated from this source.

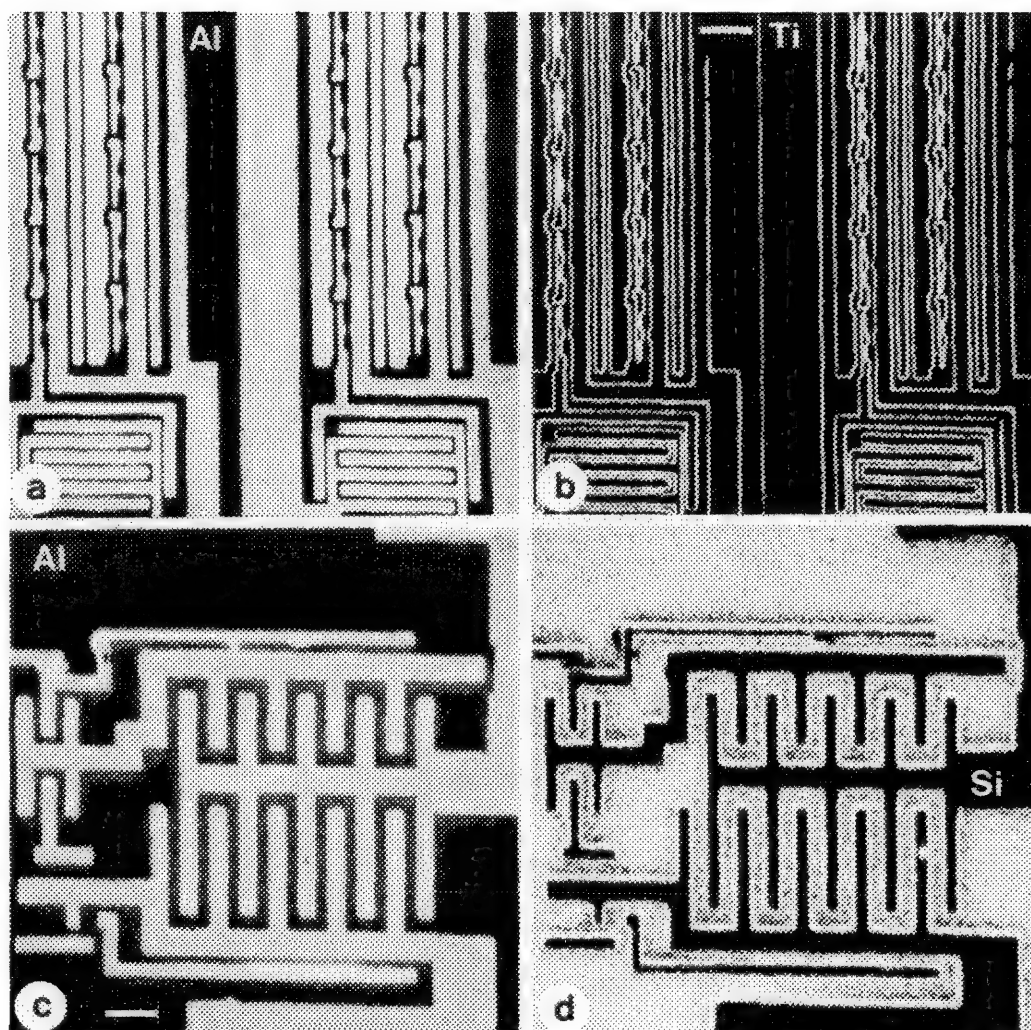


FIG. 6.--SIMS elemental images of 0.25 μm -feature-size test circuit on silicon substrate. 10 pA, 40 keV Ga^+ probe. Scale bar, 10 μm . (a) $^{27}\text{Al}^+$; 11×10^6 counts accumulated in 128 s. (b) $^{48}\text{Ti}^+$; 4.0×10^5 counts, 524 s. Scale bar, 4 μm . (c) $^{27}\text{Al}^+$; 7.8×10^6 counts, 256 s. Scale bar, 2 μm . (d) $^{28}\text{Si}^+$; 9.4×10^6 counts, 256 s.

Microcircuit Devices. The quartet of maps presented in Fig. 6 were obtained during a study¹⁶ of test circuits with 0.25 μm feature size. These circuits, constructed by e-beam lithography by IBM, consist of patterned bilayers of aluminum on titanium deposited on a uniform silicon substrate. A narrow band of the Ti layer, laying between the Al and Si, is exposed. A pair of corresponding images for $^{27}\text{Al}^+$ and $^{48}\text{Ti}^+$ (Figs. 6a and 6b) were obtained from a $40 \times 40 \mu\text{m}^2$ area. These maps of a planar sample provide excellent diagnostics of the constant secondary ion collection efficiency, and the lack of imaging aberrations, over the entire field of view. Images of comparable quality can be obtained from areas up to $0.8 \times 0.8 \mu\text{m}^2$ in size. These relatively low-resolution images (0.15 μm , determined by the probe raster spacing) possess a wealth of information. For example, several submicrometer-scale Ti circuit shorts are visible. Figures 6c and d are higher-magnification $^{27}\text{Al}^+$ and $^{28}\text{Si}^+$ maps of a circuit detail (image edge resolution for

this case is $\sim 75 \text{ nm}$). Again, nanometer-scale features are readily apparent. The faint halo surrounding the Al wires is a sputter redposition artifact that can be avoided, if necessary, by use of the gated vector-scan procedure outlined above. The picoampere currents used in the UC-HRL SIM permit sustained observations of the sample surface; unfortunately, depth profiling is time consuming.

Biological Hard Tissue. We have used our microprobe to study several biological materials. Hard mineralized tissues, such as bone and teeth, have long been popular objects for SIMS research because they can be prepared for analysis by conventional petrographic sectioning and polishing techniques. Diverse mineral and organic components, inclusive of diffusible elements, can be imaged in polished sections of hard tissue with good quantitative reliability (for a recent review, see Lodding et al.¹⁷). Specimen electrical charging is the principal difficulty encountered during ion microprobe observation of particularly

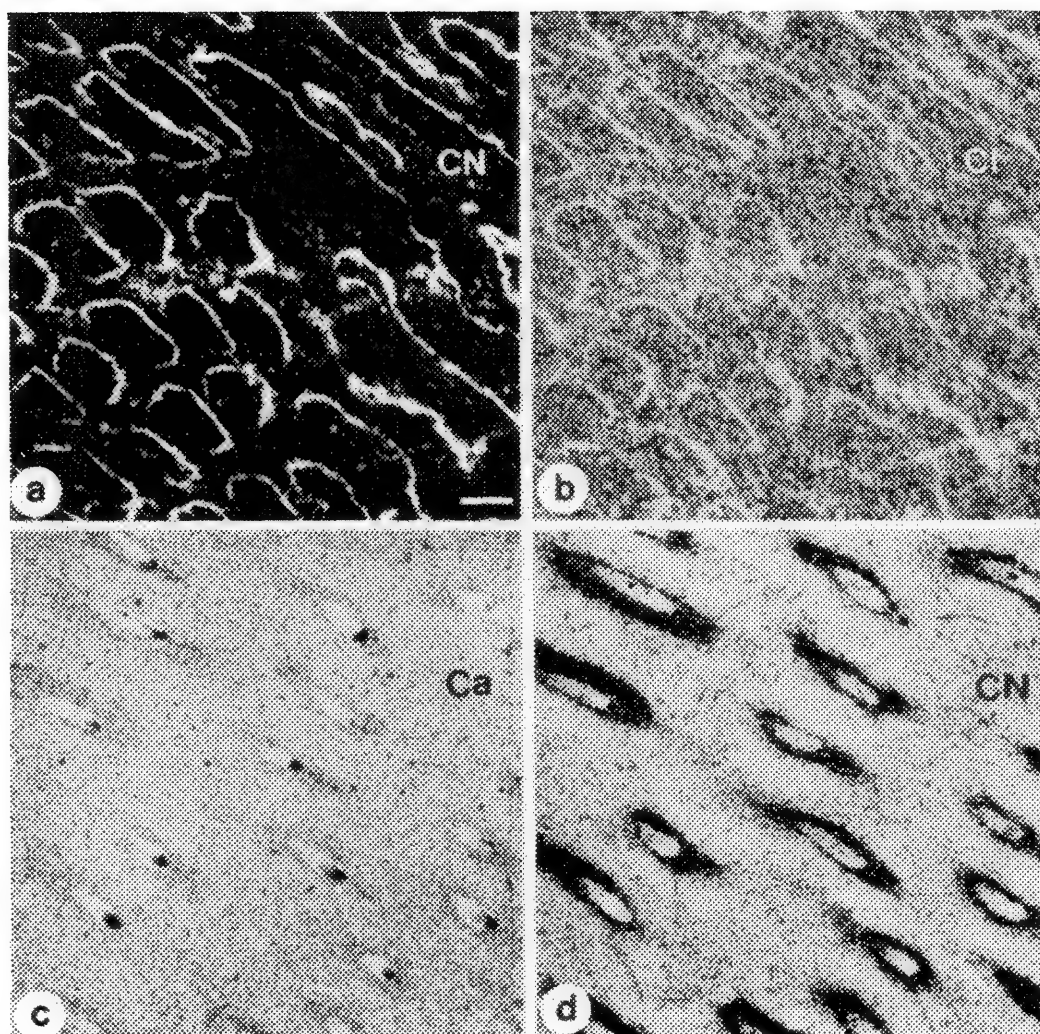


FIG. 7.--SIMS analysis of healthy human adult tooth. (a),(b) Maps of transverse cross section through enamel. (c),(d) Maps of transverse section through dentine. 10 pA, 40 keV Ga⁺ probe. Scale bar, 4 μm. (a) ²⁶CN⁻; 9.9×10^6 counts accumulated in 524 s. CN⁻ ion typically emitted from organic material. (b) ³⁵Cl⁻; 1.7×10^6 counts, 524 s. (c) ⁴⁰Ca⁺; 11×10^6 counts, 524 s.

dense materials, such as dental enamel. This restriction can be overcome by application of a thick (>30nm) conductive gold layer to the sample surface or by limiting the scans to large areas (> 80 × 80 μm²), thereby reducing the average primary ion current density (to >0.3 μA/cm²).

Detailed studies of dental hard tissues are in progress as part of a collaboration between our laboratory and the SIMS Laboratory at Chalmers University of Technology, Gothenburg, Sweden. The examples of Fig. 7 originate from these studies and are related to SIMS analyses of healthy adult tooth enamel (Figs. 7a and b) and dentine (7d and c). The ²⁶CN⁻ signal, an indicator of the presence of organic material; outlines the contours of stacked enamel prisms (Fig. 7a). The ³⁵Cl⁻ distribution (Fig. 7b), otherwise uniformly diffuse throughout the field of view, exhibits enhanced signal from the CN-rich prism sheaths. Prominent features in the ⁴⁰Ca⁺ and ²⁶CN⁻ maps of dentine (Figs. 7c and d) are the oblique, teardrop-shaped

cross sections of dentinal tubules. From a comparison of the Ca and CN images, the structure of the tubules becomes apparent. Each tubule is composed of at least three distinct concentric regions: (1) an outer layer, devoid of CN, with a Ca concentration close to that of the intertubular matrix; (2) an intermediate tubular sheath enriched in both Ca and CN; and (3) a core of pure organic material about 1 μm in diameter. The quality of these images over earlier similar observations⁷ is testimony to the substantial improvements, achieved during the last two years, in the SIMS imaging capabilities of the UC-HRL scanning ion microprobe.

References

1. R. Castaing and G. Slodzian, "Micro-analyse par émission ionique secondaire," in *Proc. Eur. Reg. Conf. on Electron Microscopy Delft*, 169-179, 1960.
2. R. Levi-Setti, G. Crow, and Y. L. Wang, "High-resolution topographic and isotopic imag-

ing with a 40 keV Ga⁺ scanning ion microprobe, in *Microbeam Analysis--1985*, 209-218.

3. R. Levi-Setti, J. Chabala, and Y. L. Wang, "Micro-secondary ion mass spectroscopy: Physical and instrumental factors affecting image resolution," *Scanning Microscopy Suppl.* 1: 13-22, 1987.

4. J. Chabala, R. Levi-Setti, and Y. L. Wang, "Practical resolution limits of imaging microanalysis with a scanning ion microprobe," *Appl. Surf. Sci.* (in press).

5. R. Levi-Setti, Y. L. Wang, and G. Crow, "High spatial resolution SIMS with the UC-HRL scanning ion microprobe," *J. Physique* 45: C9-197-205, 1984.

6. J. P. Biersack, "Computer simulations of sputtering," *Nucl. Instr. Methods Phys. Res.* B27: 21-36, 1987.

7. R. Levi-Setti, G. Crow, and Y. L. Wang, "Imaging SIMS at 20 nm lateral resolution: Exploratory research applications," in A. Benninghoven et al., Eds., *Secondary Ion Mass Spectrometry SIMS V*, New York: Springer-Verlag, 132-138, 1986.

8. R. Levi-Setti, J. M. Chabala, and Y. L. Wang, "Aspects of high resolution imaging with a scanning ion microprobe," *Ultramicroscopy* 24: 97-114, 1988.

9. Y. Nihei, H. Satoh, S. Tatsuzawa, et al., "High spatial resolution secondary ion mass spectrometry with parallel detection system," *J. Vac. Sci. Tech.* A5: 1254-1257, 1987.

10. D. R. Kingham, A. R. Bayley, D. J. Fathers, et al., "Three dimensional secondary ion mass spectrometry imaging and retrospective depth profiling," *Scanning Microscopy* 1: 463-469, 1987.

11. F. G. Rüdenauer and W. Steiger, "Sputter redeposition as a limit to spatially three-dimensional SIMS microanalysis," *Ultramicroscopy* 24: 115-124, 1988.

12. J. L. Gooding, K. Keil, T. Fukuoka, et al., "Elemental abundances in chondrules from unequilibrated chondrites: Evidence for chondrule origin by melting of pre-existing materials," *Earth Plant. Sci. Lett.* 50: 171-180, 1980.

13. For relevant references, see: L. L. Wilkening, W. V. Boynton, and D. H. Hill, "Trace elements in rims and interiors of Chainpur chondrules," *Biochimica et Cosmochimica Acta* 48: 1071-1080, 1984.

14. Y. L. Wang, G. Crow, R. Levi-Setti, and E. Olsen, "High lateral resolution SIMS mapping of meteorite chondrule," *Nucl. Instr. Methods Phys. Res.* B10.11: 716-718, 1985.

15. J. M. Chabala, R. Levi-Setti, S. A. Bradley, et al., "Imaging microanalysis of silicon nitride ceramic with a high resolution scanning ion microprobe," *Appl. Surf. Sci.* 29: 300-316, 1987.

16. J. M. Chabala, R. Levi-Setti, and Y. L. Wang, "Imaging microanalysis of surfaces with a focused gallium probe," *J. Vac. Sci. Tech.* (in press).

17. A. Lodding, J. G. Norén, and L. G. Petersson, "Applications of secondary ion mass spectrometry to biological hard tissues," in

Secondary Ion Mass Spectrometry SIMS VI, New York: Wiley (in press).

SIMS MOLECULAR ION IMAGING OF SIMPLE NEURO-COMPOUNDS

R. W. Odom

In addition to providing very sensitive elemental analysis capabilities, secondary ion mass spectrometry (SIMS) is a sensitive method in the structural analysis of a wide range of organic species. The fast atom bombardment (FAB)¹ and liquid SIMS² techniques are often utilized as routine methods in the molecular weight and structural analysis of a number of organic species adsorbed onto a variety of surfaces.³ The static SIMS techniques utilize low primary beam current densities in order to minimize beam induced damage to the adsorbed species. Several research groups have begun to employ static SIMS ion imaging techniques for molecular microanalysis.⁴ If this SIMS molecular ion imaging technique can be developed to an analytically useful level, it could provide a method for localizing the distribution of molecular species at micrometer resolutions in such organic solids as polymers and biomaterials. This paper reports the results of SIMS ion imaging of several neuro-compounds dispersed onto Ag substrates. These compounds produce relatively intense, structurally significant secondary ion signals which can be localized at lateral resolutions on the order of a few micrometers.

Experimental

A simple method of producing a spatially dispersed organic layer is to electrospray⁵ dilute methanol/distilled water solutions of the compounds through a TEM finder grid onto the Ag substrate. Approximately 5 μ L solutions of the various compounds having concentrations ranging from $\sim 10^{-2}$ to 10^{-6} M were electrosprayed over a 3mm diameter area. The molecular areal density for the most concentrated solutions was on the order of 3×10^{17} molecules/cm². The Ag substrates were high purity foil (99.999% purity, 1 mm thick) which were annealed at 600 C, polished, cleaned, and pressed flat before the depositions.

The SIMS analyses were performed on Cameca IMS 3f and 4f instruments. Positive ion SIMS was performed with O₂⁺, O⁺, and C_s⁺ primary ion bombardment and negative ion SIMS employed a C_s⁺ primary beam. Secondary ion microscope images were acquired with the resistive anode encoder (RAE) detector, which is a two-dimensional pulse counting detector with a spatial resolution of the order of 1 μ m.⁶ More intense secondary ion signals and better lateral resolutions for the molecular or pseudo-

molecular ions were obtained with a micro-focused C_s⁺ beam on the IMS-4f and positive secondary ion spectroscopy. For these microbeam analyses, a 5-20pA C_s⁺ beam was focused to a $\sim 1\mu$ m spot diameter and was rastered over a 200 \times 200 μ m area. For these ion microprobe analyses, the secondary ion signals were detected on the electron multiplier. Ion images were acquired with a specially designed primary beam raster circuit along with custom image acquisition hardware and software. The primary ion dose ranged between 8×10^{10} to 3×10^{11} ions/cm² at an impact energy of 5.5 keV.

A number of relatively simple molecules produced structurally significant positive secondary ion signals. These molecules included thymine, γ -aminobutyric acid (GABA), phenylalanine, dopamine hydrochloride, epinephrine, and acetylcholine chloride (ACh⁺-Cl⁻). Ion images of these latter two compounds are discussed below. Higher mass compounds which did not produce any apparent structurally significant fragment ions included 5-hydroxytryptamine (serotonin), several enkephalins including [D-Ala²] leucine, methionine, and [D-Met²,Pro⁵] enkephalin and two anti-malarial drugs, primaquine diphosphate and chloroquine. These substances have molecular weights above the mass range (~ 300 amu) of the Cameca instruments employed in these analyses.

Results and Discussion

Figure 1 illustrates ion images of the m/z 184, 166, and 107(Ag) ions observed in the analysis of the residue from 5 μ L of a 10^{-3} M solution of epinephrine electrosprayed onto the Ag substrate. Assuming uniform dispersion of the solution over the 7 mm² grid area, this analysis samples about 20 picomoles. The mass 184 ion corresponds to the protonated epinephrine molecule (M + H)⁺, and the m/z 166 ion is probably the (M - OH)⁺ species. Neither ion signal is observed in the mass spectrum of a Ag substrate electrosprayed with a methanol/water blank solution. The inverted "R" pattern in these images is the masking produced by the letter R on the finder grid. The gray scale to the right of the images shows the number of ion counts represented within each gray level. These images illustrate that the molecular species and the Ag ions are emitted from distinctly different regions of the sample. One can determine the relative ion yields (number of ions detected/number of molecules deposited) for these molecular ion signals by performing a "depth profile" analysis of the sample until the signals disappear. The relative ion yields

The author is with Charles Evans & Associates 301 Chesapeake Drive, Redwood City, CA 94063. Support for this work was provided by NIH SBIR grant GM39005-01.

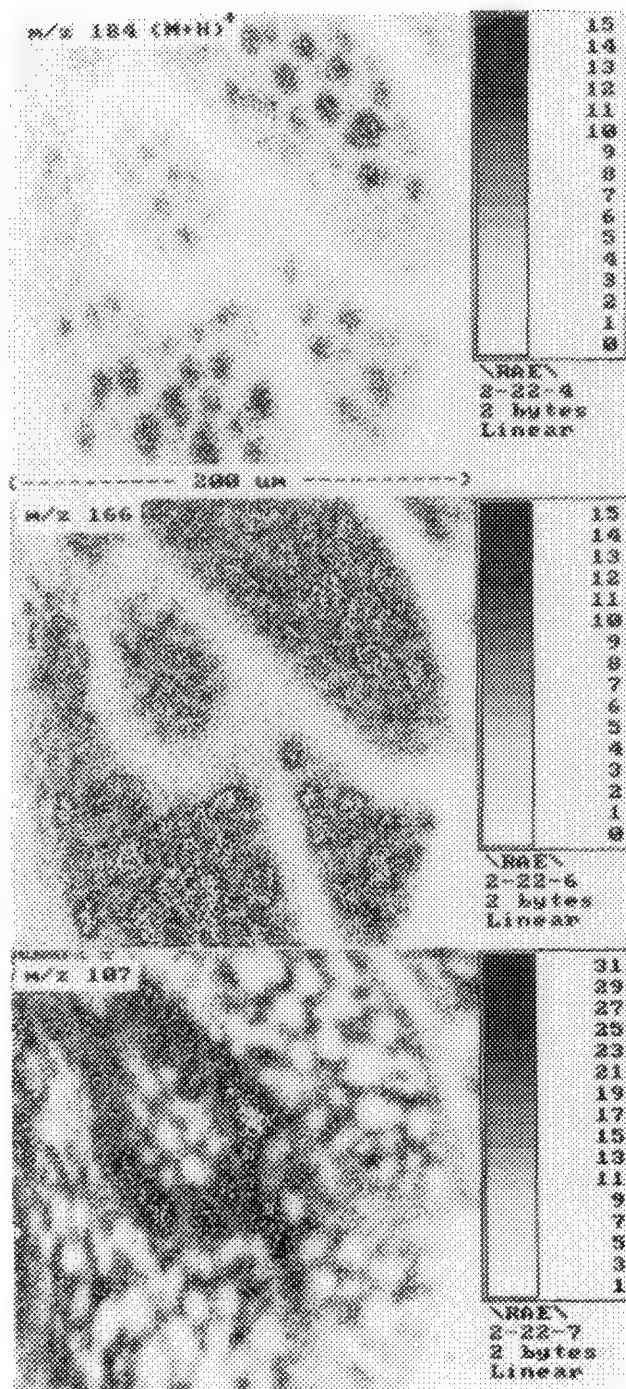


FIG. 1.--Positive-ion images of m/z 184, 166, and 107 species produced in Cs microbeam analysis of 20 picomoles of epinephrine on Ag.

for the m/z 184 and 166 ions obtained in this manner were ~ 1 and 3×10^{-8} ions/molecule, respectively.

Figure 2 shows ion images and line scan intensity profiles of the m/z 146 and 107 ions produced in the Cs^+ microbeam analysis of ~ 2 picomoles of $\text{ACh}^+\text{-Cl}^-$ dispersed on a Ag substrate. The ACh^+ ion (m/z 146) exhibits the highest ion yield of any of the compounds which produced molecular or characteristic fragment ion signals. The relative ion yield for the m/z 146 ion in this sample is $\sim 2 \times 10^{-5}$. The line scan intensity profiles display the ion intensity at each pixel along the line illustrated in the ACh^+ ion image. Each pixel

in the images is $\sim 1 \mu\text{m}$ wide and the line scans indicate that the minimum spatial distribution of ACh^+ is of the order of $10 \mu\text{m}$. The Ag^+ image exhibits enhanced emission in nearly the same region as the ACh^+ ion. Similar results are observed in the analysis of dopamine hydrochloride and a Ag substrate electrosprayed with a dilute (10^{-3} M) HCl solution. This enhanced Ag^+ emission appears to correlate with the presence of AgCl on the substrate surface.

These results illustrate the capabilities of SIMS molecular ion imaging in the analysis of rather idealized sample materials. Attempts to detect structurally significant ion signals of epinephrine, norepinephrine, dopamine and ACh in various regions of $\sim 1 \mu\text{m}$ -thick sections of rat brain tissues are underway. These samples are prepared by microtoming cross sections from frozen whole brain tissues and freeze drying these sections on a Si substrate. The sections are prepared by Joan Hunter of the Pasarow Analytical Neurochemistry Facility at Stanford University Medical School in collaboration with Dr. Kym F. Faull. Although it is possible to focus the Cs^+ microbeam onto various tissue regions, no structurally significant ions have yet been observed. The samples exhibit varying degrees of sample charging and analysis of these types of tissue sections by use of an electron flood gun is in progress.

References

1. M. Barber, R. S. Bordoli, R. D. Sedgwick, and A. N. Tyler, *J. Chem. Soc. Chem. Commun.*, 325, 1981.
2. W. Aberth, K. M. Straub, and A. L. Burlingame, *Anal. Chem.* 54: 2029, 1982.
3. A. Benninghoven, F. G. Rudenauer, and H. W. Werner, *Secondary Ion Mass Spectrometry*, New York: Wiley, 1987, chap. 5.
4. R. W. Linton in A. Benninghoven, R. J. Colton, D. S. Simons, and H. W. Werner, Eds., *Secondary Ion Mass Spectrometry, SIMS-V*, New York: Springer-Verlag, 1985, 420.
5. C. J. McNeal, R. D. MacFarlane, and E. L. Thurston, *Anal. Chem.* 51: 2036, 1979.
6. R. W. Odom, B. K. Furman, C. A. Evans, C. E. Bryson, W. A. Petersen, M. A. Kelly, and D. H. Wayne, *Anal. Chem.* 55: 574, 1983.

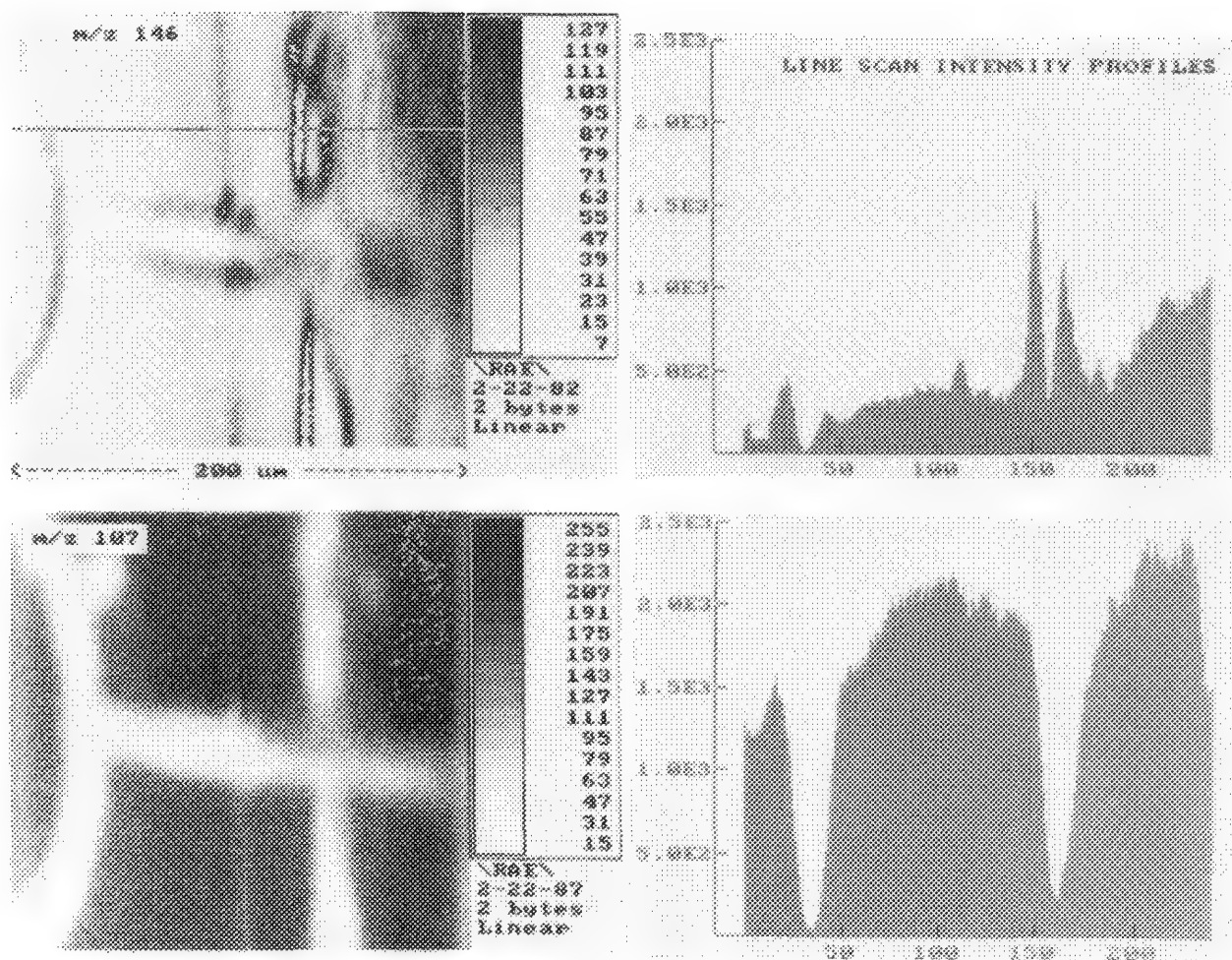


FIG. 2.--Positive-ion images and linescan intensity profiles of m/z 146 and 107 species in Cs microbeam analysis of 2 picomoles of acetylcholine⁺Cl on Ag.

COMPOSITIONAL MAPPING WITH A TV CAMERA-BASED IMAGING SYSTEM ON AN ION MICROSCOPE

Dale Newbury and David Bright

The ion microscope, the direct imaging form of secondary ion mass spectrometry (SIMS), has the potential for performing compositional mapping by simultaneously carrying out quantitative analysis for a large array of locations imaged in parallel. However, most ion microscope images recorded in practice are qualitative in nature and simply reveal the locations in the field of view at which the elemental species occur. Like all SIMS signals, ion images are subject to the well-known secondary ion yield and matrix effects, which can produce significant nonlinearities in the relation between the apparent image brightness and the true concentration. In order to prepare useful, quantitative images, it is obviously necessary to perform corrections for the yield and matrix effects. The first stage in any quantitation method for imaging must necessarily be accurate recording of the secondary ion intensities. At least three methods are available to digitize the images by use of the signal following ion-to-electron conversion at the channel plate: (1) electron-to-photon conversion at a phosphor with photography and subsequent digitization of the negative with a microdensitometer;¹ (2) television imaging of the phosphor with digitization of the TV signal;² and (3) direct digitization of the electron signals after the channel plate in a pulse counting mode with a device such as the resistive anode encoder.³ Direct digitization is the most attractive of the three methods because it has potentially the fewest instrumental artifacts, operating as it does in a pulse-counting mode. However, the resistive anode encoder, the leading device for direct digitization of ion images, is subject to a deadtime that limits the signal rate which is accurately processed by the detector to a maximum of approximately 50 kHz. Moreover, this limit applies to the whole image field. Thus, if an image has a "hotspot" of high signal intensity, this spot will limit the maximum data rate from the rest of the image.

TV Camera Image Digitization

Digitization of the signal from a TV camera that views the conventional phosphor offers certain advantages. (1) A broad range of secondary ion signals can be measured, including high ion intensities, by variation of the gain of the channel plate. (2) Because each loca-

The authors are at the Center for Analytical Chemistry, Bldg. 222, Room A121, National Bureau of Standards, Gaithersburg, MD 20899. The Al-Li specimens were kindly provided by Prof. D. B. Williams of Lehigh University.

tion in the image is measured separately and simultaneously, even if one portion of the image saturates, useful measurements can be obtained in the unsaturated portion of the image. (Blooming can affect the region of the image immediately adjacent to the hotspot.) (3) Real-time analog imaging is directly available during the digitization for continuous monitoring of the sample. In this work we have examined TV digitization of SIMS images, comparing the signal measured in the imaging mode with the signals measured with the pulse-counting electron multiplier.

The signal chain in the ion microscope consisted of (1) conversion of the secondary ions (energy: 4.5 keV) to electrons and amplification of the electrons in a dual stage channel plate; (2) conversion of the electrons to photons at the phosphor screen; (3) conversion of the photons back to an electrical signal at the charge-coupled device (CCD) TV camera; and (4) digitization of this analog electrical signal with an 8-bit analog-to-digital converter and a pixel array size of 512×512 . Of these four distinct stages in the image signal, only the CCD camera could be conveniently characterized separately. The response of the CCD camera was found to be linear when measured by means of a light source with filters of known transmittance which covered a range of two decades.

The image digitization procedure consisted of measuring the analog TV signal for an integration time of 0.033 s to create one digital frame. A total of 256 frames was added successively to produce the 16-bit digital image, which was used for all measurements and image analysis. Since the ion microscope operated at an effective lateral resolution of approximately 1 μm , a 512-square digital array substantially oversampled the image field, which was 150 μm in diameter. For subsequent processing, the 512-square image arrays were compressed to 256-square arrays.

Response of the TV Camera Imaging Detectors

In our previous work, we characterized the response of the channel plate/phosphor screen by the following procedure.⁴ Secondary ion signals from uniformly illuminated image fields of pure element and homogeneous alloy targets were measured with the ion multiplier to establish the secondary ion count rate, and digital images were acquired from these fields. By control of the primary ion current, secondary ion count rates ranging from 100 to 4×10^6 c/s over the image field were produced to determine the detector response function.

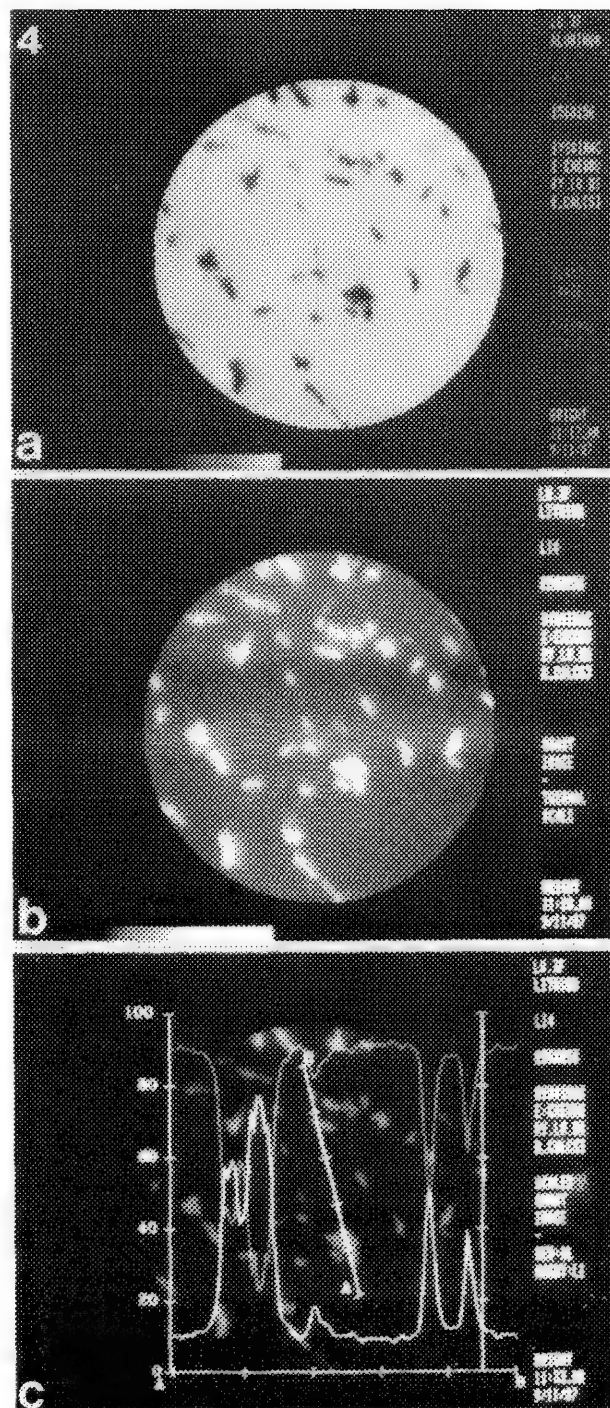
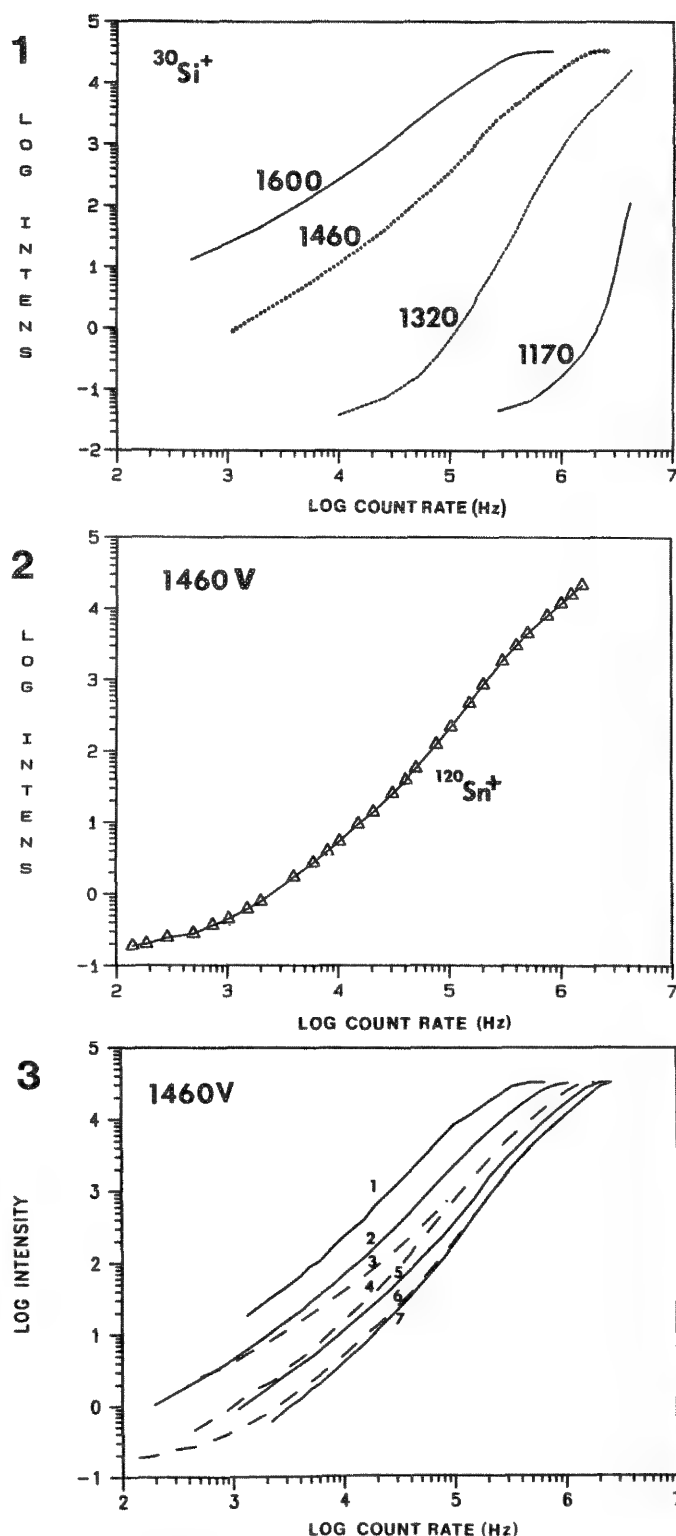


FIG. 1.--Imaging detector response curve for ^{30}Si at various channel plate voltages.⁴ Vertical axis is given in gray levels per pixel, with a maximum of 65 535 (16 bits).
 FIG. 2.--Imaging detector response curve for ^{120}Sn at channel plate voltage of 1460 V, which maximizes dynamic range.
 FIG. 3.--Imaging detector response curves for various elements at channel plate voltage of 1460 V: (1) 209-Bi, (2) 7-Li, (3) 208-Pb, (4) 27-Al, (5) ^{30}Si , (6) ^{120}Sn , (7) 115-In.
 FIG. 4.--Quantitative compositional maps for Al-10.1 at% Li alloy (heat treated at 390 C for 100 h): (a) Al image (bar = 0-100%); (b) Li image (bar = 0-100%); (c) concentration along vector AB, lower trace = Li, upper trace = Al. Vertical scale is at% Li or Al.

Figure 1 shows the effect of varying the voltage applied to the channel plate.⁴ The shape of the response curve of the channel-plate/phosphor-screen output as a function of multiplier ion count rate is found to vary strongly with the applied voltage. At the lowest applied voltage (1170 V) for which an image is first observed at high secondary ion intensity, the detection system is insensitive to incident count rates below 300 kHz. Multiplier count rates as high as 4 MHz can be measured in the imaging mode, although the response curve is extremely nonlinear. When the applied voltage is increased to 1320 V, the image sensitivity increases by 4 decades for a 1MHz multiplier count rate. At an applied voltage of 1460 V, an additional decade of sensitivity is obtained. A longer range is obtained where a linear relation is observed between the multiplier count rate and the image gray level, which indicates sensitivity to individual pulses.⁵ This voltage maximizes the dynamic range of the imaging detector and corresponds to the point at which individual noise pulses first become visible on the TV monitor with no beam (ion or neutral) incident on the specimen. A 254-frame digital image under these conditions produces an average background intensity level of 0.1 gray scale units/pixel (1 in 10 pixels is nonzero), a negligible level. The effective dynamic range which can be achieved under these conditions is illustrated in the curve for tin in Fig. 2, where over four decades of ion intensity are measured without reaching the upper saturation. Further increases in the channel plate voltage above 1460 V lead to saturation for multiplier count rates above 1 MHz and to increased background, thus reducing the dynamic range.

We next measured the imaging detector response curves for a variety of elemental species, as shown in Fig. 3. In the initial phase of this work,⁴ response curves for Li, Si, and Sn were measured (curves 2, 5, and 6 in Fig. 3). The sequence of displacement of these curves seemed to imply a decreasing sensitivity with increasing mass. Since the ions impact the detector at constant kinetic energy, increasing mass corresponds to decreasing ion velocity, which might be expected to affect the secondary electron yield at the ion-to-electron conversion in the channel plate. However, when the study was extended to heavy elements, e.g., Pb and Bi (curves 1 and 3), this trend was not confirmed. Instead, the set of response curves showed a complex behavior as a function of atomic number which did not depend on any obvious parameter such as ion velocity.

To carry out quantitative interelement analysis in the imaging mode with matrix correction by the method of sensitivity factors, it is necessary to convert the gray level measured at a particular image pixel into the equivalent multiplier count rate. The measured response curve for an element provides the mechanism for this conversion. However, it is clear from Fig. 3 that a single response curve is not ade-

quate to describe the wide range of behavior which is observed. For a specific choice of count rate as determined with the multiplier (e.g., 10 kHz), the imaging detector response response covers two decades for the limited set of elements tested. Since the behavior as a function of atomic number is not easily predictable, it is necessary to determine a response curve for each element of interest.

Application to Al-Li Alloys

Compositional mapping by ion microscopy has been applied to the study of aluminum-lithium alloys. All image manipulations were carried out with a software system developed specifically for microscopy applications.⁶ Using a homogeneous aluminum-lithium alloy, we first determined the imaging detector response curves (curves 2 and 4 in Fig. 3). From a series of these homogeneous alloys, which spanned a wide composition range, the Li-Al sensitivity factor was measured and found to be reasonably constant over the range of concentration. Pairs of images for 27-Al and 7-Li were recorded with short ion exposures (240 frames = 8 s). The 16-bit gray scale images were then converted to equivalent ion counts at each pixel by means of the appropriate imaging detector response curve. The Li-Al intensity ratio $i(\text{Li})/i(\text{Al})$ was calculated on a pixel-by-pixel basis, and the concentration ratio $C(\text{Li})/C(\text{Al})$ was calculated at each pixel from the sensitivity factor $S(\text{Li}/\text{Al})$:

$$C(\text{Li})/C(\text{Al}) = [i(\text{Li})/i(\text{Al})]/S(\text{Li}/\text{Al})$$

An example of quantified Al-Li images is shown in Fig. 4a for Al and Fig. 4b for Li. The alloy was of nominal composition Al-10.1 at% Li and was heat treated at 390 C for 100 h. Under these conditions, the phase diagram indicates a solid solution in equilibrium with an Al-Li intermetallic compound. In Fig. 4c, the Al and Li concentrations along the vector A-B are plotted, which is shown superimposed on the Li image. The vector passes through several of the second phase precipitates. From this trace, one particle (located near the 4th tick mark on vector AB) corresponds to the AlLi (50-50) composition. However, the largest particle (near the A of vector AB) shows a much higher lithium content, near 80 at%. This may be an artifact of specimen preparation. In previous work, we demonstrated that preferential leaching during mechanical polishing can lead to substantial surface enrichment of lithium, and this particle may represent an area which has not been sufficiently sputtered to reach material which is representative of the interior bulk composition.⁷

References

1. J. D. Fassett, J. R. Roth, and G. H. Morrison, "Quantitation of secondary ion mass spectrometric images by microphotodensitrometry and digital image processing," *Anal.*

Chem. 49: 2322, 1977.

2. B. K. Furman and G. H. Morrison, "Direct digitization system for quantification in ion microscopy," *Anal. Chem.* 52: 2305, 1980.

3. R. W. Odom, B. K. Furman, C. A. Evans, C. E. Bryson, W. A. Petersen, M. A. Kelly, and D. H. Wayne, "Quantitative image acquisition system for ion microscopy based on the resistive anode encoder," *Anal. Chem.* 55: 574, 1983.

4. D. E. Newbury and D. S. Bright, "Quantitative isotope and elemental ratio measurements with a camera-based imaging system on an

ion microscope," *Secondary Ion Mass Spectrometry* (in press).

5. S. R. Bryan, R. W. Linton, and D. P. Griffis, *J. Vac. Sci. Tech.* A4: 2317, 1986.

6. D. S. Bright, "A LISP-based image analysis system with applications to microscopy," *J. Microscopy* 148: 51-87, 1987.

7. D. B. Williams, R. Levi-Setti, J. M. Chabala, and D. E. Newbury, "High spatial resolution secondary ion imaging and secondary ion mass spectrometry of aluminum-lithium alloys," *J. Microscopy* 148: 241-252, 1988.

EFFECTS OF ABERRATIONS UPON THE COLLECTION EFFICIENCY OF SPUTTERED IONS

Georges Slodzian

The production of secondary ions implies the consumption of a given amount of matter from the sample. When one aims at in situ analysis of microvolumes with good sensitivity, it is of paramount importance to reduce this amount and therefore to collect secondary ions very efficiently. The parameter that controls the analytical capabilities is the useful yield, that is, the ratio of the number of mass-filtered ions arriving per unit time at the detector to the number of atoms of the same kind being sputtered during that time. Useful yields depend on the *collection efficiency* of the instrument; that is, on the ratio of the number of ions entering the mass spectrometer to the number of secondary ions of the same nature being produced at the target surface. The problem we examine concerns the improvement of the collection efficiency at high mass-resolving powers when the emitting area is reduced to the small impact area of an ion probe.

General Considerations

Consider ions of a given mass ejected from a small area with a given initial energy and with the directions of their initial velocities filling a given solid angle. After the collecting system, they form a beam of trajectories directed toward the mass spectrometer through a transfer optical system.¹⁻² The role of the transfer system is to make the beam emerging from the collecting system fit the shape of the beam that the spectrometer can accept.

When the diaphragm defining the entrance beam of the spectrometer has been optimized for a given mass resolving power, one may increase the solid angle into which secondary ions are collected by adjusting the transfer system. However, as ions emitted with larger initial angles are collected, the aberrations of the collecting and transfer systems increase and tend to limit the gain in collection efficiency. The purpose of this contribution is to examine how to adjust the transfer system to obtain the highest possible collection efficiency for secondary ions emitted from an object point. The experimental conditions are then the most favorable for the use of an ion microprobe and the production of scanning ion images with the help of the transfer system working in the dynamic mode.

The author is at the Laboratoire de Physique de Solides, Bât. 510, Université Paris-Sud, F-91405 Orsay, France. He thanks B. Daigne and F. Girard of ONERA and Dr. B. Rasser and Dr. H. Migeon of CAMECA for their help.

Aberrations of the Objective Lens and the Transfer System

The collecting system is here the objective lens of the direct imaging microscope. It can be described as an accelerating section followed by a focusing section L1. The amplitudes of the aberrations produced by the accelerating section depend on the spread of the initial energies (chromatic aberrations) and on the initial angles (aperture or spherical aberrations). The section L1 produces the same type of aberrations but with different amplitudes. In particular, the spherical aberrations of L1 may become predominant. The maximum transverse initial energy ϕ_{0m} , which defines the solid angle of collection, is fixed by the size of the "contrast diaphragm" placed in the beam. The width of the energy band accepted by the spectrometer and ϕ_{0m} control the magnitude of the aberrations.

For a given ϕ_{0m} , all the ions with initial energies ϕ_0 lower than ϕ_{0m} are collected, whereas the collected fraction of ions with an initial energy ϕ_0 higher than ϕ_{0m} is roughly ϕ_{0m}/ϕ_0 . The solid angle of collection is a function of ϕ_0 . Thus, any increase of ϕ_0 produces an increase of the collected fraction of the ions emitted with energies higher than the former value of ϕ_{0m} . As ϕ_{0m} is increased, trajectories with higher slopes (proportional to $\sqrt{\phi_{0m}/V}$, where V is the accelerating voltage) must go through the objective lens at greater distances from the optic axis.

Let us limit the investigation to trajectories in a meridian plane (the plane containing the optic axis). Each trajectory can be characterized by its intersection K with a plane π , perpendicular to the optic axis, and by its slope α with respect to this axis; K is defined by its distance r from the axis. In a drift section, α remains constant and r alone varies with the position of π along the optic axis. To unravel the beam structure throughout the optical system, it is convenient to resort to a "trace space" diagram in which each trajectory is represented by a point P defined by the coordinates (r, α) .^{3,4}

By computer simulations it is possible to draw, in the trace space, the S curve representing the beam of secondary ions emitted with a given initial energy ϕ_0 from a given point. Different energies, in the accepted energy band, have different S curves. As the position of the observation plane π is changed, the shapes of those curves are modified but it is very easy to find the particular position of π for which the beam (comprising all the accepted angles and energies) exhibits a "waist" where its section has its smallest size. A suitable position for a con-

trast diaphragm can also be determined.

As ϕ_{0m} is made to increase, the waist of the beam moves along the optic axis and its size is changed. The adjustments of the other lenses of the transfer system help to place the waist at a suitable position and optimize the slopes of the trajectories with respect to the shape of the beam accepted by the spectrometer. But since the transfer system itself is a source of aberrations, one has to take into account the overall effect of aberrations by considering the trace diagram of the beam for the entire system.

The situation is now quite different from the one that prevailed when the transfer optics was used as a "zoom" system. Besides the fact that the Gaussian approximation is no longer valid, the decomposition of the beam structure into an image of the surface and an illuminating pupil is no longer adequate. The goals are also quite different, since now one tries to fill the diaphragms defining the beam accepted by the spectrometer with the beam of ions originating from the very small impact area of an ion probe and being collected inside the largest possible solid angle. The objective lens acts like a funnel rather than as an image forming system. Ion images are obtained by rastering the ion probe over the sample and synchronously aligning the beam emerging from the objective lens along the entrance axis of the spectrometer (dynamic transfer).

Experimental Procedure and Results

Experiments are made with a CAMECA IMS4F instrument. An ion probe approximately $0.5\ \mu\text{m}$ in diameter is rastered over a field of view of $25 \times 25\ \mu\text{m}$. The detection of secondary ions is electronically gated so as to detect the ions only when the probe flies over a $1\ \mu\text{m}^2$ area in the center of the field of view. The entrance slit and the aperture stop of the spectrometer are adjusted to produce a given mass resolving power. The transfer lenses are progressively adjusted so as to increase the intensity of the secondary beam of a given mass filtered ionic species. The structure of the beam is followed with the help of trace diagrams computed for each set of excitation voltages applied to the objective and the transfer lenses.

A relative scale of collection efficiencies can be given as a function of the mass resolving power and the corresponding energy and angular limitations can be determined by calculation. The improvement of the collection efficiency can be checked by useful yield measurements. Scanning ion images at high mass resolving power with the resulting improved useful yield are available.

Conclusion

Proper adjustments of the collecting and transfer systems allow one to take advantage of the small size of the source of secondary ions to get high mass resolving powers together with high collection efficiencies. This procedure could be referred to as "probe match-

ing." In order to achieve the ultimate performances of the method, chromatic and aperture aberrations should be taken into account in the design of the transfer system.

References

1. G. Slodzian, Natl. Bur. Stand. (U.S.) Spec. Publ. 427, 1975, 33.
2. G. Slodzian and A. Figueras, *8th ICXOM*, Boston, 1977 (distributed by San Francisco Press), 1980, 65.
3. F. G. Rudenauer, *Intern. J. Mass Spectrom.* 6: 309-323, 1971.
4. C. Lejeune and J. Aubert, in A. Septier (Ed.), *Advances in Electronics and Electron Physics*, New York: Academic Press, Suppl. 13A: 159-259, 1980.

A PC-BASED BUS INTERFACE FOR THE CAMECA IMS-3f

S. F. Corcoran, W. S. Woodward, R. W. Linton, and D. P. Griffis

Over the past few years, advances in microcomputer technology have been substantial. The IBM PC (and its various clones) is one such computer that has found extensive use in the analytical laboratory. The attributes of the PC are enhanced by a large and varied list of hardware supplied by third-party vendors. Hardware advances have been paralleled by the development of high- and low-level languages which allow the programmer to access the capabilities of the PC. This paper reports on the development of a PC interface for the Cameca IMS-3f,¹ a commercial high-performance secondary ion mass spectrometer which was originally interfaced to a Hewlett-Packard 9845B desktop computer. The impetus for this project was provided by the incompatibility of the 9845B with current commonly available computer systems along with the increase in computation speed and graphics capability of the PC. Although our interface is 100% compatible with the IBM-PC architecture, a PC-AT clone based on the Intel 80286 running at 8 MHz was chosen for this work for even greater processing speed. All software for instrument control and data acquisition has been written in Microsoft Quickbasic 3.0.² Design considerations as well as present and future software implementations are described in appropriate detail.

Hardware

Primary design goals selected for the INTERFACE were:

1. Maximum facility of control for software development.
2. Implementation without modification of existing Cameca or IBM equipment.
3. Maximum electrical isolation (via optocoupler devices) of PC and IMS-3f circuitry to improve system immunity to high-voltage faults (e.g., intrasource arcs).

Achievement of design goal 1 required detailed analysis of the HP 9845 I/O architecture and its relationship with the IMS-3f interface logic circuitry. Our intent was to design the interface circuitry to bridge the disparity between the 9845B and PC I/O configurations. Accomplishing this goal required methods for encoding the 9845-style peripheral register addresses from the PC port I/O registers

and for accommodating the sixteen-bit organization of the 9845 data transfers in the predominantly eight-bit context of PC programming languages. The degree to which the interface design achieved this accommodation is illustrated by the fact that access to any IMS-3f interface register can be achieved by a single PC high-level language statement. Data transfers are accomplished by the same statements that specify the access address. This arrangement avoids cumbersome interface implementations in which access addresses must be separately provided prior to data transfer.

Achievement of design goal 2 has been equally successful. The original interface cable which formerly connected the IMS-3f to the 9845 now provides the IMS-3f/PC connection. Thus the goal of original hardware compatibility has been extended to the level of plug-to-plug interchangeability. This feature is of obvious value during the transitional period of PC software development. Periods of service work with the original 9845B system can easily alternate with intervals of PC software development.

Portions of the IMS-3f source and optics involve the use of high voltage in combination with high vacuum. Consequently the IMS-3f, in common with most such instrumentation, is prone to occasional momentary electrical arcs and the energetic electromagnetic transients such events inevitably produce. Although these events are (mostly) sufficiently contained to avoid physical damage to electronic components of the microprobe and the connected gear, it is not unusual for energy so released to disrupt (read "crash") the execution of control software in adjacent computer hardware. The resulting risk of loss of data, time, and productivity is unacceptable. Isolation of electromagnetic pulses from the delicate computing logic is difficult whenever any direct electrical path exists between microprobe and computer circuits. For this reason, Design goal 3 dictates the elimination of all such connection from the interface. Insulation of many megohms, capable of withstanding several kilovolts, is provided by optical coupling of all data and control pathways. However, this hardening of system circuitry is not brought about without cost. The isolating devices used--high-speed optocouplers--are, despite their name, slow in signal propagation time compared to most digital logic elements. They are also somewhat expensive in terms of both dollars and required circuit board area. Measures were therefore taken in interface design to minimize the impact of these inherent limitations. Optocoupler propagation delay, for example, is accommodated by interface

S. F. Corcoran and D. P. Griffis are at the Analytical Instrumentation Facility, Box 7916, North Carolina State University, Raleigh, NC 27695; S. F. Corcoran is also at the Department of Chemistry, University of North Carolina, Chapel Hill, NC 26599-3290, as are W. S. Woodward and R. W. Linton.

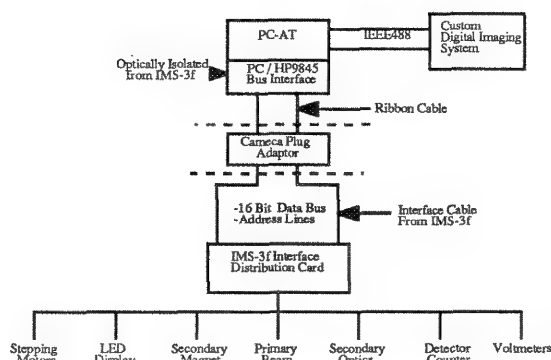


FIG. 1.-Block diagram of current hardware set-up; IEEE 488 also allows communication with HP graphics plotter as well as other off-line PCs.

timing circuitry that automatically forces the PC to generate sufficient "wait-states" to insure successful transfer of control and data signals as required by the specific I/O transaction. This automatic delay of approximately 2 μ s is practically invisible to control software. It also accommodates response delays exhibited by some of the IMS-3f interface circuits and effectively matches them to the high speed of the AT I/O bus.

The interface consists of two circuit boards. The first card is an IBM PC prototype card which resides inside and is powered by the PC. The second card resides outside the PC and is connected to the first card by a ribbon cable. The second card provides the backplane to which the IMS-3f is connected via the adaptor originally designed for the 9845B. This card is totally electrically isolated from the first card and has its own power supply. The interaction of the PC with the IMS-3f through the interface is illustrated in Fig. 1. The IMS-3f interface distribution card is used to address each of the different instrument peripherals. Four peripheral select bits allow the programmer to access each of the different peripherals. Multiplexing of address lines by the distribution card determines which I/O function is taking (e.g., Read/Write, Reset).

Software

As previously mentioned, the language that we selected was Microsoft Quickbasic. Some of the attributes of this language include its interactive program development, high-level coding, speed, the ability to use DOS 3.2 interrupts within the BASIC programming environment, and graphics commands. During the initial stages of software development all the standard I/O instructions executed by the 9845 were duplicated within the AT environment by a series of BASIC functions. Each function, when called, executes the prescribed instruction by using standard BASIC I/O statements (INP,OUT). This allows each I/O instruction to take place via a single BASIC function call. All address information required by a particular peripheral interface is contained within the function. Data is passed to or returned by the function at the time of the function call.

As mentioned previously, the ability to use DOS interrupts allows the programmer to go beyond the confines of the BASIC language. One area where Quickbasic (and other BASIC language reviewed) are deficient is in file I/O. Array storage is slow since only one array position at a time can be stored by a single statement. That can be a problem when one is storing large files such as images generated by the IMS-3f. It is desirable to store out these data quickly along with all the associated instrumental parameters. This is done in the following manner. Our standard file format consists of three arrays; the instrument parameter, mass specific information, and data vectors. Using Quickbasic we are able to determine the length and memory location of each of these arrays. Each array is written out consecutively, at rates limited by the speed of the storage device, into an open file using DOS interrupt 40H. Storing data files as series of bytes is extremely fast when compared to data-storage methods available in Quickbasic.

Each program for the IMS-3f shares a number of common variables such as calibration points that convert hall probe values to mass units (amu) and vice versa. A way of sharing these variables among programs had to be developed. One method would be to declare common variables during the start-up program; passing of these variables in Quickbasic requires that one must "CHAIN" from one program to the next. If there is an abnormal program termination, all the variables are lost. Another option is to create a file that contains all these variables and is accessed by each program at execution. The start-up program amends this file for different primary ion species as well as different primary and secondary ion polarities. We have implemented this method and have found it to work quite adequately.

As of this writing, software has been written for all the conventional modes of SIMS analysis--depth profiling, mass spectra, replotting, etc. New software implementations include cursor-assisted peak tuning for depth profiling and a replotting program for processing multilayer depth profiles.³ A listing of the current programs and their interactions are found in Fig. 2. Efforts are under way to adapt current image acquisition software written for the 9845⁴ to the AT. The authors welcome inquiries with respect to both hardware and software.

References

1. J. M. Rouberol, M. Lapateur, B. Autier, and J. M. Gourgout, in D. R. Beaman, R. E. Ogilvie, and D. B. Wittry, Eds., *Proc. 8th ICXOM*, 1976 (distributed by San Francisco Press).
2. Microsoft Corporation, Box 97017, Redmond, WA 98073-9717.
3. S. F. Corcoran, D. P. Griffis, and R. W. Linton, *Proc. Sixth Int. Conf. on Secondary Ion Mass Spectrometry*, New York: Wiley

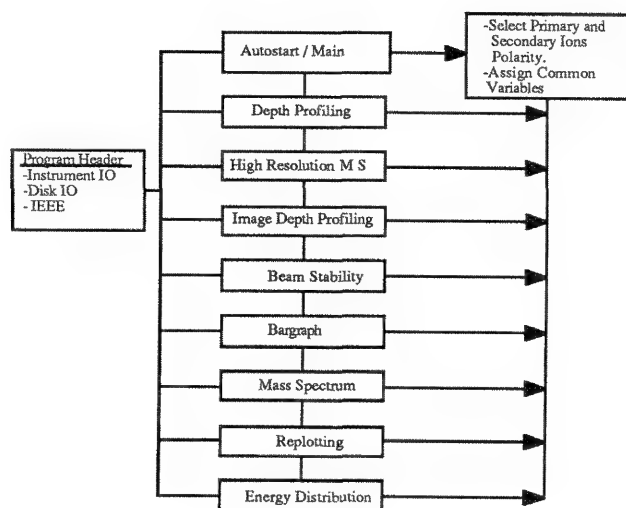


FIG. 2.--Current software arrangement. Auto-start program creates file containing common variables used by all programs (e.g., magnet calibration points, ions polarities, primary species, etc.). Program header contains all IMS-3f I/O functions and address information for IEEE.

(in press).

4. S. R. Bryan, R. W. Linton, and D. P. Griffis, "An automated method for high dynamic range secondary ion image depth profiling," *J. Vac. Sci. Technol.* A4: 2317, 1986.

RECENT DEVELOPMENTS IN QUANTITATIVE ANALYSIS WITH THE USE OF SPUTTERING TECHNIQUES

Peter Williams

Sputtering is a powerful sampling technique for solids. It allows very small numbers of atoms (on average ~ 1 -10 atoms per incident ion) to be ejected from depths as shallow as the outermost surface layer. The sampling region can be localized laterally to a spot some tens of nanometers in diameter by focusing of the primary ion beam, so that the total sampled volume can comprise as little as a few hundred atoms. If the ejected atoms are ionized in the sputtering collision or can be ionized in the gas phase, mass spectrometric detection is virtually background-free, so that the ejected atoms can be identified and detected with great efficiency: typically, as few as 1000-10 000 atoms need be sampled to produce a detected signal of 100 ion counts, measurable with a statistical precision of $\pm 10\%$. Although secondary ion mass spectrometry (SIMS), in which the atoms ionized as a result of the collisional ejection, has long suffered from difficulties of quantifying the data obtained, due to the strong influence of the nature of the sample surface on the ionization efficiency, recent developments in the production and use of ion-implanted offer a virtually universal solution to this problem. In addition, there has been a resurgence of interest in the approach of ionizing the sputtered *neutral* flux in the gas phase, which avoids the malign influence of the sample surface and promises simple and accurate quantitative sputtering analyses. This paper briefly surveys progress toward quantitative-surface and thin-film analysis by these two approaches.

Ion-implanted Standards

The use of ion-implanted standards for SIMS quantification is not new; Dearnaley, one of the pioneers in ion implantation, and his colleagues realized the strength of the technique very early.¹ The sensitivity of secondary-ion yields to the sample surface chemistry is so strong that ideally one needs a standard with major-element chemistry identical to that of the unknown. Ion implantation allows this requirement to be fulfilled because it allows at least dilute levels of impurities (which do not affect ion yields) to be quantitatively introduced into a chosen standard material, or even into the sample itself. The superimposed implant profile could be readily distinguished from the constant intrinsic level, and a calibration scale established by the implant allowed the intrinsic impurity level to be read directly.² This superimposition or standard addition³ technique is extremely powerful, since by sampling both standard and unknown in

an analysis under identical conditions all possible variables including instrument conditions and operator foibles are calibrated together.

One difficulty with the standard-addition technique was that ion-implanted standards were constrained to be dilute (>1 atom %), so that the presence of the implant itself did not alter ionization efficiencies. That meant that only dilute levels could be quantified. This difficulty may be partly removed by implantation of minor isotopes such as ^2D , ^{17}O , ^{18}O , etc., which are dilute impurities even when the levels of H, O, etc., are high. About one-third of the elements in the periodic table have minor isotopes at the 1% level or below and so may be quantified by implant standard addition of the appropriate isotope. Isotopic variations in ionization efficiency are small for most elements (a few percent); where they are significant, as in the case of hydrogen isotopes, they may either be calibrated, or eliminated by an appropriate choice of instrumental conditions, and precise analyses obtained.⁴

A more serious problem with ion implantation as a standards preparation tool has been the expense and limited accessibility of ion implanters. It led workers in several laboratories recently to investigate the possibility of using the primary ion column of a SIMS instrument as a low-energy ion implanter.⁵⁻⁷ In this way, ion implant standards could be generated in situ, at the discretion of the analyst. Because only small areas are typically implanted ($\sim 500 \times 500 \mu\text{m}$), only small ion currents (a few nanoamps) are necessary, and adequate ion beams even of minor isotopes such as ^{18}O may be generated without using isotopically enriched ion source feed gas.⁵ Diffusion processes could be studied in situ by implantation into cooled⁷ or heated samples. The most recent development in in situ implantation was the construction of a universal ion source for solids by Streit and Williams.⁸ With this inverted hollow-cathode ion source, ion currents of several nanoamps could be delivered to the sample for almost any solid element.

As a result of these developments in in situ ion implantation, implanted standards of almost any element or isotope are now available to most SIMS analysts, in any specimen of interest, at a moderate capital investment in ion source technology. Analytical accuracy better than $\pm 10\%$ has been routinely demonstrated.^{5,6} These developments allow quantitative analysis of virtually any impurity element in any sample that can be loaded into the ion microanalyzer ion source. In particular, this approach allows the use of ion

The author is at the Department of Chemistry, Arizona State University, Tempe, AZ 85287.

implantation in the analysis of liquid or biological samples that must be kept frozen, and therefore could not readily be transferred to and from a conventional ion implanter. A significant advantage of deriving from the low energy (and thus shallow penetration) of these in situ implants is that the entire implant may be contained within a single layer of a thin-film multilayer; buried layers can be subsequently implanted and analyzed as they are exposed in the course of a depth profile.⁴ This procedure would not be possible with external implantation, the high energy of which smears the implant profile over several thousand Angstroms.

Sputtered Neutral Analysis

The earliest analytical investigation of secondary ion mass spectrometry also included studies of the sputtered neutral material, ionized in the gas phase by electron impact.¹⁰ Because the sputtered neutral signals were considerably lower than the secondary-ion signals, this approach was abandoned for many years. However, as the utility of sputtering analyses and the difficulties of quantifying SIMS analyses became increasingly apparent in the 1970s, interest in the sputtered neutral signal was rekindled.¹¹

The basic thesis underlying sputtered neutral mass spectrometry (SNMS) is that the sputtered flux composition is exactly that of the solid being sputtered. This statement is true for a solid of constant composition even though sputtering can alter the near-surface composition of the solid as a result of preferential sputtering or segregation effects; this altered zone can be considered to move into the solid as sputtering proceeds, with a flux of material from the bulk entering the zone at its base and leaving at the surface. Clearly, these two fluxes must be identical. The advantage of gas phase ionization is that the ionization process is not coupled in any way to the surface chemistry of the sample; the matrix effects of SIMS are thus not present in the ionization process (although they may still affect the analysis, as discussed later), and elemental sensitivities are simple elemental and instrumental constants. In principle, relative sensitivities can be determined and stored in the system computer; at worst, a single compound standard is required to establish relative sensitivities, and there are few restrictions on the nature of the standard. It need not be dilute, or closely similar to the analytical sample; all that is necessary is that the sample is well characterized, and that the levels of the relevant elements are sufficiently high to be accurately measured with the SNMS system in use. Under such conditions it has been shown that SNMS analyses are comparable in precision and accuracy to electron microprobe or Rutherford backscattering analyses, with the added advantage of broader elemental coverage and better depth resolution than either.^{9,11,12}

There are some analytical difficulties in SNMS, which will now be discussed. First, there is the obvious fact that sputtered neutral signals depend on the sputtering yield; i.e., a component with the same concentration in two phases will be detected as a higher signal from the phase with the higher global sputtering yield. This feature becomes important in depth profiles through interfaces, where a simple plot of signal intensity vs time does not directly give the variation in composition with depth. In principle, one must either know the sputtering yield at each point, or sample *all* the sputtered species in order to express the analyte signal in question as a fraction of the entire sputtered flux. If that is done, it becomes an advantage in that depth profiles through layers of differing sputter yields can be converted simply into plots of composition vs depth (more exactly, vs the total number of atoms removed). It is very difficult for one to arrive at such a plot using other sputtering approaches without tediously measuring the thickness of each layer separately. Techniques that monitor only one sputtered entity, such as those based on resonant multiphoton ionization, may be severely affected by their blindness to sputtering yield changes.

The second analytical problem of SNMS is that surface atoms are sputtered in several states--as neutral atoms, as ions (positive or negative), or in clusters, which may be charged or neutral. However, typically only one of these species, usually the neutral atoms, is sampled. If the ions or clusters compose a significant fraction of the sputtered flux, the atom signal does not accurately represent the bulk composition for that species. Of course, the probability of ions or cluster formation is a function of the surface chemistry of the sample, and that introduces a possible matrix effect in the SNMS analysis. For the ion component, this matrix effect is simply the inverse of the SIMS matrix effect. Some attention is now being directed to the absolute magnitude of sputtered ion yields; it is clear that for many metal oxides the metal ion fraction may be several tens of percent. Similarly, alkali metal ion yields may approach 100% in many systems. All that must be borne in mind when one assesses the accuracy of SNMS analyses. There are essentially no quantitative data on the absolute abundance of sputtered clusters.

Finally, SNMS analyses depart from the ideal close to interfaces, because there an important assumption (that flux into the base of the ion beam-mixed zone is identical to that leaving at the surface) is not justified. To interpret signal variations in such a zone correctly would require detailed knowledge of the relative mobilities of various components of a sample under ion bombardment; such knowledge is not currently available. The only solution to this problem at present is to reduce the primary ion energy in order to minimize the extent of the mixed zone.

Conclusion

Secondary ion mass spectrometry is approaching maturity as an analytical technique, both instrumentally and in our ability to obtain reliable quantitative analyses in a wide range of sample types. Where SIMS analyses start to become difficult to quantify, i.e., for concentrations above about 1 atom %, sputtered neutral mass spectrometry offers an attractive (and usually analytically simpler) supplement. There is a clear need to improve the sensitivity of SNMS to improve the overlap between the two techniques, and it would be attractive to have both available in the same analytical system,⁹ each with optimized sensitivity. The coming years should see developments in this direction.

References

1. R. P. Gittins, D. V. Morgan, and G. Dearnaley, *J. Phys.* 5: 1654, 1972.
2. P. Williams, *Trans. IEEE* N26: 1809, 1979.
3. D. Leta and G. H. Morrison, *Anal. Chem.* 52: 277, 1980.
4. P. Williams, K. M. Stika, J. A. Davies, and T. E. Jackman, *Nucl. Instrum. Methods* 191: 299, 1983.
5. R. T. Lareau and P. Williams, in *Mat. Res. Soc. Symp. Proc.*, Pittsburgh: Materials Research Society, 1985, 273.
6. H. E. Smith and G. H. Morrison, *Anal. Chem.* 57: 2663, 1985.
7. C. M. Loxton and B. Ladna, *Nucl. Instrum. Methods* B15: 210, 1986.
8. L. A. Streit and P. Williams, *SIMS VI* (Paris), New York: Wiley, (in press).
9. L. A. Streit and P. Williams, *J. Vac. Sci. Technol.* A5: 1979, 1987.
10. R. E. Honig, in *Advances in Mass Spectrometry*, New York: Pergamon, 1962, 25.
11. K. H. Muller and H. Gechsner, *Mikrochim. Acta* (Wien) Suppl. 10: 51, 1983.
12. P. Williams and L. A. Streit, *Nucl. Instrum. Methods* B15: 159, 1986.

ION IMPLANTATION ARTIFACTS DETECTED BY SECONDARY ION MASS SPECTROMETRY

D. S. Simons and Peter Chi

Secondary ion mass spectrometry (SIMS) is commonly used to measure the depth distributions of dopants in semiconductors, where the dopant is introduced by high-energy ion implantation. SIMS is often used in the study of the redistribution of the dopant brought about by subsequent thermal processing. In other cases, the extent of ion channeling in a crystalline substrate is of interest, when the incident ion has been intentionally aligned along a high-symmetry axis. For these types of studies it is usually assumed that the ion implanter is delivering a pure beam of the specified ion at a well-defined energy and current. The examples presented in this paper show that this assumption is not always valid, and that SIMS can be a very useful diagnostic tool for detecting unexpected artifacts of ion implantation.

Experimental

The samples described here are single-crystal silicon wafers implanted in three different laboratories with ion implanters from different manufacturers. All SIMS profiles were made on a Cameca IMS-3F Ion Microanalyzer.¹ Typically, a primary beam of 8 keV (impact energy) O_2^+ at a current of 1 μA was rastered over a $250 \times 250 \mu m$ square area, with positive secondary ions collected from the central $60 \mu m$ -diameter area of the raster.

Results

A series of arsenic implants in silicon, with implantation energies ranging from 25 to 200 keV, was profiled by SIMS. The depths of the peaks in the arsenic implant profiles were plotted against the stated implantation energies (Fig. 1). A plateau in the data can be seen between 50 and 100 keV. The dashed line in the figure shows the predicted peak depth based on a TRIM Monte-Carlo simulation of the implantation process.² Similar results were observed for a series of boron implantations. The discrepancy between theory and experiment motivated a direct measurement of the accelerating voltage by use of a high-voltage resistive divider chain. It was discovered that the energy meter on the implanter was not giving a reading proportional to the accelerating voltage, and

The authors are with the Center for Analytical Chemistry, National Bureau of Standards, Gaithersburg, MD 20899. The contributions of J. R. Ehrstein of NBS, H. B. Dietrich of the Naval Research Laboratory, and J. F. Knudsen of the Aerospace Corp. in providing the ion-implanted samples are greatly appreciated. This paper is not subject to copyright.

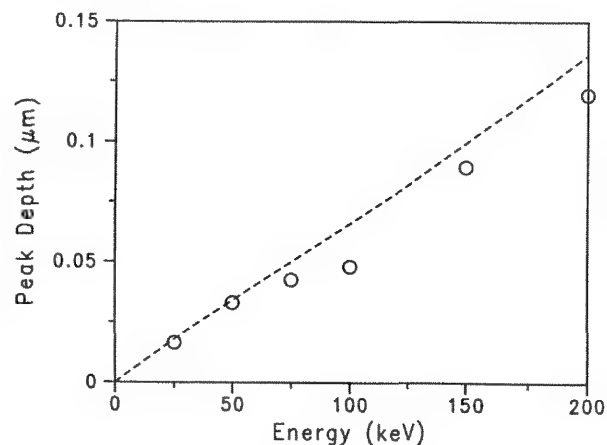


FIG. 1.--Depths of peaks of arsenic implants in silicon vs nominal implant energy as determined by SIMS (circles). Dashed line is prediction of Monte-Carlo simulation.

that the energy was overstated for values in excess of 50 keV, just as the SIMS measurements had suggested.

The remaining examples are related to a project designed to produce a standard reference material for depth profiling measurements by SIMS. The material selected for evaluation is amorphous silicon that has been ion-implanted with ^{10}B at an energy of 50 keV and a dose of 1×10^{15} at./cm².³ The ^{10}B isotope was chosen even though it is less abundant than ^{11}B because independent profiles of the former can be measured by thermal neutron depth profiling (NDP).⁴ Amorphization of the silicon was carried out by implantation of ^{28}Si at several energies up to 400 keV and at doses in excess of 10^{15} at./cm².

Figure 2 shows profiles of ^{10}B and ^{11}B from a test sample. In this case the dose of ^{10}B was only 80% of the desired value; the remaining 20% was ^{11}B . The ratio of doses of the two isotopes was determined from the SIMS data in Fig. 2; the absolute value of the ^{10}B dose was measured by NDP. Profiles of samples made in other implanters showed ^{11}B contributions to the boron dose smaller than 1%. For the case shown in Fig. 2, the ion source of the implanter produced a relatively weak boron beam, so a large mass-resolving aperture had been used to reduce the implantation time. However, this approach also allowed an unacceptable amount of ^{11}B to be implanted along with the ^{10}B . In this example SIMS has been used to determine the effective abundance sensitivity of the mass filter in the ion implanter.

In the same experiment it was noted that the background level of ^{10}B in the SIMS profile

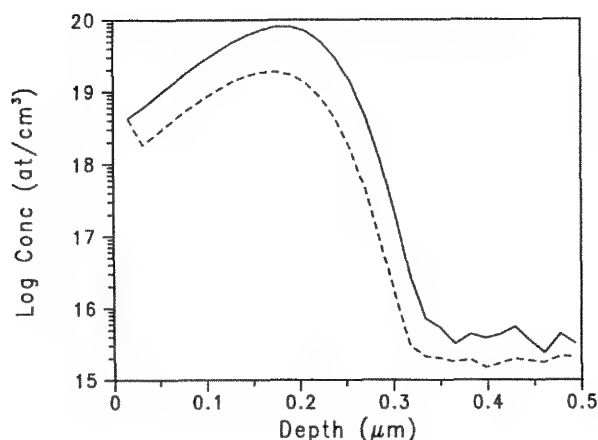


FIG. 2.--SIMS depth profiles of ^{10}B (solid line) and ^{11}B (dashed line) in amorphized silicon.

was higher than expected. A molecular ion interference at m/z 10 could produce this result. Steps are normally taken to exclude the known interference of $^{30}\text{Si}^{3+}$ when ^{10}B is profiled in silicon. Another possible interfering species is $^9\text{BeH}^+$, but for this species to be significant a substantial amount of beryllium must be present in the sample. To check this possibility, a SIMS profile of ^9Be was taken along with ^{10}B (Fig. 3). A surprisingly large beryllium signal with an unusual depth dependence was seen. The three-peak structure of the beryllium profile gave a clue to its origin. Since the amorphization of the silicon wafer had been done by implanting ^{28}Si at three different energies, it was very likely that the beryllium had been unexpectedly introduced during the Si implantation. It was learned that the cold-cathode ion source of the implanter contains beryllium components that are sputtered by the discharge, and that silicon had been introduced into the source as SiF_4 gas. Thus, beryllium was being implanted as the molecular ion $^9\text{Be}^{19}\text{F}^+$ along with the ^{28}Si . Since the level of BeH^+ detected in the SIMS spectrum is typically 0.1-1% of the Be^+ signal, the beryllium present in this sample could easily explain the high background level at m/z 10.

A different material was prepared for the same project with another ion implanter. In this case amorphization was done with implants of ^{28}Si at two different energies followed by the implant of ^{10}B . The SIMS profiles of ^{10}B and ^{11}B in this sample are shown in Fig. 4. The ^{10}B profile has a low concentration peak at a greater depth than the main peak, accompanied by a larger peak of ^{11}B . It appears that the silicon implantation step is again the cause of this unexpected result. A large mass-resolving aperture was used for the ^{28}Si implantation. Some boron must have been present in the ion source, coming from either a leak in the BF_3 gas line (that should be closed during silicon implantation), boron-containing source parts, or residual boron from a previous implantation. The boron could be ionized as

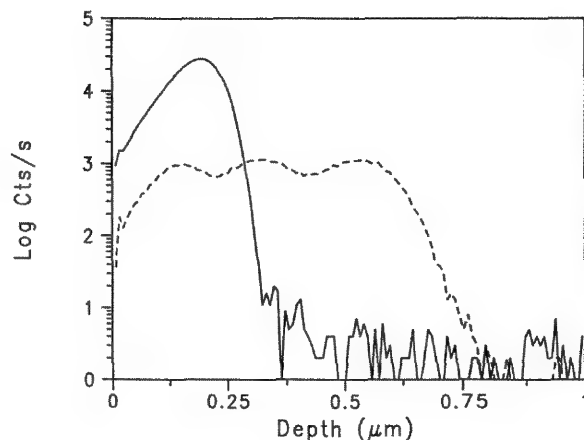


FIG. 3.--SIMS depth profiles of ^9Be (dashed line) and ^{10}B (solid line) in same sample as Fig. 2.

$^{10}\text{B}^{19}\text{F}^+$ and $^{11}\text{B}^{19}\text{F}^+$; the fluorine source was again the SiF_4 feed gas. These boron-containing species apparently accompanied the 360 keV ^{28}Si beam and passed through the large mass-resolving aperture, even though they were separated by one or two mass units from the desired species at m/z 28. Further confirmation of this hypothesis is given by the detection of an implanted fluorine peak in a SIMS profile of this sample, and by the measured depth of the deeper pair of peaks which is consistent with the depth determined from a TRIM calculation for implantation of the BF^+ molecular ion.

The final example shows a feature of implantation that remains a puzzle. Two silicon wafers were amorphized by silicon implantation under identical conditions in the same implanter. A ^{10}B implant was made in one of the wafers in the same implanter. For the other wafer, the ^{10}B implant was done in a different implanter at another laboratory. The SIMS profiles of ^{10}B in the two samples are compared in Fig. 5. An anomalous shoulder is seen in one profile, but not in the other. This shoulder is a reproducible feature of the SIMS profile. Since the amorphization treatment was identical for the two samples, the difference must be due to the boron implantation step. The sample with the shoulder in its profile had been implanted at a boron current density higher by a factor of 10 than the one without the artifact. At first it was speculated that the higher current density had led to a small amount of recrystallization of the silicon, allowing some ion channeling to occur. However, when another sample was processed in the same implanter with a boron current density lower by a factor of 10 than the first case, the shoulder in the profile remained. No satisfactory explanation has been found for this result, which must be related to the characteristics of a specific ion implanter.

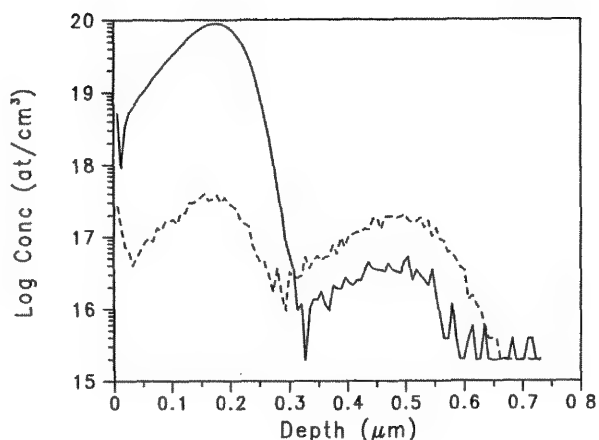


FIG. 4.--SIMS depth profiles of ^{10}B (solid line) and ^{11}B (dashed line) in another sample of amorphized silicon.

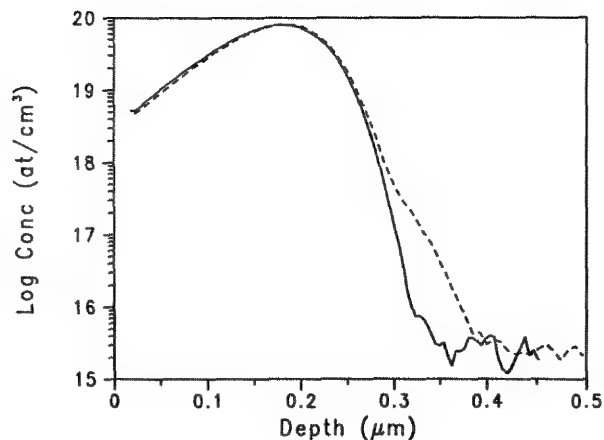


FIG. 5.--SIMS depth profiles of ^{10}B in two silicon samples amorphized by silicon implantation in same implanter, but implanted with boron in different machines.

Conclusion

The examples presented above demonstrate that one should not always accept the nominal specifications of an ion implant at face value. Unexpected species can be introduced during the implantation that may have a deleterious effect on the final product. Secondary ion mass spectrometry is the only analytical method that has the broad elemental coverage, along with sufficient sensitivity and depth resolution, to detect the contaminants introduced during ion implantation. As such, SIMS can be used advantageously to characterize the artifacts of a specific implanter so that potential problems can be avoided when the implanter is operated in a production mode.

References

1. Certain commercial equipment, instruments, or materials are identified in this paper in order to specify adequately the experimental procedure. Such identification does not imply recommendation or endorsement by the National Bureau of Standards, nor does it imply that the materials or equipment identified are necessarily the best available for the purpose.
2. John Albers, *Results of the Monte Carlo Calculation of One- and Two-dimensional Distributions of Particles and Damage: Ion Implanted Dopants in Silicon*, NBS Special Publication 400-79, Washington: USGPO, 1987.
3. D. S. Simons, P. Chi, R. G. Downing, J. R. Ehrstein, and J. F. Knudsen, "Progress toward a semiconductor depth-profiling standard," in *Secondary Ion Mass Spectrometry SIMS-VI*, London: Wiley, 1988.
4. R. G. Downing, R. F. Fleming, J. K. Langland, and D. H. Vincent, "Neutron depth profiling at the National Bureau of Standards,"

Nucl. Instrum. Methods 218: 47, 1983.

CHARACTERIZATION OF SILICON OXIDE FILMS BY A NEW SIMS TECHNIQUE

Kazuyuki Inoue and Akio Isogai

Recently, a new method to evaluate insulating properties was proposed by the authors.¹ In secondary ion mass spectroscopy (SIMS) analysis of insulating films, surface charging is not completely but slightly reduced by use of positive primary ions and a negative potential on the sample. Under this condition, a minimum intensity I_b is observed in a time dependence on the secondary ion intensity. The cause of I_b can be explained if the discharge current between the surface and rear of the specimen is taken into account; then one obtains the relationship

$$I_b/I_a = -kJ\rho d_0 + 1 \quad (1)$$

where I_a is the secondary-ion intensity in the absence of charging, k is the constant determined by the conditions of measurement, J is the discharge current, and ρ and d_0 are the resistivity and thickness of the sample. From Eq. (1), one can evaluate the insulating property ρd_0 by measuring the secondary ion intensities. The present paper describes an application of this SIMS technique to characterization of silicon oxide films, which are the most commonly employed insulator in the solid-state industry.

Experimental

SIMS analysis was performed with the ion microprobe mass analyzer (Applied Research Laboratories). The samples used in this study were silicon oxide films deposited on silicon wafers (1 Ω cm) by the rf magnetron sputtering technique. Samples of various film thicknesses, which were determined to be 140, 160, 340, and 500 nm by scanning electron microscopy, were grown in argon ambient containing 5% oxygen (sample A). Two other samples were deposited in different argon ambient containing 2% or 10% oxygen in order to vary the film properties; their film thicknesses were determined to be 180 and 300 nm, respectively (samples B and C). A thermal oxide sample prepared by heating a silicon wafer in pyrogenic steam at 1000 C for 50 min was also used; its thickness was 320 nm.

Results

The relationship between the ion intensity ratio I_b/I_a and the film thickness d_0 is shown in Fig. 1. According to Eq. (1), I_b/I_a is equal to 1 when $d_0 = 0$ and the absolute

The authors are with Toyota Central Research and Development Laboratories, Inc., 41-1 Yokomichi Nagakute, Nagakute-cho, Aichi-gun, Aichi-ken, 480-11, Japan.

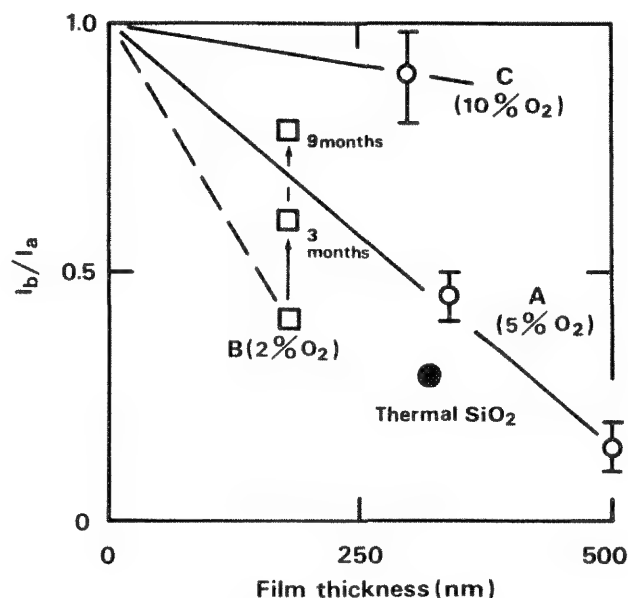


FIG. 1.--Intensity ratio I_b/I_a as a function of film thickness d_0 .

value of the gradient between I_b/I_a and d_0 , which is represented as $[1 - (I_b/I_a)]/d_0$, is proportional to resistivity. Therefore, it is found that type A samples are almost equivalent to the thermal oxide film in resistivity.

Figure 1 also illustrates that sample B has degraded in 6 months even though it exhibited the greatest resistivity in the samples. This ageing effect can be attributed to oxygen vacancies or absorbed water.^{2,5}

Conclusions

Insulating properties of silicon oxide films have been investigated by a new SIMS technique. It is shown that the insulating property of the reactively sputtered film grown in argon ambient containing 5% oxygen is equivalent to that of the thermal oxide film. Degradation of the insulating properties is observed for the sputtered film deposited in argon ambient containing 2% oxygen, although this film excelled other silicon-oxide films before 6 months.

References

1. K. Inoue and A. Isogai, "Evaluation of insulating property by secondary ion mass spectrometry," *J. Appl. Phys.* 62: 3343, 1987.
2. A. L. Shabalov and M. S. Feldman, "Optical and dielectric properties of thin SiO_x films of variable composition," *Thin Solid Films* 110: 215, 1983.
3. J. Santamaria et al., "Electrical properties of R.F.-sputtered SiO₂ films," *Thin Solid Films* 125: 299, 1985.

ARTIFACTS OBSERVED IN OXYGEN PROFILES OF SIMOX SAMPLES BY SECONDARY ION MASS SPECTROMETRY

Peter Chi, D. S. Simons, and Peter Roitman

Separation by implantation with oxygen (SIMOX) is a process in which a high dose of oxygen implanted into a silicon substrate creates a stoichiometric SiO_2 layer below the silicon surface.¹ High-quality single-crystal silicon can be regrown above the buried oxide by a high-temperature anneal. When we performed a depth profile measurement of SIMOX material by secondary ion mass spectrometry (SIMS), we noticed that the oxygen secondary ion signal was not constant in the buried oxide layer but tended to increase from the front to back interface, even though Rutherford backscattering spectrometry (RBS), Auger electron spectroscopy (AES), and transmission electron microscopy (TEM) measurements on similar materials have indicated that the buried oxide is homogeneous and stoichiometric SiO_2 .² We therefore decided to investigate the SIMS profiles more carefully to determine whether the changing oxygen signal was instead an artifact of the SIMS measurement process.

Experiment

The specimen in this experiment was a silicon wafer implanted with oxygen at 150 keV to a dose of 2×10^{18} at/cm², while the wafer was held at a temperature of 550 C. SIMS analyses were carried out in a Cameca IMS-3F ion microscope.³ An argon primary beam of 8keV net impact energy and 100nA current was focused and rastered over a 250×250 μm square area. The sample was coated with about 20 nm of Au/Pd. An electron gun was used throughout the depth profiling measurement in an attempt to neutralize the positive charge build-up on the specimen during primary ion bombardment. Positive secondary ions were collected from a circular area of 60 μm in diameter centered on the rastered area.

Results

SIMS depth profiles of oxygen ($^{16}\text{O}^+$) and silicon ($^{30}\text{Si}^+$) in the SIMOX specimens are shown in Fig. 1. The electron gun was aligned

P. Chi and D. S. Simons are at the Center for Analytical Chemistry, and P. Roitman is at the Center for Electronics and Electrical Engineering, National Bureau of Standards, Gaithersburg, MD 20899. This work was sponsored in part by the Defense Nuclear Agency under contract DNA IACRO 88-816. We acknowledge the contributions of F. A. Stevie, A. J. Filo, R. B. Irwin, and J. A. Taylor of AT&T Bell Laboratories, Allentown, Pennsylvania, for performing the RBS and AES measurements on this sample. We thank G. Gillen of NBS for his useful comments about ESD.

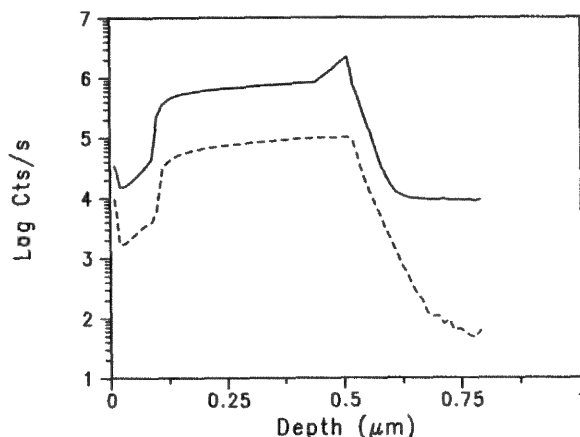


FIG. 1.--SIMS profiles of $^{16}\text{O}^+$ (dashed line) and $^{30}\text{Si}^+$ (solid line) in SIMOX sample, plotted on logarithmic intensity scale. Analysis area displaced horizontally from tuning area.

on a tuning area of the sample to flood the analyzed area with electrons. The filament current was adjusted to compensate for charging when the profile was near the center of the buried oxide layer. The criterion for adjustment was lack of translation of the "slit image" when the spectrometer lens voltage was varied. The profiles shown in Fig. 1 were taken on an area of the sample translated 1 mm horizontally from the tuning region. Figure 2 shows the oxygen profile from Fig. 1 replotted on a linear scale to emphasize the large signal change through the buried layer. We believe that this effect is due to specimen charging caused by differences in electron beam alignment between the tuning and analysis positions on the sample.

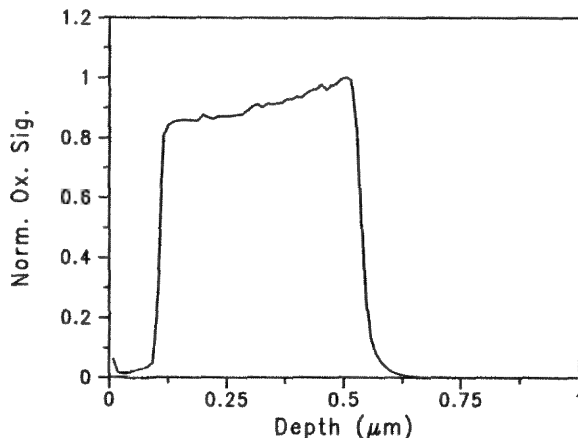


FIG. 2.--Profile of $^{16}\text{O}^+$ from Fig. 1 plotted on linear intensity scale.

To verify this hypothesis, a copper-grid-on-aluminum sample was placed in the instrument and a fluorine image of the grid pattern was obtained by electron stimulated desorption (ESD) with a 400 μ m field of view. These conditions allowed us to view the alignment of the electron beam with respect to the secondary ion acceptance area. When the grid sample was translated in both the horizontal and vertical directions, we found that misalignment of the electron beam was much more severe for horizontal translation of the sample--not a surprise, since the electron gun axis and secondary ion axis lie in the horizontal plane.

With this knowledge, a new oxygen profile of the SIMOX sample was obtained from an area translated 300 μ m vertically from the tuning region. This profile, shown on a linear scale in Fig. 3, has much less variation through the buried layer than the profile in Fig. 2; the signal change is only about 15%. This experiment indicates that the tuning of the electron beam has a major effect on the shape of the oxygen profile. The sensitivity of SIMS profiles of oxygen to charging effects in SiO₂ has also been noted by others. Kilner et al. observed an order of magnitude change in oxygen signal when profiling a thick thermal oxide on silicon.⁴ They noted that the oxygen/silicon ratio was much less sensitive to this effect.

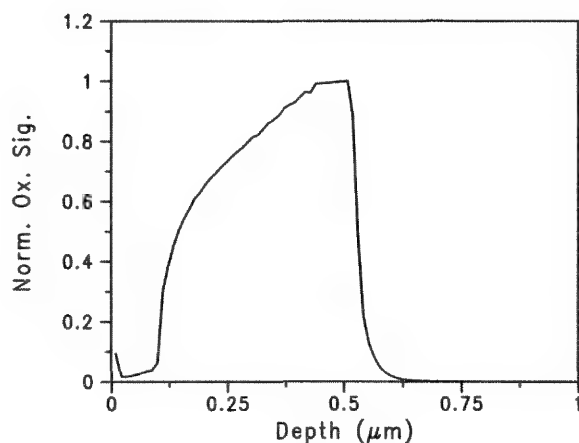


FIG. 3.--Profile of $^{16}\text{O}^+$ in SIMOX sample. Analysis area displaced vertically from tuning region.

Independent profiling measurements have been made on this sample by other methods to check the homogeneity of the oxygen concentration in the buried layer. Rutherford backscattering spectrometry and Auger electron spectroscopy both indicate that the relative variation of the oxygen concentration through the buried oxide layer is less than 5%. Thus, even the 15% variation seen in Fig. 3 must be showing the effect of specimen charging.

Conclusion

The change in oxygen secondary ion signal during depth profiling of a buried oxide layer has been observed by secondary ion mass spectrometry. The variation is due to charging of the sample during the experiment even when an electron gun is used for charge neutralization. The magnitude of the artifacts can be minimized if the analysis area is as close as possible to, and vertically displaced from, the tuning region.

References

1. R. F. Pinizzoto, "Silicon on insulator by ion implantation: A dream or a reality?" *Nucl. Instr. and Meth.* B7/8: 261, 1985.
2. P. L. F. Hemment, E. Maydell-Ondrusz, K. G. Stevens, J. A. Kilner, and J. Butcher, "Oxygen distributions in synthesized SiO₂ layer formed by high dose O⁺ implantation into silicon," *Vacuum* 34: 203, 1984.
3. Certain commercial equipment, instruments, or materials are identified in this paper in order to specify adequately the experimental procedure. Such identification does not imply recommendation or endorsement by the National Bureau of Standards, nor does it imply that the materials or equipment identified are necessarily the best available for the purpose.
4. J. A. Kilner, S. D. Littlewood, P. L. F. Hemment, E. Maydell-Ondrusz, and K. G. Stephens, "SIMS analysis of silicon on insulator structure formed by high-dose O⁺ implantation into silicon," *Nucl. Instr. and Meth.* 218: 573, 1983.

THE USE OF SECONDARY ION MASS SPECTROMETRY (SIMS) IN THE STUDY OF TOXIC TRACE ELEMENTS ON FBC FLY ASH PARTICLES

A. J. Gay, D. K. Henderson, P. J. van Duin, and Paul Humphrey

SIMS has been chosen for this study because of its ability to detect virtually all elements to very low levels (often better than ppm). It is especially useful in allowing relatively small elemental concentration changes to be determined as a function of sample depth. SIMS has been used previously to analyze the chemical composition and surface enrichment of fly ash and other environmental particles.^{1,2} The present paper is concerned with the distribution of a number of toxic elements in fly ash from a fluidized bed combustor (FBC).

The mechanism of fly ash formation during combustion of coal in pulverized coal combustors (PCC) has been extensively studied and is described in several reviews.^{3,4} Fly ash formed in an FBC conforms basically to that mechanism but differs in two aspects. First, its morphology shows that most particles are irregularly shaped, sintered, and porous, due to much lower combustion temperatures (750–950 C compared with 1300–1600 C in a PCC); consequently, the ash particles do not go through the melting stage. Second, the addition of a sorbent (e.g., limestone) introduces another component to the fly ash.

The enrichment of some elements due to their volatilization during combustion and subsequent condensation on the surface of particles in the cooler parts of the installation, first reported for PCC fly ash,⁵ has been also observed in the case of the FBC fly ash.^{6–8} As a consequence of the much higher temperature in a PCC, it is likely that the vapor phase will contain more of the volatile components than is the case in an FBC, which may result in a thicker surface layer in the former case. The thickness of the surface layer depends on such factors as the residence time of the particles in the combustion zone and their cooling rates,

and is not necessarily the same for small and large particles. After the formation of the first molecular layers, inward penetration by diffusion into the fly ash is likely to occur, giving rise to a concentration gradient.

The analytically determined bulk concentration C_b consists of two contributions: the matrix concentration C_m , the concentration in the particle before condensation occurs; and the surface concentration C_s , the concentration in the surface layer. Evidently the contribution of the latter is small for very large particles; in such a case, the bulk concentration approaches the matrix concentration. If we assume that the particles and the surface layers have equal densities and that the thickness of the surface layer is much smaller than the particle radius, the bulk concentration of the elements can be described by

$$C_b = C_m + (3/r)tC_s$$

where r is the particle radius and t the thickness of the surface layer. The dependence of the bulk concentration on particle size gives the value of tC_s as the slope of the C_b vs $1/r$ plot, as well as the value of C_m . When after a prolonged period the SIMS signal remains constant, it can be assumed that the surface layer has been sputtered off; the resulting SIMS level is identified as C_m , a value that is available from the size-dependent concentration measurements. Therefore, when the sputter rate is known, the thickness of the surface layer and also the surface concentration are experimentally available.

This approach differs from that taken earlier by Linton et al.⁹ and recently by Cox et al.,¹ who assumed that the constant ion intensities near the end of the depth profiles reflect the bulk elemental concentrations.

Experimental

Fly ash used in this study originated from a U.S. (Virginia) bituminous coal burned in the TNO 4 MW Atmospheric Fluidized Bed Boiler (AFBB) test facility with and without recirculation of the ash through the combustor. The description of the installation is published elsewhere.¹⁰ The "as received" fly ash (consisting chiefly of the fine material captured in the bag filter with a small amount of the coarse material from the cyclones) was separated into fractions by a crossflow jet classifier.¹¹ Six fractions ranging in size from 3 to 100 μm (determined with a Sympatec Helos instrument) were analyzed.

Carbon was determined by the modified Pregl

A. J. Gay and P. J. van Duin are with the TNO, Department of Environmental Technology, P. O. Box 217, 2600 AE Delft, The Netherlands; D. K. Henderson and P. Humphrey are with the Surface Analysis Service, Department of Chemistry, University of Manchester Institute of Science and Technology, P. O. Box 88, Manchester, England M60 1QD. This study forms a part of a research project, "Characterisation of fly ash from fluidised bed combustors with regard to its utilisation and safe disposal." The financial assistance by the Commission of the European Communities (Contract EN3F-0052-NL) and by the Management Office for Energy Research PEO (Contract 20.53.019.10) is gratefully acknowledged.

method.¹² Trace elements were determined by the Instrumental Neutron Activation Analysis (INAA), Atomic Absorption Spectrometry (AAS), Induction Coupled Plasma-Atomic Emission Spectrometry (ICP-AES), and Microwave-Induced Plasma-Atomic Emission Spectrometry (MIP-AES).

Surface analysis results were obtained from the three finest fractions from each run, ranging in size from 3.5 to 26 μm . A range of SIMS methods were used. Only the results from dynamic SIMS are presented here. All samples were analyzed in a VG SIMSLAB instrument operating under UHV conditions. Full instrumental details are published elsewhere.^{13,14} The primary ion beam for depth profiling was 10 kV O_2^+ produced by a duoplasmatron ion source running at 20 nA primary ion current. The fly ash samples were mounted by being pressed into an indium mirror coating on a stainless-steel sample stub. The thickness of the enriched layer was calculated from first principles assuming that the fly ash particles have a sputter yield of 0.5 and that a monolayer of 4 \AA thickness contained 10^{15} atoms/ cm^2 .

Results and Discussion

The concentrations of some trace elements vs particle size in fly ash from the run with no recirculation are presented in Table 1; those from the run with recirculation, in Table 2. Because of the high and variable carbon contents, the concentrations of the trace elements were adjusted by use of the formula

$$C_b = 100 C_b^* / (100 - C_c)$$

TABLE 1.--Concentration of elements vs particle size in fly ash from the run without recirculation.

Element		Fraction Size (μm)					
		5.4	8.5	26.3	47.4	69.7	83.3
C	wt%	31.7	44.2	63.9	58.2	9.0	40.3
As	ppm	73	69	40	35	26	25
Be		9.5	8.4	6.6	3.6	2.6	2.7
Ce		151	127	78	73	59	61
Co		91	79	65	59	40	38
Cu		606	432	274	242	233	290
Ni		375	362	219	239	144	147
Pb		206	176	86	69	87	74
Th		20	15	12	9.4	7.3	7.0
V		875	769	573	402	305	327

where C_b =bulk concentration of the element, C_b^* =concentration of the element as determined, and C_c =carbon content in the analyzed sample in wt%.

The results show that for most of the trace elements the inverse concentration-particle size dependence obtains, even for elements

that are regarded as nonvolatile, for instance Ce, Co, or Th.⁶

An examination of the SIMS profiles for similar fractions from the two runs illustrates that some of the elements are enriched to a different degree at the surface of the fly ash particles (Fig. 1). Also, the SIMS profiles show a large difference in the levels of carbon between the two runs; the run with recirculation has a level of carbon which is lower by nearly an order of magnitude than that without recirculation. Persistence of the C signal in the profile suggests that an appreciable part of the carbon is there as discrete particles.

The surface enrichment for three elements (As, Cu, V) is summarized in Table 3, giving an enrichment factor, expressed as a percentage based on bulk levels, and calculated depths over which the enrichment is observed. Arsenic has a similar level of enrichment for both the recirculated and unrecirculated material. However, the thickness of the As layer in the recirculated material is three times that of the unrecirculated. This finding shows that As probably diffuses into the matrix during the much longer residence in the hot-temperature zone in the run with recirculation. For the vanadium and copper, the layer thickness remains at a similar level (15-20 \AA), but there is an appreciable difference in the level of surface enrichment.

TABLE 2.--Concentration of elements vs particle size in fly ash from the run with recirculation.

Element		Fraction Size (μm)					
		3.5	4.0	25.4	44.0	63.7	74.9
C	wt%	15.4	16.6	45.3	32.0	20.3	13.
As	ppm	72	78	44	37	29	29
Be		11	11	5.9	3.8	3.1	2.8
Ce		160	168	73	56	46	41
Co		125	122	64	48	38	33
Cu		285	258	183	128	107	100
Ni		411	369	266	162	127	116
Pb		239	210	100	54	44	44
Th		23	22	9.7	6.6	4.9	4.1
V		976	920	510	503	118	233

References

1. X. B. Cox et al., "Microcharacterization of trace elemental distributions within individual coal combustion particles using secondary ion mass spectrometry and digital imaging," *Anal. Chem.* 59: 2018, 1987.

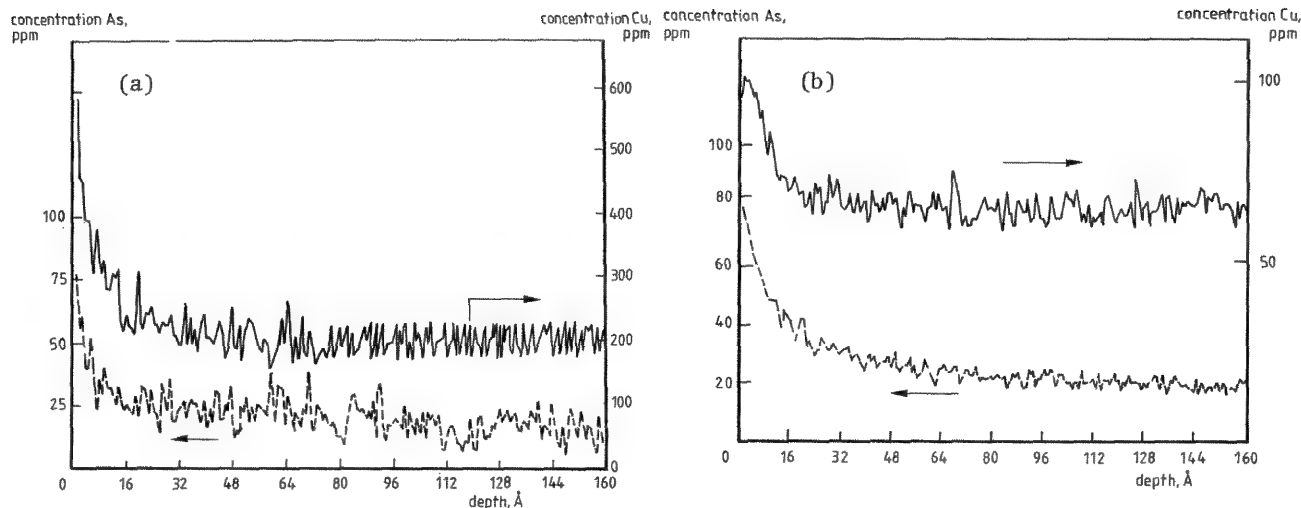


FIG. 1.--Depth profiles for As and Cu in fly ash samples from (a) run with no recirculation, fraction size 26.3 μm ; (b) run with recirculation, fraction size 25.4 μm .

TABLE 3.--Enrichment depths and percentages.

Element	Run with no circulation Fraction size 26.3 μm		Run with recirculation Fraction size 25.4 μm	
	Depth Å	%*	Depth Å	%*
As	16	370	48	380
Cu	15	256	20	158
V	15	330	16	143

2. M. E. Farmer and R. W. Linton, "Correlative surface analysis studies of environmental particles," *Environ. Sci. Technol.* 18: 319, 1984.

3. R. C. Flagan and S. K. Friedlander, "Particle formation in pulverized coal combustion: A review," in D. T. Shaw, Ed., *Recent Developments in Aerosol Science*, New York: Wiley, 1978, 25.

4. R. D. Smith, "The trace element chemistry of coal during combustion and the emissions from coal-fired plants," *Prog. Energy Combust. Sci.* 6: 53, 1980.

5. R. L. Davison et al., "Trace elements in fly ash: Dependence of concentration on particle size," *Environ. Sci. Technol.* 8: 1107, 1974.

6. D. F. S. Natusch and D. R. Taylor, *Metallic Species Derived from Fluidized Bed Coal Combustion*, Report DOE/MC/08196-T1, 1981.

7. A. J. Gay and A. P. von Rosenstiel, *A Study of the Composition and Morphology of Fly Ash from Coal-burning Installations*, TNO Report No. CL 82/55, 1982.

8. S. H. Weissman et al., "Respirable aerosols from fluidized bed coal combustion: 3. Elemental composition of fly ash," *Environ. Sci. Technol.* 17: 65, 1983.

9. R. W. Linton et al., "Determination of the surface predominance of toxic elements in airborne particles by ion microprobe spectrometry and Auger electron spectrometry,"

Anal. Chem. 49: 1514, 1977.

10. H. M. G. Temmink and J. Meulink, "Operating experiences with the TNO 2m \times 1m atmospheric fluid bed boiler facility," *Proc. 3rd European Coal Utilisation Conf.* 2: 99, 1983.

11. K. Leschonski, *Classification of Particles in Gases*, IFPRI Report, Clausthal, 1981.

12. H. Roth, *Quantitative organische Mikroanalyse*, Wien: Springer, 1958.

13. A. Brown and J. C. Vickerman, "Static SIMS for applied surface analysis," *Surf. Int. Anal.* 6: 1, 1984.

14. A. Brown et al., "Characterisation of a high transmission ion optical column for quantitative SIMS," *Proc. 6th Int. Conf. on Secondary Ion Mass Spectrometry, Versailles, 1987* (in preparation).

QUANTITATIVE ANALYSIS OF SMALL PARTICLES BY SUBMICRON SECONDARY ION MASS SPECTROMETRY

H. Satoh, M. Owari, and Y. Nihei

Submicron SIMS with a parallel detection system by use of gallium-focused ion beam was constructed.^{1,2} By this instrument, methods of quantitative analysis of small particles were studied.³

Experimental and Results

Apparatus. The schematics of the apparatus are shown in Fig. 1. Field-emitted Ga⁺ ions are accelerated to 35 kV and focused on the sample. The primary beam diameter and density are estimated to be less than 0.1 μm and $\sim 1 \text{ A/cm}^2$, respectively. When directed to fast-scan a small area or when slowly rastered, both high spatial resolution and large sputtering rate are realized. A multichannel parallel detector is placed on the focal plane of Mattauch-Herzog mass analyzer and covers a mass range of 1:2 with 120 independent channels. All ions whose m/e are within a mass of 1:2 range are detected simultaneously.

Analytical Methods. A. *Scanning mode.* Generally, secondary ion yield depends largely on the incident angle of primary ion beams to the sample surface. When the sample is not a flat plate, this fact introduces a difficult topographic effect. In order to circumvent the topographic effect, which is typically observed as edge enhancement, we examined a new kind of scanning mode. Figure 2 shows conventional raster scan mode (a) and with the new scanning mode (b).

In the conventional mode (Fig. 2a), the primary ion beam scans over an area of a particle rapidly and repeatedly in both vertical and horizontal sweeps. A particle is sputtered from exposed surface. In the new scanning mode--SHAVE-OFF mode (Fig. 2b), the fast horizontal sweep is combined with a very slow vertical sweep. The most important point of this scanning mode is that the speed of vertical sweep is slow enough to "shave-off" the sample from one edge to the other edge. The entire volume of the particle is sputtered after only a single frame raster scan. In this mode, the primary ion beam always shaves the edge of the sample. In practice, shave-off mode analysis can be performed only with a finely focused, high current density primary ion beam.

B. *Quantitative comparison of scanning modes.* Figure 3 shows the changing signal intensities during the measurement by conven-

tional mode and shave-off mode. The sample for each measurement was a single spherical coal fly ash particle held on an indium plate, and their diameters were about 3 μm . Figure 3a shows the result of conventional mode analysis. Each single frame sweep required 17 s, so the counts of signals were accumulated for every 17 s. The 17s frame sweep measurement was repeated 20 times, until the analyzed particle was completely eroded. During the initial 150 s, the peak intensities decreased monotonically. As shown in the figure, the signal intensities became stationary after 150 s; the sample particle seemed to be completely sputtered away at this time. Even after the disappearance of the sample particle, the signal counting rates were about 6 counts/s, which suggest the occurrence of sputter deposition and knock-on mixing of sample component onto the indium plate.

Figure 3b shows the result of the shave-off analysis. The primary beam sweep rate was 100 $\mu\text{m/s}$ in the horizontal direction and 0.01 $\mu\text{m/s}$ in the vertical direction. The signal counts were accumulated for every 5 s. After the single frame sweep, the sample particle was completely eroded. From 20 s to 270 s after the measurement started, the primary beam scanned over the sample particle. During this period, intensities of four signals changed almost in parallel, which indicates that the composition of the sample particle was considerably homogeneous. The changes of spectral intensities corresponded to the shape of the particle and the intensities seemed to be proportional to the cross-section area of the sample. The detecting efficiency was constant over all parts of the sample. After the primary beam passed over the sample area, the detected signal intensities (background level) were about 2 counts/s, which is 1/3 of those of conventional mode.

By shave-off mode, the angle of primary beam incidence relative to the sample surface is kept constant throughout the course of the whole particle analysis. The influence of topographic effect was held constant throughout the measurement because the topographic effect generally occurs by the variations of angle between the primary beam and sample surface. Therefore, the topographic effect is controlled and inconvenient effects of it are eliminated. In conventional mode analysis, the sputter-deposited fraction may be measured because the primary beam sweeps repeatedly over the place where sputter deposition or knock-on mixing have occurred. From the comparison of the results for those two modes, it is obvious that the shave-off mode is far more advantageous for quantitative analysis of small particles.

The authors are at the Institute of Industrial Science, University of Tokyo, 22-1 Roppongi 7 chome, Minato-ki, Tokyo 106, Japan. They wish to thank Dr. D. E. Newbury (National Bureau of Standards) and Prof. R. Shimizu (Osaka University) for providing the NBS standard reference material for glass particles.

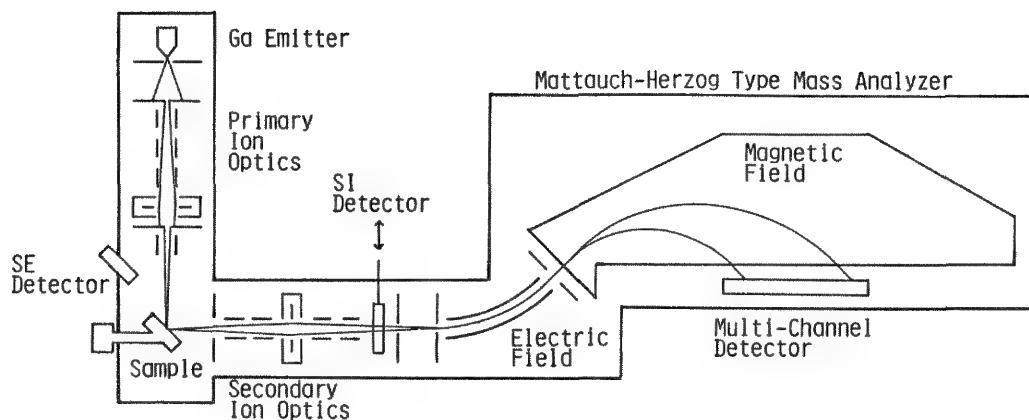


FIG. 1.--Schematic diagram of multichannel detection submicron secondary ion mass spectrometer.

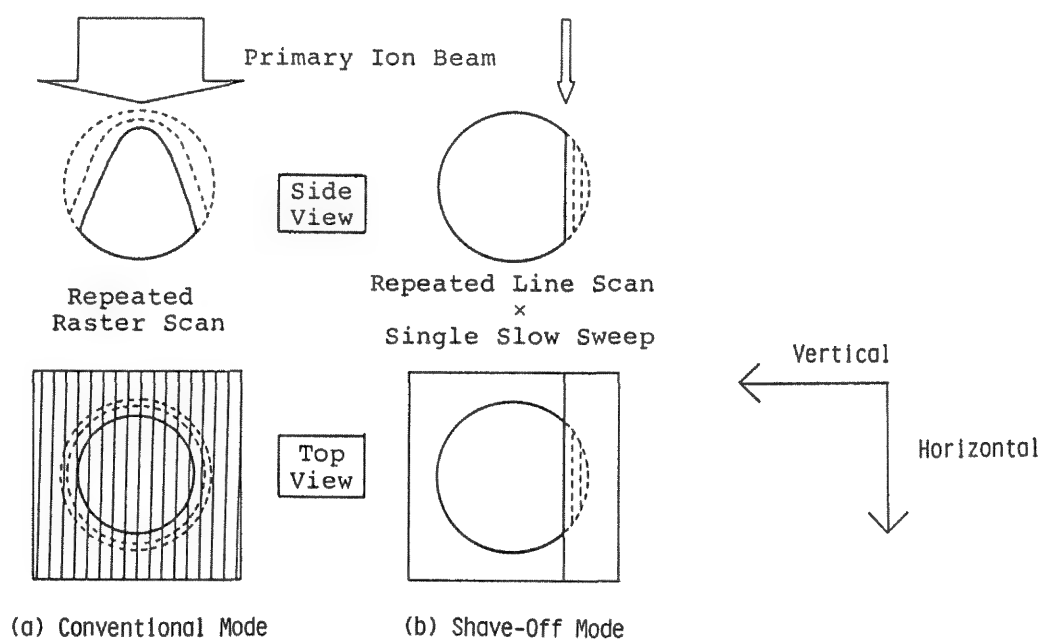


FIG. 2.--Two kinds of scanning mode for particle analysis: (a) conventional mode, (b) shave-off mode.

Quantitative Analysis. In order to perform quantitative SIMS analysis, the relative sensitivity factors of each element by use of a gallium focused ion beam are needed. An NBS K-309 Standard Reference Material was measured to get these factors. The composition of the sample is shown in Table 1.

A whole NBS K-309 particle whose diameter is $3\text{ }\mu\text{m}$ was analyzed by shave-off mode and the relative sensitivity factors of some elements were obtained. The total counts of each element, atomic concentrations, and relative sensitivity factors for using Ga^+ primary ions are shown in Table 2. The relative sensitivity factors were calculated by taking Si^+ as a standard. For the purpose of comparison, the relative sensitivity factors by use of other primary ion beams (Ar^+ , O^-) are also given in Table 2.^{4,5} Although much more experimental work is required, this preliminary study shows

that the relative sensitivity factors for Ga^+ primary ions appear to be similar to those for an Ar^+ beam.

Conclusions

A method of analysis for small particle by using submicron SIMS was studied. In order to analyze uneven samples quantitatively, the "shave-off" mode analysis has been proposed. Topographic effect is controlled and inconvenient effects of it are eliminated. The effects of sputter deposition and knock-on mixing is minimized. Therefore, the quantitative power is greatly improved.

By use of the "shave-off" mode, a quantitative SIMS analysis of standard reference glass particles was carried out, and the relative sensitivity factors for gallium primary ions were obtained.

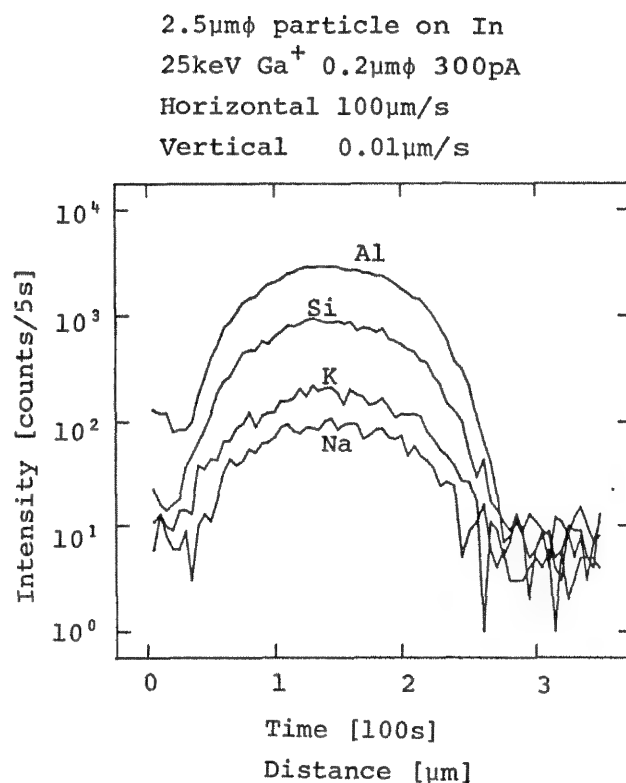
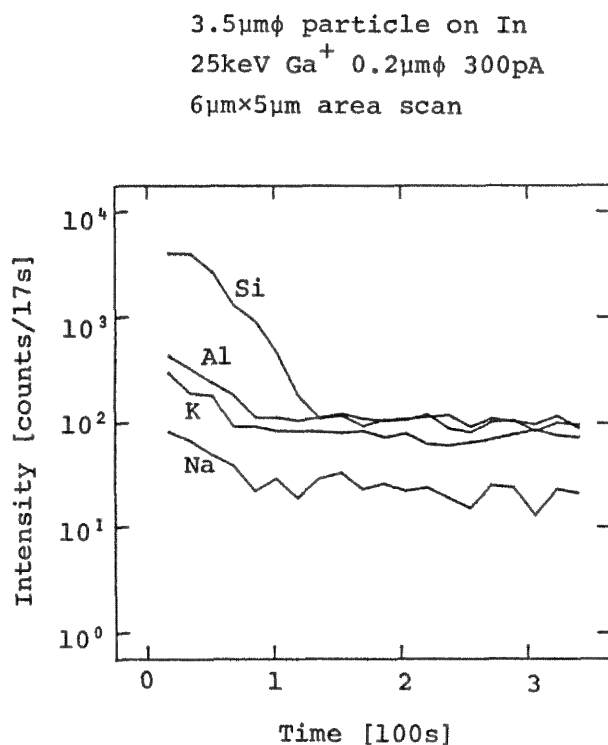


FIG. 3.--Comparison of scanning mode from quantitative aspects; (a) conventional mode, (b) shave-off mode.

TABLE 1. Composition of glass particle (NBS Standard Reference Material K-309).

Constituent	Percent by Weight
Al ₂ O ₃	15.0
SiO ₂	40.0
CaO	15.0
Fe ₂ O ₃	15.0
BaO	15.0

TABLE 2.--Analytical results of glass particle and relative sensitivity factors.

Counts/ 1.4 \times 10 ⁻¹¹ cm ³ (3 \times 10 ⁻¹⁰ A Ga ⁺)	Atomic%	Relative Sensitivity Factor		
		Ga ⁺ a) (27.5keV)	Ar ⁺ b) (12keV)	O ⁻ c) (13.5keV)
Al ⁺ 4.6 \times 10 ⁴	7.4	4.2 \pm 1.1	7.5	0.75
Si ⁺ 2.5 \times 10 ⁴	16.9	1.0	1.0	1.0
Ca ⁺ 1.20 \times 10 ⁵	6.8	12.0 \pm 0.93	-	0.39

a) This work. b) From ref.5. c) From ref.4.

References

1. Y. Nihei, H. Satoh, S. Tatsuzawa, M. Owari, M. Ataka, R. Aihara, K. Azuma, and Y. Kammei, *J. Vac. Sci. & Tech.* A5: 1254, 1987.
2. H. Satoh, M. Owari, and Y. Nihei, *Analytical Electron Microscopy--1987*, 367.
3. H. Satoh, M. Owari, and Y. Nihei, *J. Vac. Sci. & Tech.* (in press).
4. H. A. Storms, K. F. Brown, and J. D. Stein, *Anal. Chem.* 49: 2023, 1977.
5. H. E. Beske, *Quantitative Analysis with Electron Microprobe and Secondary Ion Mass Spectrometry*, Jul-Conf-8, März 1973, 249.

CHARACTERIZATION OF ELECTRON-BEAM INDUCED DAMAGE STRUCTURES IN
NATURAL FLUORITE, CaF_2 , BY ANALYTICAL ELECTRON MICROSCOPY

D. F. Blake, L. F. Allard, C. J. Echer, and Friedemann Freund

Naturally occurring fluorite, CaF_2 , develops a particular highly ordered damage structure when exposed to the primary beam in the transmission electron microscope (TEM). This structure has been variously described as "ordered defect aggregates,"¹ a "superlattice array of voids,"² and "Ca colloids produced by beam-induced loss of fluorine from the fluorite structure."^{3,4} During a reconnaissance study of optical anisotropy in natural fluorite⁵ we observed this structure under a variety of instrumental conditions. It is the purpose of this communication to further describe electron-beam induced damage structure in fluorite and to speculate, based on these new data, as to its mechanism.

Methods

Polished [100] and [111] sections of natural fluorite from the Cumberland district, England, approximately 1 mm thick, were glued to petrographic slides with Crystalbond 501™ heat-sensitive adhesive. These sections were ground by standard techniques to a thickness of 25 μm , which permitted regions that were free of optical defects to be easily located. Disks 3 mm in diameter were cut from such regions and supported on Al washers for easy handling. The disks were argon ion-milled in a Gatan Duo-Ion Mill with beams incident at 6 kV and 15°.

Energy-dispersive x-ray spectra (EDS) were acquired from ultramicrotomed thin sections of crushed grains of fluorite mixed with LR White™ embedding resin. After curing the epoxy, transmission-thin sections were cut on a Porter Blum MT-2 ultramicrotome with a diamond knife. Sections which were silver in reflected light (60-100 nm thick) were picked up on 400 mesh Cu grids covered with holey carbon support films. A thin coating of carbon was then evaporated onto the sections to insure conductivity.

Conventional and high-resolution TEM studies were conducted with a JEOL JEM-100CX having a top-entry stage with 0.7 mm C_s ultra-high

resolution polepiece. High-voltage (1.0 MeV) TEM was carried out at the HVEM Tandem Facility, Argonne National Laboratory. Analytical electron microscopy was performed with a JEOL JEM-200 CX AEM equipped with a Kevex ultrathin window detector, and an Hitachi H-500 AEM equipped with a 68° take-off angle Kevex Quantum detector.

Observations

During conventional TEM observation at 100 keV and ambient temperature, electron-beam induced damage was observed within a few seconds of exposure. The fully developed damage structures had a 10-20 nm periodicity parallel to [100], consisting of a three-dimensional periodic array of squares (in plan view), which suggest strings of corner-sharing octahedra (Fig. 1). The periodic structure was observed to grow and mature into a stable configuration in 1-2 min of viewing time. Electron diffraction patterns from undamaged regions showed a single crystal pattern with round, discrete diffraction maxima. After the beam damage structure was fully developed, individual diffraction maxima displayed satellite reflections in the [100] directions. These satellite reflections had the same periodicity as the beam-induced structure. No superlattice reflections of the type described by Murr¹ were observed in either the [100] or [111] oriented sections of the fluorite.

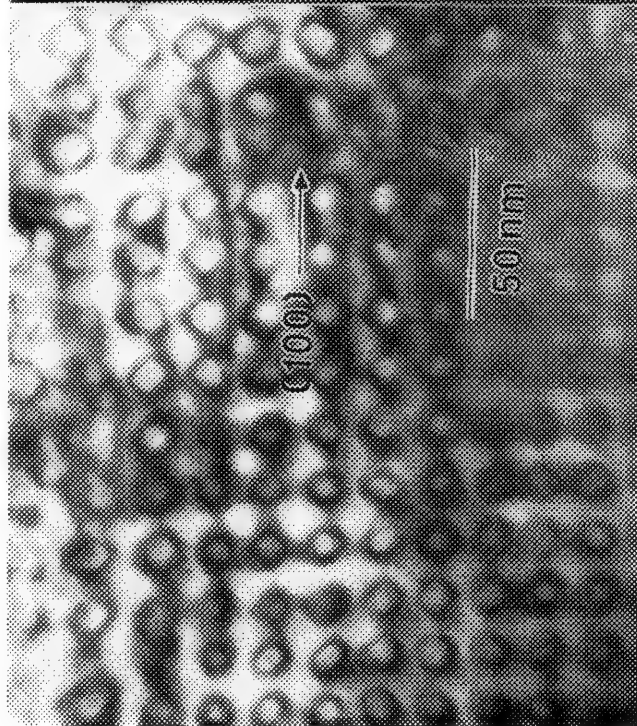
When undamaged areas of the fluorite were observed at liquid nitrogen temperature, the damage structure did not appear during periods of viewing of 10-15 min. We were thus able to produce areas of damage structure at room temperature, cool the sample in situ to -195 C, and observe adjacent damaged and undamaged areas for extended periods of time.

High-voltage TEM observations were made to determine whether the timing of onset of the damage structure was a function of accelerating voltage. We found that the damage structure developed much more slowly at 1 MeV than at 100 keV, although the resulting structure appeared indistinguishable in the two cases.

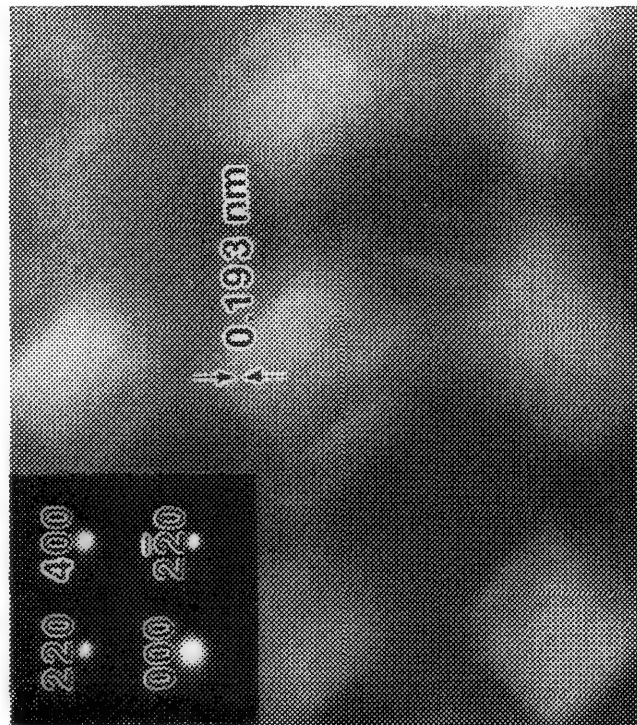
Quantitative EDX microanalyses were obtained from ultramicrotomed fluorite samples both in point mode and small area raster mode, at ambient temperature and at -165 C. Spectra were acquired for 1000s counting times and processed with theoretically derived k-factors for Ca and F. Absorption corrections were applied for fluorine based on estimated thickness of the microtome sections. The results are shown in Table 1. Fluorine loss was severe in the ambient temperature analyses, both

D. F. Blake and F. Freund are with the Planetary Biology Branch, MS 239-4, NASA/Ames Research Center, Moffett Field, CA 94035; L. F. Allard is with the High Temperature Materials Laboratory, Martin Marietta Energy Systems, Oak Ridge National Laboratory, Oak Ridge, TN 37831; and C. J. Echer is with the National Center for Electron Microscopy, Lawrence Berkeley Laboratory, Berkeley, CA 94720. Support through the Exobiology Division of NASA and the National Research Council to DFB and FF, and the Department of Energy to LFA and CJE, is gratefully acknowledged.

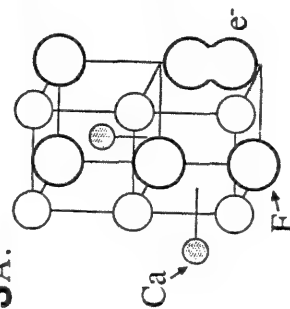
1



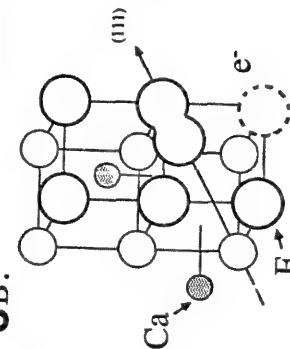
2



3A.



3B.



3C.

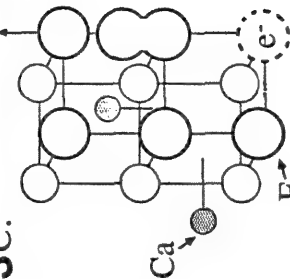


FIG. 1.--Bright-field TEM micrograph of electron-beam induced damage structure in fluorite. Rows of damage octahedra are parallel to [100].
 FIG. 2.--High-resolution TEM micrograph of fluorite damage structure, showing [220] lattice fringes (0.193 nm). Fringes in damage structure octahedra appear to be coherent and topotactically oriented with host fluorite. Differences between lattice parameters of calcium metal and fluorite are so small as to be indistinguishable. Inset diffraction pattern shows conditions used for imaging. Image was recorded with tilted beam illumination, using the four labeled diffraction maxima.
 FIG. 3.--Schematic reaction sequence for the enhanced loss of fluorine from fluorite structure: (a) Production of molecular F_2 -ion oriented with its long dimension parallel to [100]. (b) Formation of F-center and Frenkel pair parallel to [111]. (c) Formation of molecular ion which can initiate translational motion along row of densely packed F-ions parallel to [100].

TABLE 1.--Comparison of quantitative analyses of CaF_2 standards at ambient temperature and at -165 C for "large area," "small area," and "point" modes.

	Ambient Temp., At.% ¹	-165 C At.% ¹
Point Mode ²	Ca 75.47% F 24.53	Ca 51.77% F 48.23
Small-area Raster ³	Ca 65.24 F 34.76	(Data not obtained)
Large-area Raster ⁴	Ca 44.34 F 55.66	Ca 40.12 F 59.88

¹Normalized to 100%.

²Beam diameter approximately 60 nm.

³150 × 150 nm area.

⁴0.3 μm × 1.5 μm area.

in point mode and small area raster mode, but less so when the rastered area was large (0.3 × 1.5 μm). At -165 C, fluorine loss was still pronounced in the point and small area raster modes. Only the large area raster gave a value closer to the 1:2 Ca to F atomic ratio of fluorite, although some fluorine loss is still evident.

High-resolution TEM images were obtained from damaged regions to determine whether any change of lattice parameter was evident within damaged and undamaged regions. Teodorescu et al.⁴ has suggested that the structure may represent anion vacancy clusters filled with colloidal Ca metal. If this were the case, undamaged fluorite regions would have an α -parameter of 0.5643 nm, characteristic of fluorite, and regions of the "damage octahedra" would have an α -parameter of 0.5576 nm corresponding to Ca metal. Rice et al.⁶ have presented evidence that extended beam exposure in the relatively poor vacuum of tradition TEM instruments leads to oxidation of the Ca metal. If CaO were to form, the α -parameter would be 0.48105 nm. Lattice fringe images taken under 2- and 4-beam conditions with tilted illumination were measured to determine any differences in fringe spacing between the regions. We could detect no difference, although such small differences in fringe spacing are probably beyond the precision of the technique. Figure 2 shows a lattice fringe image of the damage structure from which such measurements were obtained. This image plus electron diffraction information provides clear evidence that the damage structures are perfectly coherent with the matrix.

Discussion

Our observations show that electron beam irradiation of fluorite in the TEM causes defects and defect agglomeration together with a loss of fluorine. The extent of the damage depends on the temperature at which the experiment is carried out, on primary beam energy, and on the electron flux per unit area. Low temperatures, high incident electron energies, and low irra-

diation doses clearly reduce the extent of damage.

The electrons used in the TEM for imaging purposes are those which are elastically scattered off the atoms of the sample. However, there is always an additional small fraction of electrons which interact inelastically with the target atoms and ultimately cause radiation damage. Since this fraction tends to decrease with increasing incident electron energy, samples exposed to 1MeV electrons generally suffer less damage than samples exposed to 100keV electrons. Inelastically scattered electrons give rise to various effects useful for analytical purposes. Direct knock-on processes are rare, even for electrons with energies above the threshold for atomic displacements, because electrons cannot efficiently transfer momentum onto atoms or ions and knock them off their lattice sites.⁷ Their primary mode of interaction consists of the emission of photoelectrons by ionization of core levels. When the core level holes are filled by electrons from higher levels, x rays and Auger electrons are emitted. The photoelectrons, x rays, and Auger electrons can in turn induce secondary and tertiary ionization, leading to a cascade of successive processes that eventually diminish, ending with energies sufficient to cause excitation of molecular levels and heat.

Figure 3 depicts schematically the reaction sequence for a section of the fluorite unit cell. When an F^- valence electron is elevated to an excited level, the fluorine atom bonds covalently to a neighboring F^- , forming a dumbbell-shaped F_2^- molecular ion oriented parallel to [100] (Fig. 3a). This configuration, which contains an electron in a higher molecular orbit, is metastable. There are two conceivable decay channels:^{11,12} (1) by formation of a color center, e.g., a free electron occupies the F^- site, and the nearby F_2^- molecular ion aligns parallel to [111], the direction joining adjacent octants of the CaF_2 unit cell without Ca^{2+} in their center positions (Fig. 3b); and (2) by channeling of the electronic de-excitation energy directly into a translational motion of the F_2^- complex along a row of densely packed F^- anions such as parallel to [100] (Fig. 3c). In the latter case F^- anions along the chain form a succession of transient F_2^- molecular ions with the energy traveling along the [100] direction in a way similar to a pulse which propagates along a string of billiard balls. In alkali halides the energy can thus be transported as a singular high-energy phonon spike over large lattice distances, perhaps as far as several hundred nanometers.¹³ If the spike ends at the surface of the crystal, the last atom will be ejected with a high kinetic energy.

If such high-energy phonon spikes exist in CaF_2 , they should lead to a preferential loss of fluorine from the crystal surface.¹⁴ For each F atom which is lost, a color center (i.e., a free electron), remains inside the crystal. If the F loss continues, the CaF_2 structure accumulates free electrons and Ca^{2+}

cations which have replaced some of their F⁻ ligands with electrons resonating in the anion vacancy sites. At some point during this process, clustering must occur due to long-range interactions between damaged lattice points of regions. For instance, Ca²⁺ cations which lose two of their F⁻ ligands are expected to merge with the two electrons, thus forming Ca atoms. As the reaction progresses, Ca atoms may coalesce to colloidal metallic Ca.

Another process of potential interest is the loss of F preferentially along [100] lines which in turn interact elastically so as to produce a pattern of more or less equidistant channels from which F has been removed. The observed periodic features suggest that indeed such a regular damage pattern develops and leads to regions inside the CaF₂ crystal which differ in composition. The light colored areas in Fig. 2 represent material that has less electron density per unit volume than CaF₂. Orera and Alcala³ and Teodorescu et al.⁴ have suggested that the apparent voids are filled with metallic Ca colloids. In this context it is interesting to compare structure and density between fluorite and metallic Ca. Fluorite crystallizes in the C1 structure, symmetry Fm3m, which can be viewed as face-centered cubic (fcc) packing of Ca²⁺ with the F⁻ anions occupying all tetrahedrally coordinated sites. With $a = 0.546$ nm the molar volume and density are 24.56 cm³ and 3.18 g/cm³, respectively. Ca metal at room temperature also crystallizes in the fcc structure, space group Fm3m, with lattice parameter, atomic volume and density $a = 0.558$ nm, 25.9 cm³ and 1.54 g/cm³, respectively. In other words, if the CaF₂ structure decomposes into calcium metal and fluorine, and if all fluorine were removed, the remaining Ca metal would occupy the same space within less than 2% tolerance. Since the lattice parameters are so very close, topotaxial intergrowth of the colloidal Ca precipitates is expected. Because of the identical symmetries the electron diffraction patterns in the [100] and [111] projections would be indistinguishable within the limits of the resolution of the TEM.

The pronounced loss of F (Table 1) and the observed 10-20nm periodic features with coherent fringe patterns (Fig. 2) provide support for the decomposition of CaF₂ into 2F plus Ca metal with the Ca precipitates maintaining a close topotaxial relationship with the parent CaF₂. Since the decomposition is rapid, at least at room temperature, the oxygen content in the Ca is probably insufficient to form CaO, as suggested by Rice et al.⁶ The fringes observed in the light colored areas in Fig. 2 are therefore believed to arise from Ca metal filling the strings of the corner-linked octahedra parallel to [100]. In the residual CaF₂ lattice fringes are barely observable, which suggests partial amorphization by radiation damage. By contrast the colloidal Ca crystals appear well crystallized. This is consistent with the lower Debye temperature of Ca metal which is ductile and melts around 840 C as

compared to CaF₂, which is brittle and melts around 1360 C.

References

1. L. E. Murr, "Ordered lattice defects in colored fluorite: Direct observations," *Science* 183: 206-208, 1974.
2. L. T. Chadderton, E. Johnson, and T. Wholenberg, "Observations of a regular void array in natural fluorite irradiated with 100 keV electrons," *Physica Scripta* 13: 127-128, 1975.
3. V. M. Orera and R. Alcala, "Optical properties of cation colloidal particles in CaF₂ and SrF₂," *Phys. Stat. Sol. (a)* 44: 717-723, 1977.
4. V. Teodorescu, L. C. Nistor, and S. V. Nistor, "Electron microscopy study of pure and doped synthetically grown CaF₂ crystals," *Phys. Stat. Sol. (a)* 46: 711-717, 1979.
5. D. R. Peacor, W. C. Kelly, and D. F. Blake, "Growth strain, optical anisotropy and fluid entrapment in fluorite," *Geol. Soc. Am. Abstr. W. Prog.* 16: 660, 1983.
6. P. M. Rice, P. A. Crozier and R. F. Egerton, "Control of mass loss in analytical electron microscopy," *Microbeam Analysis--1987*, 213-216.
7. J. W. Corbett, "Radiation damage, defects and surfaces," *Surface Sci.* 90: 205-239, 1979.
8. N. Itoh, T. Nakayama and T. A. Tombrello, "Electronic-excitation mechanisms in sputtering induced by high density electronic excitation," *Phys. Lett.* 108A: 480-484, 1985.
9. F. Seitz, "Color centers in alkali halide crystals," *Rev. Mod. Phys.* 26: 7-94, 1954.
10. N. Itoh, "Creation of lattice defects by electronic excitation in alkali halides," *Adv. Phys.* 82: 491-551, 1982.
11. D. Pooley, "[110] anion replacement sequences in alkali halides and their relation to F-center production by electron-hole recombination," *Proc. Phys. Soc.* 87: 257-262, 1966.
12. H. N. Hersh, "Proposed excitonic mechanism of color-center formation in alkali halides," *Phys. Rev.* 148: 928-932, 1965.
13. J. P. Biersack, "Sputtering of alkali halides under ion bombardment," *Nucl. Instr. Meth. Phys. Res.* 198: 29-32, 1982.
14. A. E. De Vries, "Chemical sputtering," *Comm. At. Mol. Phys.* 13: 127-140, 1983.

Monte Carlo Methods in Microscopy and Analysis

EXTENDING MONTE CARLO TECHNIQUES TO LOW PRIMARY-BEAM ENERGIES

K. Murata

Relatively high-resolution observations have been realized at low energies in scanning electron microscopy and electron microprobe analysis, and thanks to that a low-energy electron probe has become available now. It is generally recognized that the low-energy electron probe has several advantages such as high sensitivity and little damage to the observed sample surface. These features give SEM the capability of widespread applications. However, although the theory of electron scattering has made a great progress in the high-energy region (5-50 keV), it is not studied very much in the lower energy region (0-5 keV). For example, if one tries to develop the theory of secondary electron emission, accurate theoretical treatments have not been developed yet for low-energy primary electrons. The Born approximation does not hold yet at low energies. For example, the screened Rutherford (ScR) equation, which has seen much use, is not accurate, especially for heavy elements. Another problem in developing the theory at low energies is that the experiments that must be done to compare with the theory are difficult. Investigations of electron penetration require very thin films (of a few tens to few hundreds of Ångströms) with a clean surface, and also need accurate measurements of the films. On the other hand, measurement of electron backscattering is relatively easy and does not require thin films. If we measure the angular distributions of elastically reflected electrons (EREs) without energy losses, we can check the angular dependence of the differential cross section for elastic scattering. If we measure the angular distributions of inelastically reflected electrons (IRES) from bulk targets with energy losses, we can also check the energy-loss process indirectly. This paper, therefore, discusses the theory at low energies, with emphasis mainly on backscattering from Au targets. Since the Born approximation cannot be applied to the subject, the exact Mott cross section is used for elastic scattering.

Calculation Procedure

When an electron is incident on a solid target, it suffers elastic and inelastic collisions with the atoms composing the target. When we try to model its behavior for the purpose of simulation, we usually separate the phenomenon into two categories: the event that causes the angular deflection and the event that causes energy loss. Fortunately, these events are described by elastic and inelastic scattering, respectively, for electrons; we

can neglect both the energy loss due to bremsstrahlung radiation that accompanies elastic scattering, and the angular deflection due to inelastic scattering for low energy and heavy elements, but we may not do the latter for light elements.

Elastic Scattering Cross Section

The screened Rutherford (ScR) equation has been frequently used as the elastic differential cross section in Monte Carlo simulations of incident electrons:

$$\frac{d\sigma}{d\Omega} = \frac{Z^2 e^4}{m^2 v^4} \frac{1}{(1 - \cos \theta + 2\beta)^2} \quad (1)$$

The equation is based on the Born approximation as mentioned in the original paper by Wentzel, although the screening parameter was introduced later, based on a better atomic potential (see, for example, Motz et al.²). The condition for the approximation to hold is

$$\frac{Zc}{137v} \ll 1 \quad (2)$$

where c and v are the light and electron velocities, respectively. As calculated easily from the equation, the condition is not satisfied even for an energy of a few tens of keV for heavy elements such as Au. A previous paper³ reports some results of Monte Carlo simulations based on Eq. (1). The comparison of backscattering coefficients obtained from theory and experiment shows that their discrepancy is large even at 10 keV for Au. A more accurate expression is needed for such conditions as low energy and heavy elements.

In the present paper the Mott cross section is used, which is simply described for an unpolarized electron beam as follows:²

$$\frac{d\sigma}{d\Omega} = |F(\theta)|^2 + |G(\theta)|^2 \quad (3)$$

$F(\theta)$ and $G(\theta)$ are obtained by solving numerically Dirac's relativistic equation based on the partial wave expansion of electron waves. The potential is calculated from $Z = 79$ for Au instead of $Z = 80$ in Lin's equation⁴ for Hg. The differential cross sections are provided in numerical data. Calculated Mott cross sections are normalized by the ScR cross section and shown in Fig. 1 for Au at typical energies. For higher electron energies, such as 20 keV, the ScR equation overestimates the cross section in the angle range up to about 90° and underestimates in larger angles. As the electron energy decreases, the angle range extends where the cross section is overestimated. At 1 keV the Mott cross section is clearly subject to the diffraction effect.

The author is with the Electronics Department, College of Engineering, University of Osaka Prefecture, Sakai, Osaka 591 Japan.

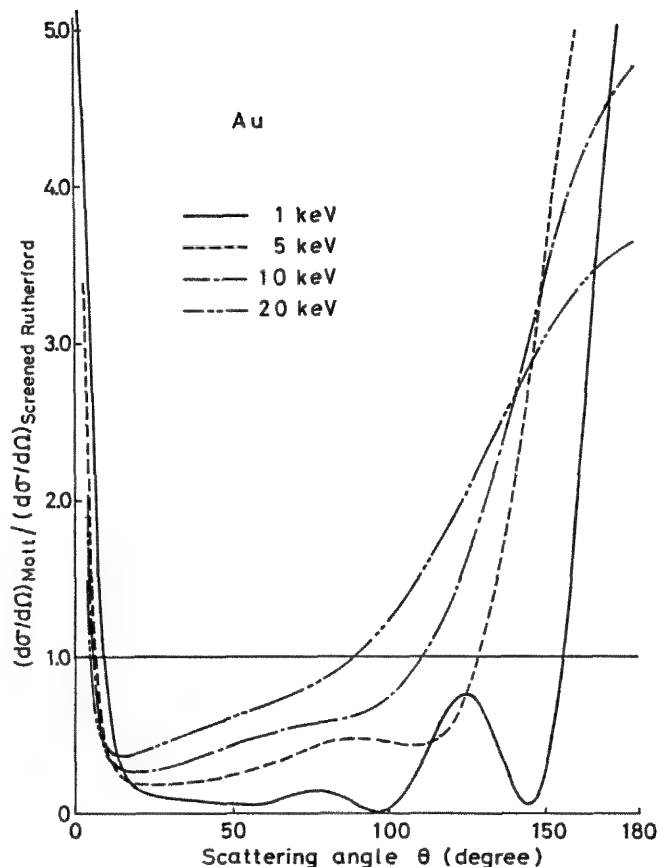


FIG. 1.--Ratio of Mott differential cross sections to screened Rutherford cross sections as function of scattering angle (Kotera et al.³).

Since the ScR equation decreases monotonically with scattering angle, it cannot predict such a diffraction effect at all.

The validity of the Mott cross sections at low energies is shown in Fig. 2 by a comparison with the experimental data of Reichert.⁵ Both cross sections are matched at an angle of 90° for easy comparison in the position of the maxima and minima and the angular dependence of the intensity. Both results agree very well. Although the absolute values are not shown in the experimental data, relative changes with energy can be compared with each other. The energy variation of the intensity is shown in Fig. 3 at a typical scattering angle of 90° . Except at an energy of 700 eV, experimental points seem to be fairly on a smooth line, although large discrepancies are seen from the theory. Both curves have a similar trend despite difficult experimental techniques. (Note that the matching of both results may not be appropriate at 0.4 keV.)

The mean free path for elastic scattering is calculated as follows:

$$\lambda_{el} = (n\sigma_{tot})^{-1} \quad (4)$$

where n is the number of atoms per unit volume and σ_{tot} the total cross section obtained by integration of Eq. (3) over all solid angles. Then an actual step length between collisions

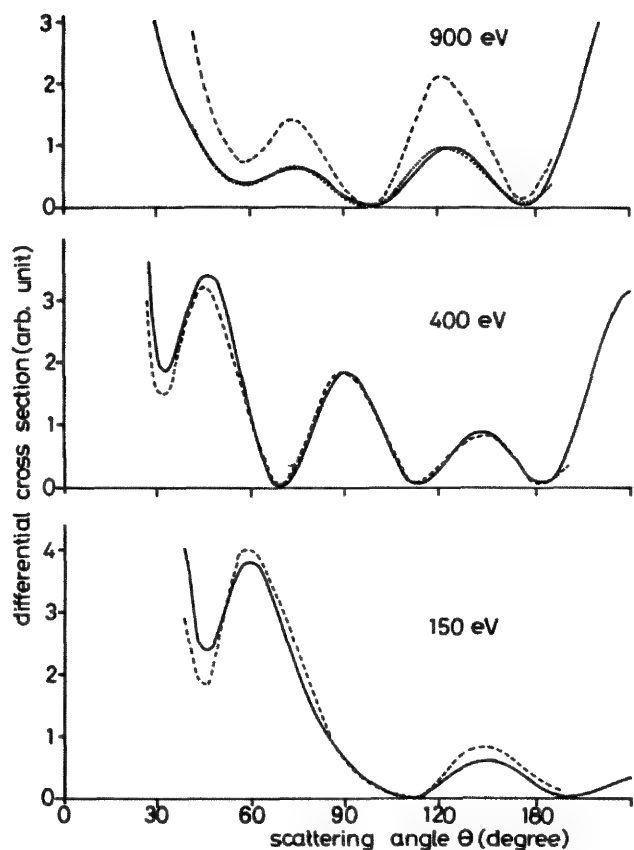


FIG. 2.--Comparison of Mott differential cross sections with experimental ones of Reichert for Au.

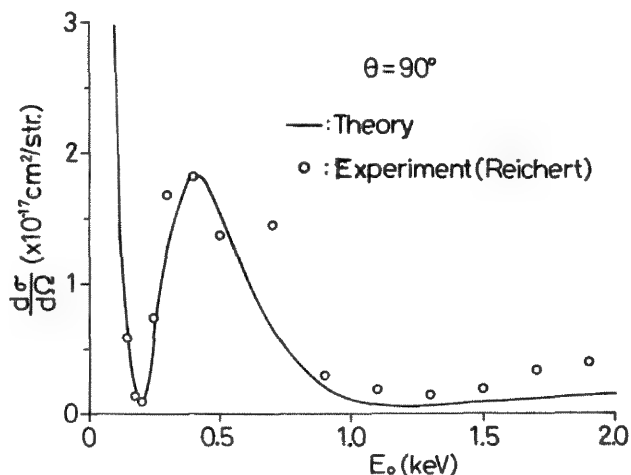


FIG. 3.--Energy variation of cross section for Au at $\theta = 90^\circ$. Theory is compared with experiment.

is calculated in the following manner by use of a generated uniform random number R :

$$\Delta s = -\lambda_{el} \ln R \quad (5)$$

Energy Loss

The modified Bethe equation is

$$-\frac{dE}{ds} = \frac{2\pi e^4 n Z}{1.259\sqrt{JE}} \quad E < 6.338J \quad (6)$$

The energy range over which this equation is applicable is $E < 6.338$ keV for Au, assuming $J = 1$ keV for the mean ionization potential. Therefore, most of the calculations in this paper are based on Eq. (6).

The energy loss ΔE in each step length is calculated as follows:

$$\Delta E = \left| \frac{dE}{ds} \right| \Delta s \quad (7)$$

For studies of EREs the number of electrons with a constant small energy loss is calculated in a previous paper.⁷ The present paper adopts Jablonski's model, which introduces the inelastic mean free path λ_{in} and in which the electrons are not counted as the number but as the intensity, with the weighting factor of the following probability that an electron escapes from the sample without energy losses:

$$p(s_{tot}) = \exp(-s_{tot}/\lambda_{in}) \quad (8)$$

where s_{tot} is the total traveling path in the sample before the electron escapes from the sample.

Results and Discussions

Electron Penetration. The electron penetration depth is the most important physical quantity to affect the overall accuracy of the simulation model. We have previously checked³ the electron range as a function of energy in the energy range of few 100 eV to 10 keV. The result is shown in Fig. 4, which also shows the curve based on the ScR equation: it is linear in the log-log plot and underestimates the penetration depth as expected from the fact that the ScR cross section is overestimated in the medium-angle region and so makes penetration depth shallower. The model based on the Mott cross section predicts the experimental plots very well. The result shows a slight curving with a decreasing energy. We also investigated the energy dependence of the backscattering coefficient, the fractional backscattering as a function of film thickness, the transmission coefficient, the depth distributions of energy dissipation, and x-ray production and obtained fairly good agreement with experimental data. However, experiments below a few keV are difficult because very thin films are required. Therefore, to check the accuracy of the simulation at very low energies, it is very important to measure backscattering from bulk targets. In more details the angular distributions of backscattered electrons is more informative as to the validity of the model.

Angular Distributions of Elastically and Inelastically Reflected Electrons. (a) *Elastically reflected electrons (EREs).* EREs are defined as electrons that do not suffer any

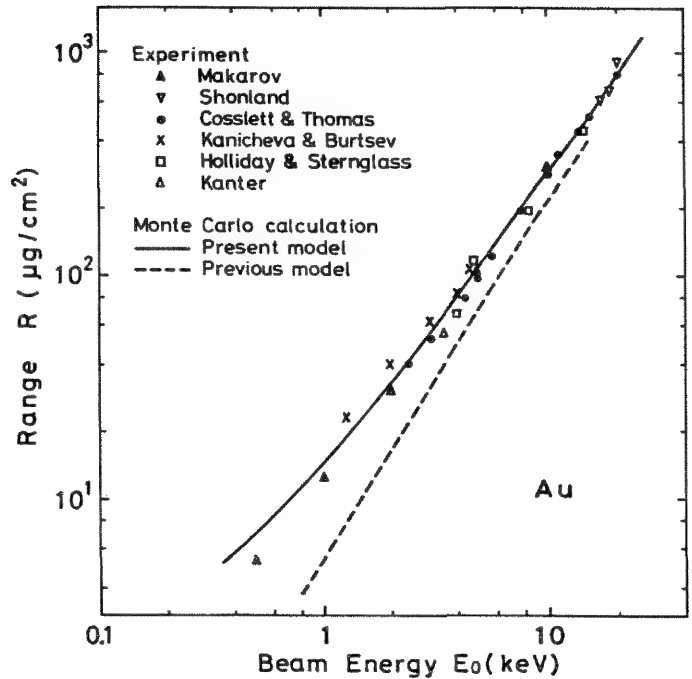


FIG. 4.--Extrapolated electron range as function of incident energy for Au (Kotera et al.³).

energy loss, so that they reflect the angular distribution due to elastic interactions between an electron beam and atoms. However, the phenomenon is complicated by the electrons that are scattered back through multiple collisions as well as by singly scattered electrons. According to the model described previously, the angular distribution $f(\theta)$ of EREs was calculated for an Au sample. The inelastic mean free path λ_{in} was calculated from the equation proposed by Seah and Dench,⁹ which has been used in Auger electron analysis. The intensity $I(\theta) \Delta\theta = 2\pi f(\theta) \sin \theta \Delta\theta$ of EREs was counted into each azimuthal angle of $\Delta\theta = 5^\circ$, which is integrated over the angles around the incidence axis due to symmetry. Then the intensity was divided by $\sin \theta$. In Fig. 5 typical results of $f(\theta)$ for normal incidence are compared with the experimental results of Bronshtein and Pronin¹⁰ in the polar diagram. Since the absolute value is not given for experimental data, both results are matched at $\theta = 155^\circ$. As seen from the figure, the positions of maxima and minima are predicted fairly well. Similar results are obtained at 0.8 and 1.5 keV. The comparison was made also at 0.1 and 0.2 keV. But the agreement is not good. The experimental curves do not show the significant maxima and minima predicted by the theory. It probably comes from a poor accuracy of the experiment because low-energy electrons are very sensitive to the surface roughness.

(b) *Inelastically reflected electrons (IREs).* IREs include electrons that have lost various amounts of energies. One of the interesting questions is whether the angular

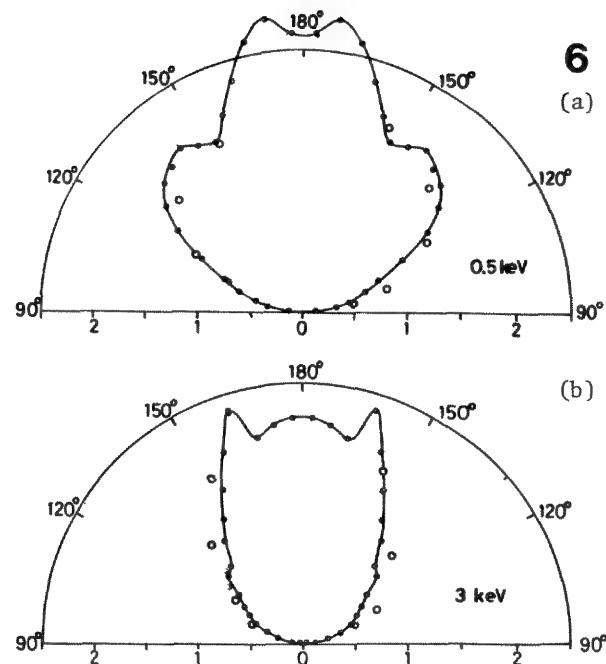
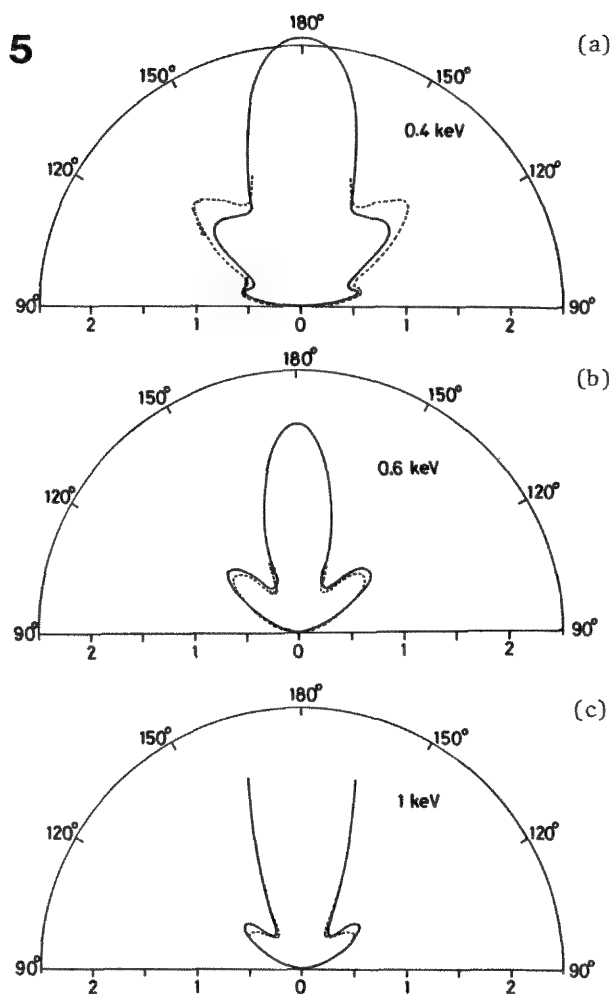


FIG. 5.--Angular distributions of EREs from Au targets in the polar diagram. Theoretical results (—) are compared with experimental ones (---) of Bronshtein and Pronin. FIG. 6.--Angular distributions of IREs at 0.5 and 3 keV. ● theory (Au), ○ experiment (W).

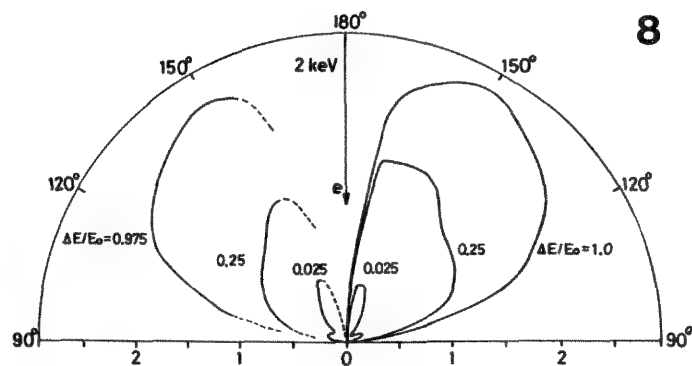
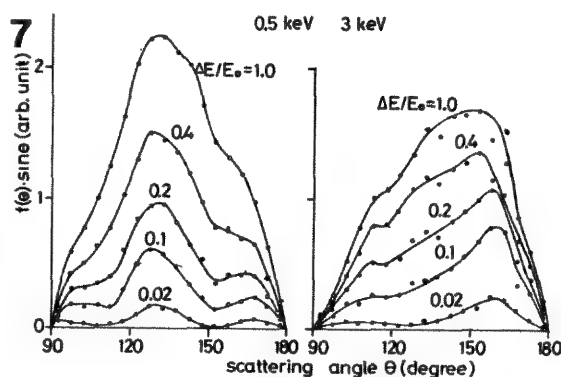


FIG. 7.--Curves of $f(\theta) \sin \theta$ for electrons with various energy losses for Au. Parameters in figure mean that all electrons that have suffered energy losses smaller than $\Delta E/E_0$ are counted. FIG. 8.--Curves of $f(\theta) \sin \theta$ in polar diagram: right, theory (Au); left, experimental (Ta) (Sommerkamp.¹²)

distribution of IREs shows anomalous distributions. Clear appearance of maxima and minima may not be expected as obtained in EREs. The theoretical results are compared with the experimental results¹¹ for W in Fig. 6 at 0.5 and 3 keV. The experimental data are measured between 90° and 155°. In this angle region both results show good agreement; no significant anomaly is seen. At 0.5 keV a dip is found around 150°, which seems to be caused by the

diffraction effect previously mentioned for EREs. The results do not simply follow the cosine law. Both results have a higher intensity in the right backward direction, reflecting a high scattering probability near 180°. It is not clear at present why the horn-shaped profiles appear in the backward direction; perhaps the effect is the result of large fluctuations due to a small number of electrons in this direction.

Let us try to classify IREs by energy. In Fig. 7 the angular distributions of $f(\theta) \sin \theta$ are shown for electrons with various energy losses: one counts the electrons with energy losses smaller than a certain amount of ΔE . The curve with $\Delta E/E_0 = 1.0$ corresponds to the results shown in Fig. 6 multiplied by $\sin \theta$. The results with the small energy loss of $\Delta E/E_0 = 0.2$ may be said to represent the angular distribution for EREs. Even for $\Delta E/E_0 = 0.2$ the diffraction effect is significant at 0.5 keV. Neither result follows the Lambert distribution of $f(\theta) = \cos \theta$ (actually, in the figure $f(\theta) \sin \theta$ is plotted) even though all electrons are detected. Present experimental data for Au are not available to compare with these theoretical results. In Fig. 8 the calculated results of $f(\theta) \sin \theta$ for Au are compared with the experimental results¹² for Ta at 2 keV. A similar tendency is seen in both results. It is especially interesting that for $\Delta E/E_0 = 50 \text{ eV}/2000 \text{ eV} = 0.025$, the maxima and minima are seen in both figures.

Conclusion

It is found that the Mott cross sections for Au are very accurate from a few keV down to 100 eV. Using a Monte Carlo simulation which incorporates these cross sections, we have investigated the electron penetration and backscattering with great success. The model has been extended to the study of the angular distribution of elastically and inelastically reflected electrons. The results were very good. The model can be applied to various problems in microbeam analysis at low primary beam energies. Further study is needed on the applicability of the model to other elements.

References

1. G. Wentzel, "Zwei Bemerkungen über die Zerstreuung korpuser Strahlen als Beugungserscheinung," *Z. Phys.* 40: 590, 1927.
2. J. W. Motz, H. Olsen, and H. W. Koch, "Electron scattering without atomic or nuclear excitation," *Rev. Mod. Phys.* 36: 881, 1964.
3. M. Kotera, K. Murata, and K. Nagami, "Monte Carlo simulation of 1-10-keV electron scattering in a gold target," *J. Appl. Phys.* 52: 997, 1981.
4. Shin-R. Lin, "Elastic electron scattering by screened nuclei," *Phys. Rev.* 133: A965, 1964.
5. E. Reichert, "Die Winkelverteilung im Bereich 30 bis 155 von elastisch an Golddampf gestreuten Elektronen mit Energien zwischen 150 und 1900 eV," *Z. Phys.* 173: 392, 1963.
6. T. S. Rao-Sahib and D. B. Wittry, "X-ray continuum from thick elemental targets for 10-50-keV electrons," *J. Appl. Phys.* 45: 5060, 1974.
7. K. Murata, H. Kawata, and K. Nagami, "Electron scattering in low voltage scanning electron microscope targets," *Scanning Microscopy Suppl.* 1: 83, 1987.
8. A. Jablonski, "Elastic backscattering of electrons from surfaces," *Surface Sci.* 151: 116, 1985.
9. M. P. Seah and W. A. Dench, "Quantitative electron spectroscopy of surfaces: A standard data base for electron inelastic mean free paths in solids," *Surf. Interface Analysis* 1: 2, 1979.
10. I. M. Bronshtein and V. P. Pronin, "Elastic reflection of moderate-energy electrons from solids," *Sov. Phys. Solid State* 17: 1363, 1976.
11. I. M. Bronshtein, V. M. Stozharov, and V. P. Pronin, "Angular distribution of inelastically reflected electrons," *Sov. Phys. Solid State* 14: 927, 1972.
12. P. Sommerkamp, "Elektronen-Rückstreuungsmessungen an Ta und Ni: Ein Beitrag zur Leistungsbilanz des Elektronen-Strahlschmelzens," *Z. angew. Physik* 28: 220, 1970.

PERFORMANCE OF A "CONVENTIONAL" MONTE CARLO PROGRAM AT LOW-BEAM ENERGY

D. E. Newbury and R. L. Myklebust

The increasing activity in microscopy, microanalysis, and microfabrication with low-energy electron beams, having incident energies of 5 keV or less, inevitably raises interest in modeling beam-specimen interactions in this energy range. Monte Carlo electron trajectory simulation has traditionally provided a powerful tool for such simulations.¹ In this paper, we examine the performance of a "conventional" Monte Carlo simulation, originally developed for application at intermediate beam energies, 10-200 keV, to the low-beam energy regime.²

Major Elements of the Monte Carlo Simulation

The "conventional" Monte Carlo simulation in use in our laboratory is based upon that of Kyser and Murata with extensive modifications to adapt it to specific problems of interest in microanalysis.²⁻⁴ This simulation assumes that the entire angular deviation of the beam electron arises from elastic scattering. The slight angular deviations due to inelastic scattering are ignored. Energy loss is treated as a continuous process rather than as a collection of discrete mechanisms because of the difficulty in describing the individual inelastic scattering cross sections.

The program makes use of the screened Rutherford cross section for calculating the mean free path λ due to elastic scattering:

$$\lambda = A/N_A \rho \sigma \quad (1)$$

$$\sigma = 5.21 \times 10^{-21} \frac{Z^2}{E^2} \frac{4\pi}{\alpha(1+\alpha)} \left(\frac{E + m_0 c^2}{E + 2m_0 c^2} \right)^2 \quad (2)$$

where E is the electron energy (keV), Z is the atomic number, A is the atomic weight, N_A is Avogadro's number, the rest mass energy equivalent is 511 keV, and α is the screening factor, given by

$$\alpha = 3.4 \times 10^{-3} Z^{0.67} / E \quad (3)$$

The partial cross section with respect to angle is used to calculate the angular distribution of elastic scattering:

$$d\sigma(\theta) = \frac{e^4 Z^2}{16(4\pi\epsilon_0 E)^2} \frac{d\Omega}{[\sin^2(\theta/2) + \alpha]^2} \quad (4)$$

The loss of energy from the primary electron due to inelastic scattering is calculated by means of the Bethe continuous energy-loss

approximation(keV/cm):⁵

$$dE/ds = -7.85 \times 10^4 (\rho z/AE) \log(1.66E/J) \quad (5)$$

where A is the atomic weight, ρ is the density, and J is the mean ionization potential given by⁶

$$J = (9.76Z + 58.5Z^{-0.19}) \times 10^{-3} \text{ (keV)} \quad (6)$$

When this Monte Carlo simulation is tested against published values of the electron backscatter coefficient at 20 keV, it is found to deviate systematically at high atomic number. To compensate for this effect, Kyser and Murata introduced a modification to the step length with the functional form³

$$\lambda^* = \lambda [1 + (Z/300)] \quad (7)$$

The need for this factor arises from the inaccuracy in the screened Rutherford elastic scattering cross section over certain ranges of scattering angle and atomic number, as has been noted by Krefting and Reimer.⁷ The performance of this Monte Carlo simulation with this path length modification is illustrated in Fig. 1. Excellent agreement is found between the experimental backscattering data of Heinrich⁸ and Monte Carlo calculations across the entire range of atomic numbers at a beam energy of 20 keV.

Backscattering as a Function of Beam Energy

To examine the performance of the Monte Carlo simulation at lower beam energy, calculations of backscattering as a function of atomic number were compared with experimental measurements at 10 keV (Heinrich⁸) and at 5 keV (Bishop⁹), as shown in Figs. 2 and 3. At both energies, the calculation systematically overestimates the backscattering coefficient for high-atomic-number targets. In order to correct for this deviation, an additional energy-dependent term is needed in the step length adjustment discussed above.

Monte Carlo calculations of backscattering as a function of beam energy over the range from 2.5-20 keV are shown in Fig. 4 for elements spanning a range of atomic numbers. The principal effect of reducing the beam energy below 10 keV is to increase the backscattering coefficient for high-atomic-number elements. The effect is especially significant at 2.5 keV. However, in view of the apparent failure of the simulation to describe adequately the experimental measurements of backscattering at high atomic number for 5 and 10 keV electrons, this result at 2.5 keV must be viewed as suspect.

The authors are with the Center for Analytical Chemistry, National Bureau of Standards, Gaithersburg, MD 20899.

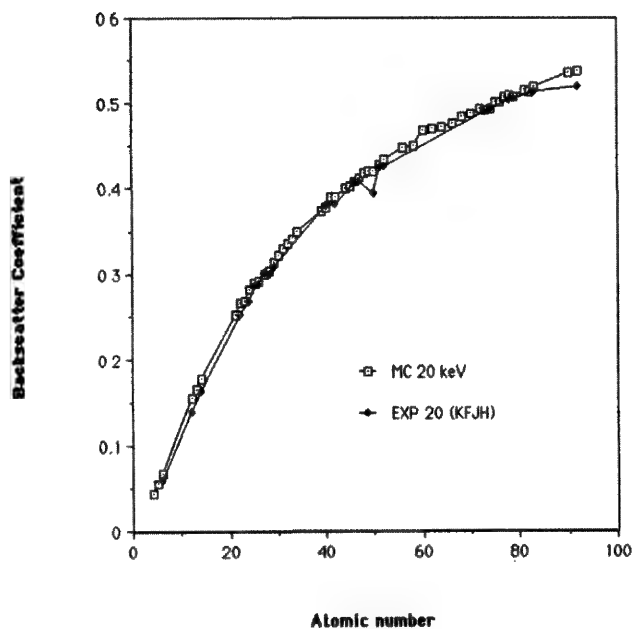


FIG. 1.--Comparison of backscattering coefficients at 20 keV as calculated by Monte Carlo simulation and as measured by Heinrich.⁸

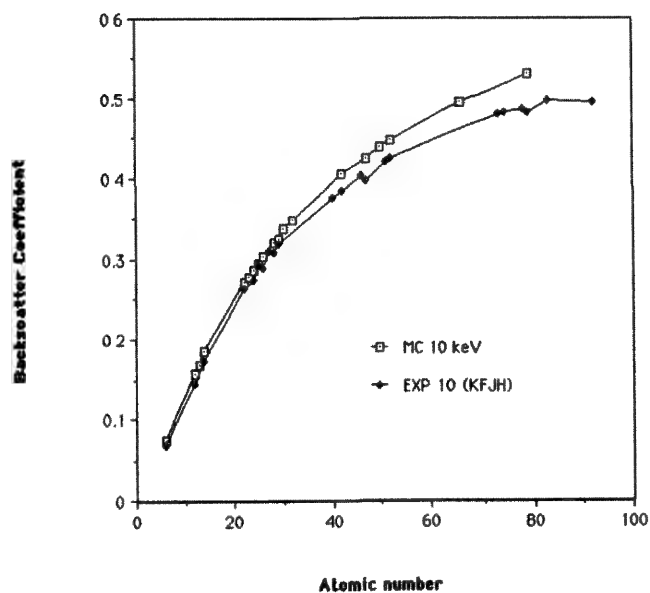


FIG. 2.--Comparison of backscattering coefficients at 10 keV as calculated by Monte Carlo simulation and as measured by Heinrich.⁸

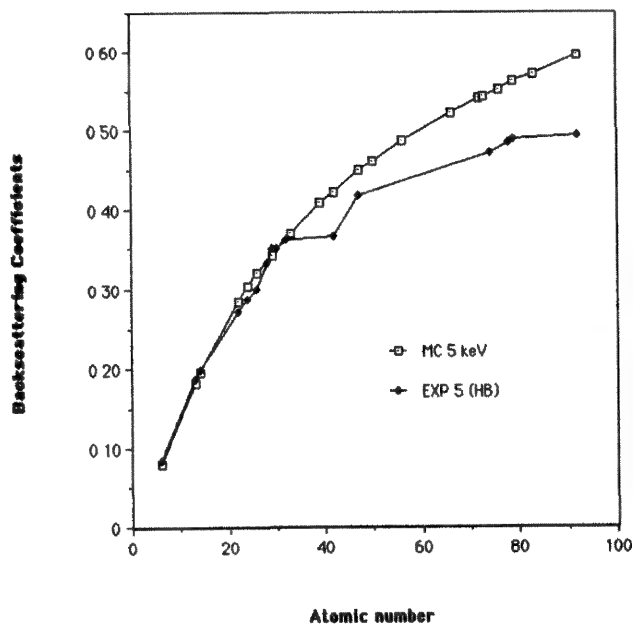


FIG. 3.--Comparison of backscattering coefficients at 5 keV as calculated by Monte Carlo simulation and as measured by Bishop.⁹

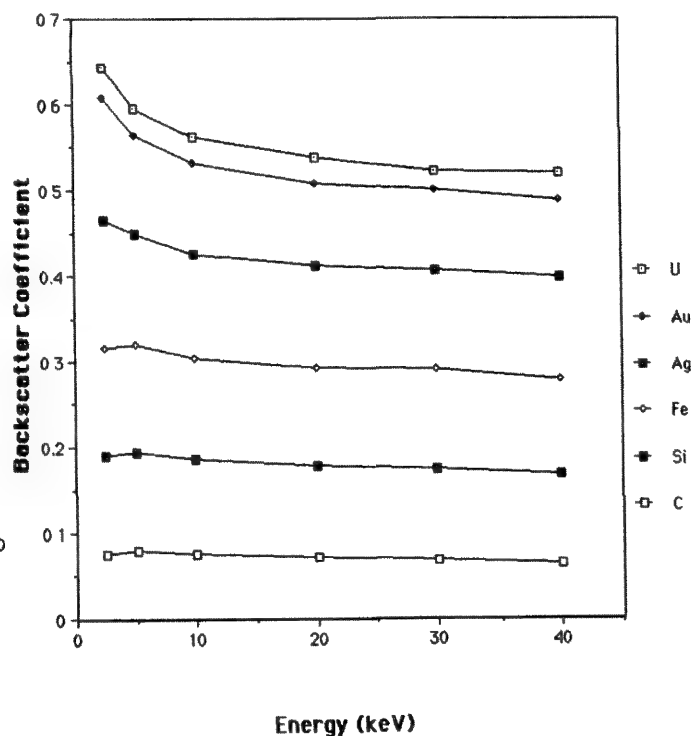
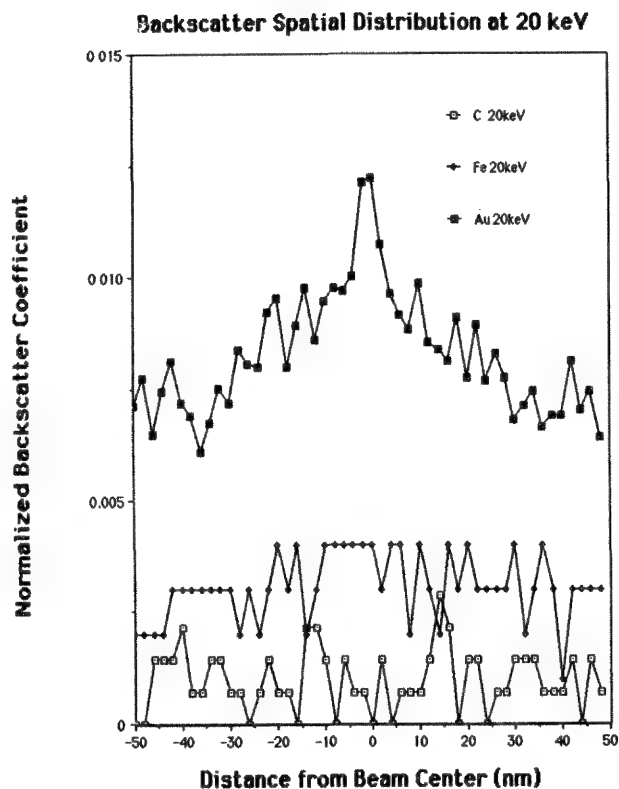
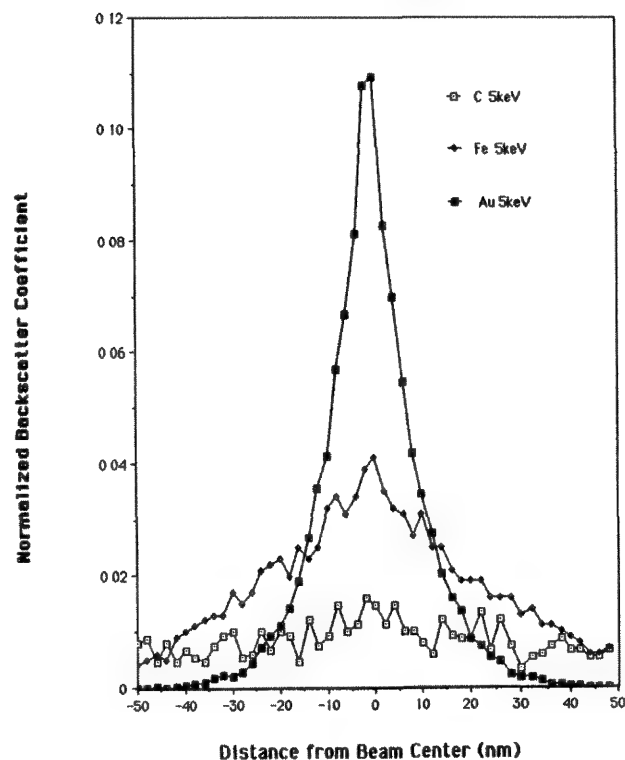


FIG. 4.--Backscattering coefficients calculated by Monte Carlo for various elements over energy range 2.5-40 keV.

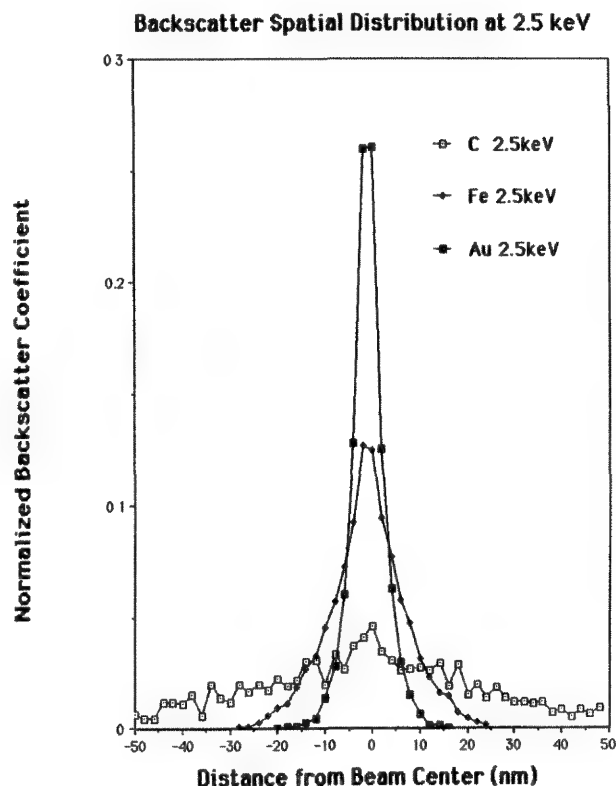
5



Backscatter Spatial Distribution at 5 keV 6



7



Iron Backscatter Spatial Distribution 8

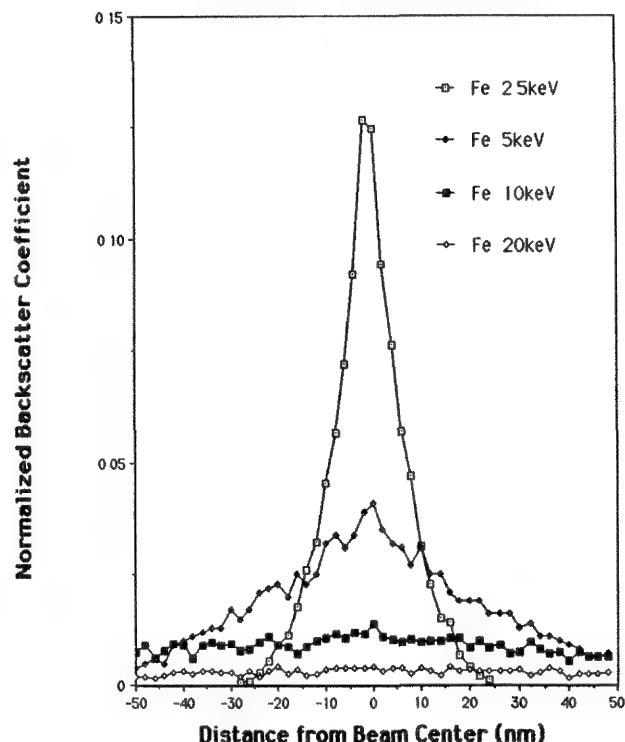


FIG. 5.--Spatial distribution of backscattered electrons calculated for 1nm-diameter probe incident at 20 keV on bulk targets of C, Fe, and Au.
 FIG. 6.--Spatial distribution of backscattered electrons calculated for 1nm-diameter probe incident at 5 keV on bulk targets of C, Fe, and Au.
 FIG. 7.--Spatial distribution of backscattered electrons calculated for 1nm-diameter probe incident at 2.5 keV on bulk targets of C, Fe, and Au.
 FIG. 8.--Spatial distribution of backscattered electrons calculated for 1nm-diameter probe incident on a bulk Fe target over energy range 2.5-20 keV.

Spatial Distribution of Backscattering at Low Beam Energy

As an example of the application of the Monte Carlo technique to an imaging problem, the spatial distribution of the backscattered electrons was calculated. This distribution was examined as a function of energy for targets of various scattering power, including C (weak), Fe (intermediate), and Au (strong). The results for a 1nm-diameter beam on the three targets at 20, 5, and 2.5 keV are summarized in Figs. 5, 6, and 7. The backscatter profiles for C and Fe at 20 keV show no peaks at the beam position; the Au profile reveals only a slight peak. At low energies, the backscattering profiles become much sharper, especially for gold. This progressive sharpening of the spatial distribution is readily seen in Fig. 8, where the distribution for iron is plotted across the energy range. The spatial distribution of the backscattered electron signal only approaches the beam diameter at low energies.

Depth Distribution of X-ray Production at Low Beam Energy

As an example of the application of the Monte Carlo calculation to a microanalysis

problem, the depth distribution of electron-excited Fe L x radiation was calculated over a range of energies (Fig. 9). Operation at beam energies of 5 keV and less produces a dramatic decrease in the generation depth of characteristic x rays. The depth distribution becomes so shallow at low energies that x-ray microanalysis under these conditions becomes highly surface sensitive.

References

1. K. F. J. Heinrich, D. E. Newbury, and H. Yakowitz, *Use of Monte Carlo Calculations in Electron Probe Microanalysis and Scanning Electron Microscopy*, National Bureau of Standards Special Publication 460, Washington, D.C., 1976.
2. D. E. Newbury and R. L. Myklebust, "Monte Carlo electron trajectory simulation of beam spreading in thin foil targets," *Ultramicroscopy* 3: 391-395, 1979.
3. D. F. Kyser and K. Murata, "Quantitative electron microprobe analysis of thin films on substrates," *IBM J. Res. Dev.* 18: 352, 1974.
4. D. E. Newbury and R. L. Myklebust, "Monte Carlo electron trajectory calculations of electron interactions in samples with special geometries," in *Electron Beam Interactions with Solids*, Chicago: SEM, Inc., 1984, 153.
5. H. A. Bethe, "Theory of the transmission of corpuscular radiation through matter," *Ann. Phys.* 5: 325, 1930.
6. M. J. Berger and S. J. Seltzer, *Tables of Energy Losses and Ranges of Electrons and Positrons*, Report NASA SP-3012, Washington, D.C., 1964.
7. L. Reimer and E. R. Krefting, "The effect of scattering models on the results of Monte Carlo calculations," in *NBS SP 460*, 45-60.
8. K. F. J. Heinrich, "Electron probe microanalysis by specimen current measurement," in *4th ICXOM*, Paris, 1965, 159-167.
9. H. E. Bishop, "Some electron backscattering measurements for solid targets," in *4th ICXOM*, Paris, 1965, 159-167.

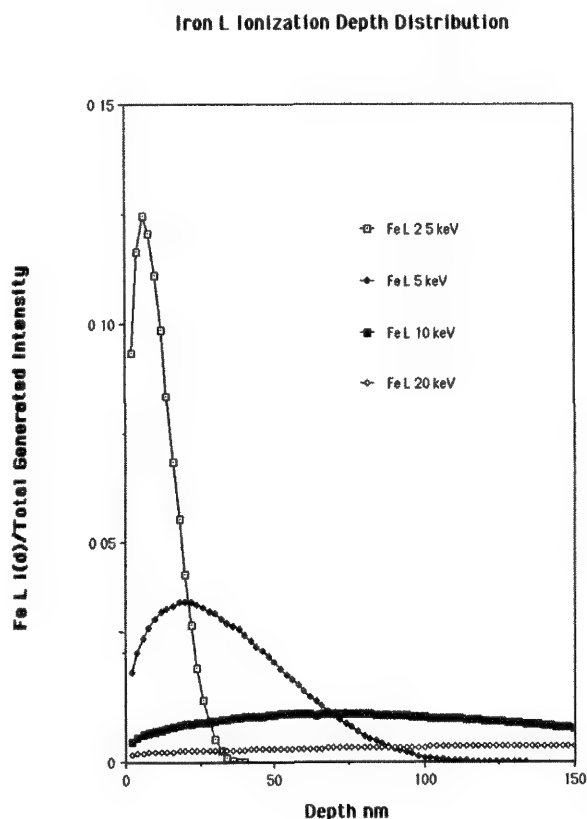


FIG. 9.--Depth distribution of electron-excited Fe L x-radiation as function of incident beam energy.

SIMULATION OF HIGH-RESOLUTION SEM IMAGES

David C. Joy

With the advent of scanning electron microscopes able to produce probes with diameters below 1 nm, interest in the use and interpretation of high-resolution secondary electron images is growing. Because at high resolution the effects of the electron beam interaction cannot be ignored, simple analytical models or optical analogies are of little value in understanding the images produced in this regime and detailed computations are required for interpretation. In this paper some preliminary Monte Carlo calculations on fundamental types of high-resolution image contrast are described. These simulations provide some basic data for evaluating and understanding these image effects and also help to clarify the electron-optical constraints imposed on these classes of images.

Principles of Simulation for Secondary-electron Images

In order to compute the expected form of a secondary-electron (SE) image it is necessary to determine the spatial distribution of SE within the sample as a function of the incident beam position and then to calculate the fraction of these SEs that escape from the specimen and can be detected. One approach to this problem^{1,2} has been to use a plural-scattering Monte Carlo simulation to compute the details of the primary beam interaction, and to employ the simple model described by Salow to find the spatial distribution of the secondary generation.³ The escape probabilities are found by a geometrical evaluation that assumes an exponential decay law. This procedure has the advantage that it is economical of computer time and when it has been used to simulate SE profiles from structures of specified geometry and composition, the results have been shown to be in excellent qualitative and quantitative agreement with comparable experimental data.⁴ However, the method is not suitable for high-resolution simulations because the Monte Carlo program divides the electron range into typically fifty steps of equal length. The granularity of the simulation is thus about 2% of the Bethe range, i.e., 50 to 60 nm for carbon at 15 keV, and it is lower than this figure. This procedure is therefore restricted to image magnifications below about 5000 \times .

The author is with the EM Facility, University of Tennessee, and the Metals and Ceramics Division, Oak Ridge National Laboratory. This research was sponsored by the DOE Division of Materials Sciences under contract DE-AC05-84OR21400 with Martin Marietta Energy Systems, Inc.

An alternative method^{5,6} has been to employ a single-scattering Monte Carlo simulation for the incident electron trajectories and to incorporate a mechanism for the generation of fast secondary electrons (FSE). These FSE are then individually tracked from their point of generation until they either escape from the specimen or are absorbed. This procedure is capable of the necessary spatial resolution, but the assumption that the FSE signal properly models the magnitude and behavior of the complete SE signal, though surprisingly good at high beam energies (> 20 keV), is increasingly unrealistic at lower beam energies.

The results discussed in this paper were obtained by an approach that combines aspects of both the above models. The incident electron trajectories are modeled by a single-scattering simulation that employs a Bethe continuous energy-loss approximation with the Rao Sahib-Wittry low-energy modification⁷ and a screened Rutherford cross section. This model is described in detail elsewhere.^{8,9} Since the typical step size is now a fraction of the electron mean free path, and thus of the order of a few nanometers, the granularity of the simulation is of the same scale and is thus consistent with the pixel size necessary for high-resolution microscopy. The Salow model³ for SE generation, which equates secondary production with the stopping power of the sample, is used as before to compute the rate of secondary generation, but the escape probability of the SE signal is computed on a point-by-point basis as discussed below.

Modeling Procedure

It is conventional to discuss the SE image in terms of two components:^{10,11} the SE1, which consists of secondaries generated by the incident beam as it impacts the specimen and before it undergoes any significant scattering; and the SE2, which are secondaries produced by multiply scattered primary and back-scattered electrons. The SE1 electrons emerge from a region of only a few nanometers in diameter about the incident beam point⁶ and so carry the high-resolution image information. However, the SE1 component can only contribute to the image when both the probe size and the pixel size are comparable with the diameter of this excitation volume. Thus both a high-performance SEM (for a small probe size) and a high ($>20\,000\times$) operating magnification are prerequisites. The SE2 signal component provides the image detail at low magnifications (20 to 5000 \times), but at high magnification only acts to provide a more or less constant background to the desired SE1 signal. Thus, although the SE2 do not contribute useful infor-

Z \ Y	2.7	2.5	2.3	2.1	1.9	1.7	1.5	1.3	1.1	0.9	0.7	0.5	0.3	0.1
0.1	365	368	370	371	375	379	386	391	400	410	422	449	490	565
0.3	243	243	246	248	249	254	259	268	276	286	306	338	385	
0.5	173	176	177	180	182	188	194	200	209	224	247	283		
0.7	127	131	133	136	137	141	148	157	168	183	210			
0.9	100	102	105	108	111	112	118	128	141	159				
1.1	76	77	78	80	85	92	99	108	120					
1.3	59	61	63	65	70	76	82	93						
1.5	47	49	52	56	60	64	72							
1.7	38	40	43	47	51	56								
1.9	32	34	37	40	45									
2.1	27	29	32	36										
2.3	22	24	26											
2.5	20	21												
2.7	17													

FIG. 1.--Matrix $p[y,z]$ showing escape probability for secondary electrons in vicinity of infinite half plane edge; y and z are in units of λ .

mation to the high-resolution image, their presence does affect the contrast level and the signal-to-noise ratio achieved, and hence the required threshold current for imaging. A knowledge of both the SE1 and SE2 components is therefore required when one assesses the form, magnitude, and likely visibility of a given feature. The practical details of SEM operation that make it possible to observe the SE1 component have been described elsewhere¹¹ and will not be considered here.

In order to model the SE1 contribution accurately the escape probability for secondaries at any given position within the sample must be known. The procedure used here has been to assume that the probability $p(s)$ of a secondary traveling some distance s is

$$p(s) = \exp(-s/\lambda) \quad (1)$$

where λ is the averaged mean free path for the emerging secondaries. This "straight-line approximation" implies that a secondary is either unscattered or absorbed, and although an oversimplification,¹² it does give good agreement with experiment under most conditions. Given

Escape probability $p[Y,Z]$
in units of 0.001 for infinite edge

By symmetry $p[Y,Z]=p[Z,Y]$

a specified sample geometry, the escape probability $p(x,y,z)$ from the point (x,y,z) can then be found by averaging $p(s)$ over the surface of interest, assuming isotropic secondary generation. By invoking the result of the "mean value theorem,"¹³ this process can be rapidly carried out by a simple Monte Carlo procedure. Figure 1 shows part of the matrix of $p(y,z)$ values for the region around a half-plane edge of infinite extension. The edge runs parallel to the x axis, so there is no x variation, and y and z are given in units of λ .

Along some segment δs of the trajectory, from (x,y,z) to (x_n,y_n,z_n) , the number of secondaries generated n_{SE} is given by

$$n_{SE} = - \frac{1}{\epsilon} \frac{dE}{ds} \delta s \quad (2)$$

where ϵ is the average energy needed to produce a secondary electron and dE/ds is the energy loss. The incremental SE1 signal is then

$$\Delta SE1 = n_{SE} \langle p(x,y,z) \rangle \quad (3)$$

where $\langle p(x,y,z) \rangle$ is the average of $p(x,y,z)$ from x,y,z to x_n,y_n,z_n computed along the segment of the trajectory. Since by definition SE1 production is associated with the initial entry of the primary electron into the solid, only the first few scattering events need be considered in this detailed way. Since under these conditions n_{SE} varies only slowly with incident beam energy, and because the lateral scattering of the beam within this surface region is small, the form of the SE1 image is determined essentially by the matrix $p(x,y,z)$ and so is not strongly dependent on beam energy. Within the simulation the SE1 component is stored separately from the total SE yield to give the best statistical accuracy in the final result.

Outside the near surface region the primary beam is increasingly scattered, and secondary production resulting from these events form the SE2 contribution to the image. Since the beam has now diffused away from the impact point, these SE carry no high-resolution information. Their incremental contribution to the SE2 yield is then written as

$$\Delta SE2 = n_{SE} p'(x,y,z) \quad (4)$$

but the escape probability $p'(x,y,z)$ is now found by an analytical approximation² in which

$$p'(x,y,z) = A \sum_i \exp(-d_i/\lambda) \quad (5)$$

where A is a constant of order 0.5, the d_i are the perpendicular distances to each of the free surfaces around (x',y',z') , and $x' = (x + x_n)/2$, etc.

This composite procedure is applied for each of the electron trajectories simulated, typically 5000 per pixel, and sufficient pixels are computed to form a line profile or two-dimensional map of the feature of interest. The code to implement these steps is written in Turbo Pascal and is run on an AT&T 6300PC equipped with an 8086 maths processor. Each pixel typically takes between 10 and 25 minutes to compute depending on the details of the problem. The result of this procedure is a profile containing both the high-resolution SE1 information and the lower-resolution SE2 intensity variations.

Edge Contrast Effects

The brightness that occurs in the vicinity of an edge, arising from the extra escape paths available to the secondary electrons, is one of the most characteristic features of the secondary-electron image. Because this brightness enhances the visibility of the edge it is a significant factor, at low magnifications, in helping to outline the morphology of the specimen, but at higher magnifications the excess brightness is more often a nuisance since it can obscure wanted detail. However, under high-resolution conditions the edge brightness again becomes useful because it serves to delineate the outlines of features that might otherwise be obscured by the poor signal-to-noise ratio. Figure 2 shows the computed profile for an edge in silicon, observed at 30 keV and assuming a 10A Gaussian probe. It can be seen that the excess brightness is visible for many micrometers from the edge, with the SE signal level approximately doubling for a region about 1 to 2 μm in extent along the edge. This edge effect, which is clearly visible at low magnifications, comes from the SE2 component of the beam interaction. The electron range at 30 keV is of the order of 10 μm , so for probe-to-edge spacings of less than this distance an increasing fraction of primary electrons reaches the edge and generates SE2 electrons. The true SE1 edge effect, which is much more dramatic in scale, occurs very close to the edge and so is only seen as a "spike" in Fig. 2. In Fig. 3 the profile in the edge region is replotted on a larger scale to show the SE1 component, now visible as a narrow and approximately Gaussian distribution about 1.3 units high and about 4 nm FWHM, superimposed on the slowly varying SE2 profile, which has a peak intensity of about 1.5 units (i.e., about 5 times the total SE yield at 10 μm from the edge). The existence of two separate contributions to the overall profile is clearly evident from the change in slope, which occurs about 10 nm from the edge.

At a lower beam energy, such as 15 or 5 keV, the form of the profile remains much as shown in Fig. 3, but the visibility (defined as the peak SE signal to the average SE signal intensity) falls because the average level of the SE2 component rises more rapidly than the contribution from the SE1 component. However, the predicted FWHM of the SE1 signal profile remains constant at about 4 nm. This width is a function both of the probe diameter, here taken to be 1 nm, and of the secondary electron mean free path λ , which for silicon has an effective value of 3 nm when averaged over the energy distribution of the emerging secondaries.¹ Since for most common materials λ falls between 2.5 and 5 nm, the width of the SE1 edge brightness feature is typically 4 to 6 nm, in agreement with experimental observations.^{1,4} Increase in probe diameter leads to an increase in the apparent width of the edge brightness, but most markedly leads to a reduction in the contrast and visibility of the bright fringe. Thus, changing from a 1nm to a 2nm probe at 30 keV increases the fringe width to about 4.5 nm FWHM, but reduces the visibility by about 30%. The visibility (and width) of the SE1 bright edge fringe is therefore a good guide to the dimension of the electron probe diameter and clear resolution of this feature is only probable for probe diameters below about 2.5 nm. Experimentally measured values of the edge brightness visibility ratio tend to be lower than the 2.5 or 3 to 1 ratios predicted, because the image transfer function of an SEM is determined not only by the probe-forming lens but also by the bandwidth and slew rate of the video chain of the instrument. Even on high-performance microscopes the performance of the video electronics is often less than ideal⁴ and a reduction in the usable resolution and a consequent fall in visibility is to be anticipated.

Particle Contrast

Most samples of interest are bounded by more than one edge, and many of the most important (such as macromolecules, semiconductor interconnects, and fibers) are defined by two edges with some variable spacing between them. When this spacing becomes small enough, the contrast profile across the feature is dominated by the edges themselves rather than by the characteristics of the specimen. The magnitude of this critical spacing is again a function of the secondary electron mean free path λ . Figure 4 shows profiles across a feature 6 nm high and 15, 9, and 6 nm wide. The actual computations were carried out for silicon, for which λ is 3 nm, and assuming a 1nm probe at 15 keV. At 15 nm (i.e., 5λ wide) the two edges are clearly resolved and the central dip is about 8%; but at 9 nm (3λ wide) and 6 nm (2λ wide), the SE1 edge brightness rims have almost merged to provide a profile in which the boundaries of the feature have disappeared and only the centroid position can be located. Peters¹¹ has called this effect "particle contrast,"

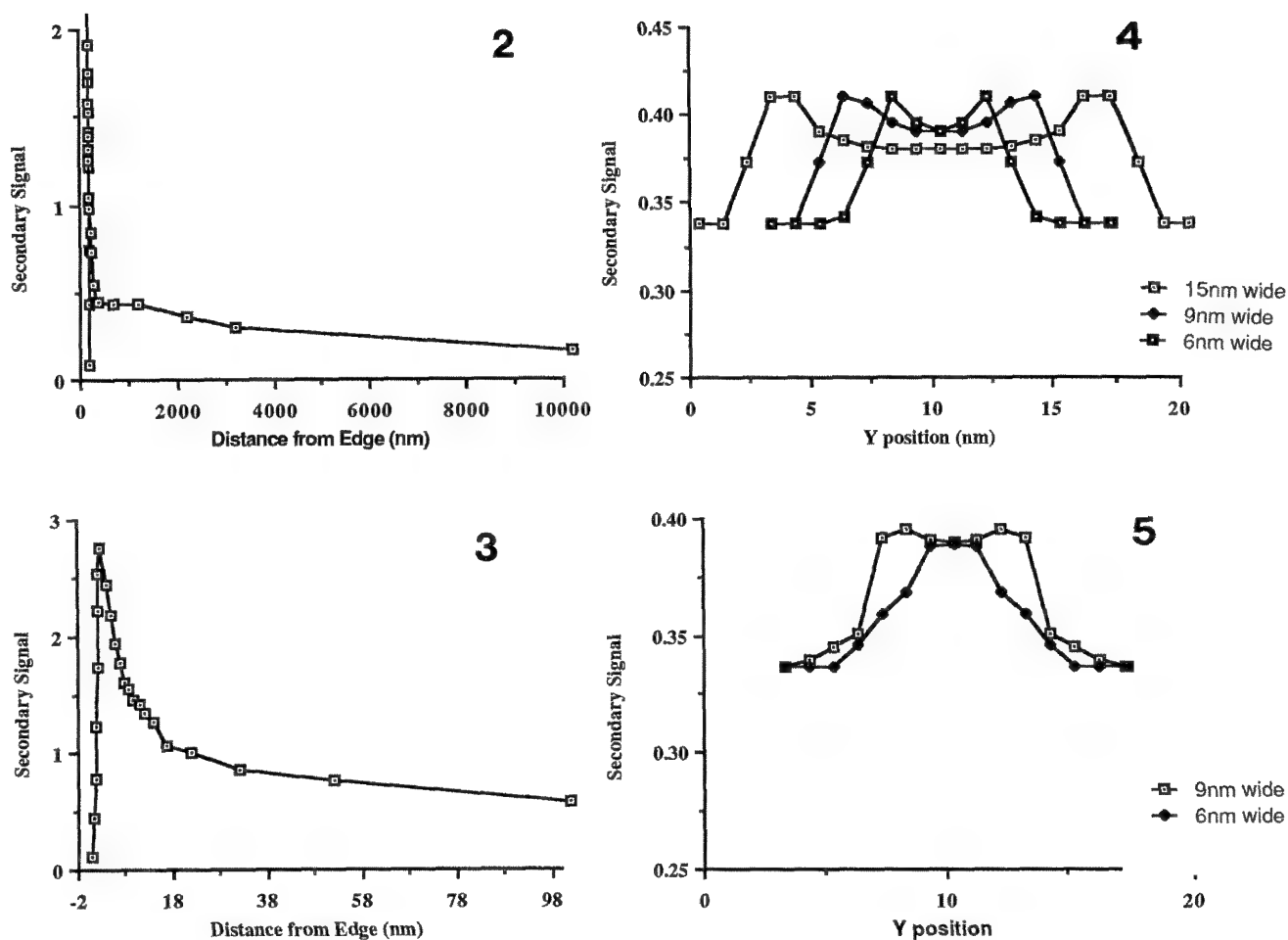


Fig. 2.--Computed signal profile across an infinite half-plane edge, for silicon at 30 keV and 1nm-diameter probe.

FIG. 3.--As Fig. 2 but on expanded distance scale.

FIG. 4.--Secondary-electron signal profiles across silicon feature 6 nm high and 15.9, and 6 nm wide, computed for beam energy of 15 keV and probe diameter of 1 nm.

FIG. 5.--Corresponding SE profiles across the 9nm- and 6nm-wide features made by 2nm probe diameter at 15 keV.

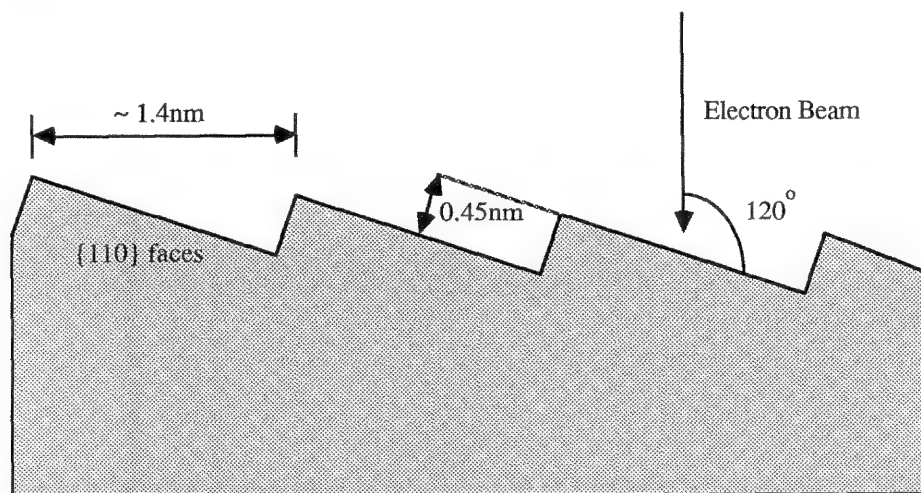


FIG. 6.--Proposed surface structure giving rise to "lattice fringe" images.

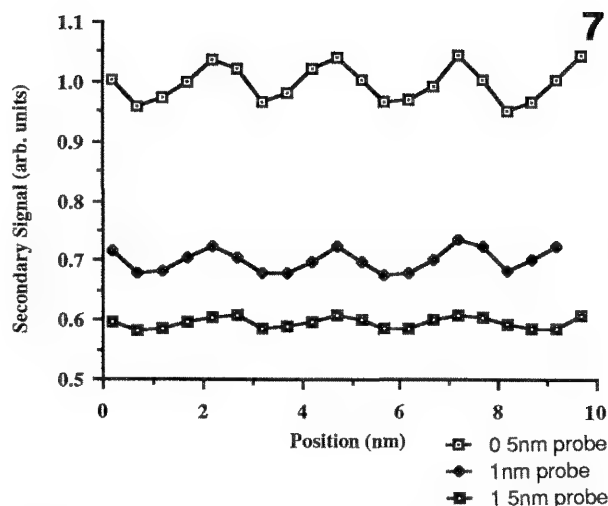


FIG. 7.--Computed SE profiles for structure and beam geometry of Fig. 6, at 15 keV, for probe diameters of 0.5, 1, and 1.5 nm.

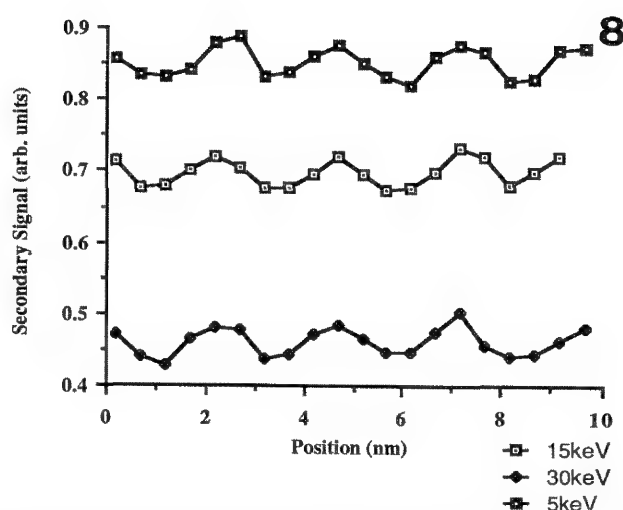


FIG. 8.--Corresponding profiles for 1 nm probe at 30, 15, and 5 keV.

and it is an undesirable condition because the profile is then essentially independent of the detailed morphology of the specimen and consequently conveys no useful information. Profiles from carbon (for which λ is 5.5 nm) or gold (for which λ is 1 nm) would be similar but the absolute spacing would be scaled by the change in secondary mean free path.

Although the data of Fig. 4 suggest that with a 10A probe features as narrow as 10 nm could be correctly resolved as spaced edges, that is actually an optimistic assessment because signal-to-noise effects have not been considered. For example, in order to visualize the 8% contrast dip at the center of the 15nm-wide feature in a scan time of 10 s, a threshold current of 6×10^{-11} A is required. Assuming a field-emission gun with a brightness β of 3×10^7 A/cm²/sterad at 15 keV, and a probe-forming lens with a C_s of 2 mm, the current available in a 1nm probe would only be about 4×10^{-11} A. Thus only by using long photoscans could one make the contrast visible. Use of a larger probe diameter makes the situation even less favorable (Fig. 5) because although significantly more beam current is available (e.g., 3×10^{-10} A into a 2nm probe for the conditions quoted above) the contrast has been considerably reduced and the threshold current required has risen more rapidly than the available probe current. At other beam energies the situation is similar. Increasing the incident beam energy raises the gun brightness and hence the beam current, but the overall signal level and contrast fall; and at lower beam energies the contrast is enhanced and the signal levels are higher but the probe current has fallen and it becomes increasingly difficult electron-optically to generate a probe of acceptable profile and diameter.¹⁵

The general principles illustrated by the specific problem addressed here show that any detail in structures spaced by less than 15 nm is likely to be lost due to the onset of par-

ticle contrast effects, even in the highest performance instruments. The use of thin metal coating films to generate edge-specific mass-thickness contrast is thus an essential technology in the utilization of high-resolution secondary imaging. A basic explanation of the theory of this type of imaging is given elsewhere.⁶

"Lattice Fringes"

The images of a tungsten field-emitter tip obtained by Kuroda et al.¹⁶ show regions of periodic contrast resembling "lattice fringes" in an TEM image. Monte Carlo methods cannot incorporate diffraction phenomena nor are they consistent with atomic-level resolution, because they implicitly assume a continuum model of the sample, and so for 'real' lattice fringes alternative methods of analysis would have to be employed.¹⁷ However, in the case demonstrated by Kuroda et al. the origin of the contrast is proposed to be the structure shown in Fig. 6, consisting of a periodic sequence of double steps at the end of (110) planes 0.45 nm high and separated by about 1.4 nm. The contrast is thus a special case of edge contrast and should be capable of being simulated by the model discussed above, even though it would be anticipated that the contrast will be low because the height of the step and the spacing of the edges are both less than the secondary mean free path for tungsten ($\lambda = 2$ nm).

The value of $p(x,y,z)$ was calculated for the structure by use of the Monte Carlo integration method and on the assumption that the steps were infinite in the x direction. The matrix was computed at steps of 0.1λ spacing. Figure 7 shows the resultant computed SE profiles for the geometry used by Kuroda et al. and shown in Fig. 6, a beam energy of 15 keV and probe diameters of 0.5, 1, and 1.5 nm. For clarity, the SE2 contribution to the signal has been partially suppressed in this plot, and the vertical axis has been shifted. Even

though the simulated data are statistically noisy, the periodic but asymmetric modulation of the profile is clearly evident. For a probe size of 0.5 nm the peak-to-peak contrast level is about 8%, falling to about 5% for a 1 nm probe and to only about 2% for a 1.5 nm probe. Since all contrast has disappeared by the time the probe diameter reaches 2 nm, it is fair to say that for contrast of this type to be visible the probe diameter should be less than about half the periodic spacing. If the beam energy is increased to 30 keV (Fig. 8) the contrast for a 10 Å probe rises to about 8% peak to peak because the scattering of the beam in the near surface region is reduced and the SEI contribution to the signal falls less rapidly than the total SE production. However, the reduction of the beam energy to 5 keV lowers the contrast, for the same probe size, to only about 4%, although the overall SE signal has increased. If the threshold current criterion is considered, as above, it is clear that this type of contrast mechanism is likely to be observed only on field-emission SEMs which are able to generate probes of 1 nm or less in diameter containing the necessary current. Even then high beam energies and long photo-record times will still be required. Other simulations show that this fringe-like contrast varies only slowly with the beam geometry relative to the lattice, whereas fringes generated by a diffraction process depend strongly on the beam orientation to the crystal. Consequently accurate alignment of the surface will not be required.

Summary

The Monte Carlo simulation procedure described here allows an initial understanding of the principles of contrast formation in high-resolution secondary images to be achieved. The agreement with experimental results is good in view of the lack of reliable data for many of the parameters of the electron beam-solid interaction required in the computation; when more quantitative imaging data from high-performance SEMs becomes available, it should be possible to refine these models and make them useful tools for image interpretation.

References

1. D. C. Joy, "A model for calculating secondary and backscattered electron yields," *J. Microscopy* 147: 51, 1987.
2. D. C. Joy, "Image simulation for the SEM," *Microbeam Analysis--1987*, 105.
3. H. Salow, "Sekundärelektronen-Emission," *Phys. Z.* 41: 434, 1940.
4. M. T. Postek and D. C. Joy, "Microelectronic dimensional metrology in the SEM," *Solid State Technology* 29(11): 145 and 29(12): 77, 1986.
5. D. C. Joy, "Beam interactions, resolution and contrast in the SEM," *J. Microscopy* 136: 241, 1984.
6. D. C. Joy, "Monte Carlo studies of high

resolution imaging," *Microbeam Analysis--1984*, 81.

7. T. S. Rao Sahib and D. B. Wittry, "X-ray continuum from thick elemental target," *J. Appl. Phys.* 45: 5060, 1974.
8. R. L. Myklebust, D. E. Newbury, and H. Yakowitz, "The NBS Monte Carlo electron trajectory program," in K. F. J. Heinrich, Ed., *Use of Monte Carlo Calculations in EPMA and SEM*, NBS Special Publication 460, 1979, 105.
9. D. C. Joy, "The interpretation of EBIC images using Monte Carlo simulations," *J. Microscopy* 143: 233, 1986.
10. H. Drescher et al., "Rückstreuoeffizient und Sekundärelektronen Ausbeute von 10-100 keV," *Z. angew. Phys.* 29: 331, 1970.
11. K.-R. Peters, "Generation, collection and properties of an SEI enriched signal," in D. Kyser et al., Eds., *Asilomar Workshop on Electron Beam Interactions*, Chicago: SEM Inc., 1984, 333.
12. Luo Suichu et al., "A Monte Carlo calculation of secondary electrons emitted from Au, Ag and Cu," *J. Microscopy* 148: 289, 1987.
13. P. K. MacKeown and D. J. Newman, *Computational Techniques in Physics*, Bristol: Adam Hilger, 1986, 137.
14. R. P. Apkarian, "High resolution signal detection," *Proc. 44th Ann. Conf. EMSA*, 1986, 658.
15. D. C. Joy, "Low voltage scanning electron microscopy," in J. N. Chapman and A. J. Craven, Eds., *Electron Microscopy and Microanalysis*, Bristol: Institute of Physics, Conf. Ser. 90, 1987, 175.
16. K. Kuroda et al., "Observation for crystal surface of W <110> field emitter tip by SEM," *J. Elect. Microsc.* 34: 179, 1985.
17. A. Howie et al., "Channelling effects in high resolution scanning electron microscopy," *Phil. Mag.* 23: 1559, 1971.

SECONDARY ELECTRON YIELD MEASUREMENTS IN THE SCANNING ELECTRON MICROSCOPE

T. E. Rothwell and P. E. Russell

Low voltage Scanning Electron Microscopy (SEM) is used frequently in integrated circuit manufacture and in other applications where specimen charging and/or beam damage must be avoided. To minimize charging of uncoated specimens, the SEM should be operated at a low beam voltage, where the secondary-electron (SE) yield is at or near unity. SE yield is highly dependent on the primary-beam energy at low operating voltages, and the crossover voltage (at which the SE yield equals unity) is material dependent. One should know the electron yield of materials when imaging at low voltages, since changing the primary beam voltage by as little as 0.1 keV can result in useful imaging vs charging. Secondary-electron emission in the SEM has recently been reviewed by Seiler.¹ In this study methods were developed for measuring secondary-electron yield as a function of voltage; gold, carbon, and silicon were used as experimental samples. The yield was determined experimentally by use of a retarding field grid and absorbed-current measurements in an SEM; the experimental results were compared with values generated by a Monte Carlo model of electron production. In addition, the electron energy vs the number of emitted electrons was measured at a series of beam energies for the materials whose SE yield curves were found with the SEM. The curves were found with a cylindrical mirror analyzer (CMA) in an Auger microprobe in which samples can be sputtered in situ with an ion gun.

Experimental Procedure

The electron yields were measured in an SEM with a sample holder containing an integral Faraday cup and shielded by a hemispherical retarding field grid (Fig. 1). A microscope with a lanthanum hexaboride filament was operated from 0.2 to 5.0 keV in steps of 0.1 keV and from 5 to 20 keV in 1keV increments. Absorbed current was measured at each incremental beam voltage both with and without the retarding field applied, and current balance equations were used to calculate the secondary and backscattered electron currents.

The beam current i_{beam} was measured with a Faraday cup. The current absorbed by the spec-

imen, i_{absorbed} , was measured with an ammeter connected to the specimen stage. The total emitted current, i_{emitted} , was calculated by use of the principle of charge conservation. The total yield is defined as the number of electrons leaving the sample divided by the beam current.

$$\sigma = \frac{i_{\text{SE}} + i_{\text{BSE}}}{i_{\text{beam}}} = \frac{i_{\text{beam}} - i_{\text{absorbed}}}{i_{\text{beam}}} \quad (1)$$

The backscattered electron yield was independently measured by biasing of the retarding field grid at -50 V. The grid repels the secondary electrons back into the sample and allows only the backscattered electrons to pass through. The backscattered yield can be calculated from current measurements taken with the retarding field on.

$$\eta = \frac{i_{\text{BSE}}}{i_{\text{beam}}} = \frac{i_{\text{beam}} - i_{\text{biased}}}{i_{\text{beam}}} \quad (2)$$

Since the total electron yield and the backscattered electron yield can both be experimentally determined the secondary electron yield δ can be found by difference, $\delta = \sigma - \eta$.

In addition, the number of electrons vs electron energy was measured by means of a cylindrical mirror analyzer (CMA) in an Auger microprobe. In a dispersive energy analyzer such as a CMA, the electrons are deflected by electrostatic fields; only a small energy band of electrons traveling in a specific direction is allowed to pass through the CMA to the detector at any one time, and one obtains entire energy spectrum by varying the deflection conditions. As in all dispersive energy analyzers, simply scanning the potential -V applied to the outer cylinder of the CMA gives the energy distribution of electrons passing through it directly, but because the transmission varies with E_0 , $E^*N(E)$ times the channelton detector response function is the energy distribution obtained.² The $E^*N(E)$ spectrum is obtained by direct recording of the output from the electron multiplier by use of beam brightness modulation (BBM).³ The $E^*N(E)$ spectra were measured by direct modulation of the primary beam intensity, as first proposed by Seah.⁴ Plots of intensity $E^*N(E)$ vs the kinetic energy of the emitted electrons were obtained at a series of primary beam voltages from 0.25 to 2.5 keV. The energy term was factored out of the intensity so that the number of electrons at a given energy was known. (The detector response was not cor-

T. E. Rothwell is with the IBM Research Triangle Park Materials Engineering Laboratory, Box 12195, Research Triangle Park, NC 27709; P. E. Russell is at North Carolina State University. This work was done as part of T. E. Rothwell's master's thesis. We acknowledge the support of the Microelectronics Center of North Carolina and Dr. D. C. Joy.

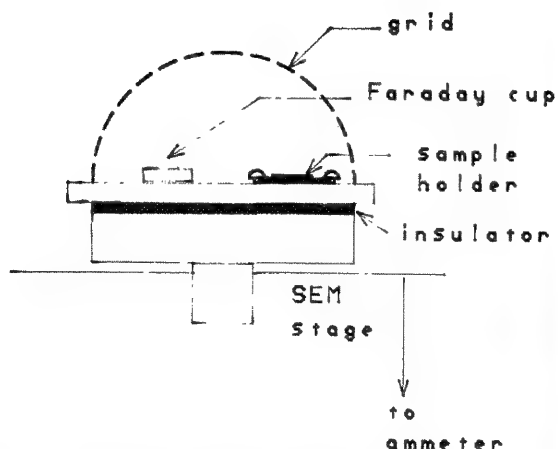
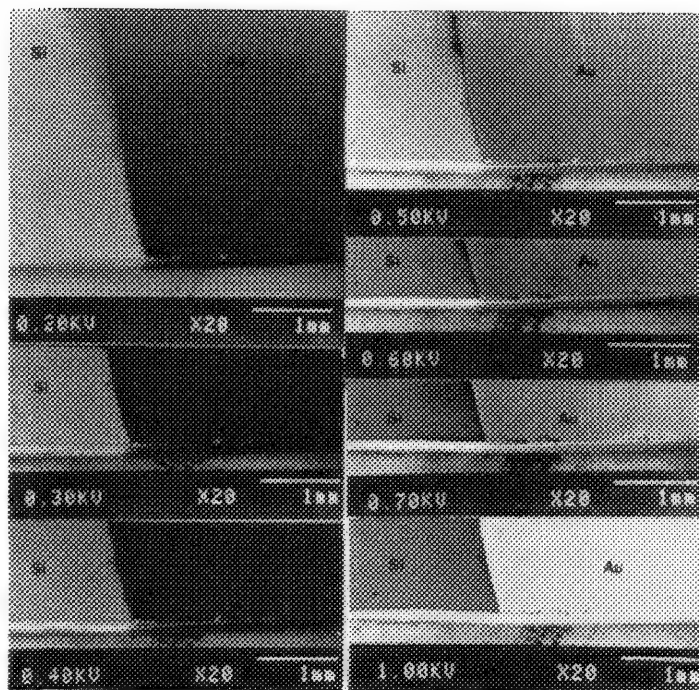


FIG. 1.--Experimental set up. Sample holder consists of integral Faraday cup recessed into lin.-diam. aluminum Hitachi sample stub and a pair of screws used to attach mounted samples, so that samples can be interchanged easily and quickly on sample holder. Faraday cup is carbon. Hemispherical retarding-field grid connected to dc power supply was formed from 68% open 100-mesh copper screen.

FIG. 2.--Micrographs of gold and silicon samples taken at 0.2-1.0keV primary beam voltages.



rected for.) Then the number of secondary electrons (electrons with an energy ≤ 50 eV) and the number of reflected electrons (all emitted electrons with an energy ≥ 50 eV) were found by Simpson's rule integration to determine the area under the $N(E)$ vs E curve for each energy range. This procedure was followed for each primary beam energy. Then the ratio of SE to total detected electrons and the ratio of SE/BSE for each primary beam voltage was calculated. Yield values cannot be directly obtained from this information. Since the transmission efficiency for CMAs is only about 10%, the number of electrons counted can be referenced only to the total number of electrons collected.

Monte Carlo Modeling

A Monte Carlo modeling program in Turbo Pascal written D. C. Joy was used to obtain predicted values of electron yield and to evaluate the discrepancies between theory and experiment. This program has been described in detail elsewhere.⁵ The model was based on the program written by Myklebust et al.⁶ The model for secondary electron production used in this program was described by Salow.⁷ The program makes significant approximations, but in general its accuracy is good; however, it is less accurate for high atomic numbers and low primary beam energies. In these cases, more sophisticated models for cross section and energy loss must be used.

In this model, screened Rutherford cross sections are used to determine the elastic cross section. The screened Rutherford model overestimates the total cross section in the low-energy regions. Mott cross sections give smaller values for average scattering angle and

scattering probability than the screened Rutherford methods.⁸ These factors explain the deviation of the Monte Carlo yield from experimental backscattered yield values at low energies (≤ 1 keV).

The Mott differential cross section is derived from a more exact treatment of elastic scattering. Kotera et al. have developed a Monte Carlo model using a procedure from Yamazaki,⁹ which used the Mott differential to determine the cross section for scattering per solid angle in the direction θ for an unpolarized electron beam. This procedure is outlined in detail by Kotera et al.⁸ There is a general consensus in the literature that Mott cross sections are more accurate; however, they are also much more complex and require more computing time and power, whereas the model used in this work was run on a personal computer.

Results

Micrographs of gold and silicon samples imaged at energies from 0.2 to 1.0 keV show changes in the relative intensity of the SE emission with energy (Fig. 2). The relative gray levels of the imaged materials can be compared with the yield values obtained from the Monte Carlo model (Fig. 3). Gold has a lower SE yield than silicon at very low voltage, as seen clearly in both micrographs and in Fig. 3. According to the Monte Carlo model, the SE yield of gold becomes greater than the SE yield of silicon at approximately 0.8 keV; the micrographs show the actual relative yield shifts at approximately 0.6 keV.

The electron yields of the gold, carbon, and silicon samples were experimentally determined by use of a retarding-field grid. The results are shown in Fig. 4, where they are compared with the Monte Carlo yields. The yield values obtained by both methods

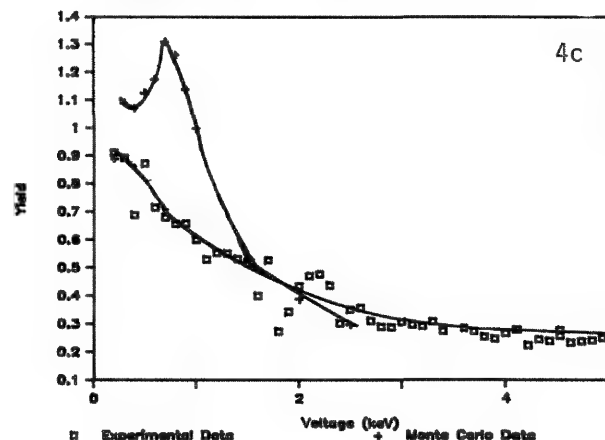
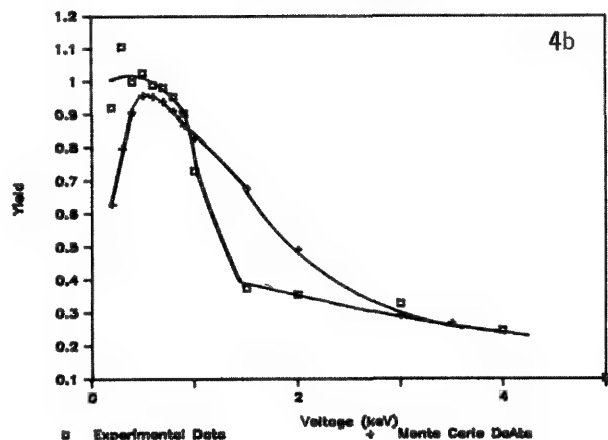
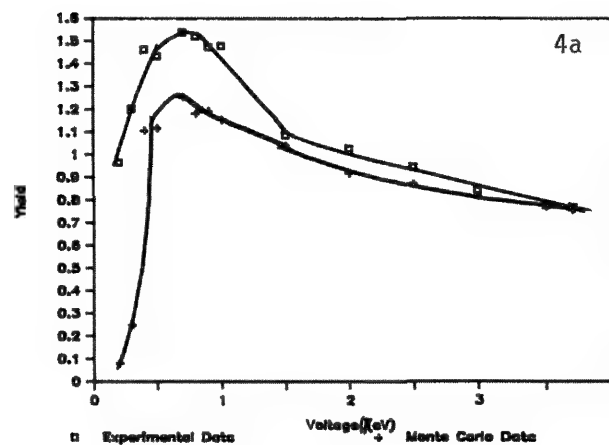
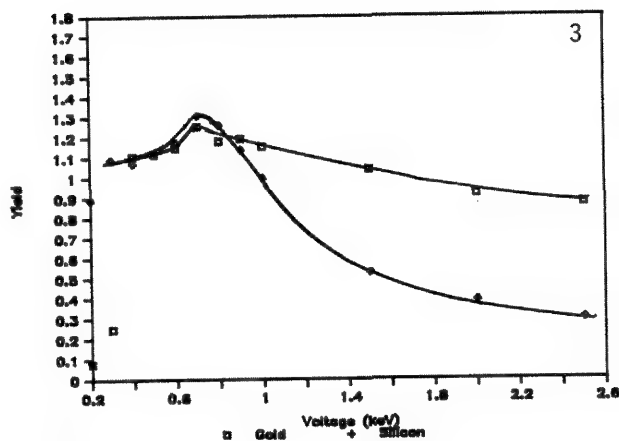


FIG. 3.--Monte Carlo simulation data of (\square) and silicon ($+$) SE yields.

FIG. 4.--Comparison of SE yield from Monte Carlo model ($+$) with results of retarding-field experiment (\square) for (a) gold, (b) carbon, (c) silicon.

agree when the beam energy is greater than 1 keV, and in addition the carbon yields correlate at all energy ranges. Some of the differences between the silicon Monte Carlo data and experimental data may be due to the thin surface film of silicon oxide on the actual silicon sample. In all cases in this experiment the silicon samples have a native oxide surface film. When the results of the Monte Carlo model were compared with the experimental results, by far the largest discrepancy occurred with the gold backscattered yield. The Monte Carlo predictions were much larger than the experimental results, especially at low voltages. This difference is attributed to the scattering model used in the program.

Among the difficulties encountered in the experiments was the effect of beam-current stability on the measurement accuracy. Under optimum conditions, with a new LaB₆ filament, the beam current fluctuated by $\sim 3\%$ /min in the voltage range 0.2-1.0 keV, and less at higher voltages. The filament saturation also needed to be optimized at every voltage to maximize the beam-current stability. Another experimental concern was contamination, which can be defined as the unintentional addition of mass to the surface during exposure to the primary electron beam. Contamination molecules from prior handling and exposure remain absorbed to

sample films unless extraordinary methods to clean the samples are taken before they are placed in the SEM. Beam damage of the resist samples was also a severe problem; measurements from these samples are therefore not included in this paper. The fact that beam damage is generally more severe in organic specimens has been well documented in the literature.¹⁰⁻¹²

The oxidized silicon surface is representative of samples seen during semiconductor processing and the measured yield values can be used to help determine the best SEM operating voltage for imaging silicon-based samples. Unfortunately, the surface oxide makes comparison of the experimental data with the Monte Carlo data of pure elements difficult. Although the measured yield values obtained from oxidized surfaces may be accurate, they cannot be used to verify the accuracy of the Monte Carlo model, since the actual atomic number and density of the near surface oxide region are unknown. Samples of carbon and gold were used to test the accuracy of the model, since these materials do not form native oxides and their large difference in atomic number gives an indication of the accuracy of the model under a range of conditions.

Conclusions

Use of a retarding field grid is an acceptable way of obtaining yield data but contamination, surface oxides, charging, and beam-current stability must be accounted for when the measurements are made. In this study experimental values of yield were obtained for very low primary beam voltages. The Monte Carlo model is accurate for SE yield at voltages >1 keV and for backscattered electron yield of low- and medium-atomic-number samples at beam voltages >1 keV. The most significant difference between the model, the theory, and the experiment is the lack of a first crossover point, which is found in the theory and the model but not always in the experimental data--perhaps because the lowest SEM primary-beam voltage available was 200 eV. Further work is needed to find a way to get crossover data from an Auger microprobe and to automate the data collection and integration of the CMA output so that the task would not be so formidable. The use of the Auger system offers the advantage of in situ cleaning, which permits measurements on clean and oxide-free surfaces.

References

1. H. Seiler, *J. Appl. Phys.* 54: R1-18, 1983.
2. J. C. Riviere, "Instrumentation," in D. Briggs and M. P. Seah, Eds., *Practical Surface Analysis*, New York: Wiley, 1983, 17-85.
3. A. Mogami, *Surface and Interface Science* 7: 241-251.
4. M. P. Seah, *Surface Science* 32: 703.
5. D. C. Joy, "A model for calculating secondary and backscattered electron yields (to be published).
6. R. L. Myklebust, D. E. Newbury, and H. Yakowitz, *NBS Special Publication 460*, 1976, 105-128.
7. H. Salow, *Phys. Z.* 41: 434-442, 1940.
8. M. Kotera, K. Murata, and K. Nagami, *J. Appl. Phys.* 52: 997-1003, 1981.
9. Y. Yamazaki, doctoral thesis, Osaka University, 1977.
10. J. J. Hren, J. I. Godstein, and D. C. Joy, Eds., *Introduction to Analytical Electron Microscopy*, New York: Plenum Press, 1979.
11. M. S. Isaacson, *Proc. 41st Ann. Mtg. EMSA*, 1983, 336-337.
12. K. Kanaya and S. Okayama, *J. Phys.* D5: 43, 1972.

Optical Microprobe Analysis

THE EVOLUTION AND PERSPECTIVE OF RAMAN MICROANALYSIS

Michel Delhayé, Paul Dhamelincourt, and Jacques Barbillat

With the advent of the laser as a nearly ideal source, Raman spectroscopy in the 1960s became a practical tool for easy molecular vibrational analysis of samples. As early as 1966 it was demonstrated clearly that focusing a laser beam onto samples greatly improved the efficiency of the Raman technique and permitted the study of small samples. But the potential for Raman characterization of true microsamples was not demonstrated until 1974, when two papers independently reported the feasibility of a Raman molecular microprobe at the Fourth International Conference on Raman Spectroscopy.^{1,2} This lapse of time arose from the necessity of developing advanced instrumentation for optical spectroscopy, i.e., low-stray-light monochromators and efficient detectors.

The Raman microprobing instruments available at present, equipped with multichannel photodetectors, have now achieved a fairly high degree of sophistication. Nevertheless, it is reasonable to expect continuing progress in several areas. The purpose of this paper is to review some of the improvements that might extend the potentiality of this technique.

Optical Microscope

Objectives. The use of commercially available lens microscope objectives has prevailed in most micro-Raman instruments. Microscope lenses are almost perfectly corrected for aberrations in a limited spectral range, chosen either in the visible, in the near UV, or in the near IR. The maximum aperture corresponds to a half angle α of nearly 72° , giving a numerical aperture $N.A. = n \sin \alpha = 0.95$ in air or vacuum, and a wide solid angle $\Omega = 1.375\pi$ sterad which enables the collection of 34% of the light if we assume homogeneous scattering in the entire space.

In order to improve light collection, one can imagine optical systems made of aspherical mirrors, for instance ellipsoids, where the light emitted by a microsample placed at a focus is captured in nearly 2π sterad with a single mirror or even 4π sterad with a symmetric system of two mirrors.³ Figure 1 illustrates a possible optical combination consisting of a plane mirror supporting the sample and of an ellipsoidal mirror that transforms a classical microscope objective ($N.A. = 0.80$) to collect 50% of the scattered light under the widest angle ($N.A. = 1$). The obvious ad-

vantages of such devices are a substantial gain in efficiency, and an extended spectral coverage from UV to IR without any chromatic aberrations. Modern diamond machining methods generate aspherical optical surfaces with excellent accuracy. The major drawback of mirror objectives in conventional microscopic observation lies in the limited field compared to the lens objectives, but this is not a serious limitation in the specific case of laser Raman microprobing, where the observed area does not exceed a few square micrometers. Special attention must be paid to the feasibility of drilling small geometric holes in the mirrors, which gives a decisive advantage when the Raman microprobe is combined with other techniques that utilize incident electron or ion beams or other radiations focused on a specimen.

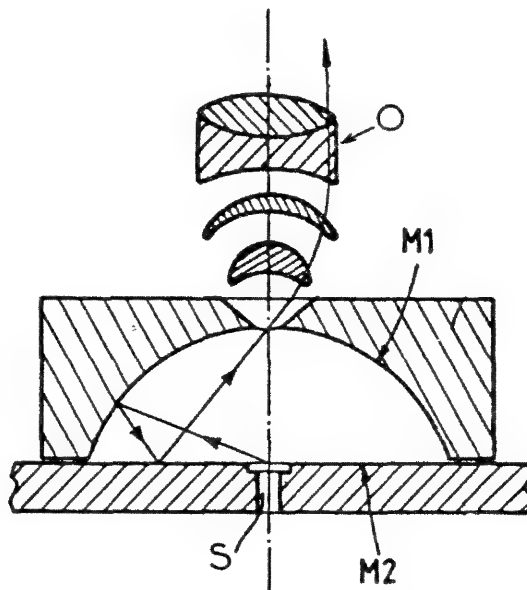


FIG. 1.--Ultimate aperture light collector. M_1 = ellipsoidal mirror, $N.A. = 1$; M_2 = plane mirror; O = microscope objective, $N.A. = 0.80$; S = sample.

Polarization Measurements. More recently we have demonstrated in our laboratory that contrary to earlier views it was possible to make accurate polarization measurements provided that the necessary correction for the effects of microscope optics were made. The strongest effect comes from the reflection coefficient of the dielectric-coated beamsplitter. It can be corrected by measurement of the power placed on the sample for different positions of the electric-field vector of the exciting radiation. As far as the polariza-

The authors are at the Laboratoire de Spectrochimie Infrarouge et Raman, CNRS, Université de Lille Flandres Artois, Bât. C5, F-59655 Villeneuve d'Ascq CEDEX, France.

tion effects introduced by the large-aperture objectives are concerned, theoretical calculations were made from optical characteristics of the objectives and the refractive index of the scattering medium in order to determine correction factors that are valid regardless of which objective is employed (Fig. 2).⁴

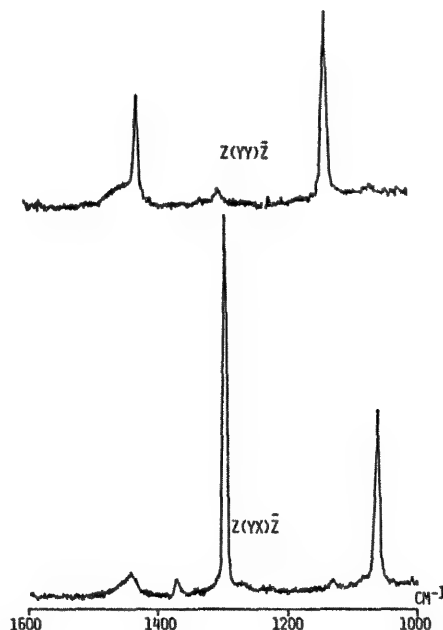


FIG. 2.--Polarized Raman spectra recorded from single polyethylene filament oriented along the Y axis; Raman scattering is observed along the Z axis.

Beamsplitter. Indeed, although the effects of the beamsplitter can be corrected for polarization measurements, the presence of this optical component is a source of an important loss of light (its global efficiency is at best 0.25 for a semitransparent plate). In order to improve the efficiency of Raman microprobes, new optical designs are being studied that completely eliminate the beamsplitter without altering the original function (illuminating and viewing of the sample) of modern research-grade microscopes which are now used in all the micro-Raman instruments.

Remote Microanalysis

Optical fibers offer an elegant means of coupling both the laser radiation to the sample and the sample scattering to the spectrometer. However, the strong depolarization of light introduced by commercially available fibers makes the assignment of polarized bands more difficult.

Direct coupling, obtained by immersion of single fibers or fiber bundles in a liquid, or by placing the end of a fiber a short distance away from a solid sample, does not clearly define the small sampling volume that is essential for a true microprobe measurement. Indirect coupling, using microscope objectives to

observe a diffraction limited area, and optical fibers to transmit the laser beam and the scattered light to the Raman spectrometer, makes easily possible a remote microanalysis in a variety of environments, ranging from industrial measurements to in situ observation of materials in biology, mineralogy, art pieces, or forensic analysis.

Rejection of Laser Line and Stray Light

The elimination of stray light background imposes stringent constraints in micro-Raman techniques, chiefly because the optical configuration routinely employed in microscopy introduces an intense reflection, specular or diffused, of the laser beam toward the monochromator. This radiation is superimposed on the weakly scattered Raman light at a very unfavorable intensity ratio. An estimate of this ratio can be given for a typical routine test: the diffuse reflection from a small particle of white, powdered aspirin generates a peak intensity of the order of 10^{10} counts per second at the laser wavelength, whereas the detector measuring Raman bands receives 10^2 to 10^3 photons per second. Most often, double or triple grating monochromators in tandem are intended to filter out the stray light efficiently, but at the expense of a rather poor throughput efficiency. The overall optical transmittance of a complete triple grating system, from the microscope to the detector, typically lies in the 1-5% range, which means that most of the precious photons scattered from microsamples are lost and never reach the photodetector.

A special effort is being made to improve the overall transmittance of the system optics. The rejection of the laser wavelength by means of Fabry-Perot or other high-quality interference filters offers a much better efficiency than a grating foremonochromator. As a serious drawback, however, the access to the low-wavenumber spectral range can be severely limited. Recently, an entirely new approach has been proposed by S. A. Asher, who introduced an efficient rejection filter based on the properties of charged polymer microspheres.⁵ Important progress may be predicted in this domain, which will significantly contribute to more sensitive detection of weak signals.

Laser Sources

The large choice of laser sources now available offers the ability to excite spontaneous Raman scattering under resonant or nonresonant conditions, from the UV to the near infrared. If the properties of photodetectors in the corresponding spectral domains are taken into account, an optimized balance may be found for each individual case of an analytical sample in order to improve the detection limit. The most severe limitations are doubtless linked to the coexistence of Raman scattering with fluorescence or luminescence background. In this respect, two approaches may be explored

for extending the spectral domain.

1. In the UV region, it is useful to benefit from resonance Raman enhancement, due to the intrinsic electronic absorption of the molecules of interest (especially in biology).

2. Excitation in the near IR region will significantly reduce the probability of fluorescence emission by the sample.

The advantages of these extensions are evidently offset by some drawbacks. The UV light efficiently excites not only resonance Raman, but also fluorescence from impurities. It also produces rapid photochemical degradation of fragile molecules. Near IR safely avoids photochemical sample damage, but the resonance enhancement is generally absent and the ν^4 dependence of nonresonant intensity combined with poorer sensitivity of photodetectors reduces the detection sensitivity.

The use of tunable dye lasers, ideally suited for resonance Raman investigations, suffers from practical limitations mainly due to the difficulties of eliminating the background arising from the active medium, which requires additional filtering of the beam.

Most of the experiments of Raman microprobing have been carried out with continuous-wave lasers. Owing to the improvements in the photodetection of weak signals, there is a marked tendency to prefer low-power lasers in place of the previous monster multiwatt argon or krypton lasers. A low excitation power favors sample survival and provides a better protection of microsamples against thermal degradation and photodecomposition. New kinds of laser sources thus became practicable, for instance the very promising semiconductor diode lasers, or the existing He-Ne or He-Cd lasers.

The use of pulsed lasers seems very attractive, both on account of the variety of accessible wavelengths and the ease with which they can be tuned, and in view of the potentialities of signal-to-noise improvement and luminescence rejection offered by pulsed excitation. Gated synchronized photodetectors, either single channel with boxcar integrator or multichannel with gated intensifiers, have been successfully explored.

Yet close attention must be paid to the inherent limitations of pulsed laser excitation in Raman microprobing. The local irradiance produced by focusing a laser beam to a small spot of a few square micrometers reaches incredibly high values in the pulsed regime.⁶ For instance, the irradiance is in the range of terawatts per square centimeter (10^{12} W cm⁻²) for a dye laser, pumped by a YAG or excimer laser, in 100 μ J nanosecond pulses, focused on a 1 μ m² probe spot. As a consequence, the threshold of destructive phenomena, such as optical breakdown, is easily exceeded in microprobing, and most kinds of materials, even refractories, are destroyed and volatilized.

The only acceptable compromise for Raman microprobing in the pulsed regime requires a laser with a relatively low peak power (10-100 W). Because of the required number of pho-

tons for a reasonable S/N at the detector level, these conditions are only feasible at high repetition rate (megahertz) at a moderate average power (milliwatt or less) in short pulses (nanoseconds to picoseconds).

Detection

For many years relatively little has changed in the way optical radiation has been detected: photomultiplier tubes have been used almost exclusively to measure sequentially light intensity from the UV to the near IR. A subsequent improvement in low-light-level detection is the substitution of multichannel detectors for the PMT. Multichannel techniques, which allow the measurement of each wavelength interval during the entire allotted measurement time, offer large signal-to-noise improvements compared to the results of sequential approaches. Standard television image tubes combined with photoelectric image intensification (first generation of multichannel detectors) have been recently replaced by intensified solid-state detectors, so that at present the most common multichannel detector used in micro-Raman installations is the intensified linear silicon photodiode array (with typically 512 or 1024 elements).⁷ The characteristics of this intensified detector are such that single photoelectron sensitivity is almost achievable by using on-chip integration. This improvement in detector sensitivity results in lower detection limits, a more rapid analysis, and the opportunity to use lower laser powers, thereby minimizing the possibilities for sample decomposition.

Two other devices are emerging as potentially competitive alternatives to the photodiode array: charge transfer devices (CCD and CID) and the intensified position sensor (i.e., resistive anode), both of which offer two-dimensional imaging capability. Because of their high quantum efficiency ($\sim 80\%$), the large number of pixels (typically a 800×800 array or larger), and low readout noise and dark current, the unintensified liquid-nitrogen-cooled CCD appears especially promising for very low-light-level detection and two-dimensional imaging with long integration time.⁸ The intensified position sensor consists of multiple cascaded microchannel plates (3 to 5) ahead of a position-encoding device (resistive anode, 400×400 pixels). Unlike the intensified photodiode array or the CCD, the intensified resistive anode is not a storage device but a very sensitive imaging device working in the photon counting mode. Its features make this detector very attractive for future Raman applications where low signal intensity is a limiting factor.⁹

Most of these multichannel detectors have a spectral response limited to photons of wavelength shorter than 1 μ m. However, it is well known that the ability to select a longer wavelength can be advantageous to avoid sample fluorescence, which is the main limitation of micro-Raman applications to complex samples excited with blue-green lasers.

Because of the availability of reliable cw Nd:YAG lasers, most fluorescence-free applications are performed with 1.064 μm excitation. Unfortunately, even the best commercially available IR detectors in that range (i.e., LN_2 -cooled Ge or InGaAs photodiodes) have a poorer detectivity than visible detectors. One can expect that linear or 2D arrays of IR detectors developed for military purposes will become rapidly commercially available. Currently, the third generation of microchannel plate image intensifier tube with GaAs photocathode coupled to a multichannel solid-state sensor can extend the response of Raman spectrometers out to 920 nm with very high efficiency.

Raman Spectrometry with IR Excitation

As a consequence of the lack of high-sensitivity IR detectors and of the fourth-power dependence of the Raman intensity on frequency, Fourier transform spectrometers that present multiplex and throughput advantages have been proposed to improve the S/N of Raman spectra in the infrared.¹⁰ Nevertheless, to obtain successful results, the exciting line must be efficiently rejected before it enters the interferometer. Otherwise the noise associated with this strong radiation will be spread over the entire spectrum and the weaker Raman lines will be obscured. In sensitive photodetectors, the ultimate limitation is due to shot noise (photon noise).

Currently, very narrowband rejection filters based on interference or diffraction phenomena are used to remove the Rayleigh line. At this time, such filters do not exhibit sufficiently sharp cutoff and the Raman spectrum close to the exciting line (typically $\bar{\nu} < 400 \text{ cm}^{-1}$) is partially rejected. Another filtering approach is to use a double subtractive foremonochromator. A very sharp cutoff of the light at the laser frequency is achieved by the intermediate slit, so that less of the low-frequency Raman spectrum should be lost.

According to recent work, Hadamard transform spectrometry (a dispersive technique with multiplex advantage) in the near IR might be an alternative to FT-Raman.¹¹ The Hadamard spectrometer could solve the multiplex disadvantage of FT-spectrometers resulting from the noise in the Rayleigh line. The encoding mask acts as a knife-edge filter for the Rayleigh line and therefore removes this strong line from the spectrum, which is then recombined onto a single-channel detector.

Raman Mapping and Imaging

Two-dimensional micro-Raman imaging has proven to be quite suitable for obtaining the distribution of a given compound within a sample and should be of special interest in many fields of research. Three methods of laser illumination have been proposed to perform Raman imaging: global, line, and point illumination.¹²

In the first experiment on Raman "micros-

copy" reported in 1974 by our laboratory, the entire sample was illuminated by unfocused laser radiation and an integral Raman image was obtained from an image-forming optical system. A tunable grating monochromator was modified so as to form an enlarged image of the sample on the gratings and then on the photocathode of an image intensifier tube. This optical setup was integrated in the MOLE microprobe but suffered from several limitations. Multichannel detection based on the use of an intensified TV camera lacked the sensitivity to reveal weak lines. Moreover, since the aperture stop of the microscope objective was imaged onto the slits of the monochromator, these slits had to be opened wide in order not to impair the spatial resolution of the final image. As a consequence, the spectral resolution was lowered and the stray light level, proportional to the slit area, was relatively high. Therefore, the use of this device was limited to the observation of strong, fluorescence-free Raman scatterers.

In order to improve the stray light rejection and the spectral resolution, Raman images can be obtained by use of a monochromator with narrow slits and scanning of the sample with the laser beam. The laser beam is either rapidly deflected or elongated by a cylindrical lens along a straight line which is imaged onto the narrow entrance slit of a tunable monochromator. This monochromator must exhibit a very good stigmatism to yield spatial information at the exit port. By using a linear intensified photodiode array, for instance, as the detector, one obtains directly the profile of Raman intensity along the line across the sample at the wavelength selected by the filter.

One can sequentially form an image by moving the sample in a direction perpendicular to the laser line and by storing these line-to-line measurements in a computer. One drawback of this technique is the time required to recover the full image, which is much longer than previously obtained by global illumination.

Image recovery time with point illumination is still less favorable and should be used only to map out just a few points across the sample.

Finally, the method we suggested more than ten years ago--use of a fixed-wavelength filter and a tunable laser rather than a tunable monochromator to select a given Raman line--might become a very promising method with the emergence of high-efficiency narrow bandpass filters and very sensitive 2D multichannel detectors (CCDs, intensified resistive anode).

Coupling Micro-Raman With Other Microbeam Analysis Techniques

The possibility of benefitting from the complementary data afforded by various methods to elucidate the analysis of microsamples seems very attractive. We proposed a few years ago to combine the information at the

molecular level from Raman microprobing with elemental x-ray electron microprobe analysis of a microsample observed with high spatial resolution in a transmission electron microscope. In order to avoid the difficulties associated with the manipulation of samples and the preservation of their integrity, these different techniques have to converge, simultaneously or sequentially, toward a unique sample configuration accurately positioned in a common observation chamber.

In a first step we have combined the optical elements of Raman microprobe, compatible with operation under vacuum conditions, with a Castaing microprobe using x-ray wavelength dispersive spectrometry.¹³ Optimized focusing of the laser beam and collection of the Raman scattered radiation is realized by an elliptical mirror system that insures a solid angle of nearly 2π sterad. The entire optical system is installed in the sample chamber of a CAMECA (MS 46) electron microprobe. The exciting laser beam and the Raman scattered light are transmitted through a sealed optical window to a Dilor multichannel spectrometer optimized for high throughput and detection sensitivity.

In the near future, further improvements may be expected in coupling Raman microprobing with other local analysis techniques. The fact that optical systems can be readily employed and perform well under controlled atmosphere conditions in liquids or under high vacuum, offers indeed promising prospects for combined instruments (Fig. 3).

Computer Data Acquisition and Treatment

In the past few years, with the enhanced capabilities of PC computers, dramatic progress has been made in the handling of data. Commercially available instruments are now all driven by such computers, which permits data acquisition in the complete defined spectral range either in the scanning or the multichannel mode. With optical multichannel detection, for example, the computer automatically converts raw data taken from several spectral segments into a unique spectrum linear in user-specified spectral units, either cm^{-1} or nm. Spectra stored as separate files on floppy or hard disks can be compared and interactively manipulated in order to improve their quality (baseline correction, removal of spurious lines, spectral smoothing, etc.) before they are plotted in user-definable formats. For micro-Raman spectroscopy, the fast multiple spectra acquisition capability offered by multichannel detectors is certainly one of the most important breakthroughs for the analysis of fragile samples. With high computer RAM capacity and direct access to the memory for fast data transfer, Raman mapping of microsamples by linear or two-dimensional intensified array detectors is now feasible at last.

But even though the data acquisition has become more and more automatic, the user still has to master the experiment by defining all the parameters (spectral range, integration

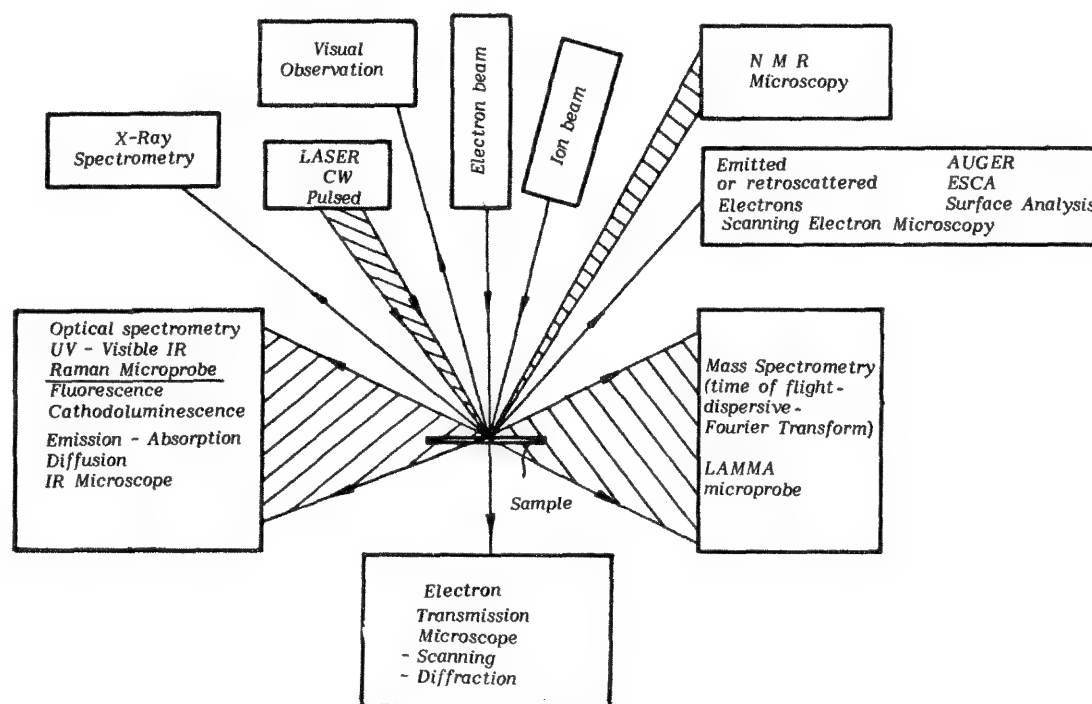


FIG. 3.--Convergence of Raman microprobing with other techniques combined in single instrument would offer complementary data for analysis of microsamples, possibly originating from the coupling with various separation techniques (e.g., chromatography, electrophoresis).

time, number of scans, etc.). The next step should certainly be the complete automation of the analytical procedure by designing "intelligent" spectrometers.

Conclusion

Future improvements of Raman instrumentation as described in this paper should lead to more efficient and more easily operated computer-based microprobes.

References

1. G. J. Rosasco et al., "Investigation of the Raman spectra of individual micron-sized particles," *Proc. of 4th ICORS*, 1974.
2. M. Delhaye and P. Dhamelincourt, "Laser microprobe and microscope," *ibid.*
3. M. Delhaye and M. Truchet, French patents CNRS-ANVAR 8 604 947 and 8 709 883.
4. P. Dhamelincourt et al., "Polarization measurements in Raman microspectroscopy," *Microbeam Analysis--1987*, 139.
5. S. A. Asher et al., "Crystalline colloidal Bragg diffraction devices: The basis for a new generation of Raman instrumentation," *Spectroscopy* 1(12): 26, 1986.
6. M. Delhaye and J. C. Merlin, *Proc. of 1st European Conf. on Spectroscopy of Biological Molecules*, Reims 1985, New York: Wiley, 1985.
7. J. Barbillat et al., "Nondestructive microprobing by means of a new generation of instruments for Raman and fluorescence spectroscopy," *Microbeam Analysis--1985*, 15.
8. P. M. Epperson et al., "Applications of charge transfer devices in spectroscopy," *Anal. Chem.* 60: 5, 1988.
9. D. K. Veirs, V. K. Chia, and G. M. Rosenblatt, "Raman spectroscopy applications of an imaging photomultiplier tube," *Appl. Optics* 26: 17, 1987.
10. B. Chase, "Fourier transform Raman spectroscopy," *Anal. Chem.* 59: 14, 1987.
11. D. Tilotta and B. Fately, "Hadamard transform spectrometry: Teaching old monochromators new tricks," *Spectroscopy* 3: 1, 1988.
12. M. Delhaye and P. Dhamelincourt, "Raman microprobe and microscope with laser excitation," *J. Raman Spectroscopy* 3: 33, 1975.
13. M. Delhaye and M. Truchet, "Transmission electron microscope with Castaing's electron x-ray and laser Raman probes for simultaneous elemental and molecular analysis at submicrometric scale," *Microbeam Analysis--1987*, 163.

ACCURATE (5.1×10^7 dyne/cm²) STRESS EVALUATION OF SILICON BY MICRO-RAMAN MAPPING SYSTEM

Teruki Ikeda, Masaaki Yumoto, and Hirokazu Okahana

Micro-Raman spectroscopy has been attracting growing interest in its application to the localized stress evaluation of semiconductor and other materials.^{1,2} The existing micro-Raman instrumentation has achieved an accuracy of 1.2×10^8 dyne/cm², incorporating multichannel detection and mathematical data handling.² However, this figure is insufficient for the stress evaluation of semiconduction materials, such as gallium arsenide (GaAs). In the present study, illustrated here, the accuracy of stress evaluation was improved approximately two-fold by precise correction of thermal effect of the micro-Raman mapping system. In this paper we describe the design improvement of our micro-Raman mapping system and its applications to the localized (10 μ m-length region) stress evaluation of silicon (Si) substrate beneath silicon dioxide (SiO₂) layer.

Instrumentation

As diagrammed in Fig. 1, our micro-Raman mapping system, model RMP-1000, was constructed around a JASCO model NR-1100 Laser Raman spectrometer, a 1024-element multichannel detector (MCD), and a microscope associated with a computer-controlled X-Y sample stage. A personal computer controls the entire system.

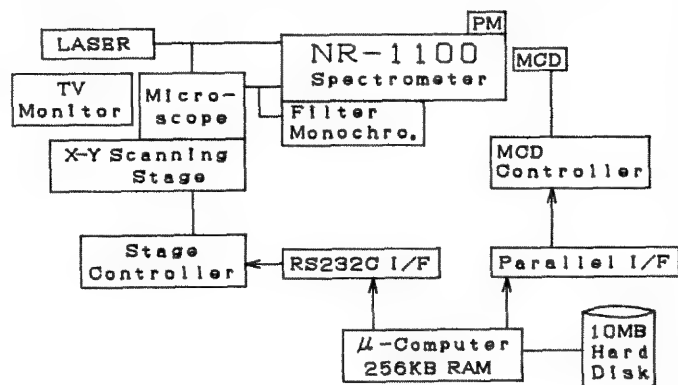


FIG. 1.--Schematic diagram of model RMP-1000 micro-Raman mapping system.

A Raman spectrometer system consists of various thermal sources within its hardware, and hence can hardly be free from a selective thermal effect that restricts frequency accu-

racy of the Raman spectrum measured. In the design of RMP-1000, precise correction of frequency deviation is carried out on line by measurement of the line spectrum of Ne lamp as reference.

Experimental

Twenty Raman spectra of stress-free Si wafer were successively taken on the RMP-1000. The excitation source used was 488nm line of argon laser and the sample was held in a backscattering configuration.

Raman spectra of Si substrate were taken on the same RMP-1000 by scanning of the laser probe spot transverse to the Si substrate and the Si substrate beneath the SiO₂ layer with steps of 0.1 μ m. The SiO₂ layer was a rectangle 710 nm thick and 5 μ m wide (Fig. 2).

Results

The Raman peak of Si in absence of stress occurs at 520.50 ± 0.007 cm⁻¹ (σ). The standard deviation (3σ) is related to the stress detection limit of 5.1×10^7 dyne/cm² by the relationship between Raman shift and two-dimensional stress of Si reported by Anastasakis and co-workers.³

In Fig. 3, the top three curves are (top to bottom) the Raman intensity, the peak width (FWHM), and the corrected frequency profiles of Raman spectra of Si plotted as function of distance along the scanning path. The lower two plots are the uncorrected frequency profile and the frequency profile of Ne lamp used as reference. The frequency profile shows that tensile stresses of 8.7×10^8 dyne/cm² occur in the Si substrate beneath the SiO₂ layer, whereas compressive stresses of 2.5×10^8 dyne/cm² were observed in the Si substrate approximately 1 μ m out of the SiO₂ layer edges. Band broadening was also observed near the stress steeping edges of the SiO₂ layer.

Conclusions

The on-line frequency correction which incorporated a Ne reference lamp has successfully improved the accuracy of the micro-Raman spectroscopy in stress evaluation nearly two-fold over the previous instrumentation. The experimental result has also suggested that further improvements of accuracy would be accomplished by selection of an appropriate convoluting function to fit the correction curve.

With the enhanced frequency accuracy, the RMP-1000 could reveal the local (10 μ m-length region) stress distribution in the partially oxidized Si structure. Developing accurate and nondistractive means to prove stress

T. Ikeda and M. Yumoto are at Japan Spectroscopic Co., Ltd., Ishikawa-cho 2967-5, Hachioji, Tokyo 192, Japan; H. Okahana is at JASCO International Co., Ltd., 4-21, Sennin-cho 2-chome, Hachioji, Tokyo 193, Japan.

distribution of semiconductor materials is of paramount importance for the advancement of production technology in the semiconductor industry. The accurate stress evaluation by micro-Raman mapping spectroscopy will be a key measurement for advanced semiconductor materials, such as GaAs.

References

1. Y. Inoue et al., Japan Soc. Appl. Phys. and Related Societies, *Extended Abstract, 34th Spring Meet.*, 1987, 548.
2. T. Ikeda et al., Ref. 1, p. 199.
3. E. Anastassakis et al., *Solid State Communications* 8: 133-138, 1970.

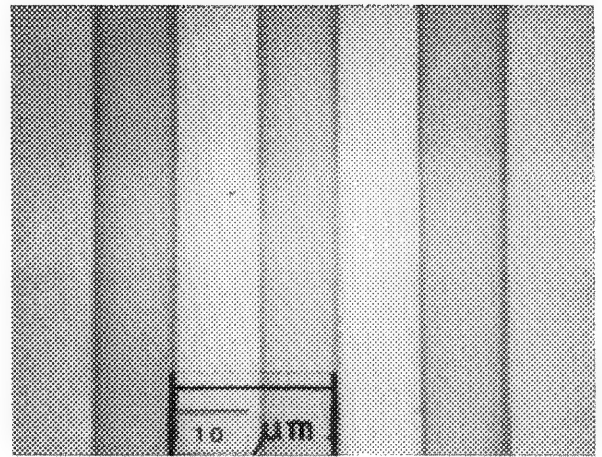


FIG. 2.--Micrograph of rectangle SiO_2 layer on top of Si substrate.

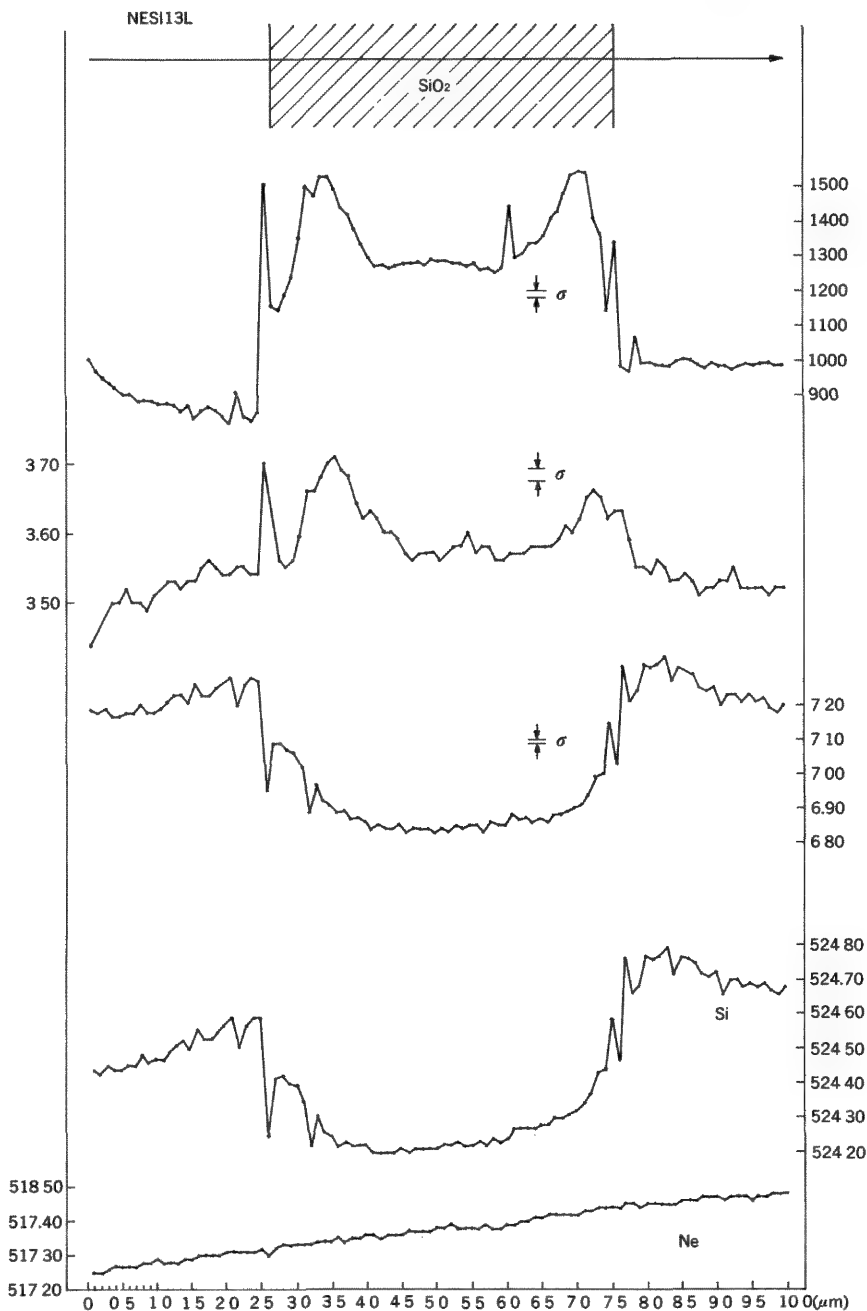


FIG. 3.--Intensity, bandwidth, and frequency profiles of Raman peak of Si plotted as function of distance along scanning path (top three plots), and uncorrected frequency profile of Si and frequency profile of Ne reference lamp (lower two plots).

HIGH-PRESSURE RAMAN MICROPROBE STUDIES OF PHOSPHAZENE TRIMERS

G. J. Exarhos and Nancy J. Hess

A representative class of molecules in which chemical bonding is controlled by marked differences in atom electronegativity as well as d-orbital involvement is exemplified by the planar cyclic phosphazene system $[NPX_2]_3$, where X represents substituent groups bonded to the ring phosphorus atoms. These materials can be viewed as inorganic analogs of benzene in which conjugation and electron delocalization should lead to significant ring stabilization. However, the symmetry of d-orbitals involved in valence bond formation precludes electron delocalization over more than 3 atoms.¹ *Ab initio* molecular orbital calculations of both chloro- and fluorotrimers using an extended basis set² also indicate the presence of highly localized bonding.³ In these molecules, the sigma electron density on nitrogen is directed inside the ring with the nonbonding pi-orbital normal to the ring. Thus, sigma bonding in the ring may be viewed as highly ionic. In addition, the ring is stabilized by only about 10 kcal/mole for $[NPCl_2]_3$. Perturbations to this bonding are expected upon alteration of substituent groups or application of high pressure, and are manifested by changes in the vibrational mode assignments for chlorotrimers and their fluorosubstituted analogs reported earlier.⁴ More recent work involving a normal coordinate analysis of the chlorotrimer was undertaken to resolve discrepancies in previously published mode assignments and to confirm the planar conformation of the molecule.⁵ Vibrational Raman spectra of chloro- and fluorophosphazene trimers as a function of applied pressure have been measured in this work and are used to confirm the mode assignments and evaluate subtle changes in chemical bonding induced by the applied pressure.

Experimental

Raman scattering measurements from samples mounted in a diamond anvil cell are similar to those reported in the literature.⁶ Two Class II low-fluorescence diamonds mounted in a hardened stainless steel holder of a Merrill-

Bassett design comprised the pressure cell.⁷ A hole 200 μ m in diameter drilled into an inconel gasket (0.5 mm thick) was located between the flat diamond faces and formed a cavity for the samples. Several crystallites of hexachlorophosphazene trimer were loaded in the cell along with a small crystallite of ruby, which served as the pressure sensor through known pressure-dependent frequency shifts of the 14 404 cm^{-1} R_1 laser-excited fluorescence line. Normal pentane was admitted to the cavity as a pressure-transmitting medium. The ruby fluorescence bandwidth, doublet splitting, and intensity of the R_1 features were monitored to verify hydrostatic conditions. The hexafluorophosphazene trimer was prepared from the chlorotrimer by refluxing with NaF in nitrobenzene, and was purified by repeated sublimation. This material exists in a solid phase below room temperature and only persists as the liquid over a limited temperature range before it vaporizes. A large crystal was loaded into a cold cell along with a ruby crystallite and compressed. The crystalline phase persisted at room temperature as long as the cell was under pressure. Raman spectra of samples in the pressure cell were excited at normal incidence in a backscattering geometry by use of the Raman microprobe (SPEX Model 1482). A long-focal-length, all-reflecting objective (Ealing, 36 power, 0.5 N/A) allowed viewing inside the cell and imaging of the probe excitation (514.5 nm, 250 mW) onto the sample. Scattered light was directed to a 0.85m SPEX Model 1403 double spectrometer and analyzed by photon-counting electronics. Spectra were recorded at increasing applied pressures from 1 bar to 70 Kbar and at lower pressures following gradual release of pressure on the cell.

Results

Vibrational frequency shifts for the strong Raman modes of the chloro- and fluoro-trimers as a function of applied pressure are shown in Fig 1, along with the reported mode assignments according to Painter et al.⁵ The pressure dependence of the mode vibrational frequency (ν_i) can be related to the isothermal compressibility K of the material and the mode anharmonicity (Grüneisen parameter γ_i) according to⁸

$$(d\nu_i/dP)_T = K\gamma_i \nu_i \quad (1)$$

The data presented in Fig. 1 enable a comparison of mode anharmonicities for analogous vibrational features in the two phosphazene molecules studied. Significant interaction between the low-frequency modes in the chlorotrimer is

G. J. Exarhos is with Pacific Northwest Laboratory, Box 999, K2-44, Richland, WA 99352; N. J. Hess is a graduate student in the Geology Department at the University of Washington, Seattle, WA 98195. Pacific Northwest Laboratory is operated by Battelle Memorial Institute for the U.S. Department of Energy under Contract DE-AC06-76RLO 1830. This research was supported by the Materials Sciences Division of the Office of Basic Energy Sciences, U.S. Department of Energy, and through a NORCUS fellowship to the second author.

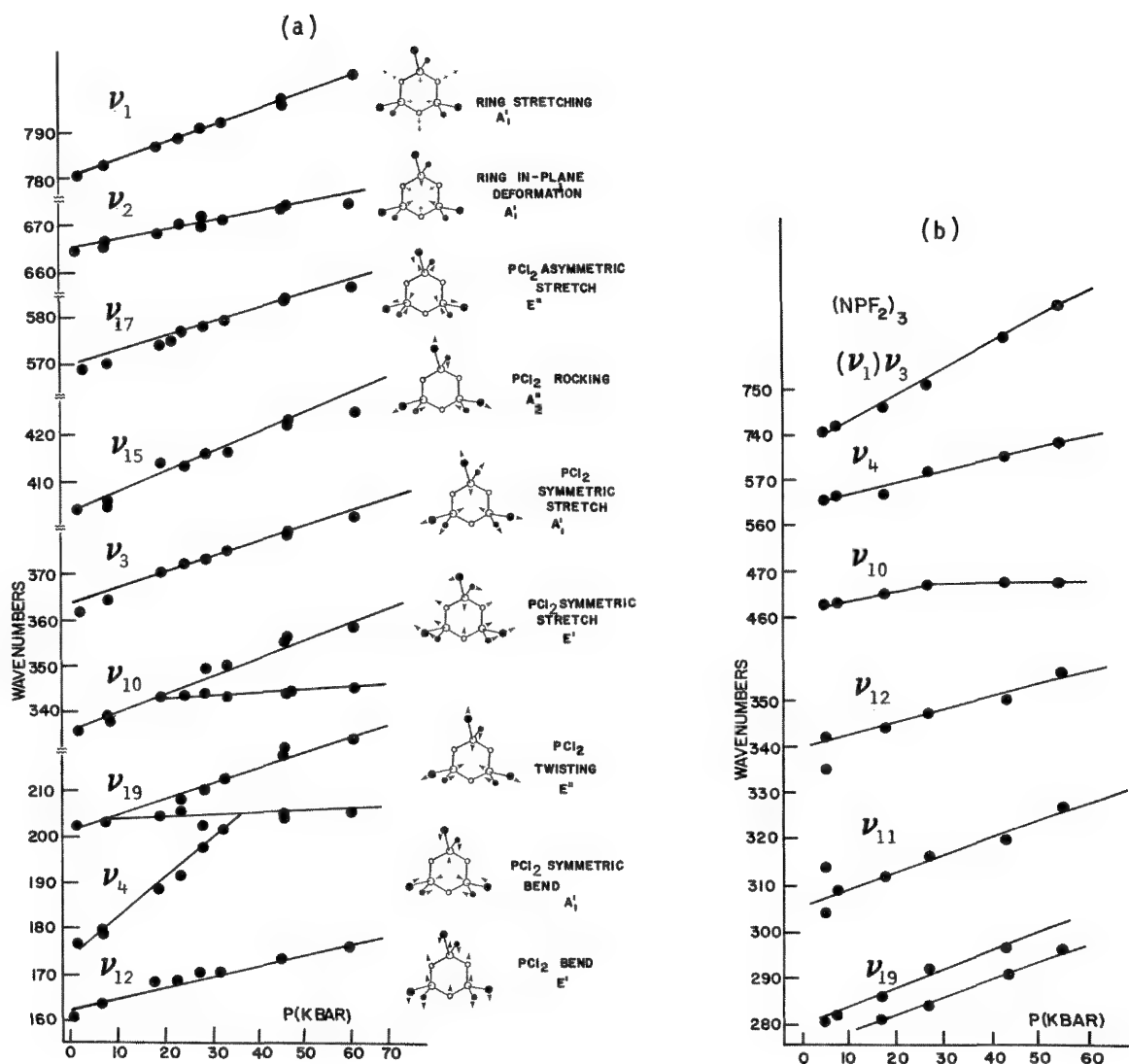


FIG. 1.--Vibrational frequency shift dependence on applied pressure for Raman active modes of (a) crystalline hexachlorophosphazene, (b) hexafluorophosphazene trimers are tabulated with associated mode assignments based on previous work by Painter et al.⁵

observed, and the PCl_2 symmetric bending vibration ν_4 exhibits a marked degree of anharmonicity. The degeneracy of the E' symmetric stretching mode ν_{10} is removed at pressures exceeding 15 Kbar. For the fluorotrimer, marked anharmonicity is observed for the 741cm^{-1} mode assigned to the symmetric PF_2 stretching vibration ν_3 , which has also been proposed to be accidentally degenerate with the ν_1 ring vibration.⁴ However, this degeneracy is not removed at applied pressures up to 55 Kbar. The 463cm^{-1} E' mode assigned to out-of-plane PF_2 symmetric stretching exhibits only a slight pressure dependence, in contrast to the analogous mode in the chlorotrimer, which also shows a pressure-induced splitting. In addition to measured frequency shifts, marked changes in band intensities were also observed and are discussed below in terms of pressure-induced perturbation to chemical bonding.

Symmetric vibrational modes involving the very polarizable P-Cl moiety are found to be relatively more intense than the ring modes at low applied pressures. However, at 70 Kbar, the PCl_2 symmetric stretching, bending, and twisting vibrations (ν_3 , ν_4 , and ν_{19}) are seen to decrease markedly in intensity relative to the ring stretching and deformation modes ν_1 , and ν_2 . In contrast, the asymmetric stretching modes ν_{15} and ν_{17} are seen to increase in intensity along with the E' wagging vibration ν_{11} , which is a very weak feature in the Raman spectrum at ambient pressure. In general, weakly active modes of E symmetry in the Raman spectrum intensify with increasing pressure, whereas the more intense modes of E symmetry exhibit an intensity decrease. At a pressure of 70 Kbar, the symmetric ring modes are comparable in intensity to the strong PCl_2 mode, ν_3 , which at 1 Kbar of applied pressure is more intense by about a factor of 3 than these features.

The intensity dependence of fluorotrimer modes as a function of pressure contrasts with results from the chlorotrimer. Here, all mode intensities monotonically decrease with increasing pressure relative to the PF_2 symmetric stretching mode ν_1 , which at a pressure of 55 Kbar is stronger by at least an order of magnitude than all other observed features.

Discussion

The observed pressure dependence of the Raman spectra for these molecular crystals can be explained qualitatively in terms of atom size and electronegativity. Compression of the chlorotrimer at high pressure leads to electron withdrawal from the P-Cl bonds into the ring due to the large electronegativity of the nitrogen atoms. This leads to intensity enhancement of the ring modes with respect to the symmetric PCl_2 modes. As the chemical bonds contract, steric hindrance between the relatively large chlorine atoms and the nitrogen lone pairs acts to distort the ring. Raman selection rules are relaxed, and the asymmetric modes appear at increased intensity at high pressure. Apparently, bonding within the ring becomes more co-

valent as a result of the electron withdrawing power of nitrogen.

The contrasting behavior exhibited in Raman spectra of the fluorotrimer as a function of applied pressure can be understood in terms of competition for electron density between the ring nitrogen atoms and the terminal fluorine atoms. Upon compaction, fluorine withdraws electron density from phosphorus thereby increasing its partial positive charge. Bonding within the ring becomes more ionic, and the PF_2 symmetric stretching mode begins to decouple from the ring. The predominance of this vibrational mode at high pressure is likely to result from this kind of interaction. In order to test these conclusions, molecular orbital calculations as a function of molecule compression will be initiated in this laboratory to determine the influence of applied pressure on electron redistribution.

References

1. H. R. Alcock, "Inorganic macromolecules: Developments at the interface of inorganic, organic, and polymer chemistry," *Chem. Engin. News* 63(11): 22-36, 1985.
2. J. S. Binkley, M. Frisch, R. Krishnan, D. J. DeFrees, H. B. Schlegel, R. Whiteside, E. Fluder, R. Seeger, and J. P. Pople, *GAUSSIAN '82*, release H., Carnegie Mellon University, 1982.
3. G. J. Exarhos, K. F. Ferris, D. M. Friedrich, and W. D. Samuels, "Molecular spectroscopic characterization of binding interactions in phosphazene-stabilized alumina dispersions," in I. A. Aksay, G. L. McVay, and T. G. Stroebe, Eds., *Atomic and Molecular Processing of Electronic and Ceramic Materials*, Pittsburgh: Mater. Res. Soc., 1988, 127-134.
4. J. Emsley, "Vibrational spectra of the triphosphonitridic fluoride chlorides," *J. Chem. Soc. A*: 109-113, 1970.
5. P. C. Painter, J. Zarian, and M. M. Coleman, "Vibrational spectra and normal coordinate calculations of chlorophosphazene compounds: I. Hexachlorocyclotriphosphazene," *Applied Spectroscopy* 36: 265-271, 1982.
6. R. J. Hemley and P. M. Bell, "Laser techniques in high-pressure geophysics," *Science* 237: 605-612, 1987.
7. L. Merrill, and W. Bassett, "Miniature diamond anvil pressure cell for single-crystal x-ray diffraction studies," *Rev. Sci. Instr.* 45: 290-294, 1974.
8. G. A. Samara and P. S. Peercy, "Pressure and temperature dependence of the static dielectric constants and Raman spectra of TiO_2 (rutile)," *Phys. Rev. B* 7: 1131-1148, 1973.

NEAR-FIELD OPTICS: APPLICATIONS OF MICROBEAMS OF LIGHT WITH WAVELENGTH-INDEPENDENT RESOLUTION BEYOND THE DIFFRACTION LIMIT

Aaron Lewis, Klony Lieberman, Victor Habib, Michael Isaacson, Alec Harootunian, and Eric Betzig

A method has been developed that permits the resolution of light to be extended below the fundamental limit imposed by the wavelength of light. The technique is based on our demonstration that significant light intensities can be passed through well-defined apertures that can be as small as 1/10 the wavelength of visible radiation.^{1,2} When such subwavelength light beams are brought within 25 nm of a surface, the illuminated area can be as small as the aperture size.³ Thus, if a surface is scanned with this light, an image of the surface with a resolution comparable to the aperture size, rather than the wavelength, can be generated. In fact, the basic principles of microscopy in the near field with apertured beams of electromagnetic radiation were detailed over a decade ago in the microwave regime by Ash and Nicholls.⁴ Nonetheless, until 1983¹ there were no reports of the extension of Ash and Nicholls's pioneering studies to visible wavelengths. The principal reasons for this were (1) the need for stringent vibration isolation requirements, (2) the need for technologies to effect movements in the nanometer range, and (3) the critical need for a well-defined aperture that could be easily fabricated and readily placed within the near field of even rough surfaces. The first two of these requirements have been met for several years. The best example of their solution is the stunning imaging of atoms obtained with scanning tunneling microscopy.⁵

The third problem was of fundamental importance; without a solution of this problem no development of near-field optics toward practical problems in microscopy and spectroscopy was feasible. In fact, the best solution of the problem has come from the application of a unique new method first developed by biologists for impaling single cells for microinjection and electrophysiological measurements.⁶ By use of microprocessor-controlled pipette pullers, pipettes made of aluminum silicate have been pulled with outer diameters of less than 20 nm and with apertures of considerably less than that. With such pipettes, appropriately coated with metal, we have been able to obtain scans of rough surfaces with a resolution better than 60 nm even when fluorescence detection at 700 nm is used.⁷

Several methods have been developed to use

these pipettes to produce small spots of light either by aperturing the light or using the pipette tips as lightning rods. In addition, several methods are available to insure that the pipette will be within the near field of the surface. Our results indicate that nondestructive spectral imaging of surfaces in air at the resolution of a scanning electron microscope can now be achieved. Of course, this form of super-resolution spectral microscopy can make use of all the advantages of light, such as fluorescence, which have been applied so successfully in the past to complex macromolecular systems. Furthermore, simply by pulling the pipette away from the surface, a far-field scan can be generated with resolution comparable to that of a conventional light microscope. Thus, in a near-field scanning optical spectral microscope (NSOM), one has the ability to zoom from the far field to the near field and even to within a few nanometers from the surface, where tunneling can be detected with the metal-coated pipettes. This is a capability that is sorely lacking in present scanning tunneling microscopes and one that is absolutely essential for the successful application of scanning tunneling microscopy to complex molecular systems.

In summary, the frontier technologies of micromovement and ultra-isolation have opened the unique properties of the optical near field. We hope to convey an understanding of the unparalleled microbeam possibilities that this advance opens, from nondestructive imaging to electronic and vibrational spectroscopy and even super-resolution photochemistry.

References

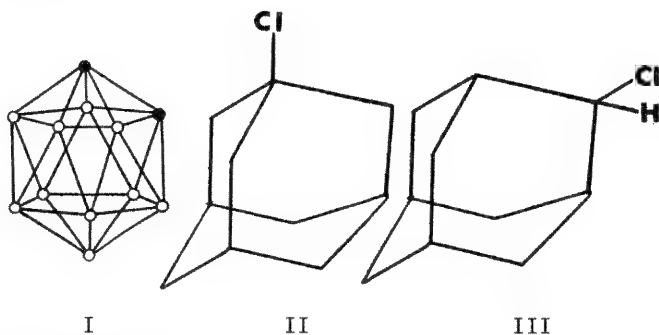
1. A. Lewis, M. Isaacson, A. Murray, and A. Harootunian, *Biophys. Soc. Abs.* 41: 405a, 1983.
2. A. Lewis, M. Isaacson, A. Harootunian, and A. Murray, *Ultramicroscopy* 13: 227, 1984.
3. E. Betzig, A. Harootunian, A. Lewis, and M. Isaacson, *Appl. Opt.* 25: 1890, 1986.
4. E. A. Ash and G. Nicholls, *Nature* 237: 510, 1972.
5. An excellent summary of present achievements in scanning tunneling microscopy appeared in a review by P. K. Hansma and J. Tersoff, *J. Appl. Phys.* 61: R1, 1987.
6. K. T. Brown and D. G. Flaming, *Neuroscience* 2: 813, 1977.
7. A. Harootunian, E. Betzig, M. S. Isaacson, and A. Lewis, *Appl. Phys. Lett.* 49: 674, 1986.

A. Lewis, K. Lieberman, and V. Habib are at the Department of Applied Physics, Hebrew University, Jerusalem, Israel; M. Isaacson and E. Betzig are at the Department of Applied Physics, Cornell University, Ithaca, N.Y.; and A. Harootunian is at the Department of Physiology, University of California, Berkeley.

APPLICATION OF HIGH-PRESSURE MICRO-RAMAN SPECTROSCOPY IN THE DETECTION OF PHASE TRANSITIONS IN ORIENTATIONALLY-DISORDERED SOLIDS

I. S. Butler, D. F. R. Gilson, R. M. Paroli, N. T. Kawai, and Gabriel Lord

Recently, we reported the successful coupling of a high-pressure diamond-anvil cell (DAC) to a micro-Raman spectrometer and demonstrated the simplicity of this spectroscopic approach in examining the properties of some inorganic materials at external pressures approaching 70 kbar ($\sim 70\,000$ atm).¹ One of our current interests involves the study of the phase-transition behavior of orientationally disordered solids or "plastic crystals," as they are sometimes termed. These materials are now attracting considerable industrial attention because of their potential uses in passive, thermal-energy storage devices for buildings and even clothing.² In the present work, we have used the DAC-micro-Raman technique to investigate several compounds with cage structures, e.g., *o*-carborane, $B_{10}C_2H_{12}$ (I, where the H atoms have been omitted for the sake of clarity) and the geometrical isomers 1- and 2-chloroadamantane $C_{10}H_{15}Cl$ (II and III). These "globular" molecules are known to exhibit order-disorder phase transitions in the solid state at low temperatures,³ and we anticipated that it might also be possible to induce the same phase transitions by application of high external pressures.



Experimental

Commercial samples of the three compounds were purified immediately prior to use by slow sublimation at reduced pressure (21° , 10^{-3} torr). Complete details of the DAC (Diacell Products) and the Instruments S.A. micro-Raman spectrometer have been reported previously.¹ The sample being analyzed and a minute piece of powdered ruby were placed in the $300\mu\text{m}$ hole of a $400\mu\text{m}$ -thick stainless-steel gasket.

The authors are at the Department of Chemistry, McGill University, 801 Sherbrooke St. West, Montreal, Quebec, Canada H3A 2K6. This research was supported by operating and equipment grants from NSERC (Canada) and FCAR (Quebec).

Since the samples are typical plastic crystals, they were difficult to manipulate at room temperature. At low temperatures, plastic crystals are much easier to handle because they are in their ordered states. Consequently, we cooled the samples with liquid nitrogen immediately before placing them in the gasket hole. The $4\times$ objective of the Nachet optical microscope proved to be the most efficient both for focusing the laser beam into the DAC and for collecting the resulting backscattered Raman and ruby fluorescence radiation. The fluorescence spectrum of ruby shifts linearly with applied pressure,⁴ and so the fluorescence spectrum of the ruby chip in the DAC was monitored before and after each Raman measurement in order to provide a measure of the actual pressure being applied between the parallel faces of the two type IIA diamonds in the DAC.

Results and Discussion

All three compounds exhibited one phase transition when subjected to high external pressures. The Raman spectra of the various high-pressure phases mirrored those produced upon lowering the temperature, which shows that the same phases were produced under both conditions. The pressures and temperatures at which the phase transitions occur and the associated enthalpies and entropies of transition (from DSC measurements) are given in Table 1. In the case of compound III, only one phase transition was detected in the pressure work, but two were observed in the variable temperature and DSC studies. The effect of pressure on the B-B stretching modes of *o*-carborane (Fig. 1) illustrates the spectral changes detectable by use of the DAC-micro-Raman spectrometer. The ease with which the laser beam can be focused onto the sample and ruby chip in the gasket hole by use of the microscope makes this technique much more convenient than that employed in traditional high-pressure Raman measurements.⁴ For this reason, we believe that other chemical applications of DAC-micro-Raman spectroscopy will soon be forthcoming, especially if the apparatus can be temperature controlled at the same time. Such combined pressure-temperature control will be of particular interest to geochemists who wish to obtain molecular information on the effects of high pressure and temperature on the structures of minerals.

TABLE 1.--Experimental data for the pressure- and temperature-induced phase transitions in compounds I-III.

Compound	Occurrence of phase transition		DSC results ³	
	(kbar)	(K)	$\Delta H^\#$ (kJ mol ⁻¹)	$\Delta S^\#$ (JK ⁻¹ mol ⁻¹)
I	10	270.6 ³	9.25	34.2
II	4	244.2 ³	6.01	24.6
III	6	242.0 ⁹	8.46	34.9
		227.0	0.52	2.3

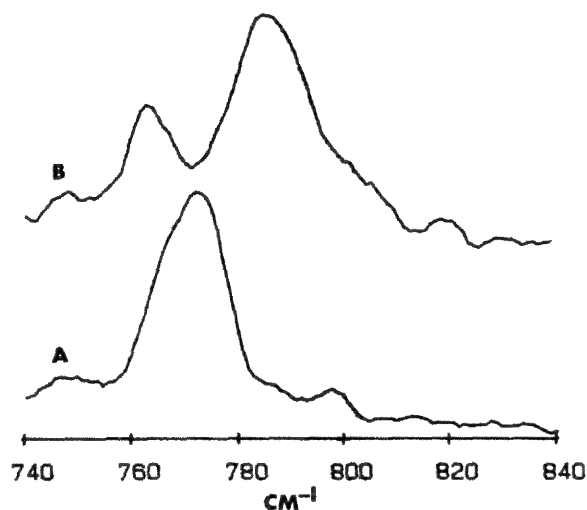


FIG. 1.--DAC-Micro-Raman spectra of o-carborane in the B-B stretching regions: (a) at ambient pressure, (b) at 30 kbar. Conditions: argon-ion laser excitation, 514.5 nm, 20 mW at sample; slit widths, 300 μ m; 3 scans at 1 s point⁻¹ in 1 cm⁻¹ steps.

References

1. V. Benham, G. Lord, I. S. Butler, and D. F. R. Gilson, "High-pressure diamond-anvil-cell micro-Raman spectra of mercuric cyanide, Hg(CN)₂, and cesium dodecahydroborate, Cs₂[B₁₂H₁₂]," *Appl. Spectrosc.* 41: 915, 1987.
2. A. C. West, "Hot/cold threads," *Popular Science* February 1988, 73.
3. R. M. Paroli, *Studies of Orientationally Disordered Organic and Inorganic Molecular Solids*, Ph.D. thesis, McGill University (in preparation).
4. J. R. Ferraro, *Vibrational Spectroscopy at High External Pressures: The Diamond Anvil Cell*, New York: Academic Press, 1984.
5. R. M. Paroli, N. T. Kawai, I. S. Butler, and D. F. R. Gilson, "Phase transitions and molecular motions in adamantane derivatives: 2-chloroadamantane," *Can. J. Chem.* (in press).

CHEMICAL BONDS AT THE INTERFACE OF GaAs/Si STUDIED BY MICRO-RAMAN SPECTROSCOPY

P. V. Huong, P. Boutinaud, S. Kazaoui, and A. Leycuras

The increasing interest in epitaxial gallium arsenide on silicon substrate promotes the studies of this semiconducting material, especially at the interfacial level. Micro-Raman spectroscopy¹⁻³ is a very suitable technique for such investigations.

Experimental

The GaAs layer was grown by metal-organic vapor-phase epitaxy on silicon (100). A beveled sample (Fig. 1) was prepared to allow the observation of various areas, from the substrate to the interface and to the outer surface of the GaAs deposit. The micro-Raman spectrometer (Dilor Model OMARS 89) was equipped with an argon-ion laser (Spectra-Physics Model 164) emitting at 514.5 nm, and a multichannel diode-array detector.

Results and Discussion

The direct growth of GaAs on silicon generally leads to highly dislocated materials with poor electronic properties. The Raman spectrum of such poorly oriented GaAs or twinned materials presents two bands at 269 cm^{-1} (TO) and 292 cm^{-1} (LO); the TO scattering is normally forbidden in the backscattering geometry on the (100) face of GaAs.⁴

The Raman spectrum of epitaxial GaAs on silicon at the interface (Fig. 2c) is different from that of silicon (Fig. 2a) and of well-oriented (100) GaAs (Fig. 2b). A band centered at 518 cm^{-1} illustrates that at the interface, the silicon becomes less ordered in comparison with single-crystal silicon characterized by a Raman band at 523 cm^{-1} with a bandwidth of 3.7 cm^{-1} . This disorder is in agreement with the broadening of the band. A very broad base of the band could correspond to a very perturbed structure of silicon caused by strong interactions with gallium arsenide.

As far as gallium arsenide is concerned, the strong enhancement of its TO phonon at 265 cm^{-1} in comparison with the LO band at 289 cm^{-1} also shows a strong perturbation of its crystalline structure. The appearance of this band has been observed when the material was heavily doped⁵ or mixed with other substances.⁶ In our case, it can be due simply to the disorder resulting from strong interactions between GaAs and silicon.

The authors are at the Laboratoire de Spectroscopie Moléculaire et Cristalline, U.A. 124 CNRS, Université de Bordeaux I, 351 cours de la Libération, F-33405 Talence, France, except A. Leycuras, who is at the Laboratoire de Physique du Solide et de l'Energie Solaire, CNRS, F-06560 Valbonne, France.

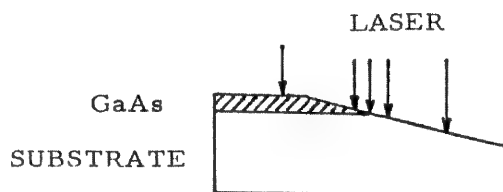


FIG. 1.--Profile of beveled sample of GaAs on silicon.

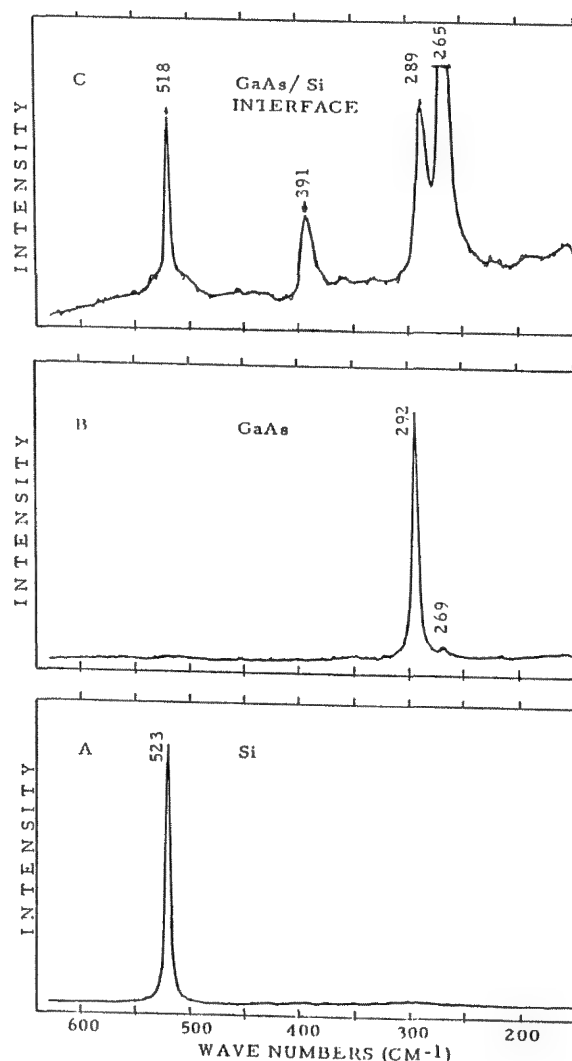


FIG. 2.--Raman spectra of semiconductor materials: Backscattering (a) on (100) surface of Si, (b) on (100) surface of GaAs, (c) at the GaAs/Si interface.

In addition, a new band appears at 391 cm^{-1} . This band may not be attributed to phonon L^+ in doped crystals which appears only for geometrical configurations not used in our experiment and whose frequency can be determined as a function of its partner L^- . We associate this new band with the presence of new chemical bonds between GaAs and silicon at the interface. In agreement with this association, no such band is observed for the GaAs/Ge interface⁷ in the same frequency range.

The frequency observed at 391 cm^{-1} corresponds roughly to what one can calculate in a first approximation by considering the reduced mass of the oscillators.

Based on very recent results obtained by photoemission core level spectroscopy⁸ showing a preference of arsenic to bond to the silicon 100 surface, we assign the new observed band to covalent-like Si-As bonds. This result is in contrast with that reported for the Ga/As/germanium interface where both As-Ge and Ga-Ge are evident at 260 and 266 cm^{-1} , respectively.⁷

Conclusion

Micro-Raman spectroscopy is a useful technique not only for characterizing the crystalline quality of the layers of GaAs on silicon but also allows to make evident the interaction mode at the GaAs/substrate interface.

In the case of GaAs on silicon, a new Si-As bond is evidenced with a characteristic phonon frequency located at 392 cm^{-1} . This result is in contrast with GaAs on germanium, where both Ge-As and Ge-Ga are present.

References

1. P. V. Huong, "New possibilities of Raman and resonance Raman spectroscopy," in L. Niinisto, Ed., *Reviews on Analytical Chemistry*, Budapest: Akademia Kiado, 1982.
2. P. V. Huong, "Laser Raman and resonance Raman spectroscopy of ferroelectrics and semiconductors," in H. D. Bist et al., Eds., *Lasers and Applications*, Bombay: Tata McGraw-Hill, 1984.
3. P. V. Huong, "Analysis of micro-electronic materials by micro-Raman spectroscopy," in M. Grasserbauer, Ed., *Analysis for the Development of Microelectronic Devices*, Amsterdam: Elsevier, 1988.
4. A. Freundlich, A. Leycuras, J. C. Grenet, C. Vérié, and P. V. Huong, *Appl. Phys. Lett.* 51: 1352, 1987.
5. A. Moodian and A. L. McWhorter, in G. B. Wright, Ed., *Light Scattering Spectra of Solids*, New York: Springer, 1969, 285 and 297.
6. G. Landa, R. Carles, J. B. Renucci, C. Fontaine, E. Bederl, and A. Munoz-Yague, *J. Appl. Phys.* 60: 825, 1986.
7. P. V. Huong (in preparation).
8. R. D. Bringans, M. A. Olmstead, R. I. Guhrberg, and R. Z. Bachrach, *Phys. Rev. B* 36: 9569, 1987.

RAMAN MICROPROBE STUDY ON FRACTURE BEHAVIOR OF YTTRIUM OXIDE CONTAINING TETRAGONAL ZIRCONIA POLYCRYSTALS (Y-TZP)

Akira Ishitani, Gen Katagiri, Hideyuki Ishida, and Takaki Masaki

The stress-induced transformation of Y-TZP has been studied extensively in our group¹⁻³ using the Raman microprobe. The shape and size of the transformation zone around a fracture edge are determined precisely by the new technique. The present study aims at clarifying fracture mechanism in a three-point bending test and a tension test through observation of the transformation zone. Two-dimensional distribution analysis of the transformation gives good insight into the fracture mechanism.

Experimental

Y-TZP containing 0.5 mol% Al_2O_3 and 2.0-4.0 mol% Y_2O_3 was prepared by hot isostatic pressing. The three-point bending test was done after a Vickers hardness indentation or without it. Tension tests were done to obtain fractured specimens with various tensile strengths. All fractured test pieces were measured on the surfaces and also on cross sections prepared by slicing perpendicular to both the surface and the fractured face. Two-dimensional mapping was carried out on the fractured face of test pieces after the tension tests.

Raman spectra were recorded with a Raman microprobe, MOLE (Jobin-Yvon), with the 4880 Å line of an Ar-ion laser. The fraction C_m is determined by the equation

$$C_m = \frac{I_m(181) + I_m(192)}{4.4 I_t(146) + I_m(181) + I_m(192)}$$

where t denotes tetragonal phase and the intensities I are measured at the indicated Raman shifts (i.e., wavenumbers) of the analytical Raman bands.

Results

Lateral and depth resolutions of the present measurements are checked experimentally.

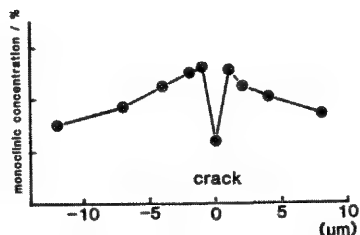


FIG. 1.--Transformation distribution across thin crack produced by bending test on 0.4 ml% Y-TZP test piece.

The authors are at the Toray Research Center, Inc., 1-1 Sonoyama 1-chome, Otsu, Shiga 520, Japan.

Figure 1 indicates variation of the values of C_m across a very thin crack. The sharp variation indicates a lateral resolution better than a few micrometers. Depth resolution is not as good as the lateral resolution by far because of the optical transparency of the material. Experimental estimation is done by a thin wedge (Fig. 2), from which is derived the maximum sampling depth of around 40 μm.

Depth distribution of C_m for 2.0 mol% Y_2O_3 Y-TZP after the three-point bending test is indicated in Fig. 3. There is a substantial difference in the transformation behavior between the tension surface and the compression surface. The transformation zone extends in complicated ways far from the fractured edge in the tension surface, whereas the transformation scarcely takes place in the compression surface.

A fractured face generated by the tension test is mapped by dividing a $100 \times 200 \mu\text{m}$ area into 160 pixels and determining C_m for each pixel. An example is given in Fig. 4, with the corresponding optical microscopic image. Fracture starts at the right upper end and extends toward the left downward. The degree of the transformation increases with extension of the fracture, which is in good correspondence with the microscopic image. A test piece with larger tensile strength indicates higher degree of transformation.

Conclusion

The Raman microprobe provides important information for understanding of the fracture mechanism of Y-TZP by mapping the distribution of the generated monoclinic phase with a lateral and depth resolution of a few micrometers and 40 μm, respectively. The shape and size of the transformation corresponds well with the observed tensile strength.

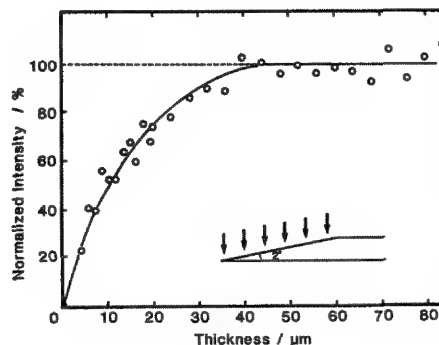


FIG. 2.--Evaluation of depth resolution of Raman microprobe on Y-TZP.

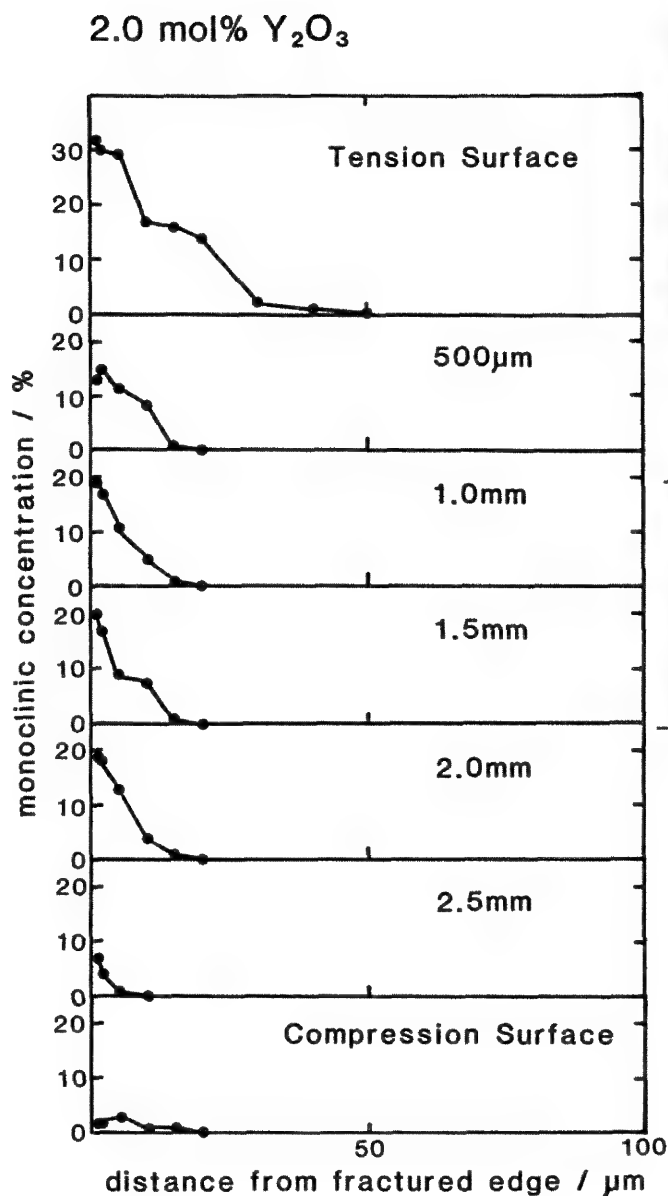


FIG. 3.--Depth dependence of transformation zone size for fractured specimen of 2.0 mol% Y-TZP after three-point bending test.

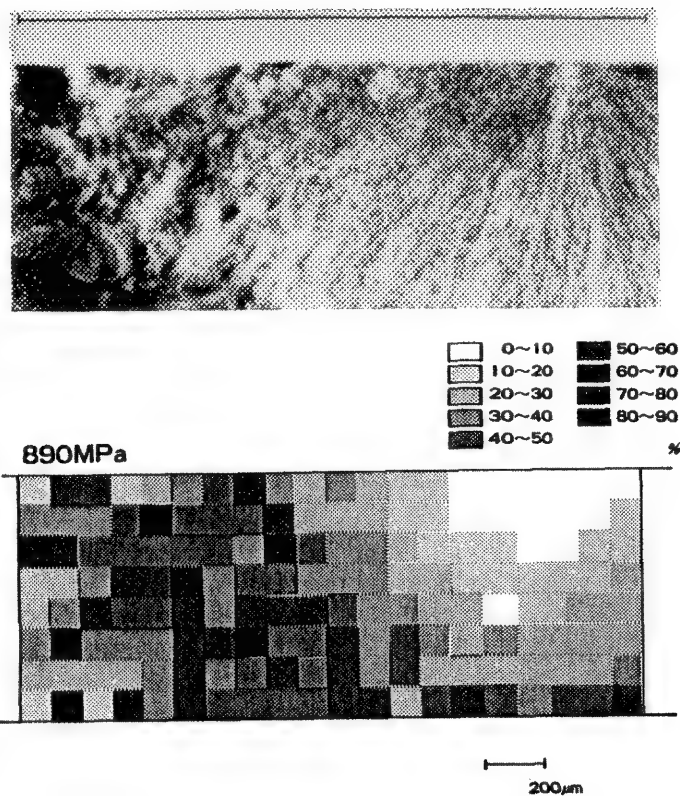


FIG. 4.--Two-dimensional mapping of degree of transformation on fractured face of a 2.0 mol% Y-TZP specimen produced by tension test which gives tensile strength of 89 kgf/mm².

References

1. G. Katagiri, M. Teramura, H. Ishida, T. Masaki, and A. Ishitani, *10th Intern. Conf. Raman Spectroscopy*, Eugene, Ore., 1986.
2. G. Katagiri, H. Ishida, A. Ishitani, and T. Masaki, *Material Research Society Symposium Proc.* 78: 43, 1987.
3. G. Katagiri, H. Ishida, A. Ishitani, and T. Masaki, "Science and technology of zirconia," *Advances in Ceramics* 24: 1988.

CALIBRATION OF A MULTICHANNEL MICRO-RAMAN SPECTROGRAPH WITH PLASMA LINES OF ARGON AND KRYPTON ION LASERS

S. K. Sharma, Naresh Pandya and D. W. Muenow

Multichannel micro-Raman spectrographs, because of their multiplex advantage, are finding increasing application in a wide variety of fields, including geochemical and materials research. However, there is a need for accurate calibration of spectral data collected with a multichannel spectrograph and diode-array detector.¹ Although algorithms for performing such calibrations in terms of wavelength or wave number have already been developed,^{1,2} they require accurate knowledge of focal length, tilt of focal plane, groove density of grating, and all pertinent angles.² Variation in any of these parameters with time or because of change in room temperature can adversely affect the calibration. Multichannel spectrographs are generally calibrated with the emission lines of neon, the spectrum of which covers the entire visible region (400-900 nm). However, to avoid error one has to make certain that the optical path of the neon light is exactly the same as that of the scattered Raman signal from the sample. Alternatively, plasma lines of Ar⁺ and Kr⁺ lasers are extensively used for calibrating conventional single-channel Raman spectrometers.³⁻⁵ In order to use these same spectra for calibrating multichannel micro-Raman spectrographs, we need a convenient and rapid recording method that does not affect the basic alignment of laser beam and microscope. In this paper we present such a method using a fiber-optics link between the laser source and the micro-Raman spectrograph.

Experimental

The multichannel micro-Raman apparatus used in our laboratory (Fig. 1) consists of a modified Leitz Ortholux I microscope optically coupled with a Spex Triplemate spectrograph and an optical multichannel detector and analyzer (OMA III, model 1421 detector and model 1460 analyzer, EG&G Princeton Applied Research). This apparatus is described in detail elsewhere.⁶

A fiber-optics system developed for calibrating the multichannel spectrograph with the plasma lines of an ion (Ar⁺ or Kr⁺) laser is also shown in Fig. 1. The fiber-optics probe was made from a 2m long and 250 μ m-diameter core silica fiber, with the protective coating re-

moved at both ends. The laser end of the fiber was sealed in an SMA-style connector (Newport Corp.) with epoxy, ground on a 600-grit silicon carbide paper, and subsequently polished with 5 μ m and then 0.05 μ m alumina powder. The microscope end of the fiber was terminated with a tungsten-carbide knife and mounted in the fiber holder. The SMA connector was mounted in a five-axis positioner (Newport FP-2) to allow precise positioning of the fiber with respect to the input laser beam. By displacing prism A on an optical bench, the fiber-optics system was positioned between the laser and the pre-monochromator in such a way that it did not affect the rest of the optical alignment of the micro-Raman spectrograph and the laser beam. The laser beam from an Ar⁺ (Spectra Physics model 2020-05) or Kr⁺ (Spectra Physics model 2025) ion laser was focused through a lens on one of the polished ends of the silica fiber (Fig. 1). After beam alignment to give maximum transmission at the other end of the fiber, the laser was detuned. The microscope end was attached to a fiber holder and positioned at the focal point of the objective (Fig. 1). In this arrangement, the light from the Ar⁺ or Kr⁺ ion laser plasma tube travels the same optical path as the Raman-scattered light in the 180° scattering geometry from the sample.

The spectra of the Ar⁺ and Kr⁺ plasma lines were recorded with 600 grooves (g)/mm gratings in the filter stage of the spectrograph and a 1200g/mm grating in the spectrograph stage. This arrangement allows recording of the plasma lines in a region \sim 1200cm⁻¹ wide about the 488.0nm Ar⁺ laser line, and in one \sim 625cm⁻¹ about the 647.1nm Kr⁺ line. However, one can double these spectral ranges by replacing the 600g/mm gratings in the filter stage with the 300g/mm gratings and by selecting the 600 g/mm turreted grating of the spectrograph stage. For such larger spectral coverage (2400cm⁻¹ wide region in the blue part of the spectrum), one has to sacrifice resolution between (as well as positional accuracy of) spectral lines because of low dispersion of the grating and finite width of the diodes in the array detector. Most of the results reported here were therefore carried out with the 1200g/mm grating. After the spectra of plasma lines were recorded in the desired range, the data were stored on a floppy diskette in the Model 1460 Optical Multichannel Analyzer (OMA). The OMA allows calibration in wavelength or wavenumbers with linear or cubic fit of the x-axis. We found that cubic-fit calibration of the abscissa, which uses a third-order equation, gave the best fit. The

The authors are with the University of Hawaii. S. K. Sharma is affiliated with the Hawaii Institute of Geophysics, 2525 Correa Rd., Honolulu, HI 96822; N. Pandya and D. W. Muenow are affiliated with the Department of Chemistry. This work is supported by the National Science Foundation grant EAR-8517888. Hawaii Institute of Geophysics Contribution No 1994.

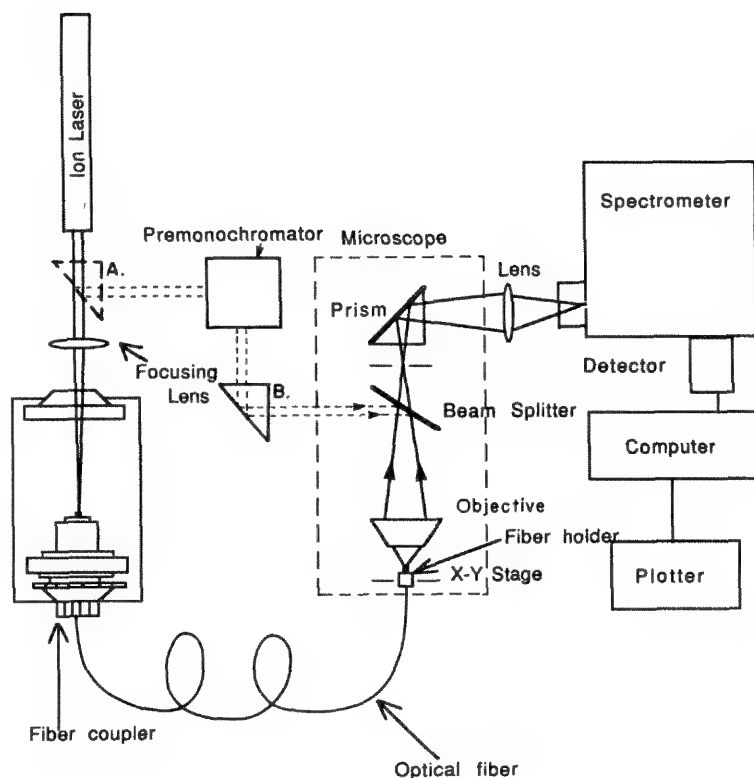


FIG. 1.--Schematic diagram of fiber-optics system for calibrating multichannel micro-Raman spectrograph with plasma lines of Ar^+ or Kr^+ laser.

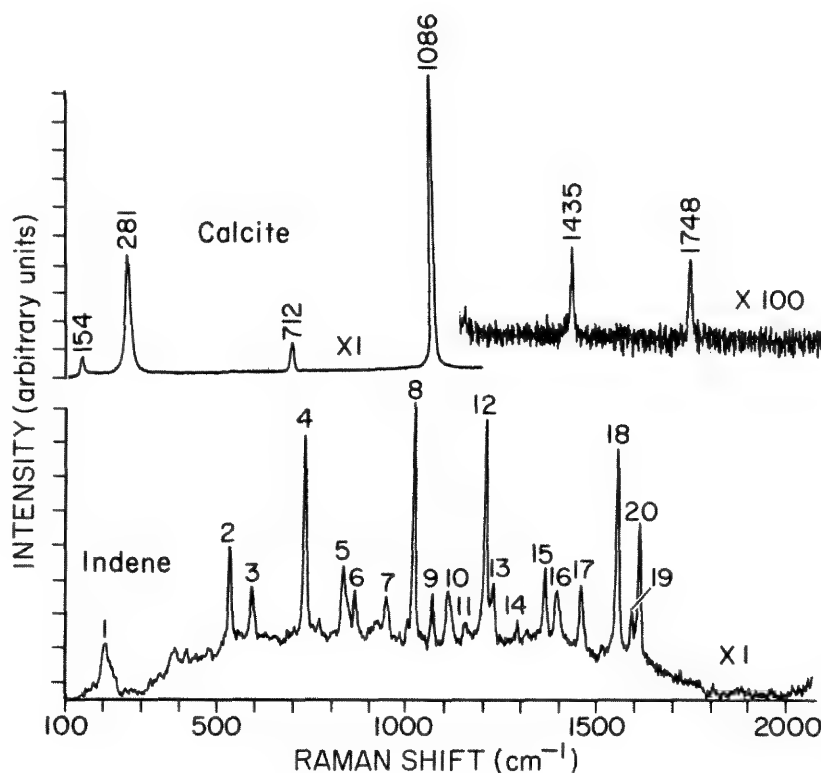


FIG. 2.--Composite multichannel Raman spectra of calcite and indene (bottom) ($100\text{--}1000\text{cm}^{-1}$ region) calibrated with Ar^+ plasma lines. Frequencies of numbered lines of indene are given in Table 1 (laser 488.0 nm , 10 mW at the sample; grating 1200 g/mm ; exposure time 1 s ; number of scans 60).

apparent Raman displacement of the plasma lines from the laser lines (488.0 nm for Ar^+ and 647.1 nm for Kr^+ laser) were used for calibration.^{4,5,7} After the spectrograph was calibrated in the desired range, the fiber-optics

system was removed and the laser was tuned to carry out Raman measurements by moving prism A into its original position (Fig. 1). The Ar^+ -plasma-line-calibrated Raman spectra of indene and calcite are shown in Fig. 2. The frequen-

TABLE 1.--Comparison of the frequencies of the Raman lines of indene recorded with single-channel and multichannel spectrometers.

Line #	Single channel Previous work ³ (cm ⁻¹)	Multichannel Present work (cm ⁻¹)	Difference (cm ⁻¹)	Lines recommended for calibration purposes
1	205.0 ± 2	204.4	0.6	
2	533.7 ± 0.5	533.7	0.0	←
3	593.0 ± 2	591.0	2.0	
4	730.1 ± 0.2	730.7	-0.6	←
5	830.5 ± 0.2	831.7	-1.2	
6	861.3 ± 0.2	861.6	-0.3	
7	947.2 ± 0.3	946.5	0.7	
8	1018.6 ± 0.2	1018.1	0.5	←
9	1067.9 ± 0.2	1068.6	-0.7	←
10	1108.9 ± 1	1108.3	0.6	
11	1154.5 ± 0.5	1154.6	-0.1	
12	1205.2 ± 0.2	1204.7	0.5	←
13	1226.2 ± 0.2	1225.7	0.5	←
14	1287.8 ± 0.2	1288.5	-0.7	
15	1361.3 ± 0.4	1362.5	-1.2	←
16	1393.2 ± 1	1393.5	-0.3	←
17	1457.8 ± 0.5	1457.5	0.3	←
18	1553.3 ± 0.5	1552.3	1.0	←
19	1589.8 ± 1	1589.7	0.1	
20	1609.6 ± 0.2	1609.5	0.1	←

cies of the Raman lines of indene in the 100-1800cm⁻¹ region are compared with previously published data³ (recorded with a single-channel spectrograph) in Table 1. It is evident from Table 1 that the positions of the indene lines measured by the two techniques are in good mutual agreement.

In the 50-1800cm⁻¹ region, the frequencies of the Raman lines in the spectrum of crystalline calcite (see Fig. 2), calibrated with the Ar⁺ plasma lines, are in good agreement with the published frequencies of these calcite Raman lines.^{8,9} The first-order Raman line of diamond measured in the multichannel spectrum at 1332 cm⁻¹ is likewise in good agreement with previous measurements. In fact, we found that between the 154 and the 1333cm⁻¹ region, one can use the cumulative set of Raman lines of optical grade calcite and diamond microcrystals as a secondary standard for routine calibration of the multichannel micro-Raman spectrograph. Such calibration was found to be accurate to within ±1.2 cm⁻¹ (or ± 1 pixel).

Similar results were obtained by calibrating with either the Ar⁺ or Kr⁺ plasma lines in the high-frequency region. In the 2800-4000cm⁻¹ region, it was sometimes difficult to assign correct apparent displacements of plasma emission lines because of alteration in their relative intensities. In order to identify the plasma lines correctly, we therefore used high-frequency Raman lines of liquids such as indene (2892, 3055, 3068 and 3113 cm⁻¹), methanol (2832, 2940 and 3030 cm⁻¹), and water (3185, 3456 cm⁻¹) for an approximate calibra-

tion of the spectrograph. Once all the emission lines were correctly identified, the calibration in the high-frequency region was carried out as before with the plasma lines of Ar⁺ or Kr⁺ lasers.

We conclude that, using a fiber-optic cable, it is possible accurately to calibrate multichannel micro-Raman spectrometers with laser plasma lines. The plasma lines of Ar⁺ and Kr⁺ ion lasers are found to be a convenient and reliable means of calibrating multichannel Raman spectrometers.

References

1. M. Diem, F. Adar, and R. Grayzel, "A simple algorithm to convert diode array spectral data to linear wavelength or wave number scales," *Computer Enhanced Spectroscopy* 43: 29, 1986.
2. J. M. Katzenberger, F. Adar, and J. M. Lerner, "An improved algorithm for linearizing in wavelength or wave number spectral data acquired with a diode array," *Microbeam Analysis --1987*, 165.
3. J. Loader, *Basic Raman Spectroscopy*, London: Heyden, 1970, 105.
4. N. C. Craig and I. W. Levin, "Calibrating Raman spectrometers with plasma lines from the argon ion laser," *Appl. Spectrosc.* 33: 475.
5. C. Julien and C. Hirlimann, "Calibration of a Raman spectrometer using the Kr laser plasma lines," *J. Raman Spectrosc.* 9: 62, 1980.
6. S. K. Sharma and J. P. Urmos, "Micro-

Raman spectroscopic studies of materials at ambient and high pressures with CW and pulsed lasers," *Microbeam Analysis--1987*, 133.

7. D. P. Strommen and K. Nakamoto, *Laboratory Raman Spectroscopy*, New York: Wiley, 1984, 138.

8. W. B. White, "The carbonate minerals," in V. C. Farmer, Ed., *The Infrared Spectra of Minerals*, London: Mineralogical Society, 1974, 227.

9. W. D. Bischoff, S. K. Sharma, and F. T. Mackenzie, "Carbonate ion disorder in synthetic and biogenic magnesian calcites: A Raman spectral study," *Am. Mineral.* 70: 581, 1985.

THE PRACTICAL ADVANTAGES OF FT-RAMAN SPECTROSCOPY FOR MACRO- AND MICRO-SAMPLING

F. J. Purcell and R. E. Heinz

Fluorescence interference has been a major impediment to significantly wider use of Raman spectroscopy for both macro- and micro-experiments. Fourier-transform Raman in the near-infrared with an interferometer-based instrument system eliminates this problem, which makes it possible to apply the unique advantages of Raman to the analysis of virtually any sample.

Experimental

The principal analytical advantages of Raman spectroscopy can be attributed to a number of factors. Among them are the noncontact nature of the technique and the simplicity of sample preparation. Raman microprobe systems also permit spatial resolution on the order of $1\mu\text{m}$ and thus facilitate analysis of minute particles within larger samples. Most important, the basic spectral fingerprint of a molecule reveals information essential to manipulating the characteristics of numerous materials. Raman spectra communicate many subtleties of molecular structure, including information about isomerization, phase changes, and conformation. Furthermore, the narrowness of the peaks and relative spectral simplicity allow easier analysis of mixtures.

In terms of experimental methodology, the past few years have seen the wider utilization of techniques like Hadamard transform Raman¹⁻⁴ and deep-UV excitation for Raman experiments.⁵⁻⁷ The availability of multichannel detectors has also contributed to expanding interest in Raman. However, despite these advances in technique and hardware, Raman has had one major drawback--fluorescence interference.

For many users, especially in industry, it is fortunate that the central problem of fluorescence has been eliminated through the development of instrument systems configured to perform Fourier-transform Raman in the near-infrared.⁸⁻¹³ Designed for economy and convenient operation, systems like the SPEX FT E/IR place a powerful analytical technique at the disposal of researchers who have been unable to apply Raman because of fluorescence.

The spectra presented with this article were taken on an FT-Raman system consisting of a 35W continuous wave Nd:YAG laser for sample excitation, laser prefilter, sample compartment with 180° collection optics and built-in power meter, Bomen 100 Michelson interferometer, and cooled InGaAs detector. A PC/AT compatible computer, which runs dedicated spectrometric software, controls the system and automates all

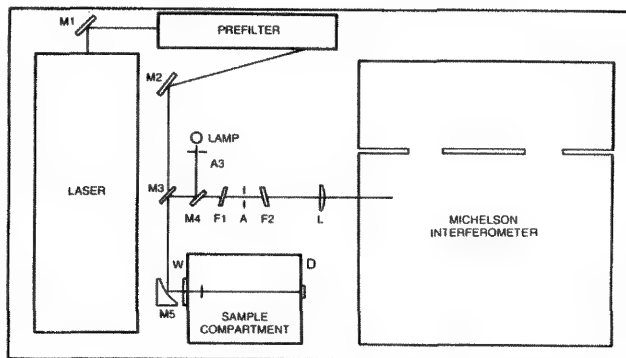


FIG. 1.--SPEX FT R/IR optical diagram. A = aperture, D = power meter, F = filter, L = lens, M = mirror, W = window.

experiments. Figure 1 is an optical diagram of the system, which affords spectral resolution of 4 cm^{-1} .

Presented for purposes of comparison, the conventional Raman spectra were acquired on a SPEX RAMALOG-9I system that includes a SPEX 1403 double spectrometer, 90° sample collection optics, and multialkali photomultiplier tube. Radiation from a Coherent Innova 70-4 4W argon-ion laser provided sample excitation. The data were accumulated with either 5.4.5nm or 488.0nm radiation at the sample and a power level of 50 mW. As with the FT-Raman experiments, resolution was 4 cm^{-1} . An optical diagram of this system has been published elsewhere.¹⁴

Since the laser in the FT-Raman system lases at $1.064\mu\text{m}$, samples are illuminated in a spectral region so far removed from the area where almost every material fluoresces that such interference no longer hinders effective analysis. To be sure, the intensity of Raman scattering at $1.064\mu\text{m}$ is less than 5% of what it would be at 514.5nm , and detectors for the near-IR are not as sensitive as photomultiplier tubes. An interferometer-based system overcomes these problems by observing an entire spectrum at once. In addition, an interferometer has better throughput than a spectrometer. Therefore, data acquisition times are comparable with those for conventional systems.

Most Raman systems acquire a spectrum point by point as the gratings scan the spectrum past the exit slit. In multichannel spectroscopy, a detector with a large number of channels observes an entire spectrum at one time. However, Fourier-transform spectroscopy changes some basic principles. The primary difference is that an interferometer replaces the spectrometer. The interferometer incorporates a beam splitter and two mirrors, one movable and the other stationary. During operation, incident

The authors are with SPEX Industries, Inc., 3880 Park Avenue, Edison, NJ 08820.

or scattered light is divided at the beam splitter, travels to the two mirrors, and is ultimately recombined at the beam splitter.

The resulting signal is the intensity of the scattered light as a function of time. Because travel for the moving mirror is only a centimeter or so, an entire scan can be accumulated in a relatively short period. The moving mirror also modulates the signal, which minimizes background problems in comparison with conventional spectroscopy. Moreover, throughput is improved with an interferometer, an advantage related to the large apertures which replace the slits of a spectrometer.

Results

The elimination of fluorescence with FT-Raman is dramatically demonstrated by the spectra shown in Fig. 2. Figure 2 shows a spectrum of rhodamine 6G obtained with a conventional Raman system and visible excitation. Only broadband fluorescence is observed in this spectrum. Because the fluorescence is inherent to the molecule itself, it is not possible to quench it or remove it by purification. Figure 2B is a Raman spectrum of the same sample obtained with the FT R/IR. Acquired in approximately 7s (the time required for a single scan), it could not be observed with excitation in the visible.

Figure 3 is a Raman spectrum of cyclohexane obtained with a conventional spectrometer. Operating conditions were 1.0 W of 514.5nm radiation at the sample, 4cm^{-1} resolution, 2cm^{-1} step size, 1s integration time and 1 scan. Data acquisition time was 37.5 min. The signal-to-noise ratio of the CH stretch peak at 2852cm^{-1} is 370:1. Figure 3 is a spectrum of the same sample taken with the FT R/IR. Experimental conditions were similar to Fig. 3, except that the number of scans was 100 and the data acquisition time was 11 min. The signal-to-noise ratio of the CH stretch peak at 2852cm^{-1} is 200:1. If the differences in collection time are taken into account, these values are the same. Thus, FT-Raman spectroscopy provides signal-to-noise performance comparable to conventional Raman spectroscopy under equivalent conditions. In fact, because the entire spectrum is observed simultaneously, it is often possible to obtain data with a satisfactory signal-to-noise ratio faster with an FT-Raman system.

Raman spectroscopy can provide a great deal of information about polymers, including data regarding composition, conformation, and isomerization, as well as degree of cross linking and crystallinity. However, polymers have been problem samples for Raman spectroscopy in the past because of fluorescence interference. This interference is sometimes from the polymer itself, but most often it is due to impurities, plasticizers, sizing, or coloring agents. For example, fibers of polyethyleneterephthalate (PET) are typically coated with a sizing that fluoresces.

In order to obtain a spectrum of a PET fiber

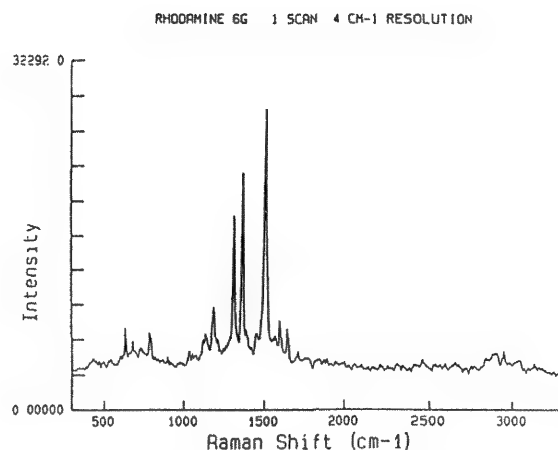
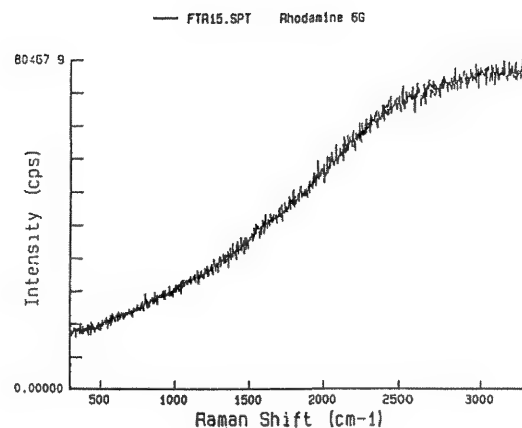


FIG. 2.--(a) Conventional Raman spectrum of rhodamine 6G obtained with 50 mW of 514.5nm radiation, 4cm^{-1} resolution, 0.05s integration time, and 2cm^{-1} step size. (b) FT-Raman spectrum of rhodamine 6G obtained with 0.4 W of $1.064\mu\text{m}$ radiation, 4cm^{-1} resolution, 1 scan.

with visible excitation, one must first wash the sizing off with methylene chloride. Figure 4 shows conventional Raman spectra of a PET fiber before and after washing. Figure 4 is a spectrum of unwashed PET fiber acquired with the FT R/IR system over a period of 11 min. Note the complete absence of fluorescence.

Another advantage gained by use of an interferometer rather than a spectrometer is greatly improved frequency accuracy. This feature becomes especially important for spectral subtractions. It is not necessary to use any special Raman difference accessories with the FT R/IR in order to obtain good spectral subtractions. Figure 5 shows FT-Raman spectra of toluene (A) and p-xylene (B). Figure 6 is a spectrum of a 44-56% mixture of p-xylene and toluene (A), a scaled p-xylene spectrum (B), and the result of subtracting a scaled toluene spectrum from the mixture. The

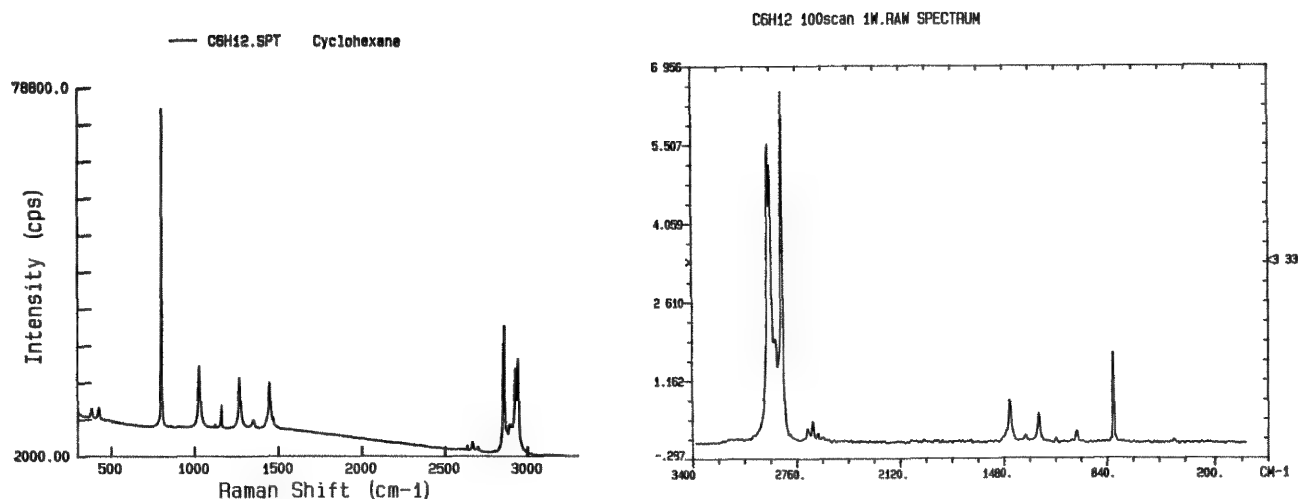


FIG. 3.--(a) Conventional Raman spectrum of cyclohexane obtained with 1.0 W of 514.5nm radiation, 4cm^{-1} resolution, 1s integration, and 2cm^{-1} step size. (b) FT-Raman spectrum of cyclohexane obtained with 1.0 W of 1.064 μm radiation, 4cm^{-1} resolution, and 100 scans.

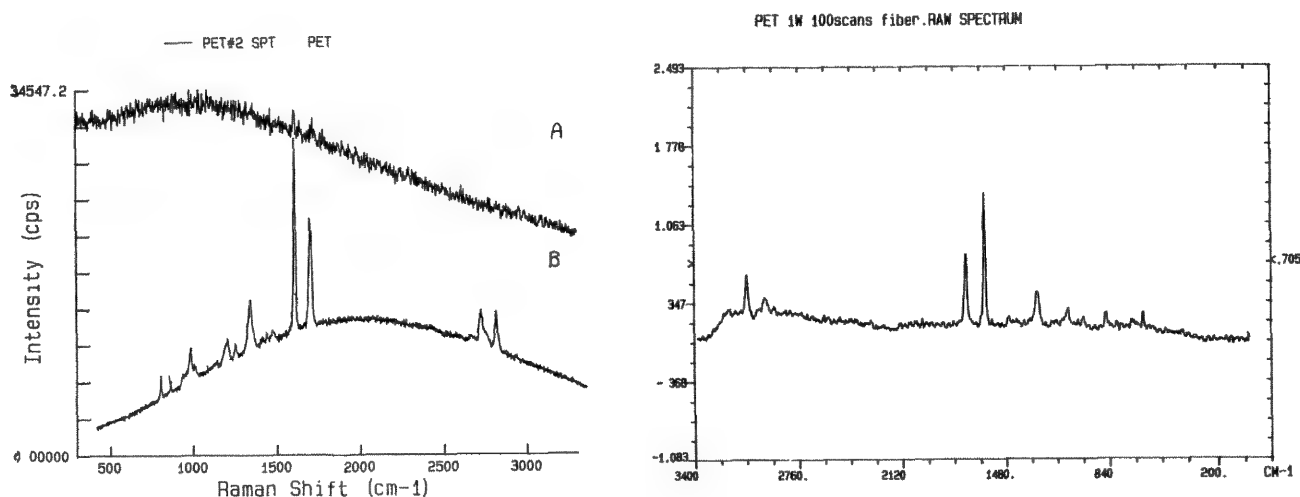


FIG. 4.--(a) Conventional Raman spectrum of polyethyleneterephthalate (PET) fiber before (A) and after (B) washing with methylene chloride. Operating parameters were 50 mW of 514.5nm radiation, 4cm^{-1} resolution, 0.5s integration time, and 2cm^{-1} step size. (b) FT-Raman spectrum of PET obtained under same conditions as in Fig. 3b.

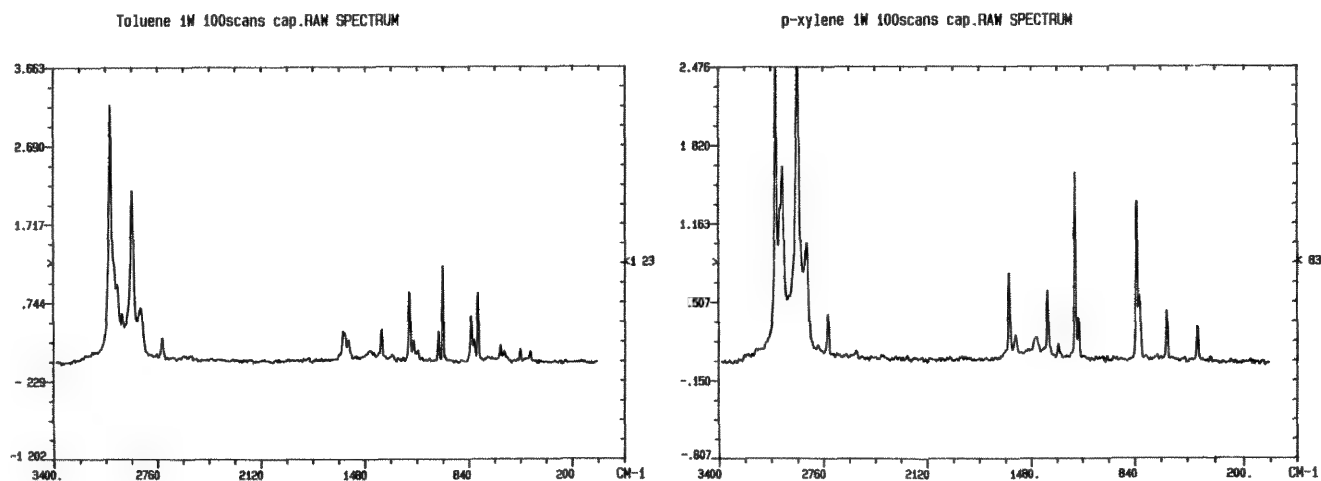


FIG. 5.--FT-Raman spectra of (a) toluene and (b) p-xylene. Operating parameters same as Fig. 3b.

dedicated FT R/IR software, similar to that available with Fourier-transform IR absorption systems, makes it easy to perform such spectral subtractions.

Conclusions

As these results indicate, elimination of the problem of fluorescence definitely establishes Fourier-transform Raman spectroscopy as a powerful analytical tool. This significant feature is complemented by data acquisition rates more than satisfactory for a large number of applications. Of course, as with any technique, FT-Raman spectroscopy has its limitations. For example, low-frequency vibrations below about 300 cm^{-1} are not observable at present. It is also impossible to obtain resonance Raman spectra in this region, since most compounds have their electronic absorption in the UV and visible. Moreover, because materials like silicon and gallium arsenide are transparent at $1.064\text{ }\mu\text{m}$, FT-Raman will be of minimal utility to researchers interested in characterizing semiconductors.

Looking toward the future, the next obvious step in the development of FT-Raman instrumentation is the implementation of micro-sampling capability. Although conventional Raman problems like sample heating due to high power densities still apply, they can be overcome. Messerschmidt et al. presented results at the 1988 Pittsburgh Conference demonstrating the feasibility of micro Raman spectroscopy in the near IR.¹⁵ A Spectra-Tech IR PLAN microscope and a Bomem DA 3 interferometer were used to examine a variety of organic and inorganic crystals as well as a polymer fiber. This work charts another dynamic direction for FT-Raman analysis, complementing the equal value of the technique for characterization of macro-samples.

References

1. D. C. Tilotta, R. M. Hammaker, and W. G. Fateley, "A visible near-infrared Hadamard transform spectrometer based on a liquid crystal spatial modulator array: A new approach in spectrometry," *Appl. Spectrosc.* 41: 727, 1987.
2. D. C. Tilotta, R. M. Hammaker, and W. G. Fateley, "Multiplex advantage in Hadamard transform spectrometry utilizing solid-state encoding masks with uniform, bistable optical transmission defects," *Appl. Opt.* 26: 4285, 1987.
3. D. C. Tilotta, R. D. Freeman, and W. G. Fateley, "Hadamard transform visible Raman spectroscopy," *Appl.*

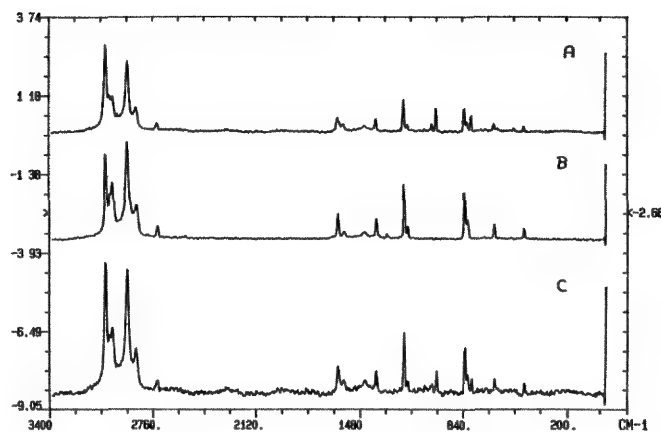


FIG. 6.--FT-Raman spectra of 44-56% mixture of p-xylene and toluene (A), scaled p-xylene (B), and subtracted result of the mixture minus toluene (C). Operating parameters same as Fig. 3.

Spectrosc. 41: 1280, 1987.

4. D. C. Tilotta and W. G. Fateley, "Hadamard transform spectroscopy: Teaching old monochromators new tricks," *Spectrosc.* 3: 14, 1988.
5. S. A. Asher, C. R. Johnson, and J. Murtaugh, "Development of a new UV resonance Raman spectrometer for the 217-400nm spectral region," *Rev. Sci. Instrum.* 54: 1657, 1983.
6. S. A. Asher, "Ultraviolet resonance Raman spectroscopy for detection and speciation of three polycyclic aromatic hydrocarbons," *Anal. Chem.* 56: 720, 1984.
7. S. A. Asher and C. R. Johnson, "Raman spectroscopy of a coal liquid shows that fluorescence interference is minimized with ultraviolet excitation," *Science* 225: 311, 1984.
8. D. E. Jennings, A. Weber, and J. W. Brault, "Raman spectroscopy of gases with a Fourier transform spectrometer: The spectrum of D_2 ," *Appl. Opt.* 25: 284, 1986.
9. T. Hirschfeld and D. B. Chase, "FT-Raman spectroscopy: Development and justification," *Appl. Spectrosc.* 40: 133, 1986.
10. D. J. Moffat, H. Buijs, and W. F. Murphy, "Interferometric observation of Raman spectra: Comparison of photomultiplier and avalanche-diode detectors," *Appl. Spectrosc.* 40: 1079, 1986.
11. D. B. Chase, "Fourier transform Raman spectroscopy," *Anal. Chem.* 59: 881A, 1987.
12. C. G. Zimba, V. M. Hallmark, J. D. Sawlen, and J. F. Rabolt, "Fourier transform Raman spectroscopy of long chain molecules containing strongly absorbing chromophores," *Appl. Spectrosc.* 41: 721, 1987.
13. V. M. Hallmark, C. G. Zimba, J. D. Sawlen, and J. F. Rabolt, "Fourier transform Raman spectroscopy: Scattering in the near-infrared," *Spectrosc.* 2: 40, 1987.
14. F. J. Purcell and W. B. White, "A Raman microprobe study of phase-separated minerals," *Microbeam Analysis--1983*, 289.
15. R. G. Messerschmidt, D. B. Chase, and J. A. Reffner, "Experimental results using near-infrared FT-Raman microprobe spectroscopy," 1988 Pittsburgh Conference and Exposition on Analytical Chemistry and Applied Spectroscopy.

TWO-DIMENSIONAL SPATIALLY RESOLVED RAMAN SPECTROSCOPY OF SOLID MATERIALS

D. K. Veirs, G. M. Rosenblatt, R. H. Dauskardt, and R. O. Ritchie

Chemical compositional analysis of solid materials often is based on vibrational spectroscopy, either infrared or Raman. Vibrational analysis is particularly valuable when information about molecular form, not only atomic composition, is desired. Many applications require analysis of small volumes necessitating sensitive instrumentation and spatial resolution. The development of multichannel detection systems for Raman spectroscopy coupled with microscopic techniques has resulted in a number of commercial Raman microprobes (from Spex Industries, Jobin-Yvon ISA, Dilor, for example)¹ capable of probing areas on the order of $100\ \mu\text{m}^2$ routinely. For macroscopic samples, with dimensions of thousands of microns on a side, an instrument which multiplexes both the spatial domain and wavelength would enhance the capability of Raman spectroscopy. We report on the development of such a Raman instrument and describe, as an example, its application to the investigation of the phase transformation accompanying crack growth in partially stabilized zirconia (PSZ).

Experimental

A Raman spectroscopy system employing an imaging photomultiplier tube (PMT) detector has been constructed. The instrument produces a one-dimensional Raman profile of a sample's chemical composition along the path illuminated by a focused slit-like laser beam. The system as configured at present achieves a resolution of $40\ \mu\text{m}$; theoretically, the spatial resolution can be improved to the diffraction limit with appropriate collection optics.² One acquires the one-dimensional Raman profile continuously without moving the sample or illuminating laser beam, and without scanning the spectrometer. By translation of the sample perpendicular to the focused illumination, a two-dimensional Raman map of the chemical composition can be obtained.

Figure 1 presents a schematic of the Raman apparatus used for obtaining spatially resolved Raman spectra. The 488nm cw Ar⁺ laser line passes through a six-cavity narrow bandpass interference filter which reduces the plasma line intensities by 10^{-6} . The laser is incident on

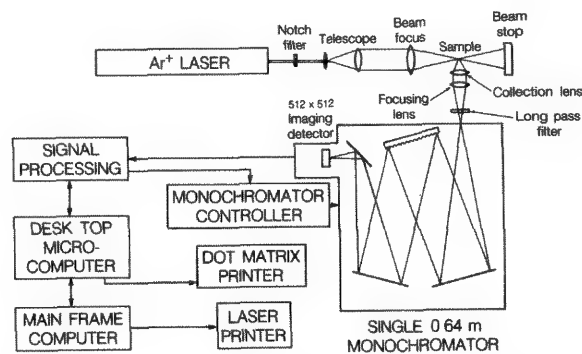


FIG. 1.--Schematic of Raman spectroscopy experimental apparatus.

a sample and the scattered light is collected and imaged onto the entrance slit of a single monochromator. A six-cavity interference filter is used to pass the spectral region of interest and to reject the Rayleigh scattered light by 10^{-6} before the monochromator. The dispersed light is detected by an imaging PMT consisting of a photocathode that generates photoelectrons with a quantum efficiency of 10-16%, five amplifying microchannel plates, and a resistive anode. The position of each arriving photon that generates a current is determined to an accuracy of $70\ \mu\text{m}$ in both the X and Y directions. The computed position of the photon is digitized in real time and passed to a digital data acquisition system. Each detected photon increments one element in a memory array which has a one-to-one correspondence with a map of the surface of the detector. Wavelength is dispersed along the X direction.

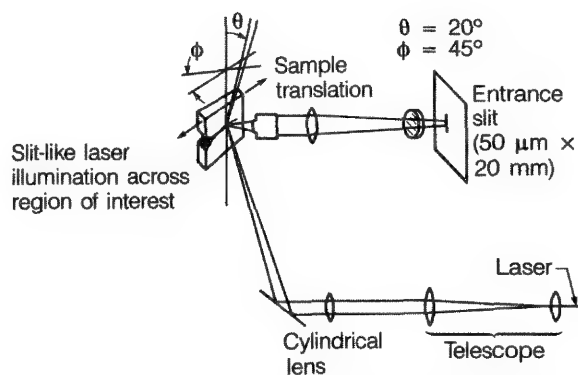


FIG. 2.--Optical arrangement used to obtain spatially resolved Raman spectra from surface of partially stabilized zirconia samples.

The authors are at the Materials and Chemical Sciences Division, Lawrence Berkeley Laboratory, Berkeley, CA 94720. R. H. Dauskardt and R. O. Ritchie are also with the Department of Materials Science and Mineral Engineering, University of California, Berkeley, CA 94720. The work was supported by the Director, Office of Energy Research, U.S. Department of Energy under Contract no. DE-AC03-76SF-00098.

The illumination and collection optics must be configured appropriately to obtain multiplexed spatial resolution. Figure 2 shows the optical design used for obtaining one-dimensional Raman profiles, in this case, on the surface of PSZ. The laser beam is expanded with a telescope to the desired diameter and then focused in one dimension by means of a cylindrical lens. The laser beam is incident on the sample at 70° from the surface normal. This angle can be varied as needed. The laser optics form a slit-like illumination at the sample with 500:1 aspect ratio. The scattered light is collected with a $f/1.3$ camera lens and focused onto the entrance slit of the monochromator. Rotation of the cylindrical lens allows the slit-like laser beam to be aligned so that the image formed by the collection lens is parallel to the entrance slit. There is a one-to-one correspondence of the Y position at the sample to the position along the entrance slit; this correspondence is maintained at the detector. Magnification of the laser illuminated area onto the detector is determined by the focal length of the collection lens. In the present arrangement each vertical (or Y-direction) pixel (row in the data array) corresponds to $28\text{ }\mu\text{m}$ at the sample. Spatial resolution in the X direction is determined by the spectrometer entrance slit width coupled with the magnification of the collection lens. In the present experiments, a $50\text{ }\mu\text{m}$ slit width corresponds to a spatial resolution of $17\text{ }\mu\text{m}$ in the X direction. Increasing the magnification by using a shorter focal length collection lens (such as a microscope lens) will increase the spatial resolution in both the X and Y directions.

A two-dimensional Raman map of the specimen surface is obtained by data collection at successive incremental sample translations. The procedure is applicable to gaseous, liquid, and solid systems; here we describe application to a technologically important ceramic.

Sample Application

Partially stabilized zirconia (PSZ) has been referred to as the "first ceramic material in which microstructural design was explicitly used to achieve optimum properties."³ When stress is applied to a crack in PSZ, material in the tetragonal phase near the crack tip undergoes transformation to the monoclinic phase, which results in a dilation and thereby relieves the tensile stress near the crack tip. Compositional mapping of the phases surrounding the crack and crack tip helps to elucidate the mechanisms of crack growth and failure in these ceramic materials.

The Raman spectra of PSZ containing both tetragonal and monoclinic phases are shown in Fig. 3. Well-resolved Raman peaks for each phase (identified in the accompanying table)⁴ can be used to determine the relative intensity of the two phases. An integrated peak intensity entirely associated with the monoclinic phase is determined by subtracting the average

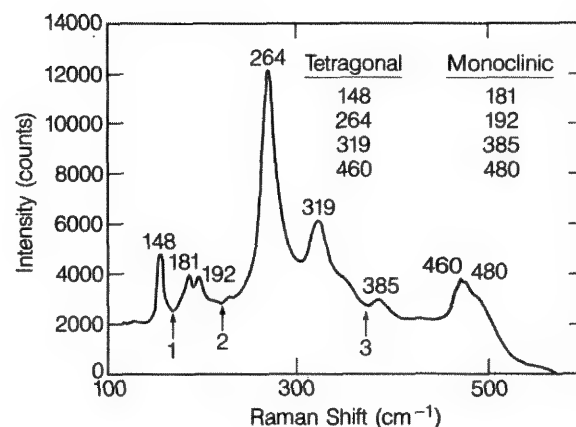


FIG. 3.--Raman spectrum of partially stabilized zirconia sample containing both tetragonal and monoclinic phases. Peak positions are identified in table. Regions used for evaluating background intensities are numbered.

background at positions indicated as 1 and 2 from the integrated area between 1 and 2. Likewise an integrated area centered at the 264 cm^{-1} peak and corrected for the average background determined at 2 and 3 yields an intensity associated solely with the tetragonal phase. The relative intensity of the monoclinic phase is computed from the intensity of the monoclinic phase divided by the sum of the intensities of the tetragonal and monoclinic phases. This calculation is carried out for each Y position (row in the data array) and yields a one-dimensional Raman profile. Figure 4 shows two such 1-D Raman profiles, one across a crack grown in PSZ and a second parallel to the first profile but in front of the crack tip. The data for each profile were collected by use of 100 mW of laser power and a collection time of 7.5 min. The laser power was limited by scattered light saturating the detector. A series of such 1-D profiles can be used to determine a 2-D surface compositional map of a sample of PSZ as previously discussed. Spectra were acquired at 12 positions separated by $250\text{ }\mu\text{m}$. Interpolation between the resulting 12 profiles was used to generate a 2-D Raman compositional map of the extent of transformation surrounding a crack, as shown in Fig. 5. An additional profile, taken parallel to and centered on the crack, was used to check the interpolation and add data in the dimension parallel to the crack. The experiment took about 1.5 h.

Conclusions

Two-dimensional detection, coupled with appropriate illumination and collection optics, yields Raman data that can be used to generate a 1-D Raman profile of the chemical composition at a surface. Successive 1-D Raman profiles can be acquired by translation of the sample and can be used to generate an accurate 2-D Raman compositional map of a surface.

Advances in detector technology and microcomputer capabilities are responsible for this new direction in Raman microprobe analysis.

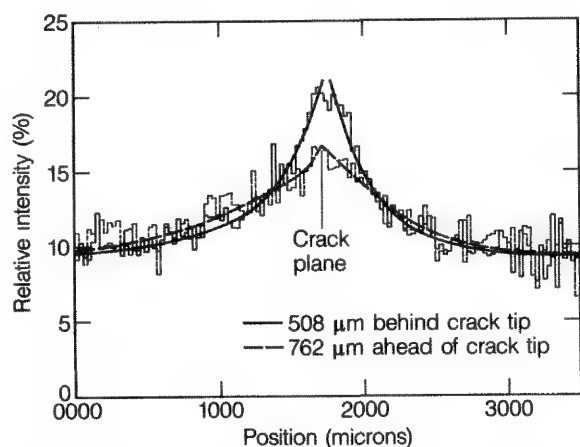


FIG. 4.--One-dimensional Raman profiles of PSZ. Spatial resolution is estimated to be 40 μm .

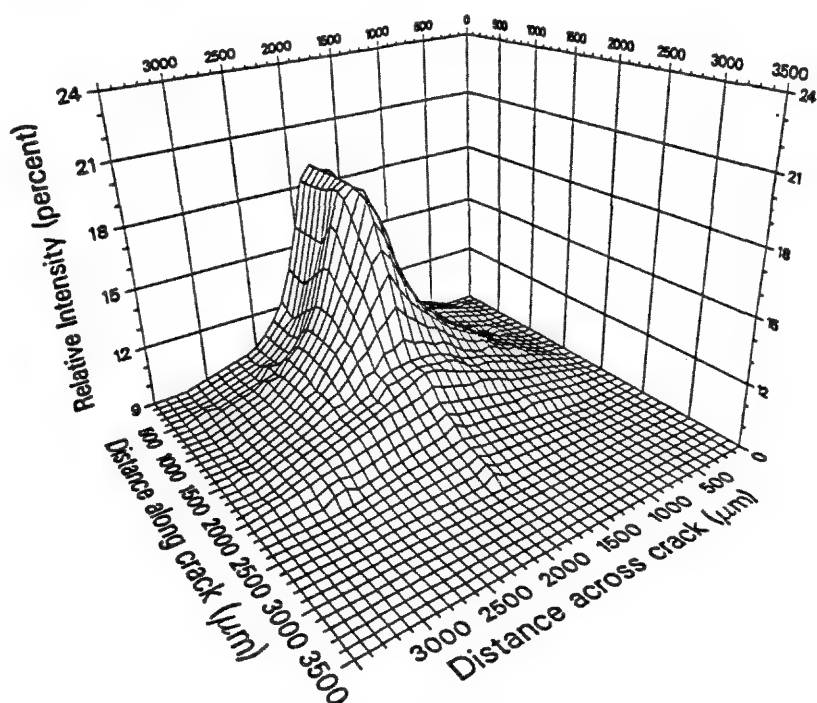


FIG. 5.--Two-dimensional Raman map of the surface of PSZ. A crack was grown partway through material. Map shows increased relative intensities of monoclinic phase, which decay to bulk values both ahead of crack tip and to the sides of crack.

References

1. P. Dhamelincourt and M. Delhaye, "Evolution and prospects of Raman microprobing techniques," *Microbeam Analysis--1987*, 119-120.
2. D. K. Veirs, V. F. K. Chia, and G. M. Rosenblatt, "Raman spectroscopy applications of an imaging photomultiplier tube," *Applied Optics* 26: 3530-3535, 1987.
3. Panel on Electrochemical Corrosion, *Agenda for Advancing Electrochemical Corrosion Science and Technology*, National Research Council Pub. NMAB 438-2: 78, 1987.
4. D. R. Clarke and F. Adar, "Measurements of the crystallographically transformed zone produced by fracture in ceramics containing tetragonal zirconia," *J. Am. Ceram. Soc.* 65: 284-288, 1982.

POLARIZED RAMAN SPECTRA OF SINGLE CRYSTALS OF $\text{YBa}_2\text{Cu}_3\text{O}_7$, $\text{EuBa}_2\text{Cu}_3\text{O}_7$, and $\text{YBa}_2\text{Cu}_3(\text{O}/\text{F})_7$

P. V. Huong, J. C. Grenier, and P. Bezdzicka

Since the discovery of Y-Ba-Cu-O materials exhibiting superconductivity at nearly 93 K, febrile activities have manifested themselves in many fields. We witness a burst of research results circulating in the form of preprints which are as authoritative as any papers published in well-established journals. The materials of the type Y-Ba-Cu-O prepared by Chu et al.¹ have been easily reproduced and their macrophysical properties have been reconfirmed and extended.² But things are going perhaps too fast. This intense competition for publishing is certainly a good thing; nevertheless, we must be careful. Many papers are concerned with Raman spectroscopy, but generally the reported spectra differ from one author to another.³⁻¹⁷ As Raman spectroscopy is well known to be a very accurate technique that allows one to investigate down to the molecular and submolecular scales,¹⁸⁻²² one may ask, what is going wrong?

In this paper, we try to find an answer for this apparent inconsistency by studying, under variable experimental conditions, the Raman spectra of $\text{YBa}_2\text{Cu}_3\text{O}_{7-\delta}$, $\text{YBa}_2\text{Cu}_3\text{O}_{7-\delta}\text{F}_{0.1}$, and $\text{EuBa}_2\text{Cu}_3\text{O}_{7-\delta}$ using micro-Raman spectroscopy, a technique that can give Raman spectra of materials of micrometer size.^{23,24}

Experimental

Materials of the type $\text{MBa}_2\text{Cu}_3\text{O}_{7-\delta}$ (M = Y, Eu; $\delta = 0.2$) were prepared from appropriate amounts of barium carbonate, rare-earth oxide (Y_2O_3 or Eu_2O_3), and copper oxide. The finely ground mixture was heated for 20 h in air at 950 °C, then quenched and reground. Pellets 8 mm in diameter were pressed and sintered at 950 °C for 2 h and finally heated at 450 °C for 2 days.

A phase containing a small amount of fluorine was prepared in the same way, starting with the following mixture: 1.95 BaCO_3 , 0.05 BaF_2 , 1.5 Y_2O_3 , and 3 CuO . As barium fluoride is very stable, it can be assumed that there is no hydrolysis and that the composition is close to $\text{YBa}_2\text{Cu}_3\text{O}_{7-\delta}\text{F}_{0.1}$.

X-ray diffraction powder analysis was carried out on a diffractometer. DC resistivity measurements versus temperature were performed

by the standard four-probe method. The Raman spectra were recorded at room temperature on a Micro-Raman spectrometer (DILOR/OMARS) by use of an argon ion laser (Spectra-Physics) emitting at 514.5 nm, and a diodes-array multi-channel detector.

Results and Discussion

$\text{MBa}_2\text{Cu}_3\text{O}_{7-\delta}$ and related compounds exhibit "normal" macrophysical properties.

X-ray Diffraction Analysis. The x-ray diffraction analysis shows quite similar patterns to those previously reported and are characteristic of the orthorhombic symmetry with the following cell parameters:

Compound	a(Å)	b(Å)	c(Å)	V _m (Å ³)
$\text{YBa}_2\text{Cu}_3\text{O}_{7-\delta}$	3.83	3.88	11.71	174
$\text{YBa}_2\text{Cu}_3\text{O}_{7-\delta}\text{F}_{0.1}$	3.82	3.88	11.66	173
$\text{EuBa}_2\text{Cu}_3\text{O}_{7-\delta}$	3.86	3.87	11.71	175

The replacement of yttrium by europium slightly increases the unit cell volume; a decrease is observed for the fluorinated compound as expected from the difference in the size of the ionic radii.²⁵

Resistivity Measurements. Typical resistivity measurements for YBaCuO and YBaCuOF are shown in Fig. 1. The superconducting transition temperatures are, respectively, 90.6 K and 89.3 K (zero-resistance T_0), in very good agreement with previous results.²

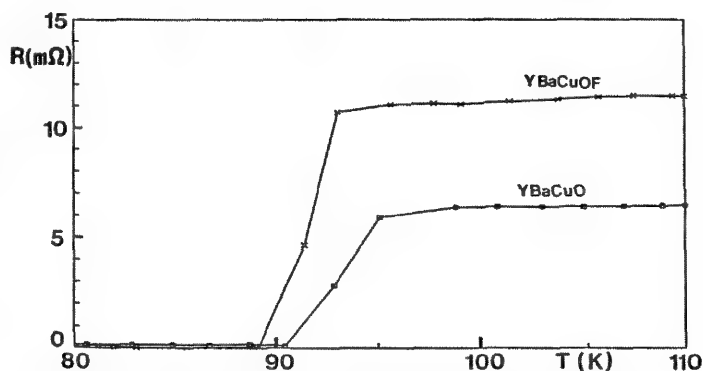


FIG. 1.--Resistance vs temperature measured at constant current of 10 mA for $\text{YBa}_2\text{Cu}_3\text{O}_{7-\delta}$ and $\text{YBa}_2\text{Cu}_3\text{O}_{7-\delta}\text{F}_{0.1}$.

The introduction of a small amount of F ions does not significantly affect the T_C value but

P. A. Huong is at the Laboratoire de Spectroscopie Moléculaire et Cristalline (UA 124), and J. C. Grenier and P. Bezdzicka are at the Laboratoire de Chimie du Solide (UP 8661), Université de Bordeaux I, 351, cours de la Libération, F-33405 Talence, France.

somewhat increases the resistivity of the sample above T_c . This result can be explained by the higher electronegativity of fluorine compared to oxygen, which increases the electronic localization. Higher concentrations of fluorine lead to multiphase materials, which become insulators. During the course of this work, Ovshinsky et al. reported on Y-Ba-Cu-O-F materials with large amounts of fluorine, showing very high superconducting temperatures;²⁶ these results do not seem to be reproducible. The Eu-Ba-Cu-O compound shows a superconducting state under 90 K, again in agreement with previous results.²⁷

Raman Spectroscopy. As noted, all the spectra reported previously are different although they are from studies of supposedly identical materials, with quite similar macrophysical properties such as resistance vs temperature, magnetic properties, etc.

1. *Effect of laser power.* Our samples were illuminated with various laser powers for obtaining Raman spectra. The Raman spectra so obtained depended strongly on the power density. That means that the structure of these superconducting materials is very sensitive to the laser beam and may drastically change with power, either due to a local increase in temperature or to photo-induced chemical changes. For reproducible Raman spectra, the illuminating laser reaching the sample must be kept below 2 mW.

2. *Heterodomains.* Thanks to the micro-Raman technique, a spatial selectivity is possible. Instead of sending the laser beam directly on the sample, as in normal Raman investigations, the incident beam is directed through an optical microscope before reaching a limited area of the sample surface; then the backscattered beam can be collected into the monochromator of a classical Raman spectrometer. In this way, Raman spectra of sample areas as small as $1 \mu^2$ can be obtained; the size of these areas is limited only by the wavelength of the laser radiation commonly used (0.3-0.8 μ m).

When investigating Y-Ba-Cu-O superconducting materials, we often observed that different areas of a particle of the same material did not give identical Raman spectra, even when the reproducibility of these measurements could be fully ascertained. Two explanations can be suggested.

As the crystal symmetry of these materials is orthorhombic, the Raman spectrum obtained for various particles may result from different orientations of these small crystallites with respect to the incident and the scattered radiation. Usually the particles are not single crystals, and the direction of the incident beam does not coincide with a given crystal axis. Consequently, the observed spectra differ only by the relative intensities, as complete extinction of a forbidden mode is rare.

The micro-Raman spectrometer (DILOR, Model OMARS) allows the acquisition of different

spectra of different intensity polarizations, even when probing different areas on the same surface of the sample. These results are in agreement with recent electron microscopy investigations^{28,29} showing that a common feature of the orthorhombic Y-Ba-Cu-O phases is the existence of twinned domains. As the spatial resolution used was 0.4 μ m, the size of these hetero domains that can be estimated as 0.16 μ^2 and larger.

3. *Heterogeneity.* For some samples, the spectra appear too different from one to the other to be considered as arising from the same chemical entity. As the Raman spectrum is directly associated with the local structure of the illuminated area or volume, some of the micro-Raman spectra do come from different "chemical species." We therefore propose the existence of heterogeneity in many samples. This heterogeneity could come from the existence of defects involving oxygen hyper- or substoichiometry in the superconducting materials.

All these reasons explain the previous controversial results.

By avoiding all these troublesome complications, and thanks to the micro-Raman technique, we obtain Raman spectra of microsingle crystals of superconducting materials.

4. *Micro-Raman spectra of single microcrystals.* Small particles of the Y-Ba-Cu-O, Eu-Ba-Cu-O and Y-Ba-Cu-O-F types of compounds were first selected under the optical microscope to present planar surfaces. The regularity was then checked by Raman spectroscopy. Various spots on the same surface might give the same Raman spectrum with the same relative intensity for all bands.

As the orientation of the crystal is not known, the first configuration may be fixed by the total extinction of at least one Raman band; the spectrum is then recorded. The other configuration is then obtained by rotation to a second orientation relative to the previous one. When the particle is changed, the study of Raman intensity extinction of other band(s) leads to the other remaining orientations.

After a series of Raman measurements, a second spectrum of the same sampling spot with the same polarization is made to check the stability of the sample and to verify that no damage by the focused laser spot has occurred. With these precautions, the following Raman spectra were obtained.

For the compound $YBa_2Cu_3O_{6.8}$, our polarized Raman spectra are displayed in Fig. 2. Except for some published spectra, which can be considered as resulting from damaged or heterogeneous samples, the following published Raman spectra can be accepted as correct, although they are generally different from one another. The reason is that each author states only one or incompletely specified polarized configuration. For instance, the Raman spectrum of McFarlane, Rosen, and Seki⁸ and of Krol¹³ is identical to our Fig. 2c; that of Liu¹¹ is not of good quality but is still similar to

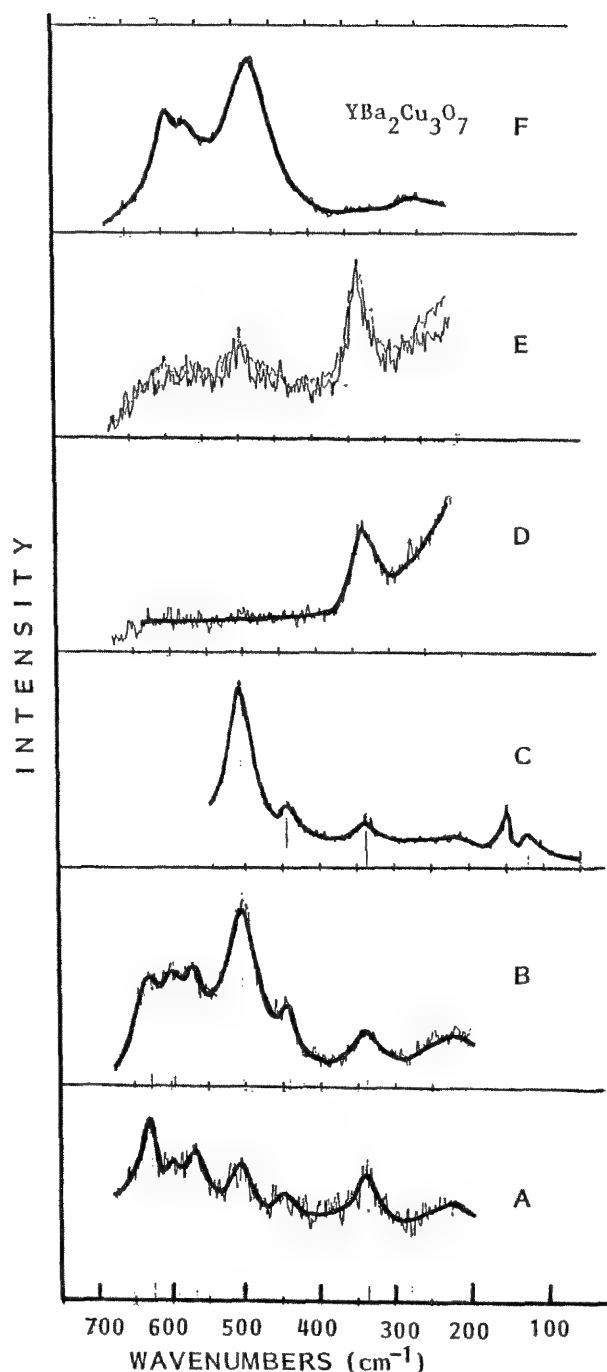


FIG. 2.--Polarized Raman spectra from various orientations of single crystal of $\text{YBa}_2\text{Cu}_3\text{O}_7$.

Fig. 2c; whereas that of Yamanaka⁵ coincides with our Fig. 2d and that of Kirby¹⁵ is the same as Fig. 2b. Again, the Raman spectra of Dai and Campion⁶ of Iqbal,⁷ of Rosen,¹⁰ of Kourouklis,¹⁴ and of Chrzanowski¹⁶ are identical to Fig. 2a, while the two polarized αZZ and αXY Raman spectra given by Hemley and Mao⁴ are identical to our configurations 2f and 2d.

In Fig. 2e are superimposed two identical Raman spectra of the same configuration recorded at the beginning and at the end of a series of measurements. This identity confirms the stability of the sample.

Thus, polarized spectra of all configurations must be taken into account in the characterization of superconducting materials. This result helps to clarify the apparent controversial published results and restores confidence in the Raman spectroscopy technique as applied to the study of new materials.

The observed Raman frequencies of $\text{YBa}_2\text{Cu}_3\text{O}_7$ are listed in Table 1 with a partial and tentative assignment.

For $\text{EuBa}_2\text{Cu}_3\text{O}_{7-\delta}$, different polarized Raman spectra are obtained by the micro-Raman technique, and are given in Fig. 3. No pronounced effect was observed when comparing these results with the Raman spectra of $\text{YBa}_2\text{Cu}_3\text{O}_7$ (Fig. 4). This is consistent with the assignment (Table 1) that the observed bands are mostly due to Cu-O vibrations, as there is no oxygen in the Y or Eu planes.

The Raman spectrum given by Batlogg and Cava³ and by Leu¹¹ is identical to our configuration 3c; that of Cardona¹² could represent an intermediary orientation between 3c and 3d.

For $\text{YBa}_2\text{Cu}_3\text{O}_{7\text{F}_{0.1}}$, the introduction of some fluorine atoms seems to affect strongly the relative intensity of the Raman bands. A new band appears at 298 cm^{-1} , which may mean that the fluorine atoms substitute in the pyramidal CuO units rather than in CuO chains, as the latter vibrate at higher frequencies.

Conclusion

A systematic study of the Raman spectra of Y-Ba-Cu-O superconducting materials under various experimental conditions allows us to clarify the controversial results given in the literature. Under carefully controlled conditions, and owing to the micro-Raman technique, reproducible polarized Raman spectra can be obtained and a coherent assignment can be suggested for $\text{YBa}_2\text{Cu}_3\text{O}_7$ and $\text{EuBa}_2\text{Cu}_3\text{O}_7$. For $\text{YBa}_2\text{Cu}_3(\text{O}/\text{F})_7$, the introduction of fluorine atoms was found to be localized in pyramidal CuO units rather than in CuO chains.

References

1. C. W. Chu, P. H. Hor, R. L. Meng, L. Gao, Z. J. Huang, and Y. Q. Wang, *Phys. Rev. Lett.* 58: 405, 1987.
2. D. W. Murphy, S. Sunshine, R. B. Van Dover, R. J. Cava, B. Batlogg, S. M. Zahurak, and L. F. Schneemeyer, *Phys. Rev. Lett.* 58: 1888, 1987.
3. B. Batlogg, R. J. Cava, A. Jayaraman, R. B. Van Dover, G. A. Kourouklis, S. Sunshine, and D. W. Murphy, *Phys. Rev. Lett.* 58: 2333, 1987.
4. R. J. Hemley and H. K. Mao, *Phys. Rev. Lett.* 58: 2340, 1987.
5. A. Yamanaka, F. Minami, K. Watanabe, K. Inoue, S. Takekawa, and N. Ivi, *Jap. J. Appl. Phys.* 26: L-1404, 1987.
6. Y. F. Dai, J. S. Swinne, H. Steinfink, J. B. Goodenough, and A. Campion, *J. Am. Chem. Soc.* 109: 5291, 1987.
7. Z. Iqbal, S. W. Steinhäuser, A. Bose, N. Cipollini, and H. Eckhardt, *Phys. Rev. B* 36: 2283, 1987.

TABLE 1.--Frequencies (in cm^{-1}) of Raman bands of superconducting materials.

YBa ₂ Cu ₃ O ₇	EuBa ₂ Cu ₃ O ₇	YBa ₂ Cu ₃ (O/F) ₇	
632	635	635	Chain Cu-O stretchings
		625	
592			
	581	584	Pyramidal Cu-O stretchings
513			
501	501	502	
492			
	450	445	
337		337	
	313		
			Cu-O bendings
		298	Pyramidal O-Cu-F stretchings
220	220	230	
		210	
150			
118			

8. R. M. MacFarlane, H. Rosen, and H. Seki, *Solid State Comm.* 63: 831, 1987.

9. I. Bozovic, D. Mitzi, M. Beasley, A. Kapitulnik, T. Geballe, S. Perrowitz, G. C. Carr, P. Lou, R. Sudharsanan, and S. S. Yom, *Phys. Rev. B*-36: 4000, 1987.

10. H. Rosen, E. M. Engler, T. C. Strand, V. Y. Lee, and D. Bethune, *Phys. Rev. B*-36: 726, 1987.

11. R. Liu, R. Merlin, M. Cardona, H. Mattausch, N. Bauhofer, A. Simon, F. Garcia-Alvarado, E. Moran, M. Vallet, and J. M. Gonzalez-Galbet, and M. A. Alario, *Solid State Comm.* 63: 839, 1987.

12. M. Cardona, L. Genzel, R. Liu, A. Wittlin, H. Mattausch, F. Garcia-Alvarado, and E. Garcia-Gonzalez, *Solid State Comm.* 64: 727, 1987.

13. D. M. Krol, M. Stavola, W. Weber, L. F. Schneemeyer, J. V. Warczak, S. M. Zahurak, and S. G. Kosinski, *Phys. Rev. B*-36: 8325, 1987.

14. G. A. Kourouklis, A. Jayaraman, B. Batlogg, R. J. Cava, M. Stavola, D. M. Krol, E. A. Rietman, and L. F. Schneemeyer, *Phys. Rev. B*-36: 8320, 1987.

15. P. B. Kirby, M. R. Harrison, W. G. Freeman, I. Samuel, and M. J. Haines, *Phys. Rev. B*-36: 8315, 1987.

16. J. Chrzanowski, S. Gyga, J. C. Irwin, and W. N. Hardy, *Solid State Comm.* 65: 139, 1988.

17. C. Thomsen, R. Liu, A. Wittlin, L. Genzel, M. Cardona, W. Konig, M. V. Cabanas, and E. Garcia, *Solid State Comm.* 65: 219, 1988.

18. J. Lascombe and P. V. Huong, Eds.,

Raman Spectroscopy, Linear and Nonlinear, New York: Wiley, 1982.

19. P. V. Huong and M. Couzi, "Spectres infrarouges et Raman des perovskites," in *L'Infrarouge en chimie des solides*, Paris: Masson, 1973.

20. P. V. Huong, in J. R. Durig, Ed., *Vibrational Spectra and Structure*, New York: Elsevier, 1980.

21. A. Freundlich, A. Leycuras, J. C. Grenet, C. Verie, and P. V. Huong, *Appl. Phys. Lett.* 51: 1352, 1987.

22. P. V. Huong, in H. D. Bist and J. S. Goela, Eds., *Lasers and Applications*, Bombay: Tata-McGraw Hill, 1982.

23. P. V. Huong, in L. Niinisto, Ed., *Reviews on Analytical Chemistry*, Budapest: Akademia Kiado, 1982.

24. P. V. Huong, in M. Grasserbauer, Ed., *Analysis for the Development of Microelectronic Devices*, Amsterdam: Elsevier, 1988.

25. R. D. Shannon and C. T. Pewitt, *Acta Cryst.* B-25: 928, 1969.

26. S. R. Ovshinsky, R. T. Young, D. D. Allred, G. DeMaggio, and G. A. Van der Leeden, *Phys. Rev. Lett.* 58: 2579, 1987.

27. B. Walz, H. Jenny, G. Leemann, V. Geiser, S. Jost, T. Frey, H. Bretscher and H. J. Guntherodt, MRS Meeting, Strasbourg, 1987.

28. Y. S. Yono, M. Kikuchi, K. Oh-ishi, K. Hiraga, H. Arai, Y. Matsui, N. Kobayashi, T. Sasaoka, and Y. Muto, *Jap. J. Appl. Phys.* 26: 498, 1987.

29. M. Hervieu, B. Domenges, C. Michel, G. Heger, J. Provost, and B. Raveau, *Phys. Rev. B*-36: 3920, 1987.

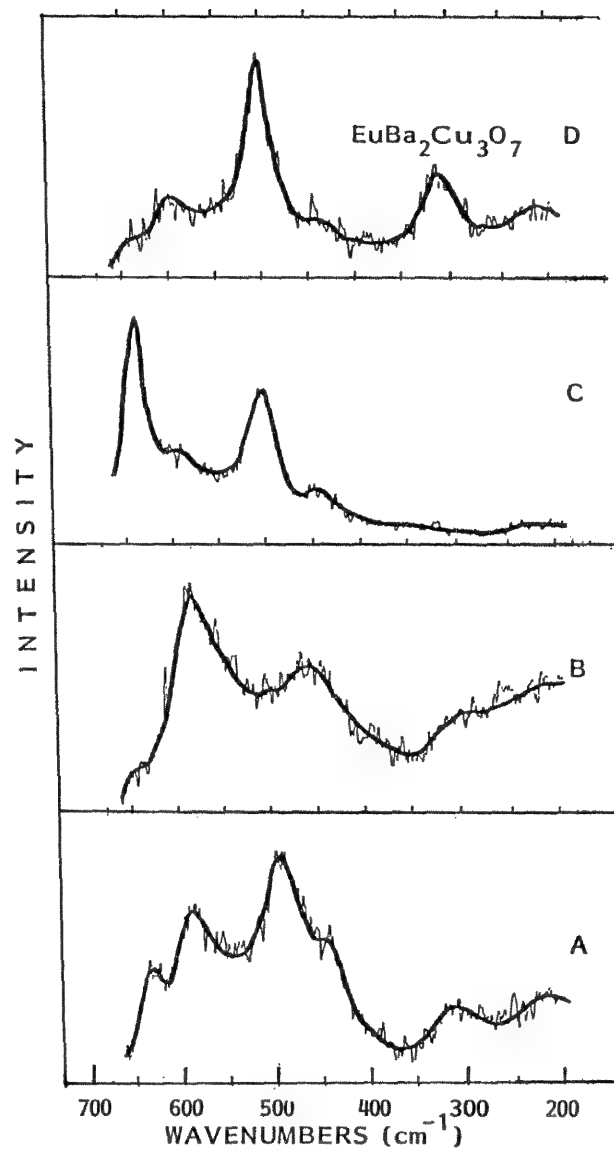
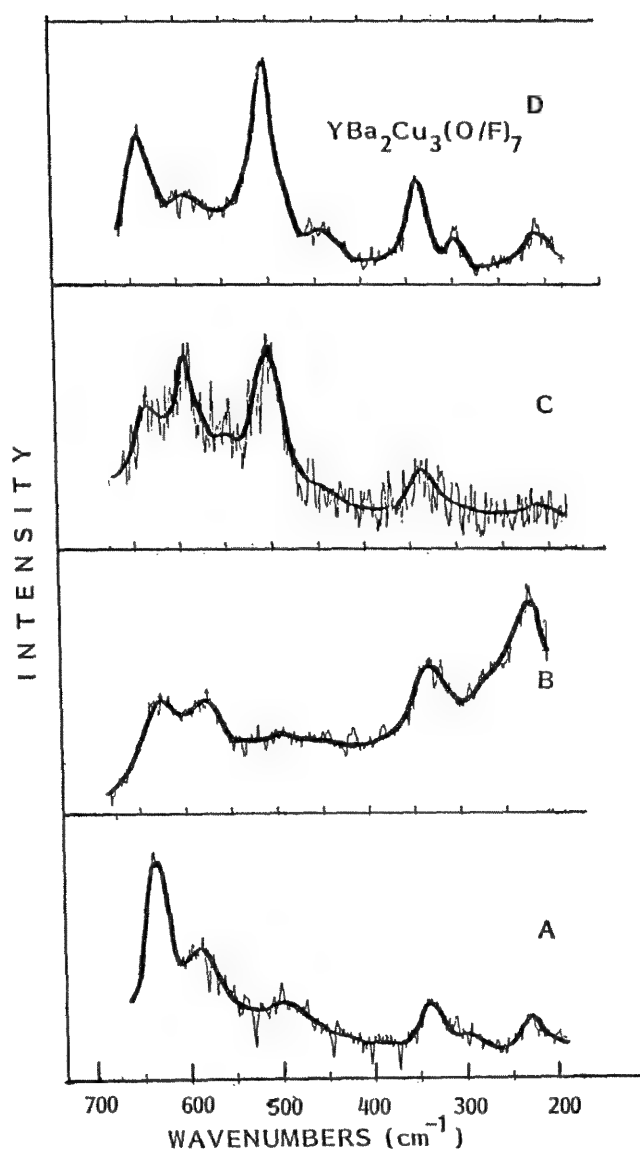


FIG. 3.--Polarized Raman spectra from various orientations of single crystal of $\text{EuBa}_2\text{Cu}_3\text{O}_7$.
 FIG. 4.--Polarized Raman spectra from various orientations of single crystal of $\text{YBa}_2\text{Cu}_3\text{O}_{7.1}$.

MICRO-RAMAN SPECTROSCOPY OF HIGH- T_c SUPERCONDUCTORS IN THE Y-Ba-Cu-O SYSTEM

E. S. Etz, Winnie Wong-Ng, J. E. Blendell, and C. K. Chiang

Currently one of the most extensively investigated materials for high-temperature superconductivity is the Y-Ba-Cu-O compound system.^{1,2} In this system, two stable single phases described by the composition $\text{YBa}_2\text{Cu}_3\text{O}_{7-x}$ ($x \approx 0$ to 1), one tetragonal ($x \lesssim 0.4$) and the other orthorhombic ($x \gtrsim 0.4$), have come under close scrutiny, as the former is semiconducting and the latter is superconducting exhibiting a transition temperature of $T_c = 95$ K.³ Much of the research into the properties and performance characteristics of this compound is directed at assessing the importance of preparation and processing techniques, microstructure, and stoichiometry (especially oxygen content), all of which are known to determine the superconductive properties of $\text{YBa}_2\text{Cu}_3\text{O}_{7-x}$. Yet numerous perplexing problems pertaining to this new class of materials remain, based on insufficient knowledge of the exact composition, the various crystal structures and phase relationships, and the microstructural features of these solids.⁴⁻¹⁰ Clearly, as more experimental information is accumulated about these compounds, T_c can be expected to rise to significantly higher temperatures. Moreover, the exact mechanism of the unprecedented high-temperature superconductivity is not at all clearly understood. It appears that measurements to elucidate the microstructure are central to the understanding of the structure-property relationships of these materials.

A variety of techniques are brought to the task to obtain compositional and structural information. In bulk characterization studies of these samples, the techniques most widely employed are x-ray and neutron diffraction, and the vibrational spectroscopies, infrared and Raman.¹¹⁻³³ The results from these structure methods are generally correlated with those from electrical resistivity and magnetic susceptibility measurements to provide a comprehensive characterization of these materials. Microstructural studies rely principally on the techniques of electron probe microanalysis (EPMA) and transmission electron microscopy (TEM), including electron diffraction, to obtain information on microscopic heterogeneity, polyphase assemblages, individual grains and grain boundaries, the arrangement of atoms and the relationship of atomic layers within the lattice, lattice defects, etc.¹⁻³

Raman and infrared spectroscopy are sensi-

tive probes of the solid state for the identification of various phases, and the detection of structural anomalies and impurities.¹⁰⁻³³ In general, the Raman spectra exhibit vibrational modes mostly related to Cu-O bonds and to the vibrations of other atoms in the lattice. Thus, numerous Raman studies have been reported for superconducting materials of the type $\text{YBa}_2\text{Cu}_3\text{O}_{7-x}$ (where $x \approx 0$) as well as their semiconducting analogs (for which $x \approx 1$). Although the normal modes have been reasonably assigned,¹³⁻¹⁹ there are still a few additional lines in the Raman spectra that may lead to erroneous assignments of the observed modes. These and other studies have also involved group theoretical analysis of phonon modes to predict the Raman active modes for the two crystallographic phases.^{15,16} A complicating factor in the examination of these samples is often the presence of impurity or parasitic phases in nominally (by x-ray diffraction) single-phase superconductor materials which more or less contribute to the observed Raman spectrum.^{10,13,31,32} Therefore, in preparations of the high-critical temperature superconductor $\text{YBa}_2\text{Cu}_3\text{O}_7$, there always exists the possibility of parasitic mixed phases like BaCuO_2 , $\text{YBa}_2\text{Cu}_3\text{O}_x$, $\text{Y}_2\text{Cu}_2\text{O}_5$, Y_2BaCuO_5 , and possibly Cu_2O as well, and also at times the unreacted parent oxides. These structural instabilities, or heterogeneities, associated with the superconducting transition may create an upper limit to the critical temperature, T_c .

In this paper we report preliminary results on the (unpolarized) room-temperature micro-Raman spectra of several preparations, and predominant phases in the Y-Ba-Cu-O (YBCO) ceramic system. It is because of the fine-grained nature of these materials that micro-analytical techniques are required for an accurate determination of the component phases, mixed stoichiometries, for these polyphase materials. These studies are part of a much broader investigation at NBS into the microstructural characterization of these materials by compositional mapping techniques employing electron beam methods (EPMA and AEM).³⁴ These measurements also contribute to a comprehensive database including the results from bulk structure studies by x-ray diffraction specifically aimed at the study of phase transitions in the $\text{YBa}_2\text{Cu}_3\text{O}_{7-x}$ system.³⁵

Experimental

The compounds examined in this study have been for the most part thoroughly characterized by the conventional (bulk) methods to establish their electrical, magnetic, and

E. S. Etz is with the Center for Analytical Chemistry and W. Wong-Ng, J. E. Blendell, and C. K. Chiang are with the Ceramics Division of the National Bureau of Standards, Gaithersburg, MD 20899. They thank D. E. Newbury for useful discussions throughout this work.

mechanical properties relative to the methods of their fabrication and processing.^{35,36} Three types of samples in the Y-Ba-Cu-O system were investigated by micro-Raman spectroscopy.

1. Several samples in a series of polycrystalline ceramic powders of $\text{YBa}_2\text{Cu}_3\text{O}_{7-x}$ ($x \approx 0$ to 1) prepared for phase transition studies by x-ray powder diffraction, all derived from a single-phase orthorhombic material by use of a quenching technique at various temperatures.³⁵

2. A sample of a superconducting sintered pellet which had been established to be of fully orthorhombic crystal structure ($x \approx 0$). This specimen was examined in parallel, as a flat-polished section, by electron probe analysis for compositional homogeneity.³⁴

3. A single-crystal material which from its processing history was expected to be predominantly in the tetragonal phase close to the $\text{YBa}_2\text{Cu}_3\text{O}_6$ oxygen stoichiometry. The synthesis of these Y-Ba-Cu-oxide ceramic powders and pellets was done by conventional high-temperature processing techniques that have been described elsewhere.^{35,36} The exploratory single-crystal specimen of $\text{YBa}_2\text{Cu}_3\text{O}_{7-x}$ was grown from a partially melting mixture by a slow cooling method. Though this specific preparation was thought to have yielded a predominantly tetragonal single-crystal phase, the presence of other impurity phases, in some of its parts, was confirmed.

For the spectroscopic measurements, we employed the Raman microprobe developed at the National Bureau of Standards,^{37,38} a dual-grating scanning spectrometer with cooled photomultiplier/photon counting detection. The fore-optical system is of a unique design (not based on the use of a standard optical microscope) for excitation and collection of the Raman scattered radiation. As a consequence of the particular collection configuration, the spectra obtained with this instrument are not subject to polarization effects; that is, the spectra are insensitive to specific orientations of small crystallites with respect to the incident and scattered radiation. All spectra reported here were excited with the 514.5 nm line of an argon/krypton laser. No spectral interferences due to sample luminescence or fluorescence are encountered from these solids. In the Raman microprobe, in a backscattering configuration, the laser beam is focused to a probe spot of variable size (5-15 μm in diameter). We generally employed an expanded beam spot of $\sim 12 \mu\text{m}$ in diameter to lessen the possibility of laser-induced sample modification, as these are opaque (i.e., black) and therefore highly absorbing solids. Under these conditions, the laser power at the sample was kept in the range from 3 to 7 mW (range of irradiance from 2.6 to 6.2 kW/cm^2 , most generally 5.0 kW/cm^2 to avoid sample degradation, especially under prolonged laser irradiation. As a rule, power densities at the sample at 514.5 nm for the totally opaque phases of the $\text{YBa}_2\text{Cu}_3\text{O}_{7-x}$ material exceeding 80 W/cm^2 were observed to be destructive; i.e., samples were

found to decompose above this threshold level of power density. These power densities are consistent with those reported in bulk- or macro-Raman measurements,¹⁴⁻¹⁶ where workers have either used a cylindrical lens to spread out the laser spot, or the spinning disk (rotating sample) technique to dissipate the incident laser energy.

The digital spectra of these materials, scanned in 1cm^{-1} steps, were obtained with 8 s integration time constants, at a scan rate of 6 $\text{cm}^{-1}/\text{min}$. All spectra were acquired with slit widths providing 5 cm^{-1} spectral resolution. The samples were in general examined as microparticulate dispersions, supported by LiF substrate, under ambient laboratory conditions. In the case of the ceramic powders--polycrystalline materials of both tetragonal and orthorhombic crystal symmetry--we examined single particles one by one, in the size range 10-35 μm . From the sintered ceramic pellet specimen, of nominally orthorhombic structure, we examined microscopic fragments, with fresh-fractured surfaces, from the interior parts of the pellet. For examination of the single-crystal material, presumed to be of tetragonal structure, we excised from the "as-grown" sample distinct microcrystallites (varying in size from 30 to 200 μm), and obtained spectra from various probe spots of their unpolished, often highly-reflecting, surfaces.

Work is in progress to examine polished sections of these superconducting materials (as well as thin film superconductors) via measurements on the same samples that are concurrently being investigated by electron-probe microanalysis to yield the compositional maps for the elements Y, Ba, and Cu.³⁴

Results and Discussion

We are reporting micro-Raman spectra obtained in the study of the three types of Y-Ba-Cu-O (YBCO) materials described above. At this time, these are preliminary results intended to illustrate the usefulness of the technique as a synergistic method for a more comprehensive microstructural characterization of these materials. Our results confirm the reported complexity of these vibrational spectra and are, in their general features, entirely consistent with conventional Raman and infrared data reported in the literature¹⁰⁻³¹ and results of other micro-Raman studies^{32,33}. Our ongoing work in this area is aimed at a clearer understanding of the subtle differences in these spectra brought about by the relevant variations in composition, structure, and phase encountered in the microscopic domain. Of principal concern in these studies is our evaluation of these spectra relative to materials unambiguously identified by several chemical and physical measurement techniques. In this regard, it is obvious from the literature that there is much controversy about the quality of the reported infrared and Raman data, largely due to poorly characterized YBCO materials. For this reason, we make no attempt here rigorously to compare the observed

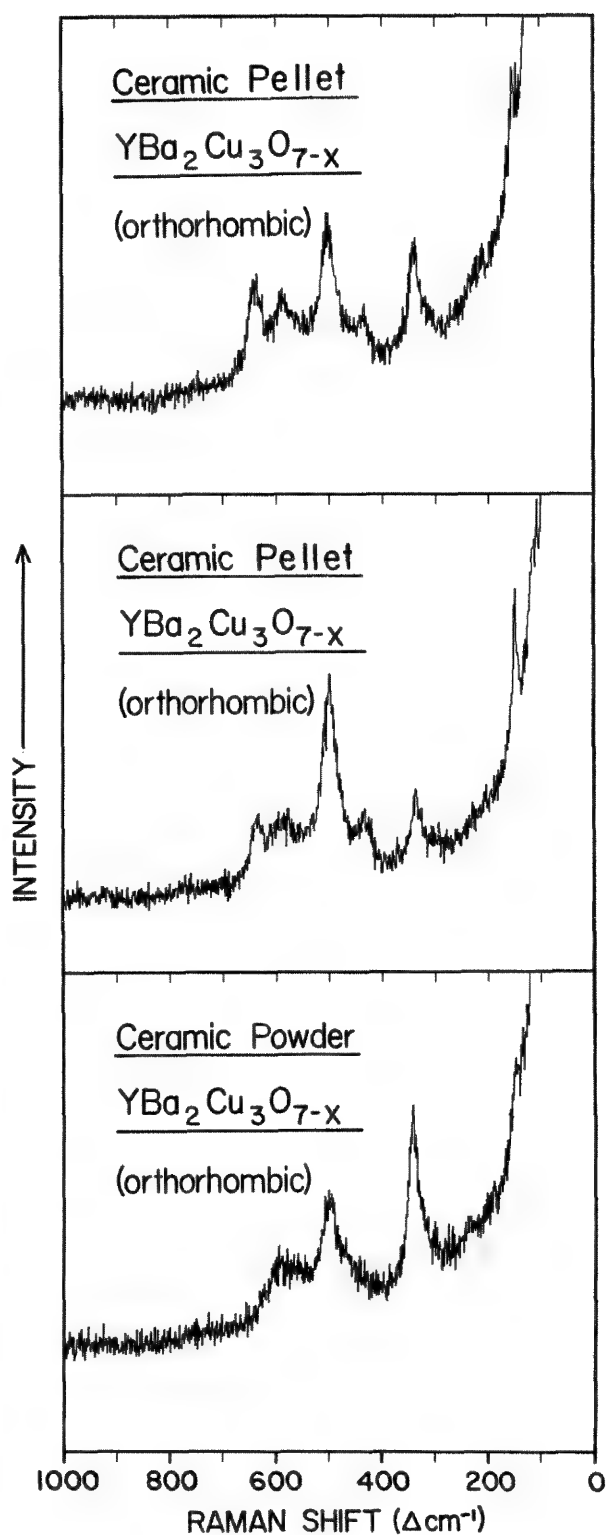


FIG. 1.--Raman microprobe spectra observed from single particles (size range, 10-35 μm) of two types of superconducting materials determined to be of orthorhombic crystal structure (by x-ray diffraction); microscopic fragments of a sintered ceramic pellet and microparticles of powdered ceramic. Samples are close to ideal $\text{YBa}_2\text{Cu}_3\text{O}_7$ stoichiometry. Spectra are excited at 514.5 nm; LiF substrate.

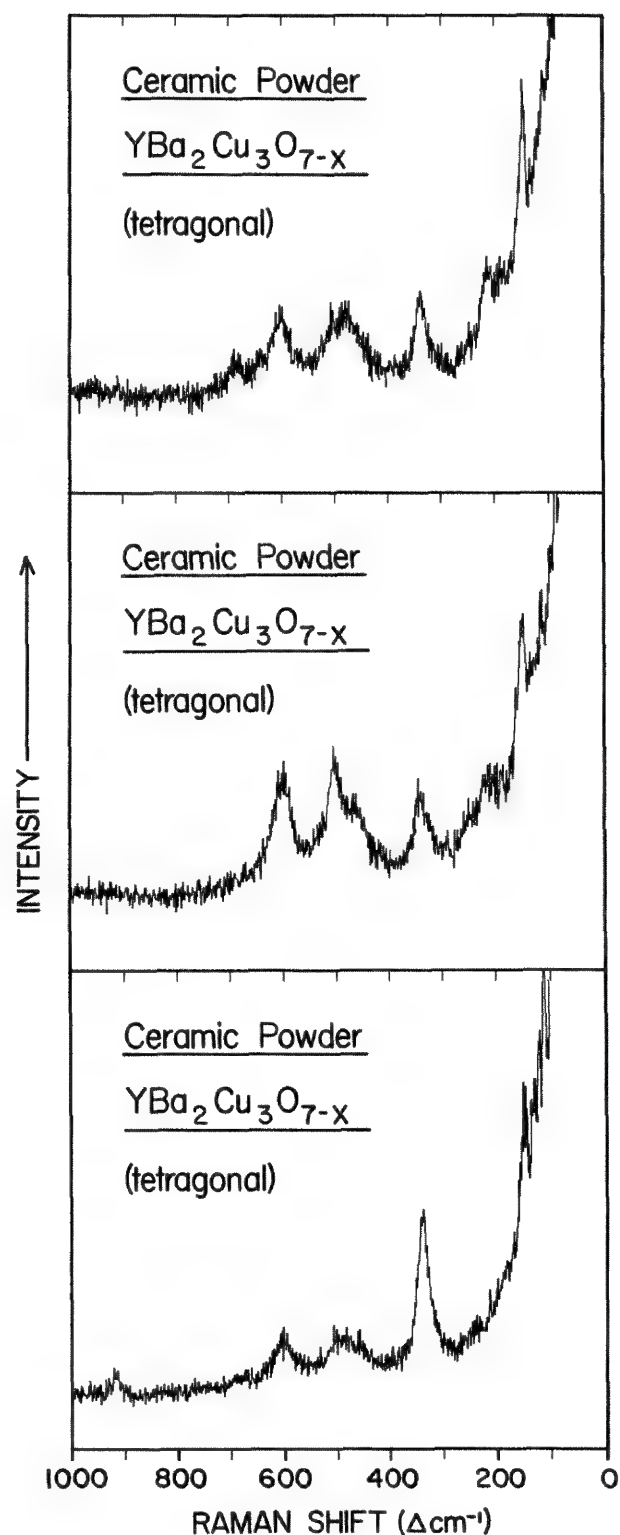


FIG. 2.--Representative Raman microprobe spectra obtained from arbitrary single microparticles of polycrystalline ceramic powder determined to be of tetragonal crystal structure (by x-ray diffraction). Ceramic is close to ideal $\text{YBa}_2\text{Cu}_3\text{O}_6$ stoichiometry. Spectra are excited at 514.5 nm; LiF substrate.

Raman features--their frequency positions, bandwidths, and relative intensities--with the wealth of vibrational data reported in the literature. Our interpretation of the micro-Raman results rests simply on a comparative evaluation of the data obtained for materials of orthorhombic and tetragonal structure, based on our current insights into the "characteristic" features of these spectra.

The results are shown in Figs. 1-3, selected as our best data obtained to date. Indeed, these spectra compare well with those reported for bulk samples, an observation from which one can conclude that the micro-Raman measurement does provide a nonintrusive (i.e., without potential sample degradation) analysis of these materials. The spectra of Fig. 1 are those of three arbitrary single particles or microfragments of two YBCO materials, a ceramic pellet and a ceramic powder, determined to be of orthorhombic structure. The spectra of these microsamples, though they have most of the principal features in common, still show considerable differences in their vibrational pattern, both in regard to the number of resolved bands and their relative half-widths and intensities. These differences are an indication of sample diversity attributable to real differences in the microstructural composition, which would suggest a sample heterogeneity not detected by bulk characterization methods. A detailed analysis and interpretation of these results is beyond the scope of this paper. Group theoretical analysis of the phonon modes of orthorhombic $\text{YBa}_2\text{Cu}_3\text{O}_7$, having no oxygen deficiency, predicts at least ten Raman bands for the orthorhombic structure.^{12-18,25} Experimentally, at room temperature (300 K), for the orthorhombic $\text{YBa}_2\text{Cu}_3\text{O}_{7-x}$, one almost always observes five distinct Raman bands, near or at 150, 340, 440, 500, and 635 cm^{-1} . All are seen in the spectra of Fig. 1, together with other weaker bands which have also been reported by other workers, such as the bands around 190, 230, and 590 cm^{-1} . In the spectra of polycrystalline and single-crystal orthorhombic samples, usually the band at 500 cm^{-1} (an A_{1g} mode, pyramidal Cu-O stretching) is the most pronounced, as is the case for the spectra from the ceramic pellet. Yet in the spectrum of the particle of the ceramic powder (and in other spectra of this sample), the band centered at 341 cm^{-1} is the most intense, and the expected band at $\sim 635 \text{ cm}^{-1}$ is largely obscured by the broad feature centered at 595 cm^{-1} . It is found that the Raman band at $\sim 635 \text{ cm}^{-1}$ is often weak and that its relative intensity differs from sample-to-sample. It is a band also associated with fundamental Cu-O vibrations (chain Cu-O stretching) and has been reported to be sensitive to surface conditions.²⁵ The $\sim 635 \text{ cm}^{-1}$ band is generally not a pronounced feature in the spectra of tetragonal $\text{YBa}_2\text{Cu}_3\text{O}_{7-x}$ samples and is thus one band sensitive to variations in phase (Figs. 2 and 3). Of the dozen or so Raman lines of superconducting $\text{YBa}_2\text{Cu}_3\text{O}_{7-x}$ that have been reported, eight Raman bands have been found to be coincident

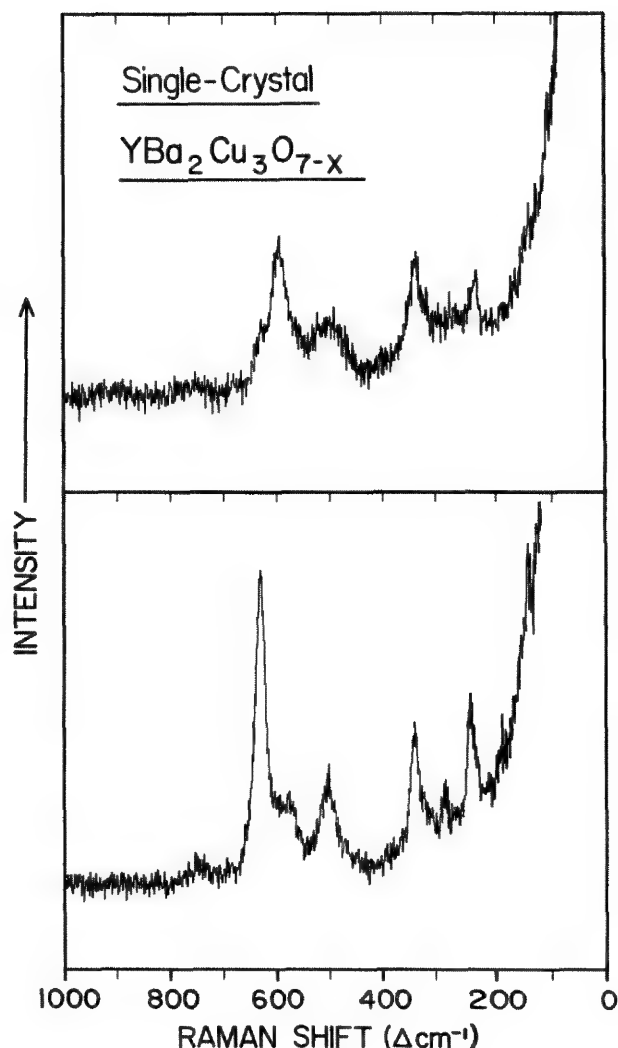


FIG. 3.--Micro-Raman spectra obtained in examination of microscopic single crystals excised from single-crystal preparation of $\text{YBa}_2\text{Cu}_3\text{O}_{7-x}$ composition. Specimen was prepared to yield single-crystal phase of tetragonal symmetry, close to $\text{YBa}_2\text{Cu}_3\text{O}_6$ stoichiometry. Spectra are excited at 514.5 nm; LiF substrate.

with the spectral features of the Y_2BaCuO_5 phase, which is the parasitic "green" phase that has been found in some preparations.^{13,31}

The spectra of microparticles and microcrystals of materials in the tetragonal structure are shown in Figs. 2 and 3. A considerable amount of Raman work pertaining to the vibrational analysis of this phase exists in the current literature, doubtless because these results are indispensable to an understanding of superconductivity in the orthorhombic Y-Ba-Cu-O system.¹⁰⁻³¹ Without question, the spectra of tetragonal $\text{YBa}_2\text{Cu}_3\text{O}_{7-x}$ are qualitatively similar to those of the orthorhombic phase. As a result workers take great care in the interpretation of these closely related patterns.^{15,16,20,24} It has been consistently reported that the Raman band corresponding to the $\sim 500 \text{ cm}^{-1}$ band in the or-

orthorhombic YBCO structure now appears at $\sim 485 \text{ cm}^{-1}$. This correspondence has been confirmed by the continuous shift of its frequency with quenching temperature (i.e., approaching $x = 1$).¹⁵ It appears therefore that the exact frequency position of the band at $\sim 500 \text{ cm}^{-1}$ may well be a sensitive indicator of the phase change. In our spectra of the particles of the tetragonal ceramic powder (Fig. 2), this band has been closely examined with respect to its frequency position and intensity. Although this band is centered at $\sim 485 \text{ cm}^{-1}$ in two of the spectra, it is distorted and centered at $\sim 500 \text{ cm}^{-1}$ in the middle spectrum, which clearly indicates an apparent inconsistency in the results from this sample. Again, this finding may well be explained by an inherent sample inhomogeneity, revealed only by single-particle analysis. Moreover, in the spectra of the two microscopic crystals of tetragonal single-crystal $\text{YBa}_2\text{Cu}_3\text{O}_{7-x}$ (Fig. 3), the appearance of the $\sim 500 \text{ cm}^{-1}$ band differs, although in both spectra this band is centered at $\sim 500 \text{ cm}^{-1}$. In a detailed study of the Cu-O vibrations of $\text{YBa}_2\text{Cu}_3\text{O}_x$ ($7 > x > 6$) for samples with well-characterized oxygen content, it was confirmed that the superconductivity properties depend critically on the value of x , and thereby on crystal symmetry. In this system, the orthorhombic-to-tetragonal transition is reported to occur for $x \approx 6.5$, where both phases are said to co-exist at room temperature.¹⁶ For tetragonal samples, these workers report characteristic Raman bands at ~ 470 and $\sim 590 \text{ cm}^{-1}$. The latter feature is indeed observed in our spectra (Figs. 2 and 3) of the tetragonal samples, with one exception, where this band is dominated by the intense 630 cm^{-1} band in the lower spectrum of Fig. 3. In some of our spectra we also find a tetragonal band centered more at 602 cm^{-1} for the ceramic powder and in several of the spectra of the single-crystal material. This may well be a characteristic mode, sufficiently different from the 635 cm^{-1} band of the orthorhombic YBCO structure. In a further analysis of these spectra, it has been reported that the frequency of the 340 cm^{-1} band is not affected by the structure change from orthorhombic to tetragonal. Yet, what has been regarded as significant is the intensity of this band relative to the band at $\sim 485 \text{ cm}^{-1}$. Thus, workers have examined the intensity ratio I_{340}/I_{485} and consistently noted that it is quite large compared to the I_{340}/I_{500} ratio observed for the orthorhombic phase.¹⁵ This observation we find generally supported by the micro-Raman spectra of the two tetragonal materials we examined.

It is clear from this tentative evaluation of our spectroscopic data derived from these materials that greater insight is required to exploit their information content fully. From a survey of the current literature, it is clear that other workers, no matter how seasoned, are wrestling with very much the same difficulties.

We cautiously conclude from these early results that micro-Raman analysis can provide unique information concerning the identity of

distinct microscopic phases not revealed by the macro- or average-structure methods. It is also evident that, as new and more complex compositions of superconducting materials are being developed,³⁹ vibrational spectroscopy may take on an increasingly important role.

References

1. D. R. Clark, "The development of high-Tc ceramic superconductors: An introduction," *Adv. Ceram. Mater.* 2: 273-292, 1987.
2. D. L. Nelson, M. S. Whittingham, and T. F. George, Eds., *Chemistry of High-temperature superconductors*, ACS Symposium Series 351, Washington: American Chemical Society, 1987.
3. For a review of the early work in this field, see A. Khurana, *Physics Today* 40: 17, 1987.
4. R. M. Hazen et al., "Crystallographic description of phases in the Y-Ba-Cu-O superconductor," *Phys. Rev.* B35: 7238-7241, 1987.
5. M. P. A. Viegars et al., "Oxygen content, microstructure, and superconductivity of $\text{YBa}_2\text{Cu}_3\text{O}_{7-x}$," *J. Mater. Res.* 2: 743-749, 1987.
6. Madoka Tokumoto et al., "Evidence of critical oxygen concentration at $y = 6.7 \sim 6.8$ for 90 K superconductivity in $\text{Ba}_2\text{YCu}_3\text{O}_y$," *Jpn. J. Appl. Phys.* 26: L1565-L1568, 1987.
7. Tsunekazu Iwata et al., "Electron probe microanalysis for multiphase superconducting Y-Ba-Cu-O compound system," *Jpn. J. Appl. Phys.* 26: L647-648, 1987.
8. R. L. Sabatini et al., "Analytical electron microscopy study of high-Tc superconductor $\text{YBa}_2\text{Cu}_3\text{O}_7$," *J. Electron Microsc. Techn.* 8: 307-309, 1988.
9. K. Ramakrishna et al., "Electron microscopic studies of local structures of high-temperature $\text{YBa}_2\text{Cu}_3\text{O}_{7-x}$ superconductor," *Solid State Commun.* 65: 831-834, 1988.
10. R. Liu et al., "Presence of Cu_2O in $\text{MBa}_2\text{Cu}_3\text{O}_6$ ($M = \text{Sm}, \text{Ho}$), semiconducting modification of high-temperature superconductors," *Solid State Commun.* 65: 67-70, 1988.
11. M. Sarikaya et al., "Microstructural characterization of $\text{YBa}_2\text{Cu}_3\text{O}_{7-x}$," *J. Mater. Res.* 2: 736-742, 1987.
12. E. Czerwosch et al., "Raman spectra of the high-Tc superconductor Y-Ba-Cu-O," *Solid State Commun.* 64: 535-536, 1987.
13. H. Rosen et al., "Raman study of lattice modes in the high-critical-temperature superconductor Y-Ba-Cu-O," *Phys. Rev.* B36: 726-728, 1987.
14. R. M. McFarlane et al., "Temperature dependence of the Raman spectrum of the high Tc superconductor $\text{YBa}_2\text{Cu}_3\text{O}_7$," *Solid State Commun.* 63: 831-834, 1987.
15. Shin-ichi Nakashima et al., "Phonon Raman scattering in orthorhombic and tetragonal $\text{YBa}_2\text{Cu}_3\text{O}_{7-x}$," *Jpn. J. Appl. Phys.* 26: L1794-L1796, 1987.
16. M. Stavola et al., "Cu-O vibrations of $\text{Ba}_2\text{YCu}_3\text{O}_x$," *Phys. Rev.* B36: 850-853, 1987.
17. R. Liu et al., "Raman scattering in the high-Tc superconductors $\text{MBa}_2\text{Cu}_3\text{O}_{7-x}$," *Solid*

State Comm. 63: 839-841, 1987.

18. J. Chrzanowski et al., "Raman scattering from Y-Ba-Cu-O high- T_c superconductors," *Solid State Commun.* 65: 139-143, 1988.

19. Yoshiyuki Morioka et al., "Raman scattering from high- T_c superconductor $YBa_2Cu_3O_{7-x}$ and its analogs," *Jpn. J. Appl. Phys.* 26: L1499-1501, 1987.

20. M. Hangyo et al., "Effect of oxygen content on phonon Raman spectra of $YBa_2Cu_3O_{7-x}$," *Solid State Commun.* 65: 835-839, 1988.

21. S. Blumenroder et al., "Raman spectroscopy as a function of the oxygen content in $YBa_2Cu_3O_{7-x}$," *Solid State Commun.* 64: 1229-1232, 1987.

22. H. D. Bist et al., "EPR and Raman spectroscopy of high- T_c superconductor $YBa_2Cu_3O_7$," *Solid State Commun.* 65: 899-902, 1988.

23. J. A. Sanjurjo et al., "Raman measurements and lattice dynamics in the high- T_c superconductor $YBa_2Cu_3O_7$," *Solid State Commun.* 64: 505-508, 1987.

24. G. Burns et al., "Raman and infrared results on $YBa_2Cu_3O_{7-x}$ type materials," *Solid State Commun.* 64: 471-476, 1987.

25. C. Thomsen et al., "Systematic Raman and infrared studies of the superconductors $YBa_2Cu_3O_{7-x}$ as a function of the oxygen concentration ($0 \leq x \leq 1$)," *Solid State Commun.* 65: 55-58, 1988.

26. M. Cardona et al., "Infrared and Raman spectra of the new superconducting cuprate perovskites $MBa_2Cu_3O_7$, $M = Nd, Dy, Er, Tm$," *Solid State Commun.* 65: 71-75, 1988.

27. Yosuke Saito et al., "Infrared properties of the oxygen-deficient triperovskite $YBa_2Cu_3O_y$ compound," *Solid State Commun.* 64: 1047-1050, 1987.

28. D. A. Bonn et al., "Far-infrared conductivity of the high- T_c superconductor

$YBa_2Cu_3O_7$," *Phys. Rev. Lett.* 58: 2249-2250, 1987.

29. L. Genzel et al., "Far-infrared spectroscopy of the high- T_c superconductor $YBa_2Cu_3O_{7-x}$," *Solid State Commun.* 63: 843-846, 1987.

30. G. A. Thomas et al., "Far-infrared spectra of polycrystalline $Ba_2YCu_3O_{9-x}$," *Phys. Rev.* B36: 846-849, 1987.

31. Masayuki Udagawa et al., "Raman and infrared spectra of a green Y_2BaCuO_{5-y} ," *Jpn. J. Appl. Phys.* 26: L858-859, 1987.

32. R. J. Hemley and H. K. Mao, "Single-crystal micro-Raman spectroscopy of phases in the Y-Ba-Cu-O superconductor," *Phys. Rev. Lett.* 58: 2340-2342, 1987.

33. P. V. Huong et al., "Polarized Raman spectra of single crystals of $YBa_2Cu_3O_7$, $EuBa_2Cu_3O_7$, and $YBa_2Cu_3(O/F)_7$," this volume.

34. R. B. Marinenko et al., "Application of wavelength-dispersive digital compositional mapping to high-temperature superconductors," this volume.

35. Winnie Wong-Ng et al., "Structural phase transition study of $Ba_2YCu_3O_{6+x}$ in air," *J. Mater. Res.* (in press).

36. J. E. Blendell et al., "Processing-property relations for $Ba_2YCu_3O_7$ x high- T_c superconductors," *Adv. Ceram. Mater.* 2: 512-529, 1987.

37. E. S. Etz, "Raman microprobe analysis: Principles and applications," *SEM/1979 I*, 67-82.

38. G. J. Rosasco, "Raman microprobe spectroscopy," in R. J. H. Clark and R. E. Hester, Eds., *Advances in Infrared and Raman Spectroscopy*, vol. 7, London: Heyden, 1980, chap. 4, 223-282.

39. M. A. Subramanian et al., "A new high-temperature superconductor: $Bi_2Sr_{3-x}Ca_xCu_2O_{8+x}$," *Science* 239: 1015-1017, 1988.

MICROSPECTROSCOPY APPLICATIONS IN TRIBOLOGY

B. E. Hegemann, Said Jahanmir, and S. M. Hsu

Tribology is the science of friction, lubrication, and wear of interacting surfaces that are in relative motion. For a full understanding of friction and wear processes, a basic understanding of the chemical reactions that occur between the substrates and the lubricants, additives, and environment must be first developed. The term tribochemical reaction is used to describe such reactions. Fourier transform infrared (FT/IR) and Raman spectroscopy are techniques that are applicable to the tribochemical analysis required for such an understanding. Tribological processes are frequently studied by wear tests, such as the four-ball wear test,^{1,2} in which friction and/or wear of materials under lubrication are monitored under various speed and load conditions. In such a test, the apparent contact area is often in the dimensional range of 0.1-1mm. Within such a contact, the tribochemical reactions between lubricant molecules and substrate material surfaces take place. Due to the minute amount of reaction product and the complexity of the chemical composition, which may not be homogeneous across the contact zone, chemical information has been difficult to obtain. In this paper, the applicability of microspectroscopy techniques for a detailed post mortem chemical analysis of wear test specimens is explored. In particular, investigations of the use of micro-FT/IR spectroscopy to post mortem four-ball wear test specimen analysis is presented. As both metal and ceramic substrates are of tribological interest, the differences in applying micro-FT/IR analysis to each case is subsequently examined. New efforts in developing a time-resolved micro-Raman spectroscopy technique for tribochemical analysis³ are also discussed.

Experimental

The micro-FT/IR system consists of an all-reflective element infrared microscope with redundant aperturing directly interfaced to a conventional 5mm retardation FT/IR optical bench with a mercury cadmium telluride (MCT) detection element. The IR microscope is operated in a reflection mode with a 100 μ m-diameter

The authors are with the National Bureau of Standards, Gaithersburg, MD 20899. Support of this research through DOE/ECUT and NBS is acknowledged. We are grateful to Dr. Patrick Pei of NBS for preparing the oxidized TCP on Alpha-alumina substrate specimens, and to Douglas Deckman of NBS for preparing the SiC unlubricated wear test specimens. We also wish to express our appreciation to Dr. Ronald Munro for his contributions to the conception and development of this work.

sampling area.

The Raman experiments use as the incident light source the 532nm frequency-doubled output of a Nd:YAG laser operating at 50 Hz with an 8ns pulse width. A triple monochromator spatially filters and frequency disperses the optically collected Raman scattering signal. A gated intensified diode array operating at -30 C subsequently detects the frequency-dispersed signal. The detector is operated either in the continuous mode or activated with a gate pulse synchronized to the laser pulse.

Results and Discussion

Micro-FT/IR is a spectroscopic technique which is extremely useful for chemical analysis.⁴ In our laboratory, this technique has been applied in the reflection mode to observe tribochemical reaction products formed in and adjacent to the contact zones of steel substrates.^{3,5} Specifically, the tribochemical reactions of tricresyl phosphate ester (TCP) additive in paraffin oil on high-chrome steel surfaces were investigated.⁵ The lubricant/substrate system was subjected to a four-ball wear test, under conditions where the lubricant oxidation rate is not diffusion limited. A constant 40kg load was applied for 25 min with a sliding speed of 25 cm/s. Representative results of the spectroscopic information obtained from post mortem analysis are presented in Figs. 1 and 2, where 1 wt.% TCP in paraffin oil was used.

Figure 1 is taken from a region outside the contact area on the metal surface where no film formation is visually apparent. This IR spectrum is identical to that of the original paraffin oil lubricant. However, either in or adjacent to the contact zone, a brownish film is observed, which characteristically exhibits

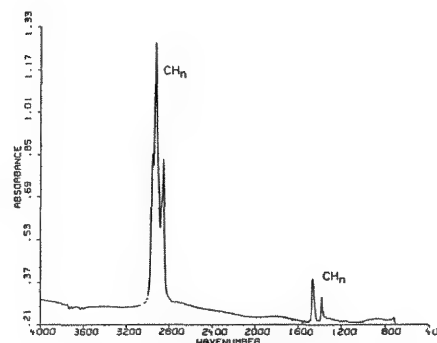


FIG. 1.--Typical micro-FT/IR spectrum of lubricant film on wear test specimen outside contact area.

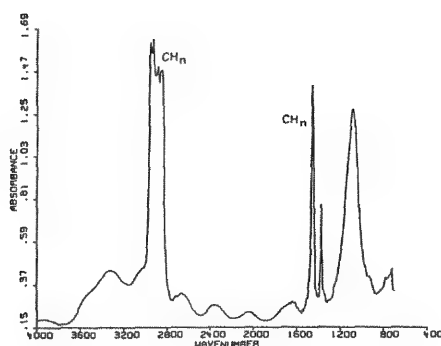


FIG. 2.--Typical micro-FT/IR spectrum of brown film deposit in contact area of wear test specimen.

the IR spectrum of Fig. 2. Noteworthy are the presence of the broad absorption peak centered at 1070 cm^{-1} , which may include polymeric C-O-C and/or P-O-C linkages and/or metallic phosphate groups,⁵ and the absence of any carbonyl absorption peaks typically found in thermally oxidized paraffinic oils.⁶ Figure 2 demonstrates that micro-FT/IR can detect tribochemical reaction products in the contact area that are not present in the original lubricant (Fig. 1). Comparison of such spectral results as a function of test conditions can now be made with spectra obtained from thermally oxidized lubricant/additive mixtures as a function of temperature, for a better understanding of the reaction conditions at the contact zone.

Ceramic materials are of considerable tribological importance, as much as metals; therefore, the use of micro-FT/IR in chemical analysis of ceramic tribological systems is also of interest. When micro-FT/IR is applied in the reflection mode to film analysis on a metal substrate, the experiment is essentially equivalent to a double-pass transmission experiment. The situation is complicated when a ceramic substrate that exhibits its own reflectance spectrum is used. Moreover, specular reflectance may also be present for sufficiently smooth test specimens and further complicates analysis. Figure 3 presents IR spectra typical of a thermally oxidized lubricant film on a ceramic substrate, TCP on alpha-alumina in this case. The resulting difficulties in spectral analysis are clear. However, in Fig. 4, the IR spectrum of the contact zone of SiC subjected to unlubricated wear clearly indicates the formation of hydrated silicates,⁷ which are not observed in any IR reflection spectra of the SiC sample outside the contact zone. Also identified in Fig. 4 is the absorption feature characteristic of graphitic/amorphous elemental carbon,⁸ which is present as an impurity in the original material. In this example, the SiC was subjected to a ball-on-three-flat wear test, as a modification of the standard four-ball wear test,⁹ with 1 kg incremental steps in the load over the range from 1 to 10 kg and a sliding speed of 4 cm/s for a total time of 100 min.

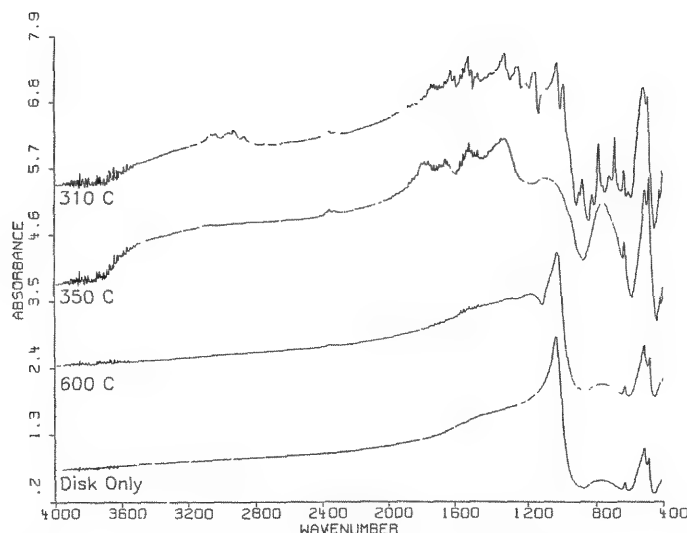


FIG. 3.--Micro-FT/IR spectra of thermally oxidized TCP on alpha-alumina disk substrate as a function of temperature. Spectra offset for clarity.

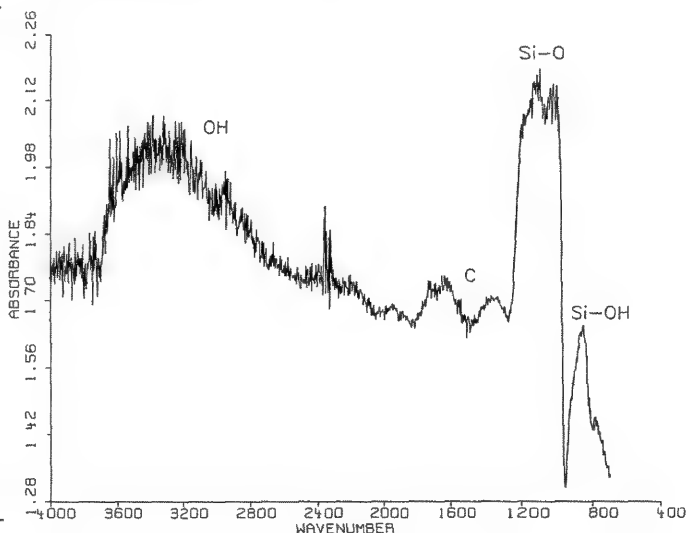


FIG. 4.--Micro-FT/IR spectrum of contact area of SiC substrate subjected to unlubricated wear test.

Applications of Raman spectroscopy to tribochemical analysis are often complicated by the presence of fluorescence. As Raman lifetimes are typically $<10\text{ ps}$ and fluorescence lifetimes are typically anywhere from nanoseconds to milliseconds, time-resolved detection techniques have been applied to reduce the fluorescence contribution.¹⁰ Therefore, the applicability of time-resolved Raman techniques to specific examples of tribological interest has been investigated. In Fig. 5, a comparison is presented of continuous and gated (20ns gate pulse) detection for an alpha-alumina substrate that exhibited considerable fluorescence with the 532nm excitation. With detection exposure time taken into account, a reduction of over two orders of magnitude in fluorescence signal was achieved.

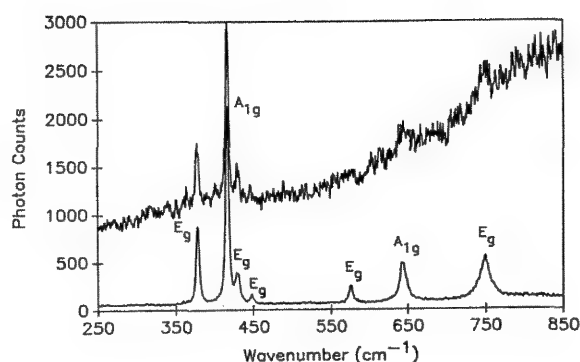


FIG. 5.--Comparison of Raman spectrum of alpha-alumina obtained with continuous detection (upper) and gated detection (lower).

For this material, the fluorescence lifetime was considerably longer than the 20ns detection time, so that excellent signal discrimination was attained.

An equivalent comparison of continuous and gated (5ns gate pulse) detection techniques for a base oil is presented in Fig. 6. This base oil sample contained an aromatic fraction that fluoresced under 532nm excitation. The reduction in fluorescence signal relative to the Raman signal is seen to be 50%. The fluorescence lifetime in this example was of the same order of magnitude as the time resolution of the experiment. This result demonstrates the ultimate limitation of the time-resolved technique: the effectiveness of signal discrimination depends on the difference between the time scales of the two processes.

The ability to combine pulsed laser excitation with micro-Raman techniques has been previously demonstrated for 1350° scattering geometries.¹¹ An upgrade of the micro-Raman optics system is now in progress. When completed, the degree to which micro-Raman and time-resolved techniques can be successfully combined will be examined as a function of spatial resolution and scattering geometry.

Conclusions

Micro-FT/IR has been found to be a useful technique for characterizing tribochemical reaction products formed in contact areas of metal substrates, and under certain conditions, ceramic substrates as well. Time-resolved Raman techniques can significantly reduce interfering fluorescence frequently found in tribological systems, provided there is sufficient difference in the time scales of the Raman scattering and fluorescence emission processes.

References

1. R. S. Gates and S. M. Hsu, "Development of a four-ball wear test procedure to evaluate

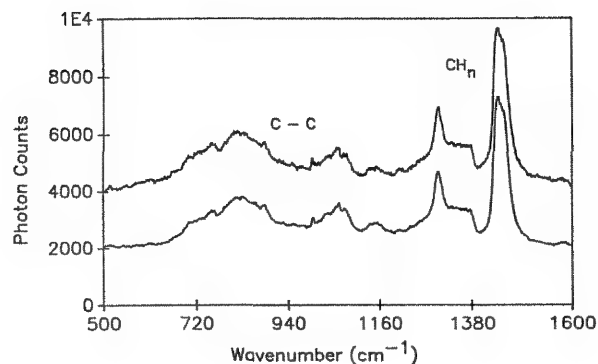


FIG. 6.--Comparison of Raman spectrum of a base oil obtained with continuous detection (upper) and gated detection (lower).

automotive lubricating oils," *Lubrication Engineering* 39: 561, 1983.

2. R. S. Gates and S. M. Hsu, "Development of an oxidation-wear-coupled test for the evaluation of lubricants," *Lubrication Engineering* 40: 75, 1984.

3. S. M. Hsu et al., *Friction and wear Characteristics of Materials*, U.S. Department of Energy, Office of Energy Utilization Research, Tribology Project Report TRIB-ECUT-87-1, 1987, 78.

4. J. A. Reffner et al., "Chemical microscopy with FT/IR microspectrometry," *Am. Lab.* 19: 86, 1987.

5. J. M. Perez et al., "Characterization of tricresylphosphate lubricating films by micro-Fourier transform infrared spectroscopy," *STLE Trans.* (submitted for publication).

6. J. P. Coates and L. C. Setti, "Infrared spectroscopic methods for the study of lubricant oxidation products," *ASLE Trans.* 29: 394, 1986.

7. G. Socrates, *Infrared Characteristic Group Frequencies*, New York: Wiley, 1980.

8. R. A. Friedel and G. L. Carlson, "Difficult carbonaceous materials and their infra-red and Raman spectra: Reassignments for coal spectra," *Fuel* 51: 194, 1972.

9. R. S. Gates, *Ceramic Tribology: Methodology and Mechanisms*, M.S. Thesis, Pennsylvania State University, 1987.

10. M. J. Wirth and S. H. Chou, "Comparison of time and frequency domain methods for rejecting fluorescence from Raman," *Anal. Chem.* (submitted for publication).

11. S. K. Sharma and J. P. Urmos, "Micro-Raman spectroscopic studies of materials at ambient and high pressures with CW and pulsed lasers," *Microbeam Analysis--1987*, 133.

"GRAPHITES" IN GEOLOGICAL SAMPLES: RAMAN SPECTROSCOPIC MISFITS?

Brigitte Wopenka and J. D. Pasteris

Raman spectra of geological carbonaceous materials indicate that in numerous cases there are significant structural and compositional deviations from well crystalline, pure carbon graphite. Some of these deviations are readily explained (and in some cases, quantifiable) by reference to the existing Raman literature on synthetically produced highly oriented pyrolytic graphite (HOPG) and graphite intercalation compounds (GICs). However, other features of Raman spectra of naturally occurring carbonaceous materials can be explained neither by theory nor by analogy with experiments done on synthetic samples. The observation of such Raman spectroscopic "misfits" is not unexpected, because of differences in the formation conditions for geologically occurring graphitic material (~ 300 - 1200 C; 1 bar to tens of kilobars) and HOPG (up to 3000 C; 1 bar), as well as the complex chemical environment of rocks. We present a brief summary of the kinds of structural characterizations and compositional inferences about "graphite" that can be revealed by Raman spectra--particularly as these data apply to several chosen examples of natural graphitic materials.

The presence of carbonaceous material in geological samples strongly affects the oxidation state and electrical conductivity of the sample, and also is an indicator of a possible organic precursor. Both the degree of crystallinity (crystallite size) and chemical purity (compared to pure carbon) are significant; the crystallite size is related to the nature of the precursor carbonaceous material, as well as the range of temperatures and pressures to which the sample has been metamorphosed. Structural deviations from well crystalline graphite and compositional deviations from pure carbon need to be accounted for in thermodynamic modeling of geological reactions that involve "graphite." Until recently, geologists assumed an essentially pure carbon composition

(the only impurity being hydrogen) for all carbonaceous materials that were well crystallized enough to produce an x-ray diffraction pattern for graphite.¹ Another technique that provides structural (and by inference, compositional) information on graphitic materials is laser Raman microprobe (LRM) spectroscopy. The LRM technique has some advantages over XRD analysis. It is nondestructive and permits in situ observation of the sample in its textural and mineralogic context. It also has excellent spatial resolution (about $2\ \mu\text{m}$), which is extremely important due to the nature of geological carbonaceous materials. The latter are frequently fine-grained, widely disseminated, and heterogeneous on a small scale.

Experimental Conditions

We use a 1983 model RAMANOR U-1000 laser Raman microprobe (Instruments SA). The one-meter, F/8 double monochromator with two plane holographic gratings is interfaced with a Nabet microscope. Instrumental details are described elsewhere.² Spectra are obtained in a scanning mode with a step size of $1\ \text{cm}^{-1}$, a counting time of 10 s per step, and a spectral resolution of about $5\ \text{cm}^{-1}$. The exciting radiation is the 514.5nm line of a 5W argon-ion laser. The power at the sample surface is about 10 mW. Geological samples can be analyzed as free unmounted grains (placed on a glass slide), as mounted microparticles (pressed into a gold substrate), or enclosed in $30\ \mu\text{m}$ -thick rock wafers in standard, polished thin sections.

Structural Characterization

Raman spectroscopy is known to be a very useful technique for distinguishing among different "degrees of order" of carbonaceous material.³ Carbon-dominated material that lacks the well-defined 3-dimensional crystal structure of graphite is called "disordered." This is a confusing term that can refer either to small crystallite size in the a- or c-direction (L_a , L_c), or to nongraphitic interplanar spacings. Because the Raman spectrum of graphite arises from in-plane vibrations, it is a reflection of the crystallite size in the a-direction (L_a). For samples with $L_a \geq 300\ \text{\AA}$, there is a single first-order Raman band E_{2g_2} at $1582 \pm 1\ \text{cm}^{-1}$, characteristic of well crystalline graphite. A second Raman-active band is so low in frequency (E_{2g_1} at $42\ \text{cm}^{-1}$) that in practice it cannot be resolved from Rayleigh scattering.

For $L_a < 300\ \text{\AA}$, the selection rules break down, and additional disorder-induced, first-order bands appear at $\sim 1360\ \text{cm}^{-1}$ and ~ 1622

The authors are in the Department of Earth and Planetary Sciences and the McDonnell Center for the Space Sciences at Washington University, Box 1169, St. Louis, MO 63130. They thank Mildred Dresselhaus (Massachusetts Institute of Technology) and Jack Fischer (University of Pennsylvania) for helpful discussions on graphite intercalation compounds. They also thank Steve Dunn and John Valley of the University of Wisconsin-Madison for the loan of interesting samples whose spectra are shown in Figs. 1a and 2c. The work was supported in part by Petroleum Research Fund grant 18786-AC2 and NASA Innovative grant NAGW122.

cm^{-1} . One of the modifications of the first-order Raman spectrum is the development of a shoulder on the high-wavenumber side of the 1582cm^{-1} band.⁴ The Raman-allowed band at 1582cm^{-1} and this disorder-induced (shoulder) band at $\sim 1622\text{cm}^{-1}$ cannot always be deconvolved, in which case the entire band appears broadened and up-shifted to about 1600cm^{-1} . The in-plane crystallite size L_a can be derived from the intensity ratio ($I_{1582}:I_{1600}$) by reference to a calibration curve relating Raman spectra to x-ray diffraction data.³ In experiments on HOPG, an L_a value of about 30Å was shown to be the lower limit for which the two first-order bands can be resolved as individual peaks.⁵ For samples with $L_a < 30\text{Å}$, and amorphous carbon films, the Raman spectrum simply shows an increased background in the $1300\text{--}1650\text{cm}^{-1}$ region.⁶

Second-order Raman bands in graphite are assigned both to overtone scattering ($2 \times 1620 = 3240\text{cm}^{-1}$; $2 \times 1360 = 2720\text{cm}^{-1}$) and combination scattering ($1620 + 830 = 2450\text{cm}^{-1}$). The theoretical reasons for the occurrence of first- and second-order Raman bands, as well as their peak positions and intensities, are relatively well understood from phonon dispersion relations based on various force constant models. The match of such models with the empirically observed band structures is extensively discussed in the solid-state literature.⁷

In practice, Raman spectroscopy can be used to monitor the in-plane crystallite size L_a from ~ 30 to $\sim 300\text{Å}$. Temperature-incremented experiments on carbonaceous materials show a rapid progress from $L_a = 30$ to 350Å over a temperature interval of only 400C (somewhere between 1600 and 2600C , depending on the carbonaceous precursor).^{8,9} Temperature changes of 400C are common in geological materials, e.g., in undergoing medium-grade regional metamorphism or baking next to an igneous intrusion. However, it is interesting to note that the specific degree of crystallinity of graphite revealed in its Raman spectrum is attained at much lower temperatures in geological samples than in HOPG (i.e., $300\text{--}700\text{C}$ vs above 1600C). The minerals and the ambient volatiles in geological samples must exert some catalytic effect on the crystallization process of graphite. The geologically important variables are time (up to millions of years), pressure (up to tens of kilobars), and chemistry (catalysts; template effect of the mineral host; initial structure of the carbonaceous precursor).

Figure 1 shows examples of Raman spectra of three different kinds of naturally occurring carbonaceous materials. The different features in the spectra of Fig. 1 can be explained by the presence of more or less disordered carbon-dominated materials, and show only small deviations from spectral data reported on synthetic samples.

Figure 1a shows the spectrum of a 2mm flake of graphite in highly metamorphosed marble from the Adirondack region of New York, which

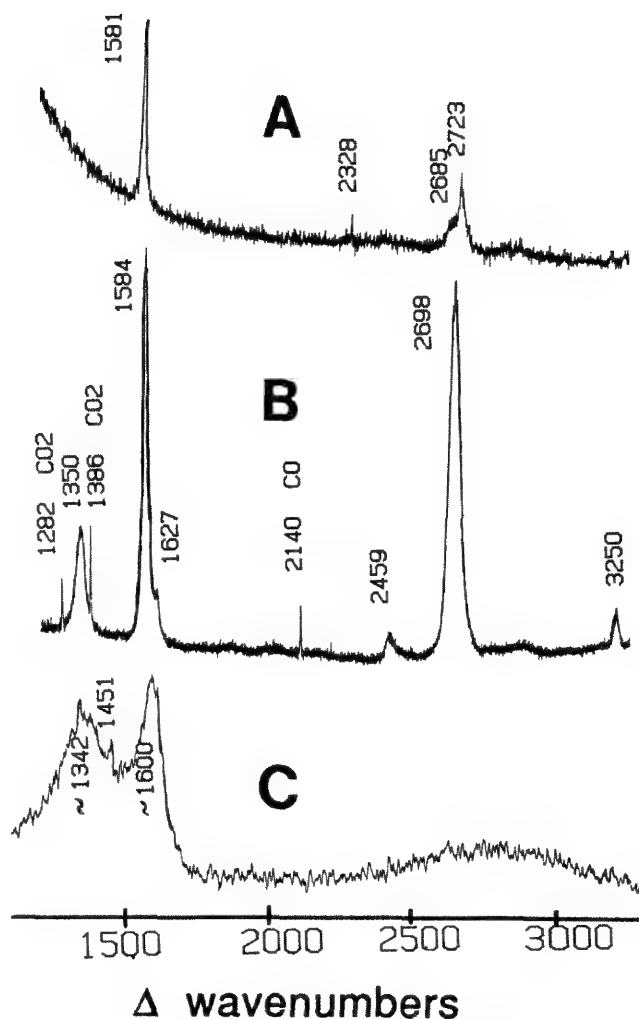
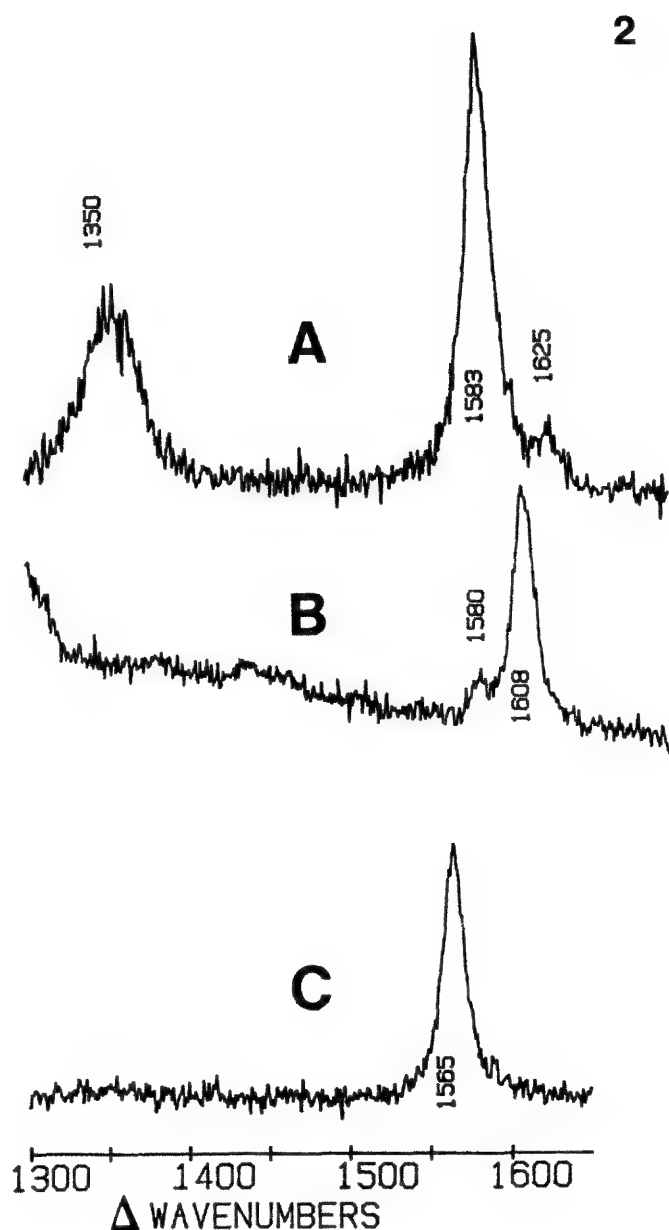


FIG. 1.--First- and second-order Raman spectra of geological carbonaceous materials of various degrees of crystallinity. (a) Well crystalline ($L_a > 300\text{Å}$), pure carbon graphite in strongly metamorphosed marble from the Adirondacks, N.Y. Grain size $\sim 2\text{mm}$. (b) Partially disordered graphite ($L_a \approx 200\text{Å}$) in CO-CO_2 fluid inclusion in olivine. Grain size $\sim 2\text{μm}$. (c) Strongly disordered carbonaceous material ($L_a = 30$ to 60Å) in interplanetary dust particle. Grain size 10μm .

consists of a single, strong first-order band at the expected position of 1581cm^{-1} , indicating an in-plane crystallite size of $>300\text{Å}$. The spectrum shows only one dominant second-order band, at about 2723cm^{-1} . This band has a shoulder on the low-wavenumber side, as reported by Elman et al.⁴ for HOPG. An additional low-intensity, but very sharp and reproducible feature appears at 2328cm^{-1} , as also reported for HOPG.⁶ However, neither the second-order band at $\sim 2450\text{cm}^{-1}$ nor the one at $\sim 3248\text{cm}^{-1}$ (both expected for HOPG) is present in the well crystallized geological sample.

Figure 1b shows the spectrum of partially disordered graphite that was synthetically induced to precipitate in a fluid inclusion in olivine.¹⁰ Although the presence of graphite was not detected optically (obscured by the wall of the fluid inclusion), the LRM detected



pounds of various stages. Bands at higher relative wavenumbers are due to graphite bounding layers. Bands at lower relative wavenumbers are due to graphite interior layers. (Reprinted from Ref. 20 with permission of Springer-Verlag.)

it. In fact, this 2 μm graphite gave the best spectrum of all carbonaceous materials analyzed in our laboratory. As noted also by Blaha and Rosasco,¹¹ the most minute grains frequently give the strongest and sharpest Raman bands. The embedding of the graphite within a fluid inclusion in a nonfluorescing, transparent matrix (olivine) also may account for the good quality of the spectrum. In addition to graphite, the volatiles CO and CO₂ are present in the fluid inclusion. The ratio $I_{1360}:I_{1600}$ (~ 0.26) indicates an in-plane crystallite size of about 200 Å.³ All of the expected second-order bands appear in this partially disordered carbonaceous material, but shifted 10-20 cm^{-1} from the theoretically predicted

positions listed above.

Figure 1c is the Raman spectrum of an individual interplanetary dust particle (IDP).^{12,13} From the $I_{1360}:I_{1600}$ intensity ratio, the in-plane crystallite size L_a is estimated to be about 30-60 Å. Comparison of Figs. 1b and 1c shows another interesting effect of disordering on the first-order Raman bands: both the Raman-allowed and the disorder-induced bands become wider upon increased disordering, and the latter are more sensitive. The full width at half height of the disorder-induced band for the IDP is $\sim 190 \text{ cm}^{-1}$ in comparison to a value of 38 cm^{-1} for the partly disordered graphite shown in Fig. 1b ($L_a \approx 200 \text{ Å}$). As long as interstitial defects are present, the "valley" between

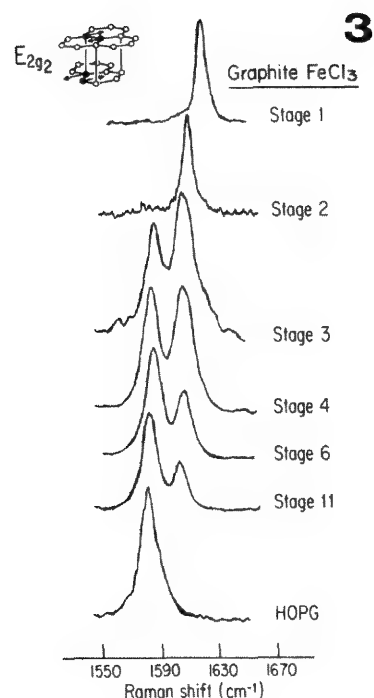


FIG. 2.--First-order Raman spectra of geological carbonaceous materials of various compositional and structural characteristics. (a) Partially disordered graphite in hydrous alteration zone in igneous Duluth Complex, Minn. Spectral characteristics consistent with either pure carbon composition or additional presence of acceptor intercalant layers. Grain size $\sim 150 \mu\text{m}$. (b) Well crystalline "graphite" in fluid inclusion in igneous olivine from Duluth Complex, Minn. May be an acceptor graphite intercalation compound. Grain size $\sim 2 \mu\text{m}$. (c) Well crystalline (no disorder-induced bands) "graphite" in strongly metamorphosed marble from Ontario. Extreme down-shift of E_{2g2} band suggests compositional deviations from pure carbon. Grain size $\sim 20 \mu\text{m}$.

FIG. 3.--Raman spectra of graphite-ferrie chloride (acceptor) intercalation com-

the Raman-allowed and disorder-induced Raman bands is elevated considerably above background, and in some cases an additional small band at $\sim 1500\text{ cm}^{-1}$ appears.⁹ Since both of the latter are observed in Fig. 1c, such interstitial defects must be present in the interplanetary carbonaceous material. The features in the second-order spectrum are also known to broaden as the in-plane crystallite size is decreased,⁷ and cannot be resolved in the IDP spectrum shown in Fig. 1c.

In summary, thus far, Fig. 1 represents geological carbonaceous samples of a wide range of crystallite sizes. The spectra demonstrate that, in at least some cases, geological carbonaceous samples produce Raman spectra that are accounted for by theoretical calculations and by analogy with synthetic HOPG.

Compositional Deviations

Our LRM studies of "graphites" in rocks of various degrees of metamorphism,¹⁴ "graphites" in hydrous alteration zones in igneous bodies of rocks^{15,16} and in fluid inclusions in hydrated olivines,^{17,18} and slightly metamorphosed carbonaceous matter in gold deposits¹⁹ resulted in the occasional observation of spectroscopic "misfits." The latter indicate the presence of more complex deviations from pure carbon graphite than just structural disorder. Some examples are shown in Fig. 2.

Figure 2a shows the spectrum of graphitic material in an alteration zone in the igneous Duluth Complex.¹⁵ As expected for partially disordered graphite, the "ordered" band develops a disorder-induced shoulder at 1625 cm^{-1} as the "disordered" band develops at $\sim 1350\text{ cm}^{-1}$. The first-order features in Fig. 2a are very similar to the ones in Fig. 1b; according to the previous discussion, this material would be identified as "partially disordered graphite." However, there is a complication to this interpretation: a similar kind of spectrum presumably also would arise from a high-stage acceptor graphite intercalation compound (GIC) with disordering of the graphitic layers. GICs are graphite-like structures in which carbon layers are separated by a layer of some other atomic or molecular species. In these sandwich structures, one distinguishes graphite interior layers (sandwiched between at least two other carbon layers) from graphite bounding layers (which sandwich an intercalant layer between them). The "stage number" is the ratio of carbon to intercalant layers.

Intercalation-induced changes in the vibrational dynamics of well ordered graphite have been studied extensively by Raman spectroscopy.²⁰ The formation of a GIC produces an additional Raman band on either the high-wavenumber (for acceptor intercalants, e.g., molecular compounds like Br_2 , MgCl_2 , FeCl_3) or low-wavenumber (for donor intercalants, e.g., metals like Rb, K) side of the 1582 cm^{-1} band (Fig. 3). In the case of an acceptor intercalant (see Fig. 3), the band at higher relative wavenumbers is identified with the graphite bounding layer mode and the one at lower relative wavenumbers

with the graphite interior layer mode. Unfortunately, Raman spectral characteristics of a GIC reflect only the electronic donor/acceptor nature of the intercalant and the stage number. Other analytical techniques such as x-ray analysis in an SEM or TEM must be used for specific elemental characterization. However, the LRM's ability to rapidly distinguish GICs from pure, well ordered carbon graphite is significant.

Compositional deviations from pure carbon graphite (such as a GIC) are a realistic possibility for many natural samples. On the basis of energy dispersive x-ray analysis, Mathez²¹ has inferred the presence of GICs in geological materials similar to those whose spectra are shown in Figs. 2a and b. Thus, the presence of GICs in the Duluth sample of hydrous alteration cannot be ruled out, and the interpretation of the spectrum in Fig. 2a (as well as the one in Fig. 1b) becomes ambiguous: the development of the 1625 cm^{-1} band could be caused simply by partial disordering of a pure carbon graphite or by the additional presence of intercalant layers in such a structure.

A less ambiguous example of the inferred presence of a naturally occurring GIC is the spectrum shown in Fig. 2b, obtained on a "graphite" precipitated in a fluid inclusion in olivine, also from the Duluth Complex.¹⁶ The Raman-allowed band is up-shifted to 1608 cm^{-1} , as would be expected in a strongly disordered graphite. However, there is no sign of a disorder-induced band at $\sim 1360\text{ cm}^{-1}$. The structural-bonding information provided by this spectrum suggests that the "graphite" is well ordered ($L_a \geq 300\text{ \AA}$), but that it has compositional deviations from pure carbon. The spectrum is consistent with a relatively low-stage (i.e., high concentration of intercalant), well crystalline GIC with an acceptor intercalant. A chloride intercalant seems to be most likely, given that Pasteris¹⁶ detected Ca, K, and Cl in opened fluid inclusions in similar Duluth olivines, using energy dispersive electron microprobe analysis. "Graphite" precipitates in fluid inclusions in partially serpentinized olivines from kimberlites yield spectra almost identical to that in Fig. 2b.¹⁸

The spectrum in Fig. 2c, obtained on a $20\mu\text{m}$ "graphite" flake from a strongly metamorphosed marble in Ontario, superficially appears analogous to that in 2b: no disorder-induced band and a displaced Raman-allowed band. However, there are important differences between this spectrum and the one in Fig. 2b. First, the Raman band is extremely down-shifted (to 1565 cm^{-1} , i.e., a shift of 17 cm^{-1}), which indicates the presence of compositional deviations from pure carbon graphite. Second, there is a complete lack of any remnant 1582 cm^{-1} band, which suggests a first- or second-stage intercalation compound.²⁰ This would require a one-to-one or two-to-one ratio of carbon planes to intercalant planes.

Our data (Fig. 2c) are not consistent with the presence of graphite intercalation com-

pounds, because no first- or second-stage GICs reported in the literature²⁰ show peak downshifts anywhere near as large as those we find. Therefore, Fig. 2c appears to be a spectroscopic "misfit" in that such spectra are not described in the Raman literature on graphitic materials or on synthetically produced intercalation compounds. As a further complication, x-ray diffraction patterns of this material show only lines for well crystallized graphite,²² whereas preliminary SEM and TEM analyses reveal large concentrations of silicon in addition to carbon in these 20 μm grains embedded in minute silicate minerals.¹⁴ We are therefore considering additional interpretations, such as an interstitial solid solution of Si in the graphite structure and very fine intergrowths (on the order of hundreds of Angstroms) of C- and Si-bearing phases.

Conclusions

Raman spectroscopic analysis of geological carbonaceous materials reveals a wide range in structural and compositional deviations from well crystallized pure carbon graphite. The LRM provides a relatively rapid, pinpoint, non-destructive means of recognizing unusual graphitic materials. The geological ramifications of impure and/or disordered graphite are numerous. Recognition of compositional and structural deviations is important in (1) thermodynamic calculations of equilibria in assemblages bearing "graphite," (2) mass balance calculations on trace elements and isotopic species in rocks,²¹ and (3) evaluating possible effects on isotopic fractionation.²²

References

1. See, for example, K. W. Wedeking and J. M. Hayes, "Carbonization of Precambrian kerogens," *Adv. Organ. Geochem.* 1981: 546, 1983.
2. B. Wopenka and J. D. Pasteris, "Raman intensities and detection limits of geochemically relevant gas mixtures for a laser Raman microprobe," *Anal. Chem.* 59: 2165, 1987.
3. See, for example, F. Tuinstra and J. L. Koenig, "Raman spectrum of graphite," *J. Chem. Phys.* 53: 1126, 1970.
4. B. S. Elman et al., "Structural characterization of ion-implanted graphite," *Phys. Rev. B* 25: 4142, 1982.
5. P. Lespade, R. Al-Jishi, and M. S. Dresselhaus, "Model for Raman scattering from incompletely graphitized carbons," *Carbon* 20: 427, 1982.
6. B. S. Elman et al., "Raman scattering from ion-implanted graphite," *Phys. Rev. B* 24: 1027, 1981.
7. See, for example, R. J. Nemanich and S. A. Solin, "First- and second-order Raman scattering from finite-size crystals of graphite," *Phys. Rev. B* 20: 392, 1979.
8. B. T. Kelly, *Physics of Graphite*, New Jersey: Applied Science Publishers, 1981, 470.
9. J. N. Rouzaud, A. Oberlin, and C. Beny-Bassez, "Carbon films: structure and microtexture (optical and electron microscopy, Raman spectroscopy)," *Thin Solid Films* 105: 75, 1983.
10. J. D. Pasteris and B. J. Wanamaker, "Laser Raman microprobe analysis of experimentally re-equilibrated fluid inclusions in olivine: Some implications for mantle fluids," *American Mineral* (in press).
11. J. J. Blaha and G. J. Rosasco, "Raman microprobe spectra of individual microcrystals and fibers of talc, tremolite, and related silicate minerals," *Anal. Chem.* 50: 892, 1978.
12. L. J. Allamandola, S. A. Sandford, and B. Wopenka, "Interstellar polycyclic aromatic hydrocarbons and the carbon in interplanetary dust particles and meteorites," *Science* 237: 56, 1987.
13. B. Wopenka, "Raman observations on individual interplanetary dust particles," *Earth Planet. Sci. Lett.* (in press).
14. B. Wopenka et al., "Si-bearing graphite in Tudor Township, Ontario," *EOS* 69: 501, 1988.
15. D. C. Sassani and J. D. Pasteris, "Preliminary investigation of alteration in a basal section of the southern Duluth Complex, Minnesota," in G. Kisvarsanyi and S. K. Grant, Eds., *Proc. North American Conf. on Tectonic Control of Ore Deposits*, University of Missouri at Rolla, 1988, 280.
16. J. D. Pasteris, "Monitoring volatile-solid reactions in mantle rocks," *Geology* (in press).
17. J. D. Pasteris, "Occurrence of graphite in serpentinized olivines in kimberlite," *Geology* 9: 356, 1981.
18. J. D. Pasteris and B. Wopenka, "Use of a laser Raman microprobe to trace geological reactions," in R. H. Geiss, Ed., *Microbeam Analysis--1987*, 205.
19. J. D. Pasteris, C. A. Kuehn, and R. J. Bodnar, "Applications of the laser Raman microprobe RAMANOR U-1000 to hydrothermal ore deposits: Carlin as an example," *Econ. Geol.* 81: 915, 1986.
20. See, for example, M. S. Dresselhaus and G. Dresselhaus, "Light scattering in graphite intercalation compounds," in M. Cardona and G. Güntherodt, Eds., *Light Scattering in Solids*, New York: Springer-Verlag, 1982, 3-57.
21. E. A. Mathez, "Carbonaceous matter in mantle xenoliths: Composition and relevance to the isotopes," *Geochim. Cosmochim. Acta* 51: 2339, 1987.
22. S. R. Dunn and J. W. Valley, "Calcite-graphite carbon isotope thermometry: Recognition of polymetamorphism, Tudor Gabbro," *Geol. Soc. of Amer. Abstracts with Programs* 19: 649, 1987.

ANALYSIS OF INDIVIDUAL FLUID INCLUSIONS BY MICRO-FTIR SPECTROSCOPY

J. K. Vry, P. E. Brown, and J. Beauchaine

Micro-FTIR (Fourier transform infrared spectroscopy) techniques offer a promising new development for fluid inclusion studies. Both H_2O and CO_2 are readily identified in moderate- to small-sized ($250\mu\text{m}^2$ or less in cross-sectional area) subequant fluid inclusions in doubly polished thick sections of quartz. Spectra from synthetic $\text{H}_2\text{O}/\text{CO}_2$ fluid inclusions ($\text{XCO}_2 = 0.25, 0.50, \text{ and } 0.75$)^{1,2} show clear signals for both H_2O and CO_2 , with negligible effects from differing inclusion depths within the quartz (Fig. 1). The high fluid densities typical of many fluid inclusions permit the use of CO_2 overtone bands (Fig. 2) for semiquantitative (and potentially for quantitative) analyses of inclusion contents. The presence of these additional alternative peaks can help avoid interferences from the quartz absorption edge, which in some cases makes absorbance estimates from the 2349cm^{-1} CO_2 peak difficult. The excellent resolution of the micro-FTIR method for H_2O provides a direct contrast to laser Raman spectroscopy and should substantially improve detection limits for H_2O in fluid inclusions. The Micro-FTIR method should also prove suitable for other important species such as CH_4 and some daughter salts.

The estimation of maximum $\text{H}_2\text{O}/\text{CO}_2$ ratios in individual fluid inclusions is of key importance in both fluid inclusion geobarometry and petrologic phase equilibria studies. Metamorphic rocks commonly contain several generations of fluid inclusions, which potentially provide information on the composition and evolution of a metamorphic fluid phase during mineral growth, recrystallization, or deformation, and on the pressure and temperature history of the metamorphic terrane. Because water preferentially wets inclusion wells, severe optical problems arise related to boundary effects and the high refractive index of CO_2 . Thus, up to 20 volume % H_2O may be present in inclusions, but visually difficult to detect. Laser Raman spectroscopy is not suitable for estimating $\text{H}_2\text{O}/\text{CO}_2$ ratios in fluid inclusions because of the low laser Raman signal for H_2O . The magnitude of uncertainties in inclusion composition estimates (20 volume % H_2O may be equivalent to 50 mole % H_2O , depending on the CO_2 density) by the best of previous nondestructive techniques can cause pressure estimates to be in error by as much as 2 kbar for granulite facies pressures and temperatures.⁵ The real need of improvements in specific areas of fluid inclusion

analysis has led to this present evaluation of micro-FTIR techniques. Early results suggest that micro-FTIR methods will extend minimum detection limits for H_2O in fluid inclusions by a factor of 2 or more (i.e., < 10 volume %), when compared to the best (nondestructive) techniques now available.

A Nicolet 55XCFT-IR, interfaced to a Spectra-Tech IR plan in microscope with $32\times$ Cassegrain objective lens, has been used to obtain spectra from inclusions in three synthetic fluid inclusion "standard" chips (doubly polished thick sections of quartz; fluid $\text{XCO}_2 = 0.25, 0.50, \text{ and } 0.75$).^{1,2} Typical measurements using 512 co-added scans at 8 to 16 wavenumber resolution require only approximately 400 s per inclusion analysis. For inclusions of known composition, it has been possible to compare the effects of differing sample characteristic such as inclusion size, shape, and position (depth) within the quartz matrix, and quartz sample thickness, on H_2O and CO_2 peak height measurements. Extremely reproducible micro-FTIR analyses (Fig. 1) can be obtained from subequant inclusions as small as $250\mu\text{m}^2$ in cross-sectional area, with virtually no depth effect. Data obtained from smaller inclusions suffer proportionally larger uncertainties, and inclusions smaller than approximately $170\mu\text{m}^2$ in cross-sectional area are difficult to analyze by present methods. Application of partial least-squares techniques shows promise for in situ quantitative fluid inclusion analyses.

The ability to obtain reproducible spectra with a narrow range of sampling errors depends critically on at least three variables in microscope configuration: the characteristics of the aperturing system, the power of the objective lens, and the general smoothness (and thus reproducibility) of the sampling operation. An inclusion must be isolated for quantitative or even semi-quantitative micro-FTIR analysis, which requires that different portions of the apertures be movable to fit almost exactly the viewed inclusion margins. The effects of stray light and imperfect aperturing are most severe in the case of small inclusions. Careful redundant aperturing, above and below the sample, increases data quality. For typical, small fluid inclusions, such careful visual aperturing is best obtained by use of a $32\times$ Cassegrain objective lens.

The data obtained in this study represent a significant improvement over previous reports in the literature,⁴ which have not obtained acceptable quality spectra from typical moderate- and small-sized fluid inclusions.

Micro-FTIR analyses of three high-density

J. K. Vry and P. E. Brown are at the Department of Geology and Geophysics, University of Wisconsin, Madison, WI 53706; J. Beauchaine is with Nicolet Instruments Corp., 5225-1 Verona Road, Box 4370, Madison, WI 53711-0370.

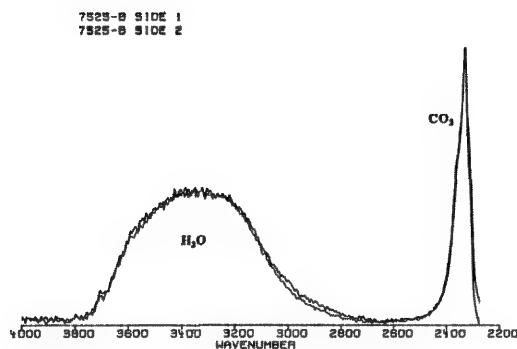


FIG. 1.--Micro-FTIR spectra of synthetic $\text{H}_2\text{O} + \text{CO}_2$ fluid inclusion ($\text{XCO}_2 = 0.25$). Inclusion is $12 \times 23 \mu\text{m}$, at depth of $8 \mu\text{m}$ in $70\mu\text{m}$ -thick double-polished quartz thick section. Figure shows clear signals obtained for both H_2O and CO_2 , to evaluate effects of differing inclusion depths within quartz. Sample was analyzed twice, by turning the chip over (side 1 and side 2), to evaluate effects of differing inclusion depths.

CO_2 -rich fluid inclusions from granulite-facies occurrences in the Adirondack Mountains, N.Y. and the Pikwitonei domain, Manitoba, have detected no H_2O or other fluid species such as methane. Phase equilibria studies⁵ indicate that such inclusions cannot represent the peak metamorphic fluid; however, the inclusions may provide information on postmetamorphic uplift paths.

References

1. R. J. Sterner and S. M. Bodner, "Synthetic fluid inclusions in natural quartz: I. Compositional types synthesized and applications to experimental geochemistry," *Geochim. Cosmochim. Acta* 48: 2659-2668, 1984.
2. R. J. Bodner and S. M. Sterner, "Synthetic fluid inclusions," in G. C. Ulmer and H. L. Barnes, Eds., *Hydrothermal Experimental Techniques*, New York: Wiley, 1987, 423-457.
3. P. E. Brown and W. M. Lamb, "Mixing of H_2O - CO_2 in fluid inclusions: Geobarometry and Archean gold deposits," *Geochim. Cosmochim. Acta* 50: 847-852, 1986.
4. O. Barres, A. Burneau, J. Dubessy, and M. Pagel, "Application of micro-FT-IR spectroscopy to individual hydrocarbon fluid inclusion analysis," *Applied Spectroscopy* 41: 1000-1008, 1987.
5. W. M. Lamb, J. W. Valley, and P. E. Brown, "Post-metamorphic CO_2 -rich fluid inclusions in granulites," *Contrib. Mineral Petrol.* 96: 485-495, 1987.

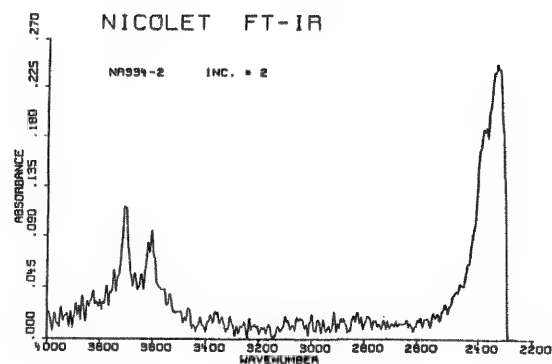


FIG. 2.--Characteristic spectrum of high-density CO_2 fluid inclusion, showing only CO_2 peaks. Inclusion is $18 \times 27 \mu\text{m}$, CO_2 density is approximately 1.02 g/cc , and quartz chip thickness is $152 \mu\text{m}$.

INFRARED MICROSCPECTROSCOPY FUNCTIONAL GROUP IMAGING AS A PROBE INTO THE COMPOSITIONAL HETEROGENEITY OF POLYMER BLENDS

M. A. Harthcock, S. C. Atkin, and B. L. Davis

The application of infrared microspectroscopic techniques for obtaining Functional Group Images (FGI) has recently been described.¹⁻³ The imaging technique provides a means to observe a material based on the absorption of infrared radiation by specific vibrational motions associated with functional groups (e.g., carbonyl stretching modes). The images are produced after infrared spectra are obtained at specific locations on a material via mapping or scanning a region of the material. The technique can thus be used to determine the homogeneity or identity of a material based on the chemical composition. The spatial resolution limit of the technique is governed by the diffraction limit of the infrared radiation (i.e., approximately 10 μm in the fingerprint region of an infrared spectrum).

We have used this technique to investigate the homogeneity of polymer blends based on the chemical composition and not made use of any implications based on the morphology of a blend which is observed using optical and/or electron microscopy.⁴ This paper describes how functional group imaging can give compositional information about polymer blend homogeneity and compatibility and outlines the experimental considerations that must be made for such investigations.

Experimental

The experimental details and data reduction techniques necessary for obtaining functional group images via (absorption) infrared microspectroscopy have been reported previously.¹⁻³ The instrumentation and data analysis methods described previously were used for the studies reported here. The samples investigated were prepared as microtomed cross sections from injection molded parts by means of a Sorvall MT-6000 microtome equipped with an FS-1000 cryo-sectioning chamber or as cast films.

Results

The morphology of polymeric blends has been investigated extensively using optical and electron microscopy.⁴ Many extrudates or molded parts exhibit what is classified as a skin-core morphology.⁴ Figure 1 presents a

schematic representation of a skin-core morphology in a cross section of an injection molded two-phase polymer blend. As can be observed, the phases are elliptical near the outer surface. As one transverses through the cross section, the phases become spherical in shape. The compositional homogeneity through the cross section cannot be conclusively determined by analysis of the image based simply on distribution of the various size and shaped phases within a given spatial region. The solubility or chemical mixing of the two phases of the blend will influence the chemical composition observed for any given phase.

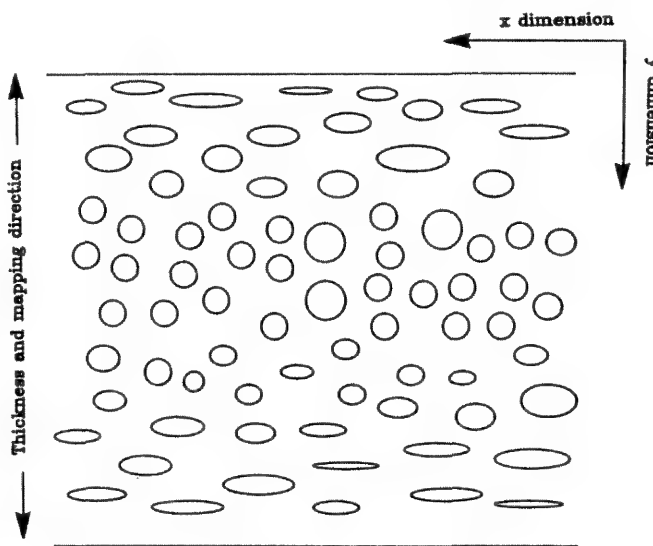


FIG. 1.--Schematic of cross section of molded polymer blend exhibiting skin-core morphology; x and y axes are defined for aperture dimensions used in infrared microspectroscopy experiment.

As an example, Fig. 2 presents an image of a polycarbonate/ester functionality blend (one-dimensional, averaged, with an aperture size of $x = 150$ and $y = 15 \mu\text{m}$, as defined in Fig. 1) based on a ratio of the carbonyl stretching frequency absorptions. The 1773 and 1736 cm^{-1} absorptions correspond to the polycarbonate and ester functionality-containing phases, respectively.

As can be observed from the averaged one-dimensional image, the composition varies throughout the cross section of the injection molded part from the region sampled. At least five distinct zones of compositional change can be defined with respect to the center of the mold thickness direction. For example, the outer 150 μm of the mold contains a higher con-

The authors are with Analytical and Engineering Sciences, Dow Chemical U.S.A., Freeport, TX 77541. Their thanks goes to E. I. Garcia-Meitin for preparing the microtomed cross sections used in the analysis, as well as to Drs. C. Kao, C. P. Christenson, and A. Platt of the Dow Chemical Company.

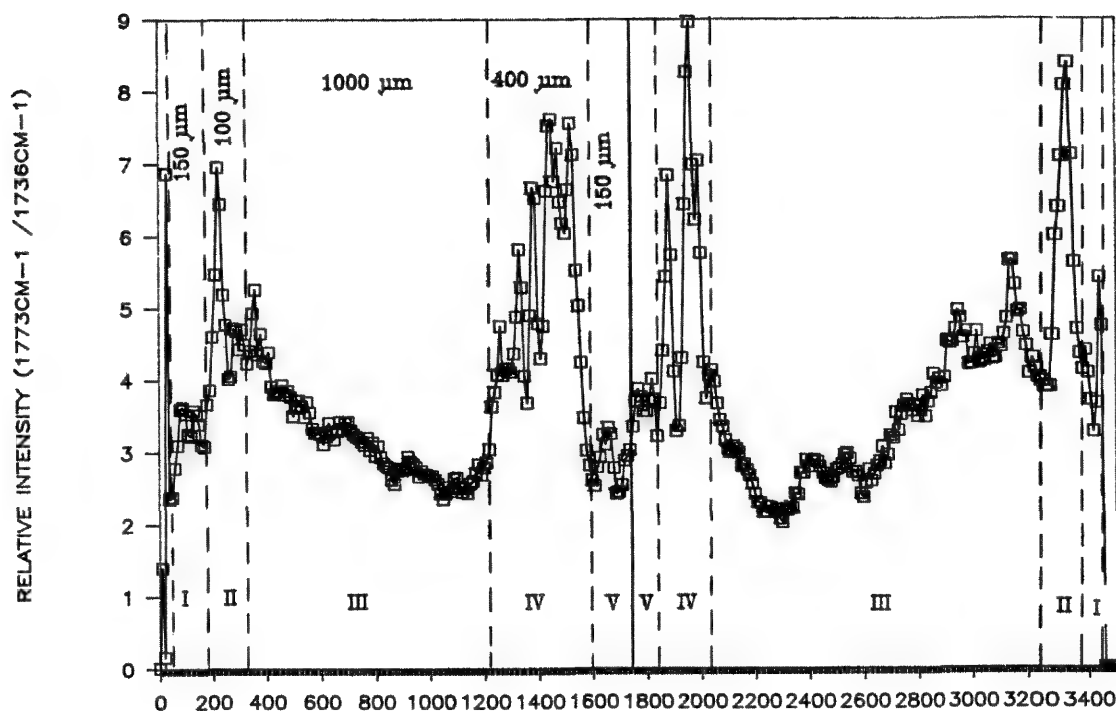


FIG. 2.--Functional group image (ratio map of 1773 to 1736 cm^{-1} absorption bands) showing compositional heterogeneity of polycarbonate/ester functionality containing blend. (Aperture dimensions: $x = 150\text{ }\mu\text{m}$, $y = 15\text{ }\mu\text{m}$; 10 μm steps, 256 scans, 8 cm^{-1} resolution.)

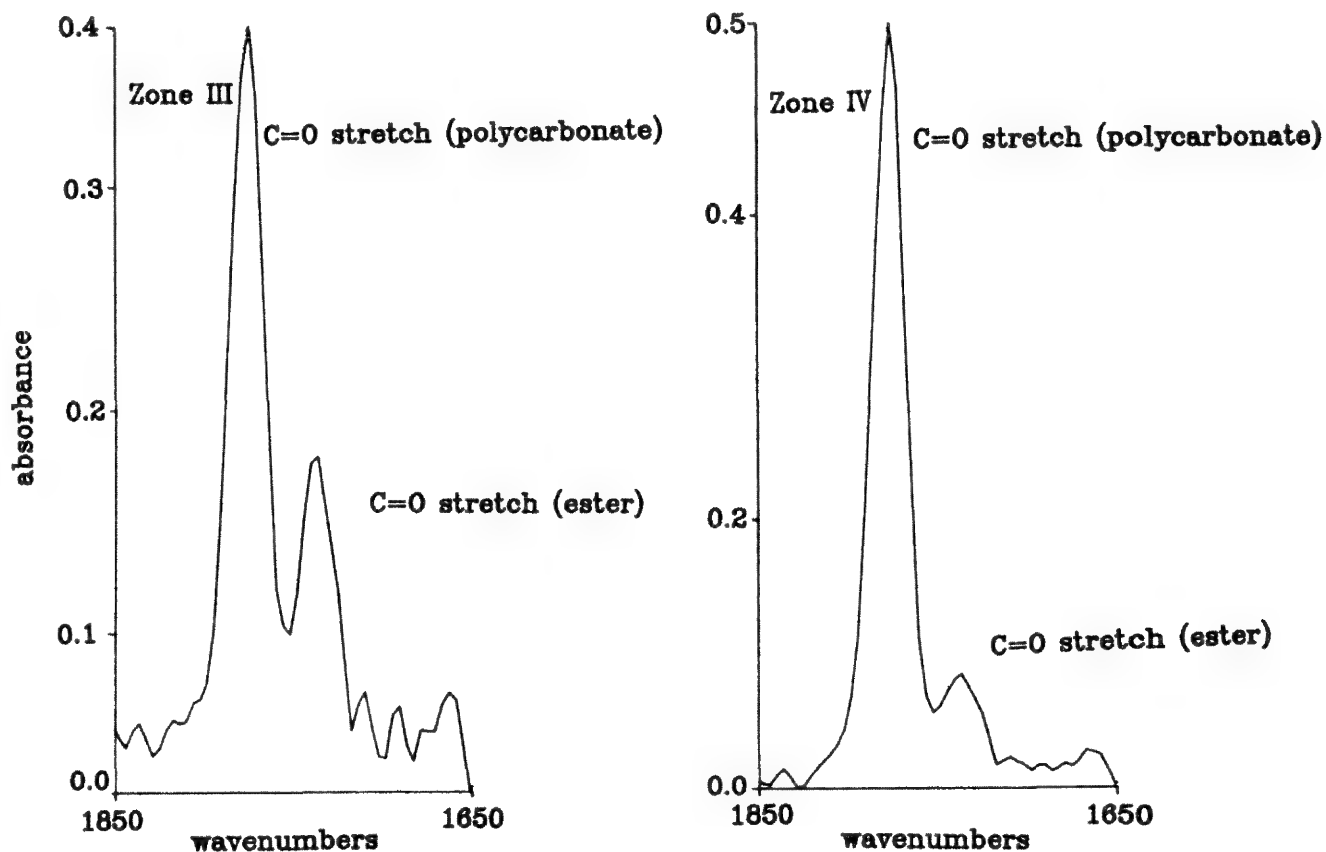


FIG. 3.--Infrared spectra representative of zone III and IV for image shown in Figure 2.

centration of the ester functionality containing phase than does the next 100 μm of the specimen. Figure 3 presents representative infrared spectra of zones III and IV, confirming that the compositional heterogeneity is not an artifact of the sample preparation.

Sample preparation is very critical to investigating the compositional homogeneity of a polymer blend system. Since infrared spectra are being recorded, the chemical composition must be representative of the material or domains of interest. Figure 4 is a schematic representation of a two-phase polymer blend.

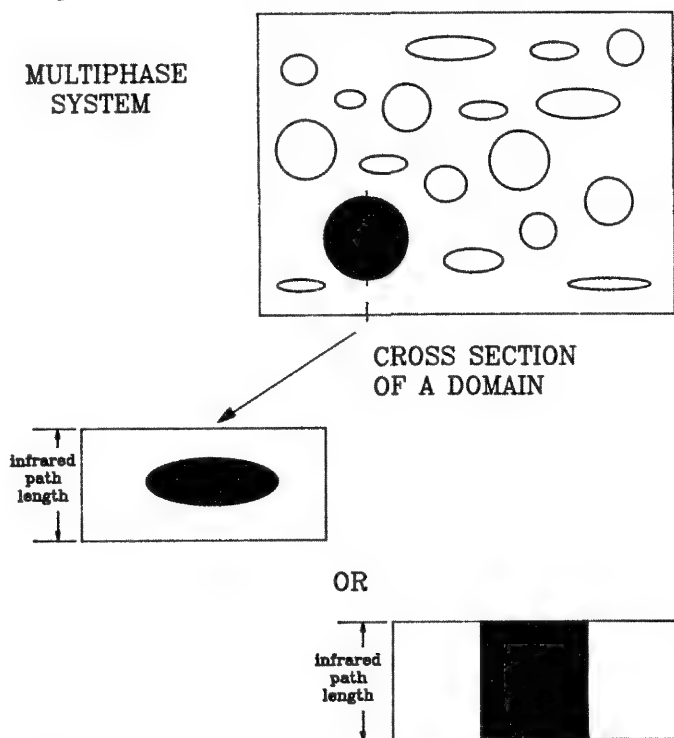


FIG. 4.--Schematic representation of two-phase polymer blend with possible cross sections of domain shown in path length direction.

The z direction or infrared path length is shown as a cross section of a domain or phase of the blend. It is apparent, if one is investigating the solubility of a polymer in the other phase of the blend, that the phase cannot be surrounded by the second phase in the infrared path direction, which results in a misrepresentation of the solubility of a particular phase in another. Thus, the physical state/morphology of the sample must be known and carefully prepared.

As a demonstration of the ability to image a polymer blend based on functional groups present in and indicative of phases of a blend, Fig. 5 presents an image of a cast film of a blend of polycarbonate and SAN (styrene-acrylonitrile copolymer). The image is based on the 2234 cm^{-1} carbon/nitrogen triple bond stretching frequency which is associated with the SAN phase. As observed from the image, polycarbonate or SAN dominant regions can be identified. The concerns expressed earlier and depicted in Fig. 4 related to the morphology of the micro-

scopic sample preclude conclusive quantitation of the solubility of the two phases in a cast film. However, in the future, we believe that quantitative determination of the solubility or mixing of the phases in a blend can be determined by a study of the specific domains. Further work in our laboratory is being done to address the direct quantitation of phase solubility in polymer blends using infrared microspectroscopy. In particular, research is being conducted on compression and injection molded polycarbonate/SAN blends.

Conclusion

Infrared microspectroscopic functional group imaging can be used to investigate the compositional homogeneity in polymer blends exhibiting a skin-core morphology. Interpretation based simply on analysis of an optical and/or electron microscopic image could misrepresent the chemical compositional homogeneity. The physical state/morphology of a sample and its preparation for the infrared microspectroscopic examination must be carefully chosen to avoid determining incorrect values for the solubility of one phase of a polymer blend in the other. With expanding application of infrared microspectroscopy to polymer characterization, of the nature reported here, a point to be made in this paper is that sample preparation and integrity are as important (if not more so) here as they are for optical/electron microscopic analyses.

Although the technique currently limits examination to phases that are larger than approximately $10\text{ }\mu\text{m}$, the potential of the method for obtaining direct information on the compatibility of two phases in a biconstituent polymer system has been demonstrated. Previous methods to investigate the use of infrared spectroscopy to study the compatibility of phases of a blend have been less direct.⁵ Now we are confronted with the $10\text{ }\mu\text{m}$ spatial resolution limit and the concerns associated with sample preparation.

References

1. M. A. Harthcock and S. C. Atkin, "Infrared microspectroscopy: Development and application of imaging capability," in R. G. Messerschmidt and M. A. Harthcock, Eds., *Infrared Microspectroscopy: Theory and Applications*, New York: Marcel Dekker (in press).
2. M. A. Harthcock and S. C. Atkin, "Composition mapping with the use of functional group images obtained by infrared microprobe spectroscopy," *Microbeam Analysis--1987*, 173.
3. M. A. Harthcock and S. C. Atkin, "Imaging with functional group maps using infrared microspectroscopy," *Appl. Spectrosc.* 42: 449, 1988.
4. See, for example, L. C. Sawyer and D. T. Grubb, *Polymer Microscopy*, London: Chapman and Hall, 1987, 196.
5. M. M. Coleman and J. Zarian, "FT-IR studies of polymer blends," *J. Polym. Sci. Polym. Phys. Ed.* 17: 1979, 837.

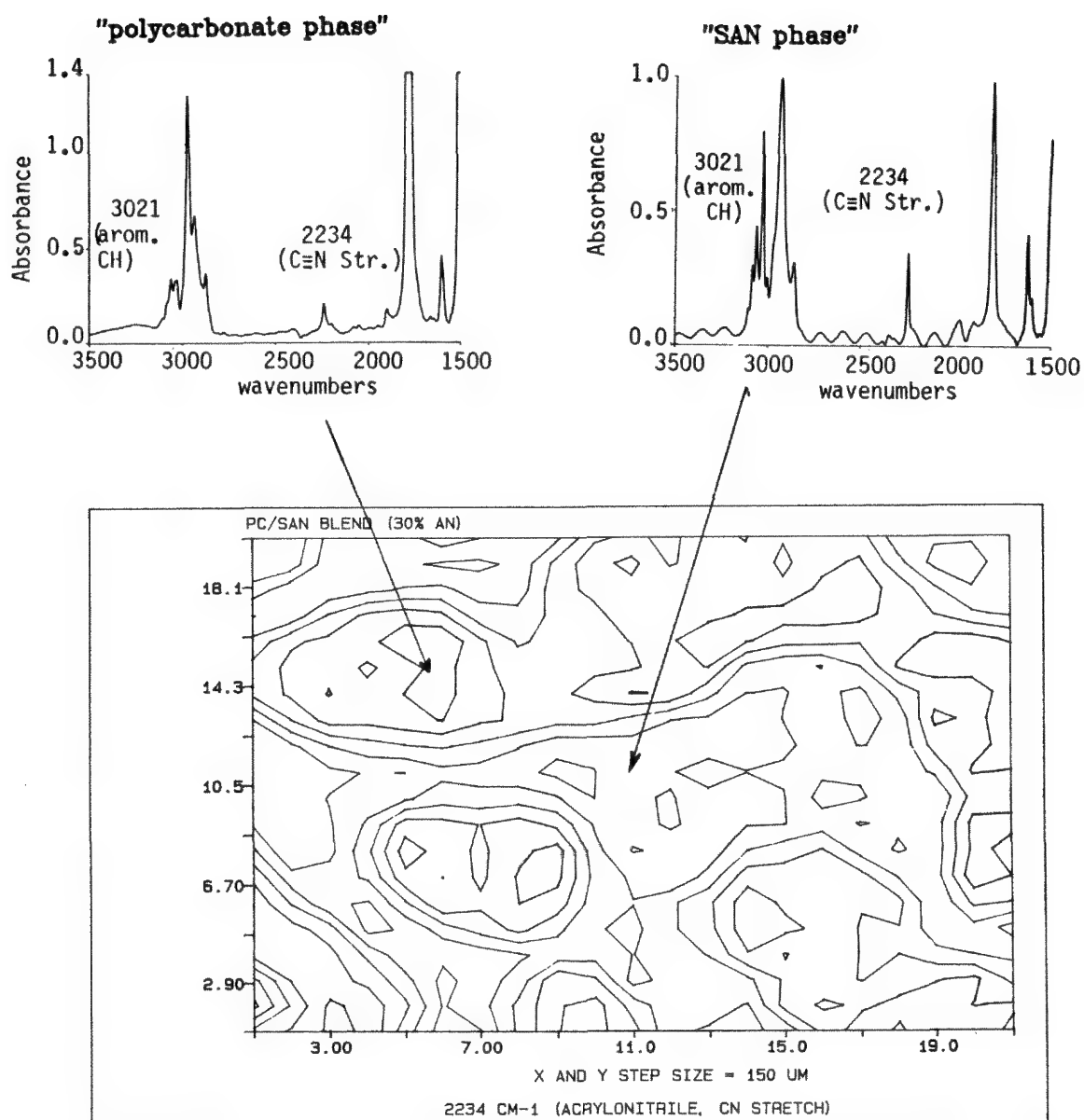


FIG. 5.--Two-dimensional functional group image based on 2234cm^{-1} absorption of a polycarbonate/SAN blend: $150 \times 150\mu\text{m}$ aperture, $150\mu\text{m}$ step size in x and y direction, 32 scans for signal averaging, 8cm^{-1} resolution.

INFRARED AND RAMAN MICROSCOPY: CRITICAL FACTORS IN SAMPLE PURITY, PREPARATION AND SIZE

A. J. Sommer and J. E. Katon

Infrared and Raman microspectroscopies have quickly gained wide acceptance in the scientific community as a result of recent technological advances, their excellent selectivity and their well-known complementarity. A comparison of each technique reveals a complementary nature not only useful for probing molecular structure but also in the more general sense of providing information when one or the other technique is restricted as a result of instrumental or sample limitations. The advantages and disadvantages of each technique in regard to macrosampling have been discussed quite extensively in the literature. In general, the same rules apply for each technique when microsampling is employed; however, there are additional considerations with regard to sample purity, sample preparation, and spatial resolution. It is the purpose of this paper to highlight these additional considerations and to demonstrate the benefits of using both techniques in a general analytical problem solving scheme.

Experimental

Transmittance infrared spectra were collected using an Analect FX-6260 refractively scanning Fourier transform infrared spectrophotometer with an Analect AQM/FXA-515 infrared microscope attachment. The microscope attachment is a fixed focus infrared microscope with a 15× (N.A. = 0.28) Cassegrainian objective. Spectra were collected at a resolution of 4 cm^{-1} and apodized by use of a Happ-Genzel function. Infrared radiation transmitted by the sample was detected with a HgCdTe liquid nitrogen cooled detector.

Raman spectra were collected with an Instruments SA U1000 double monochromator outfitted with a Nabet microscope. Raman scattering was excited with the 514.5nm output of an argon ion laser and collected 180° to the incident excitation with a 40× (N.A. = 0.75) infinity-corrected microscope objective. Laser powers at the sample were adjusted to prevent sample degradation and did not exceed 10 mW. The Raman signal was detected in single channel mode with the aid of a thermoelectrically cooled RCA 31034A photomultiplier tube. Spectra were collected at 4 cm^{-1} resolution with data points spaced every 1 cm^{-1} and integration times of 1 to 2 s.

Spectral domains were chosen to provide the most information in terms of sample identifica-

tion and common regions studied in infrared Raman spectroscopy. Sample analysis was conducted by transfer of a small portion of the sample to a potassium chloride salt plate or glass microscope slide with the aid of a stereo microscope and a fine pointed probe.

Sample Purity

Sample purity with regard to sample collection and preparation has been shown to be extremely important when microspectroscopy is used for contaminant analysis.¹⁻³ Two very common contaminants are cellulose and proteins. Figure 1 compares the infrared and Raman spectra of a 30 μm cellulose fiber sample. The infrared spectrum of cellulose exhibits major infrared absorptions located near 3344 (O-H stretch), 2901 (C-H stretch), 1430-1317 (C-H bend, CH_2 wag), 1162 (antisymmetrical bridge oxygen stretching), 1112 (antisymmetrical in phase ring stretching, and 1061-1035 cm^{-1} (C-O stretching).⁴ Prominent bands observed in the Raman spectrum are observed in the region of 300-400 cm^{-1} shift (ring torsions), 400-700 cm^{-1} shift (C-O bending and ring motions), 950-1200 (symmetric C-O and ring stretching), and 1200-1440 cm^{-1} shift (methine bending, methylene rocking and wagging, and C-O-H in plane bending).⁵ Atalla et al.⁶ has used the bands located from 200 to 600 cm^{-1} shift to determine the crystallinity of cellulose fibers.

Infrared and Raman spectra of a 35 μm skin cell (stratum corneum) are presented in Fig. 2. Characteristic infrared absorptions exhibited include the N-H stretch (3287 cm^{-1}), C-H stretch (2953, 2922, 2871, and 2850 cm^{-1}), the C=O stretch amide I (1654 cm^{-1}), the N-H deformation amide II (1541 cm^{-1}) and the CH_2 and CH_3 deformation modes (1466, 1457, 1439 and 1402 cm^{-1}).⁷ Principal Raman bands are observed at 1653 cm^{-1} (amide I), 1444 cm^{-1} (CH_2 and CH_3 bending modes), 1337 and 1295 cm^{-1} (C-H bending and possible amide III, respectively), 1121 cm^{-1} (skeletal stretch), 1061 cm^{-1} (C-N stretch), 1001 and 619 cm^{-1} (phenylalanine residue), and 957 cm^{-1} (amide III or C-C stretch of the amino acid residues).⁸

Contamination of a sample with common particulates such as skin cells and cellulose is more of a problem in infrared microspectroscopy because these materials exhibit strong infrared absorptions. Raman spectra of these particles are difficult to record due to the combined effects of their thermal instability and relatively small scattering cross sections. The infrared spectra for cellulose and the skin cell were obtained in ~2 min, whereas Raman spectra of these materials required significant signal averaging to produce the same

The authors are at the Molecular Microspectroscopy Laboratory, Department of Chemistry, Miami University, Oxford, OH 45056.

signal-to-noise level. Data collection times for the Raman spectra of cellulose sample and skin sample were 4 and 8 h, respectively.

One contaminant often detected by Raman spectroscopy is amorphous carbon. It is characterized by Raman bands located at 1350 and 1600 cm^{-1} shift. An earlier study conducted by Wada and Solin⁹ has demonstrated that Raman spectra of carbon arise from a 500Å-thick layer and as such the Raman technique is extremely sensitive for the detection of carbon contaminants. This material has no infrared spectrum; thus, Raman spectroscopy is suitable for its identification.

Care must be taken to insure that equipment used during sample manipulation is clean and free of contaminants. One example of contaminating the sample during sample preparation was experienced in the use of so-called pre-cleaned microscope slides. Observation of the slides in reflected light showed the presence of a thin white film. The film was removed with a razor blade and transferred to a KCl salt plate with a fine pointed probe. Subsequent infrared microanalysis of the resultant 25 μm -diameter sample yielded the spectrum shown in Fig. 3. Infrared absorptions observed in this spectrum are characteristic of a mixture of silica (1098 and 839 cm^{-1}), calcium

carbonate (1454 and 872 cm^{-1}) and a formate salt (2958, 2927, 2834, 2716, 1607, and 1366 cm^{-1}). The band at 1098 cm^{-1} could be due to a phosphate or sulfate moiety but a Raman spectrum of the same material (Fig. 3) exhibited bands arising only from the formate salt, calcium carbonate (1087 cm^{-1}), and an unidentified band at 920 cm^{-1} . Since phosphates and sulfates exhibit relatively strong Raman signatures in the 940-1025 cm^{-1} shift region, their absence indicates that the infrared absorption at 1098 cm^{-1} is in all likelihood a result of silica. The presence of silica and calcium carbonate can be explained from the manufacturing process and cleaning of the slides with hard water, respectively; however, the source of the formate salt is still unknown and under investigation.

One further point to be made regarding sample purity concerns the sample itself. With the aid of microspectroscopy, we are analyzing an amount of sample that can be statistically nonrepresentative of the sample as a whole. For samples large compared to the amount analyzed, multiple samplings should be conducted to insure that the spectra obtained are truly representative of the sample.

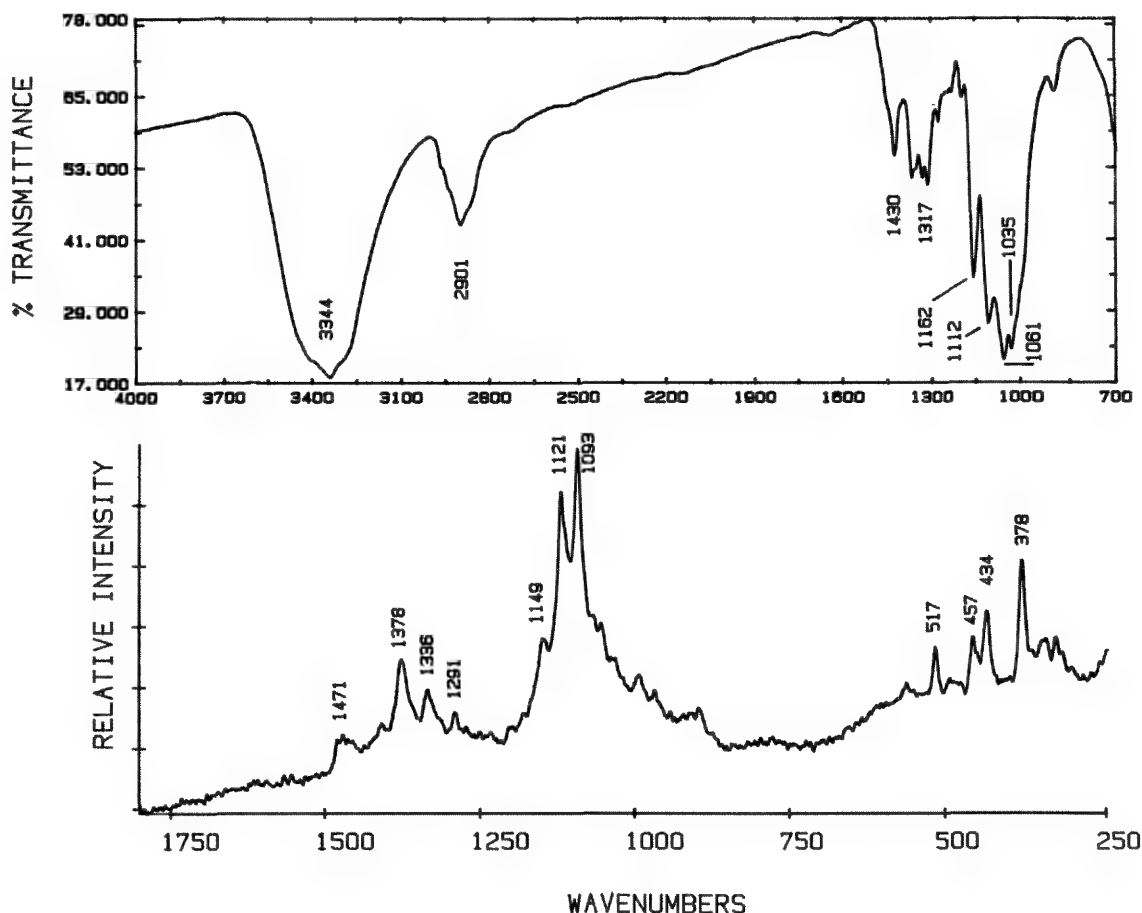


FIG. 1.--Infrared spectrum of cellulose fiber (top, 2min collection time) and Raman spectrum of same fiber (bottom, 4h collection time).

Sample Preparation

The advent of infrared and Raman microspectroscopy has drastically reduced the time needed to prepare a given sample. Many samples can be prepared "neat" and loaded onto a single salt plate or microscope slide for subsequent analysis. In Raman microspectroscopy the sample is usually brought into focus beneath the microscope with only the z-axis adjustment and little if any sample preparation is required. This single adjustment is in stark contrast to the many adjustments needed for a conventional 90° scattering macrosampling conformation. Slight sample manipulation may improve the quality of spectra recorded, especially for powdered samples. Figure 4 demonstrates the result of compacting powdered zinc oxide in comparison to direct analysis. The integrated band intensity of the transverse optic lattice vibration for zinc oxide at 435 cm^{-1} shift for the compacted sample is approximately 17 times the integrated intensity of the sample analyzed without compacting. This method works equally well for the infrared. Using a rounded probe one can exert enough pressure on a powder sample to recrystallize it into a transparent particle or pellet, thereby reducing the scattering (diffracting) nature of the sample.

Sample preparation for transmission infrared microanalysis revolves around the need for a sample to be transmitting and of proper path length. The sample path length can be adjusted by flattening the sample with a rounded probe or, if the sample has memory, the use of a diamond anvil cell. Although flattening the sample with a rounded probe or diamond anvil cell is relatively straightforward, it does introduce another step in sample preparation. In contrast the Raman experiment can be conducted merely by focusing the sample beneath the microscope.

An example that demonstrates the strengths of both techniques involved matching two paint chips from a boating accident. Observation of these chips under a stereo microscope showed that each chip consisted of two different areas. The first area was a brown transparent material; the second, a faded blue material. The chips were flattened on a KCl salt plate and analyzed via infrared microspectroscopy. No infrared spectra could be obtained on the blue areas due to the opacity of this material. The transparent material yielded the spectrum shown in Fig. 5 and exhibited infrared absorptions characteristic of a melamine/acrylate paint lacquer.

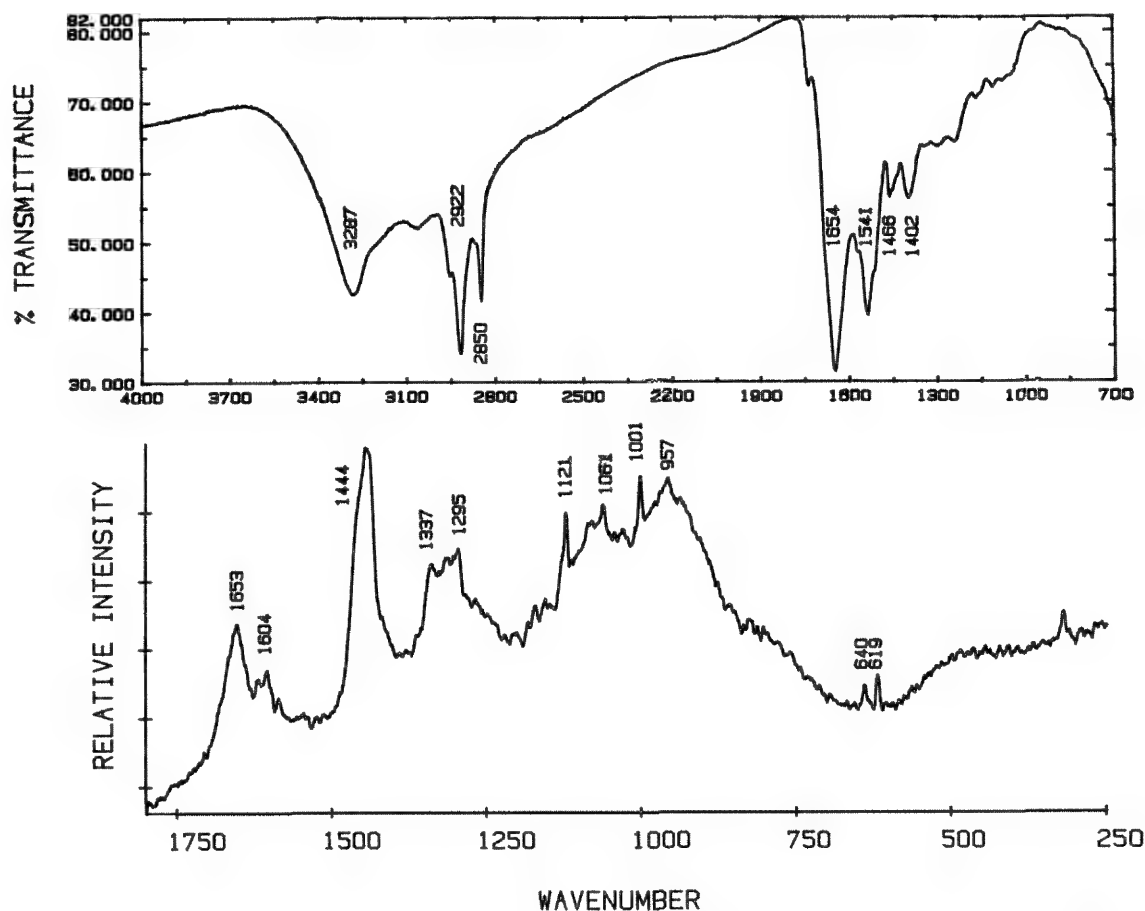


FIG. 2.--Infrared spectrum of skin cell from stratum corneum (top, 2 min collection time) and Raman spectrum of same cell (bottom, 8 h collection time).

Absorptions characteristic of the acrylate moiety are observed at 1731 cm^{-1} (C=O stretch), 1462 cm^{-1} (C-H bending), and 1240 and 1149 cm^{-1} (C-O-C stretch). Melamine is a primary amine that exhibits two N-H stretching vibrations located at 3451 and 3378 cm^{-1} , as well as the NH_2 deformation band at 1589 cm^{-1} . Analysis of the blue areas with Raman microspectroscopy produced the spectrum shown in Fig. 5. Raman transitions in this spectrum are characteristic of a mixture of copper phthalocyanine pigment and the rutile form of titanium dioxide. Titanium dioxide bands are observed at 408 and as the shoulder at 608 cm^{-1} shift. The remaining bands are characteristic of the copper phthalocyanine pigment, with some of the more prominent bands arising from the $\text{C}\beta\text{-C}\beta$ and $\text{C}\alpha\text{-C}\beta$ stretches of the pyrrole rings (1526 and 1340 cm^{-1} shift, respectively), breathing stretching vibrations of the pyrrole groups (1141 cm^{-1} shift), breathing mode of the sixteen member inner ring (678 cm^{-1} shift) and deformation mode of the isoindole ring (592 cm^{-1} shift).¹⁰

Similar analysis of the second paint chip yielded identical spectra. This example demonstrates very nicely the advantage of employing both techniques to gain as much information as possible for a given sample.

Spatial Resolution

Spatial resolution in the x-y plane is fundamentally limited by the diffraction of light employed in either technique. The diffraction limited illumination diameter D can be estimated from $D = 1.22\lambda/\text{N.A.}$, where λ is the light wavelength and N.A. is the numerical aperture of the focusing and or collecting element.¹¹ For infrared microspectroscopy, a wide range of wavelengths is employed for sample analysis. Thus the diffraction-limited sample size is determined by the lowest wave-number (longest wavelength) observed in a given spectrum. A typical spectrum ranging from 4000 to 700 cm^{-1} is diffraction limited to a sample area whose diameter is approximately $27\text{ }\mu\text{m}$ with an objective N.A. = 0.65 . It can be easily seen that the sample diameter increases as one goes to the far infrared. The diffraction-limited sample diameter for the Raman experiment with conventional $0.5145\text{ }\mu\text{m}$ excitation and the same numerical aperture is about $1\text{ }\mu\text{m}$.

In practice sample sizes down to $5\text{-}6\text{ }\mu\text{m}$ in diameter can be analyzed with infrared microspectroscopy; however, the spectra exhibit artifacts due to diffraction. Diffraction of

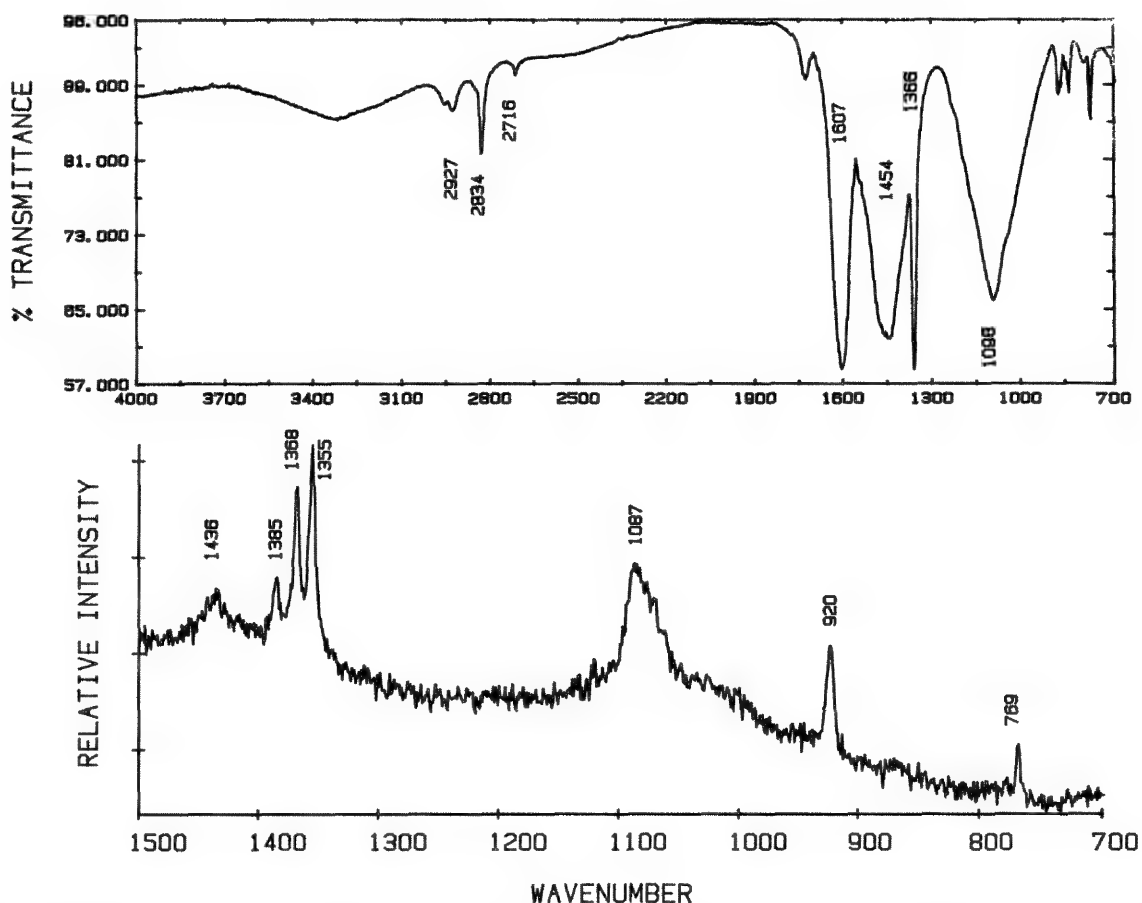


FIG. 3.--Infrared (top) and Raman (bottom) spectra of thin-film contaminant removed from pre-cleaned microscope slide.

light by the sample usually manifests itself in the infrared spectrum as a sloping baseline rising toward lower wavenumbers (longer wavelength). The quantitative effect of diffraction is a loss of photometric accuracy since light bends around the sample (diffracts) and dilutes the spectrum.^{12,13} The effects of diffraction for small continuous samples can be effectively removed by redundant aperturing.¹³ For powdered materials this problem of diffraction still exists and is more pronounced for materials such as pigments. In these cases many diffracting particles are present in the field of view of the microscope and redundant aperturing is of little help. Figure 4 shows the spectrum of methylene violet obtained from the material as spread on the slide and a spectrum of the same material diluted with KBr and pressed into a micropellet with a rounded probe. The spectrum of the neat material exhibits both severe diffraction and infrared absorptions whose relative intensities are not representative of the sample. Dilution of the pigment with KBr serves to reduce the diffraction effects by reducing the sample concentration thereby yielding a truly representative spectrum. Interference fringes from the relatively thin micropellet are also observed.

Another example which serves to demonstrate several aspects of the complementary nature of infrared and Raman spectroscopy is a four-layer polymer laminate presently used for food containers. A cross section of the laminate was made with the use of a razor blade. The spatial resolution afforded by the Raman microprobe, and the fact that a transmitting sample is not required, enabled spectra to be recorded without further manipulation of the sample. Figure 6 illustrates Raman spectra recorded on the first (300 μ m thick) and third (25 μ m thick) layers of the laminate. The identity of the first, second, and fourth layers was easily recognized as isotactic polypropylene. The fluorescent background observed in the Raman spectrum of the third layer prevents a conclusive identification. The identity of this third layer was determined to be polyvinyl alcohol from an infrared spectrum presented in Fig. 6, but only after significant sample manipulation to obtain the desired pathlength.

The application of molecular microspectroscopy to the identification of fibers serves to illustrate a number of the salient features of infrared and Raman spectroscopic strengths and weaknesses. Although optical microscopic tech-

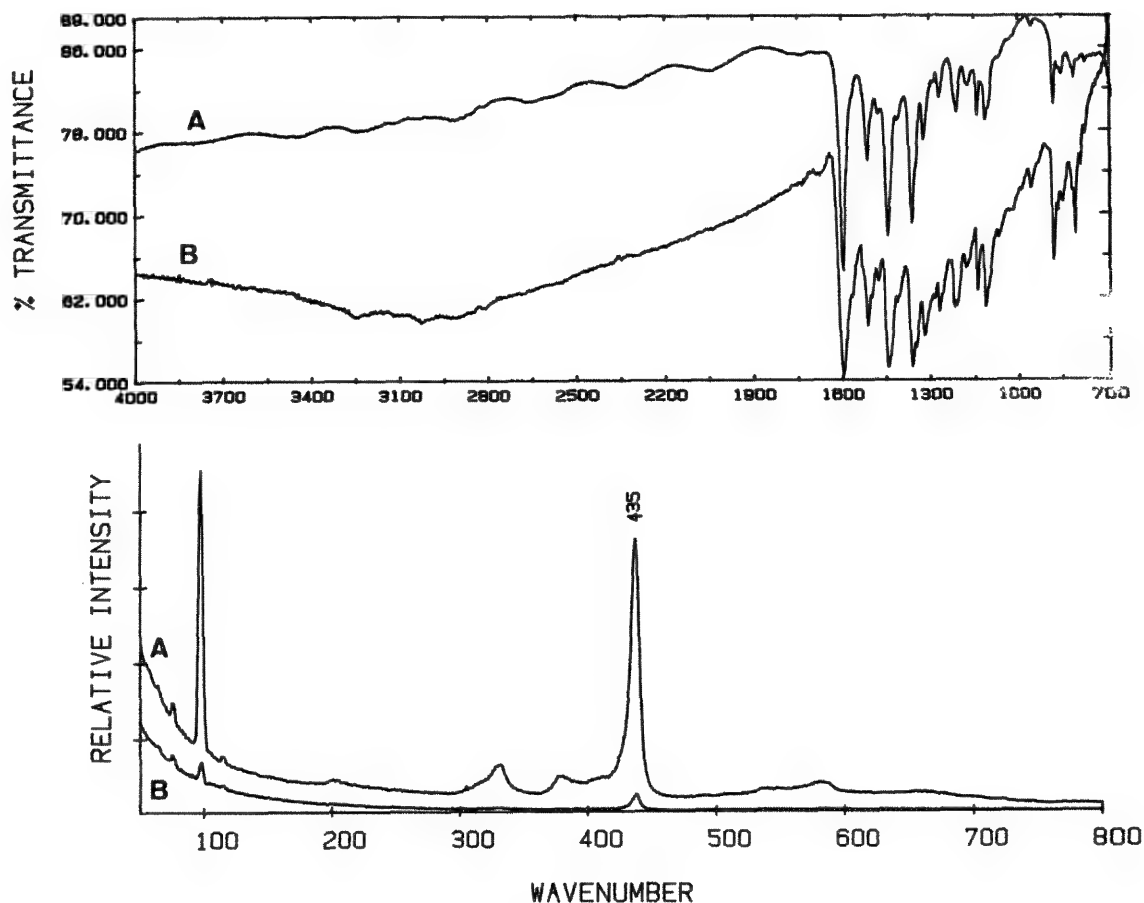


FIG. 4.--Top: Infrared spectra of methylene violet pressed into KBr micropellet (A) and "neat" (B). Bottom: Raman spectra of zinc oxide powder compacted (A) and "neat" (B).

niques for the identification of most fibers are well known, and in some cases quite accurate and efficient, they cannot match infrared microspectroscopy in terms of speed and power. These advantages are particularly true with regard to synthetic fibers since simple visual observation seldom allows identification as is often the case with natural fibers.

In addition to the path-length problems associated with infrared microspectroscopy, the cross-sectional form of the synthetic fiber may also affect the resultant spectrum. Most synthetic fibers are extruded and, as a result, exhibit a nearly cylindrical shape.¹⁴ The exact shape depends on the shape of the orifices in the spinnerette but the cylindrical shape is most common. The fiber and its shape behave as a lens to the focused infrared radiation and tend to defocus the beam.¹⁴ The end result is a loss of signal-to-noise due to the energy lost by this defocusing mechanism. This problem may be ameliorated by flattening the fiber. In doing so both the path length and sample lensing problems are avoided.

Many fibers behave as mixtures since they are chemically treated in various ways. For instance, cotton is treated with polyurethane to improve the fiber's wrinkle recovery properties.¹⁴ Such a treatment can be readily detected from the infrared spectrum of a single

fiber. Dyeing processes often result in structural changes within the fiber material and these too may be detected with infrared microspectroscopy. Although dyes are readily observed directly with the naked eye, their presence is difficult to detect with infrared spectroscopy due to the amount of material present on the fiber. Molecular structure information of the fiber obtained with infrared is complemented by Raman spectroscopy in that infrared spectroscopy is useful for the study of polymer side chains, whereas Raman spectroscopy is more informative of the backbone structure. In some cases the extreme differences in spectral intensity observed renders one form of spectroscopy completely unsuitable for the identification of a fiber and the other is very good. Two examples are glass fibers and silicon carbide fibers. The Raman spectrum of the glass fibers is extremely weak; the infrared spectrum is quite strong.¹⁴ Exactly the reverse situation occurs with silicon carbide fibers. Raman may also be useful to detect additives to synthetic fibers, especially if they are inorganic. The presence of titanium dioxide on synthetic fibers, often added as a delustering agent, can easily be detected via Raman microspectroscopy.

A somewhat more unique fiber application of Raman microspectroscopy is provided by the

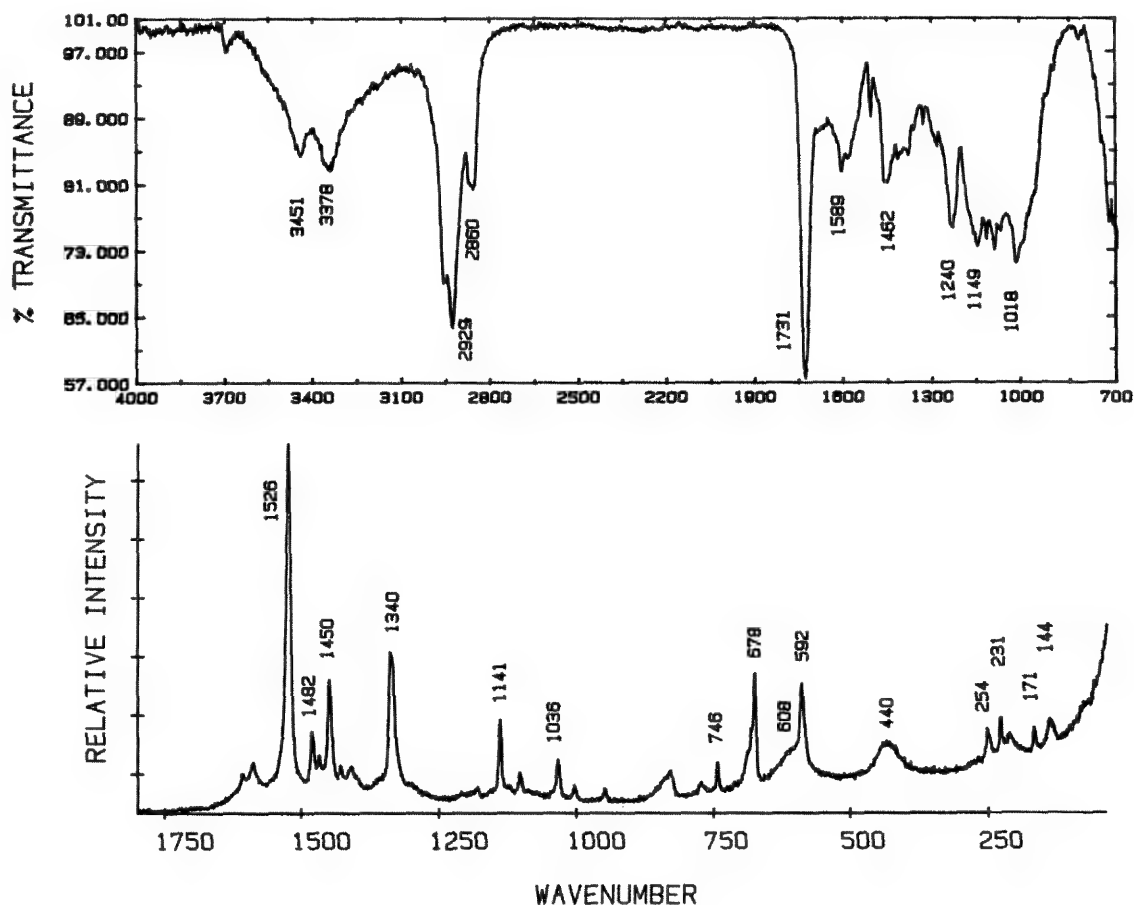


FIG. 5.--Infrared (top) and Raman (bottom) spectra of paint chips from boating accident.

differentiation of Dacron 64 from the standard Dacron 54.¹⁵ Dacron 64 differs from the standard type in that approximately 2% of the terephthalic acid groups have been replaced by other diacid molecules (e.g., sulfoisophthalic acid). This replacement makes the material more compatible to basic dyestuffs but also distorts the polymer chain and in doing so decreases the crystallinity of the polymer chain. One cannot observe the compositional changes directly by either infrared or Raman spectroscopy in a simple manner. However, one can detect differences in crystallinity by measuring the half-width of the Raman carbonyl stretching band observed at 1721 cm^{-1} . Measured half-widths for Dacron 63 and Dacron 52 are 20.1 ± 0.2 and $18.6 \pm 0.2\text{ cm}^{-1}$, respectively.

Conclusion

The examples presented in this study demonstrate the benefits of using both infrared and Raman microspectroscopy in a general analytical problem-solving scheme. In most cases, the success is not limited by instrumental constraints but by the ability to develop sampling methods for presentation of the sample to the

instruments. This problem is at present more pronounced with infrared microspectroscopy. Shortcomings of each technique include sample preparation and spatial resolution for infrared microspectroscopy and fluorescence for Raman microspectroscopy. However, these problems are currently being addressed. Infrared ultra-microspectroscopy may ultimately push spatial resolution below the diffraction limit of infrared light.¹³ The fluorescence problem in Raman spectroscopy has already been solved for macrosamples¹⁶ and it is just a matter of time before FT-Raman microspectroscopy is developed. These developments will probably help to solve the deficiencies of each technique, but there is no equal to using both techniques as complements to one another.

References

1. P. Lang and J. E. Katon, *Microbeam Analysis--1986*, 47.
2. P. Lang, J. E. Katon, A. S. Bonanno and G. E. Pacey, in R. Messerschmidt and M. Harthcock, Eds., *Infrared Microspectroscopy: Theory and Applications*, New York: Marcel Dekker, 1988, 39.
3. P. Lang and J. E. Katon, *Appl.*

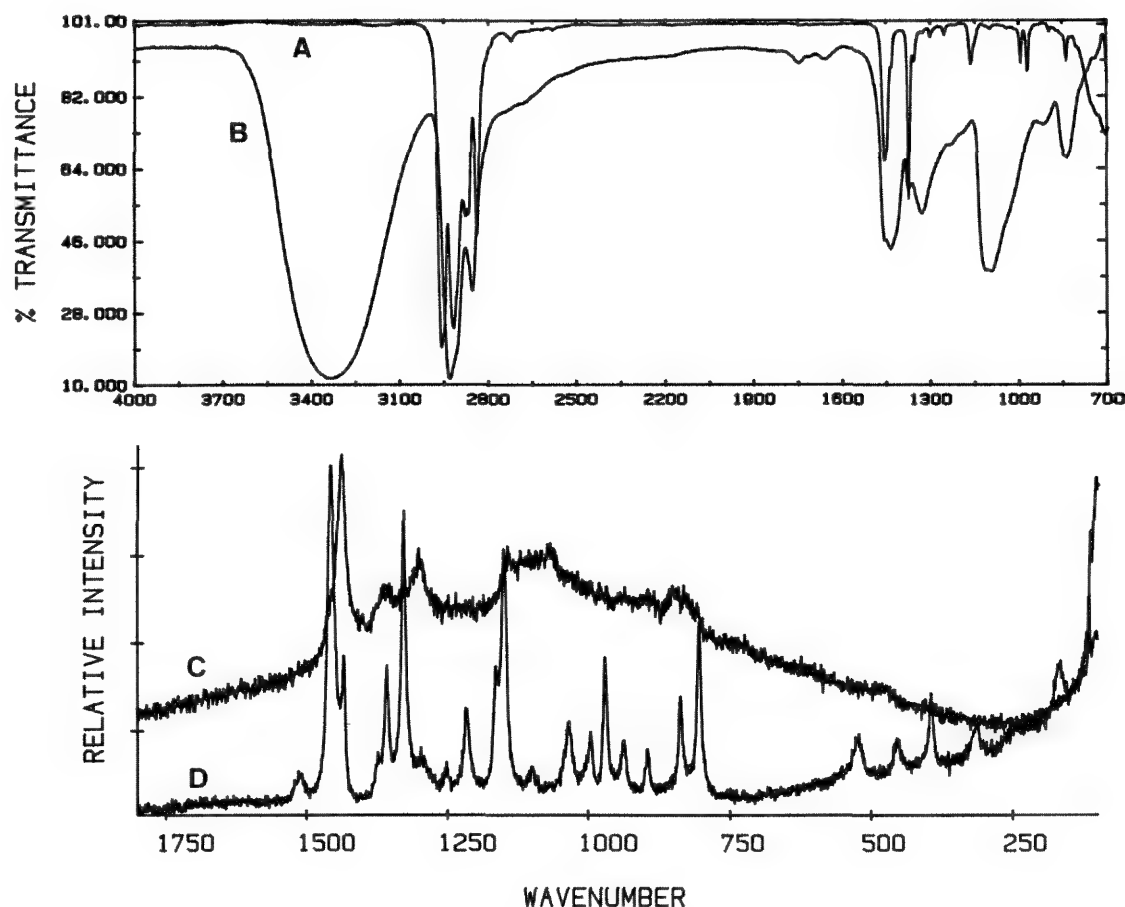


FIG. 6.--Top: Infrared spectra of first 300μm layer (A) and third 25μm layer (B) of polymer laminate. Bottom: Raman spectra of third 25μm layer (C) and first 300μm layer (D) of polymer laminate.

- Spectrosc.* 42: 313, 1988.
4. B. L. Browning, Eds., *Chemistry of Wood*, New York: Krieger, 1975, 130-131.
 5. R. H. Atalla, *J. Wood Chemistry and Technology* 7: 115, 1987.
 6. R. H. Atalla, C. P. Woitkovich, and V. C. Setterholm, *Tappi J.* 68: 116, 1985.
 7. R. P. Oertel, *Biopolymers* 16: 2329, 1977.
 8. F. S. Parker, Ed., *Applications of Infrared, Raman and Resonance Raman Spectroscopy in Biochemistry*, New York: Plenum Press, 1983, 103.
 9. N. Wada and S. A. Solin, *Physica* 105B: 353, 1981.
 10. C. Jennings, R. Aroca, A. Hor, and R. O. Loutfy, *J. Raman Spectroscopy* 15: 34, 1984.
 11. G. J. Rosasco, "Raman microprobe spectroscopy," in R. J. H. Clark and R. E. Hester, Eds., *Advances in Infrared and Raman Spectroscopy*, London: Heydon 7: 223, 1980.
 12. V. J. Coates, A. Offner, and E. H. Siegler Jr., *J. Opt. Soc. Amer.* 43: 984, 1953.
 13. R. G. Messerschmidt in P. B. Roush, Ed., *The Design, Sample Handling, and Applications of Infrared Microscopes*, ASTM STP 949, Philadelphia: ASTM, 1984, 12.
 14. P. Lang, J. E. Katon, J. F. O'Keefe, and D. W. Schiering, *Microchemical J.* 34: 319, 1986.
 15. P. Lang, *Application of Infrared and Raman Microspectroscopy and the Vibrational Spectra: Structure and Conformational Behavior of Dimethyl Dicarbonate*, Ph.D. Thesis, Miami University, 1987.
 16. T. Hirschfeld and B. Chase, *Appl. Spectrosc.* 40: 133, 1986.

FT-IR MICROSCOPY OF BIOLOGICAL SAMPLES: A NEW TECHNIQUE FOR PROBING CELLS

R. G. Messerschmidt and J. A. Reffner

The need for structural information about biological materials cannot be questioned. Yet for years the most selective probe of molecular structure, the infrared spectrum, has been left out of the biological researchers' arsenal. Light spectroscopies, except when used to measure relative concentrations or kinetics, have been applied by only a handful of researchers. Light spectroscopy in the infrared has been applied by an even smaller handful. We feel that the technique of infrared microspectroscopy using a microscope provides an ideal sampling apparatus for several fields of biological research.

For the purpose of this discussion, we must first outline the instrumentation. The modern apparatus used to obtain an infrared spectrum is the Fourier-transform infrared spectrophotometer. This type of instrument does not disperse wavelengths in space, as would be done in a grating or a prism spectrometer. Instead, the wavelength information is encoded in time, through the use of an interferometer. This type of instrument provides three advantages over the dispersive type. These are known classically as the Jacquinot or throughput advantage, the Fellgett or multiplex advantage, and Connes's advantage.

The first relates to the fact that the interferometric instrument uses no slits, as a dispersive instrument must. Instead, resolution is determined by the distance the moving mirror travels in the interferometer. However, in order to allow long travel and concomitant high resolution, the divergence of the beam must be limited. That limits throughput also, but can be overcome by an increase in the clear aperture of the interferometer. The throughput advantage of an interferometric system varies from several hundred-fold to almost nothing, depending on the spectral resolution.

The Fellgett or multiplex advantage results from the fact that the interferometer is effectively measuring all wavelengths simultaneously, instead of discretely as in a monochromator. This advantage is proportional to the square root of the number of resolution elements. For the mid-infrared spectrum, collected at 2cm^{-1} resolution, there are roughly 2000 resolution elements, leading to a 45-fold advantage. The Connes's advantage is one of wavelength precision, and does not directly influence the signal-to-noise ratio. In practice, FT-IR spectrometers tend to outperform dispersive types by several orders of magnitude. In addition, they are more rugged, containing

fewer moving parts, and do not cost much more.

The infrared microscope apparatus actually originated many years before the FT-IR instrumentation; the first units were developed in the late 1940s. Moreover, biological applications were very much one of the driving forces for the development of the infrared microscope apparatus. A large percentage of the papers published in the late 1940s and early 1950s involved biological applications, from the study of small crystals to the spectral imaging of normal and diseased tissue sections.¹⁻³ The infrared microspectrometers of three decades ago did not stand the test of time. We can find references in the literature through about 1957, and the only commercially produced instrument, the Perkin-Elmer Model 18, was not produced after the late 1950s, for various reasons--not the least of which may have been imperfect communication. In addition, the apparatus was less sensitive than today's apparatus by at least an order of magnitude and probably two, which would have precluded many of the later experiments that have so greatly contributed to the success of the technique. For example, the attainment of the spectrum of a single red blood cell (as reported on below) would not have been possible in the 1950s.

The infrared microscope apparatus has also changed in several significant ways since the 1950s. The current apparatus is as much a visible microscope as it is an infrared microscope. This feature grows more important as the spatial resolution limit is stretched. In an FT-IR microscope, the specimen is placed on a movable stage and examined under white light. The area of the specimen requiring interrogation must be clearly visible in white light. Features such as crossed polarizers and dark-field illumination have increased the utility of the instrumentation. Once the analyte has been located and placed at the center of the field of view, apertures are used at remote images of the specimen to delineate the area of the specimen that we wish to sample. This is another area in which the current instrumentation has improved. A modern FT-IR microscope places remote apertures both above and below the specimen in image planes. This advance, known as dual remote image masking or Redundant Aperturing[™] is based on theory which shows that the spatial resolution is improved by dual masking,⁴ partly due to a modification of the diffraction pattern arising from the optical system, but more particularly from the high contrast edges used to delineate the specimen. The net result is that when we are measuring the spectrum of objects of a size near the diffraction limit, Redundant Aper-

The authors are with Spectra-Tech, Inc. 652 Glenbrook Road, Stamford, CT 06906.

turing, we can measure a pure spectrum from parts of a sample as small as 10-50 μm , depending on the wavelength, and if the specimen is not near any spectral interferences, we can obtain a qualitative result from specimens as small as 5 μm . Through the use of spatial mapping and other techniques, it may even be possible to attain the elusive 1 μm resolution. Mapping techniques use the redundant information present in successively collected spectra to enhance spatial resolution mathematically.

As stated earlier, the interest in biological infrared microspectroscopy dates back almost four decades. Even then researchers were able to detect characteristic patterns that differentiated tissue sections from various body organs. They also noted that the pattern of these organs correlated across species.⁵ That is, dog lung looks like rabbit lung, and dog liver looks like rabbit liver, but dog liver does not look like dog lung, etc. This work was of course done without computer methods, and at very low spectral resolution. The tools available to the spectroscopist today will allow the furthering of this work.

Experimental

One of the more immediate applications of FT-IR microscopy is in identifying crystals and other spurious inclusions in animal tissue. We have looked at the talc particles in the lungs of a victim of a drug-related murder. The victim, an intravenous drug user and drug dealer, was given or sold a dose of heroin loaded with talc. The collection of these talc particles in his lungs caused his death by asphyxiation. Under crossed polarizers, the talc particles were clearly visible in the microtomed lung sections, and the spectrum confirmed it. This is an important point. The infrared spectrum, though complicated, provides true molecular information about the specimen. In other experiments, we have measured crystals in rat organs that arose from massive dosing of the animal. This test would be commonly done by pharmaceutical companies to determine whether a new drug was accumulating in any of the animals' organs. The detection method is normally a radioassay, a time-consuming procedure. In addition, the drug must be radioactively labeled, which could alter its effect.

The usefulness of infrared microspectroscopy has been fully appreciated by the forensic scientist. In this field, the FT-IR microscope is widely used. Fibers and traces of drugs are now routinely screened with infrared. Blood stains, human hair identification, and car paint flecks are all handled now with the FT-IR microscope. In another study, we have recently obtained spectra of single cheek (mouth) epithelial cells (Fig. 1).

Biomaterials are an increasingly important research area. As transplant techniques and heart bypasses become widely accepted, the success rate is also increasing. The understanding of the requirements for biocompatibility has been important to this achievement. The cross section of the bond between an artery and

an artificial graft may be probed with the FT-IR microscope. Contact lenses may also be studied to minimize the formation of protein deposits.

We have also recently obtained infrared spectra from single red blood cells.⁶ The infrared spectrum of blood is the special interest of our collaborator in this work, who has published numerous papers reporting on his research.⁷⁻⁹ Figure 2 shows the infrared spectrum obtained from a single red blood cell. The significance of this result is that it is now possible to research blood chemistry on extremely small quantities of blood, and study single cells in a living state. The cells are diluted in saline solution and placed between barium fluoride windows. The windows are pressed together in a sample compression device so that a very thin layer of liquid remains above or below a single red blood cell, which is 7 μm in diameter. Infusion of gases into the cell is also possible, by drilling holes into the top window and plumbing with plastic tubing. The experimental conditions are described below.

Spectra were obtained with a Spectra-Tech (Stamford, Conn.) IR-plan[™] infrared microscope mounted on a Perkin-Elmer (Ridgefield, Conn.) Model 1800 FT-IR spectrometer. The spectrometer was equipped with a glowing wire source and potassium bromide (KBr) beam splitter. The microscope was fitted with a narrow bandwidth mercury cadmium telluride (MCT) detector with a sensitive area of $0.25 \times 0.25 \text{ mm}$. The microscope was equipped with a 15 \times magnification, NA = 0.58 Replachromat[™] objective and a 10 \times , NA = 0.71 Replachromat condenser for visual and infrared use. Also available were 4 \times and 10 \times glass objectives for visual use only.

All spectra presented here were collected at 8 cm^{-1} spectral resolution. Measurement times were between 30 s and 4 min depending on the measured area. The 4min data collection resulted from the co-addition of 1000 double-sided interferograms at one level of zero filing. No additional smoothing of the data was performed. All samples were analyzed at room temperature. Samples were mounted on the sample stage of the microscope in physiological saline between two barium fluoride (BaF_2) windows, 13 mm in diameter and 0.5 mm thick. The objective and condenser were adjusted to compensate for the spherical aberration introduced by the windows, by means of a Sample Compensator[™] adjustment which is part of the Replachromat lenses. The area of interest was delineated by use of either single or dual remote image masking by means of apertures with four independent and rectilinear knife-edge blades.

These and other studies are examples of how the FT-IR microscope can aid the biological researcher. The authors expect that this will be an important tool for researchers in the near future.

References

1. R. Barer, A. R. H. Cole, and H. W. Thompson, "Infrared spectroscopy with the reflecting microscope in physics, chemistry, and biology," *Nature* 163: 198-201, 1949.
2. R. C. Gore, "Infrared spectrometry of small samples with the reflecting microscope," *Science* 110: 710-711, 1949.
3. E. R. Blout, G. R. Bird, and D. S. Grey, "Infra-red microspectroscopy," *J. Opt. Soc. Amer.* 40: 304-313, 1950.
4. R. G. Messerschmidt, "Minimizing optical non-linearities in infrared microspectrometry," in R. G. Messerschmidt and M. A. Harthcock, Eds., *Infrared Microspectroscopy: Theory and Applications*, New York: Marcel Dekker, 1988.
5. H. P. Schwarz et al., "Infrared spectroscopy of tissues: Effect of insulin shock," *Proc. Soc. Exp. Biol. and Med.* 76: 1951.
6. A. Dong, R. G. Messerschmidt, J. A. Reffner, and W. S. Caughey, *FASEB J.* (in press).
7. W. T. Potter, R. A. Houtchens, and W. S. Caughey, "Crystalization-induced changes in protein structure observed by infrared spectroscopy of carbon monoxide liganded to human hemoglobins A and Zurich," *J. Am. Chem. Soc.* 107: 3350-3352, 1985.
8. W. S. Caughey, in D. W. Darnell and R. G. Wilkins, Eds., *Methods for Determining Metal Ion Environments in Proteins: Structure and Function of Metalloproteins*, New York: Elsevier, 1980, 95-115.
9. M. W. Makinen, R. A. Houtchens, and W. S. Caughey, *Proc. Natl. Acad. Sci. U.S.A.* 76: 6042-6046, 1979.

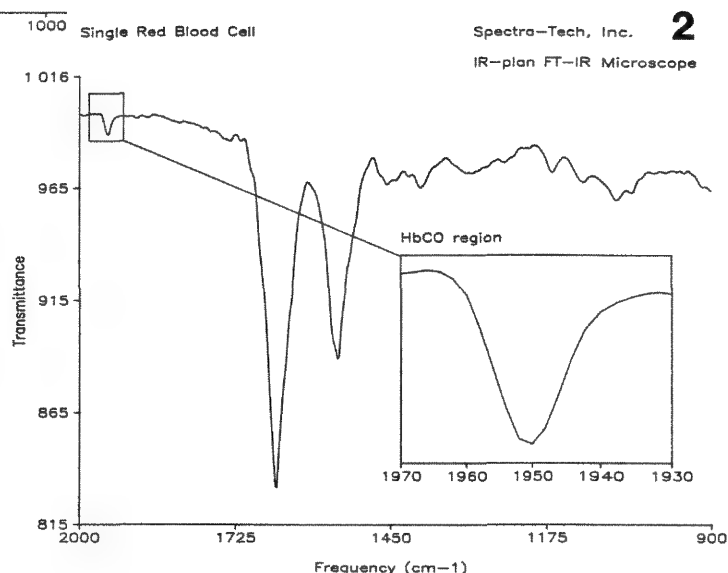
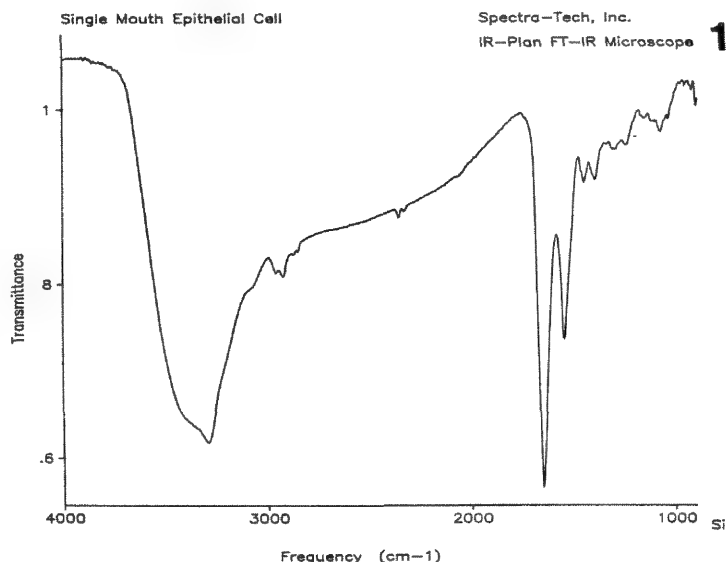


FIG. 1.--Infrared spectrum of single mouth epithelial cell. Cell smear was placed on barium fluoride window and allowed to dry. A single cell was masked down by use of dual remote image masks; 8cm^{-1} resolution spectrum was collected in 2 min of measurement time.

FIG. 2.--Infrared spectrum of single human red blood cell in solution at room temperature. Absorption band envelope with its maximum near 1950 cm^{-1} is due to carbon monoxide bound to the α and β subunits of the tetrameric hemoglobin protein complex. This 8cm^{-1} resolution spectrum was collected in 4 min of measurement time by use of an IR-Plan FT-IR microscope attached to Perkin-Elmer 1800 FT-IR spectrometer.

NONDESTRUCTIVE ANALYSIS OF ART AND ARCHAEOLOGICAL OBJECTS BY INFRARED MICROSCOPY

M. T. Baker and D. W. Von Endt

Many analytical methods are considered to be "nondestructive" because, when the analysis is completed, the sample can be recovered for more testing. However, when the article under study is an art or historical object, any technique that requires removal of a sample, however small, is "destructive." It is a common challenge in the field of conservation science to characterize and identify a coating or a pigment of an art object without disturbing it. The Fourier transform infrared (FT-IR) microspectrometer enables us to perform these studies without the removal of a sample in some cases, and allows the most discrete of sample taking when necessary. Examples of studies done at the Smithsonian Institution's Conservation Analytical Laboratory (CAL) with the FT-IR microscope follow, with a discussion of some especially difficult samples and future plans for their solutions.

Experimental

A Mattson Cygnus 100 FT-IR spectrometer was used with a Spectra-Tech IR-PLAN infrared microscope. (Most of the measurements on these art objects are made in the reflectance mode of the microscope. Where the analytical sample permits—for example on isolated fibers, thin sections, etc.—the specimens are analyzed by transmittance measurements. All spectra shown here are plotted linear in reflectance.)

The authors are with the Conservation Analytical Laboratory of the Smithsonian Institution, Washington, DC 20560.

The metal fittings and lacquered pieces came from the Arthur M. Sackler Gallery, Smithsonian Institution, and the Japanese botanical illustration was supplied by the paper conservator at CAL. The wool and cotton fibers are reference samples obtained from Test Fabrics, and the dried paint films were supplied by personnel at CAL.

Figure 1 shows the procedure for analysis of large objects by way of the side port of the microscope. The conservator is holding a Japanese lacquered piece from the 17th or 18th century. Clamping is undesirable in such cases, and the object is supported by cushioned blocks of wood and steadied with a gloved hand. Scan times are kept low in such cases, since vibrations and settling of the piece during scanning can cause anomalies in the spectrum.

Results and Discussion

Very good spectra have been obtained of clear coatings on a shiny metal surface. The coatings on the metal fittings shown in Fig. 2 were analyzed by reflectance; the original coating appears to have been shellac, as shown in Fig. 3, and the newer coating on the recently treated piece was identified as methacrylate resin (Incralac), as shown in Fig. 4. Because of the design of the pieces, the surfaces available for analysis were less than 1 mm².

Clear coatings over nonreflective substrates were more difficult to analyze. Figure 5 shows the spectra of three varnishes (B-72,



FIG. 1.--Japanese lacquered piece held for FT-IR microspectroscopic analysis.

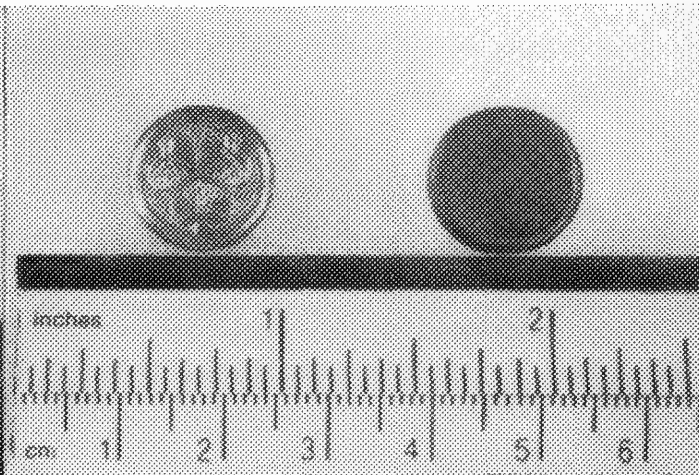


FIG. 2.--Metal fittings from lacquered piece; original on right, cleaned and treated on left.

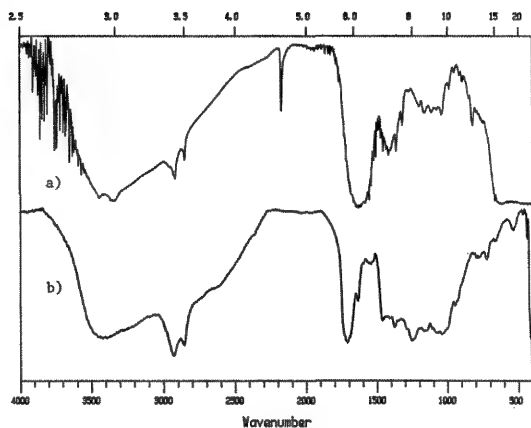


FIG. 3.--Spectra of (a) original coating on metal fitting, (b) new shellac.

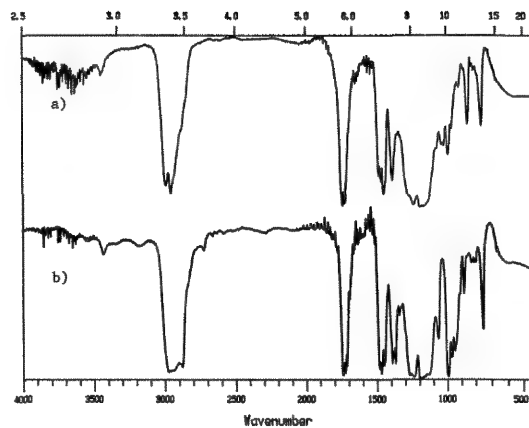


FIG. 4.--Spectra of (a) new coating on cleaned fitting, (b) Incralac.

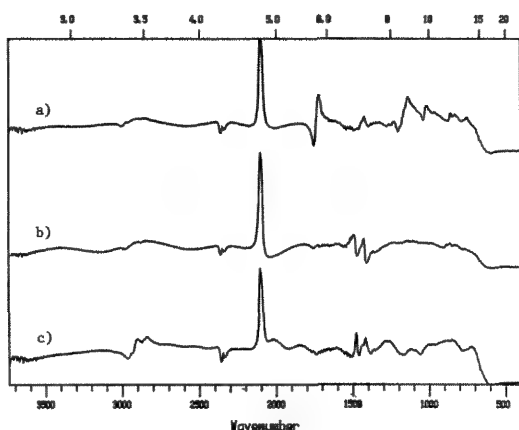


FIG. 5. Spectra of varnishes on Prussian Blue paint: (a) B-72, (b) MS2A, (c) dammar.

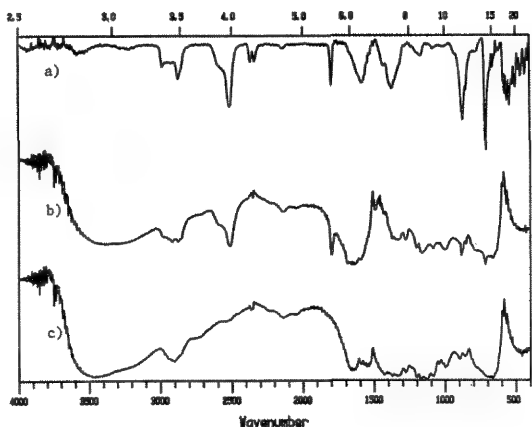


FIG. 7.--Spectra of (a) CaCO_3 , (b) coating from flowers on illustration, (c) paper from illustration.

an acrylate; MS2A, a ketone; and dammar, a natural resin) which were coating films of Prussian Blue pigment in linseed oil. The interference at about 2100 cm^{-1} is due to the paint film; the odd peaks at 1750 and 1450 cm^{-1} are



FIG. 6.--Japanese botanical illustration.

restrahlen bands commonly seen in these samples.

Reflectance measurements of highly reflective coatings are generally more successful. The small flowers in the illustration in Fig. 6 were colored with a reflective white coating. The reflectance spectra of the coating on the paper, the paper alone, and a reference spectrum of CaCO_3 (which matched the coating) are given in Fig. 7. It was not possible to subtract spectrum (c) from spectrum (b) because of differences in the cellulose bands due to the change in surface texture between the coated and noncoated paper. However, the identification could still be made.

Future Work

In some cases, small samples can be taken from the art object, such as a fiber or a flake; microscopic cross sections, minute parts of paintings and furniture finishes are often taken as part of the conservator's

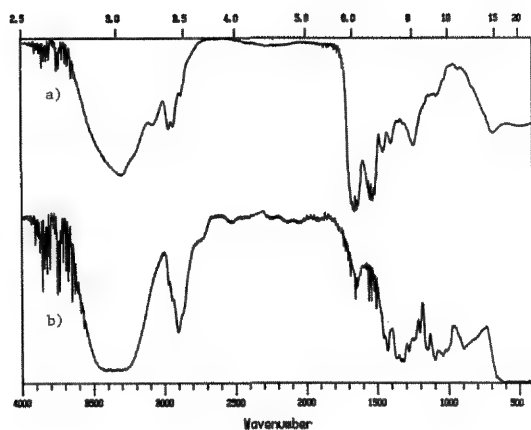


FIG. 8.--Transmission spectra of (a) wool fiber, (b) cotton fiber.

treatments. Transmission spectra of these samples can be taken with apertures to limit the field of view to the desired area. This method can be used for fiber identification; spectra of wool and cotton fibers obtained in this manner are shown in Fig. 8. Since many fibers are dyed, and traditional dye analysis requires a large sample, the development of a method to analyze the dye on a single fiber would be helpful. We also hope to adapt techniques of other workers on the analysis of laminated films¹ to the studies of paint and varnish cross sections. Finally, we plan to continue work on reflectance spectra of coatings to improve the information that can be obtained without destructive sampling.

References

1. J. A. Reffner, J. P. Coates, and R. G. Messerschmidt, *American Lab.* 86, April 1987.

RECENT APPLICATIONS OF FOURIER TRANSFORM INFRARED MICROSCOPY

Akira Ishitani, Ritsu Kamoto, and Hideyuki Ishida

We have been practicing microanalysis using FT-IR for many years^{1,2} and have been able to improve spatial resolution and sensitivity steadily. We report here recent progress with the technique and its applications.

Experimental

Bruker IFS-85 and Bio-Rad FTS 60 FT-IR spectrometers are used with microscopes. In addition, the MOLE (Jobin-Yvon) and SEM-EDX JEOL JSM 25 SIII are also used. We prepare special samples for the examination of spatial resolution (Fig. 1) by embedding polyester fibers into epoxy resin and slicing them about 1 μm thick. Gallstones are donated by Jikei University School of Medicine and samples of polyethylene used for cable insulation with "treeing" are provided by Hitachi Cable Ltd.

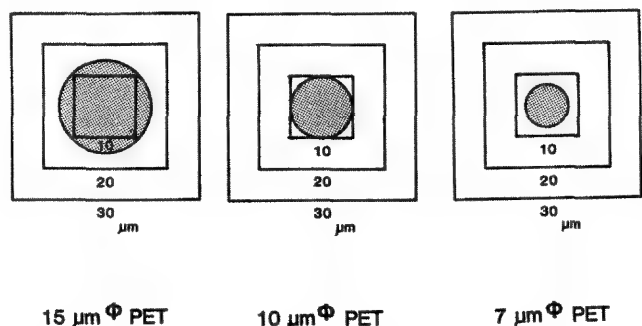


FIG. 1.--Samples used for evaluation of lateral resolution of infrared microscopy. Polyester monofilaments of various diameters embedded in epoxy resin. Squares indicate apertured used.

Results

Examination of the practical spatial resolution is done experimentally using the special samples shown in Fig. 1. An example of a polyester (polyethylene terephthalate, PET) of 10 μm diameter embedded in epoxy resin measured under 8 \times 8, 10 \times 10, and 15 \times 15 μm apertures is given in Fig. 2. The relative intensity of the polyester signal increases with decrease in aperture size. The quantitative intensity ratio from the experiment is compared with the calculated values in Fig. 3. The corrected curve, which takes the stray light effect into consideration, fits well with the observed curve down to an aperture size of 15 μm .

A cross section of a three-layered laminated film (B layer) is observed with a 10 \times 30 μm aperture (Fig. 4). Spectral contributions from

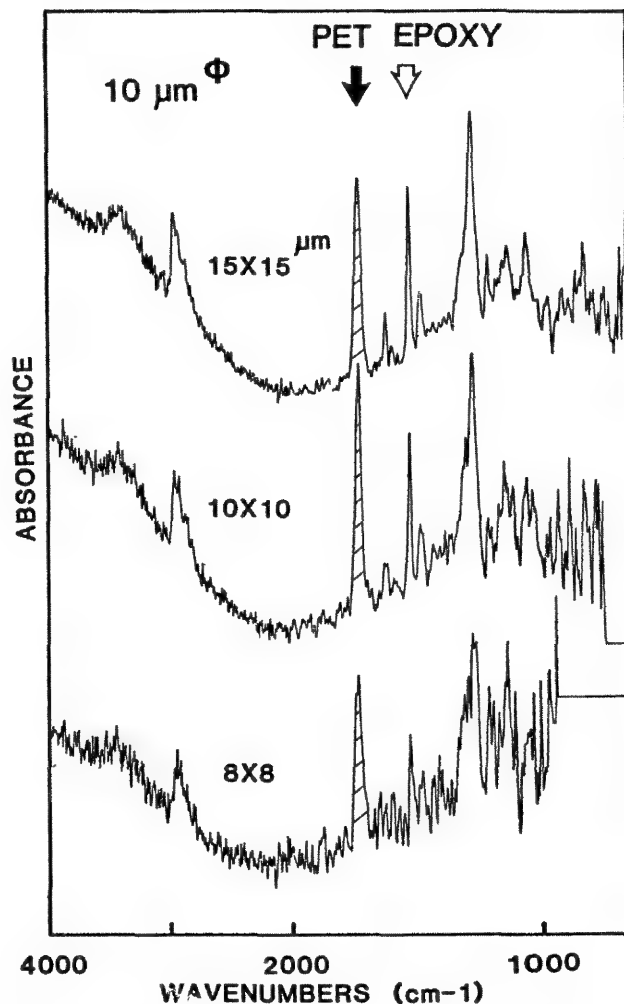


FIG. 2.--Infrared spectra of polyester/epoxy cross section.

the A layer are observed in the B-layer spectrum. The "treeing" phenomenon observed in polymer insulators under high voltage is attracting much interest. The infrared microscopy is expected to provide useful information about it (for example, whether chemical degradation is taking place or not). A measurement on a typical electrical tree is given in Fig. 5. Not much change is observed to indicate chemical structure variation in this case. Another example is a water tree or so-called "bow-tie tree" (Fig. 6). An apparent spectral change is observed in this case. The nucleus and the wing of the tree have additional 1740 and 1600 cm^{-1} bands that are not present in the control. The former band comes from ester additives condensed in the tree area; the latter, from caboxylate generated by degradation of the polymer.

A cross section of a calcium carbonate gallstone is shown in Fig. 7. The multilayers that

The authors are at the Toray Research Center, Inc., 1-1 Sonoyama 1-chome, Otsu, Shiga 520, Japan.

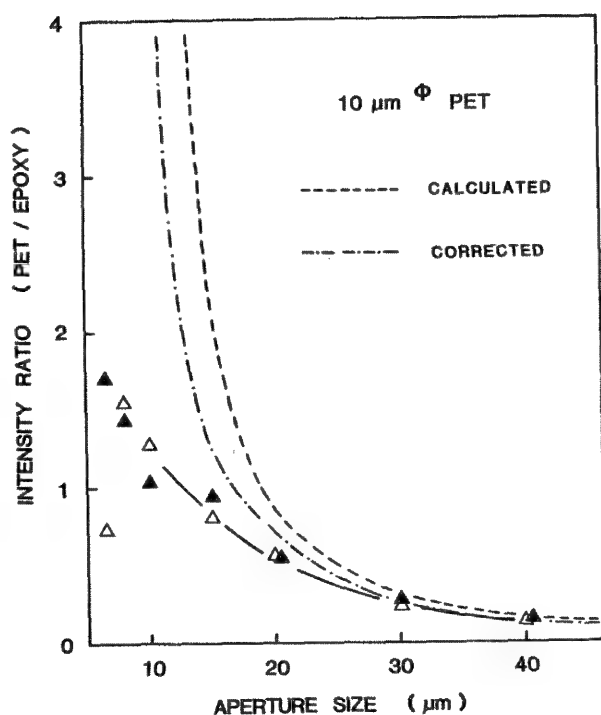


FIG. 3.--Aperture size dependence of polyester/epoxy absorption intensity ratio for 10μm-diameter polyester fiber.

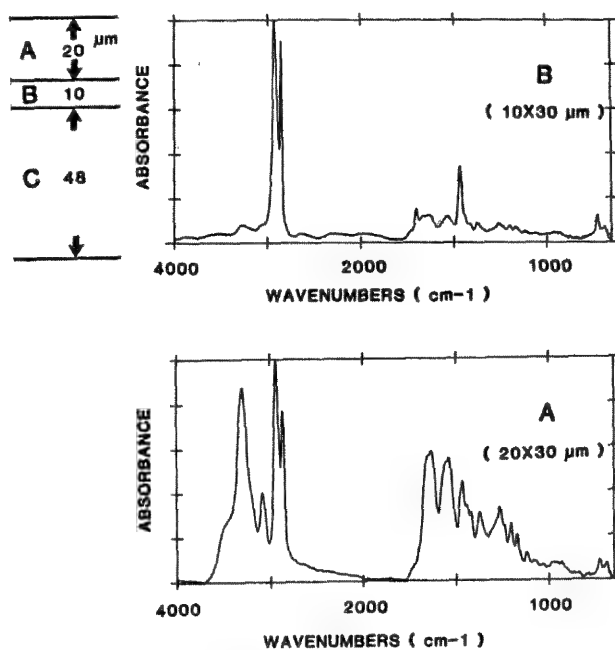


FIG. 4.--Measurement of cross section of three-layer laminated film by infrared microscope.

are observed are measured with an infrared microscope. The outer layers are made up of calcium carbonate; the inner layers contain mainly cholesterol. The intermediate layers show a gradual variation in composition. This observation gives useful insights into the mechanism of the generation of the gallstone.

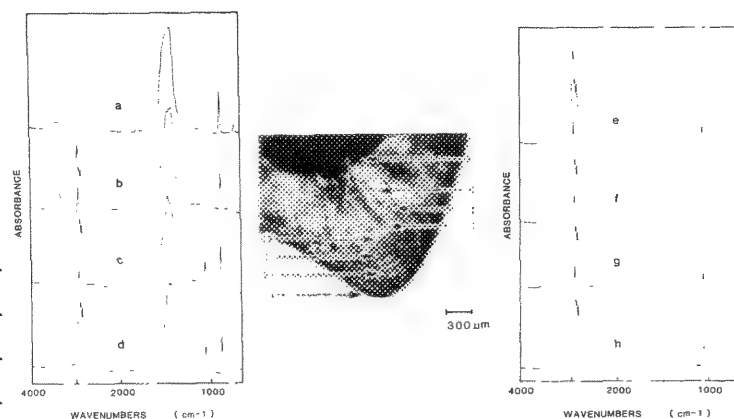
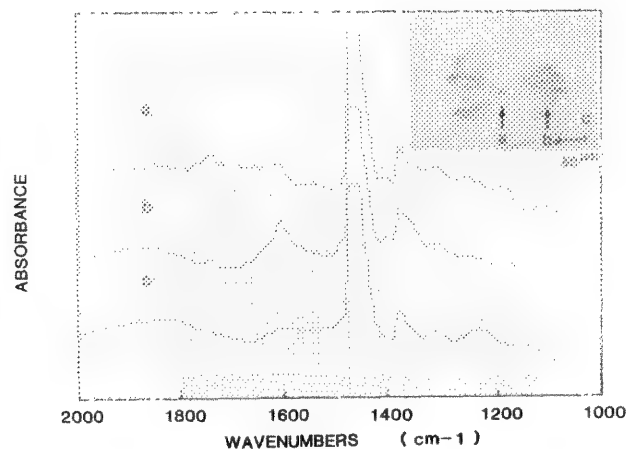
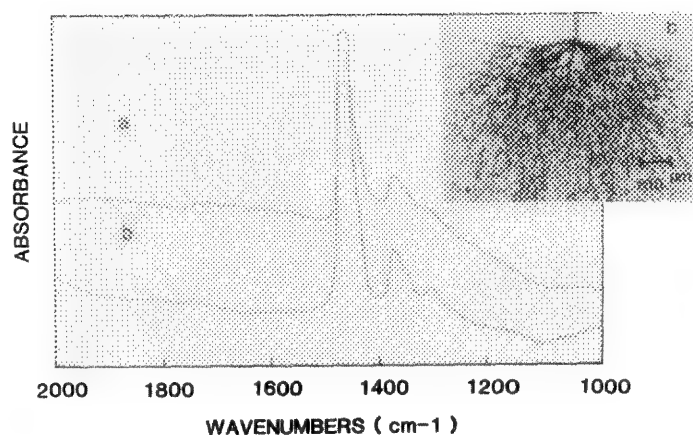


FIG. 5.--Infrared spectrum of an electrical tree of polyethylene used for cable insulation.
FIG. 6.--Infrared spectra of water ("bow-tie") tree in polyethylene.
FIG. 7.--Infrared spectra of multilayers observed in calcium carbonate gallstone.

References

1. A. Ishitani, in H. Ishida, Ed., *Fourier Transform Infrared Characterization of Polymers*, New York: Plenum, 1987, 341.
2. A. Ishitani, *Proc. 1985 Intern. Conf. Fourier and Computerized Infrared Spectroscopy*, SPIE 1985, 5533, 25.

INFRARED MICROSCPECTROSCOPY OF FIBER OPTICS

R. T. Carl

Infrared microspectroscopy has recently progressed from an exotic and difficult technique to a routine method, as a result of the merger of highly sensitive Fourier transform infrared spectrometers with precision infrared and optical microscopes. It is now widely used in a variety of fields including failure analysis, forensics, and polymer science. Currently, an area of intense interest is analysis and determination of the properties of optical fibers. Infrared microspectroscopy can play a key role in these analyses.

Fiber optics are used in a variety of applications, such as remote illumination, sensing, and data transfer in such diverse fields as biomedical monitoring, telecommunications, and analytical chemistry. Naturally, the composition of these information-carrying fibers is quite unique due to the different wavelengths being transmitted. Fiber optics transfer energy by total internal reflection. Light striking the walls of a cylinder (Fig. 1) is totally reflected provided the incident angle is greater than $\theta_c = \sin^{-1}(n_a/n_i)$, where n_i is the index of refraction of the cylinder or fiber and n_a is the index of refraction of the medium surrounding the fiber.² Normally, there will be several thousand reflections per meter of fiber. The surface of a fiber must be kept clean to prevent energy loss from the fiber by frustrated total internal reflection.³ If a large number of fibers are close together, energy may leak from one fiber to another and cause "crosstalk." To prevent crosstalk, fibers are normally clad in a thin sheath of a material with a lower index of refraction. Analysis of fiber optics by infrared microspectroscopy should yield information about their composition and formulation.

Experimental

All data were collected on a Nicolet System 740 spectrometer interfaced to an IR-PLAN[™] microscope equipped with a proprietary Nicolet high-sensitivity, narrow-band MCT detector and preamplifier. Each spectrum was collected at 8cm⁻¹ resolution in 128 scans and a measurement time of 22 s. Redundant Aperturing[™] was used in every case to collect spectra of correct spatial purity and photometric accuracy.

The fiber optics were obtained from commercial sources, mounted in Devcon[™] 5 Minute Epoxy and cross sectioned to 5 μ m by an American Optical 829 microtome. The samples were then placed on an infrared transparent window of

of barium fluoride and analyzed. Library spectra of 16cm⁻¹ resolution (Nicolet-Hummel polymer library) were searched and plotted with standard Nicolet software.

Discussion

The first sample to be analyzed was a data-transmission fiber-optic cable. When the sample was viewed with visible light and cross polarization on the IR-PLAN microscope, the presence of a black outer layer, a colorless middle layer, and a birefringent inner layer was revealed. Analysis of the outer layer by infrared microspectroscopy produced the spectrum shown in Fig. 2. The region 3200-2600 cm⁻¹ (characteristic of the C-H stretch) is totally absorbing, but there is sufficient information in the other regions to identify the composition of the sample. By use of a search algorithm that ignores the totally absorbing C-H region of the spectrum, the sample was identified as a low-density polyethylene (Fig. 2b). Analysis of the middle layer (80 \times 80 μ m) produced the spectrum shown in Fig. 3. The major component is poly(tetrafluoroethylene) (PTFE), as evidenced by the two strong bands in the 1300-800cm⁻¹ region. However, an additional component is present, since there are bands in the C-H region. Removing the PTFE bands followed by library searching shows the remaining component to be polypropylene (Fig. 3b). The inner layer seemed to contain a co-polymer of poly(methyl methacrylate) and poly(methyl acrylate), as shown in Fig. 4. This structure is consistent with the aforementioned fiber-optic design criteria, since the index of refraction of PTFE (1.3-1.4) is less than that of poly(methyl methacrylate) (1.48-1.50).

A second bundle of fiber optics were analyzed by infrared microscopy. The cross section of this fiber consisted of a quartz inner core (refraction index = 1.5-1.7) and a birefringent outer layer. The outer layer was analyzed; the spectrum is shown in Fig. 5a. The library search result showed that the major component was poly(1,4-butylene terephthalate). A second library search over the C-H region only indicated a mixed urethane polyether as a second component. An overlay plot of these two components and the sample spectrum are shown in Fig. 5b. The composite spectrum produced by addition of the library spectra of these two components (Fig. 5c) matches the sample spectrum well.

Recently, there has been interest in producing fiber optics that transmit in the infrared region, primarily due to the fact that energy losses in fibers are proportional to

The author is with Nicolet Spectroscopy Research Center, 5225-1 Verona Rd., Madison, WI 53711.

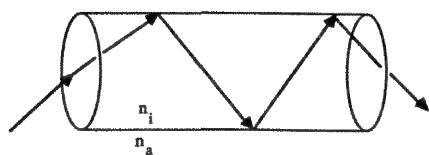


FIG. 1.--Rays reflected through cylinder.

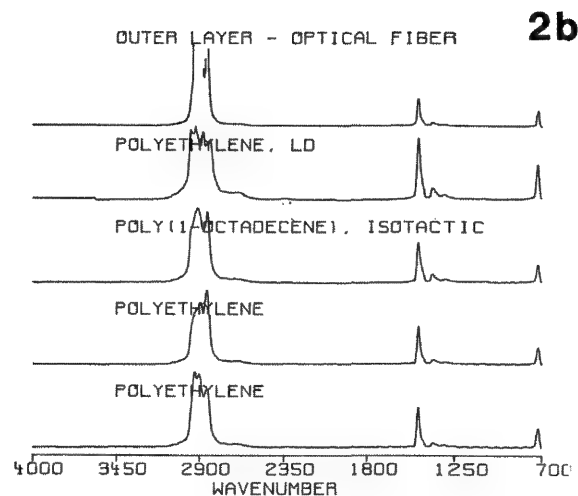
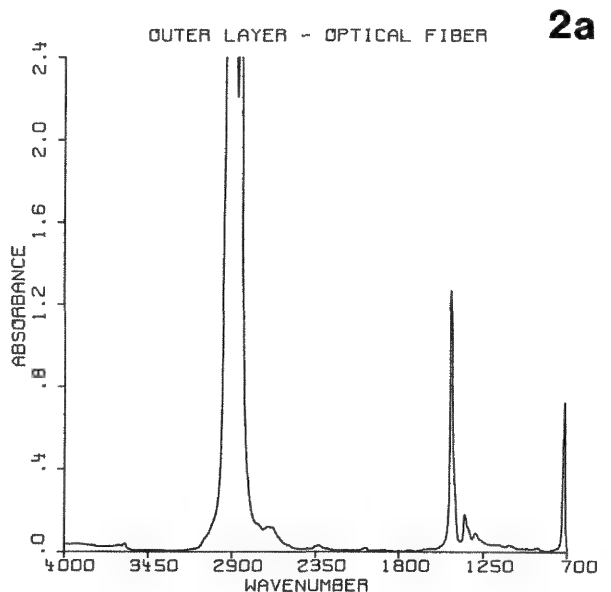


FIG. 2.--(a) spectrum, (b) search results.

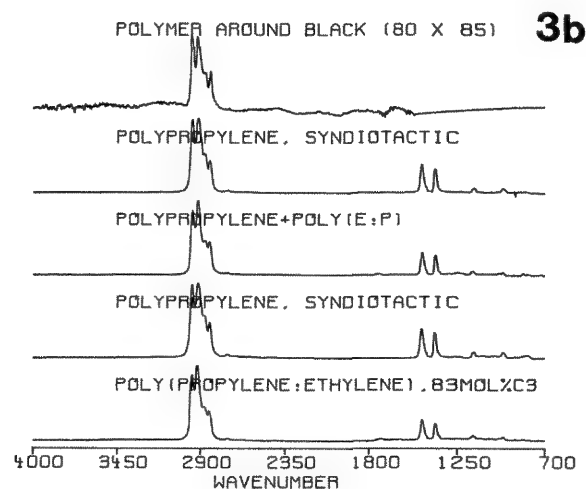
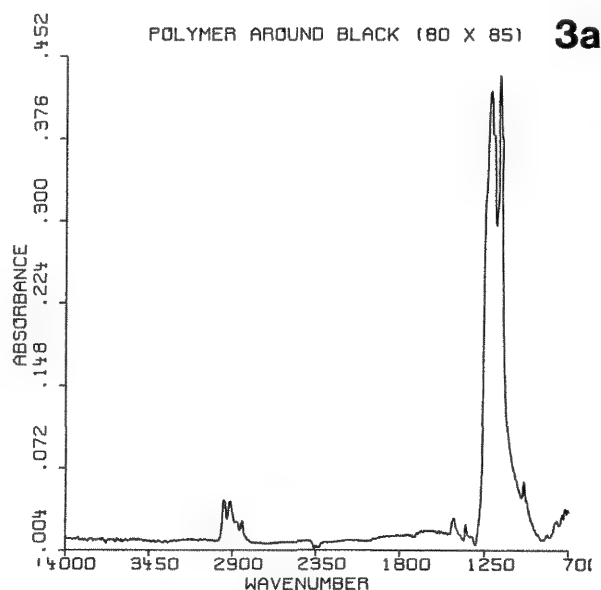


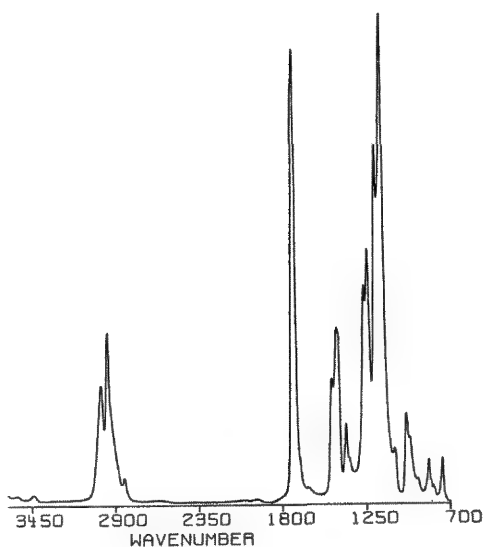
FIG. 3.--Middle layer of data transmission fiber: (a) spectrum, (b) search results.

λ^{-4} , where λ is the wavelength, so that scattering losses decrease sixteen-fold when λ is increased from 1 to 2 μm . One group of material that show promise in this field are the chalcogenide glasses: heavy-metal oxides, sulfides, selenides, and tellurides. Cross sectioning and viewing of an infrared-transmitting fiber optic shows two layers surrounding a central core of a chalcogenide. The infrared spectrum of the chalcogenide (Fig. 6a) is basically featureless, as would be expected. The "ringing" or fringing pattern is due to constructive and destructive interference of the

infrared energy as it reflects between the parallel faces of the crystal.³ Analysis of the middle layer ($16 \times 44 \mu\text{m}$) produces a spectrum indicative of poly(tetrafluorethylene) (Fig. 6b), which has a significantly lower refractive index. Analysis of the large outer layer indicates that the material consists primarily of poly(1,4-butylene terephthalate) (Figs. 6c and d). However, a co-polymer also seems to be present, as evidenced by the small differences in the C-H region.

INNER LAYER-OPTICAL FIBER (112X180)

4a



INNER LAYER-OPTICAL FIBER (112X180)

4b

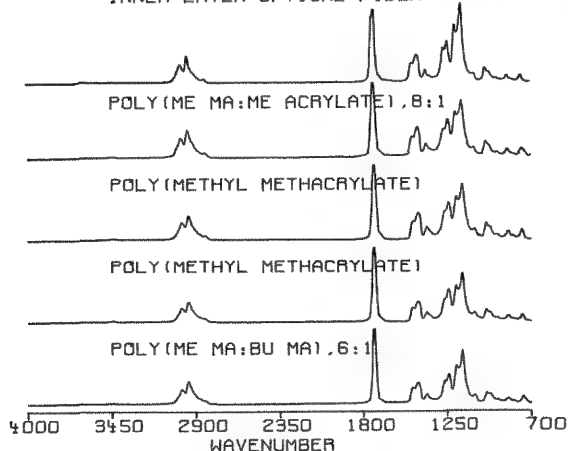
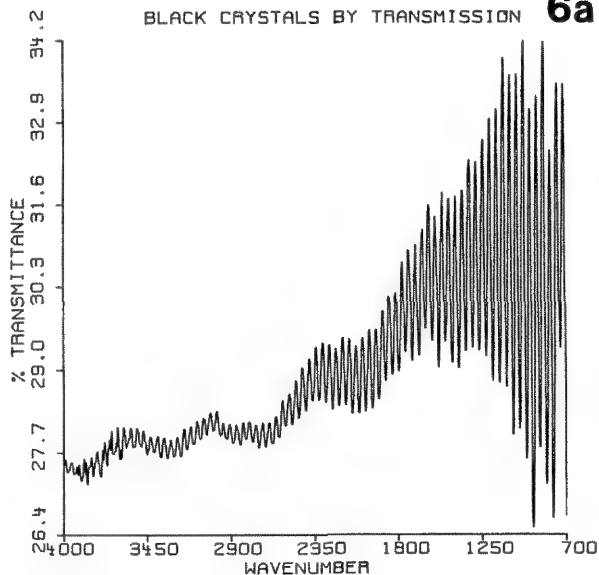


FIG. 4.--Inner layer of data transmission fiber: (a) spectrum, (b) search results.

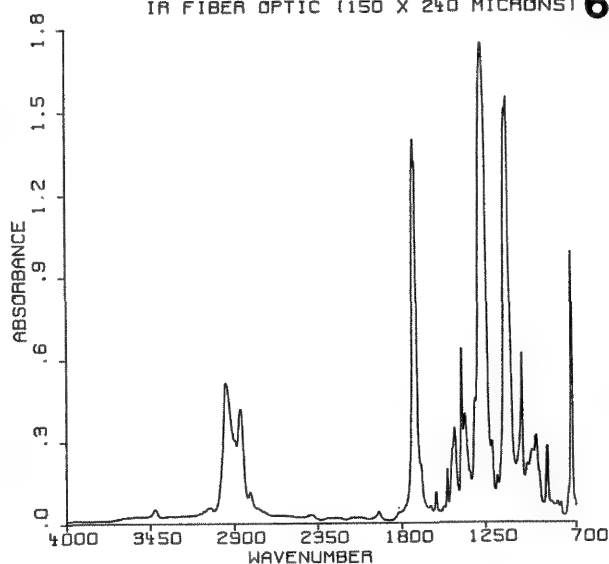
BLACK CRYSTALS BY TRANSMISSION

6a



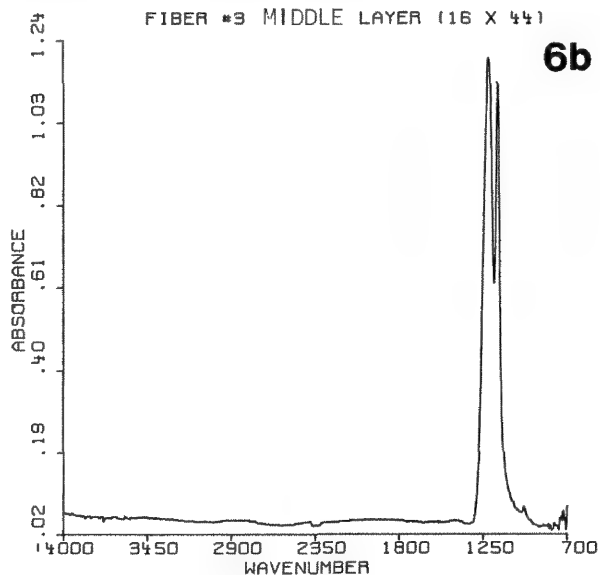
IR FIBER OPTIC (150 X 240 MICRONS)

6c



FIBER #3 MIDDLE LAYER (16 X 44)

6b



IR FIBER OPTIC (150 X 240 MICRONS)

6d

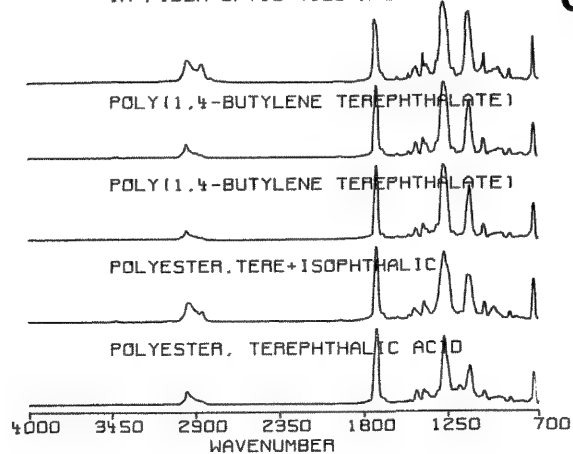


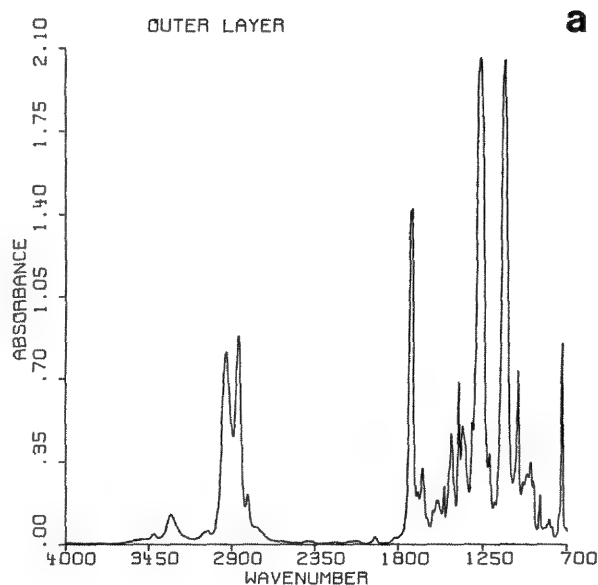
FIG. 6.--Spectra of infrared fiber: (a) core, (b) middle layer, (c) outer layer, (d) search results for outer layer.

Conclusions

The use of infrared microspectroscopy has been demonstrated for analysis of fiber optics. The technique provides uniquely diagnostic data. These data, coupled with library search capabilities and an extensive FT-IR polymer library, yield unequivocal identification of the individual materials present. The combination of infrared spectroscopy and microscopy allows the analysis of samples once thought to be unsuitable for investigation.

References

1. R. Barer, A. R. H. Cole, and H. W. Thompson, *Nature* 163: 198, 1949.
2. E. Hecht and A. Zajac, *Optics*, London: Addison-Wesley, 1974.
3. N. J. Harrick, *Internal Reflection Spectroscopy*, Harrick Scientific Corp. (Croton Dam Road, Box 867, Ossining, NY 10562), 1979.
4. R. G. Messerschmidt, *Microbeam Analysis* --1987, 169-172.



b

OUTER LAYER OF FIBER OPTIC
POLY(1,4-BUTYLENE TEREPHTHALATE)
POLYETHER URETHANE, PBO+MBI

NICOLET/HUMMEL - 10/86

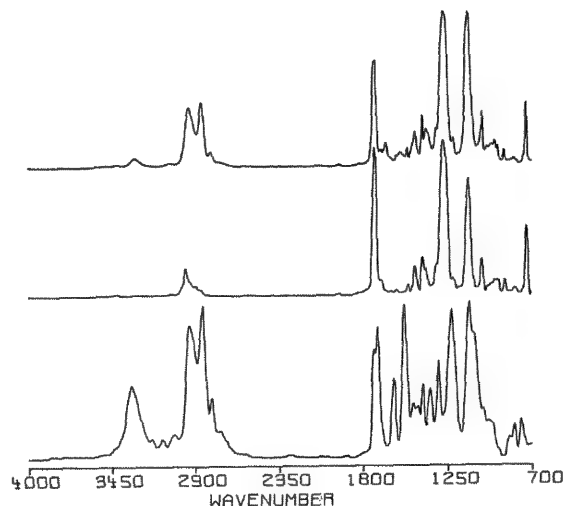
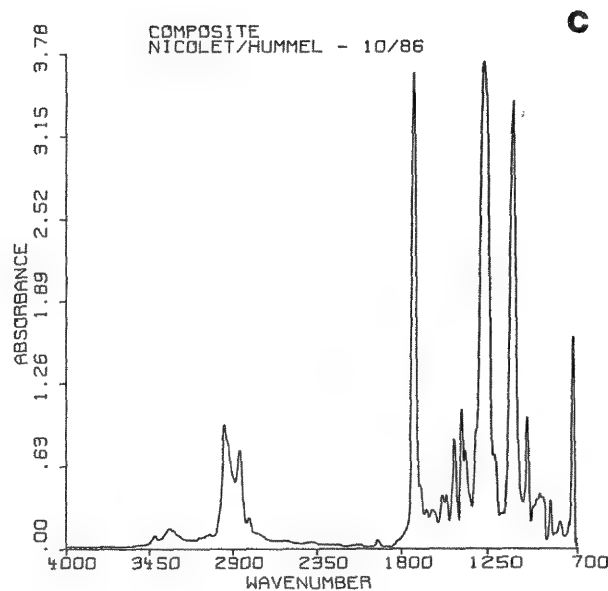


Fig. 5.--Outer layer of fiber optic cable:
(a) spectrum, (b) overlay plot of two components, (c) composite of library spectra.



MINERAL ANALYSIS BY FT-IR MICROSCOPY

J. A. Reffner

FT-IR microscopy provides molecular spectroscopic measurements of minerals without disruption of the mineral's morphological structure. With the IR-PLAN™ infrared microscope and an FT-IR spectrometer, either reflection or absorption spectra can be obtained. In the reflection mode the sample's surface geometry determines whether the recorded spectrum is predominantly diffuse reflection or specular reflectance data. With thin section, $\sim 10\ \mu\text{m}$ thick, transmission spectra may be obtained.

Mineral analysis of constituents of a rock are commonly conducted on a polished rock section. With a highly polished flat specimen, specular reflection is dominant. Since the amount of the Fresnel reflectance is affected by the optical geometry, the intensity of *reststrahlen* bands also depends on the sample's optical geometry. These optical effects cause substantial variation in the recorded spectra. Mathematical analysis of reflection data, principally the Kramers-Kronig (K-K) transformation, can yield valuable structural information. However, the use of the K-K analysis to emulate transmission spectra must proceed with caution. Attention must be given to the reflection processes being recorded, the reflection geometry, and the assumptions used in solving the Kramers-Kronig transformation.

Specular reflectance IR spectral data can be used directly to identify minerals, and with the FT-IR microscope it is possible to map the mineral species in a polished section. FT-IR microscopy also provides a direct method for the measurement of specular reflectance spectra from different faces of small single crystals.

Experimental

The spectra were all obtained with an IR-Plan™ microscope on a Nicolet 20SXB Fourier Transform spectrometer and a narrow-band $0.25 \times 0.25\text{mm}$ MCT detector. Unless noted otherwise, spectra were collected at $8\ \text{cm}^{-1}$. A gold mirror was used as the reference for all specular reflection measurements. The area of the samples was $0.00758\ \text{mm}^2$. For all measurements a $15 \times 0.58\ \text{N.A.}$, objective was used. In reflection measurements, the aperture beam splitter creates an incident beam ranging from 15.6° to 35.5° half-cone angle; specular reflections are collected over the same angular range. The angle of incidence for the median energy is 28.4° .

For recording reflection spectra of single crystals, samples were mounted on a microgoniometer stage, rotated, and tilted until a

strong specular reflection was seen for visible light; then IR spectra were measured.

Minerals for transmission measurements were sheet silicates and were cleaved to produce thin sections. The tooth cross sections were prepared by standard petrographic polishing procedures.

Results

The spectra of several minerals were obtained with the FT-IR microscope in order to demonstrate the applicability of IR spectroscopy to direct analysis of rocks and mineralized tissue. The spectra shown in Fig. 1 are the specular reflection IR spectra of tooth enamel and dentine. Both of these phases have calcium phosphate present in the form of apatite. However, the molecular spectrum of each phase is substantially different. The degree of calcification of the enamel is much higher than in the dentine, which accounts for the much higher reflectivity of the enamel. The reflectivity is 72% for the enamel and 33% for the dentine.

The sheet silicate margarite provide a direct comparison of transmission and reflection spectra. Figure 2a is the transmission spectrum of margarite (Joswig); the reflectance spectrum of the same area of the same section is shown in Fig. 2b. When the reflection spectra of the Joswig margarite is compared with that of a margarite from Chester Co., Penn. (Fig. 3), there are similarities in the silicate *reststrahlen* band at $\sim 1000\ \text{cm}^{-1}$, but there are significant differences in the water absorption band region $\sim 3650\ \text{cm}^{-1}$.

A single quartz crystal was studied. The specular reflection spectra are shown in Fig. 4 for the 001 and 110 faces. The differences in these spectra are small as expected, since quartz has a low optical birefringence. However, the splitting of the band at $700\ \text{cm}^{-1}$ and the relative peak ratios provides an indication that the infrared reflectance spectra may be useful in determining orientation effects. Polarized spectra studies are being planned.

Conclusions

The FT-IR microscope has been shown to be a direct method for obtaining molecular spectral information on minerals either in a transmission mode or in reflection. Transmission spectra are easier to interpret, but reflection spectra (diffuse or specular) can provide analytical information. With the FT-IR microscope the molecular spectra can be obtained from small areas without the sample being altered, which is of particular importance in

The author is with Spectra-Tech Inc., 652 Glenbrook Road, Stamford, CT 06902.

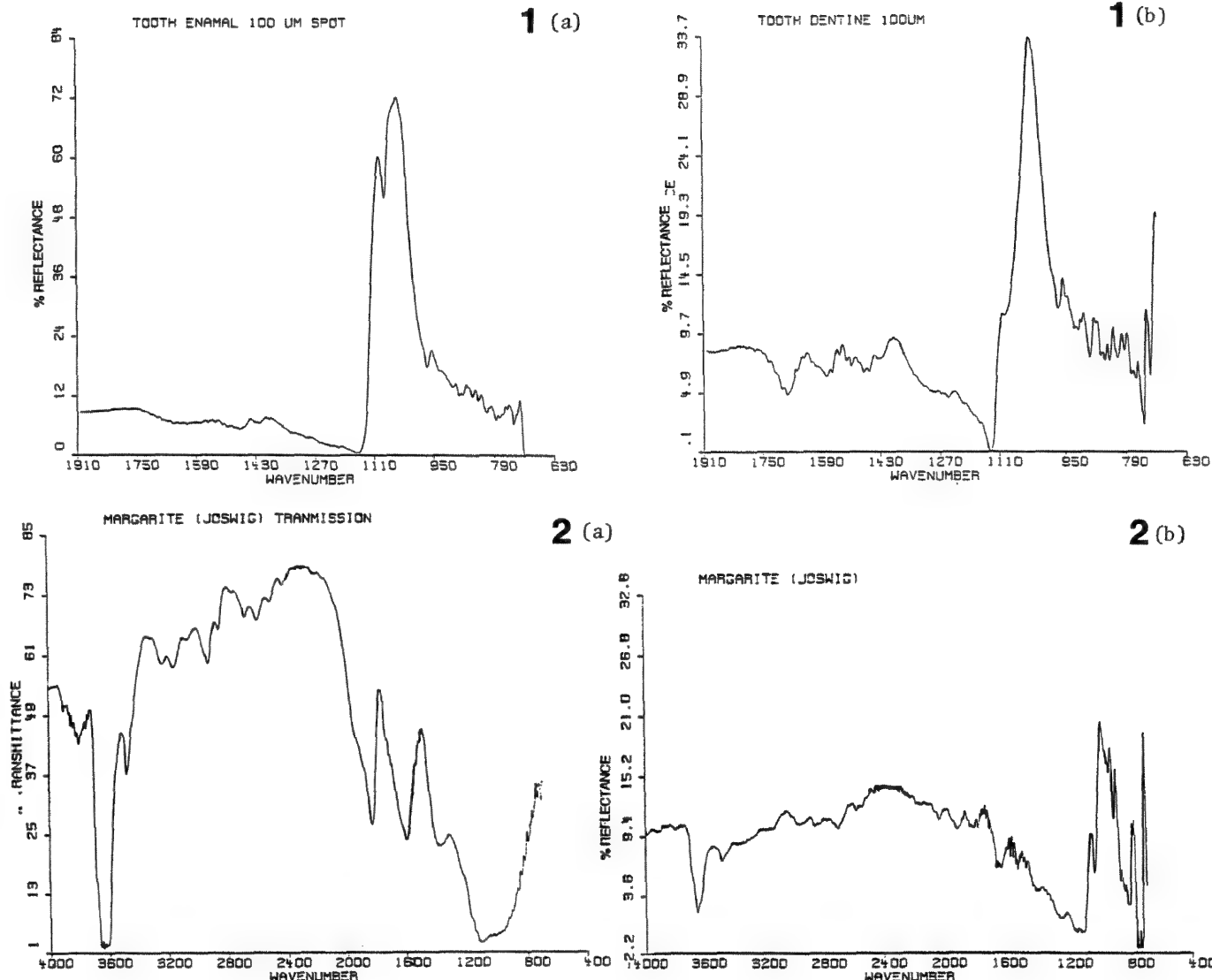


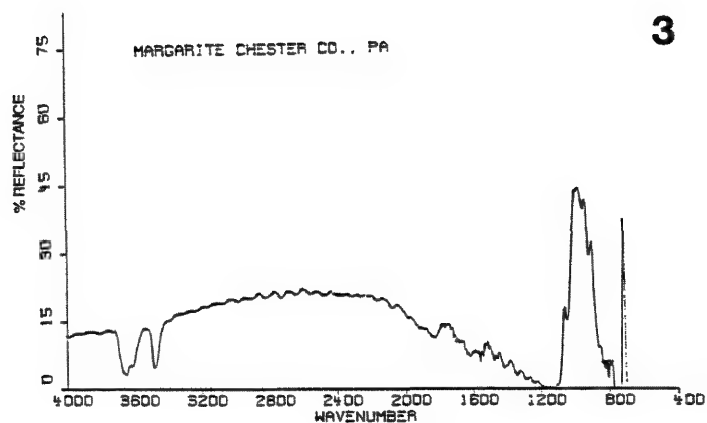
FIG. 1.--The infrared specular reflectance spectrum of (a) dentine and (b) enamel phases of human molar, measured on polished section.

FIG. 2.--Infrared spectra of margarite (Joswig) in (a) transmission and (b) reflection.

the study of the hydration of minerals, where exposure to vacuum or elevated temperatures can change the state of hydration.

References

1. H. Ishida, "Quantitative surface FT-IR spectroscopic analysis of polymers," *Rubber Chem. Technol.* 60: 497- , 1987.
2. C. Werneke and E. Salje, "A simple refinement routine for infrared reflection spectra based on Kramers-Kronig analysis and classical oscillator fit," *Infrared Phys.* 20: 59-65, 1980.
3. J. P. Hawranek, R. P. Neelakantan, and R. N. Jones, "Control of errors in IR spectrophotometry: IV. Corrections for dispersion distortion and the evaluation of both optical constants," *Spectrochim. Acta* 32A: 85-98, 1976.



3

4 (a)

4 (b)

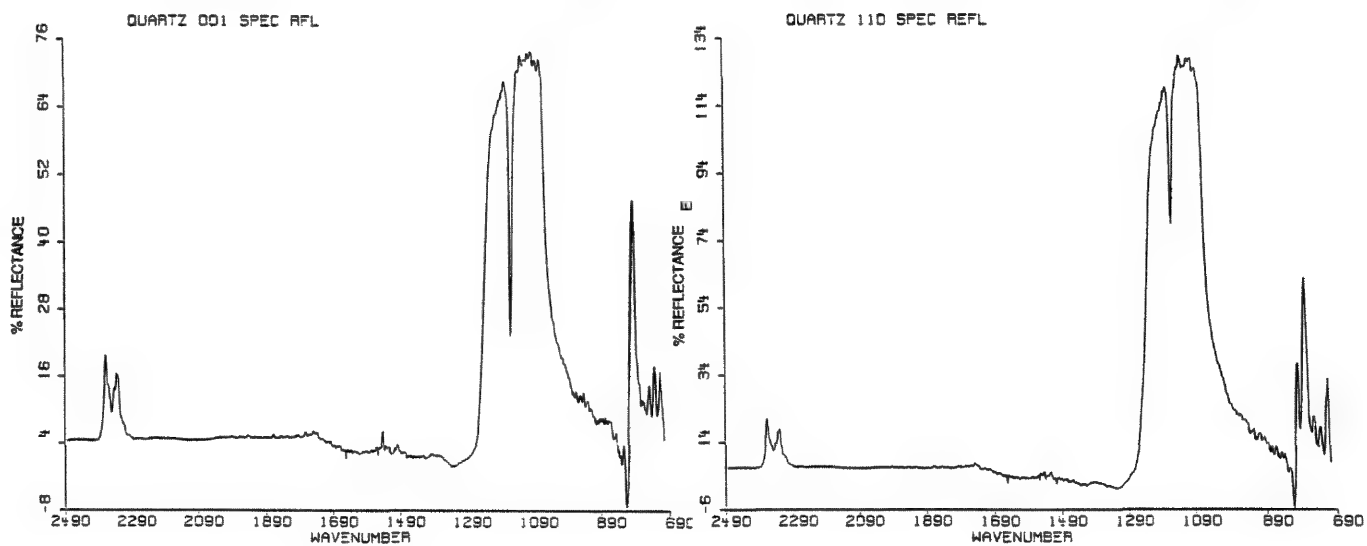


FIG. 3.--Reflection IR spectra of margarite from Chester Co., Penna.

FIG. 4.--Specular reflectance infrared spectra of single crystal of quartz. Spectra of reflection from (a) 001 face and (b) 110 face are reported.

A COMPARISON OF TWO OPTICAL DESIGNS FOR THE CROSSED-BEAM THERMAL LENS SCANNING LASER MICROSCOPE

D. S. Burgi and N. J. Dovichi

The crossed-beam thermal lens scanning laser microscope consists of two tightly focused laser beams (a modulated pump beam and a coplanar continuous-wave probe beam) crossed within the sample.¹⁻⁵ Absorbance of the pump beam generates a time-varying localized temperature rise within the sample.^{6,7} The heated region behaves like a cylindrical lens which periodically defocuses the probe beam out of the plane of the intersecting laser beams.⁸⁻¹⁰ Since the pump and probe beams interact only at their intersection volume, a point-by-point image may be generated as the sample is translated through the intersection volume. The image consists of two parts: an amplitude component, which is related to the sample's absorbance; and a phase component, which is related to the sample's thermal diffusivity. For purpose of comparison, the microscope has been applied to a botanical sample.

Experimental

There exist two generations of the microscope. Figure 1 is the optical design for the two-lens microscope; Fig. 2 is the one-lens microscope. The pump and probe beams for both designs are the 442nm line of a 4.0mW He:Cd laser and the 632.8nm line of a 510mW He:Ne laser, respectively. For the two-lens microscope, the pump beam is mechanically chopped and directed to a 18× microscope objective which focuses the beam into the sample. The probe beam is directed into a 7× microscope objective and focuses in the sample at right angles to the pump beam. The sample is translated through the intersection volume and the photothermal signal is detected as a change in the probe beam center intensity by a photodiode located behind a pinhole. The signal is sent to a vector sum lock-in amplifier for demodulation and then collection by a computer.

In the one-lens microscope (Fig. 2), the two laser beams are sent parallel and slightly offset to each other into a single microscope objective by a dichroic filter, which transmits the probe beam and reflects the pump beam. The microscope objective crosses the two beams at its focal point inside the sample creating the intersection volume. The microscope objectives

D. S. Burgi, previously at the University of Alberta, is at present at Stanford University. The work was performed in the Department of Chemistry, University of Alberta, Edmonton, Canada T6G 2G2. Paula Jaeger of Iverson Memorial Hospital kindly supplied the sample used in this study. Funding from the Natural Sciences and Engineering Research Council of Canada is gratefully acknowledged.

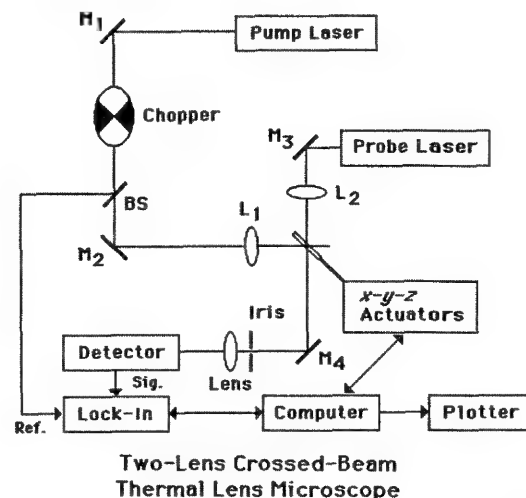


FIG. 1.--Two-lens optical diagram. M1-M4, mirrors; PUMP, unpolarized He:Cd laser; CHOPPER, mechanical chopper operating at about 1.5 kHz; BS, beam splitter; L1 and L2, microscope objectives; PROBE, polarized He:Ne laser. Sample is mounted on three-axe translation stage and moved with computer-controlled ACTUATORS; IRIS isolates probe beam center, LENS focuses the transmitted light onto DETECTOR constructed from 1cm² silicon photocell. LOCK-IN amplifier demodulates signal and sends digitized data to laboratory computer. COMPUTER plots both phase and ratio of amplitude of lock-in signal to dc probe intensity with digital PLOTTER.

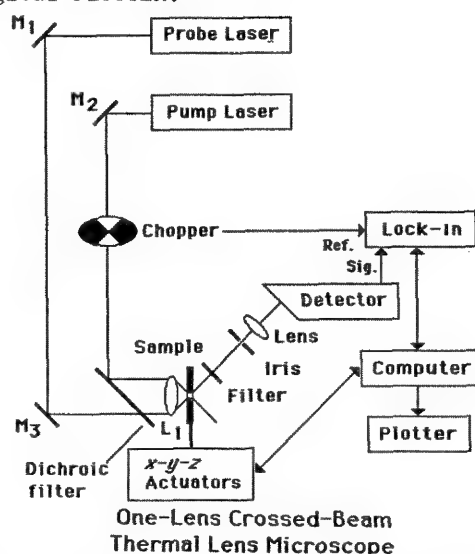
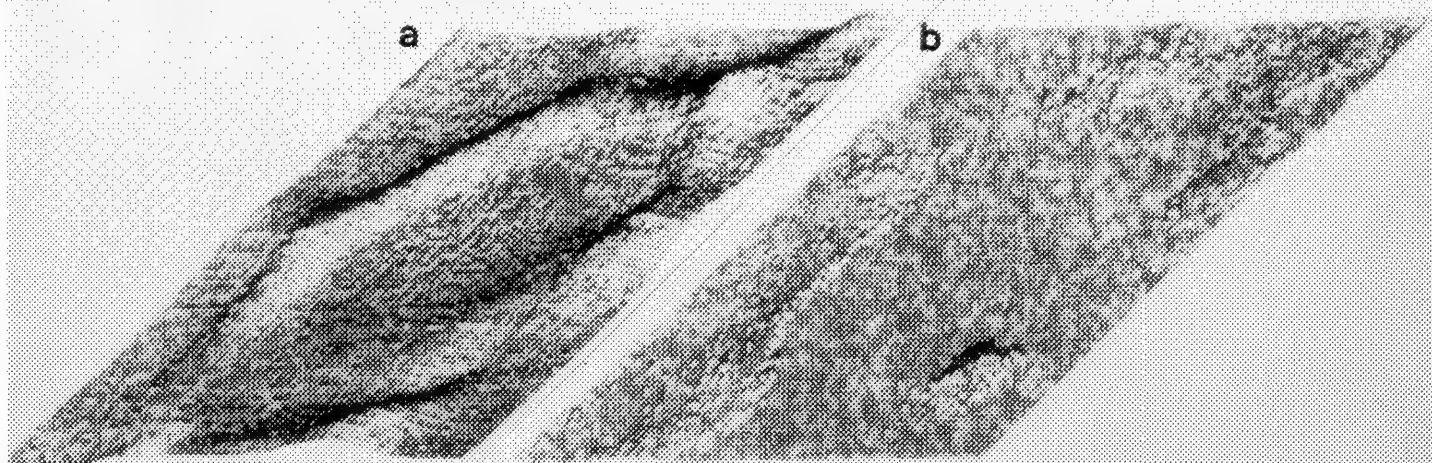


FIG. 2.--One-lens optical diagram. Same as in Fig. 1 except pump and probe beams are sent to a DICHROIC FILTER, which transmits red light and reflects blue light. FILTER after SAMPLE transmits probe beam and absorbs pump beam.



One-lens microscope

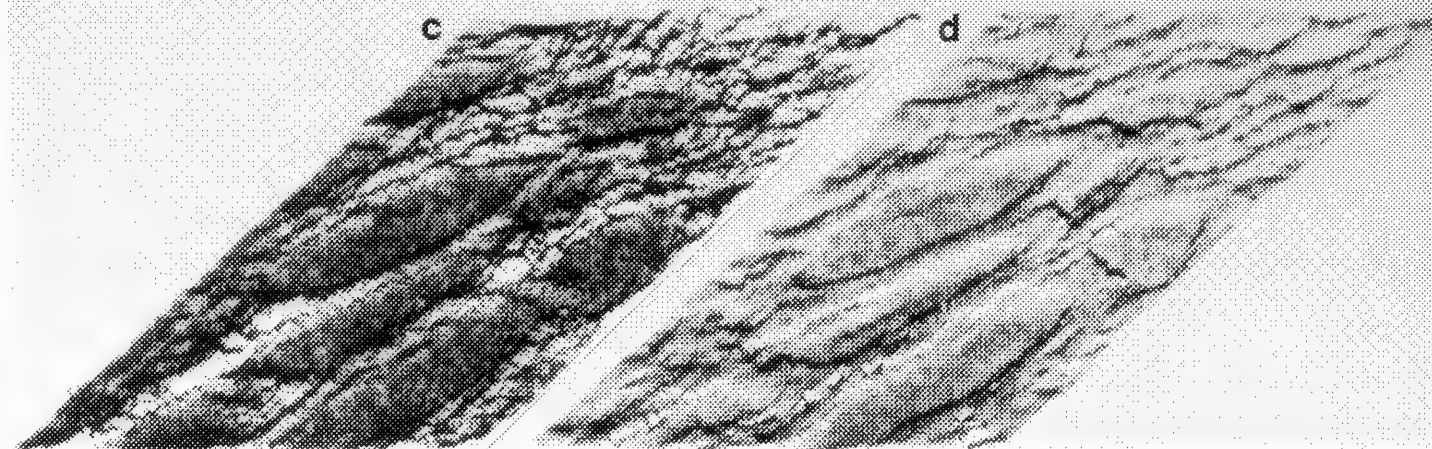


FIG. 3.--Image of one-year-old stem of *Tilia americana* taken with $1\mu\text{m}$ spacing between pixels. Two-lens microscope: (a) amplitude component; (b) phase component. One-lens microscope: (c) amplitude component; (d) phase component.

can range in power from $2.5\times$ to $100\times$; a $40\times$ objective is used in this comparison study. The photothermal signal generated in the sample is collected as described above.

The sample is a $15\mu\text{m}$ -thick cross section of a 1-year-old basswood stem (*Tilia americana*). The plant stem is stained with Safranin and Fast Green using conventional staining techniques.¹¹

Results

Figure 3 shows the amplitude and phase components of a $100 \times 100\mu\text{m}$, $1\mu\text{m}$ increment scan of the *Tilia americana* plant stem. Figures 3a and b are the amplitude and phase images, respectively, of the two-lens microscope; Figures 3c and d are the amplitude and phase images, respectively, of the one-lens microscope. Regions of large magnitude in the amplitude images correspond to regions of the sample which are stained red; regions of differing phase correspond to variations in thermal diffusivity of the sample. The large ring located in the

center of Fig. 3a is the amplitude image of a $50\mu\text{m}$ -diameter pith cell and the several rings in Fig. 3c are the amplitude images of secondary xylene cells, which range from 10 to $25\mu\text{m}$ in size. In both the amplitude and phase images, the cell walls are notably more detailed and the transition from cell interior to cell wall is sharper with the one-lens microscope than with the two-lens microscope. Spatial resolution for the microscopes is calculated by use of the rapid change in the phase signal as the intersection volume is translated from the interior of the cell to the cell wall. For the two-lens microscope and the one-lens microscope, the resolution is about $20\mu\text{m}$ and $1\mu\text{m}$, respectively. The increase in the spatial resolution coincides with a decrease in the intersection volume; the $40\times$ objective can focus the laser light to a smaller spot size than the $18\times$ objective. Unfortunately, the two-lens optical design limits the power of objective used. The shortness of the working distance of a $40\times$ objective causes the pump

and probe microscope objectives to butt up against one another. With the one-lens optical design, the intersection volume is formed in front of the objective, so that the sample can be brought up close to the face of the microscope objective. A spatial resolution of 300 nm is calculated for a 100× microscope objective.³

Conclusion

The one-lens microscope has been shown to have a higher spatial resolution than the two-lens microscope, because the one-lens microscope can use higher-power objectives, which generate smaller intersection volume. With a 100× objective, the spatial resolution approaches 300 nm and, theoretically, by use of a confocal design,^{1,2} the one-lens microscope has the potential to reach a diffraction limited spatial resolution of 120 nm.

References

1. D. S. Burgi, T. G. Nolan, J. A. Risfelt, and N. J. Dovichi, *Opt. Eng.* 23: 756, 1984.
2. D. S. Burgi, W. A. Weimer, T. G. Nolan, and N. J. Dovichi, *Am. Inst. Phys.* 146: 664, 1986.
3. D. S. Burgi and N. J. Dovichi, *Microbeam Analysis--1987*, 155-157.
4. D. S. Burgi and N. J. Dovichi, *Appl. Opt.* 26: 4665, 1987.
5. Y. F. Cheng, T. K. Lee, D. S. Burgi, and N. J. Dovichi, "Two-color photothermal microscope" (in preparation).
6. J. R. Whinnery, *Acc. Chem. Res.* 7: 225, 1974.
7. J. M. Harris and N. J. Dovichi, *Anal. Chem.* 52: 695A, 1980.
8. N. J. Dovichi, T. G. Nolan, and W. A. Weimer, *Analyt. Chem.* 56: 1700, 1984.
9. W. A. Weimer and N. J. Dovichi, *J. Appl. Phys.* 59: 225, 1986.
10. N. J. Dovichi, "Thermo-optical spectrophotometries in analytical chemistry," *CRC Critical Studies in Analytical Chemistry*, 17(4): 357, 1987.
11. E. Gurr, *Staining-Practical and Theoretical*, Baltimore: Williams and Wilkins, 1962.
12. A. Boyde, *Science* 230: 1270, 1985.

CHARACTERIZATION OF POLYMER BLENDS BY SIMULTANEOUS FOURIER TRANSFORM INFRARED MICROSCOPY AND DIFFERENTIAL SCANNING CALORIMETRY

F. M. Mirabella Jr. and M. J. Shankernarayanan

The capability of simultaneously measuring thermal property response and infrared spectra on specimens of microscopic dimensions can provide important insight into structural changes associated with thermal response for a wide range of systems.¹ The simultaneous measurement of the thermal response in a differential scanning calorimeter (DSC) and the infrared spectra in an FT-IR can provide this capability. In particular, the use of a DSC cell adapted for microscopic observation during thermal treatment, combined with an infrared microsampling accessory (IRMA) in an FT-IR, permits the simultaneous collection of such data. The various phase transitions and thermal responses of crystalline and amorphous polymers, polymer blends and copolymers, and liquid crystalline polymers, as well as small molecules, can then be correlated with the structural information derived from the simultaneously collected infrared spectra.

Experimental

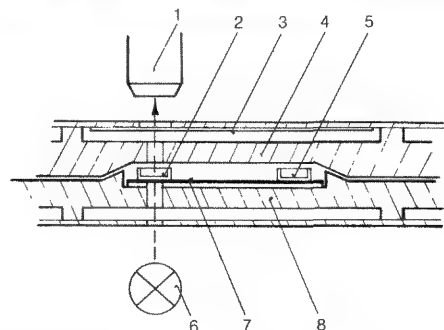
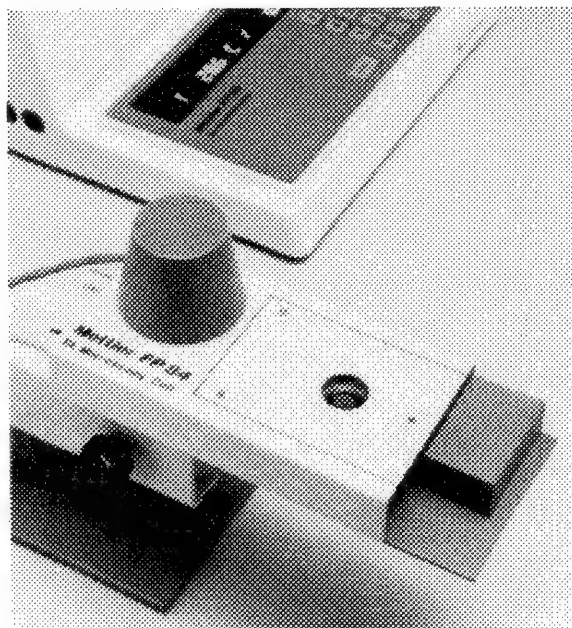
The infrared spectrometer used was a Nicolet 6000 FT-IR. All spectra were recorded at 4cm^{-1} resolution. A Spectratech Plan III IRMA with a $250\mu\text{m}$ MCT detector was used to focus the infrared radiation through the DSC cell. The DSC cell used was a Mettler FP84 thermal analysis microscopy cell. A Mettler FP80 central processor with recorder was used to control the temperature in the FP84 DSC cell. Typical DSC thermograms and infrared spectra could be simultaneously recorded with this combined apparatus. The DSC microscopy cell is shown in Fig. 1. It was placed on the stage of the IRMA. To permit both microscopical observation and transmission infrared spectroscopy, sample cups of potassium bromide were used to hold the sample. For simultaneous optical microscopy and DSC, sapphire sample cups are used.

The combination of temperature program rates in the DSC and spectral collection rates in the FT-IR offers a vast range in which to collect data simultaneously. The collection of spectra at the rate of about one per second thus results in the accumulation of a large number of spectra over a 15-20min DSC experiment. These spectra may be important for full elucidation of the thermal response.

Results and Discussion

The particular application to which the combined DSC/microscopy/FT-IR technique was put in this work was the study of polymer blends.

The authors are with Quantum Chemical Corp., Rolling Meadows, IL 60008.



- | | |
|----------------------------------|--|
| 1 Microscope objective | 6 Microscope light source |
| 2 Sapphire sample crucible | 7 DSC measuring sensor |
| 3 Heat protection filter | 8 Metal plate with heating wires and Pt100 resistance sensor |
| 4 Metal plate with heating wires | |
| 5 Sapphire reference crucible | |

FIG. 1.--Microscopy/DSC cell.

Thermal analysis of polymers is a useful technique for obtaining qualitative and quantitative information. However, the thermal analysis technique is by its nature sometimes not well suited for quantitative analysis of polymers because they lack well-defined melting points or heats of fusion; real polymer crystals are virtually never in thermodynamic equilibrium--they are formed on the basis of kinetic factors during crystallization. However, the situation may be significantly improved by simultaneous recording of the DSC thermogram and the corresponding infrared spectra as a function of temperature.

Specific studies of the interaction of

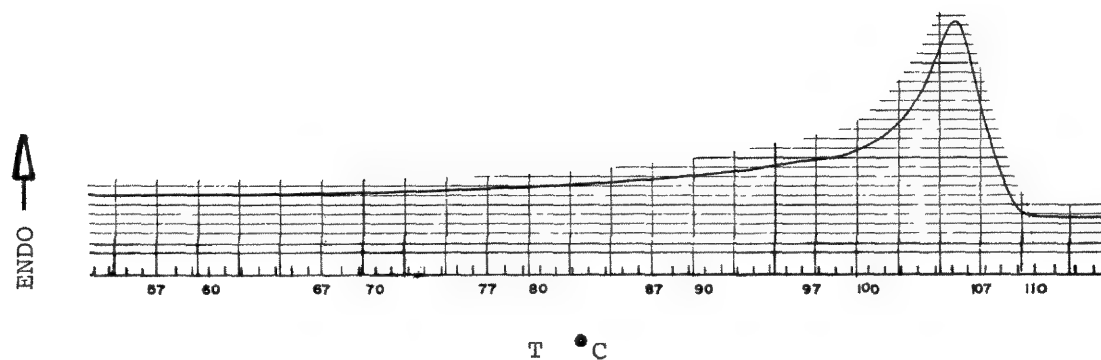


FIG. 2.--DSC thermogram of commercial LDPE resin.

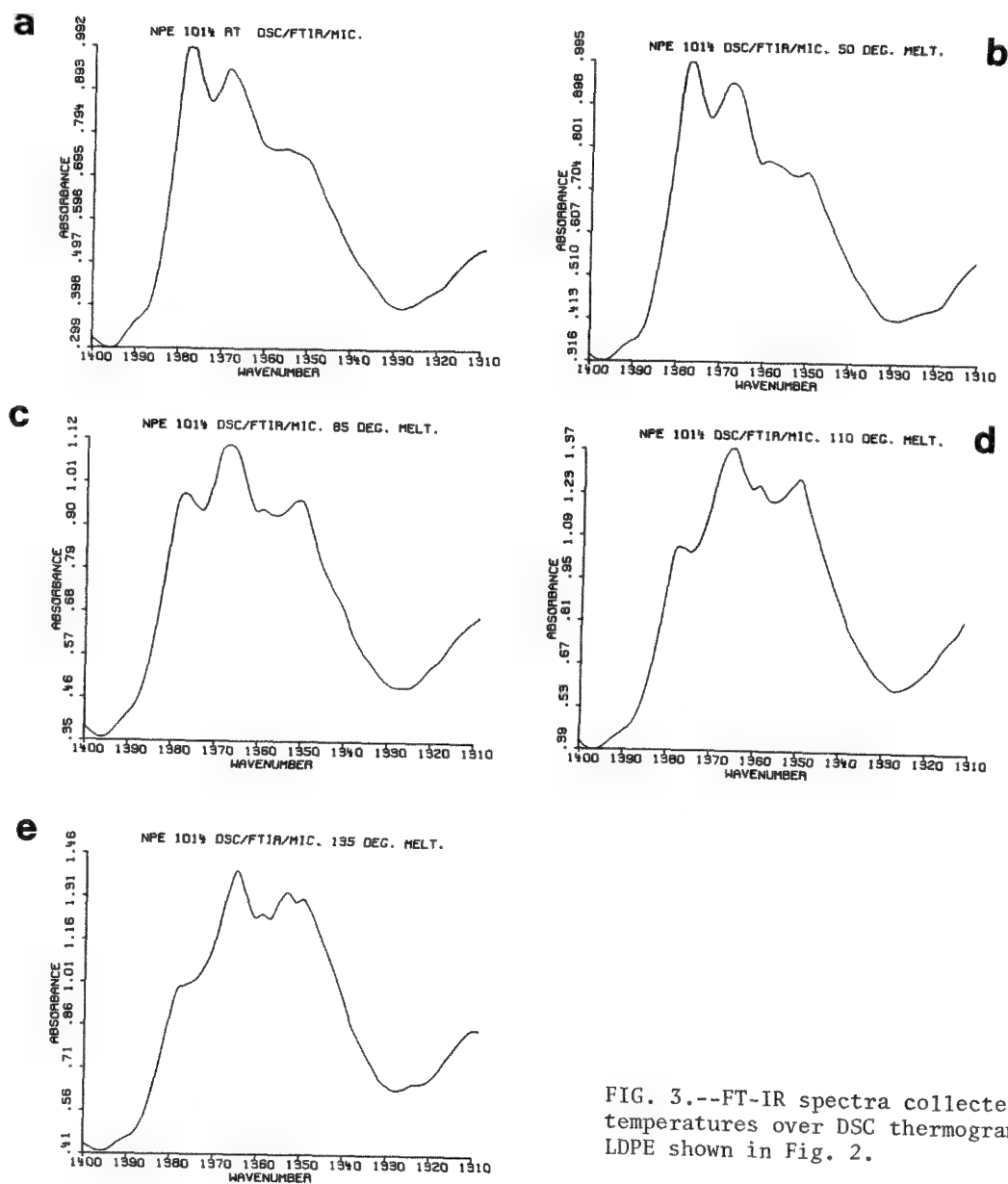


FIG. 3.--FT-IR spectra collected at specified temperatures over DSC thermogram of commercial LDPE shown in Fig. 2.

differing molecular species during crystallization and melting of polymer blends were undertaken. Commercial polyethylenes are a particularly interesting class because these polymers are often modified with comonomer, either by intentional addition of α -olefins or due to reactions that take place during polymerization and lead to short-chain branching. In each case, the resulting copolymers have a broad composition distribution: in low-density and linear-low-density polyethylene (LDPE and LLDPE), from polymer chains with little or no short-chain branching (i.e., comonomer) to chains with much higher than average branching.² One manifestation of this broad copolymer composition distribution is the melting endotherm. The modifying comonomer in the polyethylene chains acts as a crystallinity interrupter; the more comonomer present, the more defects in the crystals and the lower the fraction of crystallinity. This effect causes the melting endotherm of LDPE to be quite broadened toward the low-temperature side (compared to high-density polyethylene, HDPE) due to the presence of a large fraction of increasingly defective crystallites. Thus, LDPE exhibits the melting endotherm shown in Fig. 2. The simultaneous FT-IR spectra collected over this DSC thermogram showed some interesting variations, especially in the region of 1400-1310 cm^{-1} . Figure 3 shows some selected spectra in this spectral region, covering the temperature range of room temperature (RT) to 135 C. The first sign of melting was in the 70-80 C range in Fig. 2 and the spectra exhibited large changes in this range, as evidenced by the spectrum at 85 C in Fig. 3. As the melting endotherm maximum at about 106 C is passed, these variations in the spectra are complete and remain up to 135 C for the completely molten polymer. Inspection of Fig. 3 indicates that the methyl band at 1378 cm^{-1} remains constant in intensity at about 1 absorbance unit, whereas the methylene band at 1368 cm^{-1} grows in intensity from about 0.9 to 1.4 absorbance units. Thus, the ratio of the methyl to methylene band intensities varies from approximately 1 to 0.7 from RT through the melting maximum. A thorough analysis of the simultaneous DSC/FT-IR melting and crystallization thermograms and FT-IR spectra of LDPE and LLDPE (and HDPE for comparison) can yield important information concerning the participation of the several chemical moieties present in polyethylene in each process.

Conclusion

A technique has been demonstrated to study simultaneously the thermal response and infrared spectral changes of specimens of microscopic dimensions. This technique, which was applied to the study of polymer blends, is expected to have a wide range of applications in many areas of science, including chemistry, physics, and biology. Further studies of polymer and other systems are in progress.

References

1. F. M. Mirabella Jr., *Appl. Spectrosc.* 40: 417, 1986.
2. F. M. Mirabella Jr. and E. A. Ford, *J. Polym. Sci.* B25: 777, 1987.

MICRO/NANOSAMPLING INTERNAL REFLECTION FT-IR SPECTROSCOPY

F. J. DeBlase and N. J. Harrick

In order to apply internal reflection spectroscopy to micro- or nanosampling (10^{-6} and 10^{-9} g), close consideration of the parameters that increase spectral contrast and effective thickness is essential. These parameters include the following:

1. Electric field intensity.
2. Number of internal reflections.
3. Internal reflection angle.
4. Polarization of the infrared beam.
5. Refractive index of both the sample and internal reflection prism.

By controlling the depth at which the sample is probed, one can in some cases greatly improve the quality of useful information in the resulting spectrum over that obtained by transmission or external reflection.

This study demonstrates the developments of internal reflection microspectroscopy as an additional sampling technique. A novel configuration of internal reflection element (IRE), focusing optics, and sample presentation has been designed by Harrick and co-workers.¹ It isolates a sensitive small internal reflection element and allows in situ substrate surface analysis as well as the study of small fibers, particles, or defects. The principles associated with its operation and performance along with several applications are discussed.

Experimental

All spectra were recorded on a Mattson Sirius 100 Fourier transform infrared spectrometer equipped with a triglycine sulfate (TGS) pyroelectric detector. The spectrometer was fitted with a nanosampler internal reflection attachment. Eight wavenumber resolution spectra were recorded at mirror velocity of 0.08 cm/s; between 200 and 2000 scans were recorded, depending on the sample. The geometry of the IRE used in this attachment is shown in Fig. 1. It is a ZnSe prism designed for a 45° internal reflection angle and shaped so that the sampling surface is sharpened. In addition there is a movable knife edge which enables the exiting aperture of the element to be closed for the proper masking. Sample positioning is done by means of a special designed XYZ translator, and the sample is viewed through a $60\times$ viewing microscope. A $6\times$, 90° off-axis ellipsoidal condensing reflector focuses the beam on the entrance aperture of the prism (Fig. 2).

Funneling Effect

The internal reflection element is designed

to focus rays displaced from the central ray to the very tip of the element. We tested this funneling effect by continuously taking throughput measurements at the centerburst of the interferogram while moving the masking knife edge in increments from a fully closed position to a fully open one. In Fig. 3, the gain G as a function of mask movement is plotted, where G is

$$G = (dI/dA)/(I_{ob}/A_{ob})$$

where dI/dA is the derivative of the intensity as a function of the unmasked sampling area of the prism, and I_{ob} and A_{ob} are the intensity and cross-sectional area of the open beam at the compartment focus. This curve shows that the gain reaches a value greater than 36 times that expected for a $6\times$ beam condenser alone. In fact, it demonstrates that for areas away from the sharp tip, the gain is less than 36 times but grows as the tip is approached, reaching a maximum at about $G = 60$. This is a considerable gain in intensity for a single reflection prism. Only the gain created by use of a high-refractive-index hemisphere (where $G = 400$) is greater.

Results

Figures 4-7 show the application of the nanosampler attachment to specific analytical problems. The spectrum of inorganic materials occurring as small amounts of fine powder can be deposited on the IRE, and spectrum recorded. The peaks of the kaolinite spectrum (Fig. 4) are well resolved without the reststrahlen effects that occur in diffuse reflectance. A small optical fiber, too thick for transmission, was also studied without any problem (Fig. 5). One application for the study of synthetic fibers of poly(ethylene terephthalate) was to compare the growth of the bands associated with the transconformation of the glycol moiety as a function of increasing take-up-speed (Fig. 6). Finally, the internal reflectance spectra of samples which are even strong absorbers, in the infrared, such as a microdroplet of water or blood, were taken. The amide I and II bands from the protein in the blood are clearly visible in the spectrum.

Conclusions

The sensitivity and versatility of the internal reflection sampling technique applied to microspectroscopy has been demonstrated. Due to the nature of the effective thickness, small samples too thick for transmission are not a problem in internal reflection spectroscopy.² The characterization of polymer micro-

The authors are with Harrick Scientific Corp., 88 Broadway, Ossining, NY 10562.

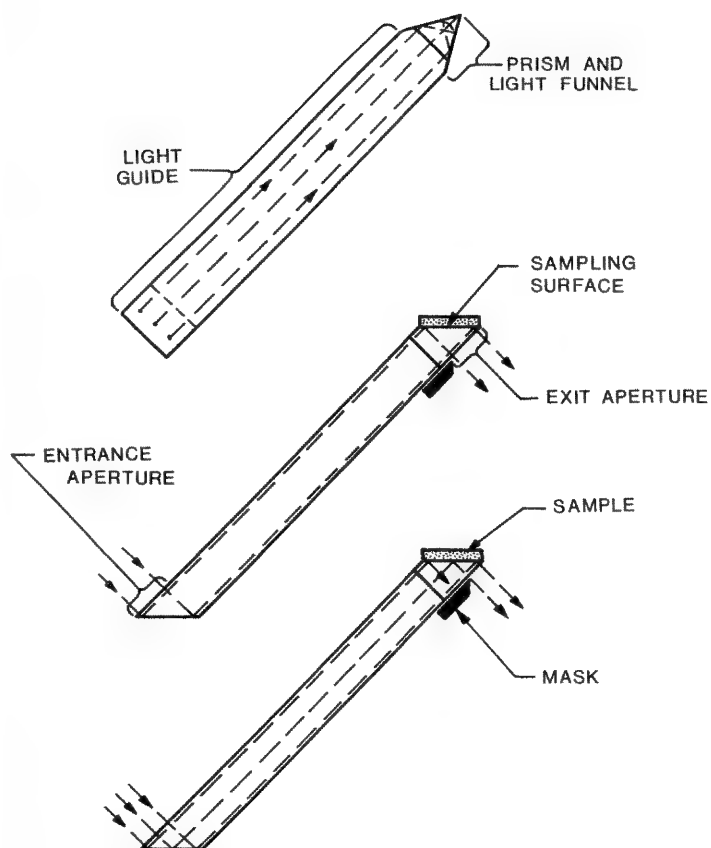


FIG. 1.--Diagram of nanosampling internal reflection element (IRE).

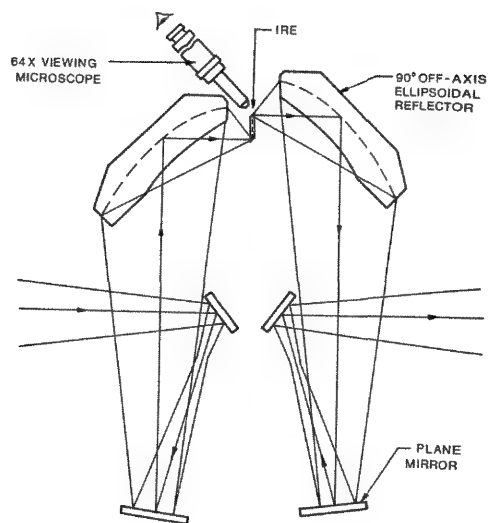


FIG. 2.--Optical diagram of nanosampling internal reflection attachment .

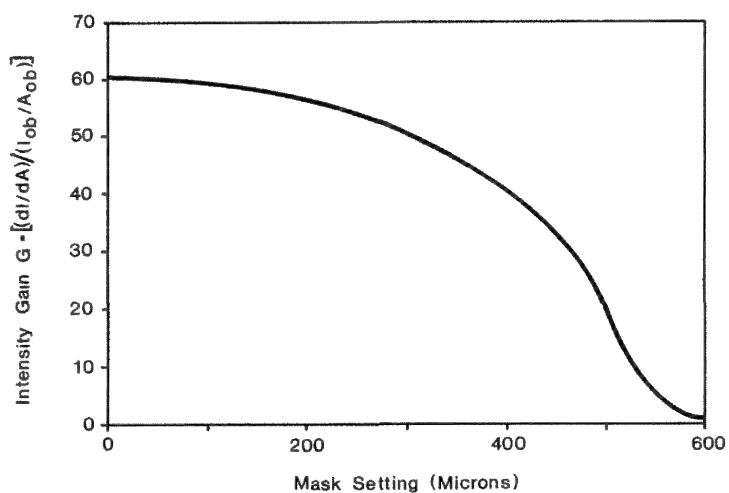


FIG. 3.--Plot of gain G in light intensity as a function of incremental area of sampling surface plotted against exiting aperture mask position from fully closed to open.

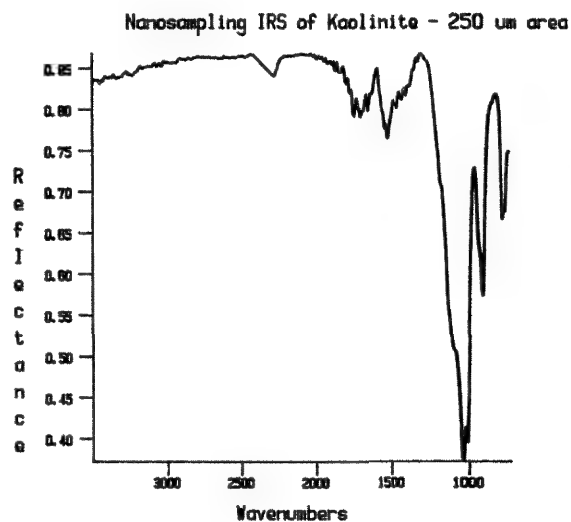


FIG. 4.--Spectrum of 250μm² area of kaolinite powder.

structure from the correlation of features in the vibrational spectrum with other experimental data³ may also lead to additional applications of this technique. Progress with sample handling and in situ analysis will doubtless develop in the future for internal reflection nanosampling.

References

1. N. J. Harrick, "Nanosampling internal reflection spectroscopy," *Appl. Spectrosc.* 41: 1, 1987.
2. F. J. DeBlase, N. J. Harrick, and M. Milosevic, "Nanosampling internal reflection FT-IR study of polymer filaments," *J. Appl. Polym. Sci.* 34: 2047, 1987.
3. F. J. DeBlase, "Conformational change, chain orientation, and crystallinity in poly(ethylene terephthalate) fibers: A Raman study," *Macromolecules* 18: 2587, 1985.

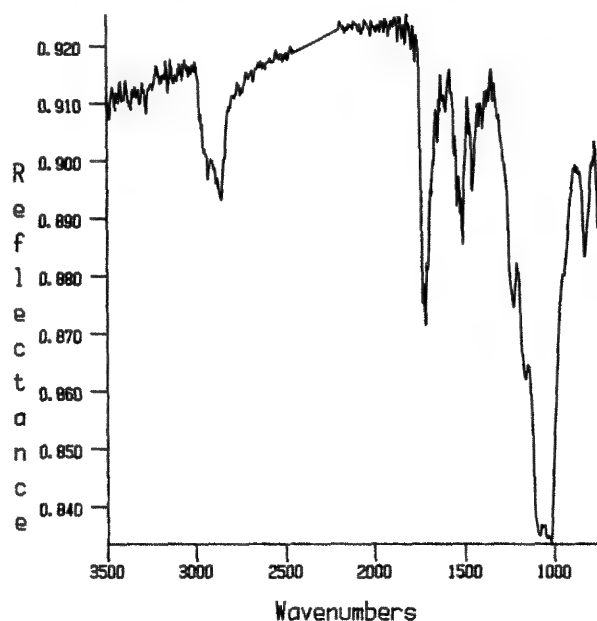


FIG. 5.--Spectrum of a 250 μ m-diameter acrylic coated optical fiber.

FIG. 6.--Spectra of series of 25 μ m filaments of poly(ethylene terephthalate) processed at increasing take-up speeds from 3.5 to 5.5 km/min. Note changes at 845 and 975 wavenumbers.

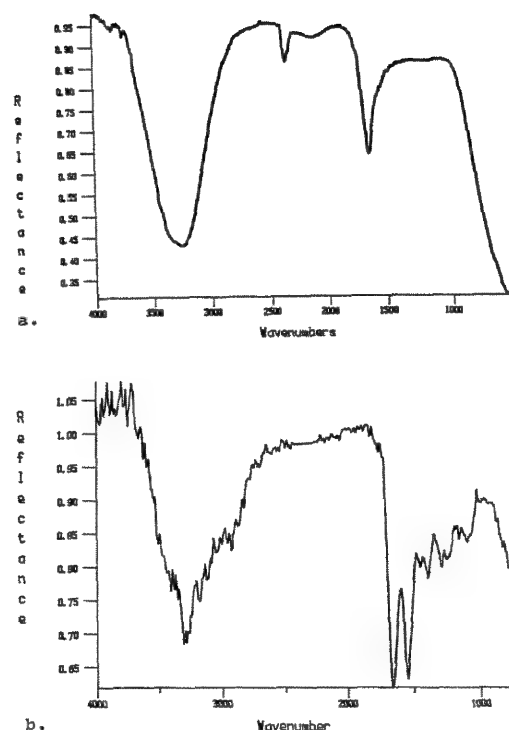
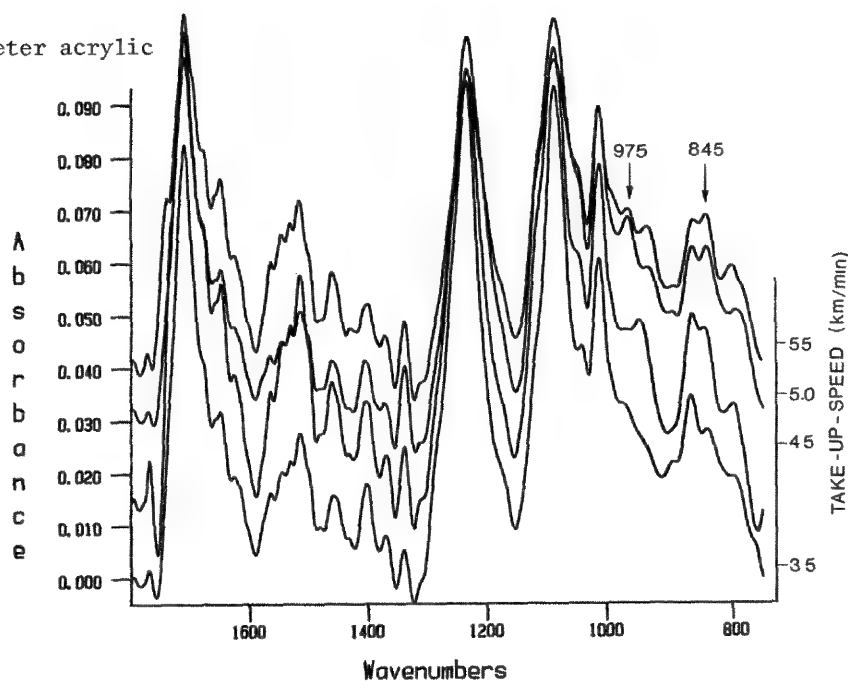


FIG. 7.--Spectrum of (a) drop of water placed on prism, (b) very thin film of type 0 blood on tip of prism.

J. T. Armstrong

enabled analyses of much higher precision than previously possible. However, some investigators appear to have confused this improved precision with improved accuracy. Conventional ZAF correction procedures produce systematic errors in the analysis of silicate materials, particularly when standards of greatly different composition (such as simple oxides) are employed.¹ Recent attempts to refine quantitative analysis correction procedures have generally involved comparison with data sets of metal alloy analyses rather than analyses of materials similar to those commonly encountered in geological applications. As a result, some of the newer correction algorithms produce poorer results in the analysis of silicate and oxide minerals than some of the earlier corrections. In the present study, data sets of analyses of silicate and oxide standards are compared with series of ZAF and $\phi(\rho z)$

Bast-I	---	GOScfh
Bast-II	---	HOScfh
Riveros	---	IOSafi
MCms-GC	---	JQSaj
MCms-WT	---	JQSak
MCms-Hu	---	JQSal
MCms-Gz	---	JQSam
MCms-Fa	---	JQSan

correction procedures as well as with recent Monte Carlo calculations.

Correction Procedures Tested

The correction procedures and parameters evaluated in this study are listed in Table 1. In a companion paper, the accuracy of α -factor correction procedures is evaluated.² Typically, the largest correction in the analysis of silicates and oxides is that for primary absorption. The various absorption corrections examined³⁻¹¹ employ different assumptions regarding the distribution with depth of the primary x-ray production.¹² The conventional Philibert correction assumes an exponential distribution with depth and no x-ray production at the surface. The Heinrich correction uses a quadratic equation to fit the absorption parameter $f(\chi)$. The Love-Scott correction assumes constant production from the surface to a mean depth and no production below that (the so-called box model). The Sewell-Love-Scott correction fits measured $\phi(\rho z)$ curves to a quadratic model. The remaining corrections, the so-called $\phi(\rho z)$ corrections, employ a Gaussian equation to express the depth distribution of primary x-ray production:

$$\phi(\rho z) = \quad (1)$$

$$\gamma_0 \exp[-\alpha^2(\rho z)^2] [1 - \{(\gamma_0 - \phi(0))/\gamma_0\} \exp(-\beta \rho z)]$$

Equations of this form have been shown to fit well experimentally determined $\phi(\rho z)$ distributions. The various Gaussian corrections employ different equations to express α , β , and γ_0 . The original model proposed by Packwood and Brown⁷ was parameterized on the basis of a simple physical model and some fitting to the measured $\phi(\rho z)$ curves. The subsequent models were more or less altered to better fit analytical data; those of Bastin et al.^{9,10} are heavily parameterized to fit binary metal alloy data; that of Armstrong⁸ makes minor adjustments to the Packwood and Brown expressions to optimize silicate and oxide analyses.

Atomic number corrections tested include the conventional Duncumb and Reed¹³ and Philibert and Tixter¹⁴ corrections, as well as the Monte Carlo calculation-based Love and Scott¹⁵ correction. In typical silicate analyses, the magnitude of the atomic-number correction is not great and these three corrections give similar results. The other atomic-number corrections examined are those based on integration of the Gaussian $\phi(\rho z)$ expressions:

$$I_p = \int_0^\infty \phi(\rho z) d(\rho z) \quad (2)$$

This author urges caution in the use of the Gaussian $\phi(\rho z)$ expressions for atomic-number corrections. Use of these expressions for the absorption correction requires only that the shapes of the curves be correct, not their absolute magnitudes. Use of them for the atomic-number correction, however, requires correct proportionality between the total integrals of

$\phi(\rho z)$ curves from different matrices. In experimental terms, this means that the thicknesses of the tracer films and the normalizing thin films used in the $\phi(\rho z)$ experiments for different matrices must be known with a high degree of accuracy--a difficult restriction, particularly when results from different investigators are compared. In addition, virtually no work has been done in determining experimental $\phi(\rho z)$ curves for multielement specimens; the atomic-number dependence is calculated strictly by comparison of different combinations of tracers and pure elements.

Monte Carlo calculations of electron trajectories were performed based on both multiple-scattering and single-scattering models to calculate $\phi(\rho z)$ distributions. These $\phi(\rho z)$ distributions were then used to calculate both absorption and atomic-number corrections. The programs employed were modifications of the programs created by Joy.¹⁶ The details of the algorithms used in these calculations are given in a companion paper.² Unlike for the Gaussian $\phi(\rho z)$ corrections, there is no a priori reason that the Monte Carlo calculations might be suspect for use in a combined absorption and atomic-number correction.

The characteristic fluorescence corrections considered include the conventional correction of Reed¹⁷ and the integral $\phi(\rho z)$ expression of Armstrong and Buseck.¹⁸ Evaluation of the commonly used correction of Reed shows that some of the approximations (made with metal analyses in mind) are inappropriate for silicates. Reed assumed that the absorption-edge jump ratio factor $(1 - r)/r$, was constant with a value of 0.88 for K-lines and 0.75 for L-lines. The jump ratio is actually a regularly variable function of Z as seen in Fig. 1 for K-lines (based on the mass absorption coefficient data of Heinrich¹⁹). The jump ratio factor is underestimated by about 10% for Mg, Al, or Si, which means that the fluorescence correction calculated for these elements is also underestimated from this factor by about 10%. Similarly, the L-line jump ratio factor for $Z = 30$ is about 0.875 instead of 0.75, which results in underestimation of fluorescence by a factor of over 10%. The jump ratios for K- and L-lines can be accurately expressed by the equations:

$$r_K = 53.46Z - 18.01 \quad (3)$$

$$(r_L - 1)/r_L = 0.9548 - 0.0026Z \quad (4)$$

In the ZAF corrections given in this paper, these equations have been used in the Reed correction.

Other simplifications in the Reed equation results in underestimation of light element fluorescence. Both Monte Carlo calculations and experimental measurements of the relative intensities of a series of pure element and compound standards made at 15 and 20 keV (Fig. 2) suggest that the Green and Cosslett²⁰ expression for the relative number of inner-shell ionizations per atom of elements A and

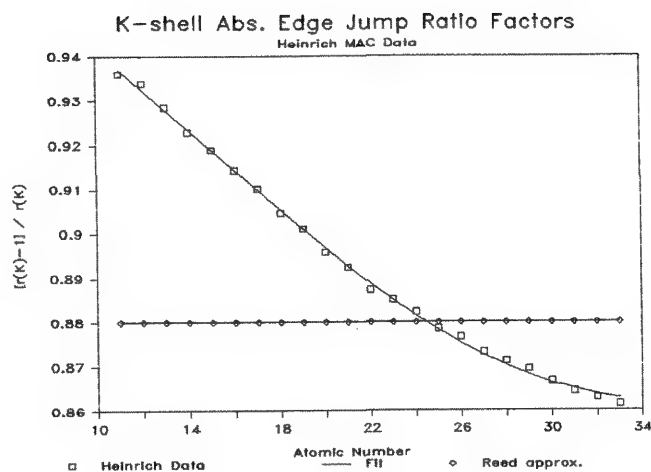


FIG. 1.--Plot of K-line absorption edge jump factor vs atomic number based on Heinrich's mass absorption coefficient data.

B as a function of the overvoltage

$$U_A = E / E_{C,A},$$

$$I_B''/I_A'' = (U_B - 1)^{1.67} / (U_A - 1)^{1.67} \quad (5)$$

significantly overestimates the difference when the two overvoltages are large and similar. The new data suggest the following alternative equations:

$$I_B''/I_A'' = (U_B - 1)^{1.59} / (U_A - 1)^{1.59} \quad (6)$$

for $(U_B - 1) / (U_A - 1) < 2/3$ and

$$I_B''/I_A'' = 1.87(U_B - 1)^{3.19} / (U_A - 1)^{3.19} \quad (7)$$

for $(U_B - 1) / (U_A - 1) > 2/3$. For elements like Mg, Al and Si at 15 keV, the new data suggest that the conventional Green/Cosslett expression underestimates the amount of fluorescence by another 10%. Finally, the data of Armstrong and Buseck¹⁸ suggest that the simple $\phi(\rho z)$ model employed by Reed underestimated the magnitude of emitted fluorescence radiation in silicates by still another 10%. In all, the magnitude of characteristic fluorescence of the major light elements in silicates may be underestimated in the Reed correction by a factor as large as 30-40% relative. Even though the absolute value of the fluorescence correction in silicates is low (typically <4%), an error of this magnitude can be of some significance.

Most ZAF correction programs do not correct for fluorescence due to the continuum, in large part due to the complexity of the correction equations. In this study, the continuum fluorescence correction of Henoc et al.²² was calculated for selected specimens to evaluate its significance. For elements lower in energy than Ti K α , the correction in typical silicates and oxides is negligible (<0.2% relative) for $E_0 = 10-20$ keV. For higher-energy lines, the

correction can start to become significant. For example, when one analyzes for Fe in $Mg_{1.85}Fe_{0.16}SiO_4$ using Fe in Fe_2SiO_4 as a standard, the magnitude of the characteristic fluorescence correction is 1.5% at 20 keV, 1.8% at 15 keV, and 2.2% at 10 keV (for $\psi = 40^\circ$).

The parameters used in the ZAF corrections can be as important as the corrections themselves. In the atomic-number correction and Monte Carlo calculation, and important parameter is the mean ionization potential. The expressions of Berger and Seltzer, Duncumb and Da Casa, Ruste, and Springer were tested and significant differences were found in the results depending on the expression used. (A comparison of the algorithms with the original references can be found in Heinrich.²³) Duncumb and Da Casa developed their expression specifically to optimize experimental results using the Duncumb-Reed atomic-number correction; the expression should be probably employed only for that correction. The authors of the other atomic-number corrections generally stated a preference in the mean ionization potential to be used; those preferences were adhered to in this evaluation.

The Gaussian $\phi(\rho z)$ and Love-Scott and Sewell-Love-Scott corrections make use of backscatter coefficients and $\phi(0)$ expressions. The various versions tested are given in Table 1. Variation of these parameters typically does not significantly affect the absorption or atomic number corrections and the preferences of the various authors of the corrections were adhered to. In the Monte Carlo calculations, a critical parameter is the ionization cross section $Q(E)$. Expressions evaluated were those of Green and Cosslett, Worthington and Tomlin, Hutchins, Gryzinski, and Fabre as tabulated and referenced by Powell.²⁷ Significant differences were seen in the results depending on the $Q(E)$ and, as seen below, the data suggest that optimal $Q(E)$ expressions can be chosen for silicates. Finally, the tabulated mass absorption coefficients of Heinrich¹⁹ were used in the comparisons.

Measurements

Replicate analyses of a large series of oxide and silicate natural and synthetic mineral standards were performed on a five-crystal spectrometer JEOL 733 electron microprobe (take-off angle = 40°) at 10, 15, and 20 keV. Space does not permit inclusion of all of the data. Table 2 lists the compositions of selected primary and secondary standards used in this study. The accuracy of the accelerating potential was determined by careful EDS determination of the Duane Hunt limit. The absence of sample tilt effects was determined by the performance of replicate analyses with the samples rotated in different orientations. Samples were repolished, recoated, and reanalyzed to determine that there were no charging or surface-hydration artifacts. Correct background settings were determined by analysis of

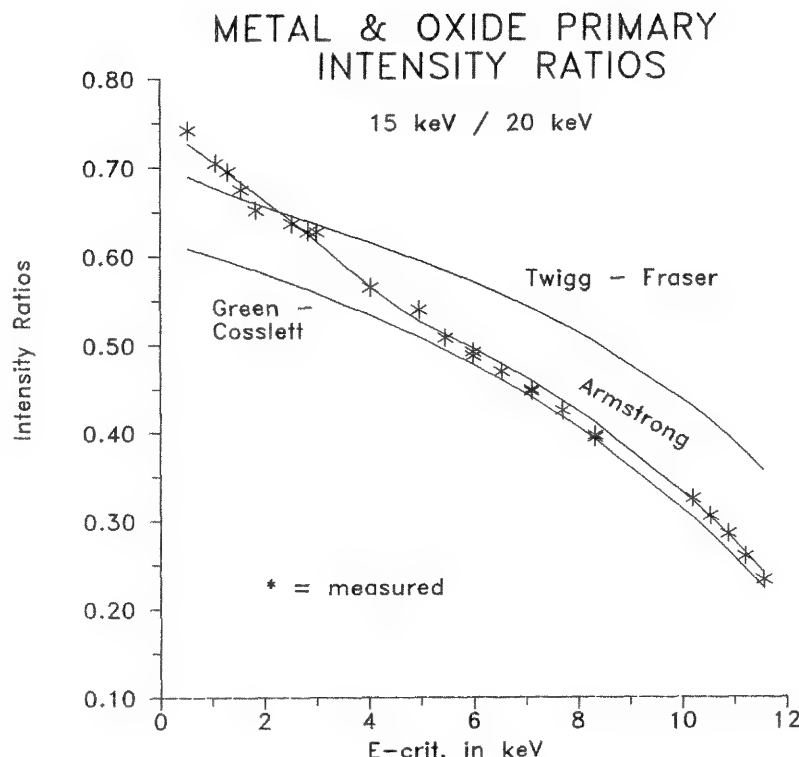


FIG. 2.--Plot of ratio of metal and oxide beam-normalized intensities (corrected for absorption) at 15 keV to those measured at 20 keV vs critical excitation potential. For high E_c , data approach equation of Green and Cosslett;²⁰ for low E_c equation of Twigg and Fraser.²¹ Equations (6) and (7) do better job of fitting data than either of above expressions.

"blank" standards, and deviations from zero background were less than 100 ppm. Deadtime was measured periodically on all spectrometers and determined reproducibly to 0.1 μ sec. Gain-shift artifacts were avoided as the output pulse energy for all elements was kept at 3 ± 0.08 V. Replicate analyses were performed at various beam currents (10-60 nA) to confirm that there were no artifacts due to counting nonlinearities or radiation damage.

Measurements were typically taken to a relative precision of 0.2%; only samples that appeared to be homogeneous at that level were considered. Effects of wavelength shift or peak shape changes for light elements were determined by repetitive high-precision wavelength scanning and peak integration. Small differences in the energy splitting between the $K\alpha_1$ and $K\alpha_2$ lines can result in significant differences in the ratio of the peak maximum to the net peak area for elements like Al and Si. The peak integration measurements made on the analyzed standards indicated that the maximum variation due to peak shape change was at or below the 1% relative level.

Elements were analyzed simultaneously with the same type of crystals on different spectrometers to check for geometry or crystal problems. Surprisingly, significant (1 to 2%) differences in k-ratios of sample to standard were detected for simultaneous analysis of Na, Mg, Al, and Si $K\alpha$ on three TAP-crystal spectrometers, and up to 5% differences were measured for Cu $L\alpha$ in Cu and 80% Au-20% Cu alloy. These differences follow the crystal when it is moved from one spectrometer to another. The measured values for a series of tested TAP crystals are almost bimodal, and the data given in this paper are from the most numerous set of crystals, the set that appears to agree most

closely with measurements made on other instruments. (The reason for this variability in crystal response is still under active investigation.)

Selected results of the analyses are given in Tables 3 to 5 and shown in Figs. 3 to 5. Tables 3 to 5 compare the analytical results with those calculated by the various Monte Carlo, ZAF, and $\phi(\rho z)$ corrections. The data are presented as the ratio of concentration relative to the standard divided by the intensity relative to the standard; i.e., $(C/K)_{\text{sample}}/(C/K)_{\text{standard}}$. The measured data for Fe and Ni has been back-corrected for fluorescence by the continuum, by use of the correction of Henoc et al.²² As can be seen in the tables, there is a significant difference in the accuracy of the different correction procedures; the mean error for the corrections tested varies by over a factor of 5. At 15 keV, the corrections that agree best with the experimental data are the Armstrong-Duncumb/Reed, Armstrong-Love/Scott, and Love-Scott corrections, with mean relative errors of 0.5-0.6%. Next best are the Philibert-Duncumb/Reed ZAF correction and the Monte Carlo multiple scattering corrections with the Hutchins, Fabre, and Gryzinski $Q(E)$ expressions, which have mean relative errors of 0.8 to 0.9%. Following them are the Sewell-Love/Scott, NBS COR2 (Philibert-Philibert/Tixier), and Monte Carlo-Green/Cosslett expressions with mean relative errors of 1.1-1.3%. Trailing the list are the $\phi(\rho z)$ corrections of Packwood and Brown, Bastin (I and II), and the Riveros and the Monte Carlo-Worthington/Tomlin expression with mean relative errors of 1.5-2.5%. The data shows that several of the corrections diverge from the measured data in higher-Z matrices.

TABLE 2.--Compositions of analyzed standards.

A. Primary standards (oxide wt %)

Elem	Std	MgO	Al2O3	SiO2	CaO	MnO	FeO	NiO	Total
Mg	MgO	100.0							100.0
Al	Kyan		62.78	37.07			0.13		100.0
Si	Qtz			100.0					100.0
Ca	Wo	0.04	0.08	51.69	48.17		0.02		100.0
Fe	Fa			29.49			70.51		100.0
Ni	NiO							100.0	100.0

B. Secondary standards (oxide wt %)

Std	MgO	Al2O3	SiO2	CaO	MnO	FeO	NiO	Total
Cor		100.0						100.0
Mel	14.79		44.08	41.13			0.01	100.0
Anor		36.65	43.19	20.16				100.0
Gros		22.63	40.02	37.35				100.0
Fo	57.30		42.70					100.0
Oliv	51.63		40.85		0.07	7.23	0.30	100.1
NiOl			28.68				71.32	100.0

TABLE 3.--Analytical results at 15 keV: (C/K)_{smp}/(C/K)_{std}.

	Mg in		Al in		Si in					
	Fo	Oliv	Me	Cor	Anor	Gros	Wo	Me	Gros	Anor
Measured:	1.044	1.119	1.179	0.981	1.047	1.058	1.026	1.080	1.114	1.172
Correction										
MCms-Hu			1.173	0.990	1.031		1.026	1.080		1.183
MCms-Fa			1.177	0.990	1.032		1.026	1.082		1.186
MCms-Gz			1.180	0.990	1.032		1.027	1.082		1.187
MCms-GC			1.183	0.990	1.033		1.028	1.085		1.194
MCms-WT			1.188	0.989	1.034		1.030	1.088		1.199
Phil-DR	1.047	1.122	1.178	0.987	1.034	1.060	1.027	1.084	1.127	1.186
NBS-COR			1.194	0.988	1.040		1.039	1.095		1.191
Love-Sc	1.045	1.119	1.168	0.989	1.029	1.052	1.022	1.076	1.117	1.176
Sewl-LS	1.043	1.113	1.157	0.990	1.027	1.048	1.019	1.073	1.113	1.173
Arms-LS	1.044	1.119	1.172	0.990	1.031	1.055	1.026	1.078	1.118	1.173
Arms-DR	1.044	1.119	1.176	0.989	1.031	1.057	1.025	1.078	1.118	1.173
Pack-Br	1.042	1.106	1.140	0.990	1.018	1.031	0.995	1.050	1.090	1.153
Bast- I	1.044	1.120	1.157	0.995	1.018	1.033	1.003	1.062	1.109	1.179
Bast-II	1.044	1.118	1.150	0.995	1.016	1.028	0.998	1.058	1.105	1.176
Riveros	1.041	1.104	1.139	0.990	1.020	1.036	1.005	1.060	1.100	1.163

	Si in		Ca in		Fe in		Ni in			
	Fa	Oliv	Fo	Kyan	NiOl	Me	Gros	An	Oliv	NiOl
Measured:	1.202	1.232	1.230	1.284	1.297	1.002	1.005	1.015	1.077	1.050
Correction										
MCms-Hu	1.207			1.313		1.002		1.014		
MCms-Fa	1.212			1.318		1.002		1.015		
MCms-Gz	1.214			1.320		1.002		1.015		
MCms-GC	1.223			1.331		1.002		1.015		
MCms-WT	1.231			1.340		1.002		1.015		
Phil-DR	1.200	1.248	1.249	1.308	1.315	1.003	1.004	1.016	1.070	1.035
NBS-COR	1.231			1.307		1.003		1.014		
Love-Sc	1.194	1.236	1.237	1.298	1.301	1.004	1.005	1.017	1.085	1.041
Sewl-LS	1.163	1.234	1.237	1.297	1.244	1.004	1.005	1.019	1.086	1.041
Arms-LS	1.214	1.232	1.229	1.288	1.328	1.004	1.004	1.017	1.084	1.040
Arms-DR	1.207	1.230	1.229	1.288	1.319	1.003	1.004	1.014	1.069	1.035
Pack-Br	1.133	1.213	1.219	1.274	1.232	1.008	1.010	1.032	1.124	1.068
Bast- I	1.199	1.244	1.245	1.315	1.257	1.008	1.015	1.039	1.087	1.055
Bast-II	1.189	1.242	1.244	1.314	1.286	1.008	1.015	1.039	1.084	1.046
Riveros	1.139	1.222	1.231	1.286	1.234	1.005	1.007	1.022	1.086	1.032

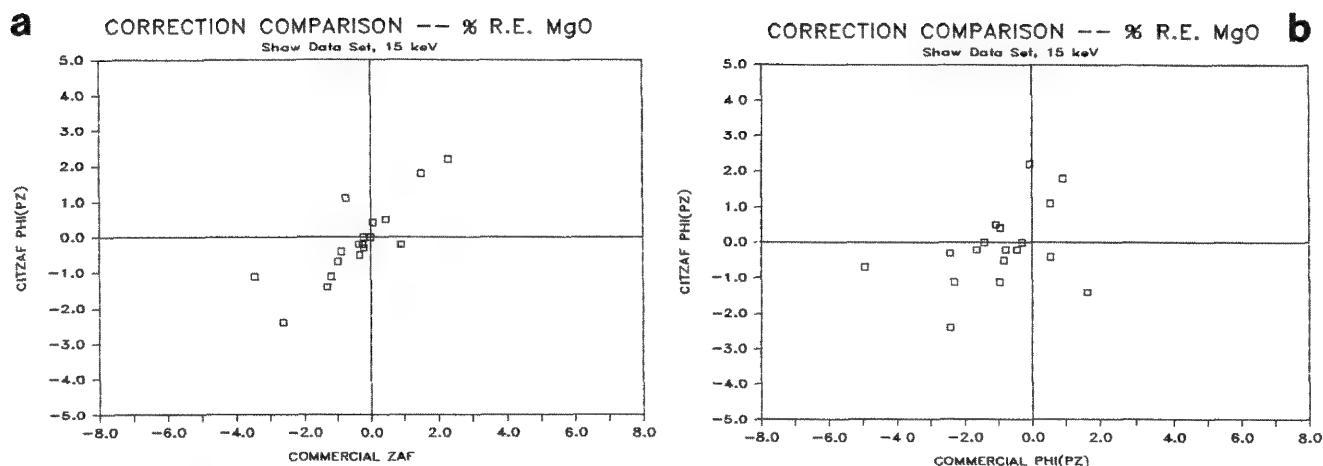


FIG. 3.--Plot of percentage relative errors for MgO in set of standard silicates and oxides based on Armstrong/Love-Scott correction procedure, CITZAF $\phi(\rho z)$, vs that based on (a) commercial ZAF program, (b) commercial $\phi(\rho z)$ program.

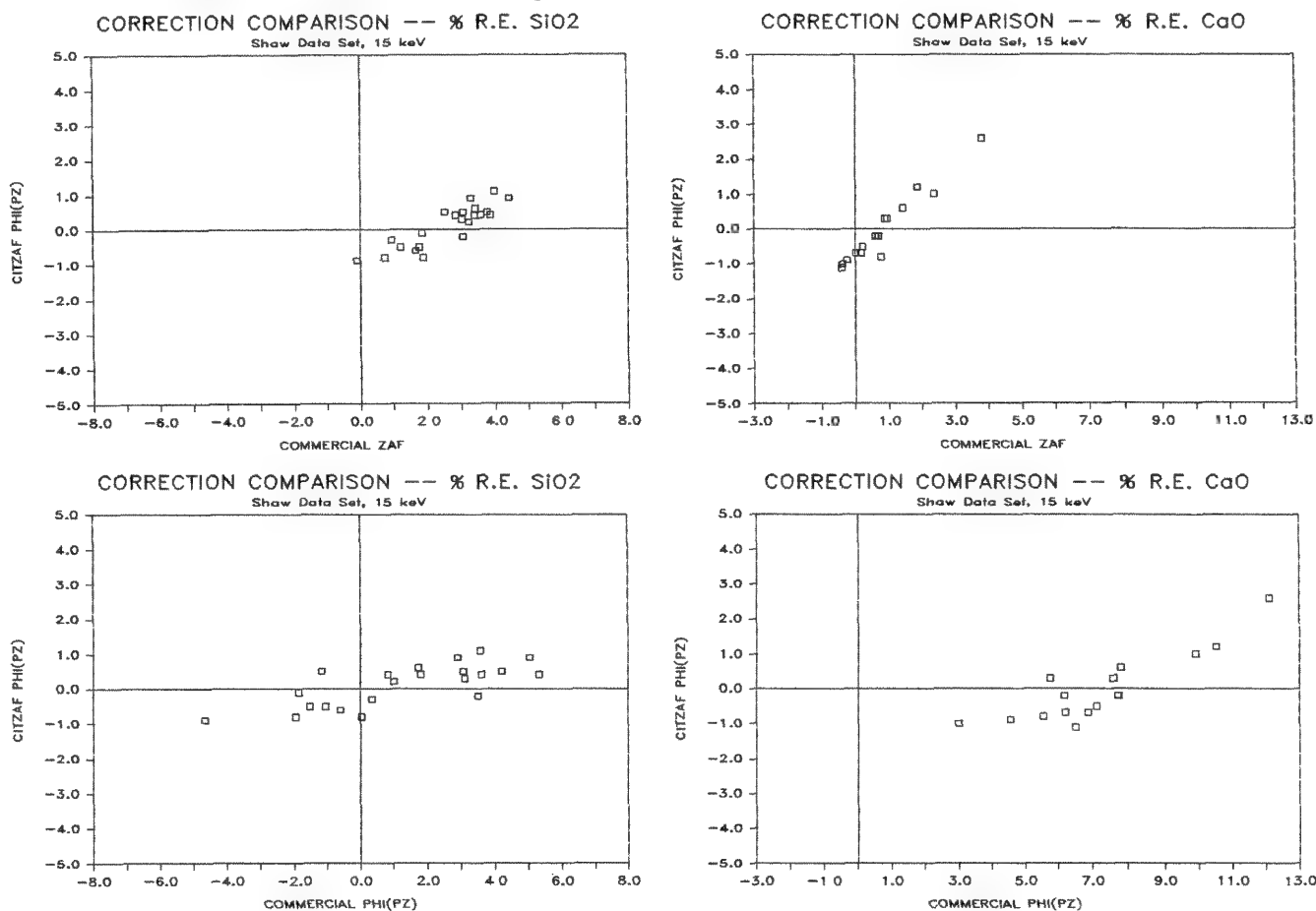


FIG. 4.--Same as Fig. 3, for SiO₂.

FIG. 5.--Same as Fig. 3, for CaO.

Figures 3 to 5 show the difference in mean percentage relative errors in the analyses of a series of Mg-Ca-Al-silicate standards processed with the Armstrong-Love/Scott correction and two commercial correction programs, one conventional ZAF and other $\phi(\rho z)$. The errors are much smaller for the Armstrong-Love/Scott correction than for either of the commercial programs. Indeed, the commercial programs perform worse than our evaluation of the

equations on which they are based, suggesting that some compromising parameterization has been used in these programs.

Conclusions

There are significant differences in the ability of the several ZAF, $\phi(\rho z)$, and Monte Carlo programs properly to correct analyses of silicate and oxide minerals. The corrections that appear to work best at present are the

TABLE 4.--Analytical results at 10 keV: (C/K)_{smp}/(C/K)_{std}.

	Mg in -- Al in --				Si in -----				Ca in --	
	Me	Cor	Anor	Wo	Me	Anor	Fa	Kyan	Me	Anor
Measured:	1.090	0.986	1.039	0.999	1.025	1.066	1.054	1.134	1.008	1.012
Correction										
Phil-DR	1.088	0.992	1.015	1.004	1.036	1.091	1.067	1.156	1.003	1.012
Love-Sc	1.074	0.994	1.011	0.997	1.024	1.074	1.044	1.133	1.004	1.014
Sewl-LS	1.066	0.994	1.009	0.994	1.023	1.075	1.011	1.138	1.004	1.016
Arms-LS	1.080	0.994	1.012	0.999	1.027	1.077	1.059	1.136	1.004	1.015
Arms-DR	1.078	0.994	1.012	1.001	1.029	1.078	1.060	1.135	1.003	1.011
Pack-Br	1.054	0.994	1.001	0.973	1.004	1.063	0.996	1.130	1.007	1.025
Bast- I	1.060	1.001	0.998	0.978	1.010	1.079	1.047	1.154	1.008	1.033
Bast-II	1.056	1.001	0.997	0.975	1.008	1.077	1.044	1.154	1.008	1.032
Riveros	1.060	0.994	1.005	0.987	1.017	1.072	1.015	1.137	1.004	1.014

TABLE 5.--Analytical results at 20 keV: (C/K)_{smp}/(C/K)_{std}.

	Mg in -- Al in --				Si in -----				Ca in --	
	Me	Cor	Anor	Wo	Me	Anor	Fa	Kyan	Me	Anor
Measured:	1.283	0.976	1.056	1.052	1.140	1.304	1.341	1.482	1.005	1.028
Correction										
Phil-DR	1.262	0.981	1.052	1.057	1.142	1.294	1.365	1.478	1.004	1.023
Love-Sc	1.271	0.983	1.050	1.051	1.138	1.304	1.377	1.510	1.004	1.024
Sewl-LS	1.259	0.984	1.047	1.046	1.132	1.296	1.342	1.502	1.005	1.026
Arms-LS	1.271	0.984	1.051	1.054	1.137	1.288	1.400	1.474	1.004	1.022
Arms-DR	1.275	0.984	1.052	1.058	1.140	1.290	1.405	1.474	1.004	1.020
Pack-Br	1.234	0.985	1.037	1.022	1.104	1.261	1.299	1.450	1.008	1.039
Bast- I	1.261	0.989	1.039	1.033	1.123	1.299	1.383	1.513	1.009	1.046
Bast-II	1.236	0.989	1.036	1.026	1.117	1.295	1.366	1.512	1.009	1.047
Riveros	1.224	0.985	1.037	1.028	1.112	1.271	1.290	1.465	1.008	1.031

Armstrong-Duncumb/Reed, Armstrong-Love/Scott, and Love/Scott corrections. Those that work worst are a series of $\phi(\rho z)$ expressions optimized for metal analyses, at least when they are used for both the absorption and atomic-number corrections. A simple Monte Carlo multiple scattering model works well in correcting for absorption and atomic-number effects in silicates (when the ionization cross section expressions of Fabre, Gryzinski, or Hutchins are employed), although not quite as well as the best ZAF or $\phi(\rho z)$ corrections.

The characteristic fluorescence correction of Reed significantly underestimates the amount of fluorescence produced in the lighter elements in silicates, although the magnitude of the error is usually not significant, since the amount of actual fluorescence is still small. The Reed equation can be easily modified to correct most of the underestimation. Finally, although the amount of fluorescence by the continuum of lines of energy less than that for Ti K α is negligible in most silicates, the continuum fluorescence correction can be significant for the higher energy lines, such as Fe and Ni K α , and should be evaluated.

References

1. J. T. Armstrong, "Quantitative analysis of silicate and oxide minerals: A reevaluation of ZAF corrections and proposal for new Bence-

Albee coefficients," *Microbeam Analysis--1984*, 208.

2. J. T. Armstrong, "Bence-Albee after 20 years: Review of the accuracy of α -factor correction procedures for silicate and oxide minerals," this volume.

3. J. Philibert, "A method for calculating the absorption correction in electron microprobe microanalysis," *Proc. 3rd ICXOM*, 1963, 379.

4. K. F. J. Heinrich and H. Yakowitz, *Analyt. Chem.* 47: 2408, 1975.

5. G. Love and V. D. Scott, "Evaluation of a new correction procedure for quantitative electron probe microanalysis," *J. Phys.* D11: 1369, 1978.

6. D. A. Sewell, G. Love, and V. D. Scott, "Universal correction procedure for electron-probe microanalysis," *J. Phys.* D18: 1233, 1985.

7. R. H. Packwood and J. D. Brown, "A Gaussian expression to describe $\phi(\rho z)$ curves for quantitative electron probe microanalysis," *X-ray Spectrometry* 10: 138, 1981.

8. J. T. Armstrong, "New ZAF and α -factor correction procedures for the quantitative analysis of individual microparticles," *Microbeam Analysis--1982*, 175.

9. G. F. Bastin, F. J. J. van Loo, and H. J. M. Heijligers, "An evaluation of the use of Gaussian $\phi(\rho z)$ curves in quantitative electron probe microanalysis," *X-ray Spectrometry*

13: 91, 1984.

10. G. F. Bastin, H. J. M. Heijligers, and F. J. J. van Loo, "A further improvement in the Gaussian $\phi(\rho z)$ approach for matrix correction in quantitative electron probe microanalysis," *Scanning* 8: 45, 1986.

11. J. H. Tirira Saá, M. A. del Giorgia, and J. A. Riveros, "Assessment of the Gaussian $\phi(\rho z)$ curves in quantitative electron microanalysis without optimization of the parameters," *X-ray Spectrometry* 16: 243, 1987.

12. R. H. Packwood, J. D. Brown, and Guy Remond, " $\phi(\rho z)$," *Microbeam Analysis--1983*, 89.

13. P. Duncumb and S. J. B. Reed, "The calculation of stopping power and backscatter effects in electron probe microanalysis," in K. F. J. Heinrich, Ed., *Quantitative Electron Probe Microanalysis*, Washington, D.C.: National Bureau of Standards Spec. Publ. 298, 1968, 133.

14. J. Philibert and R. Tixier, "Electron penetration and the atomic number correction in electron probe microanalysis," *J. Phys.* D1: 685, 1968.

15. G. Love, M. G. Cox, and V. D. Scott, "A versatile atomic number correction for electron-probe microanalysis," *J. Phys.* D11: 7, 1978.

16. D. C. Joy, "Beam interactions, contrast, and resolution in the SEM," *J. Microsc.* 136: 241, 1984; D. C. Joy, "A Monte Carlo simulation for analytical electron microscopy," *Proc. 40th Ann. Meet. EMSA*, 1982, 98.

17. S. J. B. Reed, "Characteristic fluorescence correction in electron-probe microanalysis," *Brit. J. Appl. Phys.* 16: 913, 1965.

18. J. T. Armstrong and P. R. Buseck, "A general characteristic fluorescence correction for the quantitative electron microbeam analysis of thick specimens, thin films and particles," *X-ray Spectrometry* 14: 172, 1985.

19. K. F. J. Heinrich, "X-ray absorption uncertainty," in T. D. McKinley, K. F. J. Heinrich, and D. B. Wittry, Eds., *The Electron Microprobe*, New York: Wiley, 1966, 296.

20. M. Green and V. E. Cosslett, "Measurements of K, L and M shell x-ray production efficiencies," *J. Phys.* D1: 425, 1968.

21. M. E. Twigg and H. L. Fraser, "A comparison of two models for the characteristic x-ray fluorescence correction in thin foil analysis," *Microbeam Analysis--1982*, 37.

22. J. Henoc, K. F. J. Heinrich, and R. L. Myklebust, *A rigorous correction procedure for quantitative electron probe microanalysis (COR2)*, Washington, D.C.: National Bureau of Standards Spec. Publ. 769, 1973.

23. K. F. J. Heinrich, *Electron Beam X-ray Microanalysis*, New York: Van Nostrand Reinhold, 1981.

24. K. F. J. Heinrich, "Electron probe microanalysis by specimen current measurement," *Proc. 4th ICXOM*, 1966, 159.

25. W. Reuter, "The ionization function and its application to the electron probe analysis of thin films," *Proc. 6th ICXOM*, 1972, 121.

26. G. Love, M. G. Cox and V. D. Scott,

"The surface ionization function $\phi(0)$ derived using a Monte Carlo method," *J. Phys.* D11: 23, 1978.

27. C. J. Powell, "Cross sections for ionization of inner-shell electrons by electrons," *Rev. Mod. Phys.* 48: 33, 1976.

CURVE FITTING FOR EPMA CORRECTION PROCEDURES: AN ASSESSMENT

G. Love and V. D. Scott

In order to develop a correction formula for quantitative electron-probe microanalysis (EPMA), information is needed concerning the efficiency with which characteristic x rays are generated with depth in materials at different electron energies. Such data may be in principle deduced theoretically but the limited knowledge we appear to have of electron and x-ray interaction processes has proved to be an obstacle to producing a satisfactory formula. However, the situation has been recently transformed as a result of the increased amount of experimental data on x-ray depth distributions, known as $\phi(\rho z)$ curves, obtained either by tracer measurements or by Monte Carlo simulations. These data reveal that although the magnitude and range of the curves vary as functions of electron energy and target material, their general shape remains substantially the same (Fig. 1). Hence one can adopt a purely empirical correction method that involves the development of mathematical expressions designed to match experimental $\phi(\rho z)$ data. Indeed, this has been the approach used in all the latest work in the field of quantitative EPMA.

Once equations for the $\phi(\rho z)$ curve are established, the true compositions of the specimen may be conventionally derived from the ratio k of x-ray intensities measured on specimen and standards from

$$k = c \frac{\int_0^\infty \phi(\rho z) \exp(-\chi \rho z) d\rho z]_{\text{spec}}}{\int_0^\infty \phi(\rho z) \exp(-\chi \rho z) d\rho z]_{\text{std}}} \quad (1)$$

where χ is the product of the mass absorption coefficient of interst (μ/ρ) and the cosecant of the x-ray take-off angle θ . Of course fluorescence corrections must also be applied but since these corrections appear to be well established they will not be discussed here.

In this paper we focus attention on the recent correction models of Bastin et al.^{1,2} Pouchou and Pichoir,^{3,4} and Love et al.^{5,6} We shall begin with a short description of each model, indicating the parameters the authors have used for their development and optimization, and then test each model using collections of microanalysis data drawn from various sources.

The Method of Bastin

Following Packwood and Brown,⁷ Bastin et al.¹ used a Gaussian profile to represent the

x-ray distribution $\phi(\rho z)$ versus ρz . The Gaussian was centered at the target surface (Fig. 2) and a transient function was introduced to modify the profile close to the surface so as to depict realistically the x-ray distribution here. The equation given by Packwood and Brown was

$$\phi(\rho z) = [\gamma \exp\{-\alpha^2(\rho z)^2\}] \left[1 - \frac{\gamma - \phi(0)}{\gamma} \exp(-\beta \rho z) \right]$$

The first square-bracketed term represents the Gaussian function, where α gives the decay rate and γ the amplitude. The second square-bracketed term contains the transient function β giving the rate of decay and the value of the surface ionization function $\phi(0)$. Hence the four parameters α , β , γ , and $\phi(0)$ define the $\phi(\rho z)$ profile; they were expressed in terms of specimen composition, incident electron energy, etc., based on the available experimental $\phi(\rho z)$ data. Bastin et al.¹ decided to modify Brown and Packwood's original equations for the parameters; the final formulas were obtained by an optimization process that used the database of Love et al.⁸ containing EPMA measurements on a large number of binary alloys.

Bastin et al.² later recognized that their first version of the Gaussian model had limitations and therefore produced revised expressions for β and γ based on an examination of experimental $\phi(\rho z)$ data from various sources. We shall refer to the second set of equations as the Bastin II method and the earlier attempt as Bastin I.

The Method of Pouchou and Pichoir

In the method proposed by Pouchou and Pichoir^{3,4} the x-ray depth distribution was described by a pair of intersecting parabolas. As with Bastin's approach, the $\phi(\rho z)$ curve was defined by four parameters: $\phi(0)$, the surface ionization function; R_m , the depth at which the maximum in the $\phi(\rho z)$ curve occurs; R_x , the x-ray range; and the area under the $\phi(\rho z)$ curve (Fig. 3). The equation for the parabola nearer the surface was written as $\phi_1(\rho z) = A_1(\rho z - R_m)^2 + B_1$; and the other, as $\phi_2(\rho z) = A_2(\rho z - R_x)^2$, where A_1 , A_2 , and B_1 were expressed in terms of R_m , R_x , $\phi(0)$, and R_c , the crossover point of the parabolas. The expression for R_c was established in terms of the generated x-ray intensity I_g . It may be shown that the procedure involves calculating implicitly an atomic number correction en route to the final formula, since Eq. (1) may be written as

The authors are at the School of Materials Science, University of Bath, Claverton Down, England BA2 7AY. They gratefully acknowledge SERC support.

$$k = c \frac{[Ig]_{\text{spec}}}{[Ig]_{\text{stnd}}} \frac{f(\chi)_{\text{spec}}}{f(\chi)_{\text{stnd}}}$$

where the absorption factor is given by

$$f(\chi) = \left[\int_0^\infty \phi(\rho z) \exp(-\chi \rho z) d\rho z \right] / \left[\int_0^\infty \phi(\rho z) d\rho z \right]$$

$$\text{and } \frac{[Ig]_{\text{spec}}}{[Ig]_{\text{stnd}}} = \frac{\int_0^\infty \phi(\rho z) d\rho z}{\int_0^\infty \phi(\rho z) d\rho z} \frac{\text{spec}}{\text{stnd}}$$

is the atomic number correction.

The Method of Love and Scott

The method proposed by Love et al.^{5,6} involved the separate application of atomic number and absorption corrections. That meant the height of the $\phi(\rho z)$ distribution was no longer of importance and a simple geometrical shape could be assumed to derive an absorption correction. A quadrilateral profile^{5,6} was chosen (Fig. 4) and defined by the coordinate of point A[0, $\phi(0)$], the position and height of the peak in the distribution [$\rho z_m, \phi(m)$] and the x-ray range ρz_T . It incorporated four parameters but two of them were combined into the ratio $\phi(m)/\phi(0)$ to leave only three for the fitting procedure. The quadrilateral absorption correction, when used in conjunction with the atomic-number correction of Love et al.⁹ and the characteristic fluorescence correction of Reed,¹⁰ forms the Love-Scott II correction model.

Evaluation of Correction Models

An effective way of testing a correction procedure is to see how well it performs when applied to a wide range of microanalysis measurements. This test may be achieved by calculating values of k^1/k , where k^1 refers to the predicted intensity ratio from specimen and standard. Thus, when the model works properly, $k^1/k = 1$, whereas $k^1/k > 1$ indicates overcorrection and vice versa. From these values of k^1/k , rms errors are calculated for each correction model. For reasons that will become apparent later, we prefer to separate the evaluation into two parts, the first dealing with analyses on elements of atomic number Z above 11 in the periodic table and the second with elements of lower atomic number.

Elements with $Z > 11$

We shall refer first to the use of a database consisting of 554 microanalysis measurements on binary alloys.⁶ With regard to mass absorption coefficients, the formulas derived by Springer and Nolan¹¹ from Heinrich's tabulation¹² are applied for x radiation of energy above 2 keV; for radiation below 2 keV the data of Henke et al.¹³ are adopted. In each assessment the characteristic fluorescence correction of Reed¹⁰ has been employed, but no continuum fluorescence correction has been included since it is generally very small (<1% in most cases).

When tested on the above database, Sewell

et al.⁴ had earlier reported that the Bastin I model worked very well, giving an rms error of only 3.7% (Table 1). Yet we find that when using the Bastin II model on the same data the error has worsened slightly, to 4.6%. The Bastin II model has been tested by its authors² using a new set EPMA measurements consisting initially of 681 results. Following its unsatisfactory performance when overvoltage ratios were low ($U_0 < 1.5$), the low-energy data were discarded and an rms error of 2.99% was then claimed for the remaining 627 results.

We applied the method of Pouchou and Pichoir to the microanalysis data base of Sewell et al.¹⁴ (554 measurements) and found that the model failed to produce a result in 197 cases, either because the crossover point of the parabolas occurred at a negative value of the mass depth or because the crossover point could not be established at all. When tested on the remaining 357 results, an rms error of 3.7% was found. Breakdown generally occurs when dealing with overvoltage ratios <1.5. The problem has been recognized by Pouchou¹⁵ and a solution proposed that involves giving additional degrees of freedom to their x-ray depth profile. Pouchou and Pichoir¹⁵ quoted an rms error of 2.67% when they applied their model to an unspecified collection of 978 microanalysis results.

The Love-Scott correction model was found to give an rms error of 2.9% when it was used on the database of Sewell et al.⁶ Bastin et al. when testing the Love-Scott model on their own microanalysis measurements reported an rms error of 4.33%.

Low-atomic-number Elements

Here we begin by referring to a database consisting of 94 oxygen and fluorine microanalysis measurements.⁶ With the mass absorption coefficients of Henke et al.,¹³ an rms error of 7.0% was found with the Bastin I model but this value increased to 10.7% with the Bastin II model. Yet adoption of Heinrich's mass absorption coefficients¹⁶ caused the rms error in the Bastin II model to improve to 8.1%. Bastin and Heijligers,¹⁷ in measurements on carbides (using an Fe_3C standard), quoted an rms error of 4.1% on applying their model to 117 carbon results. This low value was obtained only after Bastin's choice of mass absorption coefficients were used; much worse rms errors (12% or more) were obtained when either Heinrich's or Henke's values were used.

With Henke's mass absorption coefficients an rms error of 10.3% was produced when the model of Pouchou and Pichoir was applied to oxygen and fluorine measurements,⁶ but a much more reasonable figure of 5.8% was obtained when Heinrich's coefficients¹⁶ were substituted. As regards the 117 carbon results,¹⁷ an rms error of 6.4% was found when Bastin's selection of mass absorption coefficients was used, although errors rose to over 10% if Henke's or Heinrich's values were adopted.

Sewell et al.⁶ tested the Love-Scott model on their oxygen and fluorine measurement and reported an rms error of 4.9%; this value was obtained with Henke's mass absorption coefficients, but the error increased slightly to 6.2% when Heinrich's values were employed. Regarding Bastin's carbon measurements on carbides, the Love-Scott model produced rms errors of over 18% when either Henke or Heinrich's mass absorption coefficients were used, and 11% with Bastin's selection. In all cases the largest discrepancies occurred on heavy-element carbides such as WC and TaC, where errors of ~30% were observed. Willich¹⁸ reported similar findings with the Love-Scott model.

General Discussion

There can be no doubt that the new correction methods based on $\phi(\rho z)$ curve fitting that have been recently developed by Bastin (modified Gaussian), Pouchou and Pichoir (parabolic), and Love and Scott (quadrilateral) are superior to the quantitative ZAF routines in common use. All three methods give rms errors below 3% for heavier-element analyses which, bearing in mind the likely errors associated with the x-ray intensity measurements, must be regarded as highly satisfactory. However, when Bastin assessed his own model, he restricted the input data to systems where $U_0 > 1.5$. Similar failures at low overvoltage ratios were found when the method of Pouchou and Pichoir was applied. Here we find that on a large number of occasions the model failed to give a result at all. Hence, it may be argued that at this stage of their development there is little point in attempting to draw distinctions between these methods, at least for analyses of elements $Z > 11$.

The situation for light-element analyses appears to be less satisfactory. A major problem concerns the reliability of the mass absorption coefficients used for soft x radiation. For example, if we refer to the carbon measurements on carbides of Bastin and Heijligers,¹⁷ the corrected results are of poor quality whether we use the mass absorption coefficients of Henke or those of Heinrich. Errors are produced in excess of 10% for all three correction models; the worst performance is given by the Love-Scott program. After criticizing Henke's values, Bastin et al.² proposed an alternative set, one that showed his own correction procedure in the best possible light, with an rms error of 4.7%. Although Bastin's tactic may be justified, particularly since the other correction models also appeared to benefit, dangers may arise in pursuing this course of action too far, since some inherent fault in a correction program may remain hidden. Indeed, we have noted, as have Bastin² and Willich,⁸ that the Love-Scott model performs poorly when carbon in heavy-element matrices such as tungsten carbide at overvoltage ratios greater than 20 is measured. It would of course be simple to make the model appear better by tampering with the relevant mass absorption coef-

ficients, but a more detailed examination suggests that the mean depth equation may be at fault for these specific systems. As far as μ/ρ values for oxygen and fluorine radiations are concerned, there appear to be only those of Henke and Heinrich. Heinrich's may be better, since overall they gave the lowest rms values, but an objective assessment of correction models is difficult when so much uncertainty remains about mass absorption coefficients. Indeed, the situation has changed little over the last decade or so and the question remains, when will somebody rectify matters and produce new and reliable data?

References

1. G. F. Bastin, F. J. J. van Loo, and H. J. M. Heijligers, "Evaluation of the use of Gaussian $\phi(\rho z)$ curves in quantitative electron probe microanalysis. A new optimisation," *X-ray Spectrom.* 13: 91-97, 1984.
2. G. F. Bastin, H. J. M. Heijligers, and F. J. J. van Loo, "A further improvement in the Gaussian $\phi(\rho z)$ approach for matrix correction in quantitative analysis," *Scanning* 8: 45-67, 1986.
3. J. L. Pouchou and F. Pichoir, "Extension des possibilités quantitatives de la microanalyse par une formulation nouvelle des effets de matrice," *J. de Physique Colloque C2(Suppl. 2)*: 17-20, 1984.
4. J. L. Pouchou and F. Pichoir, "Un nouveau modèle de calcul pour la microanalyse, quantitative par spectrométrie de rayons X: Partie 1. Application à l'analyse d'échantillons homogènes," *La Recherche Aérospatiale* 3: 167-192, 1984.
5. G. Love, D. A. Sewell, and V. D. Scott, "An improved absorption correction for quantitative analysis," *J. de Physique Colloque C2(Suppl. 2)*: 21-24, 1984.
6. D. A. Sewell, G. Love, and V. D. Scott, "Universal correction procedure for electron probe microanalysis: II. The absorption correction," *J. Phys D18*: 1245-1267, 1985.
7. R. H. Packwood and J. D. Brown, "A Gaussian expression to describe $\phi(\rho z)$ curves for quantitative electron probe microanalysis," *X-Ray Spectrom.* 10: 138-146, 1981.
8. G. Love, M. G. C. Cox, and V. D. Scott, "Assessment of Bishop's absorption correction model in electron probe microanalysis," *J. Phys. D9*: 7-13, 1976.
9. G. Love, M. G. C. Cox, and V. D. Scott, "A versatile atomic number correction for electron-probe microanalysis," *J. Phys. D11*: 7-22, 1978.
10. S. J. B. Reed, "Characteristic fluorescence corrections in electron probe microanalysis," *Brit. J. Appl. Phys.* 16: 913-926, 1965.
11. G. Springer and B. Nolan, "Mathematical evaluation of x-ray emission and critical energies and of mass absorption coefficients," *Canad. J. Spectrosc.* 21: 134-138, 1976.
12. K. F. J. Heinrich, "X-ray absorption uncertainty," in T. D. McKinley, K. F. J.

Heinrich, and D. B. Wittry, Eds., *The Electron Microprobe*, 1966, 296-377.

13. B. L. Henke, P. Lee, T. J. Tanaka, R. L. Shimabukuro, and B. K. Fujikawa, "Low energy x-ray interaction coefficients: Photo-absorption, scattering and reflection," *Atomic Data and Nuclear Data Tables* 27: 1-145, 1982.

14. D. A. Sewell, G. Love, and V. D. Scott, "Universal correction procedure for electron-probe microanalysis: III. Comparison with other recent correction procedures," *J. Phys.* D18: 1269-1280, 1985.

15. J. L. Pouchou and F. Pichoir, "Basic

expression of PAP computation for quantitative EPMA," *ICXOM 11*, 1987, 249-253.

16. K. F. J. Heinrich, "Mass absorption coefficients for electron probe microanalysis," in Ref. 15, 67-119.

17. G. F. Bastin and H. J. M. Heijligers, *Quantitative Electron Probe Microanalysis of Carbon in Binary Carbides*, Technical Report, University of Technology, Eindhoven, 1985.

18. P. Willich, "Determination of the chemical state and composition of metal-carbon films by use of electron probe microanalysis," Ref. 15, 238-243.

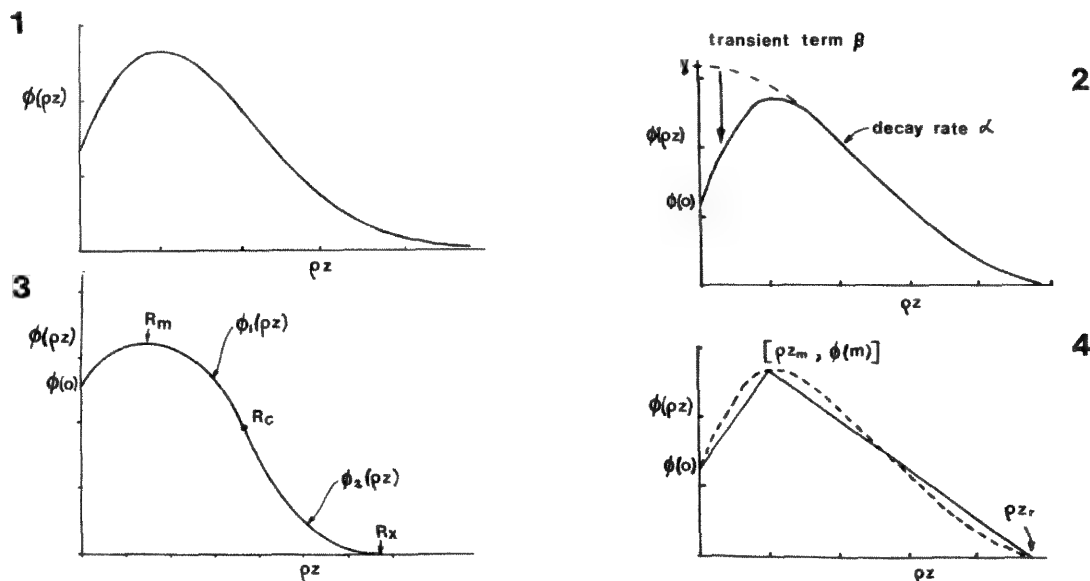


FIG. 1.--Typical $\phi(\rho z)$ curve.

FIG. 2.--Gaussian profile modified in surface region by transient function.

FIG. 3.-- $\phi(\rho z)$ distribution represented by two parabolas.

FIG. 4.--Quadrilateral simulation of $\phi(\rho z)$.

TABLE 1.--Percent rms errors: $Z > 11$.

Database	Assessor	Bastin	Models Bastin II	PAP	L & S
Sewell et al. ⁶ (554 measurements)	Love & Scott	3.7	4.6	3.7*	2.9
Love et al. ⁸ (430 measurements)	Bastin	5.46	-	-	-
Bastin et al. ² (627 measurements)	Bastin	-	2.99	-	4.33
Pouchou & Pichoir ¹⁵ (978 measurements)	Pouchou & Pichoir	-	-	2.67	-

*Data obtained on 357 results.

TABLE 2.--Percent rms errors: $Z < 11$.

Database	Assessor	μ/ρ source	Bastin II	Model PAP	L & S
Oxides & Fluorides ⁶ (94 results)	Love & Scott	Henke Heinrich	10.7 8.1	10.3 5.8	4.9 6.2
Carbides ¹⁷ (117 results)	Love & Scott	Henke Heinrich Bastin	15.0 12.8 4.7	15.5 11.6 6.4	18.8 18.4 11.0
"	Bastin	Bastin	4.11	-	7.78

MODERN COMPUTER PROCEDURES FOR ELECTRON PROBE ANALYSIS

J. R. Henoc

An experienced user visiting a microanalysis laboratory will observe that there are two phases within the laboratory during the course of the working day:

1. The Setup Phase--system operator checks for proper working conditions of the instrument (gun and column alignment, spectrometers, calibration, etc.).
2. The Analysis Phase--system operator introduces several sets of specimens into the instrument. Each specimen is associated to a LABEL, which is in fact a description of the analysis to be performed on the specimen; the output of the sequence is the chemical composition of the specimen.

The visitor will also note that if the first phase was for the most part manual, the second phase required only that the operator set up the specimens to be analyzed into the instrument (stage positions); the microanalyzer can automatically analyze the samples.

Generalities

Remember that the chemical composition, represented by the set of weight percents ($c_1 \dots c_n$) of the set ($e_1 \dots e_n$) of elements contained in the specimen, is obtained from the set ($i_1 \dots i_n$) of measured radiation intensities by resolution of the system equations:

$$i_j = I_j^k (c_1^k \dots c_n^k) \quad 1 < j < n$$

I_j designates the radiation intensity which will be measured (or calculated) in the x-ray line j ; the set of concentrations was ($c_1 \dots c_n$). This system is resolved by successive approximations.

The unit of measure is the intensity of the radiation of a standard of known composition, in the same x-ray line with the same physical and experimental conditions. The radiation intensity in each x-ray line is an independent variable. The precision of the analysis is directly related to the precision of the measurement made on the standards. A set of standards should be stored for a given laboratory; a specific procedure takes care of the acquisition and storage.

The field of routine applications in a laboratory is generally restricted. It is therefore useful to have a qualitative description of each LABEL(s) used, with the physical conditions being a part of it. It is then possible to initiate the raw data processing to calculate the matrices associated to the mix-

ture and the compound standards. These matrices are independent of the concentration. A second procedure has been written to accomplish these operations and create a permanent data output file, where the collected results are stored.

The experimental conditions (reflecting crystal, detectors, etc.) depend on the configuration of the system. Once the physical conditions of a LABEL are given, a procedure scans the calibration file to offer a choice of experimental conditions of acquisition and stores them under a file characteristic of the LABEL.

The remaining step is to organize the raw data acquisition and processing of the specimen. We have seen that the set of specimens to be processed in a laboratory is a set of LABELS open to user choice. However, the analysis of geological specimens is an exception. In this analysis mode the equation numbers resulting from the measures are generally insufficient to characterize the specimen completely. The supplementary equations are furnished by calculations that depend on the nature of the considered species; therefore, in this case we shall have a closed set of geological species (equivalent to the LABELS). A geological specimen generally contains more than one species, which makes it necessary to pass from one species to the other in the course of the same session. Input of the LABEL name must be sufficient to initiate the analysis without ambiguity.

In summary, we have defined four principal tasks:

- The acquisition and storage of the calibration.
- The declaration of the physical conditions common to a LABEL.
- The selection of the experimental conditions of the analysis.
- The analysis procedure of which the input are taken from the files created by the two preceding tasks.

Calibration of Standards

There is free play within the writing of this task; we note simply that the file usage, containing the chemical description of the standards and their respective location on the stage, is advantageous because the standard name will be sufficient to characterize the standard completely. The storage file of the standards is a succession of records of the same type, each typically containing:

- standard name
- element symbol
- symbol of the analyzed x-ray line

The author is at CAMECA, B.P. 6, F-92403 Courbevoie Cédex, France.

- reflecting crystal
- spectrometer number
- beam accelerating voltage
- peak position
- shift to background measurement
- peak minus background intensity
- counting time (fixed time)
- counting accuracy (fixed counts)
- measurement accuracy
- detection parameters (detector bias, single-channel window).

It is common practice to create two files: a sequential file permitting rapid examination of the stored quantities, and a second random-access file permitting convenient reading from a program.

Label Description

Qualitative Description. The physical description given for each element analyzed is mainly the atom symbol, x-ray line symbol, acceleration voltage, and possibly the name of the compound standard. If certain elements are not analyzed, their symbol must be entered. Also to be entered are the valence of all the elements, if one of those entered is calculated by stoichiometry. When the analysis mode of the geological specimens is announced, the correspondence between the LABEL and a list of species allows the completion of the necessary related calculations. The description is finally stored in a sequential file, which can be permanently consulted.

Matrix Calculation. Whatever the type of treatment, the matrix of the backscattering factor is calculated for a combination of the elements corresponding to the qualitative composition of the specimen and the compound standards.¹ The matrix of the fluorescence-enhancement factors² and the matrix of the absorption coefficients³ are calculated in the same way. These last play a major role in the calculation of the absorption factor; a sort routine eliminates the redundancy and sets up a temporary table. Another routine tests the consistency of the results and signals each recognized anomaly. Finally, the user can enter the values of his choice.

Calculation of Radiation Intensities of Pure and Compound Standards. The primary emerging radiation intensity is calculated following the method of Pouchou and Pichoir. The excitation by fluorescence is calculated following the method of Reed. The set of results, stored under file, will be used during the analysis.

Choice of Experimental Conditions. This task is spawned by the preceding task. In effect, it serves in locating the match between the physical parameters defined within the LABEL description, and the same stored parameters in the calibration file of the standards in order to determine the acceptable experimental conditions. When several combinations are possible, the decision is made by the user. Certain parameters can be redefined for the measurement on the specimen. The experimental conditions are stored on a file characteristic of the LABEL.

Analysis

When entering a LABEL, the parameters controlling the analysis are read from the files created for that LABEL by the two preceding tasks. The system and its accessories can be considered as peripherals, of which the management is assured by their own tasks. The microprobe equipped with the wavelength dispersive spectrometer is controlled by a task; another task takes care of the energy dispersive spectrometer. The parent task spawns the two preceding tasks, which are executed separately. When the measured results are available, they are characterized following the methods indicated above with the introduction of an iteration technique; all that remains is to calculate the concentrations from the measured intensities (forward).

These four procedures, which have been briefly described, contain the principal part of an analysis package; moreover, they contain a certain number of useful tools designed to simplify the task of the user.

References

1. J. L. Pouchou and F. Pichoir, *Proc. 11th IXC*, London, Canada, 1987, 249.
2. S. J. B. Reed, *Brit. J. Appl. Phys.* 16: 913, 1965.
3. K. F. J. Heinrich, Ref. 1, p. 67.

EFFECT OF COSTER-KRONIG TRANSITIONS ON X-RAY MICROANALYSIS

J. L. Lábár

Standardless electron probe x-ray microanalysis has been popular since the day of its invention, although it has been known for some time that analysis based on L or M lines poses the inherent danger of decrease in accuracy.^{1,2} Based on the assumption that Coster-Kronig transitions play an important role in the inner shell vacancy generation process, a standardless energy-dispersive (EDS) program was developed where the effects of these radiationless transitions were taken into account both in single-element ("standard") x-ray intensity calculations and in overlap correction.³ A significant improvement was achieved by use of this model instead of the traditional one, in which the interaction of the subshells was not incorporated. In a search for an even more accurate standardless method, various parts of the calculations were replaced by other submodels and the effect of an alternative fluorescence yield and Coster-Kronig rate data set on the results were examined. Although this investigation showed that by starting with a different model for the ionization cross section and stopping power one can improve the initial match between measurement and calculation, the improvement seen previously cannot be repeated when the effect of radiationless transitions is incorporated. That fact warns us to be cautious in drawing conclusions.

Incorporation of Coster-Kronig Transitions

Our first program for standardless analysis performed only the standard intensity calculation and ZAF correction.⁴ In an attempt to add spectrum processing, a FRAME-C type program was converted into a standardless computation. It utilized every single part of the original model in standard intensity calculation and supplemented them with $(U \ln U) - U + 1$ for the calculation of vacancy generation (referred to below as model 1). The accuracy of results for the L lines was not always satisfactory. Comparative analyses of the same samples with known composition showed that some commercial standardless programs suffered from the same limitations of reliability. Schreiber and Wims's calculation of relative L line intensities was based on the modified distribution of primary vacancies after Coster-Kronig transitions and included all the observable L lines.⁵ The original atomic-number-

independent relative intensities of FRAME-C were changed into these formulas both in overlap correction and in the calculation of the weight of the $L\alpha_1$ line compared with the integral x-ray intensity originating from the whole L shell (referred to as model 2).⁵ The latter is necessary in the standard intensity calculation. Since all other details of the FRAME-based program were retained, including the overvoltage correction of the relative line intensities, it seemed reasonable that comparison of the analytical results gained by the original and the modified program would highlight the effectiveness of the incorporation of the radiationless transitions into the model. First, $L\alpha_1$ x-ray intensities of single-element samples were recorded under the same experimental conditions and compared with the two different calculations. The match between measurement and calculation improved considerably when the better model was used (Fig. 1). As an independent and more elaborate test of the

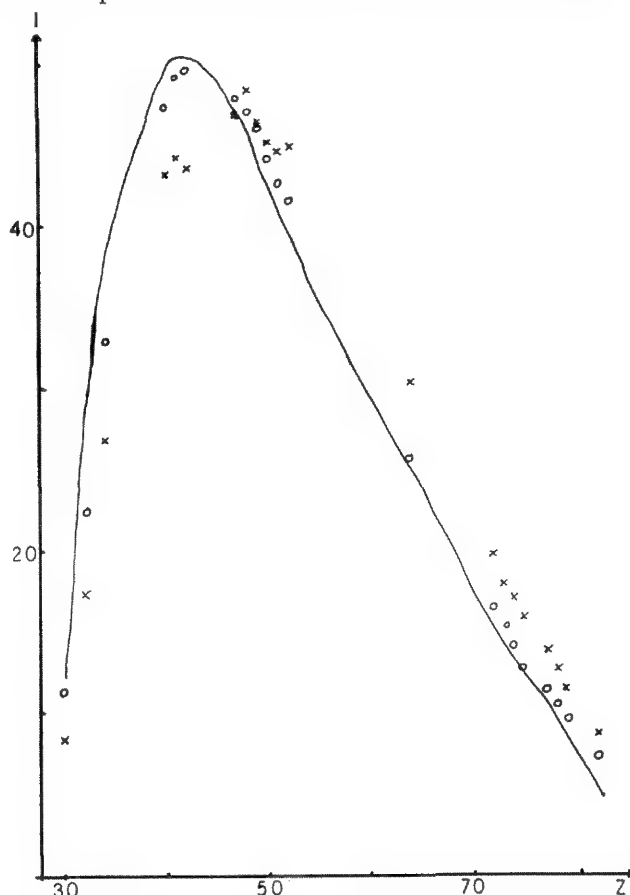


Fig. 1.--Comparison of atomic number dependence of $L\alpha_1$ line intensities, measured at 20 kV, with calculated ones. Solid line, measured values; X without Coster-Kronig transitions; O with Coster-Kronig transitions.

The author is at the Institute for Technical Physics of the Hungarian Academy of Sciences, P.O. Box 76, Budapest 1325, Hungary. The help of Dr. J. P. Jakubovics and Mr. C. J. Salter in the preparation of this manuscript is gratefully acknowledged.

method, the virtual composition of multi-element standard materials were determined by both approaches, as if they were unknown, and compared with the known real compositions. In an attempt to cover the periodic table as completely as possible, as many elements as were available were selected for analysis. Figure 2 demonstrates the distribution of elements analyzed among those that can be examined by a conventional EDS. Each sample was analyzed in several circumstances to examine the dependence not only on the atomic number but also on the accelerating voltage E_0 ; variation of E_0 from 10 to 30 kV changed both the excitation and the absorption considerably.

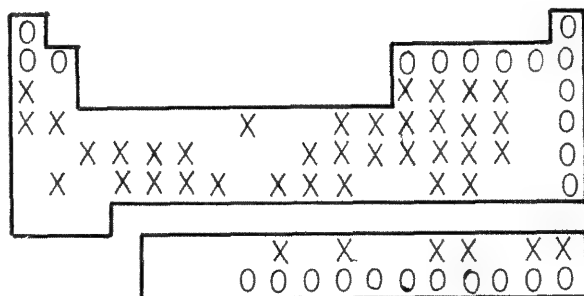


FIG. 2.--Distribution of elements used to test methods 1 and 2 over periodic table: O not available for EDS; X used for test.

The results are divided into three groups for detailed examination. First, a few measurements were performed on samples for which the K line was used for analysis for all constituents. They serve as a reference group from the point of view of achievable accuracy. Analytical results derived only from $L\alpha_1$ line intensities were classified as the second set. The third group comprised the analyses of the samples for which both K and L lines were used at the same time; i.e., the composition of at least one component was determined from its K line and at least one component from its L line. This classification seemed to be necessary because experience with commercial standardless programs suggested that reliability may vary from one of these groups to another. Table 1 presents the average relative errors

TABLE 1.--Average errors of composition determinations on multicomponent samples.

Coster-Kronig		K-K	L-L	K-L	All
	Number of meas.	22	60	95	177
no	RMS [%]	7.2	16.9	14.8	14.9
	average error [%]	5.5	12.2	10.5	10.5
yes	RMS [%]		9.6	10.2	9.7
	average error [%]		7.9	7.0	7.1

for all three groups and for both computational schemes. A noticeable reduction in errors can be observed as a result of the in-

clusion of the Coster-Kronig transitions into the calculations; moreover, the distribution of the errors among the several groups seems to be balanced. The average error of the 177 analyses, counted together as a single set, is 7.1%.

Three entities were identified as the main source of errors. First, one cannot expect better results than the quality of the match between measured and computed single-element intensities, which also includes uncertainties in the detector window absorption that can be considerable,⁶ especially for low-energy radiation. Second, errors are particularly large when constituents present in concentrations of < 5 wt% are being analyzed. Third, cases of high absorption ($f < 0.7$) lead to large errors. Their exclusion from the results yielded a set of 123 analyses with an average error of 5.8%. Of course minor components have to be analyzed as well; nor can high-absorption situations always be avoided, although they can be foreseen and proper selection of E_0 can alleviate the problem.

Comparison with Other Models

Since the most obvious area to be improved is the standard intensity calculation, attention was restricted to the success of this part of the program. In the following section the curve of experimental $L\alpha_1$ intensity vs atomic number serves as the basis of comparison and the several computation schemes are judged on their ability to describe these measured values. Since all of them contain a common multiplying factor (depending on the beam current, etc.) the calculated and measured sets were normalized together in a way that resulted in minimum rms for the given set. This type of comparison reveals the systematic errors in the calculation of atomic-number-dependence (with fixed E_0). A model that fails this test also probably cannot be successful as a general method in analysis of multicomponent samples. In an attempt to emphasize the tendencies, the relative errors of the calculations were plotted in Fig. 3.

Two details of the model were of particular interest: the way the vacancy redistribution is to be taken into account, and the ionization efficiency. All the models encountered^{4,6-9} used NQ^* for the number of generated vacancies, where N is the number of electrons in the shell/subshell and Q^* is the ionization efficiency $Q(E_0)$ for thin layers and $\int(Q/S) dE$ for bulk samples. If they take into account the radiationless redistribution at all, they do it through the multiplying $L\alpha_1/\Sigma L$ weight factor, whereas the correct formula for ionizations could be

$$V_{L_3} = N_{L_3} Q_{L_3}^* + f_{23} N_{L_2} Q_{L_2}^* + (f_{13} + f_{12} f_{23}) N_{L_1} Q_{L_1}^* \quad (1)$$

where f_{ij} are the Coster-Kronig transition rates; the weight of the analytical line should be related to the L_3 subshell only ($L\alpha_1/\Sigma L_3$).

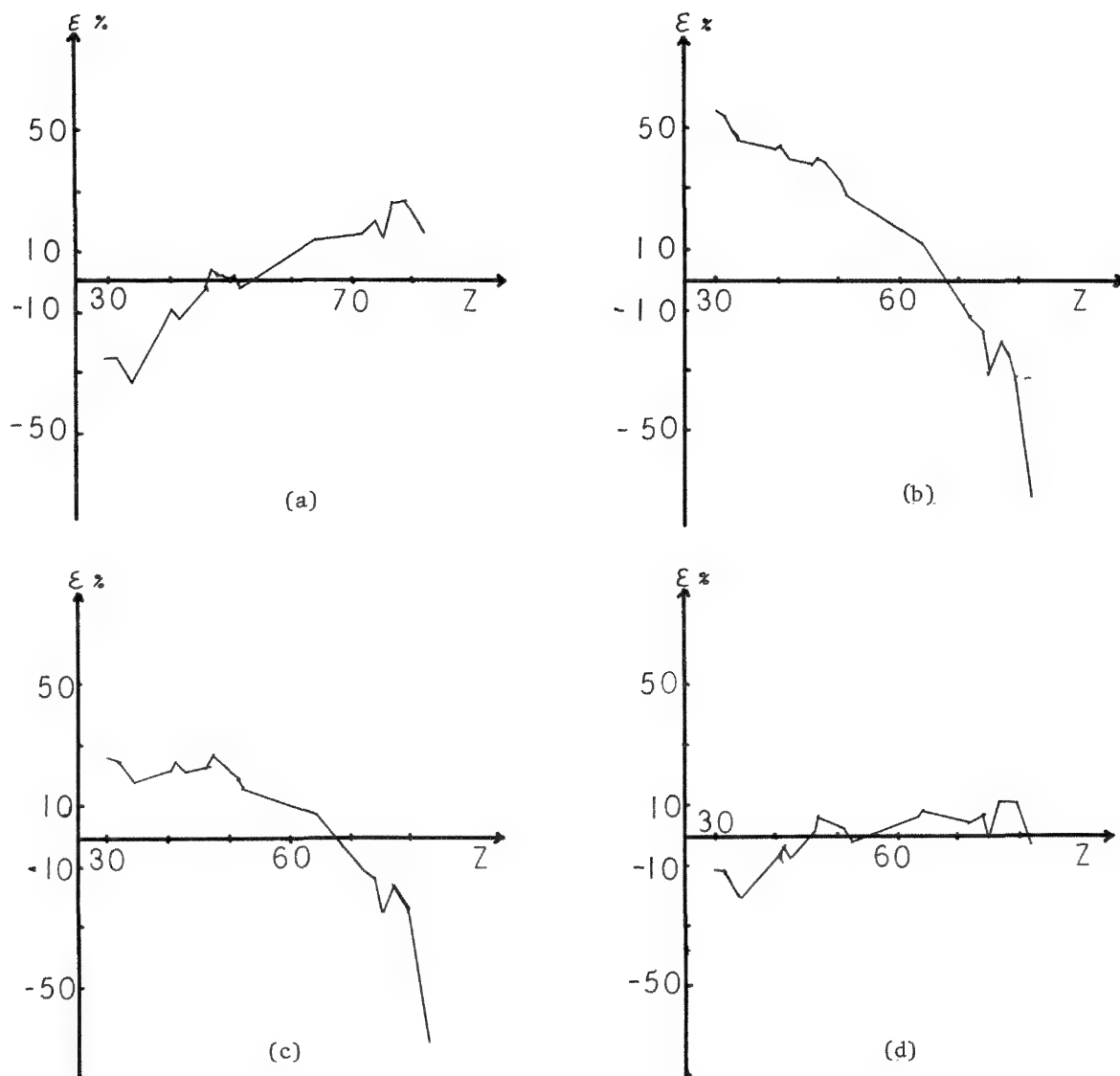


FIG. 3.--Atomic number dependence of relative errors of $L\alpha_1$ intensity calculations ($E = 20$ kV). Figs. 3a, b, c, and d correspond to models A, B, C, and D, respectively.

To illustrate the difference, Fig. 4 shows the multiplying factor necessary to convert the previously calculated standard intensities into the correctly calculated ones as a function of atomic number. Figure 4a is calculated for the case when radiationless transitions had not been involved at all; Fig. 4b demonstrates the change caused by switching over to $V_{L_3}L\alpha_1/\Sigma L_3$ from $NQ^*L\alpha_1/\Sigma L$. Both calculations assumed that E_0 is high enough to insure that the Q^* ionization efficiency is approximately the same for all three subshells and are only for illustration of the shape and magnitude of the change to be anticipated.

This modification was first applied to the model described above. It resulted only in the redistribution of errors, but the reduction in the average error was not significant compared with the average error of the model that contained the radiationless transitions in an $L\alpha_1/\Sigma L$ form. Nevertheless, it was decided to keep the approach represented by (1) because of the clearer physical image behind it.

Various combinations of models were considered and compared. They all include Heinrich's absorption model,¹² Krause's fluorescence yield, and Salem et al.'s relative line intensities, the latter for $L\alpha_1/\Sigma L_3$ calculation.^{13,14} Where appropriate Krause's f_{ij} data were used.¹³

Model A contained the Pouchou and Pichoir (PAP) calculations for vacancy generation.¹⁵ As in the original model, no interactions between the subshells were incorporated.

Model B: PAP stopping power combined with Zaluzec's ionization cross section Q .¹¹ Retaining PAP's set of symbols, we have

$$\int (Q/S) dE = (U_0/V_0M) \sum_k (U_0/V_0)^{P_k}.$$

$$\cdot [T_k U_0^{T_k} \ln(c) U_0 - U_0^{T_k} + 1 - T_k \ln(c)] / T_k^2 \quad (2)$$

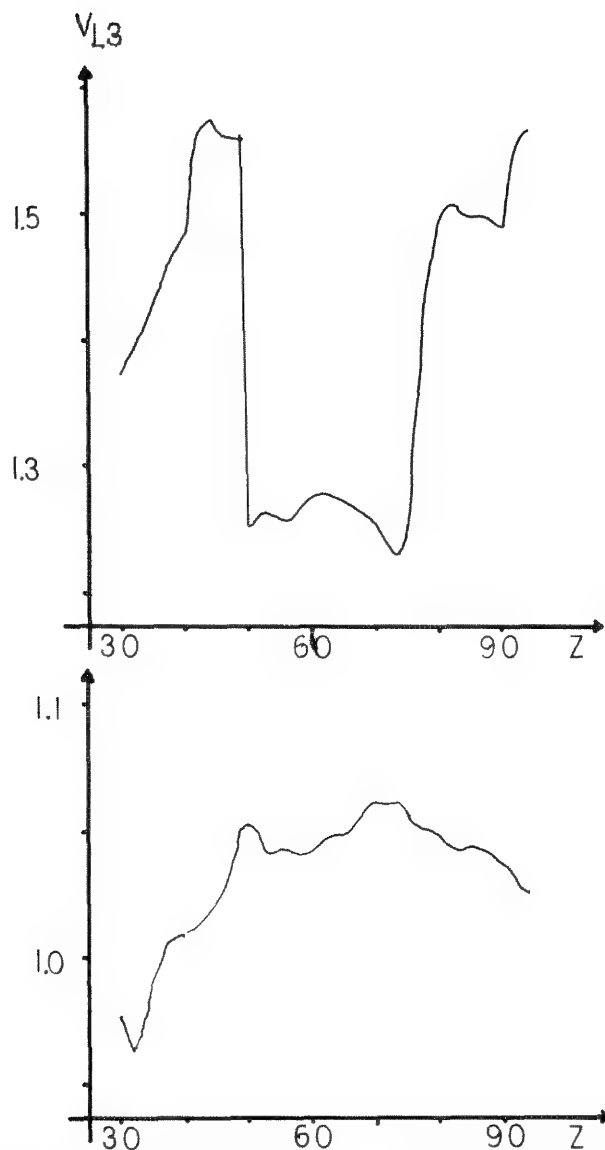


FIG. 4.--Atomic number dependence of (a) V_{L3} (Eq. 1); (b) $(\Sigma \omega_i V_i)/\omega_{L3} = (V_{L3}/Q^* N_{L3})(L\alpha_1/\Sigma L_3)/(L\alpha_1/\Sigma L)$.

but with $m = 1$ in calculation of T_k . Applied only to the L_3 subshell; i.e., no Coster-Kronig transition is assumed.

Model C: as B, with m from PAP.

Model D: as A, but multiplied by Zaluzec's 'b' factor (although $c = 1$).

Model E: as A, but radiationless transitions were incorporated. The assumption was made that all three subshells in Eq. (1) have the same ionization efficiency (the one used by PAP for the entire L shell).

Model F: as B, with all three subshells and combined as in Eq. (1).

Model G: as F, with m from PAP.

Model H: as E, but multiplied with Zaluzec's 'b' factor (although $c = 1$).

It can be seen that Eq. (2) is a generalized form of fQ/S dE given by PAP, which contains both PAP's and Zaluzec's Q as a special case, or an arbitrary combination of them as detailed above.

Figure 3 demonstrates that model A shows a marked dependence of errors on atomic number.

Model B shows an even stronger dependence, but in the opposite direction. The magnitude of these errors seems to corroborate Newbury's reservations.⁶ Complete combination of them (model C) is of very little help. Partial combination of PAP's and Zaluzec's model (D) gives the most even distribution of errors.

It is conspicuous that neither of these error distributions shows any resemblance to the atomic-number dependence of the correction introduced by the radiationless transitions (Fig. 4a). And indeed none of the models E-H gives a significant improvement over their counterparts (Table 2). The slight redistribution of errors introduced by the incorporation of Coster-Kronig transitions did not result in a serious reduction of the average errors; in fact, a slight increase of error could be observed in certain cases.

We can therefore conclude that the improvement that could be observed as a result of incorporating the Coster-Kronig transitions in models 1 and 2 described in the previous

TABLE 2.--Match of measured and calculated $L\alpha_1$ intensities of single-element samples at 20 kV.

Method	A	B	C	D	E	F	G	H
RMS %	17.2	37.5	24.0	8.4	20.8	36.2	28.5	8.8

section cannot be achieved in the case of the combinations of models described in the present section (see comparison of A with E, B with F, C with G, and D with H in Table 2), which suggests that the improvement may have been the result of partial compensation of the systematic errors of the other parts of the model.

Conclusions

A standardless method was set up for ED electron probe x-ray microanalysis, which gives about the same comparatively low average errors for both K and L lines.

Reduction in the average error achieved by changing the physical description of one part of the model does not mean that the same change will necessarily result in an improvement when different physical descriptions are used for other parts of the initial model.

References

1. J. C. Russ, *Microbeam Analysis*--1974, 22.
2. J. C. Russ, *Microbeam Analysis*--1976, 8.
3. J. L. Lábár, *X-Ray Spectrometry* 16: 33, 1987.
4. J. L. Lábár, *Magyar Kémiai Folyóirat* 87: 107, 1981.
5. T. P. Schreiber and A. M. Wims, *Microbeam Analysis*--1982, 161.
6. D. E. Newbury et al., *Analytical Electron Microscopy*--1984, 276.
7. T. P. Schreiber and A. M. Wims, *Ultra-microscopy* 6: 323, 1981.
8. J. Wernisch, *X-Ray Spectrometry* 14: 109, 1985.
9. P. Schwaab, *Scanning* 9: 1, 1987.
10. M. Sarker et al., *Nucl. Instrum. and Meth.* A255: 415, 1987.
11. N. J. Zaluzec, *Analytical Electron Microscopy*--1984, 279.
12. K. F. J. Heinrich and H. Yakowitz, *Anal. Chem.* 47: 2408, 1975.
13. M. O. Krause, *J. Phys. Chem. Ref. Data* 8: 307, 1979.
14. S. I. Salem et al., *Atom. Data and Nucl. Data Tables* 14: 91, 1974.
15. J. L. Pouchou and F. Pichoir, in J. D. Brown and R. H. Packwood, Eds., *Proc. 11th IXCOT*, London (Canada), 1987, 238.

$\phi(\rho z)$ FOR TILTED SPECIMENS IN THE ELECTRONPROBE AND SEM

Rod Packwood, Catherine Parker and Vera Moore

In his thesis Castaing¹ used cylindrical specimens to determine the absorption correction by varying the take-off angle, so that it is no exaggeration to say that tilted specimens have been used from the earliest days of microprobe analysis. However the magnitude of the difficulties presented by a non-normal incidence electron beam must not be underestimated. For example, in the early 1960s the MAC-probe was introduced. This was a compact, precise instrument, with three high take-off angle spectrometers, beam current control, excellent scanning and good light optics. A machine ten years ahead of its time, but with one single drawback: the electron beam struck the specimen at about 30° with respect to the normal. For some people this did not matter. MAC users were given an "effective" take-off angle that was fed into the standard calculations for absorption corrections, etc.² This was not entirely satisfactory but for some analysts such as mineralogists, who tend to use extensive suites of reference minerals, the errors that arise would likely cancel out. The average rock has 30-40% of oxygen and as many as 6-8 principal elements, so that the absorption corrections are generally small. Despite its many advantages, other prospective users found the idea of tilted specimens objectionable enough to veto the MAC as a research instrument, an attitude that must surely have contributed to its demise as a manufactured item. Certainly, a distinguishing feature of a present-day microprobe as opposed to an SEM is the normal incident electron beam. On the other hand a huge number of energy-dispersive x-ray spectrometer (EDXS) analyses are performed every day on tilted specimens in SEMs. It could be argued that these are not serious analyses but in many circumstances they are all that is available to the researcher, so that such data, even if gathered under less than ideal conditions, must be corrected as well as possible.

As for normal incidence, the depth distribution $\phi(\rho z)$ of x-ray production could be measured by the tracer layer technique for a variety of E_0 , E_c , Z , and ψ , where ψ is the angle of tilt of the specimen normal away from the electron beam, and the other symbols have their usual meanings. Some progress has already been made in that direction.³ As an alternative

Monte Carlo simulations could be run and used to explore the main trends in the $\phi(\rho z)$ as a function of the various physical parameters. We choose this latter route as a preliminary study to show where more detailed experimental work was required. The 1985 version of their Monte Carlo program was purchased from the National Bureau of Standards in Gaithersburg, Md. Once the initial running problems were overcome it was intended that a considerable range of parameters would be tried. Unfortunately this was not to be; for the time being we had to settle for a much smaller but still useful interim goal and managed to run simulations on Al, Cu, Ag, and Au at 20 kV and $\psi = 0^\circ$ and 30° tilt.

Theory

When a sample is tilted, to a first approximation nothing at all happens to the x-ray production. As we see in Fig. 1, for small tilt angles the loss of excitation on the low side is compensated by a roughly equal gain on the high side. The generated intensity does not change much, but the observed intensity may increase rapidly, especially if a low take-off angle is being used because of some instrumental constraint.

Before looking at the results of the Monte Carlo simulations it is worth trying to anticipate what might be found on the basis of the modified, surface-centered Gaussian approach with $\phi(\rho z)$ as

$$\phi(\rho z) = \gamma_0 \exp(-\alpha^2 \rho z^2) - (\gamma_0 - \phi_0) \exp(-\alpha^2 \rho z^2 - \beta z)$$

After all, the great advantage of a theory is that it lends itself to making predictions. With a good theory the predictions will cover situations not under consideration when it was first conceived. For the case in point, the development of the $3/2\alpha$ range,⁴ estimating the signals generated in nonuniform surface deposits and stratified specimens⁵ and the backscatter and transmission of electron beams through finite thickness films, together with the replacement of Lenard's law,⁶ are all in addition to the original goal of improving the accuracy of analyses made with soft x rays. The random walk that is implied by the Gaussian distribution immediately leads to the deduction that within reasonable limits, the magnitude of the depth distribution should be independent of the angle at which the electron beam strikes the specimen surface! Once the electrons penetrate the sample they are assumed to be randomized and hence lose directionality. Obviously this is not completely true, not even

R. Packwood and V. Moore are at the Canada Centre for Mineral and Energy Technology, 568 Booth St., Ottawa, Canada K1A-0G1; at the time of this work C. Parker was a final-year engineering student at Carleton University, Ottawa. The authors thank R. L. Myklebust of NBS and A. Euser of CANMET for advice on running the Monte Carlo program.

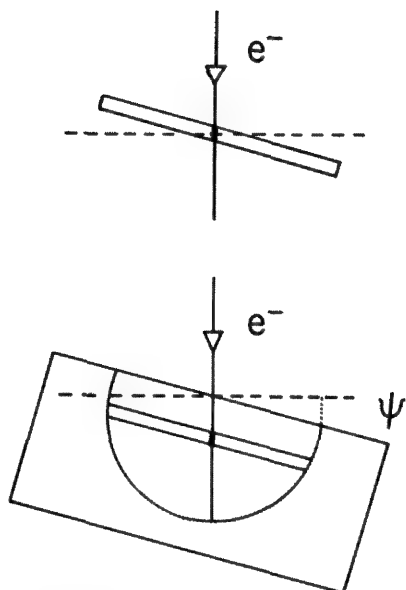


FIG. 1.--Configuration of reference and specimen tracer layers used in this work. For small tilts total x ray generation hardly alters.

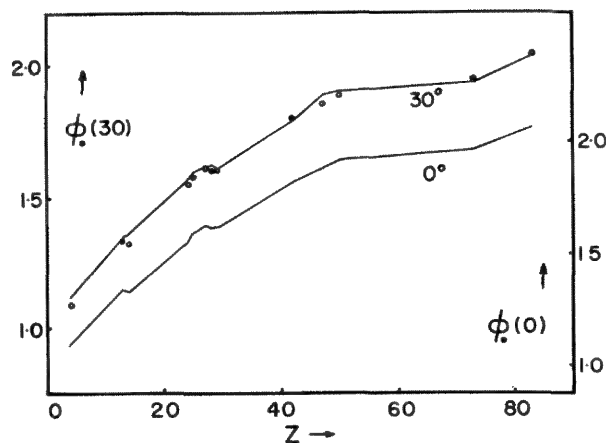


FIG. 3.--Original measurements converted to ϕ_0 for Au M α at 20 kV for 0° and 30° tilts. Solid lines join experimental data points, small circles show $\phi_0(0)$ divided by $\cos 30^\circ$.

for normal incidence; the β term describes the process of transition from collimated to random motion. But once that transition zone is traversed the remainder of the electron trajectories should be the same for normal or tilted orientations, which implies that $\alpha(\psi) = \alpha(0)$, a direct equality. It is also easy to see that when specimen and reference layer [the ratio of which defines $\phi(\rho z)$] are both tilted, $\gamma_0(\psi) = \gamma_0(0)\cos^2\psi$. This result comes about because the projected thickness of the reference and tracer layers in the specimen increase by factors of $1/\cos\psi$. This prediction is a general one and independent of the particular theory under consideration.

Results

The Monte Carlo results are shown in Fig. 2 for runs of 3000 e-trajectories at 20 kV. Evidently the maximum penetration $2/\alpha$, is always

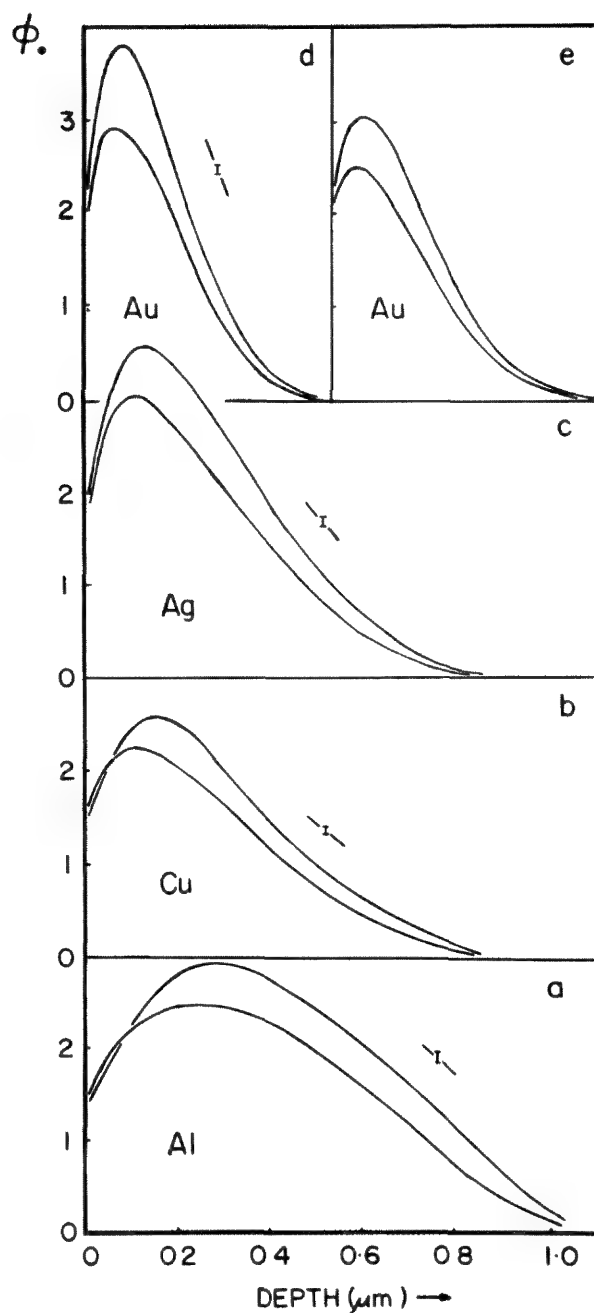


FIG. 2.--Results of Monte Carlo simulations of x-ray generation vs depth, 20 kV, 0° and 30° tilts, 3000 e-trajectories. Taller curves are for 0°. (a) Al K α , (b) Cu K α , (c) Ag L α , (d) Au M α . Error bars show observed scatter in experimental results. (Au M α in Au calculated for 0° and 30° tilts from Gaussian formula and proposed transformations.)

the same in the two orientations. In addition the $\phi(\rho z, \psi)$ distributions are very similar to their sister $\phi(\rho z, 0)$ curves. The only big change is in their respective amplitudes, which ratio out at $\sim 0.775 \pm 0.01$, close to the $\cos^2\psi$ value of 0.75 that was expected.

It can be seen that $\phi_0(\psi)$ is slightly larger than $\phi_0(0)$ for the Al and Cu curves and a

little smaller for Ag and Au, probably reflecting the increase in η the backscatter coefficient that occurs with increasing angle of tilt. The published ratio⁷ for $\eta(45^\circ):\eta(0^\circ)$ is around 1.2 and so it would be reasonable to estimate $\eta(30^\circ):\eta(0^\circ)$ at 1.15, which would almost cancel out the cosine factor to be expected from the increase in the projected thickness. In dealing with the surface ionization we should mention that prior to the Monte Carlo work we had made a series of measurements of ϕ_0 as a function of E_0 , E_c , and ϕ ; two sequences of the experimental values are shown in Fig. 3. The solid lines join actual data points. The small circles are the result of dividing the observed $\phi_0(0)$ data by $\cos 30^\circ$, i.e., the projected thickness factor.

Another noticeable fact about the behavior of the tilted $\phi(\rho z, \psi)$ is that they all have essentially the same slopes as the normal $\phi(\rho z, 0)$ curves. By differentiating the Gaussian equation we find that the slope at $\rho z = 0$ is given by

$$\frac{d\phi(\rho z)}{d\rho z} = \beta(\gamma_0 - \phi_0)$$

and therefore

$$\beta(\psi) = \frac{\beta(0) [\gamma_0(0) - \phi_0(0)]}{\gamma_0(\psi) - \phi_0(\psi)}$$

To get some idea of how well these transformations work in practice we have calculated the $\phi(\rho z)$ for Au $L\alpha$ at 20 kV (Fig. 3e). The only major difference is in the heights, which are larger by some 20% from the Monte Carlo calculations than those from the standard formula.

This is not the first work on this topic; there are Monte Carlo simulations going back many years to mention only the pioneering studies by Duncumb⁸ and experimental work noted earlier.³ However, as far as it is possible to tell from the published data those researchers used a reference layer perpendicular to the electron beam which may have concealed the underlying similarities that are so plain here.

Conclusions

Monte Carlo simulations and some experimental work indicate that the Gaussian formulation for $\phi(\rho z, \psi)$ can be obtained from $\phi(\rho z, 0)$ by some simple transformations of the four parameters involved; in particular, $\alpha(\psi)$ is nearly equal to $\alpha(0)$, $\phi_0(\psi)$ is approximately the same as $\phi_0(0)$, $\gamma_0(\psi)$ is given by $\gamma_0(0)$ multiplied by $\cos^2\psi$, and $\beta(\psi)$ is obtained from $\beta(0)$ by a simple formula containing γ_0 and ϕ_0 for the two orientations.

References

1. R. Castaing, *Application des sondes électroniques à une méthode ponctuelle chimique et cristallographique*, Pub. No. 55, ONERA, Chantillon-sous-Bagneux (Seine), 1951, 51.
2. S. J. B. Reed, *Electron Microprobe Analysis*, Cambridge: Cambridge University Press, 1975, 254.
3. See, for example: W. H. Robinson and J. D. Brown, "Corrections for electron incidence angle in quantitative analysis," *Microbeam Analysis--1982*, 159-160.
4. R. H. Packwood and J. D. Brown, "A Gaussian expression to describe $\phi(\rho z)$ curves for quantitative electron probe microanalysis," *X-Ray Spectrometry* 10: 138-146, 1981.
5. G. Remond et al., "The effect of volume and surface diffusion of impurities on the detection limit in microprobe analysis," *SEM/1984 I*, 151-166.
6. R. Packwood et al., "The electron probe microanalysis of compositionally stratified materials," *Proc. 11th ICXOM*, London, Ont., 1987, 274-279.
7. S. J. B. Reed, Ref. 2, 238.
8. P. Duncumb, in K. F. J. Heinrich et al., Eds., *Use of Monte Carlo Calculations in Electron Probe and Scanning Electron Microscopy*, NBS Spec. Pub. 460, 36.

Corrigendum

Author Packwood regrets two errors in his paper in *Microbeam Analysis--1986*, p. 268:

In Eq. (3), the first term should be

$$C_A \frac{\sqrt{\pi}}{2\alpha}$$

In Eq. (4), the first term should be

$$C_A \frac{\sqrt{\pi}}{2\alpha}$$

A REDETERMINATION OF X-RAY LOSS DUE TO ELECTRON BACKSCATTER BY MONTE CARLO SIMULATION

R. L. Myklebust and D. E. Newbury

With the advent of better electron microprobes employing more stable electronics, a new interest has arisen in the methods and parameters used to compute the matrix corrections for quantitative electron probe microanalysis. One of the two parameters employed in the "atomic number correction" part of the ZAF matrix correction procedure is the R-factor, a measure of the ratio of the total inner shell ionization actually produced in the specimen over that which would occur in the absence of electron backscattering. Several formulations of the R-factor are in use today, based on either empirical fits to experimental data on electron backscattering and backscattered electron energy distributions,¹ or on data generated by a Monte Carlo simulation for electron scattering in solids.²

Duncumb and Reed,¹ using Bishop's data³ for the energy distribution of backscattered electrons, determined the R-factors with the following equation:

$$1 - R = \frac{\int_{E_K}^1 n(W) (Q/S) dW}{\int_{E_K}^0 (Q/S) dE}$$

where the formula for the ionization cross section Q was given by Webster et al.⁴ and the equation for S was from Bethe:⁵

$$S = \text{const.} (Z/A) (1/E) \ln(1.166E/J)$$

They assumed that the value of J was given by $J = 11.5 \cdot Z$. It is obvious that the values obtained for R are affected by the values selected for J . Because of deficiencies in the expression $J = 11.5 \cdot Z$, for many years quantitative analysis programs have used values of J computed from an expression due to Berger and Seltzer,⁶

$$J = (9.76 + 58.82 \cdot Z^{-1.19}) \cdot Z$$

and the values of R determined by Duncumb and Reed or by various expressions that were fitted to their data.

The loss of x-ray generation due to backscatter of primary electrons is being reevaluated with the aid of a Monte Carlo simulation of electron scattering in solids. The Monte

Carlo simulation we have employed is a single scattering model using a screened Rutherford elastic scattering cross section, the Bethe continuous energy loss expression, and the Bethe inner-shell ionization cross section as modified by Mott and Massey.⁷ The x rays generated by electrons are computed as long as the electrons stay within the specimen. If the electron backscatters, the x rays that would have been generated if the electron had remained in the specimen are computed. The sum of these two numbers is the total generated x rays and the R-factor is the ratio of the x rays generated in the specimen to the total generated x rays.

We have been performing Monte Carlo simulations on a wide variety of pure elements at many beam voltages. Each of these simulations produces a variety of data, including the R-factor for the x-ray line of the element. These data are distributed over a range of atomic numbers and overvoltages U , so that it is difficult to plot R as a function of Z with U constant. An additional set of simulations was performed on binary alloys where the mass fraction of the matrix element was 0.999 and the mass fraction of the element whose line we were calculating was 0.001. In this manner we were able to obtain the R-factors for any x-ray line in any matrix. The matrix elements selected were Be (4), Al (13), Ca (20), Zn (30), Zr (40), Sn (50), Nd (60), Yb (70), Au (79), and Th (90). The x-ray lines calculated were Na $K\alpha$, S $K\alpha$, Ti $K\alpha$, Ga $K\alpha$, Br $K\alpha$, and Nb $K\alpha$. All Monte Carlo simulations were done with a beam voltage of 20 keV; therefore, the range of overvoltages used was $U = 1.05$ -18.66. The data calculated above are compared to Duncumb's fitted expression in Fig. 1.

We have also tested Duncumb and Reed's suggestion that we could determine the R-factor for compounds by computing the mass concentration average of the R-factors for pure elements. Four R-factors were determined by Monte Carlo simulation and by the two fitted expressions for Cu $K\alpha$ and for Au $L\alpha$ in pure gold and pure copper (Table 1). The mass concentration average for a 10%Cu-90%Au alloy was then calculated (Table 2). The values obtained are compared to values obtained from a Monte Carlo simulation of the alloy $R = 0.7046$ for Cu $K\alpha$ and $R = 0.7509$ for Au $L\alpha$. These values agree very well with the mass concentration values calculated from the Monte Carlo R-factors from Table 1. Mass concentration averaging does appear to be valid for computing the R-factors of alloys.

For the atomic number correction, the ratio of R in the alloy to R in the pure element is

The authors are at the Center for Analytical Chemistry, National Bureau of Standards, Gaithersburg, MD 20899.

Table 1.--R-factors.

Specimen	Line	Monte Carlo	Duncumb ¹	Myklebust ²
Cu	Cu K α	0.8545	0.8821	0.8468
Au	Cu K α	0.6834	0.7366	0.6860
Cu	Au L α	0.8939	0.9139	0.8687
Au	Au L α	0.7423	0.7874	0.7458

Table 2.--Mass concentration averages of R for a 10%Cu-90%Au alloy.

Line	Monte Carlo	Duncumb ¹	Myklebust ²
Cu K	0.7005	0.7512	0.7021
Au L	0.7575	0.8001	0.7581

computed (R_{AB}/R_A). For Au L α , $R_{AB}/R_A = 1.021$ by Monte Carlo and 1.016 by Duncumb. This is a relatively insignificant error for the computation of the gold composition. However, for Cu K α , $R_{AB}/R_A = 0.820$ by Monte Carlo and 0.852 by Duncumb, a 3.9% difference in the value of R for copper in this alloy.

We are computing more R-factors by Monte Carlo simulation in an effort to produce a more satisfactory expression for R. In addition, we are preparing to measure the energy distributions of the backscattered electrons from pure materials as an additional method for determining R.

References

1. P. Duncumb and S. J. B. Reed, "The calculation of stopping power and backscatter effects in electron probe microanalysis," in K. F. J. Heinrich, Ed., NBS Spec. Pub. 298, 1968, 133.
2. R. L. Myklebust, "An evaluation of x-ray loss due to electron backscatter," *J. de Physique* 45: C2, 1984.
3. H. E. Bishop, "Some electron backscattering measurements for solid targets," 4th ICXOM, Paris, 1966, 153.
4. D. L. Webster et al., "Effects of cathode-ray diffusion on intensities in x-ray spectra," *Phys. Rev.* 37: 115, 1931.
5. H. A. Bethe, "Theory of the transmission of corpuscular radiation through matter," *Ann. Phys.* 5: 325, 1930.
6. M. J. Berger and S. M. Seltzer, *Tables of Energy Losses and Ranges of Electrons and Positrons*, Report NASA SP-3012, Washington, D.C., 1964.
7. N. F. Mott and H. S. W. Massey, *The Theory of Atomic Collisions*, London: Oxford University Press, 1949, 2d ed.

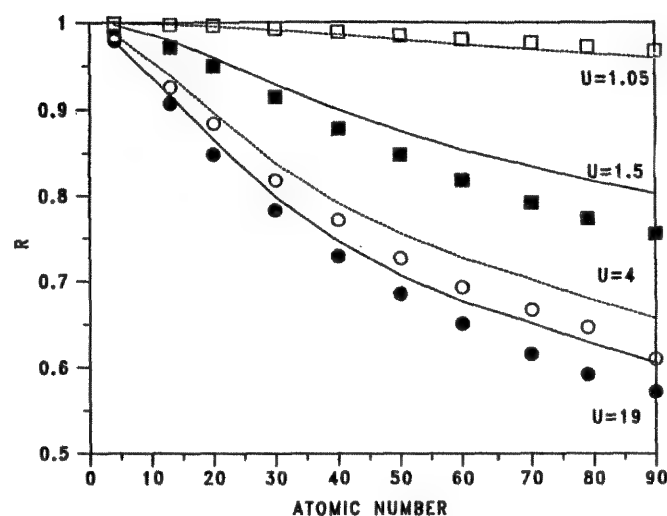


FIG. 1.--R-factors vs atomic number, from Monte Carlo simulations (points) and polynomial fit from Ref. 1 (lines). Curves are plotted at constant overvoltage U. Open boxes and dashed line, U = 1.05; solid boxes and solid line, U = 1.5; open circles and dashed line, U = 4; solid circles and solid line, U = 19.

AN ELECTRON/X-RAY OPTICAL BENCH FOR THE MEASUREMENT OF FUNDAMENTAL PARAMETERS FOR ELECTRON PROBE MICROANALYSIS

J. A. Small, D. E. Newbury, R. L. Myklebust, C. E. Fiori, A. A. Bell, and K. F. J. Heinrich

Since the development of the electron microprobe by Castaing in 1951, quantitative x-ray microanalysis has evolved into one of the most powerful methods of spatially resolved analysis.¹ For most routine analyses, the x-ray generation, absorption, and detection processes are well understood and correction procedures can be used to perform routine quantitative analyses at a relative accuracy of 2%. However, there remain several areas of microanalysis for which the electron beam-specimen interaction and the x-ray generation and absorption are not well known: analysis of particles and thin films, of specimens containing light elements such as oxygen, and of specimens by the use of low-energy electron beams. One of the main limitations to further improvements in these areas is that our knowledge of the various physical interactions is derived principally from experiments and theoretical studies performed in the period 1920-1960.² The topic of medium energy (2-50 keV) electron-target interactions has not been rigorously studied since that time. In a number of cases, data important to quantitative analysis procedures are nonexistent, or not measured with sufficient accuracy. Examples include the absorption parameter $f(X)$ and the electron backscatter loss factor R , especially at low beam energies. Conventional electron microprobes and scanning electron microscopes equipped with spectrometers are not suitable for such measurements, because the design constrains the analyst to a single value of the angle between the beam and the spectrometer axis.

During the past year at the National Bureau of Standards we have been working on the design and construction of an electron/x-ray optical measurement bench that offers flexible control of interaction parameters. This system consists of an electron gun and column, a specimen goniometer capable of three axis orientation, and an x-ray spectrometer mount that can be used to measure x-ray intensities at x-ray emergence of 0-180°. The x-ray emergence angle ψ is defined as the angle between the de-

tector and the specimen surface. The experimental bench is being constructed from the gun, vacuum, and electron-imaging subsystems of an ETEC Autoscan electron microscope augmented with a special vacuum chamber and spectrometer system.

Overall Design Approach

In order to achieve maximum flexibility in selecting experimental setups, the system (Fig. 1) was designed around a vertical axis of symmetry with the electron-beam-forming system mounted horizontally. Around this vertical axis, the x-ray detector(s) have a freedom of movement limited only by the electron-gun subsystem. The specimen may also be rotated on this vertical axis, which creates a range of beam incidence angles from 0°-90°. The combination of x-ray emergence and incidence angles allows for virtually every conceivable beam/specimen and tilt/x-ray emergence angle arrangement of interest.

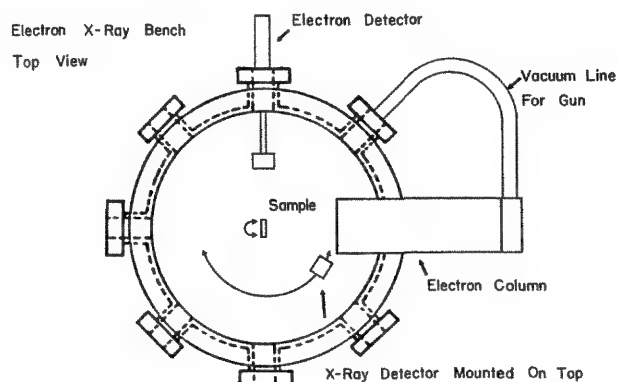


FIG. 1.--Schematic representation of instrument (top view).

Specimen Chamber

The specimen chamber from the original instrument has been replaced with a cylindrical stainless-steel vacuum chamber (Fig. 2) 45.7 cm in diameter and 30.5 cm high. The chamber was mounted directly onto the main vacuum port of the ETEC microscope and required no alterations to the ETEC vacuum system. The chamber is large enough to allow for the simultaneous mounting and the manipulation of multiple x-ray and electron detector systems. The top and bottom vacuum seals on the chamber are O-ring seals which limit the ultimate vacuum to the 10^{-6} Torr range. In addition to the main access from the top of the chamber there are eight miniflat ports. Two of the ports

The authors are with the Center for Analytical Chemistry, National Bureau of Standards, Gaithersburg, MD 20899, except C. E. Fiori, who is with the National Institutes of Health, Bethesda, MD 20892. Certain commercial equipment, instruments, or materials are identified in this paper to specify the experimental procedure. Such identification does not imply recommendation or endorsement by the National Bureau of Standards, nor does it imply that the materials or equipment identified are necessarily the best available for the purpose.

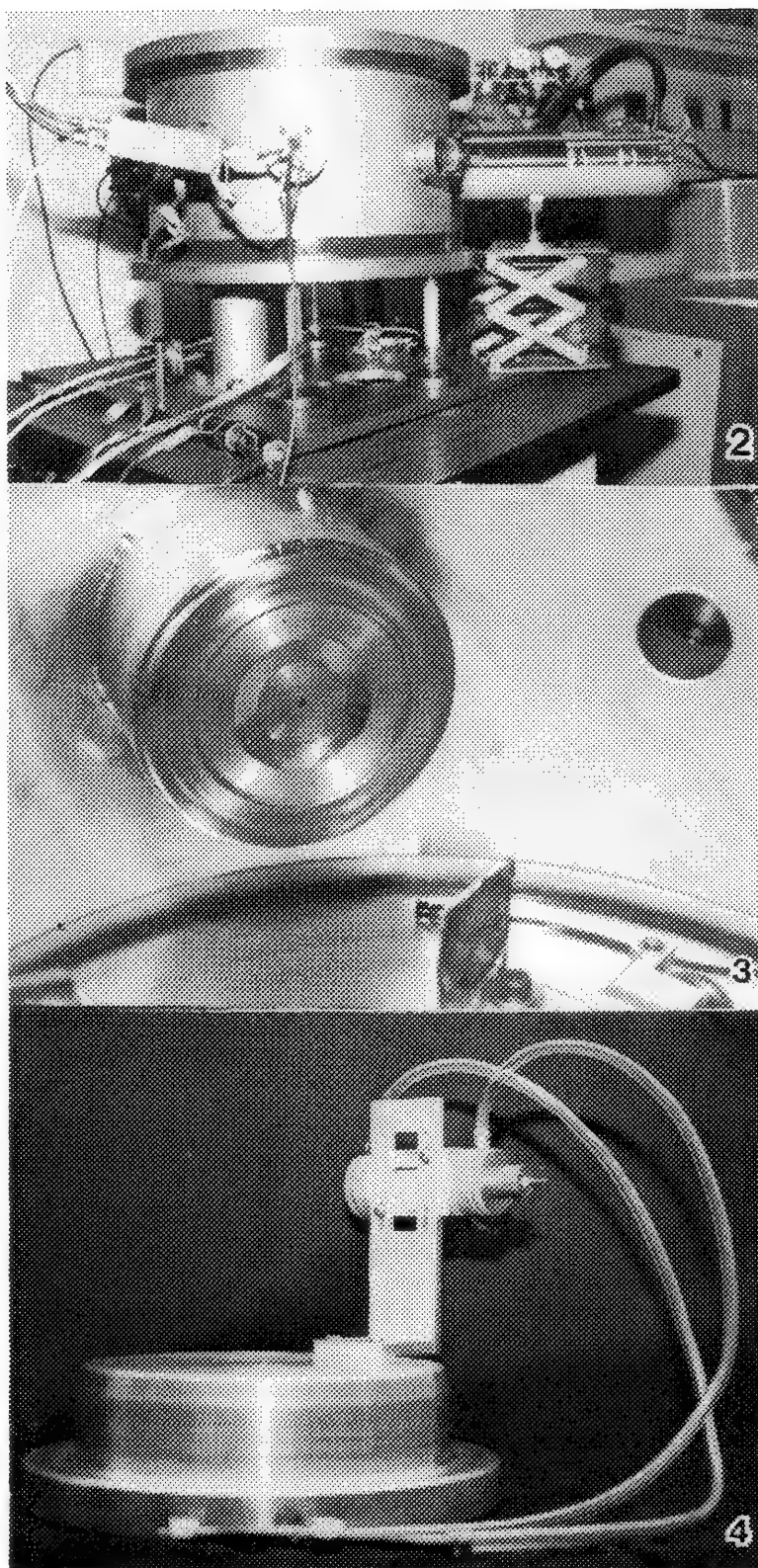


FIG. 2.--Side view of specimen chamber.

FIG. 3.--Electron column mount.

FIG. 4.--Detector mounting plug with flow-proportional counter in place.

are used for mounting the electron-gun subsystem. A third port is used to mount the secondary-electron detector. The remaining ports are used for high- and low-voltage feedthroughs for the x-ray detectors, gas feedthroughs for the flow proportional detector, and windows for observation of the experimental set-up during operation of the instrument.

Electron Gun/Lens System

The electron-gun subsystem consists of the original tungsten-filament gun and column from the ETEC scanning microscope, mounted horizontally (Fig. 3). The mount extends 7 cm inside the vacuum chamber to permit focusing of the electron beam at the centerpoint of the chamber. The horizontal mounting of the gun subsystem on the sidewall of the chamber enables us to mount the x-ray detectors off-center on the top plate of the chamber, so that they can be rotated in the horizontal plane. This configuration greatly simplifies the interfacing of the detector(s) to the vacuum system, yet allows the detectors to move through a full 180° of rotation about the sample. The gun voltage is adjustable from 2.5 to 30 keV. The electron column is equipped with two coupled condensor lenses and a third objective lens. Specimen currents range from 10^{-6} to 10^{-11} A.

Detector Systems

The x-ray detector(s) are mounted on the top plate of the vacuum chamber, made of aluminum in two sections: an outer ring 2.54 cm thick, which forms the main vacuum seal to the chamber; and an inner plug 5 cm thick, which serves as the rotating detector mount. The inner plug rotates on a compressed O-ring sleeve mounted in a groove in the outer ring. The detector mount rests on 1.3cm-diameter ball bearings and can be rotated around the central axis of the chamber. Rotation is done manually on the initial system and reference marks on the plug and outer ring are used to measure the position of the detector relative to the sample and electron beam. Two detectors are currently being mounted on the instrument. The first is a flow-proportional detector mounted directly onto the bottom of the plug (Fig. 4). In addition to rotational motion the flow-proportional detector can also be moved in a radial direction with respect to the sample

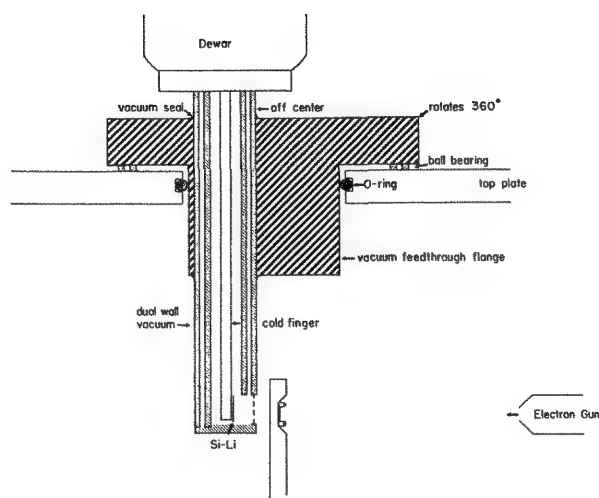


FIG. 5.--Design for Si-Li detector.

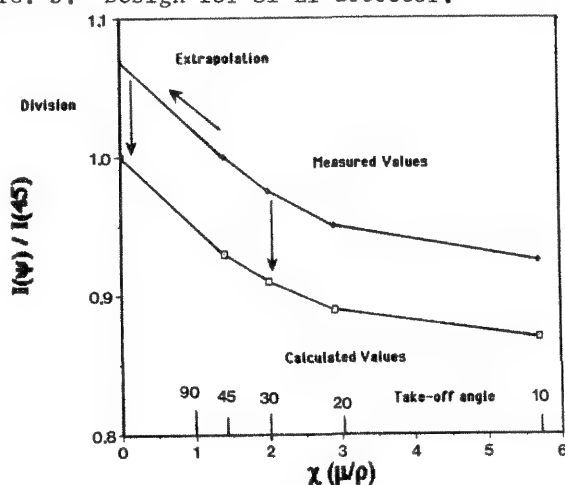


FIG. 6.--Graphical representation of Green's determination of $f(\chi)$.

to increase or decrease the solid angle. This detector will be used to measure total x-ray emission from various targets.

The second detector is an Si-(Li) detector modified as shown in Fig. 5. The tube for this detector has been lengthened and the detector crystal is oriented at right angles to the end.

Preliminary Experiment

Several expressions are used in electron-probe microanalysis for the determination of the x-ray absorption in specimens.³ These expressions are used to calculate the $f(\chi)$ value for a given element or compound, defined in Eq. (1) as the ratio of the absorbed x-ray intensity I' to the intensity I generated by the electron beam:

$$f(\chi) = I'/I_0 \quad (1)$$

In all the expressions the $f(\chi)$ value can be expressed as a function of several parameters which are related to the specimen and the experimental set up,

$$f(\chi) = f(\chi, E_0, E_c, Z, A) \quad (2)$$

where χ is related to the mass absorption coefficient (μ/ρ) and the x-ray emergence angle ψ by

$$\chi = (\mu/\rho) \csc \psi \quad (3)$$

and E_0 is the primary beam potential, E_c is the critical excitation potential for the characteristic line of the element of interest, and Z and A are the average atomic number and mean atomic weight of the specimen, respectively.⁴

In the initial experiments in this instrument we shall test existing expressions for $f(\chi)$ and compare them to new measurements of the intensity emitted from pure and multielement targets as a function of x-ray emergence angle. If we measure the emitted x-ray intensity at various x-ray emergence angles and normalize to the intensity for a particular value of ψ , such as 45° , we can determine $f(\chi)$ values for various materials following the technique used by Green.⁵ In his experiments, with an instrument similar to ours, Green obtained $f(\chi)$ values for pure elements by plotting I_ψ/I_{45° vs χ , where I_ψ is the absorbed intensity measured at the emergence angle and I_{45° is the absorbed intensity measured at an emergence angle of 45° . Green then extrapolated the curve to the hypothetical value of $\chi = 0$; i.e., no absorption. From Eq. (1), $f(\chi) = 1$ at $\chi = 0$ since with no absorption $I' = I_0$. The relationship in Eq. (4) then shows that the value of I'/I_{45° at $\chi = 0$ equals the correct value for $1/f(\chi)_{45^\circ}$.

$$I'/I_{45^\circ} = f(\chi)/f(\chi)_{45^\circ} \quad (4)$$

Green then divided the experimentally determined $f(\chi)/f(\chi)_{45^\circ}$ by the $1/f(\chi)_{45^\circ}$ determined from the extrapolation to obtain the corrected $f(\chi)$ values. This procedure is shown graphically in Fig. 6, taken from Ref. 2. In addition to repeating some of Green's measurements, we shall make measurements on other pure elements and extend the measurements to multielement targets, the importance of which has been addressed by Heinrich:⁶

The variable emergence-angle technique is potentially applicable to homogeneous multielement targets, and could be simplified and made more accurate with the use of a silicon X-ray detector. Unfortunately, there has been no further research effort in this direction.

Once we have compiled a data set of $f(\chi)$ values, they will be compared to the available experimental measurements and $f(\chi)$ terms in the literature. From this information, we hope to develop more accurate $f(\chi)$ terms than those which are currently being used in the various analysis procedures.

References

1. R. Castaing, Ph.D. Thesis, University of Paris, 1951.

2. K. F. J. Heinrich, *Electron Beam Microanalysis*, New York: Van Nostrand Reinhold, 1981.
3. *Ibid.*
4. J. I. Goldstein, D. E. Newbury, P. Echlin, D. C. Joy, C. Fiori, and E. Lifshin, *Scanning, Electron Microscopy and X-Ray Microanalysis*, New York: Plenum Press, 1981, 310.
5. M. Green, "The target absorption correction in x-ray microanalysis," in H. H. Pattee, V. E. Cosslett, and A. Engstrom, Eds., *X-Ray Optics and X-Ray Microanalysis*, New York: Academic Press, 1973, pp. 361-377.
6. Heinrich, *op. cit.*, pp. 266-271.

THE COLLECTION OF CONTINUUM SPECTRA BY ENERGY-DISPERSIVE SPECTROMETER FOR THE DERIVATION OF MODELING EXPRESSIONS

I. R. Harrowfield and C. M. MacRae

Several empirical expressions for modeling continuous radiation are available and work continues to resolve the differences among them.¹⁻³ Such expressions, which relate the measured intensity to the atomic number, incident electron energy, and x-ray photon energy, are in general applicable only to the spectrometer on which the data are acquired. Data have been collected by energy-dispersive (ED) spectrometers¹⁻⁵ and by wavelength-dispersive (WD) spectrometers.^{6,7} On the evidence available, the latter are more readily applied to data collected on other machines than the former, mainly because ED spectrometers are more susceptible to background generated by backscattered electrons (BEs).^{1,7} It appears that attempts to avoid this problem vary in their success. Some of the disagreement is due to differences in treatment of the raw spectral data, which must be corrected for self-absorption and electron backscattering before the chosen model is fitted. Also, because take-off angles of different detectors vary, correction for the anisotropy of the continuum cross sections should be made. Such corrections are not always made. In this paper we report our efforts to insure that our ED spectrometer detects x rays generated by primary electrons and not backscattered electrons or x rays generated by them. We demonstrate the need for anisotropy corrections to be applied to the raw data and consider the effects of specimen coating on measured spectra. We refer specifically in our discussion to recent databases collected by Smith and Wynne¹ and by Small et al.^{2,3}

Collection of Continuum Spectra

Pure metal standards were sited in 3mm-diameter holes in a brass block and graphite-doped resin was used to backfill the holes. The whole block was then polished and finished with 1µm diamond paste. The block was not carbon coated but electrical contact between standards and the brass was made with carbon dag. To minimize contamination during spectrum collection, the diffusion pump baffle and the condensing plate above the specimen were cooled with liquid nitrogen. Spectra were recorded with a 10mm² Link Systems 860 Mk II ED detector, which was fitted with a 1-mm diameter aluminum aperture supplied by the manufacturer, a second aperture made

of lead, and an aluminum cap on which could be mounted two very strong Cd/Sm magnets (Fig. 1). Spectra were also recorded with all apertures removed. The ED system was fitted to a Cameca "Microbeam" microprobe on which backscattered electron trapping is achieved with the magnetic field of the final lens. The beam current measurement system of the microprobe was calibrated with a carbon Faraday cup and a Keithley electrometer. The take-off angle of the detector was 40° and the detector was about 10 cm from the probe target. The pulse output and deadtime signal of the Harwell pulse processor was connected to CSIRO/MCA--a fast linear multichannel analyzer --and the accumulated spectra were stored in a DEC 11/23+ computer.

The deadtime during acquisition was set between 15 and 18% (1400 cps) to minimize pulse pile-up;³ the counting time was 200 s. After correction for residual deadtime (3 µs) and normalization to beam current, the spectra were smoothed by convolution with a normalized Gaussian function with a FWHM of 150 eV.

Results

Addition of the magnets to the collimator made no noticeable difference to the spectra even for a gold target at 50 keV (Fig. 2). If electrons are hitting the collimator they do not follow axial paths. However, the spectra changed considerably in shape when all apertures were removed, as shown in Figs. 3a and b. The accelerating voltage was 40 keV, the maximum used by Smith and Wynne¹ and Small et al.^{2,3} The spectra have been normalized so that the gold M lines of each were the same height, to correct for the reduction in exposed detector area when the aperture is fitted. The area normalized detector efficiency does not change appreciably with photon energy up to 10 keV--the L lines in both spectra of Fig. 3b are of similar height. However, in this energy range, the background in the dotted spectrum is significantly higher than the full line spectrum. In the region 1-3 keV, the dotted background is strongly enhanced, which shows that continuum is being generated in the beryllium window. The small copper peak appears when the gold target is mounted in a 25mm-diameter plastic block. It is not due to electron scatter from the primary beam and must be generated by backscattered electrons striking parts of the ED port. Above 10 keV the collection efficiency of the uncollimated detector increases, possibly because high-energy x rays penetrate the internal

The authors are at the CSIRO Division of Mineral Products, P.O. Box 124, Port Melbourne, Victoria, Australia 3207.

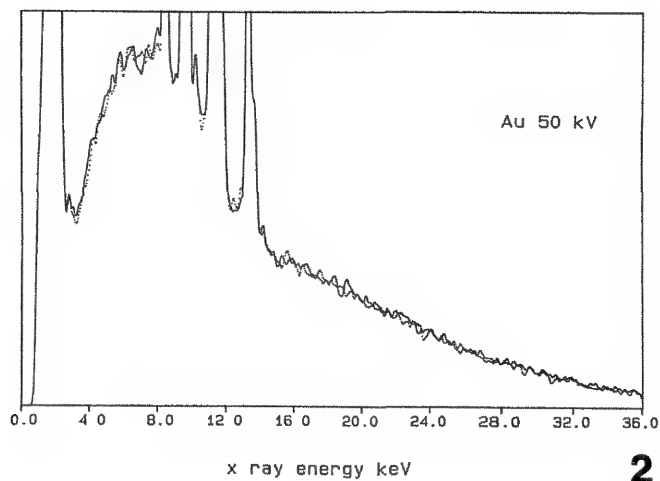
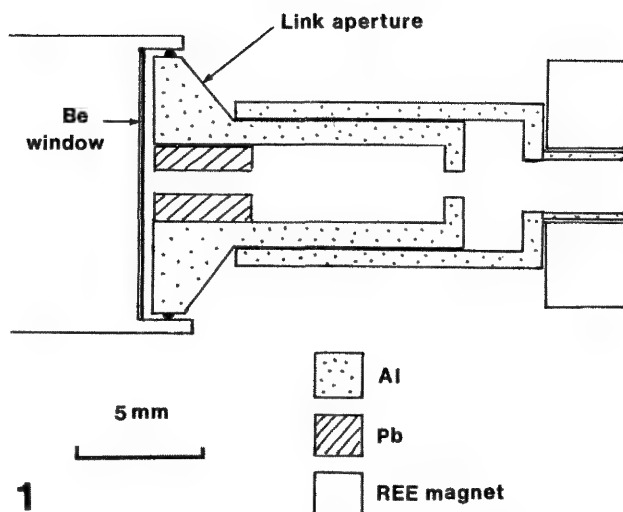


FIG. 1.--Diagram of collimator and magnets fitted to ED detector.

FIG. 2.--Spectra collected with magnets (full time) and without magnets (dotted line) at 50 kV accelerating voltage normalized to beam current.

collimator around the detector crystal itself. This effect is particularly noticeable in the silver spectrum taken at 40 kV (Fig. 3c). Here the $L\beta$ peak of the dotted spectrum at 25 keV is 1.45 times larger than that of the full spectrum. Even when the background is scaled by this factor the dotted spectrum is still significantly higher. It must be concluded that the uncollimated detector is accepting x rays generated by backscattered electrons striking the detector even after deflection by the strong field of the objective lens. Deflected electrons are scattered off the sides of the ED port and strike the uncollimated window. The effect is still present at 30 keV on silver (Fig. 3d) but is negligible at 20 keV even for gold, for which electron backscattering is high (Fig. 3e).

The effect of coating on the continuum becomes significant only at 10 kV. Gold spectra were recorded with and without a coat of 25 nm of carbon at an accelerating potential of 10 kV (Fig. 4). The difference is roughly 4% at 4 keV and 10% at 7 keV.

Discussion of Experimental Results

Smith and Wynne¹ have ascribed the poor agreement of intensities predicted by the expression of Small et al.^{2,3} with those of their own to detection of x rays generated by backscattered electrons. The experimental conditions under which spectra were collected by Small et al. would be similar to those described above when all external apertures were removed. The take-off angle, electron trapping system, ED access port, and detector area are similar, but their detector/specimen distance is smaller (5 cm).¹³ Small et al.^{2,3} have used a collimator, but its effectiveness has not been tested in the way we describe. A collimator is more effective at a larger distance from the magnetic trap, although this makes alignment more difficult. On the basis of published data, it is not possible to verify the proposal of Smith and Wynne¹ that the data of Small et al.^{2,3} are affected by electrons

entering the detector. Spectra published by Small et al.² have been taken at a maximum of only 22.5 keV. It is interesting that for low atomic numbers the agreement is poorer. At a given photon energy, the ratio of continuum to BE intensity should be slightly higher for gold than for carbon but the mean energy of BEs for gold is approximately twice that for carbon. Spurious continuum effects should therefore be greater for higher atomic numbers.

It is evident from the study of coated and uncoated gold targets that at low voltages the background computed from a model which has been derived from uncoated standards will be in error when applied to coated specimens. It would be possible to include a simple empirical correction which is a function of coating thickness, accelerating voltage and photon energy; for accurate computation of background at low accelerating voltages it is essential.

Anisotropy Corrections

Small et al.² have corrected their raw data for anisotropic production of continuum x-ray photons but Smith and Wynne¹ have not done so. The corrections are larger at high accelerating voltages and low atomic numbers. The most commonly used anisotropy correction is that by Statham,⁸ who modified the cross sections of Kirkpatrick and Weidmann.⁹ We have calculated anisotropy corrections with the Legendre polynomial coefficients given by Tseng et al.¹⁰ Large discrepancies occur between the two corrections. Our calculations are for detector take-off angles of 52.5° and 40°, the angles used by Smith and Wynne¹ and by Small et al.^{2,3} respectively.

We estimate the anisotropy correction for the production of 10 keV x-ray photons by a 15 keV electron beam incident on a carbon target by assuming that electrons with energies between 10 and 15 keV are scattered into an angular distribution described by Bothe's law,¹¹ with a most probable scattering angle of 25°. The scattering curves of Cosslett and

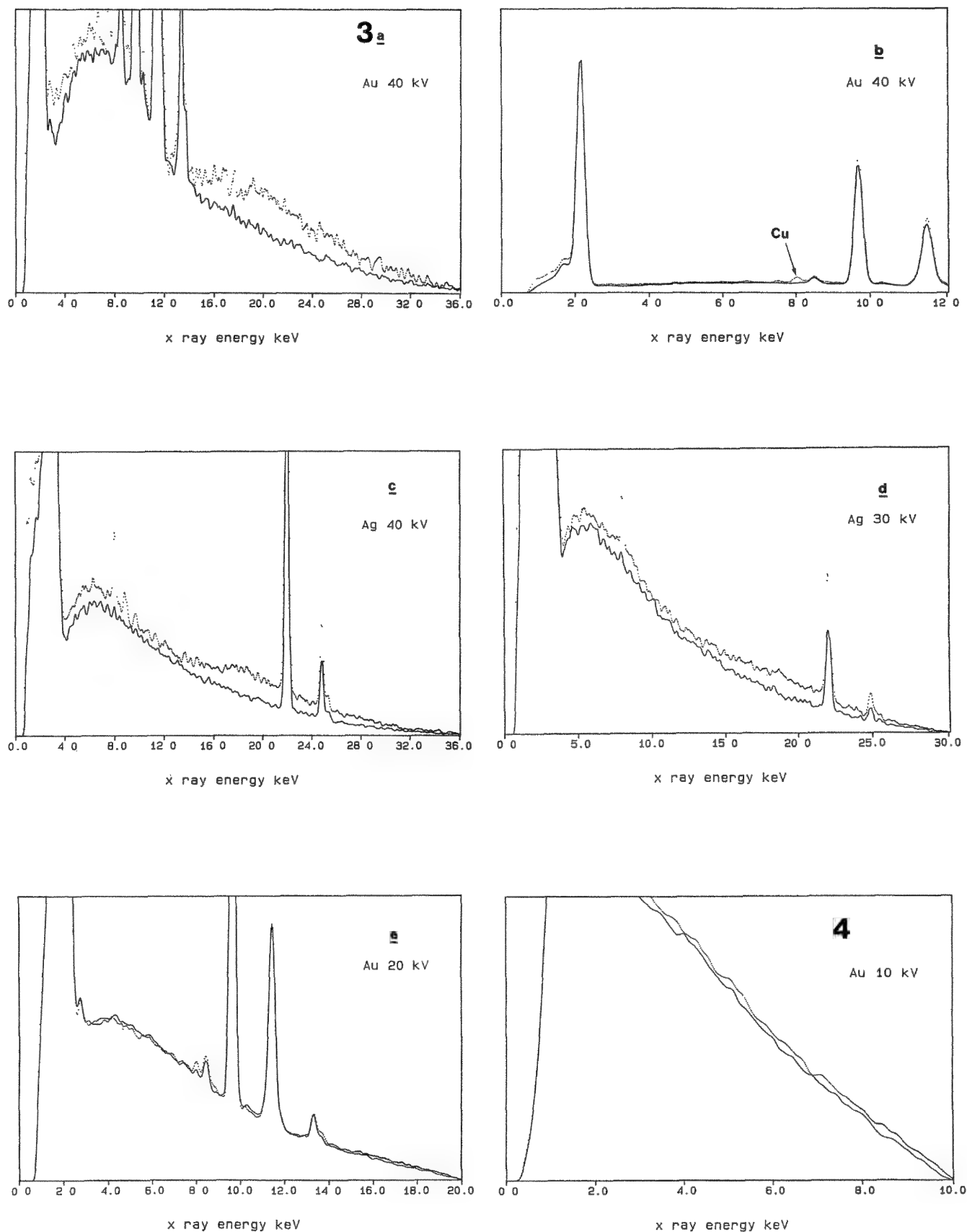


FIG. 3.--Gold and silver spectra collected with collimator and magnets (full line) and with no collimator (dotted line) at various accelerating voltages normalized so that lowest energy peaks are equal.

FIG. 4.--Spectra collected from coated (full line) and uncoated gold (dotted line) at 10 kV normalized to beam current.

Thomas¹¹ and the energy loss relation given by Love et al.¹² were used to calculate this angle for which the mean loss of energy of the electrons is 2.5 keV. We assume that the number of diffused electrons is small. The correction for a 40° take-off angle is larger by 15% or more than that for a 52.5° take-off angle. This approximate but conservative calculation shows that for light elements the anisotropy correction cannot be neglected in comparisons of spectra from detectors with different take-off angles. However, that would not explain the large discrepancies reported by Smith and Wynne¹ for carbon at a 15keV accelerating potential.

Conclusion

A modeling expression must be based on data that are free of the distortions produced by spurious x rays entering the detector. We have shown that the electron trap supplied with our microprobe is not totally effective if the ED detector is uncollimated. It is essential that similar testing be done on all detectors used for careful measurement of continuum. The data should be corrected for anisotropy in addition to absorption and backscatter loss, so that comparison of data from spectrometers at different take-off angles is possible. The available anisotropy corrections do not agree well, which may be a limitation to the derivation of a universally applicable generation expression. We are continuing work on the development of an expression that would summarize our own database as well as a modeling expression based on theoretical calculations.

References

1. D. G. W. Smith and D. A. Wynne, "The prediction of background intensities in energy-dispersive electron microprobe analysis," *Microprobe Analysis--1987*, 12-14.
2. J. A. Small, S. D. Leigh, D. E. Newbury, and R. L. Myklebust, *J. Appl. Phys.* 61: 459-469, 1987.
3. J. A. Small, D. E. Newbury and R. L. Myklebust, "Test of a bremsstrahlung equation for energy-dispersive x-ray spectrometers," *Microbeam Analysis--1987*, 20-22.
4. Von J. Heckel and P. Jugelt, "Absolute determination of the bremsstrahlung spectrum from thick targets bombarded with 15, 20 and 25 keV electrons," *Exper. Tech. der Physik* 31: 493-509, 1983.
5. N. Ware and S. J. B. Reed, "Background correction for quantitative electron microprobe analysis using a lithium drifted silicon detector," *J. Phys.* 6E: 286-288, 1973.
6. T. S. Rao Sahib and D. B. Wittry, "The x-ray continuum from thick targets," *Proc. 6th IXCOC*, Osaka, 1971, 131-137.
7. D. G. W. Smith and S. J. B. Reed, "The calculation of background in wavelength dispersive electron microprobe analysis," *X-ray Spectr.* 10: 198-202, 1981.
8. P. J. Statham, "The generation, absorption and anisotropy of thick-target bremsstrahlung and implications for quantitative energy dispersive analysis," *X-ray Spectr.* 5: 154-168, 1976.
9. Paul Kirkpatrick and Lucille Weidmann, "Theoretical continuous x-ray energy and polarization," *Phys. Rev.* 67: 321-339, 1945.
10. H. K. Tseng, R. H. Pratt, and C. M. Lee, "Electron bremsstrahlung angular distributions in the 1-500 keV energy range," *Phys. Rev.* A19: 187-195, 1979.
11. V. E. Cosslett and R. N. Thomas, "Multiple scattering of 5-30 keV electrons in evaporated metal films: 1. Total transmission and angular distribution," *Brit. J. Appl. Phys.* 13: 883-906, 1964.
12. G. Love, M. G. Cox, and V. D. Scott, "A versatile atomic number correction for electron-probe microanalysis," *J. Phys.* D11: 7-21, 1978.
13. J. A. Small (private communication).

ANALYSIS OF THIN FILMS BY ELECTRON PROBE MICROANALYSIS

J. D. Brown

The electron probe microanalyzer is a surprisingly sensitive analytical instrument for the analysis of thin films in which the sensitivity is for submonolayers for most elements in the periodic table. Many examples in the literature describe the analysis of thin films; even in the 1960s measurements were made on films as thin as 0.8 nm.¹ Most of these early measurements depended on calibration against films of known thickness for quantitative analysis.² More recently, quantitative analysis of thin and intermediate thickness films has been shown to be possible by use of only pure-element or compound standards and knowledge of $\phi(\rho z)$ curves.^{3,4} The purpose of this paper is to determine the limits to sensitivity for thin-film analysis in a modern electron probe microanalyzer and to compare measured limits of detection based on thin film standards with theoretical predictions based only on measurements from pure elemental standards.

Procedure

Thin films of Al, Cu, Ag, and Au were deposited on carefully polished substrates of Si and Ni. The deposited thicknesses were determined with an oscillating crystal thickness monitor, by measurements of deposited mass on a thin glass slide and a microbalance, and by thickness measurements in a profilometer. The intensities of the K, L, and/or M characteristic lines from the thin films were measured in a JEOL model 8600 electron probe microanalyzer with LiF, PET, or TAP crystals. Measurements were made at beam currents that were typically 30–50 nA at electron energies of 10–25 keV. The sensitivities were calculated as counts/s/nA/ $\mu\text{g}/\text{cm}^2$. To determine sensitivity for thin film analysis, the limit of detectability is defined as the thickness of film which would give a count rate 3 times the standard deviation for the background above the background count rate. The calculations are based on a beam current of 50 nA and a count time of 100 s. At the same time the count rate from pure elements combined with the $\phi(\rho z)$ curves can be used to calculate a sensitivity based on the same criterion for counts above background for the same beam currents and analysis times. Quantitatively, in terms of $\phi(\rho z)$, the minimum detectable limit ρz_{MDL} is

$$\frac{I_{\text{MIN}}}{I_{\text{A}}} = K_{\text{MIN}} = \frac{\int_0^{\rho z_{\text{MDL}}} \phi_{\text{f}}(\rho z) \exp(-\mu_{\text{f}} \rho z \csc \psi) d\rho z}{\int_0^{\infty} \phi_{\text{A}}(\rho z) \exp(-\mu_{\text{A}} \rho z \csc \psi) d\rho z}$$

where the subscript A refers to the pure-element standard and the subscript f refers to the thin film. For the calculation of K_{MIN} , the value for I_{MIN} is taken as 3 standard deviations above the background count rate for the pure substrates. These numbers are compared to evaluate the use of pure element standards as a means of establishing the sensitivity of an instrument for the analysis of thin films.

Results

Figure 1 shows the measured intensities above background for the copper thin films as counts/s/nA/ $\mu\text{g}/\text{cm}^2$ for both $K\alpha$ and $L\alpha$ lines on Si and Ni substrates. The dominant factors that seem to affect the intensity as a function of electron-beam energy are the ionization cross section and the substrate backscatter coefficient. For characteristic lines for which the overvoltage ratio is small, the intensity increases rapidly with increasing electron energy (for example Cu $K\alpha$); for large overvoltages, the intensity decreases with electron energy. This result is just in accord with the dependence of ionization cross section on electron energy. In addition, higher intensities are found for the higher atomic number substrate. Table 1 lists the sensitivity of this instrument for the analysis of thin films based on 100 s analysis time and 50 nA beam current. For most elements, characteristic lines, and electron energies studied here the sensitivity is a less than one monolayer. The advantage of using x rays for such analysis over more conventional surface analytical techniques is that such films can be seen even in the presence of hydrocarbon or oxide layers. On the other hand, the substrate must be free of the element in the thin film or sensitivity will be significantly reduced. The calculations of the sensitivity based on measurements from pure elements and based on $\phi(\rho z)$ curves are summarized in Table 2. These calculations are in good agreement with the measurements on the thin films and indicates that this method can be used to determine thickness of thin films with good accuracy.

Conclusions

The sensitivity of a modern electron probe microanalyzer for thin films has been measured with the use of both thin films and pure ele-

The author is at the Department of Materials Engineering, Faculty of Engineering Science, The University of Western Ontario, London, Ont., Canada N6A 5B9.

TABLE 1.--Sensitivity for thin-film analysis. (Measurements at 20 keV electron energy, 40 nA beam current, 100 s count time.)

Element	Element	Line	/s/nA/ μ g	Count/s/nA	Monolayers
Al	Si	K α	1.81	3.74	0.83
Al	Ni	K α	2.00	4.98	0.87
Cu	Si	K α	1.21	1.09	0.15
Cu	Ni	K α	1.54	2.84	0.29
Cu	Si	L α	0.74	0.86	0.33
Cu	Ni	L α	0.94	1.28	0.32
Ag	Si	L α	0.44	0.53	0.32
Ag	Ni	L α	0.53	1.12	0.40
Au	Ni	L α	0.36	1.92	0.41
Au	Ni	M α	1.34	14.2	0.30

TABLE 2.--Theoretical sensitivities for thin-film analysis based on measurements from pure elements and $\phi(\rho z)$ curves. (Based on measured backgrounds from Ni specimens (Table 1), 100 s count time, 20 keV electron energy, 50 nA beam current.)

Element	Line	Intensity c/s/nA	K_{MIN}	Z_{MDL} μ g/cm ²	Monolayers
Al	K α	3340	0.000056	0.031	0.56
Cu	K α	1470	0.000096	0.025	0.16
	L α	725	0.000134	0.051	0.31
Ag	L α	365	0.000232	0.073	0.36
Au	M α	695	0.000460	0.135	0.34

ments as standards. The results are comparable. The instrument is a good choice for the analysis of submonolayer thin films, particularly since calibration is relatively simple and the extreme care required to avoid surface contamination for other analytical techniques is not necessary.

References

1. G. H. Crockett and C. D. Davies, "Coating thickness measurement by electron probe microanalysis," *Brit. J. Appl. Phys.* 14: 813-816, 1963.
2. G. A. Hutchins, "Thickness determination of thin films by electron probe microanalysis," in McKinley et al., Eds., *The Electron Microprobe*, New York: Wiley, 1964, 390-404.
3. J. D. Brown, "New approaches to quantitative analysis of thin films and surfaces," *Spectrochim. Acta*. 38B: 1411-1419, 1983.
4. R. H. Packwood, G. Remond, and J. D. Brown, "Electron probe microanalysis of compositionally stratified materials," in *Proc. 11th IXCOM*, London, Ont., 274-280.

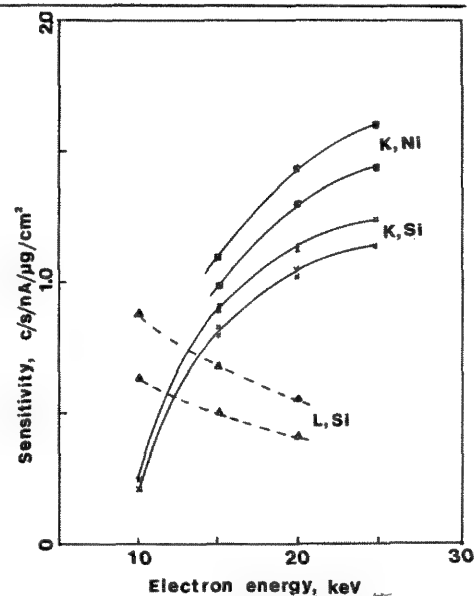


FIG. 1.--Measured sensitivity for analysis of thin Cu films on Si and Ni substrates: — Cu K α , Li F crystals; --- Cu L α , TAP crystals. Curves normalized for 1nA beam current, 1 μ g/cm² Cu film thickness. Duplicate curves are for different spectrometers.

CALCULATION OF DEPTH DISTRIBUTIONS OF X-RAY GENERATION BY THE MONTE CARLO TECHNIQUE

K. F. J. Heinrich, D. E. Newbury, and R. L. Myklebust

The correction for absorption of primary x rays within the target is of special importance in electron probe microanalysis because it can cause large errors, particularly under the inappropriate operating conditions (e.g., low-energy x-ray line excited at high operating voltage).¹ Experience has shown that, because of error compensation, errors in the absorption correction are usually small unless the ratio of absorption factors $f(\chi)$ of specimen and standard falls below 0.6. However, measurements under such conditions are still performed and reported,² and in some cases may therefore improve the quality of electron probe measurement.

Information about primary absorption includes theoretical $f(\chi)$ models (which, without experimental verification, are of uncertain accuracy), experiments with variable x-ray emergence angle,³ measurements on targets of known composition, the tracer experiments,⁴⁻⁷ and Monte Carlo calculations. Of these, the tracer experiments are the most significant. In principle, they also reveal the atomic number effects [$\phi(\rho z)$ methods].⁸⁻¹⁰ Most models that describe the depth distribution function are based on the tracer experiments. Such experiments are difficult at best and impossible to perform in many cases of interest. The Monte Carlo electron trajectory simulation can, in principle, directly calculate the depth distribution as measured by the tracer experiments and as calculated by Monte Carlo simulation and the theoretical models.

We find it convenient for the purpose of error analysis to separate the two effects of absorption and atomic number. As was shown in 1970,¹¹ the effects of the operating potential E_0 and of the critical excitation potential E_C can be described by the γ factor:

$$\gamma = E_0^{1.65} - E_C^{1.65}$$

If we divide the depth parameter z (mass thickness) by γ , we obtain a normalized depth scale that compensates for the effects of variation in E_0 and E_C . As a consequence, in order to scale the graph properly, the $\phi(z)$ axis must then be multiplied by γ . If we also adjust the generated x-ray intensities so that the area under the curve is equal to unity, we also eliminate the atomic-number effect (i.e., the effect of target composition on excitation and backscatter losses), and we are left with shape variations of the depth distribution for all energies and matrices, as illustrated for ex-

perimental data in Fig. 1a.⁵ For convenience in plotting, the $\phi(z)$ axis is scaled by 4γ , so that the normalized plot fits into the rectangular space of the graph. If we apply the same procedure to the intensities after absorption in the target, and integrate over the range of x-ray production, we obtain the factor $f(\chi)$.

The Monte Carlo simulation used for this work is based on that of Kyser and Murata, with extensive modifications to adapt it to specific problems of interest in quantitative electron probe microanalysis.¹²⁻¹⁴ This simulation assumes that all the angular deviation of the beam electrons arises from elastic scattering. The slight angular deviations due to inelastic scattering are ignored. Energy loss is treated as a continuous process rather than as a collection of discrete mechanisms, because of the difficulty in describing the individual inelastic scattering cross sections. The program makes use of the screened Rutherford cross section for calculating the mean free path due to elastic scattering, and the partial cross section with respect to angle is used to calculate the angular distribution of elastic scattering. The loss of energy from the primary electron due to inelastic scattering is calculated by means of the Bethe continuous energy loss approximation with the mean ionization potential given by Berger and Seltzer.^{15,16} For the purpose of calculating the depth distribution of primary ionization, the ionization cross section of Bethe was employed.¹⁵ There is considerable uncertainty in the choice of the constants for use in this equation at overvoltages that approach unity.¹⁷ The overvoltage is $U = E/E_C$, where E is the electron energy and E_C is the ionization edge energy. We chose to use constants (e.g., those of Mott and Massey¹⁹ or Green and Cosslett²⁰) which insure that the ionization cross section remains positive down to the threshold of $U = 1$.

Comparison of Monte Carlo Calculations with Experimental Data

We are studying all experimental depth distribution curves for normal beam incidence available in the literature and comparing the curves with the results calculated with the Monte Carlo simulation. The comparison of the normalized curves is only valid for observations relating to the absorption correction and does not imply anything concerning the atomic-number correction.

When the experimental data are compared with Monte Carlo calculations, two observations can be made. (1) For typical analysis

The authors are with the Center for Analytical Chemistry, National Bureau of Standards, Gaithersburg, MD 20899.

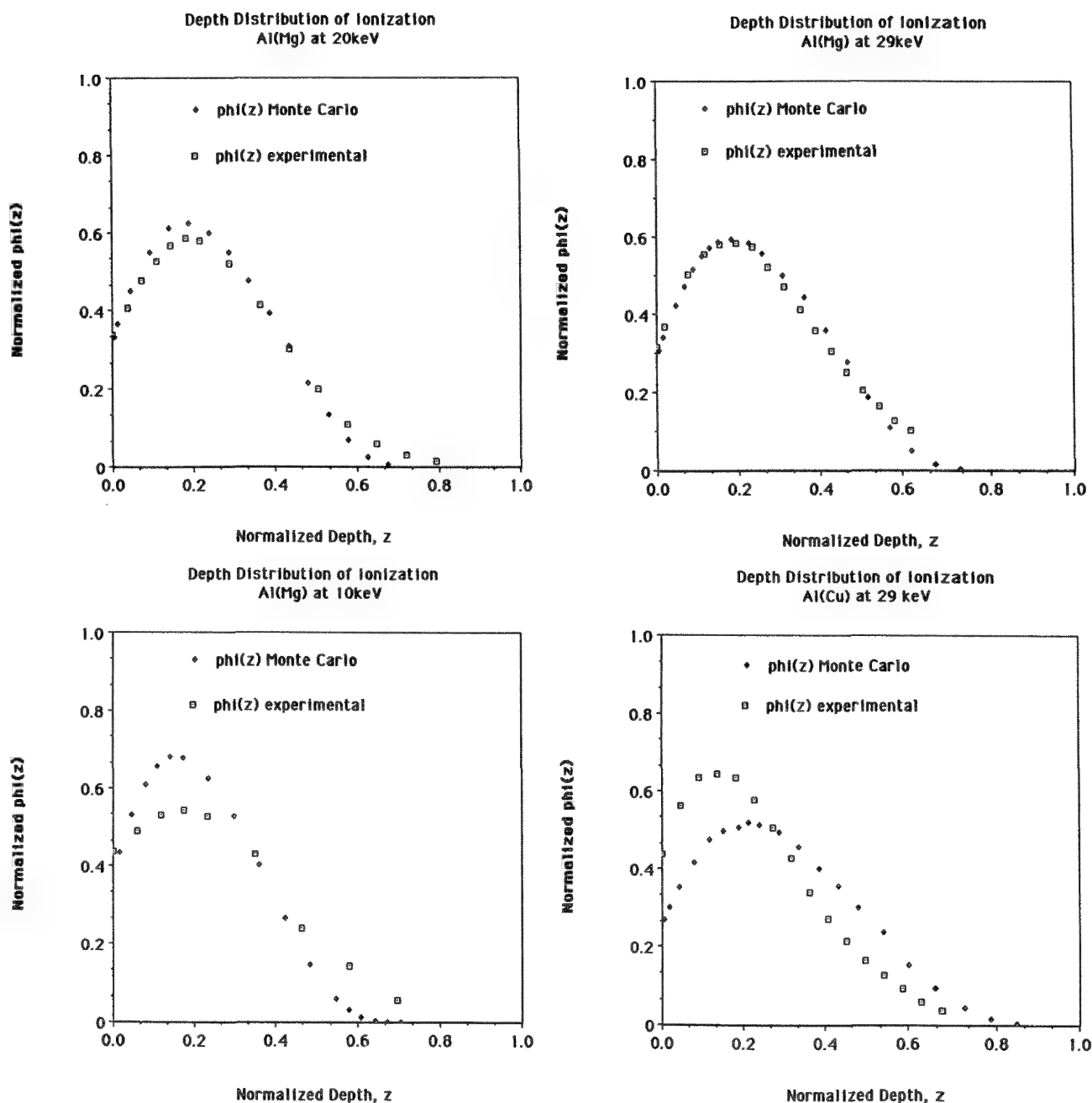


FIG. 1.--Normalized plots of experimental data⁵ and Monte Carlo calculations of depth distribution of ionization of K-edge of Al target with Mg tracer at electron-beam energy of (a) 20 keV, (b) 29 keV, (c) 10 keV. Depth scale is divided by factor γ ; vertical axis is multiplied by 4γ for proper scaling.

FIG. 2.--Comparison plots of experimental data⁴ and Monte Carlo calculations of depth distribution of ionization of K-edge of Al with Cu tracer at electron-beam energy of 29 keV. Normalized scales.

conditions of beam energy relative to critical excitation energy, the fit between the tracer experiments and the Monte Carlo calculations is very close. This close correspondence can be seen in Figs. 1a and b for the experimental data of Castaing⁵ for K-edge ionization in an aluminum matrix with a magnesium tracer, designated Al(Mg K α) at 20 keV and 29 keV. (2) For more extreme conditions, such as Al(Mg K α) at 10 keV or Al(Cu K α) at 29 keV, as shown in Figs. 1c and 2, the agreement is not as good. It is

not possible at present to determine unequivocally which description of the ionization depth distribution is best, the experimental or the Monte Carlo simulation.

Comparison of Monte Carlo Calculations with Mathematical Models

Our computer programs permit comparison of the wide range of published models for the depth distribution with the experimental data and the Monte Carlo calculations. An example

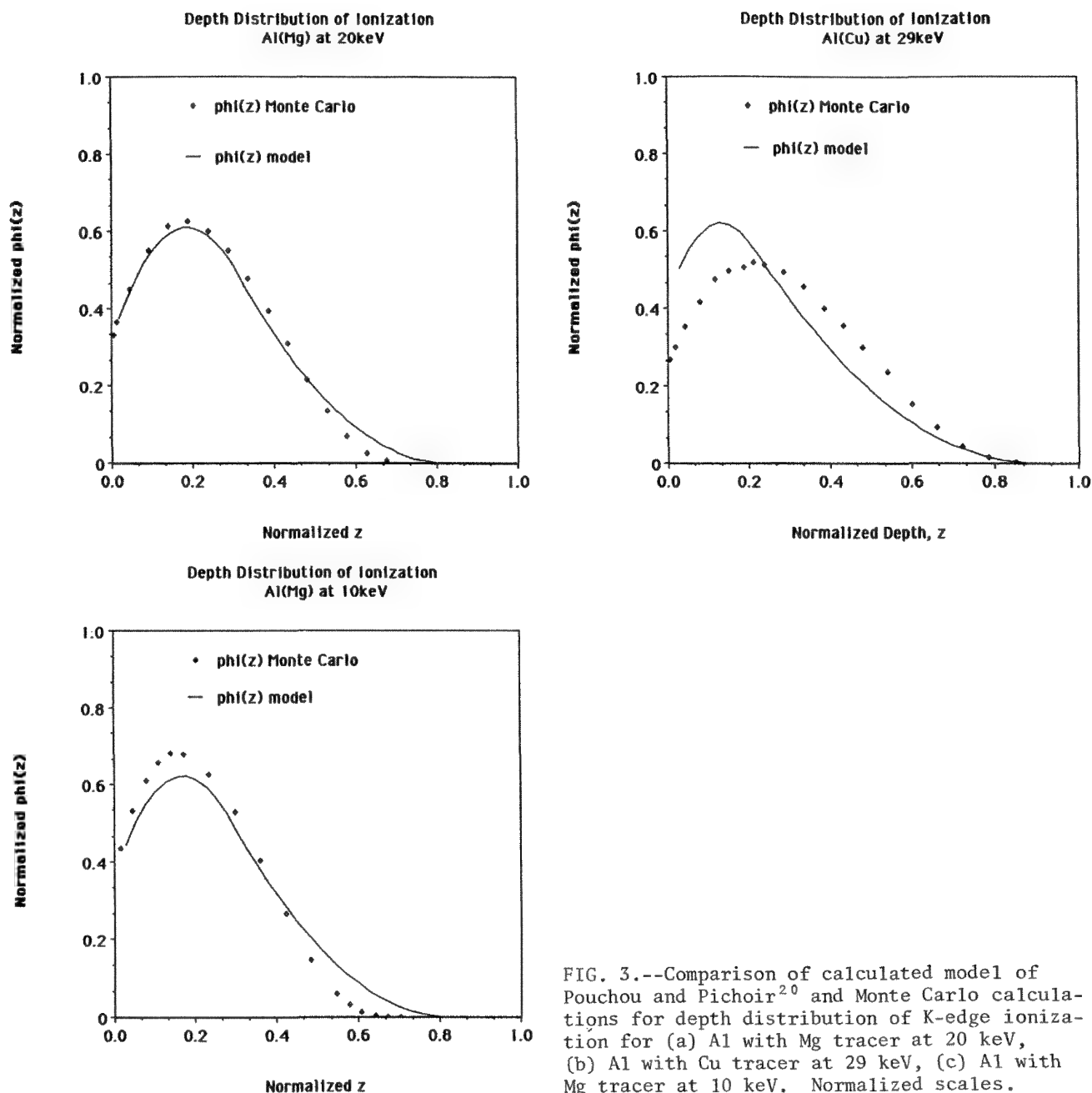


FIG. 3.--Comparison of calculated model of Pouchou and Pichoir²⁰ and Monte Carlo calculations for depth distribution of K-edge ionization for (a) Al with Mg tracer at 20 keV, (b) Al with Cu tracer at 29 keV, (c) Al with Mg tracer at 10 keV. Normalized scales.

of the model of Pouchou and Pichoir²⁰ for Al(Mg K α) at 20 keV is compared with the Monte Carlo calculation in Fig. 3a, where the correspondence is seen to be quite good. In the cases of the outliers noted above, the agreement is not as good, e.g., Al(Cu K α) at 29 keV in Fig. 3b and Al(Mg K α) at 10 keV in Fig. 3c. This result is not surprising in view of the fact that the models can be expected to fit the experimental data in preference to the Monte Carlo calculations, since most of the models were developed from the data.

Conclusions

The Monte Carlo calculations agree with experimental models for analytical conditions that correspond to practical operating condi-

tions for electron probe microanalysis. For more extreme conditions, the agreement is not as good. It is not currently possible to determine which source of information is most accurate. If Monte Carlo calculations prove to be sufficiently accurate to extend the database of ionization depth distribution functions, more robust mathematical models can be developed.

References

1. H. Yakowitz and K. F. J. Heinrich, "Absorption uncertainty," *Mikrochimica Acta* 182, 1968.
2. A. D. Romig, P. F. Hlava, and W. F. Chambers, "A comparison of correction procedures for the x-ray microanalysis of U-Nb al-

- loys," *Microbeam Analysis--1987*, 15.
3. M. Green, *Proc. 3rd ICXOM*, New York: Academic Press, 1963, 361.
4. R. Castaing and J. Descamps, *J. Phys. Rad.* 16: 304, 1955.
5. R. Castaing and J. Henoc, *Proc. 4th ICXOM*, Paris: Hermann, 1966, 120.
6. A. Vignes and G. Dez, *Brit. J. Appl. Phys.* 2: 1309, 1968.
7. J. D. Brown and L. Parobek, *Adv. X-ray Analysis* 16: 198, 1973.
8. R. H. Packwood and J. D. Brown, "Concerning x-ray production and quantitative analysis," *Microbeam Analysis--1980*, 45.
9. G. F. Bastin, F. J. Van Loo, and J. M. Heijligers, *X-ray Spectrom.* 13: 91, 1984.
10. R. H. Packwood and J. D. Brown, *X-ray Spectrom.* 10: 138, 1981.
11. K. F. J. Heinrich, *NBS Tech. Note* 521, 1970.
12. D. E. Newbury and R. L. Myklebust, "Monte Carlo electron trajectory simulation of beam spreading in thin foil targets," *Ultramicroscopy* 3: 391-395, 1979.
13. D. F. Kyser and K. Murata, "Quantitative electron microprobe analysis of thin films on substrates," *IBM J. Res. Dev.* 18: 352, 1974.
14. D. E. Newbury and R. L. Myklebust, "Monte Carlo electron trajectory calculations of electron interactions in samples with special geometries," in *Electron Beam Interactions with Solids*, Chicago: SEM, 1984, 153.
15. H. A. Bethe, "Theory of the transmission of corpuscular radiation through matter," *Ann. Phys.* 5: 325, 1930.
16. M. J. Berger and S. J. Seltzer, *Tables of Energy Losses and Ranges of Electrons and Positrons*, NASA Report SP-3012, Washington, 1964.
17. C. J. Powell, "Evaluation of formulas for inner-shell ionization cross sections," in *Use of Monte Carlo Calculations in Electron Probe Microanalysis and Scanning Electron Microscopy*, National Bureau of Standards Spec. Publ. 460, Washington, 1976.
18. N. F. Mott and H. S. W. Massey, *The Theory of Atomic Collisions*, 2nd ed., Oxford University Press, 1949, 243.
19. M. Green and V. E. Cosslett, *Proc. Phys. Soc. (London)* 78: 1206, 1961.
20. J. L. Pouchou and F. Pichoir, "'PAP' $\phi(\rho z)$ procedure for improved quantitative microanalysis," *Microbeam Analysis--1985*, 104.

PROGRESS IN THE MEASUREMENT AND CALCULATION OF THE DEPTH DISTRIBUTION OF LOW-ENERGY X-RAY GENERATION

Peter Karduck and Werner Rehbach

The knowledge of the exact depth distribution of generated x radiation in a target is a basic requirement in quantitative electron probe microanalysis. Extensive measurements of depth distribution curves $\phi(\rho z)$ have been performed in the past 35 years for electron energies between 6 and 37 keV and excitation energies $E_c \geq 1.84$ keV. Since 1963 Monte Carlo (MC) simulations of electron scattering and energy losses in targets have also been used to calculate x-ray depth distributions. Several generalized analytical expressions for $\phi(\rho z)$ have been proposed for the calculation of the absorption correction as well as the atomic number correction in matrix correction procedures. Now the development has reached a point where reliable $\phi(\rho z)$ data are also required for soft x rays, especially for the K-radiation of light elements, which have become more and more important in the quantitative analysis of modern materials such as hard coatings, ceramics, semiconductors, and alloys. Although the development of correction procedures with good performance in light-element analysis has advanced over the years, there is still no model that is based on reliable data of depth distributions for soft x rays. This paper briefly reviews the development in $\phi(\rho z)$ determination and presents the results of new measurements and MC simulations of $\phi(\rho z)$ for soft x rays.

Experimental Measurements of $\phi(\rho z)$ Curves

Castaing and Descamps first demonstrated in 1955 the usefulness of tracer experiments with the sandwich sample technique for the determination of $\phi(\rho z)$ in electron-probe microanalysis. They produced a series of $\phi(\rho z)$ curves for systems of tracer and matrix elements with atomic numbers Z matching closely. From these results they deduced absorption correction factors $f(\chi)$. Several other authors have adopted this method using a tracer layer and matrix with similar atomic numbers Z (for a review, see Ref. 2). Brown and coworkers² successfully extended this tracer technique for tracer and matrix elements with very different atomic numbers Z in order to measure the atomic number effect as well.

Schmitz et al.³ and Büchner and Pitsch³ attempted another experimental technique, in which a wedge-shaped tracer is deposited on a matrix material with an atomic number lower than that of the tracer ($\Delta Z = 1$). The characteristic intensity of the tracer element is

measured along a line across the wedge and gives the integral of $\phi(\rho z)$ for each thickness (depth) of the tracer element. The differentiation of this integral curve results in the $\phi(\rho z)$ curve itself. On the basis of a series of such $\phi(\rho z)$ curves, Büchner and Pitsch proposed an exponential description for $\phi(\rho z)$ and established empirically the so-called wedge specimen correction method.⁴

Sufficient measurements of $\phi(\rho z)$ curves were the basis for Packwood and Brown to establish a completely new approach in 1981 based on a Gaussian equation modified at the sample surface by a transient exponential function:⁵

$$\phi(\rho z) = \gamma_0 \left[1 - \frac{\gamma_0 - \phi_0}{\gamma_0} \exp(-\beta \rho z) \right] \exp[-\alpha^2 (\rho z)^2]$$

ϕ_0 is the surface ionization function and γ_0 the amplitude of the Gaussian equation. The authors deduced expressions for the parameters α , β , and γ_0 by simple theoretical considerations and established the so-called Gaussian $\phi(\rho z)$ correction procedure.

We have also applied the tracer sandwich sample technique for extremely thin tracer layers ($\sim 4 \mu\text{g}/\text{cm}^2$). In total 49 partly overlapping matrix layers were deposited on the tracer to measure $\phi(\rho z)$ curves for soft x rays at $E_c \leq 1$ keV. The layer thicknesses were determined by four independent methods, which resulted in an accuracy of about 5%. Experimental details are described in Ref. 6. The values for ϕ_0 were determined by measurements of the x-ray intensity of the tracer element on substrates with various atomic numbers Z and extrapolation to the intensity for $Z = 0$. This method was first proposed by Hutchins⁷ and Reuter.⁸

Monte Carlo Simulation of Electron Trajectories

As an alternative to tracer experiments $\phi(\rho z)$ curves can also be calculated by Monte Carlo simulations of electron trajectories from theoretical models for the elastic and inelastic electron scattering. (For details about such models in current use and the development in this specific field see also Refs. 9 and 2.) In order to investigate the production of low-energy x rays, a very complex Monte Carlo procedure first introduced by Krefting and Reimer¹⁴ has been adopted for the calculation of x-ray depth distributions. The program has been modified in some points and takes into account the following steps:

P. Karduck and W. Rehbach are with Gemeinschaftslabor für Elektronenmikroskopie der RWTH Aachen, D-5100 Aachen, Federal Republic of Germany.

1. the use of exact Mott cross sections for single elastic electron scattering with angles $> 10^\circ$ instead of the Rutherford cross sections;

2. multiple elastic small angle scattering following Lewis¹⁰ for angles $< 10^\circ$ based on a mean angular deviation after half a mean free path;

3. inelastic single electron-electron scattering after Gryzinski¹¹ including the production of secondary electrons with energies > 200 eV and their simulation up to the third generation;

4. calculation of the energy loss along a trajectory by the Bethe formula, with subtraction of the energy losses due to single inelastic events considered in three;

5. simplification of the Bethe formula for low energies according to Rao Sahib and Wittry;¹²

6. simulation of each $\phi(\rho z)$ curve with 10 000 electron trajectories; and

7. calculation of ionization cross sections for the simulation of the x-ray production according to Hutchins,¹³ with $m = 0.9$.

Krefting and Reimer¹⁴ demonstrated the excellent reliability of a similar program by calculations of backscatter coefficients in thin films and the angular and energy distribution of backscattered electrons.

Results

Some boundary conditions restrict the possibilities of experimental $\phi(\rho z)$ determinations for soft x rays by tracer experiments. Accurate intensity measurements can only succeed for low absorption coefficients of the tracer radiation in the matrix material, i.e., $\mu/\rho \ll 10\,000\text{ cm}^2/\text{g}$. Due to the low efficiency for soft x rays there is a limit of detectability for x rays emerging from depths greater than $200\text{ }\mu\text{g}/\text{cm}^2$. This result implies that for E_0 greater than 15 keV only incomplete $\phi(\rho z)$ curves can be obtained. Excessively high tracer thicknesses can have a strong effect on the shape of a $\phi(\rho z)$ curve. By definition the tracer has to be so thin that the electrons suffer no significant scattering or backscattering in it. When the electrons are partly scattered in the tracer, the intensity of the isolated tracer is too high. If all other intensities of greater depth are related to that intensity, the curve is compressed to lower values, as demonstrated in Fig. 1 for Cr $L\alpha$ in Al, and tracers with a thickness of 4 and $12\text{ }\mu\text{g}/\text{cm}^2$, respectively. The same effect can be found for very thin tracers but low primary electron energies. Such restrictions are not valid for the application of a MC program.

The Surface Ionization ϕ_0

Despite the experimental difficulties in determining ϕ_0 , the results as shown in Fig. 2 present interesting deviations from the models of Reuter⁸ or Love et al.¹⁵ used mostly in correction procedures. As opposed to the predictions, the ϕ_0 values show a slight increase

even for $U_0 > 20$ ($U_0 = E_0/E_C$), whereas the empirical curves give a ϕ_0 independent of U_0 . Furthermore, for low values of U_0 , ϕ_0 increases with a smaller slope than predicted. In spite of the experimental uncertainties, a small increase of ϕ_0 with decreasing excitation energy E_C is seen. The MC values in Fig. 3 follow the trends described above. The effect of E_C on ϕ_0 is given in detail in Table 1, as a list of MC values of ϕ_0 for Ag as matrix material. Such an E_C dependence has not been previously taken into consideration by any of the models. The increase of ϕ_0 at high overvoltage ratios U_0 is caused by the fast secondary electrons (FSE) having enough energy to produce soft x rays. In Fig. 4 the fraction of x rays generated by primary electrons is plotted separately for B $K\alpha$ in Au. The portion of ϕ_0 excited by FSE reaches 12% of the total amount. This effect has not been considered in previous investigations either, because in all experimental work for ϕ_0 performed until now Si $K\alpha$ was the lowest x-ray energy. In MC programs Krefting and Reimer¹⁴ first pointed out qualitatively the contribution of FSE to the total x-ray production but did not pursue the effects quantitatively; all other MC models do not deal with FSE. The authors have proposed a new analytical expression for ϕ_0 taking into account these new results.¹⁹

The Depth Distribution $\phi(\rho z)$

Rehbach and Karduck have already demonstrated qualitatively that experimental $\phi(\rho z)$ curves of soft x rays describe the expected physical behavior of x-ray production in depth as a function of the parameters E_0 , E_C , and Z .¹⁶ The intention of this contribution is to compare recent experimental results with the $\phi(\rho z)$ calculation by the MC program. What is to be shown is whether the MC data are in satisfactory agreement with the experimental curves, so that they can be used to optimize a generalization of the analytical $\phi(\rho z)$ description for light elements. Figures 5 through 8 show some selected $\phi(\rho z)$ curves for various tracer and matrix materials, as well as the corresponding MC data. As seen in Fig. 5, the MC curve is in good agreement with the Si $K\alpha$ data in Au for 30 keV, whereas for 10 keV the MC data exceed the experimental ones. A similar behavior has been found for nearly all systems at low primary electron energies. For soft x rays the depth of maximum x-ray generation is predicted exactly by the MC program. For relatively high E_0 the absolute values of MC and experimental $\phi(\rho z)$ are also in excellent agreement (Figs. 6 through 8). The result is that for low values of E_0 , the MC curves are systematically higher than those of the corresponding experimental curves. Recently similar results have been presented by Sewell et al., who interpreted the effect as a systematic overestimation due to their simplified MC model.¹⁷

Considering the results of the present

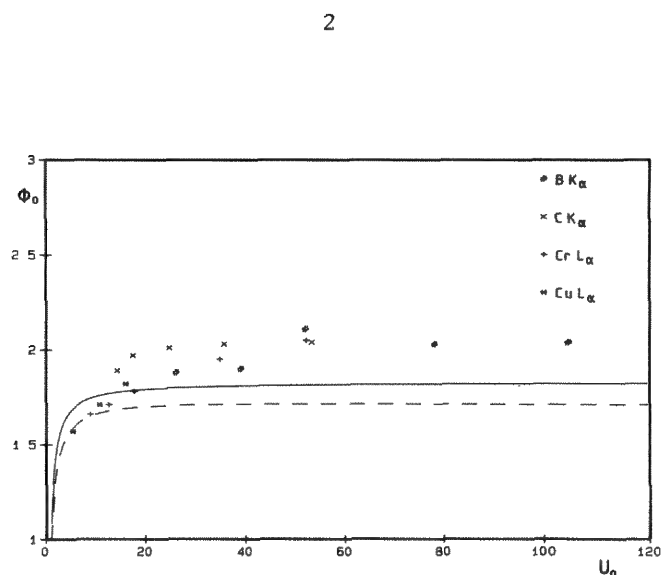
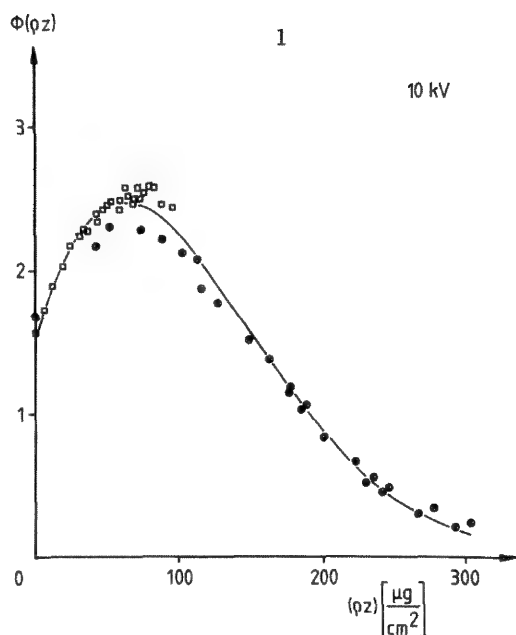


FIG. 1.-- $\phi(\rho z)$ curves of Cr L α in Al for tracer thickness 4 $\mu\text{g}/\text{cm}^2$ (\square) and 12 $\mu\text{g}/\text{cm}^2$ (\bullet).
FIG. 2.--Experimental ϕ_0 as function of overvoltage ratio U_0 for various x ray lines in Ni.

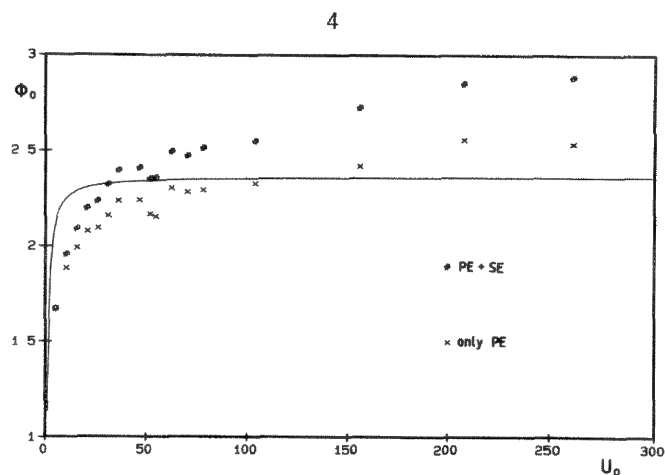
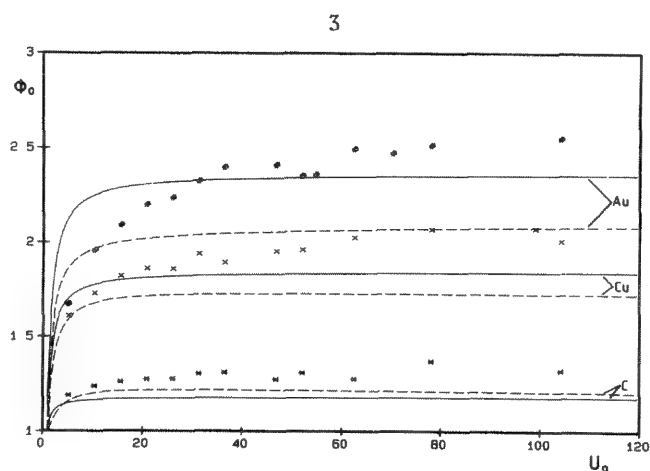


FIG. 3.-- ϕ_0 as function of overvoltage ratio U_0 for B K α in matrix materials C, Cu, and Au (MC data).

FIG. 4.--Contribution of fast secondary electrons to ϕ_0 as function of overvoltage ratio U_0 , B K α in Au (MC data).

TABLE 1.-- ϕ_0 values in Ag: Tracer radiation.

E_0 [keV]	B K α	C K α	Cr L α	Cu L α
5	2.11	2.04	1.92	1.81
10	2.24	2.15	2.14	1.99
15	2.29	2.20	2.14	2.06
20	2.35	2.24	2.18	2.10

investigation it is more likely that the influence of the tracer thickness is responsible for the discrepancy, as shown previously in Fig. 1.

The experimental curve in Fig. 5b was obtained with a tracer thickness of 20-30 $\mu\text{g}/\text{cm}^2$, but the maximum of the curve is $\rho z_m = 24 \mu\text{g}/\text{cm}^2$, which proves a tracer effect for low E_0 . The same holds for Fig. 6a with $\rho z_m = 14.5 \mu\text{g}/\text{cm}^2$ and a tracer thickness of 4 $\mu\text{g}/\text{cm}^2$. As a result the authors prefer the use of MC data for a consequent optimization of a generalized $\phi(\rho z)$ description. Detailed results of that procedure are given in Ref. 19. One reason for the good performance of the MC model in predicting $\phi(\rho z)$ curves of soft x rays is the consideration of the FSE, which contribute 19% of the generated x rays in the

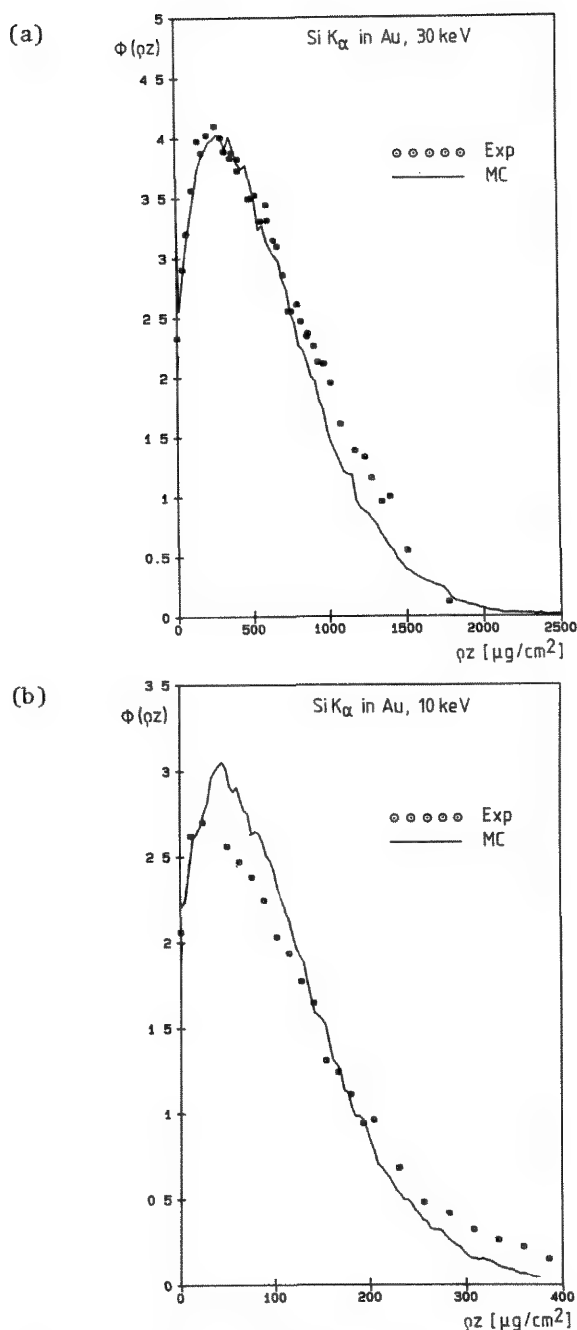


FIG. 5.-- $\phi(\rho z)$ curves for Si $K\alpha$ in Au; (a) 30 keV, (b) 10 keV.

case of B $K\alpha$ in Ag at 9 keV (Fig. 7c). Without the FSE simulation the MC model would fail for excitation energies below 1 keV. In the literature this effect is assumed to have a negligible effect on the total x-ray production.¹⁸

The Gaussian $\phi(\rho z)$ Approach

The shape of $\phi(\rho z)$ curves can be described by the Gaussian $\phi(\rho z)$ approach. Several authors have found an excellent fit of experimental data by the equation given above. But Packwood and Brown mentioned a few exceptions in an Al matrix at high overvoltage ratios, which produced anomalous values for γ_0 and β .⁵ In the range of soft x rays the experimental

data could also be fitted reasonably by the Gaussian approach.^{6,16} For example, the solid lines in Figs. 1, 6, and 9 were obtained by a least-square fit of Eq. (1) to the experimental and the MC data, respectively.

The new MC data now available for ultrasoft x rays like B $K\alpha$ in a wide range of matrix elements and for primary electron energies from a few keV up to 50 keV expand the possibility of application into the extreme but important ranges of EPMA. Figure 9 gives MC curves of $\phi(\rho z)$ in four different matrix materials for C $K\alpha$. The solid lines represent the fitted Gaussian expressions. The dashed lines show the pure Gaussian curves, which describe the depth distribution for the case that the electrons follow a random walk beginning at the sample surface. Indeed curves (a) and (b) behave according to the theoretical predictions that near the surface the state of electron randomization is controlled by the exponential with β and that the tail of the $\phi(\rho z)$ curves is completely described by the pure Gaussian.⁵

For low atomic numbers like 13 (Al) (Fig. 9d), the state of complete randomization even at $E_0 = 7$ keV is not reached at a depth important for the emitted x rays. Consequently for increasing primary electron energy this state of randomization would never take place. Although the curve can be described fairly well by the Gaussian approach, the values for γ_0 and β become unrealistic for matrices with low atomic numbers and soft x rays. In practical applications of EPMA, the situation as described above occurs in the analysis of oxides, carbides, nitrides, and borides with an average atomic number equal or less than 13. The significance of this fact for the generalization of $\phi(\rho z)$ and its application in a matrix correction routine is demonstrated quantitatively by Rehbach and Karduck.¹⁹

Conclusions

Tracer experiments with sandwich samples are a suitable technique to investigate the depth distribution $\phi(\rho z)$ of soft x rays in electron probe microanalysis. In doing so, one must obey an important boundary condition: the tracer has to be thin enough so that the primary electrons suffer no elastic scattering. Hence the limits of tracer experiments are set by the competition between this condition and the necessity for high x-ray intensities. For soft x rays a tracer thickness of $4 \mu\text{g}/\text{cm}^2$ is appropriate for electron energies of 10 keV and more. Below 10 keV a tracer effect is registered. Other restrictions of the tracer technique are given by high absorption of the x rays in the matrix material or by experimental difficulties.

The Monte Carlo simulation of electron scattering and energy loss in solids is able to overcome these problems even for the depth distribution of soft x rays, as long as a program is used that also considers single inelastic scattering and the production of x rays by fast secondary electrons. The results obtained with such a program are in good agreement with the

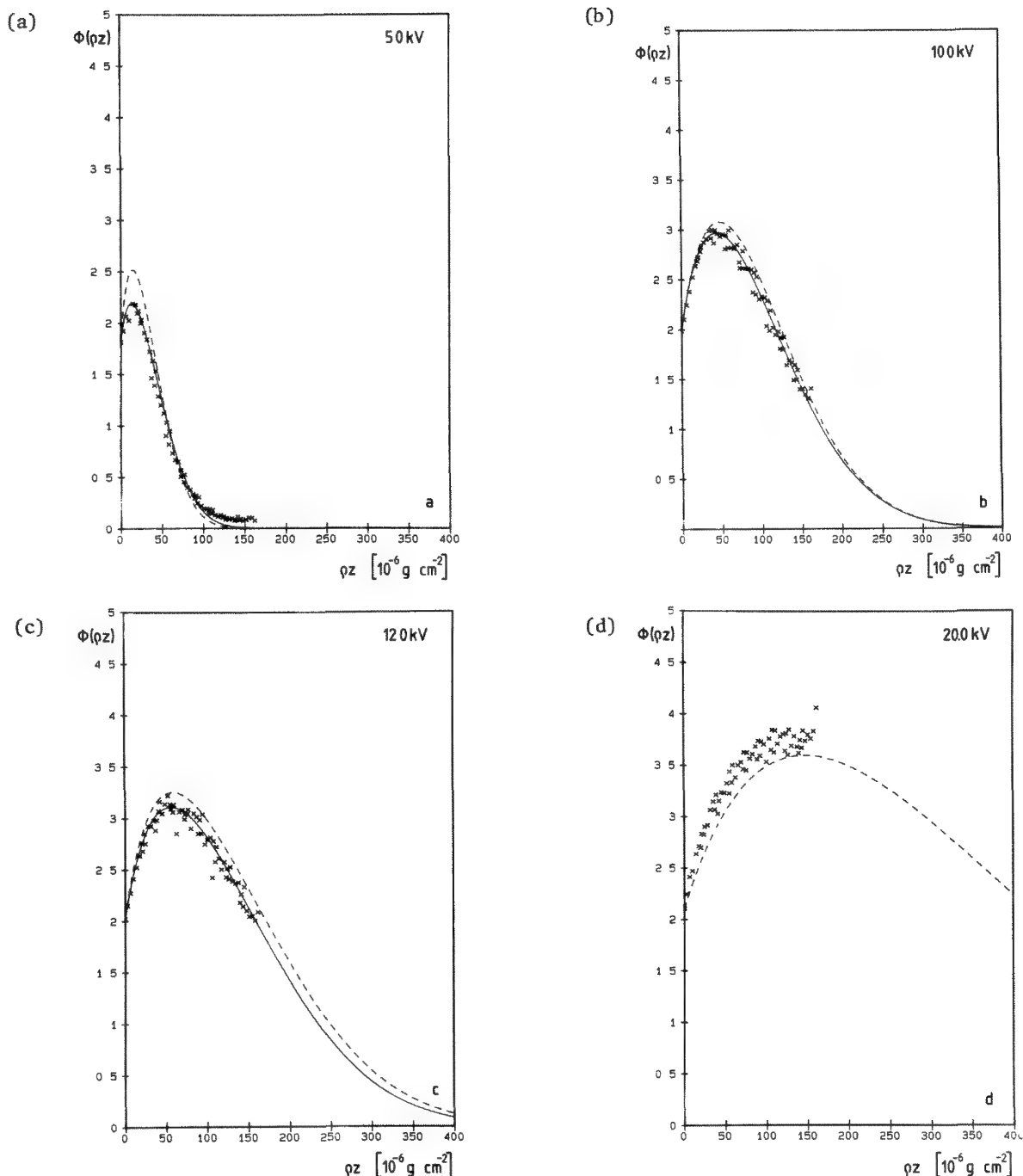


FIG. 6.--Experimental (---) and MC (×) $\phi(\rho z)$ curves for Cu $L\alpha$ in Ag.

experiments and are superior to the experimental $\phi(\rho z)$ results found for low electron energies and highly absorbing systems. The authors prefer the MC results as a basis for a systematic generalization of an analytical $\phi(\rho z)$ description for soft x rays.

References

1. R. Castaing and J. Descamps, *J. Physique et Radium* 16: 304, 1955.
2. J. D. Brown, "Modeling of depth distribution of x-ray production," in D. F. Kyser, H. Niedrig, D. E. Newbury, and R. Shimizu, Eds., *Electron Beam Interactions with Solids*, Chicago, SEM, 1982, 137.
3. U. Schmitz, R. C. Ryder and W. Pitsch, *Proc. 5th ICXOM*, Berlin, 1969, 104.
4. A. R. Büchner and W. Pitsch, *Z. Metallkunde* 62: 392, 1971.
5. R. H. Packwood and D. J. Brown, *X-Ray Spectrom.* 10: 138, 1981.
6. P. Karduck and W. Rehbach, *Mikrochim. Acta Suppl.* 11: 289, 1985.
7. G. A. Hutchins, in T. D. McKinley et al., Eds., *The Electron Microprobe*, New York: Wiley, 1966, 390.
8. W. Reuter, *Proc. 6th ICXOM*, Tokyo, 1972,

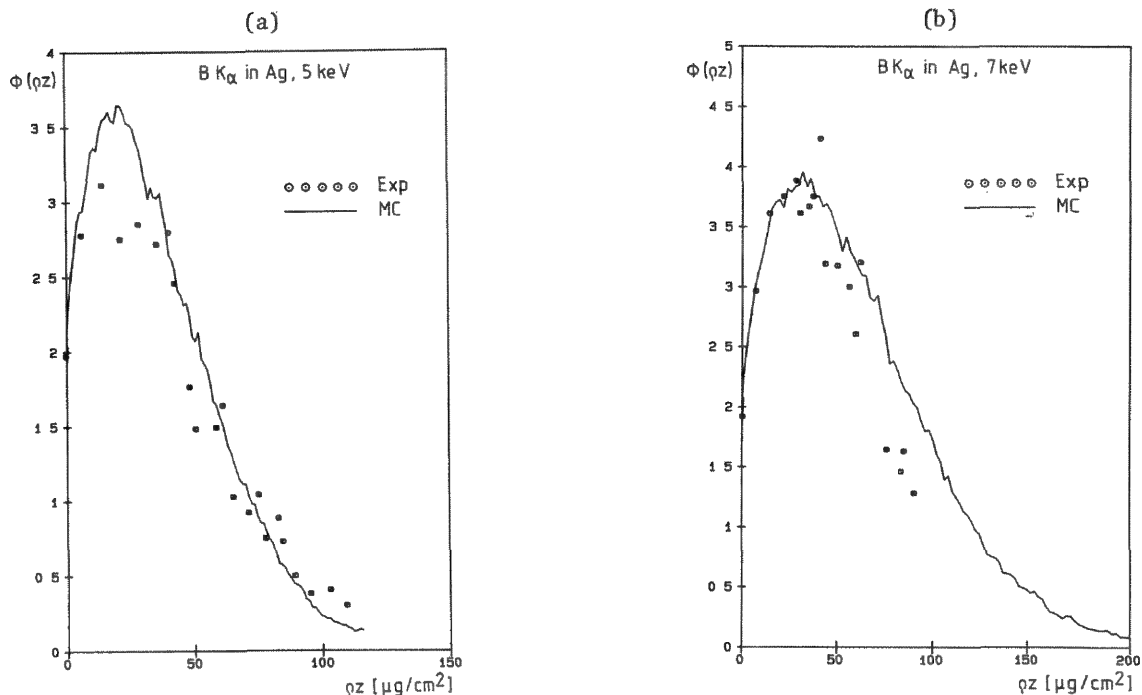


FIG. 7.--Experimental and MC- $\phi(\rho z)$ curves for B $K\alpha$ in Ag; (a) 5 keV, (b) 7 keV.

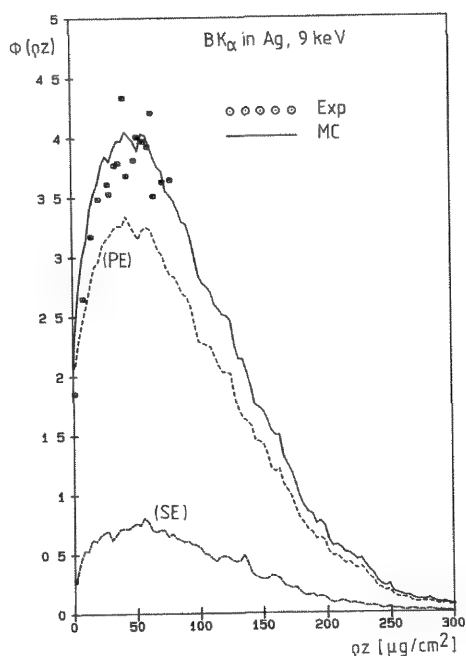


FIG. 8. Contribution of fast secondary electrons (SE) to $\phi(\rho z)$ for B $K\alpha$ in Ag, 9 keV.

121.

9. K. F. J. Heinrich, D. E. Newbury, and H. Yakowitz, Eds., *Use of Monte Carlo Calculations in Electron Probe Microanalysis and Scanning Electron Microscopy*, NBS Spec. Publ. 460, 1976.

10. H. W. Lewis, *Phys. Rev.* 78: 526, 1950.

11. M. Gryzinski, *Phys. Rev.* 138: 2A: 337, 1965.

12. T. S. Rao Sahib and D. W. Wittry, *J. Applied Phys.* 45: 5060, 1974.

13. G. A. Hutchins, "Electron probe microanalysis," in P. F. Kane and G. B. Larrabee, Eds., *Characterization of Solid Surfaces*, New York, 1974, 441.

14. Krefting and Reimer, in Ref. 9, pp. 45.

15. G. Love, M. G. Cox, and V. D. Scott, *J. Phys.* D11: 23, 1978.

16. W. Rehbach and P. Karduck, *Proc. 11th ICOM*, London, Ontario, 1987, 244.

17. D. A. Sewell, G. Love, and V. D. Scott, *J. Phys.* D18: 1233, 1985.

18. D. F. Kyser, in Ref. 2, pp. 119.

19. W. Rehbach and P. Karduck, this volume.

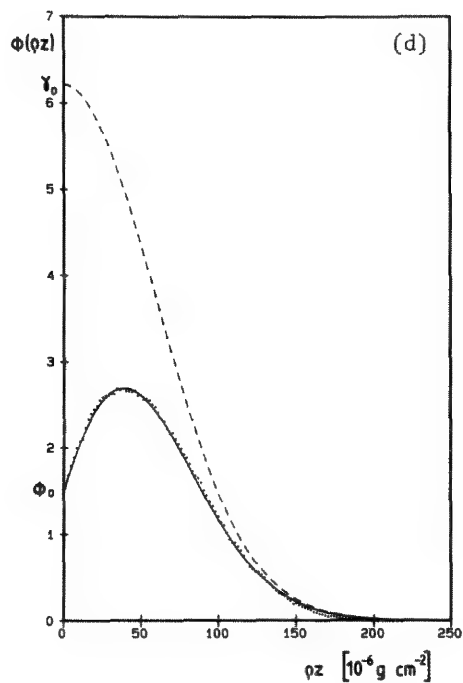
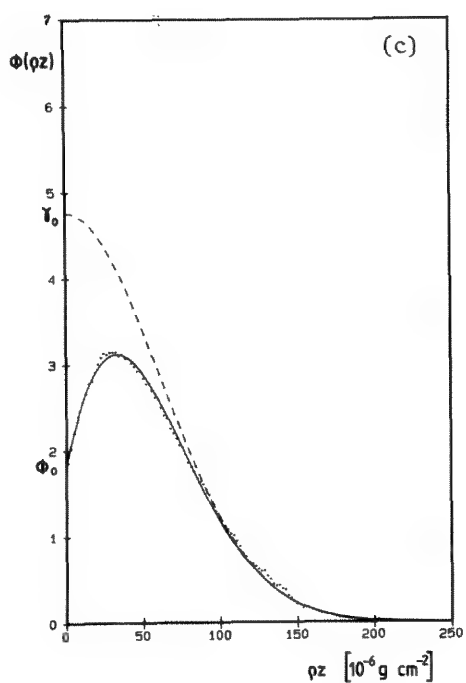
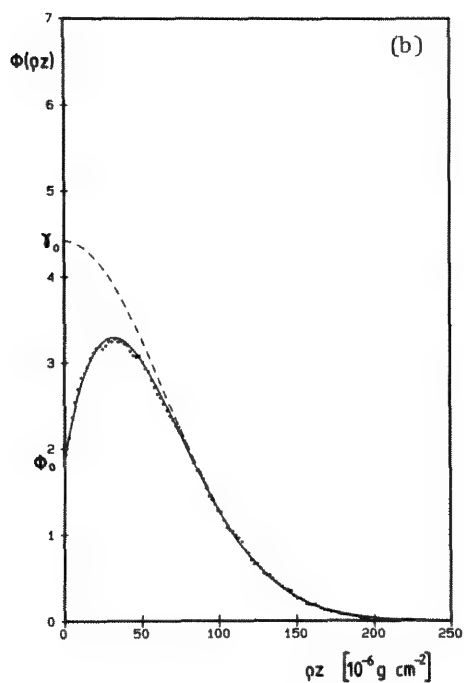
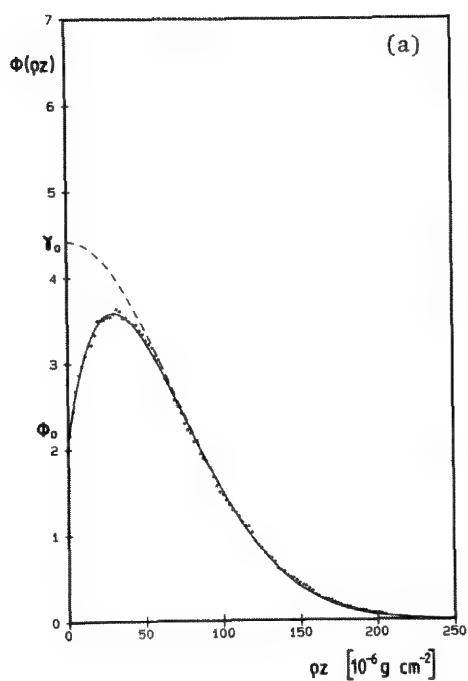


FIG. 9.--MC- $\phi(\rho z)$ curves and the corresponding pure Gaussians for C K α in (a) Ag, (b) Cu, (c) Ti, and (d) Al.

VERIFICATION OF THE GAUSSIAN $\phi(\rho z)$ APPROACH AND DETERMINATION OF THE LIMITS OF VALIDITY BY TRACER EXPERIMENTS AND MONTE CARLO CALCULATIONS

Werner Rehbach and Peter Karduck

The depth distributions for soft x rays with energies below 1 keV, found by new experiments as well as simulated by Monte Carlo (MC) calculations and described in the previous paper,¹ shall be the basis for further improvements in matrix correction procedures. The Gaussian $\phi(\rho z)$ approach, developed by Brown and coworkers^{2,3} and modified by Bastin, Heijligers, and van Loo,^{4,5} seems to be a suitable model for this purpose, since it should be able to describe any depth distribution almost exactly. One of the aims of this paper is to investigate whether this assumption proves to be valid in the complete range of primary electron energies E_0 , critical excitation energies E_C , and atomic numbers of the matrix Z .

The Surface Ionization ϕ_0

The surface ionization ϕ_0 is the only parameter required in all established $\phi(\rho z)$ descriptions. Two formulas (by Reuter⁶ and Love et al.,⁷ respectively) are commonly used. As is to be seen in the preceding paper, both the measured values and those generated by MC calculations show similar deviations from the calculated values for low-energy x rays. To allow a general formulation for the total range of E_0 , E_C , and Z used in EPMA, ϕ_0 values are calculated by Monte Carlo simulations for $2 < E_0 < 50$ keV, $0.192 < E_C < 8.98$ keV, and $6 < Z < 79$. The new analytical expression should have a form similar to that given by Reuter, which is in good agreement with the data for $E_C > 1$ keV and not too high overvoltages U_0 . The Reuter expression is:

$$\phi_0 = 1 + [1 - (0.9/U_0)] 2.8\eta$$

with a backscatter coefficient η described by a third-order polynomial fit in Z . The expression must be modified with respect to three deviations:

1. As shown in the previous paper, the curvature of the curve ϕ_0 vs U_0 is too sharp in the low- ϕ_0 region; i.e., the slope with $0.9/U_0$ has to be modified by a less rigid formulation.
2. The dependence of the curvature on E_C has to be considered.
3. X-ray production by fast secondary electrons (FSE) may not be neglected at low E_C .

Werner Rehbach and Peter Karduck are with the Gemeinschaftslabor für Elektronenmikroskopie der RWTH Aachen, D-5100 Aachen, Federal Republic of Germany. The authors wish to thank Dr. G. F. Bastin for calculating the histograms. This work was partially supported by the Deutsche Forschungsgemeinschaft.

Therefore a new approach is made by the expression

$$\phi_0 = 1 + [1 - (1/\sqrt{U_0})]^a b$$

where the parameter a takes into account the E_C dependence of the curvature and the parameter b fits the backscatter properties and the x-ray production by FSE. The logarithmic form results in

$$\ln(\phi_0 - 1) = a[1 - (1/\sqrt{U_0})] + \ln b$$

The plots of $\ln(\phi_0 - 1)$ vs $\ln[1 - (1/\sqrt{U_0})]$ are straight lines with a slope a and an intercept $\ln b$. All combinations of the 8 E_C and 8 Z values produce a set of 64 pairs of $a(E_C, Z)$ and $b(E_C, Z)$. As expected, for large E_C a is a function of Z only, given by $a_\infty = 0.68 + (3.7/Z)$, and the dependence on E_C (in keV) may be adjusted by $a = [1 + 0.005(Z/E_C)]a_\infty$.

The parameter b should be independent of E_C if E_C is large enough, so that the x-ray production by FSE is negligible. A polynomial fit of the third order in Z results in

$$b_\infty = -0.01 + 0.04805Z - 0.51599 \cdot 10^{-3} Z^2 + 0.20802 \cdot 10^{-5} Z^3$$

This parameter describes the backscattering, as is made evident in the very good description of b_∞ by $b_\infty = 3.224\eta$ Reuter in the total range of Z . The effect of FSE may be considered by

$$b = [1 + (0.05/E_C)]b_\infty \quad (E_C \text{ in keV})$$

The excellent fit of experimental and MC data is shown in Fig. 1 for very-low- E_C B K α and low- E_C Si K α in materials with low Z (Al) and high Z (Au), respectively. For all these cases the data are fitted better by the new formula than by those proposed by Reuter or by Love et al. For x rays of higher energy, e.g., Cu K α , the established formulas differ only slightly and the values of the new formula lie within that range.

The Gaussian $\phi(\rho z)$ Approach

As pointed out in the preceding paper, the experimental data and MC calculations (both given by the authors) are also in good agreement for ultrasoft x rays like B K α , C K α , Cr L α , and Cu L α . In order to make these data applicable to correction procedures, the three parameters α , β , and γ_0 of each depth distribution have to be determined first. The procedure and the determined parameters are described in detail in Ref. 8; only a short review need be given here. In a first attempt,

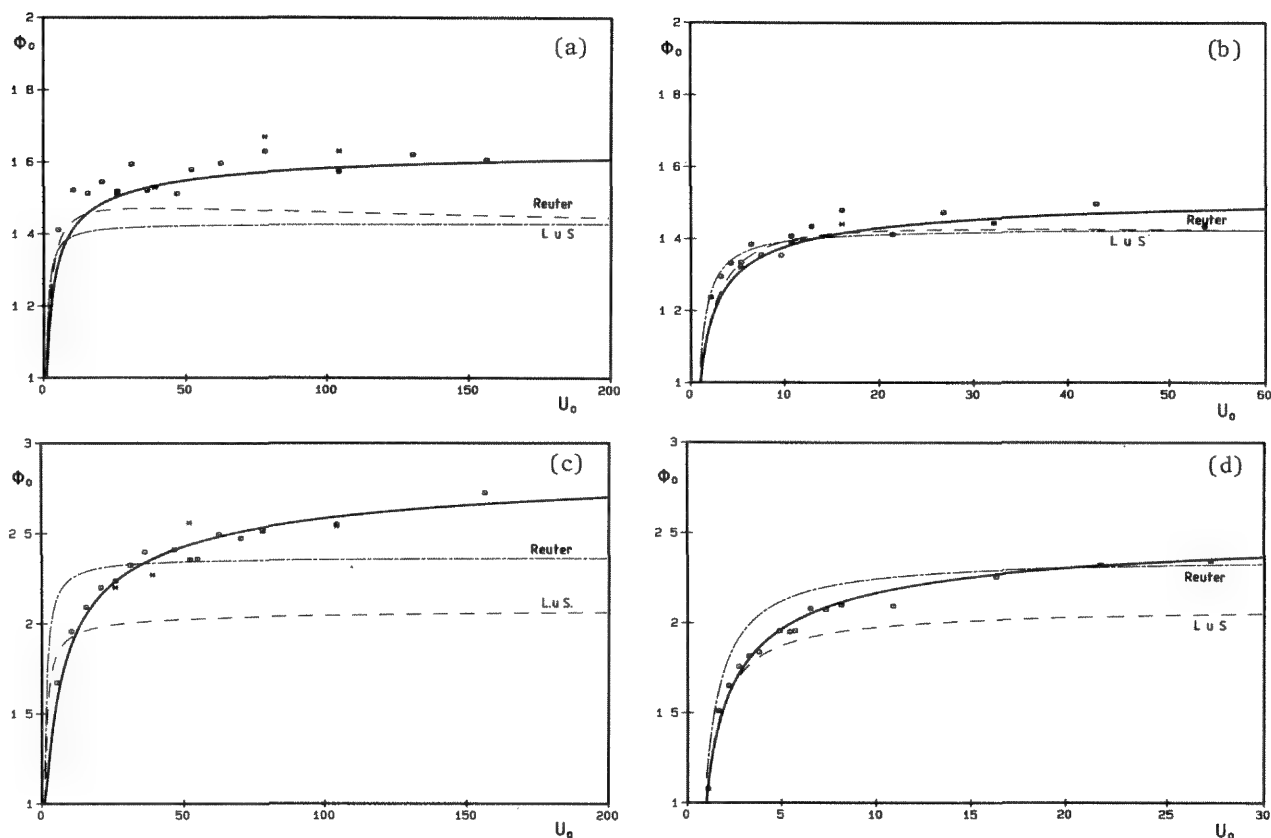


FIG. 1.--Comparison of new formula for ϕ_0 (solid line) with formulation by Reuter (dashed line) and by Love and Scott (short-long dashed line). Experimental values (*) and MC-values (o). (a) B K α in Al, (b) Cu L α in Al, (c) B K α in Au, (d) Cu L α in Au.

all three parameters were determined by a least-squares fit with a SIMPLEX algorithm. The results were not satisfactory, since the data determining the three parameters were not evenly weighted in some cases, especially when the region controlled by β was very small. Therefore a different procedure was used. First, the parameter α was determined from a plot of $\ln \phi(\rho z)$ vs $(\rho z)^2$. The slope of the straight line in the region of large ρz is $-\alpha^2$. The position and magnitude of the maximum of the depth distribution was found graphically. By an iterative computer procedure definitive values of γ_0 and β could be determined. More than 70 experimental depth distributions and 300 MC simulations were treated in this manner, all with x-ray energies below 1 keV.

Limits of the Gaussian Approach

The parameters of most of the depth distributions could be determined without problems, except for those with matrix elements of low atomic number. The parameter α is found in the described manner for high atomic numbers (Fig. 2a, corresponding to Fig. 9a in the preceding paper). For a matrix of low atomic number--e.g., 13 (Al)--the state of complete randomization of electron directions is reached only at the very end of the curve (Fig. 2b, corresponding to Fig. 9d in the preceding paper). For a depth distribution in a matrix of very low atomic number (Fig. 3) the plot of $\ln \phi(\rho z)$ vs $(\rho z)^2$ curves at its end, so that a

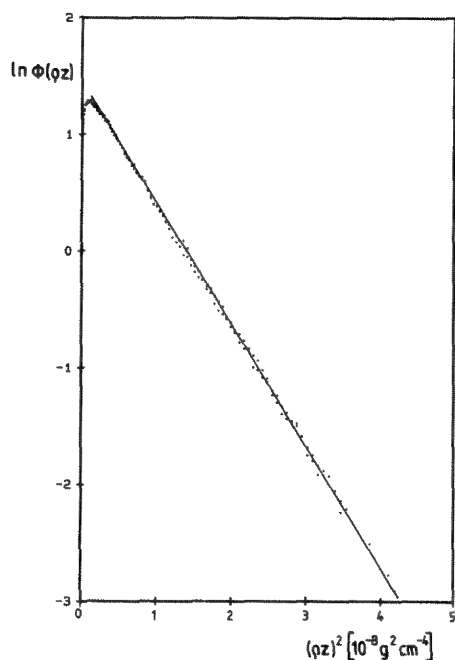
value of α cannot be found by this method. Another attempt to find α failed as well. By inputting increasing values of α into the program for determining β and γ_0 , at a fixed position of ϕ_m (Fig. 4), one can approximate the measured depth distribution by the calculated curve, but equality is never reached. For $\alpha > 10\,955$ no solution exists. Here γ_0 surpasses all limits and in consequence $\beta = 0$, which proves that the depth distribution cannot be described within the Gaussian model.

Another demonstration is shown in Fig. 5. Curves that describe the position of ϕ_m for a single value of γ_0 as β is varied are calculated for a fixed value of $\alpha = 8200$, which has been evaluated from the slope of $\ln(\rho z)$ vs $(\rho z)^2$ for large ρz , and $\phi_0 = 1.23$. For $\beta = 0 \Rightarrow \phi_m = \phi_0$ and for $\beta \rightarrow \infty \Rightarrow \phi_m = \gamma_0$. The figure shows that ϕ_m cannot be described properly even by unrealistically high values.

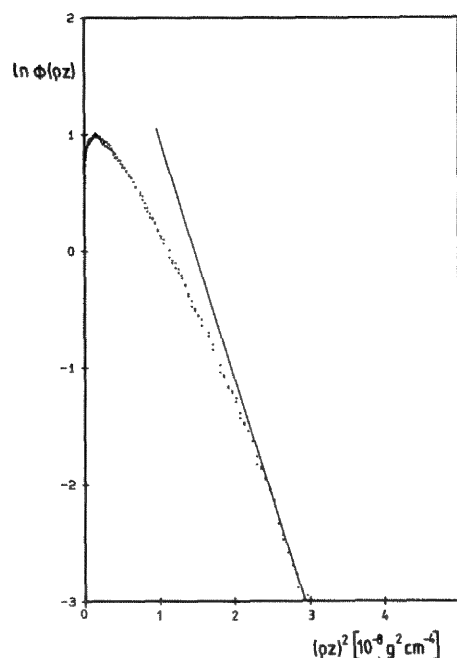
Modified Description of the Gaussian Parameters

Despite the model's disadvantages an attempt was made to show that it is possible to produce an analytical description of the Gaussian parameters based on the presented data that results in correction comparable to the established correction procedures, without the need for optimization by adjustable parameters. For α , based on the formulation of Packwood and Brown, the following equation was found:

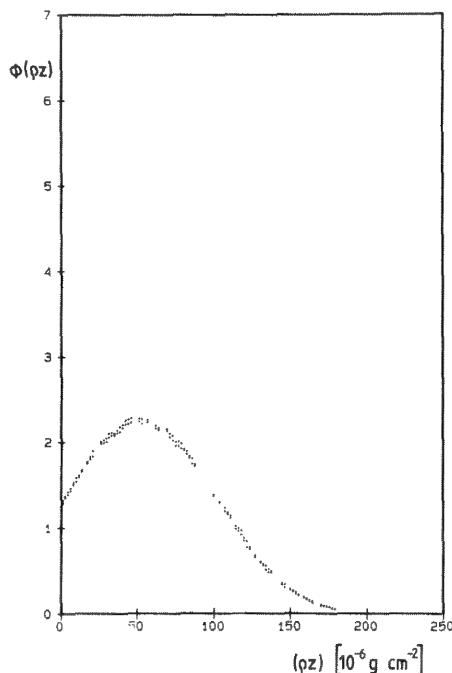
2 (a)



(b)



3 (a)



(b)

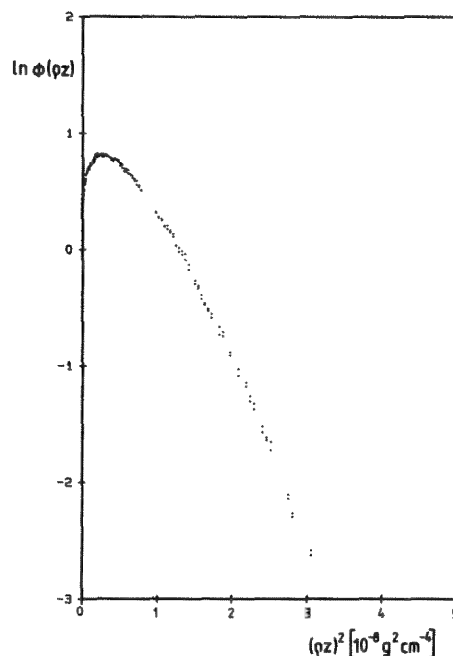


FIG. 2.--Depth distributions of C K α in (a) Ag and (b) Al, plotted as $\ln \phi(\rho z)$ vs square of the depth; $E_0 = 7$ keV.

FIG. 3.--Depth distribution of C K α in C; $E_0 = 7$ keV; (a) linear plot of $\phi(\rho z)$ vs ρz , (b) $\ln \phi(\rho z)$ vs $(\rho z)^2$.

$$\alpha = 2.66 \times 10^5 \frac{Z^{1.04}}{AE_0^{1.10}} \left[\frac{\ln(1.66E_0/J)}{E_0 - E_c} \right]^{0.5}$$

$$\beta = 2.20 \times 10^5 \frac{\ln(Z - 11)}{E_0^{1.4}} [1 + (U_0 - 1)^{-0.77}]$$

The ionization potential J of Ruste⁹ was used.

The formulation of β by Packwood and Brown has two disadvantages: β depends on γ_0 , not merely on basic physical properties such as Z , A , E_0 , and E_c . Furthermore, the dependence on E_0^{-2} seems not to be valid for soft x rays. A rather good fit for β data with $Z \geq 13$ is obtained by

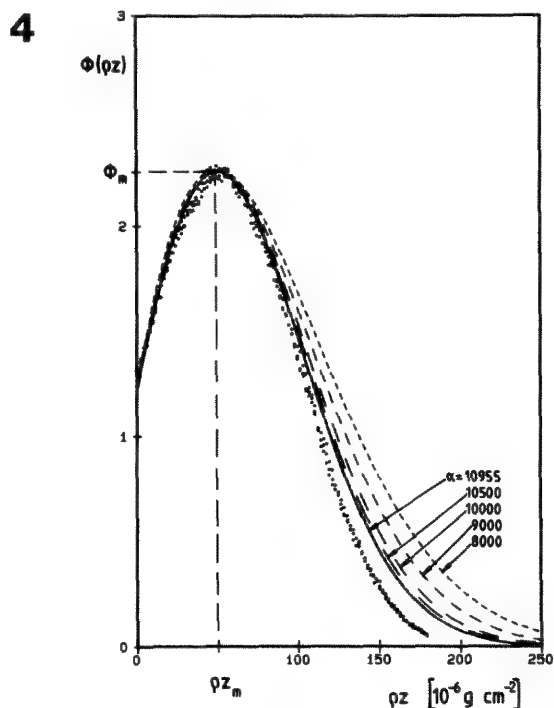
It is obvious that this formula cannot be used for $Z \leq 12$. As a rough approximation, to make the model applicable for $Z \leq 12$ for a first test, $2.20 \times 10^5 \ln(Z - 11)$ is changed to $2.08 \times 10^5 \ln Z$. The descriptions of γ_0 by Packwood and Brown and by Bastin et al., respectively, are not very obvious. Similar to a formulation by Tirira Saa and Riveros,¹⁰ the

following approach was tried:

$$\gamma_0 = b(1 + an) [\overline{Q(U)}/Q(U_0)]$$

Using the ionization cross section proposed by Hutchins,¹¹ $Q(U) \propto \ln(U/U_0)^{0.9}$, and the back-scatter coefficient according to Hunger,¹² we obtained the following equation:

$$\gamma_0 = 2.325 [1 + 0.64\eta(E_0)] \frac{10U_0(\ln U_0 - 10 + 10U_0^{-0.1})}{\ln U_0(U_0 - 1)}$$



Test of the Modified Approach

The performance of the modified approach has been compared to other correction procedures on the basis of the data set of binary carbides given by Bastin.¹³ A program similar to the program BAS 861 by Bastin was used to integrate the new parameters. The averages of Z , A , α , and β are also according to Bastin. The resulting parameters are used for the total range of Z and for the total range of E_C .

In the first test, the metal compounds of 145 binary carbides are analyzed and carbon is

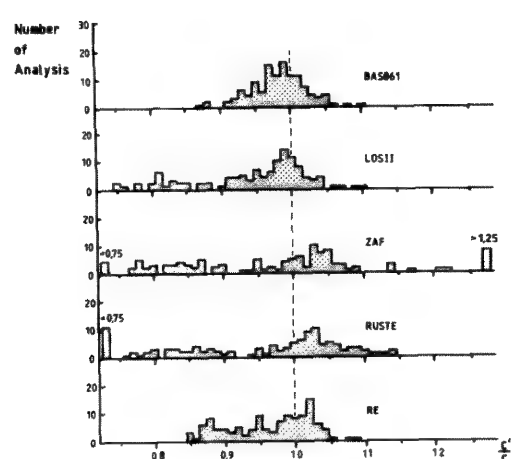
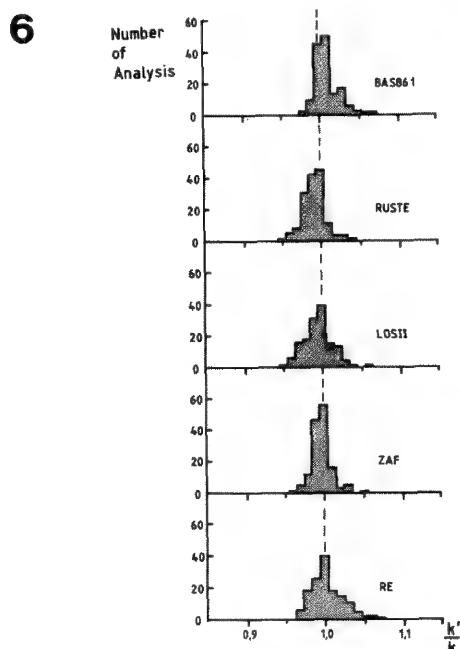
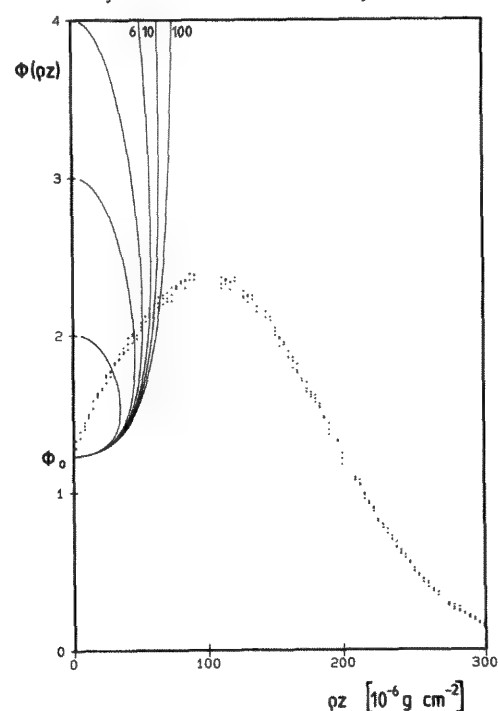


FIG. 6.--Performance of five correction procedures on database of 145 metal analyses in binary carbides.

FIG. 7.--Performance of five correction procedures on database of 117 carbon analyses in binary carbides.

calculated by difference. The results for the five correction procedures (BAS 861,¹³ Ruste,¹³ LOS II,¹⁴ a conventional ZAF-program,¹³ and the present procedure, called Re) are presented in Table 1 and Fig. 6. Although the present program is fitted with measurements of $E_C < 1$ keV only, it shows values similar to the other programs even for the metal analysis.

In a second test, carbon analyses on 117 binary carbides were compared. The results are shown in Table 2 and Fig. 7. Although the present program is only a rough approximation (especially for low atomic numbers, which are frequent in the database), it produces a comparably good average and the second best rms value. This is a further proof of the reliability of the above experimental and MC data.

Further Improvements

The breakdown of the Gaussian $\phi(\rho z)$ approach in the region of low atomic numbers is a severe disadvantage of this model. The artificial extension, made intentionally in this work (and probably only incidentally in other Gaussian approaches), is a bad remedy. A new approach has to be developed, which either combines the Gaussian approach for higher atomic numbers with a different one for low atomic numbers, or postulates a general formulation valid for the total range of EPMA.

TABLE 1.--Relative rms values and averages obtained with five correction programs on 145 metal analyses in binary carbides; k'/k = calculated/measured k-ratio.

Program	Average k'/k	r.m.s. (%)
BAS861	1.011	1.48
LOSII	0.994	1.82
ZAF	0.997	1.28
RUSTE	0.991	1.42
RE	1.003	2.02

TABLE 2.--Relative rms values and averages obtained with five correction programs on 117 carbon analyses relative to Fe_3D ; c'/c = calculated/nominal concentration (wt%).

Program	Average c'/c	r.m.s. (%)
BAS861	0.983	3.96
LOSII	0.948	7.78
ZAF	0.989	17.86
RUSTE	0.946	11.94
RE	0.964	5.76

References

1. P. Karduck and W. Rehbach, this volume.
2. R. H. Packwood and J. D. Brown, *X-Ray Spectrom.* 10: 138, 1981.
3. J. D. Brown and R. H. Packwood, *X-Ray Spectrom.* 11: 187, 1982.
4. G. F. Bastin, F. J. J. van Loo, and H. J. M. Heijligers, *X-Ray Spectrom.* 13: 91, 1984.
5. G. F. Bastin, H. J. M. Heijligers, and F. J. J. van Loo, *Scanning* 8: 45, 1986.
6. W. Reuter, *Proc. 6th ICXOM*, Tokyo, 1972, 121.
7. G. Love, M. G. Cox, and V. D. Scott, *J. Phys.* D11: 23, 1978.
8. W. Rehbach, dissertation, Aachen, 1988.
9. J. Ruste, *J. Microsc. Spectrosc. Electron.* 4: 123, 1979.
10. J. H. Tirira Saa and J. A. Riveros, *X-Ray Spectrom.* 16: 27, 1978.
11. G. A. Hutchins, in P. F. Kande and G. B. Larrabee, Eds., *Characterization of Solid Surfaces*, New York, 1974, 441.
12. H. J. Hunger and L. Küchler, *Phys. Stat. Sol.* A56: K45, 1979.
13. G. F. Bastin and H. J. M. Heijligers, *Quantitative Electron Probe Microanalysis of Boron in Binary Borides*, Eindhoven, 1985.
14. D. A. Sewell, G. Love, and V. D. Scott, *J. Phys.* D18: 1245, 1985.

QUANTITATIVE EPMA OF NITROGEN IN Ti-N COMPOUNDS

G. F. Bastin, H. J. M. Heijligers, and J. F. M. Pinxter

Quantitative analysis of nitrogen in the presence of titanium has always presented a real problem in the life of many microanalysts, caused by the severe overlap between the Ti- β (31.4 Å) and N K α (31.6 Å) emission peaks, which add up to one single peak in which no fine structure can be discerned, with the usual wavelength-dispersive analyzer crystals showing at best a resolution of approximately 3%. However, with the growing interest in Ti-N based materials (e.g., wear-resistant coatings), there is a growing demand for a procedure capable of separating the Ti- β and N K α contributions; the final goal is, of course, the accurate quantitative analysis of nitrogen. In the past, several methods for peak separation have been proposed.¹ They can be qualified either as ratio methods or as deconvolution techniques. The ratio methods are based on the assumption that there is a fixed ratio between the integral intensities of either Ti K α and Ti- β or Ti L α and Ti- β and that these ratios, once they are known from measurements on a pure Ti standard, also apply to the titanium in the Ti-N compound. The deconvolution techniques, on the other hand, do not require the ratios of Ti peaks in the standard, and are in fact multiple-least-squares fitting techniques² that are at present quite common in energy-dispersive x-ray microanalysis.

In the following sections we first give an analysis of the methods proposed so far and discuss their limitations. Next we discuss the principles of the new method we introduce, followed by a few applications on a number of examples.

Analysis of Existing Methods

In the ratio methods the ratio Ti L α /Ti- β seems to be used with preference because (1) only one spectrometer (with a lead-stearate crystal) is used and (2) the intensities of Ti L α and Ti- β are more or less comparable. One of the prerequisites for this method to work (which means that the ratio in question is indeed the same in Ti-N specimen and Ti standard) is that the absorption of both radiations is the same in Ti as well as in N.

However, as Fig. 1 shows, that is evidently not the case. The presence of the N-K absorption edge causes a marked difference in the mass absorption coefficients (mac's) for Ti L α and Ti- β . Although these values are quite similar (3320 and 4300, respectively³)

G. F. Bastin and H. J. M. Heijligers are at the Laboratory for Physical Chemistry Centre for Technical Ceramics, University of Technology, P.O. Box 513, NL-5600 MB Eindhoven, The Netherlands; J. F. M. Pinxter is at Tracor Europa BV, P.O. Box 333, NL-3720 AH Bilthoven, The Netherlands.

in pure titanium for a start, the value of Ti L α in pure nitrogen increases to approximately 25 000 and that of Ti- β is lowered to approximately 1800; i.e., a 14-fold increase in the ratio of the mac's occurs. Of course, this is an extreme case for extremely high N-contents, for which the effect is worst (assuming that Henke's mac's are correct). Yet it is a good example to demonstrate the inherent dangers in the ratio method as long as this ratio is blindly taken for granted. Perhaps the calculation of the Ti- β contribution from the known Ti content in the sample, derived from the Ti K α signal, would provide a better alternative. However, the main problem in these matters is that the Ti- β peak is so close to the N-K absorption edge (or perhaps even partly in it) that it is simply unlikely that the contribution of the Ti- β peak can be described by a single k-ratio. The extremely strong variation of the mac over the absorption edge is bound to produce a strong variation of k-ratio with wavelength. The same remarks apply to the variation in the background, which must exhibit a jump more or less, followed at increasing wavelength by a strong variation. The whole picture is not unlike the inverse of Fig. 1b. (The effects discussed so far are also the reason for the strong asymmetry usually present in the combined Ti- β + N K α peak.)

For the same reasons the deconvolution techniques are probably bound to fail because they are invariably based on the assumption that the background varies in a smooth and consistent way with energy or wavelength. The presence of an absorption edge with its typical discontinuity probably invalidates the basic assumptions. Moreover, for the reasons discussed above, it is unlikely that one single k-ratio can be applied over a wide region in wavelengths over which this k-ratio should in fact exhibit a strong variation with wavelength. Besides, these techniques rely on the tacit assumption that no peak shifts and/or peak-shape alterations occur between standard and specimen, which is in itself questionable or at least not established.

If the fine structure of the N-K absorption edge were known, one could perhaps model the background and calculate the Ti- β contribution as a function of wavelength from the known Ti content using the Ti K α signal. However, as long as the fine structure is not known, it is highly unlikely that such calculations, based on a mac of Ti- β for only a single fixed wavelength, can ever be successful. The main reason that such methods may have appeared to work well in the past is that the homogeneity region of TiN is extremely wide at high temperatures,^{4,5} ranging from 11 to approximately 22.6 wt%N, with the result that almost any answer between these limits

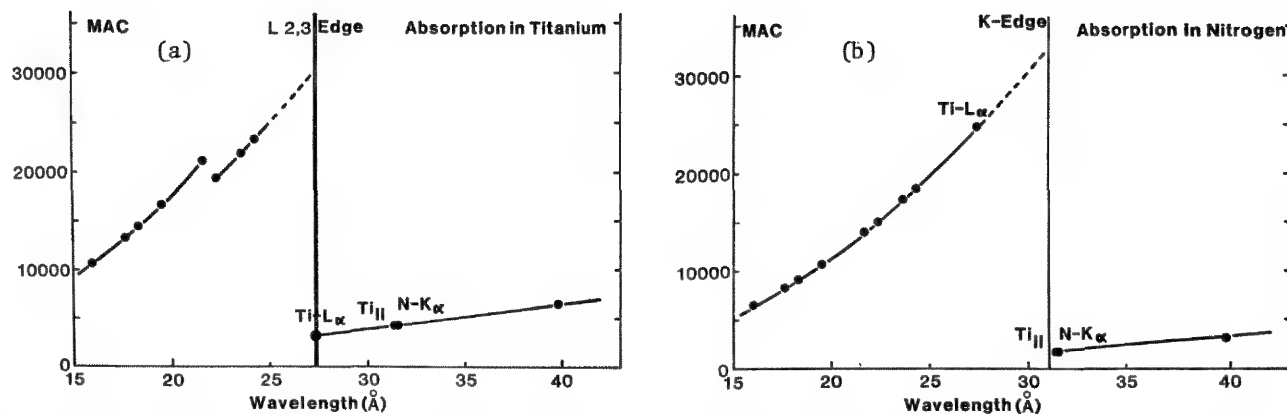


FIG. 1.--Variation of mass absorption coefficient with wavelength in (a) Ti and (b) N according to Henke et al.³ Note that mac and wavelength are plotted on linear scale.

can appear acceptable. According to our own experiences in this system and the very similar Ti-C system it is usually very difficult to find the true composition. Even when a reliable chemical analysis is available, there is always the danger of discrepancies due to variations in composition on a micron scale.

As a result of the considerations so far it might be expected that the methods hitherto used lead to systematic errors in the nitrogen content, which probably go unnoticed because the results are usually not in contradiction with the Ti-N phase diagram.

The New Method

The new method we propose here is mainly based on the consideration that although the Ti- β and N K α peaks strongly overlap, they do not coincide completely. Hence, the combined peak must inevitably be broader than that of either of the contributors. If we could find access to the true width of the N K α peak or to its width-to-height ratio, the problem would be reduced to finding the proper amount of Ti- β intensity that has to be stripped (in an integral fashion) from the combined peak in order to produce a residual N K α peak with the specified width. In the past⁶⁻⁸ we have successfully used the Area-Peak Factor (APF) concept in order to deal with peak-shape alterations in ultralight element radiations. The APF (which is simply the ratio between the integral k-ratio and the peak k-ratio for a specimen relative to a specific standard) can to a large extent be regarded and used as a measure for the relative width-to-height ratio. Unfortunately, this APF is not known a priori for Ti-N compounds and cannot be measured directly either for obvious reasons. But our experiments on a large number of nitrides indicate that, contrary to the effects in B K α and C K α peaks, the APF effects for nitrogen never diverge by more than 10% from unity, and if the results for nitrides of neighboring elements in the periodic system like V, Cr, and Fe are extrapolated toward Ti, the expected value for the APF will probably be between 0.95 and 1.0. Moreover, we have shown that within the limits of experimental accuracy the APF can be regarded as indepen-

dent of accelerating voltage. With these findings and a couple of Ti-N specimens of known compositions it is possible to start an iterative procedure aimed at obtaining the true APF. It goes without saying that the presence of the N-K absorption edge is seriously taken into account in this procedure, which means that the wavelength region of interest is treated in two distinct intervals: one interval on the left (short-wavelength) side of the edge, the other from the edge on, ranging to longer wavelengths. The k ratios on the left will be henceforth denoted by the subscript 1, those on the right hand side by r .

The first step in our procedure is the recording of the Ti L α and Ti- β peaks in a pure Ti-standard in an integral fashion. Then the same wavelength region is scanned on the Ti-N specimen under identical conditions. From the known Ti-content the k-ratio (k_1) for Ti L α is calculated and the left hand side of the Ti-spectrum up to the N K α edge is multiplied by this factor and stripped from the unknown spectrum. Alternatively, if the Ti-content is not known, this factor can be determined by trial and error: the disappearance of the Ti L α peak in the spectrum is an easy measure for success.

Next, the right side of the unknown spectrum is processed by multiplication of the Ti reference spectrum by a factor k_r , which is increased in steps of, say, 0.1; the resulting spectrum is subtracted from the unknown. After each step the residual peak is processed in order to find the APF and the integral (or area) k-ratio AKR, with respect to the particular nitrogen standard used. Both values are then plotted as a function of k_r .

In the first iteration we assume that the AKR should be equal to the calculated AKR for nitrogen using the mac's of Henke et al.³ It is then easy to find the corresponding APF value for which this equality occurs. If this procedure is repeated for several accelerating voltages and preferably for at least two different known compositions, it is possible to establish whether the APF is indeed a constant and, if this is the case, what its exact value is.

Once this value is known the procedure can be reversed and from the plots of APF and AKR

vs k_r it is easy to find the proper AKR value for a specific APF value. The experimentally obtained k_r values could even be used to make rough statements about the weighted average μ for Ti-11 in N.

Experimental

For the measurements two Ti-N compounds were at our disposal; one specimen was a 0.5mm-thick near-stoichiometric TiN specimen prepared by chemical vapor deposition, the other a Ti_2N composition prepared from a diffusion couple Ti-N₂ heated for 89 h at 1400 C. This composition was exposed by a process of grinding and polishing in a plane perpendicular to the diffusion direction. Afterward a cross section of the same diffusion couple containing the α -Ti(N) solid solution, Ti_2N , and TiN in successive layers was used in order to check the devised procedure. Such a diffusion couple is of invaluable interest for this particular type of work because it provides the almost unique possibility to find a smooth, consistent, and unambiguous variation in the nitrogen content, contrary to a number of bulk specimens with often contradicting chemical analyses.

We established the initial compositions of the calibration alloys and the nitrogen concentration profile in the diffusion couple by measuring the Ti K α signal using a near-stoichiometric TiC alloy, in equilibrium with free graphite, as a Ti standard. The nitrogen measurements were performed relative to a massive Cr_2N specimen (10.70 w/o N, 0.48 w/o O).

The spectral measurements were carried out on a fully automated JEOL Superprobe 733, equipped with four wavelength-dispersive spectrometers, two of which are specially designed for light-element work, and an energy-dispersive system (Tracor Northern TN-2000). One light-element spectrometer contained a conventional lead-stearate crystal; the other was equipped with a W/Si multilayer crystal (2d-spacing 59.8 Å, supplied by Ovonyx Corp., USA).

The nitrogen spectra for the two calibration alloys were recorded at nine different accelerating voltages between 4 and 30 kV. In many cases spectra were recorded simultaneously with the stearate and the multilayer crystal; i.e., from exactly the same location under identical circumstances. The spectrometers were thereby scanned stepwise over the range 28-35 Å. For the multilayer crystal (LDE) this was the range of 130-165 mm in steps of 0.07 mm (0.01495 Å). For the stearate crystal (STE) the range was 79-99 mm in steps of 0.04 mm (0.01426 Å). In each interval counts were accumulated during 10 s, subsequently transferred to successive channels of the multi-channel analyzer, displayed on the screen of the CRT of the EDX-system, and digitally stored after completion. In each run reference spectra from pure Ti were also recorded. Measurements in the diffusion couple were all carried out at 10 kV and counting times of 3 s/step; STE and LDE were used simultaneously.

Results and Discussion

Figure 2 shows the typical variation of APF and AKR with k_r for the near-stoichiometric TiN compound at 10 kV for both STE and LDE crystals. The calculated AKR in this case is 2.386 and the value of k_1 used is 0.437, which would lead to an APF value for STE of 0.974 at a k_r value of 0.760; for LDE in turn values of 0.980 for the APF and 0.698 for k_r are obtained.

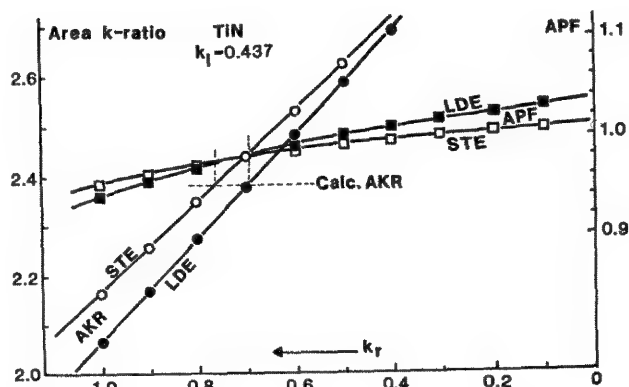


FIG. 2.--Variation of area k ratio (AKR) and Area-Peak Factor (APF) with k_r (average k ratio for Ti-11 for long-wavelength side of N-K absorption edge) for stearate and multilayer (LDE) crystals at accelerating voltage of 10 kV and k_1 value of 0.437. TiN specimen: 22.50 w/oN. Nitrogen standard Cr_2N : 10.70 w/oN, 0.48 w/oO.

This procedure has been repeated numerous times at voltages between 4 and 30 kV and it was found that the APF values could indeed be considered as a constant, independent of acceleration voltage (see bottom halves of Fig. 3a and b). The average APF value for the STE crystal was 0.971 for both calibration alloys. For the LDE crystal, which was obtained only in a much later stage, a number of measurements at 10 kV led to a value of 0.980. This result seems to be in good agreement with many of our other observations in carbon, nitrogen, and oxygen analyses where the LDE crystal always showed less sensitivity to peak-shape alterations than the STE crystal. Consequently, its APF value is usually much closer to unity.

Once the APF values are known, the procedure can be reversed and plots like Fig. 2 can be used to find the "measured" AKR starting with the specified APF. As a result the top halves of Fig. 3a and b are obtained, which show the variation of integral k ratio with accelerating voltage. Each point represents in fact the average for a large number of measurements taken over a period of several months.

The excellent agreement between expected and "measured" k ratios demonstrates that our procedure is obviously successful and that deviations rarely exceed 5% relative, which is surprising in view of the large amount of spectral manipulations involved.

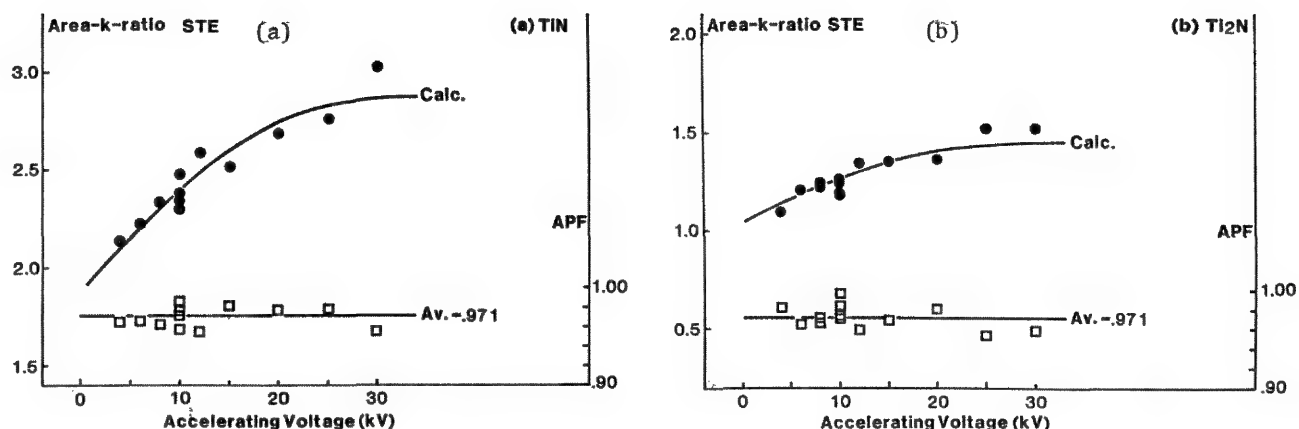


FIG. 3.--Variation of area k ratio (relative to Cr_2N) and APF with accelerating voltage for TiN (a) (22.50 w/oN) and (b) Ti_2N (11.84 w/oN).

Figure 4 gives a graphical representation of the complete procedure for the LDE crystal at 10 kV (near-stoichiometric TiN specimen). Spectrum 1 shows the combined Ti- β + N K α peak; spectrum 3, the Ti reference spectrum, which is converted into spectrum 4 by application of the appropriate k_1 and k_r factors. Spectrum 2 represents the final N K α spectrum after spectrum 4 has been stripped from spectrum 1. The shift in the peak between spectra 1 and 2 corresponds to the shift toward the true N K α peak after subtraction of the Ti- β contribution. It is clear, though, that the final spectrum shows a discontinuity at the position of the N-K absorption edge (which is, by the way, difficult enough to locate). This is the logical consequence of applying a mathematical step function representing the edge. The true edge doubtless has a different shape. However, as long as its exact shape is not known, there seems to be little point in using several mathematical functions because one procedure would be as arbitrary as another. The k_r values found experimentally strongly suggest that the mac for Ti- β in N is much higher than suggested by Henke et al.,³ which in turn means that this particular wavelength is at least partly located in the absorption edge.

A final test of our procedure was carried out at 10 kV on the diffusion couple Ti-N₂ (89 h, 1400 C). After diffusion this couple exhibited a more than 500 μm -wide diffusion zone consisting of TiN (major part) and Ti₂N covering a remaining nucleus of α -Ti(N) solid solution. From the known concentration profile a number of locations showing significant changes in the nitrogen content were selected and integral spectra were recorded on these spots. After completion the experiment was repeated (Run 2) with the specimen rotated over 180° with respect to the LDE spectrometer in order to estimate the effect of the strong rounding-off that inevitably takes place due to prolonged polishing at the interface mounting resin/TiN. The results for both runs for the LDE crystal are shown in Fig. 5. The strong rounding-off effect is clearly visible

in Run 2, where the x rays leaving for the LDE spectrometer have the poorest chance of escaping close to the mounting resin. However, overall the agreement between Ti and N measurements can be called striking for locations more than 20 μm away from the mounting resin. In fact, this conclusion holds throughout the complete diffusion zone, including the α -Ti(N) solution. At the same time the result for the near-stoichiometric TiN-alloy (arrow in Fig. 5) agrees closely with the nominal composition, thus demonstrating that the maximum nitrogen content is not yet attained at the outside of the diffusion couple.

The results for the STE crystal were quite acceptable too, although they were generally on the low side, especially for the α -Ti(N) solid solution. In the latter case this may be the result of the tacit assumption that the APF used so far also applies to this particular phase, although strictly speaking it is not really a Ti-N compound but rather a solid solution and as such its APF value may be somewhat different: a value of 1.0 would give results comparable with those of the LDE crystal. Besides, there seems to be some evidence that the APF value for STE at 10 kV is possibly somewhat higher than the average value adopted (Fig. 3). In any case the LDE crystal is definitely less sensitive to peak shape alterations due to its poorer resolution and as such it is not capable of discerning such subtle details.

A few remarks are in order here on the practical aspects of the method we propose. Because the whole method is strongly based on factors such as spectral resolution, it must be clear that all parameters in the microprobe affecting the resolution (Pulse Height Analyzer conditions, counter slit, etc.) must always be adjusted extremely carefully and reproducibly. In the same way the background limits must always be exactly the same if the highest degree of reproducibility is to be achieved. Furthermore, it is probably advisable always to run a check on a calibration specimen before or after the measurements on an unknown specimen, if only to be warned of

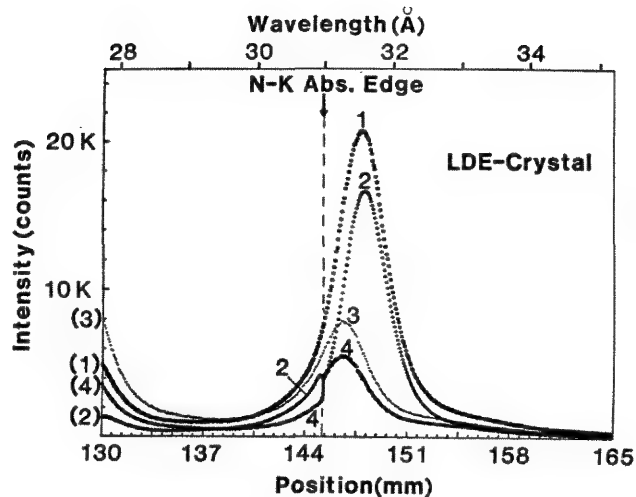


FIG. 4.--Graphical representation of our procedure for separating Ti-K and N-K contributions for LDE crystal on near-stoichiometric TiN specimen at 10 kV. Spectrum 3 is Ti reference spectrum, which is first converted into spectrum 4 by application of appropriate k_1 and k_2 factors and then subtracted from spectrum 1 to yield finally spectrum 2.

sudden changes in the equipment or settings. We realize that our method will be considered time-consuming and perhaps complex. Unfortunately, in our opinion there is little hope that there will ever be an instant solution for the complex problem at hand.

Finally we shall briefly discuss the results of the multiple-least-squares fitting technique² when applied to a number of our spectra. In fact, this is the program currently in use in EDX software, albeit the digital filter width had to be adjusted to the much higher resolution of a WD spectrometer. This program definitely gave answers; as expected, however, the results showed systematic errors. The discrepancy between expected and calculated results (which were too low) was found to increase with increasing nitrogen content, which substantiates the conclusion that the presence of an absorption edge invalidates the basic assumptions for such deconvolution techniques. The presence of the N-K absorption edge will become more and more pronounced with increasing nitrogen content.

Returning to our procedure we can state that the method we propose here, although time-consuming, offers the possibility to do quantitative analysis of nitrogen with a relative accuracy of at least 5% and perhaps better. The large number of tests under extreme conditions appear to justify our conclusions.

References

1. A. Armigliato, L. Dori, A. Garulli, and P. Venturi, "X-ray microanalysis of nitrogen in presence of titanium with an automated electron microprobe," *J. Microsc. Spectrosc. Electron.* 7: 593-603, 1982.
2. F. H. Schamber, N. F. Wodke, and J. J. McCarthy, "Least squares fit with digital filter: The method and its application to EDS

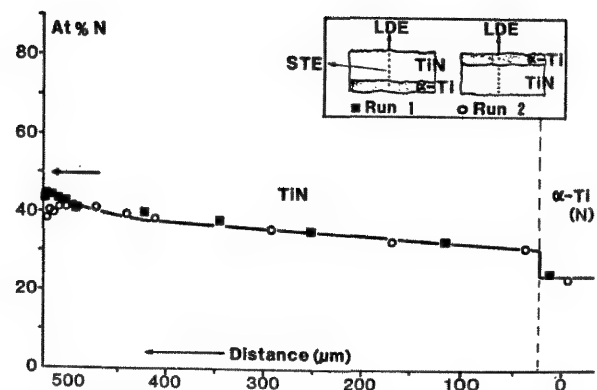


FIG. 5.--Nitrogen concentration profile in diffusion couple Ti-N₂ (89 h, 1400 C) as established by Ti K α measurements (solid line) and our new procedure for nitrogen using the LDE crystal. Squares represent results for Run 1, circles those for Run 2. Arrow shows experimental result for near-stoichiometric TiN compound in Run 2. Accelerating voltage: 10 kV. Experimental configurations for both runs are shown in the inset.

spectra," *Proc. 8th ICXOM*, 1980, 124-132. (Distributed by S. F. Press.)

3. B. L. Henke et al., "Low-energy x-ray interaction coefficients: Photoabsorption, scattering, and reflection," *Atomic Data and Nuclear Data Tables* 27: 1-144, 1982.

4. L. Wolff, G. Bastin, and H. Heijligers, "The titanium-nitrogen system," *Solid State Ionics* 16: 105-112, 1985.

5. E. Etchessahar, J. P. Bars, and J. Debuigne, "The titanium-nitrogen system: Equilibrium between the δ , ϵ and α phases and the conditions of formation of the Lobier and Marcon metastable phase," *J. Less-Common Metals* 134: 123-139, 1987.

6. G. F. Bastin and H. J. M. Heijligers, "Quantitative electron probe microanalysis of carbon in binary carbides," *Microbeam Analysis --1984*, 291-294.

7. G. F. Bastin and H. J. M. Heijligers, "Quantitative electron probe microanalysis of carbon in binary carbides," Parts I and II, *X-ray Spectr.* 15: 135-150, 1986.

8. G. F. Bastin and H. J. M. Heijligers, "Quantitative electron probe microanalysis of ultra-light elements," *J. Microsc. Spectrosc. Electron.* 11: 215-228, 1986.

A DIRECTLY CALCULATED QUADRILATERAL MODEL FOR $\phi(\rho z)$

Xu Li, Jin Guan-xiang, Wu Zi-qin, and R. J. Lee

X-ray depth distributions in aluminum, copper, and gold at 29 keV and in copper at 27.6, 23.1, 18.2, and 13.4 keV have been calculated by means of two quadrilateral models. The results have been compared with experimental curves.¹ The shape of $\phi(\rho z)$ of the direct calculating quadrilateral model is compared with that of the universal quadrilateral model created by Sewell, Scott, and Love.² The calculated functions $\phi(0)$ are close to experimental values.

Calculating the x-ray depth distribution is a foundation of standardless quantitative analysis. In this paper, we suggest a direct calculating quadrilateral model of $\phi(\rho z)$ based on a revised "full-diffusion" electron scattering model; the stepped model^{3,4} and universal quadrilateral models² were consulted. This model may be used in a direct standardless quantitative analysis program for light-element analysis.

Parameters of Direct Quadrilateral Model

In the quadrilateral model, the depth distribution of generated x-rays vs intensity is described by four parameters (Fig. 1).

a. *Full-diffusion mass depth ρ_{xb}* . In the full-diffusion electron scattering model, the incident electrons are fully diffused (as is the maximum intensity of x rays generated) at a depth

$$\rho_{xb} = 0.726 \times 10^{-5} [\cos \theta_0 / (1 + \cos \theta_0)] E_0^{1.65} \quad (1)$$

where θ_0 is the half-angle of the backscattered cone.⁴

b. *Maximum exciting depth:*

$$\rho_{xc} = 0.33 \times 10^{-5} \Sigma_i \cdot A_i / Z_i (E_0^{1.65} - E_c^{1.65})$$

and 90% ρ_{xc} was chosen as the maximum exciting depth ρ_{xm} in our quadrilateral model.

c. *Generated normalization x-ray intensity in the surface layer:*

$$\phi_0 = (1 + \eta) \gamma^b \frac{\ln(\epsilon U_0) / (\epsilon U_0)^{0.8}}{\ln U_0 / U_0^{0.8}} \frac{1 - \cos \theta_2}{1 - \cos \theta_0}$$

where η is the coefficient of the backscatter electron, ϵ is the average reduced energy of the backscattered electrons, and θ_1 is the half-angle of the backscatter cone.

d. *Maximum relative x-ray intensity:*

$$\phi_m = \frac{\ln U_b / U_b^{0.8}}{\ln U_0 / U_0^{0.8}} (\gamma_0 + \eta \gamma^b)$$

where γ^b is the coefficient of the electron scattering and γ_0 is the coefficient of the zigzag path of the electron.

Results

The two quadrilateral models (Sewell, Love, and Scott,² and ours) have been compared with each other. Both models have been compared with a sandwich sample experiment by Castaing and Brown following the paper by J. D. Brown.¹ The curves of copper for 27.6-13.4 keV were taken from the original data of Brown's experiments⁵ and smoothed. The results crossed each other between two quadrilateral models and were similar to the experimental curves (Fig. 1).

References

1. J. D. Brown, in A. J. Tonnsim and L. Marton, Eds., *Electron Probe Microanalysis*, New York: Academic Press, 1969, 45.
2. D. A. Sewell, G. Love, and V. C. Scott, *J. Phys.* D18: 1233, 1245, 1269, 1985.
3. Wu Zi-qin et al., *Acta Physica Sinica* 29: 485, 1980.
4. Zhang Ren-ji et al., *Acta Physica Sinica* 30: 209, 1981.
5. J. D. Brown, Ph.D. Thesis, University of Maryland, 1966.

The authors are at the University of Science and Technology of China, Hefei, Anhui, PRC 230029, except R. J. Lee, who is with the RJ Lee Group, Inc., 350 Hochberg Rd., Monroeville, PA 15146.

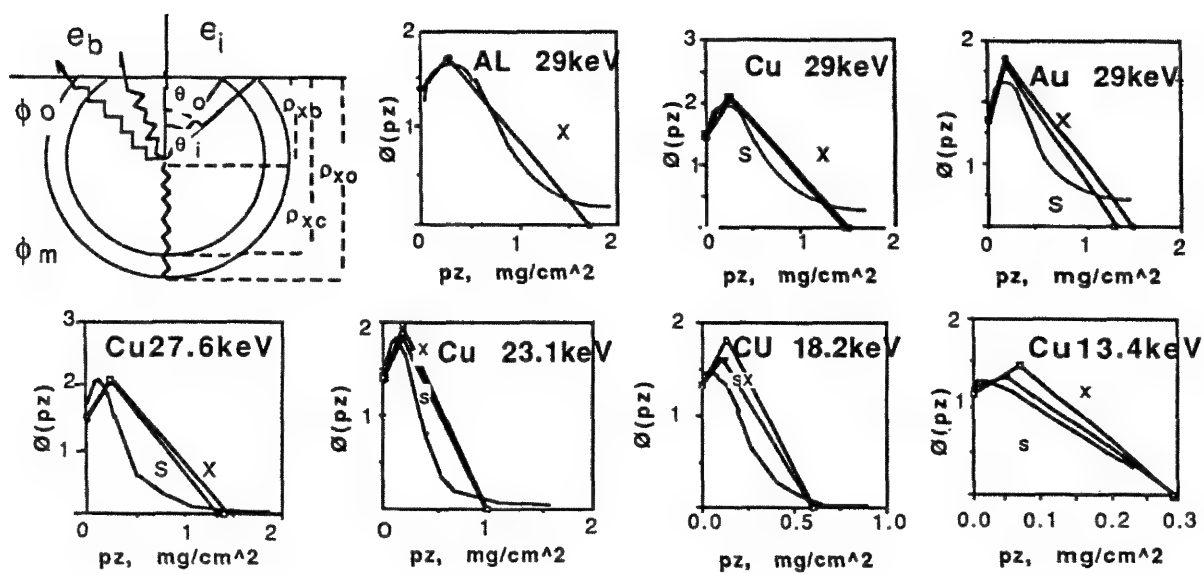


FIG. 1

QUANTITATIVE ANALYSIS OF Ti-N FILMS ON STAINLESS-STEEL SUBSTRATE WITH EPMA

Toyohiko Okumura

Coated Ti-N films on substrates, which excel in hardness and luster, are now coming into wide use for a variety of industrial products. However, the film's properties depend on the content of C, O, etc. and especially on the Ti/N ratio, all of which are greatly affected by the film preparation method and preparation conditions. The quantitative evaluation of its composition is of great importance in improving the film properties.

Problems in Composition Analysis with EPMA

EPMA is widely used for evaluation of such surface-treating films. However, since the Ti L α peak is overlapped on the N K α peak in the spectrum of the Ti-N film, it is difficult to estimate correctly the x-ray intensity of N K α alone. This problem becomes more serious to resolve in the case of thin films with thicknesses of several hundred nanometers.

Waveform Separation of Overlapped Peaks¹

The digital-filter method and the least-square-fitting method allow separation of N K α and Ti L α peaks from each other, and easily give the relative intensity of N K α . The digital-filter method is a procedure to eliminate the continuous background from the values measured at all points of the spectrum prior to application of the least-square-fitting method.

Let the measured value at the i -th point of an original spectrum be y_i (Fig. 1). Set three regions with the same width W , with the point i in the center. Let the average values in the three regions to be L_i , M_i , and H_i , respectively, and let $Y_i = F(Y_i) = 2M_i - (L_i + H_i)$, where Y_i is the filtered value of y_i . Now, we assume that an unknown spectrum is an overlap of Ref-A and Ref-B, as shown in Fig. 2. Then if we let the measured values at all points of $i = 1 \sim n$ be Y_i , RA_i , and RB_i , we get a set of simultaneous equations:

$$Y_i = e_i + (K_A RA_i + K_B RB_i) \quad (i = 1 \sim n)$$

where K_A and K_B are the coefficients by which the references A and B are to be multiplied to obtain the synthesized waveform to fit the unknown; e_i denotes the random errors.

Set $\chi^2 = \sum e_i^2$; and K_A and K_B are determined by the following conditions:

$$\delta\chi^2/\delta K_A = 0, \quad \delta\chi^2/\delta K_B = 0$$

K_A and K_B are thus found to correspond to the so-called relative intensities of separated

waveform A and B peaks, respectively.

Figure 3 shows four original spectra taken from four Ti-N films A, B, C, and D, separately. The reference spectra of N K α and Ti L α are taken from V-N alloy (N 16.1wt%) and pure Ti metal, respectively. From these data, the relative intensities of N K α (A: 4.45%, B: 9.66%, C: 3.90%, D: 9.52%) can be obtained by the waveform-separation method as mentioned above. These values are relative intensities of N K α in Table 1 together with other values.

These spectra were taken with JXA-8600M with the use of Pb-stearate operated at 10 kV.

Results of Quantitative Analysis of Ti-N Films

The relative intensities of Ti, C, and O (but not N) are obtained by the ordinary method that takes peak intensity ratio between unknown and reference samples without use of the waveform-separation method.

Table 1 shows the result of the quantitative analysis of Ti-N films. In this table, K is the relative intensity of each element, and C_{BALK} is the weight concentration taken by the ordinary ZAF correction method. Since Ti-N films are as thin as several hundred nanometers, the total value of C_{BALK} is very much lower than 100%.

C_{BALK}^{100} is the normalized value, so that the total value of C_{BALK} becomes 100%; and AB_{BALK} is the atomic concentration converted from C_{BALK}^{100} value.

From Table 1, we see that the atomic ratio of Ti/N in AB_{BALK} deviates noticeably from 1/1 only in specimen C. This specimen has been found to have lost the golden luster peculiar to TiN film. We may conclude that the golden luster of TiN films depends on the atomic ratio of Ti/N.

References

1. T. Okumura, "Deconvolution method for WDS spectra," *JEOL News* 22E(No. 1): 14, 1984.

The author is with JEOL Ltd., 1-2 Musashino 3-chome, Akishima, Tokyo 196, Japan.

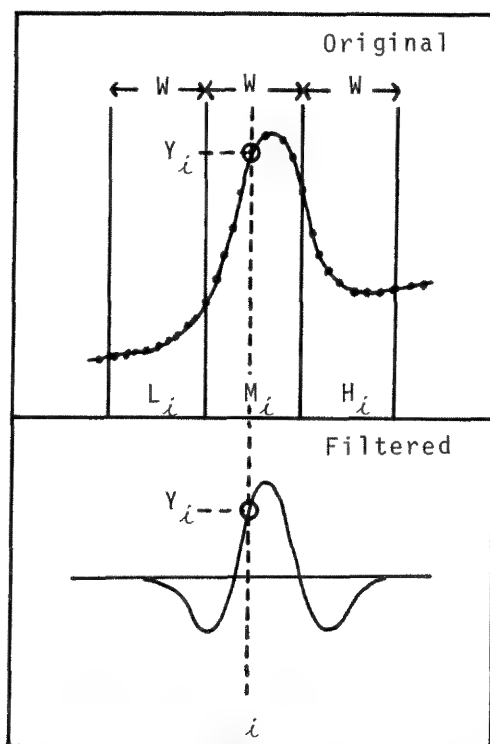


Fig. 1.--Notations in spectra used for calculation.

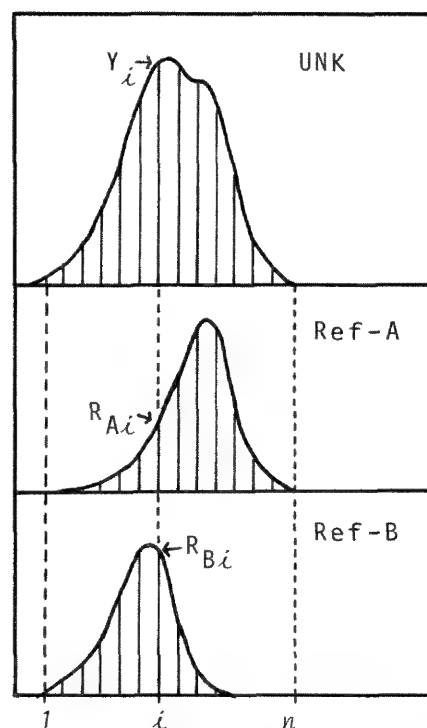


FIG. 2.--Schematic example of overlap of two spectra A and B.

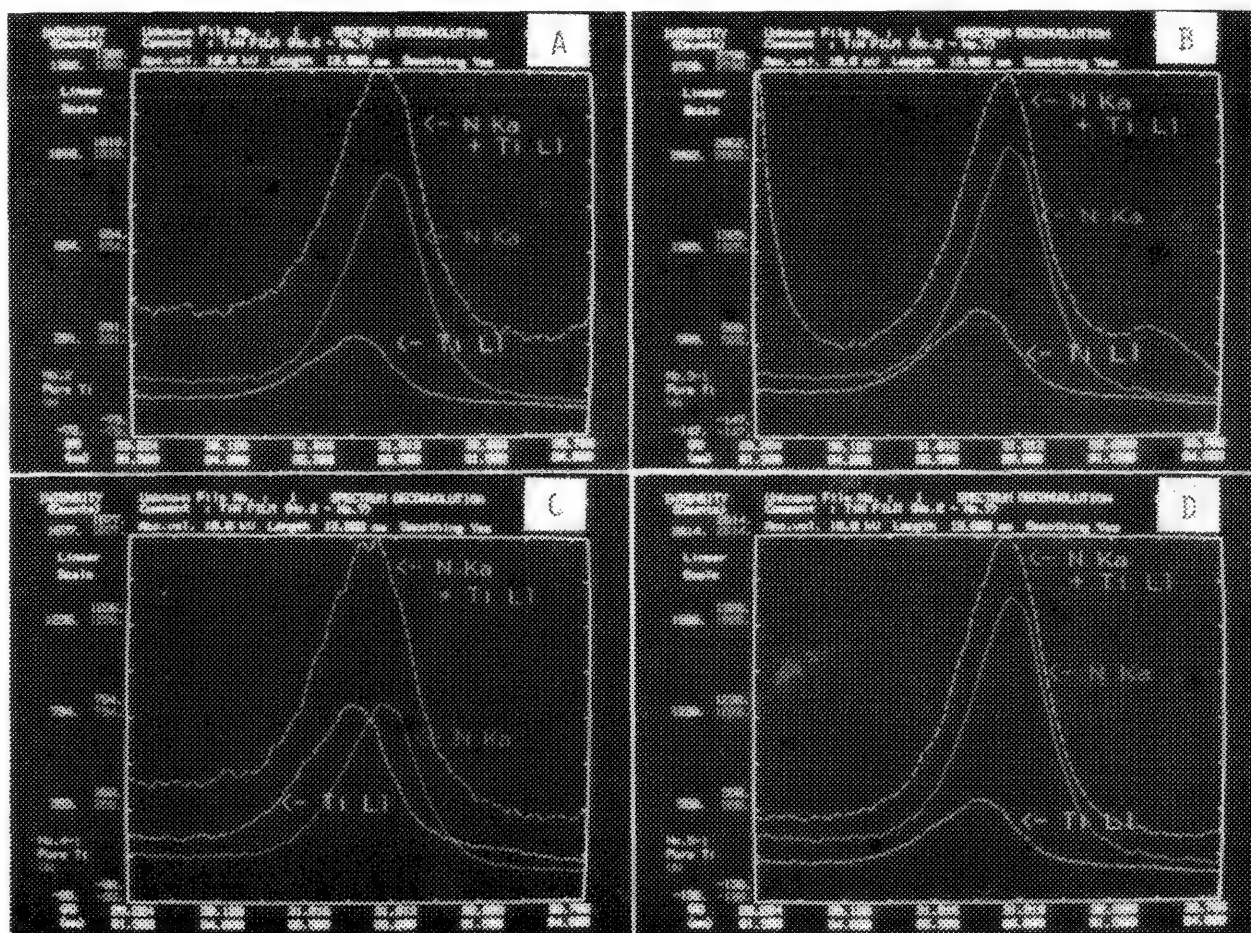


FIG. 3.--Observed spectra Ti-N films and reference specimens from V-N alloy and pure Ti metal.

TABLE 1.--Resultant composition of Ti-N films of A, B, C, and D.

Specimen		Ti	C	O	N	Total (%)	the estimated value of thickness
A	K	11.51	0.61	0	4.45	16.57	50nm
	C BALK	12.30	0.61	0	4.20	17.11	
	C ¹⁰⁰ BALK	71.86	3.59	0	24.55	100	
	A BALK	42.24	8.41	0	49.35	100	
B	K	35.84	0.54	0.89	9.66	46.93	140nm
	C BALK	37.83	0.55	2.40	8.54	49.32	
	C ¹⁰⁰ BALK	76.70	1.12	4.86	17.32	100	
	A BALK	49.51	2.88	9.38	38.23	100	
C	K	33.57	0.30	0.10	3.90	37.87	110nm
	C BALK	34.35	0.30	0.26	3.39	38.31	
	C ¹⁰⁰ BALK	89.67	0.79	0.69	8.85	100	
	A BALK	71.65	2.53	1.65	24.17	100	
D	K	26.59	0.52	0.03	9.52	36.66	100nm
	C BALK	28.16	0.53	0.09	8.46	37.24	
	C ¹⁰⁰ BALK	75.61	1.42	0.24	22.73	100	
	A BALK	47.35	3.54	0.45	48.66	100	

K : Relative intensity of each element.

C_{BALK} : Weight concentration by ordinary ZAF method.C¹⁰⁰_{BALK} : Normalized value so that total value of C_{BALK} become to be 100%.A_{BALK} : Atomic concentration converted from C¹⁰⁰_{BALK} value.

STANDARDLESS EDS ANALYSIS BASED ON A CALCULATED QUADRILATERAL MODEL

Xu Li, Jin Guan-xiang, Wu Zi-qin, and R. J. Lee

A direct relationship between the x-ray intensity ratio and the composition (wt. %) of bulk samples has been established by use of a calculated quadrilateral model of generated x-ray depth distribution. The results were compared with the stepped model program.¹ The new program, based on directly calculated quadrilateral models, is useful.

The direct relationship between the x-ray intensity ratio and the composition ratio has been established by Wu Zi-qin,² based on a revised full-diffusion model of electron scattering. That is called the stepped model of x-ray intensity depth distribution.¹ A program based on the stepped model has been used in direct standardless quantitative analysis.¹ Based on a revised full-diffusion electron scattering model and the stepped and universal quadrilateral model,¹ we suggest a calculated quadrilateral model of x-ray depth distribution.⁴

The relative generated x-ray intensity excited by incident electrons is $\phi(\rho z)$. The classical curve for $\phi(\rho z)$ was shown in Ref. 3. In the quadrilateral model, the integral intensity of $\phi(\rho z)$ is approximated by a quadrilateral, so that

$$\int_0^{\infty} \phi(\rho z) d\rho z = [\phi_0 + \frac{1}{2}(\phi_m - \phi_0)]\rho_{xb} + \frac{1}{2}m(\rho_{xc} - \rho_{xb})$$

where the parameters of ϕ_0 , ϕ_m , ρ_{xb} , ρ_{xc} are as discussed in Ref. 4.

The absorption factor $f(\chi)$ is given by the ratio of total emitted x rays divided by the total generated x rays:

$$f(\chi) = \frac{\int_0^{\infty} \phi(\rho z) \exp(-\chi \rho z) d(\rho z)}{\int_0^{\infty} \phi(\rho z) d(\rho z)}$$

where $\chi = (\mu/\rho) \csc \psi$, $\mu\rho$ is the mass absorption coefficient, and ψ is the x-ray take-off angle. Consulting the universal quadrilateral model,³ we have by substitution of the directly calculated quadrilateral model parameters for $\phi(\rho z)$

$$f(\chi) = 2\{(\rho_{xc} - \rho_{xb})(\rho_{xb} + h\rho_{xc})\chi^2\}^{-1} \cdot \{[-\exp(-\chi\rho_{xb}) + h \exp(-\chi\rho_{xc})]$$

$$+ \chi(\rho_{xc} - \rho_{xb}) - h + 1] + [\exp(-\chi\rho_{xb})(\rho_{xc} - h\rho_{xc}) + h\rho_{xc} - \rho_{xc}]\rho_{xb}^{-1}\}$$

where $h = \phi_m/\phi_0$.

The expressions for fluorescence by characteristic and continuum x rays were taken from Archard. The Heinrich and Myklebust equations were given new parameters to calculate the energy of absorption edges and emission. For the fluorescence yield, Burhop's equation⁶ with the Bambynek⁷ and Colby⁸ parameters were used. For the α line x-ray intensity ratio an empirical equation based on Colby's x-ray intensity ratio table⁸ was used. For the ionization cross section, Webster's equation⁹ was used, and Love's equation^{10,11} was used for backscattered electrons.

The results were compared with the stepped model program and a commercial standardless quantitative analysis program. The results of the quadrilateral model program for steel samples are better than results from the stepped model and EDAX programs. In other binary samples the results were the same as the stepped model program. In the future, we shall develop a new program to fit light elements analysis based on the direct calculated quadrilateral model.

References

1. Zhang Renzi, *Acta Physica Sinica* 30: 208, 1981.
2. Wu Zi-qin, *Acta Physica Sinica* 29: 485, 1980.
3. V. D. Scott and G. Love, *Microbeam Analysis--1986*, 271.
4. Xu Li et al., these proceedings.
5. K. F. J. Heinrich and R. L. Myklebust, *NBS Tech. Note* 796, 1973.
6. E. H. Burhop, *J. Phys. Radium* 16: 625, 1955.
7. W. Bambynek et al., *Rev. Mod. Phys.* 44: 716, 1972.
8. J. W. Colby, "Quantitative microprobe analysis of thin insulated films," *Advan. X-ray Analysis* 11: 287, 1968.
9. D. L. Webster et al., *Phys. Rev.* 37: 115, 1931.
10. G. Love and V. D. Scott, *J. Phys.* D11: 1978.
11. G. Love, *J. Phys.* D11: 1369, 1978.

The authors are at the University of Science and Technology of China, Hefei, Anhui, PRC 230029, except R. J. Lee, who is with the RJ Lee Group, Inc., 350 Hochberg Rd., Monroeville, PA 15146.

ACCURATE QUANTITATIVE ANALYSIS OF OXYGEN AND NITROGEN WITH A W/Si MULTILAYER CRYSTAL

J. T. Armstrong

Approximately half of the crust of the earth is composed of oxygen by weight. Oxygen is a key element in geochemical processes (e.g., oxidation, hydration, carbonation, and solution). The water content of igneous melts dramatically affects the temperatures of crystallization and the phases crystallized. The oxygen content of minerals and silicate glasses provides key information regarding the oxidation states of the cations, the amount of hydroxyl substitution for oxygen, and the amount of incorporated water, all of which provide important mineralogic and geochemical information. Despite this importance, electron microprobe analyses of oxygen in geological materials are virtually never performed. The oxygen content is inferred either based on stoichiometry relative to the measured cations, or by difference from 100%. In the former case, usually no information regarding excess oxygen can be deduced; in the latter case incorrect information regarding excess oxygen can be easily obtained. In this paper, the improved ability to analyze oxygen and nitrogen with a new W/Si multilayer crystal is examined, and results of quantitative analyses of oxygen in a series of silicate and oxide standards are presented and compared with those predicted by a series of ZAF, $\phi(\rho z)$, and Monte Carlo corrections. The results show that, with a little care, the use of the new multilayer crystals enable quantitative analyses of oxygen to be routinely performed with comparable precision and accuracy as with other major elements.

Properties of a W/Si Multilayer Crystal

The experiments described in this study were performed on a JEOL 733 electron microprobe with five two-crystal spectrometers having take-off angles of 40°. For light-element analysis the instrument has conventional TAP and stearate (STE) crystals. It also contains a vacuum-deposited W/Si multilayer on a Si (100) single-crystal substrate ($2d \approx 59.8 \text{ \AA}$). This crystal, manufactured by the Ovonic Synthetic Materials Company as the OVONYX OV-060A and marketed by the JEOL company for their in-

struments as the LDE1 (layered dispersion element) crystal, is referred to as the LDE/OV60 in this paper.

The problems of light-element analysis based on conventional TAP and STE crystals have been reported by several investigators (see, for instance, Refs. 1-5). These problems include low count rates, irregular and variable peak shapes (dependent on the chemical state and sometimes the crystallographic orientation), and the numerous interferences from multiple-order x-ray lines. The superiority of the LDE/OV60 crystal over conventional light-element crystals for oxygen and nitrogen can be easily seen in Figs 1 to 6. Figure 1 shows a wavelength scan over the O K α peak in Al₂O₃ at 15 keV with the LDE/OV60 crystal vs that taken with a TAP. The intensity scale for the TAP scan has been expanded by a factor of 40. The peak maximum intensity for the LDE/OV60 is about 10 000 cps/60 nA; that for the TAP is about 230 cps/60 nA. Note also the irregular shape of the TAP peak compared to the poorer resolution, but much more symmetric peak shape of the LDE/OV60.

Figure 2 compares the same LDE/OV60 wavelength scan with that on an STE crystal. The peak maximum count rate for the STE is less than 1/3 that for the LDE/OV60. Moreover, the STE peak shape is much more irregular and the STE scan exhibits a strong, interfering third-order Al K α peak that is not seen in the LDE scan. The only lines efficiently diffracted with the LDE/OV60 crystal are first- and second-order and result in far fewer interferences than occur with other light-element crystals.³⁻⁵

Figure 3 shows an overlay of background-subtracted wavelength scans of O K α in MgO, Al₂O₃, and SiO₂ taken with the LDE/OV60. The scans are normalized to a peak of 10 000 counts. (The peak at 92 nm is the second-order Mg K α in MgO.) Note the similar symmetrical shape of the O K α line in the three samples, which should be contrasted with the significant differences in peak shape that occur with a TAP crystal.³ However, although the peak shape of O K α is similar in different compounds with the LDE/OV60, it is *not* identical. Figure 4 shows an expanded view of the top 50% of the O K α peak from Fig. 3. The peak widths are slightly different for the three oxides. The ratio of the peak height to the net peak area is 3% more for MgO than for Al₂O₃; that for SiO₂ is about 4% less than for Al₂O₃. Figure 5 shows a more extreme case, the greatest difference found among the samples examined in this study; the ratio of the peak height to net peak area in TiO₂ is about 13.5%

The author is at the Division of Geological and Planetary Sciences, California Institute of Technology, Pasadena, CA 91125. The analytical assistance of Art Chodos and the helpful comments and provision of standard materials by G. Rossman, J. Ferry, and C. Bacon are all deeply appreciated. This work was supported in part by funds from the National Aeronautics and Space Administration through grant NAG 9-43, Division Contribution 4617 (622).

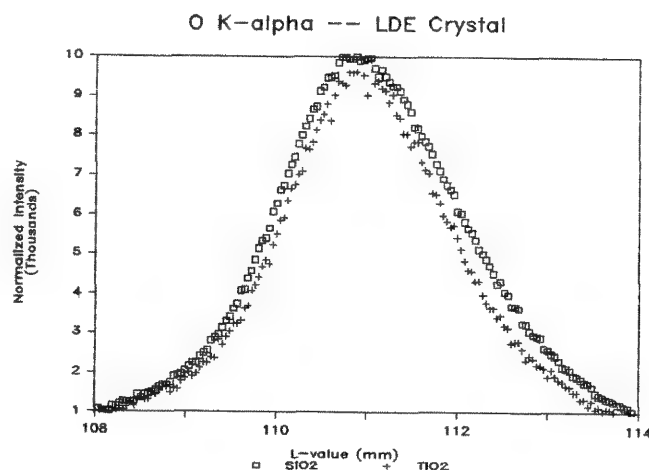
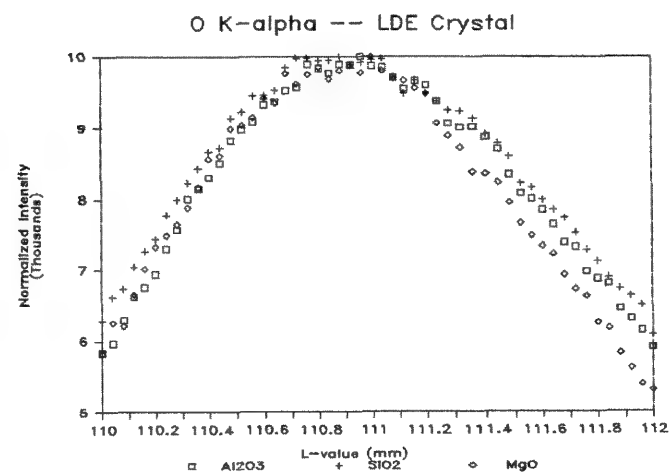
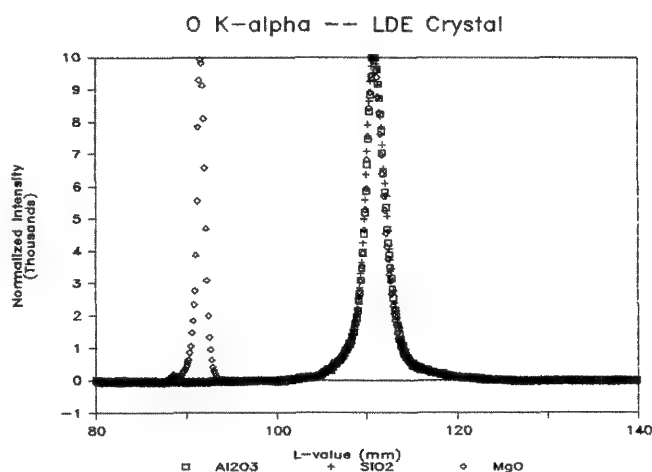
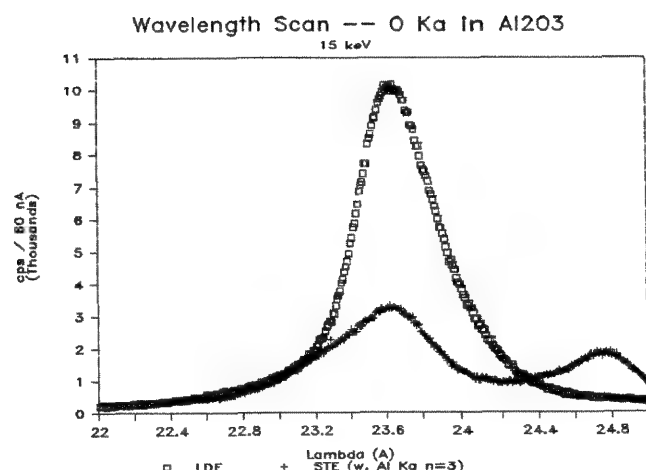
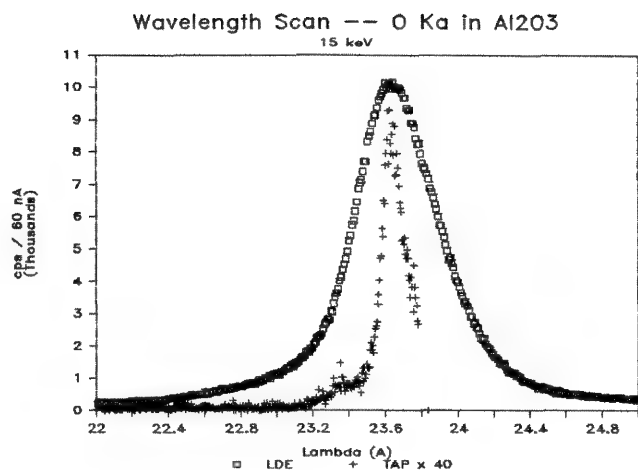


FIG. 1.--Wavelength scan over O K α peak in Al₂O₃ at 15 keV with LDE/OV60 and TAP crystals. TAP scan has been expanded in vertical scale by factor of 40.

FIG. 2.--Same as Fig. 1, comparing LDE/OV60 with STE.

FIG. 3.--Overlay of background-subtracted wavelength scans of O K α in MgO, Al₂O₃, and SiO₂.

FIG. 4.--Same as Fig. 3, showing only top 50% of peaks.

FIG. 5.--Same as Fig. 3, comparing O K α in SiO₂ and TiO₂.

greater than in SiO₂. These differences in peak width need to be accounted for when quantitative analysis is performed; however, the symmetrical, near-Gaussian shape of the LDE/OV60 peaks makes spectral fitting, background subtraction, and peak integration relatively easy to perform. In this study, wavelength scans were performed over the O K α peak for each mineral phase and the ratio of the background-subtracted peak heights to net peak areas was determined. The average measured peak intensities of the various samples were then divided by these factors to provide input

for the correction programs.

Figure 6 shows wavelength scans of the N K α peak in the mineral buddingtonite (an ammonium feldspar containing 4 wt.% nitrogen) taken with the LDE/OV60 and STE crystals. The topmost scan is an offset 3 \times expansion of the LDE/OV60 scan to show a similar level of background as measured with the STE. The STE scan barely shows the N K α peak and has prominent fourth-order Al K α and Si K α and third-order Na K α peaks. The LDE/OV60 scan shows a prominent N K α peak with no multiple-order lines except a weak second-order Fe L α peak

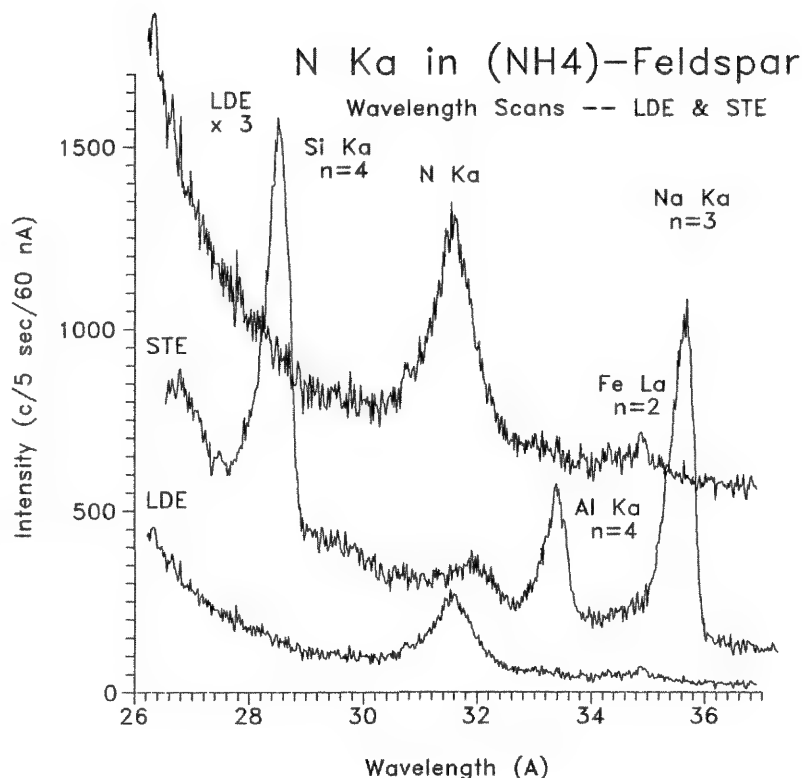


TABLE 1.--Compositions of analyzed standards (elem. wt.%).

Oxygen primary standard:										
Std	Na	Mg	Al	Si	K	Ca	Fe	O	Total	
Cor			52.92					47.08	100.0	
Analyzed standards:										
Std	Mg	Al	Si	Ca	Mn	Fe	Ni	O	Total	
Alb		10.28	32.13					48.80	91.2	
MgO	60.31							39.69	100.0	
Ryan		33.22	17.33			0.10		49.33	100.0	
Pyrp	18.09	13.38	20.90					47.62	100.0	
En	24.10	0.14	28.04	0.18				47.55	100.0	
Oliv	31.14		19.10		0.05	5.62	0.24	43.94	100.1	
Fa			13.79			54.81		31.41	100.0	
Wo	0.02	0.04	24.16	34.43		0.02		41.33	100.0	
Mel	8.92		20.61	29.40			0.01	41.08	100.0	
Anor		19.39	20.19	14.41				46.01	100.0	
NiO								78.6	21.4	100.0
Std	Na	Al	Si	K	Ti	V	Cr	O	Total	
Alb	8.72	10.28	32.13	0.07				48.80	100.0	
TiO2					59.95			40.05	100.0	
V2O5						56.01		43.99	100.0	
CrOx							68.42	31.58	100.0	

FIG. 6.--Wavelength scan of N K in mineral buddingtonite taken with LDE/OV60 and STE crystals.

(from intermixed Fe-oxide in the buddingtonite). The superior performance of the LDE/OV60 crystal for nitrogen analysis has been reported previously by other investigators.^{6,7}

Analytical Results

Quantitative analyses of oxygen in a variety of oxide and silicate minerals were performed at 10 and 15 keV with the LDE/OV60. Al_2O_3 was used as the primary oxygen standard. (SiO_2 was tried but found to suffer radiation damage during electron bombardment which resulted in a rapid increase in the oxygen signal.) The compositions of the analyzed standards are given in Table 1. The analytical procedures are described in a companion paper.⁹ Special care has to be taken regarding the carbon coat thickness and the carbon contamination rate for oxygen analysis; about 30 Å of carbon absorbs 1% of O K α x rays. Reference corundum (Al_2O_3) disks were coated simultaneously with all samples and differences in measured O K α intensities were used to correct for coat-thickness effects. Use of a LN_2 cold trap and identical time sequences for analysis of standards and samples minimized the effects of carbon contamination. In general, it was found that it was easier to obtain reproducible results at 15 keV than at 10 keV.

Results of the analyses are given in Tables 2 and 3 (shown both as raw ratios and as corrected for peak width variations) and compared with those predicted by various ZAF, $\phi(\rho z)$, and Monte Carlo correction procedures. The procedures tested are tabulated, described, and referenced in companion papers.^{8,9} The data are presented as the ratio of concentration

relative to the Al_2O_3 standard divided by the intensity relative to the standard; i.e., $(C/K)_{\text{sample}} / (C/K)_{\text{Al}_2\text{O}_3}$. As can be seen in the tables, there is a significant difference in the accuracy of the several correction procedures; the respective correction factors for individual standards vary by as much as 25%. At both 10 and 15 keV, the corrections that agree best with the experimental data are the Armstrong-Duncumb/Reed and Armstrong-Love/Scott corrections, with mean relative errors of 0.7 and 1% at 15 keV and 1.9 and 1.6% at 10 keV. Next best are the Bastin I and II $\phi(\rho z)$ corrections and Monte Carlo calculations [with any $Q(E)$ expression except that of Hutchins] with mean relative errors of 2 to 3.5%. Trailing the list in accuracy are the $\phi(\rho z)$ corrections of Packwood/Brown and Riveros and the quadratic model correction of Sewell, Love, and Scott with mean errors of up to 8%.

A critical factor in the data correction for oxygen is the set of mass absorption coefficients employed. In the tabulated set of results for the full set of corrections, the experimentally determined mass absorption coefficients of Henke et al.¹⁰ are used. Also shown are results based on the Armstrong-Love Scott correction with empirically determined mass absorption coefficients of Love and Scott³ and Ruste and Gantois.⁵ In general the Henke values produce much better results. One compound whose measured oxygen greatly deviated from that calculated by all the corrections (and not included in calculated mean error) is V_2O_5 (Table 2). The absorption edge of V L α lies very close to the O K α line. The calculated mass absorption coefficient of O K α

TABLE 2.--Oxygen analysis results at 10 keV:
(C/K)_{smp}/(C/K)_{Al₂O₃}.

	Alb	MgO	Kyan	Ens	Oliv	Fa	Pyrp
Measured:	1.034	0.916	1.058	1.030	0.994	0.877	1.018
Scan cor:	1.034	0.943	1.037	1.035	0.994	0.892	1.018
Correction							
Phil-DR	1.048	0.948	1.034	1.040	0.996	0.878	1.026
Love-Sc	1.043	0.944	1.031	1.033	0.988	0.865	1.021
Sewl-LS	1.041	0.948	1.029	1.032	0.982	0.806	1.020
Arms-LS	1.043	0.943	1.031	1.033	0.992	0.889	1.021
Arms-DR	1.044	0.943	1.032	1.033	0.992	0.897	1.021
Pack-Br	1.043	0.946	1.031	1.033	0.987	0.849	1.021
Bast-I	1.038	0.931	1.028	1.023	0.979	0.869	1.013
Bast-II	1.038	0.931	1.028	1.023	0.977	0.852	1.013
Riveros	1.042	0.949	1.030	1.033	0.984	0.828	1.021
Arms-LS w:							
LS MAC	1.044	0.957	1.030	1.037	0.997	0.883	1.023
RG MAC	1.038	0.940	1.027	1.025	0.989	0.912	1.015

	Anor	Me	Wo	TiO2	V2O5	CrOx	NiO
Measured:	1.372	1.687	1.860	2.147	7.662	0.804	0.956
Scan cor:	1.386	1.704	1.906	2.340	7.66	0.804	0.956
Correction							
Phil-DR	1.334	1.647	1.773	2.136	2.194	0.738	0.898
Love-Sc	1.336	1.655	1.784	2.220	2.278	0.731	0.880
Sewl-LS	1.311	1.602	1.718	2.046	2.078	0.708	0.731
Arms-LS	1.342	1.675	1.813	2.329	2.397	0.746	0.921
Arms-DR	1.345	1.682	1.821	2.341	2.410	0.753	0.930
Pack-Br	1.320	1.628	1.756	2.222	2.290	0.709	0.852
Bast-I	1.346	1.685	1.827	2.385	2.464	0.729	0.880
Bast-II	1.341	1.673	1.811	2.354	2.439	0.714	0.857
Riveros	1.303	1.579	1.688	2.039	2.090	0.697	0.826
Arms-LS w:							
LS MAC	1.404	1.819	1.983	2.507	2.640	0.721	0.937
RG MAC	1.309	1.608	1.733	2.342	2.307	0.770	1.067

TABLE 3.--Oxygen analysis results at 15 keV:
(C/K)_{smp}/(C/K)_{Al₂O₃}.

	MgO	Kyan	Ens	Oliv	Fa	Anor	Me	Wo	TiO2	NiO
Measured:	0.882	1.070	1.040	0.985	0.860	1.579	2.063	2.304	2.893	0.932
Scan cor:	0.908	1.049	1.045	0.985	0.875	1.595	2.084	2.361	3.154	0.932
Correction										
MCms-Hu	0.893	1.046			0.830	1.523	2.011	2.209		
MCms-Fa	0.899	1.047			0.825	1.543	2.054	2.261		
MCms-Gz	0.897	1.048			0.821	1.555	2.080	2.292		
MCms-GC	0.897	1.048			0.822	1.552	2.073	2.285		
MCms-WT	0.899	1.048			0.819	1.562	2.093	2.309		
Phil-DR	0.917	1.048	1.053	0.990	0.854	1.518	2.028	2.240	2.911	0.894
Love-Sc	0.905	1.046	1.044	0.978	0.830	1.522	2.001	2.188	2.804	0.861
Sewl-LS	0.905	1.045	1.044	0.974	0.790	1.540	2.066	2.280	2.996	0.772
Arms-LS	0.905	1.045	1.044	0.984	0.874	1.544	2.086	2.311	3.168	0.936
Arms-DR	0.904	1.046	1.044	0.985	0.885	1.550	2.099	2.326	3.193	0.952
Pack-Br	0.908	1.045	1.043	0.980	0.840	1.518	2.026	2.237	3.021	0.877
Bast-I	0.895	1.045	1.038	0.975	0.852	1.560	2.118	2.350	3.245	0.898
Bast-II	0.894	1.045	1.038	0.972	0.830	1.554	2.100	2.326	3.192	0.863
Riveros	0.915	1.042	1.042	0.976	0.806	1.465	1.887	2.053	2.597	0.822
Arms-LS w:										
LS MAC	0.925	1.044	1.050	0.992	0.860	1.653	2.336	2.607	3.486	0.961
RG MAC	0.900	1.040	1.032	0.980	0.906	1.494	1.983	2.189	3.202	0.978

required to get agreement between the correction procedures and the measured value is in excess of 60 000 as compared to the tabulated values^{3,5,10} of between 23 000 and 26 000.

Applications and Conclusions

With care, the quantitative analysis of oxygen using a LDE/OV60 crystal can be routinely performed with the same degree of accuracy and precision as for other major elements. Our laboratory now routinely analyzes oxygen in virtually all oxide and silicate samples. Even when oxidation state, hydroxyl substitution, or water incorporation are not involved, the agreement between the measured oxygen content and that calculated by stoichiometry is a good indicator of the quality of the analysis. Using oxygen analyses, we have been able to determine readily and accurately the hydroxide concentrations in minerals like chlorite and, with care, in minerals like amphibole, epidote, and clinozoisite. We have been able to determine water contents of hydro-garnets down to a

few tenths of a percent in agreement with IR measurements.¹¹ In silicate glasses, where alkali migration is not too severe, incorporated water can be accurately determined. In the case of nitrogen analysis, using budding-tonite as a standard (Fig. 6), we have been able to measure N in ammonium-containing hyalophanes at a concentration as low as 0.1% in agreement with IR measurements.¹² In short, the development of multilayer crystals and newer correction procedures have enabled accurate light element analysis that opens up a variety of new important applications in the electron microprobe analysis of geological materials. There is no longer a reason not to analyze routinely the most abundant element in the earth's crust.

References

1. G. F. Bastin and H. J. M. Heijligers, "Quantitative electron-probe microanalysis of very light elements," *Microbeam Analysis--1985*, 1.
2. G. Love and V. D. Scott, "Analyzing ultra-light elements in the electron microprobe," *Microbeam Analysis--1985*, 93.
3. G. Love, M. G. C. Cox, and V. D. Scott, "Electron probe microanalysis using oxygen x-rays: I. Mass absorption coefficients," *J. Phys. D7*: 2131, 1974.
4. G. Love, M. G. C. Cox and V. D. Scott, "Electron probe microanalysis using oxygen x-rays: II. Absorption correction models," *J. Phys. D7*: 2142, 1974.
5. J. Ruste and M. Gantois, "A quantitative analysis of very light elements by the electron probe microanalyser," *J. Phys. D8*: 872, 1975.
6. K. Kawabe et al., "Coated multilayer dispersion element for x-ray microanalysis," *Proc. 11th Int. Cong. on Elec. Microsc.*, 1986, 589.
7. H. Heijligers and G. Bastin, "The performance of an 'LSM' crystal compared to that of a conventional stearate crystal for the quantitative EPMA of nitrogen," *Beitr. Elektronenmikroskop. Direktabb. Oberfl.* 19: 1, 1986.
8. J. T. Armstrong, "Quantitative analysis of silicate and oxide materials: Comparison of Monte Carlo, ZAF and $\phi(\rho z)$ procedures," this volume.
9. J. T. Armstrong, "Bence-Albee after 20 years: Review of the accuracy of α -factor correction procedures for silicate and oxide minerals," this volume.
10. B. L. Henke, P. Lee, T. J. Tanake, R. L. Shimabukuro, and B. K. Fujikawa, "Low-energy x-ray interaction coefficients: Photo-absorption, scattering and reflection," *Atom. Data and Nucl. Data Tables* 27: 1, 1982.
11. J. T. Armstrong and G. R. Rossman, "Electron microprobe and infrared analysis of the water contents of garnets," *Amer. Mineral.* (in preparation).
12. J. T. Armstrong, G. Beran and G. R. Rossman, "Infrared and electron microprobe of ammonium ions in hyalophane feldspar," *Amer. Mineral.* (in preparation).

STEP SHAPE $\phi(\rho z)$ MODEL AND NONSTANDARD ULTRA-LIGHT ELEMENT ANALYSIS PROGRAM

Wanrong Cheng and R. J. Lee

On the basis of the physical processes involved in the excitation of x rays by electrons and the step-shape $\phi(\rho z)$ model, a wholly theoretical treatment, a direct nonstandard quantitative analysis program, was developed. Several experiments have been done to use this program to analyze heavy elements ($z \geq 11$) and ultra-light elements ($z < 11$). The results show the step-shape $\phi(\rho z)$ model is reasonable and the program can be used in a minicomputer on-line analysis. Some problems in analyzing ultra-light elements are discussed.

To analyze ultra-light elements, Tanuma,² Bastin,³ and Love and Scott⁴ proposed the Gaussian-shape, rectangular-shape, and quadri-lateral-shape $\phi(\rho z)$ curve models. The step-shape $\phi(\rho z)$ model proved to be successful in heavy elements analysis, so we extended this model to ultra-light element analysis.

The physical model for the step-shape $\phi(\rho z)$ has been described elsewhere.⁵ The primary x-ray intensity generated from the sample I_{AC}^0 is

$$I_{AC}^0 = (1 - \eta)I_{AC}^a + \eta I_{AC}^b$$

$$= [I - \eta]\phi_{AC}^a F^a + \eta\phi_{AC}^b F^b] \omega L \alpha = I^0 C_A \quad (1)$$

where η is the backscatter coefficient of the sample, ω is A element C shell yield ratio, $L \alpha$ is the ratio of α line intensity in all C shell lines, F is the absorption factor, and I_{AC}^a and I_{AC}^b represent the intensity generated by the penetration and backscatter electrons, respectively, with

$$\phi_{AC}^a = \frac{N_0 C_A}{Q_{AC}^a A_A} \frac{1}{\cos \alpha} \quad (2)$$

where Q_{AC}^a is the average ionization cross section for the absorption electrons, N_0 is Avogadro's number, C_A is the A element wt. %, A_A is the atomic weight of element A, and α is the incident angle; and similarly for ϕ_{AC}^b and backscatter electrons. We then have

$$F^a = \int_0^{\rho z_{AC}} \exp(-\mu_{\alpha} \rho z \csc \psi) d\rho z$$

$$= \frac{1 - \exp(-\mu_{\alpha} \rho z_{AC} \csc \psi)}{\mu_{\alpha} \csc \psi} \quad (3)$$

Wanrong Cheng is at the Exploration Technology Institute, Yan Jiao, Beijing, PRC; R. J. Lee is with the R.J. Lee Group, Inc., Monroeville, PA 15146.

$$F^b = \frac{1 - \exp(-\mu_{\alpha} \rho z_b \csc \psi)}{\mu_{\alpha} \csc \psi} \quad (4)$$

Finally, we have the relative x-ray intensity ratio:

$$\frac{I_i}{I_1} = \frac{I_i^0 + I_i' + I_i'' C_i}{I_1^0 + I_1' + I_1'' C_1} \quad i = 2, \dots, N \quad (5)$$

where I^0 = primary x-ray intensity (from theoretical calculation), I' = characteristic fluorescence x-ray intensity (from theoretical calculation), I'' = continuum fluorescence x-ray intensity (from theoretical calculation), and I = experimental intensity. Since

$$C_1 + C_2 + \dots + C_N = 1 \quad (6)$$

we normalize to get the result.

When we use the ordinary beryllium window detector to analyze heavy elements ($z \geq 11$), the detector efficiency formula is $T = \exp(-C_1/E^{2.8})$. For the thin-window detector, the detector efficiency is

$$T = \exp(-\mu_C^{\rho} C^t - \mu_{Al}^{\rho} Al^t_{Al} - \mu_{Si}^{\rho} Si^t_{Si} - \mu_{Au}^{\rho} Au^t_{Au}) [1 - \exp(-C_2/E^{2.8})]$$

The subscripts C, Al, Si, and Au represent carbon film, aluminum film, silicon, dead layer, and gold layer.

Since the $\phi(\rho z)$ curves of the light elements are shifted into the interior of the sample more than those of the heavy elements, we decrease the first step height for the light elements to keep the step-shape $\phi(\rho z)$ curve near the experimental $\phi(\rho z)$ curve.

In our program all the parameters (mass absorption coefficient, fluorescence yield ratio, absorption edge, etc.) must be calculated. But most empirical formulas used in heavy-element analysis programs are not suitable for ultra-light elements and must be changed when applied to light elements.

In addition we changed some model, subroutine, and detector efficiency formulas for ultra-light elements. Some experimental problems in getting x-ray intensity data of better quality should also be considered, such as the ultra-light element x-ray peak shift, oxide and carbide electrical conductivity, the surface shape effect on the relative ratio of x-ray intensity, the detector sensitivity of ultra-light elements, and the x-ray peak overlap problem.

Based on the step-shape $\phi(\rho z)$ model and the above considerations, we worked out our direct nonstandard quantitative analysis programs. Typical experimental results are found in Tables 1 and 2.

Figures 1 and 2 show the generated x-ray curve and emitted x-ray curve of experimental $\phi(\rho z)$ and step-shape $\phi(\rho z)$. Figure 3 shows the comparison between them. We note that the step-shape $\phi(\rho z)$ model is not exactly similar to the experimental $\phi(\rho z)$ curve. But after the absorption is added, the real depth distribution of emitted x rays is very close to the experimental curve. In this sense, the various shapes of the $\phi(\rho z)$ model have little effect on the depth distribution of emitted x rays. However, according to our step-shape model, the $I = \int_0^{\rho z} \phi(\rho z) \exp(-\mu \rho z \csc \psi) d\rho z$ can be simplified to:

$$I = \phi(\rho z) \int_0^{\rho z} \exp(-\mu \rho z \csc \psi) d\rho z$$

$$= \phi(\rho z) \frac{1 - \exp(-\mu \rho z \csc \psi)}{\mu \csc \psi}$$

The advantage of this program is that it does not require time-consuming numerical integration and can run faster without loss of accuracy, an important factor in minicomputer on-line analysis work.

References

1. G. D. Archard and T. Mulvey, *Proc. 3rd Int. Symp. on X-Ray Optics and X-ray Microanalysis*, 1962, 393.
2. S. Tanuma and K. Nagashima, *Microchimica Acta* 1: 299-313, 1983.
3. G. F. Bastin, F. J. J. Van Loo, and H. J. M. Heijligers, *X-ray Spectrom* 13: 91-97, 1984.
4. G. Love and V. D. Scott, *Microbeam Analysis--1985*, 93.
5. Wu Zi-qin and Zhang Rinjie, *Acta Physica* 31: 1395, 1982.

TABLE 1.--DNSQ.

Composition	Al	Si	Mo	Ti	Cr	Mn	Co	Fe	Ni	C
NBS 123C (AISI 348)		1.0			17~19	<2.0			9~13	0.08
Analysis 20KV		0.93			17.66	1.31		69.14	10.95	

TABLE 2.--LE DNSQ.

Sample	Condition Accelerate Voltage	Scan Mode	Composition %											File #
			O	Mg	Al	Si	Ti	Fe	Sn	S	Ca	Ga	Gd	
CaSiO ₃ Analysis	15 KV	area spot	41.3			24.2					34.5			111
			40.3			24.8					34.9			112
			40.6			25.0					34.4			

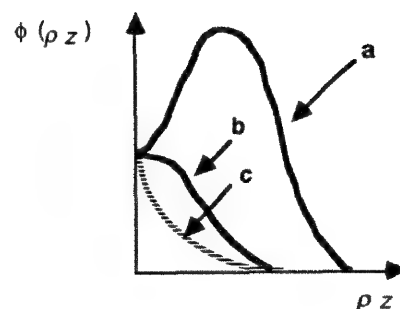


FIG. 1.--Distribution with depth of (a) experimental generated x rays and (b) emitted x rays; (c) represents absorption profile.

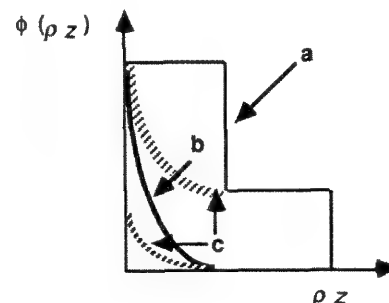


FIG. 2.--Distribution with depth of (a) step-shape generated x rays and (b) emitted x rays; (c) represents absorption profile.

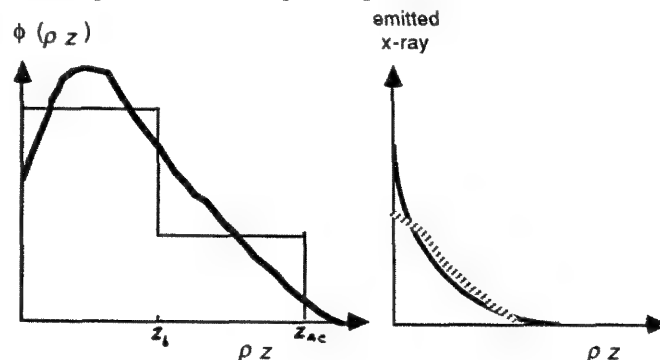


FIG. 3.--Comparison of $\phi(\rho z)$ curve and emitted x-ray curve.

QUANTITATIVE ELECTRON-PROBE MICROANALYSIS OF OXYGEN IN Y-Ba-Cu-O SUPERCONDUCTING MATERIALS

Peter Willich, Dieter Obertop, and J. P. Krumme

Electron-probe microanalysis (EPMA) is frequently used to study the composition of high-temperature superconducting oxides. Typical applications are the chemical characterization of thin films and local analysis on ceramic bulk samples. However, all investigations by EPMA reported so far are limited to the determination of the metals. In this paper we describe the complete quantitative analysis of Y-Ba-Cu-O including the direct determination of oxygen. The method is used to study the composition of thin films prepared by sputter deposition. In order to estimate the precision and accuracy of EPMA, some investigations of sintered $Y_1Ba_2Cu_3O_x$ bulk samples are discussed in comparison with the results of thermogravimetric experiments.

The possibility of high-temperature superconductivity has stimulated an intensive investigation of the $Y_1Ba_2Cu_3O_x$ ($x \approx 6.9$) perovskite-like structure, which exhibits a transition temperature T_c of about 95 K. T_c and other superconducting properties depend to a great extent on the oxygen content of the material. In the case of sintered $Y_1Ba_2Cu_3O_x$ bulk samples, the parameter x in the range of 6-7 has recently been studied by thermogravimetry.^{1,2} This method is destructive and requires at least 0.5 g of material. Application to thin films having a thickness of 0.5-2 μm and deposited on oxide substrates is not practicable. Moreover, especially in the case of films, it is preferable to use an analytical technique which, besides oxygen, enables the simultaneous determination of the cations. This requirement leads to the use of EPMA as a relatively fast and nondestructive method.

Experimental

Analyses were carried out by an automated CAMEBAX microprobe equipped with a W/Si multilayer monochromator ($2d = 50 \text{ \AA}$) for the soft x rays of O K α . The determination of oxygen is significantly improved due to net counting rates that are about 3 times higher than with a conventional monochromator of Pb-stearate. Calibration was performed by sufficiently conductive single crystals of $Y_3Fe_5O_{12}$, $BaFe_{12}O_{19}$, and $PbFe_{12}O_{19}$.³ Slight deviations from the nominal stoichiometry and the incorporation of dopants ($< 0.2 \text{ wt\%}$) were defined by x-ray fluorescence analysis. No effects of chemical shift could be observed by a comparison of the O K α spectra of the abovementioned standards with the spectra of Y-Ba-Cu-O mate-

rials. When Cu_2O is used as a standard for oxygen, the influence of peak broadening relative to Y-Ba-Cu-O has to be considered. In this case the intensities of O K α were derived from peak area measurements. Concentrations were obtained from relative intensities by the $\phi(\rho z)$ model of Pouchou and Pichoir (PAP)⁴ in combination with the mass absorption coefficients of Henke⁵ for O K α . The accuracy of the PAP model with respect to the quantitative analysis of light elements has been previously demonstrated by the example of carbon.⁶

Results

The composition of an arbitrarily selected Y-Ba-Cu-O thin film 1.8 μm thick was determined at various electron energies (E_0) of 5-20 keV (Fig. 1). Each concentration related to a particular value of E_0 represents the average of 5 measurements without a change of beam position on the sample. For this sample and the other Y-Ba-Cu-O materials discussed in this paper, possible effects of electron-beam-induced sample deterioration could not be detected. No systematic shift of the concentrations as a function of E_0 is clearly visible in Fig. 1, which proves the accuracy of the PAP correction model. This conclusion is further confirmed when one compares the results of oxygen obtained from various standards. For all elements the relative difference between the maximum and minimum concentration does not exceed 2% relative. This result may be regarded as an estimate of the analytical error, arising from fluctuations due to the relatively rough surface of films prepared by sputter deposition.

Analysis by EPMA is also compared with the well-defined bulk composition of single-phase $Y_1Ba_2Cu_3O_x$ ceramics, where x was established by thermogravimetry (Table 1). The weight concentration of the metals and oxygen based on EPMA agree within 2% relative with the bulk composition. Samples for microprobe analysis were polished by use of an oil-based slurry. Water contamination should be avoided, because Ba leaching affects the composition of $Y_1Ba_2Cu_3O_x$ within a depth of at least 0.5 μm .¹ The composition of Y-Ba-Cu-O films prepared by magnetron sputtering from a target of $Y_1Ba_2Cu_3O_x$ is strongly influenced by the temperature of the substrate during deposition (Table 1). The oxidation state of samples with a different composition of the cations can be compared by introducing the formal valency of Cu. One obtains this parameter (Table 1) by calculating the atomic composition and by assuming Y to be present as Y_2O_3 and Ba as BaO.

The determination of oxygen by EPMA was also tested by a set of $Y_1Ba_2Cu_3O_x$ ceramics with a wide variation of x . After sintering,

The authors are at the Philips Research Laboratory Hamburg, P. O. Box 54 08 40, D-2000 Hamburg 54, Federal Republic of Germany. Samples of $Y_1Ba_2Cu_3O_x$ were kindly provided by W. F. Knippenberg, Philips Research Laboratories, Eindhoven, The Netherlands.

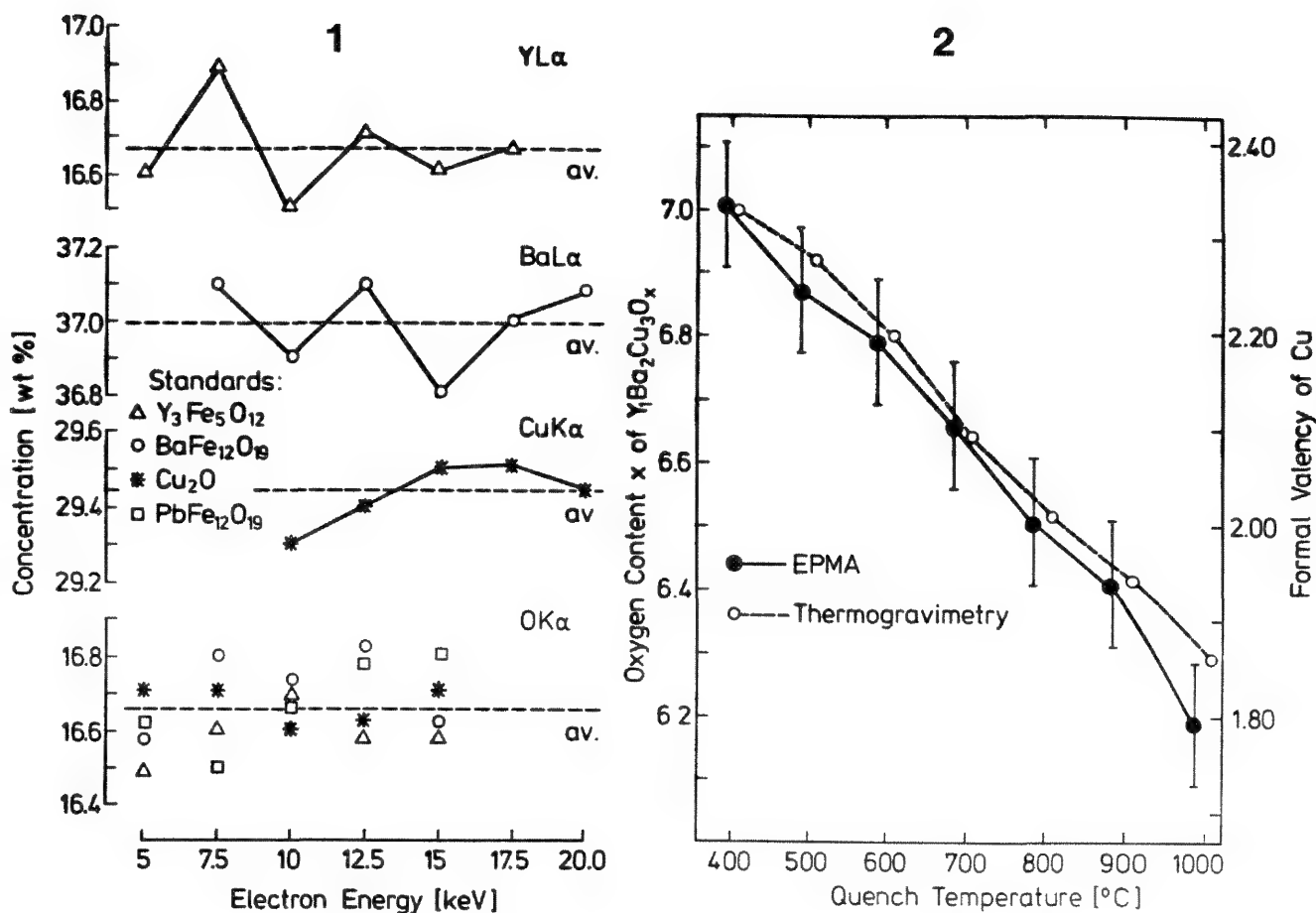


FIG. 1.--Quantitative EPMA of Y-Ba-Cu-O film at various electron energies. Calibration of oxygen by use of various standards.

FIG. 2.--Oxygen content of sintered $Y_1Ba_2Cu_3O_x$ after annealing at fixed temperatures followed by quenching. Vertical bars represent experimental reproducibility of EPMA.

each sample was annealed in an O_2/N_2 atmosphere at a different temperature (400-1000 °C) and subsequently quenched to room temperature.^{1,2} The parameter x and the corresponding formal valency of Cu as a function of quench temperature are depicted in Fig. 2. The results of EPMA are compared with those obtained by thermogravimetry, which was calibrated from weight loss measurements after reduction in hydrogen.^{1,2} EPMA was performed with an electron beam focused to a spot of 5 μm . Each data point of Fig. 2 represents the average of 10 determinations at various positions on the sample. Maximum deviations from the mean value are of the order of $x = 6.5 \pm 0.1$ or 2.00 ± 0.06 for the formal valency of Cu in $Y_1Ba_2Cu_3O_x$. Within this range of reproducibility, the results of EPMA are in agreement with those of thermogravimetry, although the oxygen contents established by EPMA show a tendency to be slightly lower than those defined by thermogravimetry. EPMA was performed at an electron energy of 12.5 keV. The corresponding depth of x-ray generation is about 1 μm . This depth seems to be sufficiently representative for the bulk composition, without noticeable effects of a possibly modified surface composition arising from polishing or contact with air.

Conclusions

Electron-probe microanalysis proves to be a fast and nondestructive method of determining the oxygen stoichiometry of multi-element oxides. The concentrations of metals and oxygen can be established within an analytical error of about 2% relative. This level includes the reproducibility of the measurements and systematic errors caused by the PAP correction model. No particularly matched standards for oxygen are required. However, depending on the choice of the standard, effects of O K α chemical shift have to be considered. As demonstrated by the example of $Y_1Ba_2Cu_3O_x$ superconducting materials, oxygen contents defined by EPMA within a depth of about 1 μm are in good agreement with the results of bulk analysis by thermogravimetry. This enables the discussion of EPMA results in relation to preparation parameters and electrical properties without influence of a nonspecific surface composition, which has to be considered when surface analytical techniques are used.

References

1. M. P. A. Vieggers et al., "Oxygen content, microstructure, and superconductivity of $Y_1Ba_2Cu_3O_{7-x}$," *J. Mat. Res.* 2: 743, 1987.

TABLE 1.--Weight composition and formal valency of Cu: $Y_1Ba_2Cu_3O_x$ ceramics and Y-Ba-Cu-O films prepared by sputter deposition.

Specimen	Composition (wt%)					Formal valency of Cu
	Y	Ba	Cu	O	Total	
Bulk $Y_1Ba_2Cu_3O_{6.29}^a$	13.6	41.9	29.1	15.4	100.0	1.86
	13.5	41.8	28.9	15.1	99.3	1.80
Bulk $Y_1Ba_2Cu_3O_{7.00}^a$	13.4	41.2	28.6	16.8	100.0	2.33
	13.4	41.6	28.4	16.9	100.3	2.37
Film $T_s=400^b$ EPMA	16.6	37.0	29.4	16.6	99.6	2.12
Film $T_s=465^b$ EPMA	20.6	42.4	19.8	15.9	98.7	2.16
Film $T_s=500^b$ EPMA	19.9	44.0	18.9	15.8	98.6	2.21
Film $T_s=560^b$ EPMA	21.6	41.2	21.6	14.8	99.2	1.53

^aOxygen content determined by thermogravimetry.

^bSubstrate temperature [$^{\circ}C$] during deposition.

2. H. Verweij, "Defect chemistry of $Y_1Ba_2Cu_3O_x$: Strong evidence for the presence of Cu^{+} ," *Solid State Communications* 64: 1213, 1987.

3. P. Willich and D. Obertop, "EPMA of oxygen and determination of oxide film thickness using Gaussian $\phi(\rho z)$ curves," *Microchimica Acta* [Wien], Suppl. 11: 299, 1985.

4. J. L. Pouchou and F. Pichoir, "A new model for quantitative x-ray microanalysis," *La recherche aérospatiale* 3: 14, 1984.

5. B. L. Henke et al., "Low energy x-ray interaction coefficients," *Atomic Data and Nuclear Tables* 27: 1-144, 1982.

6. P. Willich, "Determination of chemical state and composition of metal-carbon films by use of EPMA," in J. D. Brown and R. H. Packwood, Eds., *Proc. 11th ICXOM*, London (Canada), 1987, 238.

AN ITERATION PROCEDURE TO CALCULATE FILM COMPOSITIONS AND THICKNESSES IN ELECTRON-PROBE MICROANALYSIS

R. A. Waldo

Recent mathematical approximations of $\phi(\rho z)$, the depth distribution of electron excited x rays, have opened up the possibility of quantitative thin film analysis with the electron probe. Unfortunately, no published methods are currently available that solve the system of equations resulting from a thin-film system whose unknowns are the film and substrate composition and film thicknesses. The purpose of this paper is to describe an iteration procedure that solves the system of equations that result from a thin-film system (defined as a film on a buried layer on a substrate).

Quantitative Analysis by $\phi(\rho z)$ Curves

In this discussion, we consider a thin-film system with u elements in a surface film of thickness δ^{f1} , on a subsurface film (buried layer) of v elements extending from δ^{f1} to δ^{f2} , on a substrate of w elements. Packwood¹ found that $\phi(\rho z)$ can be approximated by a modified Gaussian function of the form

$$I_{i,obs} = \gamma_0 \exp[-\alpha^2(\rho z)^2] - (\gamma_0 - \phi_0) \exp[-\alpha^2(\rho z)^2 - \beta \rho z] \quad (1)$$

The general forms for the α , β , ϕ_0 , and γ_0 parameters were derived from a random-walk theoretical treatment of electron trajectories.² Computer fitting techniques were used to optimize the functional forms of the parameters.^{3,4}

Once the $\phi(\rho z)$ parameters have been calculated, the observed x-ray intensity for the i th element in a thin film system is found by multiplying $\phi(\rho z)$ by the x-ray absorption factor $\exp(-\chi \rho z)$ and integrating over the appropriate values of ρz . For the general case of an element in a subsurface film extending from $\rho z = \delta'(\delta^{f1})$ to $\rho z = \delta''(\delta^{f2})$,

$$I_{i,obs} = h_1 \int_{\delta'}^{\delta''} \phi(\rho z) \exp(-\chi \rho z) d(\rho z) \quad (2)$$

which can be integrated exactly:¹

$$\begin{aligned} I_{obs} = & h_2 C_i \exp[-\delta'(\chi' - \chi)] \gamma_0 \exp(\chi/2\alpha)^2 \\ & \cdot \{ \text{erf}[\alpha\delta'' + (\chi/2\alpha)] - \text{erf}[\alpha\delta' + (\chi/2\alpha)] \} \\ & - (\gamma_0 - \phi_0) \exp[(\beta + \chi)/2\alpha]^2 \\ & \cdot \{ \text{erf}[\alpha\delta'' + (\beta + \chi)/2\alpha] - \text{erf}[\alpha\delta' + (\beta + \chi)/2\alpha] \} \end{aligned} \quad (3)$$

The author is with the General Motors Research Laboratories (Analytical Chemistry Department), Warren, MI 48090.

where χ' is the x-ray absorption factor for the element i radiation in the surface film and $\text{erf}(x)$ is the error function of x . Setting $\delta' = 0$ and $\delta'' = \infty$ gives the formula for a homogeneous (semi-infinite) specimen. Setting $\delta' = 0$ and $\delta'' = \delta^{f1}$ gives the formula for a surface film of thickness δ^{f1} . Setting $\delta' = \delta^{f2}$ and $\delta'' = \infty$, with the additional absorption term $\exp[-(\chi'' - \chi)(\delta^{f2} - \delta^{f1})]$, gives the formula for a substrate covered by a surface film of thickness δ^{f1} and a subsurface film of thickness $\delta^{f2} - \delta^{f1}$. The constants h_1 and h_2 cancel in the equation which defines the experimental k -ratio for each element i .

$$k_{i,exp} = I_{i,obs}(sp)/I_{i,obs}(st) \quad (4)$$

where (sp) is the specimen and (st) is the standard.

Calculation of α , β , and ϕ Parameters for Layered Specimens

For a thin-film system, each of the parameters in $\phi(\rho z)$ will now also be a function of the electron energy, overvoltage ratio, the compositions of the films and substrate, and the film thicknesses. Packwood⁵ proposed that a weighting function be based on the error function of α times the film thickness δ , or $\text{erf}(\alpha\delta)$. The choice of which α to use--that from the surface film, buried layer, or substrate--is not too critical since α is not a sensitive function of atomic number. I have used a weighted value for α , $\bar{\alpha}$, based on $\text{erf}[\bar{\alpha}(\delta^{f1}, \delta^{f2})]$. An iterative method is required to calculate $\bar{\alpha}$ since it is not known at the start of the calculation. An initial value $\bar{\alpha}_1$ is estimated from

$$\bar{\alpha}_1 = (\alpha^{f1} + \alpha^{f2} + \alpha^S)/3 \quad (5)$$

where α^{f1} is the α for the composition of film 1, etc. By extension of Packwood's $\text{erf}(\bar{\alpha}\delta)$ weighting function to a bilayer film system, this value $\bar{\alpha}_1$ is used to calculate $\bar{\alpha}_2$:

$$\begin{aligned} \bar{\alpha}_2 = & \alpha^{f1} + (\alpha^{f2} - \alpha^{f1}) [\text{erfc}(\bar{\alpha}_1 \delta^{f1})] \\ & + (\alpha^S - \alpha^{f2}) \text{erfc}[\bar{\alpha}_1 (\delta^{f1} + \delta^{f2})] \end{aligned} \quad (6)$$

When $\bar{\alpha}_{n+1} = \bar{\alpha}_n$ within an error ϵ , the iterative solution is completed. Usually, convergence is achieved by the third iteration. A weighted ϕ_0 parameter, $\bar{\phi}_0$, is based on $\text{erf}[2\bar{\alpha}(\delta^{f1}, \delta^{f2})]$.⁵ $\bar{\beta}$ is calculated with \bar{Z} and \bar{A} which are calculated in the same manner as Eq. (6).

Once the $\bar{\alpha}$, $\bar{\beta}$, $\bar{\gamma}_0$, and $\bar{\phi}_0$ are calculated, a

system of equations is formed from Eqs. (3) and (4). To solve this system of equations, an iterative procedure similar to that used in the ZAF method of electron probe microanalysis of homogeneous specimens is required. An added complication in this iteration scheme is that additional variables are added in the unknown film thicknesses, which are present as the limits of the integrals in Eq. (3).

Initial Values for Film Thicknesses

Initial thickness estimates were made starting with estimates of the x-ray generation range ρz_r , which can be approximated by⁶

$$\rho z_r = 7.0 (E_0^{1.65} - E_c^{1.65}) \mu\text{g}/\text{cm}^2 \quad (7)$$

where E_0 is the incident electron energy and E_c is the critical excitation energy for the x-ray line. The thickness δ_0^{f1} of a surface film can be thought as being comprised of the contributions from each of the u elements in the film. Treating each element individually and neglecting absorption effects we can estimate the contributed thickness ρz_i^{f1} as the thickness at which the integral from $\rho z = 0$ to $\rho z = \rho z_i^{f1}$ of the $\phi(\rho z)$ function for the specimen ratioed to the $\phi(\rho z)$ function for the pure element standard equals the k-ratio for the element, i.e., find z_i^{f1} such that

$$k_{i,\text{exp}} = \frac{\int_0^{z_i^{f1}} \phi(\rho z)^{\text{sp}} d(\rho z)}{\int_0^\infty \phi(\rho z)^{\text{st}} d(\rho z)} \quad (8)$$

This equation cannot be used to calculate ρz_i^{f1} since the required function $\phi(\rho z)^{\text{sp}}$ can only be arrived at through subsequent iterations of the main iteration procedure.

This problem is avoided by use of a triangular approximation for $\phi(\rho z)^{\text{sp}}$ in Eq. (8), as in Fig. 1. $\phi(\rho z)^{\text{st}}$ is assumed equal to $\phi(\rho z)^{\text{sp}}$. Now, ρz_i^{f1} is the solution of the equation

$$q + [q - (q\rho z_i^{f1}/\rho z_{r,i})]/2 = (k_{i,\text{exp}} q\rho z_{r,i})/2$$

which is

$$\rho z_i^{f1} = \rho z_{r,i} (1 - \sqrt{1 - k_{i,\text{exp}}}) \quad (9)$$

$\rho z_{r,i}$ is the x-ray-generation range for the element i radiation according to Eq. (7). This solution is independent of the ordinate intercept q .

The initial thickness estimate for the surface film, δ_0^{f1} , is the sum of the contributions from each element

$$\delta_0^{f1} = \sum_i \rho z_i^{f1} \quad i = 1, u \quad (10)$$

The initial thickness estimate for the buried film, δ_0^{f2} , can be calculated in a similar manner:

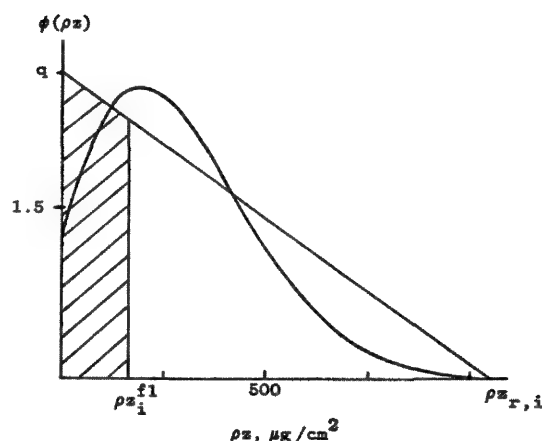


FIG. 1.--Triangular approximation for $\phi(\rho z)$ used to calculate starting film thicknesses in iteration procedure. Fractional area shaded is assumed equal to the k-ratio for the i th element.

$$\rho z_i^{f2} = \rho z_{r,i} \left[1 - k_{i,\text{exp}} - \frac{2\delta_0^{f1}}{\rho z_{r,i}} + \frac{(\delta_0^{f1})^2}{(\rho z_{r,i})^2} \right]^{1/2} \quad (11)$$

with δ_0^{f2} calculated in the same manner as δ_0^{f1} in Eq. (10).

Initial Values for Film and Substrate Compositions

For the elements in the surface film, the normalized k-ratios are used as the starting compositions $C_{i,0}$. For the buried layer, the k-ratios are first adjusted by the x-ray absorption term of the surface film, $\exp[-\delta_0^{f1}(\chi' - \chi)]$, and then normalized. Finally, for the substrate, the k-ratios are adjusted by the x-ray absorption terms for the surface layer and buried layer and then normalized. Thus

Surface film

$$C_{i,0} = \frac{k_{i,\text{exp}}}{\sum k_{i,\text{exp}}}$$

Buried layer

$$C_{i,0} = \frac{k_{i,\text{exp}} \exp[-\delta_0^{f1}(\chi' - \chi)]}{\sum k_{i,\text{exp}} \exp[-\delta_0^{f1}(\chi' - \chi)]} \quad (12)$$

Substrate

$$C_{i,0} = \frac{k_{i,\text{exp}} \exp[-\delta_0^{f1}(\chi' - \chi) - (\delta_0^{f2} - \delta_0^{f1})(\chi'' - \chi)]}{\sum k_{i,\text{exp}} \exp[-\delta_0^{f1}(\chi' - \chi) - (\delta_0^{f2} - \delta_0^{f1})(\chi'' - \chi)]}$$

Film Thicknesses and Compositions for Subsequent Iterations

The initial values for the film and substrate compositions and film thicknesses are used in Eq. (4) to calculate initial theoretical k -ratios, $k_{i,1}$, for each element. The experimental k -ratios, $k_{i,exp}$, together with $k_{i,1}$, are now used to calculate new concentrations and thicknesses $C_{i,1}$, $\delta_{i,1}^{f1}$, and $\delta_{i,1}^{f2}$, for the first iteration. The process is repeated with $C_{i,1}$, $\delta_{i,1}^{f1}$, and $\delta_{i,1}^{f2}$ being used to calculate new theoretical k -ratios $k_{i,2}$ for the second iteration. This process continues until no further change in concentrations are observed within a preset error ϵ for each element.

Of importance here is the method for calculating $C_{i,m+1}$, δ_{m+1}^{f1} , and δ_{m+1}^{f2} from $C_{i,m}$, δ_m^{f1} , and δ_m^{f2} using $k_{i,m}$ and $k_{i,exp}$. Several convergence methods were examined. The hyperbolic method of Criss and Birks used in most ZAF correction procedures for homogeneous specimens was tried first. It was not obvious that this method should work for thin films, but in fact it did produce convergence for all systems studied. The rate of convergence was slow, however, especially in the case of bilayer systems. A faster method is the relatively simple convergence method of Eq. (13), which produced solutions in 30-50% fewer iterations than the hyperbolic method:

$$C_{i,m+1} = C_{i,m} \frac{k_{i,exp}}{k_{i,m}} \quad (13)$$

For the buried layer and substrate, faster convergence is sometimes achieved when, after the $C_{i,m+1}$ are normalized, they are adjusted by:

Buried layer

$$C_{i,m+1} = C_{i,m+1} \frac{\exp[-\delta_m^{f1}(\chi' - \chi)]}{\exp[-\delta_{m+1}^{f1}(\chi' - \chi)]} \quad (14)$$

Substrate

$$C_{i,m+1} = C_{i,m+1} \frac{\exp[-\delta_m^{f1}(\chi' - \chi)] \exp[-(\delta_m^{f2} - \delta_m^{f1})(\chi'' - \chi)]}{\exp[-\delta_{m+1}^{f1}(\chi' - \chi)] \exp[-(\delta_{m+1}^{f2} - \delta_{m+1}^{f1})(\chi'' - \chi)]}$$

This adjustment increases the rate of convergence by increasing/decreasing the $C_{i,m+1}$ in line with the increase/decrease in δ_{m+1}^{f1} and δ_{m+1}^{f2} .

The best method found for successive thickness estimates was a ratio of k -ratio sums:

Surface film

$$\delta_{m+1}^{f1} = \delta_m^{f1} \cdot \frac{\sum_i k_{i,exp}}{\sum_i k_{i,m}} \quad i = 1, u \quad (15)$$

Buried layer

$$\delta_{m+1}^{f1} = \delta_m^{f1} \frac{\sum_i k_{i,exp}}{\sum_i k_{i,m}} \quad i = 1, v \quad (15)$$

Implementation of the Iteration Procedure

The $\phi(\rho z)$ thin film model and correction procedure has been used on a wide variety of specimens. The iteration procedure has never failed to converge, usually within 5-10 iterations. The convergence is only slightly sensitive to the starting values for film compositions and thicknesses. In fact, a much simpler method for calculating the initial film thicknesses δ_0^{f1} and δ_0^{f2} based on Eqs. (9)-(11) is:

Surface film

$$\delta_0^{f1} = R \sqrt{1 - \sum_i k_{i,exp}} \quad (16)$$

Buried layer

$$\delta_0^{f1} = R \left[1 - \sum_i k_{i,exp} - \frac{2\delta_0^{f1}}{R} + \frac{(\delta_0^{f1})^2}{R^2} \right]^{1/2}$$

where $R = 7.0E_0^{1.65}$ in $\mu\text{g}/\text{cm}^2$. Convergence with these equations took at most one or two more iterations than the method described above. The step to adjust the starting concentrations of elements in subsurface films and substrates for overlayer x-ray absorption reduces the number of iterations by 1-3, but is not necessary for convergence. It is likely that even more efficient convergence schemes than these may be found.

The number of unknowns in the system of equations solved in the iteration procedure is the combined number of elements in the film and substrates, $u + v + w = n$, and the two film thicknesses δ^{f1} , δ^{f2} , or $n + 2$. The number of equations totals n . There are more unknowns than equations, which means there may be no solution. The number of unknowns can be reduced in several ways. For example, the weight fraction sums for the two films can be constrained to 1.0, which reduces the number of unknowns to $n + 2 - 2 = n$. The weight fraction sum for the substrate is then allowed to float freely and becomes a test of the combined analytical procedure and $\phi(\rho z)$ model. The closer the value is to 1.0, the better the $\phi(\rho z)$ model. Due to the magnified effect of uncertainties in mass absorption coefficients and the thin-film model, the largest errors in composition will be in the substrate, whereas errors in the substrate composition will have relatively little influence on the film compositions or thicknesses. It is thus advantageous to fit the thin-film system to a model in which the film compositions are constrained to a sum of 1.0, letting errors in the model accumulate as much as possible in the substrate composition. In most specimens, the determination of film compositions and thicknesses is of more interest than the determination of substrate composition.

TABLE 1.--Concentrations and predicted k-ratios for 100 $\mu\text{g}/\text{cm}^2$ $\text{Y}_1\text{Ba}_2\text{Cu}_3\text{O}_{6.5}$ on 100 $\mu\text{g}/\text{cm}^2$ SrTiO_3 on SiO_2 substrate for 15kV beam voltage and 40° take-off angle; $\phi(\rho z)$ parameters of Bastin et al.⁴ were used.

Layer	Element, x-ray line	Concentration in layer, Wt%	k-ratio
1	Y L α	13.35	.0382
1	Ba L α	41.23	.1266
1	Cu K α	28.61	.1275
1	O K α	16.81	.0477
2	Sr L α	47.74	.1092
2	Ti K α	26.10	.0825
2	O K α	26.15	.0248
substrate	Si K α	46.74	.1194
substrate	O K α	53.26	.0120

TABLE 2.--Film and substrate compositions and film thicknesses at the end of each loop of the iteration procedure.

Iteration	Thickness, $\mu\text{g}/\text{cm}^2$		Weight Fraction									
	Layer 1	Layer 2	Layer 1				Layer 2			Substrate		
	Y	Ba	Cu	O	Sr	Ti	O	Si	O			
0(start)	81.9	90.2	.1123	.3725	.3749	.1403	.5113	.3202	.1686	.5342	.5658	
1	100.3	90.4	.1643	.5117	.3501	.1987	.4819	.2707	.2488	.3661	.4447	
2	99.1	98.7	.1315	.4074	.2841	.1651	.5254	.2873	.2793	.4809	.5002	
3	99.7	99.5	.1341	.4154	.2885	.1682	.4823	.2647	.2614	.4811	.5461	
4	99.9	99.8	.1337	.4132	.2868	.1682	.4792	.2621	.2620	.4686	.5334	
5	100.0	99.9	.1336	.4125	.2863	.1681	.4781	.2614	.2616	.4680	.5324	
6	100.0	100.0	.1335	.4124	.2862	.1681	.4776	.2612	.2616	.4675	.5327	
7	100.0	100.0	.1335	.4123	.2861	.1681	.4775	.2611	.2615	.4674	.5326	
8	100.0	100.0	.1335	.4123	.2861	.1681	.4775	.2610	.2615	.4674	.5326	

TABLE 3.--Composition and thickness of Ni-Mo multilayers.

Specimen	Mo and Ni Found, $\mu\text{g}/\text{cm}^2$				Composition, Atomic %				Thickness ^a , nm		
	$\phi(\rho z)$		ICP		$\phi(\rho z)$		ICP		$\phi(\rho z)$	XRD	ICP
	Ni	Mo	Ni	Mo	Ni	Mo	Ni	Mo			
A	138	156	155	151	59.4	40.6	62.7	37.3	308	305	322
B	149	160	169	156	60.9	39.1	63.9	36.1	325	322	343
C	140	152	153	162	60.6	39.4	63.6	36.4	307	313	345
D	138	158	158	153	59.4	40.6	62.8	37.2	310	309	328

^aLinear thickness, z, was calculated from mass thickness, ρz , with the formula:

$$z = \frac{\rho z}{\bar{\rho}} \quad \text{where} \quad \bar{\rho} = \frac{C_{\text{Ni}} \cdot A_{\text{Ni}} + C_{\text{Mo}} \cdot A_{\text{Mo}}}{\frac{C_{\text{Ni}} \cdot A_{\text{Ni}}}{\rho_{\text{Ni}}} + \frac{C_{\text{Mo}} \cdot A_{\text{Mo}}}{\rho_{\text{Mo}}}}$$

where C is the atomic fraction, A is the atomic weight and ρ is the density of each element in the film.

The combined $\phi(\rho z)$ model and iteration procedure can be demonstrated on the relatively complicated model system 100 $\mu\text{g}/\text{cm}^2$ $\text{Y}_1\text{Ba}_2\text{Cu}_3\text{O}_{6.5}$ on 100 $\mu\text{g}/\text{cm}^2$ SrTiO_3 on SiO_2 substrate. In the actual analysis of such a material, it would not be possible to find the oxygen k-ratios for each layer and substrate experimentally. However, we have analyzed such specimens in our laboratory by fixing the oxygen weight fraction at each step of the iteration according to its stoichiometry using element valences. To illustrate the operation of the iteration procedure, I have used the set of

predicted k-ratios for this system as the "experimental" k-ratios. These k-ratios can be calculated based on the procedure previously described. They are given in Table 1.

The combined $\phi(\rho z)$ model and iteration procedure should be able to determine the layer thicknesses and compositions from the set of theoretical or experimental k-ratios. Listed in Table 2 is a sample output of the program execution. The stopping criterion is $C_{m+1} - C_m \leq 0.0001$ for each element.

The composition and thickness for layer 1 is determined to within 1% in only two itera-

tions and for layer 2 in three iterations. The slow part of the iteration scheme is the determination of the substrate composition, which is extremely sensitive to the compositions and thicknesses of the two overlayers. The iteration process can be speeded up considerably if the composition of the buried layer or substrate is fixed at the start of the iteration. Fixing the composition and thickness of the buried layer to 100 $\mu\text{g}/\text{cm}^2$ SrTiO_3 reduces the number of iterations to four as does fixing the substrate composition to SiO_2 .

Application to Ni-Mo Thin Films

Table 3 shows the results of 20kV analyses of Ni-Mo multilayer arrays on SiO_2 . The bilayer thicknesses of the Ni-Mo multilayers were varied from 2.1 to 20.1 nm. The mean free paths of the analytical lines used, Mo $L\alpha$ and Ni $K\alpha$, and the electron range are all much larger than the bilayer thickness. The multilayers can thus be treated as if they were single homogeneous alloy films. The composition of each specimen was determined with an accuracy of $\pm 2\%$ by inductively coupled plasma/atomic emission spectroscopy (ICP). The thicknesses of the films were also determined by an x-ray diffraction (XRD) technique. In the XRD technique, the bilayer thicknesses were determined from the superlattice x-ray diffraction peaks and then multiplied by the number of bilayers (80-200). Accuracy of this method is estimated as $\pm 2\%$. Fluorescence corrections are not indicated for these specimens, but could easily be incorporated into the program.

The average difference in composition between the ICP and $\phi(\rho z)$ (electron-probe) methods is 11.0% for Ni and 3.8% for Mo. The average difference in thickness determinations is 1.0% comparing the electron probe with XRD and 6.5% comparing electron probe with ICP. The difference in thickness determinations between the electron probe and ICP techniques is explained by the lower Ni found with the electron probe; however, it is not clear why the ICP thickness values found were significantly thicker than those found with the XRD technique, since both are reportedly accurate to $\pm 2\%$.

An important aspect of thin-film analysis with an electron probe is the accurate modeling of the $\phi(\rho z)$ curves. Various forms of the $\phi(\rho z)$ parameters and weighting functions can now be rapidly tested on complex systems with this iteration procedure. Databases containing experimental k-ratio and composition data for a large number of thin film systems could be constructed and used to test $\phi(\rho z)$ and weighting function models.

References

1. R. H. Packwood and K. S. Milliken, *A General Equation for Predicting X-ray Intensities from Stratified Samples in the Electron Microprobe*, CANMET Research Report PMRL 85-25(TR), May 1985.
2. R. H. Packwood and J. D. Brown, "A

Gaussian expression to describe $\phi(\rho z)$ curves for quantitative electron probe microanalysis," *X-ray Spectrometry* 3: 138, 1981.

3. J. D. Brown and R. H. Packwood, "Quantitative electron probe microanalysis using Gaussian $\phi(\rho z)$ curves," *X-ray Spectrometry* 11: 187, 1982.

4. G. F. Bastin, F. J. J. van Loo, and H. J. M. Heijligers, "Evaluation of the use of Gaussian $\phi(\rho z)$ curves in quantitative electron probe microanalysis: A new optimization," *X-ray Spectrometry* 13: 91, 1984.

5. R. H. Packwood, from text of the Microbeam Analysis Society's 1986 Tour Speaker's Talk, given at Ford Motor Co., 6 May 1986.

6. K. F. J. Heinrich, *Electron Beam X-ray Microanalysis*, New York: Van Nostrand Reinhold, 1981, 419.

7. J. Criss and L. S. Birks, "Intensity formulae for computer solution of multicomponent electron probe specimens," in T. D. McKinley, K. F. J. Heinrich and D. B. Wittry, Eds., *The Electron Microprobe*, New York: Wiley, 1966, 217.

A SIMPLIFIED VERSION OF THE "PAP" MODEL FOR MATRIX CORRECTIONS IN EPMA

J. L. Pouchou and F. M. A. Pichoir

The limitations of the conventional ZAF method for quantitative EPMA have led to new models based on more realistic $\phi(\rho z)$ depth distributions of the primary ionizations. One of them is the PAP procedure,¹ the capability and reliability of which have been demonstrated for many analytical purposes (light and ultra-light element analysis,^{2,3} surface film analysis,⁴ determination of mass absorption coefficients⁵). In this model, the primary characteristic intensity emerging at take-off angle θ is directly deduced from the $\phi(\rho z)$ function according to the expression:¹

$$I(\theta) \propto C_i Q_j(E_0) \int_0^{R_x} \phi(\rho z) \exp(-\chi \rho z) d\rho z$$

where E = electron beam energy, C_i = weight concentration of the analyzed element, Q_j = ionization cross section of level j , $\chi = (\mu/\rho) \csc \theta$ = absorption factor for the emitted line, ρz = mass depth, and R_x = ultimate ionization depth.

With this expression, a combined atomic number-absorption correction is obtained, provided that the integral F of $\phi(\rho z)$ represents correctly the mean number N_j of j ionizations produced per incident electron:

$$F = N_j / [C_i Q_j(E_0)]$$

Once N_j has been calculated by use of convenient expressions¹ for the electron slowdown, the ionization cross section, and the losses due to backscattering, the $\phi(\rho z)$ function may be defined through the area parameter F and three shape parameters.¹ Apart from very low overvoltages (where an alternative shape has to be selected), $\phi(\rho z)$ is modeled by two parabolic branches which permit an analytical treatment and lead to highly reliable distributions.

Although the PAP model is quite satisfactory for the various aforementioned applications, a simpler model may be useful, for example when a small computer has to be run or when fast processing is an important requirement. For other applications, like the adaptation to oblique incidence conditions or fluorescence computations, a simpler $\phi(\rho z)$ description may also be needed.

With the parabolic PAP model, some complexity appears in practical computations for two reasons:

1. $\phi(\rho z)$ has to be integrated in two parts,

The authors are at the Office National d'Etudes et de Recherches Aérospatiales, 29 avenue de la Division Leclerc, F-92320 Châtillon, France.

between finite limits (0 to R_c and R_c to R_x , where R_c is the depth at which the two parabolas are connected). When the terms χR_c or $\chi(R_x - R_c)$ are small (i.e., for low overvoltage and low absorption), the expression of the emerging intensity has to be expanded in series, to avoid numerical rounding errors. (For the same reason, this also happens with the quadrilateral model of Love and Scott.⁶)

2. At very low overvoltage, the model has no longer any solution because $\phi(\rho z)$ has no longer any maximum. Thus, an alternative formulation has to be introduced.

The Simplified PAP Model

The criteria for a simple and efficient model are:

1. A single $\phi(\rho z)$ expression should be used in all cases. It should be integrable between 0 and infinity when applied to bulk specimens.
2. The shape of the resulting distribution should be able to vary in a realistic way from light to heavy targets, as well as from high to low overvoltages.
3. The mathematical formulation should be such that the parameters of $\phi(\rho z)$ can be calculated analytically when the integral of the distribution is imposed (combined atomic number-absorption correction).

The above conditions may be satisfied by the following expression:

$$\phi(\rho z) = A \exp(-\alpha \rho z) + [B \rho z + \phi(0) - A] \exp(-\beta \rho z) \quad (1)$$

The coefficients A , B , α , and β can be deduced from four basic parameters:

1. The integral

$$F = \int_0^\infty \phi(\rho z) d\rho z = \frac{A}{\alpha} + \frac{\phi(0) - A}{\beta} + \frac{B}{\beta^2} \quad (2)$$
2. The surface ionization $\phi(0)$ calculated as previously.¹
3. The mean ionization depth \bar{R} defined by

$$\bar{R} = \frac{1}{F} \int_0^\infty \rho z \phi(\rho z) d\rho z = \frac{A}{\alpha^2} + \frac{\phi(0) - A}{\beta^2} + \frac{2B}{\beta^3} \quad (3)$$
4. The initial slope

$$P = B - \alpha A - \beta[\phi(0) - A] \quad (4)$$

Equation (1) leads simply to the emerging intensity:

$$I(\theta) \propto C_i Q_j(E_0) \int_0^\infty \phi(\rho z) \exp(-\chi \rho z) d\rho z$$

$$I(\theta) \propto C_i Q_j(E_0) \left[\frac{A}{\alpha + \chi} + \frac{\phi(0) - A}{\beta + \chi} + \frac{B}{(\beta + \chi)^2} \right] \quad (5)$$

The bracketed term in Eq. (5) is the

Laplace transform of $\phi(\rho z)$, usually called $F(\chi)$.

The usual $f(\chi)$ absorption correction factor is then

$$f(\chi) = F(\chi)/F$$

From Eqs. (2) to (4), the coefficient α is

$$\alpha = \frac{P + \beta[2\phi(0) - \beta F]}{\beta F(2 - \beta \bar{R}) - \phi(0)} \quad (6)$$

α and β have to be positive in all cases. The slope P is positive in most cases, except in very low overvoltage conditions. When P is positive, the location of the $\phi(\rho z)$ maximum is of the order of \bar{R} . Thus, β is obviously of the order of $1/\bar{R}$. On the other hand, F is always of the order of $\phi(0)\bar{R}$. It follows that $\beta F \approx 10\phi(0)$ and that the right-hand term of the numerator in Eq. (6) is negative with an absolute value of some tens of times $\phi(0)/\bar{R}$. In practice, it can be verified that the initial slope P is always such that the numerator in Eq. (6) is negative. Consequently, the denominator should also be negative, and β should satisfy the inequality

$$\bar{R}\beta^2 - 2\beta + \phi(0)/F > 0$$

Considering the order of magnitude of β , the condition to be satisfied is:

$$\beta > \frac{1 + \sqrt{1 - [\bar{R}\phi(0)/F]}}{\bar{R}}$$

Practically, and whatever the sign of P , satisfactory $\phi(\rho z)$ distributions are obtained with:

$$\beta = 2\sqrt{2}[1 + \sqrt{1 - [\bar{R}\phi(0)/F]}/\bar{R}] \quad (7)$$

The parametrization of the mean ionization depth \bar{R} has been achieved by considering the ratio $K_1 = F/\bar{R}$. It can be easily predicted that, when the overvoltage U approaches unity, $\phi(\rho z)$ becomes close to a single exponential, which implies that F/\bar{R} tends to 1. On the other hand, when U increases to high values, the major change in $\phi(\rho z)$ shape is an expansion along the ρz axis. Thus, F/\bar{R} tends to a saturation value, which obviously increases with the atomic number of the target. An examination of the F/\bar{R} ratios given by the parabolic PAP model leads to the following expression (\bar{R} in g/cm²):

$$\frac{F}{\bar{R}} = 1 + \frac{X \ln[1 + Y[1 - (1/U^{0.42})]]}{\ln(1 + Y)} \quad (8)$$

where $X = 1 + 1.3 \ln Z_p$ (Z_p = mean atomic number), $Y = 0.2 + (Z_p/200)$, and $Z_p^{0.5} = \sum C_i Z_i^{0.5}$.

We can successfully parametrize the initial slope by relating it to the ratio F/\bar{R}^2 as follows:

$$P = K_2 F/\bar{R}^2 \quad (9)$$

where

$$K_2 = 0.22 \ln(4Z_p)\{1 - 2 \exp[Z_p(U - 1)/15]\} \quad (10)$$

The main problem with exponential models^{7,8}

is that they systematically overpeak the $\phi(\rho z)$ function near the surface. This pernicious feature is almost eliminated with the proposed formulation for light-to-heavy materials (Fig. 1), but it still remains noticeable for ultra-light targets (Fig. 2). The effects of this bias can be partly compensated by a reduction the initial slope. Thus, K_2 is multiplied by an extra factor γ^4 , with

$$\gamma = 1 - 10\{1 - 1/[1 + (U/10)]/Z_p^2\} \quad (11)$$

Scheme for Computation

- Calculation of the area F (see Ref. 1).
- Calculation of $\phi(0)$ (see Ref. 1).
- Calculation of \bar{R} from Eq. (8). If $K_1 < \phi(0)$, set $K_1 = \phi(0)$.
- Calculation of P from Eqs. (9), (10), and (11). If $K_2 > K_{2m} = 0.9\beta\bar{R}[\beta\bar{R} - 2\phi(0)/K_1]$, set $K_2 = K_{2m}$.
- Calculation of β from Eq. (7).
- Calculation of α from Eq. (6). Define $\epsilon = (\alpha - \beta)/\beta$. To avoid numerical errors, check whether $|\epsilon| < \epsilon_0$ ($\epsilon_0 \approx 10^{-6}$ depending on the computer used). If true, set $\epsilon = \pm \epsilon_0$ and $\alpha = \beta(1 + \epsilon)$.
- Calculation of $B = [\beta^2 F(1 + \epsilon) - P - \phi(0)\beta(1 + \epsilon)]/\epsilon$.
- Calculation of $A = [B/\beta + \phi(0) - \beta F](1 + \epsilon)/\epsilon$.
- Calculation of the emerging intensity according to Eq. (5). However, to avoid numerical errors, we strongly recommend computation of the $F(\chi)$ factor in Eq. (5) in the following way: $F(\chi) = \{\phi(0) + B/(\beta + \chi) - A\beta\epsilon/[\beta(1 + \epsilon) + \chi]\}/(\beta + \chi)$.

Application to Matrix Corrections

1. The reliability of the proposed model for light-to-heavy element analysis has been verified by use of a database containing 826 analyses. The main criteria for data selection were:

- conductive binary systems with no apparent ambiguity of the nominal composition;
- series of measurements performed at several accelerating voltages with pure standards;
- recent experiments with take-off angle not less than 40°, to limit the errors due to surface dirtiness;
- measurements giving k-ratios not less than 2%, to limit the relative errors coming from the counting statistics, the background subtraction and/or the nominal composition;
- consistency of data sets corresponding to similar systems analyzed under similar operating conditions.

The content of the resulting data file is summarized in Table 1. The error histogram in Fig. 3 illustrates the global results obtained with the proposed PAP-S model. As shown in Table 2, both PAP and PAP-S models are almost equally reliable and may be favorably compared with other existing approaches.

2. To check the performance for ultra-light element analysis, the most significant database is certainly the set of boron measurements by

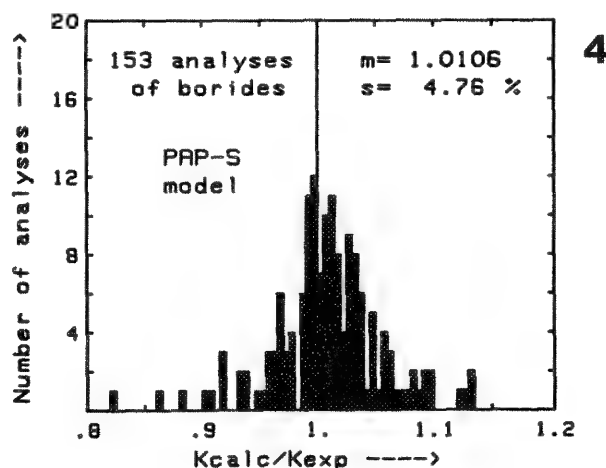
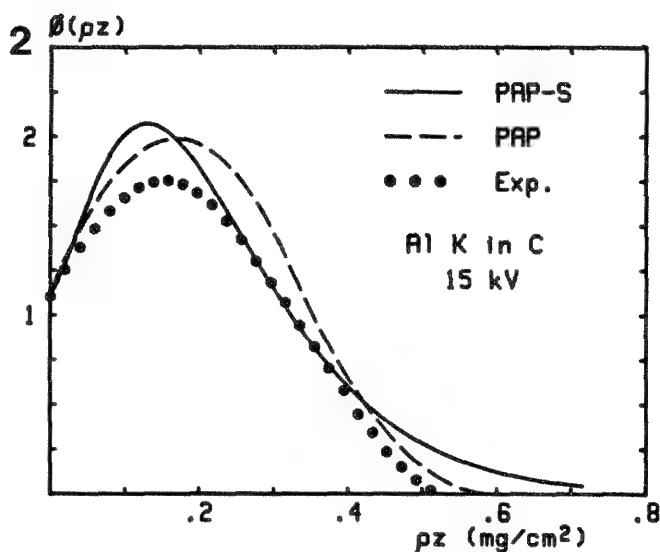
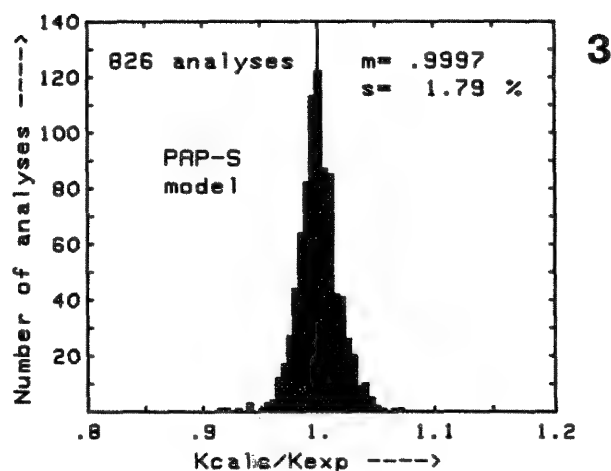
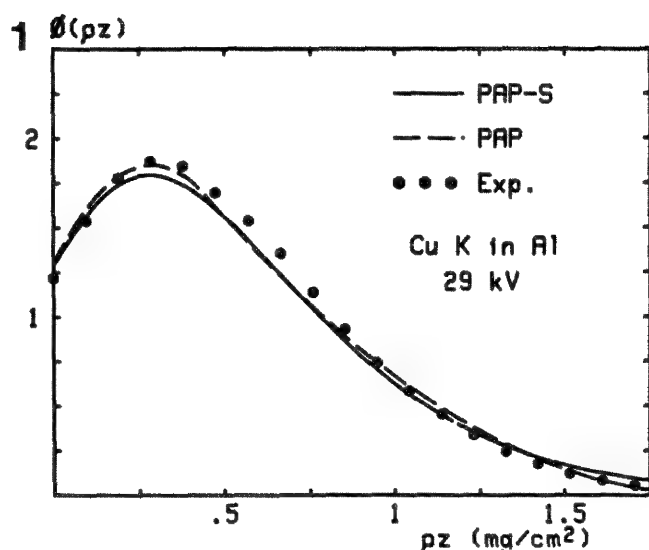


FIG. 1.--Comparison of $\phi(\rho z)$ curves given by PAP and PAP-S models with experimental data.²³ Cu K α tracer in Al matrix at 29 kV.

FIG. 2.--Comparison of $\phi(\rho z)$ curves given by PAP and PAP-S models with experimental data.²⁴ Al K α tracer in C matrix at 15 kV.

FIG. 3.--Performance of PAP-S model for 826 light-to-heavy element analyses in binary compounds of known composition.

FIG. 4.--Performance of PAP-S model for 153 boron analyses⁹ in binary borides of known composition.

Bastin et al.⁹ If nickel and cobalt borides are ignored because they exhibit an abnormal behavior, 153 analyses have to be considered. This database is a particularly severe test for exponential models, because an ultra-light standard (boron) is used. However, Fig. 4 shows that a satisfactory error histogram is obtained with the simplified PAP-S model.

A comparison with other approaches is given in Table 3.

If a compound with a medium atomic number is used as a standard, the proposed model is equivalent to the paraboloid PAP model; for example, in the case of a database consisting of 99 carbon measurements of carbides with a standard Fe₃C,¹² the PAP and PAP-S versions lead

respectively to 1.0016 and 1.0055 for the average $k_{\text{calc}}/k_{\text{exp}}$, and to 3.91% and 3.54% for the rms.

The proposed simplified version of the PAP model provides an efficient and easy procedure for matrix corrections in quantitative x-ray analysis. It should be very convenient for EDX systems, especially since the adaptation to oblique beam incidence is planned for the near future.

References

1. J. L. Pouchou and F. Pichoir, *Proc. 11th IXCXOM*, 1987, 249.
2. J. L. Pouchou and F. Pichoir, *J. Microsc. Spectrosc. Electron.* 11: 229, 1986.

TABLE 1.--Content of the database for light-to-heavy element analysis.

Number of data	Source	Selected compounds*
396	Bastin et al. ^{9,12,13}	<u>Metal</u> -(B), <u>Metal</u> -(C), Metal-(N)
148	Pouchou et al. ^{14,15}	<u>Au</u> -Cu, Ni-Al, Ti-Al, <u>Cu</u> -Al, <u>Au</u> -Pd
145	Heinrich et al. ¹⁶	<u>Au</u> -Cu, <u>Au</u> -Ag
43	Willich, cited in ¹⁷	<u>Au</u> -Cu
38	Christ et al. ¹⁸	Sb-(Bi)
36	Colby ¹⁹	U-(C), U-(N), U-(Si), U-(P), U-(S), U-(F)
14	Springer ²⁰	Fe-(S), Zn-(S), Pb-(S)
6	Shimizu et al. ²¹	Fe-Al
826	+ Elements between parentheses are not analyzed. Underlined elements are analyzed with low- and high energy lines.	

TABLE 3.--Performances of eight correction procedures for ultra-light element analysis; 153 boron measurements from Ref. 9; mass absorption coefficients proposed by Pouchou-Pichoir (P) and Bastin (B) listed in Ref. 2.

Procedure	M.a.c.	Calculated/Experimental	
		Average	r.m.s.
PAP ¹	P	1.0075	3.95 %
PAP-S (this work)	P	1.0106	4.76 %
Bastin 861 ⁹	B	1.0080	5.17 %
- idem -	P	1.0162	6.25 %
Ruste-Zeller ¹¹	P	1.0139	9.59 %
Love-Scott II ⁶	P	1.0148	12.24 %
ZAF + f(χ) Heinrich ⁸	P	1.0657	14.25 %
Tanuma-Nagashima ¹⁰	P	1.1018	17.51 %
ZAF (simpl. Philibert)	P	1.1433	19.72 %

TABLE 2.--Performances of eight correction procedures for light-to-heavy element analysis (mass absorption coefficients according to Ref. 22).

Procedure	826 analyses		577 analyses mainly submitted to Z effects		242 analyses mainly submitted to absorption effects	
	Average	r.m.s.	Average	r.m.s.	Average	r.m.s.
PAS-S (this work)	0.9997	1.79 %	0.9983	1.58 %	1.0023	2.17 %
PAP ¹	0.9982	1.91 %	0.9975	1.60 %	0.9993	2.50 %
Love-Scott II ⁶	0.9915	2.59 %	0.9941	1.79 %	0.9845	3.79 %
Tanuma-Nagashima ¹⁰	0.9917	2.73 %	0.9893	2.05 %	0.9967	3.85 %
Bastin 861 ⁹	1.0090	2.92 %	1.0138	2.84 %	0.9976	2.83 %
ZAF+f(χ) Heinrich ⁸	0.9850	2.74 %	0.9881	2.01 %	0.9765	3.84 %
ZAF (simpl. Philibert)	0.9999	4.05 %	0.9854	1.96 %	1.0339	5.50 %
Ruste-Zeller ¹¹	1.0089	4.21 %	0.9958	2.02 %	1.0401	6.07 %

* Bastin recently developed a new program in which the atomic number effects are calculated according to the PAP model. With this modification, the Bastin's program should give almost the same results as the PAP program.

3. P. Willich, *Proc. 11th ICXOM*, 1987, 238.
4. J. L. Pouchou and F. Pichoir, *J. Microsc. Spectrosc. Electron.*, 10: 279, 1985.
5. J. L. Pouchou and F. Pichoir, this volume.
6. D. A. Sewell, G. Love, and V. D. Scott, *J. Phys.* D18: 1245, 1985.
7. J. Philibert, *Métaux* 465: 157, 1964.
8. K. F. J. Heinrich, *Microbeam Analysis* --1985, 79.
9. G. F. Bastin and H. J. M. Heijligers, *THE Report*, ISBN 90-6819-006-7 CIP, 1986.
10. S. Tanuma and K. Nagashima, *Mikrochimica Acta* 265, 1984.
11. J. Ruste and C. Zeller, *C.R. Acad. Sci. Paris* B284: 507, 1977.
12. G. F. Bastin and H. J. M. Heijligers, *THE Report*, ISBN 90-6819-002-4 CIP, 1984.
13. G. F. Bastin, private communication, 1987.
14. J. L. Pouchou and F. Pichoir, *J.*

- Physique Colloq.* 45: C2-17, 1984.
15. J. L. Pouchou and F. Pichoir, *La Recherche Aéronautique* 3: 167, 1984.
16. K. F. J. Heinrich, R. C. Myklebust, and S. D. Rasberry, *NBS Spec. Publ.* 260-28, 1971.
17. G. F. Bastin, H. J. M. Heijligers, and F. J. J. van Loo, *Scanning* 8: 45, 1986.
18. B. Christ, G. Delgart, and R. Stegmann, *Phys. Stat. Solidi* 71(a): 463, 1982.
19. J. W. Colby, *Adv. in X-ray Analysis* 8: 352, 1965.
20. G. Springer, *X-ray Optics and Microanal.* 1966, 296.
21. R. Shimizu, N. Nishigori, and K. Murata, *Proc. 6th ICXOM*, 1972, 95.
22. K. F. J. Heinrich, *Proc. 11th ICXOM*, 1987, 67.
23. R. Castaing and J. Descamps, *J. Phys. Radium* 16: 304, 1955.
24. D. A. Sewell, G. Love, and V. D. Scott, *J. Phys.* D18: 1233, 1985.

DETERMINATION OF MASS ABSORPTION COEFFICIENTS FOR SOFT X RAYS BY USE OF THE ELECTRON MICROPROBE

J. L. Pouchou and F. M. A. Pichoir

During the last decade, one of the major changes in the practice of x-ray microanalysis is a more frequent use of soft radiations (from 0.1 to 2 keV). As a matter of fact, the current problems in materials science require analysis of ultra-light elements (emitters with $Z < 10$) or thin surface films characterization. In both cases, soft lines have to be used.

In recent years the analytical instruments have undergone significant improvements in the capability of soft x-ray detection, mainly with multilayered monochromators. At the same time, realistic models for data quantification have been developed. However, some limitations still remain in many cases, because of a poor knowledge of the mass absorption coefficients (mac's) to be used for low energy photons. In ultra-light element analysis, where the mac's are usually of the order of 10^4 cm²/g, 1% uncertainty in this value produces typically 1% uncertainty in the corrected concentration. Unfortunately, mac's reported by various authors may sometimes differ by a factor of 2! Hence, people who produce absorption tables for the soft x-ray region are obliged to fit some experimental data by introducing scale factors ranging from 0.6 to 1.4 to insure continuity.¹

The common method used for the determination of x-ray mac's is to measure the attenuation of a monochromatic beam through thin films of known composition and mass thickness. In the low energy range, the absorption is generally so high that such measurements cannot be performed with an acceptable accuracy. A more reliable technique is to measure the attenuation through a gas mixture with a controlled pressure.² Another method is to make reflectivity measurements,³ but the results depend strongly on the surface imperfections (roughness, oxidation). Techniques involving a proton probe to generate characteristic x rays in a partly coated and partly uncoated specimen have also been proposed.⁴

In the past, the electron microprobe has been used by several authors to derive some mass absorption coefficients, mainly for the carbon K line.^{5,6} Most of these values were greatly erroneous (up to 100%). Probably because of these unlucky experiments, some authors⁷ are now definitely considering that mac values inferred from microanalysis measurements are almost always unsatisfactory.

The present paper aims to demonstrate that the electron microprobe can produce reliable

mass absorption coefficients for soft x rays, provided that a proper method is applied.

Sources of Errors

Most mac values derived from microanalysis measurements were adjusted so that, after the experimental k-ratios had been corrected by a ZAF procedure, the nominal concentrations were obtained. This procedure is the source of several mistakes.

1. The inadequacy of the ZAF procedure for strongly absorbed radiations always produces errors, the magnitude and sign of which are difficult to predict, because they depend on the analyzed line, on the nature of the specimen, on the standard used, on the accelerating voltage, and on the take-off angle. This dependence implies that a value obtained in this way is not in fact an estimate of the true mass absorption coefficient, but only represents an adjustment parameter that compensates the inadequacy of the ZAF procedure for a given system analyzed in definite operating conditions.

2. The uncertainty in the nominal concentration of the emitter may produce an important error in the mac value resulting from k-ratio measurements. In the case of ultra-light emitters, for which the mass concentration is low in most specimens used (carbides, borides), relative errors of the order of 10% result frequently from a poor knowledge of the composition.

3. For the lightest emitters (boron, carbon, nitrogen), there may be strong effects of the chemical bonding on the spectral distribution of the characteristic bands. These effects have been most often ignored, although they can induce relative errors of several tens of percent.

4. In particular compounds, the chemical effects are such that the specific emission of particular lines can be strongly enhanced (case of Ni L α in NiAl⁸) or reduced (case of B K α in nickel borides⁹). In such cases, mac values obtained by a simple adjustment of the experimental k-ratios would be absolutely meaningless.

However, if care is taken to avoid the abovementioned sources of experimental errors and if a reliable model for matrix corrections is used, it is possible to deduce consistent mac's from conventional microanalysis measurements.

Emerging Intensity Measurements

Most of the above difficulties vanish if measurements of the emerging intensity vs

The authors are at the Office National d'Etudes et de Recherches Aérospatiales, 29 avenue de la Division Leclerc, F-92320 Châtillon, France.

accelerating voltage are considered instead of k-ratio measurements. The intensity of a given characteristic line emerging at take-off angle θ from a target with a mass absorption μ/ρ can be written as

$$I = \delta C_i Q_j(E_0) \int_0^\infty \phi(\rho z) \exp[(-\mu/\rho)\rho z \operatorname{cosec} \theta] d\rho z$$

where C_i is the mass concentration of the emitter, j indicates the ionized level for the line of interest, E_0 is the electron beam energy, $Q_j(E_0)$ is the ionization cross section of level j , ρz is the mass depth, δ is a proportionality factor including the beam current, the fluorescence yield, the weight of the line in the series, and the detection efficiency, and $\phi(\rho z)$ is the depth distribution of the j ionizations of i atoms at energy E_0 .

An effort has been made some years ago to produce a model (PAP)¹⁰ that would properly describe the $\phi(\rho z)$ function and consequently the variation of the emerging intensity with the accelerating voltage. For the application of mac determination, we have written a program called PAPMAC which includes the PAP model in an iterative scheme. The mac value producing the best adjustment of the experimental data (normalized intensity vs accelerating voltage) is obtained after two or three loops. This mac corresponds to the value of the absorption factor $\chi = (\mu/\rho)\operatorname{cosec} \theta$ that minimizes the sum S of the quadratic deviations

$$S = \sum_V [\alpha I_V - J_V(\chi)]^2$$

The emerging intensities measured at several accelerating voltages V are designated as I_V ; the intensities calculated at the same voltages for a given value of χ , as $J_V(\chi)$; and α is an unknown scale factor.

The value of α that minimizes S is given by $\partial S/\partial \alpha = 0$. It follows that

$$\alpha = \sum_V I_V J_V(\chi) / \sum_V I_V^2$$

$$\text{Hence } S = \sum_V J_V^2(\chi) - [\sum_V I_V J_V(\chi)]^2 / \sum_V I_V^2$$

The χ value that makes S minimum is obtained by numerical solution of the equation $S' = \partial S/\partial \chi = 0$.

During the iteration (Newton method), the successive values of χ are related by

$$\chi_{n+1} = \chi_n - S'/S''$$

The first- and second-order derivatives S' and S'' are calculated from

$$S_0 = S(\chi), \quad S_1 = S(\chi - \delta\chi), \quad S_2 = S(\chi + \delta\chi)$$

It follows that

$$\chi_{n+1} = \chi_n - \delta\chi(S_2 - S_1)/[2(S_1 + S_2 - 2S_0)]$$

The convergence is achieved when S_0 is less than S_1 and S_2 .

The interest of the method is that

- Self-absorption coefficients can be measured.

- The chemical bonding has no effect on the $I = f(E_0)$ variation, so that simple measure-

ments of the intensity at peak maximum are sufficient.

- No standard is needed.

- The lack of a precise knowledge of the nominal concentration of the specimen used is not a severe limitation. For example, if the absorption of the C K line in Fe is measured by use of a Fe_3C specimen, 10% relative error in the C content would only produce 0.5% error in the resulting C K/Fe mac. For titanium carbide, which has a higher C content, not more than 1.5% error would result from 10% uncertainty in the carbon concentration. For heavier emitters (e.g., the Cu $L\alpha$ line in a Ni-Cu specimen), the error in the mac is similar to the error in the concentration. However, in such a system it is no problem to obtain the composition with an accuracy of about 1% by conventional k-ratio measurements with the high energy K lines.

- The method is efficient for the determination of mass absorption coefficients ranging from some 10^2 to some 10^4 cm^2/g . Its accuracy can be estimated to 5%. Table 1 shows that a good agreement with the most recent tabulated values is obtained in various systems where the energy of the emission line is not too close to an absorption edge.

To obtain reliable mac's from emerging intensity measurements, the following precautions should be taken.

- The incident beam current has to be carefully measured in a Faraday cup at each accelerating voltage. The use of a beam regulator does not insure a constant intensity on the specimen when the accelerating voltage is changed. For example, in the case of Fe_3C , a typical shift of 3% in the beam intensity from low to high voltage would produce a 1.9% error in the C K/Fe mac.

- The accelerating voltage should be controlled within 1%. In the above example, 1% relative error along the whole voltage range would produce 1.8% error in the resulting mac.

- The specimen should be carefully polished and mounted into the specimen holder in such a way that its surface will be strictly perpendicular to the electron column axis. As an example, a deviation of 1° from the theoretical 40° take-off angle would produce an error of 2.1% in the C K/Fe mac. A good check of the geometrical configuration is to perform simultaneous measurements with two spectrometers having symmetrical positions with respect to the column axis.

- To minimize the scattering of the experimental data, it is better to measure the peak intensities at all the necessary voltages without moving the spectrometer, and to evaluate the backgrounds in a second round, by measuring the peak-to-background ratios at each voltage.

- It is not necessary to make measurements at accelerating voltages below 5 kV, except for χ factors exceeding typically 2×10^4 cm^2/g . However, in such strong absorption conditions, some residual inadequacies of the model,

TABLE 1.--Some mass absorption coefficients derived from intensity measurements vs accelerating voltage. Comparison with other sources.

Line	Energy (keV)	Absorber	Region	μ/ρ PAPMAC	μ/ρ other sources
B K	0.183	B	K-L _I	3471	3350 ¹
C K	0.277	C (diam.)	K-L _I	2170	2350 ¹ , 2147 ¹¹ , 2175 ¹² , 2052 ¹³ , 2280 ²
C K	0.277	Ti	L _{III} -M _I	8097	8090 ¹ , 8290 ¹¹
C K	0.277	Fe	L _{III} -M _I	13150	13900 ¹ , 14103 ¹¹
Cu L α	0.930	Al	K-L _I	1464	1450 ¹ , 1421 ¹¹ , 1494 ¹⁴
Cu L α	0.930	Ni	L _I -L _{II}	11879	11700 ¹ , 11776 ¹¹ , 12106 ¹⁴
Zn L α	1.012	Zn	L _{III} -M _I	1500	1520 ¹ , 1485 ¹¹ , 1581 ²
Ge L α	1.188	Ge	L _{III} -M _I	1240	1260 ¹ , 1262 ¹¹ , 1278 ¹⁴
Al K α	1.487	Al	K-L _I	393	403 ¹ , 397 ¹¹ , 404 ¹⁴
Al K α	1.487	Cu	K-L _I	4588	4550 ¹ , 4764 ¹¹ , 5410 ¹⁴
Si K α	1.740	Si	K-L _I	356	350 ¹ , 347 ¹¹ , 332 ¹⁴
W M α	1.775	W	M _V -N _I	1258	1215 ¹¹ , 1458 ¹⁴
Au M α	2.123	Au	M _V -N _I	1103	1061 ¹¹ , 1101 ¹⁴
Nb L α	2.166	Nb	L _{III} -M _I	779	726 ¹ , 718 ¹¹ , 726 ¹⁴

together with the poor reliability of the measurements and their high sensitivity to the surface imperfections, may produce uncertainties exceeding 10% in the resulting mac.

Typical $I = f(E_0)$ curves are presented in Figs. 1 to 4. Other examples can be found in earlier papers.^{8,15-18}

Coated Specimens

The PAPGLS program, which was conceived for thin-film analysis, can also be used for mac determination. In this case, the experimental data to be processed are the ratios corresponding to the intensity emitted by a coated substrate relative to an uncoated standard (the most appropriate standard being an uncoated region of the specimen itself). This technique had already been used¹⁷ to get a reasonable value of the Si K α /Ta mac. (The Si K α line is very close to the Ta M ν edge.)

In the same manner (Fig. 5), the PAPGLS program has been applied to a Mo substrate coated with Au, to determine the Mo L α /Au mac. (The Mo L α line is close to the Au M_{IV} edge.) The resulting mac (2200) lies between the values tabulated by Heinrich¹¹ (1410, M_{IV}-M_V region) and by Henke et al.¹ (3680, M_{III}-M_{IV} region).

Other interesting information near the Au M sublevels can be obtained by use of a HgS crystal (cinnabar) partly coated with gold. Ac-

cording to Ref. 19, the Hg M α line is located in the M_V-N_I absorption branch of Au; Hg M α belongs to the M_{IV}-M_V region; S K α should be in the M_{III}-M_{IV} branch, but very close to the M_{IV} edge; S K β lies on the M_{III}-M_{IV} branch. Figure 6 shows that the curves calculated from mac's tabulated in Ref. 11 agree with the experimental data for Hg M α and S K β lines, but disagree for Hg M β and S K α lines. We see from the figure that the experimental relative intensities for Hg M α and S K α are almost identical in the whole voltage range, which means that the absorption coefficients are almost equal for both lines. Figure 7 shows the best adjustment obtained with μ/ρ (Hg M β /Au) = 2170 and μ/ρ (S K α /Au) = 2200.

Figure 8 summarizes some absorption coefficients derived from microprobe measurements for radiations between 2 and 3 keV in gold. The main comment is that the M_V absorption jump in Heinrich's model¹¹ appears excessively low. Other measurements indicate the same type of inadequacy for Hf, Ta, W, and Pt absorbers.

Assessment of the Tabulated mac's

1. *Vicinity of absorption edges.* Table 2 compares some mass absorption coefficients obtained by use of the electron microprobe with tabulated values, in cases of uncertainty arising from the proximity of an edge vicinity.

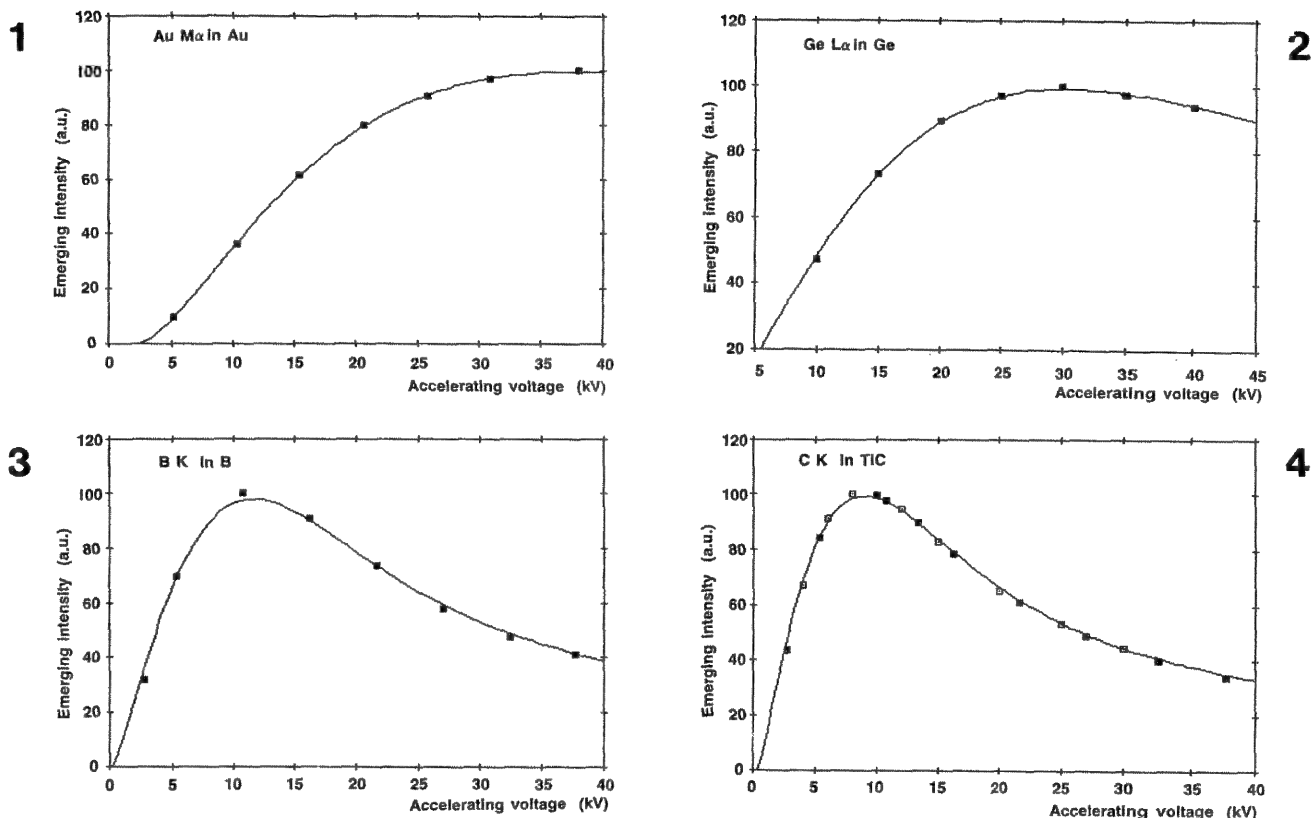


FIG. 1.--Variation of Au M α intensity vs accelerating voltage in pure Au. Best adjustment of experimental data (■) by calculated curve for $\mu/\rho = 1101$.
 FIG. 2.--Variation of Ge L α intensity vs accelerating voltage in pure Ge. Best adjustment of experimental data (■) by calculated curve for $\mu/\rho = 1240$.
 FIG. 3.--Variation of B K intensity vs accelerating voltage in pure B. Best adjustment of experimental data (■) by calculated curve for $\mu/\rho = 3471$.
 FIG. 4.--Variation of C K intensity vs accelerating voltage in TiC (18.2 wt% C assumed). Best adjustment for $\mu/\rho = 7018$. Experimental data: present work (■) and Bastin et al.⁹(□).

TABLE 2.--Example of mac's in the vicinity of absorption edges. Comparison of values inferred from microprobe with tabulated data.

Line	Energy (keV)	Absorber	Proximity	μ/ρ (cm ² /g)				
				This work	Heinrich ¹⁴	Henke ¹	Henke ²⁰	Frazer ¹⁴
Zr M ζ	0.151	Zr	M ν	4480	3508	8520	4162	-
Nb M ζ	0.172	Nb	M ν	5240	3877	7140	4659	-
B K	0.183	Zr	M ν	4400	-	8270	38410	-
B K	0.183	Nb	M ν	4500	3822	6560	4417	-
B K	0.183	Mo	M ν	4600	4208	5610	4717	-
B K	0.183	La	N ν	2500	11654	3730	3826	-
B K	0.183	U	O ν	7400	-	9020	2247	-
Mo M ζ	0.193	Mo	M ν	5460	4155	5480	4594	-
C K	0.277	Zr	M ν M ν	25000	31304	21600	31130	-
C K	0.277	Nb	M ν M ν	24000	29760	19400	33990	-
N K	0.392	Mo	M ν	25800	26458	20200	23220	-
Cu L β	0.950	Cu	L ν	6750	9595	-	-	-
Si K α	1.740	Ta	M ν	1500	1698	3760	-	-
W M β	1.835	W	M ν	2080	1617	-	-	1487
Au M β	2.205	Pt	M ν	2550	3619	-	-	-
Hg M β	2.283	Au	M ν	2170	1427	-	-	-
Mo L α	2.293	Au	M ν	2200	3437	3680	-	-
S K α	2.308	Au	M ν	2200	3380	-	-	3203
S K α	2.308	Hg	M ν	\approx 850	1499	-	-	932

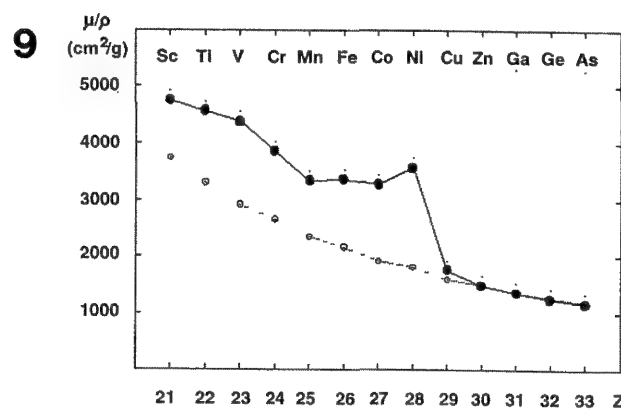
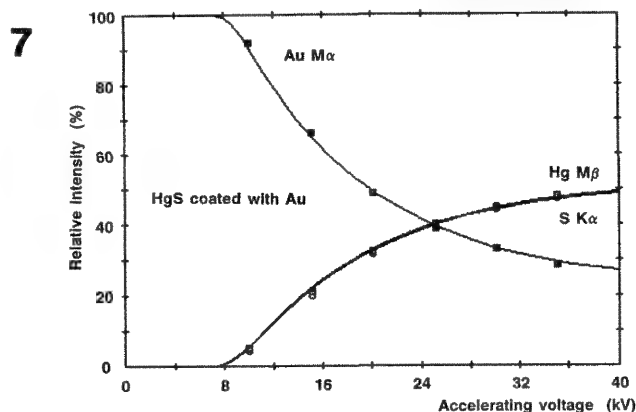
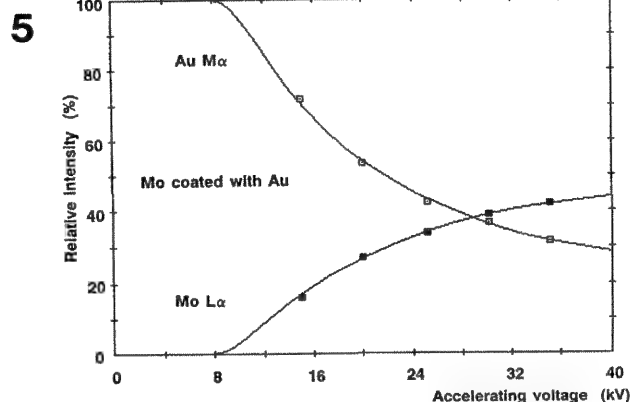


FIG. 5.--Au $M\alpha$ and Mo $L\alpha$ k-ratios (relative to pure standards) vs accelerating voltage for Mo substrate coated with $237 \mu\text{g}/\text{cm}^2$ Au (123 nm). Best adjustment of Mo $L\alpha$ data (\blacksquare) for μ/ρ (Mo $L\alpha$ /Au) = 2200.

FIG. 6.--Au $M\alpha$, S $K\alpha$, S $K\beta$, Hg $M\alpha$ and Hg $M\beta$ relative intensities vs accelerating voltage for HgS substrate coated with $207 \mu\text{g}/\text{cm}^2$ Au (107 nm). Pure standard for Au; uncoated HgS standard for S and Hg. Curves calculated with mac's from Heinrich.¹¹

FIG. 7.--Same specimen as Fig. 6. Curves calculated with adjusted mac's for S $K\alpha$ (μ/ρ = 2200) and Hg $M\beta$ (μ/ρ = 2170) in Au.

FIG. 8.--Mass absorption coefficients near M_{III} , M_{IV} and M_V edges of Au. Graph of Heinrich's tables¹¹ (—); graph of Frazer's tables¹⁴ (---); values from Henke's tables¹ (o); experimental data inferred from intensity measurements (\blacksquare); experimental data obtained with coated specimens (\bullet).

FIG. 9.-- $L\alpha$ self-absorption coefficients for elements of 4th period. Experimental values derived from intensity measurements (solid line). Comparison with Heinrich's tables¹¹ (dotted line).

The scattering of the tabulated data justifies the need for more reliable values, specially for ultra-light element analysis where the characteristic lines are frequently close to absorption edges.

2. *Transition Elements of the 4th Period.* The $L\alpha$ self-absorption coefficients of the 3d transition metals are also of interest, because they exhibit strong deviations²¹ from the tabulated values. Figure 9 shows that mac's derived from our intensity measurements are in very good agreement with Heinrich's tables¹¹ for the elements with a full 3d + 4s band (Zn to As). On the contrary, very strong deviations occur for the lighter metals (Ni to Sc)

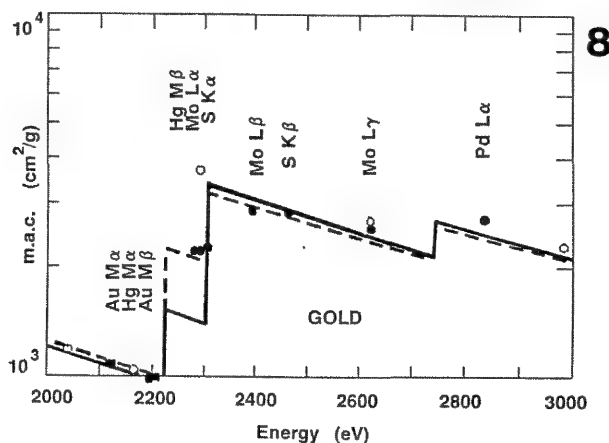
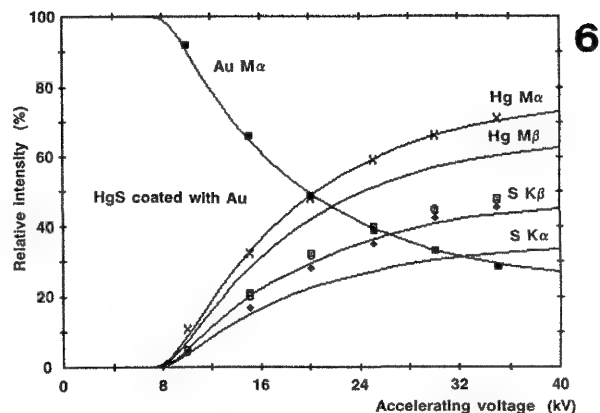


FIG. 5.--Au $M\alpha$ and Mo $L\alpha$ k-ratios (relative to pure standards) vs accelerating voltage for Mo substrate coated with $237 \mu\text{g}/\text{cm}^2$ Au (123 nm). Best adjustment of Mo $L\alpha$ data (\blacksquare) for μ/ρ (Mo $L\alpha$ /Au) = 2200.

FIG. 6.--Au $M\alpha$, S $K\alpha$, S $K\beta$, Hg $M\alpha$ and Hg $M\beta$ relative intensities vs accelerating voltage for HgS substrate coated with $207 \mu\text{g}/\text{cm}^2$ Au (107 nm). Pure standard for Au; uncoated HgS standard for S and Hg. Curves calculated with mac's from Heinrich.¹¹

FIG. 7.--Same specimen as Fig. 6. Curves calculated with adjusted mac's for S $K\alpha$ (μ/ρ = 2200) and Hg $M\beta$ (μ/ρ = 2170) in Au.

FIG. 8.--Mass absorption coefficients near M_{III} , M_{IV} and M_V edges of Au. Graph of Heinrich's tables¹¹ (—); graph of Frazer's tables¹⁴ (---); values from Henke's tables¹ (o); experimental data inferred from intensity measurements (\blacksquare); experimental data obtained with coated specimens (\bullet).

FIG. 9.-- $L\alpha$ self-absorption coefficients for elements of 4th period. Experimental values derived from intensity measurements (solid line). Comparison with Heinrich's tables¹¹ (dotted line).

the 3d band of which is partly empty. A knowledge of these anomalous mac's is useful in problems relative to thin surface films, where there may be some advantage to use soft L lines rather than K lines. However, the extra absorption due to a 2p - 3d resonance may vanish when the density of unoccupied states in the 3d band is modified by alloying.⁸ At the same time, the specific $L\alpha$ emission is enhanced. Because of this particular behavior, the use of the $L\alpha$ lines of 3d transition metals has to be avoided for routine work.

Conclusion

It has been shown that several approaches enable the electron microprobe to produce

reliable mass absorption coefficients in the soft x-ray region. Further experiments would be necessary to evaluate the possible effect of the chemical states of the emitting and absorbing atoms on absorption coefficients in the vicinity of edges.

References

1. B. L. Henke, P. Lee, T. J. Tanaka, R. L. Shimabukuro, and B. K. Fujikawa, *Atomic Data and Nuclear Data Tables* 27: 1, 1982.
2. B. L. Henke, R. L. Elgin, R. E. Lent, and R. B. Ledingham, *Norelco Reporter* 14: 112, 1976.
3. A. P. Lukirskii, E. P. Savinov, O. A. Ershov, and Y. F. Shepelev, *Optics and Spectrosc. USA* 16: 168, 1964.
4. A. Lurio and W. Reuter, *J. Phys.* D10: 2127, 1977.
5. E. Kohlhas and F. Scheiding, *Proc. 5th ICXOM* 1969, 193.
6. G. V. T. Ranzetta and V. D. Scott, *Brit. J. Appl. Phys.* 15: 263, 1964.
7. G. Love, in V. D. Scott and G. Love, Eds., *Quantitative Electron-probe Microanalysis*, 1983, 163.
8. J. L. Pouchou and F. Pichoir, *J. Microsc. Spectrosc. Electron* 10: 291, 1985.
9. G. F. Bastin and H. J. M. Heijligers, *THE Report* ISBN 90-6819-006-7 CIP, 1986.
10. J. L. Pouchou and F. Pichoir, *Proc. 11th ICXOM*, 1987, 249.
11. K. F. J. Heinrich, *ibid.*, p. 67.
12. W. Weisweiler, *Mikrochimica Acta* 2: 145, 1972.
13. D. R. Denne, *J. Phys.* D3: 1392, 1970.
14. J. Z. Frazer, *ISM Report* 67-29, 1967.
15. J. L. Pouchou and F. Pichoir, *J. Physique Colloq.* 45: C2-17, 1984.
16. J. L. Pouchou and F. Pichoir, *La Recherche Aéronautique* 3: 167, 1984.
17. J. L. Pouchou and F. Pichoir, *J. Microsc. Spectrosc. Electron.* 10: 279, 1985.
18. J. L. Pouchou and F. Pichoir, *ibid.*, p. 229.
19. J. A. Bearden, *NYO 10586 Rep.*, University of Baltimore, 1964.
20. B. L. Henke and E. S. Ebsu, *Adv. in X-ray Analysis* 17: 150, 1974.
21. D. F. Kyser, *Proc. 6th ICXOM*, 1972, 147.

CONTAMINATION PHENOMENA IN THE ELECTRON PROBE MICROANALYZER

G. F. Bastin and H. J. M. Heijligers

Contamination problems in the electron probe microanalyzer are usually discussed in terms of carbon contamination for the simple reason that this particular problem can be quite a nuisance in a very common case, the analysis of carbon in usually low concentrations in steels. It is true that in such cases the carbon build up under electron bombardment can cause an apparent carbon concentration which can be higher by at least one order of magnitude than the true content if no special precautions are taken. In the past several techniques have been proposed to deal with this problem. The most important ones are (1) the use of a liquid-nitrogen cooled cold trap surrounding the point of impact of the electron beam, and (2) an air jet by which a fine stream of air is directed toward the point of impact. Sometimes a combination of both methods is used.

Usually, one of these devices is part of the standard equipment of commercially available microanalyzers, although for some unknown reason the air jet seems to have lost some popularity with some manufacturers in the last decade. As we shall see the air jet is actually a most powerful device in the fight against carbon contamination. However, as our research in recent years (e.g., on nitrides) has shown, there are cases in which its use cannot be recommended because of the rapid oxidation of the specimen that can take place under bombardment in the poor vacuum conditions which then exist.

This effect has only become apparent after the purchase of a W/Si multilayer crystal (2d = 59.8 Å, supplied by Ovonix Corp, USA). The introduction of this crystal, next to our conventional stearate crystal, not only enabled us to detect oxygen much easier, due to its much higher count rates,¹ but also gave us the possibility to monitor two light-element radiations (N K α and O K α) simultaneously. With this new multilayer (LDE) crystal it has become clear that oxygen contamination in the microprobe is almost as bad a problem as carbon contamination (even without an air jet) and, what is worse, that the former effect is much more difficult to fight than the latter due to the relatively poor vacuum conditions in commercial microprobes. As a result it is almost impossible to measure low levels of oxygen in sensitive materials like Ti, Zr, and Hf.

The authors are at the Laboratory for Physical Chemistry Centre for Technical Ceramics, University of Technology, P.O. Box 513, NL-5600 MB Eindhoven, The Netherlands.

Experimental

All measurements were carried out with a fully automated JEOL 733 Superprobe with four wavelength-dispersive spectrometers. The automation system and additional EDX system were supplied by Tracor Northern. One of the WD spectrometers contained the conventional Pb-Stearate (STE) crystal, which was used to monitor the nitrogen or carbon count rate as a function of time; another was equipped with two multilayer crystals (LDE for nitrogen, oxygen, and fluorine), and OVH (Mo/B₄C, for beryllium and boron).

The air jet was constructed in our own laboratory and consisted essentially of a bent piece of stainless-steel capillary tubing attached to the cold trap that is part of the microprobe. The curved end of the tube ended approximately 2 mm above the specimen surface in the middle of the ring of the cold trap. The air jet could be positioned by simple turning of the cold finger in its place. The air-admittance valve (open-closed only) was fitted with a sintered piece of SiC with some residual open porosity, which in effect causes a controlled air leak. When the valve was opened, the vacuum in the instrument, measured near the gun filament, deteriorated from $\pm 10^{-5}$ to 2×10^{-4} mm Hg. Most probably the vacuum conditions in the specimen chamber are even worse than this figure. The admitted air was dried over silicagel.

Initially, our instrument was equipped with an oil-diffusion pump. A few years ago this was replaced by a turbo-molecular pump in order to remove one of the principal sources for carbon contamination.

Carbon Contamination

In a first test (Fig. 1) the performance of the cold finger and the air jet were tested on a freshly polished copper specimen. The top curve shows the carbon contamination rate when no precautions are taken. The use of the cold finger alone leads to a drastic improvement, although it is obvious that this procedure cannot match the action of the air jet, which reduces contamination to the lowest possible level. The air jet is even capable of decontaminating already heavily polluted spots. A series of tests with various gases showed that the presence of an appreciable amount of oxygen in the gas is essential; apparently it is needed to "burn off" carbonaceous deposits. It has even proved possible to burn a hole in a conductive carbon coating on a nonconducting oxide specimen, which made it possible to do oxygen analysis with the benefits of a conduc-

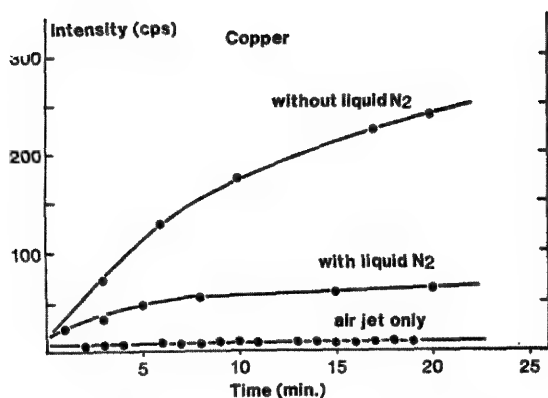


FIG. 1.--Effect of two anti-contamination devices on carbon contamination rate on copper: 10 kV, 100 nA; stearate crystal; oil-diffusion pump.

tive coating but without suffering from its disadvantages.

A further observation was that the contamination rate had a tendency to decrease with time: it was always highest immediately after the insertion of the specimen into the microprobe. This result strongly suggests that it is best to wait approximately 1 h (or better still overnight) before starting a carbon analysis. These effects must be attributed to outgasing of the specimen and its mount. In this context it must be stressed that the quality of the specimen and its mount must be of the highest possible level. We have seen notorious cases of poorly molded mounting resin with a high degree of porosity with disastrous results for the analysis of carbon; in some cases the hydrocarbons escaping from the pores caused the carbon peak from a ZrC specimen to shift more and more to the position typical for glassy carbon each time a peak search was performed, even though an air jet was used. Similarly, we repeatedly observed that the presence of pores or cavities (like those frequently present at the interface specimen/mounting resin) can be noticed at a distance of tens of microns away from the electron beam from an increase in the carbon signal.

Another important observation is that the contamination rate is *not* a fixed condition for a specific microprobe. It can vary from day to day and it depends especially strongly on the quality of all the specimens examined before a particular sample is examined for its carbon content. Our experiences in this respect show that after the analysis of a porous or powder specimen, it can take up to several hours before the contamination rate is down to its original low level again. The indication of the vacuum meter is a bad guide in such cases; apparently it is the quality of the vacuum that matters and it can take quite a long time to pump away all the hydrocarbons once they have been introduced with a bad specimen. Yet contamination can differ from one location to another, even on the same specimen, without any apparent reason. Such

differences can sometimes even be seen in the optical microscope: one spot can be bright and the next one can be brownish to black. Besides, we have found that contamination effects can differ strongly from one specimen to another. Elements such as B and Si usually show very low levels of contamination, but transition metals show much more pronounced phenomena. Some observations seem to indicate that these differences are related to differences in heat conductivity. Well-conducting materials like Cu contaminate easily; elements like B and Si, with a poor heat conductivity, hardly contaminate at all. Presumably surface temperatures on the latter elements are much higher under electron bombardment and lead to a more efficient burn-off. Likewise, there is every indication that it is beneficial to keep the best possible focus and to avoid long dwell times on areas to be analyzed, and most certainly to stay away from the edges of the specimen where it touches the mounting resin.

A somewhat disappointing conclusion is that despite all efforts it is never possible to suppress contamination completely. Using an oil-diffusion pump on our instrument, we usually find on decarburized Armco iron an apparent residual carbon level corresponding to 0.2-0.25 wt% carbon in solid solution under the best possible conditions and the use of an air jet. Clearly, this minimum or blank level must be accurately known when attempting to measure carbon contents of this order of magnitude. However, with this knowledge, it is indeed possible to do accurate carbon analysis in steels, even at very low levels (Fig. 2).

We found to our surprise that substitution of a turbo-molecular pump did not actually lower this blank level, although it might be thought that the removal of a principal source of hydrocarbons would have a beneficial effect. In any case, we still find it advisable to use the air jet.

Oxygen Contamination

As noted, the use of a multilayer crystal makes it possible to detect oxygen virtually anywhere on each specimen. This is clearly demonstrated in Fig. 3, where an oxygen peak is detected on pure gold. As the solubility of oxygen in gold is negligible, the oxygen must be in fact physically adsorbed on the specimen surface (which, by the way, shows how surface-sensitive a microprobe can be).

In the course of our systematic work on the quantitative analysis of nitrogen in a large number of nitrides, we found some cases of very strong oxygen contamination that were clearly not confined to surface adsorption effects. Because the measuring times for the integral recording of nitrogen spectra were of the order of 1 h on one spot, we initially used the air jet to prevent carbon build-up. In the majority of cases this arrangement did not give rise to noticeable adverse effects for the nitrogen signal with the exception of the nitrides of metals like Hf, Zr, Ta, and Nb, for which we were confronted with a varia-

2

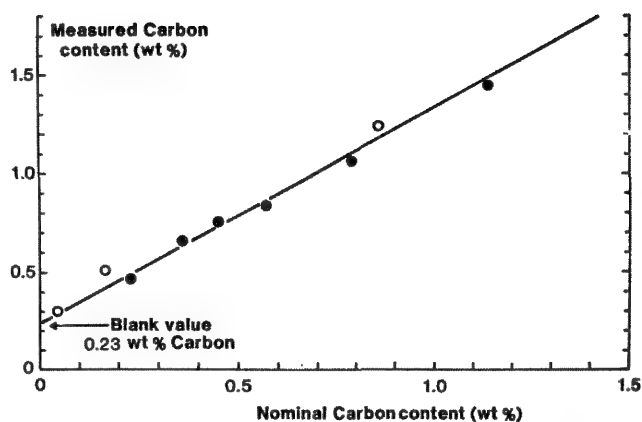
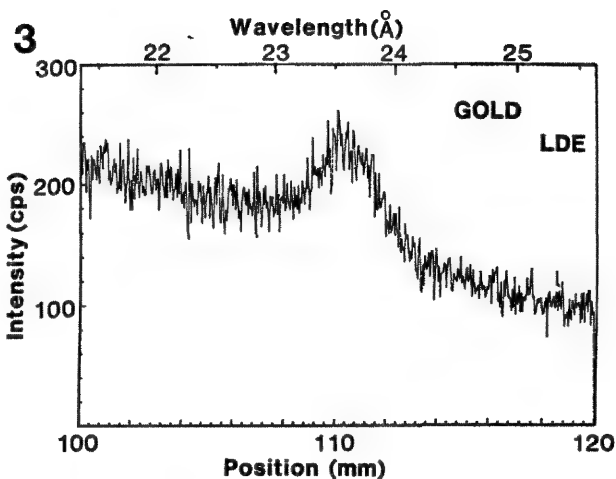


FIG. 2.--Measured carbon content compared with nominal composition for several calibration alloys. (Open and solid circles refer to different suppliers of alloys.) Blank value (as measured on decarburized Armco iron specimen) is in excellent agreement with point of intersection of straight line with vertical axis. Conditions: 10 kV, 300 nA; stearate crystal; standard, Fe_3C , turbo-molecular pump.

FIG. 3.--Oxygen peak recorded on pure gold with LDE crystal. Conditions: 10 kV, 50 nA.



tion of k-ratios with accelerating voltage that was completely inverted with respect to expectations. Further investigations into these peculiar phenomena showed that such nitrides were in fact oxidized at an incredibly high rate with the use of an air jet. This effect was established by monitoring of the $\text{N K}\alpha$ signal with the STE crystal and the $\text{O K}\alpha$ signal with the LDE crystal simultaneously. A typical example of these effects is shown in Fig. 4a for ZrN. The oxygen signal increases rapidly after the electron beam is positioned and the nitrogen signal decreases considerably which leads to final errors of $\pm 30\%$ in a period of 1-1.5 h. The effects were found to be voltage-dependent and completely explained the erratic behavior of the k-ratio with voltage.

Next, a number of tests were carried out without the air jet. It was found that, in principle, the same phenomena occurred in these sensitive nitrides (Fig. 4b), albeit to

a much lesser extent. We also found that a measuring time of 10-30 s can be sufficient to double the oxygen signal from these materials without necessarily changing the nitrogen signal. Of course, the effects are much worse on the pure elements Ti, V, Zr, Nb, Hf, and Ta.

The conclusion to be drawn from these experiments is clear: the mere positioning of the electron beam on such specimens immediately starts a process of in situ oxidation. The relatively poor vacuum conditions in commercial microprobes, as compared with typical surface-analysis instruments, are to blame for these oxygen-contamination phenomena. The practical impact of our observations is that it is highly unlikely that realistic measurements of low levels of oxygen in sensitive materials can ever be made. A sad conclusion is that it will be very difficult to fight these phenomena except by a very expensive improvement in the vacuum conditions, which would make the

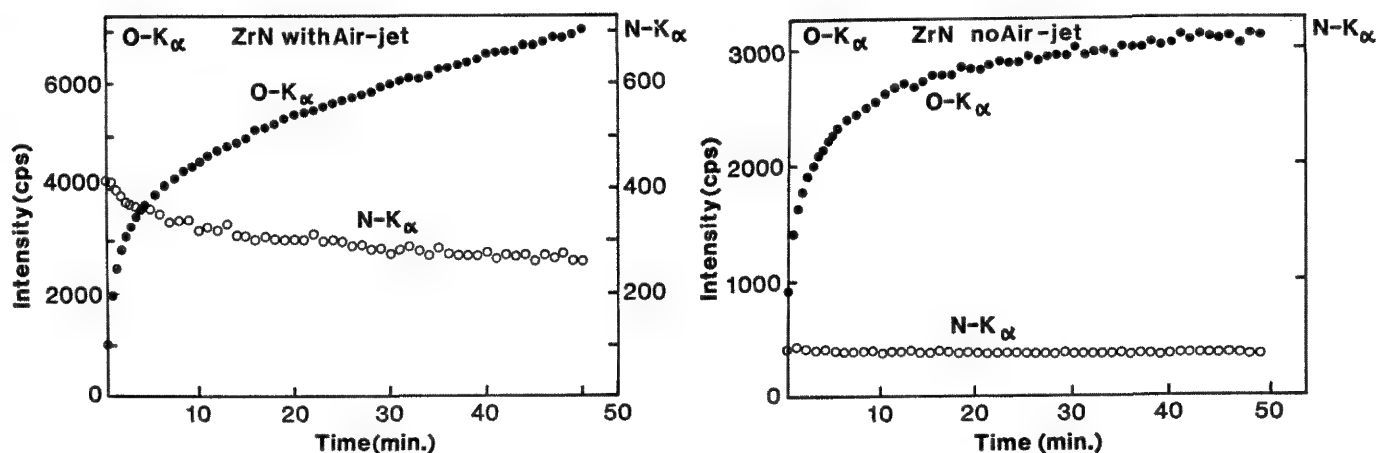


FIG. 4.--In situ oxidation phenomena on ZrN at 4 kV, 300 nA. (a) With air jet, (b) without air jet. Note differences in vertical scales for oxygen and nitrogen. Oxygen on LDE; nitrogen on STE; turbo-molecular pump.

routine use of the microprobe much more difficult. That is all the more sad because the new multilayer crystals turn out to be such an excellent improvement in the analysis sensitivity for an element like oxygen.

We conclude that it is very difficult to give hard and simple rules about carbon and oxygen contamination and the advisability of using an air jet. In each individual case, one should carefully check whether the use of the air jet has adverse side effects for the element to be determined. In the majority of cases there is nothing to be afraid of, with an exception of the cases mentioned before.

References

1. G. F. Bastin and H. J. M. Heijligers, "Recent developments in EPMA of very light elements," in *Proc. 11th ICXOM*, London, Canada, 1987, 257-261.

ELECTRON PROBE MICROANALYZER FOR ULTRALARGE SPECIMENS UP TO 12 × 12 in.

Miyuki Matsuya, Hiroaki Fukuda, Kazuyasu Kawabe, Hidehiko Sekiguchi,
Hiromi Inagawa, and Masaki Saito

An electron probe microanalyzer (EPMA) with twin inclined 4-crystal spectrometers has been developed, aiming at high-speed and high-accuracy analysis from microscopic areas to ultrawide areas on ultralarge specimens having rugged surfaces. With the conventional EPMA equipped with a wavelength-dispersive spectrometer (WDS), it is not possible to analyze the entire area of specimens of more than 5 × 5 in. However, in recent years, there is an increasing need to analyze nondestructively any position on large specimens exceeding 6 × 6 in., for example semiconductor wafers, various types of disk memories, plate-like and block-like products, and excavated materials. This paper gives an outline of an EPMA (JXA-8600B) developed to meet the above-mentioned needs, which can analyze the entire areas of specimens up to 12 × 12 in., together with a whole map of Fe distribution in a wrench.

Outline of Instrument

Figure 1 shows the entire view of JXA-8600B combined with an x-ray counting system and a computer control system. Figure 2 shows a schematic assembly of main parts. The largest specimen accommodated is 12 × 12 in.² and 0.78 in. in height (30.6 × 30.6 × 2 cm). They can be exchanged by use of an airlock system. The specimen stage moves in a range of 12 in. in the X and Y (horizontal) directions and 0.4 in. (10 mm) in the Z (vertical) direction. The detectable element ranges from B to U, and detectable wavelength ranges from 0.101 to 9.3 nm. A twin scanner-type inclined 4-crystal WDS can be installed. The large specimen chamber is evacuated by a 6in. oil-diffusion pump. The resolution of the secondary electron image (SEI) is better than 10 nm at the working distance of EPMA. An LaB₆ electron gun, a liquid nitrogen baffle (LNB), and other attachments are provided.

Inclined WDS

Figure 3 shows a sketch of a vertical WDS, showing the analysis point A, crystals C1, C2, and detectors D1, D2 on Rowland circles 1 and 2, respectively. As seen from the figure, if the Bragg angle θ_1 is less than the take-off angle α , detector D1 is located above the specimen surface; whereas if θ_2 is larger than α , detector D2 moves below the specimen surface. The latter arrangement is thus impossible for the large specimen, though the WDS has a higher sensitivity for trace elements than the energy-dispersive spectrometer (EDS).

The authors are with JEOL Ltd., 1-2, Musashino 3-chome, Akishima, Tokyo 196, Japan.

But in a inclined WDS, the Rowland circle is rotated around the path of crystal (AA') and the detector D2 remains above the specimen surface. In the present case, the Rowland circle is rotated up to a angle β (Fig. 4), which makes the Bragg angle range for large specimens extend to that of the conventional vertical WDS. Accordingly, one unit of inclined WDS with 4 crystals has the wide detectable element range from B to U. Any crystal^{1,2} can be selected among a total of 8 crystals for each element analysis, and all elements can be then analyzed with high sensitivity. Furthermore, in the inclined WDS with β , a deviation $\Delta\theta$ from the Bragg angle due to ruggedness of the specimen surface is reduced. That is, $\Delta\theta$ is given by

$$\Delta\theta = - \frac{\Delta Z \cos \alpha}{L} \cos \beta$$

where ΔZ is the vertical deviation of the analysis point from the Rowland circles and L the distance from A to C. For β near 90°, $\Delta\theta$ is small for a given ΔZ , α , and L . Thus, in the inclined WDS, the effect of the ruggedness of the specimen surface on spectral intensity is reduced. And since $L = 2R \sin \theta$, the larger the radius R of the Rowland circle, the smaller the influence of the ruggedness. These features are advantageous for high-speed analysis of a wide area of the specimen.

Ultralarge Specimen Stage

The main construction of the stage is shown in Fig. 5. The design of the stage takes the following considerations into account.

1. In order to improve the reproducibility of the specimen position, special springs CX and CY (Coping) are used. This spring maintains the spring load constant independent of the stroke.

2. A so-called cross-roller slide is applied to slide the stage smoothly on the rail. This slide system (RX in X direction and RY in Y direction) has a high rigidity, so that the reproducibility of the specimen position is improved.

3. The axial rigidity of the drive shafts (DX and DY) is so high that the natural frequency of the system is increased to more than 150 Hz even for a specimen weighing 10 kg.

As a result, the reproducibility is better than 1 μ m at any position within 6 × 6 in. for up to 15kg specimens. The resolution of SEI of Au particles (Fig. 6) is estimated to be better than 10 nm even at a 15kg load, showing small vibrations of less than 5 nm.

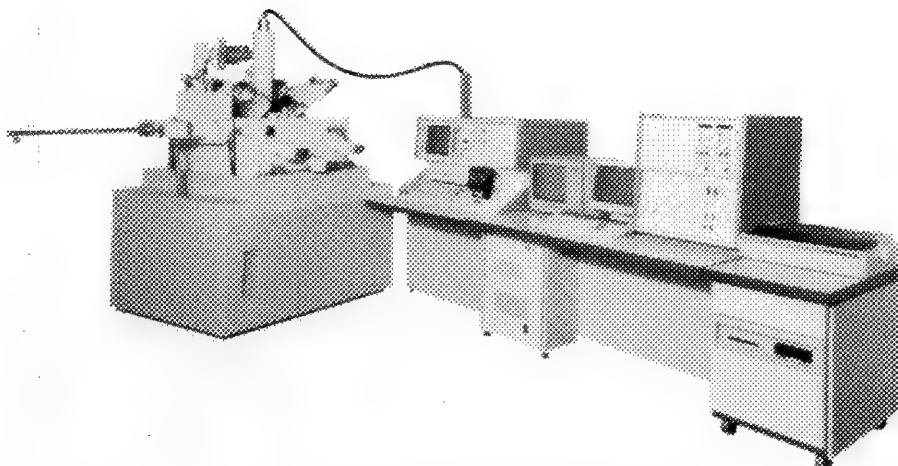


FIG. 1.--JXA-8600B combined with x-ray counting system and computer control system.

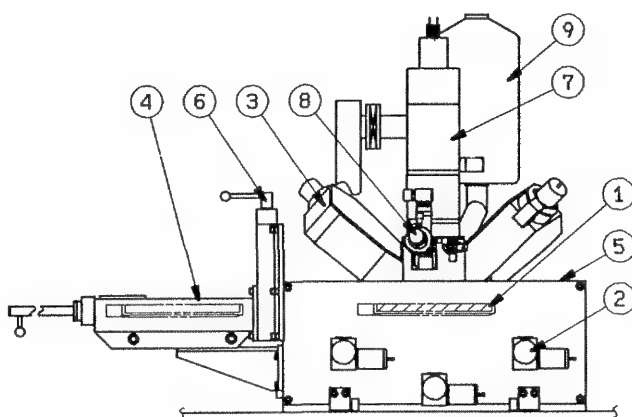


FIG. 2.--Schematic assembly of main parts: (1) specimen (up to 12×12 in), (2) ultralarge stage, (3) twin inclined 4-crystal WDS (4) specimen exchange chamber, (5) large specimen chamber, (6) airlock valve, (7) column, (8) optical microscope, (9) EDS.

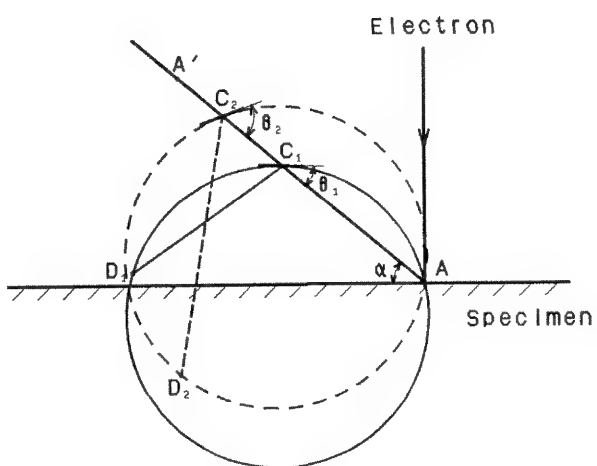


FIG. 3.--Sketch of vertical WDS.

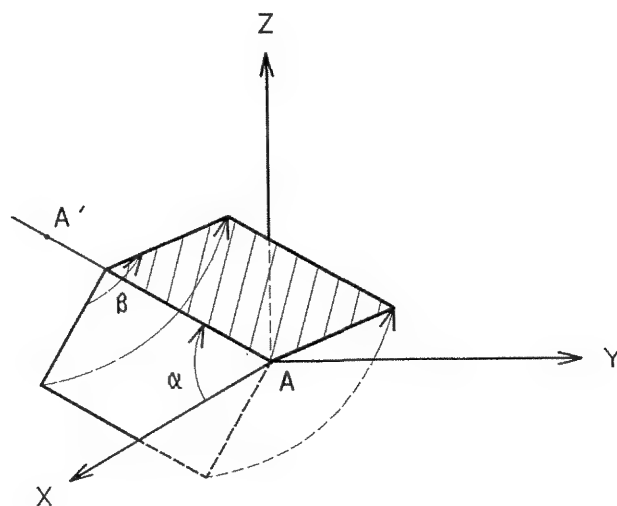


FIG. 4.--Vertical and horizontal Rowland circle plane.

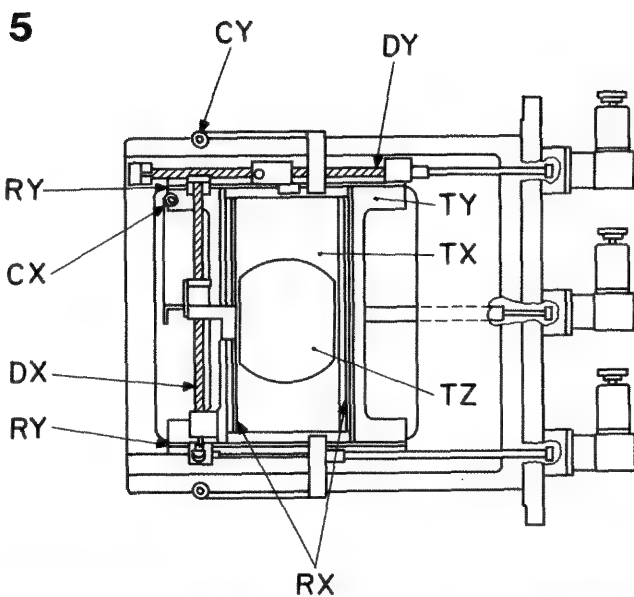


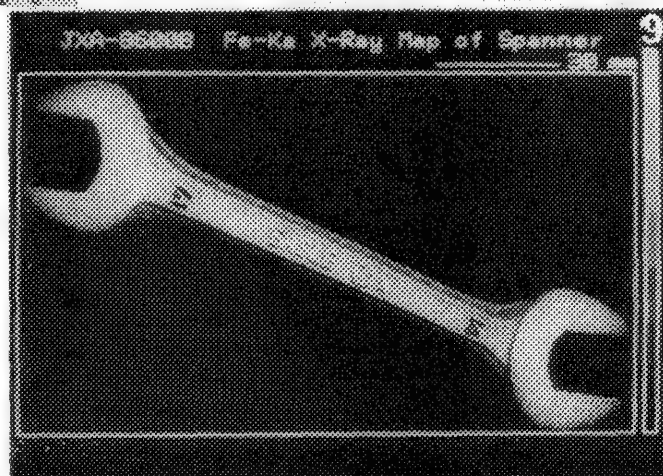
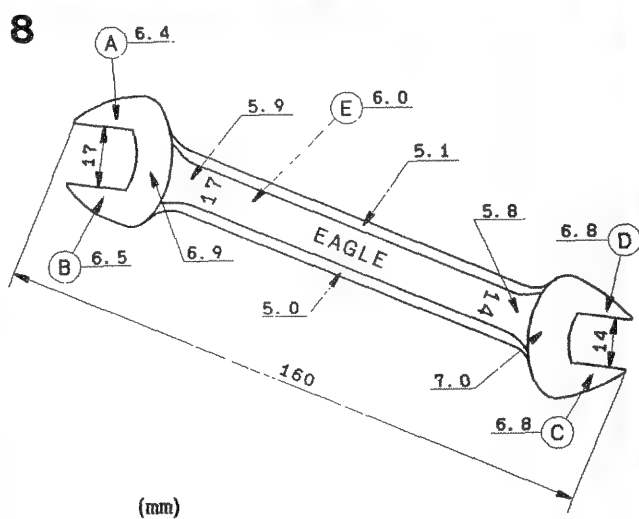
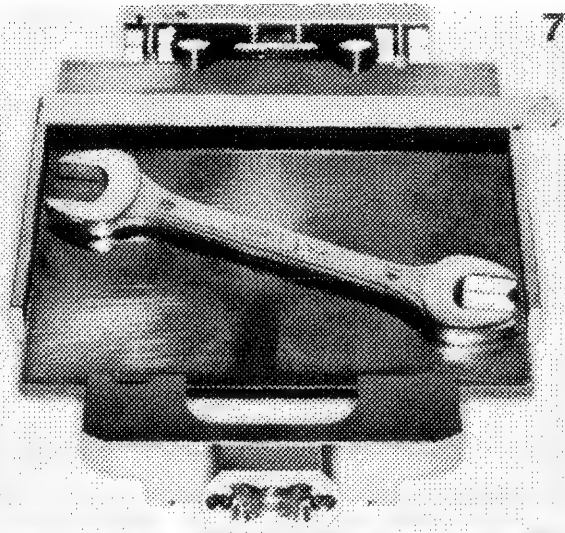
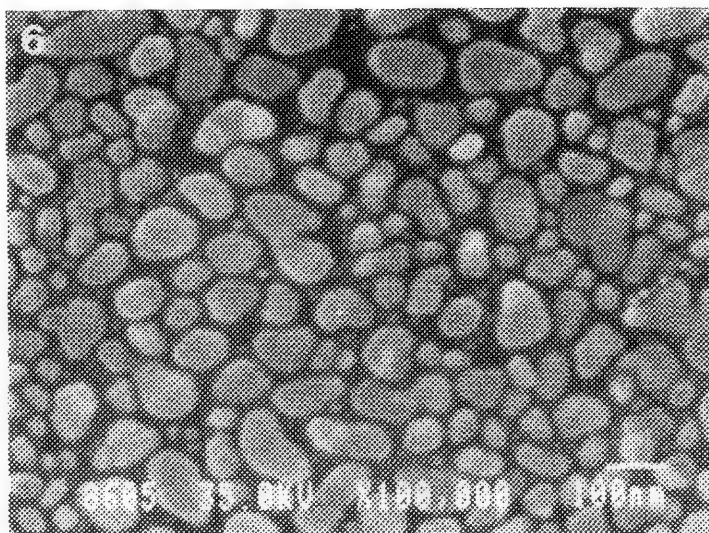
FIG. 5.--Schematic assembly of stage: TX, TY, TZ. Tables for each drive.

FIG. 6.--Image of Au evaporated particles on carbon block which is set to 15kg load-test specimen.

FIG. 7.--Specimen holder 6 × 6 in. and 17-14 wrench mounted on bottom plate.

FIG. 8.--Ruggedness of wrench surface measured from the bottom plate (mm).

FIG. 9.--Fe K α x-ray map of wrench.



Mapping⁸ of Fe Distribution of a Wrench

A wrench (Fig. 7) was fitted to the bottom plate in a specimen holder 6 × 6 in. together with a 150mm rule. The wrench is composed of irregular surfaces of varying height, which is measured in millimeter units from the horizontal bottom plate (Fig. 8). The maximum height is 7.0 mm and the minimum height is 5.0 mm, so that the difference between them is 2.0 mm.

Before mapping, an optical microscope is focused at A; then the mapping of Fe distribution is made under the following conditions: the stage drive speed is 5 mm/s, the number of pixels is 420 in the X direction and 750 in the Y direction, the pixel size is 200 × 200 μm, and the dwell time is 40 ms, by use of an LiF analyzing crystal. The intensity of Fe Kα peak was counted at an accelerating voltage of 25 kV and probe current of 0.1 μA.

As shown in the mapping image of Fig. 9, the difference of image intensity between the highest place A or D and the lowest place E is small compared with the intensity difference measured with the conventional vertical WDS.

Conclusion

A new EPMA with twin inclined 4-crystal WDS having 8 crystals can analyze the entire area of a specimen of up to 12 × 12 in. This EPMA can analyze all elements with high intensity, high speed (up to 5 mm/s), and high accuracy (reproducibility 1 μm). In addition, the resolution of SEI is better than 10 nm even with large and heavy specimens (up to 15 kg), without the effect of vibration. Also, the EPMA was applied successfully to obtain the mapping of the Fe distribution over the entire range of a wrench 160 mm long.

References

1. K. Kawabe et al., "Coated multilayer dispersion element for x-ray microanalysis," *Proc. 11th Intern. Cong. EM*, Kyoto, 1986, 569.
2. K. Kawabe et al., "Layered synthetic microstructure dispersion elements for electron probe microanalysis of carbon, boron, and beryllium," this Proceedings.
3. Y. Nagatsuka et al., "A new automated EPMA system with distributed processing capability," *Microbeam Analysis--1987*, 57.

STABILITY OF A SEMQ MICROPROBE: QUALITY CONTROL, QUANTITATIVE IMAGE ANALYSIS

E. D. Glover

The purchase of the SEMQ microprobe by the Department of Geology and Geophysics at the University of Wisconsin-Madison (UW) in 1981 was made for several reasons. The three spectrometers and six monochromators would allow counting nine elements simultaneously in the analysis of geological samples containing many elements; and, more important, the nine elements could be measured simultaneously in circumstances where automated probes are most valuable in the collection of line or area digital data (stage movement) with sufficient speed so as to cut job time to a minimum in multicomponent systems where accurate and precise data are desired. This paper describes control of the instrument for stability, production of, and transfer of data to a larger computer; and gives a number of examples to which such use has been put.

Instrument

The automation of the stage, spectrometers, PHAs, and EDS system was provided by Tracor-Northern with the distinct advantage that the SEMQ is located only 5 miles away from Tracor-Northern's plant. We spent the first 2-3 years creating our own routines for analysis. Then extension to line and area digital scans was begun and schedules were written within the limited memory available to allow disk storage. We then copied other laboratories' practice of sending the data from the probe disk to a larger computer, in this case a 'Masscomp' system just coming up to routine operation as the (departmental) interactive system. This allowed the probe to be used as a probe, with the more manageable Masscomp UNIX system to be used for massaging, printing, graphing, plotting and tape storage (Table 1).

Initial Problems

With the mechanics of collecting and organizing data into files set up and operating, attention was paid to the "quality control" aspect to check existing stability, and thus, time constraints limiting the system. A check was set up using Si K α measurement on any combination of the spectrometers; scanner #1, PET; scanner #2, ADP; and #9, ADP, a monochromator. The sample used was either silicon or silicon dioxide. An example of a successful run is shown in Fig. 1. Silicon was counted vs silicon as a standard. Correction by linear fit gave stable k ratios close to 1.0 on the three scanners. The mean and relative standard deviation

(r.s.d.) in % for the drift-corrected runs were (scanners 1, 2, and 9); 0.9963, 0.310; 1.0020, 0.325; 1.0016, 0.353 (well within the x-ray standard deviations 0.3 to 0.5%). After making a number of runs we found that it was necessary to check the filament behavior and to wait 1 to 2 h after sample entry for the vacuum to reach steady state. (Note conditions: Large sample chamber, but large diffusion pump with steady-state vacuum in the range of 3×10^{-6} Torr or less; sample chamber tie-in at 40 μ m.)

In check runs SiO₂ was used part of the time. These runs produced persistent "contamination" spots, which were used to produce a pattern giving quality control on the actual spatial distribution of the probed spots. Although the numbers on the x and y position dials read 10 μ m advancement, the pattern produced in Fig. 2 shows less accurate positioning of the sample. Since this pattern was repeatable we took care of this by simply defining a new space, SEMQ space. We are working on the conversion factors.

Application of Long Scans

A series of applications of precise long scans are next presented. The development of the method and some of the applications have been made by the author. But many of the applications given are a part of the research and development of UW probe users; much of the probe work has been done by the researchers in collaboration with the author. The users results are presented here to illustrate the usefulness of the technique.

Study of a Waveguide Device

This work by Kent Chocquette and Prof. Leon McCaughan is part of a study of Ti diffusion into Li-Niobate in waveguide devices. The measurement was made on an area covering an original section of a 5 μ m strip of Ti, scanning repeatedly across the strip along the length to establish the exact geometry. Counting times of 80 s helped gain precision at the low levels of Ti measured; k-ratios were collected and stored with a small correction made to the k-ratios measured (made from trial ZAF corrections). The scans are seen in Fig. 3, where several curves are superimposed. The goal of this work was to define the spatial precision of the diffused volume.¹

Phase Diagram Determination

A very broad application of quantitative line and image analysis has been made by Prof. Austin Chang at UW. He and his graduate students are interested in phase stability in

The author is at the University of Wisconsin (Geology and Geophysics), 1215 W. Dayton St., Madison, WI 63706.

TABLE 1.--The collection and transfer system was as follows:

Probe		RS-232	Masscomp
Main Program	Schedule	Data	
Task	Cogrid	20 sample table(s) to Disk	840 byte string Reconstituted table Masscomp file
Flextran language - - - - -		- - - - -	C language - - - - -

multicomponent systems. Recently, they have been investigating phase stability of metallic contacts to GaAs with the use of diffusion couples. In Fig. 4 is shown a digital, linear scan over a diffusion couple of GaAs vs Ni. A simple overnight run can produce an atomic composition plot which shows directly the formation of GaAsNi₃, with some variations, which the experimenter, Mr. X. Y. Zheng, can explain.

Modal or Phase Analysis

Many investigators have used stage or beam movement to count occurrences of phases present at grid locations to obtain the percentage of each phase. This method has been set up here for beam or stage movement; if the grid interval is reduced, the method gives quantitative image analysis. Present use at UW is mainly of line scans for checking concentration gradients to allow inference of P-T conditions of the formation process,² or to sort out chemical, structural, or orientation effects in minerals.

Figure 5 is a polarized light picture of a feldspar grain studied by Prof. L. G. Medaris. The superimposed Ca plot data shows that chemical effects are present. Because a focused electron beam and a 1 μ m interval were used, the Na value (which complements Ca) was variable since the heat produced causes Na mobility; however, the Ca and also the Al concentrations correlate directly with the extinction of the transmitted light by the crystal. There is a gradual increase of Ca and Al toward the center of the grain (right) and intermittent zones of high and low Ca and Al. This information with other data, allows assessment of the changes that have taken place in the development of the rock, as well as assessment of the chemical evolution of the magma from which the plagioclase has crystallized.

Homogeneity of NBS Glass K-411

The next sample, NBS Glass standard K-411, may be considered as a test for stability or a check on homogeneity. It started as a scan on a 30 \times 30 grid, 5 μ m spacing. Only 14 of the 30 passes were made in a 9.5h time interval. Data on the means and standard deviations of four elements (two duplicated) are shown in Table 2 along with the x-ray standard deviations. All are close to the x-ray standard deviations except Fe on the two scanners measured. Both are

0.55 rather than the 0.34 and 0.38 calculated. Is K-411 inhomogeneous for Fe? A look at the curves (Fig. 6) shows a "bad" point with Fe high and the other elements low. Removal of this point produced the lower set of data (Table 2) in which all the standard deviations average less than 10% more than the x-ray values. The standard gets a clean bill of health except for one point (point 420) which has a high Fe content.³

Homogeneity of Nb-Ti Alloy

This research is part of a U.S. Department of Energy sponsored effort to create Nb-Ti wire composite for superconducting magnets for use in control of accelerators in high-energy physics. Taking part in the effort are Fermi National Accelerator Laboratory, Brookhaven Laboratory, Lawrence Berkeley Laboratory, the Applied Superconductivity Laboratory at UW, plus other laboratories, as well as manufacturers and processors. In spite of the sophisticated development of the superconducting composites of Nb-Ti, a basic problem has been the production of a reasonably homogeneous alloy to produce composites with maximum current capacity.⁴ The measurement of this homogeneity has been carried out on the SEMQ by Peter Lee. This phase is only a small part of the total effort to develop the composite, but it is a basic one. What is shown here is the extremes of homogeneity development seen depending on the details of processing. The first plot (Fig. 7) shows a 400-point 10 μ m scan which was repeated after the first pass. The repetition is extraordinarily good; the two curves are hardly seen to separate. This sample is rather inhomogeneous and the curves demonstrate the spatial distribution. Figures 8 and 9 show successive improvement in the homogeneity. The collection of line scan data was usually sufficient. However, the technique was expanded in some cases to produce a quantitative image. A 50 \times 32 grid with a 10 μ m interval is displayed contour-wise in Figs. 10, 11, and 12. This 37h run was drift-corrected to give (for all points) means and r.s.ds. of 0.5315, 0.56%; 0.4677, 0.48%; 0.992, 0.14% for Nb, Ti, and the total. In spite of the high precision, the contour maps show vividly the nonrandom distribution.

TABLE 2.--MEAN and R.S.D. of k-RATIOS of NBS GLASS K-411 (20 kV, 20 NA SAMPLE CURRENT, 20s COUNT, 5 μ m GRID).

element	mean	<u>r.s.d., %</u>	<u>r.s.d., %</u>	<u>x-ray r.s.d., %</u>
		<u>as taken</u>	<u>bad point omitted</u>	
Si1	1.0000	0.38	.37	.37
Si9	1.0004	0.71	.71	.63
Ca	.9992	0.31	.25	.25
Fe2	0.9997	0.55	.38	.34
Fe4	1.0037	0.55	.40	.38
Mg	1.0035	0.69	.66	.62

Conclusions

In view of the data obtained in measurement on real systems several conclusions can be drawn. With steady-state vacuum and a well-behaved filament (properly installed), the present instrument gives high precision in measurements over a period up to 20 h (or more) with standardization only at the beginning and ends of the run. In the case of the NBS K-411 glass run on a 9.5h scan, the standard deviation was very little above the x-ray standard deviation. With the above conditions satisfied and with more frequent standardization, the precision could be routinely maintained at the x-ray standard deviation level. A very necessary condition for such precision is stable x-ray detection systems, including proportional counters and amplification. Proportional counters must be checked by such a long analysis run. If they consistently do not measure up they must be rejected. The accuracy of the stage movement on a micrometer scale can be checked by a grid pattern of contamination spots on a crystal such as quartz.

References

1. L. McCaughan and K. D. Chocquette, "Origin of and solution to crosstalk in Ti:LiNbO₃ directional coupler switches," *J. Quantum Electronics* 22: 947-951, 1986.
2. L. G. Medaris and H. F. Wang, "A thermal-tectonic model for high-pressure rocks in the Basal Gneiss Complex of western Norway," *Lithos* 19: 299-315, 1986.
3. R. Marinenko, "Preparation and characterization of K-411 and K-412 mineral glasses for microanalysis: SRMA 70," *NBS Spec. Pub.* 260-74, 1982.
4. P. J. Lee and D. C. Larbelestier, "Microstructure development in a high current density NbTi superconducting composite," *Proc. 45th Ann. Meet. EMSA*, 1985.

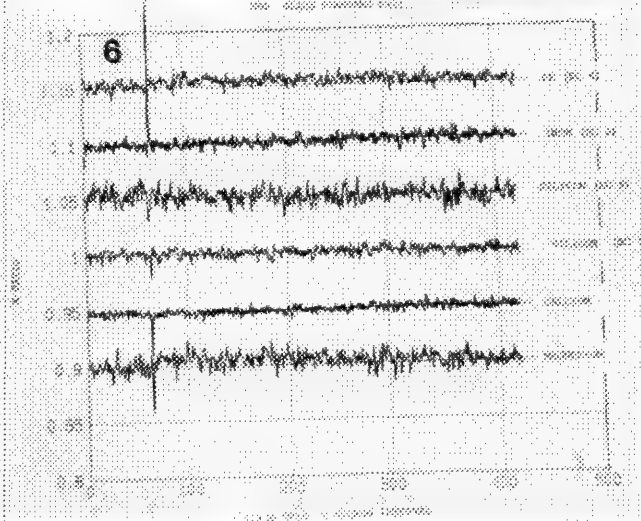
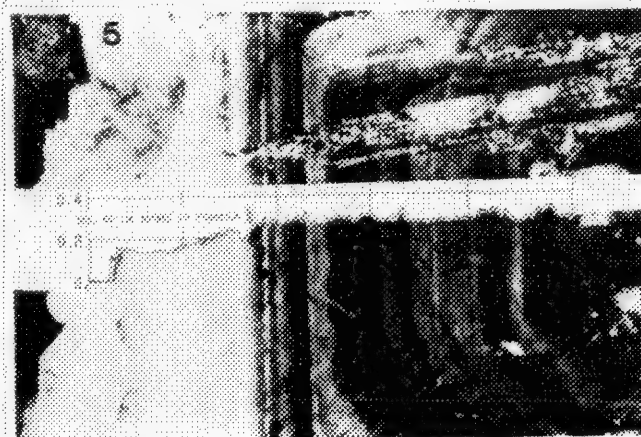
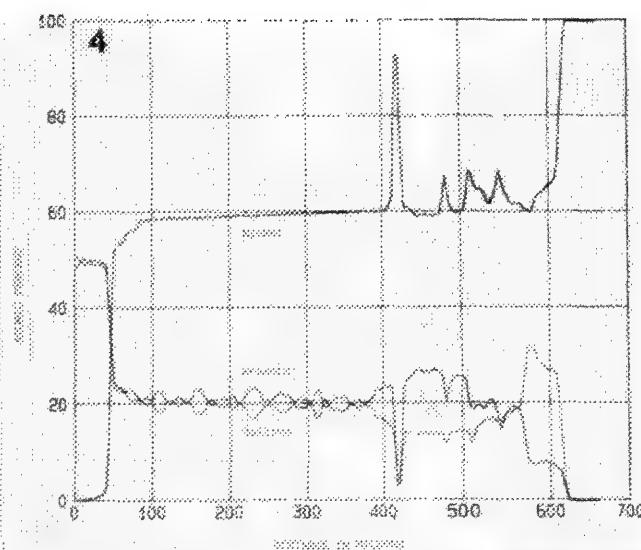
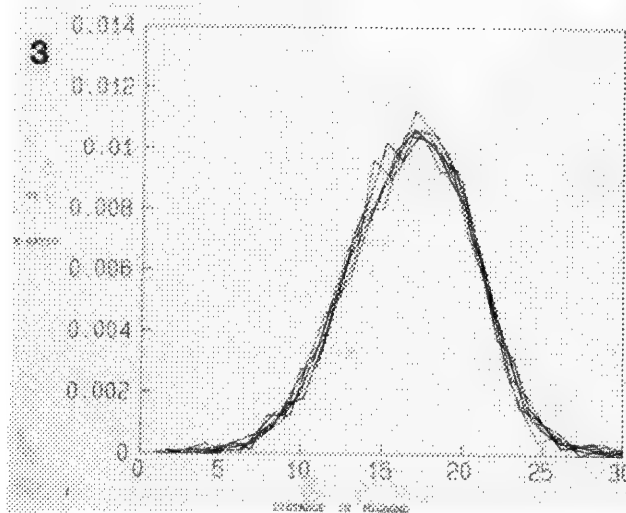
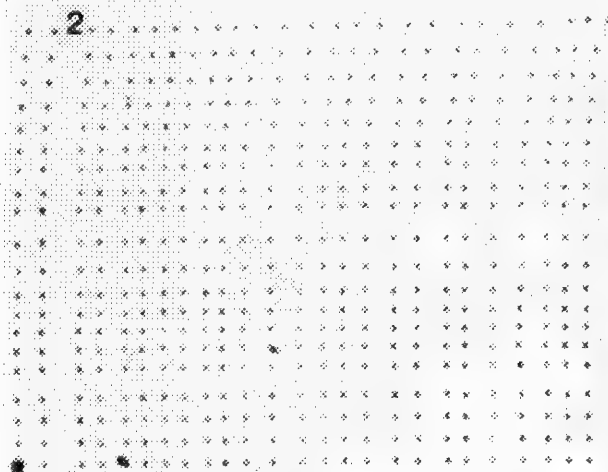
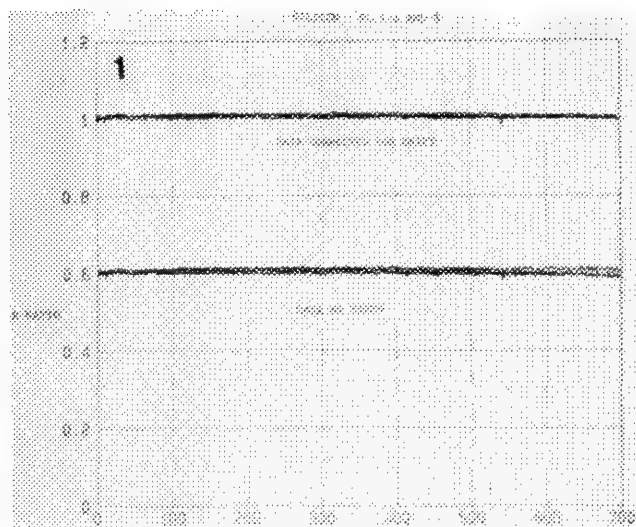


FIG. 1.--Silicon k-ratios for three scanners for a 700-point scan, 2 μ m interval, time \sim 12 h. Vertical scale is correct for upper curve/ lower curve is offset 0.4 unit.

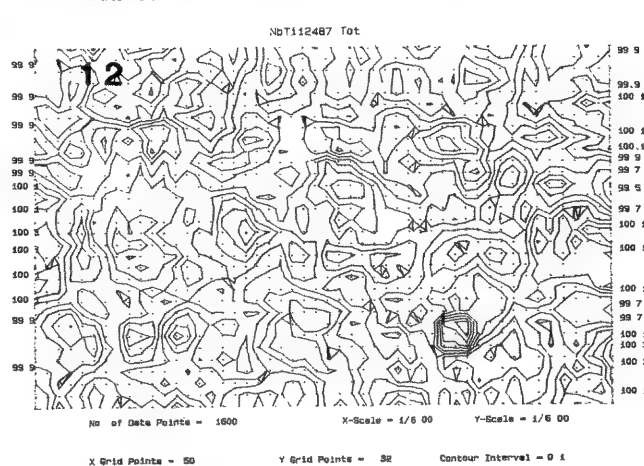
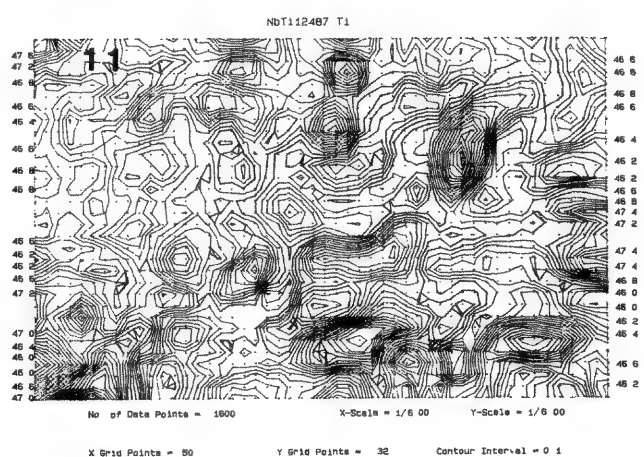
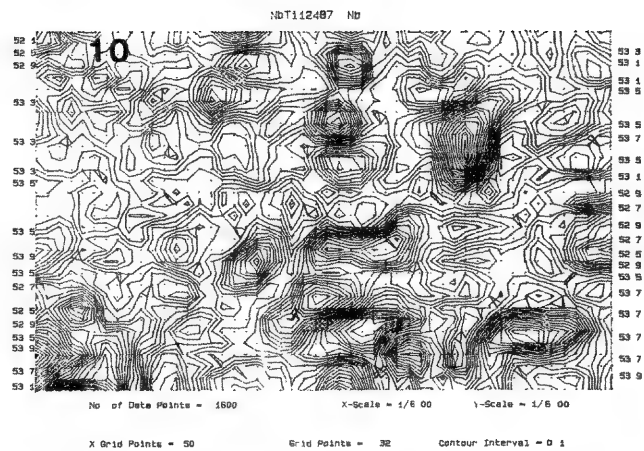
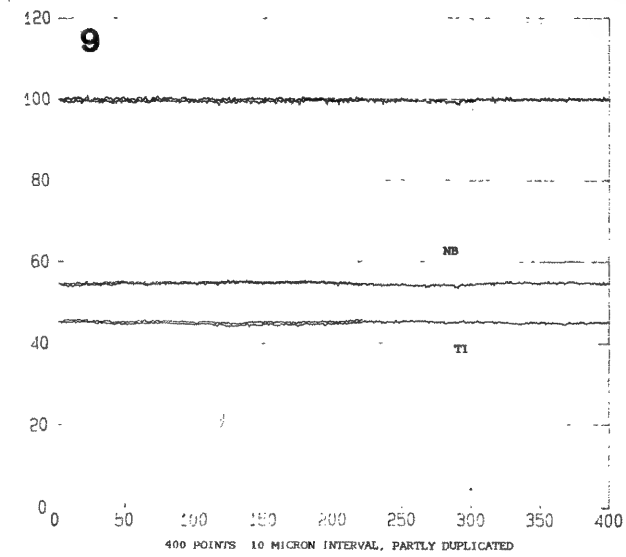
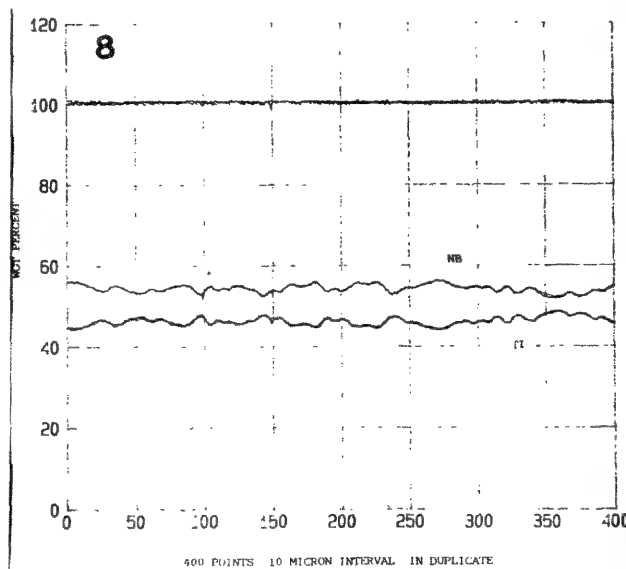
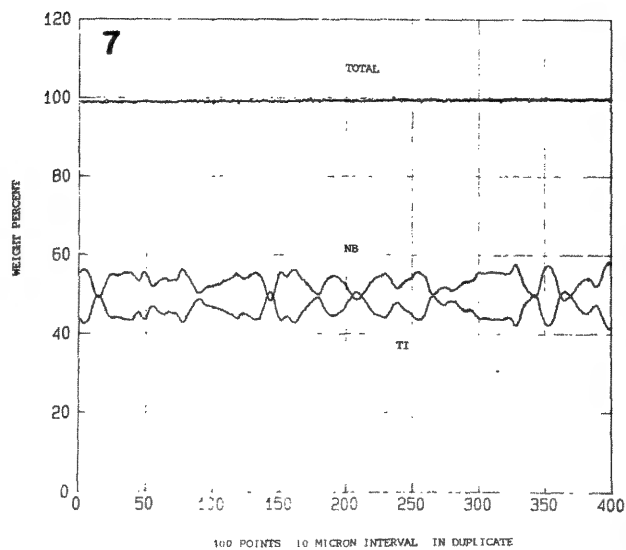
FIG. 2.--Position of the probe beam as stage moved over 10 μ m grid. Sample: quartz (SiO₂), Hot Springs, Ark.

FIG. 3.--Plot of k-ratios of Ti across several traverses of Ti strip, 5 μ m wide \times 670 \AA thick, diffused into LiNbO₃. Beam size 2 μ m; interval, 1 μ m.

FIG. 4.--Plot of atomic % of Ga, As, and Ni across diffusion boundary GaAs-Ni.

FIG. 5.--Superimposed plot of number of Ca atoms/formula [Na(Ca)Al(Al)₂Si₃(Si₂)O₈] on photo of plagioclase feldspar crystal (polarized light with crossed nicols). Scan length: 1000 points, 1 μ m interval.

FIG. 6.--Plot of k-ratios of Fe, Si, Ca, Mg in NBS K-411 glass over 5 μ m intervals. Vertical scale corresponds to Si(Sc 1). Other k-ratio curves are offset by multiple of 0.05 unit.



FIGS. 7,8,9.--Three (duplicated) linear scans on NbTi alloys of increasing homogeneity (wgt. % vs successive points at 10 μ m intervals).
FIGS. 10,11,12.--Contour map of Nb,Ti and total concentration (wgt %) of 50 \times 32, 10 μ m grid of NbTi alloy giving quantitative image with 10 μ m resolution.

MICRO CONSULTANT: A FORTH-BASED EXPERT SYSTEM FOR QUANTITATIVE MICROANALYSIS

J. F. Konopka

Micro Consultant is an interactive software program which assists new and occasional users of EDS. Given a minimal amount of information about a sample, this program lists a correct method for conducting the analysis. It suggests which lines and which kV to use, report whether or not overlaps are present, suggest a command sequence to use, and report which parameters have an effect on the result.

The motivation for this work was to complement written manuals in a way that saved time and increased security of the user. Textbooks and manuals for the most part present information in the form of static rules. It is up to the user to select which rules are relevant and how to apply them. For example, experienced users know that simple peak integration is adequate for many samples but that some kind of deconvolution technique must be used in cases of peak overlap. This software does not simply parrot this rule but instead looks at the elements being analyzed, checks for overlaps, and selects the appropriate software commands.

Another problem with written manuals is that they do not say what one has forgotten to do. This software generates a complete description of the analytical conditions and a sequence of commands tailored to the sample being analyzed. All relevant parameters are listed next to the commands they affect for ease of understanding. Default parameters are suggested where possible.

This approach brings several benefits. Compared to telephone support, a software program is available 24 h a day with no long-distance charge. A very important benefit is that the information is complete. For someone just getting started or for the occasional user, it is particularly easy to overlook something obvious to experienced users. An example is not measuring the beam current when working with standards. This software can give people confidence because the answers are complete. New users can learn from it by inputting many different element lists and observing the results. Occasional users can use it to brush up before they begin a series of analyses. It is to be regarded not as replacing warm, friendly, cheerful systems support people, but rather as extending their reach.

The rules that drive this program are written in near English so that nonprogrammers can read, verify, and modify the rule set and write new rules. A sample rule is shown in Fig. 1. The backslash character is used to separate comments from the rules. Figure 2 lists the facts about the analysis available to the deci-

sion process. All the text messages are kept in a separate text file which can be easily modified with an ordinary editor. Thus the software can be extended day by day by the applications laboratory as more is learned about analysis with a particular machine and software combination. It is very important to have a wider circle of people involved in the creative process. Only minimal support from a software engineer is required to verify correctness of the changes. This approach will prove useful in supporting systems longer than is now possible. If during the growth years of a product a solid knowledge base about it is built up and then, during the declining years, attention is focused elsewhere, a reliable, inexpensive source of support will be available for those still using these systems.

This program is written in FORTH language using FORPS which is a FORTH-base Production System developed at Oak Ridge National Laboratory. FORPS is under the copyright of Martin Marietta which operates the laboratory.¹ Typically, expert systems are written in LISP, which although very powerful is sometimes slow and require massive computer resources. I chose FORTH because it is fast and flexible, runs on microcomputers, and gives complete access to the analyzer. Moreover, FORPS is compatible with all one's other FORTH software and is also compact, fast, and flexible. There is also a precedent. At General Electric Co., an expert system designed to diagnose faults in diesel locomotives was developed in LISP on a DEC-10 and then made into a useful product by translation into FORTH to run on DEC LSI-11 microcomputers.²

To operate the program the user is asked to enter three pieces of information with a simple one-page editor. These are an element list, whether the EM is an SEM or STEM and whether or not standards are to be used. Based on this information the program then generates an informative report and chooses a path through the Kevex Quantex EDS software. Where more than one approach is possible the user is asked to make a trade-off between speed and simplicity of operation vs accuracy of the results.

A sample result is shown in Fig. 3. At the top of the page is the informative report. Below that are listed the Quantex commands and relevant parameters. The results may be printed for hard copy, viewed on the video or written to a procedure file which can be used to operate Quantex.

The current program is made up of 36 rules. It can comment on bulk analysis in an SEM whether there are overlaps or not and whether oxygen is present or not. At present, it

The author is at Kevex Corp., 1101 Chess Dr., Foster City, CA 94404.

\ This rule recognizes when to do standardless analysis.

```

RULE: Q/ASAP.R                                \ name of the rule
  *IF*
    QUANT.G IS-GOAL                            \ check that quantify is next task
    BULK                                         \ sample is bulk sample
    STD-LESS                                    \ standardless analysis request
    NO.OXIDE                                    \ non oxide sample
  *THEN*
    REMOVEGOAL                                \ delete subgoal from list
    Q/A/Z/P MSGOUT                            \ display instructions for user
  *END*

```

FIG. 1.--Sample rule used in FORPS.

Facts	
Value is true or false	
OXIDE	NO.OXIDE
OVERLAPS	NO.OVERLAPS
BULK	THIN-FILM
STDS	STD-LESS
FAST	PRECISE
ONE-LINE	MIXED-LINES

Other Data

#ELS	number of elements
ELIST	array of atomic numbers
A.LINE	array of line codes (K,L,M)

FIG. 2.--Information used to make decisions in rules.

assumes a Be window detector, so that oxygen is found by stoichiometry. The STEM case is similar but standards are not used and the thin sample is assumed to be inorganic.

The program as described has been implemented successfully and is now in the hands of the systems group. It is being distributed to some customers and appears to have gained their acceptance, especially overseas where, even more than in America, people find it difficult to read through a user's manual written in English.

References

1. C. J. Mathews, "The internals of FORPS: A FORTH-based production system," *J. of Forth Application and Research* 4: 7, 1986.
2. H. E. Johnson and P. P. Bonissone, "Expert system for diesel electric locomotive repair," *ibid* 1, 1: 7-16, 1983.

```

*****
*
*                               Micro Consultant 2.0
*
*****

```

23-Nov-87 15:12
Analyzing bulk, SEM sample without standards.
Recommended accelerating voltage is not less than 12 kV.

Elements: Cr Fe Ni
Lines: K K K

No overlaps.

```

*****
*                               *
*      Software Commands      Setup Parameters      *
*                               *
*****
Identify/List                  | No setup dependencies.
      3, 1, Cr, Fe, Ni      |
Acquire/Clear/Start           | Setup-Acquire
      Comment: Adjust beam current to keep | 1. Preset Live time
      dead time less than 35%. | 2. 100 to 200s
      Dead time is displayed during |
      acquire at bottom of screen. |
Quantify/Asap/Zaf/Normalize/Print | Setup Quantify
                                   | Menu 1
                                   | 1. Normalization      (100)
                                   | 4. kV
                                   |
                                   | Menu 2
                                   | 19. Angle.
                                   | 23. Emergence Angle.
                                   | 30. Detector Thickness
                                   |   ( Depends on detector area.
                                   |       Nominal values:
                                   |       50mm2 : 3.0mm
                                   |       30mm2 : 3.0mm
                                   |       10mm2 : 2.0mm )
                                   | 31. Window Thickness. (11)
                                   | 32. Si Dead layer.   (0.1)
                                   | 33. Gold layer.      (200)
                                   | 38. Shell Parameters.
                                   |   K (1.0)
                                   |   L (2.6)
                                   |   M (9.0)
                                   |
*****
*                               *
*      Command Sequence Finished      *
*                               *
*****

```

FIG. 3.--Sample output from Micro Consultant.

LAYERED SYNTHETIC MICROSTRUCTURE DISPERSION ELEMENTS FOR ELECTRON PROBE MICROANALYSIS OF CARBON, BORON, AND BERYLLIUM

Kazuyasu Kawabe, Shigeo Takagi, Masaki Saito, and Shojiro Tagata

Layered Synthetic Microstructures (LSM) have been used as dispersion elements for light-element analysis in x-ray spectrometry.¹⁻³ Johann-type W/Si LSM with a spacing of $2d = 60 \text{ \AA}$ has been used as a dispersion element for the detection of nitrogen and oxygen in electron probe microanalysis⁴ instead of Langmuir-Blodgett soap film (L-B film) dispersion elements, which have poor dispersion ability for N K α and O K α strongly absorbed in L-B films. Lead stearate film (STE) has been widely used as a dispersion element for carbon and boron microanalysis, because of its relatively high dispersion ability for C K α and B K α with a wavelength larger than carbon K edge (43.68 \AA). But today in the field of metallurgical engineering, improvements in the efficiency of a dispersion element for C K α and B K α are strongly needed in electron probe microanalysis. Lead cerotate film (CER) has been used as a dispersion element for beryllium microanalysis, but its low peak intensity and low peak-to-background ratio limit its practical availability. So, LSM prepared as a dispersion element for only Be K α was formerly used for the detection of beryllium in electron probe microanalysis.⁵

LSM with a spacing of $2d$ in a range from 40 to 200 \AA and composition of W/Si, W/C, V/C, Cr/C, Ni/C, and Mo/B₄C are found to be practical for x rays in the range from O K α to Be K α . These LSM are composed of the heavy element with high x-ray reflectivity and the light element with low x-ray absorption coefficient for these x rays. We have measured the peak intensity P , the peak-to-background ratio P/B , and the wavelength resolution $\Delta\lambda/\lambda$ with these LSM and have evaluated their capabilities as dispersion elements in electron probe microanalysis. As a result, we have concluded that it is desirable to have three kinds of LSM as dispersion elements for O K α ~ Be K α : one is for nitrogen and oxygen,⁴ another is for only carbon, and a third is for boron and beryllium, whose composition and $2d$ spacing can be selected to optimize the dispersion ability of each proposed x ray. This paper reports the results of LSM as a dispersion element for C K α and LSM for B K α and Be K α , and shows the improvements over L-B films in electron probe microanalysis.

Experimental Method

Five types of dispersion elements were installed in a JEOL JXA-8600 electron-probe microanalyzer. Four were Johann-

type elements with a bending radius of 280 mm: LSM for Ca, LSM for B and Be, STE, and CER. The remaining one was a new type of STE with doubly curved surface (named NEW-STE; the effective size of NEW-STE is 2.5 times that of Johann-type elements). The P , P/B , and $\Delta\lambda/\lambda$ values of spectra from graphite, metal boron, and metal beryllium specimens were measured, together with typical higher-order x-ray intensity. Furthermore, carbon in low-alloy steel, boron in surface boronized steel, and beryllium in Ni-Be alloy were analyzed by use of these dispersion elements at an accelerating voltage of 10 kV. A gas flow proportional counter with a conductive coated stretched polypropylene window was used as an x-ray detector and one-atmospheric P-10 gas was used in the detector. We have evaluated their ability as a dispersion element by comparison among these measured values.

Results

LSM for Carbon Microanalysis. To improve the dispersion ability for C K α in electron probe microanalysis, Johann-type V/C LSM with a spacing of $2d = 96\text{--}102 \text{ \AA}$ (named LDE-C; Layered Dispersion Element for Carbon) has been selected from LSM with various compositions and $2d$ spacings. Nine pieces of LDE-C made under the same coating recipe have been tested and the considerable difference between their dispersion properties was not found.

Figure 1 shows a comparison of C K α peak profiles obtained by LDE-C and STE under the same conditions. The horizontal axis represents the distance, $L = 2R \sin \theta$, where θ is the angle incident to the dispersion element and R is the radius of the Rowland circle (140 mm in our case). The P , P/B , $\Delta\lambda/\lambda$, and higher-order x-ray intensity with LDE-C are compared with STE in Table 1. C K α intensity with LDE-C is very high compared with STE. P/B and $\Delta\lambda/\lambda$ values of C K α with LDE-C are somewhat poor compared with STE, but the difference

TABLE 1.--Numerical comparison of the dispersion properties with LDE-C and STE.

X ray (Specimen)	C K α (Graphite)			B K α (Metal B)			3rd-order Fe L α (Fe)
	P	P/B	$\Delta\lambda/\lambda$	P	P/B	$\Delta\lambda/\lambda$	P-B
LDE-C/STE	7.1	0.87	1.4	2.8	0.66	1.6	0.048

The authors are with JEOL Ltd., 1-2, Musashino 3-chome, Akishima, Tokyo 196, Japan.

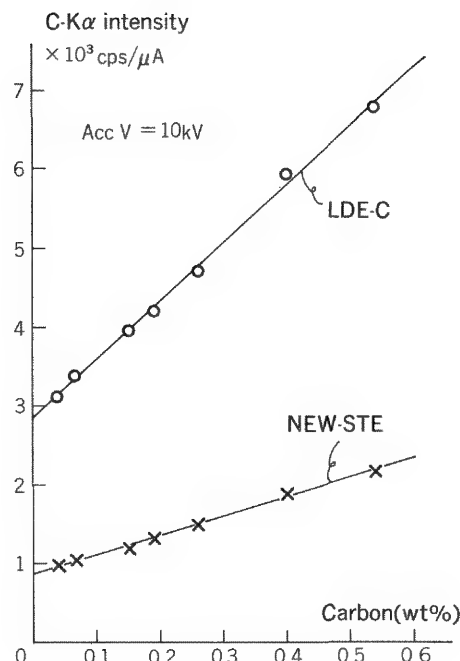
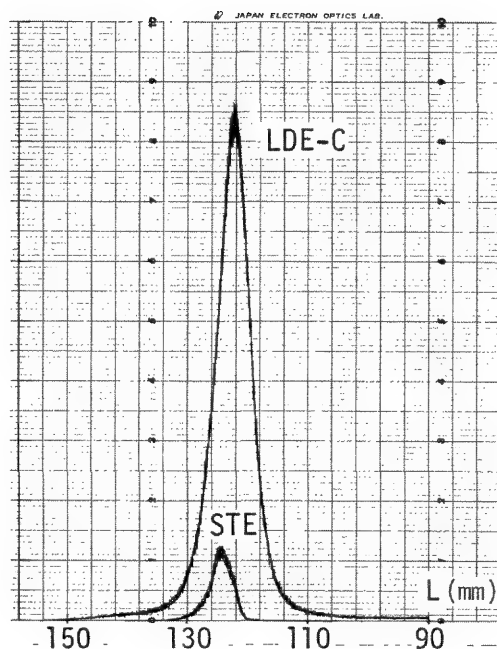


FIG. 1.--Carbon-K α peak profiles of graphite obtained by LDE-C and STE.
FIG. 2.--Analysis of carbon in low-alloy steel.

between them is not serious for the usual applications. The third-order Fe L α intensity with LDE-C is 5% compared with STE. This result is favorable for elements analysis. Figure 2 shows calibration curves of carbon in a range 0.037-0.54 wt% in low-alloy steel obtained by LDE-C and NEW-STE. The C K α intensities in the figure represent raw values including each background intensity. Each calibration curve is represented by a straight line, and the gradient A and the value B intercepting the vertical axis are different. The sensitivity defined as A/\sqrt{B} with LDE-C is 1.7 times that with NEW-STE.

LSM for Boron and Beryllium Microanalysis. To improve the efficiency of a dispersion element for B K α and Be K α in electron probe microanalysis, Johann-type Mo/B $_4$ C LSM with a spacing of $2d = 145-150 \text{ \AA}$ (named LDE-B: Layered Dispersion Element for Boron and Beryllium) has been selected from various LSM. Eleven pieces of LDE-B made according to the same coating recipe have been tested and the considerable difference between their dispersion properties was not found.

The P, P/B, and $\Delta\lambda/\lambda$ values of spectra from pure metal boron and beryllium and higher-order x-ray intensity with LDE-B are compared with STE and CER in Table 2. Peak intensities of B K α and Be K α with LDE-B are very high compared with STE and CER, respectively, whereas the $\Delta\lambda/\lambda$ value of B K α with LDE-B is poor compared with STE and CER. The third-order K α line of oxygen, which is contained in most steels, appears near B K α and its intensity with LDE-B is 5% compared with STE. The following examples in Figs. 3 and

TABLE 2.--Numerical comparison of the dispersion properties with LDE-B, STE, and CER.

X ray (Specimen)	B K α (Metal B)			Be K α (Metal Be)			3rd- order O K α (Al $_2$ O $_3$)
	P	P/B	$\Delta\lambda/\lambda$	P	P/B	$\Delta\lambda/\lambda$	P-B
LDE-B/STE	16	1.3	2.1	-	-	-	0.053
LDE-B/CER	15	8.1	1.7	15	1.2	1.2	-

4 are peak profiles from practical materials. Figure 3 shows a comparison of B K α peak profiles of Fe $_2$ B obtained by LDE-B and NEW-STE. The net intensity, P-B, and P/B value with LDE-B are 5.5 times and 1.4 times those with NEW-STE, respectively. The poor wavelength-resolving power with LDE-B is not serious for boron analysis in Fe $_2$ B. Figure 4 shows a comparison of Be K α peak profiles of the NiBe phase in Ni-Be alloy obtained by LDE-B and CER. The net intensity and P/B value with LDE-B are 16 times and 1.2 times those with CER, respectively. Figures 5a and b show boron distribution maps in the cross section of surface boronized steel, which were obtained by LDE-B and NEW-STE under the same conditions. The image quality and spatial resolution of the boron map with LDE-B are found to be better than those with NEW-STE, especially in low boron region. Figures 5c and d show beryllium distribution maps in Ni-Be alloy, which were obtained by LDE-B and

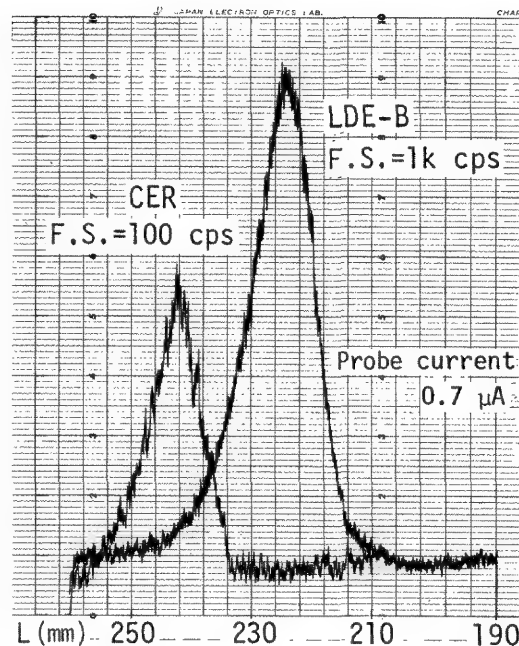
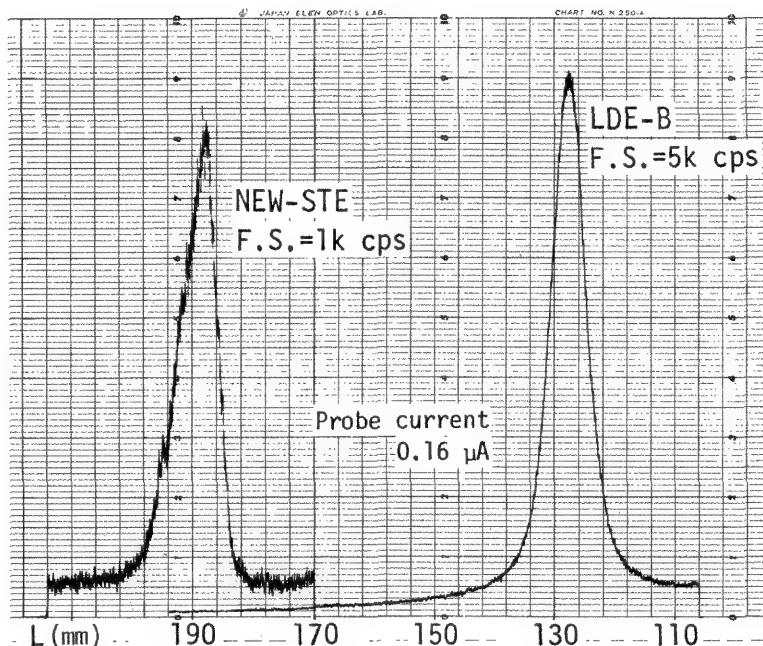


FIG. 3.--Boron-K α peak profiles of Fe₂B obtained by LDE-B and NEW-STE.

FIG. 4.--Beryllium-K α peak profiles of NiBe obtained by LDE-B and CER.

CER under the same conditions. In this case, the image quality and spatial resolution with LDE-B are clearly improved compared with CER.

Wavelength-dispersive Spectrometer (WDS) for Light-element Microanalysis. The WDS equipped with four dispersion elements, namely thallium acid phthalate (TAP), W/Si LSM for nitrogen and oxygen,⁴ LDE-C, and LDE-B, was tested and its ability was found to be better for the detection of light elements in a range from beryllium to silicon in electron probe microanalysis.

Conclusions

As dispersion elements for electron probe microanalysis, LDE-C, and LDE-B have been developed for carbon analysis and for boron and beryllium analysis, respectively. The sensitivity A/\sqrt{B} of carbon detection in low-alloy steel with LDE-C is 1.7 times that with NEW-STE. The B K α net intensity, P-B, and P/B value of boron in Fe₂B with LDE-B are 5.5 times and 1.4 times those with NEW-STE, respectively. The Be K α net intensity and P/B value of beryllium in NiBe with LDE-B are 16 times and 1.2 times those with CER, respectively.

References

1. T. W. Barbee, Jr., "Sputtered layered synthetic microstructure (LSM) dispersion elements," *Proc. Topical Conference on Low Energy X-ray Diagnostics*, New York: Am. Inst. Physics, 1981, 131.
2. B. L. Henke et al., "Low-energy x-ray interaction coefficients," *Atomic Data and*

Nuclear Data Tables 27: 1, 1982.

3. J. V. Gilfrich et al., "Layered synthetic microstructures as dispersing devices in x-ray spectrometers," *Appl. Spectroscopy* 36: 58, 1982.

4. K. Kawabe et al., "Coated multilayer dispersion element for x-ray microanalysis," *Proc. 11th Intern. Congr. EM*, Kyoto, 1986, 569.

5. D. A. Sentner et al., "Electron probe microanalysis of Be in Cu-Be alloys with the use of a layered synthetic microstructure dispersion element," *Microbeam Analysis--1987*, 65.

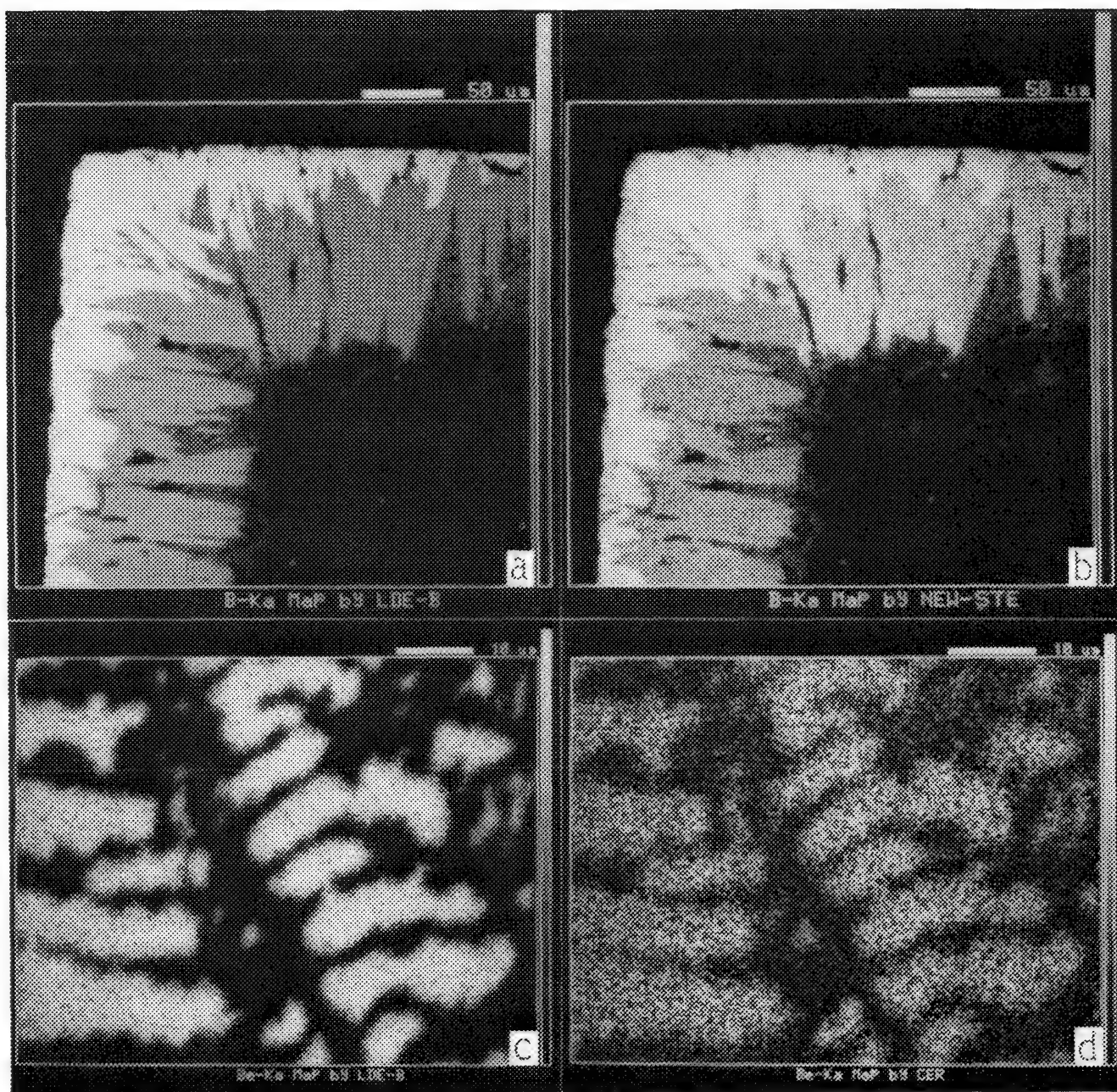


FIG. 5.--(a) (b) boron distribution maps of surface boronized steel obtained by LDE-B and NEW-STE, respectively. (c) (d) beryllium distribution maps of Ni-Be alloy obtained by LDE-B and CER, respectively.

IMPROVED ANALYTICAL CAPABILITY OF A NEW WDS/EDS COMBINED EPMA SYSTEM

Yoshitaka Nagatsuka, Masayuki Otsuki, Masaki Saito, and Shojiro Tagata

In recent years many electron probe micro-analyzer (EPMA) systems have come to be equipped with not only several wave-dispersive spectrometers (WDS), but also with an energy-dispersive spectrometer (EDS). Some of these systems have a capability to acquire data simultaneously from WDS and EDS and to process data with a host computer, realizing WDS/EDS combined EPMA systems.¹ However, in practical analysis, WDS and EDS are seldom used simultaneously because the measurement conditions, especially probe current, are quite different from each other, and it is hardly possible to use both spectrometers simultaneously. In ordinary cases, EDS is mainly used for quick qualitative analysis with lower probe current, whereas WDS is used for more precise or detailed analysis with higher probe current. Therefore, the WDS/EDS combined EPMA system offers few substantial improvements in analytical capability except convenience of use.

Under the circumstances, we have tried to bring out the original analytical merits of EDS without reducing the inherent analytical performance of WDS and have succeeded in developing a truly organic WDS/EDS combined EPMA system. We analyzed a sample of Allende stone meteorite with complex phases by this system and proved it possessed a substantially improved analytical capability in qualitative, quantitative, and area-mapping analyses.

Instrumentation

Figure 1 shows the schematic diagram of the WDS/EDS combined EPMA system, the JXA-8621. This system is a natural extension of the JXA-8600, JEOL's fundamental EPMA system, which (as previously reported in detail²) was designed to fit any modification in hardware and software. We added to the JXA-8600 a JEOL-developed EDS system that consists of a Si(Li) detector, EDS controller that includes a multichannel analyzer with EDS spectral display control and a general graphic display control, and a color monitor. The Si(Li) detector has five selectable apertures (0.12, 0.2, 0.4, 1.3, and 4 mm in diameter) and two selectable time constants (4 and 8 μ s). The EDS controller, equipped with two sets of microprocessors, has a capability of displaying WDS spectra or area maps while EDS spectra are being acquired. So it is possible to use this EDS system under a multitasking environment of the host CPU (HPU), where the EDS spectral data acquisition and other graphic displays are simultaneously executed.

The connection between HPU and EDS system

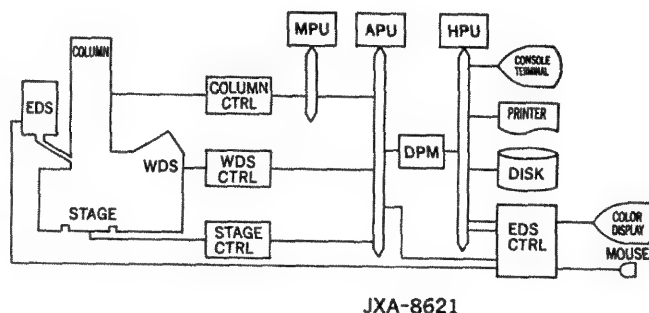


FIG. 1.--System block diagram of JXA-8621.

is made by two lines: the EDS control commands are transmitted through the serial line, and the WDS/EDS spectral data and area mapping data are transferred via the DMA line. Quantum x-ray counts generated from the specified EDS color ROIs are directly measured by data acquisition processor (APU). This facility is very effective for enabling simultaneous acquisition of WDS and EDS x-ray area mapping data.

Analysis Program

The databases of all the analysis programs, including qualitative, quantitative, and line and area mapping analysis programs, are the same as the conventional ones of JXA-8600, because we have taken EDS data into account from the beginning of JXA-8600 series instrumentations. Outlined below are some of the features that have been newly added in building the WDS/EDS combined system.

Qualitative Analysis. This program has four analysis modes: WDS only, EDS only, WDS/EDS parallel, and WDS/EDS serial mode. In the WDS/EDS parallel mode, WDS (maximum five channels), and EDS spectral data acquisitions are made simultaneously under the same probe condition. In the WDS/EDS serial mode, one can acquire WDS spectral data by changing the accelerating voltage or probe current after the EDS spectral data acquisition is finished. WDS/EDS spectral data during the data acquisition are displayed in real time. There are three display modes: WDS only, EDS only, and WDS/EDS mixed mode. It is possible to select any one of them. Spectral peak determination and the element identification from the determined peaks ranked as A, B, and C in the order of certainty of presence³ are automatically performed for WDS and EDS spectra simultaneously just after the spectral data acquisition is over. Acquired x-ray spectra of WDS and EDS are output onto a color display with the identified element labels at the corresponding peak positions. Manual peak identi-

The authors are with JEOL Ltd., 1-2 Musashino 3-chome, Akishima, Tokyo 196, Japan.

fication by KLM marker can be made for WDS and EDS spectra. This function is especially useful for reaffirming the automatically identified element peaks and removing the misidentified element labels if there are any.

Quantitative Analysis. It is possible to make a quantitative analysis of a sample for a maximum of 22 elements, in which each element is selected and measured by WDS and EDS. If we use both WDS and EDS, we can specify either the parallel or serial mode as in qualitative analysis. If we select the serial mode, we can change the probe current corresponding to WDS or EDS. This facility represents a significant advantage in analyzing beam-sensitive samples. In practical analysis, an element whose concentration is higher than 5 wt% or whose atomic number is greater than 10 can be measured by EDS without impairing the quantitative accuracy.

Area-mapping Analysis. A maximum of eight signals among several x-ray signals from WDS (maximum five channels) and/or EDS-ROIs (maximum eight channels) and/or an image signal (SEI or BEI) can be acquired simultaneously by use of stage scan or beam scan, stored on disk and displayed in real time. It is possible to change the accelerating voltage or probe current when measuring maps by WDS and EDS separately from changing the measuring sequence. As to the mapping display, three image storing memories are available, and in each of them a maximum of 128 levels of colors or black-and-white gray scales can be set. Furthermore, four types of display modes are available: 1, 2, 4, and 9 maps display mode. In each image memory, we can easily make a color modification or a line analysis for any one of the displayed maps by manipulating the mouse attached to the EDS controller.

Manipulation Job Program. We added some 20 EDS control commands to the original control commands of EPMA. Control commands such as "Acquire spectrum," "ROI setting," and "Display KLM marker" are included in these EDS control commands. Using this program, we can control EDS as well as the total EPMA instrument itself from the single keyboard as if we were controlling it manually.

Some Applications

Using the above mentioned analysis programs, we analyzed a sample of Allende stone meteorite and obtained surprisingly good results shown below.

Example of Qualitative Analysis. We used the WDS/EDS serial measuring mode in this analysis. We did not change the probe condition but used the 1.3mm-diameter aperture for the EDS detector. The analyzed point is near the center of the round shaped inclusion (chondrule) shown in Fig. 8. The elements identified by each spectrometer are as follows:

By EDS:

A-rank: Mg, Al, Si, P, S, Ca, Fe, Ni, Br, Mo
B-rank: Na, Cr

By WDS:

A-rank: C, N, O, Na, Mg, Al, Si, P, S, Ca, Cl, Fe, Ni
B-rank: K, Ti, Co, Mo, Yb
C-rank: Sc, V, Re

From these two lists, we can conclude that the elements that are definitely present in this chondrule are:

C, N, O, Na, Mg, Al, Si, P, S, Ca, Cr, Fe, Ni

The elements Br and Mo, listed on the A-rank elements identified by the EDS spectrum, are misidentified by the near-identical energy peaks of Al K α and S L α , respectively. For the other elements listed on the B and C-rank elements identified by the WDS spectra, more detailed investigation is needed to decide whether the identified elements are definitely present or not. Figure 2 shows the mixed display of WDS/EDS with the identified element labels. Figure 3 shows the WDS only display with second-order KLM marker.

Example of Area-mapping Analysis. We measured 9 maps by WDS (Mg, Al, Si, P, S, Ca, Cr, Fe, Ni), 5 maps by EDS (Mg, Si, S, Ca, Fe), and 2 maps by image signals (SEI, BEI). Figure 4 shows nine maps display of these elements, in which Al, Ca, P, Cr, and Ni maps are taken by WDS, and Mg, Si, S, and Fe maps are by EDS. This stage scan area mapping data acquisition by WDS and EDS is simultaneously carried out under the same probe condition. In these maps we can clearly recognize the typical structure of a stone meteorite (chondrite) that includes various round shaped chondrules with different element compositions. Figure 5 is a comparison of maps taken by WDS and EDS for Mg and Fe. The upper two maps are taken by WDS and the lower two maps are taken by EDS. Although the counting rate of EDS is 1/50 compared with the one of WDS, these two pairs of maps by WDS and EDS resemble each other quite closely, and are good enough for practical use. Figure 6 shows a full display of Mg by WDS with concentration values. Figure 7 shows the concentration histogram of the element. We can easily modify color by operating the mouse on this histogram. Figure 8 shows a close-up display (Fe distribution, 500 \times) of the small chondrule shown in the center of Fig. 6, taken by WDS with beam scan. We can observe the very detailed structure of this peculiar chondrule. In this map, we can recognize no defocusing effect of WDS; however, for much lower magnification maps ($\sim 200\times$), the defocusing effect appears in WDS maps but not in EDS maps. Therefore, EDS is more suited for low-magnification beam scan maps than WDS.

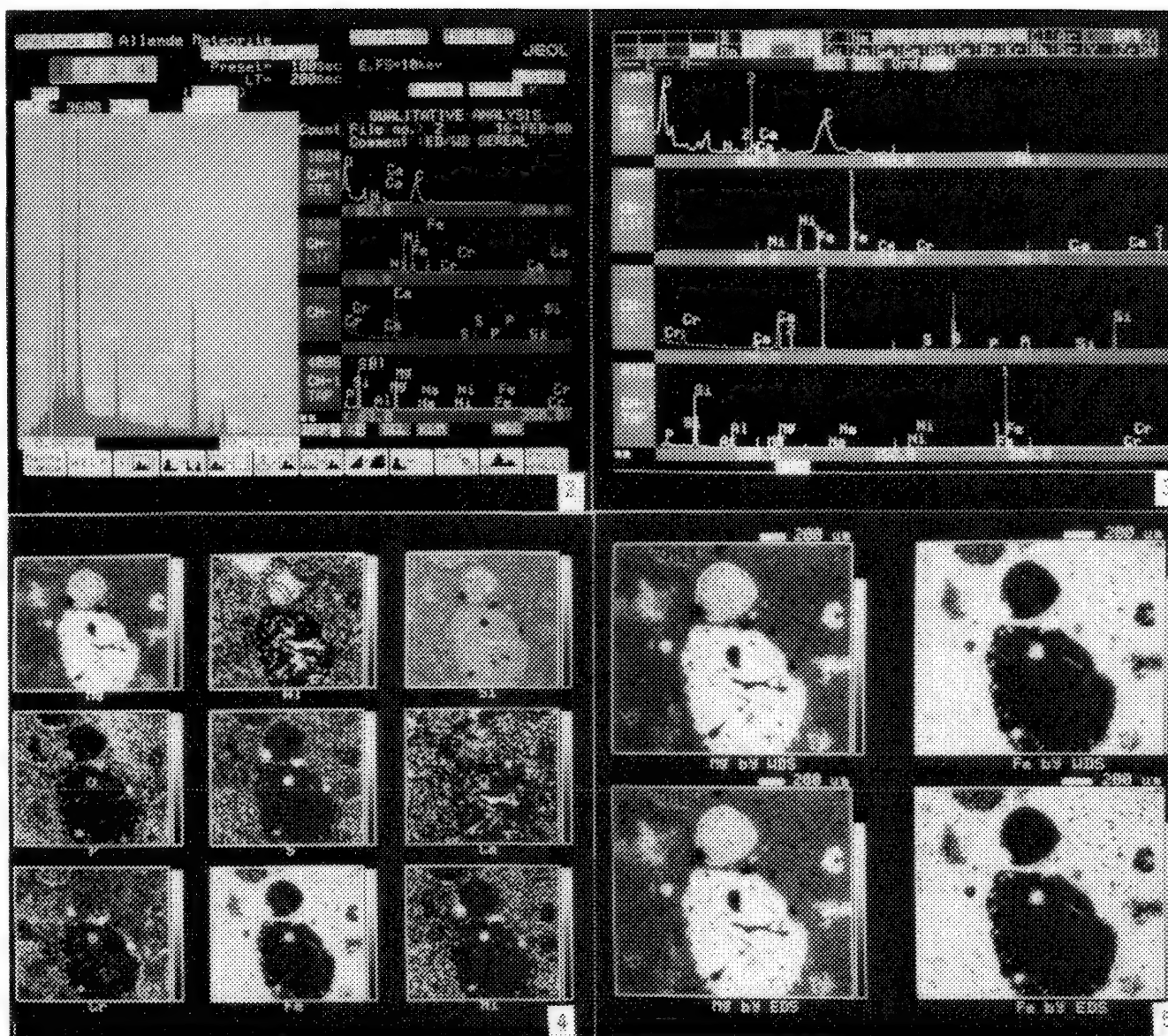


FIG. 2.--Mixed display of EDS/WDS spectral data with identified element labels.

FIG. 3.--WDS only display with KLM marker.

FIG. 4.--Nine maps display of Mg, Al, Si, P, S, Ca, Cr, Fe, Ni by WDS and EDS.

FIG. 5.--Comparison of WDS and EDS maps for Mg and Fe.

Conclusions

We have introduced in this paper a new WDS/EDS combined EPMA system and its applications. Even the few application examples demonstrate a significantly improved analytical capability for this WDS/EDS combined system. We summarize the improved points of the WDS/EDS combined EPMA system as follows:

- In qualitative analysis, a more reliable element identification is possible by use of both WDS and EDS spectral data.
- In quantitative analysis, a more rapid and delicate analysis is possible by appropriate selection of WDS and EDS.
- In area mapping analysis, a more rapid analysis is possible by use of both WDS and EDS, and defocusing free maps are available by EDS for low-magnification beam scan.

These results are accomplished by use of the same databases for WDS and EDS, and above all by accommodation of the facilities which make possible data acquisition from each spectrometer under its best measurement conditions.

References

- D. E. Newbury, "Compositional mapping of thick specimen," *Microbeam Analysis--1985*, 204.
- Y. Nagatsuka et al., "A new automated EPMA system with distributive processing capability," *Microbeam Analysis--1987*, 57.
- T. Miyokawa et al., "A new rigorous identification method for constituent element in EPMA," *11th ICXOM*, 1986, 555.

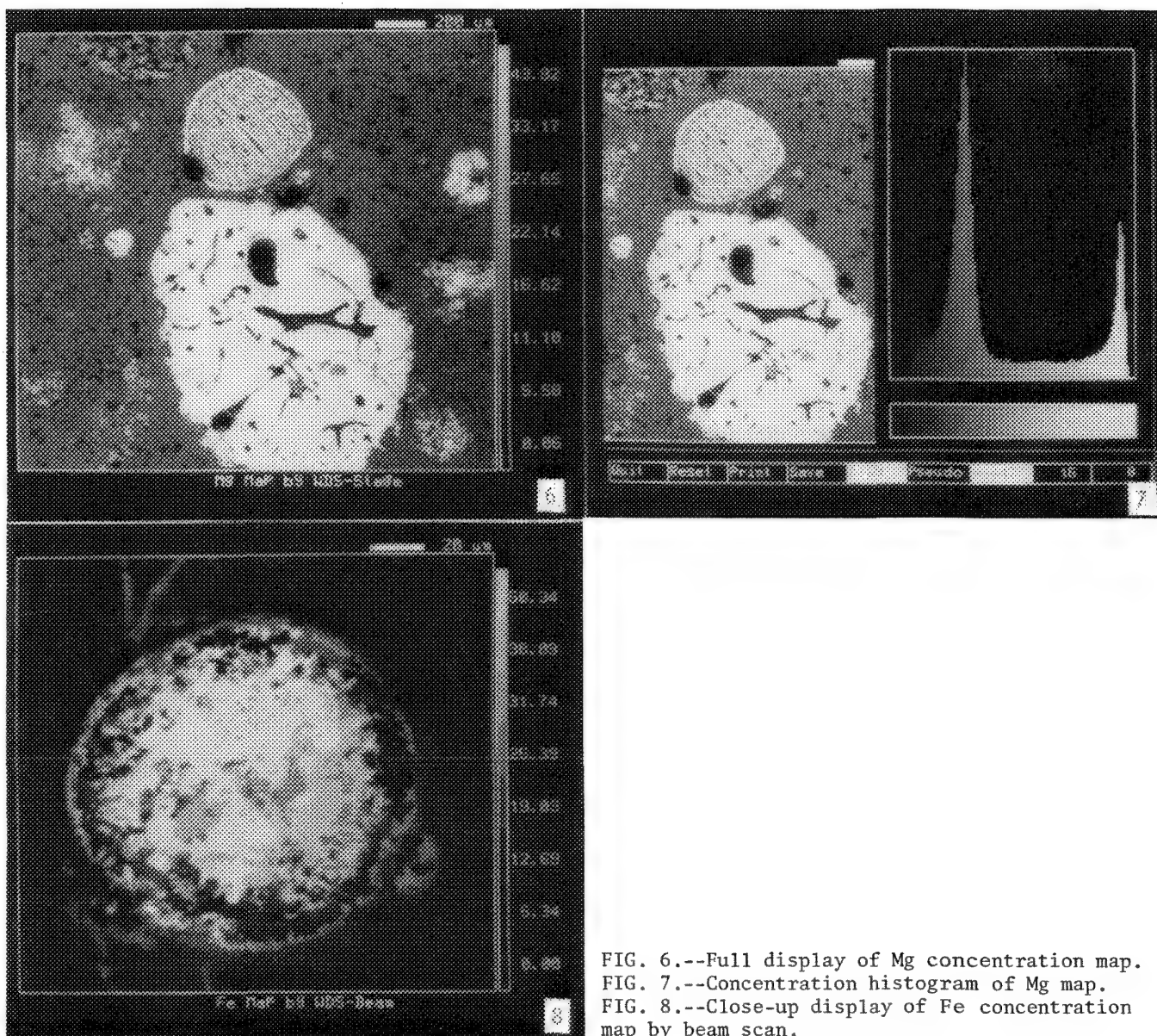


FIG. 6.--Full display of Mg concentration map.
 FIG. 7.--Concentration histogram of Mg map.
 FIG. 8.--Close-up display of Fe concentration map by beam scan.

APPLICATION OF MICRO-IMAGING TO COMPUTER-CONTROLLED SCANNING ELECTRON MICROSCOPY

W. J. Mershon, W. H. Powers Jr., H. P. Lentz, and G. D. Baughman

In the past manual methods were required for the complete characterization of particle samples by a scanning electron microscope (SEM). The sample would be characterized by having an operator search the sample for particles with a size, morphology, and chemistry of interest, and then spectra and micrographs of selected particles would be collected. A limiting aspect of performing this operation on a statistically significant number of particles was that the analysis required an inordinate amount of time. In addition, it was possible for the operator to bias the analysis through the selection process by choosing, for example, esthetically pleasing particles rather than particles representative of the sample. Also, summarizing all the data collected could be very time consuming and difficulties could be encountered in establishing correlations between chemistry and morphology.

With the advent of automated image analysis in the late 1970s, it became possible to perform such analyses in an automated fashion. By use of algorithms of various levels of sophistication to size particles and process x-ray data, information such as the size distribution of particles and tables that describe area, mass, and aspect ratio distributions, as well as average composition, could be obtained. Also, particles could be assigned to various classes based on chemistry, size, and shape.

Although this technology was a significant step forward in the evolution of scanning electron microscopy, it did not provide information on the morphology and texture of particles, which are frequently important to the interpretation of the data. In addition, with access to detailed information about particle surface texture, shape, and spatial relationships, it is often possible to draw conclusions about the conditions under which they were formed, as well as their effect on the environment. Such information is not available with current automated image analysis systems.

The present paper describes an analysis method that integrates automated image analysis with automated micro-imaging. Micro-imaging is the acquisition and storage of individual high-resolution images and is an evolution of an existing analysis method developed by U.S. Stell and Tracor Northern.¹⁻³ Automated particle analysis with micro-imaging is made possible by interfacing an X-ray microanalyzer to a conventional SEM, for the purpose of controlling the energy-dispersive spectrometer (EDS), automated stage, and digital scan

generator. In addition to collecting size, shape, position, and spectral data for an individual particle, micro-imaging enables high resolution images of the analyzed features to be acquired and stored. Images of each particle detected in an analysis can be saved. Alternatively, only a selected set of particles can be saved by use of an algorithm with x-ray, size, and shape information as the selection criteria.

Automatic particle analysis software uses a digital scan generator in the image analyzer to step the beam across a field of particles. The returned video signal is used to differentiate particles from the background substrate. When a particle is detected, a series of rotated chords drawn across it with the beam establishes its size and aspect ratio. The beam is then positioned at the particle's centroid for EDS acquisition.

To accomplish automated micro-imaging three major additions to the existing automated particle analysis have been made. The first is the use of automated stage positioning. By defining a local Cartesian coordinate system on the sample, one can store the absolute position of each particle that is analyzed. Thus, one can relocate and re-analyze particles of interest at a later date by re-initializing the system on the basis of two alignment marks on the sample. The computer can then be asked to drive the stage to a specific x,y position on the sample's coordinate system.

The second addition is the use of the digital scan generator to control the raster size and location (digital magnification and position), as well as the brightness and contrast of the resulting image. The digital beam control system interfaces the image analyzer to the SEM scan coils and electron detectors by a series of programmable digital-to-analog converters (DAC). Thus, under software control, it is possible to alter the magnification and position of the digital raster dynamically to allow micro-images of appropriate features to be acquired.

The third addition is the establishment of a high-speed data link to an off-line computer workstation. This link allows the transmission of images in real time during collection of an x-ray spectrum for the particle currently being analyzed, and provides the option of storing the images on the hard disk of the analyzer or immediately moving them to an off-line workstation, where they can be reviewed and stored. The images and data are stored on removable media so that they may be transported to remote sites or archived for future use. Figure 1 shows the

The authors are with RJ Lee Group, Inc., 350 Hochberg Rd., Monroeville, PA 15146, except G. D. Baughman, who is with Tracor Northern, Middleton, WI 53562.

flow of information between the three major elements in the system.

Micro-imaging has also been implemented in a manual mode on the Tracor Northern TN-5502 micro-analyzer. A digital image of the microscope field of view is displayed on the TN-5502 monitor. By positioning a cursor on a particle or feature in that image, one can pan and zoom the raster to display a selected portion of the original image at a higher magnification. The brightness and contrast of this micro-image can be adjusted through software so that microscope control settings need not be changed. Most of image and spectral functions normally available on the TN5502 are also available for analysis of the micro-image. This mode greatly facilitates rapid location and analysis of features of interest.

In summary, a method for automatically collecting, archiving, and summarizing data about a particulate sample has been developed. Existing hardware was utilized to its full potential and existing particle analysis software was enhanced to enable the collection and storage of micro-images and to provide a high

degree of automation. With this method it is now possible to describe a sample more efficiently than with manual methods alone, and more effectively than in existing automated analyses. For the future, the data-collection and storage techniques described above should make possible the use of technologies such as artificial intelligence, sophisticated source receptor modeling, and fractal geometry in the analysis of particulate samples.

References

1. R. J. Lee, W. A. Spitzig, J. F. Kelley, and R. M. Fisher, "Quantitative metallography by computer-controlled scanning electron microscopy," *J. of Metals*, 20-25.
2. R. M. Fisher, R. J. Lee, and J. J. McCarthy, "Applications of computers in electron microscopy," presented at 39th Ann. Meet. EMSA, 1981.
3. R. J. Lee, J. S. Walker, and J. J. McCarthy, "Microimaging: A link between manual and automated particle analysis," *SEM/1985*.

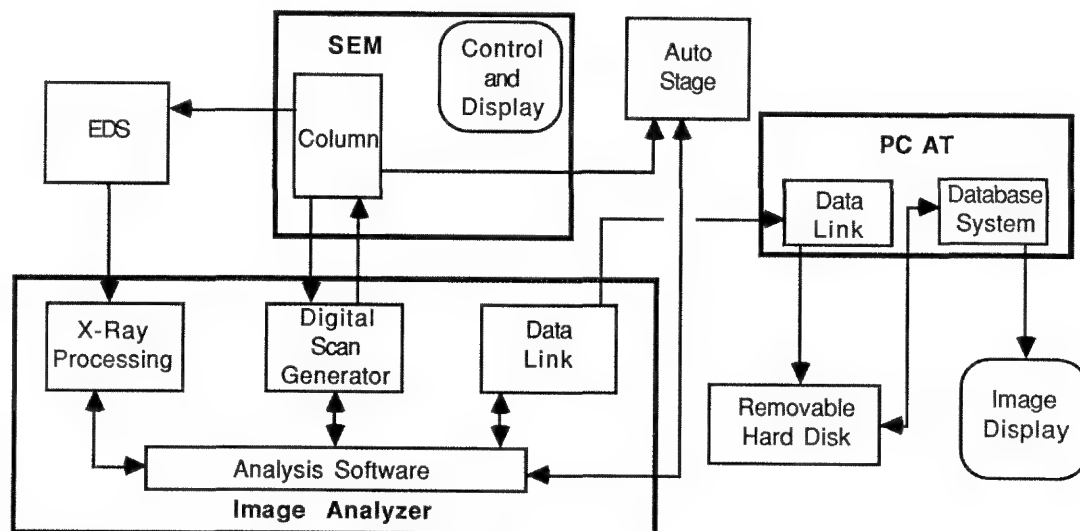


FIG. 1.--Block diagram of CCSEM with micro-imaging.

LASER MICROPROBE MASS SPECTROMETRY: POSSIBILITIES AND LIMITATIONS

L. Van Vaeck, J. Bennett, W. Lauwers, A. Vertes, and R. Gijbels

Laser microprobe mass spectrometry (LMMS) employs an intense UV pulse from a focused high-power laser to evaporate and ionize a micro-volume ($\sim 1 \mu\text{m}^3$) of solid samples at relatively elevated energy density (10^6 – $10^{11} \text{ W cm}^{-2}$). The ions produced by the interaction of photons with the condensed phase are then mass analyzed in a time-of-flight mass spectrometer and yield a complete mass spectrum on each single laser shot. Depending on the operating conditions, elemental information can be obtained, extensive speciation possibilities for inorganic species are available, and organic compounds can be characterized by means of structurally relevant molecular and fragment ions. Quantitation is difficult, but LMMS remains an excellent tool for qualitative local analysis of microscopic samples, which can be dielectric or conductive. Within the range of microbeam techniques, the method is a valuable complement to the electron and ion microprobe.

The idea of combining lasers with MS is not new and has been successfully applied to a variety of analytical purposes, e.g., pyrolysis, classification of complex materials, soft ionization of organic thermolabile compounds, as an alternative to the spark source mass spectrometer, and for bulk analysis at high power density. The first part of this presentation deals with these types of instrumentation for organic and elemental analysis and surveys the functional principles of the commercially available LMMS equipment: LAMMA 500 and 1000, and the LIMA 2A.

The polyvalent nature of LMMS results from the remarkable ease of operation of the instrument under greatly varying local conditions. The applications are unlimited. Even at the present state of the art, this statement comes very close to the truth. Review of the topics of the contributions at the recently organized triennial users' meeting yields a vast panorama of the current research in various fields. The workshop's proceedings¹

L. Van Vaeck and R. Gijbels are at the Department of Chemistry, University of Antwerp (UIA), Universiteitsplein 1, B-2610 Wilrijk, Antwerp, Belgium; J. Bennett is at the Department of Chemistry, Texas A&M University, College Station, Texas 77843; W. Lauwers is at Janssen Pharmaceutica, Turnhoutseweg 30, B-2340 Beerse, Belgium; and A. Vertes is at the Central Research Institute for Physics of the Hungarian Academy of Sciences, P.O. Box 49, H-1525 Budapest, Hungary. L. Van Vaeck and A. Vertes are indebted to the National Science Foundation (NFWO) of Belgium for its support; J. Bennett thanks the Fulbright/Hays Commission for a Visiting Researcher grant.

include papers on elemental determination of trace constituents, accurate isotope measurements, inorganic speciation, surface analysis and depth profiling, organic structure characterization in microprobe applications (but primarily on pure products), and basic research on ion formation, energy distribution, and trajectory calculations. Frequently, there is an attempt to overcome the problems arising in quantitation of complex materials, by application of a statistical treatment of fingerprint spectra. This survey elaborates on the demonstration of the versatility and outstanding potential as well as the actual limitations of LMMS in practice.

The last part of the present contribution is dedicated to research examples from the author's laboratory. During the last five years, our investigations have gradually concentrated on organic compounds. A major problem in LMMS arises from the extreme dependence of the results on the locally applied (i.e., microscopic) experimental conditions, especially when particle analysis is attempted. As a matter of fact, specific (and often very important) features of the recorded mass spectra may become prominent or completely disappear, depending on the way the operator uses his feeling and experience to cope with a variety of "hidden" parameters (e.g., physicochemical properties of the analyzed material on the micron level) that are essential to the absorption and dissipation of energy. Also important are particle size and laser focus, which critically determine the actual power density in the sample region, where ionization takes place.

We elaborated an empiric protocol, based on the use of the MS parameters (resolution, calibration, peak shape) to monitor the locally achieved experimental conditions. It appears to represent a satisfactory means of insuring the reproducibility of the results, even on a long-term basis, which is not totally obvious in LMMS. Primarily intended for organic compounds, analysis is performed under threshold conditions.

The present knowledge of laser-induced ion formation is fairly limited, particularly for organic compounds. Moreover, LMMS seems to be characterized by an ambiguity: complex disintegration of very stable molecules contrasts with the soft ionization-type features observed for thermolabile analogs. Generally, fragmentation is abundant, but the detected signals look unfamiliar in comparison with those from conventional MS techniques. Nevertheless, the major aim of the LMMS research remains the characterization of compounds intractable by other techniques. Hence, we started a systematic study of organic poly-

functionals, covering a wide range of polarity and structure. Interpretation was attempted initially on the basis of a model, including a set of tentative hypotheses about the desorption and ionization (DI) mechanisms in LMMS. Meanwhile, substantial experimental evidence could be obtained, sustaining some controversial aspects of our DI concepts, such as the role of electron ionization and thermal degradation. Selected examples are presented to illustrate the practical usefulness of this empiric approach in respect of organic-structure determination. Also, the application of LMMS to molecules, which traditionally cause problems in conventional MS (e.g., N oxides, salts, etc.), are discussed. The characteristic and sometimes remarkable complementary distribution of structural data obtained for both positive and negative ions remains an intriguing aspect of LMMS. At this moment, we feel that LMMS deserves an appropriate place among the already well-established methods of organic mass spectrometry.

Since our methods of procedure primarily aim at qualitative analyses, the characterization of organic mixtures also becomes an important challenge. Real quantitation cannot be utilized yet. However, principal component analysis by means of organic (i.e., structurally relevant) ions is reasonably feasible in rather simple mixtures--those containing up to, say, 5-10 constituents. Under threshold conditions, the mass spectra actually correspond to a simple superposition of the results for the individual analogs, and additional complications from plasma interactions appear to be negligible. An appropriate but not generally applicable sample preparation is required to insure a uniform particle-size distribution.

However, the ultimate goal remains the real microprobe applications, e.g., the in situ localization of a drug or metabolite in an embedded biological tissue sample. It is commonly accepted that the presence of such a complex and physico-chemically active matrix would lead to a variety of analytical problems. We therefore designed a series of model systems for sample simulation that makes provision for a stepwise introduction of the various interactions between the target and the surrounding environment. To our surprise the presence of a polymer barrier layer imposes a major inherent limitation. In other words, only targets originally present within the upper 5-10 nm of a 1 μ m sample effectively contribute to the detected organic ion current. Moreover, the degree of fragmentation seems to be correlated with the distance of the target from the specimen surface. This observation makes the use of selected peaks to characterize the presence of a given compound in the analyzed microvolume questionable. Nevertheless, it is feasible in a series of well-selected test cases, e.g., characterization of pigments in cryosections of microlichens and detection of organic complexes in layered silicates.

We recently found that the application of the organic protocol and operation under

threshold conditions can be profitable for inorganic speciation as well. The well-known volatilization and decomposition processes that occur during the electrothermal graphite furnace atomic absorption spectrometry (ETAAS) measurement of tin in sulfate matrices were studied by LMMS analysis of the aerosols collected from the emanating smoke. From a microscopic sample, we could obtain for the first time positive evidence to support the presence of some compounds in the gas phase. Indeed, to date ETAAS mechanisms have been based primarily on oven residue characterization, molecular absorption data (which are not very specific), and thermodynamical considerations. LMMS measurement of the aerosol in the high-laser-intensity, high-power density mode of operation, according to common practice for inorganic analyses, yielded complex spectra and partly misleading information. In contrast, under threshold conditions, the majority of cluster signals could be eliminated, which led to very simple mass spectra that could be more or less directly related to the major component. The results indicate that formation of $\text{SnO}(2)$ seems to be overestimated in comparison to the release of SnCl_2 , whereas the sulfate matrix is primarily detected by the pyrosulfite form in the gas phase.

Finally, there has been an effort to gain a better understanding of the laser-induced ion formation by model calculations on semi-infinite targets. In accordance with the experimental data, some distinction between laser desorption and plasma ionization could be explained in terms of classical absorption at low-power density or ignition by resonant plasma interactions at high irradiances. The theoretical approach applies to the reflection geometry (instead of the transmission mode for the LAMMA 500 used in our experiments), but still provides some insight regarding the various parameters involved in the relationship between the laser output and the local energy regime in which ionization takes place. Additional information is gained about the energy distributions of the released ions, matrix assisted desorption, and formation of shock waves.

For the sake of brevity, this text must be confined to the summary of the main topics. However, complete information on the results is available in Refs. 2 and 3.

References

1. F. Adams and L. Van Vaeck, Eds., *Proc. 3rd Intern. Laser Microprobe Mass Spectrometry Workshop*, Antwerp, 1986, 1-243.
2. L. Van Vaeck, J. Bennett, W. Lauwers, A. Vertes, and R. Gijbels, "Laser microprobe mass spectrometry: Possibilities and limitations," *Mikrochim. Acta* (submitted).
3. A. Vertes, P. Juhasz, M. De Wolf, and R. Gijbels, "The role of energy deposition processes in the understanding of microprobe analysis mechanisms," *Scanning Microscopy* (submitted).

IN VITRO DRUG EFFECTS MONITORED BY SINGLE BACTERIAL CELL MASS ANALYSIS WITH LAMMA

Ulrich Seydel, M. Haas, and B. Lindner

To judge the effectiveness of a treatment of a bacterial infection it is necessary to get direct information on the effect of the therapeutic agent on the physiological state (e.g., viability, ability to multiply) of the bacterial organisms. For nearly all types of bacterial infections this information is relatively easily obtained by the application of established microbiological techniques, which are based on the in vitro cultivability of the respective bacterial species. However, these techniques fail in the case of Hansen's disease (leprosy), which is caused by the in vitro noncultivable mycobacterial species *M. leprae*. The control of the effectiveness of newly developed antileprosy drugs is therefore at present only practicable in vivo in test animals. For several obvious reasons--length of time until results are available (approximately 10 months for the so-called mouse food-pad test), large number of test animals--efforts have been made toward the establishment of alternative test systems.¹⁻⁴ We have started to develop a method based on the mass spectrometric analysis of a limited number of single bacterial organisms isolated from patient or animal biopsies with the laser microprobe mass analyzer LAMMA 500. In that way, information on the effect of a drug is obtained from the measurement of the intracellular content of physiologically important cations (in particular Na^+ and K^+) and of fragment ion spectra from the organic matrix, which serve as fingerprints^{5,6} to establish numerical similarity relationships among various bacterial preparations. Moreover, this single-cell mass spectrometric methodology could be adapted to rapid in vitro drug screening,⁷ in which *M. leprae* bacteria isolated from biopsies are kept in artificial media for typically 48 h (which, of course would not allow their multiplication but a limited metabolism) and are exposed to various concentrations of the drug. The examples given in this paper demonstrate the close correlation between the results from intracellular Na^+ , K^+ -ratio measurements and the multidimensional scaling of the mass fingerprints.

Experimental

The bacteria are isolated either from tissue or--in the case of cultivable species--

The authors are at Forschungsinstitut Borstel, Division of Biophysics, D-2061 Borstel, Federal Republic of Germany. The project was financially supported by the Federal Minister for Research and Technology under grant 03 8667 and the German Leprosy Relief Association.

from culture broth, washed to remove extracellular contaminants, and prepared on Formvar-filmed EM copper meshes.⁸ From each preparation up to 500 organisms are mass analyzed for their intracellular Na^+ , K^+ -ratios to establish histograms of this value within a population (relative cumulative distributions). For fingerprinting, 120 organic fragment ion spectra are registered from each sample, from which four average spectra over 30 single-cell spectra each are generated, and the inter- and intrastain relationships are calculated. A detailed description of the applied multivariate evaluation procedures is given elsewhere.⁵

For drug-interaction studies, bacterial cultures were inoculated in Middlebrook 7H9 medium with 10^5 cells/ml and the drug (rifampicin, Merck, Darmstadt, FRG) was added in various concentrations at the beginning of exponential growth.

Results

Figure 1 gives relative cumulative distributions of the Na^+ , K^+ -ratios for two mycobacterial populations (*M. smegmatis* and *M. avium*), which had been exposed to two different concentrations of the same drug (rifampicin) for a time sufficient for a 10-fold multiplication under normal conditions. The curves corresponding to the two untreated controls are identical. As to the effect of the drug at both concentrations, obviously a significant difference in the degree of interaction (and hence of bacterial impairment) for the two species can be seen: the *M. smegmatis* population is more heavily affected than that of *M. avium*. However, the observed effect depends on concentration in both cases.

A qualitatively similar result is obtained from the numerical evaluation of the mass fingerprints of the bacteria of the same experiment as in Fig. 1. This result is shown in Fig. 2, where the two-dimensional nonlinear maps of the similarity relationships between the (a) *M. avium* and the (b) *M. smegmatis* samples prepared from the differently treated cultures are given. The average spectra (comprising 30 single cell spectra) are represented by a point on the map, and points belonging to the same sample are interconnected. The distance between the points is a measure of the numerical relationship between the corresponding spectra. Obviously, for *M. avium* (Fig. 2a) the similarity between the untreated control and the sample prepared from a population exposed to 2.5 $\mu\text{g/ml}$ rifampicin is closer than that between the latter and the sample treated with 50 $\mu\text{g/ml}$ rifampicin. For *M. smegmatis* (Fig. 2b) the situation is quite different, with a closer relationship between the two treated samples.

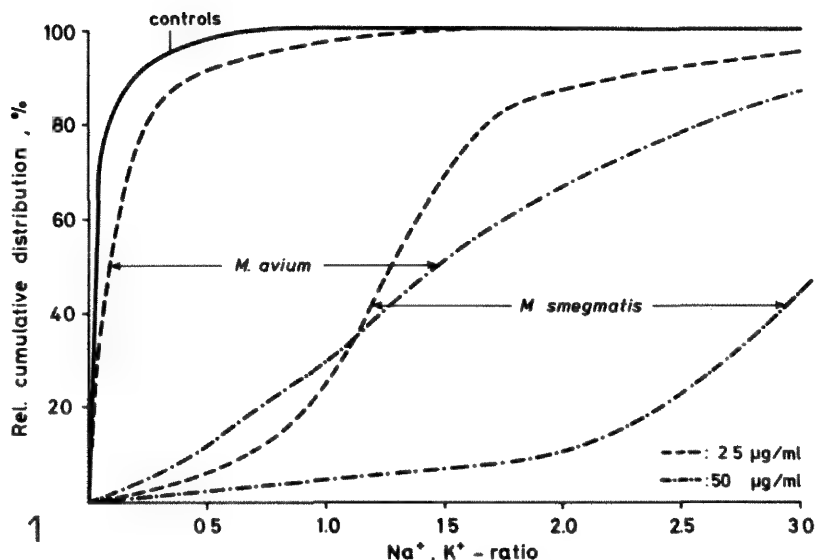


FIG. 1.--Relative cumulative distributions of intracellular Na^+ , K^+ -ratios of *M. smegmatis* and *M. avium* cultures exposed for 10 generation times to two different concentrations of rifampicin.

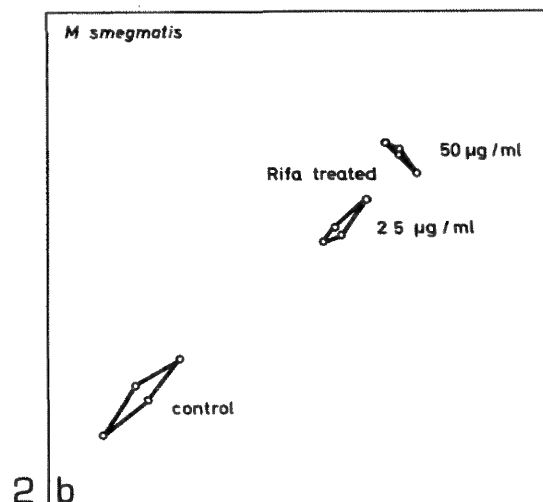
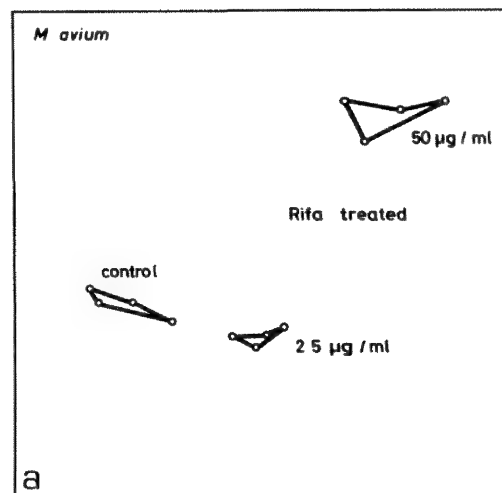
FIG. 2.--Two-dimensional nonlinear maps of similarity relationships between untreated controls and populations treated with different concentrations of rifampicin for (a) *M. avium*, (b) *M. smegmatis*.

To find out whether the effect of species-specific characteristics on the mass fingerprints is stronger than that of drug-induced characteristics, a cluster analysis was performed with three different mycobacterial strains (*M. avium*, *M. smegmatis*, *M. fortuitum*), which were compared with the corresponding rifampicin-treated (50 µg/ml) samples.

Figure 3 shows that a differentiation is first of all caused by the drug effects that lead to two clusters, which comprise the untreated control and the treated samples, respectively. The distance between these two clusters is so large that the dissimilarities between the spectra within one cluster cannot be resolved. However, close-up views of the clusters show that one can distinguish the three different samples within each cluster (see inserts). Similar experiments have been successfully performed to differentiate among samples of the same bacterial species that had been exposed to different drugs (results not shown).

Conclusions

These few examples illustrate the capability of the mass spectrometric analysis of a limited number of single bacterial cells for the acquisition of data on the effectiveness of drugs. The results from both the cation measurement and the mass fingerprint evaluation correspondingly show that different responses of different bacterial species to different drugs can be detected this way. Great advantages of this methodology are its low demand for bacteria and thus its applicability to in vivo studies of drug effects in Hansen's



disease, and the short time necessary for the evaluation of a biopsy (1-2 days). Effects of drugs on the intracellular Na^+ , K^+ -ratios as demonstrated in Fig. 1 for an in vitro experiment have already been measured in vivo for *M. leprae* isolated from patient biopsies and the kinetics for drug-induced bacterial impairments by dapsone (DDS) have been established in this way. Furthermore, early encouraging fingerprint evaluations hold out the promise of differentiating between in vivo treated and untreated *M. leprae*.⁶⁻⁷

It is our aim to establish in vivo kinetics of drug impairments of *M. leprae* for various drug regimes and (from a combination of the two evaluation procedures) on the occurrence of drug resistance.

References

1. J. T. Kvach and J. R. Veras, *Int. J. Lepn* 50: 183-192, 1982.
2. H. K. Prasad and J. Nath, *J. Med. Microbiol.* 14: 279-293, 1981.
3. A. M. Dhople, *Int. J. Lepn* 52: 183-188, 1984.
4. M. V. Mankar, R. Jagannathan, and P. R.

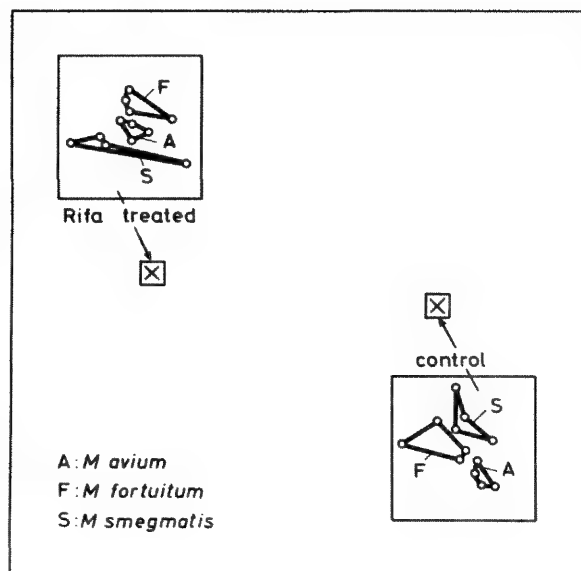


FIG. 3.--Two-dimensional nonlinear map of similarity relationships between untreated controls and preparations treated with 50µg/ml rifampicin for three mycobacterial species. Inserts: close-up views of discrimination within each of two main clusters.

Mahadevan, *J. Biosci.* 6: 709-716, 1984.

5. B. Lindner and U. Seydel, *J. Phys. Colloq.* (France) 45C-2 1: 565-568, 1984.

6. U. Seydel, B. Lindner, and A. M. Dhople, *Int. J. Lepr.* 53: 365-372, 1985.

7. U. Seydel and B. Lindner, *Lepr. Rev.* 57(Suppl. 3): 163-170, 1986.

8. B. Lindner and U. Seydel, *J. Gen. Microbiol.* 129: 51-55, 1983.

EFFECTS OF SAMPLE GEOMETRY ON INTERELEMENT QUANTITATION IN LASER MICROPROBE MASS SPECTROMETRY

I. H. Musselman, D. S. Simons, and R. W. Linton

Over the past decade, many studies have been conducted to address the prospect of multielement quantification by laser microprobe mass spectrometry (LAMMS). This paper assesses the effects of sample geometry on elemental quantification by LAMMS by the relative sensitivity factor (RSF) approach. The experiments described within address the most important aspects of the laser and spectrometer optimization procedure for quantitative elemental analysis, which is discussed in detail by Musselman.¹ These experiments include determining an einzel lens potential for the selective transmission of atomic ions as opposed to cluster ions,²⁻³ correcting ion intensities for detector saturation,⁴ and determining a laser energy for the reproducible ionization of all elements present in the sample. Unique among other quantitative studies, these experiments collected data under identical, optimized laser and spectrometer conditions from three distinct geometries (thin film, spheres, and shards) of glass samples bearing the same nominal elemental compositions. For the spheres and shards, data were collected from a range of particle sizes. The absolute elemental signal intensities and the RSFs calculated from these data are compared for the three sample geometries and for the different sphere and shard diameters.

Experimental Section

Sample Preparation. To address sample geometry effects in LAMMS quantification, three samples were made from NBS glasses each with the same nominal elemental composition but different morphologies: thin film, sphere, and irregularly shaped particle (shard).

Glass compositional characteristics desired for this LAMMS quantitation study included the presence of elements with a wide range of atomic numbers, concentrations, and ionization potentials. Alkali metals are unstable over time in a thin film morphology.^{1,5} For these reasons, NBS glass K2621 (which contains Mg, Si, Ca, Zn, Ba, and Pb, all in oxide form) was

I. H. Musselman conducted this research in the Center for Analytical Chemistry at the National Bureau of Standards while a graduate student at the University of North Carolina, Chapel Hill, NC 27514; she is currently in the Department of Materials Science and Engineering at North Carolina State University, Raleigh, N.C. D. S. Simons is with the Center for Analytical Chemistry at the National Bureau of Standards, Gaithersburg, MD 20899. R. W. Linton is at the University of North Carolina, Chapel Hill.

chosen as the target for thin-film preparation.

The sputtered thin film was made in a Gatan Dual Ion Mill, Model 600.⁶ Formvar-coated TEM grids mounted on a highly polished Si wafer were secured on a rotating sample mount (1 rpm) below the target so that they collected the sputtered glass material (2.5kV Ar beam, 0.25mA gun discharge current, 12 h). The film thickness, 3300 ± 200 Å, was determined by measuring the difference in height between the silicon substrate and the film with a profilometer (Tencor Instruments Alpha-Step 200). The sputtered thin film was determined to be homogeneous to within approximately 5% by use of a Cameca Camebax Model MB1 electron probe microanalyzer (EPMA). Its composition (which differs from the bulk target because of varying angular distributions of the sputtered elements, differential sputtering rates of elements in the target, and the presence of Cr and Fe contaminants in the film probably originating from the stainless-steel parts of the ion mill) was determined with a Japan Electron Optics Laboratory (JEOL) JEM 200 CX analytical electron microscope (AEM).⁷

The element oxide weight fractions determined for the thin film were used as a guide by the NBS glass group when making the bulk glass K2657 used for the preparation of the glass microspheres and shards. The spheres were made by dispersing micrometer-sized particles of K2657 in liquid nitrogen and aspirating them into a furnace at 1125 C. A vacuum applied at the end of the furnace draws the particles through the furnace where they are heated, form droplets, and reform as spheres upon cooling as they exit from the furnace. The spheres, which range in diameter from 1 to 6 µm, were collected on Formvar-coated TEM grids using an electrostatic precipitator. A slight change in chemistry from the bulk occurred in the preparation of these spheres due to the melting and the partial vaporization of Pb in the furnace. The composition of the microspheres was determined by use of the AEM.

The glass shards were prepared by dry grinding NBS glass K2657 into micrometer-sized irregularly shaped particles. The shards were mounted dry on Formvar-coated TEM grids. The composition of the glass shards is the same as that of the K2657 bulk glass and was determined with the EPMA. The average elemental weight fractions, $\pm 1\sigma$, are presented in Table 1 as determined for glass film, spheres, and shards.

LAMMS Analysis. All LAMMS measurements were made with the LAMMA-500 manufactured by Leybold-Heraeus. The energy of each laser pulse ($\lambda = 265$ nm, $\tau = 15$ ns) was measured

TABLE 1.--Thin-film, sphere, and shard composition.

Element	Element Weight Fraction ($\pm 1\sigma$)	Ionization Potential (eV)
Mg	0.081 \pm 0.011	7.646
Si	0.216 \pm 0.008	8.151
Ca	0.130 \pm 0.013	6.113
Cr	0.007 \pm 0.002	6.766
Fe	0.030 \pm 0.004	7.870
Zn	0.009 \pm 0.002	9.394
Ba	0.118 \pm 0.014	5.212
Pb	0.022 \pm 0.006	7.416
O	0.387 \pm -----	13.618

with a Laser Precision Corporation RjP-735 energy probe and Rj-7100 energy meter. The ions were detected by a 17 dynode Cu-Be venetian blind electron multiplier made by Thorn EMI Electron Tubes, Inc., 9643/4B, the gain of which was in the range of 10^6 . The signal from the electron multiplier was digitized by use of a LeCroy Research Systems TR8818 transient recorder. This transient recorder is nominally 8 bit, can digitize signal intervals as small as 10 ns, and has 32K of memory of which our laboratory currently utilizes 8.

Results

Optimization of Laser and Spectrometer Conditions. The purpose of the einzel lens is to collimate the ion beam for an improved transmission of ions through the mass spectrometer. However, these lenses are known to be subject to chromatic and spherical aberrations. Discrimination effects have been observed for atomic and polyatomic ions produced from TiO₂ and Ni/Au/S sandwich films when the einzel lens potential was varied.^{2,8} Both studies have confirmed the presence of broader and higher energy distributions for atomic ions compared to polyatomic species. For interelement quantitation, it is therefore necessary to optimize the einzel lens potential for the transmittance of the desired signal, in this case atomic ions.

Ten positive ion spectra were obtained from the sputtered thin film at each of 9 einzel lens potentials ranging from -749 to -1176 V while the other spectrometer conditions were kept constant.¹ The ten spectra at each of two input ranges obtained at each einzel lens potential were summed. The summed spectra obtained at 50 mV full scale from einzel lens potentials -749, -856, and -1070 V are presented in Fig. 1. Peak areas, normalized to 50 mV full scale, were determined from the summed spectra obtained at each einzel lens potential for ²⁴Mg, ²⁸Si, ⁴⁴Ca, ⁵²Cr, ⁵⁶Fe, ⁶⁴Zn, ¹³⁶Ba, and ²⁰⁸Pb. The maximum intensity of the atomic ions occurs between -962 and -1070 V.

Many cluster ions exist in the spectra taken from the sputtered thin film (Fig. 1). For quantitative analysis, it is desirable to maximize the atomic ion signal while minimizing the contribution of cluster ions as the latter increase the complexity of the mass spectrum and

often exist as isobaric interferences with atomic species, which makes it difficult to determine atomic intensities accurately. Cluster ion peak areas were determined from the summed spectra at each einzel ions potential for m/z 85, 88, 89, 96, 154, 183, 186, 187, 194, 202, and 211. The cluster ion intensities maximize at a slightly more negative potential (ca -1016 to -1124 V) with respect to the atomic ions (ca -962 to -1070 V).¹

The optimal einzel lens potential for quantitative analysis was determined from the ratio of an atomic ion (¹³⁶Ba) to various cluster ion intensities. The lens potential exhibiting the largest atomic to cluster ion intensity ratios for which there also exists sufficient atomic signal for quantitative analysis is -856 V. Compared to -1016 V, this setting results in a typical reduction in atomic signal of about a factor of 2, while increasing the typical atomic to cluster ion ratio by a factor of 9. This type of trade-off by selective energy filtering is also commonly used in secondary ion mass spectrometry to improve detection limits for atomic species where isobaric interferences from molecular ions may exist.⁹

For quantitative analysis, it is important to evaluate the characteristics of the detector system as well as to determine the laser energy necessary to achieve reproducible ionization of all elements in the glass samples. Simons reported a severe measurement bias of the LAMMA-500 detection system observed from the signal amplitude after it exited from the electron multiplier.⁴ The gain of the detection system appeared to decrease with increasing signal amplitude. Although the amplification problem was not corrected, Simons suggested a mathematical equation for its compensation. Equation (1) is a modified form of Simon's equation, where A is the actual integral intensity in the absence of detector saturation, and a₀ is a characteristic saturation intensity. When one is plotting an isotope ratio (high to low abundance) versus the integral intensity of the higher abundance isotope, Eq. (1) predicts a straight line with a₀ a fitting parameter:

$$A_{\text{corr}} = \frac{A}{1 - a_0 \cdot A} \quad (1)$$

Correction of peak integrals for detector saturation provides a more accurate quantitative interelement comparison.

Questions of detector saturation and laser energy for quantitative analysis were addressed by obtaining positive ion mass spectra from the sputtered thin film as a function of laser energy using spectrometer conditions optimized in earlier experiments.¹ Saturation parameters, which were determined from this data for Mg, Si, Ca, Cr, Fe, Ba, and Pb, using Simon's equation, are presented in Table 2.⁴ From Table 2, one can observe that there is no systematic variation of detector saturation with atomic number. It is believed that detector saturation depends primarily on the

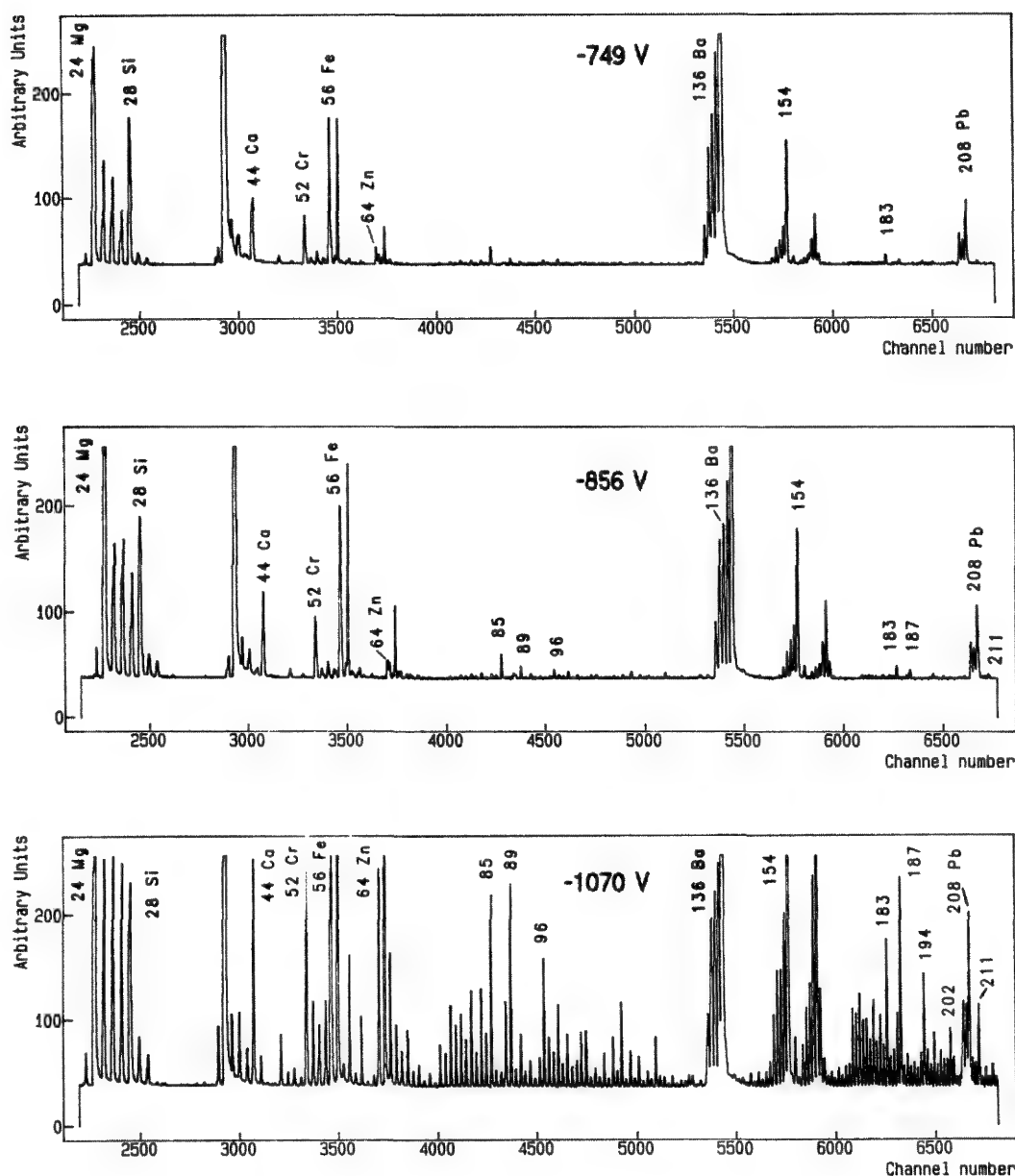


FIG. 1.--Positive ion LAMMS spectra obtained from sputtered thin film at einzel lens potentials of -749, -856, and -1070 V. Each spectrum is sum of 10 spectra.

TABLE 2.--Saturation parameters $\pm 1\sigma$.

Element Ratio	Saturation Parameter
$^{24}\text{Mg}/^{25}\text{Mg}$	$2.56\text{E-}05 \pm 1.48\text{E-}06$
$^{28}\text{Si}/^{29}\text{Si}$	$3.83\text{E-}05 \pm 4.86\text{E-}06$
$^{40}\text{Ca}/^{44}\text{Ca}$	$3.50\text{E-}05 \pm 2.55\text{E-}06$
$^{52}\text{Cr}/^{53}\text{Cr}$	$4.99\text{E-}05 \pm 6.90\text{E-}05$
$^{56}\text{Fe}/^{54}\text{Fe}$	$5.78\text{E-}05 \pm 1.42\text{E-}05$
$^{138}\text{Ba}/^{136}\text{Ba}$	$2.81\text{E-}05 \pm 4.59\text{E-}06$
$^{208}\text{Pb}/^{206}\text{Pb}$	$3.54\text{E-}05 \pm 2.47\text{E-}05$

magnitude of the signal, a charge-dependent phenomenon.

Peak areas determined from each spectrum were corrected for detector saturation using the parameters in Table 2. The corrected peak areas for ^{136}Ba are plotted vs laser energy in Fig. 2. This plot illustrates the elemental detection threshold at low energy and the manner in which the ion intensity increases with energy until a signal plateau is reached where the sample volume is maximally ionized.¹⁰⁻¹² The most reproducible elemental signal intensities are produced using a laser energy in this plateau region, which for the elements in this glass sample generally occurs at laser energies $> 1 \mu\text{J}$.

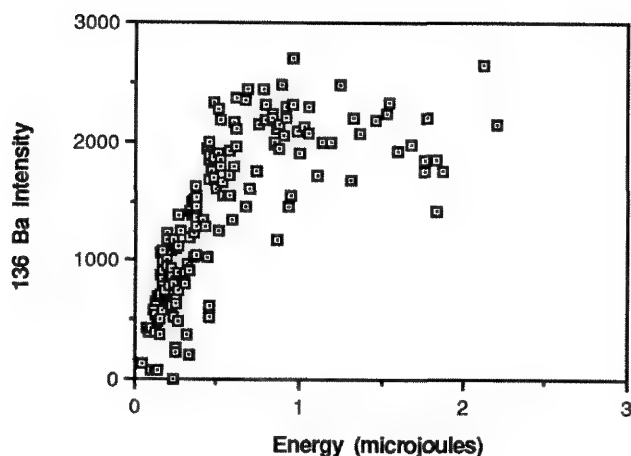


FIG. 2.--Plot of ^{136}Ba peak area corrected for detector saturation vs laser energy.

TABLE 3.--Correction of peak integrals for detector saturation.

Isotope	Isotopic Abundance	Average Uncorrected Intensity, $\pm 1\sigma$	Average Corrected Intensity, $\pm 1\sigma$	%Average Intensity Correction, $\pm 1\sigma$
^{24}Mg	79.0	18506 \pm 1616	35591 \pm 5639	46.4 \pm 4.2
^{25}Mg	10.0	4064 \pm 508	4544 \pm 633	10.4 \pm 1.3
^{28}Si	92.2	10481 \pm 2960	19131 \pm 9098	40.2 \pm 11.3
^{29}Si	4.7	862 \pm 383	898 \pm 412	3.3 \pm 1.5
^{40}Ca	96.9	20550 \pm 1317	75912 \pm 17478	71.9 \pm 4.6
^{44}Ca	2.1	1382 \pm 292	1456 \pm 325	4.8 \pm 1.0
^{52}Cr	83.8	1408 \pm 201	1517 \pm 233	7.0 \pm 1.0
^{53}Cr	9.5	257 \pm 63	260 \pm 64	1.3 \pm 0.3
^{54}Fe	5.8	448 \pm 91	460 \pm 96	2.6 \pm 0.5
^{56}Fe	91.8	4505 \pm 755	6170 \pm 1404	26.0 \pm 4.4
^{136}Ba	7.9	1920 \pm 246	2032 \pm 275	5.4 \pm 0.7
^{138}Ba	71.7	12368 \pm 784	19012 \pm 1871	34.7 \pm 2.2
^{206}Pb	24.1	682 \pm 164	699 \pm 172	2.4 \pm 0.6
^{208}Pb	52.4	1493 \pm 372	1581 \pm 414	5.3 \pm 1.3

The average percent intensity corrections for ^{24}Mg , ^{25}Mg , ^{28}Si , ^{29}Si , ^{40}Ca , ^{44}Ca , ^{52}Cr , ^{53}Cr , ^{54}Fe , ^{56}Fe , ^{136}Ba , ^{138}Ba , ^{206}Pb , ^{208}Pb signals, from the 24 spectra obtained using laser energies greater than or equal to 1 μJ , are listed in Table 3 with their corresponding isotopic abundances, average uncorrected intensities, and average corrected intensities. From these data, it is clear that the saturation characteristic of the electron multiplier is largely dependent on the absolute signal or charge available in the pulse rather than on

the nature of the isotope and/or element itself. The intensity corrections are small, 10%, for uncorrected peak areas of less than 2000. However, the correction rapidly increases above this value. The largest correction is 71.9% for ^{40}Ca , which has an average uncorrected intensity of 20 550.

Isobaric Interferences. Consideration was given to the possible isobaric interferences which exist for calcium and iron in this sample. The $^{28}\text{Si}^{16}\text{O}$ at m/z 44 overlaps with ^{44}Ca .

The contribution of $^{28}\text{Si}^{16}\text{O}$ to m/z 44 can be corrected using peak areas at m/z 45 or 46 corresponding to the $^{29}\text{Si}^{16}\text{O}$ and $^{30}\text{Si}^{16}\text{O}$ ions respectively. Since no peaks at m/z 45 or 46 were observed in these spectra, this interference is believed to be negligible and has therefore not been taken into account. Although there is conceivably an isobaric interference of $^{24}\text{Mg}^{16}\text{O}$ at m/z 40 for calcium, the correction procedure (multiplying the ^{44}Ca peak area by the $^{40}\text{Ca}/^{44}\text{Ca}$ ratio of 47.1) does not provide any additional information than is already available from the minor isotope, ^{44}Ca . The presence of a ^{54}Cr interference with ^{54}Fe at m/z 54, which ranges from 7 to 22% of the peak over this energy range, was corrected using the ^{52}Cr isotope and the $^{52}\text{Cr}/^{54}\text{Cr}$ ratio of 35.5. The ^{56}Fe peak is also subject to an isobaric interference, $^{40}\text{Ca}^{16}\text{O}$. As with calcium, it is best, however, to use the minor ^{54}Fe isotope for quantitation as the correction procedure for ^{56}Fe (analogous to Ca) does not provide any additional useful information. The use of these minor isotopes also minimizes the contribution of detector saturation as shown in Table 3 (^{40}Ca vs ^{44}Ca , ^{54}Fe vs ^{56}Fe).

Quantitative Analysis Based on Relative Sensitivity Factors. Thirty positive ion spectra were obtained each from the thin film, spheres (~ 0.5 , 0.8 , 1.0 , 1.7 , 2.1 μm in diameter) and shards (~ 0.5 , 0.8 , 1.0 , 1.7 μm in diameter) bearing the same nominal composition (Table 1) using optimized laser (2-3 μJ) and spectrometer (UToF -3000 V, ULENS -856 V, UREFL1 140 V, UREFL2 -2113 V, UCATH -6000 V, UMULT 2700 V) conditions.¹ Each spectrum was acquired simultaneously at two input ranges to the LeCroy transient recorders, 50 and 500 mV full scale.

The 30 spectra obtained from each sample were summed. The summed spectra for the thin film, 1.0 μm spheres, and 1.0 μm shards (Fig. 3) were collected at an input range of 50 mV full scale. For these spectra, many of the peaks are forced off scale in order to bring the lower abundance isotopes on scale. These spectra have a very low contribution from cluster ions, confirming the establishment of optimal einzel lens conditions for selective atomic ion transmission that is necessary for quantitative elemental analysis. The elemental peaks employed for quantitative analysis are labeled on these spectra along with the larger cluster ion peaks. The cluster ion for BaO , m/z 154, is present in the spectra obtained from all three geometries. For the thin film, a large peak is present at m/z 57 which is attributed to CaOH . The magnitude of this peak suggests that a large CaO interference is present at m/z 56 overlapping with ^{56}Fe . CaOH is also observed at a lower intensity in the shard spectra. A large peak, whose identity is unknown, is present at m/z 65 for the thin film sample only. It is possible that related species are present at neighboring masses, i.e., 64 and 66, contributing to the peak integral for Zn, which makes the Zn measurements unreliable for the thin-film sample. In the thin

film spectrum, a peak is present at m/z 162 attributed to BaC_2 or BaMg . Its presence suggests that CaC_2 or CaMg may also be an isobaric interference with ^{64}Zn . The sphere spectra exhibit peaks at m/z 59 and 157 attributed to CaF and BaF , respectively. The source of fluorine in the sphere preparation procedure is not known.

Peak areas were obtained from each spectral pair for the isotopes chosen for quantitative analysis: ^{25}Mg , ^{28}Si , ^{44}Ca , ^{52}Cr , ^{54}Fe , ^{64}Zn , ^{136}Ba . In response to the poor resolution of the lead peaks (Fig. 3) for all sample geometries, the area was obtained for all of the Pb isotopes from the envelope of peaks at m/z 206-208. The isotopes chosen for Mg, Ca, Fe, and Ba are the minor isotopes of these elements which are less subject to detector saturation (Table 3). Corrections were made to the isotopes of ^{25}Mg , ^{28}Si , ^{44}Ca , ^{52}Cr , ^{54}Fe , and ^{136}Ba for detector saturation using the parameters reported in Table 2. The ^{64}Zn peak was not corrected for saturation. The peak area for ^{64}Zn , however, is so small that one would expect a correction for detector saturation of <3%. Lead was not corrected for detector saturation as peak areas for the individual isotopes were not able to be determined; however, the correction would be negligible. In addition to the corrections for detector saturation, ^{54}Fe was corrected for the isobaric interference ^{54}Cr as described previously.

Relative sensitivity factors were calculated from the thin film, sphere, and shard data using Eq. (2), where X refers to the element of interest, R refers to the reference element, I is the peak area corrected for detector saturation and isobaric interferences (^{54}Fe only), C is the elemental weight fraction determined for each sample geometry, and f is the isotopic fraction of the peaks chosen for quantitative analysis. For all three geometries, RSFs were calculated referenced to Si, Ba, and Ca in order to compare the precision of the data relative to elements of varying ionization potentials.

$$\text{RSF}_X = \frac{I_X}{I_R} \cdot \frac{C_R}{C_X} \cdot \frac{f_R}{f_X} \quad (2)$$

Reproducibility of Absolute Intensities.

For the various sample geometries, the average uncorrected intensities for ^{28}Si , ^{44}Ca , ^{136}Ba , and ^{64}Zn are presented in Table 4. The data from the thin film are the most reproducible, which is to be expected, since it is much easier to focus the laser reproducibly on the flat regions of the film than on spheres or irregularly shaped shards. The absolute laser power density should therefore be more uniform from shot to shot. In addition, it is likely that the laser energy dissipates more uniformly through the cylindrical volume of the film than through spheres or shards. For the thin film, the relative standard deviation (RSD) $\pm 1\sigma$ for the uncorrected intensities ranges from 12 to 28 with the smallest signal variation exhib-

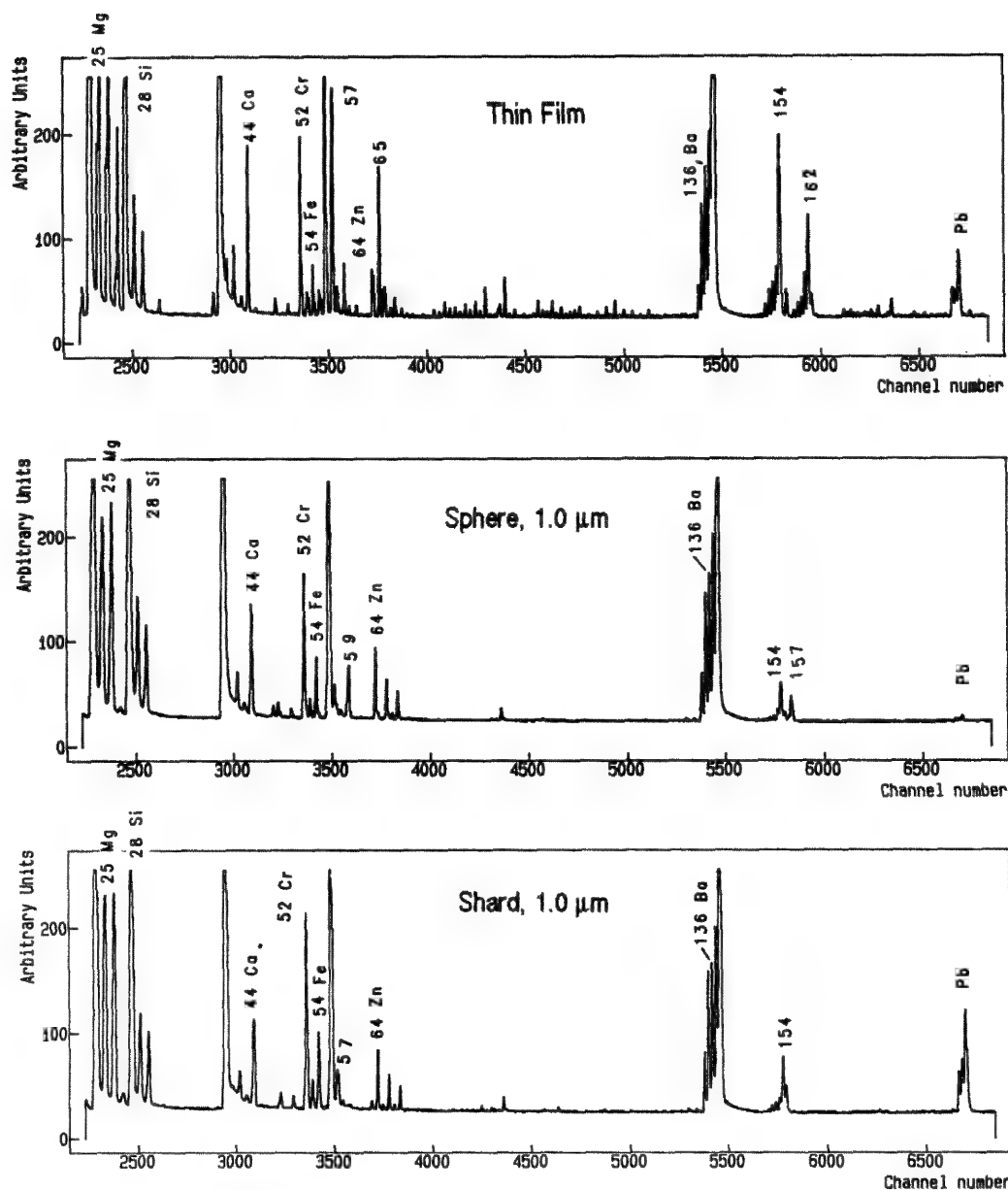


FIG. 3.--Positive ion LAMMS spectra obtained at optimized laser and spectrometer conditions from sputtered thin film, 1.0μm spheres, and 1.0μm shards. Each spectrum is the sum of 30 spectra.

TABLE 4.--Average uncorrected peak intensities, $\pm 1\sigma$.

	28Si	44Ca	64Zn	136Ba
<u>Film</u>	10370 \pm 1616 (15.6)*	840 \pm 100 (11.9)	376 \pm 106 (28.2)	1262 \pm 235 (18.6)
<u>Spheres</u>				
0.5 μm	9009 \pm 2135 (23.7)	741 \pm 163 (22.0)	181 \pm 107 (59.1)	686 \pm 214 (31.2)
0.8 μm	11280 \pm 3571 (31.7)	842 \pm 262 (31.1)	335 \pm 233 (69.6)	982 \pm 365 (37.2)
1.0 μm	14334 \pm 2857 (19.9)	861 \pm 196 (22.8)	498 \pm 208 (41.8)	1189 \pm 306 (25.7)
1.7 μm	16033 \pm 3744 (23.3)	732 \pm 161 (22.0)	425 \pm 193 (45.4)	1098 \pm 391 (35.6)
2.1 μm	17449 \pm 3466 (19.9)	763 \pm 188 (24.6)	453 \pm 192 (42.4)	1088 \pm 475 (43.7)
<u>Shards</u>				
0.5 μm	5333 \pm 3698 (69.3)	621 \pm 203 (32.7)	120 \pm 96 (80.0)	658 \pm 150 (22.8)
0.8 μm	9733 \pm 2831 (29.1)	1007 \pm 258 (25.6)	299 \pm 163 (54.5)	993 \pm 186 (18.7)
1.0 μm	11240 \pm 2278 (20.3)	922 \pm 193 (20.9)	377 \pm 141 (37.4)	1245 \pm 364 (29.2)
1.7 μm	12645 \pm 1867 (14.8)	829 \pm 298 (35.9)	482 \pm 181 (37.6)	1312 \pm 319 (24.3)

*Percent error, $\pm 1\sigma$.

ited by ^{44}Ca and the largest exhibited by ^{64}Zn . One would predict that Zn, which has a low concentration in the sample, $\sim 1\%$ by weight, and a high first ionization potential, 9.4 eV, would have a larger variation than Ca, which has a lower first ionization potential, 6.1 eV, and is present in a high concentration in the sample, $\sim 13\%$ by weight.

The variation in the uncorrected data for the spheres of all diameters is significantly greater than for the thin film. Excluding lead, which partially vaporized in the furnace, the greatest ranges of RSD, 22% to 59% and 23% to 70%, are observed for the smaller sphere diameters of 0.5 and 0.8 μm , respectively. The ranges of RSD decrease with increasing sphere diameter, 20 to 45%, 22 to 45%, and 20 to 44%, respectively for the 1.0, 1.7, and 2.1 μm spheres. For all sphere diameters, the elements of high ionization potential and/or low concentration such as Cr, Zn, and Pb generally exhibit the largest relative standard deviations, $>40\%$. The data for spheres of 1.0, 1.7, and 2.1 μm have approximately equal ranges of variability, perhaps because the signal intensities lie in the plateau region of the plot of ion intensity vs sphere diameter.¹ It is expected that the absolute signal intensity from the spheres smaller than the laser spot diameter, $<1 \mu\text{m}$, would be more subject to variation than from sphere diameters in excess of 1 μm as the particles in the former case are completely vaporized and give rise to signals proportional to the sample weight evaporated. Signal intensities for spheres $<1 \mu\text{m}$ are thus in the rising portion of the plot of ion intensity vs sphere diameter, where a slight difference in sphere diameter can produce a large change in signal intensity.¹

It is also more difficult to align and focus the laser reproducibly on very small particles, especially spheres. Although one might expect a smaller variation in the sphere data compared to shards because of the regularity of the sample shape, it is difficult to focus the laser reproducibly on glass microspheres. The glass sphere acts as a lens, which naturally provides for a substantial depth of laser focus. When the spheres and shards were analyzed, the most reproducible laser focus was noticeably attained for the particle diameters equaling that of the He-Ne laser spot, 1 μm . For this particle size, it was particularly easy to focus the He-Ne laser to form a crisp, round, bright spot in the center of each sphere or shard. For other diameters it was more difficult to focus and center the laser. This experimental observation is generally reflected in the smaller error ranges for both the spheres and shards of 1 μm in diameter (Table 4). Difficulty of laser focus for spheres was also observed by Surkyn and Adams.¹³

As with the spheres, the variability of the data for shards whose diameters are below the diameter of laser focus is greater than for those whose diameters are above the diameter of laser focus. For the shards of 0.5, 0.8, 1.0, and 1.7 μm , the relative standard deviation ranges from 23 to 80%, 17 to 54%, 16 to

37%, and 14 to 48%, respectively. With the exception of shards 0.5 μm in diameter, the greatest % relative standard deviations, $>36\%$, are exhibited by low concentration and/or high ionization potential elements, Cr, Fe, and Zn. The depth of focus, which is predicted to be a large source of error for the spheres, should not be as large of a contributing factor for the shards although it is still difficult to focus and align the laser on the smallest shards. A unique source of error for the shards, however, lies in the nature of their irregular shape. It is difficult to size them accurately with the light microscope, and nearly impossible to obtain 30 shards for each size range with exactly the same dimensions. This source of error is significant for shards whose dimensions are less than or equal to the diameter of the laser spot of $\sim 1 \mu\text{m}$.

Comparison of Relative Sensitivity Factors. Since the instrumental conditions were kept constant throughout data collection, any observed differences in the data should reflect variations in laser-solid interaction for samples of different geometries. The inherent variation in laser energy from shot to shot influences the precision of the data but should do so equally for all three geometries. Changes in laser-solid interaction are therefore the result of different focus conditions and sample absorption characteristics. Since the compositions of these samples are virtually identical, changes in sample absorption characteristics are geometry and not matrix dependent. A change in the distribution of laser energy through samples of various geometries may change the relative ion yields and hence the magnitude and precision of the RSFs.

Relative sensitivity factors referenced to Si, Ba, and Ca are presented for the thin film, 1.0 μm spheres, and 1.0 μm shards in Table 5. Not surprisingly, the smallest error is consistently observed for the thin film reflecting the enhanced reproducibility of the ion yields for this sample geometry. This good reproducibility is most likely the result of the ease of laser focus on the flat sample surface and of the uniformity of the energy dissipation through the film, as mentioned before. For all three reference elements, the RSFs from the thin film exhibit values of precision which are roughly a factor of 2 better than for the spheres or shards of varying diameters. The precision of the data for the 1.0 μm spheres and shards compares most favorably with that of the thin film. This is the result of the ability to achieve reproducible laser focus for particles whose diameters equal that of the He-Ne laser spot. From Table 5, it may be observed that the variation in RSFs referenced to Ba and Ca are somewhat lower than for Si, reflecting the relative high ionization potential of Si. Even though Si is present in a high concentration in these samples, the relative ion yield for Si is not as consistent with respect to other elements as for Ba or Ca. It may be that other high-ionization-potential elements would have more re-

TABLE 5.--Relative sensitivity factors for glass samples, $\pm 1\sigma$.Referenced to Silicon.

	Film	1.0 μ m Spheres	1.0 μ m Shards
Mg	6.31 \pm 1.97 [31.2] (5.7)*	2.37 \pm 1.32 [55.7] (10.5)	4.26 \pm 1.54 [36.2] (6.6)
Si	-----	-----	-----
Ca	3.93 \pm 1.55 [39.4] (7.1)	2.33 \pm 0.93 [39.9] (7.3)	3.67 \pm 1.51 [41.1] (7.6)
Cr	1.78 \pm 0.65 [36.5] (6.7)	1.94 \pm 0.91 [46.9] (8.8)	2.93 \pm 1.04 [35.5] (6.5)
Fe	1.68 \pm 0.60 [35.7] (6.5)	1.61 \pm 0.75 [46.6] (8.7)	3.46 \pm 1.13 [32.7] (6.1)
Zn	0.88 \pm 0.26 [29.5] (5.7)	0.90 \pm 0.35 [38.9] (6.7)	0.75 \pm 0.22 [29.3] (5.3)
Ba	1.62 \pm 0.63 [38.9] (7.4)	1.00 \pm 0.45 [45.0] (8.0)	1.31 \pm 0.39 [29.8] (5.3)
Pb	0.44 \pm 0.14 [31.8] (6.8)	-----	0.86 \pm 0.25 [29.1] (5.8)

Referenced to Barium.

	Film	1.0 μ m Spheres	1.0 μ m Shards
Mg	4.07 \pm 0.78 [19.2] (3.4)	2.34 \pm 0.70 [29.9] (5.6)	3.30 \pm 1.11 [33.6] (6.4)
Si	0.69 \pm 0.20 [28.9] (5.8)	1.20 \pm 0.56 [46.7] (8.3)	0.82 \pm 0.35 [42.7] (8.5)
Ca	2.49 \pm 0.53 [21.3] (4.0)	2.45 \pm 0.75 [30.6] (5.7)	2.86 \pm 1.23 [43.0] (8.0)
Cr	1.11 \pm 0.18 [16.2] (2.7)	2.09 \pm 0.95 [45.5] (8.6)	2.31 \pm 0.82 [35.5] (6.5)
Fe	1.06 \pm 0.19 [17.9] (2.8)	1.69 \pm 0.59 [34.9] (6.5)	2.72 \pm 0.93 [34.2] (6.6)
Zn	0.57 \pm 0.13 [22.8] (3.5)	1.00 \pm 0.38 [38.9] (7.0)	0.62 \pm 0.23 [37.1] (6.5)
Ba	-----	-----	-----
Pb	0.28 \pm 0.05 [17.9] (3.6)	-----	0.69 \pm 0.25 [36.2] (7.2)

Referenced to Calcium.

	Film	1.0 μ m Spheres	1.0 μ m Shards
Mg	1.68 \pm 0.36 [21.4] (4.2)	1.00 \pm 0.34 [34.0] (6.0)	1.21 \pm 0.22 [18.2] (3.3)
Si	0.28 \pm 0.08 [28.6] (3.6)	0.50 \pm 0.21 [42.0] (8.0)	0.32 \pm 0.15 [46.9] (9.4)
Ca	-----	-----	-----
Cr	0.47 \pm 0.12 [25.5] (4.3)	0.88 \pm 0.35 [39.8] (6.8)	0.83 \pm 0.18 [21.7] (3.6)
Fe	0.45 \pm 0.14 [31.1] (6.7)	0.70 \pm 0.19 [27.1] (5.7)	0.99 \pm 0.20 [20.2] (4.0)
Zn	0.24 \pm 0.08 [33.3] (4.2)	0.42 \pm 0.15 [35.7] (7.1)	0.23 \pm 0.10 [43.5] (8.7)
Ba	0.42 \pm 0.09 [21.4] (4.8)	0.44 \pm 0.11 [25.0] (4.5)	0.40 \pm 0.15 [37.5] (7.5)
Pb	0.12 \pm 0.03 [25.0] (4.2)	-----	0.25 \pm 0.08 [32.0] (4.0)

* Brackets [] % Relative Standard Deviation
 Parentheses () % Relative Standard Deviation of Mean

TABLE 6.--Variation of relative sensitivity factors referenced to barium among particle diameters ranging from 0.5 to 2.1 μ m for spheres and from 0.5 to 1.7 μ m for shards.

Element	SPHERES Ratio of Max. to Min.	SHARDS Ratio of Max. to Min.
Mg	1.4	1.2
Si	3.0	1.8
Ca	1.6	1.6
Cr	1.3	1.4
Fe	1.8	1.4
Zn	1.6	1.9
Ba	---	---
Pb	---	1.3

TABLE 7.--Comparison of relative elemental sensitivity. Factors referenced to barium for three sample geometries.

Element	Max. / Min. RSF All Data	Max. / Min. RSF Thin Film, 1.0 μ m Sphere and 1.0 μ m Shard
Mg	1.74	1.74
Si	5.17	1.74
Ca	1.63	1.17
Cr	2.31	2.08
Fe	2.76	2.57
Zn	2.97	1.75
Ba	---	---
Pb	2.57	2.46

producible RSFs with Si than with Ba or Ca, i.e., the ionization potential match may be more important than the absolute value. However, this sample contains no other high-ionization-potential elements. For the remaining comparisons, only RSFs referenced to Ba will be compared as they provide a useful measure of reproducibility.

For the spheres and shards, the RSFs for each element were compared across the range of experimental diameters to determine the extent of variation within a given geometry. The ratios of maximum to minimum RSFs for each element in both geometries are listed in Table 6. The extremes of RSFs referenced to Ba reach a factor of 3.0 for spheres and 1.9 for shards.

The most variation occurs for RSFs calculated for elements with high ionization potentials such as Si and Zn, 8.2 and 9.4 eV, respectively. The RSFs for elements with relatively lower ionization potentials, Ba, Ca, Cr, Pb, Mg, and Fe (5.2 to 7.9 eV), vary by less than a factor of 2 for this range of particle diameters. These results indicate that size effects are present and that they are most significant for elements of high ionization potential. This observation is not surprising because it is expected that variations in laser energy deposition with particle size would most severely affect those elements with the highest ionization thresholds.¹¹⁻¹³

The RSFs were also compared for each element

among the three sample geometries. Ratios of maximum to minimum RSFs for each element regardless of geometry are reported in Table 7 and provide a measure of the feasibility of interchanging RSFs among geometries of a limited size range in order to determine sample composition. These results indicate the presence of significant effects that may be attributed to sample geometry. The differences in RSFs referenced to Ba are largest for Si, a factor of 5, but vary by less than a factor of 3 for the other elements. By restricting the comparison to spheres and shards of 1 μm in diameter, also the diameter of laser focus, the inter-geometry effects are dramatically reduced. The variation of elemental relative sensitivity among the three sample geometries is less than a factor of three and generally less than two. The improved similarity of RSFs from the thin film and 1.0 μm spheres and shards proves by definition that the interaction of the laser with these samples gives rise to similar ratios of ionization yields for the matrix elements. It therefore appears that the optimal laser focus achieved for the thin film and spheres and shards of 1.0 μm in diameter provides for approximately equal laser power densities transmitted to the samples.

Conclusions

Based on the above results of LAMMS quantitation using the relative sensitivity factor approach, it is appropriate to provide a guideline for the quantitative analysis of a single unknown inorganic particle and to make an assessment as to the best precision and accuracy that one would expect from this method. For quantitative analysis using the relative sensitivity factor approach, it is imperative to choose a homogeneous standard of similar thermal, optical, and chemical properties as the unknown sample. This study demonstrates that it is also important to choose a standard having a geometry and size similar to the unknown sample.

The most important aspects of the optimization procedure for quantitative elemental analysis include identifying a laser energy for the reproducible ionization of all elements present in the sample and determining an appropriate einzel lens potential for the selective transmission of atomic ions. It is also necessary to evaluate the characteristics of the detection system in order to compensate for any non-linearity in the current amplification process of the electron multiplier. One should choose isotopes which are either not subject to or can easily be corrected for isobaric interferences. Based on the results from this sample, the RSFs, calculated from the data obtained from the standard, should be referenced to elements possessing low ionization potentials for the best precision and accuracy.

The best anticipated measurements of precision and accuracy for the quantitative analysis of a single inorganic particle between 0.5 and 2.1 μm are attained for elements of low ionization potential, such as for Ba in these experi-

ments, when using a RSF calculated from a particle standard (the same geometry as the unknown), as opposed to film or sphere. With these prerequisites, the precision of quantitative analysis is at best on the order to ~20-40% and is expected to be worse, up to 80%, for elements such as Si and Zn with high ionization potentials. The measurement accuracy, however, may be worse if the matrix of the standard does not quite match the matrix of the unknown.¹¹ Surkyn and Adams have observed differences up to a factor of 10 for RSFs determined for elements in a galss matrix compared with those determined for the same elements in fly ash.¹³

References

1. I. H. Musselman, *Molecular and Quantitative Aspects of Laser Microprobe Mass Spectrometry for Inorganic Particle Analysis*. Ph.D. Dissertation, University of North Carolina, 1988.
2. E. Michiels, M. De Wolf, and R. Gijbels, "Ion discrimination effects in the laser microprobe mass analyzer," *SEM/1985 III*, 947.
3. M. De Wolf, T. Mauney, E. Michiels, and R. Gijbels, "Theoretical considerations on the effect of ion formation conditions on transmission through a laser microprobe mass analyzer," *SEM/1986 III*, 799.
4. D. S. Simons, "Isotopic analysis with the laser microprobe mass analyzer," *Int. J. Mass Spectrom. Ion Phys.* 55: 15, 1983/1984.
5. P. A. Pella, D. E. Newbury, E. B. Steel, and D. H. Blackburn, "Development of National Bureau of Standards thin glass films for x-ray fluorescence spectrometry," *Anal. Chem.* 58: 1133, 1986.
6. Certain commercial equipment, instruments, or materials are identified in this paper. Such identification does not imply recommendation or endorsement by NBS, nor does it imply that the materials or equipment are necessarily the best available for the purpose.
7. G. Cliff and G. W. Lorimer, "The quantitative analysis of thin specimens," *J. Microsc.* 103: 203, 1975.
8. R. W. Linton, I. H. Musselman, F. Bruynseels, and D. S. Simons, "Inorganic cluster ion formation in the laser microprobe," *Microbeam Analysis--1987*, 365.
9. R. J. Blattner and C. A. Evans Jr., "High-performance secondary ion mass spectrometry," *SEM/1980 IV*, 55.
10. R. Wechsung, F. Hillenkamp, R. Kaufmann, R. Nitsche, and H. Vogt, "A new laser microprobe mass analyzer," *SEM/1978 I*, 611.
11. R. Kaufmann, P. Wieser, and R. Wurster, "Application of the laser microprobe mass analyzer in aerosol research," *SEM/1980 II*, 607.
12. T. Dingle and B. W. Griffiths, "Examples of quantification in laser ionization mass analysis," *Microbeam Analysis--1985*, 315.
13. P. Surkyn and F. Adams, "Laser microprobe mass analysis of glass microparticles," *J. Trace and Microprobe Techniques* 1: 79, 1982.

LAMMS ANALYSIS OF SCHOTTKY BARRIER DIODE LEAKAGE

W. M. Daniel, D. J. Delorenzo, and H. R. Wilson

Electrical analysis of leakage in Schottky barrier diodes (SBD), observed after stress testing, indicated the presence of mobile ionic charges. We report the first finding of a mobile positive ion, potassium, in a single device using Laser Microprobe Mass Spectrometry (LAMMS).

Electrical Results

In order to make more reliable semiconductor devices (chips) to study failure mechanisms, devices mounted on modules are stressed under power and temperature. One possible failure mechanism recently investigated involved the effect of process residues on Schottky barrier diode leakage. It is known that mobile alkali ions, such as sodium and potassium, can cause reliability problems in diodes.^{1,2} In this study, devices with SBDs were processed with varying degrees of incomplete photoresist removal, mounted on modules, and subjected to stress testing. Some devices showed current leakage after stressing. Exposure of modules to temperatures of 150-200 C results in a reduction of leakage in some devices. Leaky chips were then removed from the modules and surface polished to a level where the individual Schottky barrier diodes could be electrically contacted on the probe station. Diodes with various leakages were identified, and the samples were exposed to temperatures of 200-300 C to examine the recovery characteristics.

Various leakage and recovery characteristics were observed; for example, some diodes showed recovery to a level that would be acceptable for circuit operation although not to a level expected for a near ideal diode. Other diodes with excessive leakage showed little or no improvement when exposed to the same temperature range. Other leaky diodes showed similar diverse recovery characteristics when exposed to avalanche breakdown of the metal-to-semiconductor junction. One sample, which showed little or no change during high-temperature soak or avalanche breakdown, was irradiated over the entire contact with an electron beam and showed near complete recovery.

The electrical results are consistent with a positive mobile ion. Baking can cause diffusion of mobile ions away from insulator interfaces. Detrapping of sodium usually requires 150 C, and potassium requires 325 C.³ Elec-

trons, either from probes causing avalanche breakdown or from an electron beam, can neutralize the positive ion in the dielectric and temporarily eliminate current leakage.

LAMMS Results

LAMMS analysis was considered since it could provide trace analysis capability in a precisely defined small (approximately 2 μm diam.) area. The LAMMS instrument used for probing the leaky devices was a LIMA 3A (Cambridge Mass Spectrometry, Ltd.). This is a standard LIMA that has 8in. wafer capability.⁴ Previous work from this laboratory using LAMMS for organic particle analysis had been reported.⁵ All spectra taken were in the positive ion mode. The chip samples were further polished down so that the area of interest was less than 1 μm below the surface. A HeNe pilot laser was used to aim the frequency-quadrupled Nd:YAG laser on stress of interest. An area analyzed was hit repeatedly with the laser, and spectra were taken until we had penetrated through the contact. Penetration through the contact was determined by the signal being composed mainly of silicon.

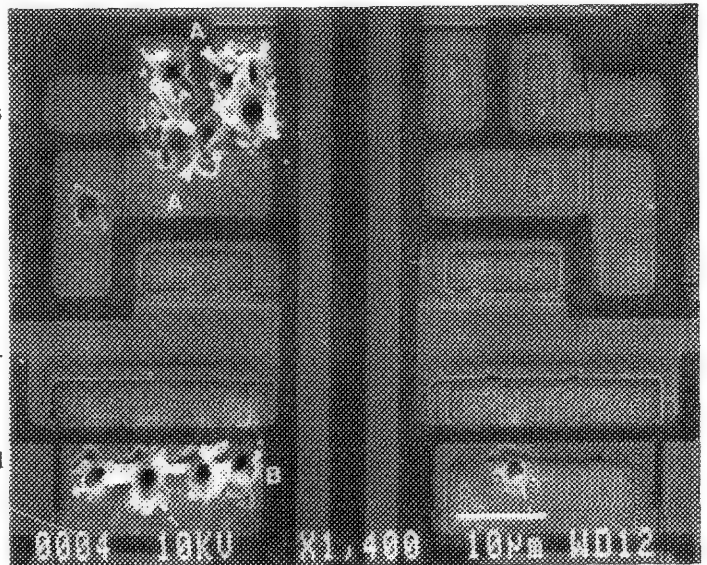


FIG. 1.--SEM micrograph showing SBD contacts both with and without laser craters following LAMMS analysis. (A) Areas where potassium was detected, (B) large $23 \times 10 \mu\text{m}$ contact. Craters to right of A had no detectable potassium. (Polishing work done by Guy Allotta, SEM work done by Ann Scheuer.)

The authors are at IBM-East Fishkill, Z/56A, Hopewell Junction, NY 12533. The use in this publication of trade names or products of manufacturers does not constitute official endorsement or evaluation of such products or manufactures, either expressed or implied, by IBM.

Figure 1 shows a scanning electron microscope micrograph of a chip after LAMMS analysis. The right side of the figure shows an area prior to analysis. The suspected location of the mobile ions causing leakage would be under the insulator edge on the contact. The left side of Fig. 1 shows some devices after they have been hit in several areas with the probe laser.

A LAMMS spectra from a device is shown in Fig. 2. In addition to the device materials (Al, Si, and Cr), a small peak at mass 39 was detected in leaky devices. Mass 39 is the most abundant isotope of potassium (93.1% of the total) with masses 41 and 40 making up the remainder (6.88% and 0.0118%, respectively). The integrated intensity of the masses 39 and 41 (from Fig. 3) are 92.6% and 7.4%. Considering the low signal level, this result shows good agreement with the natural abundances of the potassium isotopes. Because of the small signal level, mass 39 was usually the only isotope detected. To our knowledge, this is the first time a spectroscopic technique has detected a mobile ion causing electrical leakage in an individual device.

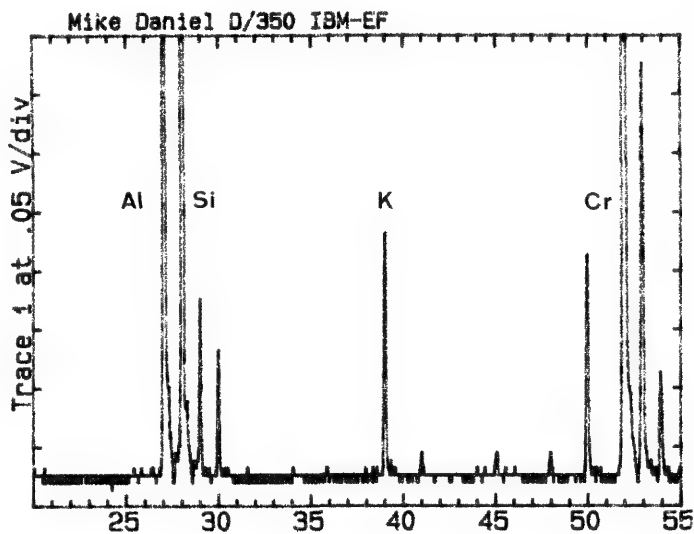


FIG. 2.--LAMMS spectra obtained from leaky device.

The potassium found was unevenly distributed on the leaky devices. In Fig. 1 the potassium was found on one side but not the other of the SBD. This localized potassium was also noticed on one of the larger (approximately $23 \times 10\mu\text{m}$) contacts where potassium was only found in one out of five areas analyzed. Two of the larger contacts are shown at the bottom of Fig. 1. Cross sections of wafers, observed on an SEM, suggested that the source of the potassium was residual resist left in the SBD contact. Chemical analysis of various batches of resist found up to 1000 ppm of potassium.

Figure 3 shows a plot of the leakage current vs the ratio of the K to the total ion current signal (IC). This ratio is for the sum of

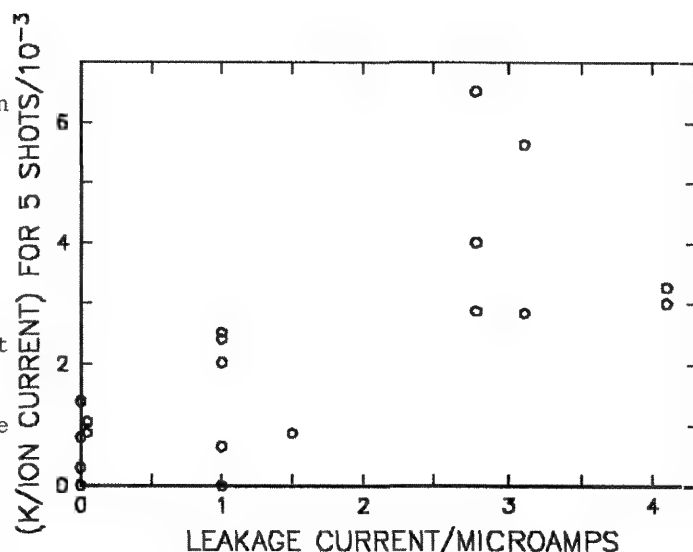


FIG. 3.--Plot of leakage current vs ratio of potassium signal to total ion current.

five spectra taken in one analysis area. Ten SBDs that were analyzed with LAMMS had zero leakage and zero $^{39}\text{K/IC}$. The scatter in these data is probably due in part to the localized discontinuous distribution of residual resist. A grazing hit on a potassium-containing area would result in a low $^{39}\text{K/IC}$ intensity. The point with $1\mu\text{A}$ leakage and zero $^{39}\text{K/IC}$ was one of the larger $23 \times 10\mu\text{m}$ contacts, where the chance of missing the localized potassium was greater. The data show an increase in potassium concentration with increasing leakage current.

Conclusion

We have used LAMMS to identify the cause of leakage in an individual electrical device. The element detected is consistent with the electrical measurements and our knowledge of the process materials and parameters.

References

1. E. H. Snow, A. S. Grove, B. E. Deal, and C. T. Sah, *J. Appl. Phys.* 36: 1664-1673, 1965.
2. D. C. Croft, *Microelectron. Reliab.* 17: 445-455, 1978.
3. M. W. Hillen and D. G. Hemmes, *Solid-State Electronics* 24: 773-780, 1981.
4. M. J. Southon, M. C. Witt, A. Harris, E. R. Walalch, and J. Myatt, *Vacuum* 34: 903-909, 1984.
5. F. A. Anderson, H. Heinen, and J. N. Ramsey, *Microbeam Analysis--1985*, 330.

PATTERN DIFFERENCES IN LASER MICROPROBE MASS SPECTRA OF NEGATIVE ION CARBON CLUSTERS

R. A. Fletcher and L. A. Currie

Laser microprobe mass spectrometry (LAMMS) provides the capability of doing chemical analysis and chemical identification on single micrometer sized particles. Most efforts have been directed toward elemental identification and molecular ion identification using laser desorption. With few exceptions,¹⁻³ carbon cluster ions have not been utilized for chemical speciation. We report some differences in negative ion mass spectra we obtained using the laser microprobe, and to convey the utility of this approach for single-particle analysis of certain causes of carbon particles found in the atmosphere.

Carbon clusters (C_mH_n)⁻ result where carbon compounds are subjected to the intense radiation resulting from the focused laser beam used in LAMMS. Carbon cluster formation is well documented in LAMMS.^{4,5} Recently, Totino et al. have studied both positive and negative ion clusters to identify coal particles and kerosenes.¹ Independently, Currie et al.^{2,3} developed a carbon ratio index, CRI, which exhibited a strong correlation with amount of contemporary carbon present in the carbon particles (i.e., quantity of ^{14}C identified by the independent technique of accelerator mass spectrometry). Early in these studies, certain laboratory-generated carbon soots were analyzed by LAMMS to gain a basis for the atmospheric particle effort. The results from these soot samples are presented here, as well as some spectra of atmospheric particles obtained from the laser microprobe.

Experimental Methods

Three separate materials were burned in controlled experiments at the NBS fire-research facility. The airborne carbon soot particles were captured by air filtration onto high-purity quartz-fiber filters. The quartz-fiber filters were previously heat treated to remove volatile compounds, especially carbon-based compounds. The filters were carefully stored and analyzed with a LAMMA 500.⁶ Due to the transmission geometry of the LAMMA 500, particles must be analyzed from a thin film or from some noncontinuous structure such as a thin fiber. Entire quartz fibers containing carbon-soot particles were transferred to a nickel transmission electron grid and mounted in the LAMMA. Individual particles and groups of particles were ablated from the fiber surface. The advantages of this approach have been discussed.⁷ The three materials that were burned

are: kiln-dried building wood, polyurethane, and heptane. Graphite particles were mounted on the same type of purified quartz fibers and analyzed for comparison to the soot. Particles were readily visible with the 32× microscope objective and when ablated with the laser, generated carbon cluster spectra. Peak areas were determined from the spectra and used in the analysis.

Results

Figure 1 presents four typical negative ion spectra for graphite, and soots of wood, heptane, and polyurethane. The first three spectra are similar with respect to the carbon cluster envelope starting at C_2^- and extending to C_9^- . In negative ions, there are no cluster numbers of higher stability ("magic numbers") such as are found at C_{11}^+ for positive ion spectra. Graphite has a low hydrogen content relative to the soots, as is evident by the clean carbon cluster formations with few hydrogen-containing clusters. Heptane soot appears to have more hydrogen present than the wood soot. Polyurethane soot has a spectrum distinctly different from the other materials; there is a strong ion at m/z of 79 that could correspond to $N_2C_4H_3^-$. Nitrogen is present in the original polyurethane molecule and is most likely the major contributor to the other dominant ion m/z 26 CN^- . The carbon cluster signature is suppressed in this soot spectrum.

One way one can analyze the carbon clusters to gain additional information is by comparing normalized peak areas.² Normalization is necessary because peak sizes vary from spectrum to spectrum as a function of laser intensity and the degree of coupling between the irradiance and the sample. One way of normalizing is to divide the area of a selected peak into the remaining cluster peaks of that spectrum and plot the ratios. It has been determined that C_4^- is a good normalizing factor and that the C_2/C_4 ratio is an excellent indicator of carbon sources.³

The data presented in Fig. 2 are the means of carbon cluster C_4 ratios derived from sets of negative ion spectra of each soot and graphite. Most of the differences are found in the first four points which are C_2^- , C_2H^- , $C_2H_2^-$ and C_3^- . There are some differences in the relative amounts of C_6 , as can be seen from the figure. The last frame, P (polyurethane soot), is scaled differently to show the large m/z 26 peak, which corresponds to CN^- .

What is the utility of such information? Identification of pyrolysis and combustion products by LAMMS would be valuable to combustion studies in general. One application already mentioned has been the identification of

The authors are at the Center for Analytical Chemistry, National Bureau of Standards, Gaithersburg, MD 20899. They thank G. Mulholland for the carbon soot samples.

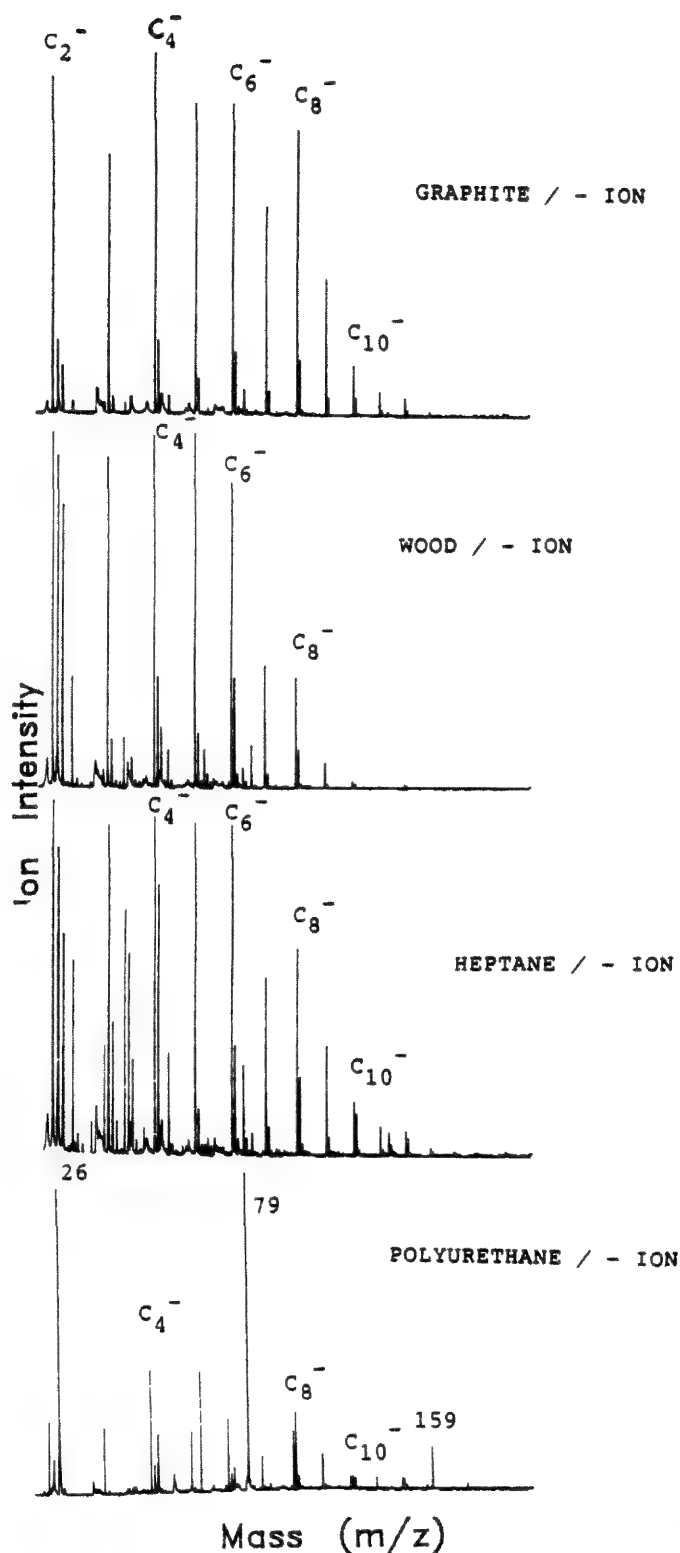


FIG. 1.--Typical single negative ion spectra for graphite, wood soot, heptane soot, and polyurethane soot.

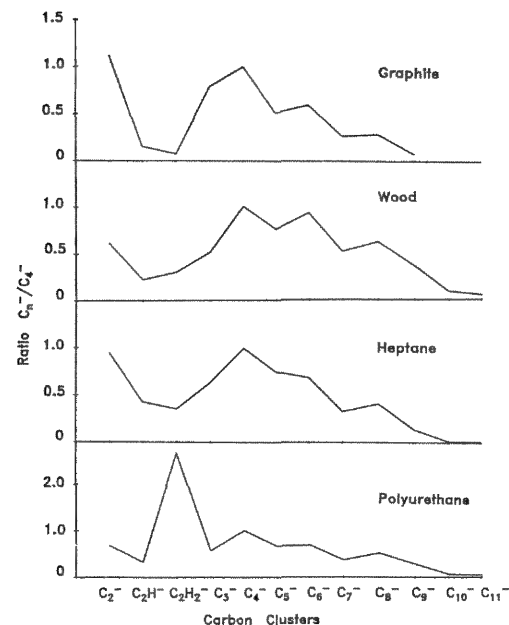


FIG. 2.--Ca cluster ratios (normalized) to C_4^- vs Ca clusters for sets of negative spectra of graphite, wood, heptane, and polyurethane soots. Points represent mean values with number of observations used as follows: graphite n-6, wood n-16, heptane n-13, and polyurethane n-16.

carbon sources in the environment from collected carbon particulate samples.³ To illustrate some of the differences in spectral features, Fig. 3 contains four averaged spectra (composed each of eight individual spectra) of atmospheric particles ablated from quartz fibers. The top spectrum contains the largest amount of contemporary carbon as indicated by the high f_c value; the bottom is composed of mostly fossil fuel combustion products and thus low f_c . The details of the samples and the ^{14}C analysis have been presented.^{3,8} Briefly, these samples are atmospheric particles collected on quartz-fiber filters. The aerosol sampling process discriminates against particles larger than $2.5 \mu m$ in diameter. One trend that appears is that the number of ions increase with increasing contemporary carbon content, and the degree of hydrogenation of the carbon material likewise increases. Some saturated mass peaks are included in the averages (Fig. 3) and thus this spectral comparison is only useful in showing qualitative differences in the data.

In summary, there are notable differences between the spectral features of soots produced from combustion of three materials. The patterns of these soots are different from those obtained for graphite. Carbon cluster ratio information has proved to be useful for environmental applications and is likely to be useful for other scientific investigations of combustion.

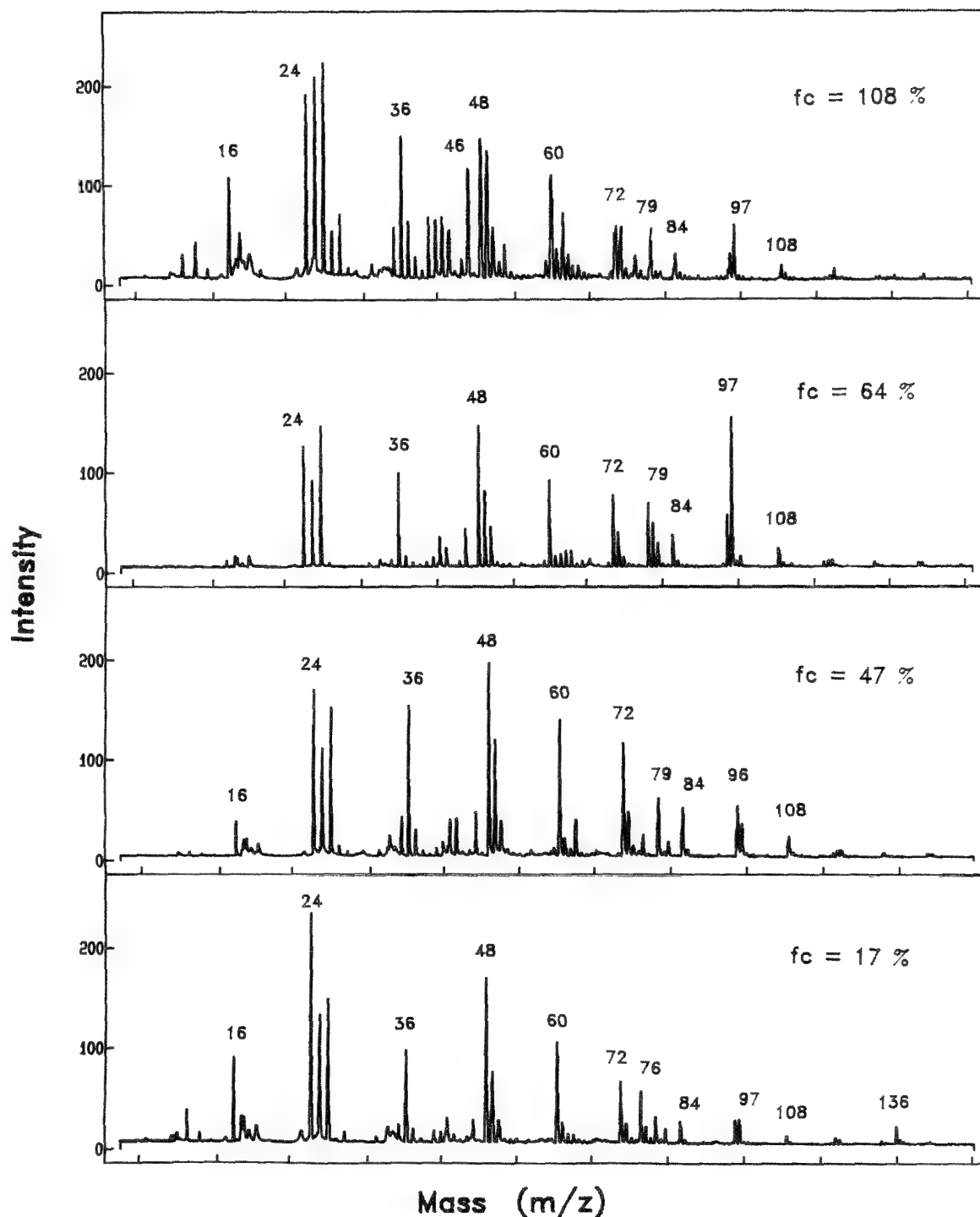


FIG. 3.--Four averaged negative ion spectra (8 spectra each) of atmospheric particulate matter; f_c value represents percentage of contemporary (or plant derived) carbon determined independently. Top f_c value, which is greater than 100%, is thought to show the influence of nuclear testing on natural abundance of ^{14}C .

References

1. E. Totino, G. Krier, and J. F. Muller, "Hydrogen ratio evaluation of coals and kerosens by LAMMA spectrometry," *Proc. Third Intern. Laser Microprobe Mass Spectrometry Workshop*, 1986, 187.
2. L. Currie, R. Fletcher, and G. Klouda, "On the identification of carbonaceous aerosols

via ^{14}C accelerator mass spectrometry, and laser microprobe mass spectrometry," *Nuclear Instruments and Methods in Physics Research B* 29: 346, 1987.

3. L. Currie, R. Fletcher, and G. Klouda, "Source apportionment of individual carbonaceous particles using ^{14}C and laser microprobe mass spectrometry," *Aerosol Science and Technology*. (in press).

4. F. Hillenkamp, in A. Benninghoven, Ed., *Ion Formation from Organic Solids*, New York: Springer-Verlag, vol. 25, 1983, 190.

5. N. Clark, A. R. Davey, and J. C. Ruckman, "Detector of cluster ions by the LIMA technique," *Microbeam Analysis--1984*, 40.

6. Certain commercial equipment, instruments, or materials are identified in this paper to specify adequately the experimental procedures. Such identification does not imply recommendation or endorsement by the National Bureau of Standards, nor does it imply that the materials or equipment identified are necessarily the best available for the purpose.

7. R. Fletcher, "A new way to mount particulate material for analysis by laser microprobe mass analyzer," *Analyt. Chem.* (submitted).

8. L. A. Currie, G. A. Klouda, D. Elmore, and H. E. Gove, *Nucl. Instr. and Meth.* B12: 396, 1985.

THE QUESTION OF ION YIELD IN LAMMS

Jonathan Housden, K. W. Hutt, J. A. Leake, and E. R. Wallach

It is well known that far more neutrals than ions are formed in LAMMS "plasmas"; typical experimental estimates for ion/neutral ratios are reported to be 10^{-4} for metals¹ and $>10^{-2}$ for ionic solids.² "Useful yield" in the Surface Analysis by Laser Ionization (SALI) method,³ defined as the number of particles detected per particle removed from the surface, is reported as being around 10^{-4} to 10^{-3} . Data such as these are important since ion yield in laser microprobe analysis is fundamental to quantification, surface sensitivity, and impurity detection levels. For instance, a major obstacle to quantification lies in understanding and being able to predict the number and types of ions detected, and in correlating these data to the original compositions of the samples. Thus, at present, experimentally derived relative sensitivity factors must be used in LAMMS instruments to correct raw data as the probability of ionization appears to vary for different atoms or molecules.

An ideal solution for improving the LAMMS technique would be total ionization of all material ablated from the sample, which would increase surface sensitivity (since less ablated material would be required), improve impurity detection levels (since every ablated impurity particle would be ionized), and simplify quantifications. Some progress toward this ideal has been reported with laser post-ionization,^{3,4} although total ionization is achieved only of the relatively small number of neutrals within the volume of the secondary laser rather than of all the material removed from the sample surface. For example, Schueler and Odom show that under certain laser irradiances, an increase of approximately 250% in ion yield can be obtained from GaAs samples.⁴ The As ion yield, in particular, is dramatically improved, probably because the higher ionization energy of As results in a relatively low yield when one is using an ablation laser alone. One problem of laser post-ionization is that on a single-shot basis the method remains selective to species; the relative ion yields in the spectra obtained depend on the delay time between ablation and ionization lasers. However, total "time averaged" accumulations⁴ of post-ionized signals can, under selected conditions, closely approach original sample compositions.

The question of ion yield and yield en-

hancement is thus of considerable importance in LAMMS. In this paper, we report on initial experiments for monitoring ion yield at source, i.e., in the laser plasma. Thus the results are independent of the mass spectrometer transmission efficiency. The method is based on a fast current probe (Tektronics CT1) and a digital storage oscilloscope (HP 54111D); the experiments were carried out on a Cambridge Mass Spectrometry LIMA 2A.⁵ Applications of the current probe are discussed in terms of:

- (a) estimating ion/neutral ratios in the laser-produced plasma, which in turn enables estimations of the overall ion transmission efficiency from plasma to detector;
- (b) providing a means of discounting any occasional multimode laser pulses as a cause of an undesired mass-peak splitting phenomenon seen at high laser powers; and
- (c) studying the effects of laser focus on ion yield in the plasma.

Use of a Current Probe to Estimate Ion Yield

Measurement of the ion yield at source in the plasma by use of a fast current probe connected to the sample stage (Fig. 1) is a new method of plasma diagnostics in LAMMS. It provides much useful information, including assessment of ion/neutral ratios, measurement of the duration of the plasma, and a means of explaining an ion discharge effect in terms of the Townsend avalanche.⁶ Figure 2 shows a typical profile of the current flowing back through the stage caused by negative ions and electrons falling back onto the sample when operation is such as to extract and analyze positive ions. The duration of this current pulse (370 ns) provides an estimate of the plasma duration and is seen to reach a maximum at 190 ns after the ablation/ionization laser pulse. It is interesting to compare these times with the time delays (200 to 2500 ns) between ablating and post-ionization lasers employed by Schueler and Odom⁴ when post-ionizing neutrals. The number of ions remaining from the original laser ablation at the onset of post-ionization will obviously depend on the delay time used.

The net charge in the plasma must be zero and it is assumed that all negatively charged particles fall back to the stage (biased at +3 kV). Thus, the total charge in the current pulse (i.e., the area under the curve in Fig. 2) can be directly equated to total positive ion production. In the example of Fig. 2 for a silicon target, the total number of positive ions produced is 1.5×10^9 . Assuming a laser-induced crater volume of about

The authors are with the Department of Materials Science and Metallurgy, University of Cambridge, Pembroke Street, Cambridge, England CB2 3QZ. They are grateful for financial support from AWE Aldermaston (J.H.) and from the Alvey Directorate and the Science and Engineering Research Council (K.W.H.).

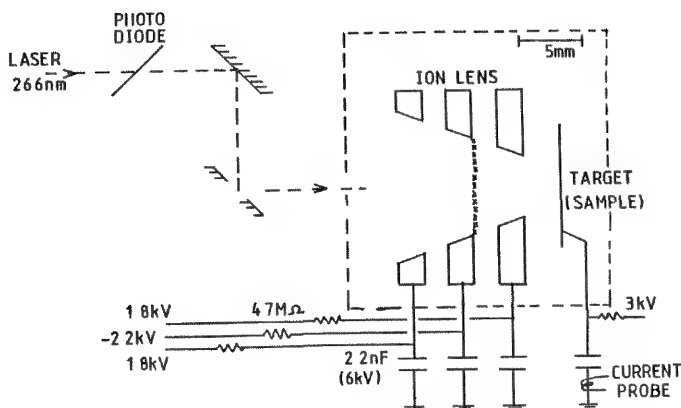


FIG. 1.--Schematic of relevant parts of LAMMS spectrometer. Ion lens and target position drawn to scale indicated. Mesh on middle plate of ion lens is 1.25×1.25 mm ($\times 0.05$ mm wire diameter).

5×10^{-18} m³, this result corresponds to an ionization efficiency of about 1:200.

Comparison of the number of ions produced in the plasma with the number detected at the electron multiplier enables measurement of bulk transmission efficiencies through the instrument. To estimate the relationship between the number of ions reaching the detector and the output signal from the detector, a statistical analysis of the signals associated with the mass 29 and mass 30 isotopes of silicon at greatly reduced laser powers was used. Figure 3 shows how the number of ions reaching the multiplier varies as a function of total ions formed for aluminum. A software correction to the multiplier signal, to simulate linear multiplier gain at all ion detection levels, has been used throughout. The multiplier signal leads to a constant value as more ions are produced and transmission efficiencies are very low. Thus these results confirm that improved ion transmission would be an effective way of increasing ion yield at the multiplier. This might be achieved by improved ion optics, which should also lead to enhanced detection limits. These initial investigations with the current probe suggest that transmission efficiency is the same for both silicon and aluminum. Further work over a wider mass range of single species samples is under way to establish whether varying transmission efficiencies contribute to relative sensitivity factors. If so, this information should be included in any quantification model.

Mass-peak Splitting

Mass-peak splitting (Fig. 4) is commonly encountered at exceptionally high ion yields (i.e., high laser powers not generally used for analysis). One explanation, that of a bimodal laser pulse, can now be discounted through monitoring of the laser temporal profile (Fig. 5) with a fast oscilloscope and photodiode, and simultaneous measurement of the current falling back onto the specimen stage (a measurement of

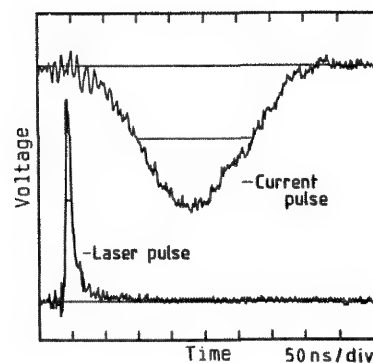


FIG. 2.--Typical target current measured for silicon target biased as anode. Time from maximum laser power to maximum current signal is 190 ns, peak current is 1.43 mA. Integrated current signal gives total charge of 2.47×10^{-10} C or 1.5×10^9 electronic charges. Full width at half maximum (FWHM) is 170 ns.

ion yield in the plasma with the current probe). Mass-peak splitting has been found to have a threshold at around 5×10^9 ions, measured at the stage (Fig. 3). With the current probe it appears that although more ions are produced above this threshold, those that are expected to appear toward the center of large mass peaks are lost at some point before the spectrum is recorded by the transient recorder. Further work is required to identify the cause of this loss in order to eliminate the phenomenon.

Current Probe and the Effects of Laser Focus on Ion Yield

Ablation/ionization laser focus is critical to laser power density and hence to the resulting total ion yield. Results for silicon ion yield (measured from the spectra) are shown in Fig. 6. Since there is an inherent random operating error in positioning the sample of approximately ± 1 μ m about focal point, variations in focus may well account for much of the shot-to-shot variation ($\pm 5\%$) typically observed in total ion yield. The current probe is being used to establish whether this effect arises from an accompanying variation in total ion yield in the plasma. An alternative explanation is the failure of the ion optics to transmit all the ions originating from the larger area of the defocused beam.

Although a focused laser is generally used for metallic and inorganic analysis, laser defocus can be advantageous in some applications, including the analysis of organic materials, as shown by Kelland and Wallach.⁷ In the focused condition, only carbon clusters are observed; when the laser power density is reduced by defocusing in either direction, more usable characteristic fragment ions are produced. Again, the current probe is being used to establish the total ion yield in the plasma in these different focal positions.

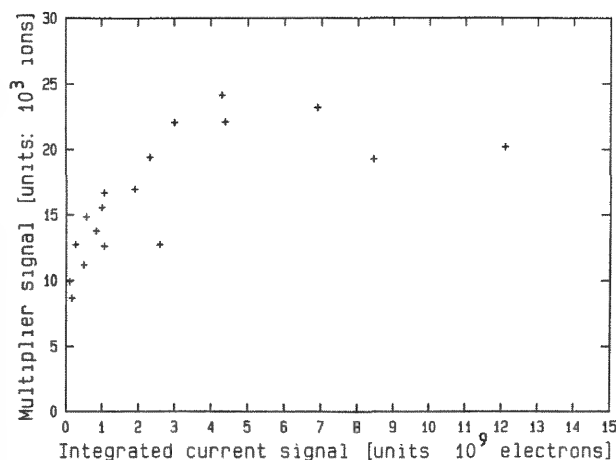


FIG. 3.--Multiplier signal as function of total ions formed.

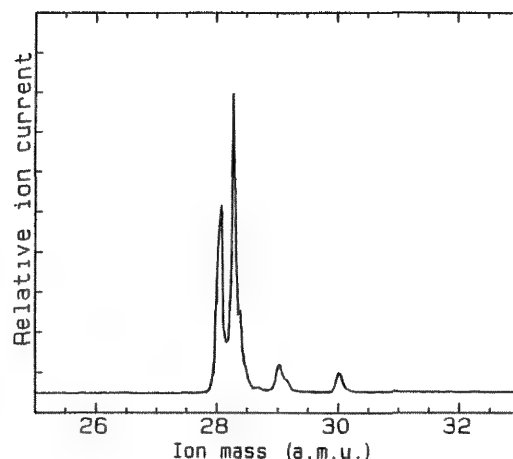


FIG. 4.--Mass-peak splitting in major isotope peak of silicon. Natural relative abundancies should be ^{28}Si :92.2%, ^{29}Si :4.7%, ^{30}Si :3.1%.

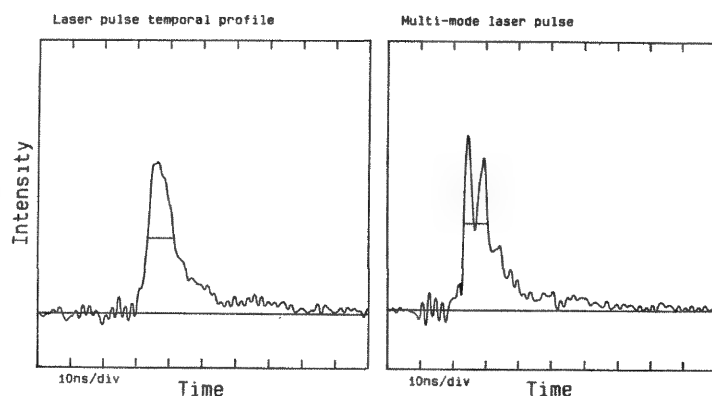


FIG. 5.--Laser pulse temporal profiles, single mode and multimode.

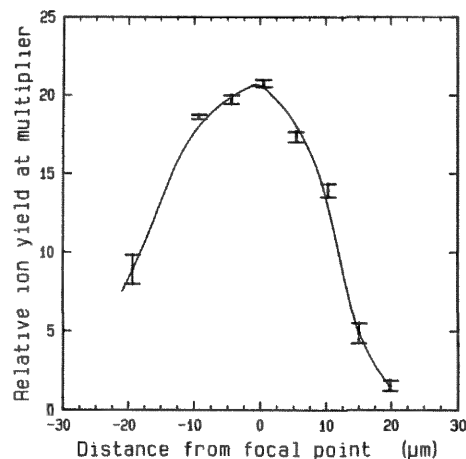


FIG. 6.--Effect of laser focus on ion yield at multiplier for Si at high laser power.

Summary

The use of a current probe connected to the specimen stage in a LAMMS instrument provides a convenient means of monitoring ion yield in the laser-formed plasma. Such data can provide estimates of ion/neutral ratios, of the order of 1:200 (for Si) and plasma duration of around 370 ns. The ion transmission efficiency from plasma to electron multiplier is observed to be around 10^{-5} . (The transmission efficiency of the mass spectrometer itself has been shown to be around 10% in recent SIMS experiments.⁹) Modifications to the ion optics could potentially result in increased total ion detection and hence improved detection limits. Mass-peak splitting is not related to any multimode laser condition. It results from the loss (possibly in the Mamyurin et al. reflectron⁸) of ions which should appear toward the center of the mass peaks. The current probe also provides a useful means of monitoring other observed phenomena, such as the effect of laser focus/power density on total ion yield in the plasma.

References

1. N. Fuerstenau and F. Hillenkamp, *Int. J. Mass Spectrom. Ion Phys.* 37: 135, 1981.
2. B. Joest, B. Schueler, and F. R. Krueger, *Naturforsch.* 37a: 18, 1982.
3. C. H. Becker, *SEM/1986 IV*, 1276.
4. B. Schueler and R. W. Odom, *J. Appl. Phys.* 61: 4652, 1987.
5. T. Dingle, B. W. Griffiths and J. C. Ruckman, *Vacuum* 31: 571, 1981.
6. K. W. Hutt and E. R. Wallach, this volume.
7. D. Kelland and E. R. Wallach, this volume.
8. B. A. Mamyurin, V. I. Karataev, D. V. Shmikk, and V. A. Zagulin, *Sov. Phys.--JETP* 37: 45, 1973.
9. S. Mullock and T. Dingle, Cambridge Mass Spectrometry, Ltd., Cambridge, England (private communication).

INITIAL RESULTS OF A CURRENT PROBE INVESTIGATION OF LASER MICROPROBE (LAMMS) PLASMA CONDITIONS

K. W. Hutt and E. R. Wallach

The current flowing through the target (sample) electrode as a consequence of the laser pulse in a LAMMS spectrometer has been monitored. With the target biased as the anode, the electric field dependence of the current was recorded. It is shown that electron drift velocity varies as $E^{1/2}$, so that the plasma has a substantially non-Maxwellian electron velocity distribution. This violates a condition required for the application of one of the most popular LAMMS quantification models (LTE). Successive Townsend avalanches are occasionally observed with the target biased as the cathode and their temporal form is briefly discussed.

In recent years, repeated attempts have been made to quantify data from laser microprobe mass analyzers (LAMMS)^{1,2} by use of the local thermodynamic equilibrium model (LTE).³⁻⁵ Inherent in this model are the assumptions that the laser-produced plasma is sufficiently dense to insure electron-collision-dominated excitation and de-excitation⁶ and that the distribution of electron velocities is Maxwellian.⁷ Thus, in general, knowledge of the LAMMS plasma conditions is essential in order to investigate the validity of the LTE or any other model. The present contribution reports initial work in which information on the plasma has been obtained by use of a current probe to monitor plasma conditions. The interpretation of these results casts doubt on the direct applicability of the LTE model for LAMMS.

Results and Discussions

Figure 1 is a schematic of the relevant features of the LIMA-2A mass spectrometer showing the experimental arrangement. A Tektronix 1 GHz current probe was used, in conjunction with a 1 Gigasample/s digital oscilloscope, to monitor the current flowing through the target electrode (sample) following the laser pulse. The temporal current profiles were observed with the target electrode biased both as the anode (Fig. 2) and cathode (Fig. 3). This work was done with silicon targets, although aluminum targets have been used and show similar features.

Target as Anode. Consider first the case of the target biased as the anode. Standard op-

erating voltages are shown in Fig. 1 and indicate an electric field in front of the target of about 8×10^5 V/m. Integration of the current recorded by the probe provides a measure of the total number of negative species, which for a silicon target are almost all electrons. The total number of negative species was typically found to be about 1×10^9 for an incident laser pulse (266 nm wavelength and duration of 8 ns), which provides at the sample an energy of approximately 0.1 mJ focused to a few microns in diameter.

The various electric fields in the plasma region were then reduced by the same proportion from their standard settings. Ten plots of the type shown in Fig. 2 were obtained at each field setting. The integrated current profile of each plot provided an (obviously) slightly different total charge. By linearizing these results, one can find the time to the maximum current for a specified total charge. The resulting plot of time to maximum current against electric field E , with the total number of negative species constant at 1×10^9 (equivalent to 1.6×10^{-10} C) was obtained and is shown as Fig. 4. Also shown are the best-fit relationships of the form $1/E^{1/2}$ and $1/E$, which show that the field dependency is well described by $t_p \propto 1/E^{1/2}$, where t_p is the time to the peak of the current pulse. The form of Fig. 4 is not significantly altered if a different total charge is chosen.

The lifetime of a LAMMS plasma depends on the time taken for the charged components to separate in the electric field. This time varies inversely as electron-drift velocity in a weakly ionized plasma. Since the stage current shape does not change for the field values used, the time to peak current can be taken to reflect the plasma lifetime and consequently the electron drift velocity. The E/p ratio, where p is the pressure, is the most useful parameter for plasma characterization.⁷ In a LAMMS plasma, the pressure depends on the energy and density distributions of the neutral component. Over the time scales involved, it is assumed that the neutral distributions vary only slowly when compared to the ionized component. Consequently, the neutral and pressure distributions will be a function of position alone, not of position and time. Justification for this assumption can be inferred from the shape of the current profile, which does not change at any value of t_p used; and from the results of Schueler and Odum,¹⁰ who found that neutral emission continued steadily for several microseconds (far longer than the plasma lifetime). It has also been assumed that there are no space-charge effects.

The authors are at the Department of Materials Science and Metallurgy, University of Cambridge, Pembroke Street, Cambridge, England CB2 3QZ. K. W. Hutt is grateful to the Alvey Directorate and to the Science and Engineering Research Council for financial support of this work.

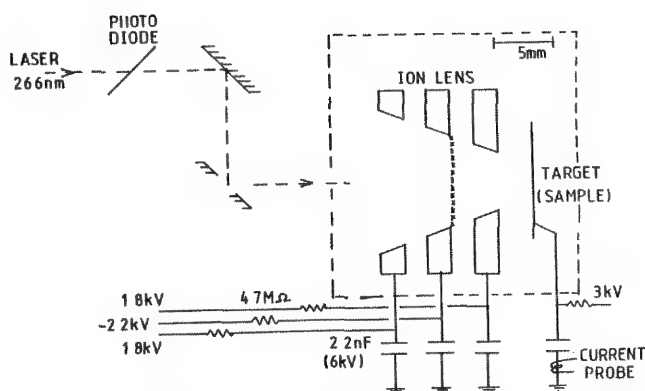


FIG. 1.--Schematic of relevant parts of LAMMS spectrometer, with ion lens and target position drawn to indicated scale. Mesh on middle plate of ion lens is $1250 \times 1250 \mu\text{m}$ ($\times 50 \mu\text{m}$ wire diameter).

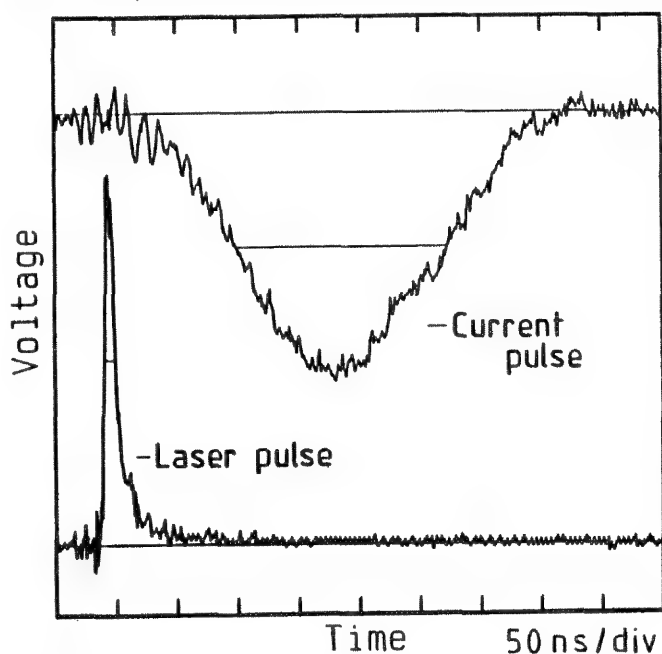


FIG. 2.--Typical target current measured for silicon target biased as anode. Time from maximum laser power to maximum current signal is 186 ns, peak current is 1.43 mA. Integrated current signal gives a total charge of $2.47 \times 10^{-10} \text{ C}$ or 1.5×10^9 electronic charges. Full width at half maximum (FWHM) is 174 ns.

The field dependency can be interpreted by considering the conditions in the laser-produced plasma to be such that electron collisions are predominantly elastic. If the field is sufficiently large, an electron can gain additional energy from the field and the electron temperature T_e is higher than the neutral or ion temperature T_n, T_i .⁸ Assuming a constant mean free path, the collision frequency is a linear function of velocity, which implies an electron drift velocity of the form⁷

$$v_d = 0.69 \kappa_{ea}^{1/4} (eE\lambda_{ea}/m_e)^{1/2} \quad (1)$$

where $\kappa_{ea} = 8m_e/3m_a$ is the average fraction of energy lost per atomic collision, with m_a equal to the atomic mass and λ_{ea} the electron-atom collision mean free path. Therefore, assuming that the time to fall back onto the surface varies inversely as drift velocity, the experimental result of $t_p \propto 1/E^{1/2}$ is predicted.

A plasma in which the E/p ratio is large enough to insure that the probability of an inelastic collision is comparable with an elastic collision, the electron temperature and ion/neutral temperature tend to the same value; that is, κ becomes a complicated function of electron energy. The electron drift velocity in this regime should vary faster than $E^{1/2}$ and would ideally⁹ approach a linear variation with E .

In a very low E/p plasma, the additional energy the electron gains between collisions is not sufficient to overcome the fraction lost per collision and no cumulative energy gain takes place. Consequently, electrons, ions, and neutrals should be defined by one temperature⁸ and again drift velocity would vary as E and not $E^{1/2}$ as observed.

The conclusion to be drawn from the experimental result is that the observed variation in drift velocity with field ($v_d \propto E^{1/2}$) is possible only for plasmas in which T_e is a linear function of field⁷ and also has a value far greater than T_n, T_i . Furthermore, in these circumstances, the electron velocity distribution is substantially non-Maxwellian, ideally with a Druyvesteyn distribution function of the form⁷

$$f_0(v) = (0.37/\pi) (\kappa_{ea})^{1/4} (m_e/E\lambda_{ea})^{1/2} \exp(-3m_e^2 v^4 \kappa_{ea}/8e^2 E^2 \lambda_{ea}^2) \quad (2)$$

where v is the random velocity. As can be observed, this function has a much stronger velocity dependence than the Maxwellian, which has important implications for quantification of LAMMS data. The LTE model with its required Maxwellian distribution will considerably overestimate the number of high-energy electrons present; yet these are the electrons that contribute crucially to the LAMMS spectrum by stepwise and direct ionization of neutrals.⁷

Target as Cathode. When the target electrode is biased as the cathode, by reversal of the polarities shown in Fig. 1, the large current breakdown shown in Fig. 3 is often observed. The temporal behavior shows the features of successive Townsend avalanches.¹¹ The theoretically predicted exponential gain in current with time is observed. However, the initial avalanche is always stunted, probably due to the nonuniform neutral distribution. The neutral density is obviously far higher around the target/cathode than at the anode immediately after the laser pulse.

Prior to this work, this phenomenon was attributed to a positive charge build-up on the surface of poorly conducting samples. As

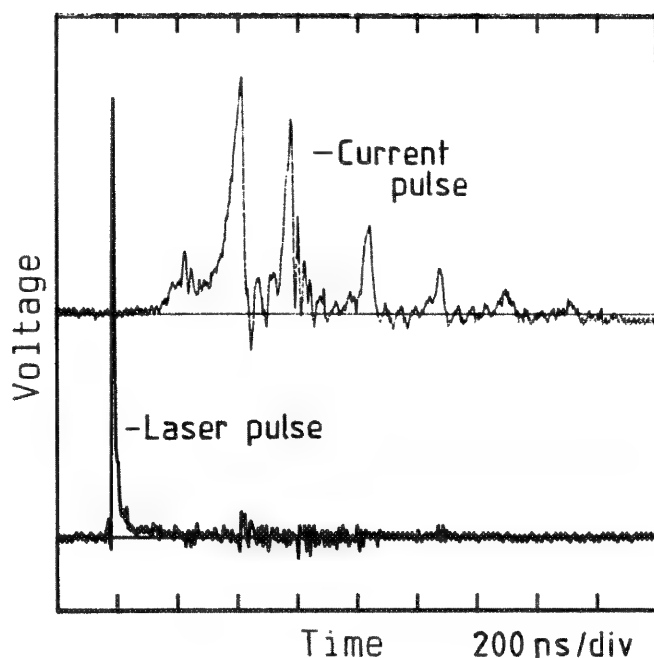


FIG. 3.--Typical breakdown condition observed with silicon target biased as cathode. Peak current is 31.4 A. Note quasi-exponential rise and very rapid fall characteristic of a Townsend avalanche.¹¹ Stunted form of initial avalanche is probably due to nonuniform neutral density distribution along avalanche path.

shown, the present observations of the nature of the large current breakdown (Fig. 3) are better explained by the Townsend avalanche. It has been shown by monitoring the current that electrons are accelerated to the middle plate in the ion extraction lens (where photoemission, probably x rays, will occur¹¹). The next avalanche is triggered by x rays incident on the sample (cathode) causing further electron emission; thus the avalanche process is repeated.¹¹ Clearly, surface charge build-up is not a requisite for this phenomenon to be observed.

Conclusion

In conclusion, we have shown that a low-cost current probe provides useful information on plasma lifetime and quasi-equilibrium state. The electron velocity distribution, for the target biased as the anode, was derived to be non-Maxwellian, which violates a condition required for the LTE model. Any successful model for quantifying LAMMS data should take into account this non-Maxwellian distribution.

References

1. F. Hillenkamp, E. Unsold, R. Kaufmann, and R. N. Itsche, *Appl. Phys.* 8: 359, 1975.
2. T. Dingle, B. W. Griffiths, and J. C. Ruckman, *Vacuum* 31: 571, 1981.
3. U. Haas, P. Wieser, and R. Wurster, *Fresenius Z. f. analytische Chemie* 308: 270, 1980.

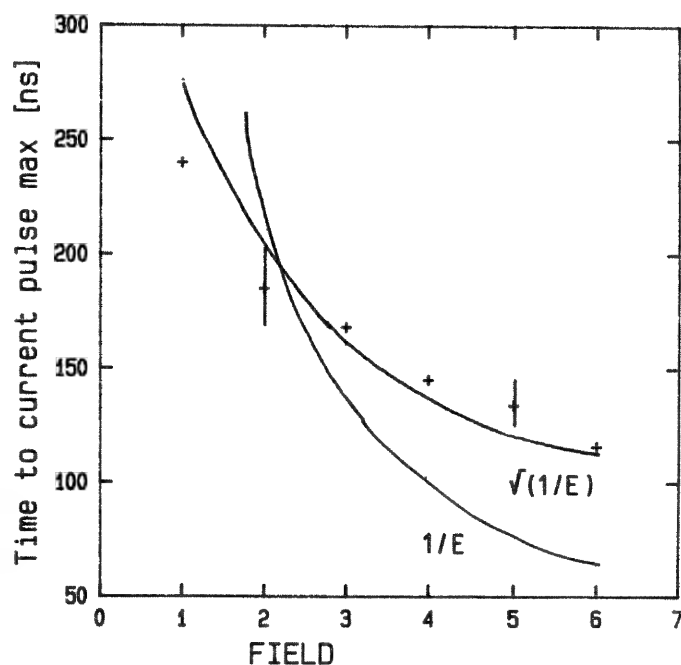


FIG. 4.--Derived time to peak current for total charge constant at 1.6×10^{-10} C, plotted against electric field. Arbitrary value of 6 has been given to field resulting from the voltages shown in Fig. 1. Best fits of form $1/E^{1/2}$ and $1/E$ are shown.

4. P. Surkyn and F. Adams, *Trace and Microprobe Techniques* 1: 79, 1982.
5. M. J. Southon, A. Harris, V. Kohler, S. J. Mullock, and E. R. Wallach, *Microbeam Analysis--1985*, 310-314.
6. R. W. P. McWhirter, in R. H. Huddlestone and S. L. Leonard, Eds., *Plasma Diagnostic Techniques*, New York and London: Academic Press, 1965.
7. V. E. Golant, A. P. Zhilinsky, and I. E. Sakharov, *Fundamentals of Plasma Physics*, New York: Wiley, 1980, chap. 5.
8. R. N. Franklin, *Plasma Phenomena in Gas Discharges*, Oxford: Clarendon Press, 1976.
9. A. Von Engel, *Ionised Gases*, Oxford: Clarendon Press, 1955, chap. 4.
10. B. Schueler and R. W. Odom, *J. Appl. Phys.* 61: 4652, 1987.
11. H. Raether, *Electron Avalanches and Breakdown in Gases*, London: Butterworths, 1964.

LASER MICROPROBE FOURIER TRANSFORM ION CYCLOTRON RESONANCE MASS SPECTROMETRY

J. T. Brenna and W. R. Creasy

Laser Microprobe Mass Spectrometry (LMMS) has established itself as a useful technique for qualitative elemental analysis of solid surfaces, particularly insulators which do not easily lend themselves to charged particle-based techniques. The pulsed nature of LMMS requires a parallel or quasisimultaneous detection system for collection of an entire spectrum from each event, and so the mass dispersing technique of choice has been time-of-flight. Over the past decade, Fourier Transform Mass Spectrometry (FTMS) has established itself as a versatile and unique technique for mass spectrometric analysis.^{1,2} It is characterized by its capability for ultrahigh mass resolution and ion storage, which allows multiple stage mass spectrometry (MS/MS...) in a single instrument. It also offers true simultaneous detection of the entire mass spectrum, and so is suitable for application to LMMS.

Experimental

A laser microprobe system has been constructed and fit to a Nicolet FTMS-2000 Fourier transform mass spectrometer (FTMS).³ A Quantel 571C Nd:YAG laser has been interfaced to the instrumental control computer and electronics to allow precisely timed and complex laser firing sequences. The system allows specimen viewing via reflected light microscope optics. The laser is operated at either 266 nm (frequency-quadrupled) or 532 nm (frequency-doubled), and is focused onto the sample by a 75 mm objective lens. The system is equipped with a specially designed specimen stage to allow motion with the sample positioned for ablation immersed in the 3T magnetic field.

Laser spot size on the specimen surface was evaluated by ablating a crater in smooth single crystal silicon and subsequent imaging by scanning electron microscopy (SEM). Preliminary data on peak height reproducibility with this system was obtained by use of National Bureau of Standards (NBS) isotopic lead and silicon standards. Radiation at 266 nm was used for this initial study.

Results

Figure 1 is a scanning electron micrograph image of a crater made in silicon in the laser microprobe with five laser shots. The crater is oval in shape because of the 33° angle (to the surface) with which the laser impinges on the surface. The smallest diameter of this spot is about 9 μm , from which we can infer that the sampled area from a single shot is in

the range of 5-8 μm .

Our studies with gas phase species show peak height reproducibility to be strongly dependent on data processing (specifically, apodization function), as expected theoretically.⁴ Data here were processed with the Blackman-Harris three-term function.⁴

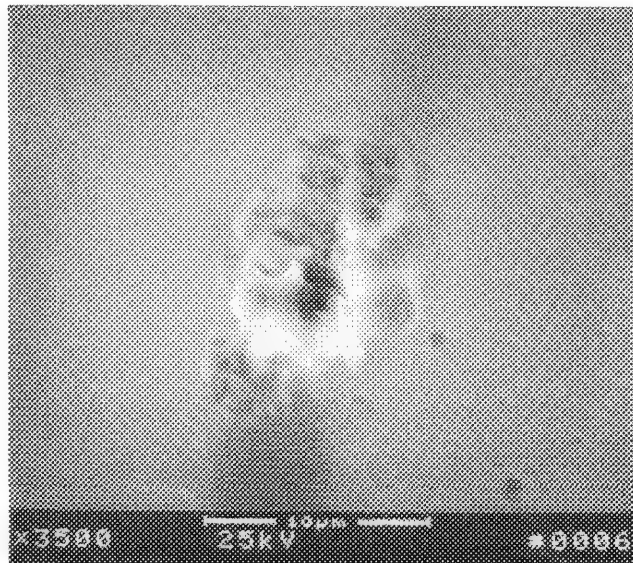


FIG. 1.--Scanning electron micrograph of crater ablated in smooth silicon wafer by laser microprobe. Note 10 μm marker.

Mass resolution exceeding $M/\delta M = 3 \times 10^5$ (FWHM) was obtained for the Pb and Si isotopes in NBS standards, which is sufficient to verify the absence of significant mass spectral interferences. Results of isotope ratio studies of these standards are shown in Table 1. Each analysis represents the average relative standard deviation (RSD) of 20 repetitions where each rep is the sum of transients from six laser shots on the same spot on the surface.

TABLE 1

Ratio (Pb)	%RSD	Ratio (Si)	%RSD
204/208	17.1	29/28	15.4
206/208	8.7	30/28	25.7
207/208	13.7		

Conclusion

A functioning laser microprobe FTMS is demonstrated; minimum spot size obtained with this system is 10 μm . Upper limits for reproducibility for elemental isotopic analysis are ob-

The authors are with the FT/ICR Laboratory, IBM Corp. (T43), Endicott, NY 13760.

tained experimentally. Further studies are in progress to improve reproducibility by optimizing trapping and measurement parameters and through the use of appropriate apodization functions. We expect the system to be of greatest utility for the molecular microprobe analysis of complex surfaces.

References

1. A. G. Marshall, *Acc. Chem. Res.* 18: 316, 1985.
2. M. B. Comisarow, *Lec. Notes in Chem.* 31: 484, 1982.
3. J. T. Brenna, W. R. Creasy, W. McBain, and C. Soria, *Rev. Sci. Instrum.* (in press).
4. J. P. Lee and M. B. Comisarow, *Appl. Spec.* 41: 93, 1987.

QUANTIFICATION OF A PESTICIDE BY LASER MICROPROBE MASS SPECTROMETRY (LAMMS)

David Kelland and E. R. Wallach

The purpose of this work is to locate and quantify a pesticide on a leaf surface and subsequently to trace the translocation of the pesticide through the leaf, by the use of LAMMS. At the moment, LAMMS is the only genuine organic microprobe with parts per million sensitivity and the ability to probe elemental and molecular compositions at a micron spatial resolution. Hence, LAMMS has been widely used in biomedical studies, probing single-celled organisms,¹ biological sections,² environmental pollutants,³ and herbicides on leaf surfaces.⁴ In this report, the framework for characterizing and quantifying a pesticide on a leaf surface is presented, with particular emphasis on the influence of various substrates and matrices on the resulting ion yield.

Methods

The LAMMS mass spectra were obtained with a laser-induced mass analyzer (LIMA-2A); this technique has been described fully.⁵ In essence, a Nd/YAG laser is used to vaporize and ionize a small volume (lateral area of a few microns square, ca 0.3 μm deep) of sample and the resulting ions are subsequently detected by a time-of-flight mass spectrometer.

A pesticide⁶ was spin-deposited on aluminum foil at five concentrations (0.05M, 0.01M, 0.001M, 0.0005M, and 0.0001M). Subsequently, the pesticide was spin-deposited at two concentrations (0.01M and 0.001M) on four different substrates (glass, aluminum foil, silver foil, and a dried leaf) and then at one concentration on aluminum foil in four different matrices:

- 0.01M pesticide : acetone : water (5:4:1:volume)
- 0.01M pesticide : acetone : 100% Na_2CO_3 (5:4:1:volume)
- 0.01M pesticide : acetone : 100% nicotinic acid (5:4:1:volume)
- 0.01M pesticide : acetone : 0.01% colloidal gold (5:4:1:volume)

The spin deposition was performed by application of one drop of the pesticide solution (approximately 20 μl) to the center of a spinning substrate,⁷ which was spun at approximately 3000 rpm by an electric motor. After about 10 s, the motor was turned off and the solvent allowed to evaporate. The samples were then analyzed by LAMMS. The LAMMS results were recorded as mean peak areas, which were calculated from 25 individual shots.

The authors are at the Department of Materials Science and Metallurgy, University of Cambridge, Pembroke Street, Cambridge, England CB2 3QZ. David Kelland thanks the SERC for financial support and Prof. D. Hull for provision of research facilities.

Each shot was taken with the Nd/YAG laser positioned 40 μm above its focus, so that characteristic pseudomolecular and fragment ions of the pesticide were obtained, as will be discussed in more detail later.

Results and Discussion

Figure 1 shows the effect of laser power density on ion formation and fragmentation of the pesticide in the positive-ion mode of LAMMS. At high laser power densities (10^{10} – 10^{11} W/cm^2), the pesticide molecules are completely fragmented and reconstructed to carbon cluster ions (Fig. 1a). At low laser power densities ($<10^9$ W/cm^2), characteristic pseudomolecular ions are detected. In between these two extremes, in a small window of laser power density (10^9 W/cm^2), characteristic pseudomolecular ions and fragment ions of the pesticide are obtained (Fig. 1b). The pseudomolecular ions can be observed but at much lower inten-

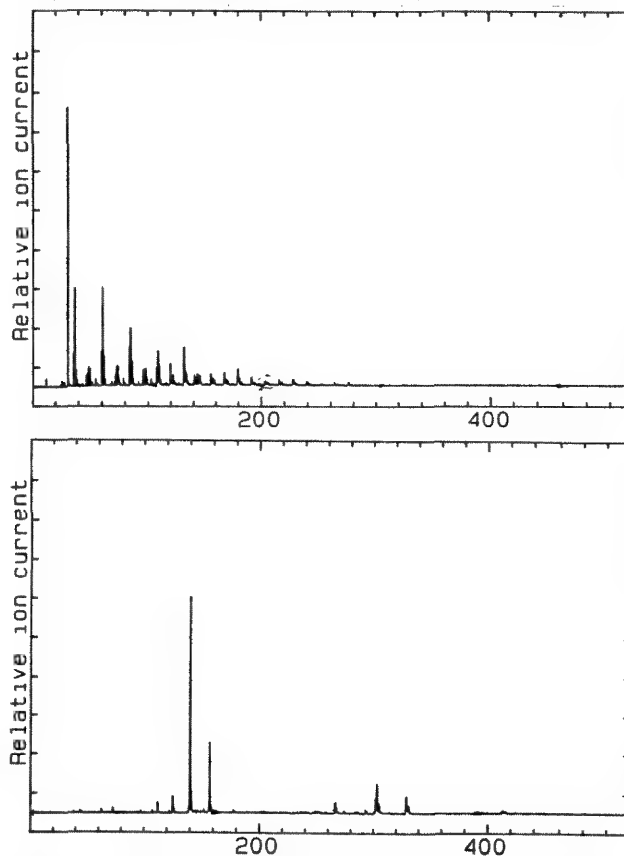


FIG. 1.--Effect of laser power density on ion formation and fragmentation of pesticide: (a) in focus, (b) 40 μm above focus.

sity than the characteristic fragment ions shown in the figure, which are thus more useful when low concentrations of the pesticide are to be monitored. The present laser/optical ar-

rangement on the LIMA-2A instrument dictates that, when operating at full laser power, the Nd/YAG laser must be 40 μm above its focus in order to obtain laser power densities of 10^9 W/cm². Hence, the LAMMS quantitative work with spin-deposited pesticide in various matrices on various substrates was all carried out with the Nd/YAG laser at full operating power and at 40 μm above its focus. However, these operating conditions are not ideal for microprobing; the laser spot size at 40 μm above its focus is approximately 20 μm in diameter. Obviously, the laser power can be turned down and characteristic ions of the pesticide can be obtained with the laser positioned less than 40 μm above its focus; with the present instrument, 20 μm above its focus corresponds to a laser spot size about 10 μm in diameter. Unfortunately, characteristic ions of the pesticide cannot be obtained when the laser is in focus, not even at the lowest power settings. However, it has been shown that the pesticide can be microprobed with the laser in focus (1-3 μm in diameter) by use of ¹⁵N labeled pesticide and monitoring of the C¹⁵N signal, which is characteristic of the labeled pesticide.⁸ The use of the ¹⁵N label means that the characteristic fragment ions are not required to identify the pesticide and so complete fragmentation causes no difficulty.

Figure 2 shows an apparent logarithmic relationship between pesticide concentration and ion yield. The reason for this relationship is unknown. However, it does show that LAMMS can be used to quantify this pesticide over a wide range of concentrations (0.0001-0.05M/20-10 000 ppm). It is unlikely that lower concentrations can be detected without modifications to the instrument that would lead to higher ion yields; the lowest concentration of 0.0001M (20ppm) results from an ion yield of around 10 ions only.* The low yield of ions at the low concentration may also account for the apparent deviation from the logarithmic dependence shown in Fig. 2, although further work is needed to account for the observed dependence. The small standard deviations for the various results also confirm that spin deposition is a good technique for producing homogeneous films.

Table 1 shows a significant difference in ion yield according to which substrate the pesticide was deposited on. It is not yet clear why. Possible explanations are that the substrate ions increase pesticide ion formation by increasing ion-attachment reactions (M + Al) or that the substrate ions create favorable plasma conditions which maintain the number of pesticide ions initially formed (i.e., reduce the number of recombination/neutralization reactions). However it may be that the actual concentrations of the pesticide on the various substrates do not reflect the initial concentration of the droplet of solution deposited; the low ion yield associated with the leaf sub-

*This level of sensitivity is characteristic of the LAMMS technique in that a similar detection limit is observed for metallic ions.⁵

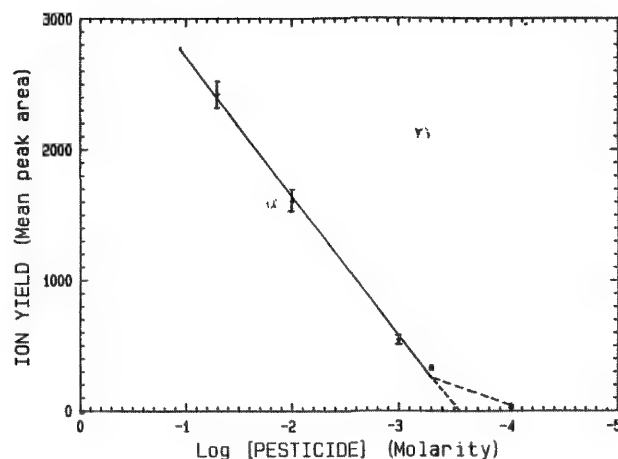


FIG. 2.--Ion yield versus logarithm of concentration of pesticide (molarity).

TABLE 1.--Variation of ion yield with substrates.

Pesticide sample (0.01M)	Mean peak area	Standard error	% Error of the mean
On leaf	59	6.5	11.1
On leaf	51	4.8	9.4
On Ag foil	242	11.7	4.8
On Ag foil	35	3.9	11.2
On glass	259	21.5	8.3
On Glass	86	9.1	10.6
On Al foil	722	27.1	3.7
On Al foil	359	26.9	7.5

strate may be due to translocation of the pesticide, and the different surface tensions between the deposited solutions and the various substrates may result in more or less pesticide solution "sticking" to the substrate surface. Further work in this area will involve the use of spectrophotometry for an independent determination of the final concentrations of the pesticide on the various substrates as well as the use of surfactants to alter surface energies.

Table 2 shows that the ion yield of the pesticide increases significantly when Na⁺ ions and nicotinic acid are added to the pesticide solutions, probably caused increased ion formation by increased ion-attachment reactions (M + Na) and protonation reactions (M + H), respectively. However, the role of these matrices in controlling the effective coupling of the laser energy into the condensed phase cannot be ignored. Further work in this area will include varying the concentration of cations and nicotinic acid while monitoring the resulting ion yield of the pesticide, to gain a better insight into how these matrices affect ion yield.

Although these results with various matrices and substrates are only preliminary, they do give an indication of some of the real problems to be encountered in quantifying a pesticide on a real biological surface which will contain a

whole spectrum of different cations and organic chemicals.

Conclusions

The current work provides an approach for the quantitative analysis of organic compounds and so provides a means for locating pesticides with micron-scale resolution on real biological surfaces. In particular, the work has led to the following conclusions:

1. In LAMMS, ion formation and fragmentation of the pesticide depends critically on the laser power density.
2. LAMMS can quantify a wide range of pesticide concentrations (0.0001-0.05M/20-10 000 ppm).
3. Spin deposition produces homogeneous films of the pesticide.
4. The ion yield of the pesticide varies with different substrates.
5. The ion yield of the pesticide is increased by the addition of Na⁺ or nicotinic acid.

TABLE 2.--Variation of ion yield with matrices.

Sample (on Al foil)	Mean peak area	Standard error	% Error of the mean
Pesticide(0.01M):acetone:water (5:4:1)	586	11.7	2.0
Pesticide(0.01M):acetone:100% Na ₂ CO ₃ (5:4:1)	709	19.1	2.7
Pesticide(0.01M):acetone:100% Nicotinic (5:4:1)	882	35.8	4.1
Pesticide(0.01M):acetone:0.01% Au (%:4:1)	501	20.4	4.1

References

1. B. Lindner and U. Seydel, *Microbeam Analysis--1983*, 106.
2. R. Kaufmann, H. J. Heinen, M. W. Schurmann, and R. M. Wechsung, *Microbeam Analysis--1979*, 63.
3. P. Wieser, R. Wurster, and H. Seiler, *Atmos. Environ.* 14: 485, 1980.
4. J. S. Brinen, M. Los, D. Kelland, and E. R. Wallach, *Surface and Interface Analysis* (in press).
5. M. J. Southon, M. C. Mitt, A. Harris, E. R. Wallach, and J. Myatt, *Vacuum* 34: 903, 1984.
6. M. Anderson, J. P. Fisher, and J. Robinson, *1986 British Crop Protection Conference: Pests and Diseases* 2B-1, 89.
7. G. Save, P. Hakansson, B. U. R. Sundqvist, U. Jonsson, G. Oloffsson, and M. Malmquist, *Anal. Chem.* 59: 2059, 1987.
8. D. Kelland, unpublished results.
9. M. Karas, D. Bachmann, U. Bahr, and F. Hillenkamp, *Int. J. Mass Spectrom. Ion Proc.* 78: 53, 1987.

QUANTITATION OF LAMMA RESULTS ON THE DISTRIBUTION OF ELEMENTS AND CHEMICAL COMPOUNDS IN BIOLOGICAL AND MEDICAL SPECIMENS

P. F. Schmidt

One criterion for the applicability of laser microprobe mass analysis in biological and medical research is the necessity to quantify LAMMA results. For example, the increase or decrease of trace element contents within cells is of pronounced importance. The effects of trace elements for pathologic symptoms and the estimation of intracellular trace element contents is of particular importance. An analytical technique by LAMMA is given which can identify and localize trace elements at a cellular or subcellular level, and under certain presuppositions the results can be quantified. The problem in quantitation of LAMMA results is that the absolute amplitude of the ion signal is not a reliable basis for quantitation, since there are variations in the evaporated volume as a result of structures of different optical absorption and of laser fluctuations. To correct variations in the evaporated volume, suitable internal standards can be used in which the ion signal of the element to be analyzed is referred to the ion signal of the reference element that serves as an internal standard. Thus normalization of the spectra and thereby relative quantitation is feasible.

Previous investigations have shown that ion signals of the organic matter can likewise serve as an internal standard, since the background of the organic mass peaks in the analysis of histological sections is quite reproducible.¹ In case specimens and external standards contain the same organic matter an absolute quantitation is possible.

Quantitative Estimation of Cd Contents in Cells of the Renal Cortex of Rats After Long-term Exposure to Cadmium

In the scope of investigations on the nephrotoxicity of cadmium, cadmium accumulations have been localized in the various structural elements of the kidney cortex of rats, including proximal and distal tubules, glomeruli, and collecting tubes. The test rats were fed a cadmium-rich diet and the control rats were fed a cadmium-poor diet. The animals were killed 40 weeks after beginning the diet. The integral cadmium concentrations were measured in tissues and in plasma by atomic absorption spectrometry.² For LAMMA analysis, small pieces of the renal cortex were prepared according to standard prepara-

tion for electron microscopy: fixation in 2.5% glutaraldehyde, dehydration in acetone, and embedding in Epon, but without any subsequent staining. Sections of this material were cut at 0.5 μm and mounted on copper grids. One typical LAMMA spectrum of a proximal tubule cell of a cadmium-fed rat is shown in Fig. 1, demonstrating the occurrence of cadmium. In order to normalize the spectra, the organic fragment ion masses $m/e = 98$ and $m/e = 109$ were chosen as the internal standards and related to the ion signal of the Cd isotope $m/e = 114$.

A standard calibration curve for absolute quantitation was prepared in the same embedding material as found in the specimens. Epon was doped with cadmium in concentrations of 0, 33, 100, 330, and 1000 ppm. The analyses were made with 0.5 μm sections. A typical result of an analysis is shown in Fig. 2a. Figure 3 shows a plot of the average values from ratios $R = I_{m=114} \text{ Cd} / I_{m=(98+109)/2}$ as a function of various cadmium concentrations. (The denominator 2 was selected optionally.) The plot demonstrates a linear relation (correlation coefficient 0.98). Using this calibration curve we could establish the cadmium concentration of the various regions of the renal cortex by evaluation of the ratio R from LAMMA spectra of the cytoplasm from different proximal and distal tubules (Fig. 2b), and from glomeruli and collecting tubes. Since the organic background in the specimen and the standard is identical, it was possible to use the calibration curve to get absolute quantitative results (Table 1). Thus, LAMMA results confirm the mechanism of cadmium absorption in the kidney; the cadmium metallothionein complex is transported to the renal tubules by means of glomerular filtration and a subsequent tubular reabsorption.³

Quantitation of PO_3 Content in Phosphate-Modified Starches

In order to determine local phosphorus concentrations in phosphate-modified starches, normalization of spectra was necessary. Figure 4 shows typical LAMMA analyses of homogenized starches which contain 0.0066% phosphorus (Fig. 4a) and 0.088% phosphorus (Fig. 4b). To estimate the phosphorus concentrations in modified starches, the PO_3^- mass line has been selected from the negative mass spectra and referred to an internal standard $m/e = 71$, a mass line of the organic background. Homogenized starches with various P concentrations were used for standards. The standards were

The author is at the Institut für Medizinische Physik, Hufferstrasse 68, D-4400 Münster, Federal Republic of Germany.

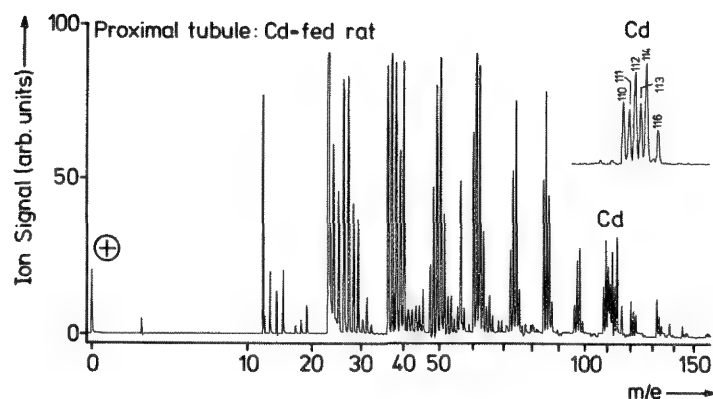


FIG. 1.--Typical LAMMA spectrum of proximal tubule cell (cytoplasm) of cadmium-fed rat.

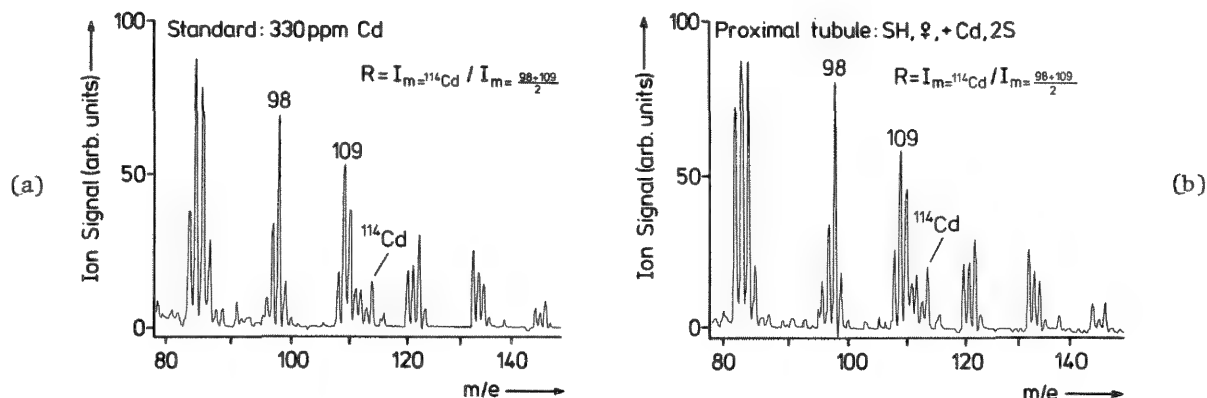


FIG. 2.--Typical segments of LAMMA spectra: (a) cadmium standard (330 ppm), (b) cadmium-fed rat. Spectra show correspondence of organic mass peaks. Mass lines $m/e = 98$ and 109 were used as reference peaks for internal standard.

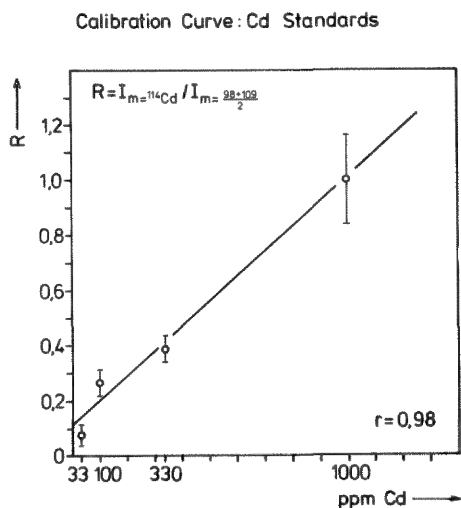


FIG. 3.--Calibration plot of average values of the ratio R vs cadmium concentrations. Mass lines at $m/e = 98$ and 109 are caused by organic embedding material.

TABLE 1.--Cadmium content in cytoplasm of various elements of renal cortex from rats with various integral cadmium concentrations. Values indicate maximum cadmium concentration.³

Rats	AAS (ppm)	LAMMA (ppm)			
		Prox tubules	Dist tubules	Glomeruli	Collecting tubes
SH, ♂, +Cd 1 R	455	1300	350	350	
N, ♂, +Cd 3 R	239	700	150		
N, ♀, +Cd 2 S	210	700	200	250	100
SH, ♀, +Cd 2 S	73	200	50	100	
Control rat SH, ♂, 1 B	0.3	—	—	—	—

N = normotensive; SH = spontaneous hypertension
R, S, B: marking of the rats

0.5 μm thick. Thirty analyses of each standard were made. The average values of $\text{I}_{\text{PO}_3}/\text{I}_{\text{m}=71}$ were plotted against the various P concentrations. The plot exhibits a linear correlation with a correlation coefficient $r = 0.995$; the standard deviation was of the order of 10 to 15%. Using this calibration curve, one could estimate the local P fluctuations in sections of P-modified starches. Thus information can be gained about the chemical reactions taking place in the starch granule by modification.⁴

Effect of Variations in Laser Power Density on the Normalization of Spectra by Reference to Organic Mass Lines

The effect of laser power density on the formation of atomic and molecular ions has to be taken into consideration if LAMMA spectra are to be normalized by organic frequent ion mass lines. The ratio of the amplitude of the atomic ion signals to the amplitude of organic ions depends on the laser power density relative to the threshold energy. Therefore, the ratio of the ion signal of an atomic element to the ion signal of the organic background could depend on the laser power density.

Investigation using standards that consisted of epoxy resin doped with lead have shown that the shift of the ratio $\text{I}_{\text{Pb}}/\text{I}_{\text{m}=30}$ ($m = 30$, a mass line of the organic background) as a function of laser power densities are measured from the transmitted laser light, which can be varied by means of filters. In this investigation the laser power density was always higher than the threshold energy.

Discussion

An essential presupposition for the applicability of the LAMMA method in medical research is the quantitation of the results. In general, several methods of quantitation are possible: (a) direct use of a working curve, (b) use of relative and absolute sensitivity factors, (c) "first principles" approach with LTE-model (see Ref. 5 for more details).

At present details of the physical process of the laser-induced ion formation are unknown. Therefore, no theoretical model can predict the ion yield in a specific situation. Empirical procedures must be applied for quantitation. This means that a correlation between ion signal and concentration has to be established by use of standards. But without information as to the actual evaporated volume, one must first normalize the spectra using internal reference elements in order to establish such a correlation. For the estimation of sensitivity factors, standards with attributes identical to those of the specimens are necessary, especially with regard to homogeneously distributed reference matrix elements in specimen and standard. For the use of LTE models, two reference elements are necessary to fit the parameters.

Since biomedical specimens do not contain homogeneously distributed matrix elements, suitable organic masses can be chosen for internal standard in order to normalize the

spectra. A characteristic of these organic mass lines must be the relatively low standard deviation in signal amplitude if the instrument parameters are constant for every analysis. Thus the condition of an homogeneous distribution is fulfilled.¹

The use of organic mass lines for a reference element enables the normalization of the spectra and thus relative quantitation is possible.

The influence of the laser power density on the various formation processes of atomic and molecular ions (in case of the described investigations) was very low. To get a sufficient ion yield, parameters of the LAMMA instrument were chosen such that the perforation of 0.5 or 1 μm -thick sections has a diameter of 0.8-1 μm . Despite optical absorption resonances and variations in the laser power density (as a result of the instability of the laser light), the laser power density to be selected does not vary considerably. Therefore the influence of the laser power on the different formation processes of atomic and organic ions may be smaller than the standard deviations of the measurements. Moreover, the organic masses of the embedding material in specimens and standards permit the normalization of the spectra from the specimens and external standards. Thus calibration curves can be established as a basis for absolute quantitation.

References

1. P. F. Schmidt and K. Ilseman, "Quantitation of laser microprobe mass analysis results by the use of organic mass peaks for internal standards," *SEM/1984 I*, 77.
2. H. Zumkley et al., "Influence of low and high cadmium diet in normotensive and hypertensive SH-rats," *Klin. Wochenschr.* 63: (Suppl. III): 70, 1985.
3. P. F. Schmidt, R. Barckhaus, and W. Kleimeier, "Laser microprobe mass analyzer investigations on the localization of cadmium in renal cortex of rats after long-term exposure to cadmium," *Trace Elements in Medicine* 3: 19, 1986.
4. R. Höpcke and P. F. Schmidt, "Topographical investigations of phosphate-modified starches," *37th Starch Convention* Detmold, FRG, 1986.
5. P. Wieser, R. Wurster, and R. Wechsung, "Methods for quantitation with LAMMA," *2nd LAMMA-Workshop*, Forschungsinstitut Borstel, FRG, 1983, 29.

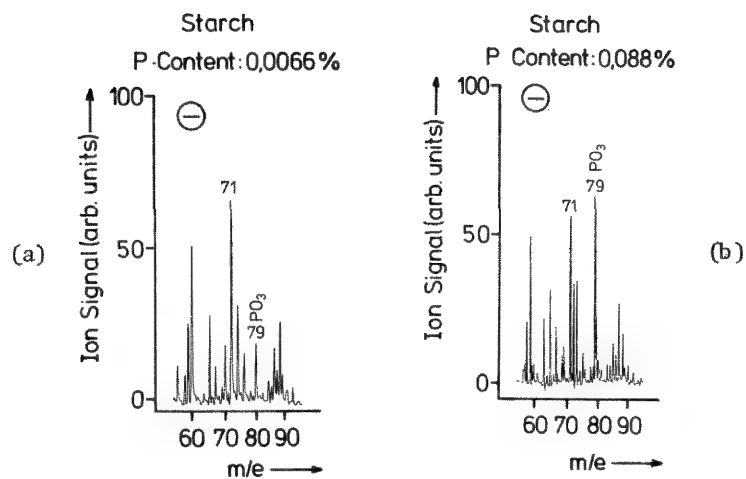


FIG. 4.--Segments of LAMMA spectra from homogenized starches with (a) 0.0066% P, (b) 0.088% P.

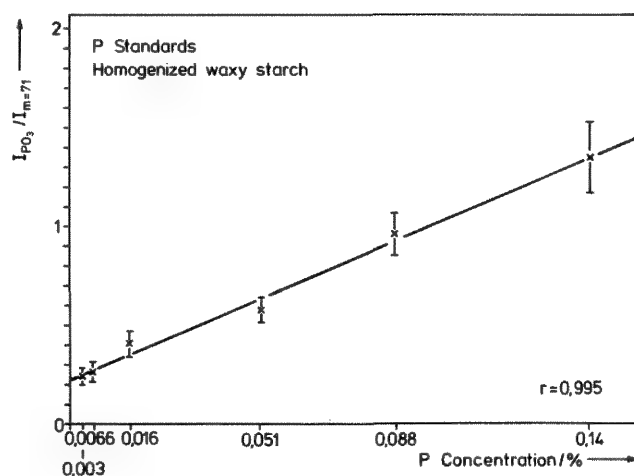


FIG. 5.--Calibration plot of average values of $I_{PO_3}/I_{m=71}$ as function of P concentrations.

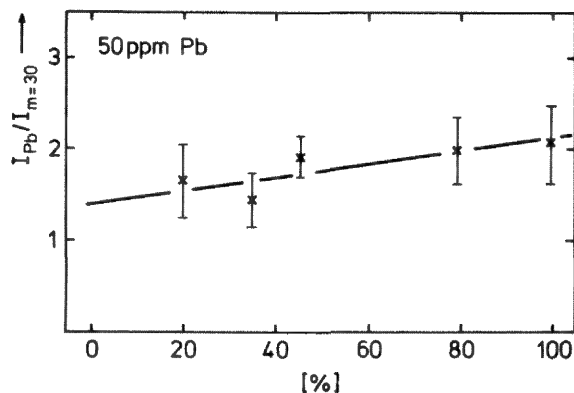


FIG. 6.--Dependence of ratio $I_{Pb}/I_{m=30}$ on laser densities.

LASER MICROPROBE ANALYSIS OF ZIRCONIUM COMPOUNDS: SURVEY MASS SPECTRA AND RELATIVE ION YIELDS

R. W. Odom and I. C. Niemeyer

Laser microprobe mass spectrometry mass spectrometry can provide a sensitive elemental micro-analysis of a wide range of inorganic and organic materials¹ and, in selected cases, appears to provide fingerprint mass spectra characteristic of the structural composition of the target materials.^{2,3} We have initiated a systematic analytical study to determine whether the laser microprobe technique can provide structural characterization for a wide variety of inorganic compounds. This paper reports the results of analyses of several homologous Zr compounds. The positive and negative ion mass spectra produced from these compounds were analyzed for structurally significant ion signal patterns, and the relative ion yields of the major elemental constituents were evaluated and compared to the known chemical composition of the compounds.

Experimental

The Zr compounds analyzed included $\text{Zr}(\text{SO}_4)_2 \cdot \text{H}_2\text{O}$, ZrS_2 , ZrC , $\text{Zr}(\text{C}_2\text{O}_4) \cdot \text{H}_2\text{O}$, $\text{Zr}(\text{CO}_3)_2$, ZrB_2 , ZrB_{12} , ZrO_2 , ZrP , and $\text{ZrO}(\text{H}_2\text{PO}_4)_2 \cdot \text{H}_2\text{O}$. The compounds were purchased from various chemical supply companies (including Chem Services, Alfa, Aldrich and Pfaltz and Bauer) in powder form. A few milligrams of each sample was pressed into a high purity In foil. The laser microprobe analyses were performed on a Cambridge Mass Spectrometry model LIMA 2A, which has been described in detail elsewhere.⁴ Both positive and negative ion analyses were performed on at least fifteen distinct regions of each sample at three different laser irradiances. These irradiances corresponded to the production of the $^{90}\text{Zr}^+$ intensities which were ~ 10 , 100, and 1000 times the noise level of the ion detection system. The actual irradiances employed were approximately 0.5, 2 and 5×10^{10} W/cm^2 . It was initially believed that a low-irradiance analysis would provide the optimum condition for observation of structurally significant molecular or cluster ion peaks, and that the higher irradiance analyses would produce more intense elemental ion signals. The peak area intensities of selected ion signals were evaluated from the 15 spectra produced at each irradiance in order to determine the average and standard deviation (SD) of these signals.

Results and Discussion

Survey Mass Spectra. In the positive ion

The authors are with Charles Evans & Associates, 301 Cheasapeake Drive, Redwood City, CA 94063. Support for this work was provided by NSF SBIR grant ISI-8700019.

analysis mode, the ZrS_2 , $\text{Zr}(\text{CO}_3)_2$, and ZrO_2 compounds all produced readily detectable pseudo-molecular or structurally significant ions of reproducible intensity. Cations of ZrS , ZrS_2 , and ZrS_3 , $(\text{ZrS})_2$, and $(\text{ZrS})_2 \cdot \text{S}$ were observed at all the three irradiances in the analysis of ZrS_2 . The $\text{Zr}(\text{CO}_3)_2 \cdot \text{H}_2\text{O}^+$ ions were observed at each irradiance in the analysis of $\text{Zr}(\text{CO}_3)_2$; the (ZrO_2H^+) ion was reproducibly detected in the analysis of ZrO_2 . Almost all the positive ion mass spectra contained relatively intense ZrO^+ signals, which suggests that all the compounds had a significant surface concentration of oxygen. The elemental composition of the various Zr compounds could be readily distinguished in the high irradiance spectra. The positive ion patterns produced from the several ZrB and ZrP compounds were qualitatively similar, as were the patterns produced from the ZrC and ZrC_2O_4 species.

In the negative ion analysis mode, ZrS formed the distinctive anions ZrS , ZrS_2 , ZrS_3 along with intense signals for S^- , m/z 64 (S_2 and/or SO_2) and 96 (S_3 and/or SO_4). The Zr sulfate also forms negative ion signals at the m/z values of 32 and 64; however, the most intense negative ion signal in the spectra of this compound is the HSO_4^- (m/z 97) ion. Thus, the unique ionization patterns observed in the positive and negative ion spectra of ZrS_2 and $\text{Zr}(\text{SO}_4)_2$ provide an unambiguous distinction between these two compounds. ZrC forms a low intensity molecular anion signal at high and intermediate laser irradiances. This ion is not observed in the spectra of $\text{Zr}(\text{CO}_3)_2$ or ZrC_2O_4 . No particular distinctive anions are observed in the spectra of $\text{Zr}(\text{CO}_3)_2$. The HC_2O_4^- ion is formed at relatively high intensity from ZrC_2O_4 at all three laser irradiances, and this signal is not observed in the negative ion spectra of any other compound. The two ZrB compounds do not form distinctive negative ion patterns. ZrO_2^- is observed in the spectra of ZrO_2 . The PO_2^- and PO_3^- anion signals are more intense in the spectra of $\text{ZrO}(\text{H}_2\text{PO}_4)_2$ than in the ZrP spectra and the relative phosphate anion intensity could serve as a general method for distinguishing phosphate and phosphide adducts. In summary, the ionization patterns produced in the laser microprobe analysis of these samples often produce distinctive peaks which are characteristic of the compound's chemical and structural composition.

Relative Ion Yields. The relative positive ion yields of the various constituent atoms in these Zr compounds were also evaluated in order to determine the yield variability of a given elemental ion from different Zr "matrices."

These ion yield data could provide an additional method of distinguishing the different chemical compositions. The positive ion yield of element X relative to Zr is defined by

$$Y(X/Zr) = \frac{i_{X^+}}{i_{Zr^+}} \frac{N_{Zr} i_{f_{Zr}}}{N_X i_{f_X}} \quad (1)$$

where i_{X^+} and i_{Zr^+} are the peak area intensities of the i th isotope of element X and Zr, $i_{f_{Zr}}$, i_{f_X} are the relative abundance of these isotopes and N_{Zr} and N_X are the atom densities of X and Zr. The ion yields were evaluated only for the high-irradiance analyses because these data generally contained the largest elemental ion intensities. The $^{94}Zr^+$ ($i_{f_{Zr}} = 0.1740$) was used as the normalizing ion intensity, since the $^{90}Zr^+$ intensity was often above the linear range of the ion detection system. Table 1 summarizes the results of this evaluation. The right-hand column lists the ion yields based on an ionization potential "model" in which $Y(X/Zr) \propto \exp\{-[IP(X)-IP(Zr)]\}$, where $IP(X)$ and $IP(Zr)$ are the ionization potentials of these elements.⁵ The ZrO_2 compound produced a detectable O^+ signal in only 5 of the 15 spectra. Consequently, the O/Zr ion yield was not evaluated. The average $^{94}Zr^+$ intensities were of the order of 9000 (± 2000) peak area units for all the analyses except ZrB_2 in which the $^{94}Zr^+$ intensity was ~ 15000 (± 3500). Thus, the

Zr^+ ion yields were uniform within a factor of ~ 2 for all these compounds, suggesting that the ionization conditions were also fairly uniform. The ZrB compounds were the only species in this sample set which exhibited similar relative ion yields, and these ion yields are close to the values calculated from the ionization model. The S^+/Zr^+ and C^+/Zr^+ yields exhibit substantial variation for the various compounds, strongly suggesting that these yields are matrix dependent at these laser irradiances. This variability, coupled with qualitative differences in the ionization patterns, could serve as a basis for distinguishing different chemical compositions. These types of analyses are in progress for other metal complexes.

References

1. R. Kaufmann, *Microbeam Analysis--1982*, 341.
2. R. W. Linton, I. H. Musselman, F. Bruynseels, and D. S. Simons, *Microbeam Analysis--1987*, 365.
3. L. Van Vaeck, J. Claereboudt, J. De Waele, E. Esmans, and R. Gijbels, *Anal. Chem.* 57: 2944, 1985.
4. R. W. Odom, C. J. Hitzman, and B. Schueler, *Materials Research Soc. Symposium* 69: 265, 1986.
5. C. A. Andersen and J. R. Hinthorne, *Anal. Chem.* 45: 1421, 1973.

TABLE 1.--Relative ion yields of selected elements in Zr compounds.

Compound	X	i_{f_X}	$i_{X^+}/^{94}Zr^+$	$Y(X/Zr)_m^2$	$Y(X/Zr)_c^3$
$Zr(SO_4)_2$	S	1.00	2.412 (1.338) ¹	0.210	0.0297
ZrS_2	S	1.00	0.024 (0.009)	0.002	0.0297
ZrC	^{12}C	0.99	0.004 (0.002)	6.5×10^{-4}	0.0121
$Zr(C_2O_4)$	^{12}C	0.99	1.351 (1.012)	0.119	0.0121
$Zr(CO_3)_2$	^{12}C	0.99	0.004 (0.002)	3.5×10^{-4}	0.0121
ZrB_2	^{10}B	0.1898	0.804 (0.545)	0.369	0.2332
ZrB_{12}	^{10}B	0.1898	3.600 (1.664)	0.275	0.2332
ZrP	^{31}P	1.00	3.391 (2.031)	0.590	0.0261
$ZrO(H_2PO_4)_2$	^{31}P	1.00	1.520 (1.156)	0.132	0.0261

¹The numbers in parentheses are the SD of these ion-intensity ratios.

²Measured relative ion yields.

³Relative ion yields calculated from the ionization potential model.

11 Unique Approaches to Microanalysis

X-RAY MICROFLUORESCENCE: A NEW ELEMENTAL IMAGING TOOL THAT COMPLEMENTS THE SEM

M. C. Nichols and D. R. Boehme

Recent developments have produced X-ray Microfluorescence (XRMF), a new analysis tool that is being used for the elemental characterization of layers and structures on and beneath the surface of materials.¹⁻³ This technique had previously been explored without the advantages of modern x-ray sources, detectors, or imaging capability,⁴⁻⁷ but never became a commonly used tool. The recent developments have resulted in commercial interest by several companies and the availability of a production unit with some of the imaging capabilities described here.

Unlike the more widely known SEM and EMPA electron optical techniques, which use a small rastered electron beam to excite elemental x-ray fluorescence, XRMF uses a finely collimated beam of x-rays to excite fluorescent radiation in a sample which is translated through the x-ray beam in a raster fashion. Elemental information is collected from successive points on the sample with an energy dispersive detector and computer-controlled multichannel analyzer. The data collected for each element can be subsequently displayed as a single- or multi-colored screen image of the scanned area, or can be combined with other elemental data to provide an image showing the position of elements in relation to each other.^{1,8}

The ability to obtain elemental information for more than one element and to provide elemental maps of surface and subsurface regions makes XRMF and SEM valuable elemental imaging techniques. XRMF and SEM methods complement one another for the analysis of subsurface regions. Although the SEM has much better resolution, XRMF can be used to obtain elemental information from further beneath the surface of the sample.⁸ XRMF can also be used without coating of the sample with a conductive film and without extensive preparation of the surface, which, coupled with the ability to examine materials in air or inert gas, allows the examination of living tissue and other materials that might be destroyed or distorted if examined in a vacuum. At present, XRMF provides 15-30 μ m resolution in a readily interpreted visual form while retaining the advantages of minimal sample preparation, nondestructive analysis, and high sensitivity inherent to XRF methods.

Experimental

Beam profiles for an XRMF prototype system

The authors are at the Materials Department, Sandia National Laboratories, Livermore, CA 94550. This work was supported by the U. S. Department of Energy under Contract DE-AC04-76DP00789.

at Sandia National Laboratories, Livermore, have shown that sufficient intensity can be obtained by use of a standard x-ray generator (1200 W, Norelco, Mo anode) and a 30 μ m aperture to image elements in most samples. This aperture results in a beam size at the sample of 35 μ m FWHM and 56 μ m FWTM, which has proved to be sufficient to provide 40 μ m resolution in the resulting image. The system uses an aperture rather than a collimation system, with the distance from the x-ray anode to the aperture large relative to the aperture-to-sample distance. For many samples of interest, the divergence of the x-ray beam as a function of the distance within the sample is not important since the x-rays penetrate only a few tens of microns into the samples. Because the effective depth from which XRF information is obtained is much greater for biological or very porous materials such as low-density catalysts, Sandia's system was designed to provide a beam that is as parallel as possible, consistent with obtaining sufficient fluorescent intensity from the sample with minimum beam divergence.¹

Results and Discussion

We have examined several samples using both XRMF and SEM techniques. Although the resolution of the SEM is considerably greater than the XRMF instrument, the depth from which the fluorescent x-rays are excited is significantly lower. With the XRMF technique, it is possible to excite fluorescent radiation at considerably greater depth than in the SEM and also obtain elemental information from beneath structures too thick for the SEM beam to penetrate. What limits the depth from which elemental information can be obtained by the XRMF technique is the escape depth of the elemental x-ray in question and the matrix from which it must escape.

We have obtained information from samples as diverse as electronic chip carriers, mineralogical samples, and organic microstructures. The data from these samples indicate that the information from the XRMF technique is coming from deeper within the sample than in the SEM. For example, in the investigation of a Te containing mineral sample, the approximate depth from which the SEM information was obtained was 1-2 μ m, but the depth from the XRMF method was approximately 40 μ m.⁸ In addition, the enhanced sensitivity and decreased bremsstrahlung radiation of the XRMF technique lends itself to the detection of minor constituents or weaker elemental signals coming from beneath the surface of the sample.

We have concentrated on qualitative imaging

of the data in most of the experiments performed to date. The use of standards allows quantitative analysis to be performed and even displayed in a false-color image format for very thin or very dense samples. However, the porous nature of most of the samples we have been investigating has made correction difficult, partly because the intensity of the radiation reaching the detector from the sample decreases with the square of the distance between sample and detector. Since the detector is placed very close to the sample, any variation in depth within the sample from which the fluorescent signal originates causes a variation in the signal received at the detector. For samples having elemental structure in both the surface and subsurface regions it is difficult to determine whether a decreased elemental signal is due to a lower elemental concentration at a given point or whether the same concentration of that element is present deeper within the sample. This variation of signal with depth can sometimes be used to advantage to supply contrast for surface or subsurface topography of samples. Such samples may have uniform compositions at the surface or on internal layers but their outer or inner surfaces may be at various elevations on or in the sample. Using the variation in signal that occurs with depth in the XRMF method, we can image these variations in topography. We have also made comparisons on samples examined using computed x-ray tomography techniques where the ability of XRMF to image multiple elements has proved to be valuable.

We have been able to learn a great deal from the XRMF images made from this prototype instrument, especially for samples with a regular or known structure for which XRMF can show variations that might otherwise be missed by other techniques. XRMF has also proven valuable for the characterization of samples having patterns of elements occurring beneath the surface of the sample. We have found the use of color to be vital in XRMF image analysis, especially for superimposed images of several elements. Several examples of the use of color in XRMF images can be found in the literature.^{1,8}

Conclusions

XRMF imaging provides a useful technique for the characterization of a wide variety of materials. It complements electron optical methods of examination and allows examination of some materials that cannot be conveniently examined by other methods. The penetrating nature of the x-ray beam provides elemental information at depth, which, when combined with surface information obtained by other techniques, gives a more complete analysis of the sample. The technique can also complement tomographic examination of samples by providing elemental analysis for a range of elements that could not be differentiated by most tomographic methods.

References

1. M. C. Nichols et al., "Parameters affecting x-ray microfluorescence (XRMF) analysis," in C. S. Barrett et al., Eds., *Advances in X-ray Anal.*, New York: Plenum, 1987.
2. M. C. Nichols and R. W. Ryon, "An x-ray microfluorescence analysis system with diffraction capabilities," in C. S. Barrett et al., Eds., *Advances in X-ray Anal.*, New York: Plenum, 1986.
3. D. Wherry and B. Cross, "XRF, micro-beam analysis, and digital imaging combined into powerful new technique," *Analyst* 12: 8, 1986.
4. I. Adler and J. M. Axelrod, "The curved-crystal x-ray spectrometer: A mineralogical tool," *American Mineralogist* 41: 524, 1956.
5. I. Adler, J. Axelrod, and J. J. R. Branco, "Further application of the intermediate x-ray probe," in W. M. Mueller, Ed., *Adv. in X-ray Anal.*, New York: Plenum, 1960, vol. 2.
6. K. F. J. Heinrich, "X-ray probe with collimation of the secondary beam," in W. M. Mueller, Ed., *Adv. in X-ray Anal.*, New York: Plenum, 1962, vol. 5.
7. H. J. Rose Jr., R. P. Christian, J. R. Lindsay, and R. R. Larson, *Microanalysis with the X-ray Milliprobe*, U.S. Geol. Survey Prof. Paper 650-B, 1969, B128-B135.
8. D. R. Boehme, "X-ray microfluorescence of geologic materials," in C. S. Barrett et al., Eds., *Advances in X-ray Anal.*, New York: Plenum, 1987, vol. 30.

A SCANNING X-RAY MICROPROBE WITH GLASS CAPILLARY COLLIMATION

D. A. Carpenter, R. L. Lawson, M. A. Taylor, D. E. Poirier, K. Z. Morgan, and G. W. Haney

Electron-beam techniques for determining elemental distributions in materials require special specimen preparation techniques as well as a high-vacuum chamber. These and other limitations have provided a driving force in recent years for the development of x-ray microfluorescence/microprobe instrumentation. As one approach to the problem of providing high primary x-ray beam intensity, a scanning x-ray microprobe analyzer with small bore pyrex glass capillary tubes (10-100 μm) placed very near the focal spot of a high brilliance microfocus x-ray tube was constructed at the Oak Ridge Y-12 Plant. Total reflection of x rays along the walls of the capillary would tend to transmit the solid angle of radiation captured at the anode end to the specimen end of the capillary, resulting in a large intensity gain when compared with metal apertures. Experiments were carried out comparing the intensity transmitted through glass capillary tubes to that passing through comparable metal apertures. In addition, the profile of the transmitted beam was examined as part of an effort to determine the potential resolution of the analyzer. Microfluorescence data were collected from several specimens to demonstrate the potential of the analyzer.

Experimental

A microfocus x-ray tube, designed for real-time radiography, was used as the source of x rays for the analyzer. The x-ray tube was designed with a vacuum system and controls for focusing and steering the focal spot. The focused spot size is 10 to 20 μm in diameter. A tungsten anode, loaded at 30 kV and 0.70 mA, was used for the experiments in this study. For beam collimation, a glass capillary tube was inserted into the x-ray tube through a vacuum port which replaced the usual x-ray window. The distance between the capillary tube and the focal spot was 4-5 mm, depending on the position of the focal spot on the anode. The capillary axis made an angle of 5.5° with the anode surface. The focal spot was aligned with the capillary tube by alternate focusing and steering of the beam until maximum fluorescent intensity was obtained.

In addition to the x-ray source, the analyzer consisted of a sample stage equipped for remote X-Y scanning and a lithium-drifted silicon [Si(Li)] detector with associated electron-

ics and a multichannel analyzer. Images were constructed from the digital data with a graphics computer.

Results

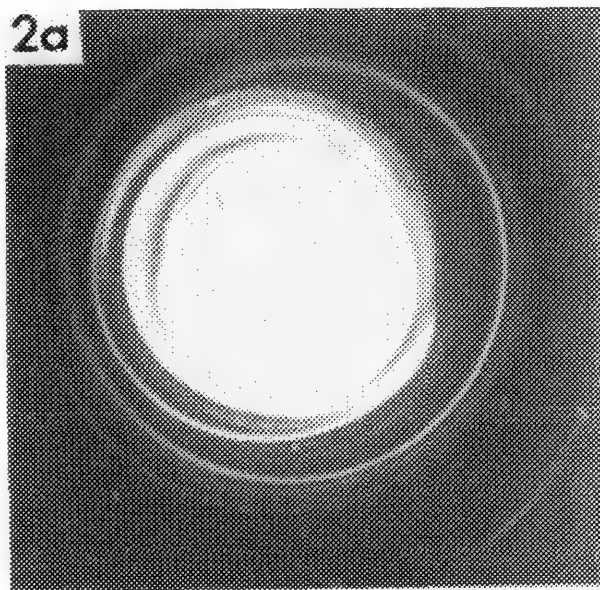
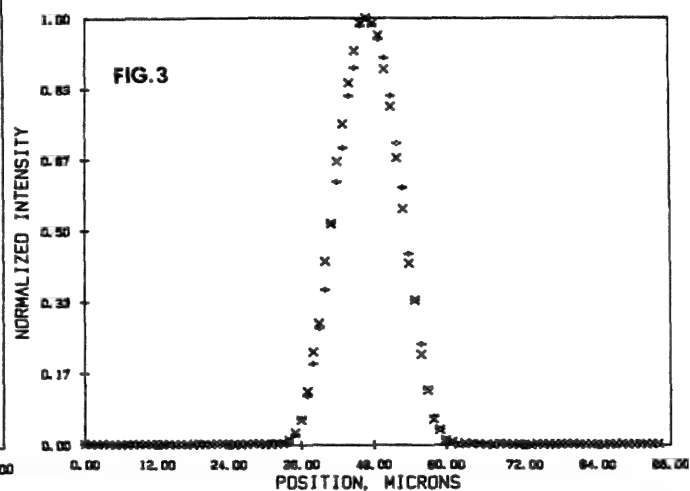
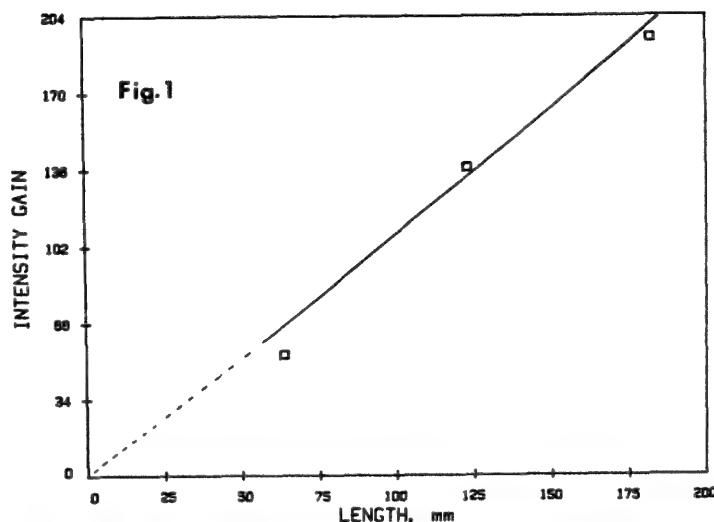
A comparison of the intensity through 25 μm capillaries placed 4.4 mm from the focal spot with the intensity through a lead aperture placed at the same distance from the anode as the specimen end of the capillary tube produced the results shown in Fig. 1. These gains are comparable with those reported for larger glass tubes of similar length-to-diameter ratios.^{1,2}

The beam profile produced by glass capillary tubes is illustrated by the x-ray exposures through a 100 μm capillary, 178 mm long, placed at a long (Fig. 2a) and at a short (Fig. 2b) distance from the film. Although the beam profile is complex under high-resolution conditions, it can be made uniform by a reduction in the distance between the capillary and the specimen, as shown in Fig. 2b. Additional exposures through a 10 μm capillary showed only a uniform profile. Fluorescence line scans over a fine nickel wire (Fig. 3), placed 0.5 mm from the end of a 10 μm capillary, gave additional evidence of the uniformity of the beam. The beam has the same profile in either the horizontal or vertical direction. Metal apertures, on the other hand, produce beams with noncircular profiles, since they are the projection of the filament image on the anode.³

As an indication of the resolution of the analyzer, two crystals of a copper-titanium-tin alloy were arranged in a "V" configuration on an aluminum block and scanned with a 10 μm capillary (Fig. 4). The distance between the two crystals was then measured with a calibrated microscope as a function of the distance from the point of intersection. This "scale" was then superimposed on the image of the tin distribution and the region where the two crystals could no longer be distinguished was found to be near 5 μm .

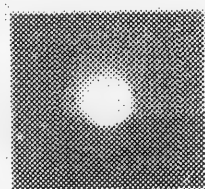
The use of the analyzer as a microprobe was demonstrated by the analysis of a tungsten/3wt%-nickel/2wt%-iron (W/3Ni/2Fe) alloy (Fig. 5). The W/Ni/Fe alloys are liquid-phase sinterable alloys containing primarily nickel and iron in the grain boundaries (0-15 μm wide) and tungsten as the matrix phase. The images were prepared from uncorrected data, taken with a 10 μm capillary, and clearly showed the expected distribution of all three elements.

The authors are at Oak Ridge Y-12 Plant, Oak Ridge, TN 37831, operated for the U.S. Department of Energy by Martin Marietta Energy Systems, Inc., under contract DE-AC05-84OR21400.

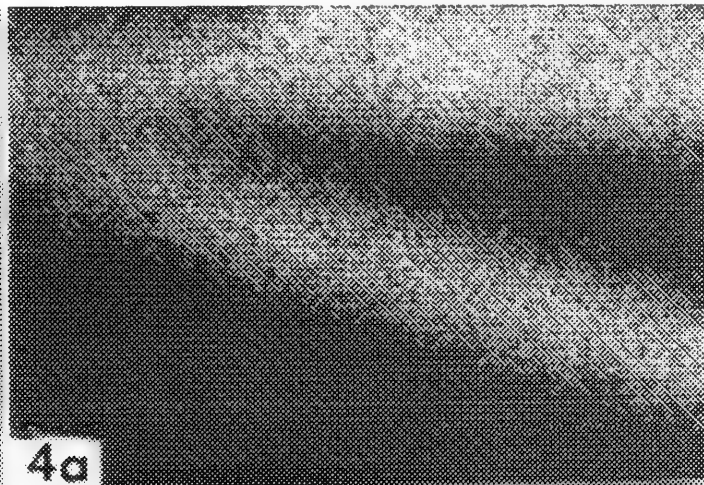


640 μm

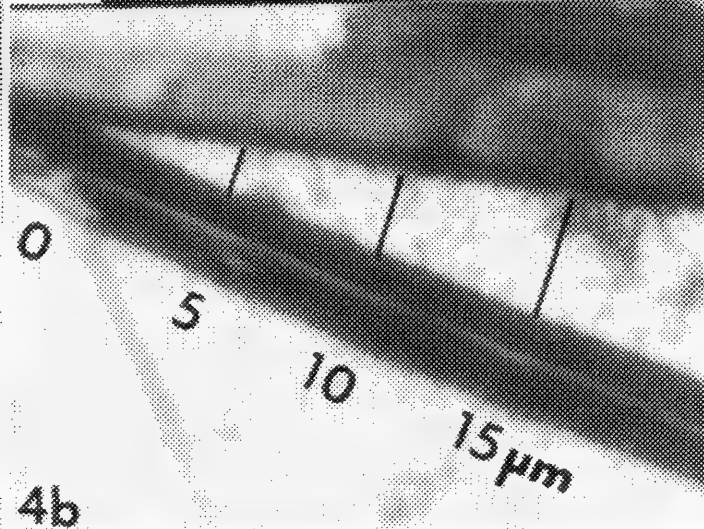
2b



130 μm



4a



4b

FIG. 1.--Intensity gain (factor) of 25 μm -diam. glass capillary tubes over comparable lead apertures with distance from focal spot.

FIG. 2.--Profile of x-ray beam through a 100 μm -diam. glass capillary tube: (a) Capillary length 178 mm, capillary-to-focal spot distance 4.4mm, placed 52 mm from x-ray film, tungsten anode, 30 kV, 0.70 mA. (b) Placed 2 mm from x-ray film; all other conditions same as in 2(a).

FIG. 3.--Fluorescent line scans over 12.5 μm nickel wire (Ni K α) with 10 μm -diam. capillary. (x) represents data collected with wire oriented vertically, scanning horizontally; (+) represents data collected with wire oriented horizontally, scanning vertically.

FIG. 4.--Resolution test of microprobe analyzer: (a) Image of tin distribution (Sn L lines) in Cu/Ti/Sn alloy single crystals, 10 μm capillary, scan area 100 \times 100 μm , 1 μm /pixel; (b) micrograph of Cu/Ti/Sn alloy of (a) showing scale of distance between needles.

Conclusions

A scanning x-ray microprobe, with a resolution of about 5 μm , has been constructed with pyrex glass capillary tubes in combination with a high brilliance microfocus x-ray tube. The x-ray microprobe could be used in many instances where an electron microprobe might or-

dinarily be used. The advantages would be that the analysis could be carried out in air and the specimen, in many cases, could be used "as-received." Although the resolution limit is still high, it could conceivably be improved either by use of a smaller capillary or by image processing to deconvolve the beam profile from the image data.

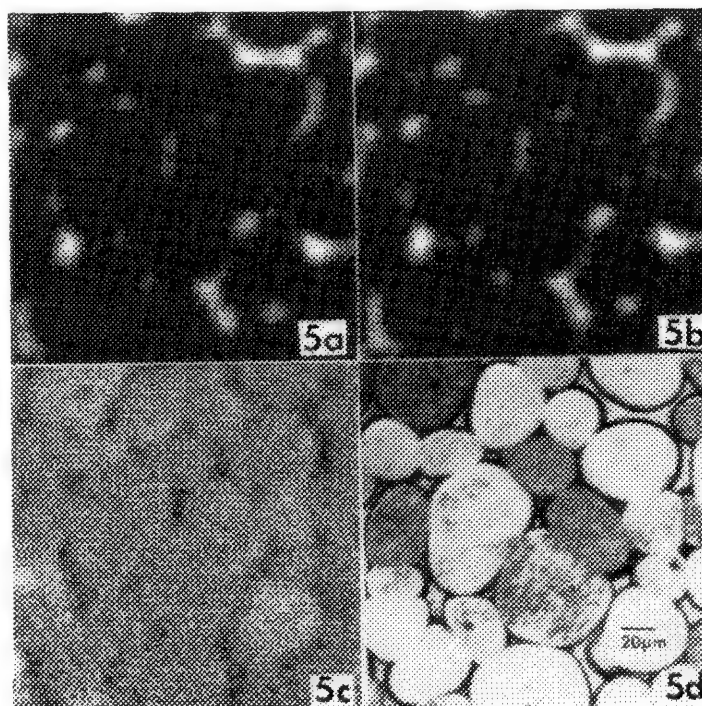


FIG. 5.--Images of elemental distributions in a W/3Ni/2Fe alloy. 10 μm capillary, scan area 200 \times 200 μm , 2 μm /pixel: (a) Fe K α distribution, (b) Ni K α distribution, (c) W L α distribution, (d) optical micrograph of area analyzed.

References

1. V. F. Jentzsch and E. Nöhling, "Die Fortleitung von Licht- und Röntgenstrahlen durch Röhren," *Zeitschr. f. techn. Physik*, 185, 1931.
3. P. J. Molloy et al., "Laser-generated plasmas as a source of x rays for medical applications," *Appl. Phys.* 45: 1891, 1974.
3. H. Nakazawa, "X-ray guide tube for diffraction experiments," *J. Appl. Cryst.* 16: 239, 1983.
4. V. B. Baryshev, G. N. Kulipanov, and A. N. Skrinsky, "Review of x-ray fluorescent analysis using synchrotron radiation," *Nucl. Instr. and Meth.* A246: 739, 1986.
5. M. C. Nichols et al., "Parameters affecting x-ray microfluorescence (XRMF)

analysis," in C. S. Barrett et al., Eds., *Advances in X-Ray Analysis*, vol. 30, New York: Plenum, 1987, 45.

DETECTION LIMITS IN MICROPROBE X-RAY FLUORESCENCE ANALYSIS

D. B. Wittry and D. M. Golijanin

Recent developments have indicated the feasibility of an x-ray microprobe based on focusing characteristic x rays from a laboratory x-ray source of high brightness with the use of doubly curved crystals.¹⁻³ The use of such an x-ray microprobe for x-ray fluorescence analysis has been called Microprobe X-ray Fluorescence Analysis (MXRF). This technique has many advantages over electron-probe x-ray microanalysis, including the following: the specimens need not be placed in a vacuum, there is virtually no charging of insulating specimens, radiation and thermal damage to specimens is low, and very little background is produced in the specimen resulting in low detection limits.

The first two of these advantages, lack of a vacuum requirement and the absence of charging effects, are self-evident. The lower specimen damage is due to the specificity of excitation by x rays; Sparks⁴ has estimated that for comparable detection limits in an x-ray microprobe based on synchrotron radiation, the energy dissipated in the specimen would be 10^{-2} to 10^{-6} times that for charged particle excitation. In a future paper, we plan to discuss this point with regard to a laboratory-based x-ray microprobe.

In this paper, we are concerned mainly with evaluating the anticipated detection limits for the MXRF technique. We assume that an element will be detectable if it produces a signal that is statistically significant compared to the rms fluctuations in background. We also assume for simplicity that the counting rate is directly proportional to the concentration, recognizing that this may not be true for specific cases because of absorption and fluorescence effects in the specimen. Finally, we assume that the instrument is sufficiently stable that instrumental drifts are not a limiting factor in determining the detection limits. With these assumptions, the minimum concentration detectable with a confidence level of 95% is given by⁵

$$C_{MD} = 3.29 C_s \sqrt{\eta B/S} \quad (1)$$

where C_s is the mass fraction of a standard specimen, B is the number of background counts, S is the number of signal counts for a concentration of C_s , and η varies between 1 and 2 depending on how accurately the background has been determined.

It can be seen from Eq. (1) that the detec-

D. B. Wittry is in the Departments of Materials Science and Electrical Engineering and D. M. Golijanin is in the Department of Materials Science at the University of Southern California, Los Angeles, CA 90089-0241.

tion limits will be reduced in direct proportion to $(S/B)^{-1}$ and $(B)^{-1/2}$, which is determined by the signal generation and collection efficiency.

For the present case, we shall assume values for the number of x-ray photons/s in the x-ray microprobe from a previous estimate.⁶ This estimate and the manner in which it was obtained is shown in Table 1. The x-ray fluorescence signal generated by monochromatic radiation was calculated by Kotera and Wittry⁷ for various characteristic x-ray lines exciting K or L levels of the elements in the specimen. The ratio of the number of photons generated to the number of photons incident is called the x-ray excitation efficiency. As shown in Fig. 1, this can range from 5×10^{-1} to 5×10^{-3} . If suitable diffractors are chosen, a typical value would be 5×10^{-2} .

TABLE 1.--X-ray intensity for laboratory-based microprobe.

Cu K α at 40 kV	Ge (333) Reflection
(1) X-ray target current	0.001 A
(2) X-ray production efficiency	0.006 phot/s
(3) Absorption factor	0.82
(4) Solid-angle factor	0.061
(5) Diffractor efficiency	0.33

$$\text{X-ray intensity} = \frac{(1) \times (2) \times (3) \times (4) \times (5)}{1.6 \times 10^{-19}}$$

$$= 6 \times 10^{11} \text{ phot/s in focal spot}$$

For determining the signal-to-background ratio and the background, two additional considerations are important: (1) the fundamental sources of background, and (2) the resolution and collection efficiency of the spectrometer used to detect the fluorescence excited x rays.

Background Considerations

The background in MXRF can be very low compared to electron-beam excitation because the incident photons can only produce a continuum background in inelastic scattering; the cross section for these effects is small except for the Compton effect. The background can also be much lower in MXRF than in conventional x-ray fluorescence analysis because continuum from the x-ray source can reach the spectrometer only if it undergoes Rayleigh scattering twice, first from the focusing diffractor and then from the specimen. In fact, if the radiation from the specimen is suitably collimated so that the spectrometer can receive only radiation from the region that is bombarded by the focused characteristic radiation, the contribution to the background due to Ray-

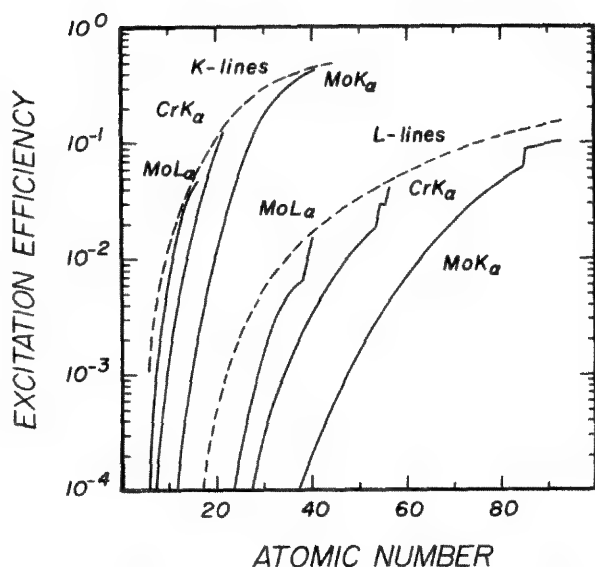


FIG. 1.--Efficiency for excitation of element with atomic number Z in thick target by various monochromatic x-ray lines.⁷

leigh scattering of the continuum can be made negligibly small.

The fundamental sources of background in MXRF include inelastic scattering, continuum due to the radiative Auger process, and bremsstrahlung due to photoelectrons. Of the many inelastic scattering processes that can take place (e.g., Compton scattering, resonance-Raman scattering, thermal diffuse scattering, double Compton scattering, Compton-Raman scattering, plasmon scattering, etc.) it appears that only Compton-Raman scattering can produce a broad continuum sufficiently removed from the Rayleigh scattered primary x-ray peak and its Compton scattered peak to represent a source of real background. However, this effect is weak and it is not expected to represent a fundamental limitation in MXRF.

The radiative Auger (RA) process may be an important source of background over a limited part of the emission spectrum (e.g., on the long-wavelength side of peaks due to major constituents) for specimens of low atomic number.⁸ However, it is not possible to evaluate its importance in determining elemental detection limits without considering specific cases and without more experimental data on the probabilities for decay of excited states by the RA process.

Background due to bremsstrahlung generated by photoelectrons is probably the most important source of background in MXRF. Although this problem has been discussed previously in conjunction with detection limits of x-ray fluorescence analysis (XRF) and proton induced x-ray emission (PIXE), it is useful to give an independent estimate based on Kramers's equation for the x-ray continuum. This equation gives the intensity of the bremsstrahlung at energy E_ν due to electrons of energy E_0 in a frequency interval $d\nu$ as:

$$I(\nu) = kZ(E_0 - E_\nu) d\nu \quad (2)$$

where the constant of $k = 2.2 \times 10^{-6}$ given by Kramers was independently evaluated by Wu and Wittry⁹ for $d\nu$ corresponding to an energy interval of 1 keV, with E_ν and E_0 in keV. Converting $I(\nu)$ to the number of background photons/s/electron = N , we would have.:

$$N = 2.2 \times 10^{-6} Z(E_0 - E_\nu) (\Delta E/E) \quad (3)$$

where $\Delta E/E$ is the energy resolution of the spectrometer.

An upper limit on the background due to photoelectrons can be obtained if we assume that every primary photon absorbed produces a photoelectron of energy equal to the energy of the primary photon and that all of the primary beam's energy is absorbed by the specimen. These assumptions lead to a gross overestimate of the background for thin specimens of low atomic number, because these specimens absorb only a small fraction of the incident beam's energy. The result of this calculation is shown in Fig. 2.

Spectrometer Considerations

For detection of characteristic x rays, either energy-dispersive spectrometry (EDS) or wavelength-dispersive spectrometry (WDS) may be used. EDS typically provides high collection efficiency and relatively poor spectral resolution; WDS provides excellent spectral resolution at the expense of collection efficiency. In many cases it is desirable to utilize both types of spectrometers with the EDS system used mainly for a survey of the major constituents, and the WDS system used for more accurate quantitative analysis and for determination of the minor constituents of the specimen.

For obtaining the ultimate detection limits of MXRF, the use of WDS is considered essential because (1) most materials which are not highly refined to provide maximum purity contain many elements in trace quantities and for these materials, the problems that occur in EDS due to overlapping peaks and their deconvolution become a serious limitation in analysis time and in accuracy of the analysis; (2) it often happens that the major peak of the element of interest is very close to a minor peak of another element present in the specimen (e.g., in the determination of Ca in biological specimens containing K); (3) the count rate limitation of EDS may result in unfavorable analysis conditions for detection of trace elements if elements present in high concentration are excited by the x-ray probe; (4) the additional "detector background" in EDS due to incomplete charge collection, which is negligible in conventional XRF and in electron probe microanalysis, can be significant compared to the fundamental sources of background in the MXRF technique; and (5) in EDS it is difficult to eliminate background coming from regions other than the region excited by the primary beam (for WDS, the focus optics of curved crystal spectrometers provide a natural collimation for the secondary radiation). In

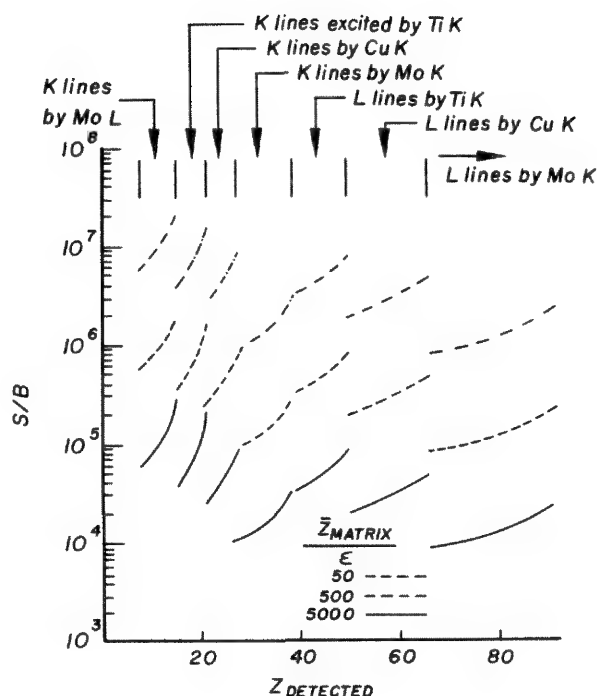


FIG. 2.--Signal-to-background ratio for bremsstrahlung due to photoelectrons for excitation by various characteristic x-ray lines exciting an element of atomic number Z in a matrix of average atomic \bar{Z} if the excitation efficiency is ϵ . For this estimate $\Delta E/E$ was assumed to be 10^{-3} .

addition, the development of automated crystal spectrometers with computer control has made WDS more efficient for multielement analysis and for analysis of unknown specimens which compensates significantly for the efficiency of the "parallel" detection provided by EDS. Moreover, the parallel detection capability of EDS must be recognized as its main advantage. It is useful for determining elements present in high concentration; for trace elements it is actually a disadvantage if the signal generation and collection efficiency is high because the EDS systems used up to now are severely count-rate limited.

Evaluation of Detection Limits

The signal levels that might be obtained from pure specimens can be very high. For example, if the number of photons incident on the specimen/s is 6×10^{11} (Table 1) and if the x-ray excitation efficiency is 5×10^{-2} (Fig. 2), the signal level for a pure specimen would be $1.5 \cdot 10^7$ counts/s. Then for a signal-to-background ratio of 10^5 x-ray efficiency of 10^{-3} , and measurement time of 100 s, the result obtained from Eq. (1) would be:

$$C_{MD} = \frac{3.29}{10^5} \frac{1}{\sqrt{1.5 \times 10^4}} = 2.67 \times 10^{-7} \quad (4)$$

On the other hand, if a complete analysis were required covering 85 elements in 300 s, about 1.5 s would be available for each measurement of peak and background and 45 s for slewing between peaks. In this case, the detection limits would be of the order of 2 ppm.

This illustrates one of the principal advantages of the MXRF technique: very low detection limits that can be obtained in a relatively short period of time. Moreover, these detection limits should be possible in regions of the order of 30 μm or less in diameter.

These estimates provide some indication of the potential of the MXRF technique to study the relationship of the concentration of trace elements to the properties of materials, electron devices, or biological systems, and also to use the concentration of trace elements for classifying materials, for studying the origin of naturally occurring materials, or for investigating materials made, processed, or altered in some way by man.

References

1. D. B. Wittry and D. M. Golijanin, "Development of an x-ray microprobe for local spectrochemical analysis," *Microbeam Analysis* --1987, 54-56.
2. D. B. Wittry and D. M. Golijanin, "Large aperture point focusing diffractor for x-rays," *Appl. Phys. Lett.* 52: 1381-1382, 1988.
3. D. M. Golijanin and D. B. Wittry, "Microprobe x-ray fluorescence analysis: New developments in an old technique," this volume.
4. C. J. Sparks Jr., "X-ray fluorescence microprobe for chemical analysis," in H. Winick and S. Doniach, Eds., *Synchrotron Radiation Research*, New York: Plenum Press, 1983, 459-512.
5. A. Curie, "Limits for quantitative detection and quantitative determination," *Anal. Chem.* 40: 586-593, 1968.
6. D. B. Wittry and D. M. Golijanin, "X-ray microprobes: A comparison of laboratory sources and synchrotron sources," *11th ICXOM*, 1986, 51-55.
7. M. Kotera and D. B. Wittry, "X-ray fluorescence analysis with monochromatic x-rays," *J. de Physique (Coll. C2)*, 45: 281-284, 1984.
8. P. Van Espen, H. Nullens, and F. Adams, "An in-depth study of energy-dispersive x-ray spectra," *X-Ray Spect.* 9: 125-133, 1980.
9. C. J. Wu and D. B. Wittry, "Measurement of surface voltages using the voltage dependence of x-ray intensities," *Proc. 10th Nat. Conf. on Electron Probe Analysis*, Las Vegas, 1975, 52A-52D.

MICROPROBE X-RAY FLUORESCENCE: NEW DEVELOPMENTS IN AN OLD TECHNIQUE

D. M. Golijanin and D. B. Wittry

Since it was applied for the first time in 1928 by Glocker and Schreiber¹ and christened by Schreiber² a year later, x-ray fluorescence spectrometry (XRF) has been one of the few techniques for materials characterization that offers a nondestructive qualitative and quantitative elemental chemical analysis. Recently, there has been an increasing need for local analysis of small volumes, which requires the formation of an intense, spatially limited x-ray microprobe for excitation. Initial attempts to accomplish this goal by collimation of the primary x-ray beam have been unsuccessful, mainly due to unacceptably low x-ray photon intensities in the probe. The solution was found in three-dimensional focusing of the x rays by diffraction from doubly curved crystals, in such a way that the diffracted beams converge to an image point. X-ray photon intensities in a laboratory-based microprobe compare favorably with the intensities achieved by the focusing of synchrotron radiation.

Doubly Curved X-ray Diffractors

Focusing geometries involving the use of spherically or toroidally curved single crystals for producing a point image from a point x-ray source have been investigated by numerous researchers over the past 36 years. Hagg and Karlsson³ and Despujols et al.^{4,5} have used toroidally curved crystals of aluminum obtained by recrystallization and plastic deformation. Berreman and co-workers⁶⁻⁸ have fabricated and evaluated quartz crystals with spherically or toroidally curved crystal planes by grinding a cylindrical slab, flattening it, and then bending it cylindrically about an axis perpendicular to that of the starting cylinder. Wassberg and Siegbahn^{9,10} attempted without success to fabricate crystals bent into a toroidal shape, but were able to bend quartz crystals into a nearly spherical surface 1 m in radius by either pressing between two circular edges or by pushing the thin slab against a spherically curved backing plate by atmospheric pressure. Barstad and Refsdal¹¹ fabricated toroidally curved NaCl and LiF crystals by hot pressing between curved glass backing plates. Eggs and Ulmer¹² made spherically curved crystals of mica and potassium acid phthalate (KAP) by pressing thin lamellae between concave and convex glass lenses. Ehrhardt et al.¹³ made spherically curved NaCl, LiF, and KBr crystals

by plastic deformation over a heated stainless-steel mold. Witz¹⁴ has reviewed various focusing monochromators for improving the intensity of diffraction patterns and has mentioned studies conducted in his own laboratory using doubly curved LiF. Das Gupta et al.¹⁵ used spherically curved mica crystals with a radius of 1.01 m obtained by pressing the crystal sheets between glass plates. Hammond et al.^{16,17} described a method of making spherically curved quartz crystals by welding a thin plate to a concave quartz backing plate. Parker¹⁸ used spherically curved silicon crystals of variable radius by applying differential pressure to a thin lamella supported by an elastomer O-ring. Recently, Chaney¹⁹ described the use of a spherically bent quartz crystal as a monochromator and focusing element for a small spot ESCA.

The design parameters of various doubly curved x-ray diffractors are summarized in Table 1. Small radius of the curved crystal planes and large crystal size become the most important contributing factors to the high "equivalent f/number." The equivalent f/number (f/no_{eq}) is defined by analogy with lenses for photography: it is similar to the conventional f/number (focal length/aperture diameter) and is derived from a circular aperture that subtends the same solid angle at the source as the crystal does in a direction perpendicular to a line joining the source and the midpoint of the crystal (Fig. 1). However, in the present case we use $f/no_{eq} = S_0/d$ where S_0 is the distance of the aperture to the source and d is the diameter of the circular aperture.

For a toroidally curved diffractor with angular limits of θ_1 and θ_2 relative to the SI axis (Fig. 2) and azimuthal angular limits ϕ_1 and ϕ_2 the solid angle is given by:

$$\Omega = \phi \int_{\theta_1}^{\theta_2} \sin \theta \, d\theta$$

Values of $\phi = (\phi_1 - \phi_2) = \pi/3$ and $\theta_1 = \pi/6$ and $\theta_2 = \pi/3$ are assumed to be possible, which would yield $f/no_{eq} = 1.16$, corresponding to a solid angle 8.3 times larger than the one listed in Table 1 and would theoretically provide 8.3 times higher intensity. The achieved detection limits would be only 2.9 times lower.²⁰

Unfortunately, the equivalent f/number alone is not sufficient for effective comparison of crystals according to their diffraction efficiencies. Only a few investigators (Barstad and Refsdal¹¹ and Ehrhardt et al.,¹³ have achieved the Johansson geometry in the plane

D. M. Golijanin is in the Department of Materials Science and D. B. Wittry is in the Departments of Materials Science and Electrical Engineering at the University of Southern California, Los Angeles, CA 90089-0241.

TABLE 1.--Doubly curved crystal diffractors for use with laboratory source.

DATE	AUTHOR(S)	f/no_{eq}	GEOM. ^a	CRYSTAL	SIZE (cm)	THICK. (mm)	RADIUS ^b (cm)	CHAR. RAD.	θ_B (deg)	APPL. ^c	REF.
1952	Hagg, Karlsson	9.30*	Jn, t	Al(200)	2.0 x 4.0	0.90	4.1 & 34	CuK α	49.59	mon, XRD	3
1952	Despujols et al.	20.19	Jn, t	Al(200)	0.5 x 3.5	-	5 & 34.5	CuK α	49.59	mon, XRF	4, 5
1954	Berberman et al.	15.27	Jn, s	SiO ₂ (052)	3.8 x 7.6	0.25	95	CuK α	71.70	mon, scat	6, 7
1958	Wassberg, Siegbahn	19.80	Jn, s	SiO ₂ (101)	ϕ 5 eff.	0.50	100	AlK α	78.50	mon, scat	9, 10
1958	Barstad, Refsdal	5.64†	Js, s	LiF(200)	4.0 x 7.0	-	40	var	var	spec, XRF	11
1965	Eggs, Ulmer	9.81†	Jn, s	MICA(002)	ϕ 6.0	0.05-0.5	70	var	var	mon/spec	12
		14.01†	Jn, s	KAP(100)	ϕ 4.2	0.05-0.5	70	var	var	mon/spec	12
1968	Ehrhardt et al.	4.74†	Js, s	LiF(200)	10 x 10	6.30	63.5	var	var	spec, XRF	13
1972	Das Gupta et al.	57.80†	Jn, s	MICA(006)	1.3 x 1.3	0.14	101	var	var	spec	15
1973	Hammond et al.	11.88	Jn, s	SiO ₂ (101)	ϕ 2.54	0.15	30.48	AlK α	78.50	mon, XPS	16, 17
1973	Parker	4.83†	Jn, s	Si(111)	ϕ 5.0	0.33	28.72	var	var	spec, XRF	18
1977	Berberman et al.	4.82	Jn, t	SiO ₂ (015)	3.8 x 7.6	0.30	18.3 & 34	CuK α	47.32	mon, scat	8
1987	Chaney	9.90	Jn, s	SiO ₂ (101)	ϕ 3.8	-	38	AlK α	78.50	mon, XPS	19
1988	Wittry, Golijanin	3.37	Js, t	Ge(333)	1.25 x 4.0	0.10	10	CuK α	44.91	mon, XRF	

a. GEOMETRY:

Jn - Johann geometry in the plane of the focal circle

Js - Johansson geometry in the plane of the focal circle

t - toroidally curved crystal; s - spherically curved crystal

b. radius of curvature of crystal planes

* - f/no_{eq} calculated for 1:1 magnification (authors use 1.54:1)

† - f/no_{eq} calculated for Bragg angle $\theta_B = 45$ deg

c. APPLICATIONS:

mon - monochromator

spec - spectrometer

scat - small angle scattering

XPS - X-Ray Photoelectron Spectroscopy

XRD - X-Ray Diffraction

XRF - X-Ray Fluorescence

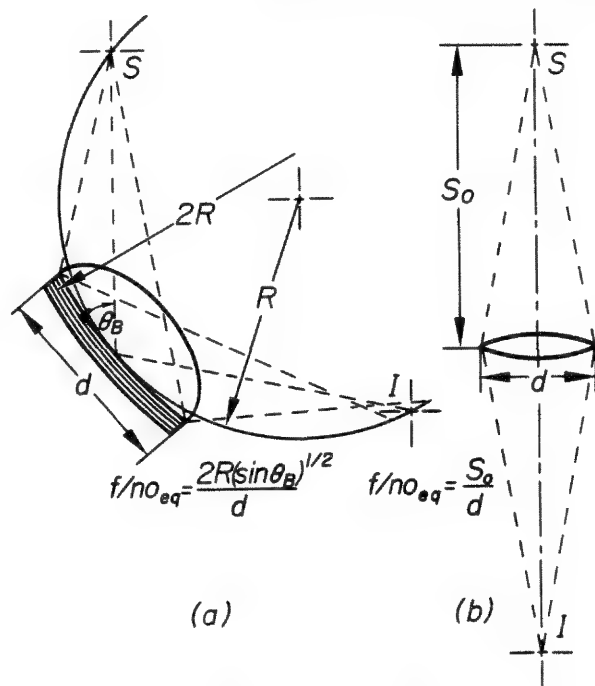


FIG. 1.--(a) Diffraction geometry of doubly curved crystal monochromator with circular crystal; (b) equivalent $f/number$ (f/no_{eq}) of a doubly curved crystal.

of the focal circle and thus the exact point-to-point focusing in one plane. Spherically bent crystals are point-to-point focusing only

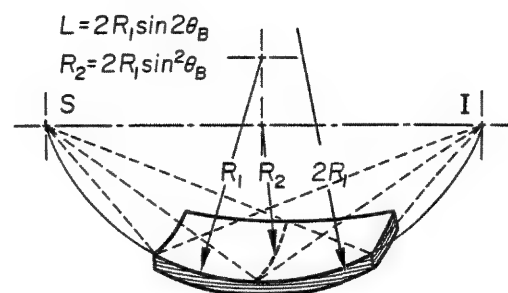


FIG. 2.--Geometry of toroidally curved x-ray diffractor for point-to-point focusing of monochromatic x rays. Crystal surface conforms to focal circle of radius R_1 ; atomic planes have radius twice as big. Johansson geometry in radial planes is obtained by rotation about line SI.

for a Bragg angle of 90° , otherwise only a part of their area is utilized for diffraction; the rest contributes significantly to the background diffraction and scattering, especially in the case of large crystals. In contrast, toroidally bent crystals with Johansson geometry can diffract a characteristic wavelength over their whole area and produce exact three-dimensional focusing.

It was found that, due to the elastic anisotropy, the central portion of the quartz

crystal wafers elastically bent by certain methods has different radii of curvature for different azimuthal directions.^{9,10} This problem, along with the most important requirement for small radii of curvature, implies that plastic deformation at an elevated temperature is the favorable bending procedure.

Only a few of the attempts in crystal bending listed in Table 1 were intended to serve as intensifying and monochromatic focusing elements for exciting x-ray fluorescence analysis.^{4,5} Many doubly curved crystals have been developed for use in diffraction experiments^{3,14} and small-angle scattering;⁶⁻¹⁰ doubly curved crystals have also been shown to be advantageous in scanning x-ray monochromators (spectrometers) used for x-ray spectroscopy,^{12,13,15,18} and they have been used to control the spatial or spectral distribution of the exciting radiation (e.g., in x-ray photoelectron spectroscopy).^{16,17} In some cases arrays of singly curved crystals have been used to approximate the use of large doubly curved crystal as described by Warren²¹ for x-ray scattering instruments; by Furnas²² and Bosslet et al.²³ for x-ray fluorescence analysis; and by Marcus et al.²⁴ and Hastings et al.²⁵ for studies of extended x-ray absorption fine structure (EXAFS).

Comparison of Laboratory and Synchrotron X-ray Sources

The main inhibiting factor in the development of an x-ray microprobe based on laboratory sources was for a long time a problem of obtaining adequate intensities. An additional limitation, that doubly curved crystals would focus x rays of only one wavelength, was shown²⁶ not to preclude their use for XRF because three or four characteristic x-ray lines are sufficient to excite effectively almost all the elements in the periodic table.

The high intensity of continuum x-ray radiation available from storage rings appeared to be the long-sought ultimate x-ray source for XRF. Synchrotron radiation can provide superior peak-to-background ratios in XRF because the wavelength (energy) of the incident beam can be varied continuously and the continuum has higher intensity than the continuum obtained with x-ray tubes.

In order to compare the intensities from synchrotron and laboratory based sources, a few points should be made: (i) characteristic lines from an x-ray tube may have an intensity of 10^4 times higher than the bremsstrahlung; (ii) the solid angle of the high-efficiency diffractor used with electron-beam-excited x rays can be as much as 10^5 times greater than the inherently very narrow angular distribution of synchrotron radiation; (iii) a microfocus x-ray source can provide 5-10 times higher brightness than a conventional x-ray tube with a large spot; and (iv) an additional 10-20-fold increase in brightness for a microfocus source compared to a conventional x-ray tube can be achieved by use of a rotating anode. Bearing these points in mind, we present the modifica-

tion of the direct comparison done by Gilfrich et al.²⁷ of the intensities obtainable from a synchrotron source with the intensities from an x-ray tube. Their comparison, drawn in dashed lines in Fig. 3 shows the superiority of the synchrotron radiation if one compares the intensities available in the continuum in a solid angle of only 0.5 μ sterad. However, it is more realistic to compare the two sources based on the intensities available when the most suitable focusing has been employed. Our comparison²⁸ takes account of high intensity of the characteristic radiation and the large solid angle from a laboratory source. We assume an energy bandwidth $\Delta E/E = 4 \times 10^{-4}$ and a solid angle of 0.77 sterad, and that 0.06 of the generated radiation can be focused for the laboratory source. After adjustment of the intensities of both sources for energy bandwidth and maximum electron currents, the comparison appears in solid lines in Fig. 3.

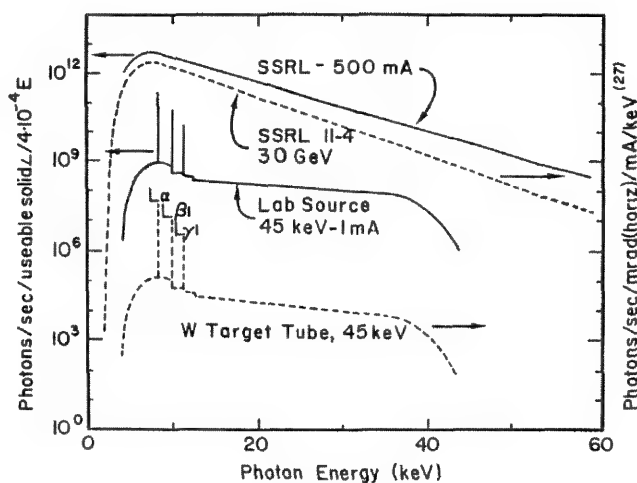


Fig. 3.--Comparison of spectral intensities for SPEAR at Stanford and a tungsten-target x-ray tube according to Gilfrich et al.²⁷ (dashed lines) and modified intensities (from Wittry and Golijanin²⁸) for a usable solid angle and $\Delta E/E = 4 \times 10^{-4}$ (solid lines).

Many authors have applied various geometries and reported²⁹⁻³⁸ measured and estimated intensities in the x-ray microprobes based on synchrotron radiation. Their parameters are summarized in Table 2.²⁸ Estimated intensity for a laboratory source compares well with the synchrotron intensities (despite a predicted electron beam current of only 1 mA, two orders of magnitude less than a synchrotron source), since a microfocus source is the most efficient for the formation of an x-ray microprobe because the source area is typically about 5000 times smaller than the storage-ring electron-beam cross section. The estimates in Table 2 for a synchrotron radiation source could be 40 to 400 times higher if wigglers or undulators were used.³⁶ However, an attractive feature of the synchrotron radiation (continuous tuning) would be lost if

TABLE 2.--Intensities of x-ray microprobes.

AUTHOR(S)	LAB	SOURCE		GEOM	M-1	PROBE SIZE		PROBE E(KV)	$\Delta E/E$ 10 ⁻⁴	INTENSITY PHOT /S/ μm^2	REF
		E(GEV)	I(MA)			H(μm)	V(μm)				
Hastings et al.	SSRL	3.7	40	a	1	2000	4000	7.1	7	1.2×10^5	29
Jaklevic/Giauque	SSRL			b	1	2000	4000	17	1	5.0×10^4	30, 31
Lemonnier et al.	DCI	1.7	120	b	1	ϕ 300 μm		8	1	2.0×10^4	32
Chen et al.	CHESS			b	1	1500	2200	8-16	10 ⁴	1.8×10^4	33
Prins et al.	SRS			c	2.6	50	50	20	1500	8.0×10^{10}	34
Sparks	BNL	2.5	500	d	10	47	80	10	1	2.8×10^8	35
Ice, Sparks	BNL	2.5	500	e	10	24	16	15	200	2.5×10^{10}	36
Jones et al.	BNL	2.5	10	f	8	30	30	8	1-200	6.0×10^5	37
Gordon, Jones	BNL	2.5	500	f	8	ϕ 30 μm		15	200	2.7×10^9	38
Wittry, Golijanin	USC	40×10^{-6}	1	g	1	ϕ 32 μm		8	4	7.5×10^8	28

FOCUSING GEOMETRY:

d - two curved crystals

* ESTIMATED INTENSITY

a - crystal monochromator - mirror

e - two curved multilayers

b - crystal monochromator - collimator

f - multilayer monochromator - mirror

c - ellipsoidal crystal

g - toroidal crystal

undulators were used.

The synchrotron-radiation-based x-ray microprobe approach also has some important problems:²⁸ (i) difficulties in fabricating x-ray optical elements to the necessary tolerance (slope error < 5 μrad), (ii) instabilities due to heating of the mirrors or diffractors, (iii) instabilities due to orbit shifts, (iv) the intensity decay with time, (v) specimen heating due to the pulsed nature of synchrotron radiation (peak power is up to 10^3 times the average power), and (vi) inconvenience due to a remote location and tight scheduling.

Laboratory X-ray Microprobe

In the previous papers^{39,40} we describe the geometry for forming a laboratory-based x-ray microprobe by using doubly curved single crystals that focus monochromatic x rays from a point source to a point image. The crystal conforms to the Johansson geometry rotated about a line joining the source S and the image I (Fig. 2). This geometry is preferably obtained by plastic deformation of the crystals because the strain involved in bending a crystal to a small radius of curvature is too great for elastic deformation without fracture.

Thin lamellae of the single-crystal slab are cylindrically cut, polished and then bent at the elevated temperature over a toroidal mold. The crystal surface in the plane of the focal circle has a radius of curvature R_1 , which is the half of the radius of the cylindrical cut. The perpendicular radius R_2 is related to R_1 via the Bragg angle according to

$$R_2 = 2R_1 \sin^2 \theta_B$$

The "parfocal" condition that several crystals with different d-spacing would focus different wavelengths from a fixed source location to a fixed image position separated by a distance L is given by

$$L = 2R_1 \sin 2\theta_B$$

In our experiments we have used Ge single crystals and the Cu K α (333) reflections which yields a Bragg angle of 44.91°. For this angle the toroidal mold is spherical to within 0.7 μm

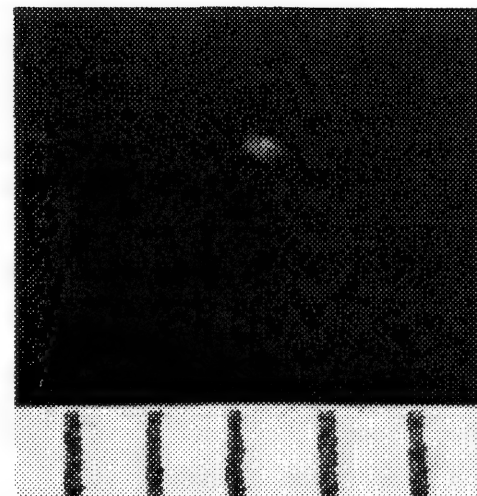


FIG. 4.--Enlarged photograph of focal spot obtained with Ge diffractor and Cu K α (333) radiation from microfocus x-ray source operated at 20 kV and 50 μA . Original photograph was exposed for 5 s on Polaroid 57 film. (1 div = 1 mm).

over the extent of the crystal (12.5 \times 40 mm), so a spherical mold has been used. After alignment of the bent crystal relative to the x-ray source, a focused x-ray spot could be observed. An enlarged photograph of the focal spot due to focusing of characteristic Cu K α line is shown in Fig. 4. The focus consists of a high-intensity central spot about 100 μm in diameter and a diffuse halo due to diffraction by the imperfectly bent portions of the crystal.

The x-ray photon flux in the focal spot was measured by a silicon solar cell. Assuming a 100% efficiency of a cell for Cu K α radiation, the current produced by a cell was measured and a flux of 9×10^5 photons/s was calculated. This flux is about two orders of magnitude lower than calculated for this size crystal and the source conditions (20 kV, 0.05 mA). The discrepancy has been attributed to one or more of the following factors: (i) imperfect bending of the crystal caused by surface irregularities of the mold and the crystal, by the formation of slip bands, and by an unaccounted for relaxation of the crystal after bending; (ii) a higher number of dislocations than required for the curvature achieved; (iii) "robbing" of the intensity in the desired direction by other coincidentally satisfied reflections; and (iv) contamination build-up or pitting of the stationary anode of the x-ray source. The last two points can account for at least ten-fold intensity reduction. Experiments with more perfectly machined molds and with alternative crystals are in progress as well as bending of bigger crystals and use of different characteristic lines and higher beam voltages and currents.

We have shown that it is possible to achieve an x-ray microprobe based on a labora-

tory x-ray source which provides a large aperture when diffractors are doubly curved to very small radii. The crystal materials with a large scattering factor at large values of $(\sin \theta)/\lambda$ are chosen with the additional requirements of being plastically deformable at a suitable temperature and possessing a slip system which is favorably oriented with respect to the desired reflection. A laboratory-based x-ray microprobe for XRF analysis would be relatively inexpensive and readily available when needed. Moreover, the use of this x-ray microprobe would not be limited to MXRF but could also be used for microprobe XPS, microfocus XRD, and fundamental investigations in x-ray physics that require a monochromatic x-ray beam of high intensity.

References

1. R. Glocker and H. Schreiber, "Quantitative Röntgenspektroanalyse mit Kalterregung des Spektrums," *Ann. Phys.* 85: 1089-1102, 1928.
2. H. Schreiber, "Quantitative chemische Analyse mittels des Röntgenemissionsspektrums," *Z. Phys.* 58: 619-650, 1929.
3. G. Hagg and N. Karlsson, "Aluminum monochromator with double curvature for high-intensity x-ray powder photographs," *Acta Cryst.* 5: 728-730, 1952.
4. J. Despujols, "Monochromateur pour rayons X à foyer ponctuel," *Compt. Rend.* 235: 716-718, 1952.
5. J. Despujols, H. Roulet, and G. Sene-
maud, "X-ray fluorescence analysis with a focused primary beam" (in French), in Pattee, Cosslett and Engstrom, Eds., *X-Ray Optics and X-Ray Microanalysis*, N.Y.: Academic Press, 1963, 445-449.
6. D. W. Berreman, J. W. M. Dumond, and P. E. Marmier, "New point-focusing monochromator," *Rev. Sci. Instr.* 25: 1219-1220, 1954; D. W. Berreman, "Single quartz crystal point focusing x-ray monochromator," *Rev. Sci. Instr.* 26: 1048-1052, 1955.
7. D. W. Berreman, *Focusing Crystal for X-rays and Method of Manufacture*, U.S. Patent 2 853 617, 23 September 1958.
8. D. W. Berreman, J. Stamatoff, and S. J. Kennedy, "Doubly curved crystal point-focusing x-ray monochromators: Geometrical and practical optics," *Appl. Optics* 16: 2081-2085, 1977.
9. G. Wassberg and K. Siegbahn, "Small-angle scattering of x-rays," *Ark. f. Physik* 14: 1-15, 1958.
10. S. Hagstrom and K. Siegbahn, "A small-angle x-ray scattering apparatus using a spherically bent crystal," *J. Ultrastr. Res.* 3: 401-419, 1960.
11. G. E. B. Barstad and I. H. Refsdal, "Sensitive, quantitative recording x-ray spectrometer," *Rev. Sci. Instr.* 29: 343-348, 1958.
12. J. Eggs and K. Ulmer, "Röntgenspektroskopie mit sphärisch gekrümmten Kristallen," *Z. angew. Phys.* 20: 118-128, 1965.
13. C. H. Ehrhardt, E. M. Banas, and J. L. Janik, "Application of spherically curved crystals for x-ray fluorescence," *Appl. Spect.* 22: 730-735, 1968.
14. J. Witz, "Focusing monochromators," *Acta Cryst.* A25: 30-42, 1969.
15. K. Das Gupta, H. Welch, P. F. Gott, J. F. Priest, S. Cheng, and E. Chu, "Some new methods of precision x-ray spectrometry," *Advances in X-ray Analysis* 16: 251-259, 1972.
16. D. L. Hammond, L. V. Knight, H. Yoshida, and V. L. Peickii, *Crystal Monochromator and Method of Fabricating a Diffraction Crystal Employed Therein*, U.S. Patent 3 772 522, 13 November, 1973.
17. D. L. Hammond and H. R. Fellner, *Bent Diffraction Crystal with Geometrical Aberration Compensation*, U.S. Patent 3 777 156, 4 December 1973.
18. D. L. Parker, "A spherically bent crystal x-ray spectrometer with variable curvature," *Advances in X-ray Analysis* 17: 521-530, 1973.
19. R. L. Chaney, "Recent developments in spatially resolved ESCA," *Surface and Interface Analysis* 10: 36-47, 1987.
20. D. B. Wittry and D. M. Golijanin, "Detection limits in microprobe x-ray fluorescence analysis," this volume.
21. B. E. Warren, "Monochromatic x-rays for single crystal diffuse scattering," *J. Appl. Phys.* 25: 814-815, 1954.
22. T. C. Furnas Jr., *X-ray Monochromatic and Focusing System*, U.S. Patent 3 898 455, 5 August 1975.
23. J. A. Bosslet Jr., R. L. R. Towns, R. G. Megargle, K. H. Pearson, and T. C. Furnas Jr., "Determination of parts per billion levels of electrodeposited metals by energy dispersive x-ray fluorescence spectrometry," *Anal. Chem.* 49: 1734-1737, 1977.
24. M. Marcus, L. S. Powers, A. R. Storm, B. M. Kincaid, and B. Chance, "Curved-crystal (LiF) x-ray focusing array for fluorescence EXAFS in dilute samples," *Rev. Sci. Instrum.* 51: 1023-1029, 1980.
25. J. B. Hastings, P. Eisenberger, B. Lengeler, and M. L. Perlman, "Local-structure determination at high dilution: Internal oxidation of 75-ppm Fe in Cu," *Phys. Rev. Lett.* 43: 1807-1810, 1979.
26. M. Kotera and D. B. Wittry, "X-ray fluorescence analysis with monochromatic x rays," *J. de Physique (Colloque C2)* 45: 281-284, 1984.
27. J. V. Gilfrich, E. F. Skelton, D. J. Nagel, A. W. Webb, S. B. Quadri and J. P. Kirkland, "X-ray fluorescence analysis using synchrotron radiation," *Advances in X-Ray Analysis* 26: 313-323, 1983.
28. D. B. Wittry and D. M. Golijanin, "X-ray microprobes: A comparison of laboratory and synchrotron sources," *11th ICXOM*, London, Ont., 1986, 51-55.
29. J. B. Hastings, B. M. Kincaid, and P. Eisenberger, "A separated function focusing monochromator system for synchrotron radiation," *Nucl. Instrum. Methods* 152: 167-171, 1978.
30. J. M. Jaklevic, R. D. Giaque, and A. C. Thompson, "Quantitative x-ray fluores-

cence analysis using monochromatic synchrotron radiation," *Nucl. Instrum. Methods* B10/11: 303-308, 1985.

31. R. D. Giaque, J. M. Jaklevic, and A. C. Thompson, "The application of tunable monochromatic synchrotron radiation to the quantitative determination of trace elements," *Advances in X-Ray Analysis* 28: 53-60, 1985.

32. M. Lemonnier, R. Fourme, F. Rousseaux, and R. Kahn, "X-ray curved-crystal monochromator system at the storage ring DCI," *Nucl. Instrum. Methods* 152: 173-177, 1978.

33. J. R. Chen, N. Martys, E. C. T. Chao, J. A. Minkin, C. L. Thompson, A. L. Hanson, H. W. Kraner, K. W. Jones, B. M. Gordon, and R. E. Mills, "Synchrotron radiation determination of elemental concentrations in coal," *Nucl. Instrum. Methods* B3: 241-245, 1984.

34. M. Prins, S. T. Davies and D. K. Bowen, "Trace element analysis and element mapping by scanning x-ray fluorescence at Daresbury SRS," *Nucl. Instrum. Methods* 222: 324-328, 1984.

35. C. J. Sparks Jr., "X-ray fluorescence microprobe for chemical analysis," in H. Winick and S. Doniach, Eds., *Synchrotron Radiation Research*, New York: Plenum Press, 1980, 459-512.

36. G. E. Ice and C. J. Sparks Jr., "Focusing optics for a synchrotron x-radiation microprobe," *Nucl. Instrum. Methods* 222: 121-127, 1984.

37. K. W. Jones, B. M. Gordon, A. L. Hanson, J. B. Hastings, M. R. Howells, H. W. Kraner, and J. R. Chen, "Application of synchrotron radiation to elemental analysis," *Nucl. Instrum. Methods* B3: 225-231, 1984.

38. B. M. Gordon and K. W. Jones, "Design criteria and sensitivity calculations for multielemental trace analysis at the NSLS x-ray microprobe," *Nucl. Instrum. Methods* B10/11: 293-298, 1985.

39. D. B. Wittry and D. M. Golijanin, "Development of an x-ray microprobe for local spectrochemical analysis," *Microbeam Analysis--1987*, 54-56.

40. D. M. Golijanin and D. B. Wittry, "Alignment and characterization of doubly curved x-ray diffractors," *Microbeam Analysis--1987*, 51-53.

TOTAL-REFLECTION X-RAY FLUORESCENCE: PRINCIPLES AND APPLICATIONS

D. E. Leyden, D. J. Leland, D. B. Bilbrey, P. Wobrauschek, and H. Aiginger

Total-reflection x-ray fluorescence spectrometry (TXRF) is emerging as a powerful new analytical tool based on x-ray emission. The basic instrumentation consists of a high-wattage focused x-ray tube whose output is collimated into a thin, ribbon-like beam incident on the specimen at a few milliradians measured from the surface. The specimen is placed on the surface of a reflector (e.g., quartz) which is optically flat. The angle of the incident radiation is below the critical angle for the reflector material; therefore, the x radiation undergoes specular reflection from the air-reflector interface. The x-ray detector [Si(Li)] is placed at 90° to the surface of the reflector plate. Specimens are deposited on the reflector as thin films. Two advantages are realized when the total-reflection configuration is used. First, there is dramatic reduction in background over the more usual optical configurations. Second, matrix and interelement effects are essentially eliminated because the low incidence and reflection angles result in extremely thin penetration depths so that the specimen is in effect infinitely thin in most cases. This paper presents some recent applications of TXRF to the determination of picogram quantities of elements in materials such as oil and atmospheric aerosols.

Experimental

The spectrometer used is a prototype TXRF spectrometer described previously.¹ A Siemens 100kV stabilized x-ray generator is used to supply power to a fine-focus 2700W Siemens x-ray tube irradiating an area of 0.2×12 mm and equipped with a copper anode operated at 40 kV and 50 mA. X radiation is detected with a Princeton Gamma Tech (Princeton, N.J.) Si(Li) detector with an active area of 12 mm² and a FWHM of 165 eV at 5.9 keV. A Canberra Model 2020 amplifier is used along with a Nuclear Data ND66 multichannel analyzer. The cutoff energy is adjusted to approximately 10 keV to minimize the continuum above the characteristic lines of the x-ray tube. The quartz sample reflector is adjusted to 1.5 millirad to be below the angle required for total reflection. Standards used to determine sensitivity factors were counted for 250 s livetime. K α intensities were extracted from the spectra using a modified version of SEEK (Ortec, Oak Ridge, Tenn.)

D. E. Leyden, D. J. Leland, and D. B. Bilbrey are at the Department of Chemistry, Colorado State University, Fort Collins, CO 30523; P. W. Wobrauschek and H. Aiginger are at the Atom Institute of the Austrian Universities, Vienna, Austria.

Aerosols. The aerosol samples used in this study were collected in Linz, Austria, during January 1985. Linz is a city of approximately 200 000 inhabitants and contains two large industrial complexes situated near residential areas. Air quality in the region is regularly monitored by local authorities for SO₂, NO_x, CO, and total suspended particulate matter. Standard aqueous solutions were prepared from commercial standards (Merck) or from reagent grade salts.

Oils. Conostan standard oil solutions (Conoco Oil Co.) were applied either directly to the quartz reflector or as a solution in chloroform. Mixtures of oil and chloroform were prepared by dissolving 1 g of oil in 10 ml of high purity chloroform. Reproducible films on the reflective substrate with the oil sample were obtained by pipetting 1 μ l of the solution onto the reflector and evaporating the solvent. The mass of oil on the reflector was varied by making a serial dilution of oil in chloroform and always pipetting 1 μ l onto the substrate and allowing the solvent to evaporate. The spectrometer design mounts the reflector vertically and as a result the concentration of oil could not exceed 0.1 g oil/ml chloroform or 1 μ l total, else the oil film would flow. A 1 μ l aliquot of a 0.1g/ml solution of oil in chloroform left approximately 1.5 mg oil/cm² on the reflector surface after solvent evaporation. Multielement oil specimens were made by blending of Conostan single-element standards and dilution with Conostan-75 base oil. Nickel was arbitrarily chosen to use as an internal standard. Measured quantities of a nickel single element Conostan standard were mixed directly into the oil samples.

Results

Determination of SO₄²⁻, Cl⁻, K⁺, and Ca²⁺ atmospheric aerosol samples was accomplished by evaporation under vacuum of a 20 μ L aliquot of a 2ml aqueous extraction of between 38 and 387 μ g samples of aerosol onto a quartz reflector plate. Cobalt (II) was used as an internal standard by addition of 20 μ L of a 120 μ g/l cobalt solution to the 2ml extract prior to taking of the 20 μ L aliquot. Table 1 shows the results found for the various size fractions for one sampling of the aerosol near Linz, Austria. It was assumed that all sulfur present in the aerosol was in the form of sulfate. For all samples collected, plots of results of determinations by ion chromatography (IC) versus those by TXRF gave slopes of 1.09, 0.982, and 0.822 for sulfate, potassium, and chloride, respectively. IC results were not available for calcium. TXRF appears to give good results for all aerodynamic diameters

TABLE 1.--TXRF determination of SO_4^{2-} , Cl^- , K^+ , and Ca^{2+} in an aerosol sample collected 17 January 1985 in Linz, Austria.

Stage	Size fraction (μm a.d.)	Ambient aerosol Mass ($\mu\text{g}/\text{M}^3$)	Concentration ($\mu\text{g}/\text{M}^3$)				Mass used for extraction (μg)
			SO_4^{2-}	Cl^-	K^+	Ca^{2+}	
1	0.04-0.1	4	0.51	0.01	0.02	0.01	38
2	0.1 -0.4	20	2.96	0.06	0.14	0.03	217
3	0.4 -1.6	48	7.82	0.25	0.21	0.10	387
4	1.6 -6.5	15	1.60	0.48	0.04	0.048	163
5	6.5 -2.5	7	0.17	0.95	0.02	0.53	72

TABLE 2.--Results of determinations based on internal standardization.

Sample	Ti	V	Cr	Mn	Fe	Cu	Zn	Pb
A	91 \pm 6 ^a	-	96 \pm 4	-	102 \pm 3	105 \pm 4	-	99 \pm 2
	100 ^{**}		100		100	100		100
B	-	318 \pm 5	300 \pm 6	315 \pm 4	295 \pm 4	297 \pm 4	324 \pm 3	309 \pm 3
		300	300	300	300	300	300	300
C	-	455 \pm 8	265 \pm 4	-	566 \pm 4	-	396 \pm 5	328 \pm 4
		496	262		569		396	328
D	607 \pm 9	-	221 \pm 2	1005 \pm 4	518 \pm 1	748 \pm 1	628 \pm 4	488 \pm 3
	589		232	950	503	770	624	482
E	266 \pm 5	514 \pm 4	-	595 \pm 3	389 \pm 7	555 \pm 5	-	1980 \pm 11
	282	560		579	384	559		1969
F	-	72 \pm 1	41 \pm 1	-	97 \pm 1	-	68 \pm 1	52 \pm 2
		83	44		96		67	55

* Found ppm value.

** Known ppm value.

^aError values are one standard deviation for replicate samples.

(a.d.) of the aerosol particle size ranges shown in Table 1.

Table 2 shows the results of the determination of trace elements in oil by TXRF compared with those given for standards. In the majority of cases, the precision of these determinations is 5% or better, and the relative error within 10% of given values.

Conclusions

TXRF appears to be a promising method for trace element determinations. Absolute detection limits are on the order of 10 to a few hundred picograms. Determinations made from small samples such as in the aerosol samples is particularly promising. Because the detection limits increase significantly with increased

increased film thickness, TXRF will have limited applications to bulk determination.

References

1. H. Aiginger and P. Wobrauschek, *Adv. X-ray Anal.* 28: 1, 1985.

THREE-DIMENSIONAL X-RAY MICROTOMOGRAPHY: PRINCIPLES AND APPLICATIONS

J. H. Kinney, Q. C. Johnson, M. C. Nichols, U. Bonse,
R. A. Saroyan, R. Nusshardt, and R. Pahl

In this paper we describe the principles and applications of nondestructive, chemically specific three-dimensional x-ray microtomography. We have developed a method for characterizing materials in three dimensions with a spatial resolution of 5 to 10 μm . Though the method does not at present have the spatial resolution afforded by electron-optical methods, the superior penetrating power of x rays allows fully three-dimensional characterization of materials that cannot easily be examined in any other way. We therefore expect x-ray microtomography to be a technique complementary to electron microscopy.

Principles

Most of us are familiar with the process of x-ray computed tomography (CT), which is a powerful tool in diagnostic radiology. CT is performed by measuring x-ray absorption through a material at a variety of viewing angles. The absorption information from each viewing angle can be used to obtain the value of the x-ray mass attenuation coefficient μ at each volume element sampled by the x-ray beam.¹ With proper knowledge of the x-ray energy, μ can be used to map directly the sample density, and in some cases the chemical composition, with an accuracy of better than 1%. In medicine, CT is a powerful tool for mapping the interior structures of the human body. It is superior to radiography because the interior structures can be imaged

without being obscured by surrounding variations in tissue density.

In the past several years CT has been developed for use in the nondestructive evaluation of materials. CT has been used to inspect engine turbine blades as well as rocket motor casings. In most nondestructive testing applications, only straightforward extensions of medical x-ray technology are required. A spatial resolution of 100 μm , easily achieved with conventional x-ray technology, is sufficient for most industrial applications.

The development of complex supported catalysts and composite materials, as well as increased interest in the materials community in studies in interfaces, adhesion, and bonding, have led to renewed interest in the nondestructive x-ray inspection of materials, especially to obtain three-dimensional information on materials with a spatial resolution of a few micrometers. Electron optical methods, though possessing great spatial resolution, cannot yield three-dimensional information on samples without the destructive thin sectioning of the material. Furthermore, many materials, especially nonconductive polymers, cannot be easily imaged by electron techniques without the application of coatings of a conductive overlayer. Therefore we were willing at first to sacrifice spatial resolution to obtain three-dimensional characterization of samples with the ability to look nondestructively within the interior.

In order to perform high-resolution CT it is necessary either to collimate the x-ray beam to a small size or use a position-sensitive detector. Collimation of the x-ray beam was the first technique used to perform high-resolution CT because it does not require any extension of conventional radiography practices.² Collimation techniques, because each projection for each viewing angle is measured sequentially, are very time consuming. With a conventional sealed-anode x-ray source, 24 h is often required to obtain a single cross-sectional slice through a typical sample with 5-10 μm spatial resolution. Even when a much more intense synchrotron light source is used in place of the sealed anode, times of the order of 1 h are required for the same CT measurement. Though experiments using collimator slits provide justification for using x-ray CT for studies in materials science, the time required to obtain three-dimensional images (by acquiring many CT cross sections of an object) is too great to make collimation techniques practical.

J. H. Kinney, Q. C. Johnson, and R. A. Saroyan are with the Chemistry and Materials Science Department, Lawrence Livermore National Laboratory, Livermore, CA 94550; M. C. Johnson is with the Materials Science Department, Sandia National Laboratories, Livermore, CA 94550; and U. Bonse, R. Nusshardt, and R. Pahl are at the Department of Physics, Dortmund University, Dortmund, Federal Republic of Germany. The authors wish to acknowledge the support of W. D. Bonivert for providing us with the supported catalysts and A. Knabe for his technical support. This work was performed under the auspices of the U.S. Department of Energy by the Lawrence Livermore National Laboratory under contract W-7405-ENG-48; by the Sandia National Laboratories under contract DE-AC04-76DP00789; and by SSRL, Stanford, California, which is supported by the Department of Energy (Office of Basic Energy Sciences) and by the National Institutes of Health (Biotechnology Resource Program, Divisions of Research Resources). Work at HASYLAB in Hamburg was supported by the Bundesminister für Forschung und Technologie, Bonn, FRG, under contract 03-BO-1DOR-1.

The inadequacy of collimation methods, which require all absorption measurements to be made sequentially, led us to develop a detector system in which all the projection data in horizontal and vertical dimensions can be taken in parallel.³ This method enables us to make measurements with high resolution on volumes of several cubic millimeters with great speed. In our CT system, x rays are passed through a sample and are converted to visible light on a high-resolution phosphor screen. The visible image is magnified and projected onto a thermoelectrically cooled charge coupled device (CCD) array detector. The array detector is operated in a charge-integrating mode. At the end of an exposure, electron charge in each CCD pixel (which is directly proportional to the x-ray fluence) is read out into a minicomputer which performs a filtered backprojection and calculates the x-ray absorption coefficient within each volume element in the sample. Using a conventional sealed-anode x-ray generator we obtain a spatial resolution of approximately 30 μm , which is determined by the geometric unsharpness due to a finite source size. Using a synchrotron radiation source we obtain spatial resolution of the order of 5-10 μm . In the case of synchrotron radiation, the resolution is limited by x-ray scatter and phosphor graininess. We expect that improvements in the system design will soon allow us to achieve spatial resolution of the order of 1 μm .

Synchrotron radiation, in addition to having high brightness, also has a high spectral density. We can continuously tune the energy of the synchrotron beam from a few eV to tens of keV with a very narrow bandwidth (<1 eV at 10 keV). By using monochromatic radiation, we can use a technique of dual-energy CT (energy-modulated CT) to obtain elemental and chemical information about a sample.^{4,5} The near-discontinuity of the x-ray absorption coefficient at an edge, as well as variations in the coefficient caused by chemical shifts, can be used to provide increased CT contrast of a particular chemical state. We have successfully used this technique to image regions of iron sulfide in coal.

Applications

Several applications for our high-resolution three-dimensional imaging system exist within the materials and biological sciences.^{6,7} We have been driven to develop the technique of microtomography to aid us in our study of supported catalysts. We have also applied this technique to the study of crack growth and propagation in porous materials, and intend soon to begin studies of interfaces and composite materials.

Supported catalysts are usually made by pyrolyzing polystyrene into low-density carbon foams. These foams are subsequently loaded with small crystallites of catalytic materials, or in some cases they are coated with the catalyst by use of electroless deposition techniques. Because of the three-dimensional random networking of these catalysts, they

cannot be characterized by conventional electron-optical or x-ray radiography techniques. Small-angle x-ray scattering, which is sometimes used to characterize these materials, does not lend itself easily to unambiguous interpretations of particle size and homogeneity. Because of these difficulties with traditional characterization techniques, we have applied microtomography to the investigation of the quality and environmental stability of these catalysts. In particular, we have examined supported catalysts containing Pd to determine the uniformity of the Pd coating. Results such as these are best observed in color, where small variations in the Pd coatings can be easily visualized. Results comparable to those of the catalysts are available in the literature.⁷

Conclusions

In this paper, we have described the principles and applications of the newly developed technique of x-ray microtomography. X-ray microtomography will find increasing application in many areas of materials research and characterization. X-ray microtomography is not intended to compete with electron-optical techniques; rather, it will become an important complementary tool, much as other x-ray methods have done. With improvements in x-ray optics, three-dimensional, chemically specific x-ray microtomography will soon provide spatial resolution of 1 μm and finer.

References

1. G. T. Herman, *Image Reconstruction from Projections: The Fundamentals of Computerized Tomography*, New York: Academic Press, 1980.
2. J. C. Elliott and S. D. Dover, *J. Microscopy* 126: 211, 1982.
3. U. Bonse et al., *Nucl. Inst. Meth.* A246: 644, 1986.
4. L. Grodzins, *Nucl. Inst. Meth.* 206: 541, 1983.
5. J. Kinney, et al., *Appl. Optics* 25: 4583, 1986.
6. B. P. Flannery et al., *Science* 237: 1439, 1987.
7. J. Kinney et al., *MRS Bulletin* 13: 13, 1988.

NEUTRON MICROPROBE: PROSPECTS AND POTENTIAL APPLICATIONS

R. M. Lindstrom, R. F. Fleming, and H. L. Rook

In the past decade the use of neutron beams for chemical analysis has come of age. Slow neutrons are a gentle probe, carrying to the sample no electric charge and only about 0.03 eV of kinetic energy. The prompt gamma rays emitted when neutrons are captured by a target nuclide have proved to be a valuable tool for nondestructive quantitative chemical analysis, especially for light elements which have no long-lived radioactivation products and for elements with large capture cross sections.^{1,2} A small number of nuclides--notably ³He, ⁶Li, ¹⁰B, and ¹⁴N--emit charged particles on absorbing low-energy neutrons. By measuring the energy spectrum of these particles, one can determine both the concentration and the depth distribution of the target elements in a specimen.³ The applications of analytical techniques based on neutron beams have been somewhat limited by the low intensity of available beams, although this restriction can sometimes be compensated by use of large sample areas or long irradiation times. In the next generation of analytical instruments, the sensitivity can be improved by the employment of advanced neutron optics to focus long-wavelength neutrons into narrow, intense beams.

A neutron beam extracted from a reactor cold source, such as the one recently installed in the 20MW NBS Reactor (NBSR), might have a flux of $1 \times 10^9/\text{cm}^2\text{s}$ over a $10 \times 10\text{cm}$ area. (Flux is a scalar quantity defined as the product of neutron density n and velocity v ; the rate of nuclear reactions in a sample smaller than the beam is equal to the product of the flux, the reaction cross section, and the number of atoms of target element in the sample.) If this beam could be focused to $1 \times 1\text{mm}$, the flux would be $1 \times 10^{13}/\text{cm}^2\text{s}$, comparable to that in the sample irradiation position of a high-flux research reactor. Because of the low background of fast neutrons and gamma rays in cold neutron beams, it has been shown that the analytical use of these beams can lead to greatly improved detection sensitivities compared with existing thermal neutron instruments, even with no focusing at all.⁴ A beam with small size could be intimately surrounded by detectors of prompt induced radiation with high detection efficiency for single-particle and coincident events. If a spot size as small as a millimeter can be attained, the analysis of small samples will be attractive, and by rastering of the sample across the beam a neutron-probe image of a large sample may be constructed.

By use of the methods of neutron optics it

The authors are at the Center for Analytical Chemistry, National Bureau of Standards, Gaithersburg, MD 20899.

appears possible to produce a high flux in an external beam. For two reasons, this is an active field of study, with many incompletely explored avenues. First, neutron optics has been studied for only a few decades, so that the physics is less well developed than that for charged particles and photons, which have had centuries and millennia of history, respectively. Second, neutron optics has been most thoroughly studied in conjunction with scattering measurements, in which much of the information is derived from the angular distribution of the scattered particles. For these experiments the ideal incoming probe beam is parallel, so reflecting elements and collimators are shaped with this intent. By contrast, the sensitivity of nuclear reaction analysis for a given analyte is determined only by the number of neutrons crossing a unit area of the target per second, independent of direction; for many applications a nearly isotropic field would be ideal.

A fission reactor produces a continuous spectrum of neutrons with a mean energy of about $2 \times 10^6\text{eV}$. These neutrons are slowed by a hundred or so elastic collisions with a low- A moderator at room temperature until they are nearly in thermal equilibrium at $kT \sim 0.025\text{eV}$. If a moderator at still lower temperature is introduced into this thermal neutron field, the energy of the neutrons is reduced further and their average wavelength increases inversely as the square root of the neutron temperatures. In the NBSR cold source⁵ (16 liters of D_2O ice at an effective temperature of 65 K), the neutron wavelength corresponding to the most probable velocity $v = (2kT/m)^{1/2}$ is 3.8Å.

For neutrons with wavelengths in the Angstrom range, as for x rays, the index of refraction is at most a few parts per million different from unity, so refraction in prisms or mirrors is very small. For example, consider a slab of quartz 1 cm thick set at 45° to a beam of visible light or of 4Å neutrons. For light, with a refractive index of 1.46, the photons are deflected 16° at each surface to emerge offset from the original ray by 3.2 mm. The beam of neutrons, with a refractive index of 0.999 989, is refracted 0.0006° at each surface and offset 0.15µm (in the opposite direction). Refractive focusing has been demonstrated for long wavelength (20Å) neutrons; four spherical quartz surfaces 2.4 mm in radius gave convergence over a 10m flight path.⁶ Shorter wavelengths require still smaller radii of curvature, with correspondingly small apertures. Diffraction by a Fresnel zone plate has been used as an analog to a lens. The technical requirements for construction of these optical elements are

severe, but a plate with 2.5m focal length has been satisfactorily tested.⁷ As with refracting elements, the aperture is necessarily small.

Reflective optics have been used to better effect. For an angle of incidence shallower than a characteristic critical angle, total reflection is observed from most surfaces, analogous to the total internal reflection in optical fibers. The critical angle is proportional to the neutron wavelength; its cosine is the refractive index of the reflecting surface. For a wavelength of 4Å the critical angle for nickel (a good reflector) is 0.39°; for the Ni-58 isotope, 0.45°.

Reflective neutron conducting tubes have come into extensive use since their properties were first pointed out in the early 1960s.⁷⁻⁹ These guides, most successfully made of optically flat glass slabs assembled into a rectangular pipe and lined with a mirror film of nickel, employ total internal reflection to transport the neutrons without substantial loss for tens of meters from the reactor, and in so doing perform an angular collimation to about 0.3°. Their application has "liberated experimenters from the tyranny of the inverse square law which had confined their work to close proximity of the reactor core".¹⁰ Bent guides or a set of straight sections forming a segmental arc are used to separate the long-wavelength neutrons from faster neutrons and gamma rays which contribute to background. Existing guides are typically 5 × 5 cm by 50 m long, so the number of reflections experienced by a neutron in traversing the guide at the critical angle is only five to ten. "Supermirrors" have recently been developed with larger critical angles than even ⁵⁸Ni, which reflect a larger fraction of the incident neutrons.¹¹

Clearly, if a neutron beam is sent down a converging reflector without losses the beam flux will increase. However, a neutron reflected at the critical angle from one side of a straight converging guide will arrive at the opposite surface at greater than the critical angle and thus will be lost. The goal of a focusing device is to increase the flux at the expense of angular divergence. This problem has been studied in detail by Maier-Leibnitz,¹² who concluded that the appropriate shape for such a surface is a logarithmic spiral.

The manufacturing tolerances required for a good focusing device are stringent: a reflector tens of centimeters across and tens of meters long, aligned to a tolerance less than a few tenths of a degree, and figured and finished to better than optical accuracy. If the optical elements are designed for one-dimensional focusing--a line, not a spot--the practical requirements may be less severe than for two dimensions, and by application of tomographic techniques, high-resolution reconstructed images may be obtained. Research is under way to develop the necessary theoretical and experimental background to use narrow, intense neutron beams for elemental analysis. When this work is completed we expect to be able to create

an exciting facility at NBS with greatly improved detection sensitivity compared with existing thermal neutron instruments.

References

1. R. M. Lindstrom and D. L. Anderson, in S. Raman, Ed., *Capture gamma-ray Spectroscopy and Related Topics*, (AIP Conf. Proc. 125), New York: Am. Inst. Physics, 1985, 810.
2. R. E. Chrien, in B. J. Allen, I. Bergqvist, R. E. Chrien, and D. Gardner, Eds., *Neutron Radiative Capture*, Oxford: Pergamon, 1984, 187.
3. R. G. Downing, J. T. Maki, and R. F. Fleming, in L. A. Casper, Ed., *Microelectronics Processing: Inorganic Materials Characterization*, (ACS Symp. Ser. 295), Washington, D.C.: Am. Chem. Soc., 1986, 163.
4. R. M. Lindstrom, R. Zeisler, and M. Rossbach, *J. Radioanal. Nucl. Chem.* 122: 321, 1987.
5. National Research Council, *Major Facilities for Materials Science and Related Disciplines*, Washington, D.C.: National Academy Press, 1984.
6. R. Gähler, J. Kalus, and W. Mampe, *J. Phys.* E13: 546, 1980.
7. J. Christ and T. Springer, *Nukleonik* 4: 23, 1962.
8. H. Maier-Leibnitz and T. Springer, *Reactor Sci. Technol.* 17: 217, 1963.
9. H. Maier-Leibnitz, in N. Ryde, Ed., *Neutron Capture Gamma-Ray Spectroscopy*, Vienna: IAEA, (STI/PUB/235), 1969, 93.
10. A. G. Klein and S. A. Werner, *Repts. Prog. Phys.* 46: 259-335, 1983.
11. C. F. Majkrzak, *Appl. Optics* 23: 3524, 1984, and references therein.
12. H. Maier-Leibnitz, *Nukleonik* 8: 61, 1966.

OBSERVATION OF Si CRYSTAL SURFACE BY SCANNING RHEED MICROSCOPY

Yuji Sakai, Shinichi Kitamura, and Takeo Ichinokawa

Reflection high-energy electron diffraction (RHEED) is one of the most important techniques for crystallographic analysis of surface microstructures. Observations of surface atomic step and reconstructed structure on Si(111) by the RHEED technique,^{1,2} low-energy electron reflection microscopy (LEERM),³ and the low-energy electron diffraction (LEED) technique⁴ have been reported. However, these techniques for surface imaging have used other methods.

In our approach, the direct observation of the structure is obtained by simultaneous use of scanning Auger microscopy (SAM), which is included in the other techniques as an ultra-high vacuum (UHV) scanning electron microscopy (SEM), and electron energy-loss microscopy (ELS). These combined electron microscopies based on multiple techniques are of great advantage to surface microstructure analysis. For a scanning RHEED image observation it is necessary to have high spatial resolution and high sensitivity detection. To observe the step structure, a scanning RHEED microscopy with a new signal-detection system has been developed. In this paper, the new detection methods are presented and the atomic steps for Si(111) surface are imaged as a demonstration.

Experimental

A schematic diagram of the scanning RHEED microscopy is shown in Fig. 1. The RHEED technique is added to the SAM (JEOL, Auger Microprobe JAMP-30). The electron beam from an LaB₆ filament is focused on the sample surface at 0-60° tilt angle by the magnetic lenses. To observe the RHEED pattern, the sample is tilted up to 85-88° by the eucentric goniometer stage, which allows little sample movement. The analyzing point is kept at almost the same position (within a few microns) in the beam-irradiated direction. SAM and ELS are performed simultaneously at the same analyzing point by a cylindrical mirror analyzer. The RHEED patterns are observed on a fluorescent screen through a viewing port.

To observe a dark-field image (the scanning RHEED image), a particular diffraction spot or a part of the spot is selected by means of the other small fluorescent screen with an aperture. The electron beam is focused on the sample at the primary beam current of 10^{-10} - 10^{-11} A and a spatial resolution of 10-30 nm.

Y. Sakai and S. Kitamura are with JEOL Ltd., 1-2 Musashino 3-chome, Akishima, Tokyo 196, Japan; T. Ichinokawa is at the Department of Applied Physics, Waseda University, 3-4-1 Ohkubo, Shinjuku-ku, Tokyo 160, Japan.

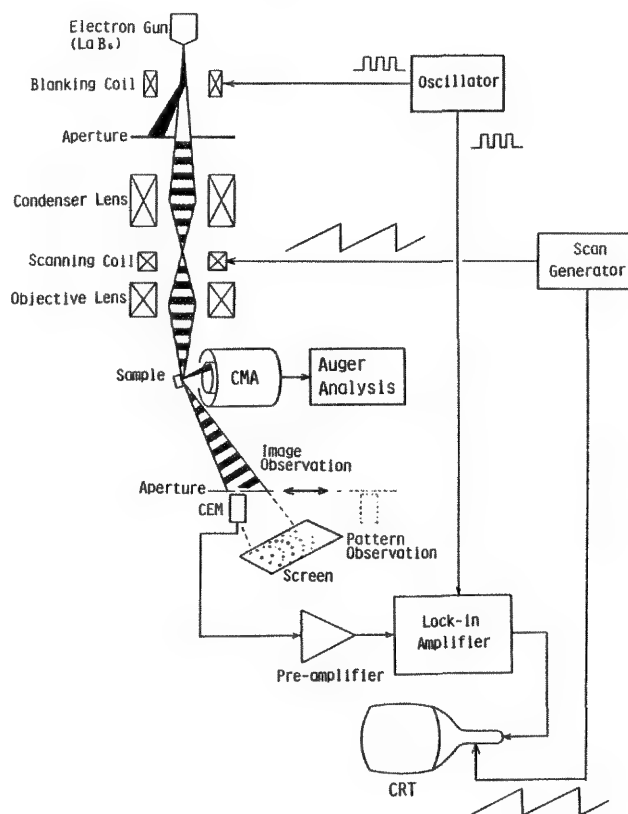


FIG. 1.--Schematic diagram of scanning RHEED microscopy.

Under these conditions, a beam-blanking technique has to be used for high-sensitivity signal detection. The beam-blanking detection method has been used previously as the high-sensitivity signal detection for SAM. A channel electron multiplier is used to detect the diffracted electrons passing through the aperture on the small screen. The dark-field images are taken with the following beam conditions: beam diameter about 20 nm, accelerating voltage 15 kV, current 0.2 nA, angular divergence of the electron beam of 2 mrad. To clean the Si(111) surface, the sample is heated by direct electric current in the analyzing chamber at a vacuum of 6×10^{-8} Pa.

Observation on Si(111) Surfaces

The step structure of Si(111) is formed by high-temperature annealing up to 1200 C for 5 s. Several step bands are observed in the secondary-electron image (Fig. 2). A step band consists of many steps one or several monolayers high. However, the steps have not been observed by the secondary-electron image.

Figure 3 shows the RHEED pattern from the Si(111) surface. The 7×7 structure became visible after the annealing. The fine step structures required the dark-field imaging capability of the scanning RHEED microscope. The dark-field images are observed by selection of the specular beam spot, indicated by a mark in Fig. 3. Figure 4a shows the secondary electron image of the Si(111) surface. This image shows only a structure of the surface modification caused by the sample heating. Figure 4b shows the dark-field image, which shows height of the several monolayers on the terraces of a stepped Si(111) surface. The surface became a higher monatomic layer by a monatomic layer from upper to lower. After the sample heating at 850 C during 2 min, the inverse grown-up monatomic layers are observed in Fig. 4c. We suppose that these inverse atomic steps are caused by the surface modification of the annealing during the evaporation or diffusion process. The steps are observed only on the center area (bright contrast area of Fig. 4b). However, the step bands are observed on the right and left side (dark contrast area). When the aperture is moved in the direction of the higher-angle or lower-angle part of the spot, the images of the bright contrast area and the dark contrast area are interchanged. This contrast reversal of the image means that the center area had a different height to the right and left side.

Conclusions

The detection methods of the scanning RHEED microscopy combined with SAM are described. Preliminary applications to Si(111) surface are carried out and the atomic steps are observed. The technique of scanning RHEED microscopy will be available in the direct observation such as reconstructed structure, initial stages of epitaxial growth, and diffusion. In situ observations of these processes are very important for surface studies. Furthermore, in this combined system, AES is performed with the same glancing incidence. Under this glancing incidence, the more surface-sensitive AES is performed.

References

1. N. Osakabe, Y. Tanishiro, K. Yagi, and G. Honjo, *Surface Sci.* 97: 393, 1980.
2. T. Ichikawa, T. Doi, M. Ichihashi, and Hayakawa, *Japan J. Appl. Phys.* 23: 913, 1984.
3. W. Teliëps and E. Bauer, *Ultramicroscopy* 17: 57, 1985.
4. T. Ichinokawa, Y. Ishikawa, M. Kenmochi, N. Ikeda, Y. Hosokawa, and J. Kirschner, *Surface Sci.* 176: 397, 1986.

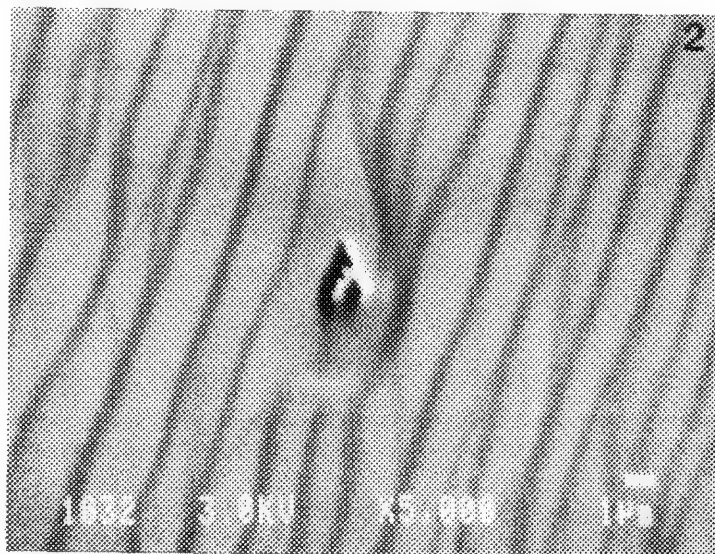


FIG. 2.--SEM image of Si(111) surface after cleaning process of high-temperature annealing.

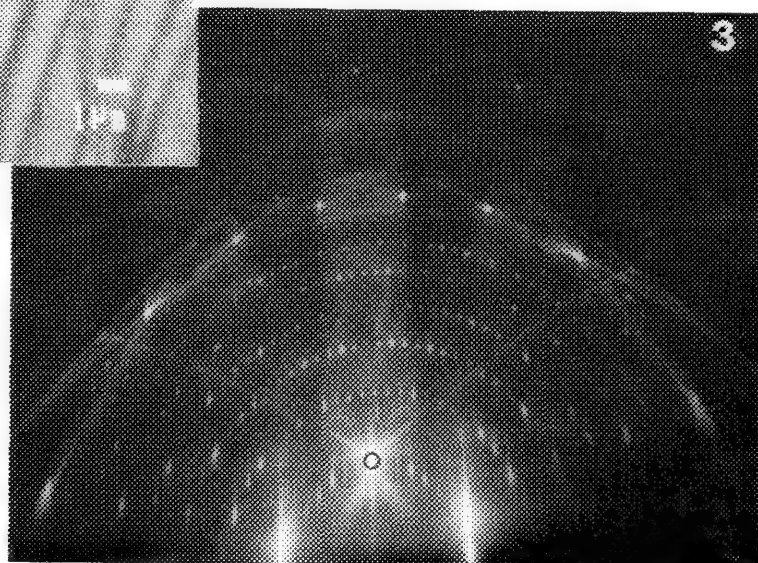


FIG. 3.--RHEED pattern of Si(111) surface.

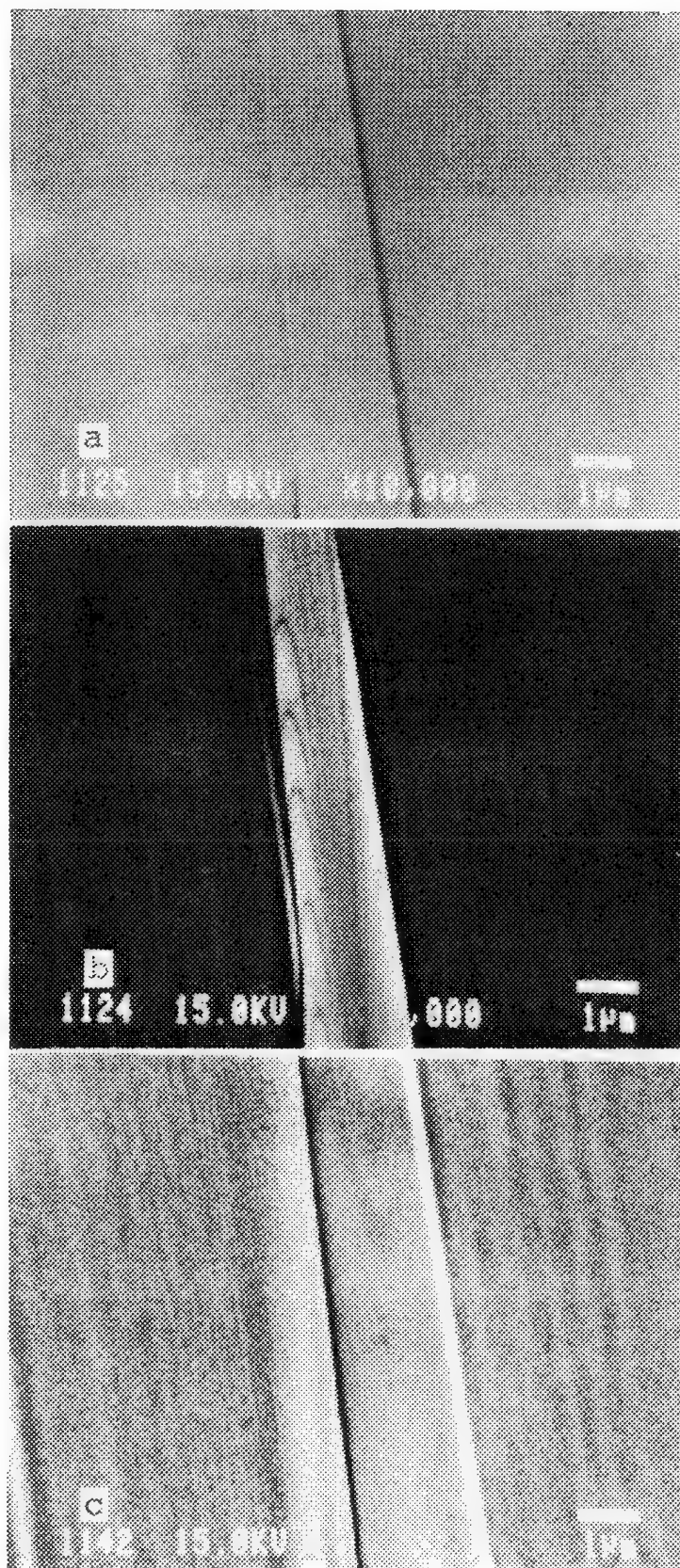


FIG. 4.--Step structures on Si (111) surface: (a) SEM image, (b) scanning RHEED image taken by specular reflection spot in Fig. 3, (c) scanning RHEED image after 850 C, 2 min annealing.

SURFACE ANALYSIS OF SMALL PARTICLES

John Gavrilovic

Surface properties of small particles have been studied for a long time in various scientific disciplines. Catalysis, fluidized bed reactors, air-pollution studies, ore processing and enrichment, and in general all solid-liquid or solid-gas chemical reactions are determined by the surface characteristics of small particles. In most cases the properties of small-particle surfaces were derived from tests performed on a very large number of particles by observation of the cumulative effects of all particles. In an assembly of small particles alike in size and appearance, there is no reason to assume that all the individual particles will have very similar surface properties.

In the past 40 years since the introduction of instrumentation for small-particle analysis, detailed knowledge of individual-particle chemistry has become very important in the study of the properties of small-particle assemblies. Perhaps the best examples are air-pollution samples. The bulk chemistry of samples collected on various filters is of limited value. To reveal the full chemistry of such samples, an array of automated procedures can be used to supply chemical identification from a statistically viable number of individual particles for each sample.^{1,2} A similar approach would be useful for understanding the surface chemistry of particulate or powder-type samples. A principal reason that no comparable method is available to examine the surface chemistry of small particles is the difficulty in routine surface analysis of particles below 100 μm in size. Many microscopic and micro-analytical techniques can reveal the surface chemistry of a small particle. Optical microscopy coupled with a fluorescent illuminator may be used for detection of a thin surface layer of tin on float glass.³ Raman microspectroscopy can detect thin layers of certain compounds on the surface of small samples.⁴ Such examples are rather unique and cannot be used for routine analysis of thin films on small particles. Transmission electron microscopy (TEM) is not commonly regarded as a surface-analytical technique. Recent developments in this field⁵ have resulted in stunning revelations of the surface chemistry of microparticles in particular micrometeorites. The discoveries are the result of the ingenious preparative techniques that include preparation of ultrathin cross sections of particles in the size range of 10 to 50 μm . Such cross sections can be observed and analyzed for all elements in the new generation of analytical electron microscopes (AEM). Thin films only a few

atomic layers thick on small particles can thus be detected and analyzed. Even crystallographic data from such films can be obtained in an AEM (Fig. 1). This is by far the most comprehensive method for surface analysis of thin films on small particles, but because of the elaborate sample-preparation procedure, it can only be applied to a limited number of particles.

Two common surface-analytical techniques that are appropriate for routine small-particle surface analysis are scanning Auger microanalysis (SAM) and secondary ion mass spectroscopy (SIMS).

Preparation of Particles for Surface Analysis

Small particles for surface analysis must first be isolated individually and mounted on a suitable substrate. It is possible to disperse them randomly on a substrate. However, in order to disperse them and to prevent the loss of particles from charging during the analysis, a solvent and a residual medium is then used. If an adhesive in a solvent is used, the surface of the particles will also be coated with the adhesive. Certain adhesives are essentially solvent free and may circumvent this problem. For example, adhesive tapes may be used as mounting substrates. Unfortunately, most tapes present an insulating mounting medium that can interfere with interpretation of spectral results. In addition, the high-energy beams commonly used in SAM can seriously degrade the tape, producing volatile components that may affect the vacuum system and/or contaminate particles to be analyzed.

Small particles down to 10 μm in size can be manually mounted on a minute (10-15 μm) patch of rubber cement that is sufficiently soft to retain particles, but not liquid enough to contaminate them. This method requires great manual dexterity in small-particle handling, but provides 40 to 60% of the particle surface for analysis. Figure 2 is an ion induced secondary electron image of such a mounting on a carbon plate. With careful handling, the free particle surface does not suffer serious contamination. The small size of the patch of adhesive does not present charging problems.

Choice of the mounting substrate depends on three principal factors: analytical technique, small-particle composition, and the general analytical requirement. In SAM analysis, the choice of the substrate is perhaps less critical than in SIMS. The main reason is the low escape depth of the Auger electrons, which at low take-off angles can only be 0.5-0.1 nm.

The author is with McCrone Associates, 850 Pasquinelli Drive, Westmont, IL 60559.

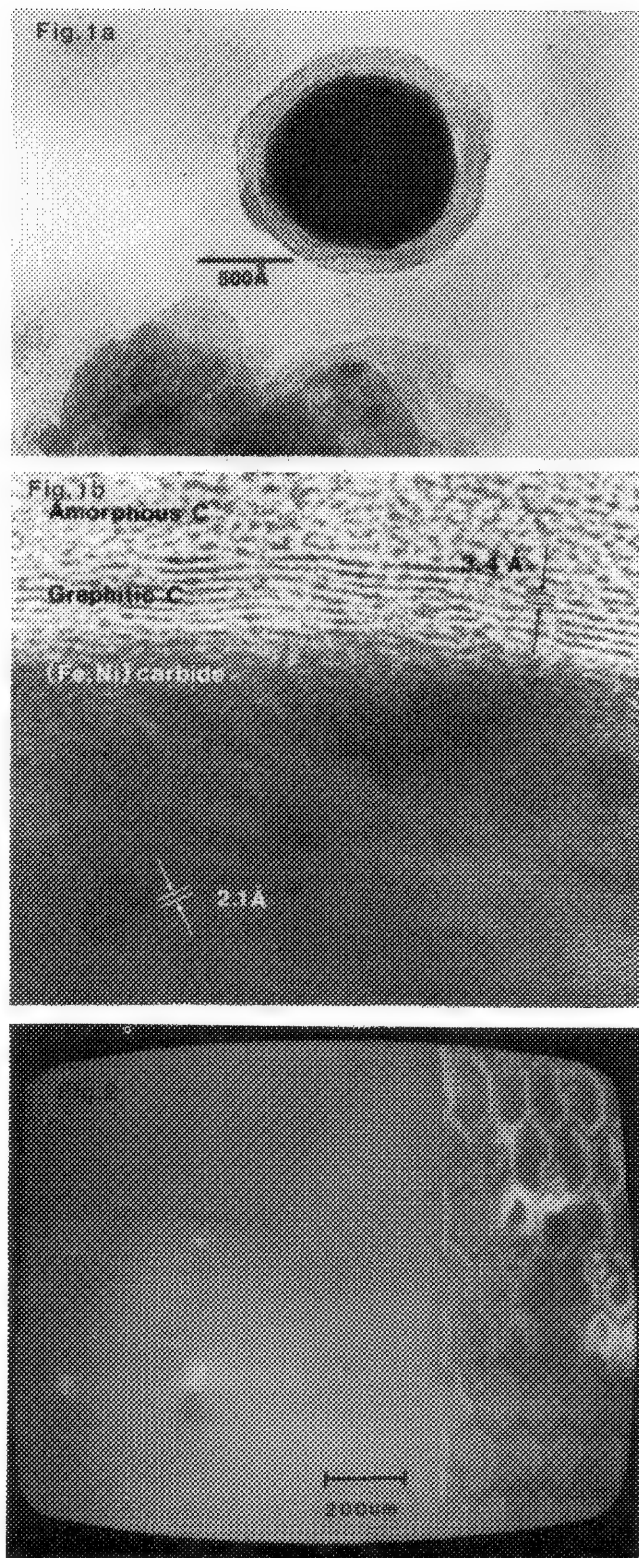


FIG. 1.--(a) Cross section of small particle observed in analytical electron microscope. (b) Detail of a cross section showing various components of thin surface film on particle.⁵ FIG. 2.--Ion induced secondary electron picture of small particles on carbon mount. TEM grid is glued on carbon block to mark position of small particles.

At such depths, almost all of the surface signal originates from airborne carbon-oxygen surface contamination. In SIMS surface analysis, secondary ions are at least partly derived from the surface. Therefore, the substrate choice is more critical. Various types of substrates have been used. In general, either pure (99.999%) gold or pyrolytic carbon produce mass spectra with minimum substrate interference easing interpretation of the particle spectre. Polished silicon, aluminum foil, tantalum, and indium have also been used for specific types of samples.

Surface Analysis of Particles by Auger Spectrometry

Scanning Auger microanalysis has two significant advantages for surface analysis of small particles: secondary electron imaging and the nondestructive nature of the primary electron beam, both related to the electron-beam generation of Auger electrons. Many scanning Auger analyzers have a spatial resolution in the 20-50nm range, comparable to scanning electron microscopes. This feature enables one to traverse the sample surface with the electron beam to select the most appropriate surface for analysis. Such a surface must be at optimum orientation with respect to three components of the analytical instrument: the electron source, the electron spectrometer and the ion sputtering gun.

Under ideal conditions, Auger spectra can reveal the surface chemistry of two to five monolayers on the small-particle surface which, in many cases, is carbon and oxygen airborne contamination. On most particles, the analyzed surface is tilted with respect to the electron analyzer, which further reduces the depth of analysis because of the low take-off angle of the escaping Auger electrons. When particles smaller than 1 μm are analyzed, the size of the electron beam for rapid Auger microanalysis becomes comparable to the particle size, which renders selection of the optimum surface for analysis very difficult. To obtain an Auger spectrum of the particle surface composition, airborne contaminants must be removed from the surface of the small particle by etching of the particle with an argon ion gun. The geometry of an excitation beam vs the ion etching gun in many Auger instruments is such that the argon ions strike the sample at a glancing angle and introduce the signal from unetched segments of the small-particle surface into the Auger spectrum of the "clean surface" (Fig. 3). The best arrangement for cleaning the particle surface with an argon ion gun would be to have coaxial etching and excitation beam.

Small Particle Surface Analysis by Micro-focused Secondary Ion Mass Spectrometry

Surface analysis of small particles by secondary ion mass spectroscopy is, in principle, possible by the same technique that is applied to large samples. The major difference stems

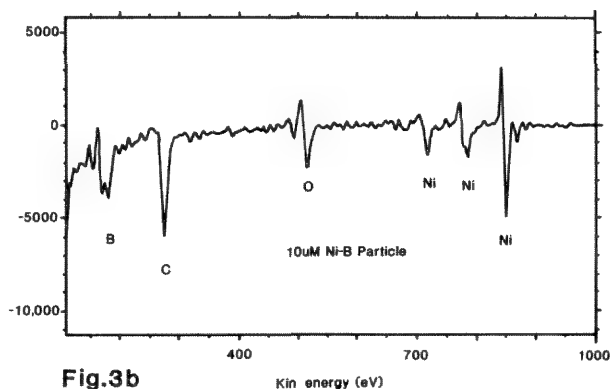
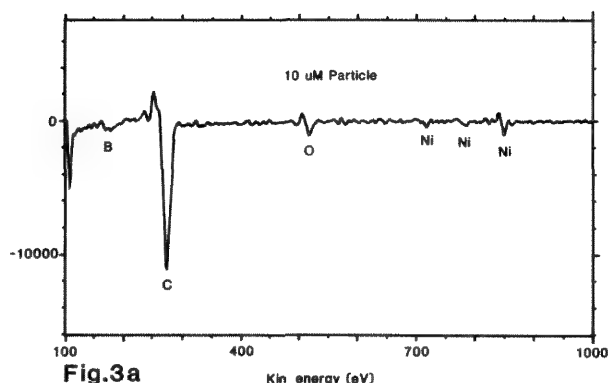


FIG. 3.--Auger spectra of Ni-B particle (a) before and (b) after argon sputter cleaning of airborne contamination.

from the very small area available for analysis coupled with the destructive nature of the SIMS technique. Small particles, above 10 μm in size, have a number of surface atoms sufficient to enable detection of all major and minor elements. Trace elements (in the ppm range) will probably not be detectable because of the low collection efficiency and possible low secondary ion (SI) yield of certain ions. Particles smaller than 10 μm have a very limited number of atoms on the surface (Table 1), which result in good detection limits of the elements with high secondary ion yields only.⁶ The low SI yield of certain elements is somewhat compensated by the re-sputtering process. In the ion microbeam instrument, a significant fraction of the secondary ions and neutrals condense on the substrate around the particle. This condensation phenomenon is important: it provides additional material for analysis with a defocused primary ion beam, which requires low density of the small particles on the substrate. Figure 4 is an example of the degree of scattering due to condensation of material from the particle on the substrate during sputtering with the primary ion beam.

Elements with high SI yield are readily detectable when present as thin films on small particles. Figure 5 shows the data from the analysis of a small (10 m) Ni-B particle before and after coating with a thin (5nm) aluminum

TABLE 1.--Surface atoms as percent of a volume of small particle.

Size of a particle (μM)	Proportion of surface atoms (%)
100	0.001
10	0.01
1	0.1
0.1	1.0
0.01	10.0

film. The ratio of the Al signal from a particle with and without a thin film is $4 \times 10^6 / 2.33 \times 10^4$ or over 170 times higher. In theory this result indicates that SIMS detection of a fraction of the monolayers of high SI yield emitters is possible from the surface of small particles. This number suggests vastly superior performance of the SIMS technique for analysis of thin films on the surface of small particles. Unfortunately, several other factors inherent in SIMS can minimize its detection capability. The destructive nature of the technique and the low SI yield of many common elements are the two major limiting factors. Elements with a low SI yield may be undetectable on small particles. Figure 6 shows the mass spectra from 10 μm silicate particles with and without a thin film of gold. The gold signal at mass 197 is barely distinguishable above the molecular ions background and is difficult to identify. Analyzing the same thin film with an Auger microprobe would be far better since a low-energy Auger line of gold would be strong and the high-energy line would encounter virtually no interference (Fig. 7).

The choice of substrate for mounting small particles for SIMS analysis is probably more critical than it is for other surface analytical techniques. Since the primary ion beam constantly sputters away the surface of the analysis area, surface attrition is minimized by scanning of an area much larger than the projected area of the small particle. Secondary ions from the substrate are thus always present in the small-particle mass spectrum. The best overall substrate for small-particle surface analysis, and small-particle analysis

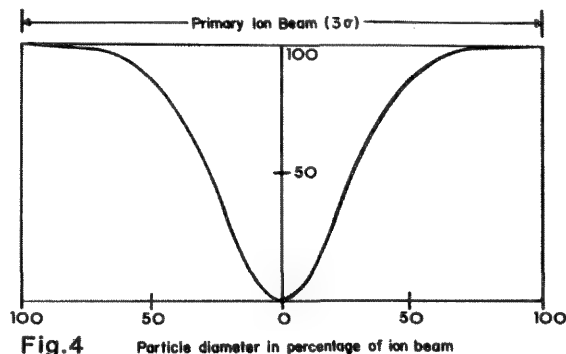


FIG. 4.--Condensation phenomenon during analysis of small particle. (From J. K. Beddow, "Particle characterization in technology," in Ref. 6, with permission.)

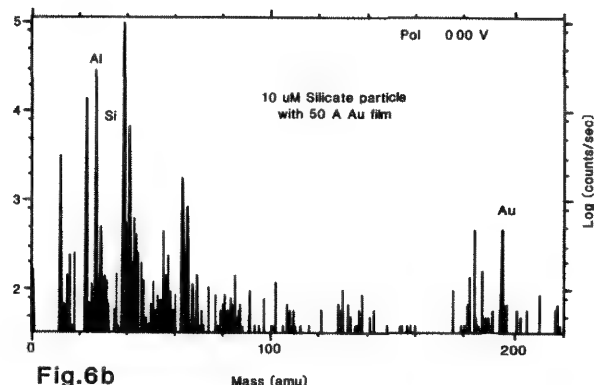
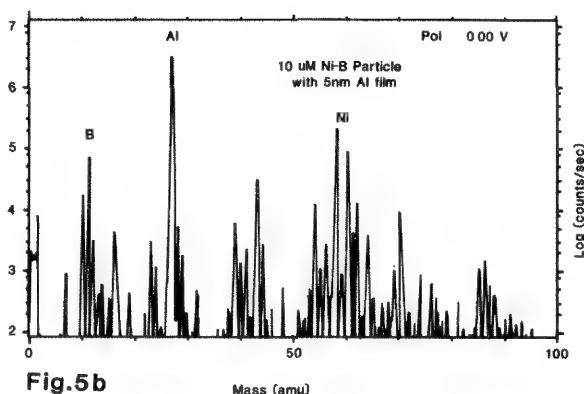
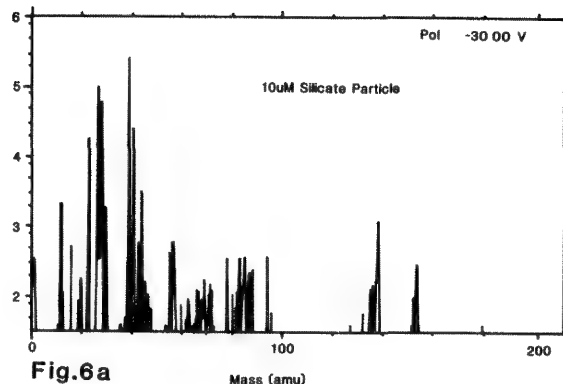
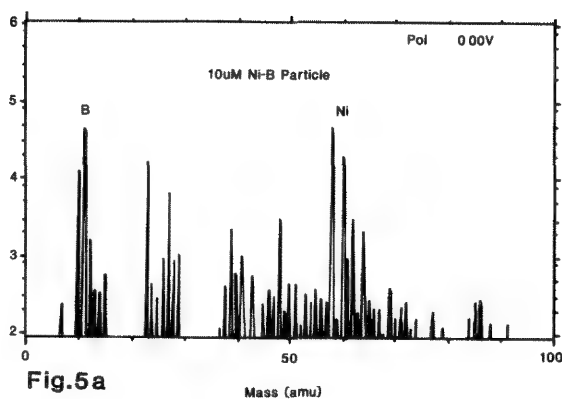


FIG. 5.--SIMS surface analysis of small Ni-B particle (a) without and (b) with thin (50Å) aluminum film.

FIG. 6.--SIMS surface analysis of small silicate particle (a) without and (b) with thin (50Å) aluminum film.

in general, is pyrolytic, nuclear purity carbon. Such a substrate in an UHV environment contributes relatively few interfering molecular ions. Other substrates such as gold or tantalum can be used in special circumstances. For particles smaller than 10 μm , the mounting medium and/or a high atomic number substrate may produce significant molecular interferences.

Concluding Remarks

Surface analysis of small particles in the size range of 10 μm and up is now possible on a routine basis with SAM and SIMS techniques. There is no optimum method. Small particle mounting for individual particle analysis is definitely nonroutine and requires much developmental work. Thin films are readily detectable on small particles that are mounted on the proper substrate. The particles must not be contaminated by the mounting medium. The first analytical technique to be tried on an unknown particle is SAM, as it is nondestructive. That may be followed by a destructive method such as SIMS. Alternately, a single particle may be mounted, cross sectioned, and examined in an analytical transmission microscope.

References

1. K. F. J. Heinrich, Ed., *Characterization of Particles*, NBS Spec. Publ. 533, Washington: National Bureau of Standards, 1980.
2. J. T. Armstrong, "Rapid quantitative analysis of individual microparticles using the A-factor approach," *Microbeam Analysis--1980*, 193.
3. J. Locke, "A simple microscope illuminator for detecting the fluorescence of float glass surfaces," *The Microscope* 35: 1987.
4. H. Ishida and I. Ishitani, "Raman microprobe analysis of thin films formed on the surface of silver electrical contacts utilizing the surface-enhanced raman scattering effect," *Appl. Spectroscopy* 37(5): 1983.
5. J. P. Bradley et al., "Carbon compounds in interplanetary dust: Evidence for formation by heterogeneous catalysis," *Science* 223: 56-58, 1984.
6. J. Gavrilovic, "Surface analysis of small individual particles by secondary ion mass spectroscopy," in J. K. Beddow, Ed., *Particle Characterization in Technology*, Boca Raton, Fla.: CRC Press, 1984.

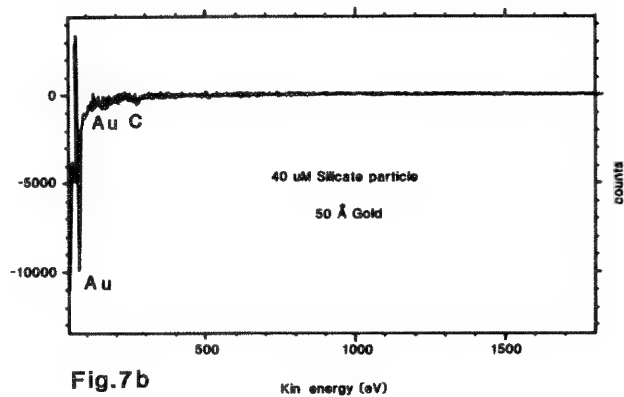
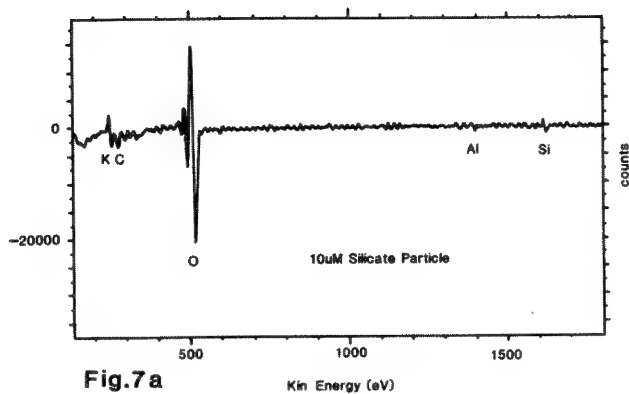


FIG. 7.--Auger surface analysis of small silicate particle (a) without and (b) with thin (50Å) gold film.

NEAR-FIELD OPTICAL IMAGING

M. Isaacson, E. Betzig, H. Barshatzky, K. Lin, and A. Lewis

The spatial resolution of most convention imaging or characterization methods used at present is fundamentally limited by the wavelength of the exciting or emitted radiation being used. In order to visualize small structures, short wavelengths are used; but in general, the smaller the wavelength of the exciting probe, the greater the structural damage to the object under study. Thus, the requirements of non-destructive imaging and high spatial resolution seem to be at odds with one another. However, the reason for this situation is the far-field optics used for producing the radiation probe or for detecting the radiation signal of interest. If one could form images without using far field optics, this wavelength-dependent resolution limit would no longer exist and higher spatial resolution could be attained.

Recently, a novel class of microscopies has been developed that does not depend on far-field optics. This class goes under the broad title of "scanned-tip microscopies."¹ The unifying principle of these scanned-tip methods is that the interaction between a sharp probe and an object is used in a mechanical-scanning arrangement to generate an image formed by scanning of the probe and object with respect to one another. The spatial resolution of such an image is determined by a convolution of the effective probe diameter with the probe-to-sample separation. The most widely used and publicized of the methods is scanning tunneling microscopy, in which the probe can effectively be that of an individual atom (e.g., 2) and atomic resolution can be achieved.

Our contribution to scanned-tip microscopy is an optics-based method called near-field scanning optical microscopy (NSOM). This technique is particularly attractive because it combines the best aspects of conventional optical microscopy and complementary scanning-tip microscopies in terms of flexibility and nondestructiveness. In addition, the spatial resolution limit of this method is competitive with scanning electron microscopy (at least when visible light is used). Since this near-field imaging method does not use far-field optics, the spatial resolution attainable can be smaller by more than an order of magnitude than the wavelength of the radiation used.

This method of near-field imaging has general applicability for all types of radiation probes (i.e., light, x rays, and sound). It is based on the fact that the distribution of radiation in the near field of an object (either considered as a source or receiver of radiation)

can be highly collimated, and that the degree of collimation does not depend to any great extent on the wavelength used. This concept was first described by O'Keefe more than 30 years ago³ and was experimentally implemented with 3cm microwaves by Ash and Nicholls in 1972.⁴ More than a decade elapsed before technology had developed to a point where the idea could be used at visible wavelength.⁵⁻¹¹

Three possible modes have been demonstrated for NSOM (see Ref. 12 for a more complete description). In the illumination mode (Fig. 1a), a subwavelength-diameter aperture in an opaque screen is placed in the near field with respect to an object and is illuminated on the opposite side. The radiation transmitted through the aperture is initially collimated to the aperture size.¹³ By scanning this aperture relative to the object and collecting light transmitted through the sample in the far field, one can form an image of the surface nearest the aperture with a resolution determined by the aperture size. In the collection mode (Fig. 1b), the aperture is used as a receiver rather than as a transmitter of near-field radiation.¹⁴ A microscope objective focuses light onto a sample, a small portion of which is collected by the aperture. In this case, the optical information is collected only from the region in the vicinity of the aperture that is within the near field (which extends to a fraction of the aperture size). Finally, in the reflection mode (Fig. 1c), the illuminated aperture serves as a subwavelength light source and a subwavelength receiver to collect light reflected (or emitted) from the sample surface. Alternatively, one can illuminate the sample at grazing incidence and use the aperture as a receiver.^{6,15}

Each of these methods has advantages and disadvantages;¹² the choice is ultimately made by the type of object to be imaged. Although the experimental NSOM technique is quite new and several methods are being used for implementing the scanning apertures,¹⁵⁻¹⁷ spatial resolutions of the order of one-tenth of the wavelength have been demonstrated and further improvements in resolution can be expected. The limits of resolution and detectability have not yet been reached and the indications are that NSOM coupled with other scanned-tip methods might have many potential applications as a non-destructive high-resolution microscopic tool.¹⁸

References

1. K. Wickramasinghe, *Proc. Soc. Photo-Opt. Instr. Eng.* (in press).
2. G. Binnig and H. Rohrer, *Physica* B127: 37, 1984.
3. J. A. O'Keefe, *J. Opt. Soc. Amer.* 46:

The authors are at the Department of Applied and Engineering Physics, Cornell University, Ithaca, NY 14853.

359, 1956.

4. E. A. Ash and G. Nicholls, *Nature* 237: 359, 1956.

5. A. Lewis, M. Isaacson, A. Muray, and A. Harootunian, *Biophys. J.* 41: 405a, 1983.

6. A. Lewis, M. Isaacson, A. Harootunian, and A. Muray, *Ultramicroscopy* 13: 227, 1984.

7. D. W. Pohl, W. Denk, and M. Lanz, *Appl. Phys. Lett.* 44: 651, 1984.

8. U. C. Fischer, *J. Vac. Sci. Technol.* B3: 386, 1985.

9. E. Betzig, A. Lewis, A. Harootunian, M. Isaacson, and E. Kratschmer, *Biophys. J.* 49: 269, 1986.

10. A. Harootunian, E. Betzig, M. Isaacson, and A. Lewis, *Appl. Phys. Lett.* 49: 674, 1986.

11. U. Durig, D. W. Pohl, and R. Rohner, *J. Appl. Phys.* 59: 3318, 1986.

12. E. Betzig, M. Isaacson, H. Barshatsky, K. Lin, and A. Lewis, *Proc. Soc. Photo-Opt. Instr. Eng.* (in press).

13. E. Betzig, A. Harootunian, A. Lewis, and M. Isaacson, *Appl. Optics* 25: 1890, 1986.

14. E. Betzig, M. Isaacson, and A. Lewis, *Appl. Phys. Lett.* 51: 2088, 1987.

15. U. C. Fischer, U. T. Durig, and D. W. Pohl, *Appl. Phys. Lett.* 52: 249, 1988.

16. E. Betzig, M. Isaacson, H. Barshatsky, A. Lewis, and K. Lin, *Ultramicroscopy* (in press).

17. D. W. Pohl, U. C. Sicher, and U. T. Durig, *Proc. Soc. Photo-Opt. Instr. Eng.* (in press).

18. This work is supported by U.S. AFOSR grant 84-0314. E. B. is an IBM graduate fellow.

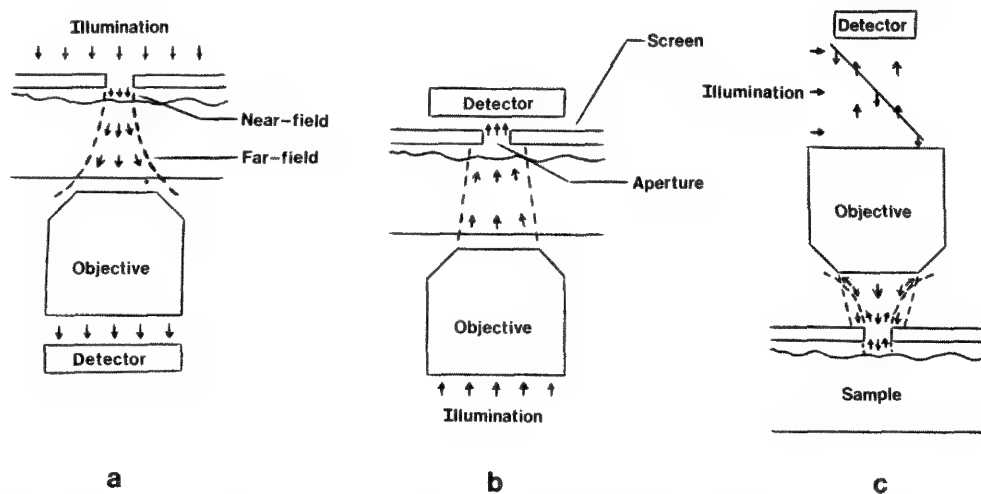


FIG. 1.--Configuration for near-field scanning optical microscopy (NSOM): (a) illumination mode, (b) collection mode, (c) reflection mode.

ACOUSTIC MICROSCOPY

L. W. Kessler

Acoustic Microscopy is an outgrowth of the ultrasonic visualization field that specializes in producing very-high-resolution images through the use of short-wavelength VHF and UHF ultrasound. Two major approaches, SLAM (scanning laser acoustic microscopy) and C-SAM (C-mode scanning acoustic microscopy), are currently applied, both using ultrasound but conceptually different. In understanding their differences and applications, we can see the direction of the future use of this technology and anticipate the problems confronting acoustic microscopy in its bid for wide recognition.

Before we discuss where the field may be heading, we shall describe the key aspects of each approach. In the scanning acoustic microscope (SAM), a point source of ultrasound is produced in a fluid such as water by a highly focused ultrasonic transducer.¹ The transducer is pulsed and alternately acts as a transmitter and receiver. In the imaging process, the transducer (or the sample) is mechanically scanned in a rectilinear raster pattern and ultrasonic signal levels returned from the sample are stored in memory along with address information. The data are subsequently read out as an image on a CRT. A full scan of the field of interest with SAM takes approximately 10 s.

SLAM utilizes another approach.² Here a focused laser beam is employed as an ultrasonic wave detector by the fact that displacement at an insonified surface modulates light reflected from the surface. The displacement is localized within the acoustic wavelength dimensions. To produce an image, the sample is insonified with a plane wave of ultrasound and the laser is scanned rapidly over the field of view. The rate of scan is 30 images/s, which is 300 times faster than can be achieved with SAM's mechanical device. Scanning speed is more important in industrial and quality control applications of acoustic microscopy than in basic research.

SLAM and SAM utilize quite different methods with regard to their applications and operating principles. SAM is generally best utilized in a reflection mode. In order to circumvent absorption of ultrasound in the fluid coupling, focal lengths of SAM acoustic lenses are kept short. After the ultrasound reaches a solid sample, surface penetration is not governed by sample absorption as much as it is limited by geometric refraction. SLAM utilizes a plane-wave transducer for generating the ultrasound

and a focused laser for reception; therefore, SLAM is best utilized in a transmission mode. The "illuminating" ultrasound beam (insonification) is collimated and remains collimated as it crosses a liquid-solid boundary. Therefore, SLAM is not as susceptible to penetration limitation unless it is due to intrinsic attenuation by the sample.

A suitable coupling fluid must be employed in both SAM and SLAM to conduct the ultrasound to the sample. The fluid choice is dictated by several factors. As noted, fluids are absorptive to ultrasound. Distilled water, the most common fluid employed, has a 2.2db/mm absorption loss at 100 MHz. The absorption increases with frequency squared, so that at 1 GHz absorption losses amount to 220 db/mm. In SLAM applications, one can keep the fluid-layer thickness to a minimum by sandwiching the sample between a flat fused quartz buffer rod and the coverslip (mirror scanned by the laser). With SAM, the focused spot is produced one focal length away from the lens, so that there is the risk of significant absorption losses. To minimize these losses, the focal lengths are kept short, as little as 50 μ m at 1 GHz, and the water is heated to decrease the absorption significantly. In another SAM approach, the focus is established at liquid-helium temperatures, where acoustic absorption is also very low. In this case a SAM has been operated at 8 GHz where a resolution of 200 Å has been achieved at Stanford University.³

Besides absorption losses, another factor concerning coupling fluids is the problem of contamination. For example, water may cause sample corrosion. Alternate fluids such as oils and Fluorinert^R are acceptable alternatives in certain cases with regards to contamination, and have been successfully employed with both SAM and SLAM.

The resolution obtained with acoustic microscopes is intrinsically governed by the ultrasonic frequency and wavelength of sound in the material of interest. SLAM has been operated up to 500 MHz; however, the upper frequency of SLAM (and therefore resolution), is limited by the smallest laser spot that can be made. At 500 MHz the acoustic resolution is on the order of 4 μ m in solid materials. Since laser spots can be produced at 0.5 μ m, an eightfold increase in frequency to 4 GHz could be realized.

The resolution attainable with SAM is ultimately limited by acoustic-lens performance. If good lenses can be made and ultrasonic waves generated, there is no limit to the attainable resolution. For example, recent work at Stanford, with very-low-temperature liquid helium as the coupling fluid, has

The author is with Sonoscan, Inc., 530 East Green Street, Bensenville, IL 60106.

produced resolution of 250A.³ A somewhat confusing issue arises when the resolutions of SAM and SLAM are compared. The conditions under which the resolution specification applies to a given sample must be considered. The resolution capability for SLAM is generally limited to 0.5-1 the wavelength of sound in the sample under investigation. For example, at 100 MHz in an aluminum sample, the resolution (and the wavelength for shear) is about 30 μ m. However, at 100 MHz the SAM can produce a 10 μ m spot in water at the surface of the aluminum sample. If this 10 μ m spot is positioned at or up to a wavelength below the sample surface, high resolution is obtained. However, deeper into the sample, the resolution then reverts to the wavelength limit in the material rather than in the water.

Although acoustic microscopy is becoming better known in the technical community, what is its future and what are some of the obstacles facing its acceptance? The following are some of the salient points.

1. Knowledge of acoustic-wave propagation is not as widespread among technical people as light-wave propagation. This lack of familiarity causes reluctance on the part of a potential user to interpret the images comfortably and, in particular, to understand the contrast mechanism. The situation is complicated by the fact that acoustic images inside optically opaque samples cannot be compared to an optical reference. As the acoustic-microscopy concepts gain wider recognition, educational institutions will be required to offer more educational support of this field in order to satisfy the demands of technology and so increase data and ease future interpretations of imagery.

2. Acoustic microscopy began as a scientific curiosity with the anticipation that this new way of imaging "structure" would provide unique and useful new information. This information was provided, but its practical applications must now be developed. As an example, materials scientists always search for ways to characterize materials. Thus, metallurgists have learned to associate grain structure with mechanical properties--but grains can only be visualized at a surface that has been polished and etched. Acoustic microscopy utilizes elastic-wave illumination; therefore, the images relate directly to elastic properties on a micro-scale. With acoustic microscopy grains can be visualized at and below a surface without etching. That is an advantage, but a relatively insignificant one in comparison to the capability of acoustic microscopy in providing elastic modulus information at the grain level. Although this new information is not available by any other technique, it will take time before we learn how to make effective use of it.

3. Acoustic microscopy extends the application of nondestructive testing to small samples requiring higher resolution than had been previously available. This feature is especially important with the use of new high-strength and high-temperature state-of-the-art materials such as nickel-based superalloys and fine-

grain ceramics, where tiny defects cause large reliability problems. Advances in non-destructive-testing techniques, such as acoustic microscopy, will play an important role in the successful employment of these new materials.

4. Although the original motivation for acoustic microscopy development came in biomedical applications, research in this area is in a very early phase. One of the obstacles is a lack of funding to enable researchers to purchase equipment without extensive justification.

5. In the industrial application of new technology, incorrect decisions are made due to insufficient data. SLAM and SAM are applied to specific problems and the merit of the technique is quickly determined by the user, but they are quite different conceptually. The fact that one type of instrument may be inapplicable to a particular problem cannot be extrapolated to the other type of instrument. This limit of application or misapplied application often precludes future considerations of the technology and discounts the rapid change in the state of the art of acoustic microscopy; applications that are not possible today may be routine tomorrow. Dissemination of information regarding new research is needed on a broad scale to combat this tendency.

Future trends in acoustic microscopy involve new applications as well as new instrument developments to improve resolution, penetration, sample handling, and image interpretation. The acoustic microscopist may share some of the traditional microscopist's interest in resolution, but in view of attenuation in samples, resolution and penetration must be traded off. The acoustic transmission spectrum of materials does not provide "windows of transparency" as in the electromagnetic spectrum. With acoustic waves, acoustic attenuation increases monotonically with frequency for all materials (as far as current research suggests).

Acoustic microscopes are commercially available, although various models differ in concept; i.e., SLAM or SAM, frequency ranges, sample handling capability, etc. Acoustic microscopes cover a broad range of applications. Recently developed SLAM systems are in use for testing ceramic tubes that are 20 in. long and 10 in. in diameter. At the other end of the spectrum, SAMs with submicron resolution are available for probing the sub-surface of VLSI silicon wafers.

In conclusion, the dedicated work being performed by acoustic microscopists will overcome the barriers of acceptance and allow this new technique to mature fully and prosper.

References

1. L. W. Kessler and D. E. Yuhas, "Acoustic microscopy," *Proc. IEEE* 67: 526, 1979.
2. C. F. Quate, "Acoustic microscopy," *Trans. IEEE* SU-33: 132, 1985.
3. J. S. Foster and D. Ruga, "Low-temperature acoustic microscopy," *Trans. IEEE* SU-32: 139, 1985.

SUPERRESOLUTION IN LIGHT MICROSCOPY

J. G. Dodd and L. K. DeNoyer

Although the performance of the laboratory microscope has increased dramatically since the time of Leeuwenhoek, so have the demands of the light microscopist. The evolution of modern light microscopy should convince us that a flood of discoveries awaits one who can invade a still smaller world, and if the example of the electron microscope carries any lesson it is that cost and complexity would be unimportant obstacles. Yet the pace of advances in light microscopy has slowed as our resolution limits approach the wavelength of the illuminating light. Are we nearing the end of the race?

Resolution Limits

The resolving power of the light microscope is limited by the objective numerical aperture and by the wavelength of light.¹ Both variables have been extended to their apparent limits. What else can one do?

Let us examine the image behavior on the back focal plane of the objective--the Fourier domain. Under Kohler illumination, the back focal plane (BFP) "image" consists of a re-sorting of the information carried by the light, so that the information representing fine detail in the object is concentrated at the periphery of the field, and the coarse regions contribute to the central illumination.² Blocking off the peripheral region of this distribution reduces the resolution of the microscope by preventing the passage of high-spatial-frequency (fine-detail) information. To increase the resolving power of such a system, one must somehow restore this information. But how can one know what to restore?

Resolution Enhancement

If the information is present to some degree, but attenuated, then restoration should be easy if the signal-to-noise ratio (SNR) is large enough. One need only divide the Fourier transform of the image by that of the aperture function to remove the attenuating effects of the latter; the inverse transform is then the image with fully restored resolution. This procedure seems simple, but the result is so poor that it is not worth showing here. The catch is that a SNR at least as great as the attenuation is required to restore the infor-

mation, and even that won't help if the information is actually missing anywhere in the Fourier domain, and not just attenuated. Since attenuation due to a sharp aperture stop rises rapidly to infinity, data of exquisite quality are necessary if significant restoration is to be achieved. Data of such quality almost never exist, and if they did, would require at least a 32-bit A/D converter to capture. The problem sounds hopeless, but it is not.

First, the information attenuation does depend on whether the aperture is hard or soft--abrupt or gradual. Wiener developed an optimal filter that restores data to the limit the noise spectrum permits, and is useful for soft-aperture functions.^{3,4} The Wiener filter is easy to implement, fast, and optimal in the least-squares sense, and requires only the aperture stop function (separately measurable) and a reasonable noise estimate. Unfortunately, as for all linear filters the Wiener restoration cannot promise to satisfy certain kinds of constraints that apply to optical images, particularly positivity. In the presence of noise (and one is always in the presence of noise), negative intensities and other artifacts can appear in Wiener restorations. Nevertheless, the Wiener filter is useful where the artifact structure does not confuse the parts of the image where detail is required, and it is very fast.

Figure 1a shows a synthetically produced object, and Fig. 1b shows that object viewed through the "aperture" function depicted in Fig. 1c. Gaussian noise of 0.5% of peak signal level has been added. Figure 1d shows a Wiener restoration of Fig. 1b. The resolution certainly has been improved, but there are unpleasant artifacts and negative intensities.

Figure 2 shows power spectra of the image and its Wiener restoration. (The power spectrum is the intensity distribution observed in the BFP of the objective.) Comparing Figs. 2a and 2b, one notes the increase in power present in the higher spatial frequency region of the power spectrum produced by the filter. But the sharp drop-off in Fig. 2b at the same point as that in Fig. 2a shows that restoration could not proceed beyond this point because the information is simply not there in the original image. The aperture was too "hard." The result is the production of artifacts, in fact the one-dimensional equivalent of diffraction rings from a poorly placed stop. No one has ever been really satisfied with restorations of this kind--often called "deconvolutions"--and because of these artifacts the whole field of signal restoration has received a bad press. To avoid artifacts

J. G. Dodd is with Spectrum Square Associates, Inc., 755 Snyder Hill, Ithaca, NY 14850, and Colgate University, Hamilton, N.Y.; L. K. DeNoyer is with Spectrum Square Associates and Cornell University, Ithaca, N.Y. They acknowledge the generous support of Walter C. McCrone and the McCrone Research Institute.

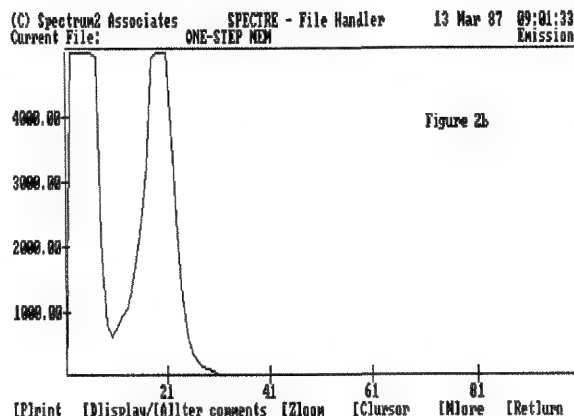
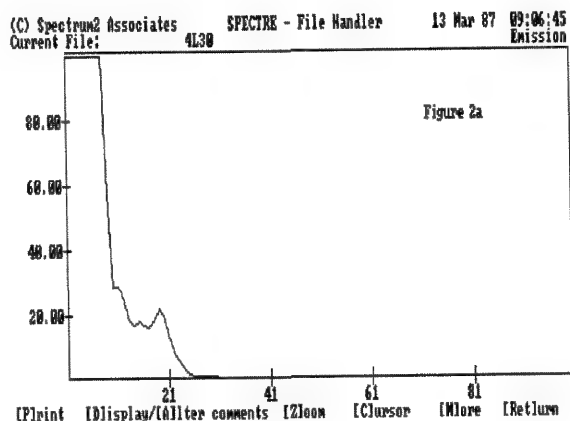
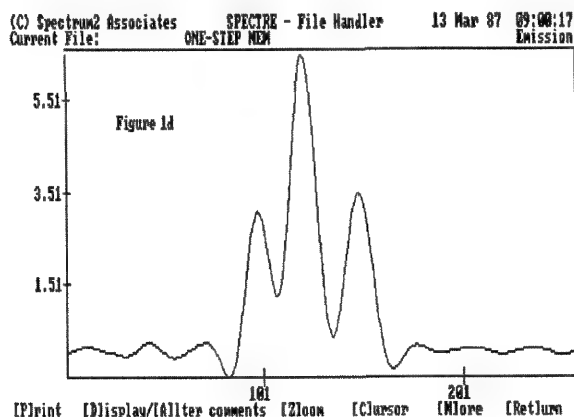
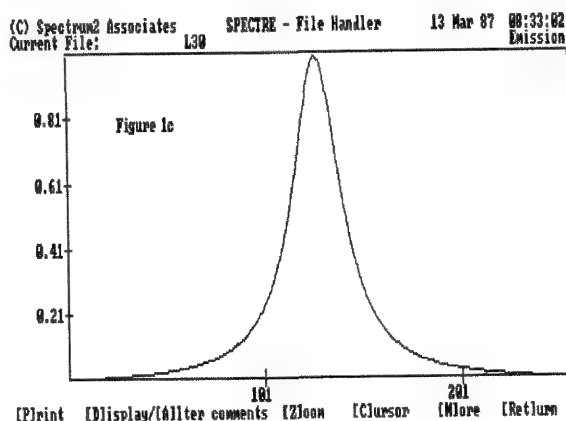
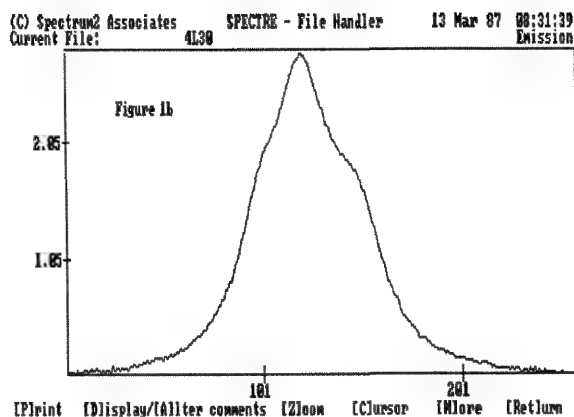
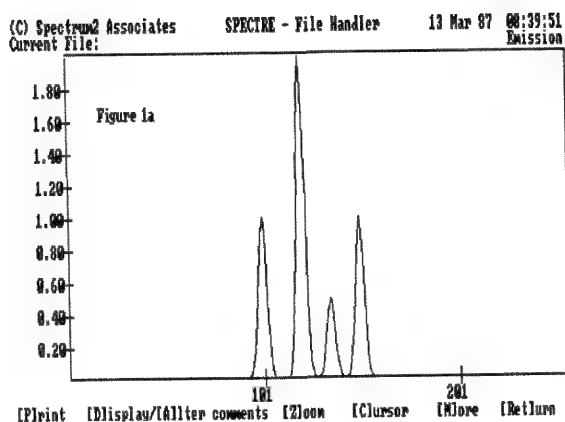


FIG. 1.--(a) Synthetic object spectrum. (b) Synthetic image spectrum. (c) Synthetic transfer function. (d) Wiener restoration of Fig. 1d.

FIG. 2.--(a) Power spectrum of Fig. 1b. (b) Power spectrum of Fig. 1d.

and still achieve resolution improvement we need to restore the information that is missing in the image, as well as to remove the attenuation, which the Wiener filter certainly does.

But to restore information that is simply not in the data is a problem different in kind. Can it be done?

Super-resolution

In mathematical terms, the Fourier transform of a finite object is a continuous function with continuous derivatives. Any such function is completely defined if its values are known over any finite interval. If we measure the illumination over any part of the BFP, no matter how small, then by analytic continuation we may reconstruct the rest of the field out to infinity, if we choose, as if no aperture were present.⁵ Again, however, the SNR required to obtain acceptable results is in the millions, and even if the necessary hardware existed, noise would defeat the attempt. Noise is the demon; what Milton

called "a dismal universal hiss" that fills the universe.

Noise introduces uncertainty; and where uncertainties exist exact results do not. Statistical analyses provide the only answers.

Maximum Entropy and Maximum Likelihood Methods

In 1949 Shannon defined an entropy function of information.⁶ Jaynes first suggested that the probable information state of a system is one that maximizes the information entropy subject to whatever other constraints are applicable.⁷ Burg developed the first efficient algorithm to apply a maximum entropy method (MEM) to experimental data.⁸ It works well.

Since its inception MEM has grown many branches, reflecting mostly variations in the types of additional constraints upon the data that are implicitly or explicitly present. Most modern methods of signal and image restoration are equivalent to some subset of superset of MEM, even if the concept is not explicitly used in the method's development. It is the dominant paradigm in image restoration, because it works. For more than 20 years radio astronomers have used MEM-based programs to make scattered radio telescopes behave like a single large dish by estimating the signal between the dishes from the dish samples.⁹ It has been used to extend the resolution of FTIR systems by a factor of eight!¹⁰ It is not the ultimate tool, but it works.

How does MEM work, and why does it work so well? One answer to this question is, unfortunately ... very slowly! But let us examine the structure of MEM-based algorithms.

The Structure of MEM

First, the information entropy function of the system is defined either as $N \ln(N)$ or as $\ln(N)$ (depending on whether the quanta of information obey Boltzmann or Bose statistics), where $N = N(k)$ is the number of ways the quanta can be rearranged among the k detector bins. This function is then maximized subject to conservation of the various constraint equations. Typical constraints for optical images are the following.

1. The image is a "good" sample of images of this particular object taken under these conditions.
2. The image has been observed through an instrument with a known transfer function which has converted the actual object field to the image field.
3. Total energy is conserved.
4. Noise of a known power spectrum has been added to the system, either before or after the instrument, or both.
5. The object is positive definite.

The list is in random order. More or different constraints may apply in particular cases. Note that these constraints are a priori and are not explicit in the data. The constraint set is the secret of statistical res-

toration methods. We have said that the aperture has blocked fine detail from our view, and that is true; and that noise has corrupted what is left, and that is true. But we know something about the nature of the blockage and corruption, and a good deal about the domain of acceptable objects that can produce such images; it would be surprising if we could not put this knowledge to some use. We use it, in fact, to constrain the object properties to be consistent with this knowledge.

But why maximize the entropy?

From thermodynamics we know that a system is stable if arbitrary perturbations from the present state always increase the entropy of the universe. We presume, therefore, that the maximum entropy state is the most probable state.¹¹ (In fact, this may not be true, although it usually is; we shall discuss this surprising result later.) Thus we choose from the set of possible objects that satisfy the constraints the one at the peak of the entropy distribution; that object is our "best guess." This is the rationale of MEM.

Unfortunately, the resulting set of equations is exceedingly difficult to solve quickly and stably.¹² Under the best of conditions an image will occupy a fast mainframe computer for most of an hour. However, the result, when it finally emerges, can exhibit a resolution enhancement of as much as a factor of eight or more, depending on how well the constraints are known, and what the SNR is.

The noise tolerance of MEM-based methods is impressive. Some degree of restoration can be obtained from SNRs of 2 or 3, if the noise statistics and power spectrum are well known.¹³ So, why does it work so well?

The entropy functions of large data sets are very sharply peaked. An example is the uniformity of air density in a room; the uniform state is so much more probable than the neighboring states that a statistical fluctuation of, say, 0.001% will probably not occur during billions of years. Since MEM entropy functions are already selected from permissible object sets that obey specified constraints, where these constraints are poorly chosen the probability that an "accurate" measurement of the system will deviate from a properly constructed MEM estimate is very small, and if it occurs, can usually be traced to an improper, inaccurate, or missing constraint. If the constraints properly represent the physics of the data-taking system, the reconstruction will be close to an image taken with a "better" system.

Having said all this, we must point out that an MEM estimate can be wrong. It is, after all, based on just one sample of data. Sources are only statistically steady. The next sample will certainly be a little different, and occasionally a lot different. And since detector noise is present, a noise fluctuation in a critical region *can* change a feature radically. MEM is a statistical method, after all, and although, for example, we can say that an honest coin has an equal probabil-

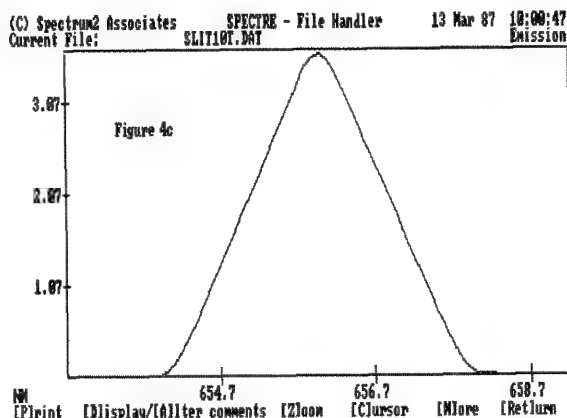
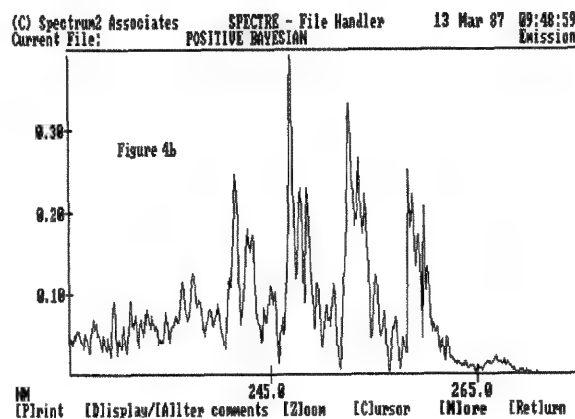
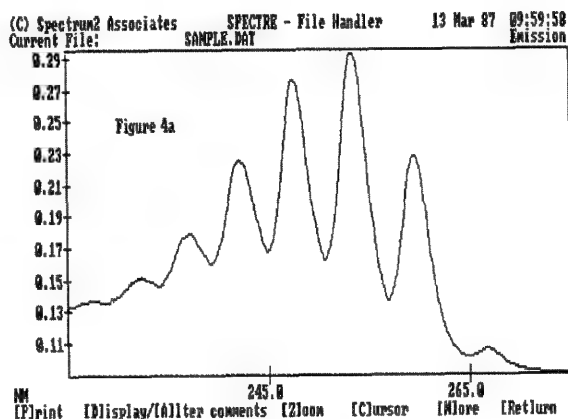
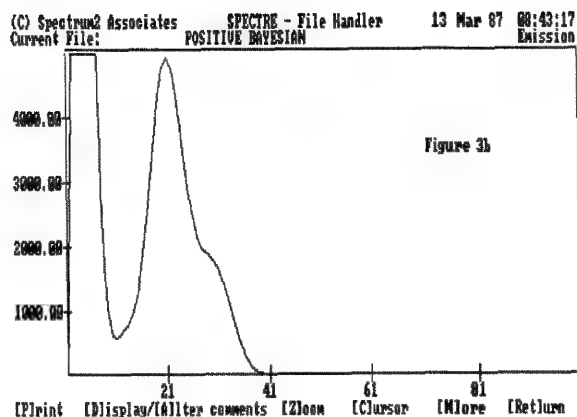
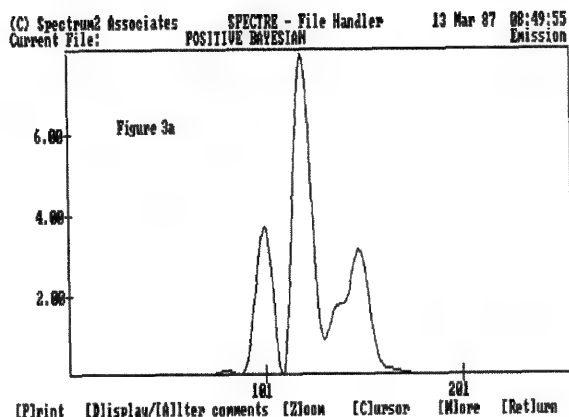


FIG. 3.--(a) Maximum-likelihood restoration of Fig. 1b. (b) Power spectrum of Fig. 3a. FIG. 4.--(a) DU benzene spectrum. (b) Maximum-likelihood restoration of benzene spectrum. (c) DU transfer function.

ity of landing heads or tails when flipped, it may stand on end without violating the laws of probability!

But MEM is not the end of the hunt. The maximum entropy principle described above does not necessarily represent a *maximum likelihood* principle, and that, after all, is what every experimenter wants to achieve. The MEM algorithm is based on the statistics of the entropy function alone; the assumed constraints are deterministic. That may not always be the case. Often constraints may themselves be statistical. In that case, we

should write the joint probability function for the entropy and the statistical constraints, and maximize that function.¹⁴ The result is usually close to a MEM result, but if the constraints are statistical, and especially if the signal flux is very low, such a *maximum likelihood* (ML) result may be much different from that produced by MEM.

Equations resulting from an ML algorithm are no easier and often harder to solve than those arising from MEM. The differences in the algorithm arise from the nature of the statistical constraints, which typically reflect particle statistics (Bose-Einstein for photons, Fermi-Dirac for electrons and protons, and Maxwell-Boltzmann for everything else), and from various kinds of a priori knowledge of the object, which is usually only statistical in nature. Although ML may reduce to MEM in many common cases in which "classical" statistics apply and a priori object knowledge is not available, MEM must be considered a subset of ML.¹⁵

In any case one is faced with a number of unknowns equal to some multiple of the number of data points, and as many equations. The

equations are highly nonlinear and "stiff," in the sense that at least a lower bound, and sometimes both a lower and an upper bound, exist on permissible solutions. In fact, the development of the theory awaited that of the computer, because the principles of statistics certainly existed before there was any possibility of applying them to the kinds of problems discussed here.

If the mathematics seems difficult and complex and the demands on the computer seem overwhelming, the reader has correctly understood the nature of this problem. The practical barrier to the use of ML is still speed, speed, speed.

Some Results

We have made some algorithmic advances that now bring certain kinds of ML processing within the reach of most laboratories. With an AT-class computer, and a suitable image capture board, ML restorations of a 128×128 pixel image may now be carried out in about 15 min. The equipment cost of such a system, excluding the camera, is under \$6000.

Here, we show a simple one-dimensional example by restoring Fig. 1b by a fast ML method. Figure 3a shows the restoration, and Fig. 3b shows its power spectrum. Comparing Figs. 2b and 3b, we see that information in the Fourier domain has been extended into the originally empty higher frequency region. The effect is exactly the same as if an objective of larger N.A. were used. The restoration of these 256-point spectra took about 30 s.

One cannot help wondering whether such a restoration will work as well on real data. Figures 4 and 5 show that it works even better. Figure 4a is a UV absorbance spectrum of benzene taken on a Beckman DU spectrophotometer with 2nm resolution. Figure 4b is the restoration using the measured instrument line shape of Fig. 4c. The data are very good; the SNR was conservatively set at 500. The restoration compares quite well with published spectra taken at a slit setting representing a resolution about eight times as great. (The comparison spectrum was taken on a different machine;

the DU is not capable of producing such a well-resolved spectrum.) The power spectra of the original and restored files are shown in Fig. 5.

But one must be careful not to assume that good microscopic images can therefore be super-resolved. There are two differences between the one-dimensional examples shown above, and microscopic images at the limit of resolution of the light microscope: the two-dimensional nature of the image, and the partial coherence of microscopic illumination. The first difference is trivial. The second is crucial and will force substantial algorithmic changes.

Coherence and Restoration

It is necessary that the transfer function, or point spread function, be known as precisely as possible. For incoherent illumination, it is simply a matter of measurement. The principle of superposition holds, so the illumination at a given point is simply added to by the spreading-light pattern from surrounding points.

However, if the illumination is coherent, the spreading-light pattern has a phase relationship to the light at the given point, and the sum is no longer that of simple intensities, but of amplitudes and phases. Two overlapping patterns may constructively or destructively interfere, depending on relative phases. An image is no longer a unique result of a given object. Unfortunately, illumination of a microscopic object near the resolution limit is always partially coherent.¹⁶ Extension of ML algorithms to the coherent case is not automatic. Although in principle the mathematics of the extension is easy, the fact that the intensity image is not a unique representation implies that an image taken for the purpose of restoration must have phase as well as intensity information. Such an image is called a *hologram*. Fortunately, image plane holography will suffice and is not hard to arrange in microscopy.¹⁷ Tests are now being designed.

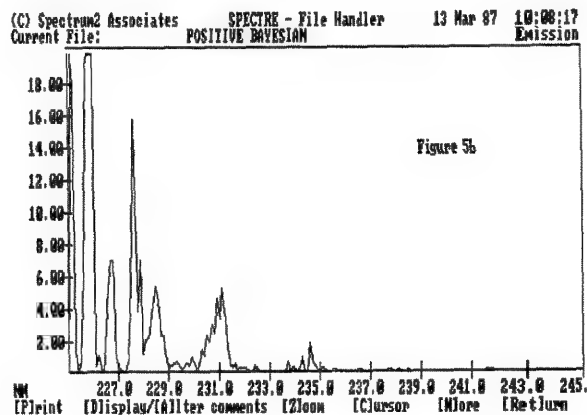
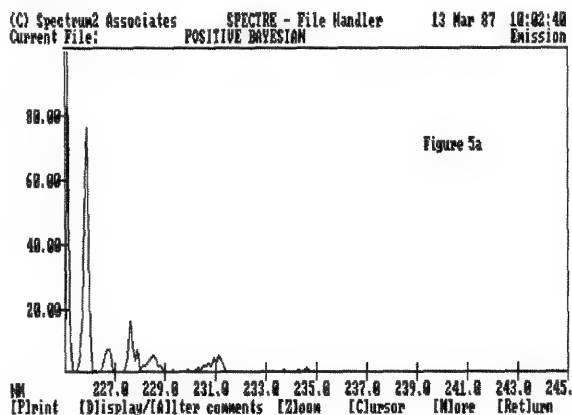


FIG. 5.--(a) Power spectrum of Fig. 4a. (b) Power spectrum of Fig. 4b.

Conclusions

Superresolution of one- and two-dimensional images may now be accomplished by use of maximum-likelihood methods of data processing. The degree of superresolution attained depends on the signal-to-noise ratio of the image, and on a knowledge of the behavior of the imaging system. Processing time on an AT-class computer is of the order of 15 min for a 128×128 pixel image. Application to partially coherent images requires holographic images, since phase information may be necessary.

References

1. F. Zernike, in J. Strong, *Concepts of Classical Optics*, San Francisco: Freeman, 1958, 533 (Appendix K).
2. *Ibid.*, p. 551.
3. N. Wiener *Extrapolation, Interpolation, and Smoothing of Stationary Time Series*, Cambridge, Mass.: MIT Press, 1958.
4. B. Saleh, "Wiener restoration of defocused partially coherent images," *Appl. Optics* 19: 3646, 1980.
5. R. Churchill, *Complex Variables*, New York: McGraw-Hill, 1948, 32.
6. C. Shannon and W. Weaver, *The Mathematical Theory of Communication*, University of Illinois Press, 1949.
7. E. T. Jaynes, *Trans. IEEE SSC-4*: 227, 1968.
8. J. P. Burg, "Maximum entropy spectral analysis," *37th Ann. Int. Mtg. Soc. Expl. Geophys.*, Oklahoma City, 1967.
9. R. Narayan and R. Nityananda, "Maximum entropy image restoration in astronomy," *Ann. Rev. Astron. and Astro.* 24: 127, 1986.
10. S. Kawata, K. Minami, and K. Minami, "Superresolution of Fourier transform spectroscopy data by the maximum entropy methods," *Appl. Opt.* 22: 3593, 1983.
11. B. R. Frieden, "Restoring with maximum likelihood and maximum entropy," *J. Opt. Soc. Am.* 62: 511, 1972.
12. J. Skilling and R. K. Bryan, "Maximum entropy image reconstruction: General algorithm," *Mon. Not. R. Astr. Soc.* 211: 111, 1984.
13. Ref. 11, p. 516.
14. B. R. Frieden, "Unified theory for estimating frequency of occurrence laws and optical objects," *J. Opt. Soc. Am.* 73: 927, 1983.
15. B. R. Frieden, "Dice, entropy, and likelihood," *Proc. IEEE* 73: 1764, 1985.
16. M. Born and E. Wolf, *Principles of Optics*, London: Pergamon, 4th ed., 1970, 522.
17. J. Dodd, "A holographic attachment for the light microscope," *The Microscope* 25: 55, 1977.

ELEMENTAL IMAGING TECHNIQUES IN STUDIES OF STRIATED MUSCLE

M. E. Cantino and D. E. Johnson

Analytical electron microscopy has, in recent years, provided unique and valuable information about the subcellular distributions of elements in cells and tissues. However, the substantial time required for collection and analysis of data makes the possibility of automated acquisition and processing of spectra particularly attractive. We have been exploring the use of digital elemental images in our studies of the regulation of contraction in striated muscle, and have found that imaging capabilities augment previous methods for collection and analysis of data in several important respects. In this paper we discuss and illustrate some of the advantages of digital elemental imaging in muscle studies.

Methods of Image Acquisition and Analysis

The data described here were collected in the STEM mode in a JEOL 1200EX electron microscope, with a Link AN10000 analytical system and Link analytical software for the acquisition and processing of elemental and electron images. This software, which has been described elsewhere,¹ applies a digital filter and least-squares fit to the data acquired at each pixel. Quantitative information can then be extracted from specific subcellular regions in elemental images by masking techniques described previously.^{2,3} In brief, a binary mask is created over the region of interest by use of automated thresholding routines or an interactive device such as a mouse to draw in the mask. The pixel values within the masked area of each map are then added and averaged to determine elemental composition.

Analysis of Periodic Structures

The periodic structure of muscle has always made it well suited to digital image analysis, since averaging techniques can improve signal-to-noise ratios while total exposure (and hence, radiation damage) is minimized. Although radiation damage cannot be eliminated in analytical studies, there are several advantages to elemental imaging in studies of elemental distributions along the sarcomere. First, the sarcomere pattern does not always lend itself to the use of rectangular analysis rasters (Fig. 1). In this case, a series of masks was applied along the sarcomere in such a way that lateral skew within myofibrils was accounted for. By application of such masks to both halves of all sarcomeres, nearly all of the data in the field of view can be used. Av-

erage sulfur counts per pixel for the series of masks shown are included at the bottom of Fig. 1. Although some elements (such as calcium) may contribute only a few counts per pixel above background, the summed counts over several thousand pixels in a particular band become significant, and provide high resolution data reflecting calcium binding to myofilaments. An additional benefit of digital images is that they can be re-analyzed without a return to the microscope, should new questions arise.

Identification of Subcellular Organelles

Identification of organelles from electron images alone may be difficult, particularly in cryosections, where the structural preservation is not always optimal. In such cases, spectral data can provide elemental "fingerprints" for particular subcellular compartments. An example is shown in the transverse cryosection of a rabbit papillary muscle (Fig. 2a). Although mitochondria are generally characterized by high electron density, freeze damage toward the center of the cell makes positive identification difficult in some cases. Fortunately, mitochondria are also characterized by high phosphorus levels (Fig. 2b). In this study, we selected mitochondrial areas by making a binary mask on the STEM image (i.e., thresholding on low pixel values), and multiplying it by a binary mask created on high-intensity pixels in the phosphorus image. The resulting binary mask selects only pixels low in the STEM image and high in the phosphorus image (eliminating, for example, nuclear regions). Average counts/pixel from elemental images were then normalized to film corrected counts/pixel from the bremsstrahlung image and multiplied by appropriate proportionality constants to yield concentrations. Table 1 shows cytosolic and mitochondrial dry-weight concentrations for several elements, derived from the digital maps. Although mitochondrial phosphorus is clearly elevated in the raw (un-normalized) image, P concentrations in cytosol and mitochondria are quite similar.

TABLE 1.--Elemental concentrations from digital map of papillary muscle (mmol/kg dry wt.).

	Na	Mg	P	Cl	K	Ca
Mitochondrial	91	36	415	64	380	0.88
Cytostolic	112	54	430	112	556	0.57

The authors are at the Center for Bioengineering, WD-12, University of Washington, Seattle, WA 98195.

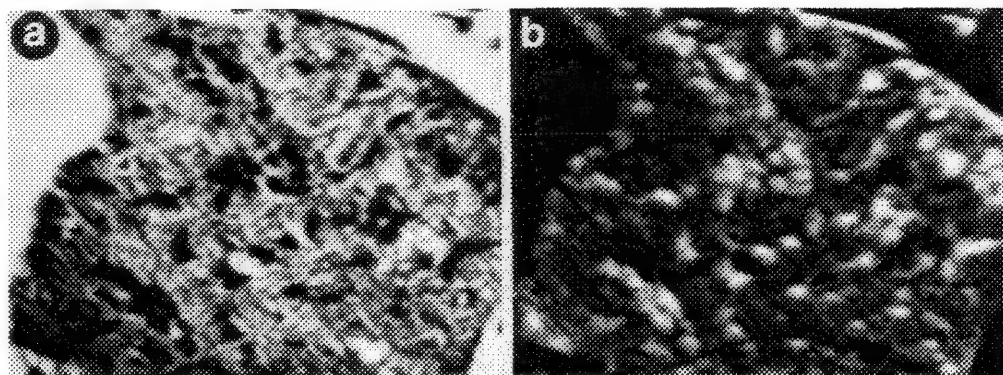
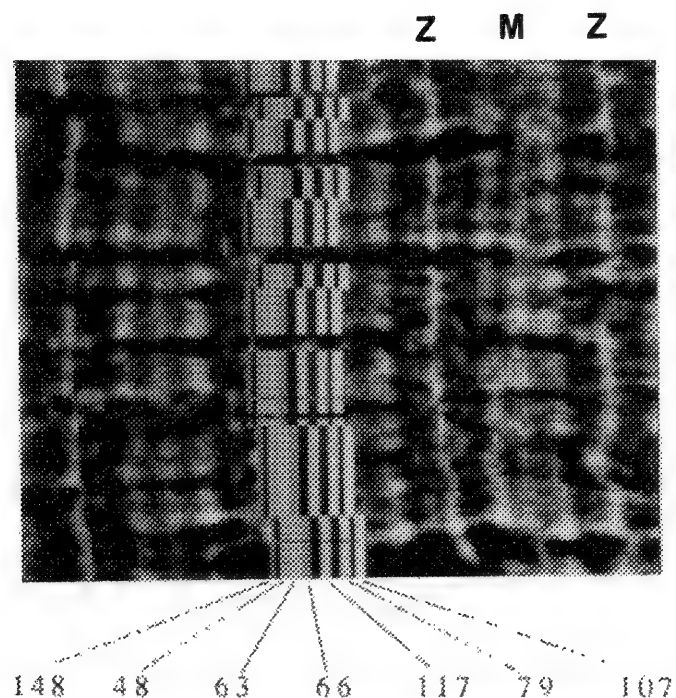


FIG. 1.--Sulfur x-ray image of several sarcomeres in cryosection of glycerinated rabbit psoas muscle. Multibanded mask shown over one half sarcomere was applied to other half sarcomeres in the field, and pixels in each band were averaged separately to obtain average sulfur counts per pixel shown below micrograph. Similar data can be obtained from each elemental image. Z = Z line, M = M line.

FIG. 2.--(a) Digital STEM image of transverse cryosection of rabbit papillary muscle. (b) P image of same muscle. Mitochondria are characterized by high P levels.

Unanticipated Results

Although statisticians generally prefer questions to be formulated a priori, the most important information may easily be missed in an analysis scheme that specifies that only certain subcellular regions should be sampled. One of the greatest benefits of digital imaging is in providing a broad view of elemental distributions in an entire field, whether it includes a single cell or a group of cells. With this information in hand, the investigator may return to ask new and potentially more important questions in the next round of experiments.

References

1. P. J. Statham, "Quantitative digital mapping with drift compensation," *Analytical Electron Microscopy--1987*, 187-189.
2. D. E. Johnson, K. Izutsu, M. Cantino, and J. Wong, "High spatial resolution spectroscopy in the elemental microanalysis and imaging of biological systems," *Ultramicroscopy* 24: 221-236, 1987.
3. J. G. Wong, M. E. Cantino, L. E. Wilkinson, K. T. Izutsu, and D. E. Johnson, "Quantitative elemental analysis of digital x-ray images," *Analytical Electron Microscopy--1987*, 191-194.

PROGRESS AND APPLICATION OF QUANTITATIVE ELEMENTAL MAPPING

P. J. Statham

A technique for x-ray spatial mapping was reported last year that aimed at improving both the accuracy and quantity of information extracted during a long experiment. The present work shows how this "quantitative elemental mapping" method has been developed further to improve corrections for drift and to extract additional parameters for subsequent x-ray correction calculations and diagnostic purposes. The use of statistical data such as "standard deviation images," which was suggested as a means of suppressing artifacts, is developed further as an aid to interpretation and evaluation of experimental results.

Summary of Technique

The quantitative mapping technique introduced last year¹ performs the following operations:

1. Position the beam on a grid of up to 1024×1024 pixels.
2. Acquire x-ray and electron image data for preset dwelltime.
3. Correct x-ray spectrum for drift and perform all background subtraction, peak overlap correction, and statistical calculations by a "filtering and least-squares" (FLS) approach.
4. Extract up to 32 parameters to be used as pixel intensities for up to 32 individual maps.
5. Periodically, interrupt the acquisition to track a reference feature and deduce a spatial drift correction.

Figure 1 summarizes how these operations are achieved but does not represent the exact order of events, because every opportunity is taken to save time whenever one operation can be commenced and run simultaneously with another. If polished bulk specimens are being analyzed, apparent concentrations are calculated with reference to stored standard intensities; otherwise, peak areas are computed. To process data for a single pixel to obtain 8 window integrals and fit 8 profiles by FLS takes 1.2 s; since data can be acquired while calculation is in progress, it is realistic to consider dwell time as short as 1 live second per pixel. The tracking routine typically takes about 1 s to find a good match to the reference image and is usually invoked at the end of each grid line.

The use of images of the standard deviation for each parameter was also suggested as an objective method of eliminating artifacts.¹ If

the image describing a given parameter is smoothed, a simple algorithm can be used to correct the corresponding standard deviation image so that it can still be used for statistical-significance testing.¹

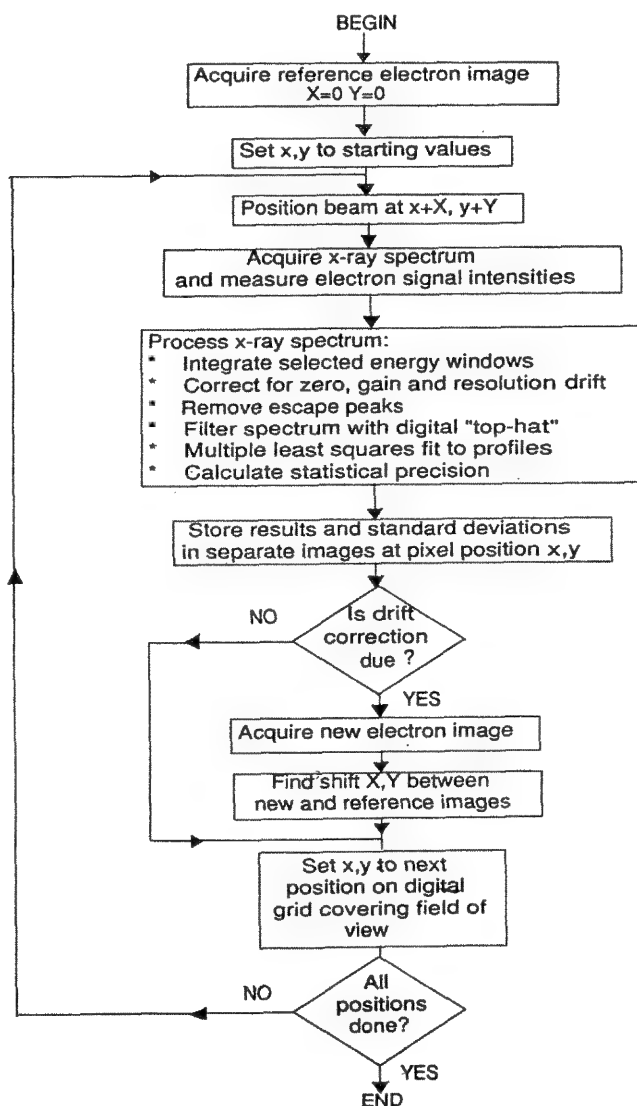


FIG. 1.--Outline of stages involved in quantitative mapping with drift correction.

Figure 2 illustrates a problem in a difficult application that exemplifies the advantages of this technique; the L line profiles of the rare earth elements are convoluted and the counts in simple energy windows are inadequate as an indication of elemental concentration. In a mineralogical sample of a diagenetic rhabdophane, the quantitative mapping technique was used to investigate a new theory of

The author is with Link Analytical Ltd., Halifax Road, High Wycombe, Bucks, England HP12 3SE. He is indebted to M. Jones for considerable technical assistance in the experimental work for this paper.

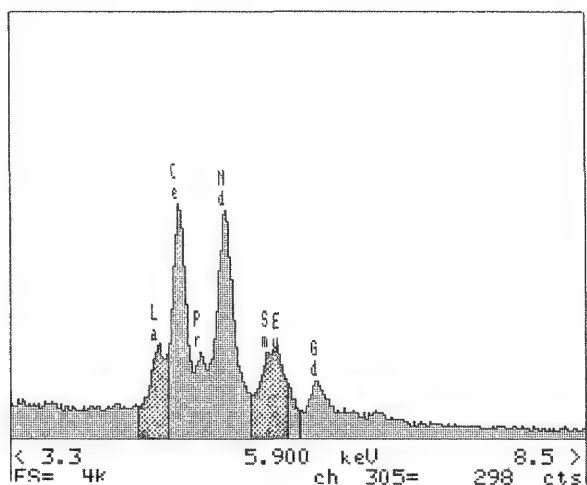


FIG. 2.--Example spectrum from diagenetic rhabdophane. Labels show approximate positions of $L\alpha$ lines of rare earth elements. Window regions are shaded for La and Sm.

zonation² which runs contrary to popular models. The digital maps recorded from simple energy regions set around each major peak (Figs 3a and b) do not show any clear change in contrast across the field of view. However, the maps obtained by full spectral processing at each pixel show that the major element is concentrated in the rim (Fig. 3c) and even though Sm is only present at less than 5 wt%, the fact that it is more concentrated toward the core is clearly apparent from Fig. 3d.

Figure 4 illustrates the importance of the standard deviation image in a run where Ba and Ti concentrations were measured. The FLS-derived image of Ti (Fig. 4c) appears to show a slight increase in Ti in areas obviously rich in Ba (Fig. 4a). However, further analysis reveals that there is a greater statistical fluctuation in these regions and the higher excursions appear as brighter pixels in the image; when the image is divided by the corresponding standard deviation image (Fig. 4d), it is clear that there is no area of Ti enrichment. The images of Figs. 4b and d can be regarded as statistical confidence distributions to which we can refer if we wish to validate structure that seems to be apparent in an image. Alternatively, pixels can be zeroed if they fall below a suitable significance value such as twice the standard deviation.¹

New Additions

The present paper describes the following extensions to the technique.

1. An option to compute and store a value for "FIT INDEX" (i.e., goodness of fit) at each pixel.
2. In addition to simple window integrals, the option to record the integral of a window after stripping away the peaks.
3. A method for monitoring and correcting for beam current drift.

FIT INDEX Images. The FIT INDEX is equal to

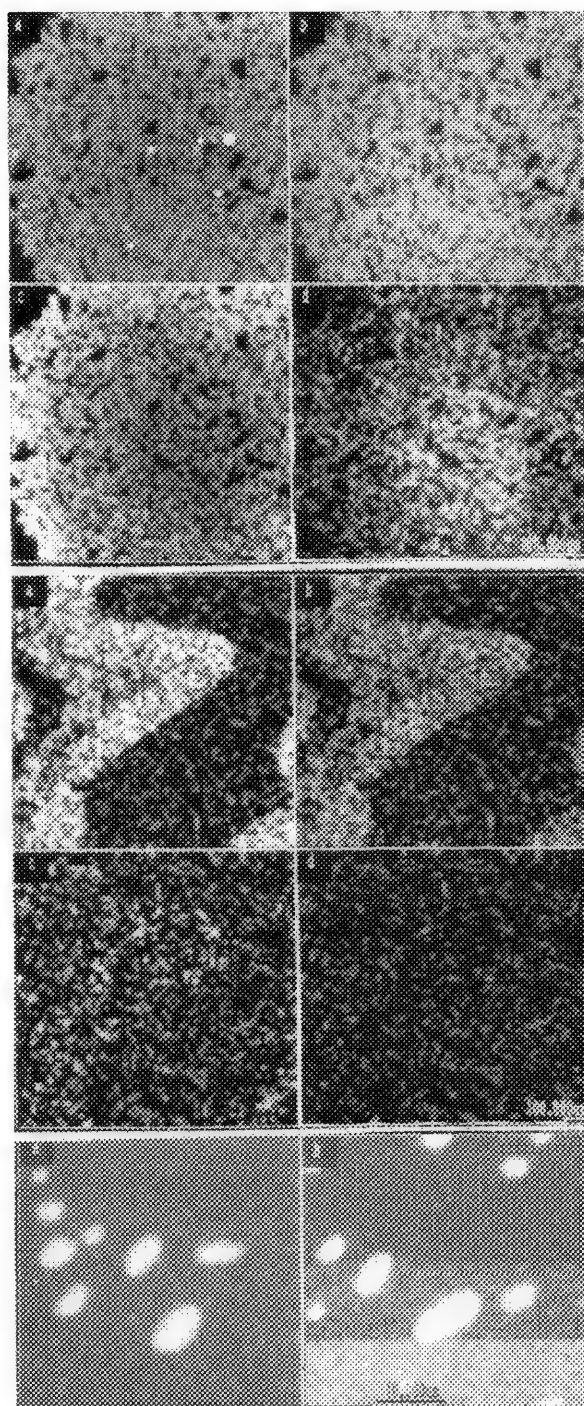


FIG. 3.--Images from sample as for Fig. 2 obtained with 64×64 scan with 1 live second dwell per pixel: (a) La window counts, (b) Sm window counts, (c) La apparent % by FLS (max = 20%), (d) Sm apparent % by FLS (max = 5%).

FIG. 4.--Images from mineralogical sample obtained with 64×64 scan with 1 live second dwell per pixel: (a) Ba apparent % by FLS, (b) Ba%/std. dev., (c) Ti apparent % by FLS, (d) Ti%/std. dev., Maximum brightness: (a) 5%, (b) 3, (c) 2%, (d) 3.

FIG. 5.--Examples of FIT INDEX images from two experiments performed with 64×64 scan and 1 live second dwell per pixel.

the average value of r^2/v over all channels used for the FLS fit, where r is the residual channel count after the fitted profiles are subtracted from the filtered spectrum and v is the estimated variance at each channel.³ It is similar to a "normalized χ^2 " value but is not exactly the same because, after filtering, the individual channel statistics are no longer independent.³ Nevertheless, the FIT INDEX is a sensitive indicator of the goodness of fit and although the average value should be close to 1, values greater than 2 are usually indicative of a poor fit to the data. Poor fits can arise if the peak shapes used for fitting do not conform exactly to those in the acquired spectrum. Although this problem is largely overcome by the use of a stored library of standard profiles,³ there can still be a problem if the resolution, gain, or zero change during the course of an experiment. Furthermore, the simple omission of a peak in processing will give rise to a poor fit.

Figure 5 shows the FIT INDEX images for two different experiments. In Fig. 5a, most of the pixel values are close to unity (a satisfactory fit) but the bright area describes a region where the fit is always poor; in this experiment profiles for Cr and Fe were included but that for Mn was omitted in FLS processing, so that the FIT INDEX map effectively highlights the regions where Mn is present. In Fig. 5b, the FIT INDEX image not only contains similar bright regions due to an omitted peak, but also exhibits bands of increased brightness toward the bottom of the image; in this experiment the EDS electronics were purposely misadjusted to upset the gain during the course of the run, yet no attempt was made in the processing to correct for such drift and the fit deteriorated. These two examples show how useful the FIT INDEX map can be as a diagnostic tool to monitor unexpected events during the course of a long unattended run.

Continuum Intensity Maps. In bulk specimens, drift in probe current will obviously affect x-ray maps; and in thin specimens, variations in thickness will further modulate observed intensities. One solution to these problems is to measure the continuum intensity in a fixed energy band; if the specimen composition and hence efficiency of bremsstrahlung generation is known (or obtained by iterative calculation), characteristic intensities can be adjusted so that they are independent of such variations. This is the basis of the well-known "Hall" procedure for microanalysis of thin biological material, but can also be applied in principle to bulk specimens.⁴ In the case of particles or rough surfaces, the ratio of peak area to background intensity immediately beneath the peak can also make the results insensitive to geometric variations that alter the absorption correction for characteristic radiation.⁵

As illustrated by Fig. 6a, a simple integral of the raw spectrum over the desired continuum energy window may include counts from characteristic peaks and thus be unsuitable for use

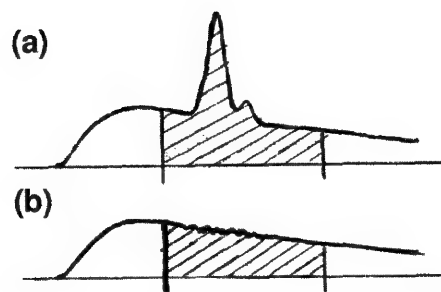
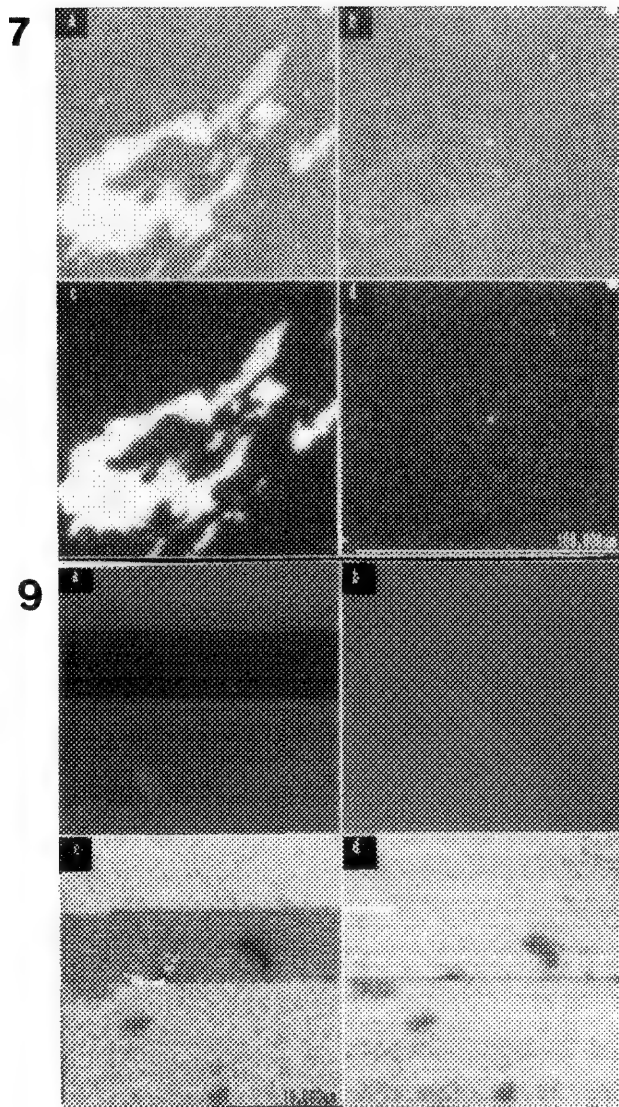


FIG. 6.--(a) Window integral including characteristic peak counts; (b) continuum integral obtained after peak stripping.

in any of the above correction methods. Therefore, after FLS processing, peaks are stripped from the spectrum⁵ so that integration yields a result proportional to the mean bremsstrahlung intensity as required (Fig. 6b). Figure 7 is an example where images formed from the continuum window both before (Fig. 7a) and after (Fig. 7b) stripping are compared. Here, a window spanning the K $K\alpha$ and K $K\beta$ peaks was set in an experiment on a mineralogical sample. The potassium distribution revealed in Fig. 7c is also reflected in Fig. 7a, but Fig. 7b shows that this component is effectively removed by stripping. Since Fig. 7b should in theory be a fair representation of mean atomic number of this bulk sample, it would appear that there are a few small regions of high atomic number toward the center and upper right of the image. However, examination of the FIT INDEX image in Fig. 7d also shows these bright areas, which suggests that the fit is bad and consequently the derived results are likely to be unreliable in these regions. Such results can be explained by the presence of an element (e.g., Ca) with a profile that overlaps the potassium peaks yet which has been omitted from the fitting procedure; the useful point to note is how the FIT INDEX map can be used to avoid misleading interpretation of image data.

Correction for Probe Current Drift. A direct method to correct for variations in excitation is to monitor and record an image representing aperture current, provided it is proportional to probe current. Alternately, if an automated Faraday cage is available, measurements can be made periodically during the course of a long run and used to correct spectra for current fluctuations. In many instruments, neither of these options is available, so a technique has been devised that only requires that a small area of conductive bulk material be within the limits of beam deflection during the experiment. The principle should be clear with reference to Fig. 8, which shows the full field of view accessible via beam deflection. The boxed area represents the area scanned when the digital maps are acquired. At the end of each line of the scan, the beam is directed to the position



shown by the cross and a measurement of some signal is taken. Provided this signal is directly related to probe current, the result can be used to form an image where each line contains a number proportional to probe current. An integral across any region of the x-ray spectrum would suffice, but better signal-to-noise ratio can usually be achieved by the use of backscatter or secondary electron detector signals, provided they are DC coupled and no black-level correction has been applied. It does not matter that the signal may be affected by composition of the sample under the cross because the same position is used for all measurements.

Figure 9 illustrates how this technique can be used in practice. Figure 9a shows an image constructed in the above fashion where each line records the secondary electron detector output at a chosen reference position. (Artificial current fluctuations were introduced during the experiment by adjustment of lens current on the SEM; although this shifted the image slightly, the experiment was only performed to test the procedure.) Since it is

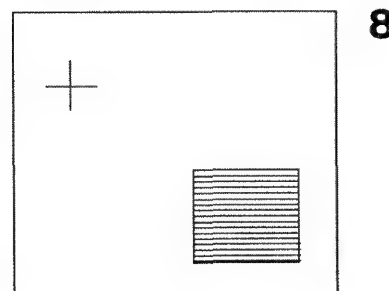


FIG. 7.--Example use of continuum integral: (a) raw window counts, (b) continuum integral after peak stripping, (c) potassium K peak area by FLS, (d) FIT INDEX.

FIG. 8.--Diagram of field of view in probe current correction method.

FIG. 9.--Example showing correction for current fluctuations: (a) reference signal R at end of each line, (b) R corrected, (c) Cr apparent % by FLS, (d) Cr % corrected. (Correction is to divide by R then scale by first R pixel intensity.) Shearing is result of lens current changes used to simulate genuine current fluctuations.

reasonable to assume that probe current remains stable for a short time, the intensity value for the first line in this image can be used as the reference value to represent the desired probe current level. The variations in current evident in Fig. 9a are also reflected in the apparent concentrations for Cr shown in Fig. 9c. If both images are divided pixel by pixel by the intensity value for Fig. 9a and scaled by the reference value from the first line, the resulting images (Figs. 9b and d) are corrected for the major fluctuations in probe current. Alternative reference measurements, such as the integral of all counts in an x-ray spectrum, are insensitive to amplifier drift and may prove to be a more practical indication of probe current than the secondary electron signal.

References

1. P. J. Statham, "Quantitative digital mapping with drift compensation," *Analytical Electron Microscopy--1987*, 187.
2. A. Kearsley, personal communication, October 1987.
3. P. J. Statham, *Analytical Chem.* 49: 2149-2154, 1977.
4. C. Nockolds, *10th Australian Conf. on EM*, 1988.
5. P. J. Statham, *Mikrochimica Acta* (Wien), Suppl. 8: 229, 1979.

QUANTITATIVE ELEMENTAL X-RAY IMAGING OF BIOLOGICAL CRYOSECTIONS

Peter Ingram, Ann LeFurgey, S. D. Davilla, J. R. Sommer,
L. J. Mandel, Melvyn Lieberman, and J. R. Herlong

Quantitative elemental imaging (mapping) from electron probe x-ray microanalysis is now practiced in a number of laboratories as a powerful tool for addressing problems in cell physiology.¹⁻⁴ Not only is a considerable amount of time saved in the acquisition of data, but an essential degree of overall perception is added.⁵ Furthermore, by judicious combination with supplementary static probes, reliable statistics should be obtainable⁶ from regions of cryosections with element content near the limit of detectability. Even the most awkward elements to deconvolute (such as calcium, which suffers from peak overlap from a neighboring peak, potassium) can be quantitated.

In the present paper we describe improvements to the system outlined previously.⁷⁻¹⁰ We have now incorporated the acquisition and spectral processing functions into a workstation (Digital Equipment Corporation, VAXstation 2000) and the data storage, image display, processing, and retrieval of quantitative image information into a microcomputer (Macintosh II, Apple Computer). Figure 1 is a schematic arrangement of the new system, the details of which are given elsewhere.⁸

The workstation provides a major simplification in both operation and programming. It retains the multiprocess virtual memory qualities of the previous system, but is also equipped with a large 1024 × 870 bitmapped virtual screen and a virtual keyboard by which one can have several windows simultaneously open on the physical display screen with each window mapped to a separate process. In addition, processes can create their own windows for graphics or text display. This feature eliminates the need for ancillary external graphics terminals for plotting acquired spectra. Since the virtual display is an integral component of the workstation, plotting speed is increased

manyfold. Realtime display of several stages in processing spectra (such as plots of the raw spectra and the filtered spectra) can be shown, as well as plots of spectral peak values vs livetime or other cumulative graphic information.

As with the previous programming structure of interprocess data sharing (a global section), this system uses several small simple programs that handle specific tasks, rather than one large program that handles both control of data acquisition and display of acquisition results. For example, a program that handles plotting the current raw spectrum only needs to know that there is a current or new spectrum to plot and how to plot it. Details of acquiring the spectrum are left to another program (the acquisition program, ACQ). The acquired spectrum is available from the shared data areas, as is information about its status.

The multiprocess operating system transparently handles the distribution of CPU time among the current processes. The current acquisition and spectral processing system consists of several programs that all run simultaneously as independent processes. There are two required processes, the acquisition process (ACQ) and the controlling process (DUKMLS). The controlling process incorporates a pulldown menu command structure to simplify operation further and to reduce operator error, and is used to set up the acquisition parameters (probe mode, image mode, map size, data file name, reference set, etc.) as well as to start or stop the actual acquisition. Numerical results and acquisition status are displayed by the controlling process. The acquisition process handles the details of directing the x-ray analyzer in spectrum acquisition or beam positioning, and filtering and fitting the current spectrum by use of a multiple least-squares routine against a set of precollected reference spectra.¹¹⁻¹³ The acquisition parameters and results are available to the other processes through a shared data area (VAX/VMS global sections) and the processes themselves are controlled by the setting or clearing of programmable global event flags.⁹ The other support processes are used for the realtime display of the raw spectra, filtered spectra, video line profiles, or a cumulative plot of peak vs livetime to monitor mass loss (gain) or image shift.

Cost considerations and ease of use were persuasive factors in placing image display and manipulation on another microcomputer (Macintosh II) rather than on the workstation. The microcomputer is equipped with the standard gray scale or color monitor (640 × 480

P. Ingram is with Research Triangle Institute, Research Triangle Park, NC 27709; A. LeFurgey, S. D. Davilla, L. J. Mandel, M. Lieberman, and J. R. Herlong are with the Department of Physiology, School of Medicine, Duke University, Durham, NC 27710; and J. R. Sommer is with the Departments of Pathology, Duke University and VA Medical Centers, Durham, NC 27710. This work was supported by NIH grants HL-07101, HL17670, HL27105, DK-37794, DK-26817, and HL-12486, and the VA Research Service. The authors would like to thank Drs. A. P. Somlyo and H. Shuman for generously supplying them with the original multiple-least-squares program, and Mr. Larry Hawkey and Ms. Teresa High for expert technical assistance in specimen preparation and photography.

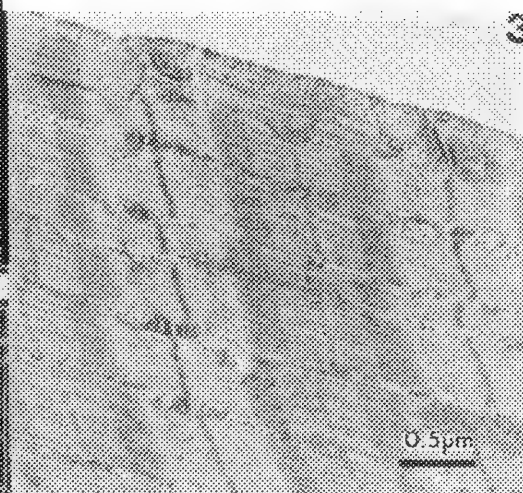
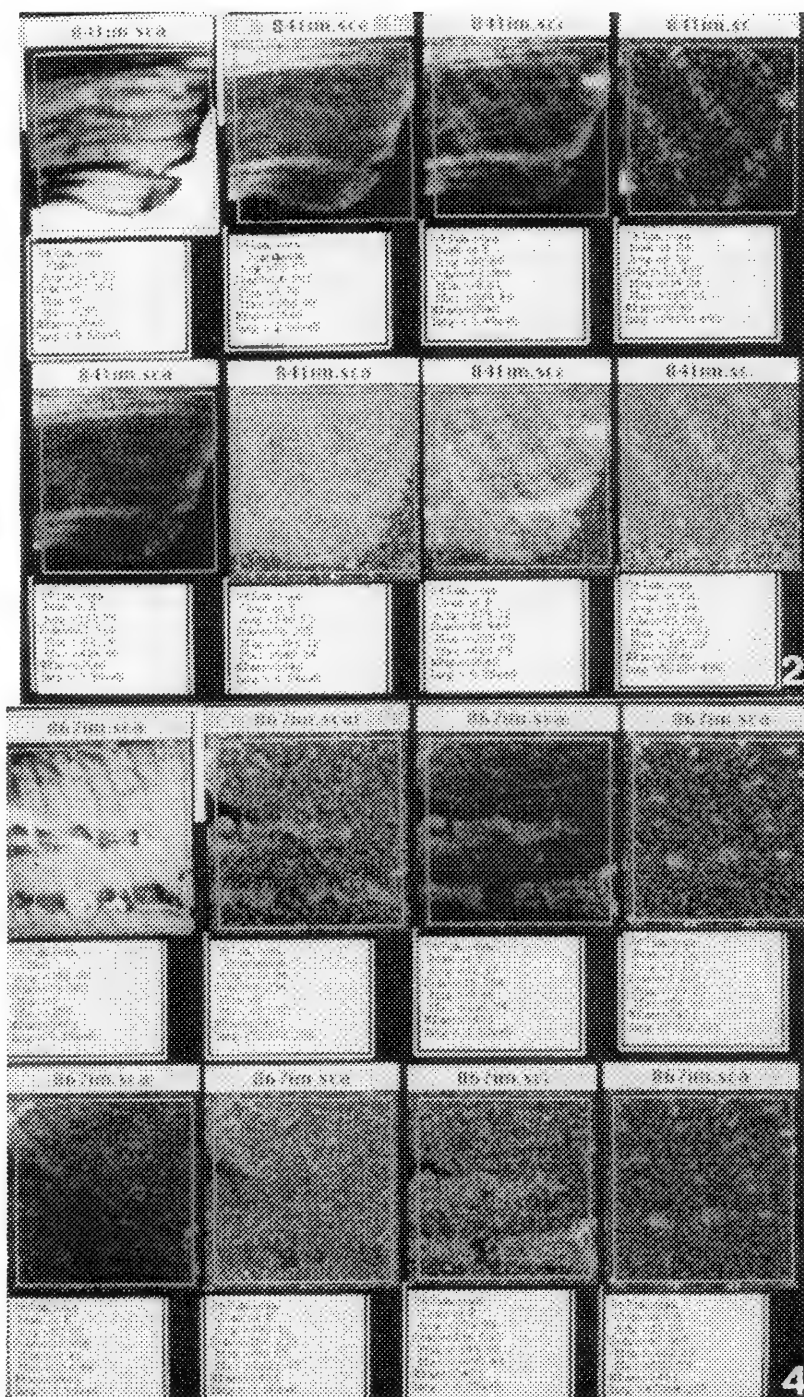


FIG. 2.--Quantitative 64 × 64 pixel x-ray maps from quick-frozen, freeze-dried cryosection of single intact skeletal muscle fiber. (Magnification: 4500×.)

FIG. 3.--TEM of freeze-substituted, quick-frozen single intact skeletal muscle fiber. Region immediately adjacent to that in Fig. 2. Note absence of cryoartifacts. (Magnification: 20 000×.)

FIG. 4.--Quantitative x-ray maps from quick-frozen, freeze-dried cryosection of single intact skeletal muscle fiber. (Magnification: 4500×.)

ultrastructure upon rapid freezing is well known.¹ However, the elemental images, especially for calcium in the junctional sarcoplasmic reticulum (JSR) (storage sites) and phosphorus in the banding pattern, dramatically reveal the quality of chemical and structural preservation. Such sections in fact are better for quantitation since there is less ice crystal damage. Were it not for the elemental imaging capability, they would ordinarily be ignored because one would not know where to probe. This can be considered a true form of microchemical microscopy at the ultrastructural

level.

A second point is the unambiguous demonstration that the Hall continuum normalization procedure¹¹ is clearly effective in thin (~100nm) cryosections. Several horizontal regions of contrast in the section seen in the STEM and continuum images are revealed as mass thickness effects in the P and K peak maps and are totally eliminated (normalized) in the respective concentration maps. A partial band of P remains, very likely due to the presence of mitochondria, which are seen better in the conventional TEM of the same

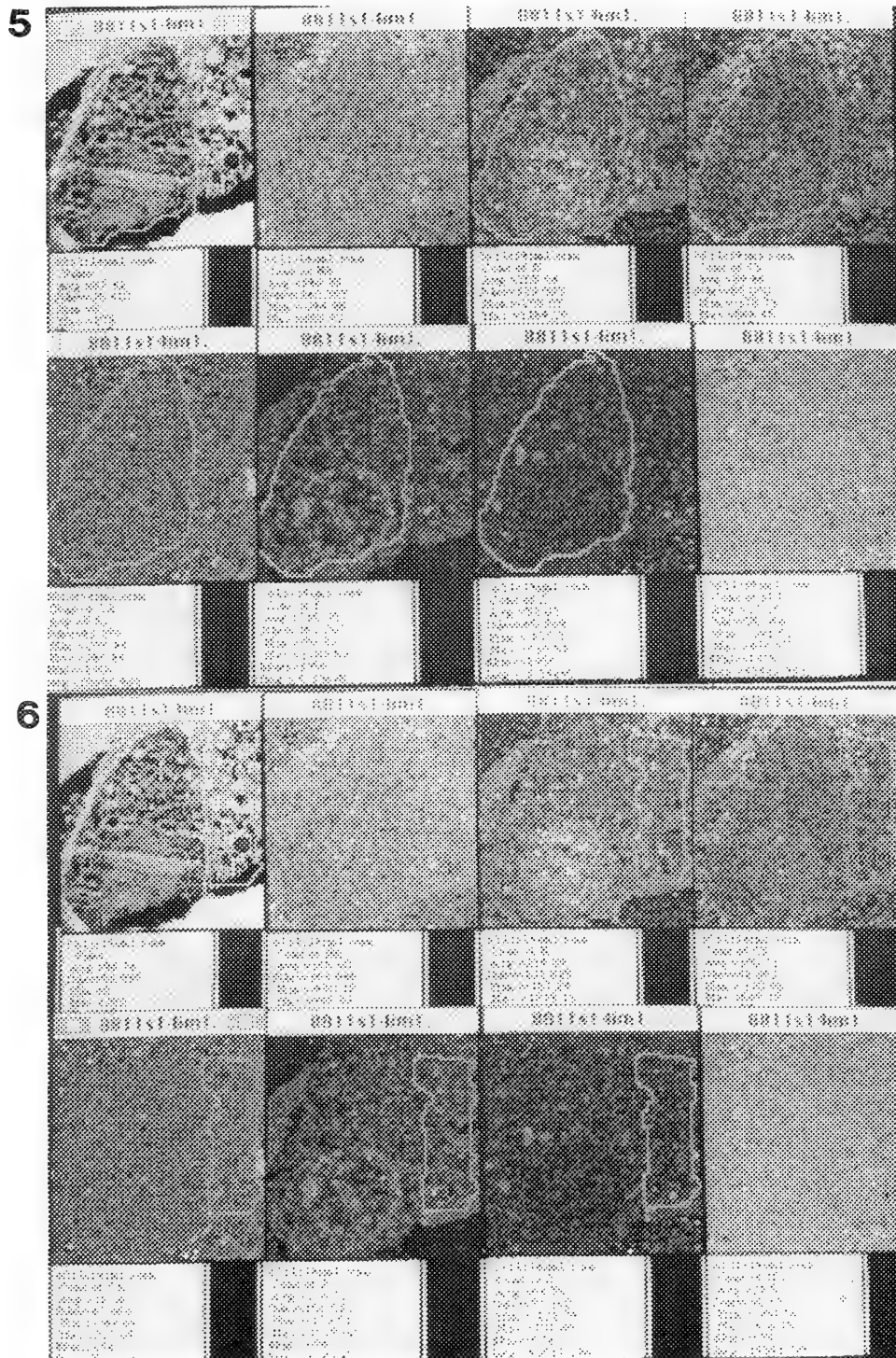


FIG. 5.--Quantitative x-ray maps from quick-frozen, freeze-dried cryosection of rabbit kidney proximal tubule. Outlined area is of normal morphology and shows expected cell element content. (Magnification: 2800 \times .)

FIG. 6.--Quantitative x-ray maps from quick-frozen, freeze-dried cryosection of the same rabbit kidney proximal tubule as in Fig. 5. Outlined area is of altered morphology and shows different element concentrations.

section (Fig. 3).

The obvious converse effect of absence of ultrastructural detail in STEM is that the appearance of good contrast does not necessarily indicate the presence of locally high elemental concentrations. Figure 4 is a similarly prepared intact single skeletal muscle fiber¹⁴

which shows considerable ultrastructural detail. However, not every dense morphological detail contains significant amounts of elements, as is clear from the individual maps.

The heterogeneity in element content that can be found among cells from the same population is illustrated in Figs. 5 and 6. The

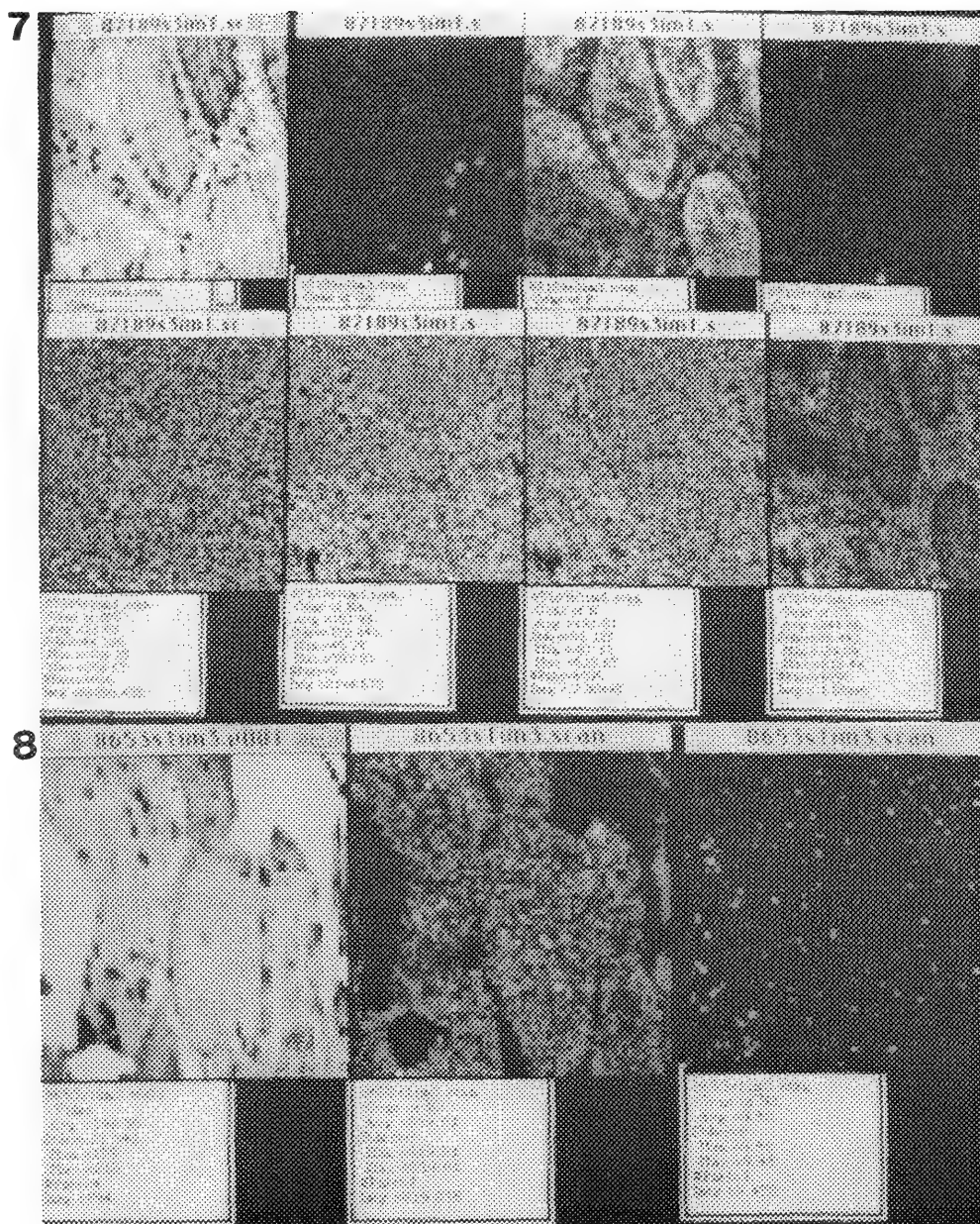


FIG. 7.--(Quantitative x-ray maps from quick-frozen, freeze-dried cryosection of human nasal epithelium. (Magnification: 3700 \times .)

FIG. 8.--Quantitative x-ray maps from quick-frozen, freeze-dried cryosection of cultured embryonic chick heart cells. (Magnification: 5000 \times .)

quick-frozen, cryosectioned kidney proximal tubule cell¹⁵ circled in Fig. 5 has normal morphology and, as enumerated in the written text below each element map, a K:Na ratio of approximately 2:1 and an overall cell calcium content of 5.5 mmol/kg dry weight. An adjacent cell, circled in Fig. 6, in which there is increased vacuolization and swelling of the mitochondria, has a K:Na ratio of approximately 1.3:1 with total cell calcium doubled (11.2 mmol/kg dry weight) in comparison. This type of mapping makes calculation of total cell element content obtainable simultaneously with calculation of individual organelle content. For correlation with other techniques, such as atomic absorption spectroscopy, which measure

average total cell content from a bulk sample, it is essential to obtain by EPXMA values for total cell contents from as many cells as possible.

The general usefulness of quantitative concentration mapping is illustrated in Fig. 7. In this field of approximately 5 to 6 epithelial cells from the human nasal passage (quick-frozen and cryosectioned as above), only one cell contains localizations of calcium in organelles. Although x-ray dot mapping could provide similar information, in less clear-cut cases this type of imaging also could be misleading since quantitation becomes almost impossible. As Fiori and colleagues have pointed out, the effects of mass-thickness

cannot be corrected in dot maps.⁶ However, if only static probes from individual cells or regions of cells are taken, the investigator obtains a statistically smaller sample and may not recognize an elemental compartmentation that occurs in only a small fraction of the cell population. In other words, static probing not only requires a tremendous amount of time to obtain comparable sampling statistics, thus placing an unnecessary burden on the operator's patience and productivity, but the investigator may actually miss "trends" if changes in element distribution occur as a result of an experimental manipulation. This is what is inherent in the term "essential degree of overall perception": vital nonuniform events could easily be overlooked. If subtle changes are detected, or if a particular region is suspected of having a statistically unacceptable level of element, these same regions can subsequently be probed with a static beam or small area of a rastered beam of a size that can be gauged optimally from the results of the quantitative mapping.

Generally, elemental maps are also scaled relative to each other within the same image, so that one can visually compare ratios of elements such as sodium and potassium. (An image can also be made from this ratio.) In every eukaryotic cell type the K:Na ratio is an indication of cell viability: heart cells cryopreserved¹⁶ during basal conditions display a K:Na ratio of 10-15 to 1; those subjected to reversal of the transmembrane sodium gradient for as little as 4 min are identified by a change in this ratio of an order of magnitude (Fig. 8). Images also immediately make evident that the change in Na content occurs in all compartments--mitochondria, cytoplasm, and nucleus.

There are several refinements which have been or can readily be incorporated into the quantitative imaging system, but which will be reported elsewhere.⁸ Another is the ability to scale individual images to a predetermined concentration level within the 8-bit gray scale, which will enable direct visual comparison between small changes in concentration, and which of course can then be color-coded. A similar procedure is the application of the standard deviations of measurements to the absolute values at each pixel. Thus concentrations with more than two standard deviations, for example, could be eliminated from the image,¹⁷ or a color-coded "statistical error" map formed. This feature is particularly important with regard to evaluating images consisting primarily of statistical noise when they originate from regions of very low counts. Standard image-processing functions¹⁸ in both spatial and frequency domains are clearly appropriate. The ability to store individual spectra (rather than the processed data) at each pixel would be an advantage since image data could then be updated for example if one wanted to fit to alternative or refined reference spectra. One only needs additional memory, which is fortunately becoming fairly inexpensive.

Finally, since image acquisition can take between nearly 2 h and up to possibly tens of hours for high-resolution maps, the specimen will inevitably suffer some drift in the microscope. Such drift is corrected either during acquisition by feedback to the scan coils (tracking)¹⁷ or post facto by an image correlation program.^{7,8}

References

1. A. LeFurgey et al., "Frontiers in electron probe x ray microanalysis: Application to cell physiology," *Ultramicroscopy* 24: 185-219, 1988.
2. A. P. Somlyo, "Compositional mapping in biology: X rays and electrons," *J. Ultrastructure Res.* 88: 135-142, 1984.
3. D. Johnson et al., "High spatial resolution spectroscopy in the elemental microanalysis and imaging of biological systems," *Ultramicroscopy* 24: 221-236, 1988.
4. A. J. Saubermann et al., "Quantitative digital x ray imaging using frozen hydrated and frozen dried tissue sections," *J. Microscopy* 146: 169-182, 1987.
5. T. L. Hayes, "Biophysical aspects of scanning electron microscopy," *SEM/1980 I*, 1-10.
6. C. E. Fiori et al., "Quantitative x ray mapping of biological cryosections," *Ultramicroscopy* 24: 237-250, 1988.
7. P. Ingram et al., "Real-time quantitative elemental analysis and imaging in cells," *Analytical Electron Microscopy--1987*, 179-183.
8. S. D. Davilla et al., "Real time quantitative elemental analysis and mapping: Microchemical imaging in cell physiology," *Scanning* (submitted).
9. S. D. Davilla et al., "Simple multi-process data sharing with the VAX/VMS operation system," *J. Electron Microsc. Tech.* 8: 227-228, 1988.
10. S. D. Davilla et al., "Real time graphic display of mass variation or elemental concentration during electron beam microanalysis using a general purpose computer," *J. Microscopy* 149:153-157, 1988.
11. T. Hall, "Biological x-ray microanalysis," *J. Microscopy* 117: 145-163, 1979.
12. H. Shuman et al., "Quantitative electron probe microanalysis of biological thin sections: Methods and validity," *Ultramicroscopy* 1: 317-339, 1976.
13. T. Kitazawa et al., "Quantitative electron probe analysis: Problems and solutions," *Ultramicroscopy* 11: 251-262, 1983.
14. J. R. Sommer et al., "Quantitative x-ray elemental imaging in stimulated single intact skeletal muscle fibers: The fate of calcium after ryanodine," *Proc. 45th Ann. Mtg. EMSA*, 1988 (in press).
15. A. LeFurgey et al., "Heterogeneity of calcium compartmentation: Electron probe analysis of renal tubules," *J. Membrane Biology* 94: 191-196, 1986.
16. A. LeFurgey et al., "Na-Ca compartmentation in cultured heart cells," *Microbeam Analysis--1987*, 267-268.

17. P. J. Statham, "Quantitative digital mapping with drift compensation," *Analytical Electron Microscopy--1987*, 187-190.
18. D. E. Newbury et al., *Advances in Scanning Electron Microscopy and X-Ray Microanalysis*, New York: Plenum Press, 1986, 181-242.

CAPACITATION AND DECAPACITATION: IONICALLY DISTINCT PHYSIOLOGICAL STATES OF THE MAMMALIAN SPERM

K. N. Colonna and G. Oliphant

Despite a high level of morphological sophistication, ejaculated mammalian spermatozoa cannot immediately fertilize an ovum. Prior to the acquisition of fertilizing ability, spermatozoa must undergo a series of maturational events within the female reproductive tract. These events are separable into two distinct phases, capacitation and the acrosome reaction. Ejaculated (noncapacitated) spermatozoa undergo capacitation, a reversible process¹ that is associated with the removal or alteration of macromolecular sperm surface components and is an absolute prerequisite for the subsequent acrosome reaction.² The acrosome reaction, the release of hydrolytic enzymes through fenestrated membranes, permits penetration of the acellular zona pellucida by the sperm and subsequent fusion of the sperm-egg plasma membranes.^{3,4}

A glycoprotein, isolated from whole seminal plasma, decapacitates capacitated sperm and renders it incapable of undergoing the acrosome reaction. The isolated glycoprotein has been named the Acrosomal Stabilizing Factor (ASF).⁵ The mechanisms involved in capacitation and decapacitation are poorly understood, but it is well established that the acrosome reaction is clearly linked to a complex and coordinated series of ionic fluxes.^{3,6,7} To gain a better understanding of events prior to the acrosome reaction, energy-dispersive x-ray microanalysis (EDS) was used to analyze changes in the subcellular distributions of Na, K, Ca, and Mg in ejaculated (noncapacitated), capacitated, and decapacitated spermatozoa. The data obtained provide direct evidence for changes in the subcellular elemental distribution and support ion-specific alterations in membrane permeability occurring concomitant with capacitation and decapacitation.

Experimental Protocol

Cell Preparation. New Zealand white rabbits

K. N. Colonna is at the Department of Anatomy and Cell Biology, University of Virginia School of Medicine, Charlottesville, VA 22908. The authors express their appreciation to Drs. C. E. Fiori, Richard Leapman, Richard Ornberg, and Carol Swyt of the National Institutes of Health, both for the extensive use of their equipment and for invaluable conversations during the course of the research. The authors also thank Dr. Ted Thomas of the Department of Obstetrics and Gynecology and Dr. Barry Hinton of the Department of Anatomy and Cell Biology, University of Virginia School of Medicine, for critically reviewing the manuscript. This research was supported by NIH grant HD21086.

were used through the study. Ejaculated or noncapacitated sperm were obtained via semen collection. Semen was collected from mature bucks of proven fertility by use of an artificial vagina and a teaser doe.⁸ In vivo capacitated sperm were acquired by surgically flushing the uterine horns of mature estrous does with 4 ml warm HEPES buffered medium (50 mM HEPES, 80 mM NaCl, 4.78 mM KCl, 1.71 mM CaCl₂, 1.19 mM KH₂PO₄ (nonbasic), 1.19 mM MgSO₄ · 7 H₂O, 1.2 mM Na pyruvate, 0.05 g gentamycin sulfate, 11.1 mM glucose, 24.76 mM NaHCO₃, 2.0 ml 60% Na lactate syrup, and 4 mg/ml bovine serum albumin, 285 mOsm., pH 7.4) 6 h post-coitus. Decapacitated sperm were obtained after incubating in vivo capacitated sperm in a phosphate-buffered saline solution (0.15 M NaCl, 1 mM sodium phosphate, 285 mOsm, pH 7.4) containing affinity purified and dialyzed ASF⁹ at a final concentration of 300-330 µg/ml, a level previously shown to promote decapacitation in a bioassay.⁵ The protein concentration was determined spectrophotometrically from an established extinction coefficient.¹⁰ Buffers used in the decapacitation medium and to recover uterine capacitated sperm had no effect on the subcellular elemental distribution observed in capacitated and decapacitated spermatozoa (data not shown).

One microliter volumes of the ejaculated, capacitated, and ASF-decapacitated spermatozoa were immediately loaded onto the freezing head of a Med-Vac cryopress¹¹ and rapidly frozen against a liquid helium cooled silver block. Ultrathin cryosections, 60-90 nm thick, were then prepared by use of a Reichert Model E/FC-4 cryoultramicrotome and a diamond cryoknife. Cryosectioning temperatures were maintained between -135 and -145 C. All cryosections were collected on carbon- and Formvar-coated folding grids and transferred in the frozen hydrated state to the electron microscope. The cryosections were internally freeze-dried in the microscope vacuum.

System Analysis. The cryosections were examined and analyzed in a Hitachi H-700H analytical electron microscope equipped with a scanning-transmission attachment and a 30mm² side-looking Tracor Northern Si(Li) energy-dispersive spectrometer (EDS). EDS spectra were collected from specific regions of the acrosome and nucleus for 100 s at a 1 nA probe current and 100 kV. The EDS pulses were routed either to a Tracor Northern 5500 x-ray analysis system or to a Kevex 7000 computer-based multichannel analyzer. EDS spectra were processed for quantification on a DEC PDP 11/60 host computer by the multiple-least-squares fitting routine and analysis programs developed and described by Shuman et al.¹² The spectral fitting routines were calibrated with standard

specimens. The spectral region of 1.37-1.61 keV was designated as the background or continuum region.

To eliminate errors in both the quantitation of calcium, as caused by the overlap of the $\text{CaK}\alpha$ and the $\text{KK}\beta$ x-ray peaks, and in the quantitation of sodium, as caused by the curvature existing in the local background, the method developed by Kitazawa et al.¹³ was employed. Finally, although each cryosection was maintained in a Gatan 626 low-temperature sample holder and analyzed at -100 C, beam-induced radiation damage and mass loss were carefully monitored.

EDS spectra generated from 50-60 acrosome-intact spermatozoa per experiment ($n = 7$) were statistically analyzed by the Statistical Analysis System (SAS) analysis of variance (ANOVA). The null hypothesis was tested by the F-statistic and interpreted by Duncan's Multiple Range Test. Only significance levels less than or equal to 0.01 are reported.

Results and Discussion

EDS analysis of the acrosomal region in ejaculated, capacitated, and ASF-decapacitated spermatozoa demonstrated dramatic differences in the dry-weight concentrations of Na, K, Ca, and Mg. The acrosomal region of ejaculated sperm contained Na levels of 180 ± 12 mM/kg (dry weight concentrations are expressed as the mean \pm standard error of the mean), K levels of 456 ± 22 mM/kg, Ca levels of 2.3 ± 0.5 mM/kg, and Mg levels of 1.4 ± 0.4 mM/kg. Capacitated sperm demonstrated acrosomal Na levels of 838 ± 41 mM/kg, K levels of 230 ± 14 mM/kg, Ca levels of 9.4 ± 1.2 mM/kg, and Mg levels of 0.3 ± 0.1 mM/kg. Associated therefore with capacitation is a substantial increase in acrosomal Na and Ca and a decrease in K and Mg.

EDS analysis of the same subcellular regions in ASF-decapacitated sperm demonstrated an intracellular elemental profile different from that observed in capacitated sperm. The acrosomal region of ASF-decapacitated spermatozoa contained Na levels of 140 ± 14 mM/kg, K levels of 330 ± 18 mM/kg, Ca levels of 2.0 ± 0.5 mM/kg, and Mg levels of 28 ± 2.0 mM/kg. Thus, concomitant with decapacitation is a significant decrease in acrosomal Na and Ca and an increase in K and Mg.

EDS analysis of the sperm nuclei in the three groups revealed virtually no statistically significant elemental differences ($p < 0.01$). Nuclei of the ejaculated, capacitated, and decapacitated sperm contained Na levels of 20 ± 3.2 , 17 ± 2.4 , and 14 ± 2.8 mM/kg; K levels of 116 ± 8.5 , 96 ± 6.1 , and 104 ± 7.9 mM/kg; Ca levels of 1.2 ± 0.3 , 1.1 ± 0.2 , and 0.52 ± 0.06 mM/kg, and Mg levels of $9.2 \pm 8.7 \pm 2.8$, and 10 ± 3.5 mM/kg, respectively. The lack of statistically significant elemental differences between the nuclei of the three treatment groups allows an internal control against changes observed in the acrosome.

Although the absolute quantitation of free or diffusible ions by EDS analysis is not possible, the changes observed in total element (free and

bound) are indeed reflective of transport phenomena across compartmental membranes.¹⁴ Concomitant with capacitation were substantial increases in acrosomal Na and Ca, and decreases in K and Mg. The net movement of the monovalent cations Na^+ and K^+ may be explained to a large extent by an ATPase-mediated Na^+/K^+ exchange pump such as that located on the outer acrosomal membrane of the sperm head in several mammalian species.¹⁵ Activation of the Na^+/K^+ ATPase would facilitate increased acrosomal levels of K and decreased levels of Na. This ATPase, like the Na^+/K^+ ATPase of the erythrocyte plasma membrane,¹⁶ is activated by Mg and inhibited by both Ca^{17} and elevations in cAMP.¹⁸ Inhibition of the ATPase would allow the monovalent cations to move down their electrochemical gradients and result in an accumulation of intracellular Na and a depletion of K. EDS analysis of the acrosomal region in capacitated sperm, revealing substantial increases in Na and Ca and decreases in K and Mg, is supportive of an inhibition of the Na^+/K^+ ATPase via increased levels of Ca.

Levels of Ca in the acrosome of capacitated spermatozoa were four times greater than levels found in the same subcellular region of ejaculated spermatozoa. This finding is of particular interest as increased levels of intracellular Ca have been associated with the state of development following capacitation, the acrosome reaction.¹⁵ Ca serves to activate membrane phospholipases, convert proacrosin to enzymatically active acrosin, and promote membrane fusion, each a necessary prerequisite for completion of the acrosome reaction.¹⁵ Although the functional relationship between the presence of calcium and the induction of the acrosome reaction is well established, mechanisms for calcium accumulation in the acrosome are ill defined. However, there is cytochemical evidence that a Mg^{2+} -dependent Ca^{2+} ATPase exists on the rabbit and guinea pig acrosomal membrane.¹⁹ This ATPase could play a role in mediating the movement of the divalent cation across the acrosomal membrane and thus contribute to the observed accumulation of acrosomal Ca.

The subcellular elemental distribution observed in the acrosomal region of capacitated spermatozoa, increased levels of Na and Ca, and decreased levels of K and Mg was reversed upon ASF-decapacitation, which supports the view that capacitation is indeed a reversible process.¹ Concomitant with ASF-decapacitation were substantial decreases in acrosomal Na and Ca, and increases in K and Mg. The exact mechanisms involved in the decapacitation of spermatozoa by ASF is not clear. It is speculated that the decapacitating glycoprotein exerts its effects at the level of the plasma membrane. Interaction of ASF with the sperm surface could alter or influence plasma membrane-associated ion transport mechanisms. Such alterations could ultimately lead to changes in the elemental composition of the acrosome via indirect mechanisms. It appears as if interaction of the capacitated sperm with

the decapacitating factor ASF significantly alters the subcellular elemental composition of the maturing sperm, thereby preventing the cell from establishing the intracellular ionic triggers necessary for the activation of the final stage of sperm maturation, the acrosome reaction.

Conclusion

The critical role that ion transport exerts in the control of mammalian cell metabolism and proliferation is becoming increasingly evident. The information obtained with EDS clearly demonstrates that changes in the subcellular elemental distribution and plasma membrane permeability are specific to both particular ions and particular stages of sperm maturation. The information obtained with EDS has provided further characterization of the dynamic intracellular ionic milieu and is thus another step in the definition of the developmental changes occurring in the mammalian sperm.

References

1. M. C. Chang and R. H. F. Hunter, "Capacitation of mammalian sperm: Biological and experimental aspects," in R. O. Greep, Ed., *Handbook of Physiology*, Section 7, Vol. 5, Washington, D.C.: Amer. Physiol. Society, 1977, 339-351.
2. G. Oliphant, "Removal of sperm-bound seminal plasma components as a prerequisite to induction of the rabbit acrosome reaction," *Fertil. Steril.* 27: 1, 1975.
3. R. Yanagimachi, "Mechanisms of fertilization in mammals," in L. Mastroianni and J. D. Biggels, Eds., *Fertilization and Embryonic Development in Vitro*, New York: Plenum Press, 1981, 81-182.
4. P. Talbot, "Events leading to fertilization in mammals," in R. F. Harrison and J. B. W. Thompson, Eds., *Fertility and Sterility: Proceedings of the 11th World Congress on Fertilization and Sterilization*, Boston: MTP Press, 1984, 121-131.
5. L. A. Eng and G. Oliphant, "Rabbit sperm reversible decapacitation by membrane stabilization with a highly purified glycoprotein from seminal plasma," *Biol. Reprod.* 19: 1083, 1978.
6. R. Yanagimachi and N. Usui, "Calcium dependence of the acrosome reaction and activation of guinea pig spermatozoa," *Exp. Cell. Res.* 89: 161, 1974.
7. P. Talbot, R. G. Summers, B. L. Hylander, E. M. Keough, and L. E. Franklin, "The role of calcium in the acrosome reaction: An analysis using ionophore A23187," *J. Exp. Zool.* 198: 383, 1976.
8. B. G. Brackett and G. Oliphant, "Capacitation of rabbit spermatozoa *in vitro*," *Biol. Reprod.* 12: 260, 1975.
9. A. B. Reynolds and G. Oliphant, "Production and characterization of monoclonal antibodies to the sperm acrosome stabilizing factor (ASF): Utilization for purification and molecular analysis of ASF," *Biol. Reprod.* 30: 775, 1984.
10. T. S. Thomas, W. L. Wilson, A. B. Reynolds, and G. Oliphant, "Chemical and physical characterization of rabbit sperm acrosome stabilizing factor," *ibid.*, 33: 691, 1986.
11. J. E. Heuser, T. S. Reese, M. J. Dennis, Y. Jan, and L. Evans, "Synaptic vesicle exocytosis captured by quick freezing and correlated with quantal transmitter release," *J. Cell Biol.* 81: 275, 1979.
12. H. Shuman, A. V. Somlyo, and A. P. Somlyo, "Quantitative electron probe microanalysis of biological thin sections: Methods and validity," *Ultramicroscopy* 1: 317, 1976.
13. T. Kitazawa, H. Shuman, and A. P. Somlyo, "Quantitative electron-probe analysis: Problems and solutions," *Ultramicroscopy* 11: 251, 1983.
14. R. L. Ornberg, G. A. S. Kuipers, and R. D. Leapman, "Electron probe microanalysis of the subcellular compartments of bovine adrenal chromaffin cells: Comparison of chromaffin granules *in situ* and *in vitro*," (in press).
15. R. Yanagimachi, "Mammalian fertilization," in E. Knobil and J. Neill, Eds., *The Physiology of Reproduction*, New York: Raven Press, 1988, 135-185.
16. R. M. Dowben, "Composition and structure of membranes," in R. M. Dowben, Ed., *Biological Membranes*, Boston: Little, Brown & Co., 1969, 1-38.
17. N. Usui and R. Yanagimachi, "Cytochemical localization of membrane-bound Mg^{2+} -dependent ATPase activity in guinea pig sperm head before and during the acrosome reaction," *Gamete Res.* 13: 271, 1986.
18. R. J. Mersny and S. Meizel, "Initial evidence for the modification of hamster sperm Na^+ , K^+ -ATPase activity by cyclic nucleotide mediated processes," *Biochem. Biophys. Res. Commun.*, 112: 132, 1983.
19. M. J. Gordan and R. J. Barnett, "Fine structural cytochemical localizations of phosphatase activities of rat and guinea pig," *Exp. Cell. Res.*, 48: 395, 1967.

QUANTITATIVE COMPARISON OF LOW-TEMPERATURE PREPARATION METHODS FOR THE X-RAY MICROANALYSIS OF BIOLOGICAL BULK SAMPLES

A. T. Marshall and R. J. Condron

It is generally recognized that for biological x-ray microanalysis the frozen-hydrated sample preserves with greatest fidelity the distribution of elements that prevails in living cells and tissues. Frozen-hydrated samples present the analyst with numerous technical difficulties and on occasions it may be preferable, or necessary, to use other methods of sample preparation. We show in the present study that although freeze-dried embedded and freeze-substituted embedded bulk samples lack the absolute element concentrations found in frozen-hydrated bulk samples, they do retain elemental differences in control and experimental tissues, produced in this case by pathophysiological manipulation. Previous comparisons¹⁻⁵ of these preparation techniques have been largely qualitative in nature.

Methods and Procedures

The preparation and analysis of frozen-hydrated bulk samples has been reviewed elsewhere.⁶ Briefly, samples were frozen by being pushed into solid nitrogen, fractured at -180 C, coated with 20 nm Be, and analyzed at -172 C (15 kV, beam current 0.2 nA). Intracellular water was calculated from O concentrations.

Small (1mm³) samples were frozen in liquid propane and processed by freeze-drying or freeze-substitution. In both cases the samples were embedded in Cl-free Spurr's resin, previously dried over a Linde molecular sieve. Freeze-drying was carried out at -96 C for 10 days at 5×10^{-6} Torr and gradually brought to room temperature over 24 h. Freeze-substitution was carried out in anhydrous 20% acrolein in diethyl ether, containing a Linde molecular sieve, at -96 C for 30 days and raised to room temperature in 20 C steps over 5 days.

Embedded freeze-dried and freeze-substituted samples were polished on an ultramicrotome and the surfaces were coated with 20 nm Al. Analyses were carried out at -172 C and at 15 kV with a beam current of 0.25 nA.

In all cases images were processed with a Dindyma temporal filter to aid in structure recognition, and quantitation was carried out by referencing of specimen x-ray intensities to standard intensities (Biorad microprobe standards) and correcting for absorption and atomic number effects by means of the $\phi(\rho z)$ ionization function.

The tissue samples used for this investigation

were chicken kidneys from normal healthy chickens and chickens that had been infected with infectious bronchitis nephritis virus (IBV), which causes perturbations in the normal kidney physiology. Several cells in each of several proximal tubules within each kidney were analyzed.

Results

Analytical results are shown in Table 1. There are consistent significant differences in Na and Cl concentrations between normal and infected kidney tubule cells in each preparation method. However, there is a lack of agreement between methods with respect to absolute concentration values. Some loss of K, Mg, Ca, and P in the resin-embedded samples is apparent.

Discussion and Conclusion

Significant element retention can be obtained by freeze-drying and freeze-substitution followed by resin embedding. In the experiments described here some elemental loss did occur. However, it did not disturb the differences in elemental distribution between normal and infected cells in the kidney tubules. Comparison of freeze-dried and frozen-hydrated samples suggests that most element loss is a consequence of infiltration and embedding in epoxy resin. It is possible that this loss may be avoidable by use of methacrylate resins. The methods used in the present study would seem to be adequate for comparing differences in cellular composition arising as a consequence of physiological intervention.

References

1. O. G. Forrest and A. T. Marshall, "Comparative x-ray microanalysis of frozen-hydrated and freeze-substituted specimens," *Proc. 6th European Congress Electron Microsc.* 2: 218, 1976.
2. A. T. Marshall, "Freeze-substitution as a preparation technique for biological x-ray microanalysis," *SEM/1980* II, 395.
3. J. A. Chandler, "X-ray microanalysis of biological tissues--an examination of comparative specimen preparation techniques using prosthetic tissue as a model," *SEM/1985* II, 731.
4. R. Meyer et al., "The influence of different cryopreparations on the distribution of ions in bullfrog myocard cells," *SEM/1985* I, 419.
5. R. Wroblewski et al., "Freeze-drying and related preparation techniques for biological microprobe analysis," *SEM/1985* I, 447.

The authors are at the Department of Zoology, La Trobe University, Bundoora (Melbourne), Victoria 3083, Australia. This work was carried out with the aid of a grant from the Australian Research Grants Scheme.

6. A. T. Marshall, "Progress in quantitative x-ray microanalysis of frozen-hydrated bulk biological samples," *J. Electron Microsc. Techniques* (in press).

TABLE 1.--Comparison of specimen preparation techniques (FH, frozen-hydrated; FD, frozen-dried; FS, freeze-substituted).

	Na	K	Cl	Mg	Ca	P	S	N	n	s
	m mol l ⁻¹			m mol kg ⁻¹						
FH										
Normal	43 ₊₂	125 ₊₄	41 ₊₁	27 ₊₁	12	109 ₊₂	72 ₊₁	2	21	105
Infected	36 ₊₃	114 ₊₂	30 ₊₂	26 ₊₁	12	107 ₊₂	70 ₊₁	2	20	100
FD										
Normal	71 ₊₄	82 ₊₇	70 ₊₄	18 ₊₁	7 ₊₁	67 ₊₂	75 ₊₂	1	9	126
Infected	46 ₊₂	84 ₊₅	55 ₊₃	16 ₊₁	6	68 ₊₃	74 ₊₂	1	8	112
FS										
Normal	55 ₊₂	60 ₊₅	28 ₊₂	15 ₊₁	7	56 ₊₂	60 ₊₁	1	7	98
Infected	44 ₊₂	67 ₊₉	23 ₊₁	13 ₊₁	7	58 ₊₄	60 ₊₃	1	7	98
Pvalues										
Paired t-										
test	<0.10	ns	<0.05	ns	ns	ns	ns			
Two way										
ANOVA	<0.01	ns	<0.01	ns	ns	ns	ns			
Norm.vs.Inf.										
Two way										
ANOVA	<0.01	<0.01	<0.01	<0.01	<0.01	<0.01	<0.01			
FHvsFDvsFS										

Mean \pm SE. N = number of animals, n = number of proximal kidney tubules, s = number of analysis sites.

EFFECTS OF TISSUE PREPARATION ON DISTRIBUTION OF CN^- AND O^- IN SCANNING ION MICROPROBE ANALYSIS

M. S. Burns, J. Chabala, P. Hallegot, and R. Levi-Setti

In order to interpret elemental microlocalization studies in secondary ion mass spectrometry (SIMS), we need to understand ion emission from various tissue areas. For this purpose we have processed rat retinal tissue using five different preparative methods, and have examined (1) the CN^- emission to see whether it is an appropriate normalizing factor, and (2) the O^- emission to look for potential sites of ionization enhancement.

Experimental

Retina and choroidal tissue from pigmented Long-Evans rats was prepared by (1) freeze-drying,¹ (2) freeze-substitution in acetone alone,³ (3) freeze substitution in acetone and osmium,² (4) fixation in Karnovsky's containing potassium oxalate followed by postfixation with osmium containing potassium pyroantimonate,³ and (5) fixation in pyroantimonate mixed with formaldehyde.⁴ All tissues were embedded in Polybed 812 and ca 2 μm -thick sections were dry cut, mounted on boron-doped silicon wafers, and overcoated with ca 20 nm 99.999% Au.

The University of Chicago Hughes Research Laboratory scanning ion microprobe⁵ (SIM) was operated with a 20 pA, 40 keV Ga^+ primary ion beam focused to a 35 nm-diameter spot that was digitally rastered over a 60 \times 60 μm^2 area. Lateral resolution of ion images under these conditions is ca 0.2 μm . The ion images are stored directly in a digital image processor (Kontron IPS).

Results

The freeze-dried sample is used as the reference specimen, since this preparation has given quantitative data for elemental content in lens,⁶ and the specimen has never been exposed to solvents. The CN^- signal (Fig. 1a) is relatively even throughout the retina and more intensely emissive from the melanocyte regions of the choroid. The CN^- signal represents the presence of tissue that corresponds to the morphological appearance in the light microscope. The freeze-substituted specimens gave similar CN^- images. The CN^- image was not due to topology of the specimen (Fig. 1b), which is even throughout the retina region, but shows some topographic features in the choroid. The O^- image (Fig. 1c) is relatively nonemissive except for the melanin-containing areas of the choroid. A sodium image of this

region (Fig. 1d) is shown for reference.

The tissues fixed with aldehyde fixatives containing oxalate and/or pyroantimonate were qualitatively similar to each other. The CN^- image was emissive from the melanocytes of the choroid, and also from the outer nuclear layer; a distinction between the inner and outer segment of the photoreceptor cell was obvious (Fig. 2a). The CN^- was not due to topography (Fig. 2b), although some edge effects are seen in the CN^- and O^- image (Fig. 2c). These features probably represent initial surface roughness during specimen cutting. O^- emission is seen in the melanin-containing choroid. A Na^+ image of this region is shown in Fig. 2d for comparison.

Conclusions

The presence of oxygen in melanin-rich regions of the choroid may be responsible for the intense emission of Na, K, and Ca from these areas, although there may also be topographic enhancement of ion emission, as previously shown.⁷

As noted by Galle,⁸ CN^- images give an adequate representation of tissue morphology. However, the CN^- image varied considerably between the freeze-dried or substituted samples and the fixed specimens. It would be expected that loss of small molecules such as amino acids, which may contribute to the CN^- signal, could occur during aqueous fixation and dehydration procedures, but our preliminary results indicate that the average CN^- counts are the same in the rod outer segment layer with various preparative methods. However, the CN^- counts are doubled in the outer nuclear layer in the fixed specimens, as are the Na^+ counts, but not K^+ counts. It appears that some step in the fixation process changes the tissue to augment ionization of some but not all ions in specific areas. Experiments to define this alteration need to be done before CN^- can be used to normalize ion count rates for quantitative analysis.

References

1. M. S. Burns, D. M. File, K. T. Brown, and D. G. Flaming, "Localization of calcium and barium in toad retina by secondary ion mass spectrometry," *Brain Res.* 230: 173, 1981.
2. G. L. Fain and W. H. Schroeder, "Calcium content and calcium exchange in dark-adapted toad rods," *J. Physiol.* (London) 368: 641, 1985.
3. J. L. VanReempts, M. Borgers, S. R. DeNollin, T. C. Garrevoet, and W. A. Jacob, "Identification of calcium in the retina by the combined use of ultrastructural cytochemistry and laser microprobe mass analysis,"

The authors are at the University of Chicago, Enrico Fermi Institute, Chicago, IL 60637, except M. S. Burns, who is at the University of California, Davis, CA 95616. Supported by NSF Grant BBS 8610518 and NIH Grant EY05979.

FIG. 1.--Freeze-dried retina and choroid. (a) CN^- emission from choroid (CH), rod outer segments (ROS), rod inner segments (RIS), and outer nuclear layer (ONL). Regions are exactly the same in (b), (c), and (d). (b) Integrated secondary-ion image showing surface topography. (c) O^- image showing emission from melanin granules of choroid. (d) Na^+ image showing emission from melanin granules and RIS, and less from other structures. Bar = 10 μm .

1

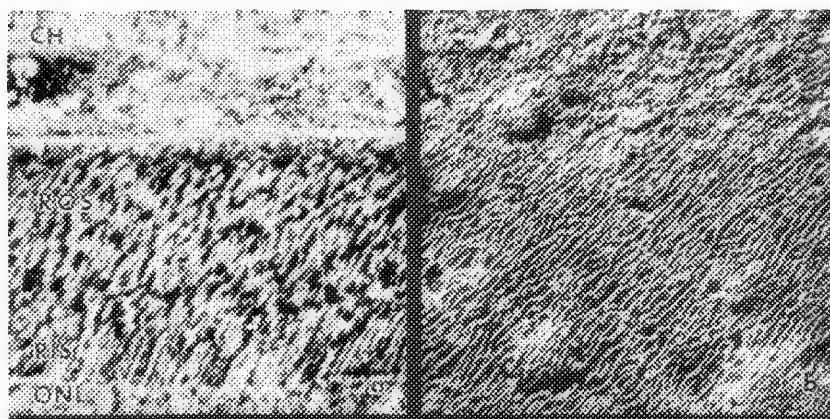
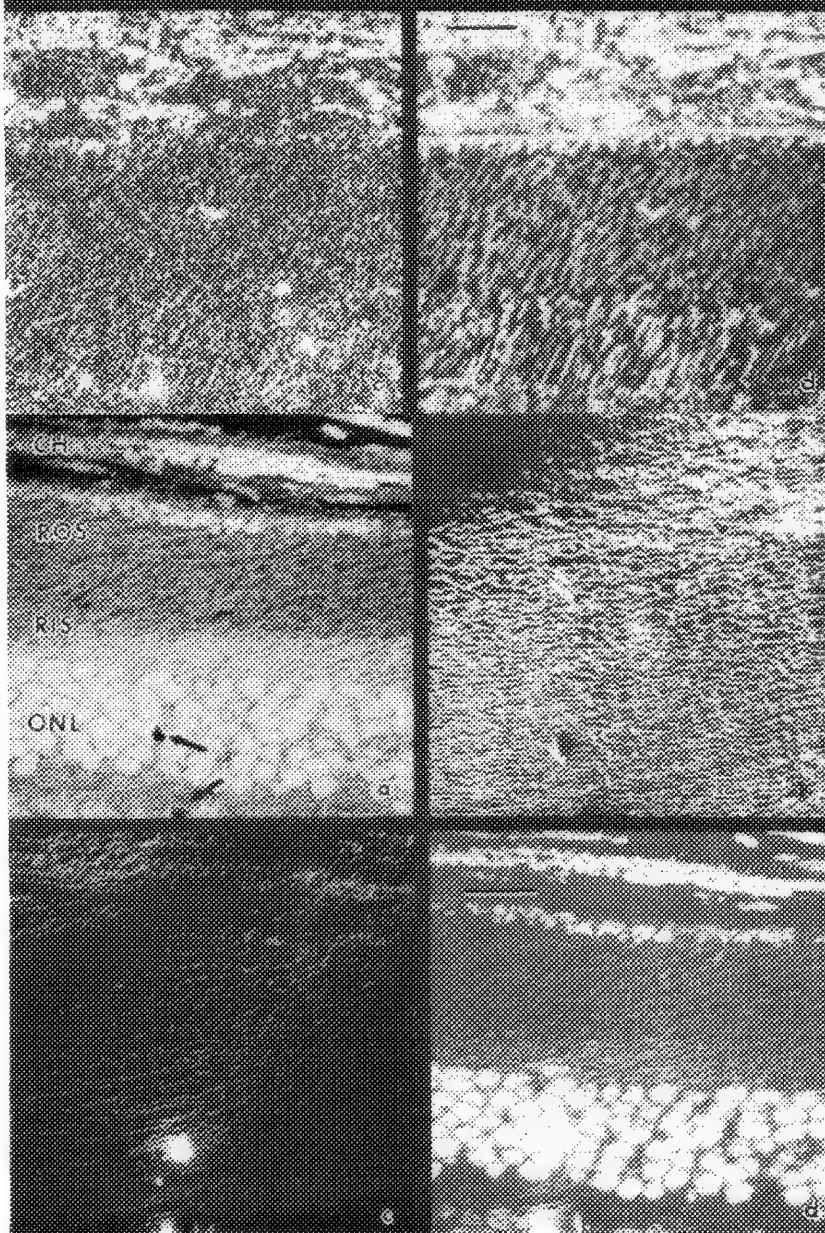


FIG. 2.--Retina and choroid fixed with glutaraldehyde containing oxalate and postfixed with osmium containing pyroantimonate. (a) CN^- image showing intense emission from melanin granules of choroid and ONL. Arrows indicate artificial dirt on specimen surface. (b) Integrated secondary ion image showing surface topography. Dark area in upper left is a swale in specimen. (c) O^- image showing slight emission from choroid region, along edges of surface topography and from dirt on sample (d) Na^+ image showing intense emission from melanin granules in choroid and outer nuclear layer, similar to intense CN^- emission. Bar = 10 μm .

2



J. Histochem. Cytochem. 32:788, 1984.

4. M. L. Fishman, M. A. Orbec, H. H. Hess, and W. K. Engel, "Ultrastructural demonstration of calcium in retina, retinal pigment epithelium and choroid," *Exp. Eye Res.* 24: 341, 1977.

5. R. Levi-Setti, "Structural and microanalytical imaging of biological materials by scanning microscopy with heavy ion probes," *Ann. Rev. Biophysics and Biophysical Chem.* (in press).

6. M. S. Burns and D. M. File, "Quantitative microlocalization of diffusible ions in normal and galactose cataractous rat lens by secondary ion mass spectrometry," *J. Microscopy* 144: 157, 1986.

7. M. S. Burns, D. M. File, V. Deline, and P. Galle, "Matrix effects in secondary ion

mass spectrometric analysis of biological tissue," *SEM/1986* IV, 1277.

8. E. Hindie, B. Coulomb, F. Escaig, and P. Galle, "Intracellular dynamics of a fluorinated drug, dexamethason: A study by ion microscopy," *SIMS VI* (in press).

QUANTITATIVE X-RAY IMAGING OF HUMAN CYSTIC FIBROSIS NASAL EPITHELIUM

J. R. Herlong, Ann LeFurgey, Peter Ingram, J. D. Shelburne, L. J. Mandel, and L. A. Hawkey

Cystic fibrosis (CF) is the most common lethal genetic disease which afflicts Caucasians. The respiratory system is almost universally affected in CF patients, and the basic defect in this organ system as well as in others appears to be an abnormality of the regulation of chloride ion transport; the transport of other ions may also be either primarily or secondarily affected.¹ Both the nasal mucosa and the lower respiratory tracts of CF patients exhibit this defect, but the nasal mucosa is much more readily accessible and is free of the infectious complications common in the lower-tract regions.² There is unfortunately no perfect animal model of cystic fibrosis.³ Thus the human nasal mucosa is an ideal site for studying the respiratory tract pathophysiology of CF. Electron-probe x-ray microanalysis (EPXMA) promises to be a useful tool in the investigation, at the cellular and subcellular levels, of this ion transport defect as well as possible defects in the transport of other ions. Indeed, EPXMA has been used to considerable advantage in the study of CF by Quinton (using microdroplet analysis),⁴ Roomans,⁵ and Izutsu.⁶ In addition, quantitative elemental x-ray imaging expands the usefulness of EPXMA in these studies by providing both a statistically larger sample size and greater ease of recognition of elemental compartmentation.⁷ This report presents preliminary results of quantitative elemental x-ray imaging of normal and CF nasal epithelia.

Methods

Nasal mucosa was obtained from human volunteers (CF patients and normal volunteers) by scraping of the inferior surface of the inferior turbinate (concha) with an ear curette by Alford's method.⁸ This is the anatomic site in the nose that is least affected by cuboidal or squamous metaplasia.⁹ The scraping was placed onto a wooden stub and quickly hand-plunged into liquid ethane at -184 C. Total time from removal of the scraping to freezing

was less than 20 s. Cryosections were obtained in an ultramicrotome with a cryo attachment; dry glass knife temperature was maintained at -150 C and specimen temperature at -140 C. The cryosections were placed onto carbon-coated nickel grids, freeze-dried, carbon-coated, and viewed unstained.¹⁰ Subsequent scrapings were obtained both for freezing followed by freeze substitution with 2% osmium in acetone¹¹ and for fixation in 2% glutaraldehyde in isosmotic 0.05 M Na-cacodylate buffer, followed by processing for routine transmission electron microscopy (TEM).¹⁰ The freeze-substituted tissue was removed from the specimen stub and rotated 90° prior to embedding, so that both the first and last points of impact with the ethane were present in each section.

Quantitative elemental x-ray images (maps) were obtained as previously described.⁷ Briefly, image maps of 64 × 64 pixels were obtained for physiologically important ions (K, Na, Mg, Ca, P, Cl, and S) with an electron microscope (JEOL 1200EX) operating at 80 kV and equipped with scanning attachment, an additional hard x-ray aperture, and an energy-dispersive x-ray analyzer (TN5500). Acquisition and spectral processing were performed by a multitasking graphics workstation (Vaxstation 2000, Digital Equipment Corp.); and data storage, image display, processing, and retrieval of quantitative image information were performed by a microcomputer (Macintosh II, Apple Computer). Data were analyzed by the Hall procedure for ultrathin specimens and quantitation was done by a multiple-least-squares fitting routine on filtered x-ray spectra.¹² In order to compensate for possible shifts in detector calibration that would otherwise limit the accuracy of the Ca measurements, first and second derivatives of the potassium reference peaks were included in the fit.¹³

Results

The scrapings each contained hundreds of nasal epithelial cells suspended in mucus. There were areas in which the cells were randomly oriented as well as areas in which the native pseudostratified architecture was maintained. No ultrastructural differences were noted between normal and CF cells. Routine TEM revealed intact intercellular junctions and no membrane damage. There was mild to marked swelling of the mitochondria, endoplasmic reticula, and nuclear envelopes. The degree of this swelling varied from cell to cell. In the freeze-substituted tissue, adequate preservation (no noticeable ice crystal damage at 20 000×) was obtained in the first several cell layers from the point of first

J. R. Herlong, A. LeFurgey, L. J. Mandel, and L. A. Hawkey are with the Department of Physiology, School of Medicine, Duke University Durham, NC 27710; P. Ingram is with Research Triangle Institute, Research Triangle Park, NC 27709; J. D. Shelburne, with the Department of Pathology, Duke University and VA Medical Centers, Durham, NC 27710. This work was supported by the NC United Way. The authors gratefully acknowledge the contributions of Dr. M. R. Knowles, who performed all cell harvests and without whom this work would not have been possible.

impact, and progressively severe ice crystal damage was observed in deeper layers; however, there was occasionally varying severity of ice-crystal damage among adjacent cells in the same layer. Because of the usually random orientation of cells in the scrapings, sections through the apical portion of the cells could not be assured, but ciliated cells and goblet cells could be identified in some cryosections. Sufficient ultrastructural detail was preserved in the cryosections so that nuclei, mitochondria, and mucous granules could be reliably discerned in many sections. The morphological results of this preparation are presented in detail elsewhere.¹⁴

X-ray images have thus far been obtained from 24 cells from 6 normal volunteers and from 7 cells from 2 CF patients. In 10 cells from normal volunteers and 3 cells from CF patients, ultrastructural detail could be discerned. The K:Na ratios obtained from whole cell data varied considerably from cell to cell; these ratios ranged from 0.5 to 4.2 in normal volunteers and from 1.1 to 2.3 in CF patients. In contrast, the K:Na ratios were remarkably similar among cells from the same patient. In both normal volunteers and CF patients, accumulations of Ca and P were observed in the mitochondria of some cells; this phenomenon was variable from cell to cell and had no correlation with an alteration in K:Na ratio. This phenomenon is illustrated in Fig. 1, which presents a transmission electron micrograph as well as video (STEM) and x-ray images of two adjacent ciliated cells from a CF patient. The encircled cell has Ca accumulated in its mitochondria, and its neighboring cell does not. Elevated P is also observed in the encircled cell. The mucous granules of both normal volunteers and CF patients accumulated S; in some granules this was associated with an accumulation of Ca; again, the presence or absence of Ca accumulation in the mucous granules had no correlation with an alteration in K:Na ratio. Figure 2 presents a transmission electron micrograph as well as video (STEM) and x-ray images of a cryosection in which both mucous granules and mitochondria are seen. The mucous granules can be seen to accumulate S and Ca, and the mitochondria demonstrate an accumulation of P and Ca. The combined data from all normal volunteers and all CF patients are presented in Table 1. These concentration values are not corrected for the contribution of the carbon film; the actual concentrations are therefore 15-20% higher than the presented concentrations.

Discussion

Given the limited database thus far established, physiological interpretation of the data is premature. However, certain trends indicate similarities between CF nasal mucosa and other CF tissues that have been studied. The variable mitochondrial accumulation of Ca and P and the heterogeneity of mitochondrial swelling noted in routine TEM studies are strongly suggestive of varying degrees of

sublethal cell injury. This injury may either reflect the native state of this rapidly regenerating epithelium which is constantly exposed to turbulent air flow, or may result from mechanical trauma during extraction (scraping) of the cells. The lack of association of these accumulations with a decreased K:Na ratio remains puzzling in light of the current concept of cell death being associated with the accumulation of Ca and P in mitochondria.¹⁵ The accumulation of S in the mucous granules is likely a reflection of the sulfated mucins contained in these granules. Roomans has reported an elevated Ca content of CF bronchial goblet cells.¹⁶ In the present study, the Ca content of mucous granules was greater in CF patients than in normal volunteers, but did not reach statistical significance; however, the Ca content of the cytoplasm was significantly greater in CF patients than in normal volunteers. This finding is consistent with proposed alterations in Ca-dependent pathways in CF.¹⁷ Izutsu et al.⁶ have reported elevated S content of CF labial gland mucous granules, a finding paralleled in the present study of CF nasal epithelial mucous granules. Increased sulfation of mucins in CF has been proposed as a contributing factor to the altered rheology of CF mucous, which is important in the pathophysiology of CF respiratory disease.¹⁸

In conclusion, this paper documents the development of techniques for obtaining EPXMA images of cryosections of nasal epithelium from normal volunteers and CF patients and presents preliminary data from these images.

References

1. R. A. Frizzell, "Cystic fibrosis: A disease of ion channels?," *Trends in Neurosciences* 10: 190, 1987.
2. M. R. Knowles et al., "Abnormal respiratory epithelial ion transport in cystic fibrosis," *Clinics in Chest Medicine* 7: 285, 1986.
3. R. M. Muller, *Exocrine Glands in Animal Models for Cystic Fibrosis*, Stockholm: University of Stockholm (Ph.D. dissertation), 1987.
4. J. Bijman and P. M. Quinton, "Influence of abnormal Cl⁻ permeability on sweating in cystic fibrosis," *Am. J. Physiology* 247: C4, 1984.
5. G. M. Roomans, "Cystic fibrosis," in *Microprobe Analysis in Medicine*, New York: Hemisphere (in press).
6. K. Izutsu et al., "Electron microprobe analysis of human labial gland secretory granules in cystic fibrosis," *J. Clinical Investigation* 75: 1951, 1985.
7. P. Ingram et al., "Quantitative elemental x-ray imaging of biological cryosections," this volume.
8. B. R. Alford et al., "Atraumatic biopsy of nasal mucosa," *Arch. Otolaryngology* 90: 88, 1969.

Fig. 1.--(a) Quantitative x-ray maps corresponding to (b) TEM micrograph of ciliated respiratory epithelial cells of CF patient. In images, lighter shading indicates greater concentration. Conc. = concentration; M = mitochondria; C = cilia; arrow indicates corresponding regions of the TEM and video (STEM) image.

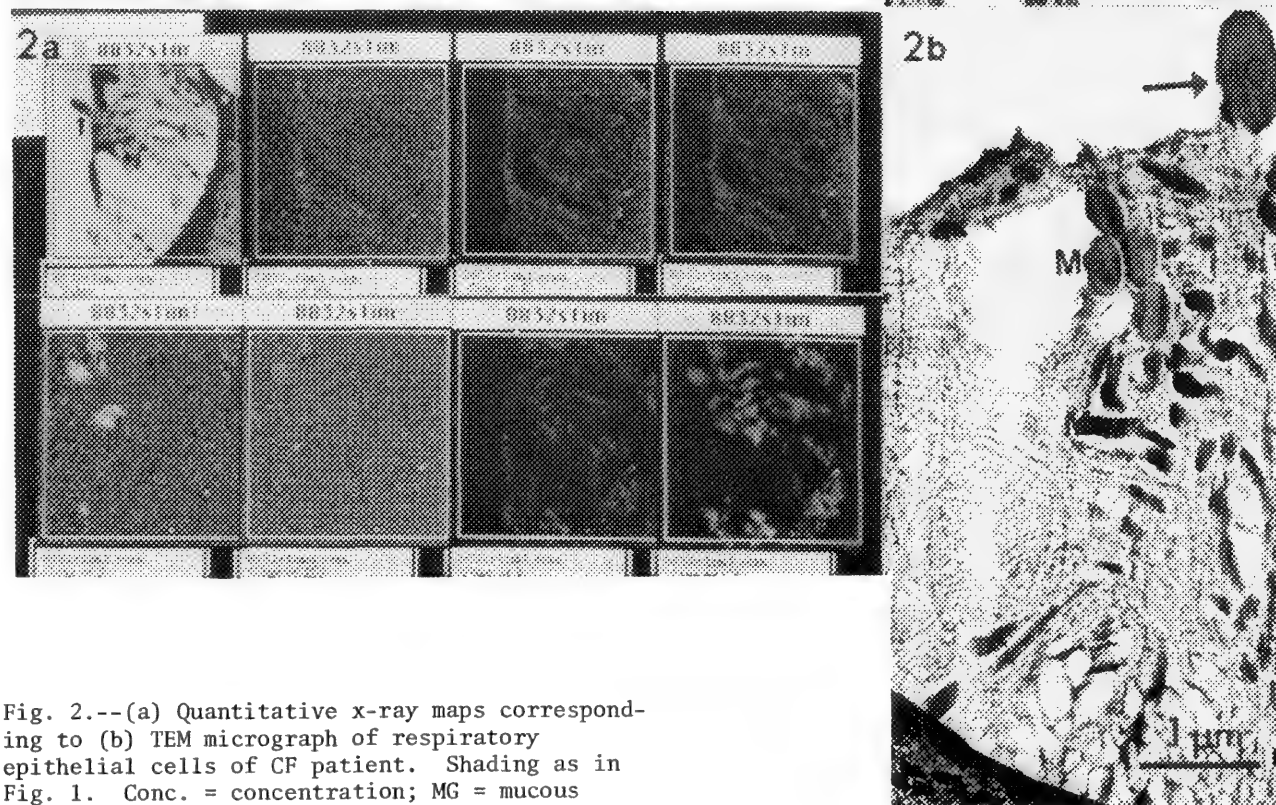
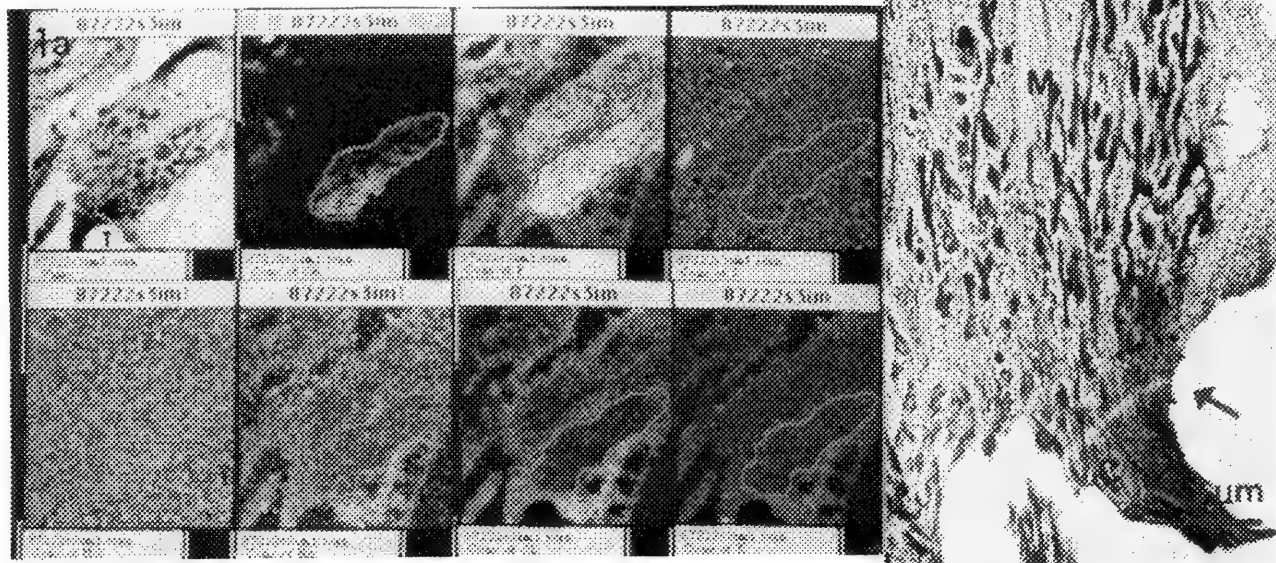


Fig. 2.--(a) Quantitative x-ray maps corresponding to (b) TEM micrograph of respiratory epithelial cells of CF patient. Shading as in Fig. 1. Conc. = concentration; MG = mucous granules; M = mitochondria; arrow indicates corresponding regions of the TEM and video (STEM) image.

9. M. R. Knowles et al., "Measurements of nasal transepithelial electric potential differences in normal human subjects in vivo," *Am. Rev. Respiratory Diseases* 124: 484, 1981.

10. Ann LeFurgey et al., "Heterogeneity of calcium compartmentation: Electron probe analysis of renal tubules," *J. Membrane Biology* 84: 191, 1986.

TABLE 1^a.--Combined concentration data from 3 normal controls (10 cells) and 2 CF patients (2 cells). Concentrations are given as mean \pm SEM in mmol/kg dry weight and are not film-corrected. Statistical significance was determined by Student's t-test. N = number of regions analyzed.

Elemental concentration (mmol/kg dry wt.)	Cytoplasm		Mucous Granules	
	Normal controls (N = 50)	CF patients (N = 20)	Normal controls (N = 12)	CF patients (N = 3)
Ca	7 \pm 1*	14 \pm 3*	83 \pm 36	182 \pm 47
P	211 \pm 16	222 \pm 14	162 \pm 33	100 \pm 60
S	28 \pm 2	33 \pm 5	97 \pm 12**	245 \pm 42**
Cl	123 \pm 17	186 \pm 40	105 \pm 26	124 \pm 9
K	215 \pm 10**	298 \pm 10**	224 \pm 15*	181 \pm 24*
Na	270 \pm 14	253 \pm 26	152 \pm 37	80 \pm 14
Mg	21 \pm 4	21 \pm 6	36 \pm 10*	12 \pm 4*

*p < 0.05.

**p < 0.0005.

^aNote that this tabulation includes data from all cells investigated to date and thus that physiological interpretation of these mean values is premature. For example, in normal controls, if one includes *only* cells categorized as viable on the basis of a K:Na ratio of >2:1, the cytoplasmic elemental contents (mean \pm SEM) in mmol/kg dry wt. are as follows: P, 193 \pm 19; S, 47 \pm 4; Cl, 105 \pm 10; K, 241 \pm 15; Na, 90 \pm 10; and Mg, 31 \pm 9.

11. R. Nassar et al., "The quick freezing of intact skeletal muscle fibers at known time intervals following electrical stimulation," *SEM/1986* I, 309.

12. H. Shuman et al., "Quantitative electron probe microanalysis of biological thin sections: Methods and validity," *Ultramicroscopy* 1: 317, 1976.

13. T. Kitazawa et al., "Quantitative electron probe analysis: Problems and solutions," *Ultramicroscopy* 11: 251, 1983.

14. J. R. Herlong, "Cryopreservation of cystic fibrosis nasal epithelium," *Proc. 46th Ann. Meet. EMSA*, 1988, 88.

15. B. F. Trump et al., "The role of ion shifts in cell injury," *SEM/1979* III, 1.

16. G. M. Roomans et al. "X-ray microanalysis of goblet cells in bronchial epithelium of patients with cystic fibrosis," *J. Submicrosc. Cytol.* 18: 613, 1986.

17. S. Katz et al., "The calcium hypothesis of cystic fibrosis," *Cell Calcium* 5: 421, 1984.

18. T. F. Boat et al., "Tracheobronchial mucus secretion in vivo and in vitro by epithelial tissues from cystic fibrosis and control subjects," *Modern Problems in Paediatrics* 19: 141, 1977.

BIOLOGICAL ELECTRON-PROBE X-RAY MICROANALYSIS: AN UNFULFILLED PROMISE?

Patrick Echlin

It is now more than twenty years since the first papers appeared describing how electron-probe x-ray microanalysis could be used to detect and measure the amount of elements in biological specimens. The trace element analysis technique, which came to biology from the material sciences, gave the promise of being able to measure the distribution and local concentration of elements $Z > 11$, in small microvolumes at a spatial resolution of 1-10 μm , in cells and tissues that in theory required no chemical intervention during sample preparation. For the first time, it would be possible to measure and compare elemental concentrations at the individual cell level within tissues.

Twenty years on, thanks to improvements in instrumentation and quantitative algorithms, and a better understanding of the processes of specimen preparation, the technique has developed into methods which, in thin sections and under ideal conditions, can measure elemental amounts as small as 10^{-18} g, in concentrations down to 1 mmol/kg and at a linear spatial resolution of 10 nm.¹ Electron-probe x-ray microanalysis has emerged as one of the most useful methods of quantitative *in situ* analysis that may be carried out at the ultrastructural level of biological materials. It is now possible to measure the local concentration of a number of diffusible, physiologically active elements, in volumes as small as 100 attoliters (10^{-16} l) at specific sites within the cytoplasm and organelles of an individual cell. Yet despite these remarkable advances, the technique does not appear to be widely used in the biomedical sciences.

Since the mid-1960s, and during a period of unprecedented interest in the relationship between ultrastructure and physiological function, only about 2650 papers in the biological sciences have used electron-probe x-ray microanalysis as a method for elemental analysis. Of these papers, 71% have been on animal and human tissue, 18% on plant material, and 11% on microorganisms.² During the same time period there have been 6050 references to electron-probe x-ray microanalysis in the material and geological sciences.^{3,4} This increased usage should come as no surprise, for much of the success of electron-probe x-ray microanalysis in the nonbiological sciences is related to the relative ease of specimen preparation, the precision of the popular ZAF quantitative procedure, and the fact that inorganic samples are rarely damaged by the electron beam. It

is appropriate to ask why this seemingly sensitive and accurate analytical technique appears relatively underused in the biomedical sciences. This paper considers some of the present limitations of the technique and considers what we may do to improve the quality of analysis within the constraints of the existing technology.

Spatial Resolution and Sensitivity

We should first examine the claims of high spatial resolution and sensitivity. The best that biological x-ray microanalysis can do has been achieved only by a small number of workers in a small number of cases. For example, a minimum detectable mass of 10^{-15} g Fe has been reported in ferritin,⁵ minimum detectable concentrations of 0.3 mmol Ca/kg dry weight in smooth muscle⁶ and 0.5 mmol Fe/kg wet weight in cerebellar tissue.⁷ A number of similar examples may be found in the appropriate literature. The sensitivity of measurements of elements such as K, Ca, and Fe is estimated to be in the range 0.1-0.5 mmol/kg wet weight.⁷ Although electron-probe x-ray microanalysis has been used successfully for the detection of calcium where the cellular concentration is unusually high, the technique is not sufficiently sensitive to detect the low concentrations (10 to 100 $\mu\text{mol/kg}$ FW) of the element that are considered to play a pivotal role as second messenger in cell metabolism. Analytical results from studies on the lighter elements such as Na and Mg are less sensitive; it is generally accepted that a minimum detectable concentration of 5-10 mmol Na/kg wet weight is the lowest amount that may be reliably measured.

High spatial resolution depends on both the probe size and the biological matrix being analyzed. A field-emission STEM instrument produces a minimum probe size of 3-5 nm and when used to analyze the closely knit organic matrix of membranous organelles such as mitochondria, can achieve an analytical spatial resolution better than 10 nm.⁸ In thick (1-2 μm) sections the linear spatial resolution is 0.1-0.5 μm ,⁹ and in bulk samples the resolution is no better than 3-5 μm .^{10,11} Bulk samples present an additional problem in that unseen structures below the specimen surface can contribute to the analyzed microvolume. Such specimens should only be used where the volume of the compartment being analyzed is considerably larger than the size of analyzed microvolume, as is the case with many extracellular spaces and the vacuoles of mature plant cells. If we convert these linear dimensions into volumetric measurements, we find that with a 50nm probe, the analyzed micro-

The author is at the Department of Botany, University of Cambridge, Cambridge, England CB2 3EA.

volume is 10-100 femtoliters (10^{-15} l) in thick sections; with a 100nm probe the analyzed microvolume is 1-10 picoliters (10^{-12} l) in bulk material analyzed at 10 kV. These are the best values that may be obtained under optimal conditions--and are rarely obtained in practice.

Major Areas of Application

Although these impressive statistics are encouraging, we should perhaps inquire how far this precision and accuracy is being achieved generally, and whether this high degree of resolution and sensitivity is necessary for all biological microanalysis. Many analyses are of a routine qualitative and essentially static nature, in which the end product of a metabolic or physiological event is analyzed. Although high spatial resolution is frequently necessary, it is usually sufficient to state that a particular element is either present or absent and/or that it is x times greater in one cell compartment than another. This type of analysis is usually associated with abnormally high or unusual local concentration of an element such as may be found in clinical pathology, in heavy-metal pollution and contamination, and in the vacuolar contents of halophytic and glycophytic plants. Apart from marginal improvements in specimen preparation, the existing technology can solve these types of problems.

The other major area of application for biological x-ray microanalysis is in cell and tissue physiology, where one is generally concerned with making quantitative measurements of the spatial distribution and transport of diffusible elements in concentration gradients both within and between cells, tissues, and extracellular spaces. Precision and accuracy are at a premium, although high spatial resolution may not be always necessary. In this second situation one would look for improvements in both sample preparation and the analytical procedures. It is particularly important to maintain the cells and tissues in a physiologically defined state up to the moment of sample preparation and to insure that the in vivo distribution of the elements remains unaltered throughout sample preparation, examination, and analysis. A large amount of important physiological data, including electrolyte concentration and water content, has been found by x-ray microanalysis, and the validity of both the preparative and quantitative procedures has been established independently by the use of alternative methods.¹² Although the analytical technology is capable of sustained productivity, the properties of the specimens themselves will be the limiting factors to further improvements in resolution and sensitivity. As long as high spatial resolution analysis of local concentrations of elements remains a significant factor in cell physiology, electron-probe x-ray microanalysis (particularly x-ray mapping) will remain an important analytical tool. Alternatively, if interest in physiol-

ogy turns more toward in vivo studies, then perhaps x-ray microanalysis is beginning to reach the end of its usefulness. Information on dynamic physiological processes will come only by means of other, less invasive technologies such as indicator dyes and ion-specific probes coupled with digital imaging fluorescent microscopy. However, the spatial resolution will be decreased and the new methods will doubtless bring their own preparative problems.

Sample Preparation and the Promises of Cryotechnology

Throughout the brief history of biological x-ray microanalysis, the technology of instrumentation and the computational procedures for quantitation have always been ahead of the methods of sample preparation. Low-temperature techniques appear to be the best way to preserve a wet, three-dimensional dynamic sample for examination in the arid low-pressure confines of an electron-beam instrument. Such methods serve both to preserve the sample in a near-lifelike state and to minimize the damage that invariably occurs during examination and analysis. The arguments for this approach are well rehearsed and need not be repeated here, although it is frequently forgotten that low-temperature techniques are not the panacea for all sample preparation. High-resolution high-sensitivity analysis has only been achieved with frozen dried sections. A major limitation to this approach is that it inevitably results in considerable displacement of diffusible elements in the matrix-free extracellular spaces of tissues and the large aqueous vacuoles, which are the principal component of plant cells. We shall briefly consider some of the limitations of low-temperature techniques in biological x-ray microanalysis.

There is now general agreement that hydrated biological samples, unsullied by chemical intervention prior to cooling, when cooled at a rate of $10\text{--}50 \times 10^3 \text{ K s}^{-1}$ will contain ice crystals no bigger than 10 nm down to a depth of 20 μm from the surface. This result may be achieved by impact cooling onto a polished copper plate cooled to 77 K with liquid nitrogen (liquid helium gives only a marginal improvement) and a few sections, at worst containing microcrystalline ice, may be cut from the first few micrometers of the frozen sample. Alternatively, small isolated samples, up to $\sim 50 \mu\text{m}$ in diameter, can be cooled by jet, spray, or immersion procedures to produce ice crystallites of the same dimensions. It has been calculated that the technique of high-pressure cooling will vitrify hydrated samples to a depth of 500 μm .¹³ If this promise is fulfilled, it will remove one of the major limitations to the preparation of hydrated specimens for biological microanalysis.

At present, high-spatial resolution x-ray microanalysis can only be achieved in the microcrystalline regions of rapidly cooled samples if they are either sufficiently small, or

if the analysis is confined to the surface regions of larger specimens. However, in many instances the experimental procedure only requires analyses to be carried out at the whole-cell level. Under these circumstances larger ice crystallites and their consequent phase separations may be tolerated, although resolution will be compromised. It would be imprudent to use small probes for such analyses as their improved lateral resolution could give rise to misleading experimental data. An example will suffice to illustrate this point.

A 1 μm -thick frozen hydrated section would typically have ice crystals of between 0.1 and 0.2 μm . Analysis of such a section with a 50nm probe would indicate alternately regions of very low elemental concentration within ice crystals and regions of high concentration within the frozen eutectic. This problem is overcome either by use of a much larger probe size or a reduced raster of 0.5 μm^2 that would encompass both ice crystals and eutectic and give an average concentration. Under these circumstances, the volumetric spatial resolution in thick sections would fall from 10-100 femtoliters to 1-10 picoliters. If we assume 0.5 μm ice crystals in the larger bulk samples, which would necessitate the use of a 1.0 μm^2 reduced raster to analyze the sample properly, the volumetric resolution would fall to 20-50 picoliters.

At cooling rates of 10^5 K s^{-1} , theory¹⁴ predicts that water and aqueous solutions will vitrify and all the structural components and soluble species will be arrested in the position they assumed immediately prior to rapid cooling--an ideal state for subsequent analysis and microscopy. Although thin (100nm) suspension films of water and particulate matter have been vitrified and imaged in the transmission electron microscope, truly vitrified samples have yet to be used for x-ray microanalysis. With the size and type of samples we normally use for a microanalysis, the best we can hope for is to cool them at an initial cooling rate of 10^4 - 10^5 K s^{-1} and convert the water to microcrystalline ice.

The water in the first 10 μm of a hydrated sample cooled at a rate of $40 \times 10^4 \text{ K s}^{-1}$ will be converted to ice (cryofixed) in $5 \times 10^{-4} \text{ s}$.¹⁵ The cooling rate will become progressively lower as the freezing front penetrates deeper into the sample. The same depth of material (10 μm) would take 5-10 s to be immobilized by conventional chemical fixation.¹⁶ Clearly, cryofixation is faster than chemical fixation, and although low-temperature techniques are routinely used to arrest electrophysiological events that occur at a rate of $1\text{-}5 \times 10^{-3} \text{ s}^{-1}$, there is some doubt whether rapid cooling is equally effective at stopping diffusive processes. The average diffusion rate of water and electrolytes at 293 K is about 10 μm in $5 \times 10^{-7} \text{ s}^{-1}$, which (at the cooling rates we can realistically hope to achieve with the type of sample we use for microanalysis) gives water molecules more than enough time to migrate to a growing ice crystal, and for diffusible elements to be

moved tens of micrometers from their original position in the cell. Diffusion slows down as the viscosity of water increases during the undercooling of water prior to nucleation and it is generally assumed that electrolytes become enmeshed (or bound?) to the constituent structures of the cellular cytomatrix. Although there is little experimental evidence to support the notion that components of the aqueous phase are deposited onto adjacent fixed macromolecular structures, diffusible elements within cells are relocated only over quite short distances. The problem is more serious in extracellular spaces and plant vacuoles that are devoid of matrix components and the growth of ice crystals may cause substantial electrolyte relocation. A simple examination of frozen dried specimens, including thin sections, will reveal the presence of ice-crystal ghosts of between 0.1 and 1.0 μm ; it is these dimensions that must be used to judge the efficacy of the cryopreparation protocol and, in turn, the expected accuracy and precision of the microanalysis.

It is unfortunate that the choice of rapid cooling procedures for biological x-ray microanalysis is unduly influenced by quoted rates of cooling. It is unrealistic to expect that a procedure that gives a cooling rate of $80 \times 10^4 \text{ K s}^{-1}$ with a 70 μm thermocouple should produce microcrystalline ice throughout a 0.25mm⁵ piece of wet tissue. We should adopt a different approach when planning our experimental protocols and first set the limits of cryopreservation that are necessary for the type of analysis to be carried out. Data should then be collected on the thermophysical properties of the sample, the cryogen(s), the method(s) available for rapid cooling, and the expected upper limit for the size and distribution of ice crystals for the type of microscopy and analysis to be carried out. A series of theoretical equations may be used,¹⁷ to calculate the critical cooling rates necessary for optimal cryopreservation. This approach provides a positive way forward in our understanding of what happens as a hydrated specimen is cooled rapidly.

The Promises Fulfilled and Denied

In many respects biological microanalysis is fulfilling its promises, although it will probably never be used to its full potential. The problems of specimen damage in high-resolution quantitative analysis of frozen hydrated sections, with probe sizes smaller than 100 nm, may limit the usefulness of this type of sample. That is unfortunate, for all the collected wisdom of specimen preparation predicts that this type of specimen probably most closely resembles the natural state of the sample. In physiological investigations, the static trace element approach of x-ray microanalysis is likely to be further supplemented by optical fluorescence methods that more closely reflect the dynamic state of living matter. This approach would circumvent

the tiresome preparative procedures that are necessary for so much of this type of biological microanalysis. Advances in immunocytochemistry and labeled antibody techniques are going to allow some elemental species to be identified and localized by virtue of their association with specific macromolecules. In the past five years alone there have been nearly 5700 papers² that have used immunocytochemical techniques as a means of analysis. These procedures are arguably less invasive and do not require expensive instrumentation, and the quantitative procedures appear relatively simple. The current interest in the organization of the genetic script and in the processes of gene sequencing and manipulation means that organic molecules and macromolecules are of more interest than local concentrations of elements. An examination of the figures below, which gives the number of literature citations in electron probe x-ray microanalysis (EPXMA) and immunocytochemical techniques (ICCT) over the past two decades, reflects this change in the biological sciences.

	1966-73	1974-78	1979-83	1984-88	TOTAL
EPXMA	195	663	1002	690	2550
ICCT	53	627	2546	5274	8500

Entirely noninvasive methods such as nuclear magnetic imaging, although they still lack the spatial resolution of x-ray microanalysis, are able to localize and provide information on the binding state of several elements of biological interest in living material. A hydrated sample converted to a vitrified state is the near-perfect sample for biological microanalysis, but dynamic processes can only be followed in living organisms.

There is a final matter we might consider when assessing the apparent underusage of x-ray microanalysis by experimental biologists. This is not a question that turns on the scientific method, but is more concerned with the availability of technical resources and the need for more thorough exploration of the attributes and limitations of x-ray microanalysis as a tool for biomedical research. The equipment required for innovative biological x-ray microanalysis is both expensive and complex. Funding for the equipment is only part of the problem; there is also a need for full-time experts to insure that the equipment is working properly. Advances in technology may insure more accurate analysis, and hence more reliable experimental results, but they will not make the process of analysis and data acquisition any easier. We need a much closer collaboration between the cognoscenti and the end-user biologist, who may well be technically illiterate about x-ray microanalysis but has nevertheless specific problems that could be resolved by the technique.

A change is also needed in the attitude of the funding agencies to permit support of projects whose primary aim would be the general improvement of the technique rather than

concentration on using existing technologies to solve narrow (although doubtless eminently worthy) biological problems. There is an alarming paucity of thorough studies that have sought either to develop entirely new methods of specimen preparation, or to assess carefully the limitations of existing methods. Sample preparation alone is a major impediment to the wider use of x-ray microanalysis in biology.

It is now generally accepted that advances in biology come from the application of a variety of techniques to the study of a particular problem. These techniques--and they are after all only techniques and a means to an end--are expert systems in which most biologists need only occasional access. Such expert systems should be an integral part of centralized instrumentation facilities, staffed by experts who, in addition to advising and assisting visiting biologists, would be involved in developing improved methods of biological analysis. The few such national and regional facilities that exist have proved the worth of this approach as they are all acknowledged centers of excellence. They are still few and far between and more are needed to insure that biologists can take advantage of the full impact of x-ray microanalysis as a means of studying the distribution and concentration of elements in plant and animal material.

References

1. T. A. Hall, "Capabilities and limitations of probe methods for the microanalysis of chemical elements in biology: A brief introduction, *Ultramicroscopy* 24: 181, 1988.
2. BIOSIS Computer Literature Search, February 1988.
3. METADEX Computer Literature Search, February 1988.
4. GEOREF Computer Literature Search, February 1988.
5. A. P. Somlyo and H. Shuman, "Electron probe and electron energy loss analysis in biology," *Ultramicroscopy* 8: 219, 1982.
6. M. Bond et al., "Release and recycling of calcium by the sarcoplasmic reticulum in guinea pig portal vein smooth muscle," *J. Physiol.* 355: 677, 1984.
7. C. E. Fiori et al., "Quantitative x-ray mapping of biological cryosections," *Ultramicroscopy* 24: 237, 1988.
8. A. V. Somlyo et al., "Calcium content of mitochondria and endoplasmic reticulum in liver frozen rapidly in vivo," *Nature* 314: 622, 1985.
9. T. A. Hall and B. F. Gupta, "Quantification for the x-ray microanalysis of cryosections," *J. Microscopy* 126: 333, 1982.
10. A. T. Marshall, "Scanning electron microscopy and x-ray microanalysis of frozen hydrated bulk specimens," in R. A. Steinbrecht and K. Zierold, Eds., *Cryotechniques in Biological Electron Microscopy*, Berlin: Springer-Verlag, 1987.
11. P. Echlin and S. E. Taylor, "The

preparation and x-ray microanalysis of bulk frozen hydrated vacuolate plant tissue, *J. Microscopy* 141: 329, 1986.

12. A. P. Somlyo et al., "Quantitative electron probe analysis in biology," *Microbeam Analysis--1986*, 196.

13. H. Moor, "Theory and practice of high pressure freezing," in Ref. 10.

14. U. Riehle, "Schnellgefrieren organischer Präparate für die Elektronen-Mikroskopie," *Chem. Ing. Technol.* 40: 213, 1968.

15. G. J. Jones, "On estimating freezing times during tissue rapid freezing," *J. Microscopy* 136: 349, 1984.

16. B. Ph. M. Mersey and M. E. McCully, "Monitoring of the course of fixation of plant cells," *J. Microscopy* 114: 49, 1978.

17. W. B. Bald, *Quantitative Cryofixation*, Bristol: Adam Hilger, 1987.

**SELECTED-AREA CHANNELING PATTERN AND DEFECT ETCH STUDY OF
SILICON IMPLANTED WITH OXYGEN**

Peter Roitman and G. E. Davis

Thin-film silicon-on-insulator materials are under serious investigation for use in advanced integrated circuits. A currently popular candidate technology is SIMOX, in which a silicon crystal is heavily implanted with oxygen and annealed at high temperature. If enough oxygen is implanted, a layer of amorphous SiO_2 forms underneath a thin surface layer of silicon. The silicon is heavily damaged by the implant, but is not driven amorphous. Various implantation and annealing conditions are being studied in an attempt to develop a defect-free layer of silicon on top of the oxide.

Most of the defect studies of this material to date have used cross-sectional TEM. Although this technique works well and is extraordinarily sensitive, there are three difficulties. Sample preparation remains time consuming and painstaking; the technique is inherently destructive, hence it cannot readily be used for quality control; and TEM suffers from the general "microscopy problem," which is the difficulty of examining small defects in a large amount of perfect material. As defect densities are pushed below 10^7 cm^{-2} , a large number of samples must be examined to find one defect.

Electron channeling pattern analysis and etch-pit counting are two techniques that have been employed to study defects in other systems. In this study we report on their utility for the silicon-on-insulator case.

Experimental

The samples were all implanted with oxygen at 150 kV to a dose of $1.7 \times 10^{18} \text{ cm}^{-2}$ at a temperature of 505-535 C. They were all annealed at 1250 C in $\text{N}_2 + 1\% \text{O}_2$. Samples E and F were internally oxygen gettered prior to implantation by heating at 700 C for 24 h, 900 C for 4 h, and 1050 C for 16 h. Samples B, C, and D were not heat treated prior to implantation. Sample B was annealed for 6 h; samples C, D, E, and F were annealed for 2 h. During the anneal samples C and E were coated with $\sim 500 \text{ nm}$ of oxide, which was removed prior to observation. Samples B, D, and F were not coated. Sample A was a control sample of unimplanted, unannealed single crystal silicon. In fact, a portion of each sample was etched clean of the surface silicon and buried oxide layers

after annealing to provide this reference.

Previous work¹⁻³ has shown that these implant conditions and annealing temperatures result in a well-defined layered structure of single crystal silicon, silicon dioxide, and bulk silicon. The top silicon layer is $\sim 200 \text{ nm}$ thick and includes a large number of threading dislocations and oxide precipitates. The oxide layer is $\sim 300 \text{ nm}$ thick and is stoichiometric. The quality of the top layer is of particular concern for device fabrication.

The electron channeling patterns were acquired in single deflection selected area channeling pattern mode⁴ by use of an annular silicon diode backscatter detector. In this mode the electron beam is collimated; i.e., the beam is a pencil of parallel rays rather than a focused cone. The beam diameter was approximately 10-20 μm . The beam spot was held stationary on the sample while the angle of incidence was rocked by the scan coils. Distance on the channeling micrograph therefore corresponds to the angle of incidence of the electron beam and not to any physical distance on the sample. The beam energy used was 7 keV, which was derived from the following considerations. To sample a 0.2 μm layer with backscattered electrons, the electron range must be $> 0.4 \mu\text{m}$, which implies a beam energy greater than 6 keV.⁵ The detector is an unbiased silicon diode located above the sample. The signal from this detector is proportional to the energy of the detected electrons; i.e., this type of detector is insensitive to low-energy electrons. The 7keV electrons lose $\sim 6 \text{ keV}$ in 0.4 μm . Thus 7keV electrons backscattered 0.2 μm deep emerge with 1 keV of energy. The use of higher-energy electrons increases the total backscattered signal, but reduces the amount of modulation of that signal caused by the top silicon layer. Therefore, the real signal-to-noise ratio decreases. The use of lower-energy electrons reduces the depth of the sample probed and, because of the detector sensitivity, reduces the amount of modulation in the total backscattered signal. Also, the 7keV electrons have the advantage that they ionize a track through the oxide (which extends to a depth of 0.6 μm), which precludes charging from being a problem. Resolution is determined by the degree of collimation achieved, which is not directly related to beam current. A beam current of 0.1 μA was used to provide a good signal-to-noise ratio.

The samples were etched according to the Wright etch formulation.⁶ This solution etches crystalline silicon at a rate of 1.7 $\mu\text{m}/\text{min}$ and etches dislocations somewhat faster. For these 200nm-thick films an etch time of 10 s was

P. Roitman is at National Bureau of Standards, Semiconductor Electronics Division, Gaithersburg, MD 20899; G. E. Davis is at Northrop Electronics Division, Hawthorne, CA 94026. The work was sponsored in part by the Defense Nuclear Agency contract DNA LACRO 88-816.

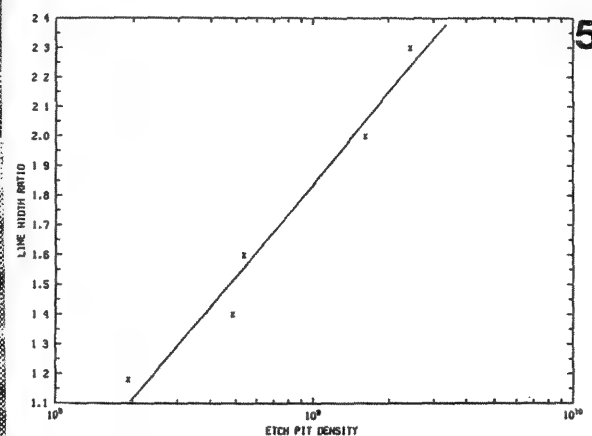
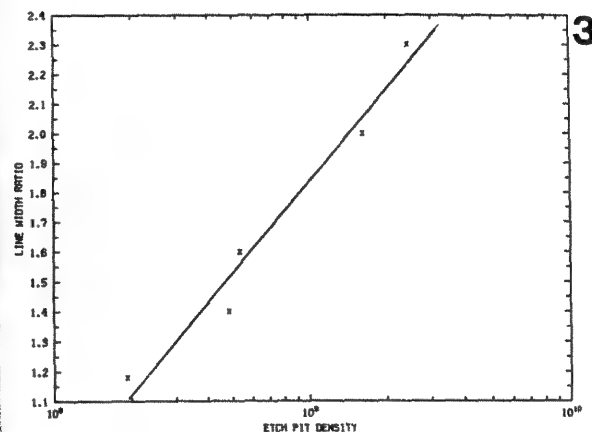
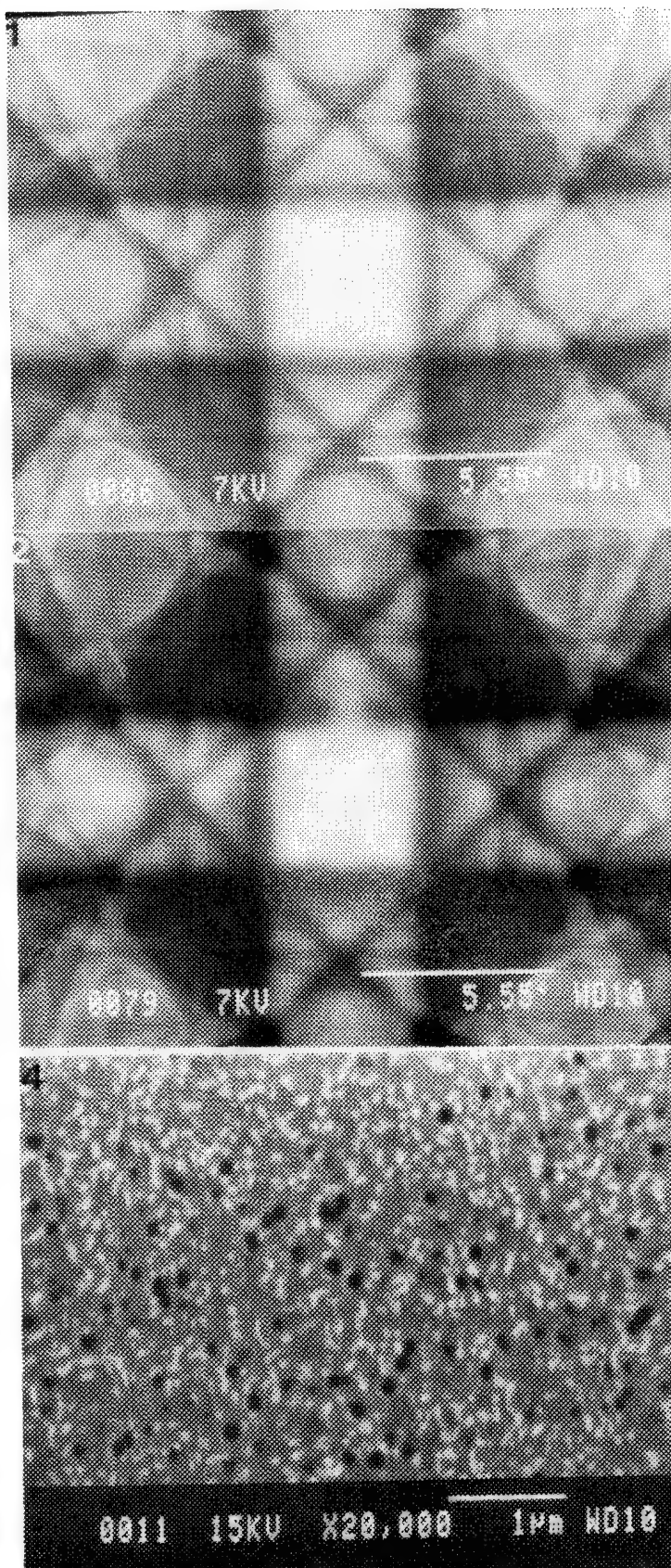


FIG. 1.--Selected-area channeling pattern for single crystal silicon.
 FIG. 2.--Selected-area channeling pattern for oxygen-implanted silicon sample C.
 FIG. 3.--Linescans on channeling patterns for samples A-E.
 FIG. 4.--Etch pits on sample D.
 FIG. 5.--Channeling pattern linewidth vs defect density.

determined to be effective. Etch times longer than 20 s resulted in a loss of the entire top layer. The diameter of the etch pits was therefore 50-100 nm. The samples were observed in the SEM in the normal secondary electron

mode at 20-40k× magnification.

Results

Two channeling pattern micrographs are shown in Figs. 1 and 2. Figure 1 is the reference pattern for single crystal silicon; Fig. 2 is the pattern from sample F. The patterns are superficially the same: the bright square in the center is the $\langle 100 \rangle$ Bragg reflection, the bands running horizontally and vertically are from the $\langle 110 \rangle$ planes, and the fainter and wider bands at 45° that touch the corners of the $\langle 100 \rangle$ pole are from the $\langle 100 \rangle$ planes. The fainter lines are due to reflections from increasingly higher-order planes. These geometric features are not altered by the presence of defects and disorder in the lattice. Rather, the width of the lines is increased.⁷⁻⁹ Since this effect is difficult to perceive in the pictures, a series of linescans were recorded through the center of the $\langle 100 \rangle$ pole in $\langle 110 \rangle$ direction for each sample; they are collected in Fig. 3. The angular scale was derived from the known spacing of the $\langle 100 \rangle$ and $\langle 110 \rangle$ planes in silicon;¹⁰ the vertical scale is arbitrary. The fine features clearly visible in the trace from sample A widen and decrease in amplitude in the traces for samples B, C, and D, and E and F. The width of the fine line in the center of each trace was measured and the ratio with a reference line measured on an etched portion of the same sample was determined. The ratios varied from 1.18 to 2.3.

Figure 4 is a micrograph of the etched surface of Sample C. The black dots are the etch pits due to dislocations. The white dots are believed to be due to oxide precipitates which have not etched as rapidly as the silicon matrix, which appears gray. The other samples appeared similar, except that sample B, which received a longer anneal, exhibited almost no precipitates. A series of micrographs was recorded and the etch pit densities were counted. The etch pit densities varied from 1.3×10^8 cm^{-2} to 2.4×10^9 cm^{-2} .

These results are collected in Fig. 5. There appears to be a linear relation between the width of the lines in the electron channeling pattern and the log of the dislocation density, at least over the range studied. This agrees with the results in Ref. 11 for steel.

Conclusions

Silicon films on buried oxide layers formed by oxygen implantation have been studied by selected-area channeling patterns and chemical etching. Neither technique provides the detailed information on defect morphology available from cross-sectional TEM, but both techniques appear capable of providing useful information on defect densities. Sample preparation for both is certainly easier than for TEM, and the channeling pattern approach is nondestructive. There is some promise that they can be extended to lower defect densities, although it is not clear how far. The analysis of the channeling pattern data and the correlation of that analysis with film quality need

to be more firmly established.

References

1. P. L. F. Hemment, E. Maydell-Ondruss, K. G. Stephens, J. Butcher, D. Ionannou, and J. Alderman, "Formation of buried insulating layers in silicon by the implantation of high doses of oxygen," *Nucl. Instr. and Methods* 209/210: 157, 1983.
2. B.-Y. Mao, P.-H. Chang, C.-E. Chen, and H. W. Lam, "The effects of oxygen dose on the formation of buried oxide silicon-on-insulator," *J. Appl. Phys.* 62: 2308, 1987.
3. Previous work in our laboratories.
4. D. C. Joy, "Electron channeling patterns: Principles and techniques," in *Quantitative Scanning Electron Microscopy*, New York: Academic Press, 1974.
5. T. E. Everhart and P. H. Hoff, "Determination of kilovolt energy dissipation vs penetration distance in solid materials," *J. Appl. Phys.* 42: 5837, 1971.
6. M. Wright Jenkins, "A new preferential etch for defects in silicon crystals," *J. Electrochem. Soc.* 124: 757, 1977.
7. J. P. Spencer, C. J. Humphreys, and P. B. Hirsch, "A dynamical theory for the contrast of perfect and imperfect crystals in the scanning electron microscope using back-scattered electrons," *Phil. Mag.* 26: 193, 1972.
8. E. M. Schulson, "Interpretation for the widths of SEM electron channeling lines," *Phys. Stat. Sol.* B46: 95, 1971.
9. D. C. Joy, D. E. Newbury, and D. L. Davidson, "Electron channeling patterns in the scanning electron microscope," *J. Appl. Phys.* 53: R81, 1982 and references therein.
10. R. W. G. Wyckoff, *Crystal Structures*, New York: Wiley, 1963.
11. R. Stickler, C. W. Hughes, and G. R. Booker, "Application of the SA-ECP method to deformation studies," *SEM/1971 I*, 473.

ANALYSIS OF METAL FILMS SUITABLE FOR HIGH-RESOLUTION SE-I MICROSCOPY

R. P. Apkarian and D. C. Joy

Accurate assessment of metal films used for high-resolution "SE-I mode" scanning electron microscopy (SEM) is integral for their application in high magnification ($>100\,000\times$) studies of biological structure.¹ Since modern SEMs equipped with condenser/objective (c/o) lens specimen stages can produce beam diameters of 0.7–2.0 nm when operated at high accelerating voltages (15–30 kV) and can operate in the SE-I mode, biological structures ranging from 2–10 nm can be accurately imaged with topographic contrasts. The sample to be observed must be coated with a metal film. The purpose of this coating is not primarily to eliminate charging, but to generate a defined contrast mechanism in which the topography of the sample is precisely delineated by changes in the SE-I yield occurring as a result of variations in the mass thickness of the deposited film. It is necessary that the metal film be continuous; ultra-thin (1–2 nm), so that the SE-I yield from it varies monotonically with its thickness; and of a grain size that is small in comparison with the image pixel size.^{1,2} Metals such as gold (Au), platinum (Pt), or gold/palladium (Au/Pd) are not ideal for the production of ultra-thin films because these materials have high mobility during deposition and tend to form island structures, and also have high electron scattering, which produces a noisy and low resolution background signal. Chromium (Cr) and tantalum (Ta) by comparison have low mobilities and low electron scattering, and thus "enrich" the SE-I signal.² Particulate test specimens of colloidal gold (20–40 nm) and ferritin (5 nm core diameter, 11–12 nm apoprotein particle diameter) deposited on a silicon chip have been used to determine suitable metal-deposition techniques and record available contrast.^{3,4}

Experimental

In this paper images of ferritin particles were analyzed in order to assess their dimensions and their contrast after coating with Cr and Au/Pd films. Test specimens of ferritin and colloidal gold particles were spread on silicon wafers as previously described.^{3,4} A 3 nm film of 60:40 Au/Pd was applied onto a group of specimens in a conventional low-volt-

age sputter system; another group of specimens was observed uncoated.⁵ A third group of samples were coated with 2 nm of Cr in a Denton DV-602 turbo-equipped sputter deposition system. The integral water cooled cathode (DSM-300A) was operated at 150 mA for 4 s at a target distance of 5 cm (2 in.). The deposition thickness had previously been calibrated by both an optical method and a quartz crystal thickness monitor.⁶ All specimen were imaged on both a Hitachi S-900 cold-cathode field-emission gun (FEG) SEM operated at 20 kV, and an ISI DS-130 SEM with a LaB₆ cathode, operated at 30 kV. Normal SE-I images were recorded from the CRT in the conventional manner; Y-modulated images (in which the normal brightness modulation signal is used to deflect the display spot in the y axis of the CRT) were also recorded to provide a means of measuring the width and relative contrast of the ferritin cores.

Results

Uncoated ferritin particles appear as diffuse disks⁷ approximately 10 nm in diameter when imaged in the ISI DS-130 with the LaB₆ cathode and c/o lens, and as bright disks again of about 10 nm diameter when imaged by the S-900 with the FEG and c/o lens (Figs. 1a–b). The FEG Hitachi S-900 was operated at 20 keV rather than at 30 keV because at the highest accelerating energy the uncoated ferritin cores created the predominant contrast and the apoprotein shell was lost in the background,⁸ whereas at 20 keV the entire ferritin particle was visible. Measurements from Y-modulation pictures of the uncoated cores showed that the maximum vertical excursion of the contrast profile varied from 6 to 10 units indicating visualization of either an individual core or the entire apoprotein (Figs. 1c–d). The Cr-coated samples were only marginally visible in the LaB₆ instrument (Fig. 2a), but the FEG SEM produced high-quality SE-I images of the cores with a diameter of about 13 nm and a vertical deflection in the y-modulation image of 15 units, i.e., about 50% greater than in the uncoated case, showing the contrast enhancement produced by the coating (Figs. 2b–c). Both SEMs imaged Au/Pd coated ferritin to the same 15 nm-diameter dimensions and produced maximum contrast levels of about 15 units, the same as the value recorded from the Cr-coated sample.

Increased background intensity was observed in the Hitachi S-900 images from the Au/Pd-coated specimens compared to that generated from the Cr-coated sample due to the enhanced electron scattering of the heavier material. Although there is also an increase in the contrast produced by the ferritin particle that we

R. P. Apkarian is with Yerkes Regional Primate Research Center, Emory University, Atlanta, GA 30329; D. C. Joy is with the EM Facility, University of Tennessee, Knoxville, TN 37996-0810. This research was supported by NIH grant RR-00165 from the Division of Research Resources to Yerkes Regional Primate Research Center.

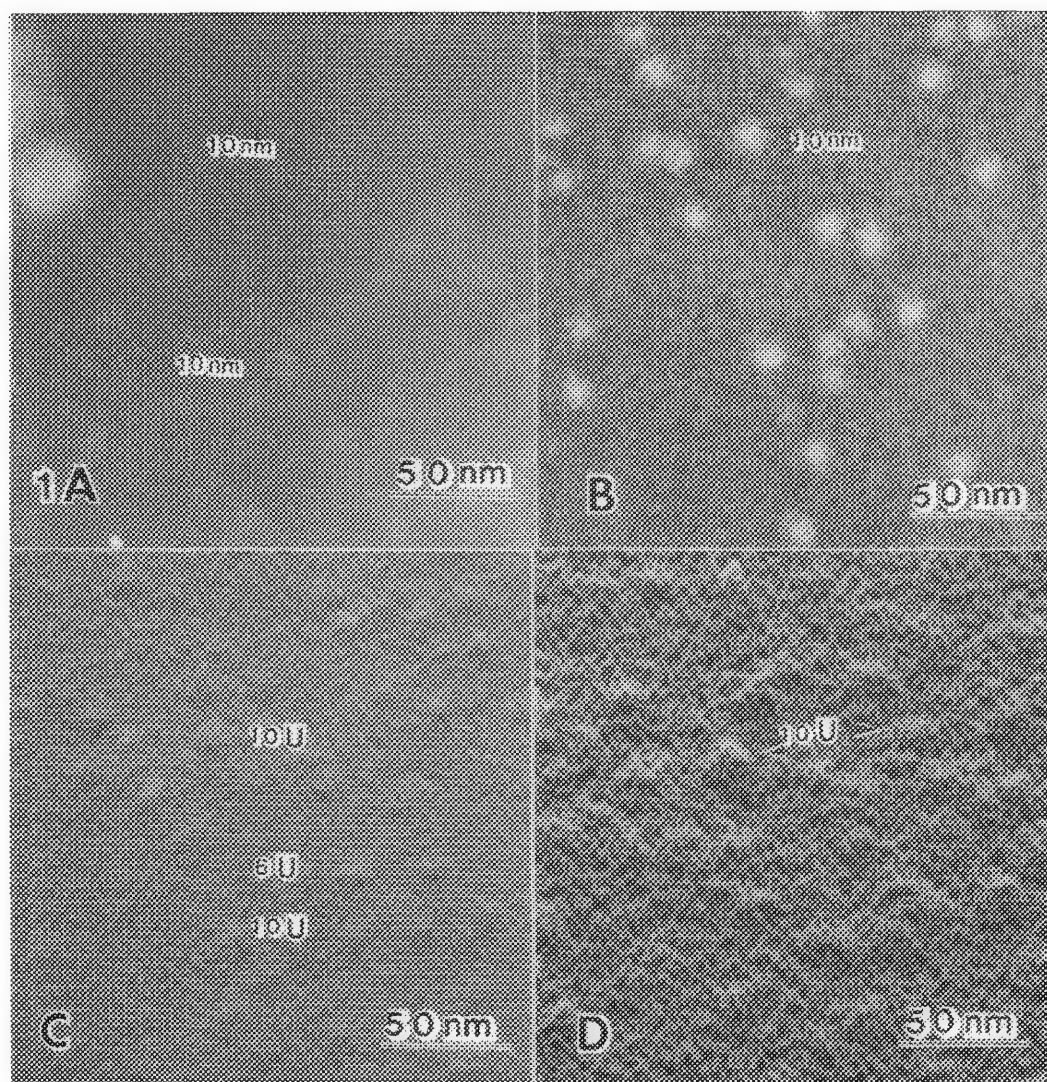


FIG. 1.--(a) and (c) Profiles of uncoated ferritin (from ISI DS-130/LaB₆ c/o lens SEM); (b) and (d) profiles of uncoated ferritin (from Hitachi S-900 FEG c/o lens SEM).

wish to image, the background intensity increases more rapidly than the particle intensity, leading to an overall decrease in the delineation of the ferritin. Although the same sort of variation must also occur for the ISI DS-130 images, the lower signal-to-noise ratio has the effect of partially masking the unwanted background contrast and so improving the edge definition of the particles.

Conclusion

On the basis of the images presented above we conclude that, when observed by either of the microscopes used in this investigation, the whole ferritin particles appeared to be evenly coated by the ultra-thin continuous metal films of either Cr (2 nm) or Au/Pd (3 nm). The measured width of the Cr and Au/Pd-coated ferritin particles was enlarged by approximately two times the metal-coating thickness; thus, quality images provided a useful measurement of the actual deposition thickness. Using this information one can therefore make an accurate de-

termination of the actual size of small (i.e., less than 10 nm) biologically significant structures in ultra-thin metal-coated bulk biological specimens. Due to the increased scattering of the secondary electrons in the Au/Pd film, resulting in a higher background signal component and a lower SE-I yield, quality images were not available from structures smaller than 10 nm in size. It is therefore evident that chromium represents the optimum choice for a coating metal for this regime of operation.

References

1. R. P. Apkarian, "Condenser-objective lens SE microscopy," *Proc. 45th Ann. EMSA*, 1987, 564.
2. K.-R. Peters, "Working at higher magnifications in scanning electron microscopy," *SEM/1985 IV*, 1579.
3. K.-R. Peters, in J. K. Koehler, Ed., *Advanced Techniques in Biological Electron Microscopy III*, New York: Springer-Verlag,

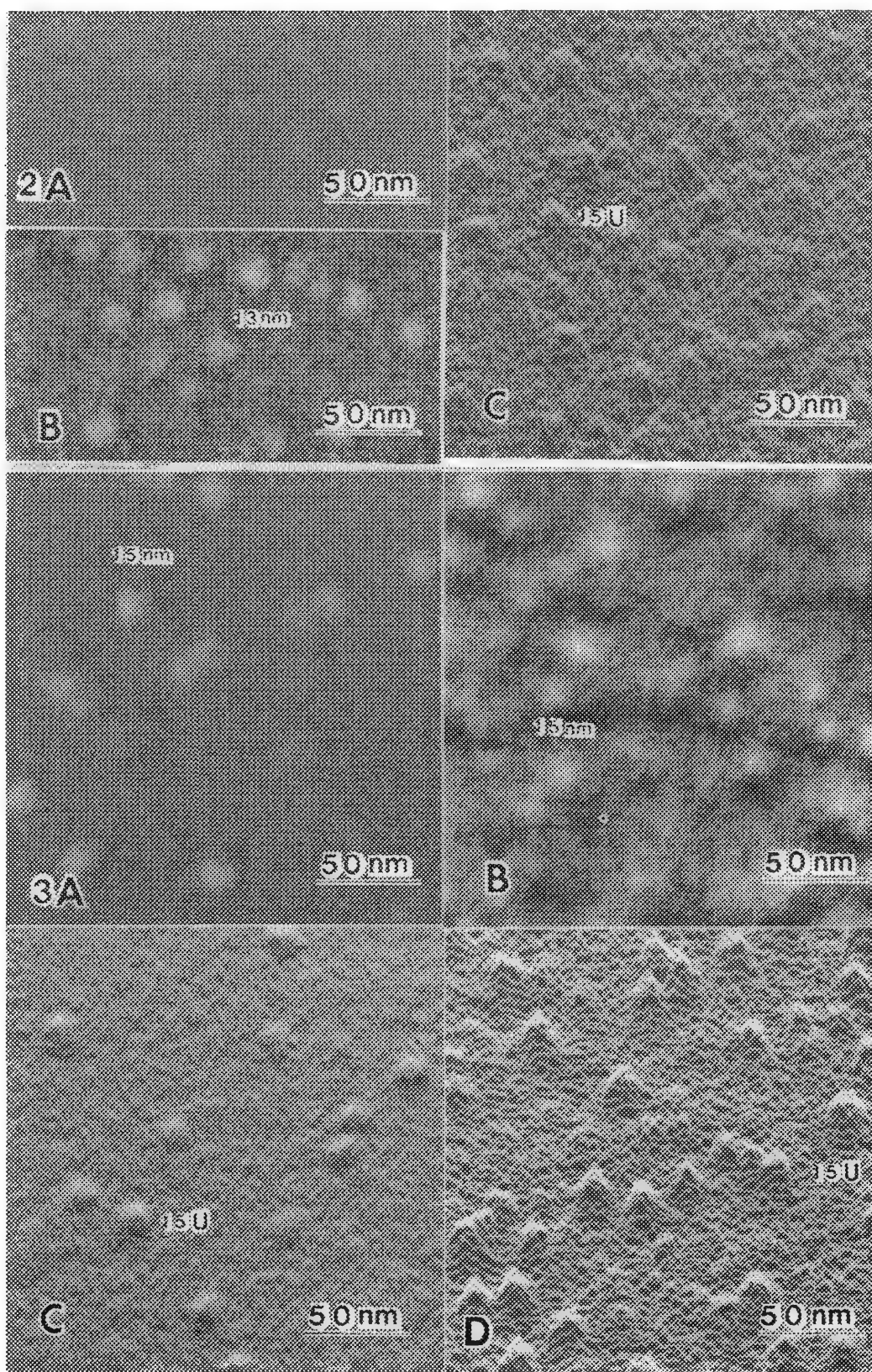


FIG. 2.--(a) 2nm Cr-coated ferritin from DS-130 SEM with LaB₆; (b) 2nm Cr-coated ferritin from S-900 with FEG.

FIG. 3.--(a) and (c) normal and Y-modulation images of 3 nm Au/Pd coated ferritin from DS-130; (b) and (d) normal and Y-modulation images of 3nm Au/Pd coated ferritin from S-900.

1986.

4. R. P. Apkarian, "High-resolution signal detection," *Proc. 44th Ann. EMSA*, 1986, 658.

5. R. P. Apkarian and J. C. Curtis, "Hormonal regulation of capillary fenestrae," *SEM/1986 IV*, 1381.

6. R. C. Specht and G. J. Lutz, "Chromium deposition by sputtering," *Proc. 44th Ann. EMSA*, 1986, 662.

7. D. C. Joy, "Simulation of high resolution SEM images," these proceedings.

8. R. P. Apkarian, "Ultra-thin metal coatings enhance high resolution SE-I contrast," 12th ed. (T. Nagatani, Ed.), *Hitachi Inst. News*, 1987, 22.

LOW-VOLTAGE SEM FOR METROLOGY AND INSPECTION

P. E. Russell

The SEM has rapidly evolved, in the two and one-half decades since commercialization, from a basic picture-taking instrument to become a highly sophisticated quantitative measurement system. The semiconductor industry has greatly benefited from the continuing expansion of capabilities and performance of the SEM and has led the drive for many of the recent development in the field.¹ In this paper, we discuss the development, use, and problems of low-voltage SEM for in-line inspection and metrology applications for semiconductor device manufacturing.

As pointed out by Postek and Joy,² in early uses the SEM, as a measurement tool for semiconductor device features, was regarded as the "correct" measurement. All too often a technician in a manufacturing environment would check the accuracy of his standard measurement technique (typically light optical imaging or electrical measurements) by comparing it to an SEM micrograph. The SEM micrograph was often considered to be the correct image, without distortion or calibration errors.

Historically, the SEM came to serve in semiconductor inspection and metrology as a complement to or extension of light microscopy techniques, which were then and remain today the standard techniques. Clearly, from the inspection point of view, the SEM provided two major advantages over light microscopy: magnification (or resolution) and depth of field. From the metrology side, the SEM provided what was in fact often a false sense of measurement accuracy. The SEMs utilized were typically those designed for general-purpose, high-resolution, and/or depth-of-field imaging of relatively small samples (typically 25 mm or less in maximum dimension). The SEMs simply were not designed to be metrology tools, and thus were highly limited in their ability to achieve reasonable precision and accuracy.

There are many important issues of relevance to both inspection and metrology, beginning with large differences between the two objectives, yet there is a growing tendency in many applications for the two techniques to merge. An example is automated mask inspection for defect identification.³

One of the most obvious issues to be considered is that of electron optics. The single most important improvement in SEMs for metrology and inspection has been in low-beam voltage optics.⁴ Low-voltage operation has the advantages of reduced specimen charging, reduced beam damage, and reduced volume of the beam

specimen interaction volume. Each warrants further discussion.

Specimen charging in an SEM results from an imbalance between the current of the primary beam into the sample and the current of the emitted electrons out of the sample. For examples such as integrated circuits with complex topographical and materials structures, charging effects are somewhat difficult to model and control. A typical device structure may contain several layers of material deposited on an Si substrate. The thickness of these layers may vary from 10's to 1000's of Angstroms. One or more of these layers will be an electrical insulators serving electrically to isolate the various conducting layers. SEM operators quickly realized that at normal SEM operating conditions of ~20keV beam voltages, these samples charged extensively. It was quickly determined by skilled operators, however, that at carefully chosen voltages, the charging could be reduced or in some cases eliminated. In general, this effect is due to high-voltage electron-beam-induced conductivity (EBIC) in the insulating regions: because of the extent of the interaction volume, all layers are in effect electrically connected to the conducting substrate. When the accelerating voltage is too low, the excitation volume is reduced and the excess charge (although generated in a region of induced conductivity) cannot bleed off to the substrate. When the beam voltage is too high, a complex relationship of the shape and size of the interaction volume and the reduction in secondary electron yield comes into play. In addition sample tilt can dramatically change the beam-excitation volume within a sample, which can also be used to avoid charging. The problem is that the applicable voltages are by design large enough to include the many sensitive interface and other active regions of a device within the excitation volume. The result is a high probability of beam-induced damage, particularly to interface states. Thus, the reduction of charging by proper choice of a relatively high beam energy (≥ 10 keV) partially solves the charging problem, but the technique is destructive and often has little or no advantage over metal-coating techniques to avoid charging. A more practical solution to the charging problem is to use lower accelerating voltages, where the total emitted electron yield (secondary plus backscatter yield) is equal to unity. Under these conditions, no net surface charge results and hence insulators can be imaged adequately. An important side effect of the low voltage needed for unity electron yield is a tremendous reduction in excited

The author is with the Materials Science and Engineering Department of North Carolina State University, Raleigh, NC 27695-7907.

volume which, in general, protects sensitive device areas from beam damage.

The problems of low-voltage SEM optics are of importance. In the past SEM optics were optimized for the smallest possible final spot size. Thus, in order to reduce the effect of chromatic aberration (which is proportional to $\Delta E/E$, where ΔE is the spread in the beam energy and E is the beam energy), high beam energies (i.e., > 25 keV) were commonly utilized. In addition to lens aberrations, source brightness, was found to limit attainable resolution, and hence brighter electron sources have been rigorously pursued and developed. In terms of brightness, this evolution followed from the W hairpin filament to LaB₆ filaments, both as thermionic emitters, to field-emission sources (and the closely related Schottky emitters). Fortunately, from the point of view of the low-voltage microscopist, the brighter sources also have a narrower energy spread, since LaB₆ has a lower emission temperature than W and cold-field emission even lower. Thus, the major optical improvement needed for the low-voltage SEM was a reduction of C_c of the objective lens.

The low-voltage SEM has been found to have a large number of additional problems that appear once the basic optics is in place: the effect of external fields,⁵ the effect of internal fields due to contamination or other column defects, and the effect of the detector and its associated field. Also, in addition to optics-related effects, the beam-specimen interaction effects are considerably different at low voltages.^{6,7}

Perhaps the easiest of the problems to control is the detector and its associated electric fields--by the use of an above-the-lens detector, a symmetric pair of detectors, or axially symmetric microchannel plate detectors.⁸ All these approaches have now proved to be viable in commercial metrology systems: the detector is not the limiting factor in LVSEM metrology systems. Yet for non-normal beam incidence, the above detector solutions all have particular problems. Thus, for inspection applications, where sample tilt is often required, continued detector development is needed. A final point of importance regarding detectors is the energy response function of detectors. Although straightforward to characterize for a particular detector system, the optimization of detector response (vs electron energy) cannot be performed until more detailed understanding of the emitted electrons and their various energy components is attained.

The area of greatest importance in the author's opinion to the further development and quantification of LVSEM is beam-specimen interaction effects.⁷ There is a parallel here to the development of quantitative x-ray microanalysis, which has benefited greatly from improved modeling and understanding of the beam specimen interaction effects, including excited volume effects. The current effects to model and experimentally determine the

LV beam-specimen interaction effects are very small by comparison with the effects extended in the x-ray analysis case. However, the need is certainly as large and the problems are perhaps more complex.⁹ A casual review of the beam-specimen-interaction modeling literature quickly reveals a lack of consistency in the low-voltage (< 5 keV) area. As this voltage regime is not critical to the x-ray analysis community, it has largely gone undeveloped. As evidenced by this conference, however, current work in progress is aimed at resolving these present shortcomings.

For the particular applications of LVSEM metrology and inspection of semiconductor wafers, there is an ever-present problem of beam-induced specimen contamination. The source of contamination is typically the sample itself, or the vapors present in the SEM vacuum. We have found extensive experimental differences in LVSEM results obtained in a typical diffusion or turbo-pumped SEM and an ultrahigh-vacuum SEM. Secondary-electron yields are found to vary substantially depending on the actual surface conditions of a sample. This is a critical point with respect to modeling the beam-specimen interaction in that it is very difficult to model actual surface conditions of the samples of interest. Experiments are under way to combine in situ ion-beam sputtering with a retarding field analyzer in an ultrahigh-vacuum SEM with an Auger electron spectrometer to quantify the effect of surface chemistry on secondary and backscattered yields. This in turn is being utilized to aid the development of edge detection algorithms for metrology and automated inspection applications.

Although considerable effort has been and continues to be devoted to the development of edge-detection algorithms, it is clear that truly accurate edge detection can only occur after our understanding of low-voltage beam-specimen interaction effects are developed. Other issues of importance to LVSEM metrology and inspection systems, which can only be briefly mentioned here, include sample stage automation and interfacing to a CAD-based design system, sample alignment on the stage, scan calibration, sample exchange systems, and the user interface appropriate for nonscientific operators.⁸⁻¹⁰

It is important to consider the overall approach currently being pursued to address to above problems. From the progress to date, it is evident that LVSEM will play an important role in metrology and inspection systems, and thus move more and more into a manufacturing regime, far afield from the original imaging purpose for SEMs were developed. We must also look at potential new techniques that can contribute to the field. An example is the use of a scanning tunneling microscope for metrology applications. This concept has been around for many years and is being aggressively pursued from slightly different points of view. It is, however, low-voltage (< 5 eV) scanned-electron-beam (via the source) microscopy.

The elimination of lenses has many of the advantages of the current LVSEM approach. The mechanical versus electromagnetic deflection system offers some unique opportunities for calibration. Again, the limiting factor is in the understanding of the beam-specimen interactions and particularly the true surface of the sample under manufacturing conditions. This example underlines that we must not limit our effects to only one possible solution of the very important issue of micrometrology.

In summary, many of the areas of importance to LVSEM for metrology and inspection have recently approached maturity. Other areas, in particular beam-specimen effects, are still in their infancy. LVSEMs are rapidly finding their place in manufacturing environments as tools rather than research instruments, and the research needed to perfect these tools will continue.

References

1. P. E. Russell, "SEM-based characterization techniques," in N. Chang and M. A. Nicolet, Eds., *Materials Characterization*, Materials Research Society, 1986, 15-22.
2. M. T. Postek and D. C. Joy, "Submicrometer microelectronics dimensional metrology: Scanning electron microscopy," *J. Res. NBS* 92: 205-228, 1987.
3. S. Tukeuchi, K. Saitoh, N. Yoshioka, and T. Kato, "E-beam inspection technology for x-ray masks," *J. Vac. Sci. Tech.* 86: 146, 1988.
4. M. T. Postek, W. J. Keery, and R. D. Larrabee, "The relationship between accelerating voltage and electron detection modes to linewidth measurements in a SEM," *Scanning* (in press).
5. J. B. Pawley, "Strategy for locating and eliminating sources of mains frequency stray magnetic fields," *Scanning* 7: 43-46, 1985.
6. D. C. Joy, "Resolution in low voltage scanning electron microscopy," *J. Microsc.* 140: 283-292, 1985.
7. D. C. Joy, "Image modeling for SEM-based metrology," *Proc. 44th Ann. Meetg. EMSA*, 1986, 650-651.
8. P. E. Russell and J. F. Mancusco, "Microchannel plate detector for low voltage SEM," *J. Microscopy* 140 (Pt. 3): 323-330, 1985.
9. S. Erasmus, "Damage to resist during SEM inspection," *J. Vac. Sci. Technol.* B5: 409-413, 1987.
10. T. Ohtaka, S. Saito, T. Furuya, and O. Yamada, "Hitachi S-6000 field emission CD-measurement SEM," *SPIE Proc.* 565: 205-208, 1985.
11. P. E. Russell, T. Namae, M. Shimada, and T. Someya, "Development of SEM-based dedicated IC metrology system," *SPIE Proc.* 480: 01-108, 1984.
12. H. Yamaji, M. Miyoshi, M. Kano, and K. Okumura, "High accuracy and automatic measurement of the pattern linewidth on very large scale integrated circuits," *SEM/1985 I*, 97-102.

SEM IMAGING AND ANALYSIS OF SUBMICROMETER PARTICLES IN AIR AND WATER SAMPLES

E. B. Steel

The scanning electron microscope (SEM) has seen considerable use in characterizing the particulate populations associated with air and water samples. However, the SEM is limited in particle visibility and analytical sensitivity as the particle size decreases below a micrometer and into the nanometer range. In this range, the secondary-electron, backscatter-electron, and x-ray yields from a particle can be very small compared to a bulk filter sample substrate. This paper describes results from research into various ways of improving imaging and x-ray analysis from such small particles. Many parameters were studied that would affect the imaging of submicrometer particles. Image contrast was measured as a function of types of substrate filters, sample substrate thickness, conductive coatings, accelerating voltage, and CRT raster rate. The particle applications used as test specimens were chrysotile and amosite asbestos and a fiberglass. A method of sample preparation was found that enhances the visibility of small particles and allows for improved x-ray sensitivity.

Sample Substrate

The ideal sample substrate for these small particles would be used to collect the specimen directly with no need for subsequent transfer, require a minimum of sample preparation, contribute negligible electron and x-ray signal compared to the particles, have a minimum of texture or surface detail to allow easy imaging and thresholding of the particles for automated analysis, and be stable under the electron beam for normal electron doses used for imaging and x-ray analysis.

Filters

A convenient way of collecting particulate matter from gases and liquids is through filtration, where the number and type of particles can be determined quantitatively as a function of the volume of the filtrate. It was found that the type of filter could dramatically affect image quality and particle visibility on the SEM. Three types of filters commonly used for air and water sampling were investigated: a 0.4 μ m polycarbonate, a 0.45 μ m cellulose ester filter, and a 0.45 μ m polyvinyl chloride (PVC) copolymer filter. These filter materials each give different secondary electron yields and have differing electron beam damage rates and quite different morphological structures.

The author is with the National Bureau of Standards, Center for Analytical Chemistry, Gaithersburg, MD 20899.

The polycarbonate filter is approximately 10 μ m thick, with a flat surface and randomly dispersed pores over the surface. At all voltages, the secondary electron yield around the pores is high and gives the image a complexity that cannot be avoided and that may give image analyzers problems differentiating between filter artifacts and particles.

Both the mixed cellulose ester (MCE) and copolymer (PVC) filters are tortuous-path filters that have considerable surface topography which impairs the visibility of small particles (Fig. 1). To overcome this difficulty, these filters may be collapsed in acetone vapor or with a dimethyl formamide solution to yield a flat surface with the particles at or near the surface of the filter.^{1,2} An oxygen plasma etch is performed to expose the small particles near the surface. This step etches away the surface of the filter and places the particles on mesa-like pedestals. When the three filters are compared with this treatment applied to the MCE and PVC filters (Fig. 2), the MCE has the lowest secondary electron yield, the PVC next, and the polycarbonate the highest. From this information it was decided to try using the MCE filters; however, after a short time it was noted that the MCE filters damage readily under the electron beam, so that their utility is reduced as both surface topography and mottled surface contrast are introduced. The PVC and polycarbonate filters are relatively stable. From these experiments it was determined that if filters were to be used as substrate, the PVC filter yielded the best compromise for a smooth nondetailed background image with a low secondary-electron yield, which produces a high particle-to-background secondary-electron signal and a minimum of confusing detail (pores) for automated particle analysis.

Specimen Substrate Thickness

At 15 kV the submicrometer particles are generally at least partially transparent to the electron beam: the electron may pass directly through the particles into the specimen substrate or filter and can cause the emission of secondary electrons and x rays there. In order to maximize the particle-to-substrate secondary-electron ratio and increase the characteristic x-ray signal from the particle compared to the continuum x-ray emanating from the substrate, it is most useful to use a thin substrate, i.e., to eliminate the filter altogether.³ One can achieve this goal by carbon coating the surface of the filter, placing a section of the filter on a transmission electron microscope (TEM)

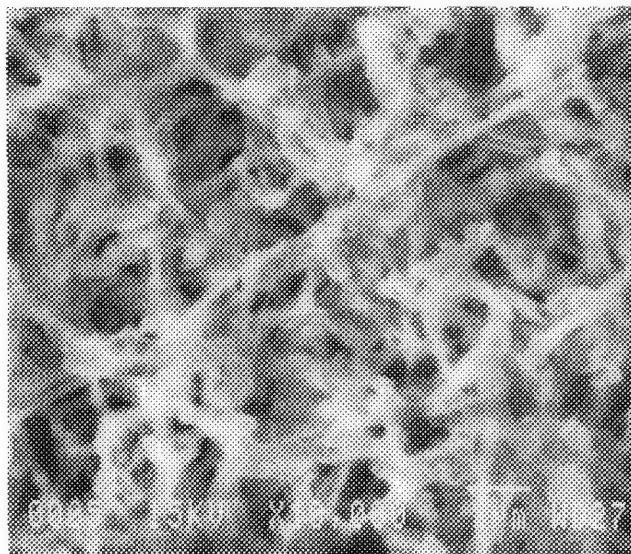


Fig. 1.--Electron micrograph of surface of MCE filter before collapse showing detailed topography of tortuous-path filters that reduces visibility of small particles. Asbestos fibers are visible when they pass over voids in filter, but in areas where they touch the filter, they are very difficult to see.

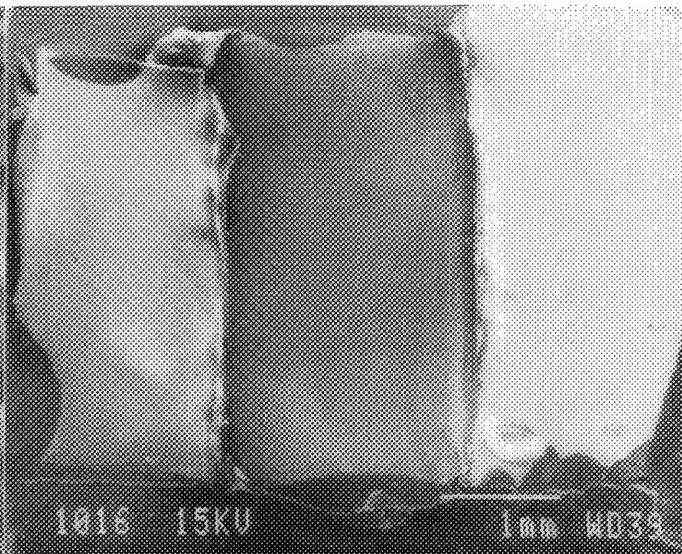


Fig. 2.--Electron micrograph comparing the three filter types. Polycarbonate filter at right has highest emission; PVC at left, intermediate; and MCE, in middle, lowest secondary-electron emission at 15 kV.

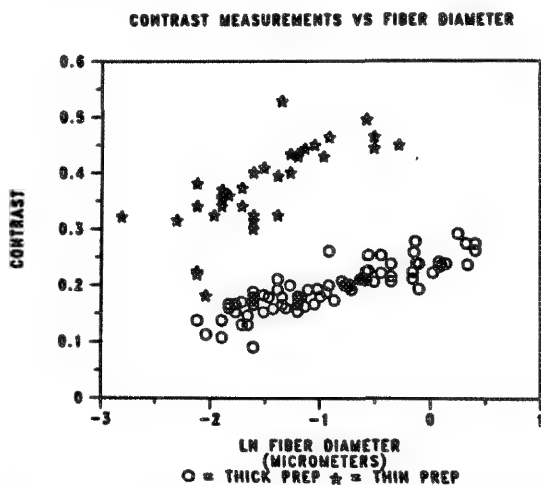


Fig. 3.--Plot displaying higher contrast of particles on thin-films than particles on bulk filters.

specimen grid, and dissolving the filter in a solvent. This dissolution leaves the particles trapped in a thin-film carbon replica of the filter surface supported by a TEM grid.^{1,2} Figure 3 shows the relative secondary-electron signal contrast for a set of carbon-coated thin particles over a filter substrate and the contrast after the substrate has been dissolved away. It was found that the thin-film preparation from the collapsed, etched, carbon-coated MCE and PVC filters yielded the highest image quality for the smallest particles, probably due to the fact that the topographical features immediately surrounding the particles are enhanced by the etching process. The same sample-preparation process with no or very

little plasma ashing shows much lower particle image contrast.

Primary Beam Voltage

All the filter types and sample-preparation techniques consistently show that low voltages favor the imaging of the particles on the surface over the imaging of the filter. If only imaging is desired, a low voltage (<5 kV) can be chosen that optimizes beam current, spot size, and signal information for the specific application, and dissolution of the filter is not necessary. However, if x-ray analysis is necessary for determining the chemical nature of the particles, a higher voltage is most likely necessary. Since our samples often have the elements from Na through Fe, we chose a voltage of 15 kV, well above the Fe K absorption edge, so that the Fe K lines are reasonably efficiently excited. At this voltage most elements in the periodic table have an x-ray line observable in the range 0-10 keV. Again, 15 kV is a compromise. One sacrifices some particle visibility to gain chemical composition data.

CRT Raster Rate

It is well known that the SEM raster rate affects image quality.⁴ However, little data appear to be available on this effect. It is the raster rate that often controls the image visibility during live-time viewing of a specimen on the SEM. When dealing with SEM imaging capability, researchers often overlook the significant difference between the slow-raster, statistically high-quality SEM micrographs and the typically fast-raster and therefore statistically poor-quality live-time images. Figure 4 shows a line scan across two

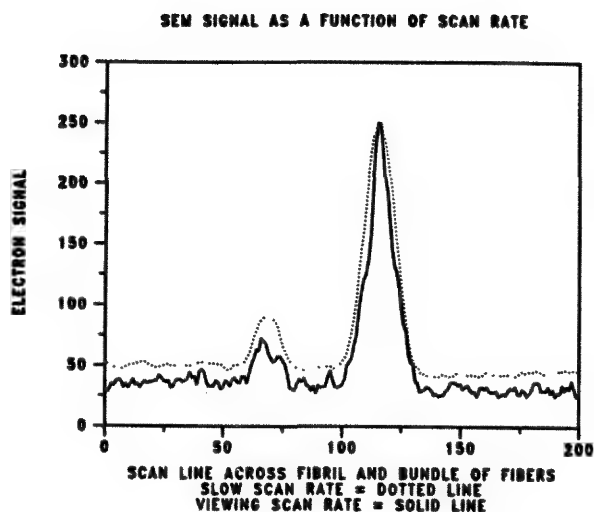


Fig. 4.--Secondary electron signal as seen in linescan across two fibers at two scan rates. Smaller peak is from a single fibril (approximately 40 nm thick) of chrysotile; larger peak is thicker bundle of fibers. Lower trace (with higher noise) is 0.9 s raster; upper trace (with lower noise) is 60 s raster.

fibers showing the difference in the contrast due solely to raster rate (or digital sampling rate for digitally controlled systems). The signal-to-background for the thick fiber is well above the noise level and could be discerned at either the fast (viewing) or slow (photographic) raster; however, the thin fiber is barely visible at the fast raster while easily visible at the slow raster. Thus, care must be taken to analyze image contrast conditions in the state in which the instrument is actually used for analysis. This means that particles visible in micrographs may not be visible in the live-time viewing mode. As a consequence it is extremely misleading to employ scanning SEM micrographs of small particles, such as asbestos fibers, as a proof of the imaging capability of an SEM when these samples are analyzed manually from a high-speed raster CRT image and not from photographs.

Conclusions

A sample-preparation scheme using collection of particulate on MCE or PVC filters followed by collapsing, oxygen plasma etching, carbon coating, and filter dissolution allows very small, thin particles to be readily seen, photographed, and analyzed with good image contrast and high-sensitivity x-ray analysis. Methods employing bulk substrates such as filters or graphite blocks have both poorer image contrast and elemental sensitivity in x-ray analysis. Thin film techniques that do not employ the plasma ashing have greatly reduced particles visibility or contrast in comparison.

References

1. G. J. Burdett and A. P. Rood, *Env. Sci. Technol.* 17: 643-648, 1983.
2. National Institute of Occupational Safety and Health Method 7402, 1987.
3. J. A. Small et al., K. F. J. Heinrich, Ed., *Characterization of Particles*, NBS Special Publication 533, Gaithersburg, MD., 1980.
4. J. I. Goldstein et al., *Scanning Electron Microscopy and X-ray Microanalysis*, New York: Plenum Press, 1981, 175.

BENCE-ALBEE AFTER 20 YEARS: REVIEW OF THE ACCURACY OF α -FACTOR
 CORRECTION PROCEDURES FOR OXIDE AND SILICATE MINERALS

J. T. Armstrong

Twenty years ago, Arden Albee and Ted Bence wrote a paper in the *Journal of Geology* proposing the use of empirical α -factors to correct electron microprobe analyses of oxide and silicate minerals,¹ similar to procedures proposed by Ziebold and Ogilvie for binary metal alloys² and by Lachance and Traill for x-ray fluorescence analyses.³ This paper has become one of, if not the most cited paper in the geological sciences, which is a tribute both to the success and popularity of the analytical technique and to the important role microbeam analysis plays in geology. In the intervening years, although the original papers emphasized that new empirical α -factors should be developed,^{1,4} and other studies indicated that the original α -factors produced some systematic errors in processing geological data, most investigators have continued to use the corrections as originally formulated. In the present study, the Bence-Albee correction is evaluated in comparison with the current generation of ZAF, $\phi(\rho z)$, and Monte Carlo corrections. We show that with some modifications the α -factor corrections can be as accurate as any other correction procedure currently available and much easier and quicker to process.

Basics of the α -factor Procedures

The Bence-Albee correction is based on two assumptions.^{1,4}

1. In binary oxide systems AB, there is a hyperbolic relation between concentration and intensity such that

$$(1 - K_{AB}^A)/K_{AB}^A = \alpha_{AB}^A(1 - C_{AB}^A)/C_{AB}^A \quad (1)$$

or

$$C_{AB}^A/K_{AB}^A = \alpha_{AB}^A + (1 - \alpha_{AB}^A)C_{AB}^A \quad (2)$$

where C_{AB}^A is the concentration of A in the binary relative to the end member oxide (i.e., the oxide weight fraction), K_{AB}^A is the ratio of the background-subtracted x-ray intensity of A in the binary relative to that in the end member oxide, and α_{AB}^A , the α -factor, is a con-

stant for the binary. If this assumption is correct, the plot of C/K vs C is a straight line, the y-intercept of which is equal to the α -factor, as is 1 minus the slope.

2. In multicomponent oxide systems, C/K is equal to the concentration-weighted sum of the α -factors for each of the binaries:

$$C_{ABC...n}^A/K_{ABC...n}^A = \sum_1^i (C_{ABC...n}^i \alpha_{Ai}^A) / \sum_1^i C_{ABC...n}^i \quad (3)$$

One can determine the α -factors either experimentally by performing a multiple least-squares fit of C/K vs composition for a series of analyzed standards,^{1,5} or theoretically by calculating C/K from a ZAF correction procedure for various compositions in binary oxide systems, and then performing least squares fits of C/K vs C .⁴

Bence and Albee noted in their initial paper that in binary systems where there was either a large fluorescence or a large absorption correction, the linear relationship between C/K and C did not hold. Other investigators have proposed that more accurate results could be obtained if the constant α -factor term was replaced with a polynomial function of concentration,^{6,7} although this conclusion has been disputed.⁵ In none of these papers were the magnitudes of the deviations from linearity of the Bence-Albee equation evaluated for any considerable range of binary oxides. In a recent series of papers,⁸⁻¹⁰ Armstrong has demonstrated that the α -factor approach can be successfully applied to the quantitative analysis of particles and thin films, in addition to conventional thick polished specimens, but that the accuracy of the procedure can be significantly improved if α -factors are calculated from newer ZAF and $\phi(\rho z)$ algorithms. However, these papers did not evaluate the magnitude of the nonlinearity in C/K vs C relations, either.

α -factor Calculations

Series of α -factors were calculated for a 102×102 oxide matrix spanning the periodic table. ZAF and $\phi(\rho z)$ correction procedures employed were those tabulated in a companion paper (see Table 1 in Ref. 11). Correction factors were calculated for the 1:0, 3:1, 1:1, 1:3, and 0:1 oxide combinations for each binary (e.g., CaO, Ca₃SiO₅, CaSiO₃, CaSi₃O₇, and SiO₂ for the binary CaO--SiO₂). From these values a least-squares fit was made of C/K vs C , and the α -factor was calculated. The maximum deviations of C/K from the least-squares-fit lines were stored along with the α -factors. In cases where the deviation exceeded a threshold value (typically 0.05%),

The author is at the Division of Geological and Planetary Sciences, California Institute of Technology, Pasadena, CA 91125. The analytical assistance of Art Chodos, the provision of Monte Carlo calculation programs by David Joy, and the helpful comments of Arden Albee are all deeply appreciated. This work was supported in part by funds from the National Aeronautics and Space Administration through grant NAG 9-43. Division Contribution 4616(621).

the nominal α -factor for each composition was calculated from the relation:

$$\alpha = [(C/K) - 1]/(1 - C) \quad (4)$$

and a second-order polynomial fit was performed to determine the variation of the α -factors with concentration.

Monte Carlo calculations of electron trajectories were performed by use of both multiple-scattering and single-scattering models to calculate $\phi(\rho z)$ distributions for similar ranges of compositions in selected binary oxide systems. These $\phi(\rho z)$ distributions were then used to calculate absorption and atomic number corrections and combined with a conventional characteristic fluorescence correction¹¹ to calculate C/K vs C. The calculations were performed with modified versions of the Monte Carlo programs written by David Joy.^{12,13} The multiple-scattering program uses a screened Rutherford cross section based on the models of Cargenven and Duncumb¹⁴ and constants of Bishop¹⁵ and Myklebust et al.¹⁶ The single-scattering model is similar to that developed by Newbury et al.¹⁶⁻¹⁸ The programs were modified to work with multi-element samples by generating a random number at each electron step and determining which element in the sample is involved in the scattering by application of the random number to the relative values of the atom-concentration-weighted ionization cross sections for the given electron energy. The number and energy distribution of electrons passing through each ρz increment were stored and then multiplied by a series of ionization cross section expressions to calculate the $\phi(\rho z)$ distributions. The ionization cross section expressions tested were those of Green and Cosslett, Worthington and Tomlin, Hutchins, Gryzinski, and Fabre (see Powell¹⁹ for equations and references).

All the ZAF, $\phi(\rho z)$, and Monte Carlo corrections agree closely in the shapes of the C/K vs C curves or lines for all the systems tested, although the magnitude of the intercepts and slopes varies from expression to expression. Table 1 lists selected α -factors calculated for an accelerating potential of 15 keV and a take-off angle of 40° with the $\phi(\rho z)$ absorption correction of Armstrong and atomic-number correction of Love and Scott (Arms-LS).¹¹ Figure 1 shows typical C/K vs C values determined from Monte Carlo calculations.

Table 2 lists the maximum percentage deviations of C/K from the best-fit α -factor lines for the binary systems given in Table 1. As can be seen, many of the binary systems show significant deviations from the constant α -factor assumption. In many cases, the deviations exceed 1% (including geologically important binaries such as Na₂O:Al₂O₃, MgO:Al₂O₃, Al₂O₃:SiO₂, MgO:FeO, and Na₂O:CaO) and in extreme cases are greater than 30%.

All the correction procedures tested give similar results regarding the frequency and nature of the deviations from linear fits of

C/K vs C. An element in a binary system that has small absorption and fluorescence corrections closely fits the straight-line C/K vs C relation (i.e., it has a composition-independent, constant α -factor). In binary systems where the two elements are similar in atomic number, but one is heavily absorbed (the fluorescing element), that element exhibits significant deviations from a straight-line C/K vs C relation. However, the calculated α -factors in those cases are found to vary linearly with concentration. In binary systems where the two elements are dissimilar in atomic number and one is heavily absorbed (particularly when it is also heavily absorbed by oxygen), a plot of calculated α -factor vs oxide concentration precisely fits a second-order polynomial function. In binary systems where one of the elements is significantly fluoresced by other, a plot of α -factor vs oxide concentration for the fluoresced element approximately fits a second-order polynomial. Figure 2 shows typical α -factor vs concentration plots for these cases.

Table 3 gives the results of second-order polynomial fits of α -factors vs concentration for selected of the binary systems presented in Table 1 (using the same Armstrong--Love/Scott correction) and Table 4 lists the maximum percentage deviations of C/K from the second-order polynomial α -factor fits for all the cases shown in Table 2. As can be seen, the deviations drop dramatically when the polynomial expression is used. The maximum relative deviation is 1% and deviations greater than 0.1% are rare. This has been found to be true for all of the binaries spanning the periodic table and all the major ZAF, $\phi(\rho z)$, and Monte Carlo calculations examined. In other words, replacing the constant α -factor approximation with a simple second-order polynomial function of concentration results in the α -factor procedure *exactly* duplicating the results of the correction procedure on which it is based. The only modifications to the conventional Bence-Albee procedure required to use this polynomial approach are (1) to replace the constant α -factor in Eq. (3) with the polynomial equation:

$$\alpha_{AB}^A = c + d[C_A/(C_A + C_B)] + e[C_A/(C_A + C_B)]^2 \quad (5)$$

where C_A and C_B are the oxide weight fractions of the elements in each calculated binary, and (2) to store three matrices of c , d , and e coefficients instead of the single α -factor matrix. Under these circumstances, there is no reason not to replace the ZAF, $\phi(\rho z)$, or Monte Carlo correction by the much simpler and faster polynomial-modified Bence-Albee correction when one is analyzing silicates or oxides.

Best-fit α -factors

To determine the accuracy of the newly calculated α -factors, a set of standards minerals and glasses in the system MgO-Al₂O₃-SiO₂-CaO previously described by Shaw and Albee⁵ were

TABLE 1.--Calculated oxide α -factors from Armstrong/Love-Scott correction.

EO = 15 KEV, PSI = 40 DEGREES

Emitting																								
Line.:	O	K	C	K	F	K	Na	K	Mg	K	Al	K	Si	K	P	K	S	K	Cl	K	K	K	Ca	K
O	1.000	1.169	6.460	1.846	1.372	1.213	1.114	1.085	1.052	1.152	1.102	1.070												
CO2	2.003	1.000	5.546	1.625	1.258	1.145	1.074	1.061	1.038	1.144	1.102	1.072												
F	1.064	1.685	1.000	2.171	1.519	1.277	1.131	1.075	1.024	1.108	1.046	1.012												
Na2O	1.486	3.109	2.310	1.000	2.037	1.589	1.326	1.205	1.114	1.180	1.086	1.042												
MgO	1.693	3.598	3.183	1.154	1.000	1.722	1.414	1.271	1.158	1.226	1.120	1.073												
Al2O3	1.868	3.927	3.727	1.261	1.027	1.000	1.474	1.305	1.183	1.235	1.118	1.068												
SiO2	2.100	4.316	4.264	1.372	1.099	1.016	1.000	1.361	1.225	1.273	1.145	1.091												
P2O5	2.292	4.533	4.607	1.440	1.136	1.042	0.971	1.000	1.254	1.290	1.146	1.088												
SO3	2.545	4.854	5.036	1.522	1.187	1.082	1.007	0.975	1.000	1.325	1.169	1.108												
Cl	6.281	11.36	3.649	1.206	0.987	0.925	0.869	0.831	0.763	1.000	1.271	1.152												
K2O	7.025	1.098	5.078	1.571	1.199	1.074	0.988	0.951	0.898	0.943	1.000	1.203												
CaO	6.951	1.167	5.869	1.757	1.309	1.153	1.051	1.010	0.959	1.018	0.861	1.000												
TiO2	5.889	1.297	6.665	2.071	1.463	1.235	1.093	1.034	0.977	1.044	0.933	0.858												
V2O3	7.348	1.400	7.122	2.295	1.575	1.294	1.122	1.046	0.980	1.042	0.933	0.865												
Cr2O3	1.237	1.616	7.131	2.530	1.704	1.376	1.177	1.086	1.011	1.072	0.965	0.902												
MnO	1.326	1.797	7.653	2.913	1.900	1.484	1.235	1.116	1.024	1.075	0.961	0.901												
FeO	1.452	2.065	2.098	3.226	2.072	1.592	1.305	1.167	1.062	1.110	0.991	0.932												
NiO	1.755	2.684	2.247	4.002	2.490	1.846	1.464	1.275	1.139	1.172	1.034	0.975												
ZnO	2.103	3.472	2.382	3.081	3.017	2.145	1.633	1.371	1.191	1.202	1.038	0.971												
SrO	4.466	5.978	3.726	1.538	1.151	1.005	0.937	1.848	1.615	1.491	1.138	1.027												
ZrO2	4.740	4.694	4.529	1.727	1.266	1.089	0.967	0.951	1.536	1.549	1.181	1.066												
BaO	1.501	1.126	1.709	2.694	2.389	1.991	1.521	1.269	1.087	1.077	0.885	0.804												
HfO2	2.971	2.596	3.117	1.518	1.172	1.038	1.863	1.491	1.329	1.482	1.095	0.973												
ThO2	3.323	0.410	3.549	2.315	1.657	1.361	1.150	1.035	0.936	0.966	0.842	1.023												

Emitting																								
Line:	Ti	K	V	K	Cr	K	Mn	K	Fe	K	Ni	K	Zn	K	Sr	L	Zr	L	Ba	L	Hf	L	Th	M
O	1.114	1.149	1.142	1.184	1.175	1.177	1.240	1.169	1.129	1.340	1.548	1.255												
CO2	1.119	1.155	1.149	1.191	1.183	1.186	1.250	1.139	1.110	1.346	1.560	1.253												
F	1.050	1.080	1.072	1.110	1.101	1.102	1.160	1.208	1.135	1.262	1.447	1.204												
Na2O	1.070	1.098	1.088	1.124	1.113	1.112	1.169	1.389	1.263	1.287	1.459	1.258												
MgO	1.098	1.126	1.115	1.152	1.140	1.138	1.196	1.462	1.320	1.320	1.494	1.298												
Al2O3	1.089	1.115	1.103	1.139	1.127	1.124	1.181	1.518	1.354	1.309	1.475	1.299												
SiO2	1.110	1.137	1.123	1.160	1.147	1.144	1.201	1.069	1.410	1.335	1.500	1.333												
P2O5	1.101	1.126	1.112	1.147	1.134	1.129	1.185	0.917	1.049	1.324	1.481	1.339												
SO3	1.118	1.142	1.127	1.162	1.148	1.143	1.199	0.970	0.896	1.345	1.499	1.369												
Cl	1.095	1.098	1.067	1.088	1.065	1.046	1.087	0.774	0.654	1.317	1.363	1.566												
K2O	1.135	1.134	1.100	1.119	1.094	1.073	1.114	0.981	0.886	1.366	1.397	1.145												
CaO	1.164	1.164	1.130	1.151	1.126	1.105	1.147	1.069	0.984	1.401	1.439	0.730												
TiO2	1.000	1.028	1.098	1.115	1.089	1.066	1.106	1.131	1.050	1.202	1.387	0.901												
V2O3	0.975	1.000	0.989	1.100	1.070	1.041	1.074	1.164	1.071	1.171	1.350	0.910												
Cr2O3	0.815	1.011	1.000	1.032	1.087	1.054	1.086	1.222	1.119	0.747	1.365	0.966												
MnO	0.834	0.789	0.971	1.000	0.987	1.028	1.053	1.287	1.167	0.732	1.327	1.003												
FeO	0.885	0.853	0.776	1.014	1.000	1.045	1.067	1.358	1.220	0.803	1.346	1.071												
NiO	0.952	0.943	0.890	0.858	0.775	1.000	1.082	1.510	1.326	0.991	1.302	1.224												
ZnO	0.955	0.959	0.924	0.922	0.870	0.738	1.000	1.667	1.422	1.081	1.251	1.230												
SrO	0.969	0.966	0.935	0.948	0.923	0.897	0.922	1.000	1.902	1.164	1.157	1.414												
ZrO2	1.006	1.003	0.971	0.986	0.961	0.936	0.964	0.930	1.000	1.209	1.209	1.467												
BaO	0.834	0.839	0.902	0.937	0.908	0.843	0.837	1.546	1.299	1.000	1.063	0.964												
HfO2	0.888	0.870	0.826	0.818	0.773	0.786	0.794	1.887	1.543	1.029	1.000	1.383												
ThO2	0.929	0.931	0.893	0.872	0.823	0.760	0.749	1.207	1.084	1.115	0.951	1.000												

analyzed. Series of replicate analyses of each of the standards were performed under conditions described by Armstrong.¹¹ Results of the analyses are given in Fig. 3, which shows the percentage relative errors for the standards obtained from the new polynomial α -factors--or from the Armstrong/Love-Scott $\phi(\rho z)$ correction; both give the same results--against those obtained from the Albee and Ray⁴ α -factors. As can be seen, systematic errors produced by the

older α -factors are eliminated with the new polynomial expressions. Table 5 compares the best-fit α -factors determined by a multiple linear regression of the analytical data with those calculated from the new polynomial correction. The two sets of factors are very similar, which shows that the Armstrong/Love-Scott correction comes close to a best-fit correction for the data.

Conclusions

The conventional Bence-Albee α -factor correction produces significant deviations from the correction procedures on which it is based. Substitution of the composition-independent α -factor with a simple second-order polynomial function of concentration results in the procedure producing identical results to the ZAF, $\phi(\rho z)$, or Monte Carlo correction on which it is based. This new modified Bence-Albee expression results in significantly improved accuracy in the correction of silicate and oxide analyses, and is essentially as fast and straightforward a procedure as the initial Bence-Albee correction.

References

1. A. E. Bence and A. L. Albee, "Empirical correction factors for the electron microanalysis of silicates and oxides," *J. Geol.* 76: 382, 1968.
2. T. O. Ziebold and R. E. Ogilvie, "An empirical method for electron microanalysis," *Analyt. Chem.* 36: 322, 1964.
3. G. R. Lachance and R. J. Traill, "A practical solution to the matrix problem in x-ray analysis," *Can. J. Spectros.* 11: 43, 1966.
4. A. L. Albee and Lily Ray, "Correction factors for electron probe microanalysis of silicates, oxides, carbonates, phosphates, and

sulfates," *Analyt. Chem.* 42: 1408, 1970.

5. H. F. Shaw and A. L. Albee, "An empirical investigation into possible non-linearities of the microprobe correction factors in the system $\text{MgO-CaO-Al}_2\text{O}_3\text{-SiO}_2$," *Microbeam Analysis--1979*, 227.

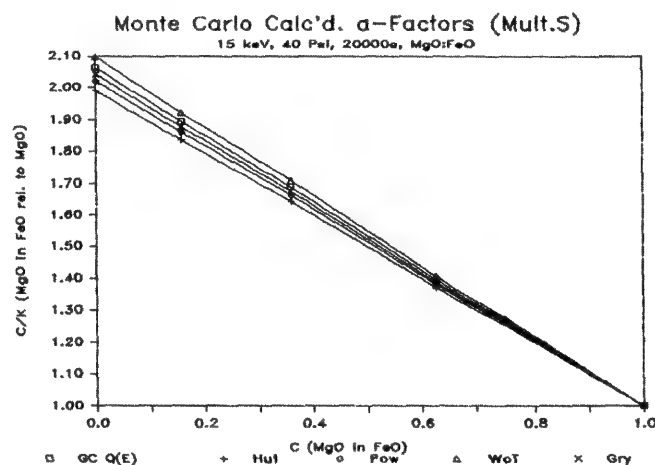


FIG. 1.--Plot of C/K vs C for $\text{Mg K}\alpha$ in MgO:FeO , calculated from Monte Carlo multiple-scattering calculations from various ionization cross section expressions.

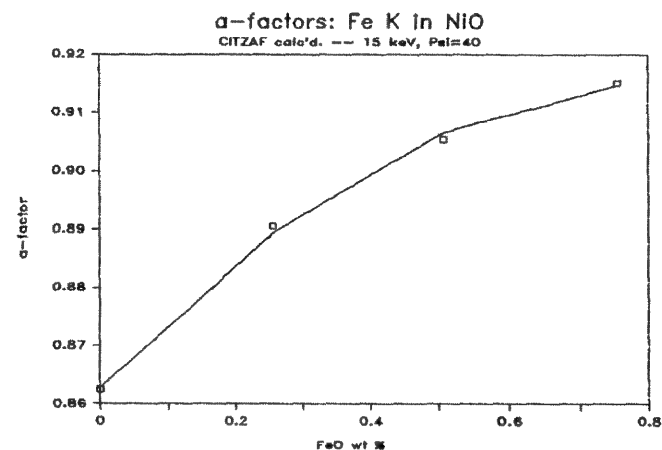
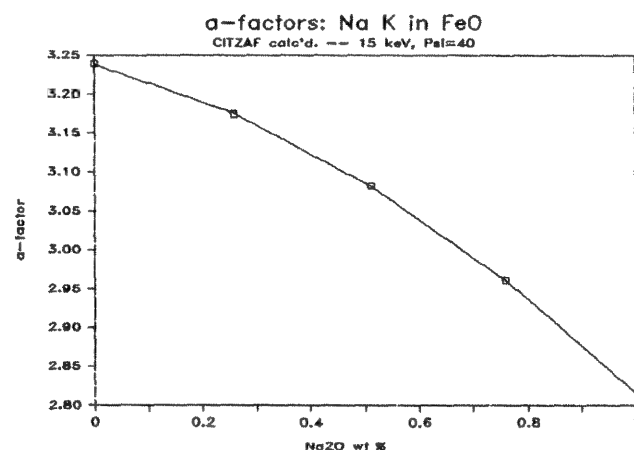
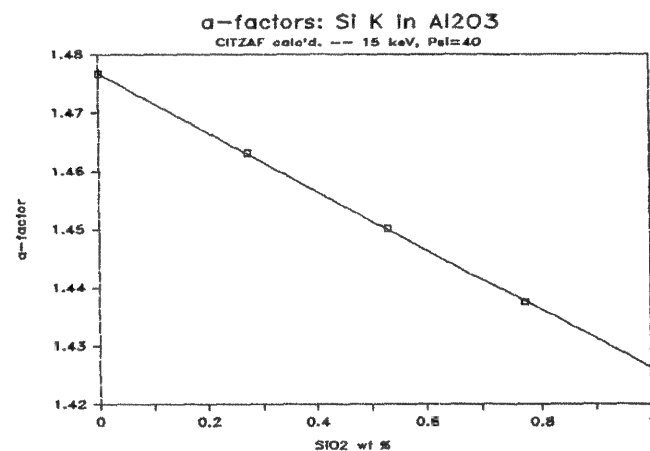
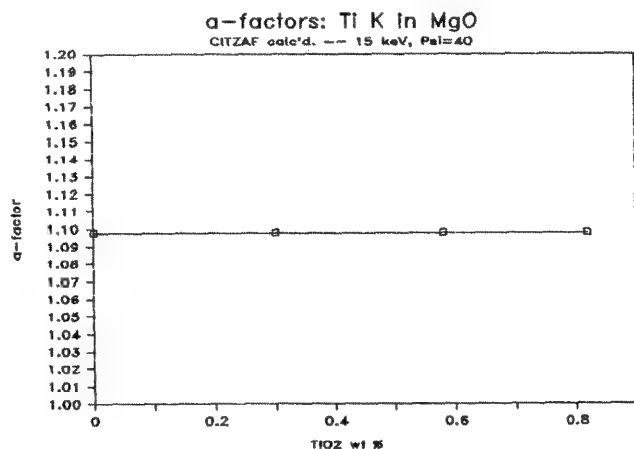


FIG. 2.--Plots of calculated α -factor vs concentration, in oxide weight fraction, for (a) Ti $\text{K}\alpha$ in $\text{TiO}_2\text{:MgO}$, (b) Si $\text{K}\alpha$ in $\text{SiO}_2\text{:Al}_2\text{O}_3$, (c) Na $\text{K}\alpha$ in $\text{Na}_2\text{O:FeO}$, (d) Fe $\text{K}\alpha$ in FeO:NiO .

TABLE 2.--Maximum % deviations from linear fit of C/K vs C for α -factors in Table 1.

Emitting																								
Line:	O	K	C	K	F	K	Na	K	Mg	K	Al	K	Si	K	P	K	S	K	Cl	K	K	K	Ca	K
O	0.0		0.0		36.2		2.7		0.7		0.2		0.1		0.1		0.0		0.1		0.1		0.1	
CO2	3.5		0.0		27.6		1.6		0.4		0.1		0.1		0.0		0.0		0.1		0.1		0.1	
F	0.9		1.5		0.0		4.9		1.5		0.5		0.3		0.1		0.1		0.3		0.2		0.1	
Na2O	0.8		6.8		4.3		0.0		3.9		1.6		0.6		0.3		0.1		0.3		0.2		0.1	
MgO	1.5		8.2		10.0		0.3		0.0		2.0		0.8		0.4		0.2		0.3		0.1		0.1	
Al2O3	2.4		9.8		14.3		0.1		0.4		0.0		1.1		0.5		0.2		0.4		0.2		0.1	
SiO2	3.5		11.0		18.0		0.4		0.2		0.5		0.0		0.6		0.3		0.4		0.2		0.1	
P2O5	4.6		11.8		20.7		0.6		0.0		0.3		0.5		0.0		0.4		0.6		0.2		0.1	
S2O3	6.0		12.5		23.3		0.9		0.1		0.1		0.3		0.7		0.0		0.6		0.2		0.1	
Cl	25.2		20.3		10.2		0.2		0.2		0.3		0.6		1.3		2.4		0.0		0.4		0.1	
K2O	30.3		0.5		18.8		0.5		0.1		0.1		0.1		0.3		0.6		2.6		0.0		0.2	
CaO	30.6		0.4		24.6		1.1		0.1		0.0		0.1		0.1		0.3		1.5		4.2		0.0	
TiO2	26.2		0.2		32.2		2.7		0.7		0.2		0.0		0.0		0.1		0.4		1.5		2.4	
V2O3	33.8		0.3		33.8		3.6		1.0		0.2		0.0		0.0		0.1		0.2		0.9		1.5	
Cr2O3	0.2		0.1		32.8		4.4		1.3		0.3		0.0		0.0		0.0		0.1		0.6		1.0	
MnO	0.4		0.2		33.8		5.9		1.8		0.5		0.1		0.0		0.1		0.0		0.3		0.5	
FeO	0.3		0.5		1.7		7.0		2.3		0.7		0.2		0.0		0.0		0.1		0.1		0.3	
NiO	0.4		1.5		2.0		9.9		3.8		1.4		0.4		0.1		0.0		0.1		0.0		0.0	
ZnO	1.4		3.1		2.6		5.7		6.3		2.6		0.9		0.3		0.0		0.2		0.0		0.0	
SrO	10.7		4.8		8.0		0.1		0.2		0.2		0.1		1.6		0.9		1.1		0.2		0.0	
ZrO2	13.2		4.2		13.1		0.7		0.0		0.1		0.1		0.1		0.8		1.2		0.2		0.0	
BaO	1.7		2.4		0.5		2.5		2.4		1.8		0.8		0.6		0.4		0.4		0.2		0.1	
HfO2	2.1		5.3		3.2		0.1		0.1		0.3		1.6		0.9		0.6		1.3		0.3		0.1	
ThO2	4.2		2.8		3.5		1.1		0.5		0.8		0.7		0.8		0.7		0.6		0.4		0.3	

Emitting													
Line:	Ti K	V K	Cr K	Mn K	Fe K	Ni K	Zn K	Sr L	Zr L	Ba L	Hf L	Th M	
O	0.0	0.0	0.1	0.1	0.1	0.2	0.1	0.3	0.2	0.6	0.5	1.0	
CO2	0.0	0.0	0.1	0.1	0.1	0.2	0.1	0.2	0.2	0.6	0.5	0.9	
F	0.1	0.1	0.1	0.1	0.2	0.2	0.2	0.8	0.6	0.8	0.6	1.5	
Na2O	0.1	0.1	0.1	0.1	0.1	0.2	0.1	1.3	0.8	0.7	0.5	1.3	
MgO	0.0	0.0	0.1	0.1	0.1	0.1	0.1	1.3	0.8	0.6	0.4	1.2	
Al2O3	0.0	0.1	0.1	0.1	0.1	0.1	0.1	1.6	1.0	0.6	0.4	1.3	
SiO2	0.0	0.0	0.1	0.1	0.1	0.1	0.1	0.1	1.0	0.6	0.4	1.2	
P2O5	0.0	0.0	0.1	0.1	0.1	0.1	0.1	4.1	0.1	0.6	0.4	1.4	
SO3	0.0	0.0	0.1	0.1	0.1	0.1	0.1	3.4	4.5	0.6	0.4	1.3	
Cl	0.0	0.0	0.0	0.0	0.0	0.1	0.0	5.3	7.8	0.6	0.3	2.0	
K2O	0.0	0.0	0.0	0.0	0.0	0.0	0.0	1.9	3.0	0.6	0.3	0.5	
CaO	0.0	0.0	0.0	0.0	0.0	0.1	0.0	1.1	1.9	0.6	0.2	11.2	
TiO2	0.0	0.0	0.1	0.1	0.1	0.1	0.1	0.1	0.5	0.3	0.3	6.5	
V2O3	0.0	0.0	0.0	0.1	0.1	0.1	0.1	0.2	0.2	0.3	0.4	5.5	
Cr2O3	3.0	0.0	0.0	0.0	0.1	0.1	0.0	0.2	0.1	9.9	0.3	4.7	
MnO	1.7	3.4	0.0	0.0	0.0	0.0	0.0	0.5	0.2	9.6	0.3	2.9	
FeO	1.0	2.3	3.6	0.0	0.0	0.0	0.0	0.6	0.2	8.8	0.3	1.9	
NiO	0.3	0.8	1.5	3.1	4.6	0.0	0.0	0.9	0.4	4.7	0.0	0.4	
ZnO	0.0	0.1	0.4	1.0	1.7	4.2	0.0	1.6	0.7	1.7	0.1	0.5	
SrO	0.0	0.1	0.0	0.0	0.0	0.0	0.0	0.0	2.7	0.1	0.0	0.9	
ZrO2	0.0	0.1	0.0	0.0	0.0	0.0	0.0	2.5	0.0	0.2	0.1	1.1	
BaO	0.3	0.3	0.1	0.1	0.0	0.1	0.0	1.1	0.5	0.0	0.0	1.5	
HfO2	0.4	0.4	0.4	0.4	0.3	0.0	0.1	2.4	1.2	0.2	0.0	0.5	
ThO2	0.3	0.3	0.2	0.1	0.0	0.0	0.0	0.5	0.4	0.1	0.0	0.0	

6. A. E. Bence and W. Holzwarth, "Non-linearities of electron microprobe matrix corrections in the system MgO-Al₂O₃-SiO₂," *Proc. 12th MAS Conf.* 1977, 38.

7. D. Laguitton, R. Rousseau, and F. Claisse, "Computed alpha coefficients for electron microprobe analysis," *Analyt. Chem.* 17: 2174, 1975.

8. J. T. Armstrong, "Rapid quantitative analysis of individual microparticles using the α -factor approach," *Microbeam Analysis--1980*, 193.

9. J. T. Armstrong, "New ZAF and α -factor correction procedures for the quantitative analysis of individual microparticles," *Microbeam Analysis--1982*, 175.

10. J. T. Armstrong, "Quantitative analysis of silicate and oxide minerals: A reevaluation of ZAF corrections and proposal for new Bence-Albee coefficients," *Microbeam Analysis--1984*, 208.
11. J. T. Armstrong, "Quantitative analysis of silicate and oxide materials: Comparison of Monte Carlo, ZAF, and $\phi(\rho z)$ procedures," *Microbeam Analysis--1988*.
12. D. C. Joy, "Beam interactions, contrast, and resolution in the SEM," *J. Microsc.* 136: 241, 1984.
13. D. C. Joy, "A Monte Carlo simulation for analytical electron microscopy," *Proc. 40th Ann. Meet. EMSA*, 1982, 98.
14. L. Curgenven and P. Duncumb, *Simulation of Electron Trajectories in a Solid Target by a Simple Monte Carlo Technique*, Report 303, Tube Investments Co., Saffron Walden, England, 1971.
15. H. E. Bishop, "Calculations of electron penetration and x-ray production in a solid target," *Proc. 4th ICXOM*, 1965, 112.
16. R. L. Myklebust, D. E. Newbury, and H. Yakowitz, "NBS Monte Carlo electron trajectory calculation program," in K. F. J. Heinrich, D. E. Newbury, and H. Yakowitz, Eds., *Use of Monte Carlo Calculations in Electron Probe Microanalysis and Scanning Electron Microscopy*, Washington, D.C.: National Bureau of Standards Spec. Publ. 460, 1976, 105.
17. D. E. Newbury and H. Yakowitz, "Studies of the distribution of signals in the SEM/EPMA by Monte Carlo electron trajectory calculations," in Ref. 16, p. 15.
18. D. E. Newbury, R. L. Myklebust, and K. F. J. Heinrich, "A hybrid Monte Carlo procedure employing single and multiple scattering," *Proc. 8th ICXOM*, 1977, 57.
19. C. J. Powell, "Cross sections for ionization of inner-shell electrons by electrons," *Rev. Mod. Phys.* 48: 33, 1976.

TABLE 3.--Calculated oxide polynomial α -factor expressions from Love-Scott correction; for each oxide, line 1 contains c factors, line 2, d factors; line 3, e factors.

EO = 15 KEV, PSI = 40 DEGREES													
Emitting	Na K	Mg K	Al K	Si K	K K	Ca K	Ti K	V K	Cr K	Mn K	Fe K	Ni K	
Line:													
Na2O	1.000	2.047	1.593	1.327	1.086	1.042	1.070	1.099	1.088	1.125	1.114	1.112	
	0.000	-0.169	-0.069	-0.030	-0.007	-0.006	-0.002	-0.003	-0.004	-0.005	-0.005	-0.006	
	0.000	-0.016	-0.003	0.000	-0.000	-0.000	-0.000	-0.000	-0.000	-0.000	-0.001	-0.001	
MgO	1.153	1.000	1.727	1.417	1.120	1.073	1.098	1.126	1.115	1.152	1.141	1.139	
	0.025	0.000	-0.086	-0.037	-0.007	-0.005	0.000	-0.002	-0.003	-0.004	-0.005	-0.006	
	-0.017	0.000	-0.007	-0.001	0.000	-0.000	0.000	0.000	0.000	0.000	-0.000	-0.001	
Al2O3	1.261	1.025	1.000	1.477	1.118	1.068	1.089	1.116	1.103	1.139	1.128	1.125	
	0.001	0.026	0.000	-0.050	-0.008	-0.006	-0.002	-0.003	-0.003	-0.004	-0.005	-0.006	
	-0.008	-0.015	0.000	-0.001	0.000	-0.000	0.000	0.000	-0.000	-0.000	-0.000	-0.001	
SiO2	1.373	1.098	1.014	1.000	1.145	1.092	1.110	1.137	1.124	1.160	1.147	1.144	
	-0.014	0.012	0.032	0.000	-0.008	-0.006	0.000	0.000	-0.003	-0.003	-0.004	-0.005	
	-0.005	-0.007	-0.017	0.000	0.000	0.000	0.000	0.000	0.000	0.000	-0.000	-0.001	
K2O	1.572	1.199	1.073	0.988	1.000	1.204	1.135	1.134	1.100	1.119	1.095	1.073	
	-0.017	0.004	0.005	0.008	0.000	-0.010	0.000	0.000	0.000	0.000	-0.002	-0.002	
	-0.013	-0.002	-0.001	-0.002	0.000	-0.000	0.000	0.000	0.000	0.000	0.000	0.000	
CaO	1.760	1.309	1.153	1.050	0.841	1.000	1.164	1.165	1.130	1.151	1.126	1.105	
	-0.041	-0.004	0.000	0.004	0.334	0.000	-0.002	-0.002	0.000	0.000	-0.002	-0.002	
	-0.019	-0.003	0.000	-0.001	-0.238	0.000	-0.000	-0.000	0.000	0.000	0.000	0.000	
TiO2	2.078	1.465	1.235	1.093	0.925	0.847	1.000	1.028	1.098	1.115	1.089	1.066	
	-0.108	-0.027	-0.006	0.000	0.119	0.184	0.000	0.000	-0.003	-0.004	-0.004	-0.004	
	-0.040	-0.007	-0.002	0.000	-0.083	-0.126	0.000	0.000	0.000	0.000	0.000	-0.000	
V2O3	2.303	1.577	1.294	1.122	0.929	0.858	0.975	1.000	0.989	1.101	1.070	1.041	
	-0.129	-0.035	-0.008	0.000	0.068	0.110	0.000	0.000	0.000	-0.004	-0.003	-0.003	
	-0.069	-0.014	-0.004	0.000	-0.043	-0.068	0.000	0.000	0.000	0.000	0.000	0.000	
Cr2O3	2.540	1.707	1.377	1.177	0.962	0.898	0.803	1.011	1.000	1.032	1.087	1.054	
	-0.151	-0.046	-0.012	0.000	0.040	0.067	0.212	0.000	0.000	0.000	-0.003	-0.003	
	-0.099	-0.021	-0.005	0.000	-0.024	-0.039	-0.123	0.000	0.000	0.000	0.000	0.000	
MnO	2.924	1.904	1.485	1.235	0.960	0.899	0.828	0.774	0.971	1.000	0.987	1.028	
	-0.168	-0.057	-0.016	-0.000	0.020	0.034	0.118	0.244	0.000	0.000	0.000	-0.002	
	-0.178	-0.043	-0.012	-0.004	-0.011	-0.017	-0.062	-0.143	0.000	0.000	0.000	0.000	
FeO	3.239	2.076	1.593	1.305	0.990	0.931	0.881	0.843	0.761	1.014	1.000	1.045	
	-0.184	-0.069	-0.023	-0.004	0.010	0.018	0.071	0.163	0.258	0.000	0.000	0.000	
	-0.238	-0.059	-0.016	-0.004	-0.006	-0.009	-0.036	-0.091	-0.150	0.000	0.000	0.000	
NiO	4.016	2.497	1.848	1.465	1.034	0.975	0.951	0.939	0.884	0.845	0.755	1.000	
	-0.212	-0.101	-0.043	-0.014	0.000	0.000	0.018	0.056	0.105	0.222	0.333	0.000	
	-0.423	-0.115	-0.032	-0.008	0.000	0.000	-0.009	-0.029	-0.056	-0.133	-0.205	0.000	

TABLE 4.--Maximum % deviations from polynomial fit of C/K vs C for α -factors in Table 3.

Emitting Line:	O	K	C	K	F	K	Na	K	Mg	K	Al	K	Si	K	P	K	S	K	Cl	K	K	K	Ca	K
O		0.0		0.0		0.3		0.0		0.0		0.0		0.0		0.0		0.0		0.0		0.0		0.0
CO2		0.0		0.0		0.0		0.0		0.0		0.0		0.0		0.0		0.0		0.0		0.0		0.0
F		0.1		0.0		0.0		0.0		0.0		0.0		0.0		0.0		0.0		0.0		0.0		0.0
Na2O		0.0		0.0		0.0		0.0		0.0		0.0		0.0		0.0		0.0		0.0		0.0		0.0
MgO		0.0		0.1		0.0		0.0		0.0		0.0		0.0		0.0		0.0		0.0		0.0		0.0
Al2O3		0.0		0.1		0.0		0.0		0.0		0.0		0.0		0.0		0.0		0.0		0.0		0.0
SiO2		0.0		0.2		0.0		0.0		0.0		0.0		0.0		0.0		0.0		0.0		0.0		0.0
P2O5		0.0		0.2		0.1		0.0		0.0		0.0		0.0		0.0		0.0		0.0		0.0		0.0
SO3		0.0		0.3		0.1		0.0		0.0		0.0		0.0		0.0		0.0		0.0		0.0		0.0
Cl		0.4		2.3		0.1		0.0		0.0		0.0		0.0		0.0		0.0		0.0		0.0		0.0
K2O		0.6		0.0		0.2		0.0		0.0		0.0		0.0		0.0		0.0		0.2		0.0		0.0
CaO		0.5		0.0		0.3		0.0		0.0		0.0		0.0		0.0		0.0		0.1		0.4		0.0
TiO2		0.3		0.0		0.3		0.0		0.0		0.0		0.0		0.0		0.0		0.0		0.1		0.2
V2O3		0.6		0.0		0.5		0.0		0.0		0.0		0.0		0.0		0.0		0.0		0.1		0.1
Cr2O3		0.0		0.0		0.5		0.0		0.0		0.0		0.0		0.0		0.0		0.0		0.0		0.0
MnO		0.0		0.0		0.7		0.0		0.0		0.0		0.0		0.0		0.0		0.0		0.0		0.0
FeO		0.0		0.0		0.0		0.1		0.0		0.0		0.0		0.0		0.0		0.0		0.0		0.0
NiO		0.0		0.0		0.0		0.2		0.0		0.0		0.0		0.0		0.0		0.0		0.0		0.0
ZnO		0.0		0.1		0.0		0.1		0.0		0.0		0.0		0.0		0.0		0.0		0.0		0.0
SrO		0.0		0.7		0.1		0.0		0.0		0.0		0.0		0.0		0.0		0.0		0.0		0.0
ZrO2		0.2		0.4		0.2		0.0		0.0		0.0		0.0		0.0		0.0		0.0		0.0		0.0
BaO		0.1		0.0		0.0		0.0		0.0		0.0		0.0		0.0		0.0		0.0		0.0		0.0
HfO2		0.2		0.0		0.0		0.0		0.0		0.0		0.0		0.0		0.0		0.0		0.0		0.0
ThO2		0.2		0.0		0.0		0.1		0.0		0.0		0.0		0.0		0.0		0.0		0.0		0.0

[illegible]

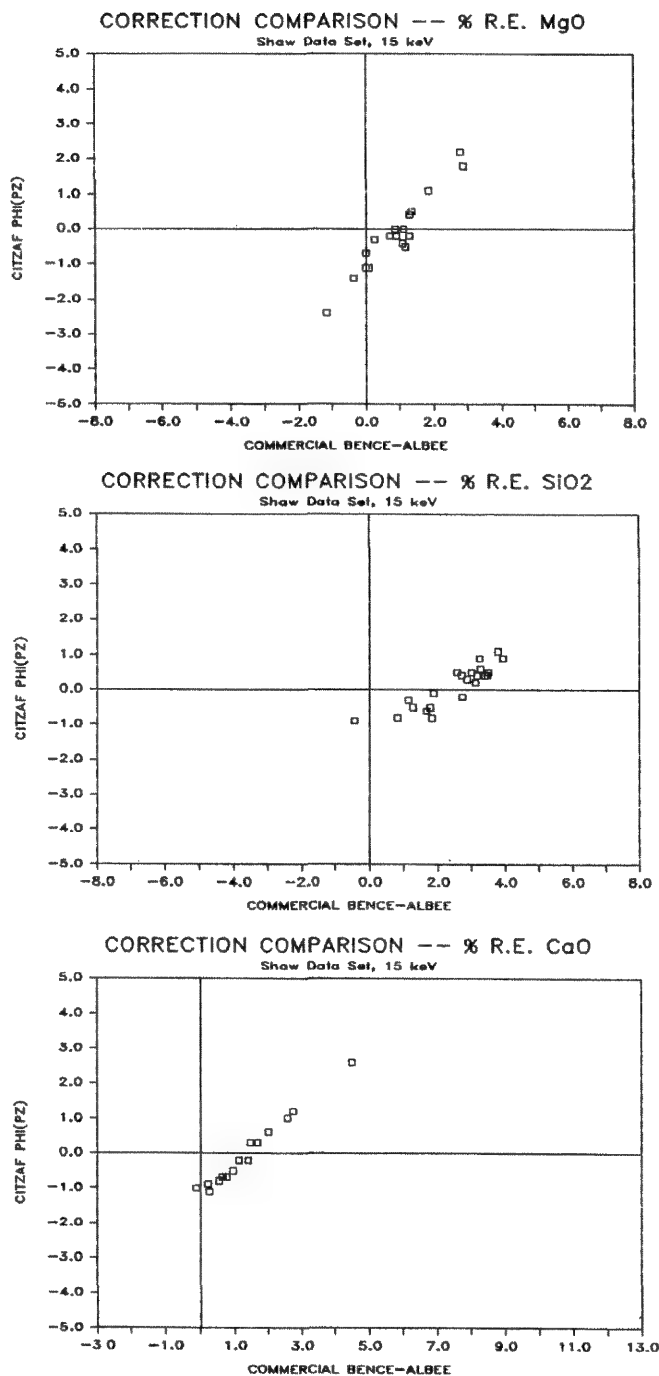


TABLE 5.--Comparison of Armstrong/Lov-Scott $\phi(\rho z)$ calculated α -factors with best fit α -factors from analyses of Caltech "Shaw" standards (15 keV, $\Psi=40$).

Best fit ZAF calc'd. (α -fac for 1:1 mix)		
Mg by Al2O3	1.046	1.038
SiO2	1.127	1.102
CaO	1.287	1.306
Al by MgO	1.724	1.682
SiO2	1.010	1.026
CaO	1.215	1.153
Si by MgO	1.398	1.398
Al2O3	1.461	1.452
CaO	1.049	1.052
Ca by MgO	1.079	1.072
Al2O3	1.073	1.065
SiO2	1.092	1.089

FIG. 3.--Plot of percentage relative errors in a set of standard silicates and oxides based on the new polynomial α -factor correction procedure, CITZAF $\phi(\rho z)$, vs that using a commercial Bence Albee program for (a) MgO, (b) SiO₂, (c) CaO.

EVALUATION OF STANDARDS AND CREATION OF ARTIFICIAL STANDARD RECORDS THROUGH ZAF-BACKWARD CALCULATIONS IN QUANTITATIVE ELECTRON MICROPROBE ANALYSIS

S. V. Yang and G. A. McKay

Through ZAF-backward calculations, the electron microprobe analyst can easily evaluate the laboratory standards and various ZAF packages, and create artificial-standard records for quantitative analysis. Examples are given in this report.

Procedures

All data presented in this report were acquired by the CAMECA CAMEBAX scanning electron microprobe at NASA-Johnson Space Center, Houston, Tex. ZAF data reduction was done by the CAMECA ZAF,¹ CAMECA PAP,¹ and DUST² packages, and by the IBM PC attached to the Digital PDP11/23 computer that operates the microprobe. Individual standard records, which cover the peak position, peak intensity, and pulse-high-analyzer setups, were collected for various elements on various standards. For each standard record, a correspondent record that represents the pure-element standard was created by use of the net peak intensity divided by its k-ratio. The k-ratio is the theoretical ZAF-backward correction factor calculated by the off-line quantitative analysis program. Eventually, different ZAF packages give different results. An example is shown in Table 1, in which record no. 1 is the real data set of the Si K α peak acquired by the electron microprobe and record no. 2 is the artificial one derived from record no. 1. Technically, there is no difference between the two records in real quantitative analysis. Based on such artificial standard records, one can evaluate specific element among different standards, and even among different ZAF packages.

Figure 1 shows the wavelength counts per second per nanoampere of the silicon K peak of various Si standards. All data points present the converted pure element peak intensities by the aforementioned ZAF packages.

In some cases, the artificial standard record of a target element can be created through projecting data points from the calculated pure-element standard records of the adjacent elements. Records 5 and 6 in Table 1 were created based on the data point projection shown in Fig. 2. Any extrapolation over an element absorption edge (e.g., argon absorption edge when gas flow detector is used) should be avoided.

The peak position can be determined by peak scanning over the target specimen. The other way is using the data point projection method

that takes the atomic numbers as the X axis and the Y axis as the offset between the theoretical peak position and the measured peak positions (Fig. 3). The background can either be determined by the peak profile of the target specimen, or one can select the background positions that have the least x-ray interference possibility.

Conclusions

A data plot similar to that shown in Fig. 1 is helpful for the microprobe analyst who wishes to avoid selecting undesired standards for a specific quantitative analysis. Similar plots may also be useful in interpreting abnormal analysis results and calibrating the reported concentration of the standards involved. If the laboratory has a broad spectrum of the microprobe standards, the analyst can set up the instrument with various analysis parameters to evaluate various standard groups. ZAF data reduction packages, and even instrument performance. Through careful preparations, one can analyze element by the artificial standard records without the real microprobe standards.

References

1. Available at CAMECA Instruments, Inc., 2001 W. Main St., Stamford, CT 08902.
2. Available from John Armstrong (Caltech).

The authors are at NASA-JSC, Houston, TX 77058 (S. V. Yang at C23 and G. A. McKay at SN2).

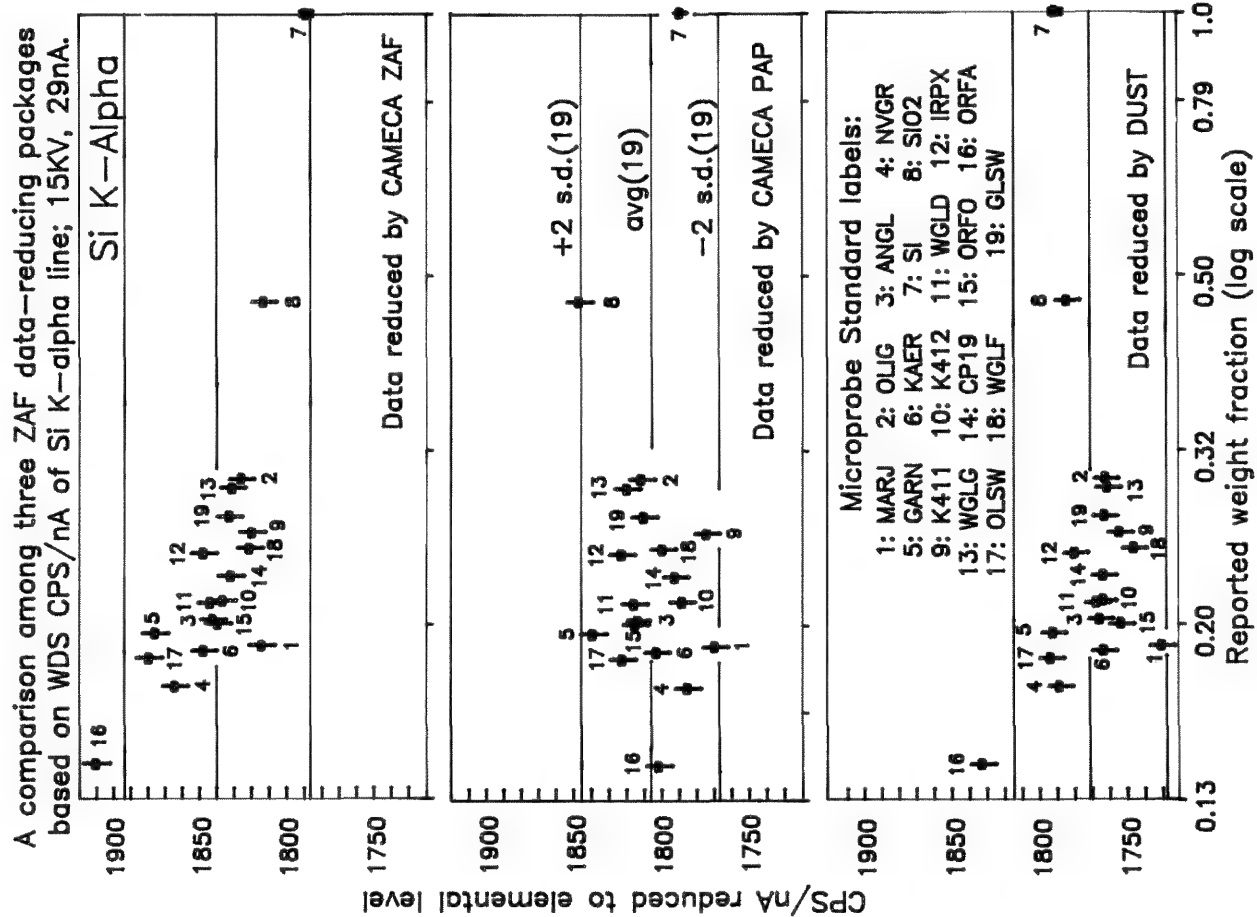


FIG. 1.--Calculated pure-element peak intensities of Si K α line of some electron microprobe standards.

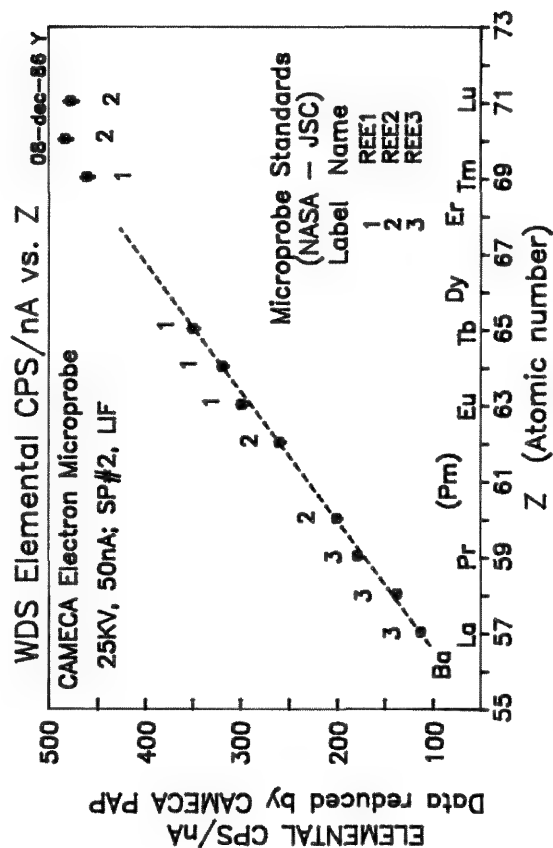


FIG. 2.--Calculated pure-element peak intensities of some rare-earth elements.

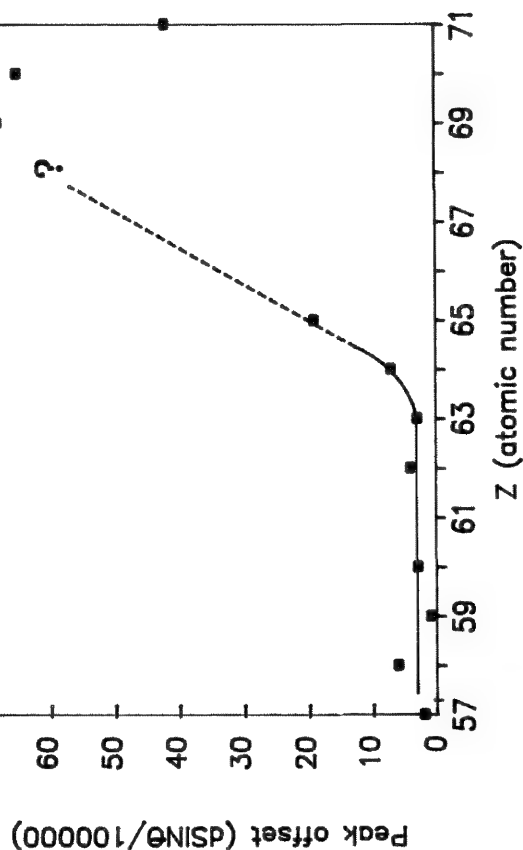


FIG. 3.--Offsets between theoretical and measured peak positions.

TABLE 1.--Examples of real and artificial standard records.

REC. NO.	STD NAME	ELEM	XTAL	KV	PEAK POS.	BG. OFF.	PK-BG C/S/nA	SIGM %	DET. BIAS	D.T. -7	INT DIF
1+	SIO2	Si	TAP	15	27753	600	744.70	0.2	1220	20	0
2*	SI	Si	TAP	15	27753	600	1846.64	0.2	1220	20	0
3+	REE2	Sm	LIF	25	54630	600	7.15	0.9	1607	20	1
4*	SM	Sm	LIF	25	52670	600	260.12	0.9	1607	20	1
5**	PM	Pm	LIF	25	56850	600	234.45	1.0	1607	20	1
6**	ER	Er	LIF	25	44309	600	460.00	1.0	1607	20	1

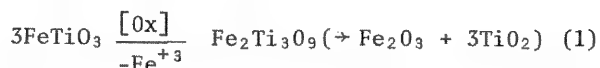
*: By data conversion. **: By data projection (Fig. 2).

+: Real data

MICRODIFFRACTION AND MICROANALYSIS OF IRON-TITANIUM MINERAL SAMPLES WITH A VG STEM

G. L. Shoemaker, J. D. Stephens, and R. G. Teller

Examination of iron-titanium mineral samples has revealed a close crystallographic and structural relationship between two phases, ilmenite (FeTiO_3) and pseudorutile ($\text{Fe}_2\text{Ti}_3\text{O}_9$). The conversion of ilmenite to pseudorutile is the result of a weathering and oxidation process that occurs in nature over long periods of time. This process is summarized as follows:



Pseudorutile has been identified as a distinct stoichiometric metastable phase, although independent synthesis of pseudorutile has not been accomplished. This phase is thought to be an intermediate in the oxidative decomposition of ilmenite to rutile (TiO_2).

X-ray diffraction and neutron diffraction analysis of a weathered mineralogical iron-titanium oxide sample indicated the presence of pseudorutile and ilmenite and a Vacuum Generators HB501 STEM study was initiated to examine the detailed microscopic relationship between the phases.

Single-grains of thinned mineralogical samples were examined. They contained areas where both the Fe/Ti elemental ratios and microdiffraction patterns showed abrupt changes. A reflected-light micrograph of an exemplary grain is shown in Fig. 1. On either side of the boundaries represented by the abrupt changes, microdiffraction patterns indicated the presence of one of the two phases identified in preliminary diffraction work, ilmenite, or pseudorutile. The changes in EDX and ED across the boundaries, relationships between the ED patterns, and the fact that both phases are found within a single grain indicate that a close crystallographic relationship exists between ilmenite and pseudorutile.

Mixed mineral grains that show both ilmenite and pseudorutile were examined by scanning electron microscopy (SEM), secondary ion mass spectrometry (SIMS), and a laser Raman microprobe. A reaction zone separates the ilmenite from the pseudorutile. Alkali and alkaline earth elements have migrated into the grains with the pseudorutile alteration and are concentrated at the reaction zone between the two minerals.

Alteration of the original ilmenite particle proceeds from the outside inward. It is likely that oxidation of the Fe in ilmenite from +2 to +3 is followed by leaching of Fe^{+3} from ilmenite

to form pseudorutile. (numerous organisms have an extremely high affinity for Fe^{+3} and practically no affinity for Fe^{+2} .) As weathering proceeds, the pseudorutile structure accommodates transport of Fe^{+3} from inside of each grain to the environment, either through crystallographic channels or through porosity developed in the minerals. Diffraction (x-ray and neutron) studies of the pseudorutile structure indicate that approximately one-half of the octahedral interstices are occupied by cations and that, on the average, these filled sites are only partially occupied. This partial cation occupation suggests a facile cation "hopping" mechanism for the transport of ferric ions through the pseudorutile structure. A complete electrochemical cycle would require an oxidizing reagent (such as H^+) to migrate inward, oxidize Fe^{+2} to Fe^{+3} , and be itself reduced ($\text{H}^+ + \frac{1}{2}\text{H}_2$) and migrate back to the environment.



FIG. 1.--Reflected polarized-light micrograph of typical weathered grains showing core of ilmenite with weathered layer of porous pseudorutile. (Magnification 500 \times .)

The authors are with BP America Research & Development, 4440 Warrensville Center Road, Cleveland, OH 44128.

THE AUTOMATED SCANNING ELECTRON MICROSCOPE AS A TOOL FOR GOLD MICROPROSPECTING

I. R. Harrowfield, C. M. MacRae, and P. F. Simmonds

Gold particles with diameters as low as 1 μm have been located in polished sections of ore samples with an automated scanning electron microscope (SEM). Average concentrations of gold have been as low as 1 ppm by weight. The system we describe uses backscatter electron (BE) intensities to discriminate possible gold grains and x-ray acquisition on an energy-dispersive (ED) spectrometer to resolve the remaining gray-level ambiguities. It was developed because microprobe searching by wavelength (WD) spectrometers was found to be too slow and therefore too expensive. McConnell et al.¹ described a search technique for gold particles that uses only x-ray testing by WD spectrometers. Testing of 50 \times 50 μm frames for the gold M x rays without direct measurement of background was considered to be sufficiently sensitive to find 2 μm particles. However, the minimum detectable concentration in a frame depends on the background, which must be measured directly if the atomic number of major phases in the sample varies widely. Using the experimental parameters of McConnell et al., the expression for minimum detectable concentration of Ancey et al.,² and the count rates on pure gold for our CAMECA "Microbeam" microprobe (50 cps at 250 nA), we find that if background measurement is done, a search for 2 μm particles with 95% confidence would take more than six times the time given by McConnell et al.¹ (56 h). Zuiderwyck³ constructed a rapid bright particle location system as a prototype for inclusion in the QEM*SEM mineral analyzer.⁴ This system used both BE and ED testing. In this system, and others that use the rapidly measured BE signal to carry out the initial discrimination, the amount of slow x-ray testing is minimized. Total search time is reduced to several hours.

In this paper we describe the major design parameters of our automated gold searching system, which is a refinement of Zuiderwyck's prototype. Since most samples have been found to have only a low fraction of bright material that must be tested, speed and cost effectiveness are increased. In the small number of samples where x-ray testing time becomes large, we describe search strategies that can reduce it to acceptable levels.

Method

Our automated system uses both stage and beam stepping of 1 mm and 1 μm step sizes, respectively. For a 25 mm-diameter polished section, 346 frames are scanned by the beam; each

frame contains 1 million points. These are initially tested by comparison of their BE levels with a preset window that includes all discrete gold-rich phases thought to be present. It is desirable to make the frame as large as possible to minimize the number of slow stage steps needed to traverse the section. At each point the beam dwells for 11 μs for BE testing. If BE discrimination is satisfied, x-ray testing of 40 ms duration takes place. Counts are accumulated in preset x-ray energy windows for gold M α and gold L α photons. If the count in both windows exceeds preset levels, the coordinates of the point are recorded. Upon completion of a frame scan, all such coordinates are recorded in a personal computer file. The stage is then stepped and the process repeated.

Upon completion of the search, gold points are relocated via the personal computer. The composition of each gold-rich particle and the associated minerals can be examined to assist in the design of extraction processes for the ore. Another direct output of this method is a ratio of the gold-rich points to the total number tested. This ratio is equivalent to a volume fraction of gold in the polished section and can be usefully compared to a bulk assay of the ore, provided the sampling strategies are sound and no systematic error is introduced during embedding and polishing.

At present we search about 70% of every block. If x-ray testing time is negligible (e.g., for rare gold particles in quartz) the total search time is about 1 h. The search strategies of Jones et al.⁵ can be used to reduce this time still further, provided the size ranges of particles searched for can be defined. X-ray testing adds to search time depending on the area of ambiguous phases. Typically, four polished sections are scanned overnight; the average time for each is 2.5 h for the ore types we have encountered.

We have not yet searched gold ore bodies containing large amounts of galena, zircon, or tungsten minerals, etc. These minerals would significantly increase the search times due to the BE gray-level overlap. If the search in such samples can be restricted to gold grains not associated with abundant ambiguous phases, or if on other grounds the occurrence of gold grains in these phases can be discounted, the total search time can be reduced. If only the first few consecutive bright points are tested with x rays and gold is not confirmed, then testing is stopped until a change in BE level is registered. The bright grain is thus considered to be uniform and of no interest. So far we have found that to be a good assumption.

The modified BE scan for this strategy takes longer than before because there is more soft-

The authors are at the CSIR Division of Mineral Products, P. O. Box 124, Port Melbourne, Victoria, Australia 3207.

were testing. We assume for simplicity that the particle sections are $P \mu\text{m}$ by $P \mu\text{m}$ squares and N consecutive x-ray tests are done for M particles in each frame. The modified search should be used only when

$$\text{MPN}(40 \times 10^{-3}) + 33 < \text{MP}^2(40 \times 10^{-3}) + 11$$

$$\text{or } \text{MP}(P - N) > 550$$

For example, if a frame contains square bright particles of side $10 \mu\text{m}$ and $N = 3$, then $M > 7.9$. If, on average, these frames contain 8 bright particles, then the modified scan is more efficient. We are forced to conduct an unmodified search on a sample block, choose the parameters of the modified search, and then assume that these parameters are appropriate for all others in the suite.

Results and Discussion

A number of drill core sections of gold-bearing ores with average concentrations between 1 and 5 ppm by weight have been examined. Gold grains down to $0.5 \mu\text{m}$ in diameter have been found, although typical sizes range from 2 to $10 \mu\text{m}$. Figure 1 shows a BE micrograph of gold grains found by the first scanning method. Only 2 gold points were actually registered. To improve the success rate we are considering reducing the step size by shortening the working distance of the SEM (at present, 43 mm). Figure 2 shows gold next to a copper sulfide particle. Since the BE window had to be set wide enough to include both native gold and gold alloys, the copper sulfide was x-ray tested and was correctly rejected. It may be possible to reduce the working BE window widths by lowering the noise in the detector and making it more isotropic in its response, as suggested by Robinson.⁶

Conclusion

An SEM equipped with a BE detector and an ED spectrometer has been automated so that $2 \mu\text{m}$ -diameter grains of gold can be located with 100% probability very rapidly. Grains $1 \mu\text{m}$ in diameter are found only 10% of the time but increasing the spatial resolution of the scan will improve this yield. This system is far more efficient for particulate gold location than the frame searching described by McConnell et al.,¹ except where ambiguous phases that include gold are very common. However, search strategies can be used to minimize the amount of slow x-ray testing in intermediate cases. Also, a volume fraction of gold in the polished section is available immediately when this automated facility is used. A great deal more testing of real samples is required to improve both spatial resolution and the efficiency of search strategies.

References

1. M. D. McConnell, R. B. Bolon, and W. T. Grubb, "Microprospecting for precious metals with an automated electron microprobe," *Microbeam Analysis--1983*, 125-127.

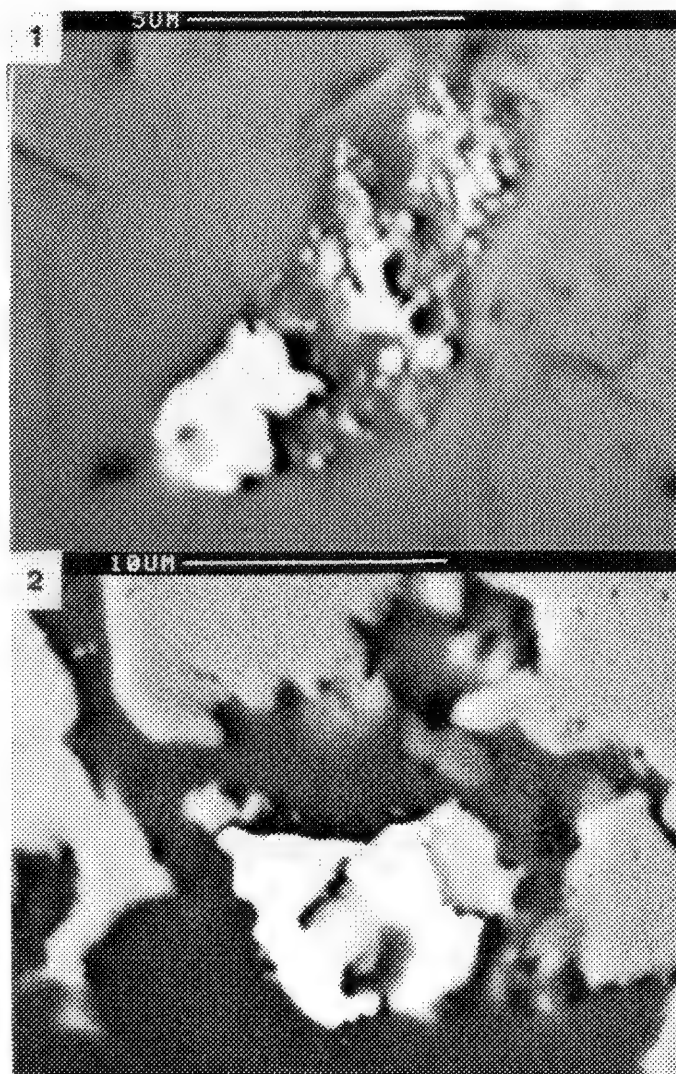


FIG. 1.--Backscattered electron micrograph of gold grains in iron oxide matrix.

FIG. 2.--Backscattered electron micrograph of gold grain intergrowth with copper sulfide and surrounded by quartz.

2. M. Ancey, F. Bastenaire, and R. Tixler, "Application of statistical methods to electron microprobe analysis," *J. Phys.* D10: 817-830, 1977.
3. M. A. Zuiderwyck, Paul Gottlieb, and V. H. Quittner, *A Method for the Detection of Sparingly Distributed Mineral Grains in Polished Sections*, CSIRO Division of Mineral Engineering Restricted Report V16/353.
4. K. J. Reid, and S. Pignolet-Brandom, "Capabilities for automated liberation analysis at the Minnesota QEM*SEM laboratory," presented at SME, 117th annual meeting, Phoenix, Ariz., 1988.
5. M. P. Jones and J. Gavrilovic, "Automated searching unit for the quantitative location of rare phases by electron-probe x-ray microanalysis," *Trans. Inst. Min. Metall.* 77: B137-143, 1968.
6. V. Robinson, "Theory and application of an efficient backscatter electron detector in scanning electron microscopy," *Beitr. elektronermikroskop. Direktabb. Oberfl.* 20: 1987.

RARE EARTH MINERALS IN BLACK SANDS OF THE BIG MEADOW PLACER DEPOSIT, IDAHO

C. R. Knowles and T. H. Kiilsgaard

Extensive black sand placer deposits are present throughout central Idaho.¹ Of these, the Big Meadow placer, along Bear Valley Creek, Valley County, Idaho, was selected for mineralogical study.² This deposit was mined for niobium, tantalum, and uranium during the 1950s.³ The black sands are composed predominantly of ilmenite (FeTiO_3) and magnetite (Fe_3O_4). The principal minerals of economic interest are monazite $[(\text{Th}, \text{La}, \text{Ce}, \text{Pr}, \text{Nd})\text{PO}_4]$ and euxenite $[(\text{Y}, \text{Ce}, \text{Ca}, \text{U}, \text{Th})(\text{Nb}, \text{Ta}, \text{Ti})_2\text{O}_6]$. Other minerals of lesser economic value include columbite (FeNb_2O_6), allanite $[(\text{Ce}, \text{Ca}, \text{Y})_2(\text{Al}, \text{Fe})_3(\text{SiO}_4)_3(\text{OH})]$, sphene (CaTiSiO_5), garnet $[(\text{Fe}, \text{Mn})_3\text{Al}_2(\text{SiO}_4)_3]$, and zircon (ZrSiO_4). Some minerals previously reported from the deposit were not found in our study.³

The chemical composition of these minerals was determined by an electron microprobe. Phase identification was made where mineral separations were possible by x-ray diffraction spectroscopy.

The principal source of black sand minerals in the alluviated valleys of central Idaho is the Cretaceous Idaho batholith and its associated pegmatite dikes. Other source rocks include plutonic and related hypabyssal rocks of Tertiary age. The Big Meadow deposit, in the upper part of Bear Valley Creek, is approximately 80 miles north of Boise and about 18 miles north of the settlement of Lowman.

The samples used in this study were collected from the site of the abandoned Porter Bros. Corp.'s electromagnetic concentrator, which formerly processed dredge concentrates from the Big Meadow deposits. Five samples were collected of which one was from dump material and four were from various piles of material that probably represented various products in the electromagnetic separation process. One of the concentrator samples consisted almost entirely of yellow sand grains; another had red-orange sand grains, and the others had gray to black sand. In addition to the five samples, Mr. Richard Porter, Boise, Idaho, furnished us with two samples, one of euxenite and the other of monazite. Both of these samples were from the Big Meadow concentrates that had been further processed at the Lowman concentrator.

Experimental

The major minerals in the black sand placers are opaque oxides of magnetite-ilmenite, which

C. R. Knowles is at the Idaho Geological Survey, University of Idaho, Moscow, ID 83843; T. H. Kiilsgaard is at the U.S. Geological Survey, Spokane, WA 99201. Some of the samples were supplied by Richard Porter, Boise, ID 83707.

were found to be mixtures of exsolved phases of ilmenite and titanium-rich magnetite. The garnet ($\text{Sp}_{52}\text{-Al}_{48}$) was found to be unzoned, and roughly 52 mole percent spessartine $[\text{Mn}_3\text{Al}_2(\text{SiO}_4)_3]$ and 48 mole percent almandine $[\text{Fe}_3\text{Al}_2(\text{SiO}_4)_3]$. The radioactive minerals were predominantly monazite and euxenite, with minor amounts of allanite. Small amounts of sphene, zircon, columbite, and tantalites were found in the samples studied.

The samples were analyzed by an ARL-EMX electron microprobe equipped with a Tracor Northern energy-dispersive x-ray analyzer (EDX).^{*} The polished samples were examined qualitatively with EDX and reflected light microscopy.

A series of standards was used for quantitative analysis. The rare earth elements (REE) standards were from Drake and Weil of the University of Oregon.⁴ These standards are glasses containing approximately 4% REE oxides. Several pure (99.99+%) metal standards were used, as were three Corning Glass standards obtained from Art Chodos at the California Institute of Technology.⁵ When REE were present in a mineral as seen by EDX, all the lanthanide series elements were analyzed in a quantitative manner and compared to the REE glasses.

The correction of these data was made by use of ZAF and Bence-Albee corrections in some cases. However, the Bence-Albee correction program used with the Tracor Northern 880 system cannot correct for the REE. To attempt a moderate correction, the REE were examined as though they were all BaO_2 . These data were then compared with the ZAF matrix correction for the ten most abundant elements. The two methods showed some success in comparison; the estimated error was less than 5%. All the data are shown in Table 1.

Results

The iron oxide minerals were found to be ilmenite and an intermixed titanium-rich magnetite. Exsolution of two phases was seen, but whether Ti or Fe exsolved from the mineral could not be determined. The phases ranged from ilmenite with inclusions of titanomagnetite to grains of mostly titanomagnetite in which laminar inclusions of ilmenite were present. The titanomagnetite contained about 18% TiO_2 . Both oxides contained MnO, but the ilmenite had the larger amount.

Garnet in the samples was not zoned, a condition best explained by its igneous-rock origin. The mineral is Mn and Fe rich with small

^{*}Use of brand names in this report is for descriptive purposes only and does not imply endorsement by the University of Idaho or the U.S. geological survey.

TABLE 1.--Results of microprobe analysis of black sand minerals and the mineral formula.

<u>Euxenite</u>	<u>Monazite</u>	<u>Allanite</u>	<u>Garnet</u>
U ₃ O ₈ = 22.7%	U ₃ O ₈ = 0.0%	U ₃ O ₈ = 0.0%	SiO ₂ = 35.8%
ThO ₂ = 6.0	ThO ₂ = 8.6	ThO ₂ = 0.0	Al ₂ O ₃ = 20.3
Y ₂ O ₃ = 18.9	Y ₂ O ₃ = 0.0	Y ₂ O ₃ = 0.0	MnO = 21.9
Nb ₂ O ₃ = 26.9	Nb ₂ O ₃ = 0.0	SiO ₂ = 29.5	FeO = 22.3
Ta ₂ O ₃ = 0.4	Ta ₂ O ₃ = 0.0	Al ₂ O ₃ = 14.9	CaO = 0.67
TiO ₂ = 19.7	TiO ₂ = 0.0	TiO ₂ = 1.4	TiO ₂ = 0.17
FeO = 1.9	Fe ₂ O ₃ = 0.3	Fe ₂ O ₃ = 17.0	<u>Ilmenite</u>
CaO = 0.3	CaO = 0.6	CaO = 10.8	FeO = 50.1%
La ₂ O ₃ = 0.0	P ₂ O ₅ = 25.9	MgO = 1.4	TiO ₂ = 46.5
Ce ₂ O ₃ = 0.0	La ₂ O ₃ = 13.8	La ₂ O ₃ = 8.3	MnO = 4.1
Pr ₂ O ₃ = 0.3	Ce ₂ O ₃ = 27.5	Ce ₂ O ₃ = 11.3	<u>Titano-Magnetite</u>
Nd ₂ O ₃ = 0.3	Pr ₂ O ₃ = 6.1	Pr ₂ O ₃ = 2.7	FeO = 80.7%
Sm ₂ O ₃ = 0.4	Nd ₂ O ₃ = 10.3	Nd ₂ O ₃ = 2.1	TiO ₂ = 18.2
EuO = 0.1	Sm ₂ O ₃ = 1.9	Sm ₂ O ₃ = 0.33	MnO = 1.0
Gd ₂ O ₃ = 1.3	EuO = 1.0	EuO = 0.16	
Tb ₂ O ₃ = 0.4	Gd ₂ O ₃ = 3.4	Gd ₂ O ₃ = 0.0	
Ho ₂ O ₃ = 1.4	Tb ₂ O ₃ = 0.2		
Er ₂ O ₃ = 2.4	Ho ₂ O ₃ = 0.2		
Dy ₂ O ₃ = 3.9	Er ₂ O ₃ = 0.0		
<u>Formula</u>			
Ilmenite	Ti _{1.9} Fe _{1.0} Mn _{0.09} O ₃	Garnet	Mn _{3.0} Ti _{0.2} Ca _{1.1} Fe _{3.1} Al _{3.9} Si _{5.9} O ₂₄
Titano-magnetite	Ti _{1.6} Fe _{2.8} Mn _{0.03} O ₄	Monazite	(REE) _{5.9} Th _{0.5} Ca _{0.2} Fe _{0.05} P _{5.5} O ₂₄
Euxenite	U _{1.4} Th _{0.4} Y _{2.9} Nb _{3.5} Ti _{4.3} Fe _{0.5} Ca _{1.1} Dy _{0.4} O ₂₄		
Allanite	(La,Ce,Pr,Nd) _{4.6} Ti _{0.5} Mg ₁ Ca ₆ (Al ₉ ,Fe _{6.6})Si ₁₅ O ₆₈		

amounts of Ca and no Mg or Cr. A computer program to recast garnet end members was used to determine the best garnet mole % end member composition.⁶ A garnet of Sp_{51.6}-Al_{46.4}-An_{2.0} is the best fit to the data (where Sp is spessartine, Al is almandine, and An is andradite).

Monazite, the Th-rare earth element phosphate, contained larger amounts of the light REE with few REE above Gd. La and Ce accounted for nearly half the REE. The mineral contains 8.6% of ThO₂, but no U was found.

Euxenite, a radioactive black mineral, is U rich and Th poor with more heavy REE (larger than Eu) than light. This mineral contains large amounts of Y and Nb, and some Ta. The grains were found to vary in U₃O₈ from a high value of 26.6% to a low of 11.1%. An average value was used in Table 1. The amount of REE varied slightly with the change in U concentration. When U was high the REE were lower. The Fe concentration was lower with the increase of U as well.

Allanite commonly is a radioactive REE silicate, but no Th or U was found in the allanite that was studied. The REE in allanite were at the lighter end of the lanthanide series. Other minerals were found in the placer concentrates, but only a qualitative scan was made. Future studies will include these other minerals if a suitable means of concentration can be found.

Conclusions

The electron microprobe examination of the placer black sands showed fewer mineral varieties than described in previous studies.³ The misinterpretations in the previous studies were probably due to bulk chemical analysis and possible contaminations in the analyzed samples. The site specific microprobe chemistry methods

showed the exact mineral in question excluding foreign material or inclusions in the analyses.

The minerals of most commercial importance in the placers are the U-, Nb-, and Y-rich euxenite, the REE-rich monazite, and allanite. Although sphene, zircon, garnet, ilmenite, and titano-magnetite are present, the market value for these minerals is low.

The Big Meadow deposit has been estimated by Porter Bros. Corp. to contain 67 000 000 yd³ of alluvial material, the average grade of which is 0.40 lb of euxenite and 0.75 lb of monazite per cubic yard.¹ At this mineral content, and at recent market values of \$97/kg for Y₂O₃ and \$581/short ton of monazite, the total amount of euxenite and monazite in the deposit would have a value of \$239 million.

References

1. T. H. Kiilsgaard and W. E. Hall, *Radioactive Black Sand Placer Deposits of the Challis 1° × 2° Quadrangle, Idaho*, U.S. Geological Survey Open-File Report 86-0633, 1986.
2. J. H. Mackin and D. L. Schmidt, *Reconnaissance Geology of Placer Deposits Containing Radioactive Minerals in the Bear Valley, Valley County, Idaho*, U.S. Geological Survey Open-File Report 53-01676, 1953.
3. Mining World, "Idaho placer is source of 99 percent of U.S. columbium-tantalum output," *Mining World*, 20: 38, 1958.
4. M. J. Drake and D. F. Weil, "New rare earth element standards for electron microprobe analysis," *Chemical Geology*, Amsterdam: Elsevier, 1972, 179.
5. A. A. Chodos, "Caltech glass standards V, W, and X," personal communication, 1973.
6. C. R. Knowles "A BASIC program to recast garnet end members," *Computers and Geosciences* 13: 655, 1987.

ELECTRON MICROPROBE TRACE ELEMENT ANALYSIS

T. N. Solberg

This paper presents our approaches for measuring trace elements. Each analytical situation is unique and usually presents options that should be individually evaluated with regard to limits of detection. By choosing optimum analytical conditions, we can reduce counting times and beam damage to the samples.

We limit our discussion to x-ray diffracting spectrometers rather than Li-drifted silicon detectors. However, an electron microprobe should ideally have an integrated energy and wavelength-dispersive x-ray system using the same computer. The energy spectra display is invaluable in trace-element analysis, particularly when used with the scanning mode for identifying inclusions. We usually raster our beam at 10 000 \times during analysis observing the secondary-electron image of the sample, which allows one to avoid surface irregularities and identify inclusions.

Many minerals, such as zircons, apatites, sphalerites, etc., should be examined with cathode luminescence before trace-element analysis is done. Cathode luminescence is invaluable in many microprobe analytical situations such as the examination of potential carbonate standards to reveal trace-element zoning.

Limits of detection (LD) for this study are defined as three times the square root of background of the unknown divided by the peak intensity of the standard times the standard elemental concentration. There are several ways to improve the limits of detection on an electron microprobe. One should calculate the limits of detection when varying microprobe conditions. Never assume.

Trace-element analysis was hindered on our electron microprobe because of the time-consuming and imprecise analog x-ray spectral scanning methods provided with our instrument. Spectral scans to determine background and peak shape used a strip chart recorder or an x-y plotter in conjunction with a potentiometer coupled to the x-ray spectrometer and a ratemeter to indicate intensity. This procedure proved to be unworkable for many reasons. Ratemeter time lag, lack of deadtime correction, noisy electrical signals, noise from stepping motors moving the x-ray spectrometers, the need to mark and calibrate charts, and lack of storage of spectral x-ray data all made trace-element analysis tedious if not impossible.

We developed a computer program to scan and plot x-ray spectra that has eliminated most of

the problems associated with the analog methods of x-ray spectra recording. The features of our scan program are signal averaging of multiple scans, performing a digital smooth, plotting the resultant spectra with the position and dead time-corrected x-ray intensity information, printed out in both linear and logarithmic scales with spectra storage for later reference. The ability to scan a given x-ray spectral region by multiple scans averaged over many hours enables us to determine elemental concentrations of down to 50 parts per million (ppm). Backgrounds for trace element analysis were easily determined by our scan program. We could generally determine the presence of 100 ppm of an element, whether there were any interfering lines to account for, and where to make background measurements. This capability was particularly important in doing rare earth analysis.

X-ray Spectrometer

The most important factor affecting electron microprobe trace element analysis is the type and perfection of the x-ray diffracting element of an x-ray spectrometer. One should not confuse high count rates or superior peak to background (P/B) rates with having the lowest possible limits of detection. The P/B ratio is usually highest for the narrowest slit width as seen from the plot of the LD vs slit width in Fig. 1. The slit settings for the lowest LD do not correspond to the slit settings for the highest P/B ratio. Also, the LiF plot in Fig. 1 is not smooth, because the $K\alpha_1$ and 2 lines are partially resolved at the smaller slit widths (Fig. 2).

Several of our analytical schemes require measurement on the sides of interfering spectra to subtract its contribution from an x-ray line of interest. Generally, too narrow an x-ray peak implies some difficulty with trace-element analysis because slight changes in sample focus affect peak position.

Accelerating Potential

A general rule of thumb is that the best P/B ratio is achieved at 2.5 times the energy of x-ray line of interest. For calcium we should use an accelerating potential of about 10 kV. However, if we plot LD of calcium vs kV for two of our scanners and the fixed calcium channel (Fig. 3), we note that the limits of detection are optimum at 25 kV. Nor is this the whole story, since the x-ray analytical volumes at the higher voltages may be too large for our microanalytical needs.

T. N. Solberg manages the Electron Microprobe Laboratory, Department of Geological Sciences, Virginia Polytechnic Institute and State University, Blacksburg, VA 24061-0796.

X-ray Detectors

Light-element analysis depends on low x-ray absorbing detector windows for the flow-proportional detector. Any x rays that enter the proportional detector should ideally cause ionizations near the electron collecting wire. We can affect x-ray counting efficiency by choosing the correct proportional-detector gas mixture and pressure to "tune" the efficiency to x rays of interest.

The proportional counter for our PET crystal spectrometer initially used an argon-filled detector. When we started doing trace-element analysis of uranium, we had to use the $M\beta$ x-ray line instead of the $M\alpha$ line. The absorption edge of argon lies between the two uranium lines and argon is not efficient at stopping uranium $M\alpha$ x rays. Substantially higher count rates are obtained with the U $M\beta$ line, and therefore better limits of detection. We have replaced the argon proportional detector with a xenon proportional detector and now use the uranium $M\alpha$ line to obtain improved analysis for that x-ray wavelength region due to higher xenon ionization efficiencies.

Contamination

Long counting times are needed to determine low concentrations of elements. Our initial diffusion-pumped vacuum system contaminated the sample surface where the electron beam impinged and made trace-element analysis nearly impossible. We replaced our diffusion pump with a cryogenetically pumped system and vacuum contamination was virtually eliminated.

Pulse Height Analysis

Pulse height analysis (PHA) can be used to reduce higher order x-ray line interferences. Fluorine analysis of apatites requires PHA settings to discriminate against a set of phosphorus third-order K lines (Fig. 4). Careful selection of PHA is required to discriminate against the phosphorus and yet allow counting of sodium x rays, since the same spectrometer is used for both elements.

If one calculates the LD vs PHA window settings, the widest windows or even integral settings yield the lowest limits of detection. (This is not true if one wants high P/B ratios.) This relationship is fortunate, since one may obtain high count rates from standards used for trace-element analysis. High count rates into proportional detectors have the effect of lowering the gas amplification factor and narrow PHA window settings are unworkable for widely varying concentrations of an element. In general, it is therefore best to have as wide as possible a window for good trace-element analysis. Some analysts use a low beam current on a standard and then increase the beam current for trace elements.

Sample Preparation

A smooth surface is especially important for trace-element analysis. A vibrating lap as a

final step has generally provided the best sample surfaces. However, the vibrating lap has caused some contamination and alteration of samples. Small pyrites in particular react when polished in water and another polishing fluid must be used. We once found copper contamination in a lead tin telluride that was due to an electrochemical reaction with a brass weight on the vibrating lap.

Soft materials, such as gold, require special care since polishing debris is embedded in the sample surface. Separation of the gold from the host rock is the ideal way to look for trace elements in gold. We usually crush the gold-bearing rock and pan the gold ore to free any gold grains for individual mounting and polishing. Suppose one wishes to determine copper in a gold grain adjacent to chalcopyrite in a polished section. The gold is being loaded with chalcopyrite during polishing. We usually etch to remove surface contamination from the gold, but the problem remains of x rays from the gold and back-scattered electrons exciting copper radiation from the chalcopyrite.

The tendency of scattered electrons and x-ray fluorescence causing adjacent materials to contribute characteristic spectra to the unknown is a serious problem in microprobe analysis, a problem whose magnitude one should test. For example, one may place a polished rod of iron metal in a hole drilled in a pure gold sample, then traverse for Fe and Au across the gold/iron interface from different directions as if this were a diffusion couple, and plot the results to determine the magnitude of the problem on one's instrument.

Backgrounds

Our ARL-SEMQ electron microprobe has three scanning spectrometers and six fixed x-ray channels set for Fe, K, Ca, Si, Al, and Mg. The spectrometers have variable slit widths for the two Lif/PET and PET/Lif crystal scanners, and a fixed-slit-width, long-wavelength scanner with RAP/PBSD crystals. For most analyses, we generate working graphs to determine backgrounds vs average atomic number.

The exercise of plotting backgrounds vs average atomic number is valuable because points that fall off a straight line indicate a possible problem with backgrounds: note Fig. 5 and the relative slopes to the backgrounds of Ti, K, and Mn. Compare these sloping backgrounds to the Fig. 6 flat backgrounds for Mg, Al, Si, and Na. Note the anomalous Mg background value at atomic number 18, obtained in a measurement on a supposedly pure synthetic tephroite. The tephroite was checked and found to contain 0.3% MgO.

We find that backgrounds fit a linear plot if the background standards are free of any interfering spectra or are indeed free of the element of interest. The point to be made is that we can predict the backgrounds for most of our analytical schemes and thereby save considerable time during analysis. We also

find that fluorine backgrounds are virtually flat for all average atomic materials.

Using these graphical backgrounds works most of the time for measuring concentrations in the tenths of a percent range. It is best to have a pure background standard identical to the material being analyzed. We use this approach when analyzing calcites, zircons, feldspars, and apatites. We are evaluating many background standards for dolomite and calcite. Quartz is a good background standard for calcite since their average atomic numbers are so similar.

We calculate the average atomic number during analysis and print this value along with the measured composition. For some of our analytical schemes we program background corrections to the analysis based of measured average atomic numbers.

Interfering Spectra

When there are interfering first-order spectra in the unknowns, one can perform an empirical correction to the analysis. For example, we find using the LiF crystal spectrometer for Ti and Ba analysis, that there is a 0.5wt% contribution from the Ti K α to the Ba L α x-ray line. The amount of interference is controlled by the slit width. Therefore, we could program a simple Ti subtraction from all barium values. The maximum correction for a biotite would be in the order of 0.02% with LiF. The Ti/Ba interference would be much greater had we used the PET crystal for barium analysis, since there is less dispersion for the lower scanner settings and therefore less resolution.

The choice of diffracting crystals and x-ray lines is a major part of analytical strategy. For example, we use the M β x-ray line for determining mercury in gold because the gold M β overlaps the mercury M α line. Tables of interfering x-ray lines are essential for trace element analysis.

When there are x-ray line interferences, we can often choose a background offset on a portion of the interfering spectra which equals the spectra under the peak of interest. Consider zinc L α interferences with sodium K α (Fig. 7). Here is an example of using our scan program to determine where to make background measurements. First determine where the sodium peak will be. Then acquire the zinc spectrum from a standard chemically similar to the unknowns we wish to analyze. Next determine the intensity of the zinc spectra at the sodium peak position. The zinc spectrum has three equivalent background measurement locations on the high-wavelength side of the sodium peak position. I prefer the two closest "valley" background positions for measuring the zinc background contribution to the sodium analysis. The log display helps one choose where to measure backgrounds. This method of selecting equivalent interfering spectra measurement positions is how we handle rare-earth analysis on a wide range of minerals.

Counting Time and Beam Current

Counting times are a variable we can adjust to improve our LD. As an example, consider Fig. 8, where we plot the LD for calcium in an atomic-number material of about 11. This plot indicates that 40 s of counting is optimum and yields a calcium detection limit of about 50 ppm. Although a single 40s count would do, it would be better to have three 10s counts than the single 40s count.

Beam currents have to be adjusted to reduce destruction and contamination of standards and unknowns. Thick carbon coatings may provide better thermal conductivity for some sensitive materials. The electron beam is blanked while x rays are not being counted to reduce beam damage to the sample. Contamination of the unknowns by electron-beam decomposition of standards could be a problem.

We could not use cinnabar (HgS) as a mercury standard because it was unstable at the beam conditions needed for trace-element gold analysis and caused contamination of the electron microprobe. Livingstonite (HgSb₄S₈) proved to be stable enough for our needs.

Carbonates seem stable when analyzed with a 15kV, 10nA beam scanning at 10 000 \times magnification. The calcium signal from a calcite standard changed by less than 3% after 120 s. Varying the accelerating potential while maintaining a 10nA sample current rastered over a 10 μ m area gave similar stability results.

When we traverse calcite samples, using a 40s counting time, we usually achieve a 300 \pm 100ppm LD for iron and manganese. We prefer to do three traverses across a carbonate and then average the scans to give better statistics for the trace elements. Because we choose relatively nondestructive beam conditions for the calcite analysis, we can repeat analysis as often as needed.

X-ray Mapping

Homogeneity of standards and unknowns is always in question. When one has an indication of a trace element being present in a sample, x-ray mapping should be done to insure that the trace elements are not present as inclusions. For example, when we studied strontium in calcite and used x-ray mapping to examine suspect areas, we found that the strontium was really contained in inclusions of strontianite.

Similarly, during our studies of gold for iron and arsenic, we found the iron and arsenic were present as inclusions of arsenopyrite. X-ray mapping also revealed calcium silicate exsolutions in our Rockport fayalite iron standard.

Example

As an example of what we usually do to determine whether a trace element is present, let us determine the LD of iron for our LiF x-ray spectrometer (Fig. 9). We would scan a standard to calibrate for iron, in this case using an NBS SRM 610 trace-element glass stan-

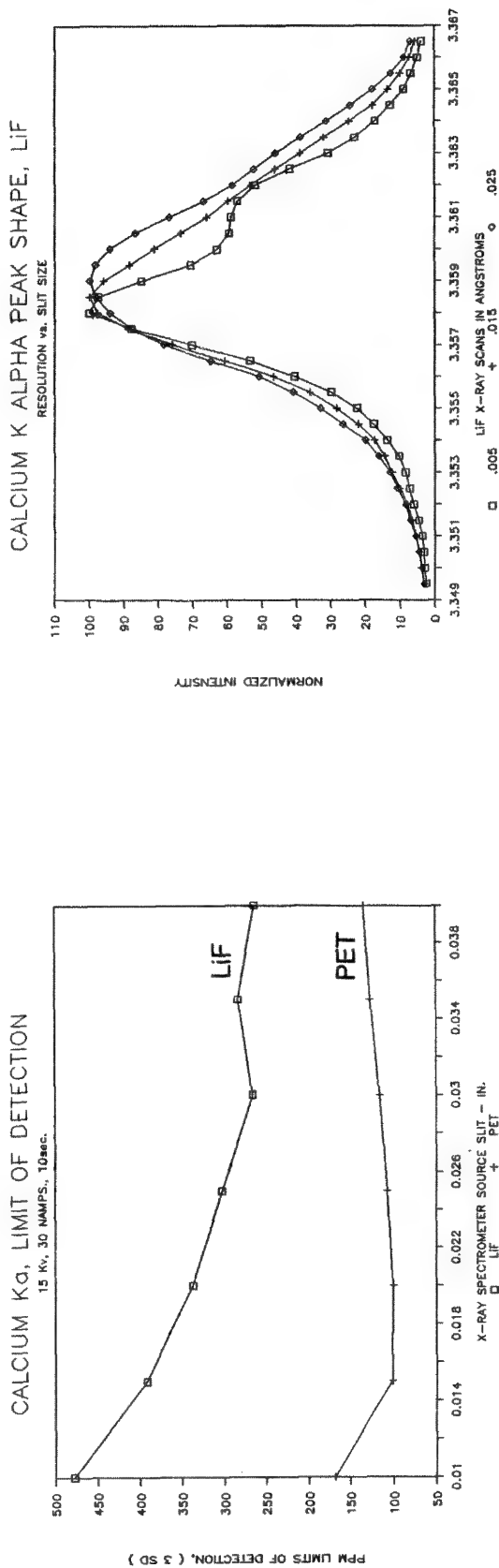


FIG. 1.--Calcium limit of detection vs slit width for LiF and PET x-ray spectrometers. LiF plot is affected by K α 1 and 2 lines being partially resolved. Lowest LD is not at smallest slit settings.

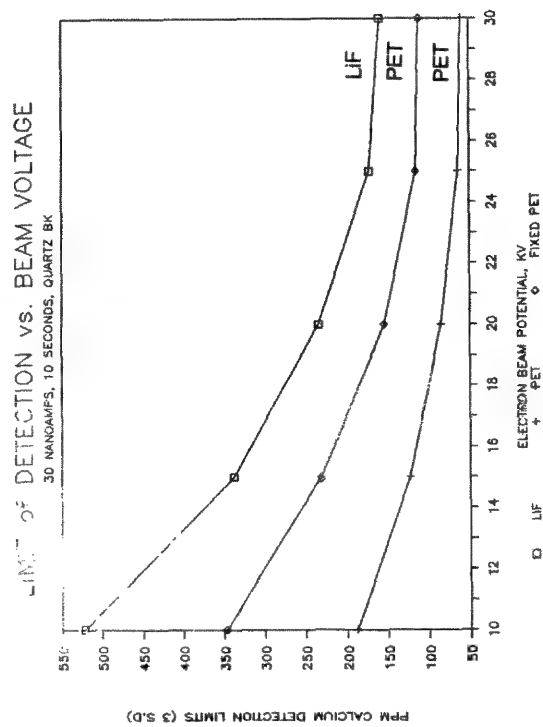


FIG. 3.--Plots of limits of detection (3 S.D.) of calcium vs accelerating potential for LiF and PET x-ray spectrometers and fixed calcium channel.

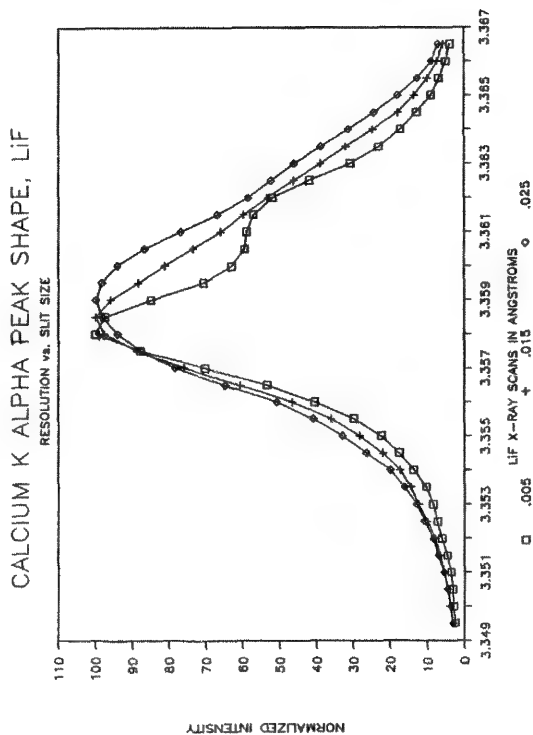


FIG. 2.--Normalized calcium K α peak scans from LiF x-ray spectrometer with slit widths of 0.005, 0.015, and 0.025 in. Partially resolved K α 1 and 2 lines are at smallest slit width.

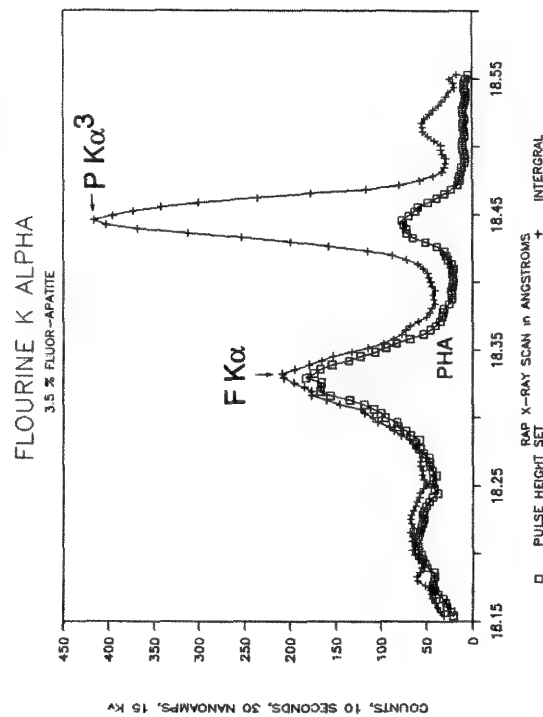


FIG. 4.--Fluorine x-ray spectral scans on a fluor-apatite with and without pulse height discrimination. Third-order phosphorus K lines are reduced when PHA is used.

MN, K, & TI BACKGROUNDS

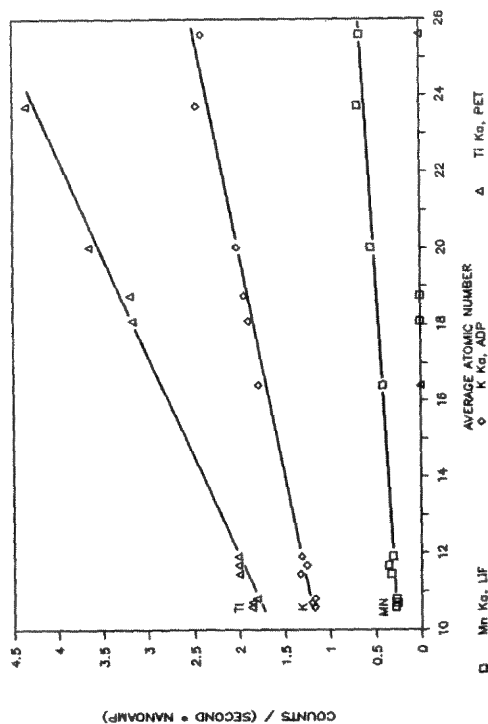


FIG. 5.--Backgrounds for Mn, K, and Ti vs average atomic number. (Compare slopes of these backgrounds to Fig. 6.)

SODIUM K ALPHA AND ZINC L ALPHA

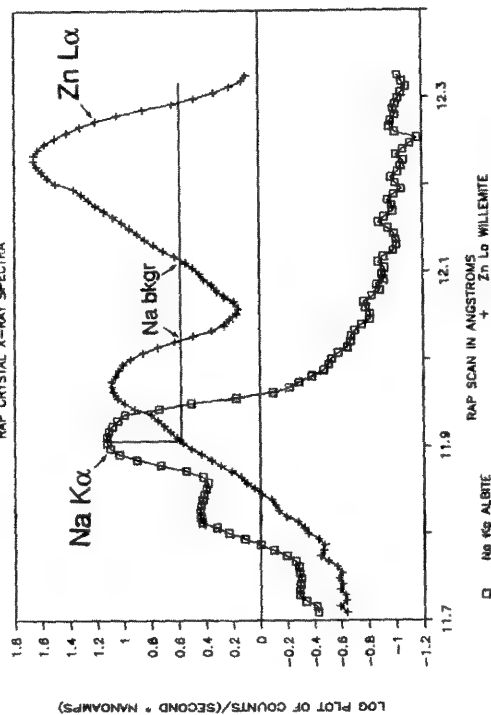


FIG. 7.--X-ray spectra of sodium K α and zinc L α showing where sodium background can be measured to correct for zinc spectrum contribution to sodium peak.

MG, AL, SI, NA BACKGROUNDS

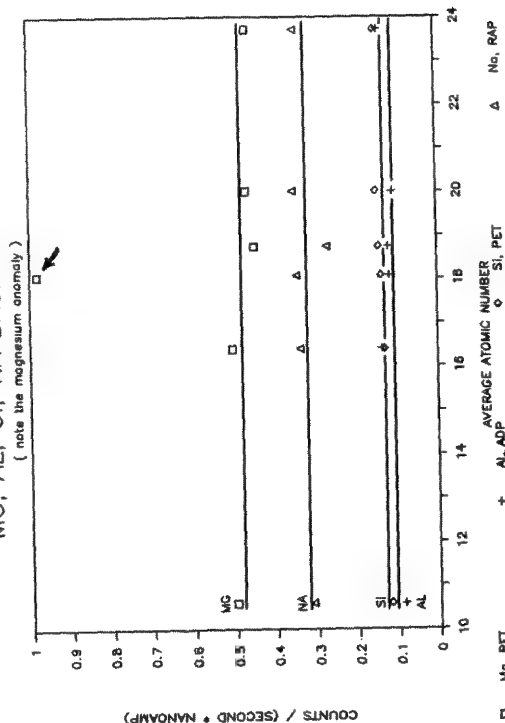


FIG. 6.--Backgrounds for Mg, Al, Si, and Na are relatively flat when plotted vs average atomic number. Anomalous Mg background is due to supposedly pure tephroite standard, actually containing 0.3 wt% MgO.

LIMIT OF DETECTION VS COUNTING TIME

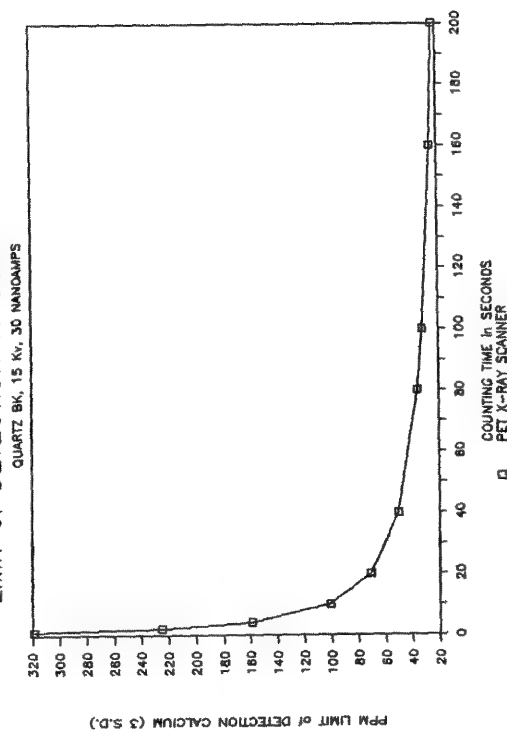


FIG. 8.--Calcium limits of detection vs counting time for PET x-ray spectrometer.

dard which contains 458 ppm of iron. Then we would scan overnight on unknowns, in this case other lower trace element NBS SRM glasses containing 51 and 13.3 ppm Fe. Although we could easily determine a 100ppm iron peak, we would question the 51ppm iron peak. We could certainly not detect 13ppm iron. We could say there is less than 50 ppm of iron present in the 13ppm Fe-bearing glass.

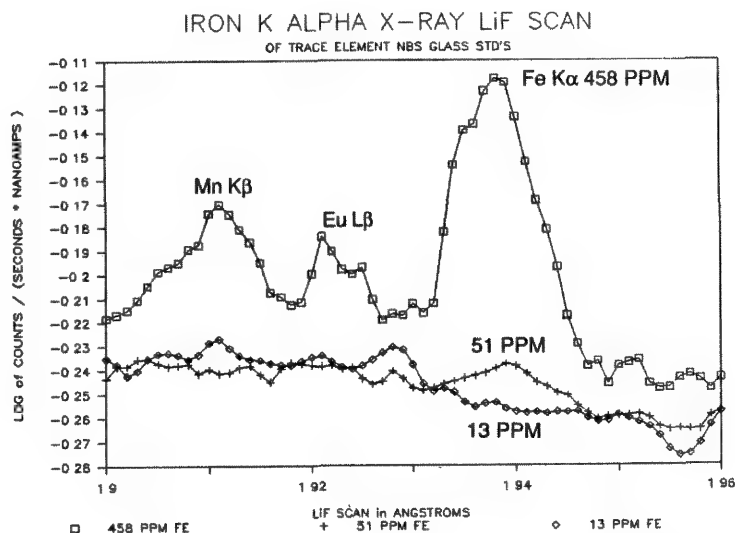


FIG. 9.--Iron $K\alpha$ spectra from trace-element NBS glasses having 458, 51, and 13 ppm iron. Interfering Mn and Eu x-ray lines are seen in 458 ppm NBS glass. Scan for 458ppm Fe glass took 1.7 h; other scans were about 10 h; a 50nA beam was used and glass was moved during analysis.

ANALYSIS OF METEORITIC MINERALS BY PROTON MICROPROBE (PIXE)

Alfred Kracher, T. M. Benjamin, C. J. Duffy, and P. S. Z. Rogers

Differentiated meteorites are samples whose parent bodies underwent a stage of partial or complete melting. The temperature range of melting for chondritic material is large, and we should expect to see a range of materials depending on the maximum temperature during differentiation. Achondrites like the eucrite clan and "magmatic" iron meteorite groups¹ (IIAB, IIIAB, IVA) come from fully differentiated parent bodies. The IAB-IIICD association of irons and winonaites may represent one or more partially differentiated bodies.² The partitioning of some trace elements among metal, sulfide, and oxide phases in meteorites can be used to infer the conditions during differentiation and subsequent fractional crystallization.³ In this paper we evaluate the use of proton probe microanalysis (PIXE) in order to study this partitioning behavior, and compare the results with other analytical techniques applied to the same samples, such as electron probe microanalysis⁴ (EPMA), radiochemical¹ and instrumental neutron activation analysis⁵ (RNAA and INAA), secondary ion mass spectroscopy⁵ (SIMS), and spark source mass spectroscopy⁶ (abbreviated SSMS in this paper).

Techniques and Samples

The instrument used in this study was part of the Ion Beam Facility at the Los Alamos National Laboratory.⁷ A 20 μ m-diameter, 3.0MeV proton beam with a beam current of 0.5-1.5 nA was used. Since all analyzed phases contained Fe as a major element, x-ray filters had to be used to reduce dead time and pile-up peaks caused by the intense Fe K radiation. Absorbers of 77.18 mg/cm² Be and 80.675 mg/cm² Al still allowed the use of Fe as the normalizing element in the data reduction. Data-reduction methods were those developed at Los Alamos National Laboratory for use with this instrument.⁸

Five samples from three iron and two stony meteorites were included in this exploratory study. The classification of the meteorites, with the minerals analyzed in parenthesis, is given below; the discussion of analytical results (by minerals) follows.

Landes (kamacite) is a IA iron meteorite with abundant silicate inclusions. A small kamacite chip from this meteorite was used as secondary standard in the EPMA determination of

Ge in A77081,⁴ and analyzed in this study.

Cape York (troilite, chromite) is a IIIA meteorite. All data are from sulfide inclusions from the Agpalilik specimen of this meteorite shower.

Henbury (troilite, daubréelite, chromite) is a IIIA iron meteorite. Although the host metal is similar to Cape York, the inclusion analyzed here is texturally different. No comparative data are available for this inclusion.

Allan Hills A77081 (kamacite, chromite) is a stony meteorite similar to the silicate inclusions in IAB irons.⁹ A previous EPMA study⁴ showed that small kamacite grains differed in their content of Co, Ni, and Ge from the larger ones, but the anomalous grains were too small for PIXE analysis at the time these measurements were made.

Uden (troilite, chromite) is a highly equilibrated L chondrite. This sample was included as representative of primitive material highly metamorphosed but not melted.

Results

Kamacite. Kamacite is the most abundant metallic phase in most meteorites. Landes kamacite was used as reference material for EPMA determinations of Ge⁴ because of its homogeneity and high Ge content. Since the abundance of metallic phases other than kamacite in Landes is negligible, bulk chemical analyses¹ can be directly compared to microprobe analysis with little sampling bias. Relative to the Chilean hexahedrites, a group of meteorite samples that is even more homogeneous, Landes has about twice the Ge content, which makes this element more easily detectable by electron microprobe.

Table 1 gives results for Landes and Allan Hills A77081. All quoted errors are 1 σ . The EPMA technique is discussed in detail in Appendix 1 of Ref. 4. The EPMA data may be systematically lower than NAA data because of problems with the dead-time correction in EPMA.⁴ This potential error is not included in the 1 σ figures, which only concern reproducibility. The relative error quoted in Table 1 for NAA analyses of Ga and Ge in Landes is $\pm 4\%$, the typical accuracy claimed for this type of analysis.¹⁰ The PIXE errors are propagated from counting statistics, fitting error, uncertainty in the concentration of the normalization element (Fe in this case), and an assumed error of 1.5% in the product of the mass absorption coefficient and the thickness of the Al filter. Attenuation by the filter increases exponentially with decreasing x-ray energy, resulting in low sensitivity for elements near Fe. The 2 σ errors of

A. Kracher is at the Department of Earth Sciences, Iowa State University, Ames, IA 50011; the other authors are at INC-7, Los Alamos National Laboratory, Los Alamos, NM 87545. This work was financially supported by NASA grant NAG9-112.

TABLE 1.--Minor and trace element contents (in $\mu\text{g/g}$) of kamacite in the Landes and Allan Hills A77081 meteorites. EPMA analyses are from the same samples as the PIXE data.⁴ All quoted errors are 1σ .

meteorite	Landes			Allan Hills A77081		
method	PIXE	EPMA	NAA	PIXE	EPMA	INAA
reference	[4]		[1]	[4]		[9]
Cu				<228		227 ± 12
Ga	112 ± 20		88.7 ± 3.6	45 ± 20		38 ± 2
Ge	473 ± 20	340 ± 30	414 ± 17	248 ± 17	230 ± 40	330 ± 70
Mo	6 ± 2			≤ 6		7 ± 1

the PIXE and RNAA determinations of Ge in Landes overlap, but the 14% difference may also reflect some sample heterogeneity.

The INAA data for A77081 are from a metal separate. As in Landes, kamacite is by far the dominant metallic phase in A77081, and the composition of this metal separate should be very close to that of pure kamacite. The error bars of the Ge determination by INAA overlap the PIXE and EPMA uncertainties.

The agreement for Ga in both cases (Table 1) is within the error of the PIXE analysis. The PIXE determination of Cu in a Fe,Ni matrix has low sensitivity because of the thick Al filter. Two samples (Landes kamacite and Cape York troilite/chromite) mounted in brass tubes may have been slightly contaminated during polishing. Therefore Cu and Zn is not reported for these minerals, except for Zn in chromite, whose concentration is so much higher than that of Cu that any contribution from brass must be trivial.

Only an upper limit could be obtained for Mo in A77081, but this is close to the INAA determination. No comparative Mo analysis is available for Landes, but the concentration determined by PIXE is typical of this type of meteorite.

Troilite. Table 2 shows comparative analyses of troilite by five different methods, including some elements not determined in these particular PIXE analyses. Se was easily detected by PIXE. The Se/S ratio shows little variation in meteorites, within about $\pm 25\%$ of the cosmic value. Analyses of Se in Cape York troilite by different techniques agree very well, except for one of the two mass spectrometric values, and Henbury troilite is similar to Cape York. Uden troilite has a higher Se/S ratio, in complete agreement with average S and Se concentration in L chondrites.¹² As in the metal phase, the upper limits for Mo are close to the values obtained with other methods.

On other elements, there is generally adequate agreement between EPMA, INAA, SIMS, and SSMS, with some exceptions (e.g., Mn). Thinner Al x-ray filters and reduced beam currents would permit analysis of these elements by PIXE. EPMA,¹¹ PIXE, and SSMS⁶ data are from

splits of the same inclusions. Some of the variation between that sample and the one studied by INAA and SIMS⁵ may be real.

Daubreelite. This mineral was found only in Henbury, and Se ($310 \pm 50 \mu\text{g/g}$) and Ga ($<72 \mu\text{g/g}$) are the only trace elements detected by PIXE. The Se/S ratio of daubreelite appears to be higher than that of troilite. For mass balance reasons troilite in iron meteorites containing daubreelite should have a lower Se/S ratio than troilite in chondrites. This is indeed observed within our limited selection of troilite samples (Table 2).

Chromite. In iron meteorites, chromite is an important indicator of formation conditions.¹³ Two types of chromite are included in this study. The two group IIIA iron meteorites, Cape York and Henbury, contain practically pure FeCr_2O_4 , which probably formed from small amounts of Cr and O dissolved in the metallic melt. Chromite with minor Mg and Al is associated with silicates in Allen Hills A77081 and Uden. The major element compositions are given in Table 3.

Comparative trace element data exist for the Cape York sample only (Table 4). A sectional study of a sulfide inclusion by SSMS⁶ revealed strong enrichments of some elements (V, Cr, Mn, Zn, Ga) at one end of the inclusion. It was due to small chromite inclusions, and from the Cr concentration it can be calculated that the most enriched sample contained 10.6% chromite by weight. If we subtract the data for pure troilite, we can infer the chromite composition (SSMS column in Table 4). This calculation is probably valid for all elements except Cu, which is mostly present as metallic veinlets,^{5,11} and Zn, which is present in sphalerite (ZnS) in addition to chromite.¹¹ Considering the uncertainties, the agreement among all analytical methods is very good.

Comparison of Methods

Our PIXE analyses represent counting times between 30 min and 1 h. Count rates for routine analysis are five times higher, without overloading the EDS detector, with the new accelerator at the Ion Beam Materials Laboratory,

TABLE 2.--Minor and trace element contents (in $\mu\text{g/g}$) of troilite in the Cape York, Henbury, and Uden meteorites.

meteorite	Cape York					Henbury	Uden
method	SSMS	INAA	SIMS	EPMA	PIXE	PIXE	
reference	[6]	[5]	[5]	[11]			
V	7.6	3.7	9				
Cr	1000		1600	1300			
Mn	170	200	1070	190			
Cu	50	110	120			1110 ± 115	≤ 266
Zn	<19	8.7				220 ± 34	<104
Ga	0.2	<1.5			<15	<32	<56
Se	38;92	90.4			97 ± 6	87 ± 9	150 ± 20
Mo	8.6	5.6			≤ 4	≤ 5	<12

TABLE 3.--Major element composition (by EPMA, in weight percent) of chromite in the Cape York, Allen Hills A77081, and Uden meteorites.

	Cape York	A77081	Uden
Cr_2O_3	67.33	60.95	55.90
Al_2O_3	.07	6.76	5.49
TiO_2	-	1.02	2.77
SiO_2	.07	.62	.33
FeO^2	31.55	22.23	32.70
MnO	.49	1.26	.60
MgO	.07	6.58	1.73
CaO	-	.05	.06
Total	99.58	99.47	99.58

TABLE 4.--Minor and trace element contents (in $\mu\text{g/g}$) of chromites in the Cape York, Henbury, Allan Hills A77081, and Uden meteorites.

meteorite	Cape York				Henbury	A77081	Uden
method	SSMS	SIMS	EPMA	PIXE	PIXE		
reference	[5]		[11]				
V	2100	720	1840				
Mn	3570	5120	3820				
Cu	4020	122		896 ± 72	<79	<60	<94
Zn	12660	3200	1290	1290 ± 59	2680 ± 74	8100 ± 190	738 ± 33
Ga	112			129 ± 10	≤ 18	77 ± 14	25 ± 7
Ge	1.0			<12	<14	<10	<12

Los Alamos. Thus the detection limits could probably be reduced by more than a factor of 2 without an increase in counting time.

Most trace elements included in this study show a strong preference for one particular phase, leading to low concentrations in all the other phases. This is an unfavorable situation for determining partitioning behavior. However, Ga is present in amounts easily detected

by PIXE in both kamacite and chromite. INAA and PIXE are both sensitive for Ga, but its concentration in troilite appears to be too low to be easily determined by either method.

In bulk samples like iron meteorites, Ge usually has to be determined by RNAA, because of large uncertainties in INAA, PIXE is much more reliable, and allows the study of Ge microdistribution. Comparison of the sensitivity

for Ge of the EPMA and PIXE results given in Table 1 is difficult, because the EPMA analyses were optimized for Ge, but the analytical parameters for PIXE analysis were chosen to obtain data on as many elements heavier than Fe as possible. Separate experiments¹⁴ have shown that the ultimate PIXE sensitivity for Ge is about 3 µg/g (2σ level). Scaling of this result to the 12min counting time used for the EPMA analysis gives a comparable sensitivity of 20 µg/g, about four times better than the estimated detection limit (75 µg/g) of the EPMA determination for this element.⁴ However, the further important advantage of PIXE is that all elements with x ray energies between 7 and 35 keV can be determined simultaneously in a single 1h count with similarly low detection limits. For the Landes spectrum of Table 1, PIXE analysis found 34 elements with detection limits below 100 µg/g.

Molybdenum is an important indicator of partial differentiation, since it has significant affinity to both kamacite and troilite. Our data show that it is quite feasible to study its microdistribution by PIXE. For troilite this approach may require longer counting times. For Mo analysis in kamacite higher beam currents and a heavier absorber could be used. In this case, trace element concentrations could be normalized to Ni rather than Fe, or external standards could be used rather than internal normalization. EPMA is not useful for studying the microdistribution of Mo, since the Mo K radiation is outside the range of all commercial WDS spectrometers, and L lines do not afford nearly the same sensitivity.

In principle the sensitivity of PIXE for individual transition metal elements could be greatly enhanced by the addition of WDS spectrometers, which would allow the determination of elements whose x-ray energy is lower than that of the heaviest major element (e.g., Cr in troilite), and reduce the detection limit for most elements. Even with the present EDS system, PIXE is a very useful tool in the study of trace element distributions that elucidate the history of differentiated meteorites.

References

1. J. T. Wasson, *Meteorites*, New York: Springer, 1974, 316 pp.
2. A. Kracher, "The evolution of partially differentiated planetesimals: Evidence from iron meteorite groups IAB and IIICD," *Proc. Lunar Planet. Conf.* 15 (*J. Geophys. Res.* 90): C689-698, 1985.
3. A. Kracher and M. L. Pierson, "Elements Cu through Ge: Cosmochemical significance and microanalysis in meteorites," *Microbeam Analysis--1986*, 151-152.
4. A. Kracher, "Metal with low Ni and Ge contents in the Allan Hills A77081 winonaite," *Proc. 18th Lunar and Planetary Science Conference* (Cambridge University Press), pp. 485-491.
5. C. Koeberl et al., "Cape York IIIAB iron meteorite: Trace element distribution in mineral and metallic phases," *Memoirs of National Institute of Polar Research (Japan)*, Special Issue 41: 297-313, 1986.
6. K. P. Jochum et al., "Distribution of minor and trace elements in the elongated troilite inclusions of the Cape York iron Agpalilik (abstract)," *Meteoritics* 10: 419-422, 1975.
7. T. M. Benjamin et al., "Development and application of the Los Alamos nuclear microprobe: Hardware, software, and calibration," *Microbeam Analysis--1985*, 236-240.
8. C. J. Duffy et al., "Los Alamos PIXE data reduction methods," *Nuclear Instruments and Methods* B22: 91-95, 1987.
9. L. Schultz et al., "Allan Hills 77081: An unusual stony meteorite," *Earth Planet. Sci. Lett.* 61: 23-31, 1982.
10. E. R. D. Scott et al., "The chemical classification of iron meteorites: VII. A reinvestigation of irons with Ge concentrations between 25 and 80 ppm," *Geochim. Cosmochim. Acta* 37: 1957-1983, 1973.
11. A. Kracher et al., "Cape York: The extraordinary mineralogy of an ordinary iron meteorite and its implication for the genesis of IIIAB irons," *Geochemical J.* 11: 207-217, 1977.
12. J. T. Wasson and C.-L. Chou, "Fractionation of moderately volatile elements in ordinary chondrites," *Meteoritics* 9: 69-84, 1974.
13. A. Kracher et al., "Partitioning of gallium into chromite, and consequences for iron meteorite formation," *Lunar Planet. Sci.* XVIII: 515-516, 1987; A. Kracher, "Behavior of chromium during differentiation of chondritic asteroids (abstract)," *Meteoritics* 22: 431, 1987.
14. P. S. Z. Rogers et al., "Accuracy of standardless nuclear microprobe trace element analyses," *Nuclear Instruments and Methods* B22: 133-137, 1987.

ELECTRON MICROPROBE ANALYSIS OF BASALTIC GLASSES AND ASSOCIATED ALTERATION PRODUCTS

M. J. Jercinovic and Klaus Keil

The alteration of basaltic glass (SiO_2 from 45 to 52 wt%) is a process of interest as a possible analog for the formation of a Martian regolith component,¹ in understanding the ocean crust/seawater chemical budget,² and in modeling the long-term corrosion of nuclear waste-form glasses.³ The alteration of basaltic glass proceeds by hydrolytic replacement of the glass and results in an amorphous aluminosilicate gel (palagonite), and formation of various cementing phases, such as smectite clays, zeolites, and calcite.^{1,2,4,5}

A major consideration in the electron microprobe analysis (EMPA) of glass is the behavior of alkalis, particularly sodium, when exposed to the electron beam.⁶⁻¹³ In addition, the resulting alteration products (hydrated, alkali-bearing minerals) are also subject to beam damage.¹⁴ Efforts to minimize the problem of alkali diffusion have included use of high accelerating potential and low beam current,¹⁵ broadening the beam,¹⁶ beam rastering,¹¹ empirical corrections, and cryogenic techniques.¹⁰

Experimental

Alkali diffusion tests were performed on basaltic glasses and associated alteration products in samples from Iceland (GI2), Alaska (TT2), Hawaii (KK2), New Mexico (IM1), British Columbia (TB2 and TB5), and the Antarctic (An3). Intensity (counts $\cdot \text{nA}^{-1} \cdot \text{s}^{-1}$) vs time relationships were determined for sodium and potassium on a number of points on glasses, palagonites, and zeolites with a 20 nA, 2 μm beam. An ARL EMX-SM with four spectrometers (three automated and one fixed) was used for the diffusion tests. Phase compositions were established by EMPA after methods were developed to account for alkali diffusion. These analyses were done on the ARL EMX-SM and on a JEOL 733 Superprobe.

Results

In each case, Na exhibits a greater relative loss in intensity than K; consequently, only Na results are presented, since they represent the worst case. Up to 59% loss was seen for Na in glass over the time of a typical ten-element analysis, 162 s (Figs. 1a and b). Note that diffusion curves cannot be predicted from the initial Na x-ray intensity. Thus, a measurement of Na counts at 90 s could not be extra-

polated back to the true intensity at time zero without knowledge of the precise nature of the curve for the glass of interest. It is interesting that the initial slopes of the diffusion curves do not correlate well with the Na_2O content of the glass (Fig. 2a). However, a good correlation exists between the initial slope of the Na-diffusion curves and the MgO content of the glass: more MgO-rich glasses exhibit lower diffusion rates (Fig. 2b). Defocusing of the beam to a diameter of 40 μm results in no discernable diffusion over the period of analysis of glasses (Fig. 1c).

Diffusion tests for Na on palagonite (Fig. 1d) in most cases show decreasing x-ray intensity with time. However, some of the tests on An3 palagonite show increasing Na intensity with time. An increase in intensity is also seen after 100 s for other points of An3 palagonite and for IM1 palagonite. Such effects may be due to beam-induced damage of the conductive coating, which would allow surface-charge buildup.⁷ Increasing intensity with time may also result from high sample temperature without destruction of the conductive coating.¹⁷ Palagonite rinds range in thickness from a few to several hundred micrometers. To analyze thin palagonite rinds and to investigate compositional heterogeneities (e.g., zoning) within thicker rinds, a nearly focused beam must be used. The diffusion curves in Fig. 1d indicate that the loss (or gain) of Na counts within the first several seconds of beam bombardment is well within the estimated counting error. A single 2 s, 10 nA, 4 μm point analysis gives an Na_2O value of 1.53 ± 0.14 wt% for TB2 palagonite and 0.22 ± 0.07 wt% for TB5 palagonite. Point analyses performed at 20 s, 2 nA, and 4 μm give similar counting statistics ($\text{Na}_2\text{O} = 1.53 \pm 0.12$ wt% for TB2 and 0.22 ± 0.05 wt% for TB5 palagonite).

Diffusion tests were done on phillipsite (K-Ca zeolite) and chabazite (Na-Ca zeolite) in samples TB2 and TB5 (Fig. 1e). Zeolite crystal sizes limit the possible beam diameter to 15 μm . Na diffusion can be substantially reduced over the analysis time of zeolites (70 s for six elements with a four-spectrometer (three automated and one fixed) ARL EMX-SM, 90 s for eight elements with a five-spectrometer JEOL 733) by use of a 10 nA, 15 μm beam.

Conclusions

Alkali diffusion curves are not always a simple exponential decrease in x-ray intensity with time. Increasing Na intensity is also seen, either initially or after a period of decreasing intensity. Analysis with a

The authors are at the Department of Geology and Institute of Meteoritics, University of New Mexico, Albuquerque, NM 87131. The following have provided samples: J. M. Hoare and R. J. Motyka (Alaska); W. E. LeMasurier (Antarctica); and Carlton C. Allen (Hawaii). The work was conducted under NASA Grant NSG-7579 to K. Keil.

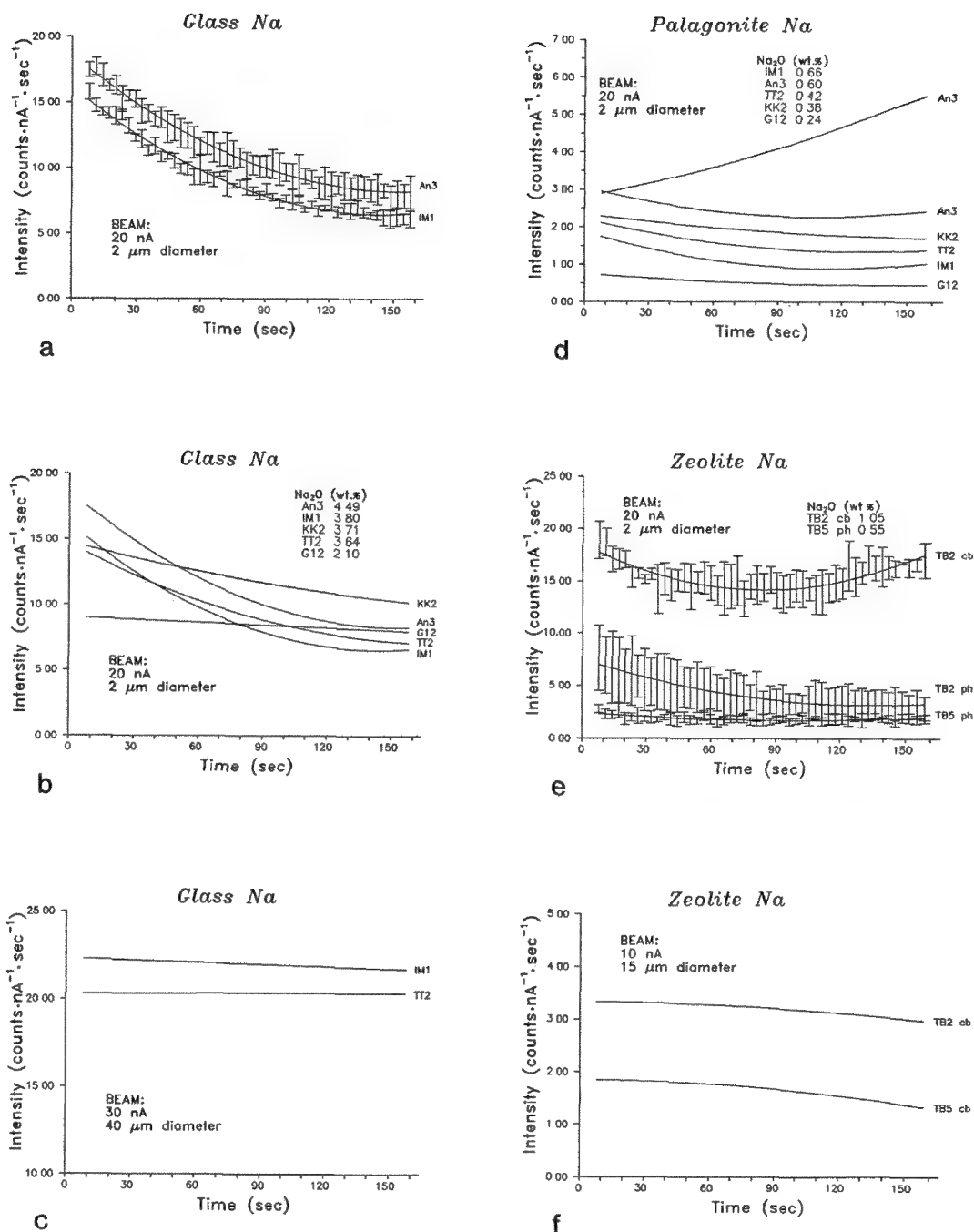


FIG. 1.--Results for diffusion tests for glass, palagonite, and zeolite. Best-fit curves were calculated by polynomial regression. (a) Examples of two glasses with error bars to indicate variation. (b) Focused-beam diffusion curves for all glasses. (c) Diffusion curves for two glasses with defocused beam. (d) Diffusion curves for palagonites. (Tests exhibiting increase in intensity with time for An3 are plotted separately from those exhibiting decrease.) (e) Focused-beam diffusion curves for zeolites (cb = chabazite, ph = phillipsite). (f) Diffusion curves for zeolites with defocused beam and lowered beam current.

defocused beam is reasonable for analysis of bulk glass or large crystals, but if one wishes to preserve the microscale analytical capability of EMPA (a necessity for analysis of palagonites and small crystals, or studies of compositional heterogeneities), counting times must be decreased or the current density must be lowered relative to the beam diameter by lowering of

the beam current. The use of short times (2 s), averaged over a number of points, is safest considering possible beam damage to the conductive coating. More MgO-rich glasses (which have the lowest alkali diffusion rates) may allow the use of higher current density during EMPA, with resulting improvements in precision and detection limits.

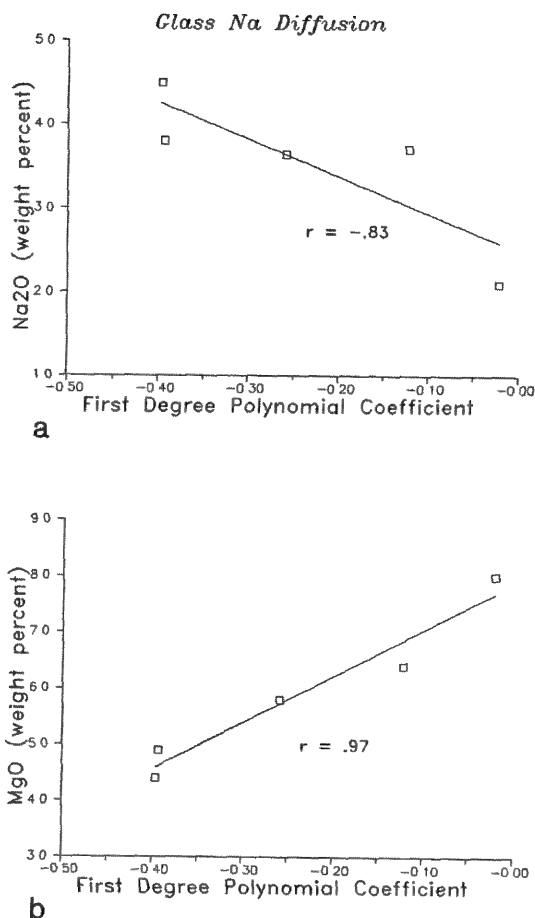


FIG. 2.--Plots of initial slope of diffusion curves for Na in glass (estimated by use of first-degree polynomial coefficient of best-fit curves) vs (a) Na₂O content and (b) MgO content from defocused-beam microprobe analysis.

References

1. C. C. Allen, J. L. Gooding, M. J. Jercinovic, and Klaus Keil, "Altered basaltic glass: A terrestrial analog to the soil of Mars," *Icarus* 45: 347, 1981.
2. Hubert Staudigel and S. R. Hart, "Alteration of basaltic glass: Mechanisms and significance for the oceanic crust-seawater budget," *Geochim. Cosmochim. Acta* 47: 337, 1983.
3. Werner Lutze, Gunter Malow, R. C. Ewing, M. J. Jercinovic, and Klaus Keil, "Alteration of basalt glass: Implications for modelling the long-term stability of nuclear waste glasses," *Nature* 314: 252, 1985.
4. R. L. Hay and A. Iijima, "Nature and origin of palagonite tuffs of Honolulu Group on Oahu, Hawaii," *Geol. Soc. Am. Memoir* 116: 338, 1968.
5. R. L. Hay and A. Iijima, "Petrology of palagonite tuffs of the Koko Craters, Oahu, Hawaii," *Contrib. Min. Pet.* 17: 141, 1968.
6. P. H. Ribbe and J. V. Smith, "X-ray-emission microanalysis of rock-forming minerals: IV. Plagioclase feldspars," *J. Geol.* 74: 217, 1966.
7. M. P. Borom and R. E. Hammerman, "Local composition changes in alkali silicate glasses

during electron microprobe analysis," *J. Appl. Phys.* 38: 2406, 1967.

8. W. G. Melson et al., "A catalog of the major element chemistry of abyssal volcanic glasses," *Smithsonian Contrib. Earth Sci.* 19: 31, 1977.

9. Eugene Jarosewich, A. J. Parkes, and L. B. Wiggins, "Microprobe analyses of four natural glasses and one mineral: An inter-laboratory study of precision and accuracy," *Smithsonian Contrib. Earth Sci.* 22: 53, 1979.

10. C. H. Nielson and Haraldur Sigurdsson, "Quantitative methods for electron microprobe analysis of sodium in natural and synthetic glasses," *Am. Mineral.* 66: 547, 1981.

11. M. B. Strobe, "A method of combating alkali metal loss during microbeam analysis of basaltic glass," *Microbeam Analysis--1984*, 154.

12. Rachel Cowan and R. C. Ewing, "Alteration products of basaltic glass, Hanauma Bay, Oahu, Hawaii," *Microbeam Analysis--1986*, 131.

13. J. M. Walker and D. G. Howitt, "Alkali metal loss in glass from a characterizing electron probe," *Microbeam Analysis--1986*, 299.

14. Helene Bizouard, "Geological samples, glasses and ceramics: Preparation and analysis," in F. Maurice, L. Meny, and R. Tixier, Eds., *Microanalysis and Scanning Electron Microscopy*, Orsay: Les Editions de Physique, 1979, 377.

15. P. J. Goodhew and J. E. C. Gulley, "The determination of alkali metals in glasses by electron probe microanalysis," *Glass Tech.* 15: 123, 1974.

16. J. H. Natland and W. G. Melson, "Composition of basaltic glasses from the East Pacific Rise and Siqueiros fracture zone, near 9°N," in B. R. Rosendahl et al., Eds., *Init. Rep. DSDP 54*, Washington: U. S. Govt. Printing Office, 1980, 705.

17. L. F. Vassamillet and V. E. Caldwell, "Electron-probe microanalysis of alkali metals in glasses," *J. Appl. Phys.* 40: 1637, 1969.

NITRIDE LAYER GROWTH IN IRON AND TITANIUM ALLOYS: STUDIES BY ELECTRON PROBE MICROANALYSIS

E. Metin, A. D. Romig Jr., O. T. Inal, and R. E. Semarge

The surface properties of metals are often modified by the addition of small amounts of alloying elements. When the primary motivation for surface and modification is a higher hardness, and typically better wear resistance, the added alloying element is often an interstitial element. The increased surface hardness is due to the formation of a hard martensitic layer and/or the formation of hard compound layers (or a high density of near surface compound precipitates). The present study addresses the surface hardening of Fe and Ti by plasma nitriding. The work reported here describes quantitative electron probe microanalysis of the nitride layers and composition gradients which form during the nitriding process in iron (600 C) and titanium (800-1080 C). Such measurements are the key to developing quantitative diffusion models for the nitriding process (e.g., prediction of microstructural evolution as a function of time and temperature).

It is the objective of the present work to develop the quantitative electron probe microanalysis (EPMA) techniques to determine the compositions of Fe and Ti nitrides and to measure concentration gradients of N in metallic phases of Fe and Ti. Such measurements are not routine for several reasons: (1) the difficulty in obtaining standards of sufficient quality for quantitative analysis, (2) the N K α x rays are readily absorbed in both metal matrices, requiring large absorption corrections, and (3) for Ti only, interference between the N K α and the Ti L β x-ray lines. The difficulties can be addressed by the judicious choice of standards, EPMA operating conditions, and matrix correction algorithm.

Background

Ion Nitriding. Ion nitriding, also known as nitrogen plasma nitriding and glow discharge nitriding, is a fast and efficient process for the hardening of metallic surfaces by the in-

troduction of nitrogen. A schematic of the process is given in Fig. 1. A potential field of less than 1 keV (far less than that used in ion implantation) is placed across the anode and cathode, which ionizes the N gas and drives the ionized N to the surface of the workpiece. The potential field can be varied as a means to vary the temperature of nitriding. (The variation in potential changes the N ion kinetic energy and hence energy transfer to the workpiece.) Heating is accomplished solely by energy transfer from the plasma and an external heating source is not used. The anode is typically a Ni or stainless-steel plate (often other stainless-steel components of the nitriding chamber are also at the anode potential) and the workpiece to be nitrided is typically the cathode. Ultrahigh purity (UHP) dry nitrogen, often mixed with various amounts of H, is passed into the system, where it is ionized. The hydrogen appears to improve the nitriding process, perhaps because of its ability to aid in initial cleaning of the metal surface. The total pressure in the nitriding chamber is typically a few torr.

Ion nitriding is of commercial interest because it is much faster and more efficient than conventional gas nitriding. For the diffusion of an interstitial element, such as N into Fe or Ti, the increased rate of nitriding is believed to be due to increased thermodynamic activity of N at the surface during ion nitriding relative to conventional gas nitriding.¹ The mechanism involves the formation of metastable nitrides at the surface which subsequently decompose, giving rise to the high surface activity of the nitrogen. For more detail on the ion nitriding process, the reader is referred to the original work by Metin.¹

EPMA Analysis of N. The quantitative measurement of N concentration at high spatial resolution in metals by EPMA is a nontrivial experiment. As a low-atomic-number element, N is not well suited for x-ray microanalysis. The element, although readily ionized by the incident beam, has a low fluorescence yield and hence does not efficiently produce characteristic x rays. Furthermore, the x rays are low energy (392 eV) and are readily absorbed in the metallic matrix. Hence, quantitation often requires a large absorption correction. Quantitation also requires homogeneous standards of known composition. Nitrides have a stoichiometric range, making it often difficult to obtain well characterized standards. Quantitation is made more difficult in a matrix containing Ti, since the Ti L β line (395 eV) interferes with the N K α line (392 eV). The overlap is so severe that interference is a

E. Metin and O. T. Inal are with the New Mexico Institute of Mining and Technology, Socorro, NM 87801; A. D. Romig Jr. and R. E. Semarge are with Sandia National Laboratories (Div. 1831), Albuquerque, NM 87185. The work performed at New Mexico Institute of Mining and Technology was supported by the Research and Development Division of the New Mexico Institute of Mining and Technology and by a grant from the New Mexico Chapter of the American Vacuum Society to E. Metin. The work performed at the Sandia National Laboratories was supported by the U.S. Department of Energy under contract DE-AC04-76DP00789.

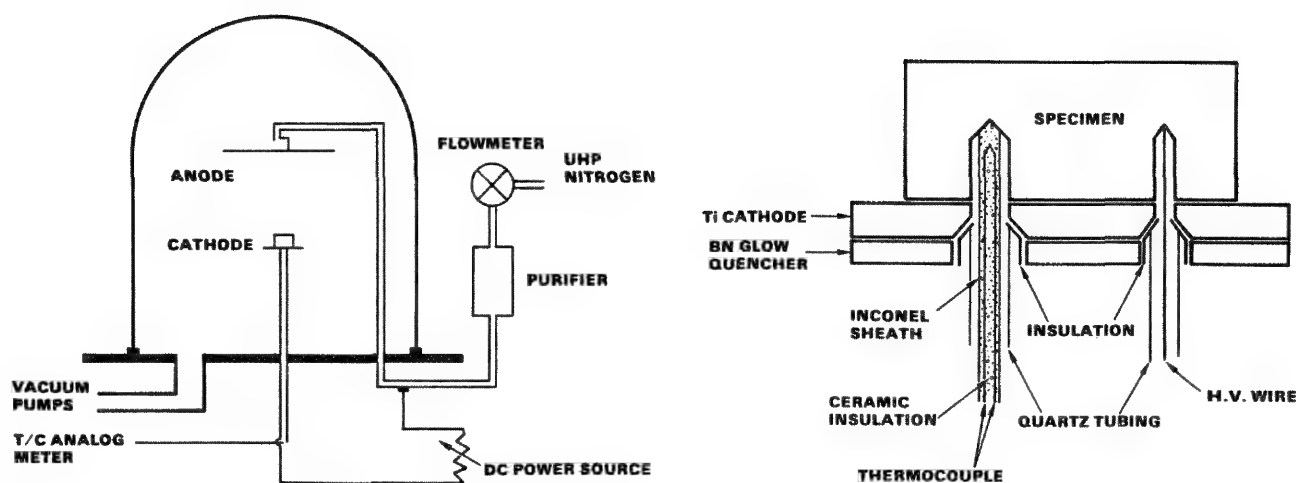


FIG. 1.--(a) Schematic of ion nitriding system, (b) details of cathode arrangement.

problem even with high-resolution wavelength-dispersive system (WDS) analyzing crystals.

Diffusion Modeling of the Ion Nitriding Process. During ion nitriding, N diffuses into the substrate metal. If the N surface activity is great enough, one or more metal nitrides layers form on the surface, with the most N-rich compound forming as the outermost layer. At greater depths, one or more nitrogen-bearing metallic phases may form. The interface between each pair of phases is in local thermodynamic equilibrium, so that the interface compositions are those given by the incoherent phase diagram.² The diffusional models which describe such layer growth are well developed.^{1,3-7} These various models are essentially equivalent, although there are some subtle differences with respect to their ability to accommodate terminal phase solubility. Some of the solutions are formal error-function solutions; others assume steady-state diffusion. Error function solutions allow for non-linear composition gradients in each phase. The position of each phase interface is calculated by numerical solution of a system of $3N + 1$ coupled equations, where n is the number of phases. The equations are derived by use of both a flux and a mass balance. Steady-state solutions assume linear concentration gradients in each phase. The interface positions are calculated by solution of a system of n coupled equations, where n is still the number of phases. The equations are derived by use only of a mass balance, where the mass is taken to be equal to the area under the concentration-distance curve for each phase. The steady-state models are capable of accommodating a compositionally dependent diffusion coefficient. For a complete discussion of the various models and their derivations, the reader is referred to the literature.^{1,3-7}

The experimental observations and the diffusional analysis can be used in two complementary ways. If the diffusion coefficients in the various phases are unknown, measured layer thicknesses and concentration profiles in the various layers can be mathematically analyzed

to determine the diffusion coefficients. If the complete set of diffusion coefficients are known, they can be used to model, in a predictive way, the evolution of the microstructure during the nitriding process.

Experimental Procedure

Ion Nitriding. The potential field was varied between 0.5 and 1.0 keV as the means to control the nitriding temperature. The anode was a stainless-steel plate and the cathode was a plate of Ti. The workpiece to be nitrided was placed in electrical contact with a Ti cathode. Ultra-high purity (UHP) dry nitrogen (20%) with UHP hydrogen (80%) was used for the nitriding of Fe. Pure UHP dry nitrogen was used for the nitriding of Ti. Gas was fed into the system at a flow rate of 0.35 l/min. The total pressure in the nitriding chamber was 10 torr for the nitriding of Fe and 5 torr for the nitriding of Ti. The Fe was nitrided at only 600 C. The Ti was nitrided at 800, 900, 1000, and 1080 C.

Electron Probe Microanalysis. The nitrided specimens were mounted and polished by traditional metallographic techniques. A tight Al foil wrap was used around the specimens for edge retention during polishing. The specimens and N standards were lightly C coated for EPMA. Pure Ti and Fe were used as standards for the metals. Stoichiometric BN, containing 56.45 wt.%N, was used as a standard for N. The background for N was measured on pure Ti. The analysis was performed in a Cameca-MBX EPMA operated at 15 kV at a beam current of 22 nA. Under these conditions, spatial resolution for microanalysis was approximately 1 μ m. A pentaerythritol (PET) analyzing crystal was used for the Ti K α x-ray line, a lithium fluoride (LiF) analyzing crystal was used for the Fe K α x-ray line, and a high-resolution dedicated light element, lead stearate (LSD) analyzing crystal, was used for the N K α x-ray line. Compositions were measured at 1 μ m steps in the near surface regions. In the deeper regions, where the N content varied more slowly, measurements were

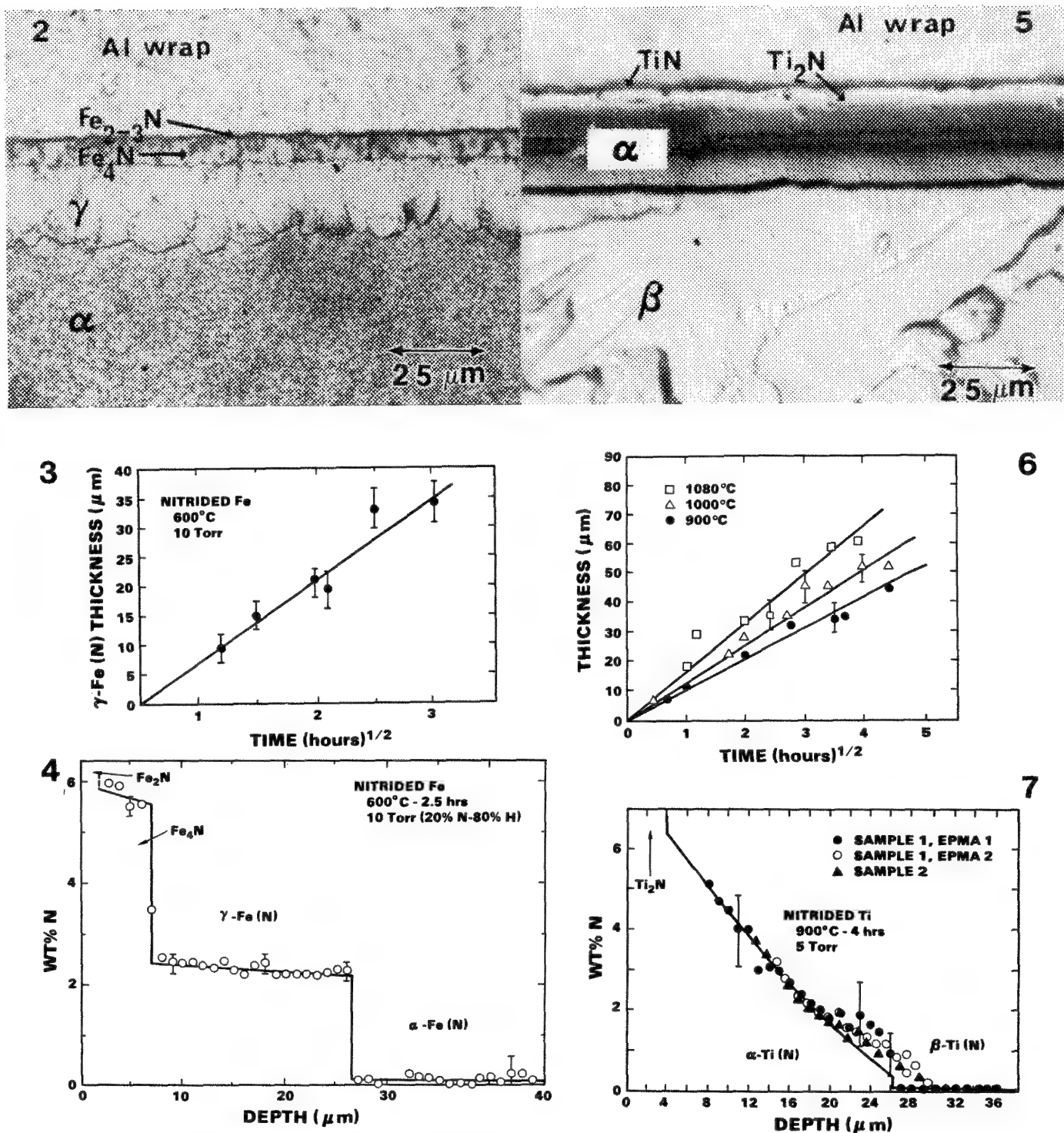


FIG. 2.--Optical micrograph of Fe sample nitrided at 600 C for 2.5 h at N pressure of 10 torr. Phases shown on micrograph are those formed during diffusion anneal. Subsequent transformations occur on quenching that alter crystal structure but do not alter bulk phase composition.

FIG. 3.--Thickness of $\gamma\text{-Fe(N)}$ layer vs time at 600 C under N pressure of 10 torr.

FIG. 4.--N profile, as measured by EPMA, in sample of Fig. 2 nitrided at 600 C for 2.5 h under N pressure of 10 torr.

FIG. 5.--Optical micrograph of Ti sample nitrided at 900 C for 4 h at N pressure of 5 torr. Phases indicated on micrograph are those formed during diffusion anneal. Subsequent transformations occur on quenching that alter crystal structure but do no alter bulk phase composition.

FIG. 6.--Thickness of $\alpha\text{Ti(N)}$ layer vs time at 900, 1000, and 1080 C under N pressure of 5 torr.

FIG. 7.--N profile, as measured by EPMA, in Fig.5 sample. Discrepancies between experimental data and diffusion model at low N levels in $\alpha\text{-Ti(N)}$ phase are believed to be due to compositionally dependent diffusion coefficient. Models developed here cannot accommodate compositionally dependent diffusion coefficient.

made at greater intervals. In all cases, measurements were taken until the N intensity reached the background level.

The x-ray intensity data were converted to weight percent composition with the $\phi(\rho z)$ data reduction algorithm,⁸ operated under Sandia Task8.⁹ The algorithm uses the absorption coefficients of Heinrich¹⁰ for $Z \geq 10$ and of Henke and Ebisu¹¹ for $Z = 5, 7, 8$, and 9.

Diffusion Analysis and Modeling. The diffusion coefficients of N in Fe and Fe nitrides are known. Hence, these experiments served as a means to verify the capability to perform quantitative EPMA analysis for N (in the absence of characteristic line interference) and the capability to model multiphase layer growth by use of a number of different mathematical formulations. In fact, the results can be used to evaluate the relative merits of each of the diffusional growth models.

The diffusion coefficients of N in most of various phases formed during nitriding of both Fe and Ti are not well known, and the analysis of layer thickness and composition profiles in the phases can be used to determine the diffusion coefficients.

Results and Discussion

Nitrided Fe. Examination of the Fe-N phase diagram¹² suggests that the Fe-N "diffusion couple" formed during nitriding at 600 C should contain, from the outer surface inward, Fe_2N , Fe_{2-3}N , Fe_4N , $\gamma\text{-Fe(N)}$, and $\alpha\text{-Fe(N)}$, where the Fe(N) indicates that the N is dissolved in a metallic Fe phase. The $\gamma\text{-Fe(N)}$ and $\alpha\text{-Fe(N)}$ phases have the fcc and bcc crystal structures, respectively. The optical micrograph (Fig. 2) shows that the predicted layers did indeed form in an Fe sample nitrided at 600 C for 2.5 h. The presence of the thin outer Fe_2N layer (a few tens of nanometers thick) was confirmed by reflection electron diffraction.¹³ Figure 3 shows the thickness of the $\gamma\text{-Fe(N)}$ layer as a function of time at 600 C at a N pressure of 10 torr. The parabolic time dependence of the layer thickness is indicative of a volume diffusion controlled reaction. Figure 4 shows the N concentration profile, as determined by EPMA, in the sample nitrided at 600 C for 2.5 h at an N pressure of 10 torr. The outer Fe_{2-3}N layer was too thin to be properly retained during metallographic polishing. Hence, accurate measurements of N content in the Fe_{2-3}N layer could not be made. The linear concentration gradients in each phase are a consequence of steady-state diffusion.

The linear concentration profiles in each phase indicate that a steady-state diffusion solution is appropriate. The steady-state solution requires only layer thickness, and not the explicit concentration profile in each phase, to determine the diffusion coefficients of N in each phase. The analysis of the present data reveals a N diffusion coefficient of 1.89×10^{-11} , 1.11×10^{-9} , and $3.78 \times 10^{-9} \text{ cm}^2/\text{s}$ in Fe_{2-3}N , Fe_4N , and $\gamma\text{-Fe(N)}$, respectively. These results compare favorably with those re-

ported in the literature for $\gamma\text{-Fe(N)}$, where at 600 C Grozier et al.¹⁴ report a value of $2.2 \times 10^{-9} \text{ cm}^2/\text{s}$. Grozier et al. determined the diffusion coefficient by using completely different experimental procedures. The agreement between these results suggest that the EPMA techniques used to measure N are adequate and the mathematical solutions to the diffusion equation used in the present work are correct and appropriate.

Nitrided Ti. Examination of the Ti-N phase diagram¹² suggests that the Ti-N "diffusion couple" formed during nitriding should contain a number of different phases, as a function of the nitriding temperature. As with Fe-N, the number of phases predicted by the phase diagram do indeed form. At nitriding temperatures in excess of 882 C, the sequence of phases from the outer edge inward are TiN, Ti_2N , $\alpha\text{-Ti(N)}$, and $\beta\text{-Ti(N)}$, where the Ti(N) indicates that the N is dissolved in a metallic Ti phase. The $\alpha\text{-Ti(N)}$ and $\beta\text{-Ti(N)}$ phases have the hcp and bcc crystal structures, respectively. At temperatures below 882 C, the $\beta\text{-Ti}$ does not form. Figure 5 shows a metallographic cross section of a Ti sample nitrided at 900 C for 4 h at an N pressure of 5 torr. The entire sequence of phases has formed, although the two nitride layers are quite thin ($\leq 2 \mu\text{m}$). Figure 6 shows the growth of the $\alpha\text{-Ti(N)}$ layer as a function of time at various temperatures. Again, the parabolic growth is indicative of a volume diffusion controlled reaction. Figure 7 shows the N concentration profile, as determined by EPMA, in the sample nitrided at 900 C for 4 h at a N pressure of 5 torr. The data for three independent measurements from two different samples are shown in Fig. 6. Under these particular nitriding conditions the outer nitride layers were too thin to be properly retained during metallographic polishing. Hence, accurate measurements of N content in the nitride layers could not be made. The concentration gradient in the $\alpha\text{-Ti(N)}$ has an error function profile. Hence, a steady-state solution is not appropriate and a modified form of the Wagner error function solution is required to determine the diffusion coefficient in each phase.^{1,4,7} The deviation between the experimental data and the model prediction at low N contents in the $\alpha\text{-Ti(N)}$ phase is believed to be due to a compositionally independent diffusion coefficient. The models developed here all assume a compositionally independent diffusion coefficient. Since the diffusion experiments were conducted at various temperatures, it is possible to construct the Arrhenius relationship for N diffusion through each phase (Fig. 8). From the Arrhenius analysis, the diffusion coefficients of N in each phase in the temperature range 800 to 1080 C are given by

$$D(\text{TiN}) = 4.4(\pm 1.6) \times 10^{-5} \left[\exp \left(\frac{-36500 \pm 1400}{RT} \right) \right] \text{ cm}^2/\text{s}$$

D (Ti₂N)

$$= 2.7(\pm 1.1) \times 10^{-3} \left[\exp \left(\frac{-35760 \pm 2530}{RT} \right) \right] \text{ cm}^2/\text{s}$$

D (α-Ti)

$$= 9.6(\pm 0.8) \times 10^{-1} \left[\exp \left(\frac{-51280 \pm 505}{RT} \right) \right] \text{ cm}^2/\text{s}$$

where R is 1.987 (cal/mole K) and T is the temperature in K. These results agree well with values reported in the literature for the α-Ti phase.¹⁵⁻¹⁷ The agreement with the literature for the α-phase suggests that once again the measurement of Ti by EPMA and the mathematics of the diffusional growth model are adequate and correct.

Conclusions

1. Quantitative electron probe microanalysis has been demonstrated to be a useful technique for studying diffusion-controlled nitriding reactions. N concentration profiles can be measured accurately in both Fe and Ti, despite the numerous experimental difficulties with each measurement.

2. Diffusion-controlled nitride layer growth is a steady-state process, as evidenced by linear concentration gradients through each phase. The diffusion coefficients of N at 600 C are 1.89×10^{-11} , 1.11×10^{-9} , and 3.78×10^{-9} cm²/s in Fe₂₋₃N, Fe N, and γ-Fe(N), respectively.

3. Diffusion-controlled layer growth in nitrified Ti is a nonsteady-state process, resulting in error function profile in each phase. The diffusion coefficients of N in each phase in the temperature range 800 to 1080 C are given by the equations in the preceding section.

References

1. E. Metin, *Multiphase Diffusion and Microstructural Effects in Ion Nitrided Ti*, Ph.D. Dissertation, New Mexico Institute of Mining and Technology, 1988.
2. A. D. Romig Jr., "Thermodynamic considerations in the analysis of phase stability: The role of interfacial equilibrium in the determination of phase diagrams by x-ray microanalytical techniques," *Bull. of Alloy Phase Diagrams* 8: 308, 1987.
3. W. Jost, *Diffusion*, New York: Academic Press, 1960, 8.
4. C. Wagner, "The evaluation of data obtained with diffusion couples of binary single phase and multiphase systems," *Acta Met.* 17: 99, 1969.
5. G. V. Kidson, "Some aspects of the growth of diffusion layers in binary systems," *J. Nucl. Mat.* 3: 21, 1961.
6. S. R. Shatynski, J. P. Hirth, and R. A. Rapp, "A theory of multiphase binary diffusion," *Acta Met.* 24: 1070, 1976.
7. E. Metin, O. T. Inal, and A. D. Romig Jr., "Solutions to multiphase diffusion in binary metal interstitial systems," *Metall. Trans.* (submitted).

8. G. F. Bastin, F. J. J. van Loo, and H. J. M. Heijligers, "Evaluation of the use of Gaussian $\phi(\rho z)$ curves in electron probe microanalysis: A new optimization," *X-Ray Spectr.* 13: 91, 1984.

9. W. F. Chambers, *Sandia Task8: A Sub-routined Electron Microprobe Automation System*, SAND85-2037, Sandia National Laboratories, Albuquerque, N.M., 1985.

10. K. F. J. Heinrich, "X-ray absorption uncertainty," in T. D. McKinley, K. F. J. Heinrich, and D. B. Wittry, Eds., *The Electron Microprobe*, New York: Wiley, 1966, 296.

11. B. L. Henke and E. S. Ebsu, "Low energy electron absorption in solids," *Adv. in X-ray Analysis* 17: 150, 1974.

12. M. Hansen, *Constitution of Binary Alloys*, New York: McGraw Hill, 1958, 670 and 989.

13. E. Metin and O. T. Inal, "Formation and growth of iron nitrides during ion-nitriding," *J. Materials Sci.* 22: 2783, 1987.

14. J. D. Grozier, H. W. Paxton, and W. W. Mullins, "The growth of austenite into ferrite in the iron-nitrogen system," *Trans. AIME* 233: 130, 1965.

15. R. J. Wasilawski and G. L. Kehl, "Diffusion of oxygen and nitrogen in titanium," *J. Inst. Metall.* 83: 94, 1954-1955.

16. F. W. Wood and O. G. Paasche, "Dubious details of nitrogen diffusion in titanium," *Thin Solid Films* 40: 131, 1977.

17. A. Anttila, J. Raisanen, and J. Keinonen, "Diffusion of N in a titanium," *Appl. Phys. Lett.* 42: 498, 1983.

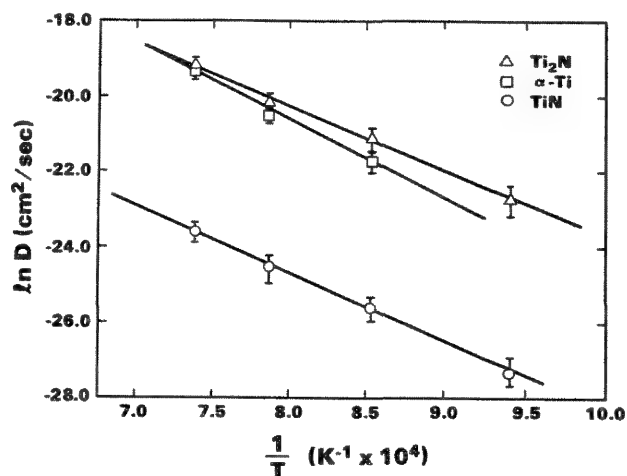


FIG. 8.--Arrhenius relationships for diffusion of N through Ti₂N, TiN, and α-Ti(N) in temperature range 800-1080 C.

MICROSCOPY AND MICROANALYSIS OF SHOCK-PROCESSED MATERIALS

M. J. Carr and R. A. Graham

The passage of a shock compressive pulse through a material consists of a brief excursion to high pressure and temperature, concurrent with high-strain-rate deformation, followed promptly by a return to nominal conditions. The short duration of the shock pulse and the rapid quench combine to produce complex chemical and microstructural changes on a very fine scale. The analytical electron microscope and electron microprobe have been successfully employed to analyze a variety of materials systems exposed to shock loading. Case studies of rutile, Al-Ni reacting powder mixtures, and zinc oxide-hematite reactions are used to illustrate the applicability of these methods to the characterization and analysis of shock processed materials.

The passage of a shock wave through a solid or a powder is an energetic process.^{1,2} In a simplistic sense, a compression wave enters a specimen or target, accelerating its particles from rest to a velocity in the neighborhood of 1 km/s within a rise time of a few tens to a few hundreds nanoseconds. Local pressures of 10-100 GPa develop, and a temperature rise from a few tens to hundreds of degrees Celsius occurs. Powders deform and compact quickly to solid density; further uniaxial compression strains of the order of 5-30% develop at strain rates of 10^7 - 10^9 s⁻¹. A few microseconds later, a trailing tensile or release wave enters the specimen, reduces the pressure to near or below zero, and adiabatically cools the specimen substantially. A reverse strain occurs that can return a solid specimen to nearly its starting dimensions. Depending on the design of the fixturing, ring-down (repeated compression/tension cycles) or secondary collisions can occur which may further modify the microstructure.

A solid understanding of the chemical reactions and microstructural changes that occur during the shock process is required in order to optimize the performance of ordnance, armor, materials synthesis, and fabrication technologies. For example, it is important to understand the development of microstructure as a function of peak pressure, peak temperature, and pulse duration.³⁻⁵ Similarly, it is important to recognize the effects of mixing and flow separately from diffusional effects to efficient exploitation of the shock process for the synthesis of novel metastable structures.⁶ Late-time processes are likewise important, since residual strain and heat can lead to re-

crystallization and possibly the loss of useful defect structures developed under shock loading.³

The experimental study of shock effects on materials is a complicated enterprise. Meaningful results are best achieved when well-characterized starting material is exposed to well-characterized shock-loading conditions and then analyzed with the proper techniques. The fine structure of a shock pulse depends on the details of fixture design; careful modeling and analysis of the shock conditions are needed to quantify the conditions experienced by the material at various locations in the specimen because microstructural development depends critically on the details of the shock pulse. The chemical and structural changes resulting from shock loading usually occur on a very fine scale, so electron optical methods are relied upon heavily for analysis of these materials. The purpose of this paper is to illustrate typical applications of electron microscopy and electron microanalysis to the characterization of shock-loaded powders, with an emphasis on the insight they have provided into this complex process.

Experimental Procedure

Shock loading of materials can be achieved by a variety of methods, including gas guns, explosively driven flyer plates, explosively imploded cylinders, exploding foils, and explosive plane wave loading.⁷ Each method possesses advantages and disadvantages for the experimentalist. In the cases discussed below, explosive plane-wave loading was achieved in special "Sandia Bear" fixtures, which were developed specifically for loading and recovering powdered specimens and have been thoroughly characterized in terms of pulse shape and duration in several pressure levels.^{8,9} A schematic of a shock recovery fixture is shown in Fig. 1. It consists of a detonator and plane-wave generator positioned on a cylindrical slab of explosive, all atop a massive steel block. The specimen (powder) is pressed into a copper capsule to a predetermined density, typically 40-60% of theoretical density. The lower the starting density, the higher the peak temperature during the shock. The temperature rise in powdered specimens is relatively high (50-900 C) compared to solid specimens (10-100 C) due to the increased pressure-volume work done to compress the specimen to full density. The capsule is pressed into a chamber in the steel block and capped with a tamper. The material used for the tamper affects the shape of the pressure pulse during the shock. All surfaces are lapped flat to insure good contact and avoid spurious reflections.

The authors are at Sandia National Laboratories, Albuquerque, NM 87185. This work was supported by the U.S. Department of Energy under contract DE-AC04-76DP00789.

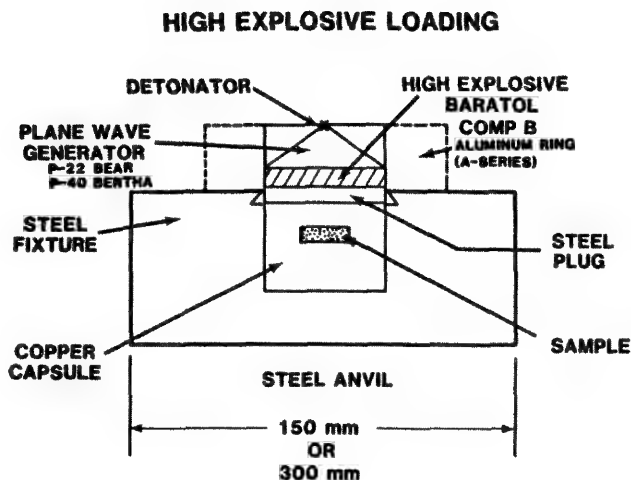


FIG. 1.--Schematic drawing of "Sandia Bear" fixture for controlled shock loading of powders.

Upon detonation, the plane wave generator spreads the detonation front from a point to a plane when it enters the main explosive. The thickness of the main explosive controls the pulse duration, and the type of explosive and size of the sample capsule controls the peak pressure. A planar shock wave propagates through the steel block containing the specimen, first compressing a powder specimen to full density and then raising the pressure to a peak and holding it briefly. There is a radial component of the pressure pulse, which leads to a characteristic zoning of the specimen. The outer edge of the specimen gets hottest, and the center briefly reaches a higher pressure, but the majority of the volume of the specimen sees a uniform pressure, temperature, and pulse duration. The massive steel block confines the specimen for later recovery and acts somewhat as a heat sink after the shock pulse passes.

After the shock experiment, we ordinarily recover a chunky powder when the capsule is opened. For peak pressures in the range 5-27 GPa and a duration of 1-2 μ s, we find that neither the average particle size nor the total surface area of ceramic powders are significantly altered. Analytically, one is faced with the problem of preparing specimens for microstructural and microchemical analysis in a manner that does not alter the deformation microstructure, chemistry, nor morphology of any products. For TEM samples, a generally satisfactory procedure has been developed to overcome this problem.¹⁰ It consists of mixing the powder with metallographic epoxy and centrifuging the mixture in special molds to produce a densely compacted, well-bonded powder preform. The preform is ground to ~ 100 μ m thick, and the usual 3mm-diameter specimen disks are trepanned. Pieces of the preform may also be mounted and polished for optical analysis, and further carbon coated for SEM or microprobe analysis. TEM specimens are mechanically dimpled to reduce ion milling time, and then thinned to perfora-

tion by ion milling in a liquid-nitrogen-cooled stage, which minimizes milling artifacts. Most of the epoxy in the composite sample is milled away, but enough remains in shielded places between particles to hold the sample together. Ion milling in this manner produces random sections through polycrystalline particles and provides an accurate view of the microstructure of the most friable materials. TEM specimens were examined at 200 keV in a JEOL 200CX, or in a JEOL 100C at 100 keV equipped with a Tracor-Northern TN2000 X-ray Analyzer. Microprobe data were obtained with a Cameca MBX equipped with a TN2000.

Results and Discussion

Microstructural Development in Shock-Modified Rutile. An early application of these techniques in our laboratory was a study¹¹ of the microstructure of the rutile form of titanium oxide, TiO_2 . Rutile is both an important ceramic material and an interesting geologic material. Its properties under shock loading and more nominal conditions are well known. Rutile has been used as a model material in numerical simulations of recovery fixtures for shock-loaded powders. The defects that form in rutile over a wide range of low-strain-rate, low-pressure conditions have been characterized. These data provide a basis for comparison with the structures that develop under shock-loading conditions. Rutile was also of interest because it was found to exhibit enhanced catalytic activity,¹² an extraordinarily large concentration of point defects, and unusual electrical conductivity¹³ after being shock modified.

Well-annealed, high-purity rutile powder was shock loaded to peak pressures between 5 and 22 GPa and peak temperatures between 80 and 500 C. The microstructures that resulted were found to depend on both the peak pressure and the peak temperature reached during the shock process. The microstructure of the unshocked powder was also examined and provides a good example of the value of the epoxy/centrifuge sample preparation technique. The starting powder (Fig. 2) consisted of polycrystalline particles of 102 μ m grains, isolated 0.1-0.5 μ m intergranular pores (often at triple points), and isolated 0.05 μ m intragranular pores (often faceted). A few [001] dislocations and annealing twins on [101] planes were observed in a mainly defect-free structure. However, when prepared by being ground under n-butanol and dispersed on holey carbon support films, the same powder appeared to consist of individual rutile grains bearing fine twins, an artifactual structure resulting from intergranular fracture during grinding. The polycrystalline nature of the particles was completely lost and the defect structure introduced by grinding would be difficult to distinguish from some of the features resulting from the shock loading. The shock-modified powders prepared by the epoxy/centrifuge technique exhibited a microstructure of dense dislocations and deformation twins in mainly

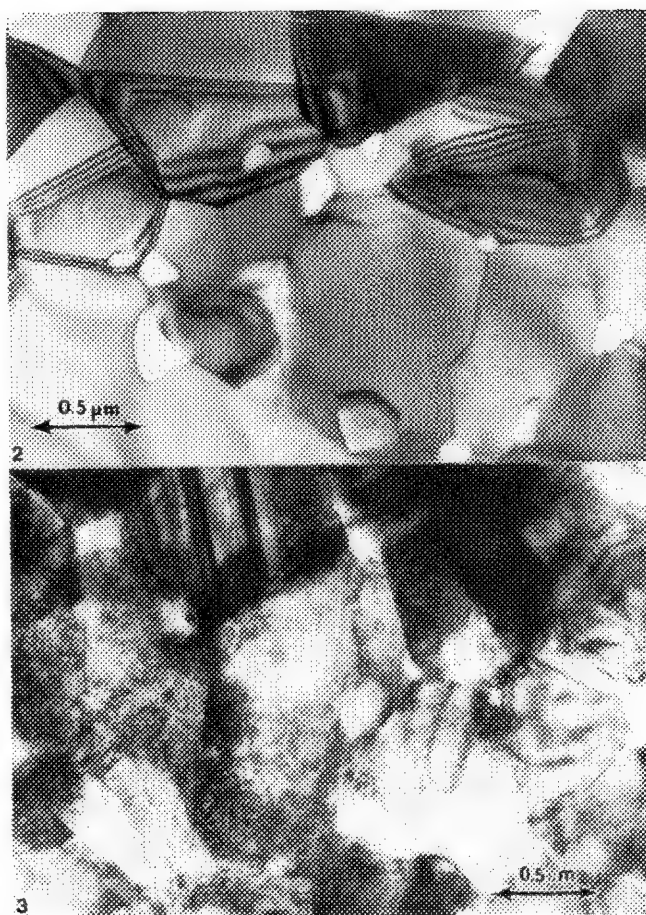


FIG. 2.--TEM micrograph of interior of polycrystalline particle of well-annealed, unshocked rutile powder.

FIG. 3.--TEM micrograph of interior of polycrystalline particle of rutile powder shock-loaded to 5 GPa and 80 C.

polycrystalline particles lacking the voids observed in the starting material (Fig. 3). Retention of many polycrystalline particles after shock loading indicates that the individual grains flowed plastically under shock to close the pore spaces, and did not shatter or fracture in an intergranular manner. The relative lack of cracking can be interpreted as an effect of the high-hydrostatic-compression component of the shock wave. Some intergranular cracking was observed, as well as localized {100} cleavage in some grains, which could be interpreted as a secondary effect of tensile stresses associated with the release wave. An indication that deformation processes depend on crystal orientation during shock loading was taken from the fact that grains containing annealing twins often deformed primarily by twinning on side of the twin boundary and by slip on the other. Dislocation density increased rapidly with increasing pressure and exceeded 10^{11} cm^{-2} above 8 GPa. Deformation was uniform from grain to grain; no grains were observed to pass through the process unaffected. This observation permitted the onset of recrystallization to be observed in specimens shocked at the

highest pressures and with the greatest peak temperatures, although it was not possible to determine to what extent the recrystallization occurred after the shock had passed.

TEM images of the shocked rutile were used to explain several unusual property measurements. Shocked rutile was found to exhibit unusually high electrical conductivity compared to nonstoichiometric reduced rutile with the same Ti^{3+} point defect density. TEM images showed that the difference between the two materials was that point defects in reduced rutile were organized into crystallographic shear defects, whereas in shocked rutile the defects remained isolated and available for conduction. Also, a relationship was found between shock modification and catalytic activity in rutile for the oxidation of CO. A decrease in catalytic activity was found to correlate very well with a decrease in dislocation density in post-shock annealed rutile.¹⁴

Shock-induced Chemical Reactions in Al-Ni Powder Mixtures. Enhanced mixing has been cited as one of the mechanisms by which shock processing of material leads to enhanced reactivity.⁶ In a series of experiments^{15,16} on aluminum and nickel powder mixtures, the electron microprobe and the AEM were employed to observe the fine-scale mixing that resulted from shock compression of two morphologically different powders. The first type of powder was a mixture of 30vol% $\sim 10\mu\text{m}$ pure aluminum powder, and 70vol% $\sim 60\mu\text{m}$ pure nickel powder. The second powder consisted of $\sim 65\mu\text{m}$ -diameter 'composite' particles, each of which had a pure aluminum spherical core surrounded by a dense pure nickel coating. Each particle was about 80vol% nickel. These powders were pressed into a Sandia Bear fixture at 60% of theoretical density. The powders received a 16GPa shock pulse $\sim 1 \mu\text{s}$ long.

The recovered specimen of the mixed Al-Ni powders was first sectioned along a diameter and examined optically, then re-polished and examined in the electron microprobe. The optical examination revealed a reacted region around the periphery of the specimen where the highest temperatures are reached during the shock process. Nickel and aluminum undergo an exothermic reaction to form Ni_3Al at the composition used in this work if the reaction goes to completion. The reacted region showed structural evidence of having been molten, and microprobe analysis found the major phase in this region to be Ni_3Al . Most of the rest of the specimen appeared unreacted but was essentially fully dense. Close examination of this unreacted area revealed that the aluminum had flowed extensively around the mainly unaffected nickel particles (Fig. 4). Some submicron streams of nickel-rich aluminum appeared to exceed the equilibrium solid solubility of nickel in aluminum, although no discrete particles of a second phase were found. The Al-Ni phase diagram is complex, and between the once-molten reacted area and the unreacted region of the sample, regions were

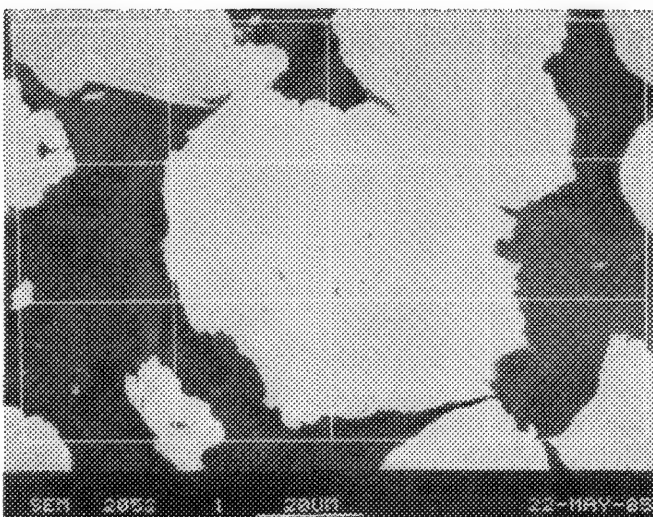


FIG. 4.--Backscattered electron image of shocked Ni-Al mixed powder. Aluminum has flowed around and between relatively undeformed nickel particles.

found that contained NiAl and Ni_2Al_3 , both of which were identified by electron diffraction as well.

The recovered specimen of the composite powder was similarly sectioned on a diameter and examined by optical microscopy and microprobe. Reaction to form Ni_3Al occurred around the periphery as in the previous specimen. The reacted region was surrounded by layers of NiAl and Ni_2Al_3 as in the first sample, but the layers were less extensive. The unreacted area presented a morphology (Fig. 5) distinctly different from that of the mixed-powder specimen discussed above. In this case, the thick nickel coating surrounding each Al particle prevented aluminum from flowing widely and limited mixing mainly to the internal Ni-Al boundary.

When small pieces of the unreacted area of these two specimens were further studied by differential thermal analysis, it was found that the shocked mixed powders were much more reactive than the shocked composite powder, reacting at 100-200 C below the normal reaction start temperature (650 C). A ready explanation for this behavior was found in the microanalytical results. Elemental maps from the same specimen plainly showed that the shocked mixed powders were 'pre-mixed' on a microscopic scale, whereas the composite powders were deformed but not mixed to any significant extent. These studies were the first quantitative observations of mixing due to shock processing and were immediately applied to a materials engineering problem. Since there was still a large component of material that reacted at 650 C, continued research is under way to optimize process parameters such as particle size and distribution, composition, shock pressure and duration, and post-shock heat treatment in an attempt to fabricate large pieces of high-density, crack-free, solid intermetallic material.

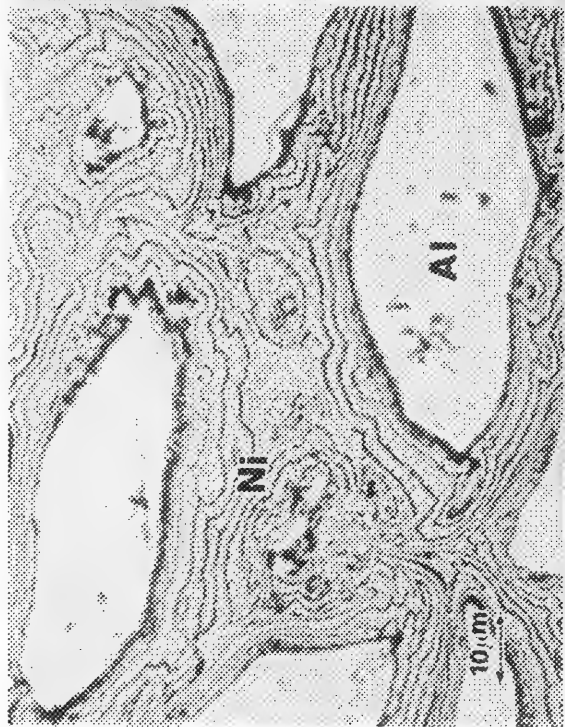
Shock Synthesis of Zinc Ferrite. Electron diffraction and analytical electron microscopy were used to study¹⁷ the synthesis of ZnFe_2O_4 from a mechanical mixture of ZnO and Fe_2O_3 . The starting powder was a well-blended 1:1 mixture of ZnO and hematite (Fe_2O_3), the correct stoichiometry for ZnFe_2O_4 . Powders from three different conditions were examined. The first was blended but unshocked starting powder. The second was shocked to 22 GPa and a peak temperature of 300 C, and the third was shocked to 27 GPa and a peak temperature of 725 C. These powders were prepared for examination by the epoxy/centrifuge technique described above. A fourth powder of a known homogeneous solid solution spinel ($\text{ZnFe}_2\text{O}_4 + \text{MnO}$, 95:5 wt%) was prepared in the same manner and used as a standard to obtain a k-factor for these elements ($K_{\text{Zn/Fe}} = 0.735$) under the analytical conditions used with the unknowns (JEOL 100C, 100 keV, 45° tilt).

TEM examination of the unshocked starting powder showed that blending was complete, down to the individual grain level, with 2000Å grains of both oxides exhibiting a very low defect density (Fig. 6). The powder shocked at 22 GPa was found to be unreacted insofar as it contained no detectable ferrite. Its microstructure consisted of heavily dislocated, deformed, but unbonded grains (Fig. 7). Electron diffraction patterns revealed the presence of both ZnO and Fe_2O_3 , but only individual grains of hematite could be easily imaged in dark field. The softer ZnO had apparently been comminuted, smeared, or flowed between the harder hematite grains. EDS profiles from one hematite grain to another showed that zinc was concentrated between hematite grains. Some hematite grains, although unreacted to ferrite, appeared to contain as much as a 5wt% Zn. The powder shocked to 27 GPa was found to contain some ferrite in addition to the deformed mixture found in the unreacted shocked powder. The ferrite grains were distinct from the unreacted material in the same sample because they possessed a fine recrystallized microstructure (Fig. 8), apparently due to the plastic deformation and high temperature caused by the shock, as in the case of rutile. The ferrite grain size was 5000 Å, and a clear identification was obtained on the basis of electron diffraction. EDS data showed the Zn/Fe stoichiometry to be $\text{Zn}_{1-x}\text{Fe}_2+\text{xO}_4$, with $x = 0.09 \pm 0.02$. The zinc-deficient stoichiometry found by AEM was applied to the interpretation of corresponding magnetic measurements on the same materials that had showed them to be ferrimagnetic; stoichiometric zinc ferrite is paramagnetic, and zinc-deficient zinc ferrite is ferrimagnetic.

Conclusion

The microanalytical and crystallographic capabilities of the electron microscope and electron microprobe are well suited to the characterization of microstructural details on a fine scale and have proved to be very effective.

5



6



7



8



FIG. 5.--Optical micrograph of shocked Ni-Al composite powder. Nickel coating each particle has remained intact after shock compaction.
 FIG. 6.--TEM micrograph of unshocked blended ZnO and Fe₂O₄ powders.
 FIG. 7.--TEM micrograph of blended ZnO and Fe₂O₃ powders, shocked at 22 GPa.
 FIG. 8.--TEM micrograph of recrystallized shock synthesized ferrite.

tive in providing critical information on the deformation and chemical processes that occur under shock loading in powder materials.

References

1. M. A. Meyers and L. E. Murr, "Defect generation in shock wave deformation," in M. A. Meyer and L. E. Murr, Eds., *Shock Waves and High-Strain-Rate Phenomena in Metals*, New York: Plenum Press, 1981, 487.
2. M. A. Mogilevsky, "Mechanisms of deformation under shock loading," in Ref. 1, p. 531.
3. M. J. Carr, "Deformation microstructures in shock deformed ceramic powders," in R. A. Graham and A. B. Sawaoka, Eds., *High Pressure Explosive Processing of Ceramics*, Trans Tech Publications, 1987, 341.
4. G. T. Gray III, P. S. Follansbee, and C. E. Frantz, "Effect of residual strain on the substructure development and mechanical response of shock-loaded copper," *Materials Science and Engineering* (submitted).
5. R. N. Wright, D. E. Mikkola, and S. Larouche, "Short duration shock pulses as a tool to study the time dependence of plastic deformation," in Ref. 1, p. 703.
6. R. A. Graham, "Shock compression of solids as a physical-chemical-mechanical process," in S. C. Schmidt and N. C. Holmes, Eds., *Shock Waves in Condensed Matter--1987*, North Holland, 1988, 11.
7. R. A. Graham, "Explosive processing methods," in Ref. 3, p. 29.
8. R. A. Graham and D. M. Webb, "Fixtures for controlled explosive loading and preservation of powder samples," *Shock Waves in Condensed Matter--1983*, 211.
9. R. A. Graham and D. M. Webb, "Shock-induced temperature distributions in powder compact recovery fixtures," *Shock Waves in Condensed Matter--1986*, 831.
10. M. J. Carr, "A method for preparing powdered specimens for transmission electron microscopy," *J. Elect. Microsc. Tech.* 2: 439, 1985.
11. M. J. Carr and R. A. Graham, "The effect of shock pressure and temperature on the deformation microstructure of rutile," in L. E. Murr, K. P. Staudthammer, and M. A. Meyers, Eds., *Metallurgical Applications of Shock-wave and High-strain-rate Phenomena*, Marcel Dekker, 1986, 369.
12. J. Golden, F. Williams, B. Morosin, E. L. Venturini, and R. A. Graham, "Catalytic activity of shock-loaded TiO_2 powder," *Shock Waves in Condensed Matter--1981*, 72.
13. E. L. Venturini and R. A. Graham, "Metallic microwave conductivity in shock-loaded rutile," *Mat. Res. Soc. Symp. Proc.* 24: 383, 1984.
14. M. J. Carr, R. A. Graham, B. Morosin, and E. L. Venturini, "Transmission electron microscopy of shock-modified and annealed rutile," *ibid.*, 343.
15. W. F. Hammetter, R. A. Graham, B. Morosin, and Y. Horie, "Effects of shock modifications on the self-propagating high temperature synthesis of nickel aluminides," *Shock Waves in Condensed Matter--1987*.
16. I. K. Simonsen, Y. Horie, R. A. Graham, and M. J. Carr, "Formation of amorphous nickel aluminides under shock loading," *Mat. Lett.* 5(No.3): 75, 1987.
17. R. A. Graham and M. J. Carr, "Analytical electron microscopy study of shock synthesized zinc ferrite," in Ref. 9, p. 803.

THE FORMATION OF TITANIUM SILICIDES IN DIFFUSION COUPLES

Erkki Heikinheimo, Jorma Kivilahti, and Markku Pajunen

Owing to their high thermal stability and good electrical conductivity, various metal silicides are used in contacts and interconnections in electronic devices. In particular, titanium disilicide, TiSi_2 , has been extensively studied because it has one of the lowest resistivities among the metal silicides. Generally, the TiSi_2 is produced by annealing of very thin sputtered layers of titanium on silicon. However, in this study we investigated the formation sequence of the silicides in "bulk" Ti-Si diffusion couples by utilizing the SEM/EPMA technique.

Stability of the Silicides in the Ti-Si System

When predicting the existence of possible silicides in diffusion couples it is common practice to start by searching the phase diagram compilations and literature. In the present case the most reliable experimentally determined phase diagram is that given by Svechnikov et al.¹ Making use of this diagram, new experimental solubility results, and the available thermodynamic data we assessed² the stabilities of the silicides Ti_3Si , Ti_5Si_3 , Ti_5Si_4 , TiSi , and TiSi_2 , and the temperature-composition diagram in Fig. 1a by the THERMO-CALC program.³ All these silicides are stoichiometric except Ti_5Si_3 , which has a narrow homogeneity range.

Experimental

The diffusion couples were prepared from CP (grade 1, Avesta) or high-purity Ti (99.99+%) sheet and semiconductor-grade single-crystal Si (Okmetic) in $\langle 100 \rangle$ and $\langle 111 \rangle$ orientations. Titanium was ground with SiC paper and polished both with diamond paste and electrolytically. The materials were etched in dilute HF solutions before being pressed together in a stainless steel (ASTM 310) or Ti holder. The purpose of the holder was merely to bring the two reacting materials in good contact; no effort was made to control the pressure accurately. The samples were annealed at 1100 C in a vacuum furnace ($P < 10^{-4}$ mbar) for varying periods and cooled within 30 min to below 500 C. Several samples were also annealed in vacuum or Ar-filled ampoules; the cooling rate was considerably higher in this case.

The authors are at the Department of Materials Science, Helsinki University of Technology, SF-02150 Espoo, Finland. They are grateful to Dr. G. F. Bastin, Eindhoven University of Technology, The Netherlands, for introducing the methodology to us; and to Dr. J. Bigot, Centre d'Etudes de Chimie Metallurgique, Vitry, France, for supplying the high-purity titanium.

Microanalysis was performed by a JEOL JSM-840A SEM equipped with a Tracor Northern TN-5500 EDS system.

Results

When the stainless-steel (SS) holder was used, microanalysis revealed sulfur up to 5 wt% in the Ti-rich silicide Ti_3Si . After the holder material was changed to CP Ti, and contamination disappeared from the Ti_3Si . It was concluded that under high-vacuum annealing conditions the MnS inclusions in the SS holder decomposed and sulfur dissolved through the gas phase into the Ti_3Si silicide. The thermodynamic and structural reasons for this specific dissolution must be clarified.

Both in the vacuum furnace and in vacuum ampoules, the silicide layers in the diffusion couples retained their original dimensions; but in Ar-filled ampoules lateral spreading of the silicides was observed on the Ti surface. SEM investigation revealed concentric zones of the silicides on the Ti surface, each silicide with its unique particle morphology. The analyses of the concentric zones corresponded to the stable silicides going away from Si in the same order as they appear in the phase diagram. It is likely that the lateral spreading of the silicides is caused by oxygen, which is the main impurity in the Ar-gas (<20 ppm) and which cannot be easily prevented from intruding into the ampoule.

The first silicides to form were TiSi_2 and TiSi (<1 h), followed by Ti_5Si_4 (in 4 h). The last ones to form were Ti_3Si and Ti_5Si_3 (in 10 h). After long annealing, up to 100 h, mainly the Si-rich silicides gained thickness; the TiSi_2 was the quickest to grow, followed by TiSi and Ti_5Si_4 , in that order. The growth rate of Ti_3Si and Ti_5Si_3 was very slow (Fig. 1b). Apparently, Si diffusion is the rate-controlling step in the process. It was surprising to find out that the most stable silicide, Ti_5Si_3 , was the last one to appear; this is the phase which cannot be easily prevented from growing into Ti-Si alloys during and after solidification.

On the titanium side of the diffusion couple a Si depletion zone was established; its extent depended on the cooling rate. As shown in the phase diagram (Fig. 1a), the equilibrium solubility of silicon increases with temperature and is about 3 at% at the annealing temperature. When temperature is decreased after long annealing, the Ti_3Si layer starts to grow into the α -solution, which consumes dissolved Si from the vicinity of the $\alpha/\text{Ti}_3\text{Si}$ interface.

We were not able to detect any significant difference in silicide formation between the two orientations of the Si single crystals.

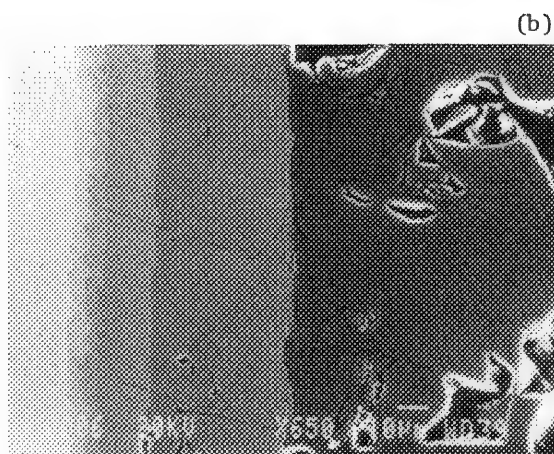
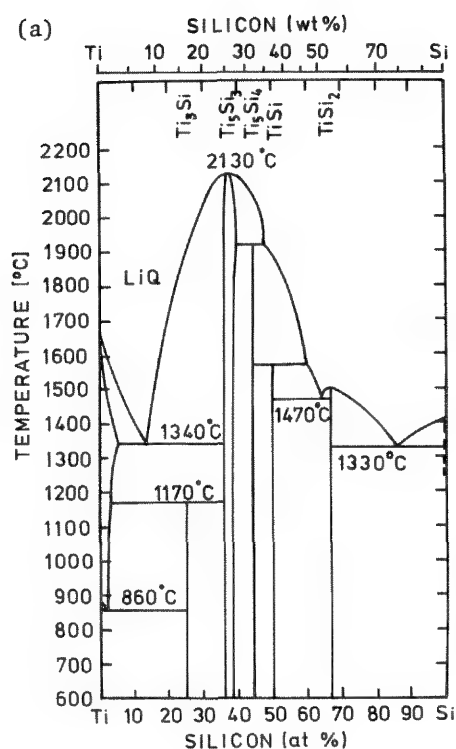


FIG. 1.--(a) Phase diagram of titanium-silicon system²: stable silicides starting from titanium side: Ti_3Si , Ti_5Si_3 , Ti_5Si_4 , $TiSi$, $TiSi_2$; (b) BSE image of diffusion couple cross section, annealed for 100 h at 1100 C. Successive layers from left to right are Ti and all silicides given in phase diagram.

Conclusion

The diffusion couple method, combined with accurate microanalysis, is a very powerful tool for studying stability and diffusion behavior of binary systems. However, great effort is required for insuring sufficiently clean annealing conditions for the diffusion couples. For example, the morphology of silicide growth is altered by impurities. We were able to observe the existence of the Ti-rich silicide Ti_3Si in the high-purity Ti diffusion couple as well.

References

1. V. N. Svechnikov, Y. A. Kotserzhinskiy, I. M. Yupko, O. G. Kulik, and E. A. Shiskin, *Dokl. Akad. Nauk. SSSR, Khim. Tekh.*, 1970, 393.
2. J. Kivilahti and O. Tarasova, to be published.
3. B. Sundman, B. Jansson, and J.-O. Andersson, *CALPHAD*, 1985, 153.

Rh AND Pt DISTRIBUTIONS IN Rh/Al₂O₃ AND Pt/Al₂O₃ CATALYSTS

J. S. Hepburn, H. G. Stenger, and C. E. Lyman

In catalyst co-impregnation, a secondary impregnant is added to the impregnating solution. In a chromatographic fashion, the precursor and the co-impregnant compete for adsorption sites during imbibition; the less strongly adsorbed species is driven ahead of the more strongly adsorbed one. The theory of co-impregnation has been extensively reviewed by Lee and Aris,¹ and the technique has been demonstrated extensively with platinic acid and various secondary impregnants.²⁻⁵ However, little work with other precursors has been done, and very few experimental internal concentration profiles of catalysts prepared by this method have appeared in the literature. Becker and Nutall have shown Pt distributions in alumina spheres which were impregnated with citric acid.² The analysis was carried out by x-ray microanalysis in an electron microprobe. Few details of the analysis were stated, and no quantification was given. In this study, HF co-impregnation of RhCl₃ and PtCl₄ into γ -alumina is examined. Quantitative internal concentration profiles determined by EPMA are presented and discussed.

Experimental

γ -alumina monoliths, Corning Celcor EX78, of rectangular cell geometry (Fig. 1), were impregnated with aqueous solutions of RhCl₃/HF and PtCl₄/HF. Impregnation was conducted under vacuum for 30 s, which assured complete imbibition but suppressed any redistribution due to diffusion. Immediate calcination followed for 1 h at 500 C. The monolith walls were sectioned and placed in a single epoxy mount alongside of Rh, Pt, and γ -alumina standards. The mount was given a standard metallographic polish and left unetched. Rh and Pt profiles were determined by WDS x-ray analysis on a JEOL 733 EPMA with Tracor Northern automation, model TN-2000/1310. The L α line of Rh, the M α line of Pt, and the K α of Al were analyzed on PET, LiF, and TAP crystals, respectively. Raw data were corrected by Basting's $\phi(\rho z)$ for quantification; oxygen was calculated by difference. Line traces (Fig. 1) were collected in 10 μ m steps with a beam approximately 10 μ m in diameter to average the effects of surface relief in the porous alumina support. To obtain a reasonable number of counts, it was necessary to count for 120 s per point with a

J. S. Hepburn and H. G. Stenger are at the Department of Chemical Engineering and C. E. Lyman is at the Department of Materials Science and Engineering, Lehigh University, Bethlehem, PA 18015. This work was supported by the Department of Energy under contract DE-FG02-86ER45269. Also, thanks is given to Corning for the donation of the γ -alumina monoliths.

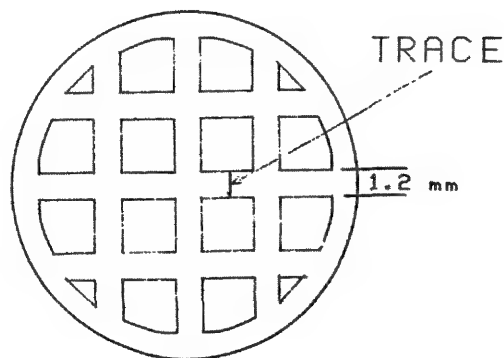


FIG. 1.--Top view of monolith with rectangular cell geometry.

nominal probe current of approximately 100 nA at 10 keV.

Results and Discussion

The Rh and Pt profiles of the HF co-impregnation are shown in Figs. 2-5. The impregnations with no HF (Figs. 2 and 4) show the Rh and Pt to be located in narrow bands near the exterior of the monolith wall. Impregnations with HF (Figs. 3 and 5) reveal the Rh and Pt profiles to be peaked beneath the external surface of the support. The Pt profile, unlike that of Rh, indicates that the chromatographic effect of the HF enabled the Pt precursor to be driven to the center of the support from both sides producing a single peak. With Rh, the effect of the HF was weaker, and the two precursor fronts did not meet.

The qualitative shape of the profiles are as predicted by Lee and Aris for $K_{HF} > K_{RhCl_3}$ and $K_{HF} > K_{PtCl_4}$, where K_{HF} , K_{RhCl_3} , and K_{PtCl_4} are the equilibrium constants for adsorption of HF, RhCl₃, and PtCl₄, respectively. For the same concentrations of HF, the Rh and Pt distributions indicate that the Pt has penetrated farther into the interior of the support, which shows that the PtCl₄ precursor requires either more sites or a larger area on the alumina for adsorption than the RhCl₃ precursor and hence travels farther into the alumina seeking open adsorption sites.

The data were found to be above the minimum detectability limit, ~ 0.02 wt% for the experimental parameters used, as calculated by the Ziebold MDL approximation for both Rh and Pt.⁶ The quantitative data were checked by a comparison of the amount of Rh and Pt imbibed with the amount obtained by graphical integration of the quantitative profiles; the deviation from the mass balance was within 30% and 20% for Rh and Pt, respectively. The

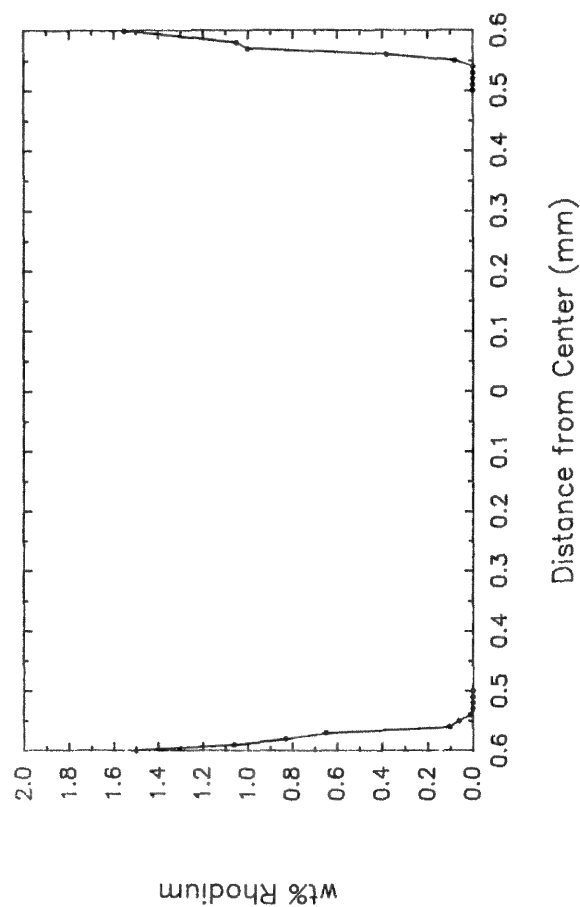


FIG. 2. --Rh distribution in co-impregnated γ -alumina.
 $C_{\text{RhCl}_3} = 3.8 \times 10^{-5} \text{ mol/cc}$, $C_{\text{HF}} = 0 \text{ mol/cc}$.

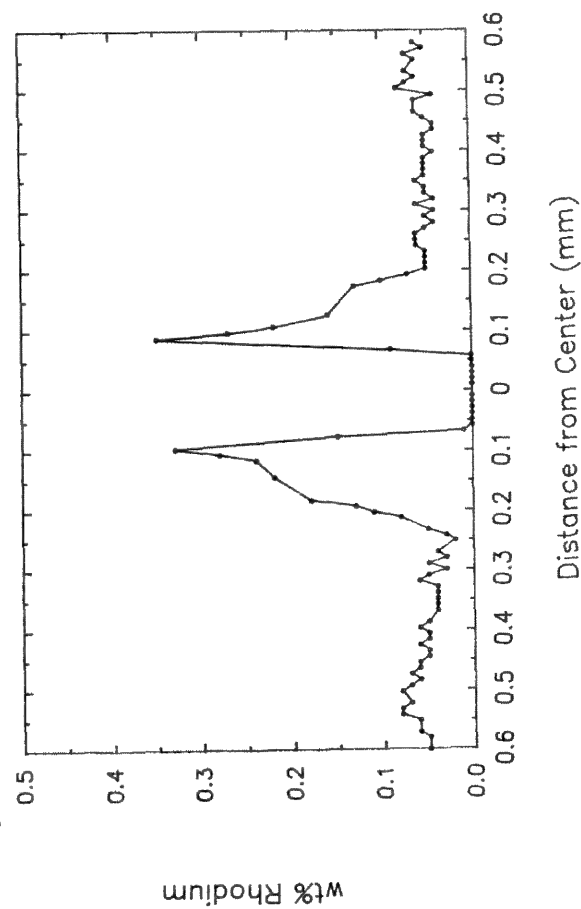


FIG. 3. --Rh distribution in co-impregnated γ -alumina.
 $C_{\text{RhCl}_3} = 3.8 \times 10^{-5} \text{ mol/cc}$, $C_{\text{HF}} = 9.9 \times 10^{-3} \text{ mol/cc}$.

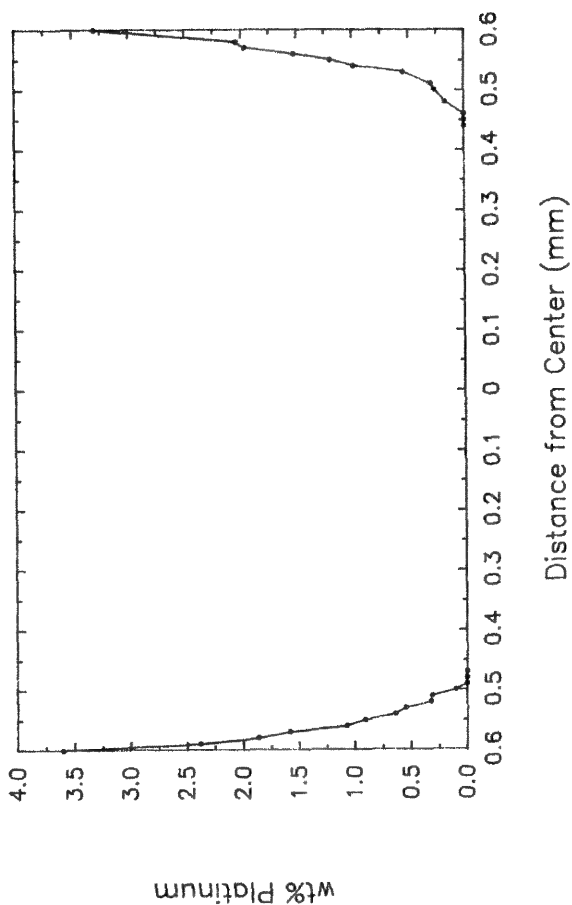


FIG. 4. --Pt distribution in co-impregnated γ -alumina.
 $C_{\text{PtCl}_4} = 3.8 \times 10^{-5} \text{ mol/cc}$, $C_{\text{HF}} = 0 \text{ mol/cc}$.

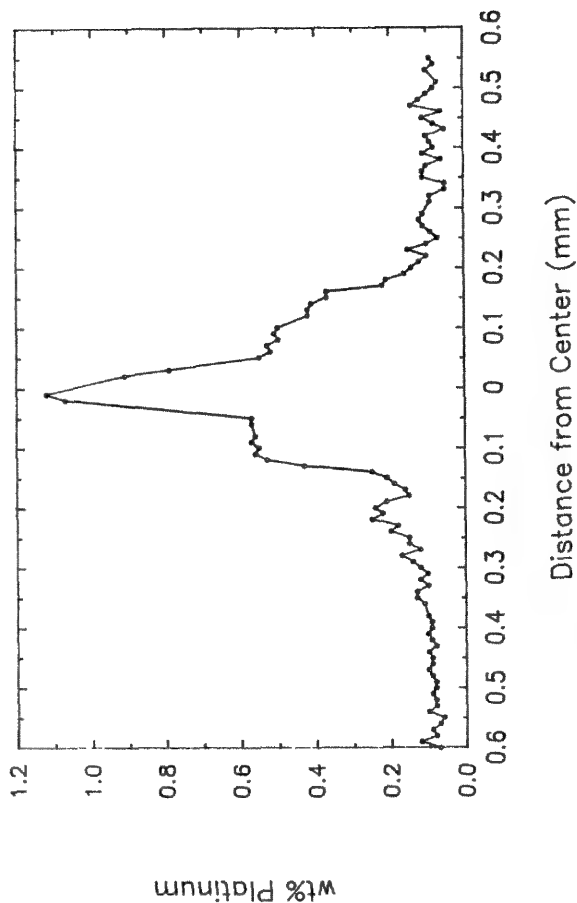


FIG. 5. --Pt distribution in co-impregnated γ -alumina.
 $C_{\text{PtCl}_4} = 3.8 \times 10^{-5} \text{ mol/cc}$, $C_{\text{HF}} = 9.9 \times 10^{-3} \text{ mol/cc}$.

aluminum to oxygen ratio was consistently within 2% of the calculated value for Al_2O_3 .

In Figs. 2-5, the statistical error in the data points which are close to the detectability limit, ~ 0.02 wt% for both Rh and Pt, is quite large, ~ 20 -50%. However, these points have a very small effect on the mass balance; points far removed from the detectability limit, which have a relatively small degree of statistical error, influence the mass balance the most. This statistical error only accounts for less than 3% of the error in the mass balance for both Rh and Pt.

The porosity and surface relief in the alumina support may have resulted in probe analysis errors. The effect of porosity reduces the effective atomic number of the specimen; hence, more Rh or Pt x rays are generated. This effect cannot explain the errors in the mass balance, but needs to be addressed further. Absorption and fluorescence should not be affected appreciably by porosity. Although x rays are generated farther below the surface, the effective path length for absorption and fluorescence, ρz , is unchanged. Surface relief produces a mass effect: from Rh or Pt x rays are generated because more electrons are back-scattered out of the specimen with non-normal beam incidence. This effect can explain the errors incurred in the mass balance. The effect of surface relief on absorption and fluorescence should be averaged out because the beam diameter is much greater than the size of the relief features.

The errors incurred in the mass balance may be explained in terms of an exclusion or filtering effect. Many of the pores in the alumina are less than 30 Å in size. Although these small pores are accessible to the imbibed water, they may be too small for the relatively large precursor molecules (which may be polymeric) to enter. Thus, not all the Rh or Pt available in solution can enter the support. The higher degree of error in the Rh mass balance may be associated with the fact that RhCl_3 in its solid state is hydrated to an unknown degree; therefore, the quantity of Rh available for imbibition is not exactly known.

References

1. S. Y. Lee and R. Aris, "The distribution of active ingredients in supported catalysts prepared by impregnation," *Catal. Rev.-Sci. Eng.* 27: 207, 1985.
2. E. R. Becker and T. A. Nutall, "Controlled catalyst distribution on supports by co-impregnation," *Preparation of Catalysts I, Proc. 1st Intern. Symp. Scientific Bases for the Preparation of Heterogeneous Catalyst*, Amsterdam: Elsevier, 1976.
3. Y. S. Shyr and W. R. Ernst, "Preparation of nonuniformly active catalyst," *J. Catal.* 63: 425, 1980.
4. R. W. Maatman, "How to make a more effective platinum-alumina catalyst," *Ind. Eng. Chem.* 51: 913, 1959.
5. D. M. Price and A. Varma, "Preparation

of $\text{Pt}/\text{Al}_2\text{O}_3$ pellets with internal step-distribution of catalyst: Experiments and theory," Paper 14c, *AIChE Annual Meeting*, New York, 1987.

6. J. I. Goldstein, D. E. Newbury, P. Echlin, D. C. Joy, C. Fiori, and E. Lifshin, *Scanning Electron Microscopy and X-Ray Microanalysis*, New York: Plenum Press, 1981, 436.

PHASE TRANSFORMATIONS AT STEEL/IN625 CLAD INTERFACES

Raghavan Ayer, R. R. Mueller, D. P. Leta, and W. J. Sisak

The microstructures of 4130 and $2\frac{1}{4}$ Cr-1Mo steels clad to IN625 were studied by analytical electron microscopy (AEM) and secondary ion mass spectroscopy (SIMS). The article describes the microstructural analysis of the interface regions and models are proposed to explain the microstructural evolution at the interface and their potential effect on the mechanical properties.

R. Ayer, R. R. Mueller, and D. P. Leta are with Exxon Research and Engineering Co., Route 22 East, Annandale, NJ 08801; W. J. Sisak is with Exxon Production Research Co., Box 2189, Houston, TX 77001.

Experimental Method

An approximately 0.25in.-thick IN625 layer was clad on to both AISI 4130 and $2\frac{1}{4}$ Cr-1Mo steels by welding and hot isostatic pressing (HIP). Specimens from the steel/IN625 interface were examined in Philips EM400-FEG and 430 electron microscopes. SIMS analyses were performed with a CAMECA IMS-3f SIMS both in the positive and negative modes.

Results

The clad samples provided for the present study were in the fully heat treated condition. Table 1 lists the thermal history of the clads provided by the manufacturers.

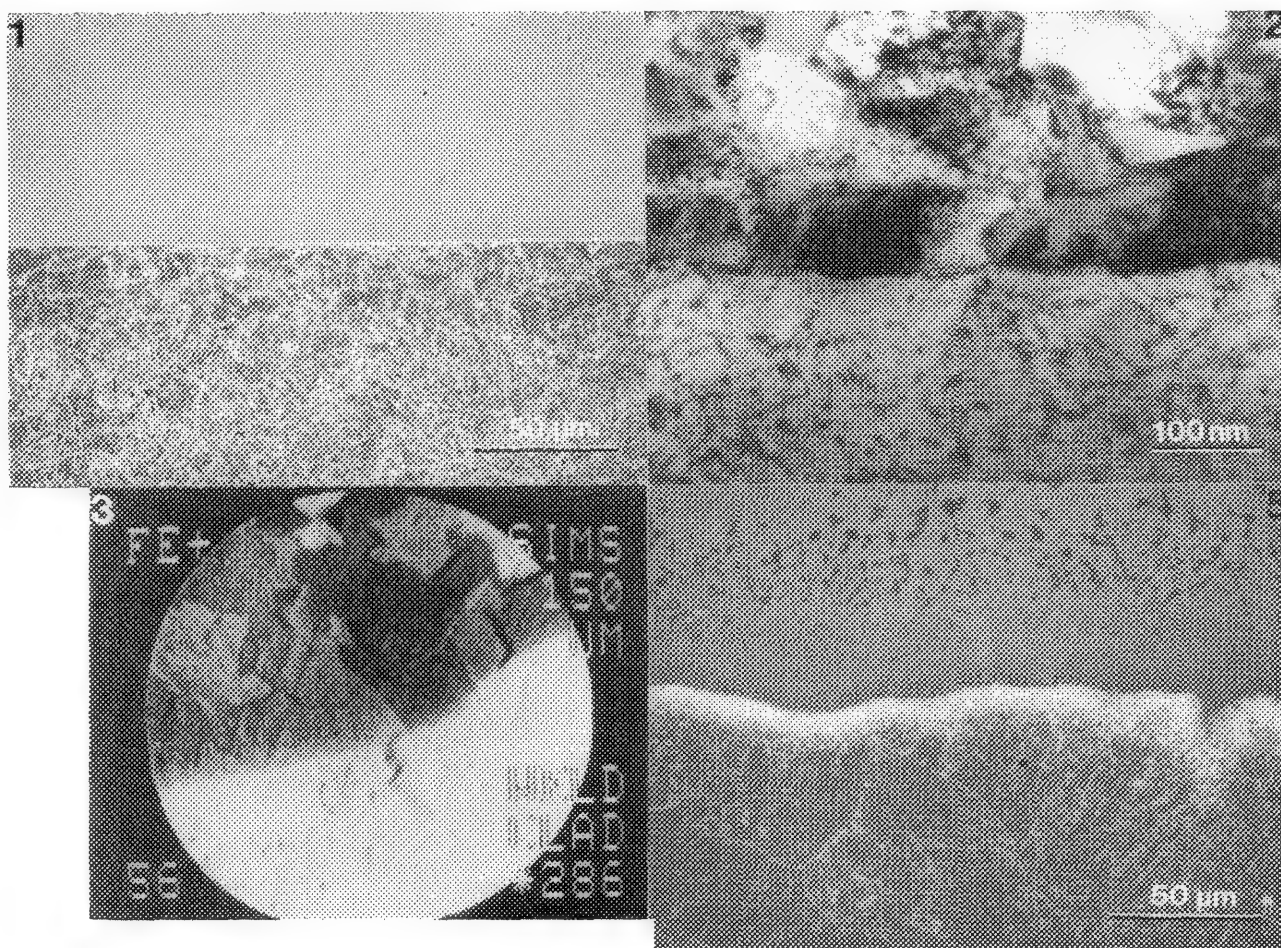


FIG. 1.--SEM image of weld interface.

FIG. 2.--TEM image of untempered martensite and carbides in weld-clad specimen.

FIG. 3.--Fe⁺ SIMS image of weld-clad interface.

FIG. 5.--SEM image of HIP-clad interface.

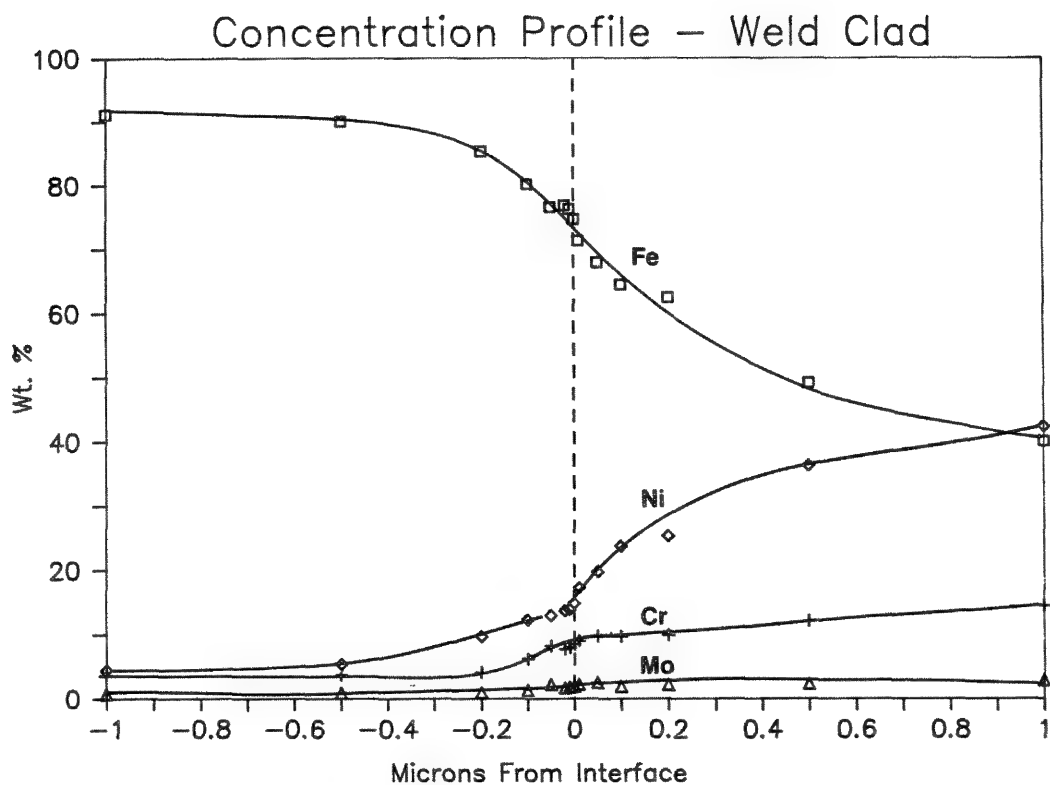


FIG. 4.--Concentration profiles across weld-clad interface.

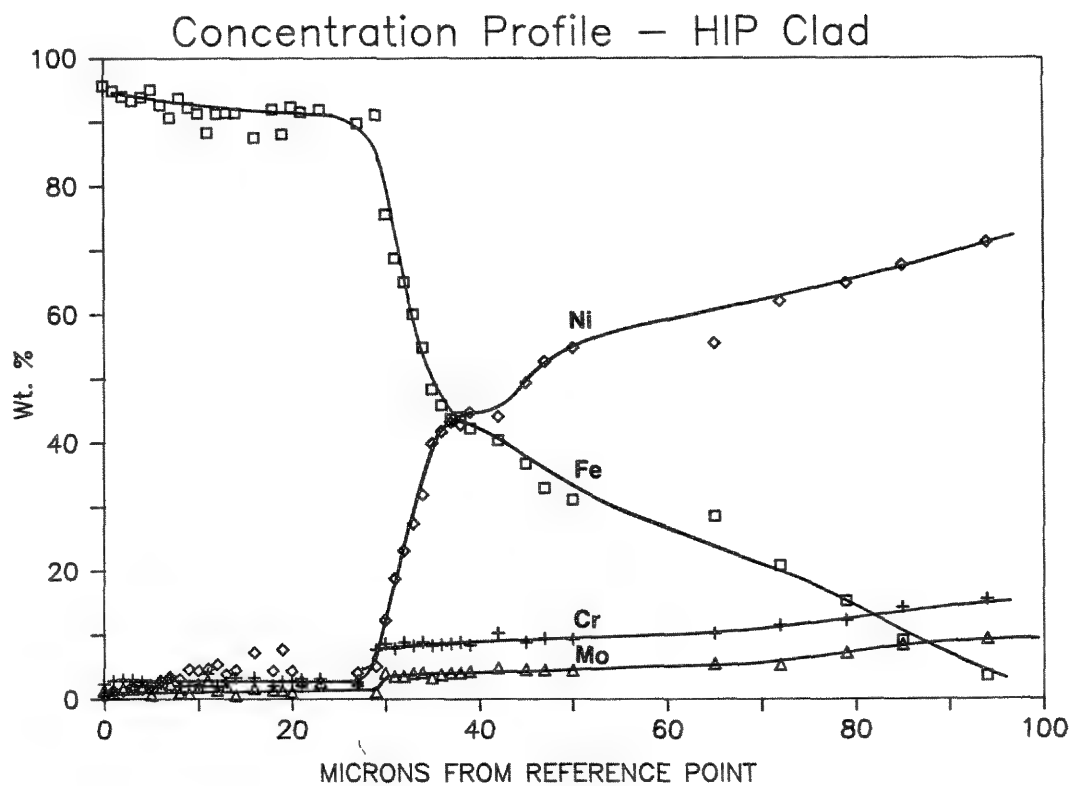


FIG. 6.--Concentration profile across HIP-clad interface.

TABLE 1.--Processing parameters for the clad materials.

<u>Step</u>	<u>Weld Clad</u>	<u>HIP Clad</u>
1.	Normalization 1650°F/4hrs	Cladding 2050°F; 15 ksi
2.	Austenitization 1575°F/4hrs/WQ	Normalization 1650°F/3hrs/AC
3.	Tempering 1120/15hrs	--
4.	Cladding	Austenitization 1600°F/3hrs/WQ
5.	Stress Relieving	Temper#1, #2 1225°F/6hrs/WQ

Figure 1 shows a set of SEM micrographs from interface regions of the weld and HIP clad specimens. TEM studies of the weld clad interface showed the presence of untempered martensite and $M_{23}C_6$ carbides (Fig. 2). Figure 3, a SIMS Ni^+ image of the interface, shows a sharp change at the interface that indicates absence of lack of extensive interdiffusion. Compositional profile across the interface by x-ray microanalysis is shown in Fig. 4.

The microstructure of the HIP-clad specimens contained regions of varying precipitate density at the interface regions (Fig. 5). The microstructure consisted of a high density of precipitates in the ferrite, followed by a zone essentially void of precipitates in the austenite, and a zone containing high density of coarse carbides. The precipitates in the ferrite were identified as $M_{23}C_6$ carbides; the carbides in the austenite consisted of a mixture of $M_{23}C_6$ carbides and M_6C carbides. To determine the origin of the precipitates, samples were heat treated to reproduce the microstructure of the individual steps. It was shown that the carbides in the austenite formed during the HIPing step, and the carbides in the ferrite formed during the tempering step. Concentration profiles determined across the interface of the heat treated specimens (Fig. 6) showed that the concentration change occurred over a larger distance (50 μm) compared to the weld-clad specimen.

Conclusion

The interface microstructures of the clad specimens observed in the present study have a significant effect both on their mechanical properties and resistance to hydrogen embrittlement. Also, based on the microstructural analysis conducted in the present study, a model for the development of the microstructure at the interface region is presented.

STABILITY OF SECOND-PHASE DISPERSOIDS IN AUSTENITIC STAINLESS STEELS

C. F. Klein and Raghavan Ayer

Austenitic stainless steels find extensive service under moderate temperatures (900-1300 F) in the petrochemical industry. It is well known that these steels are prone to the formation of chromium carbides at grain boundaries during service, which impairs their resistance to stress corrosion cracking. This phenomenon is generally accentuated in the heat-affected zone (HAZ) associated with weldments. Traditionally, formation of chromium carbides is minimized by stabilization of the steel with the addition of strong carbide-forming elements, such as titanium, niobium, etc. More recently, stabilization of the steel by the addition of nitrogen has also been demonstrated.¹

The current research was directed toward examination of the microstructural changes, both in the bulk and in the HAZ, of three steels during simulated exposure to service temperatures. The first was 347, which is stabilized with niobium. The second was alloy 374AP, which is a modified form of alloy 347 with the intentional addition of nitrogen, and the third alloy was an experimental alloy composed of 304 stainless steel stabilized with hafnium. Table 1 lists the nominal compositions of these alloys.

Experimental Procedure

Bulk samples of the three alloys were exposed at 1100 F for 8400 h. The microstructure of the HAZ was simulated by a thermal treatment. The procedure consisted of rapidly heating the sample to 1300 C and air cooling to room temperature; the entire cycle lasted 7 min.² These cycled samples were then aged at 1200 F for 1000 h to induce precipitation. Specimens for scanning and transmission electron microscopy were prepared from the heat treated samples.

Results

The microstructural analysis of the three alloys in the as-received condition showed that alloy 347 contained niobium carbides (NbC) uniformly distributed in the microstructure, alloy 374AP contained finely dispersed chromium niobium nitrides (CrNbN), and the experimental alloy contained uniform precipitation of hafnium carbides (HfC). The CrNbN precipitates found in alloy 374AP were similar to those reported by Jack and Jack;³ however, diffuse intensities were found indicating ordering, presumably of vacancies.⁴ The grain size of all the alloys varied in the range of 50-100 μm

(Fig. 1).

The microstructural studies of the bulk of the steels exposed for 8400 h at 1100 F showed that the steels modified with hafnium and nitrogen formed no chromium carbides, whereas the niobium-modified alloy showed moderate levels of precipitation. After the weld-simulation treatment, the grain sizes of alloy 347 and the hafnium containing alloy were unchanged but the grains in alloy 374AP had grown in excess of 1 mm (Fig. 2). The propensity for the growth of grains can be related to the stability of the second-phase particles at temperatures attained during welding. When the specimens subjected to weld simulation were subsequently aged at 1200 F for 1000 h, it was observed that alloys 347 and 374AP formed precipitates both at the grain boundaries and in the grain interior while the experimental alloy stabilized with hafnium remained unchanged. The electron microscopy analysis of the decomposition reaction in these alloys is available.

References

1. S. Abe and T. Ogawa, *Metals Progress*, September 1979, 61.
2. J. Y. Koo, unpublished research, Exxon Research and Engineering Co., 1987.
3. Jack and Jack, *J.I.S.I.* 210: 790-792, 1972.
4. Raghavan Ayer, C. F. Klein, and J. W. Steed, unpublished research, 1987.

The authors are with the Corporate Research Science Laboratory, Exxon Research Engineering Co., Annandale, NJ 08801.

ELECTRON MICROPROBE ANALYSIS OF $\text{YBa}_2\text{Cu}_3\text{O}_{6+x}$ HIGH-TEMPERATURE SUPERCONDUCTORS

Eric Lifshin, L. A. Peluso, and R. H. Arendt

The recent discovery of superconductors with critical temperatures in excess of 90 K has resulted in some of the most extensive characterization studies ever done of any materials. The universal hope is that a detailed understanding of microstructure, crystal and electronic structures, and composition will lead to practical materials with higher transport currents and possibly higher transition temperatures. Principal methods used include x-ray and neutron diffraction, transmission electron microscopy, and photoelectron spectroscopy, although many other techniques are also being tried (see Refs. 2-5 for examples). It is therefore surprising that the electron microprobe is rarely mentioned, since elemental analysis on a micron scale is essential to unraveling the complex multiphase mixtures produced by the wide variety of processing schemes used at present. This paper describes a series of electron microprobe measurements made on samples of orthorhombic $\text{YBa}_2\text{Cu}_3\text{O}_{6+x}$ determined to be both homogeneous and of high phase purity.

Experimental

Powder samples of orthorhombic $\text{YBa}_2\text{Cu}_3\text{O}_{6+x}$ were prepared from reagent grade BaCO_3 (J. T. Baker), Y_2O_3 (Research Chemicals, 99.9%), and CuO (EM Sciences, analyzed by H_2 reduction as 99.9% CuO). The reactants were wet-milled 1 h in a polyethylene jar with dense zirconia media, with a dilute aqueous solution of Triton X-100 used as the fluid. The milled material was oven-dried overnight at 120 C. The dry reactants were placed in a shallow alumina boat as a powder bed less than 1 cm deep. The materials was heated in air at 100 C/h to 950 C, maintained at this temperature for 24 h, then cooled at 150 C/h to room temperature. The reaction product was gently ground in a porcelain mortar, then dry-milled in a polyethylene jar with dense zirconia media for 25 h. X-ray diffraction analysis of the powder showed it to be nearly phase pure, containing only a trace of BaCuO_2 .

We prepared bar specimens by pressing 2.00g portions of the powder in a 0.25×0.75 in. die at 30 kpsi, then isostatically pressing the bars at 60 kpsi, to obtain final bar thick-

nesses of approximately 0.25 in. The pressed bodies were placed on a dense alumina card lightly dusted with the powder to facilitate separation of the sintered bars. The assembly was heated at 100 C/h to 950 C, maintained at this temperature for 10 h, then cooled at 20 C/h to <100 C, all in a flowing, over-pressured oxygen atmosphere. We minimized contact of the bars with the room atmosphere by keeping them in a desiccator when not in use. Previous x-ray powder diffraction of similarly prepared samples has shown them to be orthorhombic phase, which exhibits superconducting behavior.

Samples for metallography and electron microprobe examination were prepared both by water and kerosene polishing, to determine whether the more conventional practice of water polishing would alter the results, since significant reactivity of $\text{YBa}_2\text{Cu}_3\text{O}_{6+x}$ with water has been described.⁶⁻⁷ All samples were mounted in epoxy; the polishing sequence included hand grinding with silicon carbide papers (180, 400, 600, 8 μm , 3 μm), followed by automatic polishing (Jarrett) with diamond on cloth (9 μm , 3 μm , 1 μm and 1/2 μm). Samples designated HP are those for which water was used as the lubricant for all the steps listed; for those designated KP, only kerosene was used. Final cleaning for HP samples was an aqueous Alconox rinse; KP samples were cleaned in high-purity hexane.

Bulk chemical analysis for Y, Ba, and Cu was done with inductively coupled plasma spectrometry (ICP). To minimize the effects of water adsorption, the following procedure was found to be most effective: the samples were first oven dried at 110 C, then ground with an alumina mortar and pestle under dry nitrogen in a glove box. Individual samples of approximately 100 mg were dissolved in hot hydrochloric acid and sufficient de-ionized water was added to bring the sample volumes to 500 ml. The samples were then analyzed in an Instrumentation Laboratories Plasma 200 ICP. Diluted 1000 ppm Y, Ba, and Cu standards obtained from Spex Industries were used for calibration.

Oxygen analysis was performed by observation of the mass loss that occurs as a result of hydrogen reduction. Measurements were made with a Du Pont 9900 thermal analyzer. Approximately 100mg samples were heated in a hydrogen atmosphere at 10 C/min to a temperature of about 970 C. At this temperature, all the Cu is present as elemental copper, whereas Y and Ba remain fully oxidized. Since the mass fractions of Y and Ba are known, the amount of oxygen associated with each can be calculated and added to the oxygen associated with the

The authors are with GE Corporate R&D, Schenectady, NY 12301. They wish to acknowledge the ICP work of W. E. Balz and E. M. Skelly, the materials preparation effort of M. J. Curran, the metallography of A. Barbuto, the Auger microscopy of M. D. McConnell, the x-ray diffraction of M. F. Garbaskas, and the helpful discussions of R. B. Bolon.

copper determined by reduction. The total mass of oxygen can then be used to calculate the oxygen stoichiometry.

Electron microprobe analysis was done with a Cameca MBX equipped with a Tracor Northern automation package run under the TASK program. The crystals selected were TAP for Y L α , PET for Ba L α , and LiF for Cu K α . The standards used were Y₂O₃, NBS glass standard K458 for Ba, and Cu metal. Most of the work described was done at 15 kV and a beam current of 56 nA measured on the copper standard. Measurements were made at normal incidence and at a take-off angle of 40°. All data were corrected for background by the use of average values obtained at $\pm 0.005 \sin \theta$ units. The typical counting time on the sample and standards was 100 s for point counts and 50 s for step scan, which insured that at least 800 000 counts were obtained on the standards and 300 000 counts for the 100s readings on the samples. Although both samples and standards were then given thin carbon coatings, it was determined that the YBa₂Cu₃O_{6+x} is a sufficiently good conductor so that no coating was necessary, and that no differences in counts were noted between coated and uncoated samples. Three basic sets of measurements were taken:

1. Large numbers of individual grains were sampled to look for grain-to-grain variations.
2. Several grains were compared between water- and kerosene-polished samples mounted in the instrument at the same time.
3. Step scans were made across individual grains to look for any variation in composition from the exterior to the interior of the grains.

Relative intensity ratios (K ratios) were determined for all data points and these values were compared to calculated K ratios obtained from a conventional ZAF calculation. The actual calculation was done with the CITZAFOD and CITZAFID programs made available by John Armstrong.⁸ The corrections used are the Philibert absorption correction, the Duncumb/Reed atomic number correction, and the Reed fluorescence correction.

Checks of sample homogeneity with depth were measured with a PHI600 scanning Auger microscope operated at 5 kV. An argon ion gun was used for in situ cleaning and depth profiling. With 4kV ions, a sputter rate of approximately 200 Å/min is possible and the composition of several grains was determined to a depth of about 1.0 μm .

Results

Oxygen analysis by TGA and the ICP data made it possible to determine that the samples prepared by the above method are YBa₂Cu₃O_{6.7}. Table 1 shows a comparison between calculated mass fractions of the elemental constituents and the ICP results. These results provide additional evidence that the cation ratios are very close to the frequently quoted 1:2:3. The oxygen concentration is also consistent with independent determinations done on single

TABLE 1.--Bulk elemental analysis.

Element	Calculated weight fraction	ICP Results	Calculated weight fraction
	YBa ₂ Cu ₃ O _{6.7} (Orthorhombic)		YBa ₂ Cu ₃ O ₆ (tetragonal)
Y	0.134	0.134 \pm 0.004	0.136
Ba	0.415	0.419 \pm 0.010	0.422
Cu	0.288	0.288 \pm 0.007	0.293
O	0.162	0.162*	

*Determined by TGA.

crystals of similarly prepared materials, whose complete structures have been determined by x-ray diffraction.² Included for further comparison are the calculated weight fractions of the elemental constituents of the tetragonal phase YBa₂Cu₃O₆, which is known to be nonsuperconducting.

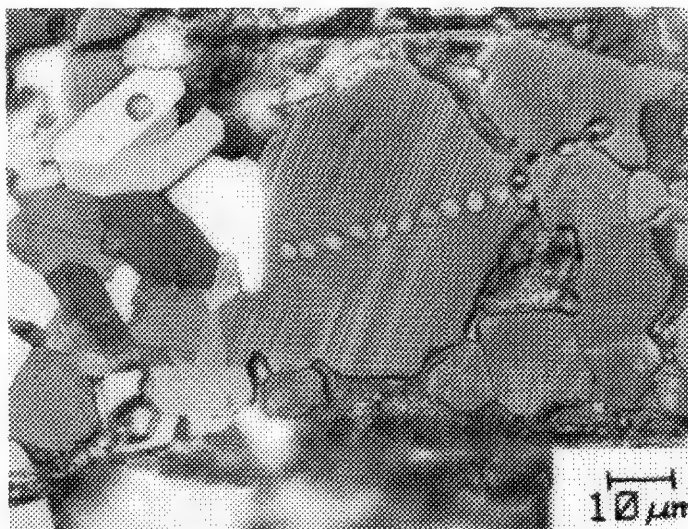


FIG. 1.--Polarized light micrograph of water polished sample of YBa₂Cu₃O_{6+x}.

Figure 1 shows a representative microstructure of one of the KP samples viewed in polarized light, which accentuates the abundant twins observed in the orthorhombic phase. Typical grain sizes are of the order of 10 μm . Larger grains of the type shown are also present, and were used for the step scans (note the presence of the contamination spots). The materials do not achieve 100% density, as indicated by the presence of pores, and grain pull-out has also occurred. Regions for analysis were therefore carefully selected to avoid peculiar geometric effects. The structures observed in both the HP and KP samples were basically the same, although some enhanced grain boundary delineation was observed in the HP samples, presumably due to an etching effect.

Table 2 contains a set of measured K values obtained at both 15 and 20 kV from 10 different points measured at each voltage. The low

TABLE 2.--Measured K ratios from 20 grains compared to ZAF calculations.

Point	15KV			20KV		
	Y L	Cu K	Ba L	Y L	Cu K	Ba L
1	0.0955	0.286	0.365	0.0848	0.282	0.370
2	0.0948	0.288	0.356	0.0848	0.282	0.365
3	0.0974	0.291	0.365	0.0856	0.283	0.368
4	0.0967	0.291	0.365	0.0861	0.283	0.368
5	0.0969	0.292	0.363	0.0848	0.283	0.373
6	0.0935	0.290	0.362	0.0856	0.283	0.368
7	0.0936	0.285	0.363	0.0862	0.283	0.370
8	0.0950	0.289	0.359	0.0874	0.284	0.368
9	0.0956	0.286	0.365	0.0878	0.285	0.367
10	0.0954	0.287	0.364	0.0871	0.285	0.369
Average K_m	0.0954	0.288	0.363	0.0860	0.283	0.368
Standard Deviation	0.00130	0.00246	0.00302	0.00111	0.00106	0.00212
ZAF K_z/K_m	0.0964	0.292	0.366	0.0864	0.282	0.378
$(K_m - K_z)/K_m$	-0.00963	-0.0110	-0.00909	-0.00441	0.00290	-0.0264

standard deviations for each of the elements indicates very little, if any, grain-to-grain variation in composition. Excellent agreement with the ZAF-calculated K values suggests that this method will work well in the analysis of these materials. Table 3 contains two sets of data taken at 15 kV on two different days. The comparison of HP and KP data taken from two points on each sample, as well as other measurements, shows that the specimen preparation lubricant does not appear to alter the results. In addition, results from a typical step scan across one of the KP samples shows no significant variation across individual grains. Average values of all the data in Table 2, and their comparison to ZAF calculated data, are also given to illustrate the excellent day-to-day agreement between the data sets. The magnitude of individual ZAF correction factors is given in Table 4, where it can be seen that the largest correction is for Y L α absorption, followed by a significant atomic number correction for Ba L α . Very little correction of the Cu K α data is needed to convert K ratios to concentrations.

The Auger findings indicated that no detectable changes in composition with depth occurred, although it was established that samples left in the air, even for a brief period of time, would develop a thin surface layer, possibly due to water adsorption, that disappears if the sample is allowed to sit in the vacuum system for a few hours.

Conclusions

The present study has shown that we can perform accurate electron microprobe analysis on the superconducting material YBa₂Cu₃O_{6+x} using conventional ZAF procedures. Results support expected cation ratios of 1:2:3 with reasonably high accuracy. The problem of distinguishing orthorhombic from ideal tetragonal material is currently under investigation; however, as seen from Table 1, measurement of

TABLE 3.--Effects of polishing and step scan data K ratios (at 15 kV).

Point	Y L α	Cu K α	Ba L α
KP 1	0.0975	0.29	0.368
HP 1	0.0971	0.286	0.366
KP 2	0.0974	0.289	0.370
HP 2	0.097	0.288	0.369
1	0.0976	0.286	0.368
2	0.0972	0.282	0.369
3	0.099	0.281	0.370
4	0.097	0.288	0.367
5	0.0965	0.286	0.368
6	0.0965	0.286	0.366
Average	0.09634	0.286	0.368
Standard Deviation	0.00227	0.00272	0.00131
ZAF	0.09636	0.292	0.366
$(K_m - K_z)/K_m$	-0.00020	-0.0191	0.00500

differences in cation weight fraction between the phases is only marginally amenable to electron microprobe analysis at best. The element with the largest difference (about 9.4%) between the two phases is oxygen, which is also currently being investigated. The variations between YBa₂Cu₃O₆ and YBa₂Cu₃O_{6.7} might be detectable, but more subtle spatial variations in oxygen composition present a significant challenge. It is also recognized that the oxygen concentration alone does not determine whether a sample is orthorhombic or tetragonal, since the tetragonal phase has been observed with $x > 0.7$ and the orthorhombic phase $x < 0.5$.⁹

References

1. K. A. Muller and J. G. Bednorz, *Science* 237: 1133-1139, 19
2. M. F. Garbauskas, R. H. Arendt, and J. S. Kasper, *Inorganic Chem.* 26: 3191-3193, 1987.

TABLE 4.--ZAF correction factors.

Element	Concentration weight fraction	Operating voltage (kV)	Relative intensity K_z	Atomic number Z	Absorption A	Fluorescence F
Y	0.1344	15	0.0964	1.047	1.342	0.993
		20	0.0864	1.040	1.510	0.990
Ba	0.4153	15	0.366	1.161	1.000	0.976
		20	0.378	1.137	1.001	0.964
Cu	0.2882	15	0.292	0.985	1.024	1.000
		20	0.282	0.973	1.049	1.000

3. H. You, R. K. McMullan, J. D. Axe, D. E. Cox, J. Z. Liu, G. W. Crabtree, and D. J. Lam, *Sol. State Comm.* 94: 739-742, 1987.

4. J. Tafto, M. Suenage, and R. L. Sabatini, *Appl. Phys. Lett.* 52: 667-668, 1988.

5. Z. Iqbal, E. Leone, R. Chin, A. J. Signorelli, A. Bose, and H. Eckhardt, *J. Mat. Res.* 2: 768-774, 19

6. M. F. Yan, R. L. Barns, H. M. O'Bryan Jr., P. K. Gallagher, R. C. Sherwood, and S. Jin, *Appl. Phys. Lett.* 51: 532-534, 1987.

7. N. P. Bansal and A. L. Sandkuhl, *Appl. Phys. Lett.* 52: 323-325, 1988.

8. J. T. Armstrong, Division of Geological and Planetary Science, California Institute of Technology, Pasadena, CA 91125.

9. M. F. Garbaskas (private communications).

IDENTIFICATION OF PARTICULATE DEFECTS IN CAST PRODUCTS BY ASEM

L. D. Fitch and W. E. Votava

We present an improved method for analyzing casting defects by analytical scanning electron microscopy (ASEM), with the use of a backscatter electron detector and energy-dispersive x-ray system, available on most AMESSs. Currently the raw materials are introduced to the casting process before analysis. To compare the spectra for analysis, we use a computer matching program (X-Match), a general spectrum-matching program that compares an unknown spectrum with a series of (standard) spectra stored on disk by means of a χ^2 best fit. The results of the X-Match program show that the new method of analyzing defects is an improvement over the earlier work.

We discuss the continued work on the defect-analysis method described previously,¹ in which unreacted raw material standards were matched to defects found in gray iron piston bodies; we showed that the raw materials may be made up of more than one phase and that one or more of the phases may dissolve during the casting process leaving the other phases behind in the defect. Which raw material generated the defect was unknown if this phase did not show up in one of the unreacted standards.

The current research addresses the problem of such compositional changes. Better results would be obtained even if the materials did not change composition, because the material causing a defect undergoes the temperatures involved during the casting process and now the raw material standards would also.

Experimental

The standards used to show the compositional changes were cast as slugs 3 in. in diameter and 1 in. thick in a mold (Fig. 1). Approximately 1 cm³ of a different raw material was placed in each of the four runners and swept into the four mold cavities by the molten metal during pouring. In this way four different samples could be prepared at once. The standards were then cut and polished metallographically and sputtered with 200 Å of Au-Pd to provide conduction in the areas where the reacted raw material was present. A scanning electron microscope (SEM), equipped with a detector for the observation of atomic number contrast (BSE), along with an energy-dispersive x-ray system (EDS), was used to collect standard spectra. The new reacted raw-material standard spectra were stored on floppy disk with the unreacted raw-material standard spectra, so that computer matching programs could be run.

The authors are with the New York State College of Ceramics at Alfred University, Alfred, NY 14802. The research was funded by a contract from NYSERDA, Agreement 966-EEEd-AEP-87.

Analysis of Defects

The first foundry problem (FDP35) is a casting defect from a gray iron piston body (Fig. 2). A sample of the body was cut and polished metallographically and sputtered with 200 Å of Au-Pd. An examination of the defect indicated the presence of clay. Since the casting may come into contact with clay in many areas of production, it was impossible to pinpoint the cause of the defect definitely, but it was suspected that the clay used to seal the molds (Cedar Heights Clay) was the cause. To prove it, alumina was added to the Cedar Heights Clay to act as a tracer, and a reacted raw material standard of Cedar Heights Clay and alumina was prepared and characterized.

When subsequent samples of the defect arrived they were analyzed and found to contain distinctive agglomerates of alumina. The conclusion was that Cedar Heights Clay was the cause of the defect. When the matching pro-

TABLE 1.--X-Match program listing of best matches to spectrum FDP35A from foundry problem FDP35.

MATCH TO SPT FDP35A			
1.	S861	AL ADDED B4-A	2.9
2.	S551	AL ADDED TO CLAY	21.7
3.	S852	DEFECT AREA B3-A	33.1
4.	S472	MINRO FIRE MATRIX	40.0
5.	S860	CLAY W/AL B4-A	50.8
6.	S701	GEN AREA A1-B	55.9
7.	S704	LARGER BRIGHT AREAS A1B	57.6
8.	S700	GEN AREA A1-A	60.4
9.	S602	LARGE CA PHASE WITH FE A4B	64.5
10.	S703	VERY DARK, SIMILAR SIZE 700	64.6
11.	S850	B3B-S GRAIN	64.9
12.	S862	B4B BRIGHT PHASE T1	67.7
13.	S800	GEN AREA INDUCALLOY A2A	68.0
14.	S604	DARK S PHASE A4C	68.5
15.	S130	INDUCALOY SI-CA GRAIN	69.0
16.	S600	GENERAL DEFECT AREA A4A	69.3
17.	S132	INDUCALOY SINGLE PHASE SI	69.4
18.	S851	B3A MEDIUM DEFECT AREA	69.7
19.	S831	B1A DARK GENERAL AREA	70.7
20.	S820	GENERAL AREA A3A	73.2
21.	S601	MEDIUM PHASE A4B	73.6
22.	S131	INDUCALOY SI-FE GRAIN	73.7
23.	S603	GENERAL AREA A4A	74.2
24.	S830	B1A MED PHASE IN DEFECT AREA	75.0
25.	S160	CALOY (2)	75.2
26.	S702	GENERAL DEFECT AREA-A1A	76.5
27.	S803	BRIGHT AREAS IN SI GRAIN A2C	77.7
28.	S801	SM DK ON SM BR DK DEFECT A2A	83.3
29.	S821	BRIGHT AREA A3A	88.6
30.	S802	LIGHT DEFECTS A2A	95.3

TABLE 2.--X-Match program listing of best matches to spectrum FDP34C from foundry problem FDP34.

MATCH TO SPT FDP34C		
1.	S562	MINRO AL MATRIX 3.0
2.	S482	MINRO AL MATRIX 3.6
3.	S560	MINRO AL GENERAL AREA 7.4
4.	S480	MINRO AL UPPER CASE THROAT 7.5
5.	S291	ELECTRIC FURNACE PATCH LIGHT 7.9
6.	S503	SLAG LINE AL GRAIN 10.9
7.	S481	LG BLOCKY GRAINS - AL 11.9
8.	S561	MEDIUM DARK PHASE, AL 13.6
9.	S290	ELECTRIC FURNACE PATCH 14.1
10.	S471	MINRO FIRE SM GRAIN IN MATRIX 14.2
11.	S483	MINRO AL BRIGHT IN MATRIX 19.7
12.	S471	MINRO FIRE MATRIX 24.7
13.	S486	MINRO AL SEMI-BRIGHT PHASE 26.9
14.	S500	SLAG LINE RAM GENERAL AREA 31.7
15.	S505	SLAG LINE MATRIX 33.0
16.	S473	MINRO FIRE LG BLOCKY GRAINS 39.4
17.	S484	SM BRIGHT PHASE IN MATRIX 39.5
18.	S493	MINRO MAG LG BLOCKY GRAIN 41.2
19.	S470	MINRO FIRE GENERAL AREA 43.1
20.	S292	ELECTRIC FURNACE PATCH DARK 45.0
21.	S506	SLAG LINE SM BRIGHT PHASE IN AL 47.1
22.	S490	MINRO MAG INDUCTOR, MATRIX 47.7
23.	S485	BRIGHT PHASE IN SM AL GRAIN 50.8
24.	S492	MINRO MAG BRIGHT PHASE SI-ZR 50.9
25.	S564	BRIGHT PHASE, T1 51.1
26.	S491	MINRO MAG MG-SI-CA IN MATRIX 52.5
27.	S501	SLAG LINE LIGHTER PHASE IN AL 55.5
28.	S474	MINRO FIRE BRIGHT PHASE SI-ZR 56.9
29.	S502	SLAG LINE BRIGHT PHASE IN AL 57.0
30.	S504	SLAG LINE BRIGHT PHASE#2 IN AL 57.9

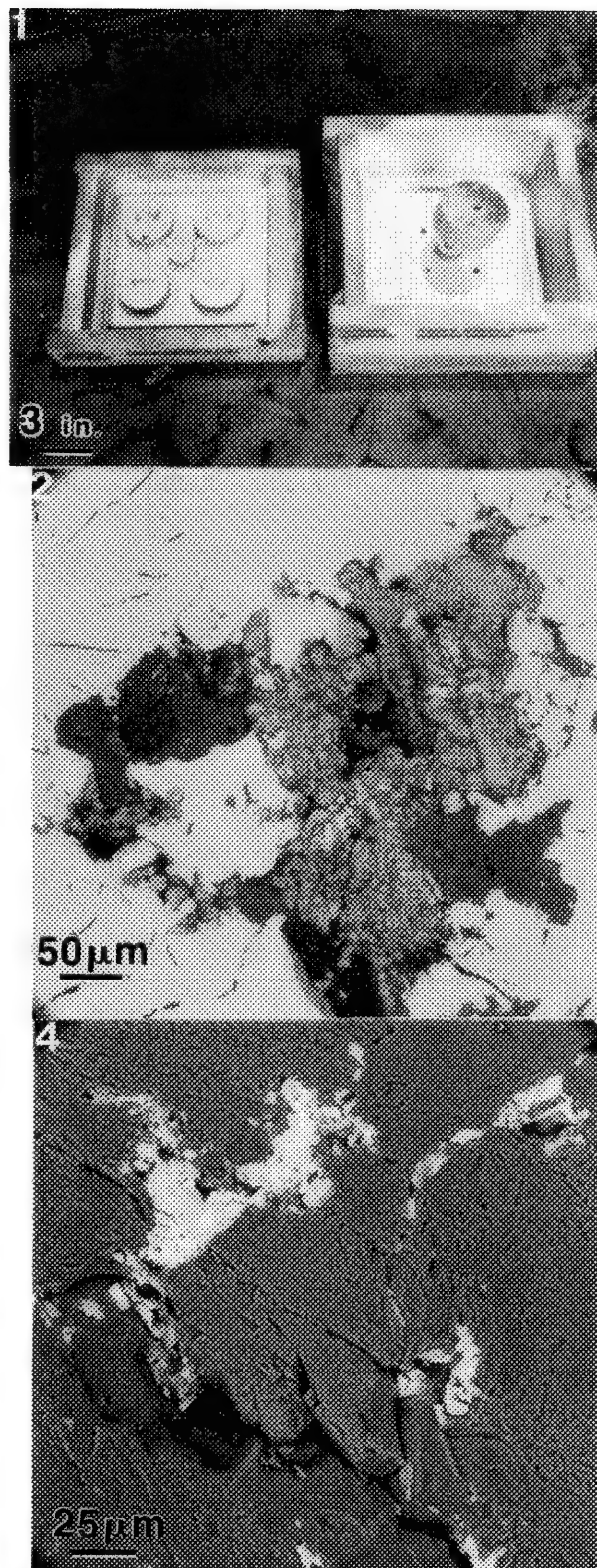


FIG. 1.--Master mold used to manufacture 3-in. test slugs of reacted raw materials. (Mold is pictured before being packed with sand.)
 FIG. 2.--Defect area (multiphase area in center) of gray iron piston body (FDP35) at 200× (BSE).
 FIG. 4.--Material clogging inductor showing Al matrix (dark gray) and Ti inclusions (bright) at 400× (BSE).

gram was run (Table 1) the reacted standard spectra of Cedar Heights Clay gave a match of 2.9 (Fig. 3), which is considered very good.

The second foundry problem (FDP34) is the clogging of a furnace inductor (Fig. 4). A sample of the material clogging the inductor was polished metallographically and sputtered with 200 Å of Au-Pd. EDS examination of the

material showed that it was mainly Al with inclusions of Ti (small bright areas). Standards were made from all the refractory materials lining the induction furnace and the computer-matching program was then used to compare the defect spectra with these unreacted raw-material spectra.

Two spectra from the problem (FDP34) were

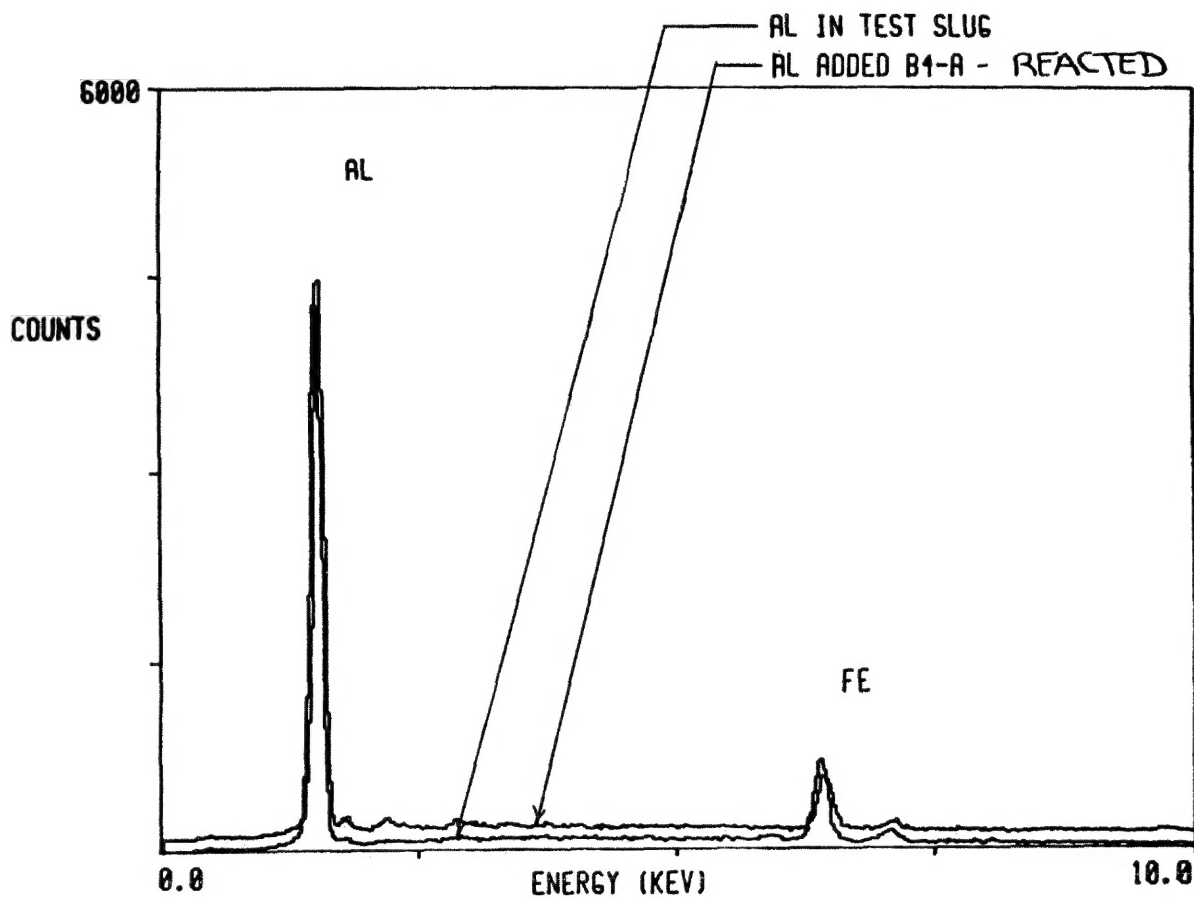


FIG. 3.--Plot of best match from Table 1.

compared by use of the matching program. The first area matched (FDP34C) showed that the four best matches were from Minro Al (Table 2 and Fig. 5). The other spectra matched (FDP34E) from the problem also showed Minro Al (the bright Ti inclusions) as the best match. We concluded that the material clogging the inductor was Minro Al, a cement material that is rammed into the spaces between the refractory brick.

The second spectrum matched was then put through the matching program again, but this time with the reacted raw material of Minro Al included in the list of standard spectra. The results of the matching program showed that the reacted raw material spectrum had a better match (12.2) than the unreacted raw-material spectrum (15.6).

Conclusions

A method for the analysis of particulate defects in cast iron has been presented. The analysis of particulate defects in a timely manner is of utmost importance to the foundry. The method described makes use primarily of the backscattered electron signal and the EDS signal, combined with the spectrum-matching program to eliminate all but a few sources of contamination. It has been shown that the standards generated by the introduction of raw

materials subject to compositional change with the metal provide a much more accurate match to defects caused by those raw materials. The standards developed are easy to produce and characterize, and the programs used for the matching are generally available on most EDS systems. Even the smallest foundry should be able to set up a cost-effective analysis program with local service organizations or universities equipped with instrumentation similar to that used for this project.

References

1. W. E. Votava, "ASEM analysis of casting defects," *J. Metals* 39: 20-22, 1987.

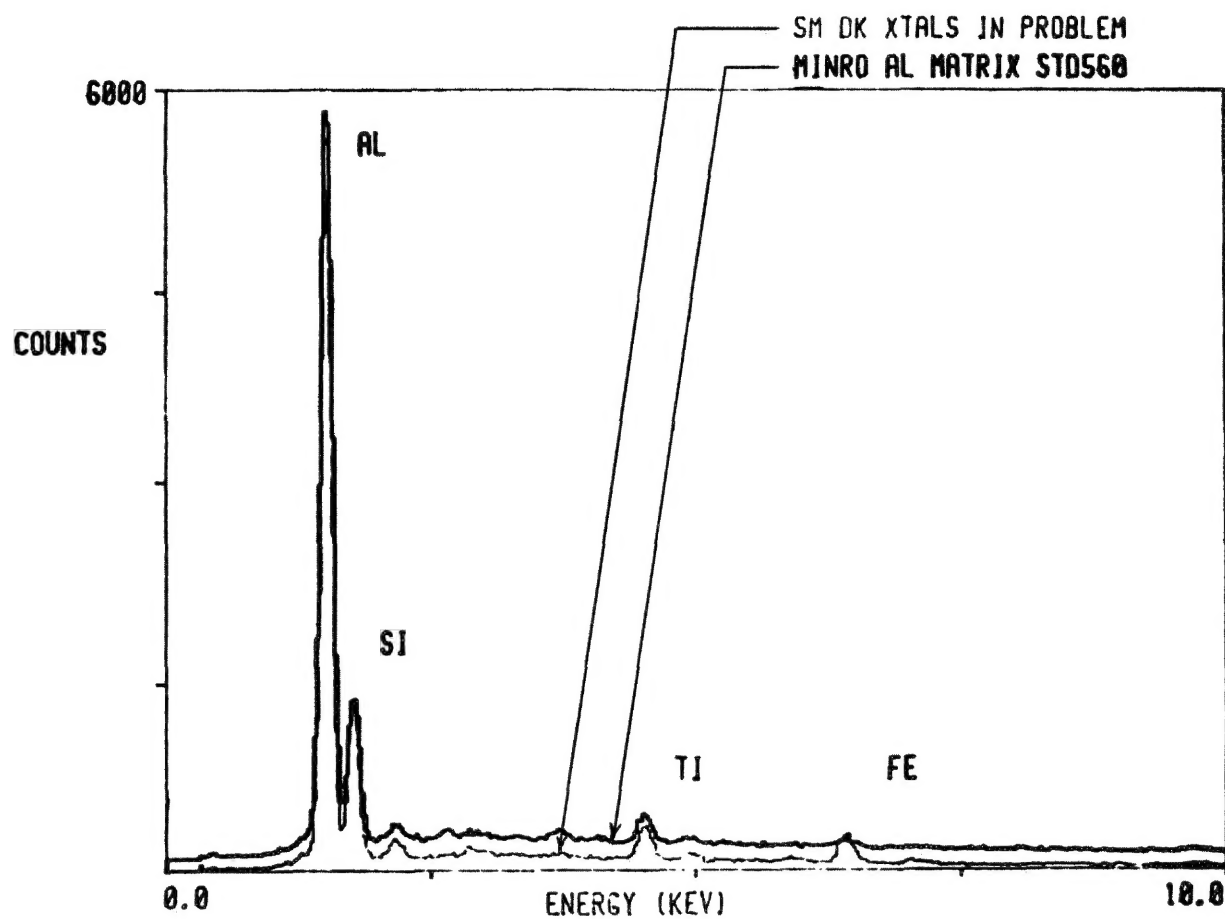


FIG. 5.--Plot of best match from Table 2.

AUTHOR INDEX

A

Ahn, C. C., 47
Aiginger, H., 403
Allard, L. F., 129
Apkarian, R. P., 459
Arendt, R. H., 519
Armstrong, J. R., 239, 301, 469
Atkin, S. E., 203
Ayer, R., 514, 517

B

Baker, M. T., 218
Barbillat, J., 153
Barshatzky, H., 417
Bastin, G. F., 290
Baughman, G. D., 44, 349
Beauchaine, J., 201
Bell, A. A., 263
Benjamin, T. M., 491
Bennett, J., 351
Betz, E., 164, 417
Bezdzicka, P., 182
Bilbrey, D. B., 403
Blake, D. F., 129
Blendell, J. E., 37, 187
Boehme, D. R., 389
Bonse, U., 405
Boutinaud, P., 167
Brenna, J. T., 377
Bright, D. S., 18, 25, 105
Brown, J. D., 271
Brown, P. E., 201
Burgi, D. S., 230
Burns, M. S., 445
Buskes, H. A., 44
Butler, I. S., 165
Butler, J. H., 69

C

Cantino, M. E., 427
Carl, R. T., 223
Carpenter, D. A., 391
Carr, M. J., 503
Chabala, J. M., 93, 445
Cheng, W., 305
Chi, P., 117, 121
Colonna, K. N., 440
Conron, R. J., 443
Corcoran, S. F., 111
Creasy, W. R., 377
Currie, L. A., 367

D

Daniel, W. M., 365
Dauskardt, R. H., 179
Davilla, S. D., 433
Davis, B. L., 203
Davis, G. E., 456
DeBlase, F. J., 236

DeNoyer, L. K., 421
Delhaye, M., 153
Delorenzo, D. J., 365
Dhamelin-court, P., 153
Disko, M. M., 47
Dodd, J. G., 421
Dovich, N. J., 230
Duffy, C. J., 491

E

Eades, J. A., 75
Echer, C. J., 129
Echlin, P., 1, 451
Etz, E. S., 187
Exarhos, G. A., 161

F

Fiori, C. E., 263
Fitch, L. D., 523
Fleming, R. F., 407
Fletcher, R. A., 367
Freund, F., 129
Friel, J. J., 41
Fritz, G. S., 33
Fukuda, H., 329

G

Gastin, G. F., 325
Gauvin, R., 57
Gavrilovic, J., 412
Gay, A. J., 123
Gijbels, R., 351
Gilson, D. F. R., 165
Glover, E. D., 333
Golijanin, D. M., 397
Graham, R. A., 503
Grenier, J. C., 182
Griffis, D. P., 111

H

Haas, M., 353
Habib, V., 164
Hallégot, P., 93, 445
Haney, G. W., 391
Harootunian, A., 164
Harrick, M. J., 236
Harrowfield, I. R., 267, 481
Harthcock, M. A., 203
Hawkey, L. A., 447
Hegemann, B. E., 193
Heijligers, H. J. M., 290, 325
Heikinheimo, E., 509
Heinrich, K. F. J., 263, 273
Heinz, R. E., 175
Henderson, D. K., 123
Henoc, J. R., 251
Hepburn, J. S., 511
Herlong, J. R., 433, 447

Hess, M. J., 161
Housden, J., 371
Hsu, S. M., 193
Humphrey, P., 123
Huong, P. V., 167, 182
Hutt, K. W., 371, 374

I

Ichinokawa, T., 409
Ikeda, T., 159
Inagawa, H., 329
Inal, O. T., 498
Ingram, P., 433, 447
Inoue, K., 120
Isaacson, M., 164, 417
Ishatani, A., 221
Ishida, H., 169, 221
Ishitani, A., 169
Isogai, A., 120

J

Jahanmir, S., 193
Jercinovich, M. J., 495
Jeulin, D., 9
Jin, G.-X., 295, 300
Johnson, D. E., 427
Johnson, P. F., 41
Johnson, Q. C., 405
Joy, D. C., 143, 459
Juzwak, T. J., 41

K

Kamoto, R., 221
Karduck, P., 277, 285
Katagiri, G., 169
Katon, J. E., 207
Kawabe, K., 329, 341
Kawai, N. T., 165
Kazaoui, S., 167
Keil, K., 495
Kelland, D., 379
Kennedy, G., 57
Kessler, L. W., 419
Kiilsgaard, T. H., 483
Kinney, H. H., 405
Kitamura, S., 409
Kivilahti, J., 509
Klein, C. F., 517
Knowles, K. R., 483
Konopka, J. F., 338
Kracher, A., 491
Krivaneck, O. L., 47
Krumme, J. P., 307

L

Lábár, J. L., 253
Lauwers, W., 351
Lawson, R. L., 391
Leake, J. A., 371

AUTHOR INDEX

Lee, R. J., 295, 300, 305
 LeFurgey, A., 433, 447
 Leland, D. J., 403
 Lentz, H. P., 349
 L'Esperance, G., 57
 Leta, D. P., 514
 Levi-Setti, R., 93, 445
 Lewis, A., 164, 417
 Leycuras, A., 167
 Leyde, D. E., 403
 Lieberman, K., 164
 Lieberman, N., 433
 Lifshin, E., 519
 Lin, K., 417
 Lindner, B., 353
 Lindstrom, R. M., 407
 Linton, R. W., 111, 356
 Liu, D.-R., 55, 84, 87, 91
 Lord, G., 165, 247
 Lyman, C. E., 511

M

McKay, G. A., 477
 MacRae, C. M., 267, 481
 Mandel, L. J., 433, 447
 Marinenko, R. B., 18, 37
 Marshall, A. T., 443
 Masaki, T., 169
 Matsuya, M., 329
 Meitzner, G., 47
 Mershon, W. J., 349
 Messerschmidt, R. G., 215
 Metin, E., 498
 Michael, J. R., 60
 Mirabella, F. M., Jr., 233
 Moore, V., 258
 Morgan, K. Z., 391
 Mueller, R. R., 514
 Muenow, D. W., 171
 Murata, K., 133
 Musselman, I. H., 356
 Myklebust, R. L. 37, 139, 261,
 263, 273

N

Nagatsuka, Y., 345
 Newbury, D. E. 18, 37, 105, 139,
 261, 263, 273
 Nichols, M. C., 389, 405
 Niemeyer, I. C., 387
 Nihei, Y., 126
 Nusshardt, R., 405

O

Obertop, D., 307
 Odom, R. W., 102, 387
 Okahana, H., 159
 Okumura, T., 297
 Oliphant, G., 440
 Otsuki, M., 345
 Owari, M., 126

P

Packwood, R., 258
 Pahl, R., 405
 Pajunun, M., 509
 Pandya, N., 171
 Parker, C., 258
 Paroli, R. M., 165
 Pasteris, J. D., 196
 Peluso, L. A., 519
 Pichoir, F. M. A., 315
 Pinxter, J. F. M., 290
 Poirier, D. E., 391
 Pouchou, J. L., 315, 319
 Powers, W. H., Jr., 349
 Purcell, F. J., 175

R

Reffner, J. A., 215, 227
 Rehbach, W., 277, 285
 Roitman, P., 121, 456
 Romig, A. D., Jr., 498
 Rook, H. L., 407
 Rosenblatt, G. M., 179
 Rothwell, T. E., 149
 Russ, J. C., 14
 Russell, P. E., 149, 463

S

Saito, M., 341, 345
 Saito, N., 329
 Sakai, Y., 409
 Sarikaya, M., 81
 Saroyan, R. A., 405
 Satoh, H., 126
 Schamber, F. H., 33
 Schmidt, P. F., 383
 Scott, V. D., 247
 Sekiguchi, H., 329
 Semarge, R. E., 498
 Seydel, V., 353
 Shankernarayanan, M. J., 233

Sharma, S. K., 171
 Shelburne, J. D., 447
 Shoemaker, G. L., 480
 Simmonds, P. F., 481
 Simons, D. S., 117, 121, 356
 Sisak, W. J., 514
 Slodzian, G., 109
 Small, J. A., 263
 Solberg, T. N., 485
 Sommer, A. J., 207
 Sommer, J. R., 433
 Statham, P. J., 50, 429
 Steel, E. B., 466
 Stenger, H. E., 511
 Stephens, J. D., 480

T

Tagata, S., 341, 345
 Takagi, S., 341
 Taylor, M. A., 391
 Teller, R. G., 480
 Titchmarsh, J. M., 65
 Treacy, M. M. J., 69

V

van Duin, P. J., 123
 Van Vaeck, L., 351
 Veirs, D. K., 179
 Vertes, A., 351
 Von Endt, D. W., 218
 Votava, W. E., 523
 Vry, J. K., 201

W

Waldo, R. A., 310
 Wallach, E. R., 371, 374, 379
 Williams, D. B., 87, 91
 Williams, D., 114
 Willich, P., 307
 Wilson, H. R., 365
 Wittry, D. B., 394, 397
 Wobrauschek, P., 403
 Wong-Ng, W., 187
 Woodward, W. S., 111
 Wopenka, B., 196
 Wu, Z.-Q., 295, 300

X

Xu, L., 295, 300

Y

Yang, S. V., 477
 Yumoto, M., 159